Advances in Natural and Technological Hazards Research

Sebastian Krastel · Jan-Hinrich Behrmann
David Völker · Michael Stipp
Christian Berndt · Roger Urgeles
Jason Chaytor · Katrin Huhn
Michael Strasser · Carl Bonnevie Harbitz *Editors*

Submarine Mass Movements and Their Consequences

6th International Symposium

Springer

Submarine Mass Movements and Their Consequences

Advances in Natural and Technological Hazards Research

Volume 37

For further volumes:
http://www.springer.com/series/6362

Sebastian Krastel • Jan-Hinrich Behrmann
David Völker • Michael Stipp • Christian Berndt
Roger Urgeles • Jason Chaytor • Katrin Huhn
Michael Strasser • Carl Bonnevie Harbitz
Editors

Submarine Mass Movements and Their Consequences

6th International Symposium

Springer

Editors
Sebastian Krastel
Institute of Geosciences
Christian-Albrechts-Universität zu Kiel
Kiel, Germany

Roger Urgeles
Institute of Marine Sciences (CSIC)
Barcelona, Spain

Katrin Huhn
MARUM Center for Marine
Environmental Sciences
University of Bremen
Bremen, Germany

Carl Bonnevie Harbitz
Norwegian Geotechnical Institute
Oslo, Norway

Jan-Hinrich Behrmann
David Völker
Michael Stipp
Christian Berndt
GEOMAR Helmholtz Centre for Ocean
Research Kiel
Kiel, Germany

Jason Chaytor
United States Geological Survey
Woods Hole, MA, USA

Michael Strasser
ETH Zurich
Geological Institute
Zurich, Switzerland

ISSN 1878-9897 ISSN 2213-6959 (electronic)
ISBN 978-3-319-00971-1 ISBN 978-3-319-00972-8 (eBook)
DOI 10.1007/978-3-319-00972-8
Springer Cham Heidelberg New York Dordrecht London

Library of Congress Control Number: 2013948753

Printed on acid-free paper

Springer is part of Springer Science+Business Media (www.springer.com)

Preface

The morphology of continental slopes and rises around the world as well as flanks of oceanic islands are marked with major landslide scars. Many of these involve thousands of square kilometers of sea floor, and their formation represents an important mechanism for transferring sedimentary material to the deep sea. Sand-rich gravity flow deposits form many of the world's largest oil and gas reservoirs, while mud-rich deposits may sequester globally significant volumes of organic carbon. The geohazards associated with submarine slope failures include destruction of sub-sea infrastructure such as pipelines and cables as well as tsunamis induced by landslides and their effects onshore. Due to the source characteristics, tsunamis induced by landslides cause more local effects than those caused by earthquakes. The 1998 Papua New Guinea tsunami that followed from a 5–10 km^3 submarine landslide and killed ~2,200 people along a 30 km coastal section illustrates the hazard and risk resulting from such local events. Very large submarine landslides with volumes of several thousands of cubic kilometers are rare, but may cause tsunamis with more widespread effects. Volcanic flank collapses on oceanic islands may also cause tsunamis inducing distant destruction, although their tsunamigenic potential is highly disputed.

The causes of submarine mass movements are manifold, but not yet well understood. Surprisingly many of the larger landslides are associated with much gentler slopes than required to destabilize the sea floor under static conditions. Slope failure is often attributed to some combination of earthquake triggering, rapid sedimentation, the presence of weak layers, excess pore pressures, ice-induced forces in glaciated areas, steeping from tectonic, diapiric or erosional activity, as well as volcano development, but only for very few slope failures a robust scientific case has been made.

The complex nature of submarine mass movements and their consequences calls for a multidisciplinary approach including state-of-the-art seafloor and sub-seafloor mapping, investigations of physical properties (in situ and on cores), numerical

modeling of landslides and associated tsunamis as well as hazard and risk assessment. In order to bring 'submarine landslide' scientists together and to minimize the consequences of submarine failures, the International Union of Geological Science (IUGS) and the United Nations Educational, Scientific and Cultural Organization (UNESCO) have sponsored two International Geoscience Programs on 'Earth's Continental Margins: Assessing the Geohazard from submarine Landslides' (IGCP-585) and its predecessor 'Submarine Mass Movements and Their Consequences' (IGCP-511).

A central activity of IGCP 585 is the organization of a bi-annual symposium in order to present an up-to-date perspective of submarine mass movements and their consequences by assembling excellent contributions from active international academic, government and industry researchers. The 6th symposium was held in Kiel (Germany) in September 2013; this new volume of the book series on 'Submarine Mass Movements and their Consequences' presents new peer-reviewed contributions by international experts in the field. The book is organized in nine parts covering geological, geophysical, engineering and environmental aspects of submarine slope failures. It contains (among others) investigations of physical properties of landslide deposits, partly on samples collected during some of the first attempts at scientific ocean drilling in thick sequences of mass transport deposits, the analysis of long-term records of submarine landslides and their usage in paleoseismology, repeated surveys of active slope failures, as well as a chapter on landslide generated tsunamis. The focus is on understanding the full spectrum of challenges presented by this major coastal and offshore geohazard.

Research on submarine mass movements and their consequences spans several disciplines and several open questions need to be addressed in the future. It is crucial to identify potential precursors of submarine landslides. The emergent field of submarine geodesy will hopefully provide us with the means of measuring small movements on the sea floor, which may occur prior to a catastrophic failure. The new science plan of the 'International Ocean Discovery Program (IODP)' identified geohazards as one of the key objectives. First results from dedicated drilling campaigns for understanding submarine landslides are currently published (e.g., offshore Japan, around the Lesser Antilles, the Gulf of Mexico). Future systematic monitoring of *in situ* parameters in drill holes may allow identification of transient signals indicating imminent slope instability. Sophisticated hazard assessment for tsunamis caused by submarine landslides is another important step for mitigating their impacts. So far, most tsunami hazard assessments have been scenario-based and focused on earthquake tsunamis. More recently a probabilistic tsunami hazard assessment approach has been developed, which is largely inspired from probabilistic seismic hazard investigations. However, insufficient age sampling and changing conditions for landslide triggering are major obstacles in translating a probabilistic tsunami hazard assessment approach from earthquake to landslide tsunamis. It is further expected that the landslide tsunami risk is dominated by

the long return periods, generally carrying the largest uncertainties. Hence, a more robust scenario-based tsunami hazard assessment will probably still be the most efficient one to use for landslide tsunamis.

Kiel, Germany — Sebastian Krastel
Kiel, Germany — Jan-Hinrich Behrmann
Kiel, Germany — David Völker
Kiel, Germany — Michael Stipp
Kiel, Germany — Christian Berndt
Barcelona, Spain — Roger Urgeles
Woods Hole, MA, USA — Jason Chaytor
Bremen, Germany — Katrin Huhn
Zurich, Switzerland — Michael Strasser
Oslo, Norway — Carl Bonnevie Harbitz

Contents

Part I
Physical Properties of Sediments

Chapter 1
Weak Layers: Their Definition and Classification from a Geotechnical Perspective

Jacques Locat, Serge Leroueil, Ariane Locat, and Homa Lee

Abstract Weak layers play a major role in the development of many large submarine landslides. A definition of a weak layer is proposed here using a geotechnical perspective: a layer (or band) consisting of sediment or rock that has strength potentially or actually sufficiently lower than that of adjacent units (strength contrast) to provide a potential focus for the development of a surface of rupture. Such a layer or a band can follow stratigraphic horizons, but this is not a requirement. From this it is proposed to define two types: inherited and induced weak layers. In addition, weak layers can develop in strain softening sediments where progressive failure can generate a surface of rupture without the need to invoke the role of excess pore pressures.

Keywords Submarine landslides • Weak layers • Strength • Strain softening • Sedimentology • Geotechnical properties • Surface of rupture • Earthquake • Gas hydrates

1.1 Introduction

In many studies on submarine mass movements, weak layers are invoked to explain their occurrence and extent, particularly those taking place on nearly horizontal surface of rupture (Lee et al. 2007; Masson et al. 2010; Locat and Lee 2002, 2009). However, it is not always clear if these weak layers existed prior to the landslide or resulted from the failure mechanism. What is clear is that a rupture surface is the

J. Locat (✉) • S. Leroueil • A. Locat
Laboratoire d'études sur les risques naturels, Université Laval, Québec, Canada
e-mail: Jacques.locat@ggl.ulaval.ca

H. Lee
Retired Research Scientist, United States Geological Survey, Menlo Park, CA, USA

S. Krastel et al. (eds.), *Submarine Mass Movements and Their Consequences*, Advances in Natural and Technological Hazards Research 37, DOI 10.1007/978-3-319-00972-8_1,

locus of an existing surface of lower resistance or a surface where there is a reduction in the shearing resistance of a layer of sediment to a point where it cannot resist the gravitational driving forces. For subaerial landslides, the presence of weak layers was invoked as early as 1943 (Kardos et al. 1943) and for submarine landslides, the first direct mention of weak layers is found in Lewis (1971). They are also well recognized in snow avalanches (Heierli et al. 2008). By their very nature, weak layers are often linked directly to sediments showing some level of stratification (or layering), which, in a marine environment, can cover quite large areas (few hundreds of square kilometres, Kvalstad et al. 2005). They may also result from landslide re-activation on a pre-existing surface of rupture (Leroueil et al. 1996). For the purpose of this paper, we will mostly focus our analysis of weak layers in marine sediments.

In many cases, the failure surface on which submarine mass movements originated, appears to follow stratigraphic horizons that are identified on seismic lines by strong reflectors (Levesque et al. 2004). As indicated by Masson et al. (2010): "The sedimentology of weak layers is not well understood, mainly because they are destroyed in areas where landslides have occurred and it is not known how to identify them before they fail".

In order to improve our understanding of weak layer formation and their role in the development of landslides, we would like to take an approach coupling sedimentological and geophysical observations, and geotechnical concepts. This approach will be centred around three main points: (1) definition of weak layers, (2) observations of weak layers, and (3) a proposed classification system for weak layers. As part of this analysis we will also underline the potential role of progressive failure as a way of explaining large submarine landslides without the need to invoke excess pore pressures.

1.2 Weak Layer Definition

If failure is taking place, this is because the factor of safety F of the slope has been reduced to unity or less according to the following relationship:

$$F = \frac{\tau_f}{\tau_{mob}} \tag{1.1}$$

where τ_f is the shearing resistance of the soil at failure and τ_{mob} the mobilized shearing forces. Changes in this equilibrium can come from either a loss of strength of the sediment or an increase in external forces like sediment loading at a delta front.

Where weak layers have been identified, it is common that some processes produced a layer that is relatively weak prior to failure or during the failure process. That is to say that the shearing resistance of the layer was reduced or the gravitational forces exceeded the shearing resistance to a degree for which the

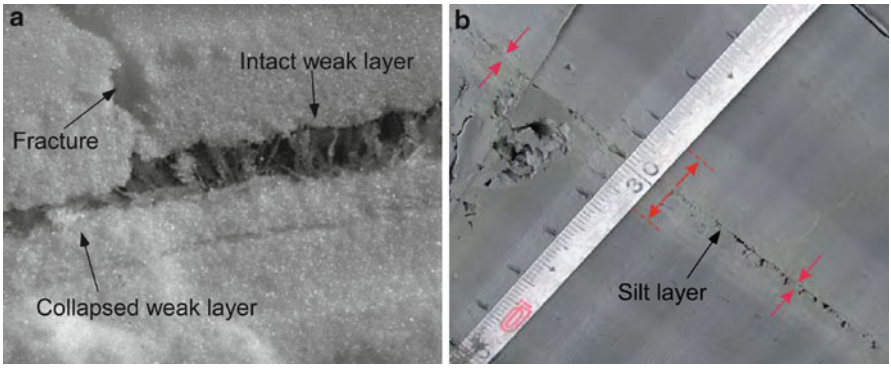

Fig. 1.1 Thin weak layer in (**a**) snow and (**b**) marine clay. The collapsible structure in the snow is about 2 cm thick and formed by hoar crystals (modified after Heierli et al. 2008). In (**b**) the weak layer is a silt layer (about 1 mm thick) that failed (remoulded, ∼10 cm of displacement) and the failure itself has softened about 1 cm on either side (*red arrows*, modified after Locat et al. 2011b)

resisting forces of that layer are exceeded by gravitational forces. The components leading to the formation of a weak layer are contained within a Mohr-Coulomb failure criterion:

$$\tau_f = c + (\sigma - u)\tan\phi' \tag{1.2}$$

where c is the cohesion, σ the total stress, u the pore pressure and ϕ' the friction angle. From this equation it is clear that the formation of a weak layer will require a modification of either, the cohesion, the total stresses, the pore pressure, the friction angle or a combination of them.

A weak layer can be very thin (e.g. Fig. 1.1), for example a single clay layer, or a thicker band of multiple layer. In either case, they can be transformed by processes like liquefaction during earthquakes. Leroueil et al. (2002), considering the effect of layering, show that the effective strength envelope of a marine clay deposit from Louiseville (Québec) is lower along stratigraphic horizons than along arbitrary planes at some angle with these horizons. This was explained by the roughness of the marine clay that is lower parallel to bedding. Very thin (∼1 mm) silt layers can also be remoulded to develop a surface of rupture as observed for the St. Jude slide in leached Champlain marine sediments (Fig. 1.1a, Locat et al. 2011b). Therefore, layers of sediments having little or no cohesion can also act as a plane of weakness under certain conditions that may be similar to very thin weak layers seen in snow avalanches (Fig. 1.1a).

For marine sediments, Kvalstad et al. (2005) have shown that sediment having a strain softening behaviour could develop progressive failure along large surfaces of rupture. Leroueil et al. (2012) have also shown that progressive failure can develop in various types of material.

Taking into account the great diversity (origin and formation) of weak layers, we would like to propose the following definition: *a layer (or band) consisting of sediment or rock that has strength potentially or actually sufficiently lower than that of adjacent units (strength contrast) to provide a potential focus for the development of a surface of rupture. Such a layer or a band can follow stratigraphic horizons, but this is not a requirement*.

With such a definition for weak layers we will continue our analysis by reviewing some observations and then look at the classification system.

1.3 Weak Layer Observations

In the submarine environment, weak layers are more often deduced from observations and interpretation rather than direct sampling (Masson et al. 2010), with a few recent exceptions like the Storegga slide (Kvalstad et al. 2005), the Nice airport failure (Dan et al. 2007) or submarine landslides in fjords (Hansen et al. 2011; L'Heureux et al. 2012; Levesque et al. 2004). An example of a weak layer, taken from the work of L'Heureux et al. (2012), is presented in Fig. 1.2. It consists of a layer, at a depth of around 3 m, deposited during a rapid sedimentation event (turbidite). It is recognizable by its lower density and lower strength of the underlying layer. This band could likely be responsible for the location of the rupture surface in a fjord (e.g. Saguenay Fjord, Fig. 1.2a). Another example is presented in Fig. 1.3, where a flow slide is mapped in the Saguenay Fjord (Levesque et al. 2004). The rupture surface can be seen as a strong reflector but the transparent layer above it, consisting mostly of normally consolidated silty clay (resting on a sandy layer), as seen on the flanks, has been removed by the slide process (disintegrative slide, Fig. 1.3). Here, if the remoulding energy (Leroueil et al. 1996) is sufficient, the material will evacuate the landslide scar and a retrogressive mechanism can be maintained.

A compilation of weak layers observed in submarine landslides studies is presented in Table 1.1. This table shows that there is no common element: there can be various sediments types and failure processes involving weak layers.

The first two types of sediments listed in Table 1.1 are for weak layers that result from an increase in pore pressure due to gas hydrate dissociation and/or resulting loss of cementation along contourites (Elverhoi et al. 2002; Sultan et al. 2004b; Camerlenghi et al. 2007), or high sedimentation rates inducing an increase in excess pore pressure in some layers (underconsolidation, e.g. Huvenne et al. 2002; Sultan et al. 2004b).

The next two types of sediments consist of weak layers for which both pore pressure increase and strength reduction have taken place. The first one is for sandy layers, which may liquefy during earthquakes (Lewis 1971) or in which seepage forces can develop along a confined permeable layer (Dan et al. 2007). In some stratigraphic conditions with hydraulic conductivity contrast between layers (e.g. sand and clay layering), earthquakes can also produce planes of weakness by

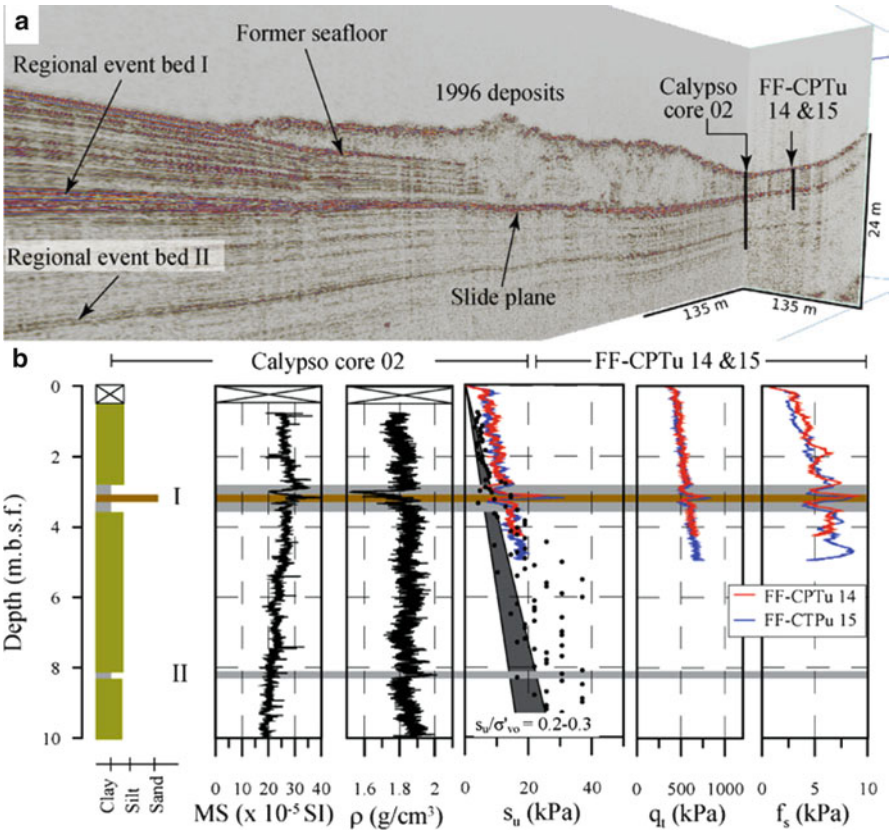

Fig. 1.2 Example of a surface of rupture (**a** and **b**) identified as an event layer (turbidite) sandwiched between more resistant layers (Modified after L'Heureux et al. 2012)

forming a film of water with little shearing resistance (Kokusho and Kojima 2002). The second type of sedimentary weak layer results from rapid accumulation events (event layers like a turbidite or a debris flow, e.g. Fig. 1.2) over a clay-rich bed (Hansen et al. 2011; L'Heureux et al. 2012).

The last two types of sediments involved in weak layers in Table 1.1 are those whose properties favour the development of strain softening behaviour and the potential for progressive failure along nearly flat rupture surfaces. Such a mechanism was proposed to explain the large spread failures observed near the head of the Storegga slide (Kvalstad et al. 2005) and also for large sub-aerial spreads in sensitive clays either normally consolidated (Locat et al. 2011a) or overconsolidated by erosion (Locat et al. 2008). An interesting aspect of the progressive failure mechanism is that, if it can be initiated, it can develop into a complete surface rupture. The resulting final failure can take place without the need to have excess pore pressures at the onset of failure. Moreover, rupture surface does not need to

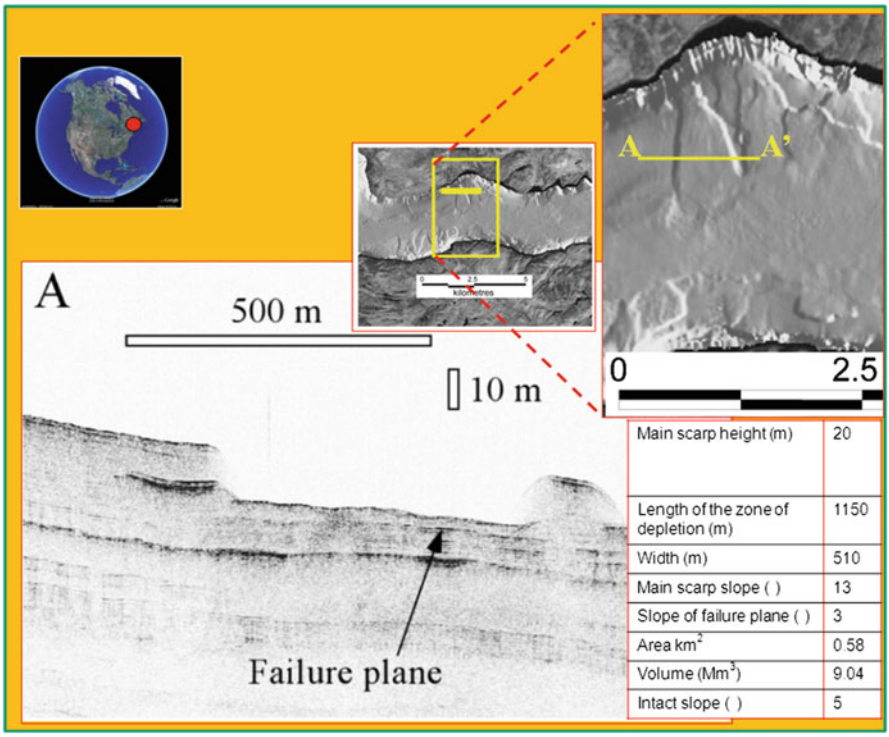

Fig. 1.3 Sandy weak layer for a flow slide in Saguenay Fjord showing that most of the sliding mass (transparent layer seen on the flanks of the slide) has been removed (Modified after Levesque et al. 2004)

follow a specific stratigraphic horizon (Locat et al. 2011a). In few cases, submarine mass movements were considered to involve quick clay layers. These acted as weak layers for the observed flow slides along fjord walls (Longva et al. 2003) or at the heads of deltas (Sultan et al. 2004a). It could also happen in deep marine sediments where gas hydrates dissociation could bring the salinity to a critical value that can influence its remoulded strength (Hyndman et al. 1999). In these cases, the higher sensitivity also promotes a strain softening behaviour for the sediment and the low remoulded shear strength which can play a major role in the development of a retrogressive failure. In both cases, development of sensitivity caused by leaching is promoted by a groundwater flow, which may also cause seepage forces (excess pore pressures, Sultan et al. 2004a).

With these observations, weak layer formation can result from various processes: sedimentological (e.g. layering), geotechnical (e.g. strain softening) and geochemical (e.g. leaching). In the next section we will introduce a classification system that integrates these various observations.

Table 1.1 Examples of weak layers involved in submarine slide studies

Type of sediment	Description	Main effect	References
Contourites	Sandy layers in which hydrates can accumulate	Pore pressure increase due to gas hydrate dissociation	Buenz et al. (2003), Dan et al. (2007), Camerlenghi et al. 2007, and Sultan et al. (2004b)
UC clayey sediment layers	In areas of high sedimentation rates, excess pore pressure can accumulate at depth	Pore pressure	Sultan et al. (2004a), Huvenne et al. (2002), and Dugan and Flemings (2000)
Sandy silt layers	Provide a locus for seepage forces to accumulate (e.g. Nice airport slide) and can also liquefy. Contourites could also by liquefy by earthquakes	Pore pressure increase and strength reduction	Lewis (1971), and Hampton and Bouma (1977), Kokusho and Kojima (2002), Sultan et al. (2004a), and Urgeles et al. (2010)
Clay event layers -	Rapid accumulation of sediments which will not allow the underlying sediment to consolidate completely, thus providing a lower shearing resistance	Pore pressure and lower strength	Hansen et al. (2011), and L'Heureux et al. (2012)
NC to OC sediments	Clayey sediments normally consolidated or overconsolidated with strain softening behaviour	Strength reduction	O'Leary (1991), Elverhoy et al. (2002), and Kvalstad et al. (2005)
Quick clay	Increase in sensitivity and reduction in undrained remoulded shear strength due to leaching of salts	Lowered remoulded strength	Longva et al. (2003), and Sultan et al. (2004a)

1.4 Classification System from a Geotechnical Approach

From the above analysis and Table 1.1, it is possible to consider that various factors can lead to the development of weak layers either before the landslide takes place or as part of the failure process. According to the definition and the observations mentioned above, we propose a classification system, shown in Fig. 1.4, where weak layers are separated in two groups: (1) inherited and (2) induced, by either pore pressure changes or strength reduction as a result of various sedimentological, geochemical or geomechanical processes. The classification system is further developed by considering the primary effects of the processes involved either on pore pressure generation or on strength.

An inherited weak layer is a layer (or stratigraphic horizon) where strength was already low before landslide initiation. For example, a relatively lower strength

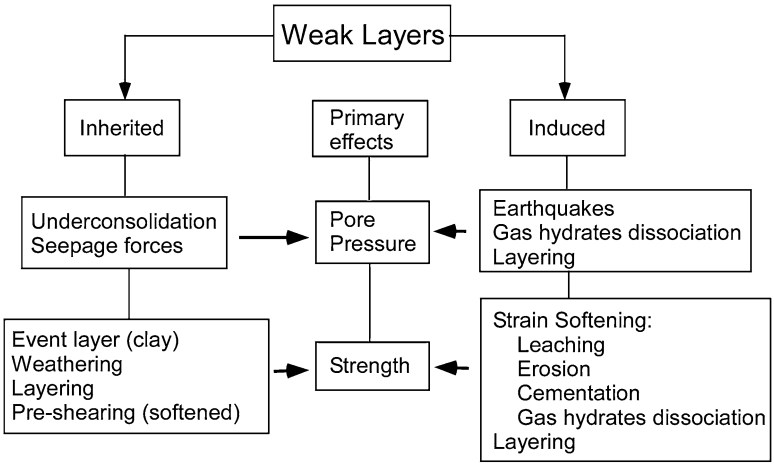

Fig. 1.4 A sedimentological and geotechnical classification system for weak layers. The *horizontal arrows* point in the direction of the primary effect of the process involved

can be maintained since deposition due to non-equilibrium consolidation and the presence of excess pore pressure (or equivalently, gas hydrates). Amongst the inherited weak layers are those that have developed as part of an older landslide event which may be re-activated over the same surface of rupture (pre-sheared softened surface). The long term weathering, due to some diagenetic processes, that result into a reduction in the friction angle or cohesion of the sediment, may also favour the formation of an inherent weak layer. The presence of joints or aligned pock marks could also help to reduce the strength at the head of a potential landslide.

An induced weak layer is a layer in which the strength is reduced during the slide process. This can result from external forces (e.g. earthquakes), local liquefaction within a sandy layer, gas hydrate dissociation, or from the development of strain softening behaviour. Cementation can increase the strength of sediment, but may generate sediment with a higher sensitivity and a corresponding strain softening behaviour (Locat and Lefebvre 1986).

1.5 Concluding Remarks

This paper presents a first attempt at defining and proposing a classification system for weak layers. Although this remains a complicated issue, such a classification may prove useful in understanding various types of landslides. When considering the geotechnical characterization of mass movements proposed by Leroueil et al. (1996), such a classification system may help identify predisposition and preconditioning factors.

Weak layers may be inherited or induced. Inherited derives from the original depositional properties of the sediment. Induced requires an external factor or

factors. Strain softening behaviour is one such example of this latter, and likely a requirement for progressive failure in many types of sediments and rocks (Leroueil et al. 2012). For large spreads or retrogressive failures where progressive failure can develop, there is no requirement for high pore pressures as part of the triggering process. Such consideration may lead to reviewing cases of submarine slides where earthquakes are not clear triggers for the slide.

Acknowledgements This paper is the result of long discussions amongst the submarine landslide community and everyone who participated is acknowledged. We would like to thank Roger Urgeles and Dave Mosher for their constructive reviews of the manuscript.

References

Buenz S, Mienert J, Berndt C (2003) Geological controls on the Storegga gas-hydrate system of the mid-Norwegian continental margin. Earth Planet Sci Lett 209:291–307

Camerlenghi A, Urgeles R, Ercilla G, Bruskmann W (2007) Scientific ocean drilling behind the assessment of geo-hazards from submarine slides. Sci Drill 4:45–47

Dan D, Sultan N, Savoye B (2007) The 1979 nice harbour catastrophe revisited: trigger mechanism inferred from geotechnical measurements and numerical modeling. Mar Geol 245:40–64

Dugan B, Flemings PB (2000) Overpressure and fluid flow in the New Jersey continental slope: implications for slope failure and cold seeps. Science 289:288–291

Elverhoi A, De Blasio F, Butt FA, Issler D, Harbitz C, Engvik L, Solheim A, Marr J (2002) Submarine mass-wasting on glacially-influenced continental slopes: processes and dynamics. In: Dowdeswell JA, Cofaigh C (eds) Glacier-influenced sedimentation on high-latitude continental margins, vol 203, Geological Society London special publications., pp 73–87

Hampton MA, Bouma AH (1977) Slope instability near the shelf break, Western Gulf of Alaska. Mar Geotechnol 2:309–331

Hansen L, L'Heureux J-S, Longva O (2011) Turbiditic, clay-rich event beds in fjord-marine deposits caused by landslides in emerging clay deposits – palaeoenvironmental interpretation and role for submarine mass-wasting. Sedimentology 58:890–915

Heierli J, Gumbsch P, Zaiser M (2008) Anticrack nucleation as triggering mechanism for snow slab avalanche. Science 321:240–243

Huvenne VAI, Croker PF, Henriet J-P (2002) A refreshing 3D view of an ancient sediment collapse and slope failure. Terra Nova 14:33–40

Hyndman RD, Yuan T, Moran K (1999) The concentration of deep sea gas hydrates from downhole electrical resistivity logs and laboratory data. Earth Planet Sci Lett 172:167–177

Kardos LT, Vlasoff PI, Twiss SN (1943) Factors contributing to landslides in the Palouse region. Proc Soil Sci Soc 8:437–440

Kokusho T, Kojima T (2002) Mechanism for postliquefaction water film generation in layered sand. J Geotech Geoenviron Eng 128:129–137

Kvalstad TJ, Andresen L, Forsberg CF, Berg K, Bryn P, Wangen M (2005) The Storegga slide: evaluation of triggering sources and slide mechanics. Mar Petrol Geol 22:245–256

L'Heureux J-S, Longva O, Steiner A, Hansen L, Vardy ME, Vanneste M, Haflidason H, Brendryen J, Kvalstad TJ, Forsbeg CF, Chand S, Kopf A (2012) Identification of weak layers and their role for the stability of slopes at Finneidfjord, Northern Norway. In: Yamada Y et al. (eds) Submarine mass movements and their consequences, vol 31, Advances in natural and technological hazards research., pp 321–330

Lee HJ, Locat J, Desgagnés P, Parsons JD, McAdoo BG, Orange DL, Puig P, Wong FL, Dartnell P, Boulanger E (2007) Chapter 5: Submarine mass movements on continental margins.

In: Nittrouer CA, Austin JA, Field ME, Kravitz JH, Syvitski JPM, Wiberg PL (eds) Continental-margin sedimentation: from sediment transport to sequence stratigraphy, vol 37, IAS special publication. Blackwell Publishing Ltd, Oxford, pp 213–274

Leroueil S, Vaunat J, Picarelli L, Locat J, Faure R, Lee H (1996) A geotechnical characterisation of slope movements. In: Proceedings of the 7th international symposium on landslides, Trondheim, vol 1. Balkema, Rotterdam, pp 53–74

Leroueil S, Hamouche K, Tavenas F, Boudali M, Locat J, Virely D (2002) Geotechnical characterization and properties of a sensitive clay from Québec. In: Proceedings of the symposium on characterisation and engineering properties of natural soils, Singapore, vol 1. Swets & Zeitlinger, Lisse, The Netherlands, pp 363–394

Leroueil S, Locat A, Eberhardt E, Kovacevic N (2012) Progressive failure in natural and engineered slopes. In: Eberhardt EB et al. (eds) Landslides and engineered slopes: protecting society through improved understanding. CRC Press, Leiden, pp 31–46

Levesque C, Locat J, Urgeles R, Leroueil S (2004) Preliminary overview of the morphology in the Saguenay Fjord with a particular look at mass movements. In: Proceedings of the 57th Canadian geotechnical conference, Québec, Session 6, pp 23–30

Lewis KB (1971) Slumping on a continental slope inclined at 1-4. Sedimentology 16:97–110

Locat J, Lee HJ (2002) Submarine landslides: advances and challenges. Can Geotech J 39:193–212

Locat J, Lee HJ (2009) Submarine mass movements and their consequences: an overview. Chapter 6. In: Sassa K, Canuti P (eds) Landslides – disaster risk reduction. Springer, Berlin/Heidelberg, pp 115–142

Locat J, Lefebvre G (1986) The origin of structuration of the Grande-Baleine marine sediments, Qu6bec, Canada. Q J Eng Geol 19:365–374

Locat A, Leroueil S, Bernander S, Demers D, Locat J, Ouehb L (2008) Study of a lateral spread failure in an eastern Canada clay deposit in relation with progressive failure: the St. Barnabé-Nord slide. In: Locat J, Perret D, Turmel D, Demers D, Leroueil S (eds) Proceedings of the 4th Canadian conference on geohazards. Canadian Geotechnical Society, Engineering Geology Division, Laval, pp 88–96

Locat A, Leroueil S, Bernander S, Demers D, Jostad HP, Ouehb L (2011a) Progressive failures in eastern Canadian and Scandinavian sensitive clays. Can Geotech J 48:1696–1712

Locat P, Fournier T, Robitaille D, Locat A (2011b) Glissement de terrain du 10 mai 2010 Saint-Jude, Montérégie rapport sur les caractéristiques et les causes. Ministère des Transports du, Québec

Longva O, Janbu N, Blikra LH, Boe R (2003) The 1996 Finneidfjord slide; seafloor failure and slide dynamics. In: Locat J, Mienert J (eds) Submarine mass movements and their consequences. Kluwer, Dordrecht, pp 531–538

Masson DG, Wynn RB, Talling PJ (2010) Large landslides on passive continental margins: processes, hypotheses and outstanding questions. In: Mosher DC et al. (eds) Submarine mass movements and their consequences, vol 28, Advances in natural and technological hazards research., pp 153–165

O'Leary DW (1991) Structure and morphology of submarine slab slides: clues to origin and behavior. Mar Geotechnol 10:53–69

Sultan N, Cochonat P, Canals M, Cattaneo A, Dennielou B, Haflidason H, Laberg JE, Long D, Mienert J, Trincardi F, Urgeles R, Vorrene TO, Wilson C (2004a) Triggering mechanisms of slope instability processes and sediment failures on continental margins: a geotechnical approach. Mar Geol 213:291–321

Sultan N, Cochonat P, Foucher J-P, Mienert J (2004b) Effect of gas hydrates melting on seafloor slope instability. Mar Geol 211:379–401

Urgeles R, Locat J, Sawyer DW, Flemings PB, Dugan B, Binh NTT (2010) History of pore pressure build up and slope instability in mud-dominated sediments of Ursa Basin, Gulf of Mexico continental slope. In: Mosher DC et al. (eds) Submarine mass movements and their consequences, vol 28, Advances in natural and technological hazards research., pp 179–190

Chapter 2
Field Measurements to Investigate Submerged Slope Failures

Alexander van Duinen, Adam Bezuijen, Geeralt van den Ham, and Victor Hopman

Abstract Many flood defences in The Netherlands have been disapproved for flow slides of the Holocene subsoil. Traditionally these flow slides are assumed to be induced by static liquefaction. Only in recent times it has been recognized that flow slides may also concern breach flows, which do not necessarily require loosely packed sand. For both static liquefaction and breach flow the inaccuracy of the currently applied methods to determine in situ density lead to high computed probabilities of failure, which is one of the main problems in the safety assessment of flow slides. In order to reduce this uncertainty, based on a literature study a number of methods were selected and applied on four test locations: two sites where flow slides occurred and two sites where no flow slides occurred, but for which high probabilities on flow slides were calculated based on current Dutch assessment rules for liquefaction and breach flow. For these sites CPT's and electrical resistivity cone tests available from earlier investigations, were extended with seismic CPT's and interpreted for relative density and state parameter. The results of this study lead to the conclusion that some of the historical flow slides in The Netherlands may have been the result of static liquefaction in loosely packed sand. For many other slopes, however, it is more reasonable to assume that the failures must have been breach flows in medium or densely packed layers.

Keywords Sand • Static liquefaction • Breach flow • Relative density • State parameter • Cone penetration test

A. van Duinen (✉) • G. van den Ham
Department of Geo-engineering, Deltares, Delft, The Netherlands
e-mail: alexander.vanduinen@deltares.nl

V. Hopman
Department of Subsurface and Groundwater Systems, Deltares, Delft, The Netherlands

A. Bezuijen
Department of Geo-engineering, Deltares, Delft, The Netherlands

Faculty of Engineering and Architecture, Department of Civil Engineering, Geotechnics Laboratory, Ghent University, Ghent, Belgium

S. Krastel et al. (eds.), *Submarine Mass Movements and Their Consequences*, Advances in Natural and Technological Hazards Research 37, DOI 10.1007/978-3-319-00972-8_2,

2.1 Introduction

Hundreds of flow failures of submerged slopes have been observed in the southwestern estuary of The Netherlands (Zeeland) since 1800. It is generally assumed that many of these flow failures are initiated by static liquefaction in loosely packed sand. However, in recent times it has been recognized that many of these flow slides may also concern breach flows, which do not necessarily require loosely packed sand.

The soil layers that might experience static liquefaction or breach flow are part of tidal and coastal deposits. These deposits contain alternating fine sand and clay laminae. The geological past of the southwestern estuary and the coast of The Netherlands is characterised by rapidly shifting coastlines and alternating sedimentation and erosion along the tidal channels and the coast. Generally the upper 30 m of the subsoil consists of Holocene deposits. Most of these consist of (medium) fine sand, which, in general, is loosely packed due to high deposition rates. The variation in tidal currents often resulted in the deposition of thin clay layers in between the thicker sand layers.

In a loosely packed sand layer static liquefaction can occur, given a sufficiently high and steep under water slope and the presence of a trigger, such as a local slip failure or rapid drop of water level. Static liquefaction involves the sudden undrained collapse of the soil structure leading to an increase of pore water pressure, resulting in a dramatic reduction of shear strength and consequently instability of the slope. In densely packed sand, a breach flow can occur. A breach flow entails the upslope retrogression of a breach, induced by erosion or scour. According to de Groot and Mastbergen (2006) and van den Ham et al. (2013) it is reasonable to believe that many flow slides in the Holocene tidal and coastal deposits, which are characterised by alternations of densely and loosely packed sand layers, concerned combinations of static liquefaction and breach flow.

According to the current Dutch assessment procedures (Rijkswaterstaat 2007; TAW 2001) a large number of levees in the Netherlands are not sufficiently safe with respect to flow sliding. Besides uncertainty in the models for liquefaction and breach flow, a large part of the relatively high calculated probabilities of failure can be ascribed to the large uncertainty of the in situ void ratio of the sand, which is relevant for both static liquefaction and breach flow and is an important input parameter of the calculation models.

In this paper (i) various published interpretation methods to determine the in situ void ratio of sand and silt are given, (ii) application of a number of these methods on four test sites is presented and (iii) conclusions are drawn with respect to the accuracy and practical applicability of the methods are given.

The deposits at four sites are investigated. At Oude Tonge and Hoofdplaat (both in Zeeland) a failure occurred (1972 and 1973 respectively). Stoutjesdijk and de Groot (1994) found that these failures could have been caused by static liquefaction. Tabak (2011) analysed the failure at Oude Tonge and found that this failure could also be explained as a breach flow failure. At the sites at the river Spui (near

Oud-Beijerland) and Petten (along the Noordzee) no failures occurred, but for these sites calculation models yielded unacceptably high probabilities of failure. The soil layers at these four sites belong to the same geological deposits as described above. The site investigations were carried out with CPT trucks and CPT track rigs on land, in the zone between the dikes and the shoreline.

2.2 Interpretation Methods of Field Measurements

2.2.1 Relative Density

In Dutch practice relative density is today the most widely used expression to estimate the susceptibility for static liquefaction. An estimation of the in situ relative density can be made using a correlation with the cone tip resistance (q_c) of a cone penetration test (CPT) or directly with the electric resistivity of a resistivity CPT (RCPT). In the literature, several CPT correlations are available. In the Dutch engineering practise the correlation of Baldi et al. (1982) is often used, because this correlation estimates the relative density in the middle of other well-known relative density correlations.

According to the (roughly chosen) criteria generally applied in the Dutch engineering practice a relative density below 33 % indicates very liquefiable sand, a value between 33 and 67 % indicates potentially liquefiable sand and above 67 % the sand is assumed to be not liquefiable (i.e. dilative).

In none of the relative density correlations is the effect of fines taken into account and in most of them the soils' compressibility neither, whereas it is known that fines are an important factor of influence to the susceptibility of a sand layer to liquefaction (Lade et al. 2009) and variations in soils' compressibility may lead to 15–20 % deviation of the average relative density, as can be concluded from Schnaid (2009). In some of the correlations the importance of soil compressibility has been recognized (i.e. Kulhawy and Mayne 1990; Jamiolkowski et al. 2001). However, today there is no approach to quantify the effect of the soil compressibility in the CPT based relative density estimation.

Most relative density correlations assume drained behaviour during the CPT.

2.2.2 State Parameter

The state parameter, ψ, introduced by Been and Jefferies (1985), is defined as a measure of the deviation between the void ratio at the in situ state and the void ratio at the critical state. A negative ψ indicates dense, dilative soils, whereas a positive ψ indicates loose contractive soils. Been et al. (1987) developed an approach to derive ψ from a CPT. After the Been et al. (1987) approach other approaches

were formulated, varying from simple screening methods based on CPT only to advanced methods requiring seismic CPT (SCPT) and laboratory tests. The most important are (i) the screening method of Plewes et al. (1992), including partially drained conditions with the normalized excess pore pressure B_q and estimating the soil compressibility λ from the normalized friction ratio F_r, (ii) the screening method of Been and Jefferies (1992), including partially drained conditions with the normalized excess pore pressure B_q and estimating the soil compressibility λ from the soil type index I_c, (iii) the Shuttle and Jefferies (1998) universal framework, which accounts for in situ soil stiffness G_0, plastic hardening modulus H and stress level bias, (iv) the Schnaid and Yu (2007) theoretical approach, which relates ψ to the ratio of the cone tip resistance q_c and the small strain stiffness G_0, (v) the method of Robertson (2010), which is a simplified and approximate relationship between ψ and the normalised equivalent clean sand cone tip resistance $Q_{tn,cs}$ and (vi) the method of Ghafghazi (2011), who extended the Shuttle & Jefferies framework and performed spherical cavity expansion analysis with a finite element model.

An important shortcoming of some of the listed state parameter interpretation methods is that they are only valid for completely drained cone penetration, with pore pressure parameter $B_q \approx 0$, whereas in clayey sands (substantial) excess pore water pressures may be generated during cone penetration. The Plewes et al. (1992) screening method and the Been and Jefferies (1992) screening level assessment are initial steps to estimate the state parameter for partially drained soils. However these methods are first approximations and might be argued as rather speculative (Jefferies and Shuttle 2011). Shuttle and Cunning (2007) and LeBlanc and Randolph (2008) developed a more advanced approach for partially drained soils. DeJong et al. (2012) suggest modifying the penetration rate of the CPT to obtain fully drained or fully undrained soil behaviour. But these methods need further development and validation (Jefferies and Shuttle 2011; DeJong et al. 2012).

2.3 Application on Test Locations

Figures 2.1, 2.2, 2.3, and 2.4 present typical values of the normalized cone tip resistance Q_t, $(= (q_t - \sigma_{v0})/\sigma'_{v0})$, normalized shear wave velocity V_{s1}, normalized pore pressure parameter B_q, Been and Jefferies (1992) soil behaviour index I_c, which include the pore pressure parameter B_q, state parameter ψ and relative density R_e of the four investigated sites respectively. Both the results of the state parameter interpretations of Plewes et al. (1992) and Shuttle and Jefferies (1998) are shown. The normalized shear wave velocity V_{s1} from SCPT, soil compressibility λ and friction angle φ' from triaxial tests and estimations of the hardening modulus H are used in the Shuttle and Jefferies (1998) method. Relative density is in each case calculated from the cone tip resistance with the Baldi et al. (1982) correlation and derived from the resistivity cone (R_e A and R_e B) according to de Graaf and Zuidberg (1985). The state parameter and the relative density are only presented

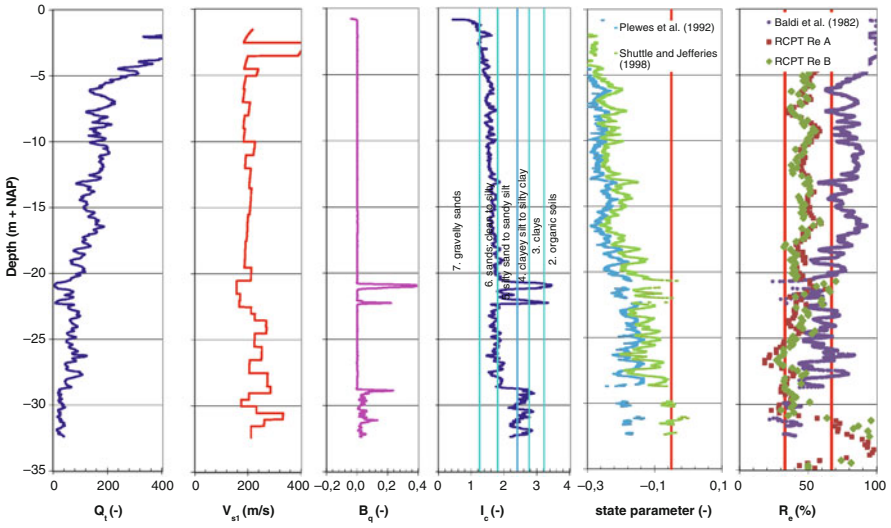

Fig. 2.1 Results and interpretations of Oude Tonge

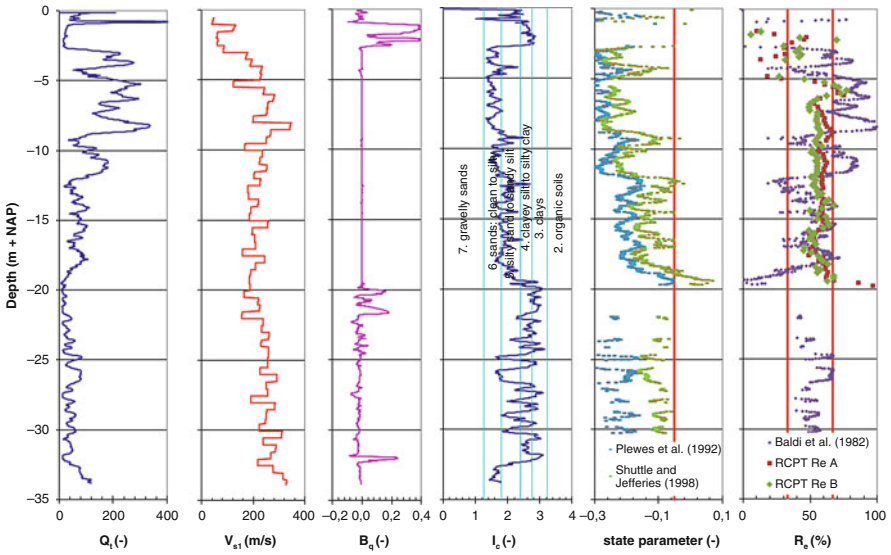

Fig. 2.2 Results and interpretations of Hoofdplaat

if $I_c < 2.4$. The boundary between contractive and dilative response suggested by Shuttle and Cunning (2007) at $\psi = -0.05$ is shown on each figure as well as the relative density boundaries of 33 and 67 %.

At Oude Tonge (Fig. 2.1) the soil behaviour index I_c indicates mainly clean sand to silty sand to a depth of 28 m below the reference level NAP. Below NAP –28 m the

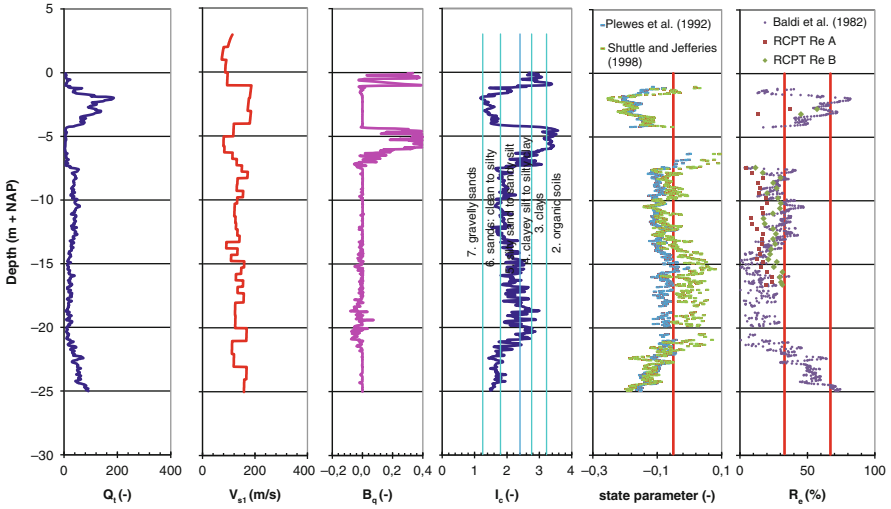

Fig. 2.3 Results and interpretations of Spui

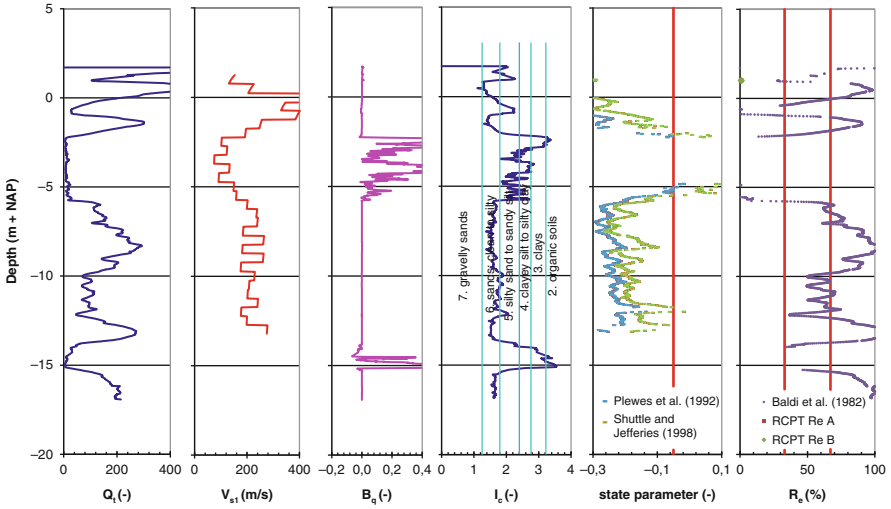

Fig. 2.4 Results and interpretations of Petten

soil behaviour index indicates clayey and silty material. The sand deposit behaves dilative according to the state parameter interpretations ($\psi < -0.05$). According to the relative density as calculated with the Baldi et al. correlation the sand layer behaves dilative above NAP –18 m only. The relative density derived from the resistivity cone indicates generally potentially liquefiable sand (33 % $< R_e <$ 67 %) and very liquefiable sand around NAP –27 m ($R_e <$ 33 %).

At Hoofdplaat (Fig. 2.2), the soil behaviour index I_c shows mainly clean sand to silty sand above NAP –19 m. Below NAP –19 m the deposits are alternations of sandy, silty and clayey layers. Again the state parameter interpretations indicate dilative behaviour of the above silty sand layer. The relative density from the Baldi et al. correlation and the relative density from the resistivity cone are in reasonable agreement at this site. Both results indicate potentially liquefiable sand in the deposit above NAP –19 m.

At Spui (Fig. 2.3), the deposits between NAP –8 m and NAP –22 m are indicated by the soil behaviour index as silty sand and sandy silt with various thin layers of clayey silt and silty clay. Between NAP –8 m and NAP –13 m the silty sand layer is very liquefiable according to the relative density methods. In the most clayey part of the deposit below NAP –13 m both the Shuttle & Jefferies state parameter interpretation and the relative density calculated from the Baldi et al. correlation show very liquefiable sand. However the Plewes et al. interpretation, which includes pore pressure effects, gives a state parameter which indicates dilative sand behaviour. This is an interesting result, because the soil behaves partially drained ($B_q \neq 0$).

At Petten (Fig. 2.4), the soil layer between NAP –4 m and NAP –6 m is of particular interest. This layer is characterised as silty sand to silty clay (sand with up to 9 % silt and 7 % clay). Both the state parameter interpretation of Shuttle & Jefferies and the relative density methods indicate this layer as potentially liquefiable to very liquefiable. Again the Plewes et al. method classifies this layer as mainly dilative.

2.4 Discussion

Some important reasons argue in favour of application of the state parameter as the most suitable method for defining the in situ state of sand. Compared to relative density the state parameter is a more objective measure and has a better theoretical basis. The Shuttle and Jefferies (1998) universal framework uses physical parameters of the soil behavior, which can be derived from field and laboratory tests. Thus an accurate state parameter determination can be made for each sand deposit and each site, which account for fines content, soil compressibility and soil stiffness.

At the four investigated locations the state parameter approach indicates less liquefiable sand (i.e. more dilative sand) compared to the traditional Dutch assessment criteria based on relative density. The $\psi = -0.05$ state parameter boundary between dilative and contractive response seems to correspond with the $R_e = 33$ % relative density boundary. Sand with a relative density between 33 and 67 % seems to be not liquefiable according to the state parameter methods.

A remarkable result is that at the locations where flow slides occurred, i.e. Oude Tonge and Hoofdplaat, the sand deposits appear to be denser, based on CPT interpretation, than those at Spui and Petten, where no flow slides occurred. From

the traditional Dutch point of view in which flow failures are assumed to be the result of static liquefaction in loose sand deposits this seems to be a paradox.

The findings could be explained by a number of reasons: (i) other conditions required for flow slides at each site were different, such as height and steepness of the slope or the absence of changing geometry by sedimentation and erosion, (ii) the two slope failures concerned breach flow slides in densely packed dilative sand (triggered by erosion of the slope) as could be underpinned by calculations with a breach flow model by Tabak (2011), (iii) the two slope failures are initiated by static liquefaction in a thin layer of loose sand, triggering a breach flow as soon as liquefaction induced instability reached the dense sand, (iv) at Spui and Petten the void ratio of the sand layers is underestimated due to partially drained conditions during cone penetration that were not taken into account. The sand at Oude Tonge and Hoofdplaat behaves more or less drained compared to the other two locations.

2.5 Conclusions and Recommendations

This study underpins that not only static liquefaction of the loosely packed Holocene deposits but also breach flow in densely packed deposits has to be evaluated in the safety assessments of flood defences. This study makes clear that, as already suggested by Tabak (2011), flow failure is possible also in denser sand in the form of a breach flow. This makes it worthwhile to further investigate the breaching failure mechanism (for which conditions it occurs, what trigger is necessary etc.). For a clear understanding of the slope failures at Oude Tonge and Hoofdplaat and to understand why no failures have yet occurred at Spui and Petten further study is required. Relevant aspects of CPT interpretation might be the drainage conditions during cone penetration and the effect of aging on cone tip and shear wave velocity measurements (Wride et al. 2000).

Acknowledgements Dr. A. Kort and prof. P.K. Robertson are very much appreciated for reviewing this paper. Rijkswaterstaat, who commissioned this study as a part of the research programme ‘Sterkte en Belastingen Waterkeringen´ (SBW) is also appreciated.

References

Baldi G, Bellotti R, Ghionna V, Jamiolkowski M, Pasqualini E (1982) Design parameters for sands from CPT. In: Proceedings of the 2nd European symposium on penetration testing, Amsterdam, pp 425–432

Been K, Jefferies MG (1985) A state parameter for sands. Géotechnique 35(2):99–112

Been K, Jefferies MG (1992) Towards systematic CPT interpretation. In: Proceedings of the wroth symposium, Oxford, pp 44–55

Been K, Jefferies MG, Crooks JHA, Rothenburg L (1987) The cone penetration test in sands: part II, general inference of state. Géotechnique 37(3):285–299

de Graaf HC, Zuidberg HM (1985) Field investigations. In: de Leeuw EH (ed) The Netherlands commemorative volume XI, ICSMFE, The Hague, pp 29–52

de Groot MB, Mastbergen DR (2006) Scour hole slope instability in sandy soils. In: Proceedings of the 3rd international conference scour and erosion, CURNET, Gouda, The Netherlands, pp 126–127

DeJong JT, Jaeger RA, Boulanger RW, Randolph MF, Wahl DAJ (2012) Variable penetration rate cone testing for characterization of intermediate soils. In: Coutinho RQ, Mayne PW (eds) Geotechnical and geophysical site characterization 4. Taylor & Francis Group, London. ISBN 978-0-415-62136-6

Ghafghazi M (2011) Towards comprehensive interpretation of the state parameter from cone penetration testing in cohesionless soils. Ph.D. thesis. The University of British Columbia. April 2011

Jamiolkowski M, Lo Presti DCF, Manassero M (2001) Evaluation of relative density and shear strength of sands from cone penetration test and flat dilatometer test. In: Soil behavior and soft ground construction, vol 119, GSP. ASCE, Reston, pp 201–238

Jefferies M, Shuttle D (2011) Understanding liquefaction trough applied mechanics. In: 5th international conference on earthquake geotechnical engineering, Santiago, Chile, January 2011, pp 10–13

Kulhawy FH, Mayne PH (1990) Manual on estimating soil properties for foundation design. Electric Power Research Institute, EPRI, Palo Alto, Augustus 1990

Lade PV, Yamamuro JA, Liggio CD (2009) Effects of fines content on void ratio, compressibility, and static liquefaction of silty sand. Geomech Eng 1(1):1–15

LeBlanc C, Randolph MF (2008) Interpretation of Piezocones in silt, using cavity expansion and critical state methods. In: The 12th international conference of International Association for Computer Methods and Advances in Geomechanics (IACMAG), Goa, India, 1–6 October 2008

Plewes HD, Davies MP, Jefferies MG (1992) CPT based screening procedure for evaluating liquefaction susceptibility. In: Proceedings of the 45th Canadian geotechnical conference, Toronto, pp 4:1–4:9

Rijkswaterstaat (2007) Voorschrift Toetsen op Veiligheid Primaire Waterkeringen. Ministerie van Verkeer en Waterstaat, Delft, September 2007

Robertson PK (2010) Estimating in-situ state parameter and friction angle in sandy soils from CPT. In: 2nd international symposium on cone penetration testing. Huntington Beach

Schnaid F (2009) In situ testing in geomechanics – the main tests. Taylor & Francis, London/New York, 327 p

Schnaid F, Yu HS (2007) Interpretation of the seismic cone test in granular soils. Géotechnique 57(3):265–272

Shuttle DA, Cunning J (2007) Liquefaction potential of silts from CPTu. Can Geotech J 44:1–19

Shuttle DA, Jefferies MG (1998) Dimensionless and unbiased CPT interpretation in sand. Int J Numer Anal Methods Geomech 22:351–391

Stoutjesdijk TP, de Groot MB (1994) Verificatie SLIQ2D aan de Zeeuwse praktijk. Rapport Grondmechanica, Delft CO-341940/21, April 1994

Tabak F (2011) Analysis of breach flow slides with HMBreach. Deltares, Delft, 1204202.019

TAW (2001). Technisch Rapport Waterkerende Grondconstructies – Geotechnische aspecten van dijken, dammen en boezemkaden. Technische Adviescommisie voor de Waterkering. Delft, Juni 2001

van den Ham GA, de Groot MB, Mastbergen DR (2013) A semi-empirical method to assess flow slide probability. Submarine mass wasting and their consequences. In: 6th international symposium on submarine mass movements and their consequences, Kiel, Germany, 23–25 September 2013

Wride CE, Robertson PK, Biggar KW, Campanella RG, Hofmann BA, Hughes JMO, Küpper A, Woeller DJ (2000) Interpretation of in situ test results from the CANLEX sites. Can Geotech J 37:505–529

Chapter 3
Elemental Distribution and Microfabric Characterization Across a Buried Slump Scar: New Insights on the Long-Term Development and Reactivation of Scar Surfaces from a Microscopic Perspective

Helen Eri Amsler, Eric Reusser, Kitty Milliken, and Michael Strasser

Abstract This study presents a detailed characterization of the sedimentology, microfabric and elemental distributions across a prominent unconformity drilled at 78 m below sea floor at Integrated Ocean Drilling Program (IODP) Site C0004 in the Nankai accretionary prism, offshore Japan. This stratigraphic contact has previously been interpreted as buried landslide scar, which likely experienced multiple failure events. Our study aims at testing this hypothesis and at contributing new insights on the long-term development and reactivation of submarine landslide scars from a microscopic perspective. X-ray fluorescence spectroscopy documents increased values of sulfur and iron across the unconformity. Pyrite mineralization occurring in small fractures immediately below the unconformity is identified with energy dispersive X-ray analysis. Cross-cutting relationships between fractures and pyrite minerals, as imaged by X-ray computed tomography and scanning electron microscopy reveals that precipitation has occurred before the formation of the unconformity. A few mm-to-cm above the studied surface and thus within the overlying hemipelagic sediment, preferred mineral alignment along thin deformation bands are observed. Inferred shear bands are hypothesized as incipient evidence for a potential future submarine landslide. Compiled data confirm the hypothesis of recurrent submarine landslides along the same surface.

Keywords Submarine landslide • IODP • Nankai accretionary prism • SEM-EDX • Mineralization • Microfabrics

H.E. Amsler (✉) • M. Strasser
Geological Institute, ETH Zurich, Zurich, Switzerland
e-mail: sedimentdynamics@erdw.ethz.ch

E. Reusser
Institute of Geochemistry and Petrology, ETH Zurich, Zurich, Switzerland

K. Milliken
Bureau of Economic Geology, University of Texas at Austin, Austin, TX, USA

S. Krastel et al. (eds.), *Submarine Mass Movements and Their Consequences*, Advances in Natural and Technological Hazards Research 37, DOI 10.1007/978-3-319-00972-8_3,

3.1 Introduction

Submarine landslides often occur on continental slopes and especially along active tectonic margins. These mass flows and their related turbidity currents are attracting interest because they pose geohazards, such as tsunamis, to submarine infrastructure as well as to human life in coastal regions (e.g. Yamada et al. 2012). During submarine landslides, thick piles of sediment can be eroded, exposing older and more consolidated strata at the seafloor. With time and ongoing sedimentation the erosional surface is buried and the slope may become "recharged" to potentially fail again in a subsequent submarine mass movement event. Such loading and unroofing cycles should also affect the geochemical equilibrium in the pore water and thus may facilitate dissolution and/or precipitation of mineral phases along critical stratigraphic contacts, which in turn may affect the overall mechanical stability of the surface for future failure events. To investigate such processes of repeated movements along a surface and to test related conceptual hypotheses, however, we often lack access to buried landslide scars deep below the ocean floor. Over the last decade the Integrated Ocean Drilling Program (IODP) has provided samples and data at critical depth for submarine landslides investigation (e.g. IODP Exp 308 in the Gulf of Mexico (Sawyer et al. 2009), IODP Exp 333 Nankai Trough (Strasser et al. 2012) and IODP Exp 340 Lesser Antilles (Expedition 340 Scientists 2012)), and first detailed studies using microstructural analysis on mass transport deposits have been presented in the literature (Behrmann and Meissl 2012).

In this study, we use samples and data obtained through scientific ocean drilling within the IODP Nankai Trough Seismogenic Zone Experiment (NanTroSEIZE). This drilling project acquired several lines of evidence for submarine slumping and mass transport deposits at various drill sites along the active subduction margin offshore SW Japan (Kinoshita et al. 2009; Kitamura and Yamamoto 2012; Strasser et al. 2011, 2012). In particular, we present a detailed characterization of the sedimentology, the elemental distribution and the microfabric across a prominent unconformity drilled at 78 m below the seafloor (mbsf) at Site C0004, located along the upper slope of the outer Nankai accretionary wedge (Fig. 3.1). This stratigraphic contact has previously been interpreted as buried landslide scar, which likely experienced multiple failure events as evidenced by stacked mass transport deposits in an adjacent basin (Strasser et al. 2011). Our study aims at testing this hypothesis and at contributing new insights on the long-term development and reactivation of submarine landslide scar surfaces from a microscopic perspective.

3.2 Geological Setting

Along the Nankai Trough (Fig. 3.1) the Philippine Sea plate is being subducted underneath the Eurasian plate in a northwestward direction at a rate of 4–6 cm/year (e.g. Moore et al. 2009). The SW-NE striking accretionary prism mainly consists

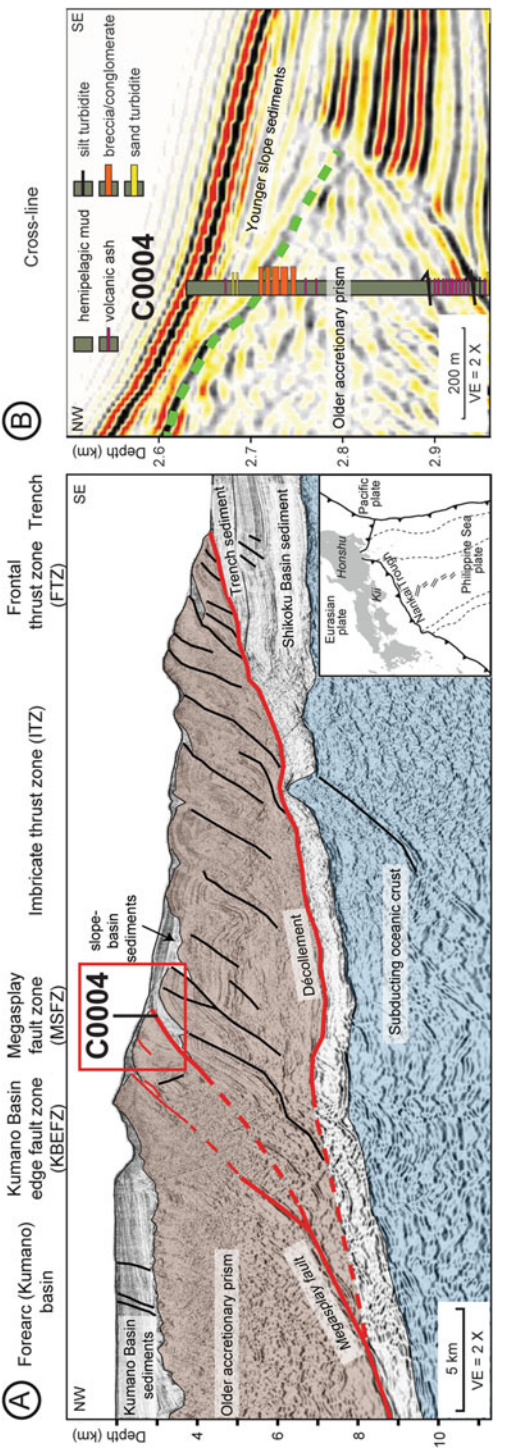

Fig. 3.1 (**a**) Interpreted seismic line with inlet showing the geological setting of the Nankai Trough. (**b**) Close-up of seismic line across Site C0004; *green-dashed line* indicates unconformity (Modified after Moore et al. 2009; Strasser et al. 2011)

of off-scraped and underplated strata from the incoming trench fill and the Shikoku Basin. Our study site is located along the Kumano transect, which is divided into six morphotectonic zones: the trench, the frontal thrust zone (FTZ), the imbricate thrust zone (ITZ), the megasplay fault zone (MSFZ), the Kumano Basin edge fault zone (KBEFZ) and the Kumano fore-arc basin (Moore et al. 2009). Along this transect, the accretionary prism is cut by several landward dipping thrust faults. Beneath the upper slope and the Kumano Basin a regional splay system, termed "megasplay", discontinuously cuts the older accretionary prism (Moore et al. 2009). The shallow part of the MSFZ is a complex thrust system with backward breaking branches that truncate the imbricate thrust faults within the accretionary prism and override younger slope basin sediments (Moore et al. 2009; Strasser et al. 2009).

Site C0004 is located in the hangingwall of the shallow MSFZ. The drilled angular unconformity (dipping about 50° towards SE) corresponds to the transition between the younger hemipelagic slope sediments and the older accretionary prism, which in the uppermost part is brecciated (Kinoshita et al. 2009) (Fig. 3.1). At this unconformity, there is an age gap derived from nannofossil biostratigraphy (between 1.46–1.6 and 2.06–2.512 Ma) and magnetostratigraphic data (between 1.77 and 1.95 Ma) (Kinoshita et al. 2009; Strasser et al. 2011). At another drill site about 1 km further downslope (Site C0008) time equivalent mass transport deposits were found (Strasser et al. 2011). Due to these observations these authors interpreted the prominent stratigraphic contact as a buried landslide scar along which slope failure event(s) excavated part of the upper accretionary prism and slope apron. The contact also represents a mineralization horizon, suggesting a complicated paragenetic sequence that encompasses burial, chemical alteration, erosion and seafloor exposure, followed by burial beneath younger slope sediments.

3.3 Investigation of Remineralization at the Unconformity

In the following section, detailed observation and analysis across the C0004 unconformity are presented, along with a brief introduction of the methods used. Results derived by X-ray Computed Tomography (X-CT), X-ray Fluorescence Spectroscopy (XRF), Scanning Electron Microscopy (SEM) and Energy Dispersive X-ray analysis (EDX) are then discussed towards testing the proposed landslide and mineralization hypothesis.

3.3.1 X-ray Computed Tomography (X-CT)

All cores were scanned immediately after core retrieval using an X-CT instrument onboard *D/V Chikyu* (Kinoshita et al. 2009). X-CT scans show the internal pattern of 3D-objects based on the composition and density/porosity changes.

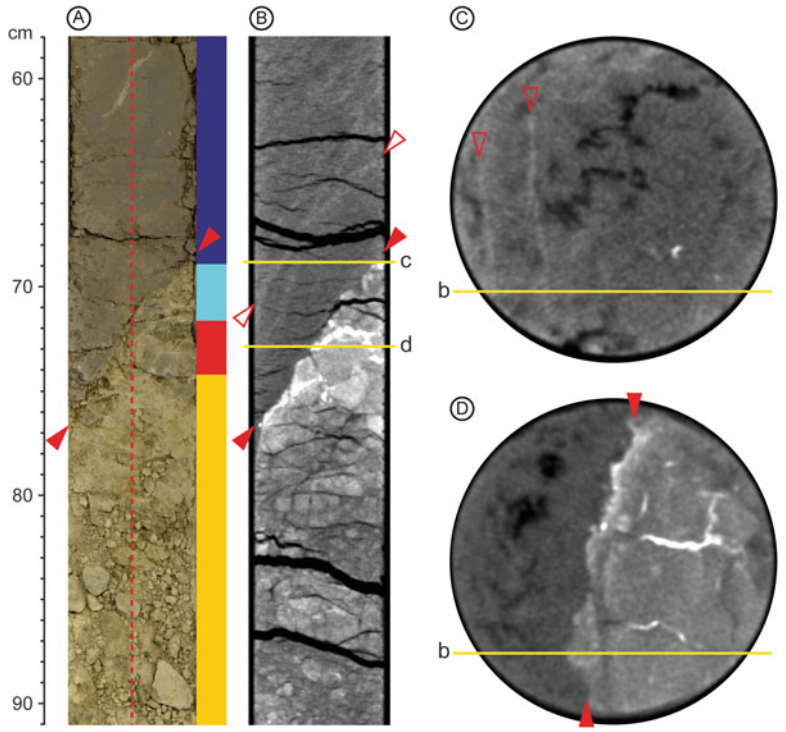

Fig. 3.2 Section 316-C0004C-9H-5 across the unconformity with *red filled triangles* indicating its location. (**a**) Core picture with section depth. *Red dashed line* shows approximate course of the XRF scan and *colors* on the *right* of the core picture correspond to the different intervals in the *core section* shown in Fig. 3.3. (**b**) X-CT image with mineralized fractures below the unconformity and *lighter colored* bands above the unconformity indicated by *red open triangles*. Axial plane in (**c**) shows the *lighter colored* bands and in (**d**) the mineralized fractures. The *horizontal lines b*, *c* and *d* show the approximate position of the corresponding X-CT image. Brightness and contrast of X-CT images are enhanced

Sediments below the unconformity are generally denser and less homogeneous than overlying sediments (Fig. 3.2). Very high CT-numbers (white in Fig. 3.2b, d) suggest the presence of a dense mineral in the first 5 cm below the unconformity. The mineral fills fractures within the sedimentary breccia (Fig. 3.2b, d). Because these mineral-filled fractures end abruptly at the surface of the unconformity, we interpret that mineralization above the unconformity has been eroded.

About 4–5 cm above and parallel to the unconformity surface, there are a few mm-thick bands of slightly higher CT-number. They are visible in the coronal (Fig. 3.2b) as well as in the axial plane (Fig. 3.2c) of the core. It remains unclear from X-CT alone if these bands are related to lithological difference or have arisen by localized compaction or cementation (see further discussion below).

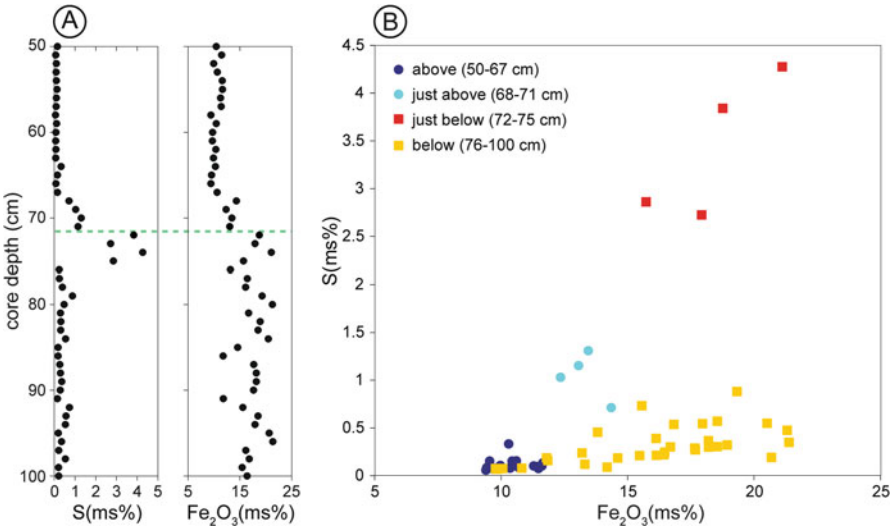

Fig. 3.3 XRF data of sulfur and iron. Approximate *scanning line* depicted in Fig. 3.2 as *red dashed line*. (**a**) Concentration plotted against core section depth; the green dashed line indicates the unconformity. (**b**) Element cross plot. The *colors* correspond to different intervals in the core section (compare to Fig. 3.2)

3.3.2 X-ray Fluorescence Spectroscopy (XRF)

Analysis of the elements Na, Mg, Al, Si, P, S, K, Ca, Ti, Mn, Fe, As, Rb, Sr was performed using the Kochi Core Center (KCC) XRF Core-Imaging Scanner TATSCAN-F2, which provides non-destructive and semi-quantitative measurements on split cores (Sakamoto et al. 2006). The rhodium target was operated at 30 kV accelerating voltage and a current of 0.01 mA. The diameter of the collimator was set to 7 mm and the scanning was performed at an accumulation live time of 150 s. The measured data are reported as intensities (counts per second) on the elemental peak and also in weight percent (ms%) and molecular percent (mol%) of the element oxides. The oxide percentages are calculated from the X-ray intensities using the bulk fundamental parameter approach for the matrix correction (Tertian and Claisse 1982) with the software provided by the vendor of the TATSCAN-F2. Since the surfaces were unpolished (split core surface), elemental data should be considered semi-quantitative at best.

Notable changes across the unconformity are observed in the concentrations of sulfur and iron (Fig. 3.3a). The sulfur values are lower than 1 ms% above and below the unconformity and rise up to the 4–5 fold of the background value at the unconformity. The iron values are rather constant above the unconformity and are higher and more scattered below. The values start to rise at the same depth as the sulfur values. The rise is not abrupt.

When sulfur is plotted against iron (Fig. 3.3b) distinct differences in the different parts of the core section become evident. Above the unconformity sulfur and

iron values are closely clustered and rather low. This suggests that the iron in the sediment covering the unconformity is presumably of terrigenous origin. High values both in sulfur and iron within the first 4 cm below the unconformity (from 72 to 75 cm) are interpreted to be due to Fe-sulfide mineralization, which corresponds to the appearance of aggregates with a high density observed in X-CT images. Low sulfur values combined with high iron values further below the unconformity are probably a signature of Fe-oxides (e.g. as indicated in Figure 10 of Richter et al. (2006)).

Given the positive identification of pyrite by EDX analysis (see below), the co-occurring high sulfur and iron concentrations just below the unconformity are best interpreted in terms of pyrite distribution.

3.3.3 Scanning Electron Microscopy (SEM) and Energy Dispersive X-ray Analysis (EDX)

Mineral analysis with high spatial resolution on a micrometer scale was performed using the SEM (JEOL, JSM 6390LA), which is equipped with a backscattered electron (BSE) detector and an EDX-analyzer. The sample was impregnated with Laromin C 260 and Araldite DY 026 and was coated with carbon by high vacuum evaporation. The EDX measurements were carried out in the high vacuum mode with a voltage of 15 kV and a live time of 30 s. The BSE imaging was utilized to further examine the sediment fabric as seen in the section.

The dense mineral takes the form of cubes and aggregates of cubes. These pyrite cubes occur in spatially restricted aggregations (Fig. 3.4b, c) and are observed only below the unconformity. The aggregates of pyrite fill fractures in the sedimentary breccia, which clearly indicates that pyrite precipitation postdates the deposition of the breccia.

A thin planar feature a few millimetres above and parallel to the unconformity is observed in the thin section (Fig. 3.4a). In SEM photomicrographs, this feature is visible as a band of brighter BSE intensity (Fig. 3.4d, e). Elongated mineral grains (presumably phyllosilicates) in the band are aligned parallel to the orientation of the band itself (indicated with an arrow in Fig. 3.4e). EDX measurements on square areas, both in the bright band and in the surrounding sediment, show the same elemental spectrum.

Of the several possible phyllosilicate alignment processes (Milliken and Reed 2010), planar deformation as indicated by deformation bands, is the most probable one to explain the observed feature. Since there is no difference in the elemental spectra, the higher BSE intensity could arise from porosity loss within the bands, whereby the electron beam intersects more material and thus a stronger signal is generated (Milliken and Reed 2010). Similarly, the thin bands observed in X-CT images are interpreted as such deformation bands, along which shearing, possibly induced by instability and incremental creep of the overlying sedimentary succession, resulted in mineral alignment, shear compaction and porosity reduction.

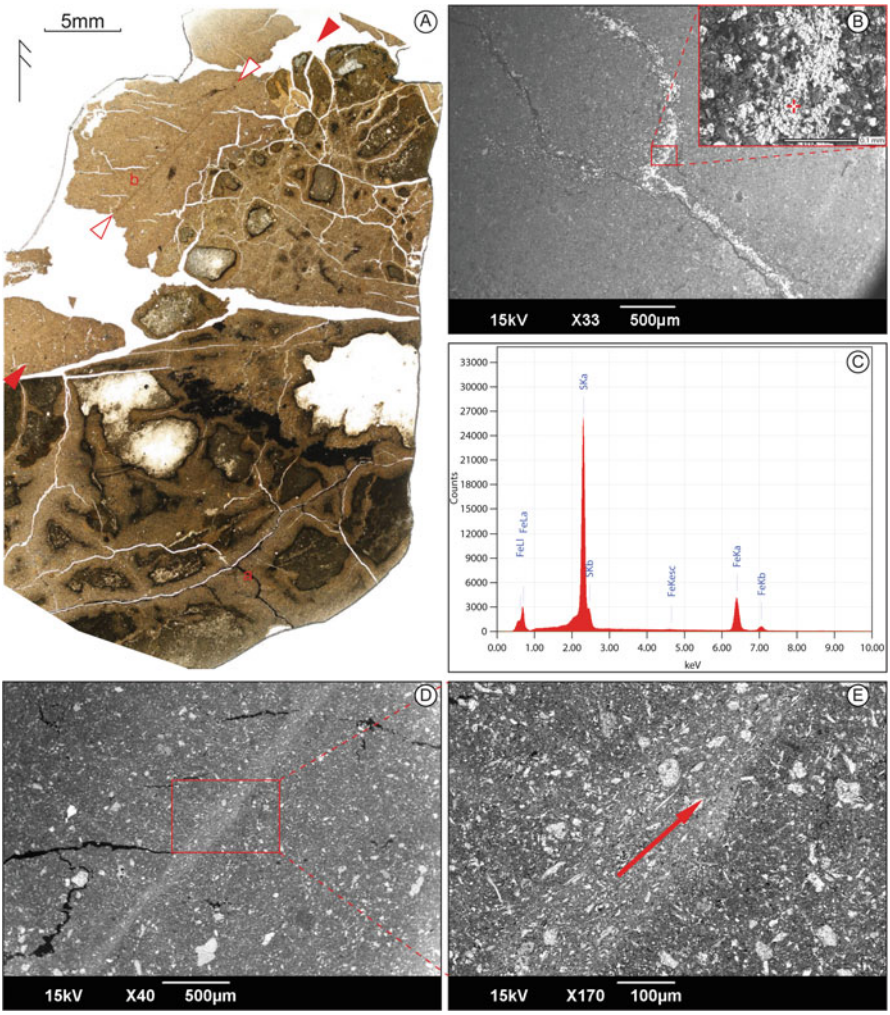

Fig. 3.4 (**a**) Thin section across the unconformity. *Red filled triangles* indicate unconformity; *red open triangles* indicate a deformation band; (**b**) Photomicrograph of point *a* in thin section showing a *pyrite filled crack*; close-up with measuring point of the EDX analysis in (**c**). (**d**) Photomicrograph of point *b* in *thin* section showing the deformation band. (**e**) Close-up of band with aligned mineral grains along the *arrow*

3.4 Discussion and Conclusion

Microscopic observations reveal pyrite mineralization after deposition of the brecciated sediment immediately below the unconformity. Pyrite mineralization must have occurred in a reducing environment and thus is unlikely to have taken place on the seafloor or within the water column, since a pronounced oxygen minimum

zone in this setting cannot be expected. Subsurface pore water sulfate reduction or sulfur-rich deep-sourced fluids rising along faults and stratigraphic contacts are the most likely source of sulfur to react with dissolved iron to form iron sulfides (Berner 1970; Moore and Vrolijk 1992). XRF data indicate that pyrite mineralization is spatially linked to the unconformity, suggesting that at the time of mineralization a predefined stratigraphic contact, buried by younger sediments, was already present. Yet, given that pyrite mineralization is cut abruptly by the unconformity, mineralization must predate a younger erosion phase along the unconformity. Together, the presented data therefore support the hypothesis of multiple slope instabilities along the unconformity.

The deformation bands in the overlying slope sediments indicate shear due to slope movement parallel to the unconformity after burial of an older erosional surface. Shearing is likely linked to gravitational slope instability, potentially enhanced during earthquake shaking events. However, given the fact that the slope cover has not been eroded, progressive shear band propagation during such instability events has not grown to reach a critical shear displacement to initiate "catastrophic" failure and initiation of a submarine landslide (Puzrin et al. 2004). Shear bands, however, can be interpreted as incipient evidence for a potential future submarine landslide, which would likely erode the slope sediments down to the unconformity.

In conclusion, this study displays the potential of microscopic analysis for finding indications of recurrent submarine landslides along the same surface, which, also due to mineralization after burial, evolves as distinct stratigraphic contact over geologic times. The base of a sedimentary package immediately overlying such prominent stratigraphic surfaces then is likely a locus for instability by shear band propagation and initiation of recurrent landslide events.

Acknowledgments Samples and data for this research were provided by the Integrated Ocean Drilling Program (IODP). The dedication of the researchers, technicians and curation staff at Kochi Core Center is greatly appreciated. This study was supported by the Swiss National Science Foundation (grant Nr. PP00P2-133481). The authors acknowledge the constructive comments by the reviewers Susann Henkel and Yuzuru Yamamoto. Further thanks go to Judith McKenzie, Weiren Lin and Frowin Pirovino.

References

Behrmann JH, Meissl S (2012) Submarine landslides, Gulf of Mexico continental slope: insights into transport processes from fabrics and geotechnical data. In: Yamada Y, Kawamura K, Ikehara K, Ogawa Y, Urgeles R, Mosher D, Chaytor J, Strasser M (eds) Submarine mass movements and their consequences, vol 31, Advances in natural and technological hazard research. Springer, Dordrecht, pp 463–472

Berner RA (1970) Sedimentary pyrite formation. Am J Sci 268(1):1–23

Expedition 340 Scientists (2012) Lesser Antilles volcanism and landslides: implications for hazard assessment and long-term magmatic evolution of the arc. IODP Prelim Rep 340. doi:10.2204/iodp.pr.340.2012. http://publications.iodp.org/preliminary_report/340/340pr_2.htm

Kinoshita M, Tobin H, Ashi J, Kimura G, Lallement S, Screaton EJ, Curewitz D, Masago H, Moe KT, and the Expedition Scientists (2009) Proceedings of the integrated ocean drilling program, vol 314/315/316. Integrated Ocean Drilling Management International, Inc., Washington, DC. doi:10.2204/iodp.proc.314315316.2009

Kitamura Y, Yamamoto Y (2012) Records of submarine landslides in subduction input recovered by IODP expedition 322, Nankai Trough, Japan. In: Yamada Y, Kawamura K, Ikehara K, Ogawa Y, Urgeles R, Mosher D, Chaytor J, Strasser M (eds) Submarine mass movements and their consequences, vol 31, Advances in natural and technological hazard research. Springer, Dordrecht, pp 659–670

Milliken KL, Reed RM (2010) Multiple causes of diagenetic fabric anisotropy in weakly consolidated mud, Nankai accretionary prism, IODP expedition 316. J Struct Geol 32(12):1887–1898

Moore JC, Vrolijk P (1992) Fluids in accretionary prisms. Rev Geophys 30(2):113–135

Moore GF, Park J-O, Bangs NL, Gulick SP, Tobin HJ, Nakamura Y, Sato S, Tsuji T, Yoro T, Tanaka H, Uraki S, Kido Y, Sanada Y, Kuramoto S, Taira A (2009) Structural and seismic stratigraphic framework of the NanTroSEIZE Stage 1 transect. In: NanTroSEIZE stage 1: investigations of seismogenesis, Nankai Trough, Japan. Proceedings of the integrated ocean drilling program 314/315/316

Puzrin AM, Germanovich LN, Kim S (2004) Catastrophic failure of submerged slopes in normally consolidated sediments. Géotechnique 54(10):631–643

Richter TO, van der Gaast S, Koster B, Vaars A, Gieles R, de Stigter HC, De Haas H, van Weering TCE (2006) The Avaatech XRF Core Scanner: technical description and applications to NE Atlantic sediments. Geol Soc Lond Spec Pub 267(1):39–50

Sakamoto T, Kuroi K, Sugawara T, Aoike K, Iijima K, Sugisaki S (2006) Non-destructive X-ray fluorescence (XRF) core-imaging scanner, TATSCAN-F2. Sci Drill 2:37–39

Sawyer DE, Flemings PB, Dougan B, Germaine JT (2009) Retrogressive failures recorded in mass transport deposits in the Ursa Basin, Northern Gulf of Mexico. J Geophys Res 114:B10102

Strasser M, Moore GF, Kimura G, Kitamura Y, Kopf AJ, Lallemant S, Park J-O, Screaton EL, Su X, Underwood MB, Zhao X (2009) Origin and evolution of a splay fault in the Nankai accretionary prism. Nat Geosci 2:648–652

Strasser M, Moore GF, Kimura G, Kopf AJ, Underwood MB, Guo JH, Screaton EJ (2011) Slumping and mass transport deposition in the Nankai fore arc: evidence from IODP drilling and 3-D reflection seismic data. Geochem Geophys Geosyst 12:Q0AD13

Strasser M, Henry P, Kanamatsu T, Thu MK, Moore GF, Expedition Scientists (2012) Scientific drilling of mass-transport deposits in the Nankai accretionary wedge: first results from IODP Expedition 333. In: Yamada Y, Kawamura K, Ikehara K, Ogawa Y, Urgeles R, Mosher D, Chaytor J, Strasser M (eds) Submarine mass movements and their consequences, vol 31, Advances in natural and technological hazard research. Springer, Dordrecht, pp 671–681

Tertian R, Claisse F (1982) Principles of quantitative X-ray fluorescence analysis. Heyden, London

Yamada Y, Kawamura K, Ikehara K, Ogawa Y, Urgeles R, Mosher D, Chaytor J, Strasser M (2012) Submarine mass movements and their consequences. In: Yamada Y et al (eds) Submarine mass movements and their consequences, vol 31, Advances in natural and technological hazard research. Springer, Dordrecht, pp 1–12. doi:10.1007/978-94-007-2162-3_1

Chapter 4
Evidence for Mass Transport Deposits at the IODP JFAST-Site in the Japan Trench

Hiske G. Fink, Michael Strasser, Miriam Römer, Martin Kölling, Ken Ikehara, Toshiya Kanamatsu, Dominik Dinten, Arata Kioka, Toshiya Fujiwara, Kiichiro Kawamura, Shuichi Kodaira, Gerold Wefer, and R/V Sonne SO219A Cruise Participants

Abstract Several studies indicate that the 2011 Tohoku-Oki earthquake (M_w 9.0) off the Pacific coast of Japan has induced slip to the trench and triggered landslides in the Japan Trench. In order to better understand these processes, detailed mapping and shallow-coring landslides at the trench as well as Integrated Ocean Drilling Program (IODP) deep drilling to recover the plate boundary décollement (Japan Trench Fast Earthquake Drilling Project, JFAST) have been conducted. In this study we report sediment core data from the rapid response *R/V SONNE* cruise (*SO219A*) to the Japan Trench, evidencing a Mass Transport Deposit (MTD) in the uppermost section later drilled at this JFAST-site during IODP Expedition 343. A 8.7 m long gravity core (GeoB16423-1) recovered from ~7,000 m water depth reveals a 8 m sequence of semi-consolidated mud clast breccias embedded

H.G. Fink (✉) • M. Römer • M. Kölling • G. Wefer
MARUM – Center for Marine Environmental Sciences, University of Bremen, Bremen, Germany
e-mail: hfink@marum.de

M. Strasser • D. Dinten
Geological Institute, ETH Zurich, Zurich, Switzerland

K. Ikehara
AIST, Geological Survey Japan, Ibaraki, Japan

T. Kanamatsu • T. Fujiwara • S. Kodaira
IFREE, JAMSTEC, Yokosuka, Japan

A. Kioka
AORI, Tokyo University, Tokyo, Japan

K. Kawamura
Departement of Geosphere Science, Yamaguchi University, Yamaguchi, Japan

R/V Sonne SO219A Cruise Participants:
Christian dos Santos Ferreira (MARUM, University of Bremen, Germany), Patrizia Geprägs (MARUM, University of Bremen, Germany), Kazuya Ishitsuka (University of Kyoto, Japan), Yann Marcon (MARUM, University of Bremen, Germany), Lina Podszun (MARUM, University of Bremen, Germany), Takeshi Sato (JAMSTEC, Japan)

S. Krastel et al. (eds.), *Submarine Mass Movements and Their Consequences*, Advances in Natural and Technological Hazards Research 37, DOI 10.1007/978-3-319-00972-8_4,

in a distorted chaotic sediment matrix. The MTD is covered by a thin veneer of 50 cm hemipelagic, bioturbated diatomaceous mud. This stratigraphic boundary can be clearly distinguished by using physical properties data from Multi Sensor Core Logging and from fall-cone penetrometer shear strength measurements. The geochemical analysis of the pore-water shows undisturbed linear profiles measured from the seafloor downcore across the stratigraphic contact between overlying younger background-sediment and MTD below. This indicates that the investigated section has not been affected by a recent sediment destabilization in the course of the giant Tohoku-Oki earthquake event. Instead, we report an older landslide which occurred between 700 and 10,000 years ago, implying that submarine mass movements are dominant processes along the Japan Trench. However, they occur on local sites and not during each megathrust earthquake.

Keywords Japan Trench • Tohoku-Oki earthquake • IODP-JFAST • Mass-transport deposit • Physical properties • Geochemistry

4.1 Introduction

Since the Grand Banks earthquake off Newfoundland and the subsequent submarine landslides and landslide-induced tsunami (e.g. Heezen and Ewing 1952; Fine et al. 2005), the science community became aware that earthquakes can trigger submarine slope failures initiating large-scale downslope sediment mass transfer, causing tsunamis and shaping seafloor topography (e.g. Hampton et al. 1996). In the aftermath of the 2011 Tohoku-Oki earthquake (M_w 9.0) off the Pacific coast of Japan, several studies are now being conducted to identify and study earthquake-related submarine landslides processes in the Japan Trench and its potential link to the devastating tsunami event (Fujiwara et al. 2011; Kawamura et al. 2012; Strasser et al. 2013; Ikehara 2012). This study aims to contribute to this research by presenting detailed sedimentological, physical property and geochemical observation and measurements, respectively, from a gravity core that recovered the uppermost 8.7 m of the sedimentary succession at the same location, where the Integrated Ocean Drilling Program (IODP) has conducted the Japan Trench Fast Earthquake Drilling Project (JFAST; Chester et al. 2012). Here we report data from the shallow subsurface, in order to unravel if the slope region around the JFAST-site has been affected by submarine landslides related to the 2011 earthquake or to earlier events.

4.2 Background and Geological Setting

The Japan Trench convergent margin stretches some 700 km parallel to the northern Japanese island Honshu (Fig. 4.1a). Here, the Pacific plate underthrusts the Okhotsk plate with a convergence rate of 8.0 to 8.6 cm/year to NW direction (DeMets et al.

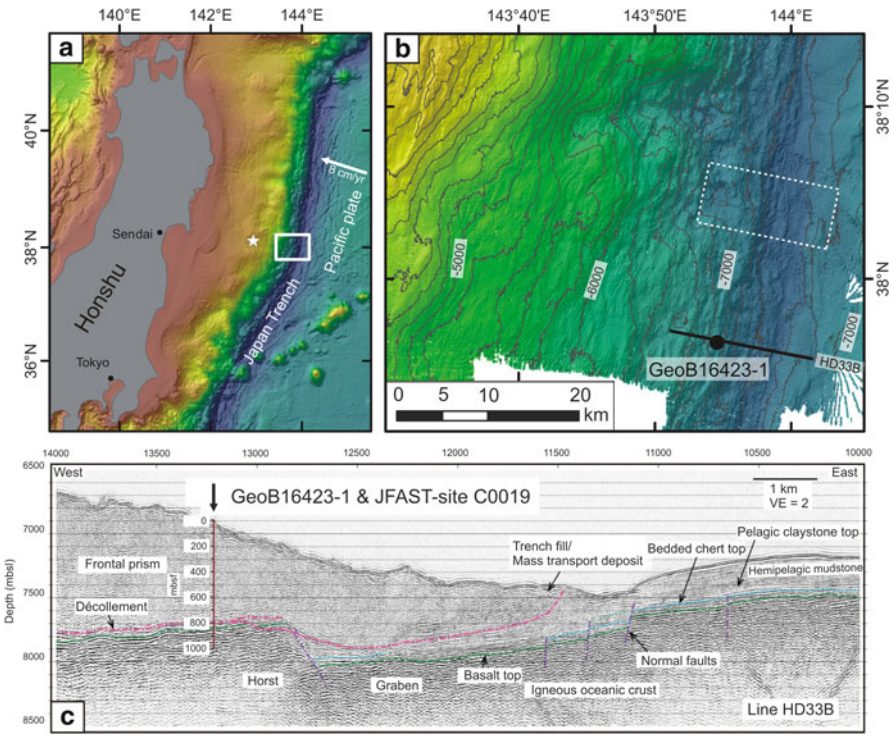

Fig. 4.1 (**a**) Overview map of Japan Trench convergent margin off northern Honshu; the *star* shows the location of the 2011 Tohoku-Oki epicentre; the *box* indicates the study area. (**b**) Bathymetric map of the study area: Shown are the sampling location of sediment core GeoB16423-1 at the JFAST-site and the track of seismic line HD33B (Chester et al. 2012); the *dashed rectangle* indicates the area where major changes in seafloor morphology triggered by the 2011 earthquake have been observed (see e.g. Kodaira et al. 2012). (**c**) seismic line HD33B (partially interpreted) through JFAST-site modified after Chester et al. (2012); sampling location of sediment core GeoB16423-1 and JFAST-site C0019 is indicated

2010). The Japan Trench subduction zone is characterised by tectonic erosion in contrast to sediment accretion as e.g. in the Nankai trough (Taira and Ogawa 1991). This is evidenced by the subsidence of the continental crust associated with basal subduction erosion of the upper plate, as well as by the absence of young accreted strata (Scientific Party 1980). The frontal prism in the deep Japan Trench is mainly composed by sediments originating from the (partly unstable) continental slope and, moreover, multichannel seismic records revealed that a major portion of the incoming sediments are subducted (Tsuru et al. 2002). These processes caused a landward retreat of the trench at least since the Miocene (Scientific Party 1980; von Huene and Lallemand 1990).

The Japan Trench subduction plate boundary system is an active seismogenic zone, where frequently large, tsunamigenic megathrust earthquakes occur. Since the

seventeenth century there are 8 M ≥7 and 4 M ≥8 earthquakes known from the region (Tajima et al. 2013), which was hit most recently in March 2011 by the giant (M_w) 9.0 Tohoku-Oki earthquake. The 2011 Tohoku-Oki megathrust earthquake was larger than anticipated for this region and numerous studies analysing seismic, geodetic and tsunami data of the Tohoku-Oki event revealed that propagating rupture at the plate's interface has reached the trench floor (see review by Tajima et al. 2013). The coseismic slip resulted in the horizontal displacement of the overriding plate of ∼50 m to SE and in a vertical uplift of ∼10 m (Fujiwara et al. 2011).

The Tohoku-Oki earthquake triggered a devastating tsunami, which hit the Pacific coast of northern Honshu with run-up heights of up to 40 m (Mori et al. 2011). Tsunami waveform inversion analysis indicates that the tsunami was generated by both, a deep interplate slip and large displacement near the trench axis (Fujii et al. 2011). In fact, prominent changes in seafloor morphology in the course of the 2011 earthquake have been found east of the epicentre (∼38°10′ N), at the trench axis and the lowermost continental slope, respectively (Fig. 4.1b, Fujiwara et al. 2011). Here, differential bathymetry data revealed 50 m up- and downward changes in seafloor elevation (Fujiwara et al. 2011), which have been suggested to result from earthquake propagation to the trench and a major earthquake-triggered rotational slump (Kodaira et al. 2012; Strasser et al. 2013). Additionally, further to the north along the continental slope (∼38°40′ N), fresh open fractures and sharp scars have been observed on the seafloor, indicating recent fracturing and sliding possibly induced by the Tohoku-Oki earthquake (Kawamura et al. 2012).

The study site presented here is located on the lower slope around 20 km south of the area where major changes in seafloor morphology in the course of the Tohoku-Oki event have been observed. Here the rapid response IODP-JFAST project was conducted subsequent to the 2011 earthquake (Chester et al. 2012). JFAST was aimed to recover sediment core from the plate boundary décollement and to investigate the level of frictional stress and further physical characteristics therein, in order to better understand the physical mechanisms and dynamics of large slip earthquakes (Chester et al. 2012). Due to challenging water depth and limited amount of operation time, JFAST coring was only conducted below 176 m below seafloor (mbsf) and therefore unable to provide sediment core data from possible 2011 triggered slope failures.

4.3 Material and Methods

In order to characterize and study the slope region and shallow subsurface sediments of the JFAST-site, detailed multibeam bathymetry mapping and sediment sampling by gravity coring has been conducted during expedition *SO219A* with the German *R/V SONNE* in March 2012 about one year after the 2011 Tohoku-Oki earthquake.

4.3.1 Bathymetric Mapping

A KONGSBERG multibeam echosounder EM120 has been used to record the bathymetric data along the Japan Trench. The operational mode onboard *R/V SONNE* has a frequency of 12 kHz and uses 191 beams with a total swath width of 150°, resulting in 2° resolution (footprint). The data is real time motion compensated. MB-System software was used for post-processing of the data and resulting grids were visualized with Esri Arcmap 10.0.

4.3.2 Sediment Core

During *SO219A* cruise, prior to IODP JFAST drilling, a sediment core (GeoB16423-1) has been collected along continental slope of the Japan Trench at IODP JFAST-site C0019 (37°56.301′ N, 143°54.840′ E). The core was recovered from a water depth of 6,936 m by using a gravity corer (1.5 t weight, 12 m pipe length).

4.3.2.1 Physical Properties

Undrained shear strength was determined on the working half of the sediment core by using a Wykeham-Farrance cone penetrometer WF 21600 and following the procedures after Wood (1985). Core photographs and gamma density of the sediment were obtained with a *Geotek* Multi Sensor Core Logger at MARUM-Center for Marine Environmental Sciences, University of Bremen. Data were processed following the procedure after Blum (1997).

4.3.2.2 Pore-Water Analyses

The closed sediment core was sampled onboard *R/V SONNE* immediately after core retrieval for interstitial water by using rhizon samplers (Seeberg-Elverfeldt et al. 2005). The samples were analysed offshore for alkalinity and ammonium.

4.4 Results

The bathymetry around the study site shows generally a rough topography. Overall, the lower continental slope in the area has an average slope angle of ∼4° but locally dip to more than 7°. Reflection seismic profiles published in Chester et al. (2012; Fig. 4.1c) image the frontal prism as a wedge shaped body with an acoustically chaotic character and without continuous reflectors (Chester et al. 2012).

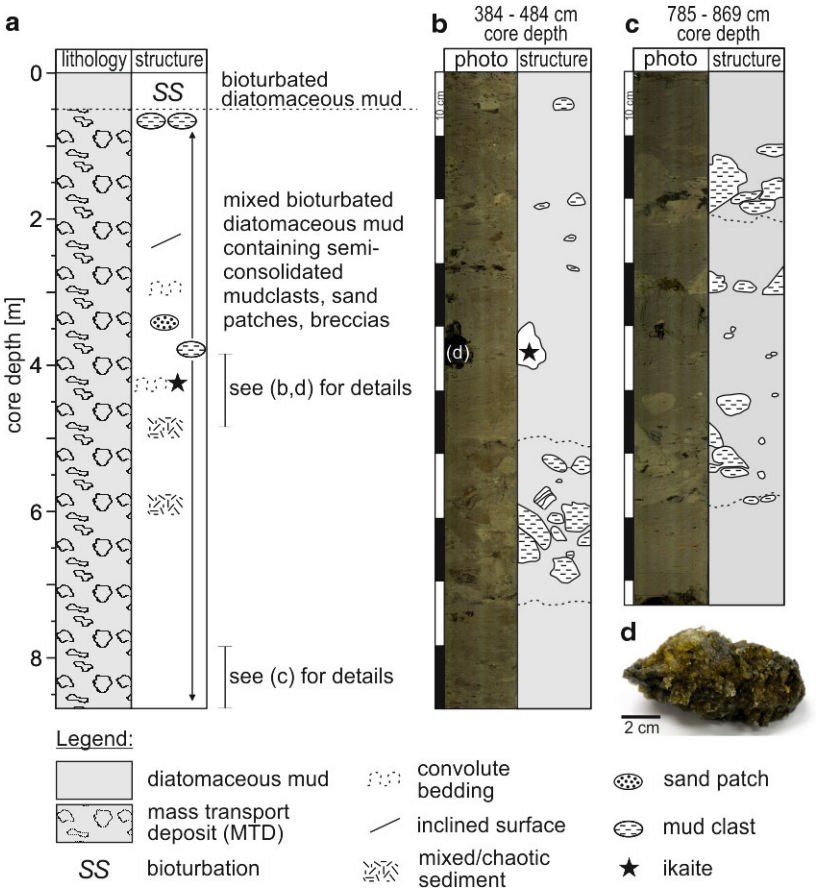

Fig. 4.2 Sedimentary data of core GeoB16423-1: (**a**) core description; (**b**), (**c**) core photographs and detailed structures of selected core intervals: (**b**) 384–484 cm and (**c**) 785–869 cm core depth; (**d**) photograph of the cleaned authigenic mineral ikaite, scale bar 2 cm, the sampling position is indicated in (**b**)

The sediment core GeoB16423-1 has a total length of 869 cm (Fig. 4.2a). The upper 50 cm consist of hemipelagic bioturbated silt containing diatoms, radiolarians and sponge spicules as well as volcaniclastic components like e.g. glass shards. In the entire section below, the sediments are characterised by semi-consolidated (mud-) clasts, sand patches and breccias embedded in a chaotic distorted sediment matrix. The clasts are up to 7 cm in diameter and consist of different lithologies with varying colours (Fig. 4.2). In a core depth of 430 cm, a large (6 cm in diameter, see Fig. 4.2b, d) translucent amber authigenic mineral has been formed, that has been identified as ikaite (calcium carbonate hexahydrate; Suess et al. 1982).

The shear strength values obtained on the sediment core vary between ~3 and ~220 kPa (Fig. 4.3b). For the upper 50 cm the shear strength gradually increases

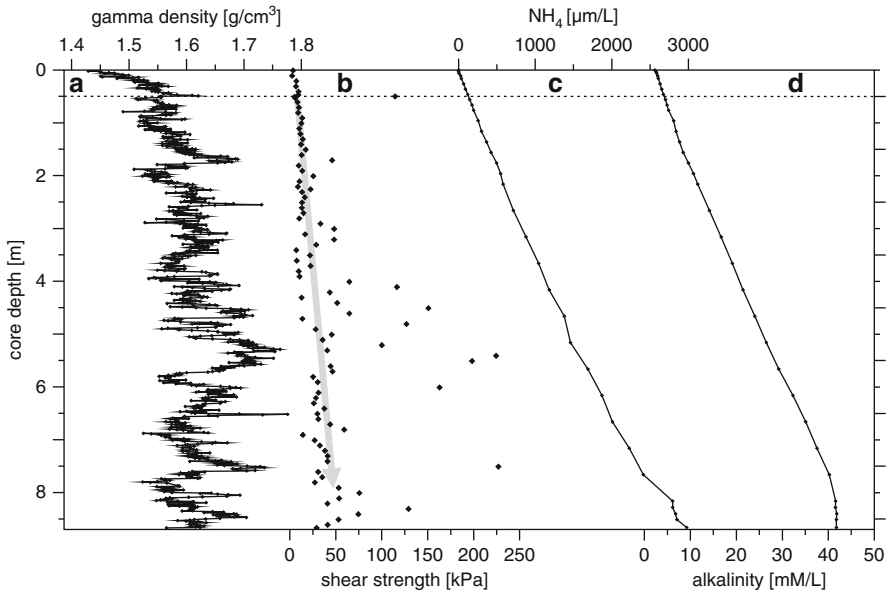

Fig. 4.3 Physical properties and geochemical data of sediment core GeoB16423-1: (**a**) density [g cm^{-3}]; (**b**) undrained shear strength [kPa], the *arrow* indicates the overall down-core increasing trend; (**c**) ammonium [µm/L]; (**d**) alkalinity [mM/L]

from 3 to 10 kPa. Below, within the distorted sediment sequence, the shear strength shows a scattering pattern. High values mainly represent the embedded breccias and mud clasts, whereas the shear strength of the sediment matrix reveals a rather gradual downcore increase to ~50 kPa.

A similar pattern is evident in the bulk density of the sediment (Fig. 4.3a). Within the upper sediment sequence the density increases linearly from around 1.44 g cm^{-3} at the top to 1.6 g cm^{-3} in a core depth of 50 cm. In contrast, the chaotic sediments beneath are characterised by highly variable values between 1.53 and 1.75 g cm^{-3}.

Overall the geochemical pore-water profiles show linear trends (Fig. 4.3c, d). Samples obtained on the core top, reveal values in equilibrium with seawater. Further down-core alkalinity and ammonium values increase linearly with depth.

4.5 Discussion

4.5.1 Evidencing Mass Transport Deposits at the JFAST-Site

The sedimentary record of core GeoB16423-1 gives clear evidence for submarine mass movements at the study site: The sedimentary and physical properties data

of the core allow to distinguish between two distinct stratigraphic units within the obtained sediment sequence. The upper unit (0–50 cm, Fig. 4.2a), consisting of bioturbated diatomaceous mud and characterised by a gradual downcore increase in density and shear strength, is considered to reflect hemipelagic sedimentation processes.

The second unit comprises the ∼8 m long chaotic sediment sequence below, which reveals characteristics of a Mass Transport Deposit (MTD) embedding various mud clasts and breccias in a distorted sediment matrix (Fig. 4.2). The scattering bulk density of this unit shows the inhomogeneous distribution within the reworked material of the MTD (Fig. 4.3a). Moreover, the clasts within this unit reveal various lithologies. Their scattered varyingly high (up to 220 kPa) shear strength values likely reflect their previous consolidation states. This may indicate different source regions or, alternatively, different previous subsurface depths of the components mobilized by submarine landslide processes and subsequently embedded within the MTD. In contrast, the general trend of downward increasing shear strength of the matrix sediment is considered to represent the overall consolidation state of the MTD (Fig. 4.3b).

Reflection seismic data from the study area depict a mass-transport influenced deposition of the sedimentary trench-fill (Chester et al. 2012). However, at the coring site this data fails in exploiting the presence of similar MTDs. This is due to the chaotic reflection pattern of the frontal prism that likely results from the presence of inclined and faulted bedding and the relatively uniform physical properties of the sediment (Chester et al. 2012). The combination of seismic (Chester et al. 2012) and shallow sediment core data presented here reveals that the continental slope and trench south of 38° N has also experienced slope failure and mass movements, similar as observed in other parts of the Japan Trench (Fujiwara et al. 2011; Kawamura et al. 2012; Strasser et al. 2013).

4.5.2 Estimating the Age of the MTD Formation

The question arises if the MTD described here is linked to the 2011 Tohoku-Oki earthquake, as suggested for a large slump northward of the study site (Kodaira et al. 2012; Strasser et al. 2013), or related to an older event. A useful tool to date relatively young sediment remobilisation is pore-water geochemistry: Several studies have shown the impact of submarine mass-movement events on the shape of steady state pore-water profiles, subsequently to the disturbance often resulting in kink-shaped profiles (e.g. Henkel et al. 2012; Völker et al. 2011). Over time molecular diffusion causes a transition to a concave shape until a linear profile again indicates the steady state of the pore-water. Modelling approaches allow to re-calculate the time since the disturbance, thus to date the event. However,

since these processes occur in a certain period, this method enables only to date sedimentary sequences remobilised in a maximum of several 1,000 years before sampling (Henkel et al. 2012).

By analysing the pore-water profiles of the core in detail, no distinct features indicating a recent sediment remobilisation are evident. In fact, the linear trends of the pore-water profiles are typical of undisturbed records and represent normal values for a region characterized by high marine productivity (Schulz 2006) like here off Honshu (Antoine et al. 1996). This is supplemented by the presence of the authigenic mineral ikaite, which precipitates in organic carbon-rich deep-marine sediments (Suess et al. 1982).

With respect to determine the age of the MTD the linear pore-water profiles exclude to apply any modelling approach. However, as very recent mixing with seawater would be evident in pore-water geochemistry this implies in turn, that the MTD deposition is not related to the giant 2011 earthquake occurring only one year before core recovery.

We can estimate a maximum age of the MTD by using the thickness of the 50 cm hemipelagic top unit and sedimentation rates reported from the region, ranging between 5 and 70 cm/kyr (Suyehiro et al. 2003). Thus, we suggest that the post-MTD hemipelagic background sediments have been deposited within the past ~700–10,000 years.

4.6 Conclusions

The sedimentary record obtained from the uppermost sediment sequence at the JFAST-site along the continental slope of the Japan Trench gives clear evidence for submarine mass movements. The MTD emplacement here was not related to the giant 2011 Tohoku-Oki earthquake, which caused a major slope failure north of the study site. Instead, lithological and geochemical data reveal that the studied MTD is older and represents a submarine landslide event that occurred between 700 and 10,000 years ago. This indicates that submarine landsliding is a dominant process along the Japan Trench convergent margin, but occurring on local sites and not during each megathrust earthquake. Considering studies aiming to use MTDs for paleo-seismology these results show that a sound understanding of the local sedimentation regime is essential.

Acknowledgments We thank captain and crew of *R/V SONNE* for onboard assistance during cruise *SO219A* in 2012. The cruise and the research leading to this study were funded by the German Bundesministerium für Bildung und Forschung (BMBF) and the Deutsche Forschungsgemeinschaft (DFG-project WE 992/58-1) and was supported by the DFG-Research Center/Cluster of Excellence "The Ocean in the Earth System". Vera Lukies is kindly thanked for lab assistance with the MSCL Core Scanner at MARUM-Center for Marine Environmental Sciences, University of Bremen, Germany. We further acknowledge B. McAdoo and J. Geersen for their constructive reviews. All data are available via the database Pangaea (http://www.pangaea.de).

References

Antoine D, André J-M, Morel A (1996) Oceanic primary production: 2. Estimation at global scale from satellite (Coastal Zone Color Scanner) chlorophyll. Global Biogeochem Cycles 10(1):57–69. doi:10.1029/95gb02832

Blum P (1997) Physical properties handbook: a guide to the shipboard measurement of physical properties of deep-sea cores. Ocean drilling program technical note 26. doi:10.2973/odp.tn.26.1997

Chester FM, Mori JJ, Toczko S, Eguchi N, The Expedition 343/343T Scientists (2012) Japan Trench Fast Drilling Project (JFAST). Integrated ocean drilling program preliminary report 343/343T. doi:10.2204/iodp.pr.343343T.2012

DeMets C, Gordon RG, Argus DF (2010) Geologically current plate motions. Geophys J Int 181(1):1–80. doi:10.1111/j.1365-246X.2009.04491.x

Fine IV, Rabinovich AB, Bornhold BD, Thomson RE, Kulikov EA (2005) The Grand Banks landslide-generated tsunami of November 18, 1929: preliminary analysis and numerical modeling. Mar Geol 215(1–2):45–57. doi:10.1016/j.margeo.2004.11.007

Fujii Y, Satake K, Si S, Shinohara M, Kanazawa T (2011) Tsunami source of the 2011 off the Pacific coast of Tohoku earthquake. Earth Planets Space 63(7):815–820

Fujiwara T, Kodaira S, No T, Kaiho Y, Takahashi N, Kaneda Y (2011) The 2011 Tohoku-Oki earthquake: displacement reaching the trench axis. Science 334(6060):1240. doi:10.1126/science.1211554

Hampton MA, Lee HJ, Locat J (1996) Submarine landslides. Rev Geophys 34(1):33–59. doi:10.1029/95rg03287

Heezen BC, Ewing WM (1952) Turbidity currents and submarine slumps, and the 1929 Grand Banks [Newfoundland] earthquake. Am J Sci 250(12):849–873. doi:10.2475/ajs.250.12.849

Henkel S, Schwenk T, Hanebuth TJ, Strasser M, Riedinger N, Formolo M, Tomasini J, Krastel S, Kasten S (2012) Pore water geochemistry as a tool for identifying and dating recent mass-transport deposits. In: Yamada Y et al (eds) Submarine mass movements and their consequences, vol 31, Advances in natural and technological hazards research. Springer, Dordrecht, pp 87–97. doi:10.1007/978-94-007-2162-3_8

Ikehara K (2012) Offshore earthquake- and/or tsunami-induced sediment transports and their deposits: Importance of marine sediment study for understanding past earthquakes and tsunami. J Sedimentol Soc Jpn 71(2):141–147

Kawamura K, Sasaki T, Kanamatsu T, Sakaguchi A, Ogawa Y (2012) Large submarine landslides in the Japan Trench: a new scenario for additional tsunami generation. Geophys Res Lett 39(5):L05308. doi:10.1029/2011gl050661

Kodaira S, No T, Nakamura Y, Fujiwara T, Kaiho Y, Miura S, Takahashi N, Kaneda Y, Taira A (2012) Coseismic fault rupture at the trench axis during the 2011 Tohoku-oki earthquake. Nat Geosci 5(9):646–650

Mori N, Takahashi T, Yasuda T, Yanagisawa H (2011) Survey of 2011 Tohoku earthquake tsunami inundation and run-up. Geophys Res Lett 38:L00G14. doi:10.1029/2011gl049210

Party S (1980) Initial reports of the deep sea drilling project 56/57. U.S. Government Printing Office, Washington, DC

Schulz HD (2006) Quantification of early diagenesis: dissolved constituents in pore water and signals in the solid phase. In: Schulz HD, Zabel M (eds) Marine geochemistry. Springer, Berlin/Heidelberg, pp 73–124

Seeberg-Elverfeldt J, Schlüter M, Feseker T, Kölling M (2005) Rhizon sampling of porewaters near the sediment-water interface of aquatic systems. Limnol Oceanogr Methods 3:361–371

Strasser M, Kölling M, dos Santos Ferreira C, Fink HG, Fujiwara T, Henkel S, Ikehara K, Kanamatsu T, Kawamura K, Kodaira S, Römer M, Wefer G, The R/V Sonne Cruise SO219A and JAMSTEC Cruise MR12-E01 scientists (2013) A slump in the trench: tracking the impact of the 2011 Tohoku-Oki earthquake. Geology 41(8):935–938. doi:10.1130/g34477.1

Suess E, Balzer W, Hesse KF, Müller PJ, Ungerer CA, Wefer G (1982) Calcium carbonate hexahydrate from organic-rich sediments of the Antarctic shelf: precursors of glendonites. Science 216(4550):1128–1131. doi:10.1126/science.216.4550.1128

Suyehiro K, Sacks IS, Acton GD, Oda M (2003) Proceedings of the ODP, scientific results, vol 186, College Station, TX (Ocean Drilling Program). doi:102973/odpprocsr1862003

Taira A, Ogawa Y (1991) Cretaceous to Holocene forearc evolution in Japan and its implication to crustal dynamics. Episodes 14(3):205–212

Tajima F, Mori J, Kennett BLN (2013) A review of the 2011 Tohoku-Oki earthquake (Mw 9.0): large-scale rupture across heterogeneous plate coupling. Tectonophysics 586:15–34

Tsuru T, Park J-O, Miura S, Kodaira S, Kido Y, Hayashi T (2002) Along-arc structural variation of the plate boundary at the Japan Trench margin: implication of interplate coupling. J Geophys Res 107(B12):2357. doi:10.1029/2001jb001664

Völker D, Scholz F, Geersen J (2011) Analysis of submarine landsliding in the rupture area of the 27 February 2010 Maule earthquake, Central Chile. Mar Geol 288(1–4):79–89

von Huene R, Lallemand S (1990) Tectonic erosion along the Japan and Peru convergent margins. Geol Soc Am Bull 102(6):704–720. doi:10.1130/0016-7606(1990)102<0704:teatja>2.3.co;2

Wood DM (1985) Some fall-cone tests. Géotechnique 38:64–68

Chapter 5
Preliminary Investigations of Rheological Properties of Busan Clays and Possible Implications for Debris Flow Modelling

Sueng Won Jeong, Sang-Nam Yoon, Sung-Sik Park, Gil Young Kim, Seong-Pil Kim, Jang-Jun Bahk, Nyeon-Keon Kang, Sang Hoon Lee, and Sung-Gyo Chung

Abstract To investigate the post-failure dynamics of subaerial and subaqueous landslides in various environments, we need a detailed analysis of the geotechnical and rheological behaviour of fine-grained sediments. For fine-grained sediments found in the subaerial and subaqueous environments, rheological research should be conducted as a prelude to understanding flow behaviour and hazard assessment. In this paper, the rheological characteristics of Busan clays from the Nakdong deltaic plain are examined in a shear rate-controlled system. A comparison is made between the Busan clays and low-activity clays in terms of rheometer geometry. Flow curves obtained from the controlled shear rate and the shear stress mode are examined. The viscosity and yield stresses obtained from different geometries, which may produce wall-slip among cylinder, ball-measuring and vane-measuring systems, are highlighted. Based on the relationship between the liquidity index and rheological values (viscosity and yield stress), flow motions are compared. Results

S.W. Jeong (✉)
124, Geologic Environmental Division, Korea Institute of Geoscience and Mineral Resources, Daejeon 305-350, Republic of Korea
e-mail: swjeong@kigam.re.kr

S.-N. Yoon
Business Department, CM Corporation Ltd, Seoul, Republic of Korea

S.-S. Park
Department of Civil Engineering, Kyungpook National University, Daegu, Republic of Korea

G.Y. Kim • S.-P. Kim • J.-J. Bahk • N.-K. Kang
Petroleum & Marine Research Division, Korea Institute of Geoscience and Mineral Resources, Daejeon, Republic of Korea

S.H. Lee
Korea Institute of Ocean Science and Technology, Ansan, Republic of Korea

S.-G. Chung
Department of Civil Engineering, Dong-A University, 840 Hadan-dong, Saha-gu, Busan 604-714, Republic of Korea

S. Krastel et al. (eds.), *Submarine Mass Movements and Their Consequences*, Advances in Natural and Technological Hazards Research 37, DOI 10.1007/978-3-319-00972-8_5,

show that the differences in mobility are significant when assuming that the flowing materials behave as a Bingham fluid. The runout distance is controlled by the yield stress of fine-grained sediments. Differences in yield stress may be caused by wall roughness and the distance between the ball (vane) and the wall in the rheometer. Under the same geomorphological conditions, the runout distance calculated from vane-measuring systems is much lower than that from ball-measuring and cylinderic systems. These difficulties must be minimized to predict debris flow mobility and to correctly perform hazard risk assessment.

Keywords Rheological properties • Busan clays • Ball-measuring and vane-measuring rheometer • Debris flow mobility

5.1 Introduction

The high mobility of subaqueous debris flows is strongly influenced by the geotechnical and rheological properties of the fine-grained sediments. To estimate the runout distance and velocity of debris flows, we need yield stress and plastic viscosity values. Yield stress is one of the most important parameters in debris flow modelling. There are two ways to determine yield stress: (i) geomorphological analysis and (ii) laboratory experiments using rheometers. For specific research sites, rheometrical analysis is required. For sediment-water mixtures, we can use different types of measuring rheometers, such as coaxial cylinder, cone-plate, plate-plate, vane-penetrated and ball-rotated measuring rheometers. Rheological parameters are generally influenced by physical and chemical factors such as grain sizes, clay minerals, soil types, volumetric concentrations of solids, salinity, liquidity index, and so on (Locat 1997; Jeong et al. 2010). In particular, the influence of grain size distribution in a debris flow is essential. The effect of rheometer geometry also cannot be neglected. Rheological parameters are very sensitive to the effects of the geometry of the rheometer, such as wall-slip, roughness at the wall and end effect (Coussot 1994). In this study we determine the general flow behaviour of Busan clays using ball-measuring and vane measuring rheometry and compare the differences between the Busan clays and low-activity clays as found in the literature. The aim of this study is to examine the rheological properties of Busan clays and implications for debris flow modelling from different rheometric systems.

5.2 Materials and Methods

The material examined was obtained in the city of Busan, in the deltaic plain of the Nakdong River, which is located on the southeastern coast of Korea. The normally consolidated Busan clay is known as an unusually thick deposit, varying from 20 to 70 m thickness (Chung et al. 2010). Ongoing research projects related to reclamation

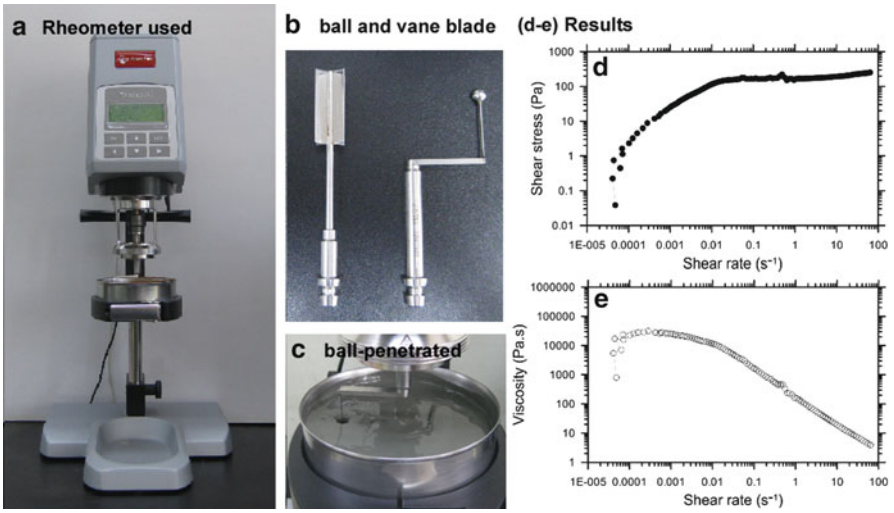

Fig. 5.1 Rheometric system and testing results: (**a**) Rheometer (RheolabQC, Anton Paar series), (**b**) ball and vane blade, (**c**) set up for rheological measurements, (**d**) plot of shear stress against shear rate and (**e**) plot of viscosity against shear rate

works in the Nakdong deltaic plain are focused on consolidation and hydraulic characteristics, which are still poorly understood (Chung et al. 2009). The Busan clays used in this study consists of soft silty clay to soft clay. These clays consist of illite-rich materials with small proportions of kaolinite, quartz and hornblende, with a very low percentage of montmorillonite. The natural water content of the Busan clays ranges from 35 to 60 %. The salinity and organic matter of the Busan clays range from 5 ~ 15 % and 2 ~ 8 %, respectively. The liquid limit and plasticity indices are approximately 43 ~ 72 % and 18 ~ 35 %, respectively. In general, the liquidity index is very close to unity with depth. In short, Busan clays have low to medium activities (i.e., $A_c = 0.5 \sim 1.2$). The geotechnical and rheological properties of these clays can thus be compared with that of low-activity clays (e.g., rheological compilation from Locat 1997). Furthermore, the geotechnical properties of the Busan clays are similar to the low-activity clays examined by Jeong et al. (2010).

The rheological analyses were carried out using either ball-measuring or vane-measuring rheometry on the <0.075 mm fraction. Ball and vane types (RheolabQC, Anton Paar series, Fig. 5.1) were developed to determine the yield stress and viscosity for large-particulated fluids. The ball and vane-measuring systems consist of a sphere (8 mm diameter) and a vane blade (20 mm wide × 40 mm high), which penetrate the soil samples. The maximum volume of the soil samples is 500 cm^3. The rotational speeds are recorded when the torques exerted on the sphere and vane blade is recorded within a wide measuring range. The distance between the sphere and the container wall is 20 mm. For the vane-measuring system, it is 48 mm. The ball-measuring and vane-measuring systems and the testing program are described in detail by numerous researchers (e.g., Schatzmann et al. 2009; Sosio

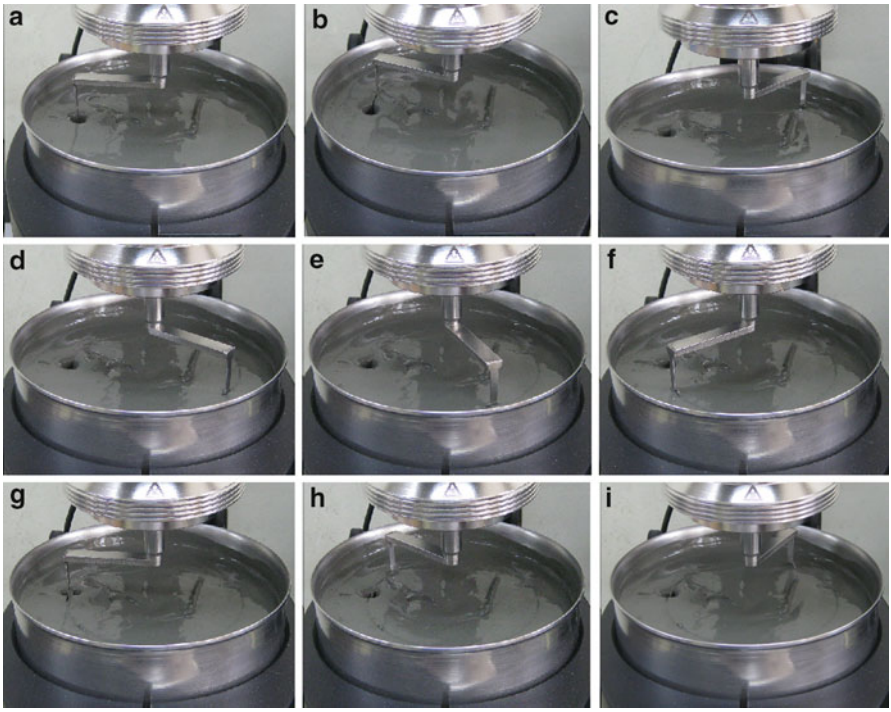

Fig. 5.2 Ball-measuring system for examining the rheology of the Busan clays (**a–g** is the first rotation; **g–i** is the post-failure stage)

and Crosta 2009; Scotto Di Santolo et al. 2012). Two types of shear mode can be applied: (a) shear stress controlled and (b) shear rate controlled. The measurements of torques are fully automated within the range of shear rates of $0.001 \sim 100\ s^{-1}$. Shear stress (T) and shear rates (D) can be measured within $0.5 < T < 10{,}000$ Pa and $0.001 < D < 4000\ s^{-1}$. Figure 5.1 shows the rheometrical system with the ball and the vane blade, set up for rheological measurement, and test results in the shear stress-shear rate and viscosity-shear rate plots. Figure 5.2 depicts the ball-inserted rheometric system and shows how rheological measurements were performed.

For each rheological test, the soil-water mixtures were prepared by adding a given amount of water to the solid fraction and thoroughly mixing by hand to ensure complete homogenization. The mixtures were left at rest for $30 \sim 60$ min for hydration. Before performing the rheological tests, the mixtures were re-mixed. The mixtures were then poured into the container and were left at rest for 5 min. For the next desired level, the liquidity index (water content) was slowly increased at a constant salinity of the pore water by adding water with the same salinity. Following each step the remoulded undrained shear strengths was measured using the Swedish fall cone (i.e., 60°–30 g and 60°–60 g cones) according to ASTM and BNQ

standards. The flow curves were obtained for the given shear rates. An example is shown in Fig. 5.1d (see the log-log plot of shear stress against shear rate).

5.3 Results

5.3.1 Rheological Behaviour of the Busan Clays

Figure 5.3 presents the flow curves of the Busan clays when the shear rates were given in the range of 10^{-4} to 10^{2} s^{-1} for various liquidity indices. The liquidity index varied between 2.2 and 5.4; this value was determined using the empirical relationship proposed by Leroueil et al. (1983). Figure 5.3a, b show the test results from the controlled shear rate in the ball-measuring system, while Fig. 5.3c, d present the test results from the controlled shear rate in the vane-measuring system. The Busan clays generally exhibited a shear thinning flow behaviour; i.e., viscosity decreases with an increasing shear rate (Fig. 5.3b, d). In the shear rate controlled system, the rotational speed gradually increased with time (i.e., the variation in shear rate = $0.0001 \sim 62$ s^{-1}). The shear stress increases with increasing shearing mode at the beginning of rotation and at the shear rate between 10^{-5} and 10^{-3} s^{-1}. The

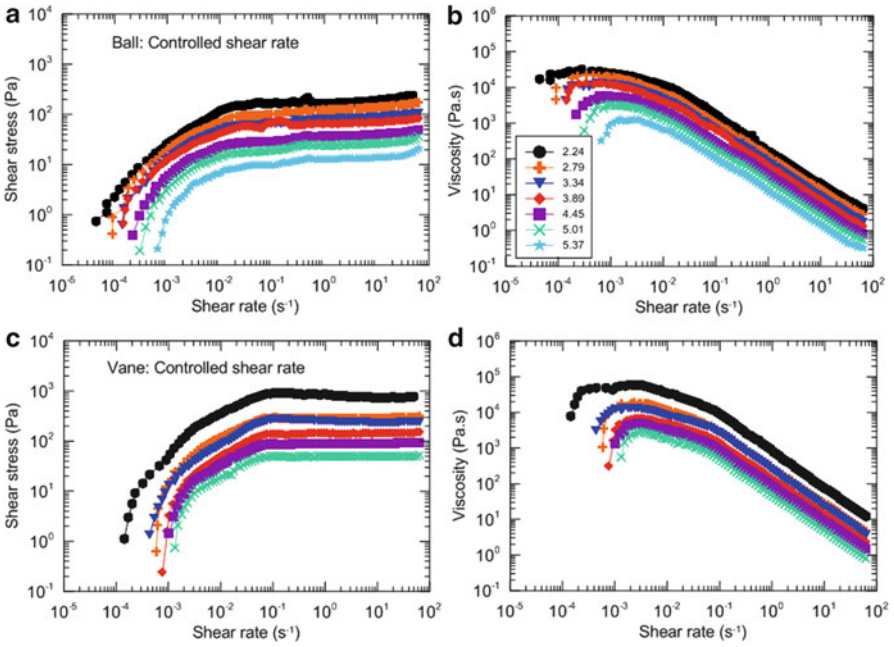

Fig. 5.3 Flow curves of the Busan clays: (**a**–**b**) ball measuring system and (**c**–**d**) vane measuring system. *Symbols* indicate the liquidity index

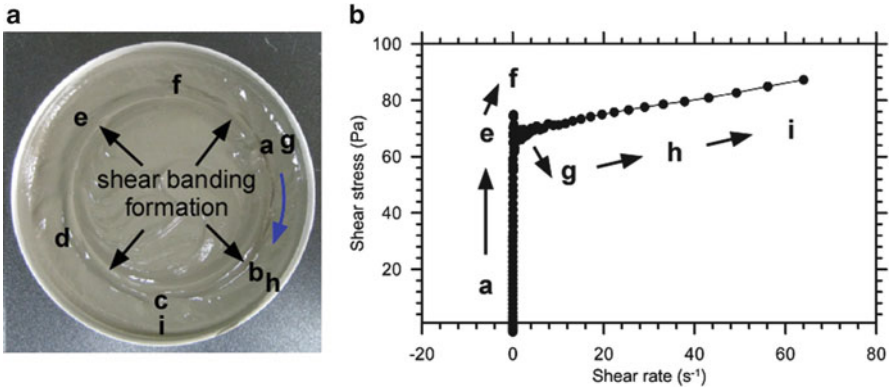

Fig. 5.4 Shear banding in ball-measuring rheometry and flow curve for $I_L = 3.9$

transition from a Newtonian plateau to a power-law regime is observed when the shear rate is larger than 10^{-3} s^{-1} (see Fig. 5.3b, d). A sudden abrupt change in shear stress was often observed in ball-measuring systems for relatively sticky materials (i.e., high plasticity), because of the small uplift just before the ball returns to the original position (see Fig. 5.2f, g for $I_L = 2.2$, 2.8 and 3.3). However, this change is almost undetectable in the vane-measuring system. The power-law regimes are distinct in the range of 10^{-1} and 10 s^{-1}, both for the ball and the vane-measuring systems. Similar results were found by Barnes (1999). When the shear rate reaches the highest value (i.e., shear rate $\rightarrow$ 100 s^{-1}), the Busan clays examined behave as an ideal Bingham fluid (see Fig. 5.4b). This occurs in the stage where the sphere rotates from point (g) to point (i) in Fig. 5.2 (see Fig. 5.3a, c).

Assuming that the flow behaves like a Bingham fluid, we can determine the plastic viscosity (η_h) and the Bingham yield stress (τ_c) for various volumetric concentrations of solids. It should be noted that, for fine-grained sediments, the Bingham yield stress is very close to the apparent yield stress (i.e., Imran et al. 2001) when the bi-viscosity model was applied (Jeong 2013). Hereafter, we can use the term Bingham yield stress rather than apparent yield stress. The shear banding formation after one rotation of the sphere in the soil samples is shown in Fig. 5.4a for an $I_L = 3.9$. The flow curve for this specific test is shown in Fig. 5.4b. Here the letters (a) to (i) represent the different location of the ball during the test (also see Fig. 5.2). The first rotation is completed when the ball reaches point (g). An apparent yield stress appears just before reaching point (g). After the appearance of yield stress, the results show that plastic viscosity governs the flow (from point **g** to point **i**). The same results were observed for coaxial cylinder and vane rheometry.

For fine-grained sediments encountered in various environments, rheological properties can be correlated with a liquidity index in a semi-logarithm or log-log diagram (Locat 1997): (*i*) liquidity index and plastic viscosity and (*ii*) liquidity index and yield stress. It is generally accepted that these findings can be utilized as input parameters to model subaerial and subaqueous debris flows. Based on these relationships, a comparison between Busan clays and low-activity clays is

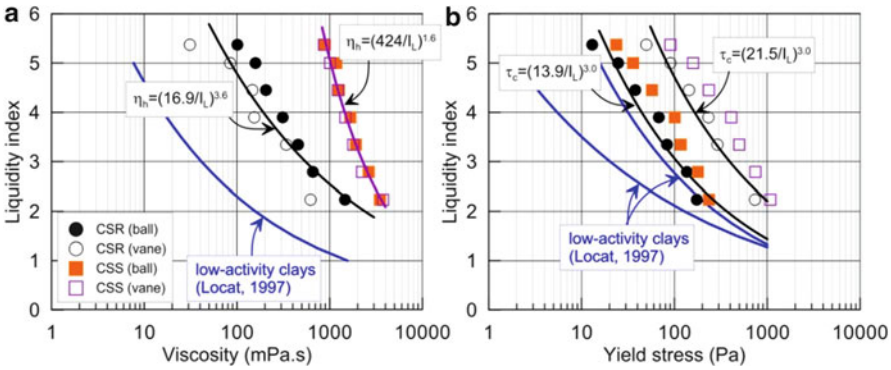

Fig. 5.5 Relationship between liquidity index and rheological values: (**a**) viscosity and (**b**) yield stress

shown in Fig. 5.5. There is a positive relationship between the liquidity index and the rheological values, but the differences in correlations are significant in the controlled shear rate mode. The viscosities determined from the ball and the vane are very close, but the differences in yield stress are distinct. Similar findings are also observed in the controlled shear stress mode.

5.4 Discussion

The rheological characteristics of Busan clays typically exhibit a shear thinning and thixotropic behaviour. Similar results were observed for low-activity clays (e.g., Coussot and Piau 1994; Møller et al. 2006; Locat 1997). The flow motion of clay-rich materials can be modelled using the bi-viscosity rheological law (Locat et al. 2004). These findings will help in understanding the motion of a debris flow with a long travelling distance. Practically, Fig. 5.5 may be useful for a preliminary numerical analysis for subaerial and subaqueous landslides (Locat and Lee 2002). Similar research using these relationships for fine-grained sediments was completed by Locat et al. (2009). In general, rheological characteristics depend on shear rate and geometry. In this research, it was assumed that the observed rheological differences for the Busan clays between cylinder, ball and vane geometries will be the same as those of marine clays found in the Ulleung basin, East Sea, Korea. For the same geomorphological and geotechnical conditions, therefore this study can compare the flow mobility using the rheological properties obtained from different geometries of viscometers.

Based on the geomorphological features in the Ulleung Basin, East Sea, various types of submarine landslides are identified (Fig. 5.6a), including slumps, slides, rockfalls, debris flows and turbidites that occurred along the entire margin of the basin overlain by Holocene hemipelagic muds (Chough et al. 1985). Flow

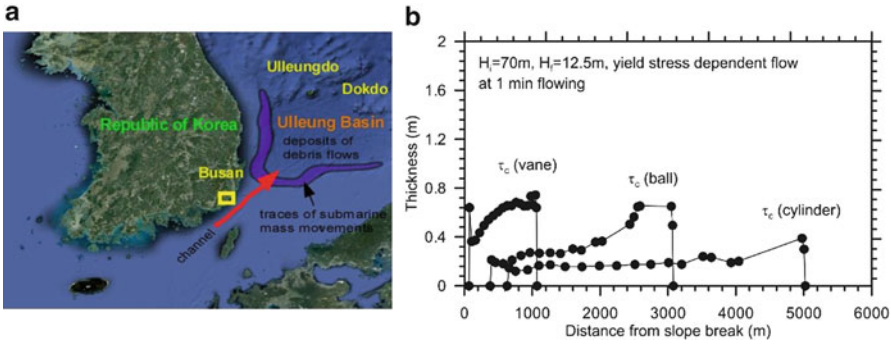

Fig. 5.6 Shearing in the post-failure stage and possible implications of debris flow modelling: (**a**) submarine mass movements in the Ulleung Basin, East Sea and (**b**) runout distance prediction for the Bingham fluid case

transformation (i.e., the transition from slide to flow) may be one of the possible mechanisms for explaining high mobility mass movements encountered in the Ulleung Basin. To investigate the post-failure dynamics of submarine landslides in the Ulleung Basin, we need a detailed investigation of geotechnical and rheological characteristics of fine-grained sediments and to develop a robust rheological model.

In debris flow mobility, yield stress is an important parameter for estimating the final deposition. For the determination of rheological properties for fine-grained sediments, a detailed analysis of the rheological properties and the complete methodology are described by Locat and Demers (1988). We compared debris flow mobility as a function of yield stress determined from Fig. 5.5. At the liquidity index equal to 3, the yield stresses can be given as 20, 100 and 400 Pa (these values are most likely too low to compare in situ conditions, but in this research the authors tried to compare flow motion; in other words, this paper doesn't deal with the exact determination of rheological characteristics of fine-grained sediments encountered in the Ulleung Basin) for cylinder, ball and vane-measuring rheometry, respectively. The yield stress calculated from vane geometry is the largest value, and the yield stress calculated from cylinder geometry is the lowest value, which may be because the wall-slip cannot be avoided. Based on geotechnical and rheological compilations, debris flow mobility was analyzed using a BING (Imran et al. 2001). Based on the Bingham rheological law (for numerical simulation, mud density = 1,500 kg/m^3, Herschel-Bulkley exponent $n = 1$, and reference shear rate = 1), the yield stresses can be determined: τ_c vane > τ_c ball > τ_c cylinder. As a consequence, assuming that the materials behave as a Bingham fluid, runout distances can be predicted at 1 min flowing conditions when the height and deposits of the debris flows are 70 and 12.5 m (data from Locat et al. 2004 for comparison), respectively (Fig. 5.6b). It should be noted that rheological measurements are related to wall roughness and the distance between soil samples and the wall. In a coaxial cylinderic system, there are no rough surfaces in a viscometer with a very small container (the samples can be placed in a container of $6 \sim 70$ cm^3).

The ball-measuring and vane-measuring systems are relatively larger (0.5 L) than the cylinderic type. The distance between the ball and the container wall is much smaller than the distance between the vane and the container wall. Wall-slip has a minor effect for highly diluted suspensions; however, for sticky materials (highly structured soil samples), the wall-slip effect cannot be neglected. Therefore, geotechnical and rheological tests should be carried out in the future for muddy sediments, which are sampled from the landslide deposits in the Eastern part of the Ulleung Basin. A comparison should be made for the materials from the Busan clays in the Nakdong deltaic plain and from muddy sediments from the Ulleung Basin.

5.5 Conclusions

Rheological properties of the Busan clays were examined using ball-measuring and vane-measuring rheometry. In particular, the effect of wall-slip was emphasized. The Busan clays have characteristics of a shear thinning fluid similar to other low-activity clays. Rheological properties are positively correlated with index properties. For this reason, the relationships between liquidity index and rheological properties can be used to provide a first estimate of debris flow mobility. However, to provide guidance in the selection of strength parameters where numerical models are used to simulate debris flows, technical errors should be minimized. There are significant differences in rheological properties between coaxial cylinder and ball (vane)-measuring systems. The yield stresses can be determined: τ_c vane $> \tau_c$ ball $> \tau_c$ cylinder. Different yield stresses directly affect the runout distance of flowing materials, and wall-slip is the main cause of inconsistency in the results. More laboratory data and field observations are needed to confirm the relationships proposed in this study.

Acknowledgments The authors would like to thank the KIGAM research project (11-7622, 13-3212) and Integrated Ocean Drilling Program at KIGAM (12-9102-1) for their support. We also thank J.S. L'Heureux for valuable comments and reviewing parts of an earlier version of the manuscript.

References

Barnes HA (1999) The yield stress – a review or 'παντ ρει' – everything flows? J Non-Newton Fluid Mech 81:133–178

Chough SK, Jeong KS, Honza E (1985) Zoned facies of mass-flow deposits in the Uleung (Tsushima) Basin, East Sea (Sea of Japan). Mar Geol 65:113–125

Chung SG, Lee NK, Kim SR (2009) Hyperbolic method for prediction of prefabricated vertical drains performance. J Geotech Geoenviron Eng 135(10):1519–1528

Chung SG, Chung JG, Jang WY, Lee JM (2010) Correlations between CPT and FVT results for Busan clay. Mar Georesour Geotechnol 28(1):49–63

Coussot P (1994) Steady, laminar, flow of concentrated mud suspensions in open channel. J Hydraul Res 32(4):535–559

Coussot P, Piau J-M (1994) On the behavior of fine mud suspensions. Rheol Acta 33:175–184

Imran J, Harff P, Parker G (2001) A numerical model of submarine debris flows with graphical user interface. Comput Geosci 274(6):717–729

Jeong SW (2013) The viscosity of fine-grained sediments: a comparison of low- to medium-activity and high-activity clays. Eng Geol 154:1–5

Jeong SW, Locat J, Leroueil S, Malet J-P (2010) Rheological properties of fine-grained sediments: the roles of texture and mineralogy. Can Geotech J 47:1085–1100

Leroueil S, Tavenas F, LeBihan JP (1983) Propriétés caractéristiques des argiles de l'est du Canada. Can Geotech J 20:681–705

Locat J (1997) Normalized rheological behaviour of fine muds and their flow properties in a pseudoplastic regime. In: Proceedings 1st international conference on debris-flow hazards mitigation, San Francisco. ASCE, New York, pp 260–269

Locat J, Demers D (1988) Viscosity, yield stress, remoulded strength, and liquidity index relationships for sensitive clays. Can Geotech J 25:799–806

Locat J, Lee HJ (2002) Submarine landslides: advances and challenges. Can Geotech J 39:193–212

Locat J, Lee HJ, Locat P, Imran J (2004) Numerical analysis of the mobility of the Palos Verdes debris avalanche, California, and its implication for the generation of tsunamis. Mar Geol 23:269–280

Locat J, Lee H, ten Brink US, Twichell D, Geist E, Sansoucy M (2009) Geomorphology, stability and mobility of the Currituck slide. Mar Geol 264:28–40

Møller PCF, Mewis J, Bonn D (2006) Yield stress and thixotropy: on the difficulty of measuring yield stresses in practice. Soft Matt 2:274–283

Schatzmann M, Bezzola GR, Minor HE, Windhab EJ, Fischer P (2009) Rheometry for large-particulated fluids: analysis of the ball measuring system and comparison to debris flow rheometry. Rheol Acta 48:715–733

Scotto Di Santolo A, Pellegrino AM, Evangelista A, Coussot P (2012) Rheological behaviour of reconstituted pyroclastic debris flow. Geotechnique 62(1):19–27

Sosio R, Crosta GB (2009) Rheology of concentrated granular suspensions and possible implications for debris flow modelling. Water Resour Res 45:W03412, 1–16

Chapter 6
Utilizing Cone Penetration Tests for Landslide Evaluation

M.E. Jorat, S. Kreiter, T. Mörz, V. Moon, and W. de Lange

Abstract Pore pressure and shear strength are two important parameters that control the stability of slopes. These parameters can be derived *in-situ* by cone penetration testing (CPT) with pore pressure measurements. This paper presents the results from three static, vibratory and dissipation CPT profiles deployed into a landslide headwall at Pyes Pa, Bay of Plenty, New Zealand. The landslide strata consist of volcanic ashes and ignimbrites. Studying the stability of slopes in this area using *in-situ* geotechnical testing is of societal-economic importance since several other landslides within comparable strata caused considerable property damage. Three CPT profiles were collected across the headwall of the slide scar with 2 m spacing in undisturbed sediments using static, vibratory and dissipation test modes. Static CPT results are used to evaluate soil grain size variations, geotechnical parameters of sediments such as shear resistance, probable slip surface and sensitivity of sediments. Liquefaction potential of sediments is assessed using vibratory CPT results. For dissipation tests, the cone remained stationary in the sediment for ~60 min to monitor pore pressure dissipation at the depths of 6, 9 and 11 m. With the use of pore pressure dissipation data, values of soil horizontal permeability are calculated. The liquefaction probability from static CPT results is compared to liquefaction potential evaluation from vibratory CPT. Last but not least, an unstable soil layer is defined based on static CPT, vibratory CPT and dissipation results.

Keywords CPT • Landslide • Static • Vibratory • Dissipation

M.E. Jorat (✉) • S. Kreiter • T. Mörz
Marum – Center for Marine and Environmental Sciences, University of Bremen, Klagenfurter Strasse, 28359 Bremen, Germany
e-mail: jorat@uni-bremen.de

V. Moon • W. de Lange
Department of Earth and Ocean Sciences, University of Waikato, Private Bag 3105, Hamilton 3240, New Zealand

S. Krastel et al. (eds.), *Submarine Mass Movements and Their Consequences*, Advances in Natural and Technological Hazards Research 37, DOI 10.1007/978-3-319-00972-8_6,

6.1 Introduction

Slope failure is an important factor which causes damage to public and private properties every year. Slope failure can be manifested as landslides and may destroy or damage buildings and infrastructure located on or in the path of a landslide (Ozcep et al. 2010). In extensive areas of New Zealand, prevalent severe landslips result from intensive rainstorms or prolonged winter wetness (Trustrum et al. 1984). Infiltration of rainwater into soil increases the pore water pressure which reduces the effective stresses and alters structure of soil that finally results in a reduction or even elimination of frictional and cohesional strength (Reddi 2003). Protracted and intense rainfall in New Zealand dramatically increases pore water pressure in soils which boosts shear stresses on materials and causes slopes to fail (Brown 1983). Slope failures induced by excessive rainfall may cause shallow landslides which trigger small volumes of earth and/or debris with considerable velocity and high impact energy (Giannecchini et al. 2012).

There have been several studies on different landslides in New Zealand (e.g. Brown 1983). In this paper, a landslide which is located at Pyes Pa, Bay of Plenty, New Zealand is geotechnically investigated as a typical example of a shallow onshore landslide. We describe its morphological and structural characteristics and discuss the possible mechanism of emplacement by using static, vibratory and dissipation cone penetration data. With static CPT (SCPT) data, soil behavior type, undrained shear strength, sensitivity and liquefaction potential are calculated. Vibratory CPT (VCPT) is performed to evaluate liquefaction potential by a second measurement. Permeability properties of layers are evaluated with the use of CPT dissipation test.

In-situ cone penetration test measurements were undertaken at three different locations at 463 Pyes Pa Road, Tauranga, New Zealand (Fig. 6.1). Table 6.1 shows SCPT, VCPT and dissipation test locations which were performed at Pyes Pa landslide to evaluate the static, dynamic and permeability behavior of soil.

6.2 Site Characterization

The geology of the Tauranga area consists of Pliocene to Pleistocene volcanic materials derived predominantly from the Taupo Volcanic Zone; the materials are mainly rhyolitic in composition. At the study site, Late Pleistocene and Holocene tephras from the surface horizons overlie fluviatile sands and silts and older pyroclastic units. Below these, the Waimakariri Ignimbrite, a partially welded pumice-rich ignimbrite, overlies the non-welded Te Ranga Ignimbrite (Briggs et al. 1996). Houghton et al. (1995) suggest that the Waimakariri Ignimbrite has an age between 0.32 and 0.22 Ma. Based on visual inspection at the landslide area, the first 3 m of the soil profile consists of an ash sequence that continues with a paleosol layer from 3 to 6.80 m. From the depth of 7–13.70 m, a clayey layer was observed, which

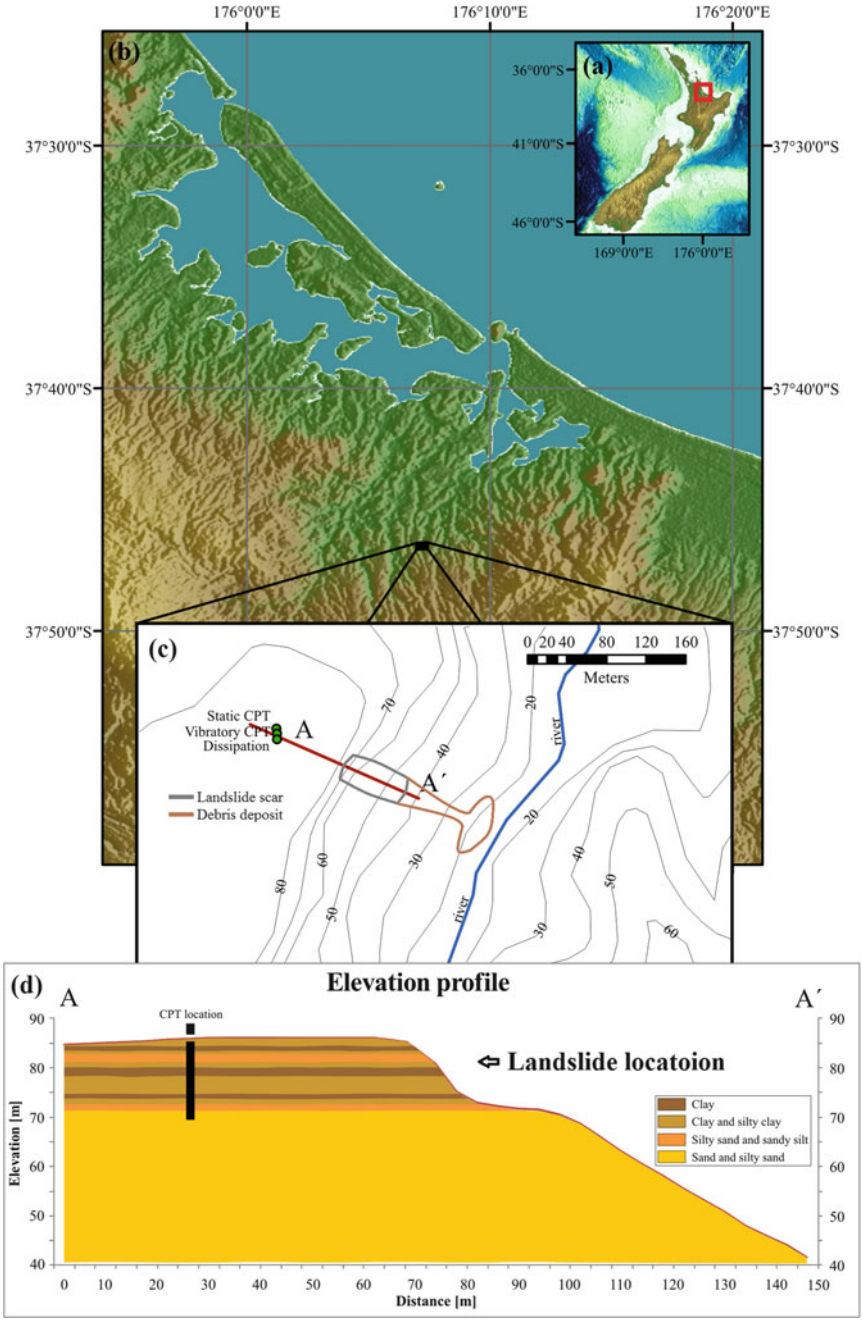

Fig. 6.1 Map of (**a**) New Zealand, (**b**) Bay of Plenty, (**c**) Topography, landslide location and location of CPTs at Pyes Pa and (**d**) landslide cross section. "Map a, b and c are generated from LINZ (Land Information New Zealand) data" Layering at (**d**) is derived from soil behavior type calculated by SCPT

Table 6.1 Cone penetration test location details in Pyes Pa landslide

CPT location/Type	Coordinate	
Static	37.774358° S	176.118563° E
Vibratory	37.774309° S	176.118561° E
Dissipation	37.774299° S	176.118527° E

likely contains halloysite with accumulation of clay at the base of the sequence. From the depth of 13.70–16 m, a poorly welded, loose and coarse grain sized ignimbrite was observed.

A river flows down the low lying valley floor that indicates the vicinity of the ground water table. According to Foundation Engineering Geotechnical and Environmental Consultant Company (2006), standing ground water levels were not encountered below the elevated and gently sloping portions of 52 Pyes Pa Road, suggesting free drainage of coarse volcanic particles. Yet, across the valley floor, they observed seepage of groundwater at a layer between 0.60 and 1 m. This indicates the presence of a complex ground water regime, with mostly free drainage due to the coarse nature of many of the primary pyroclastic units. However, perched water tables associated with local aquitards clearly exist. These aquitards are the result of the accumulation of secondary clay minerals, most commonly associated with weathering of fine-grained tephra units. The spatial distribution of these aquitards is difficult to predict.

6.3 Methods

6.3.1 In-Situ CPT Measurements

In-situ measurements of sediment physical and mechanical properties were carried out with a CPT unit which is called GOST. GOST, a new geotechnical offshore seabed CPT tool developed at University of Bremen, Center for Marine and Environmental Sciences (Marum), was utilized for the investigations (Fig. 6.2). GOST possesses a cone with a projected area of 5 cm^2. Compared with normal cones with projected area of 10 cm^2, 5 cm^2 cones react more sensitively and precisely to rapid changes in thin layered soils via the pore water pressure response, which leads to increased vertical resolution and provides more detailed profiles (Lunne et al. 1997; Hird and Springman 2006). The penetration rate for static tests is the standard rate of 2 cm/s (e.g. Lunne et al. 1997). The vibrocone used in this study was vertically forced with a frequency of 15 Hz and an amplitude of 25 mm.

SCPT, VCPT and dissipation tests were conducted within 1 m of each other. The tests were conducted in early autumn on 6th of March 2012. Rainfall in Tauranga is approximately evenly distributed throughout the year, with little seasonal variability. Instruments were transported to the location and positioned by truck crane, and a mobile generator was used to provide power for the instruments. Since GOST is designed and manufactured to work on/off shore, no modification was required to operate on land.

Fig. 6.2 Geotechnical Offshore Seabed Tool (*GOST*) sketch

Table 6.2 Classification of sensitive clays (Skempton and Northey 1952)

Sensitivity (S_t)	Classification
~1	Insensitive
1–2	Low sensitive
2–4	Medium sensitive
4–8	Sensitive
8–16	Extra sensitive
>16	Quick

6.3.2 *Physical and Mechanical Properties*

Soil behavior type (SBT) is evaluated based on SCPT results and the SBT chart through the CLiq (2008) software program based on the Robertson et al. (1986) classification scheme. Schmertmann (1978) explained that the sensitivity of soils is inversely related to the CPT friction ratio. He proposed a correlation for analyzing the sensitivity of sediments as follows:

$$S_t = N_s / R_f \tag{6.1}$$

Where, N_s is constant and R_f is friction ratio.

Lunne et al. (1997) suggested a value of $N_s = 7.5$ for mechanical CPT data. Skempton and Northey (1952) defined sensitivity of clay as a ratio of maximum undrained shear strength of undisturbed clay over maximum undrained shear strength of remolded clay. They proposed a classification for sensitive clay which is shown in Table 6.2.

Interpretation of undrained shear strength from CPT results was performed using total cone resistance (Lunne et al. 1997). In order to compare static and vibratory tip resistance, Sasaki et al. (1984) proposed a formula for direct comparison of these two values, which is defined as the reduction ratio *(RR)* and explained as:

$$RR = 1 - q_{cv} / q_{cs} \tag{6.2}$$

Where, *RR* is the reduction ratio, q_{cv} is the vibratory cone penetration resistance and q_{cs} is the static cone penetration resistance. Values of *RR* near unity demonstrate small measured values of q_{cv} compared with q_{cs}, an *RR* of zero identifies equal values of q_{cs} and q_{cv} (Bonita et al. 2004), while negative values of *RR* show greater q_{cv} than q_{cs}. The soil liquefaction potential index (LPI) is used to interpret the liquefaction susceptibility in terms of severity over depth which was developed based on methodology proposed by (Iwasaki 1986). He proposed four discrete categories based on the numeric value of LPI as follows:

LPI = 0	: Liquefaction risk is very low
0 < LPI <= 5	: Liquefaction risk is low
5 < LPI <= 15	: Liquefaction risk is high
LPI > 15	: Liquefaction risk is very high

GeoLogismiki, in collaboration with Gregg Drilling Inc. and Prof. Peter Robertson have developed a software which is called CLiq (2008). This program is a CPT based SBT and liquefaction assessment software. SBT is evaluated based on a chart proposed by Robertson et al. (1986) and soil liquefaction assessment procedure based on static CPT results is developed according to Robertson and Wride (1998). Robertson in 2009 revised his former procedure and that procedure is used in CLiq software for evaluation of liquefaction resistance of soils.

6.4 Results and Discussion

6.4.1 Static CPT

According to the origin of soil at the study area described in Sect. 6.2, ignimbritic layers showing different degrees of weathering interlayered with weathered ashes and other pyroclastites are the cause for changes in the CPT profile (Fig. 6.3). Specifying the location of saturated zones within the sequence is very important in interpreting the pore water pressure response during CPT. Pore water pressure values measured in unsaturated materials represent induced pore water pressures in response to the undrained loading applied by the cone penetration. In contrast, pore water pressure values measured within saturated zones represent these induced pressures, as well as the hydrostatic head associated with the standing water.

Below 13.7 m the measured pore water pressure rapidly falls, indicating that free-draining material lies below this level. This material is interpreted as ignimbrite

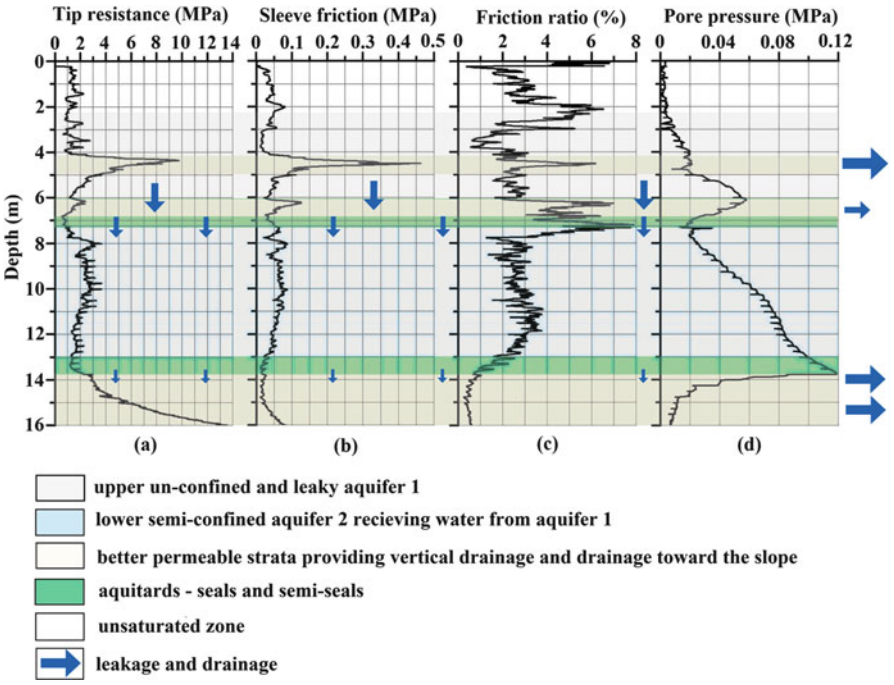

Fig. 6.3 Static CPT result (**a**) tip resistance, (**b**) sleeve friction, (**c**) friction ratio and (**d**) pore water pressure and hydrological situation of layers to a penetration depth of 16 m

based on the known local stratigraphy. This ignimbrite has a sandy, pumiceous texture with minimal weathering. The material is highly permeable and induced pore water pressures from the cone penetration are insignificant. Immediately above the ignimbrite, a rapid rise in pore water pressure with depth is seen from 12.5 to 13.7 m. This zone marks the transition from the lower, uniformly free-draining material to an overlying sequence of clay and silt materials that show marked variations in the pore water response. These layers are mostly tephras from different eruptive events and have variable textures associated with the characteristics of each eruption.

The primary textures are overprinted with different levels of weathering representing the time of exposure at the ground surface; this weathering is expressed in the clay content, and in the extreme can be seen as well-developed paleosols in the sequence. The hydrological conditions of these layers above 13.70 m are illustrated based on SCPT results (Fig. 6.3). A lower semi-confined aquifer 2 extends from 7.20 to 13 m, and is surrounded by two sealed and semi-sealed aquitards at 6.90–7.20 m and 13–13.70 m. Above this is an upper aquifer 1 which extends from the unsaturated zone to 6.90 m; this aquifer contains two better permeable strata. Aquifer 2 receives water from aquifer 1 through the semi-sealed overlying aquitard. The upper leaky and unconfined aquifer 1 and lower semi-confined aquifer 2 are responsible for the pore water pressure increase seen in the layer between 7.20

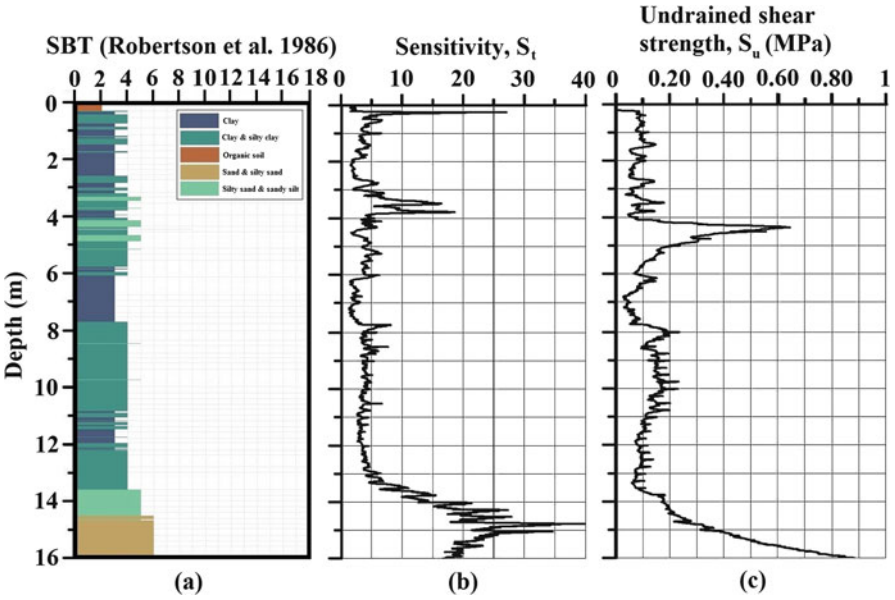

Fig. 6.4 CPT based (**a**) soil behavior type (**b**) sensitivity and (**c**) undrained shear strength calculated from SCPT results

and 13.70 m which is believed to represent both saturated pore pressure and an induced pore pressure signal due to penetration. The pore water pressure in the aquitard located at 6.90 to 7.20 m is low which is related to the permeable layer immediately above the aquitard that drains pore water from the upper unconfined and leaky aquifer and transfers it to lower semi confined aquifer 2. In contrast, because of the buildup of pore water pressure at the lower semi-confined aquifer 2 and very low permeability characteristics of the aquitard located at the depth of 13–13.70 m, pore water pressure is high at the depth of 13.70 m. This results in a reduction of effective stress. Therefore, excessive rainfall can result in the situation of zero effective stress at the depth of 13.70 m, leading to failure of the slope.

Taking the results of Fig. 6.4b and values of Table 6.2 into consideration, the first 14.60 m of soil layers are predominantly categorized as medium sensitive/sensitive materials. Two extra-sensitive layers occur within this sequence: from 3.20 to 3.80 m and from 13.70 to 14.60 m. The apparent rapid increase of sensitivity at the depth of 0.20 m resulted from great values of sleeve friction in organic soils (Figs. 6.3b and 6.4a). Given the coarse grain size of particles below the depth of 14.60 m, a sensitivity calculation cannot be applied for this layer. High sensitivity values of the layers between depths of 3.20–3.80 m and 13.70–14.60 m indicate a dramatic decrease of remolded undrained shear strength compared with undisturbed undrained shear strength. This indicates a vulnerability of the layers to disturbance. Accordingly, at circumstances like earthquakes, the respective layers would be potential slip surfaces.

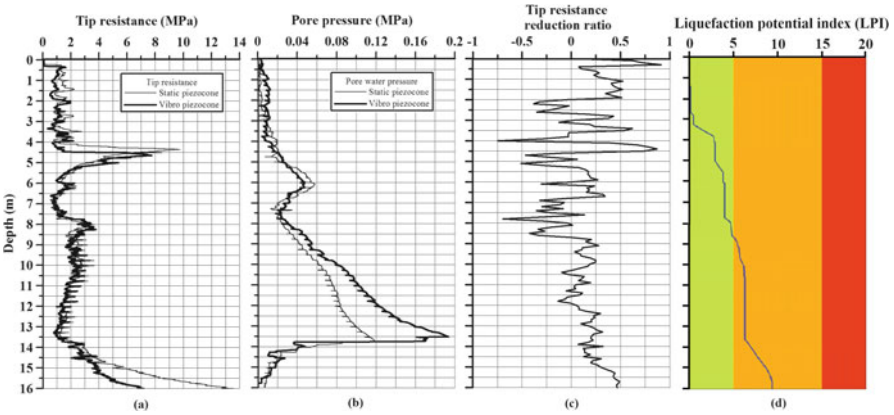

Fig. 6.5 Static and vibratory piezocone test results of (**a**) tip resistance and (**b**) pore water pressure (**c**) tip resistance reduction ratio. Calculated values of *RR*, SCPT and VCPT results are presented together to show the key role of vibration on sediments. (**d**) Soil liquefaction potential index analyzed by CLiq software using SCPT data

Undrained shear strength values are shown in Fig. 6.4c. From the depth of 8 m until 13.70 m, S_u decreased continuously. The same reduction trend is also observed in tip resistance, sleeve friction and friction ratio profiles of the same layer (Fig. 6.3a–c). On the other hand, pore water pressure at the respective layer increased progressively from the depth of 8 m and reached to its maximum at 13.70 m (Fig. 6.3d). Fine grained materials started from the depth of 8 m until 13.70 m, created a relatively impermeable layer which kept water during precipitation. Very low values of tip resistance, sleeve friction, friction ratio and undrained shear strength and an increased sensitivity at the depth of 13.70 m indicate the vulnerability of the layer to fail under the effect of driving forces. Accordingly, on the occasion of excessive rainfall, the weak soil layer located at the depth of 13.70 m would be considered as the most probable slip surface.

6.4.2 Vibratory CPT

A slight decrease in values of tip resistance under the effect of vibration is observed in the first 4 m of the VCPT profile (Fig. 6.5a), whilst the most significant reduction of tip resistance is observed at a layer between 4 m and 4.50 m. From 4.50 m until 13.70 m, static and vibratory tip resistances become compatible with each other and from 13.70 m until the end of CPT profile, vibratory tip resistance decreased progressively. Based on static and vibratory tip resistance, *RR* was defined (Fig. 6.5c). According to Tokimatsu (1988), soils with *RR* values more than about 0.80 have high liquefaction potential. Thus, the layer from 4 to 4.50 m is vulnerable to liquefaction. The 0.20 m of topsoil layer has $RR > 0.80$, however, since this layer consists of organic materials, it is not considered as a liquefiable layer (Fig. 6.4a).

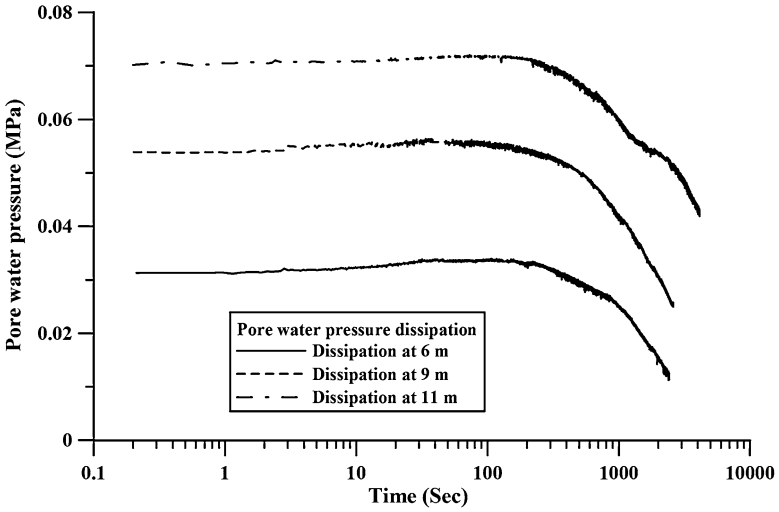

Fig. 6.6 Dissipation of pore water pressure vs. time performed at penetration depths of 6, 9 and 11 m following static cone penetration

An apparent increase of pore water pressure was observed under the effect of vibration at layer from 7.80 to 13.70 m (Fig. 6.5b). Konrad (1985) made an experiment to evaluate effects of cyclic loadings on saturated silty soils and based on his observations in all tested samples, the residual pore water pressure increased progressively with cycles of loading. Accordingly, a greater concentration of silt is verified at the above-mentioned layer which causes increased pore water pressure under the effect of vibration. With the increase of pore water pressure, effective stress decreases respectively. Maximum increase in pore water pressure under the effect of vibration occurred at the depth of 13.50 m which indicates the vulnerability of this layer to failure due to dynamic loads which are predominately induced by earthquake.

6.4.3 Dissipation Test

As can be observed from dissipation curves, pore water pressures first increased from an initial value to a maximum and then decreased to the hydrostatic value (Fig. 6.6). These kinds of dissipation curves are called non-standard dissipation curves (Chai et al. 2012). According to Teh and Houlsby (1991), volumetric expansion, resulting from movement of soil element from the tip to the sleeve of the penetrometer, is the possible reason for occurrence of non-standard dissipation curves.

According to Robertson (2010), the most precise soil permeability (k_h) estimation formula based on CPT dissipation tests is defined by the following equation:

$$k_h = (c_h.\gamma_w)/M \tag{6.3}$$

Where: c_h is the coefficient of consolidation in the horizontal direction, γ_w is the unit weight of water and M is compressibility.

Robertson (2010) reported his findings to estimate 1-D constrained modulus (M) using:

$$M = \alpha_M\,(q_t - \sigma_{vo}) \tag{6.4}$$

When $I_c > 2.2$:

$$\alpha_M = Q_{tn} \quad \text{when } Q_{tn} \leq 14$$

$$\alpha_M = 14 \text{ when } Q_{tn} > 14$$

$$I_c = \left[(3.47 - \log Q_{tn})^2 + (\log F_r + 1.22)^2\right]^{0.5} \tag{6.5}$$

$$F_r = [f_s/(q_t - \sigma_{vo})]\ 100\% \tag{6.6}$$

$$Q_{tn} = [(q_t - \sigma_{vo})/p_a]\ \left(p_a/\sigma'_{vo}\right)^n \tag{6.7}$$

$$n = 0.381(I_c) + 0.05\ \left(\sigma'_{vo}/p_a\right) - 0.15 \tag{6.8}$$

α_M = coefficient of constrained modulus
q_t = CPT corrected total cone resistance = $q_c + (1-a)u$
σ_{vo} = pre-insertion in-situ total vertical stress
p_a = reference atmospheric pressure = 100 kPa
I_c = soil behavior type index
Q_{tn} = normalized cone resistance
f_s = CPT sleeve friction
a = area ratio of the cone = (A_n/A_c)
σ'_{vo} = pre-insertion in-situ effective vertical stress
n = stress exponent
F_r = normalized friction ratio

To facilitate calculation of I_c, the value of the stress exponent (n) is assumed to be 1.

The most widely used formula for calculating c_h is the one proposed by Teh and Houlsby (1991):

$$c_h = \left(C_p \cdot r_0{}^2 \cdot I_r{}^{(0.5)}\right) / t_{50} \tag{6.9}$$

C_p = is a factor related to the location of the filter element and for a cone with shoulder filter element is equal to 0.245 (Teh and Houlsby 1991)
r_0 = radius of the cone
I_r = rigidity index
t_{50} = time required for 50 % of dissipation

$$I_r = G/s_u \tag{6.10}$$

$$G = \rho \cdot V_s{}^2 \tag{6.11}$$

Where, G is shear modulus, s_u is undrained shear strength, ρ is mass density (γ/g) and V_s is the shear wave velocity.

Hegazy and Mayne (1995) proposed a formula for shear wave velocity calculation based on CPT results which is as follows:

$$V_s = [10.10 \log q_t - 11.40]^{1.67} [f_s/q_t]^{0.30} \tag{6.12}$$

To calculate values of t_{50}, an equation which was proposed by Lunne et al. (1997) is introduced as follows:

$$U = (u_t - u_0)/(u_i - u_0) \tag{6.13}$$

Where, U is a degree of dissipation, u_t is pore pressure at time t, u_0 is *in-situ* equilibrium pore pressure and u_i is pore pressure at start of dissipation test.

Since the target is to calculate t_{50} for all dissipation tests, $U = 50$ % is considered. According to the hydrological information of the study area as the ground water level was located down the slope and it was not touched by the cone during penetration, value of *in-situ* equilibrium pore pressure is considered to be zero. Having values of u_i from dissipation test, u_t at 50 % of dissipation is calculated. Accordingly, with the use of dissipation curves (Fig. 6.6), values of t_{50} are calculated.

Chai et al. (2012) proposed an empirical equation to correct the value of t_{50} for non-standard dissipation test as follows:

$$t_{50c} = t_{50} \Big/ \left[1 + 18.50 \cdot (t_{u\ max} / t_{50})^{0.67} \cdot (I_r/200)^{0.30}\right] \tag{6.14}$$

Taking the above-mentioned equations into consideration, k_h in respective depths are calculated and presented in Table 6.3.

According to Table 6.3, values of k_h are very low in all samples which indicate the presence of fine grained materials in the layers. The lowest value of k_h is calculated at the depth of 9 m while the greatest value of k_h is achieved at the depth of 6 m.

The greatest value of k_h is achieved at the depth of 6 m which is located in the upper unconfined and leaky aquifer 1. As this point is situated above the permeable strata, it has greater permeability (Fig. 6.3). Values of k_h at depths of 9 and 11 m are very close to each other and are lower than k_h at the depth of 6 m. These points are located at the lower semi-confined aquifer 2 which is surrounded by aquitards at depths of 7 and 13.70 m.

Taking the very low horizontal permeability values of layers at depths of 9 and 11 m and pore water pressure condition of the layer between depths of 7.20–13.70 m into consideration the aquitard located at the depth of 13.70 m is considered as the most impermeable layer (Fig. 6.3). Because of this characteristic, at times of precipitation, infiltrated water cannot percolate rapidly toward the groundwater table causing excessive extra weight cumulating on the weakest and the most impermeable layers and increasing the failure potential of the slope.

6.4.4 Liquefaction Analysis with CLiq Software

Liquefaction potential index derived using SCPT data was analyzed by CLiq software and results are presented in Fig. 6.5d. Considering discrete categories of LPI proposed by Iwasaki (1986), the first 2.70 m of the profile has a very low risk for liquefaction (Fig. 6.5d). Soil layers between depths of 2.70 and 8.60 m are at low risk of liquefaction and from the depth of 8.60 m until the end of CPT profile, soil layers are potentially at high risk of liquefaction (Fig. 6.5d). The layer located at the depth of 13.70 m, which was indicated before as the most probable slip surface, is in the zone with high risk of liquefaction. Comparing the results of this section with the liquefaction probability evaluation discussed in the VCPT section, CLiq specifies greater areas with a risk of liquefaction than VCPT. Areas that CLiq indicates with high liquefaction potential by using SCPT data to make assumptions about cyclic behavior of layers are basically concentrated at the lower part of CPT profile while in VCPT, liquefiable layers are detected at the upper part of CPT profile by measuring the change in fabric upon small strain activation. For analysis of liquefaction in CLiq, the software considers coarse grain sized materials concentrated at the lower part of CPT profile as loose pulverized sand while these materials are actually the product of ignimbrite weathering and are not considered necessarily as pulverized sand which is the proof for a significant difference between the two methods.

Table 6.3 Horizontal soil permeability calculation details based on pore pressure dissipation test

Depth(m)	q_t (kPa)	V_s (m/s)	G (kPa)	I_r	t_{50} (sec)	$t_{u\,max}$ (sec)	t_{50c} (sec)	C_h (m^2/s)	F_r	Q_{tn}	I_c	α_M	M (kPa)	k_h (m/s)
6	1,156.87	43.50	3,556.98	55.10	1,949	3,898	88	3.13E-06	2.21	8.48	2.98	8.48	8,359.97	3.67E-09
9	2,458.38	55.97	6,292.89	43.18	2,383	4,766	115	2.11E-06	2.04	10.19	2.90	10.19	22,429.16	9.23E-10
11	1,940.52	55.52	6,175.56	57.97	5,155	10,310	229	1.23E-06	2.76	6.72	3.21	6.72	10,905.37	1.11E-09

6.5 Summary and Conclusion

In this study a preliminary evaluation of the site conditions was made by using the map of the study area and site history as reported by published geological information. Static, vibratory and dissipation tests were performed by using the cone penetration test unit which is called GOST at the top of the slide scar. Cone penetration tests were performed to provide subsurface information. A static cone penetration test provided information in regard to soil grain size variations and the local strength variations with depth. The location of a possible slide plane was detected at a depth of 13.70 m based on low values of tip resistance, sleeve friction, undrained shear strength. Sensitivity of subsurface layers was also evaluated by using static cone penetration test results. The upper 14.60 m of layers were considered as medium sensitive/sensitive materials except for the layers between depths of 3.20 and 3.80 and 13.70 and 14.60 m which were identified as extra sensitive layers and indicated the vulnerability of the latter mentioned layers to disturbance. A vibratory cone penetration test was basically performed to evaluate subsurface layers liquefaction probability. Accordingly, the layer between depths of 4 and 4.50 m is potentially vulnerable to liquefaction. Pore water pressure increased under the effect of vibration in the layer between depths of 7.80 and 13.70 m which indicates the reduction of effective stresses under the effect of vibration. The maximum increase in pore water pressure happened at the depth of 13.70 m. Dissipation tests were performed at depths of 6, 9 and 11 m to evaluate the *in-situ* horizontal soil permeability at the respective depths. These measurements gave an average value of horizontal permeability of 1.9×10^{-9} m/s. The low values of horizontal permeability showed impermeable properties of layers above the proposed slip surface. Least permeable layers provided a barrier to infiltrated rain water which causes extra weight on the slope. The extra weight is an important factor in triggering the slide. The CLiq software was used to evaluate soil layers liquefaction potential. The software results showed the layers between 8.60 and 16 m to be at high risk for liquefaction. The software was unable to specify any liquefiable layer at the first 8.60 m of cone penetration test profile while vibratory cone penetration test specifies vulnerable layers to liquefaction in that area. Software considered coarse grain sized materials located at the bottom of the CPT profile as the pulverized sand and reported high risk of liquefaction for the respective layers while the materials are weathered ignimbrite.

In conclusion, based on static CPT, Vibratory CPT and dissipation test, the layer located at the depth of 13.70 m is identified as the most probable slip surface. The landslide is a shallow translational slide with a length of approximately 30 m and 6 m wide, and is formed on a slope of 27°. This equates to the scarp base at approximately 14 m depth. The lower portion of the scarp itself is covered by debris, but ignimbrite is exposed immediately below the base of the scarp. Therefore, the depth of 13.7 m observed in the CPT results is believed to be entirely consistent with the geomorphic evidence of the scarp face.

In this investigation cone penetration testing provided valuable information in landslide characterization when evaluated in conjunction with topographical and geological information.

Acknowledgment The authors acknowledge funding by Deutsche Forschungsgemeinschaft (DFG) via the Integrated Coastal Zone and Shelf Sea Research Training Group INTERCOAST and the MARUM Center for Marine Environmental Science at the University of Bremen. We would like to thank the Department of Earth and Ocean Sciences at University of Waikato for their help and support during the project, and Mr and Mrs Lucas for access to the site. We appreciate the effort of Prof. Dr. Haflidi Haflidson from University of Bergen and Prof. Dr. Kate Moran from University of Victoria for reviewing the manuscript. Special thanks to Mr. Wolfgang Schunn for managing instruments and operation CPT unit.

References

Bonita J, Mitchell JK, Brandon TL (2004) The effect of vibration on the penetration resistance and pore water pressure in sands. In: da Fonseca V, Mayne PW (eds) Proceedings of the ISC-2 on geotechnical and geophysical site characterization. Millpress, Rotterdam, pp 843–851

Briggs RM, Hall GJ, Harmsworth GR, Hollis AG, Houghton BF, Hughes GR, Morgan MD, Whitbread-Edwards AR (1996) Geology of the Tauranga area. Sheet U14 1:50,000. Occasional report 22. Department of Earth Sciences, University of Waikato, Hamilton, New Zealand

Brown WJ (1983) The changing imprint of the landslide on rural landscapes on New Zealand. Landscape Plan 10:173–204

Chai J, Sheng D, Carter JP, Zhu H (2012) Coefficient of consolidation from non-standard piezocone dissipation curves. Comput Geotech 41:13–22

CLiq (2008) Geologismiki. Geotechnical liquefaction software at http://www.geologismiki.gr/

Foundation Engineering Geotechnical and Environmental Consultants (2006) Geotechnical investigation report on proposes rural residential subdivision at 52 Pyes Pa Road, Tauranga, For Pyes Pa Investments Limited. Project No. 12921, pp 77–99

Giannecchini R, Galanti Y, D' Amato Avanzi G (2012) Critical rainfall thresholds for triggering shallow landslides in the Serchio River Valley (Tuscany, Italy). Nat Hazard Earth Syst Sci 12:829–842

Hegazy YA, Mayne PW (1995) Statistical correlations between V_s and cone penetration data for different soil types. In: Proceedings of the international symposium on cone penetration testing. CPT'95, vol 2. Swedish Geotechnical Society, Linköping, Sweden, pp 173–178

Hird CC, Springman SM (2006) Comparative performance of 5 cm^2 and 10 cm^2 piezocones in a lacustrine clay. Geotechnique 56(6):427–438

Houghton BF, Wilson CJN, McWilliams MO, Lanphere MA, Weaver SD, Briggs RM, Pringle MS (1995) Chronology and dynamics of a large silicic magmatic system: central Taupo Volcanic Zone, New Zealand. Geology 23:13–16

Iwasaki T (1986) Soil liquefaction studies in Japan: state-of-the-art. Soil Dyn Earthq Eng 5(1):2–70

Konrad J-M (1985) Undrained cyclic behaviour of Beaufort sea silt. In: Proceedings of Arctic'85, ASCE, San Francisco, 25–27 March, pp 830–837

Lunne T, Robertson PK, Powell JJM (1997) Cone penetration testing in geotechnical practice. Taylor & Francis Group, London and New York

Ozcep F, Erol E, Saracoglu F, Haliloglu M (2010) Seismic slope stability analysis: Gurpinar (Istanbul) as a case history. Sci Res Essays 5(13):1615–1631

Reddi LN (2003) Seepage in soils. Wiley, Hoboken, p 07030

Robertson PK (2009) Performance based earthquake design using the CPT. Keynote lecture, In: International conference on performance-based design in earthquake geotechnical engineering – from case history to practice, IS Tokyo, June 2009

Robertson PK (2010) Estimating in-situ soil permeability from CPT & CPTu. In: 2nd international symposium on cone penetration testing, Huntington Beach, CA, USA. vol 2–3, Technical Papers, session 2, Interpretation, paper No. 51

Robertson PK, Wride CE (1998) Evaluating cyclic liquefaction potential using the cone penetration test. Can Geotech J 35:442–459

Robertson PK, Campanella RG, Gillespie D, Greig J (1986) Use of Piezometer cone data. In: Insitu'86 use of in-situ testing in geotechnical engineering. GSP 6, ASCE, Reston, VA, Specialty Publication, pp 1263–1280

Sasaki Y, Itoh Y, Shimazu T (1984) A study on the relationship between the results of vibratory cone penetration tests and earthquake-induced settlement of embankments. In: Proceedings, 19th annual meeting of JSSMFE, Tokyo, Japan

Schmertmann JH (1978) Guidelines for cone penetration test, performance and design. US Federal Highway Administration, Washington, DC, Report, FHWATS-78-209, p 145

Skempton AW, Northey RH (1952) The sensitivity of clay. Geotechnique 3(1):30–53

Teh CI, Houlsby GT (1991) An analytical study of the cone penetration test in clay. Geotechnique 41(1):17–34

Tokimatsu K (1988) Penetration tests for dynamic problems. Penetration testing 1988, vol 1, In: Proceedings of the ISOPT-1, Balkema, Rotterdam, pp 117–136

Trustrum NA, Thomas VG, Lambert MG (1984) Soil slip erosion as a constraint to hill country pasture production. Proc N Z Grassl Assoc 45:66–71

Chapter 7
Geomechanical Characterization of Submarine Volcano-Flank Sediments, Martinique, Lesser Antilles Arc

Sara Lafuerza, Anne Le Friant, Michael Manga, Georges Boudon, Benoit Villemant, Nicole Stroncik, Barry Voight, Matt Hornbach, Osamu Ishizuka, and The Expedition 340 Scientific Party

Abstract Onshore-offshore geophysical studies conducted on Martinique have identified major flank collapse events of Montagne Pelée that generated large submarine mass wasting deposits. Here, we evaluate the preconditioning factors involved in the deformation and failure of marine sediments related to volcano-flank collapse events. We use core logging, sedimentological and geotechnical data of the upper 200 m of core at sites U1397, U1398, U1399 and U1400 drilled during the Integrated Ocean Drilling Program (IODP) expedition 340, west of Martinique. We find that the low hydraulic conductivity of hemipelagic sediment causes low rates of dewatering of turbidites and tephra layers allowing excess pore fluid pressures to persist at depth. Overpressure generation was likely enhanced during major flank collapses, leading to low shear strength and subsequent deformation of large volumes of marine sediments, as found at Site U1400.

S. Lafuerza (✉) • A. Le Friant • G. Boudon
Institut de Physique du Globe de Paris, Sorbonne Paris Cité, Univ Paris Diderot, UMR 7154 CNRS, F-75005 Paris, France
e-mail: lafuerza@ipgp.fr

M. Manga
Department of Earth and Planetary Science, University of California, Berkeley, CA 94720, USA

B. Villemant
Laboratoire de Petrologie, Geochimie, Volcanologie, University Pierre et Marie Curie-Paris 6, UMR 7193, ISTEP, F-75005 Paris, France

N. Stroncik
Department of Geology and Geophysics, Texas A & M, College Station, TX 77845, USA

B. Voight
Geosciences, Penn State University, University Park, PA 16802, USA

M. Hornbach
Department of Earth Sciences, Southern Methodist University, Dallas, TX 75275, USA

O. Ishizuka
Geological Survey of Japan, AIST, Central 7 1-1-1 Higashi, Tsukuba, Ibaraki 305-8567, Japan

S. Krastel et al. (eds.), *Submarine Mass Movements and Their Consequences*, Advances in Natural and Technological Hazards Research 37, DOI 10.1007/978-3-319-00972-8_7,

Keywords Undrained shear strength • Consolidation properties • Overpressure • Sediment deformation • Volcano-flank collapse • Martinique

7.1 Introduction

Volcano-flank collapses and subsequent debris avalanches are a major hazard in coastal areas of volcanic islands. Their entry into the sea can have catastrophic effects on-land and on nearby islands by generating tsunami waves (Harbitz et al. 2012). Along the Lesser Antilles volcanic arc, many prehistoric flank collapses have been recognized based on submarine deposits offshore Montserrat (Le Friant et al. 2004; Lebas et al. 2011; Watt et al. 2012a, b), Dominica (Deplus et al. 2001; Boudon et al. 2007), Martinique (Le Friant et al. 2003), St. Lucia (Deplus et al. 2001) and St. Vincent (Le Friant et al. 2009). A well-documented flank collapse occurred on Montserrat in 1997 (Voight et al. 2002).

Marine geophysical and on-land studies in Martinique have identified three submarine mass wasting deposits related to three major flank collapse events of Montagne Pelée volcano at ~100 ka (D1, 1100 km^2), ~25 ka (D2, 700 km^2) and ~9 ka (D3, 60 km^2) (Fig. 7.1) (Le Friant et al. 2003). Seismic reflection data for these deposits suggest that they consist of debris avalanche material that incorporate shallow marine sediment (Deplus et al. 2001). Incorporation of marine sediments increases the overall landslide volume and mobility, with important implications for tsunami modeling (e.g. Voight et al. 2012).

To improve our understanding of both eruption history and the consequences of flank collapses, IODP expedition 340 obtained sediment records offshore Montserrat, Dominica and Martinique (Le Friant et al. 2011). For the first time ever, submarine mass wasting deposits in volcanic islands were successfully drilled and revealed the importance of marine sediment deformation. Here we report physical properties obtained from core logging as well as sedimentological and geotechnical analyses that we use to infer the consolidation state of the upper 200 m of sediment drilled at sites U1397, U1398, U1399 and U1400 (Fig. 7.1). Our objective is to evaluate the preconditioning factors involved in the deformation and failure of marine sediments during major volcano-flank collapses on Martinique.

7.2 Geomechanical Characterization

Our study focuses on the consolidation state of materials, which is the gradual reduction in volume and water content of low permeability material, due to the dissipation by drainage of excess pore water pressure caused by increased external loading (Terzaghi et al. 1996). Materials are considered “normally consolidated” when excess pore pressures (exceeding hydrostatic) are completely dissipated.

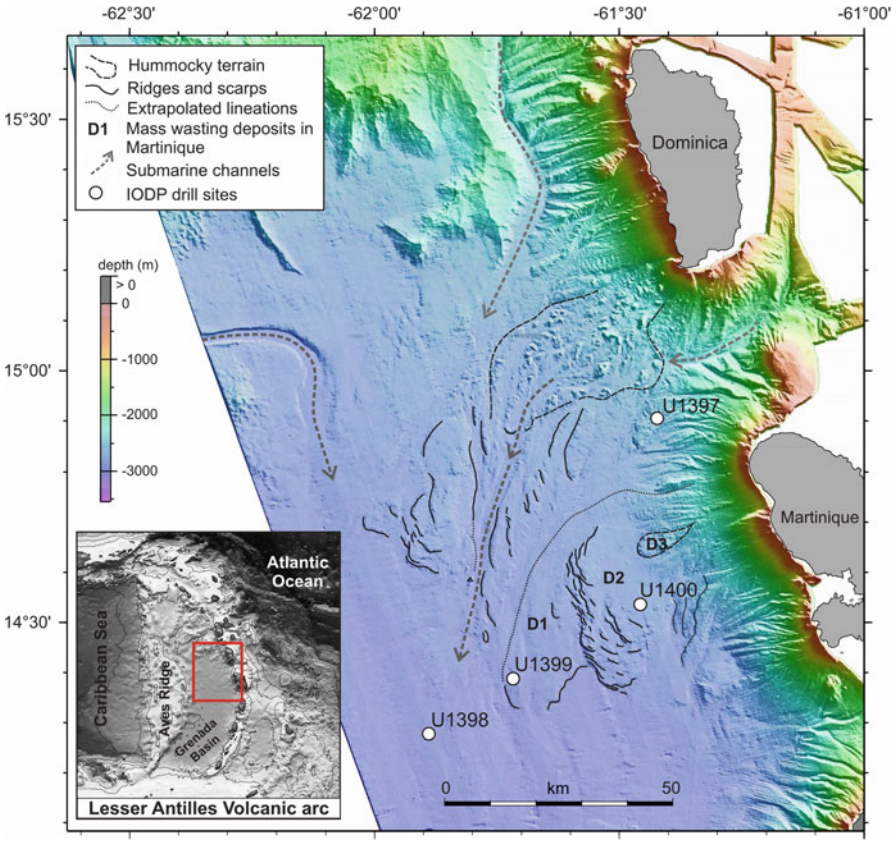

Fig. 7.1 Location of IODP drill sites west of Martinique. Inset map shows satellite bathymetry of the Lesser Antilles (Smith and Sandwell 1997). Multibeam bathymetry map (water depth given by color scale) from CARAVAL 2002 and AGUADOMAR 1999 cruises (IPGP-IFREMER) shows main geomorphologic features (based on Le Friant et al. 2003)

From laboratory uniaxial consolidation experiments, which measure how porosity decreases with increasing stress, the maximum effective vertical stress that has acted in the past – the preconsolidation pressure (σ'_p) – can be estimated. The ratio between σ'_p and the in situ vertical effective stress σ'_v is referred to as the overconsolidation ratio (OCR), which indicates whether a sediment is normally consolidated (OCR = 1), i.e. current overburden is the largest ever supported; whether previous stresses exceeded that of current overburden, reflecting processes such as erosion, deformation or cementation (OCR > 1); or if excess pore pressures maintain abnormally high porosities at depth (OCR < 1). When OCR < 1, excess pore pressure Δu can be expressed as:

$$\Delta u = \sigma'_v - \sigma'_p \tag{7.1}$$

Table 7.1 Physical properties measured on whole-round samples collected at Hole U1400C

	5H6	7H2	10H4	13H4	19H4
Depth (mbsf)	47	61	84	109	159
Description	Carbonate ooze	Carbonate ooze	Pink tephra	Carbonate ooze	Carbonate ooze
σ'_v (kPa)	251	309	597	489	1,240
wc (%)	74.4	80.2	52.1	82.8	37.1
PI (%)	11	12	17	28	12
Clay (%)	23.6	23	35.6	11	24.6
Silt (%)	48.9	59.1	36.7	28.6	42.9
Sand (%)	27.5	17.9	27.7	60.4	32.5
e_0 (−)	2.07	2.23	1.40	2.41	1.08
e_0 (at σ'_v)	2.02	2.18	1.31	2.34	1.03
$\Delta e/e_0$	0.02	0.02	0.07	0.03	0.04
σ'_p (kPa)	299	505	219	592	811
OCR (−)	1.19	1.63	0.37	1.21	0.65
Δu (%σ'_v)	–	–	63	–	35
k (m·s^{-1}) at σ'_v	$2.0{\cdot}10^{-9}$	$3.4{\cdot}10^{-10}$	$1.5{\cdot}10^{-10}$	$1.2{\cdot}10^{-9}$	$2.8{\cdot}10^{-9}$
k (m·s^{-1})	$4.5{\cdot}10^{-10}$	$1.8{\cdot}10^{-10}$	$3.8{\cdot}10^{-11}$	$1.7{\cdot}10^{-10}$	$2.8{\cdot}10^{-9}$

σ'_v effective vertical stress, *wc* water content, *PI* plasticity index, e_0 initial void ratio before loading, σ'_p preconsolidation pressure, *OCR* Overconsolidation ratio, Δu excess pore fluid pressure considering hydrostatic conditions, k hydraulic conductivity

Standard consolidation experiments require minimally disturbed samples, but such sampling interferes with continuous sediment core recovery. Thus only a few undisturbed whole-round samples were obtained during IODP expedition 340. Here we report only uniaxial consolidation (oedometer) tests performed on five samples collected from Hole C at Site U1400 (Table 7.1). We also use the Skempton empirical method to predict the shear strength-overburden stress ratio for normally consolidated (OCR = 1) marine sediments:

$$Su/\sigma'_v = 0.11 + 0.0037\,PI \tag{7.2}$$

where Su = undrained shear strength, σ'_v = effective stress, and PI = plasticity index (e.g. Bryant et al. 1986).

Hydraulic conductivity (k) was measured by the falling-head method immediately after reaching effective stress conditions and before the last loading stage during consolidation experiments. A handheld penetrometer (Soiltest 29-3729) and an automated shear vane (Wykeham Farrance) were used to measure *Su* onboard when materials were sufficiently fine-grained to ensure undrained conditions. Grain size measurements were performed with a particle size analyzer Coulter LS 230 and Atterberg limits and *PI* according to Feng (2001). Interpretation of σ'_p follows the bi-logarithmic approach of Onitsuka (Grozic et al. 2003). σ'_v is calculated from bulk density from shipboard gamma ray attenuation measurements on whole-round samples (Expedition 340 Scientists 2012).

7.3 Results

7.3.1 Summary of Hole Stratigraphy

For our purposes, we distinguish three main lithologies: (i) hemipelagic, (ii) volcanic (turbidite and/or coarse tephra) and (iii) hemipelagic with intercalations of fine turbidite/tephra (Fig. 7.2). Site U1399 penetrated distal area of mass wasting

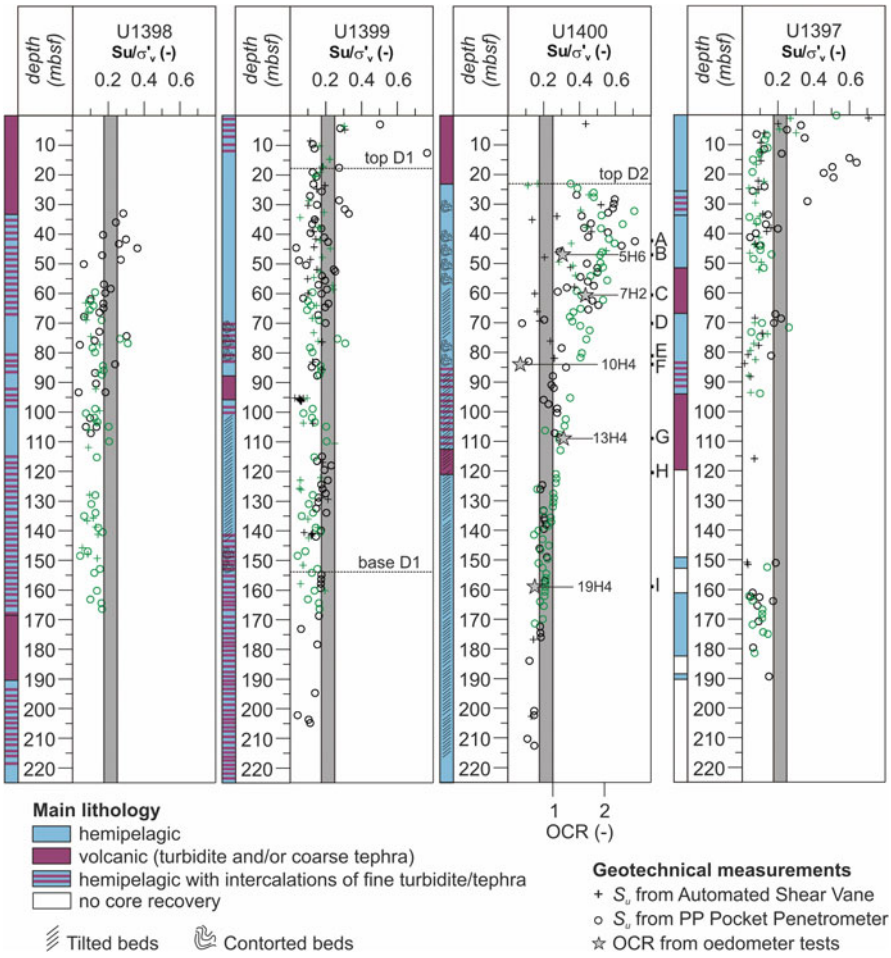

Fig. 7.2 Depth distribution of ratio Su/σ'_v. *Gray shading*, normally consolidated materials. *Black* and *green colors* are used to differentiate *Su* measurements at holes *B* (*black*) and *C* (*green*) at each drilling site, except for site U1397, with hole *A* in *black* and hole *C* in *green*. *A* to *I*, location of photos in Fig. 7.4. *Circles*: *Su*-handheld penetrometer; crosses: *Su*-automated shear vane

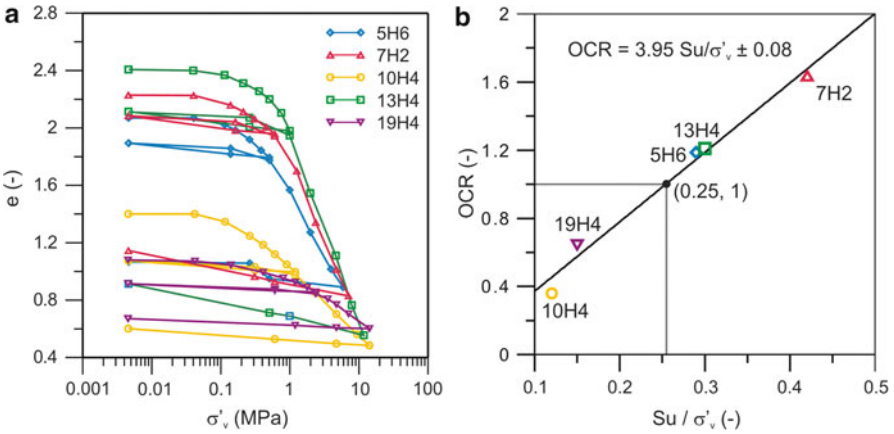

Fig. 7.3 (**a**) Consolidation curves showing porosity reduction (decreasing void ratio *e*) during uniaxial loading (increasing stress σ'_v) of whole-round samples (5H6 to 19H4; Hole U1400C). (**b**) Linear relationship between overconsolidation ratios (*OCR*) and Su/σ'_v

deposit D1 (~100 ka) and Site U1400 penetrated mass wasting deposits D1 and D2 (~25 ka) described by Le Friant et al. (2003). Deformation in these is characterized mainly by tilted bedding (Expedition 340 Scientists 2012).

7.3.2 Consolidation State

Evaluation of quality for our whole-round samples (Hole U1400C), based on the change in pore volume (Δe) relative to the initial pore volume (e_0), was possible for samples with OCR > 1 (Lunne et al. 2006). These data suggest that samples 5H6, 7H2, 13H4 are of high quality ($\Delta e/e_0 < 0.04$, Table 7.1).

OCR obtained from oedometer tests (Table 7.1) are plotted together with obtained Su/σ'_v (Fig. 7.3). A linear regression results in $Su/\sigma'_v = 0.25 \pm 0.08$ for normally consolidated sediments (OCR = 1). The Skempton approach used for U1400C data with average $PI = 16$ (Table 7.1) yields $Su/\sigma'_v = 0.17$. Given mean *PI* values of 17–21 in hemipelagic sediments in sites U1397, U1398 and U1399, we assume materials are underconsolidated if Su/σ'_v <0.17–0.25.

Ratios Su/σ'_v <0.17–0.25 indicate underconsolidated sediments in the upper 200 m at site U1397 and >50 m below seafloor (mbsf) at U1398, and underconsolidated to marginally normally-consolidated sediments at U1399 (Fig. 7.2). At U1400, Su/σ'_v suggest materials <120 m are overconsolidated (exceedingly so <85 m, with 85–120 m transitional), 120–180 m are normally consolidated, and >180 m are underconsolidated. The latter condition implies excess pore pressures (Δu). Two consolidation samples from U1400C suggest overpressures with $\Delta u = 63$ % of vertical stress (63 $\%\sigma'_v$) in sample 10H4 (fine-grained pink tephra) and 35 $\%\sigma'_v$ in sample 19H4 (hemipelagic sediment with dark tephra)

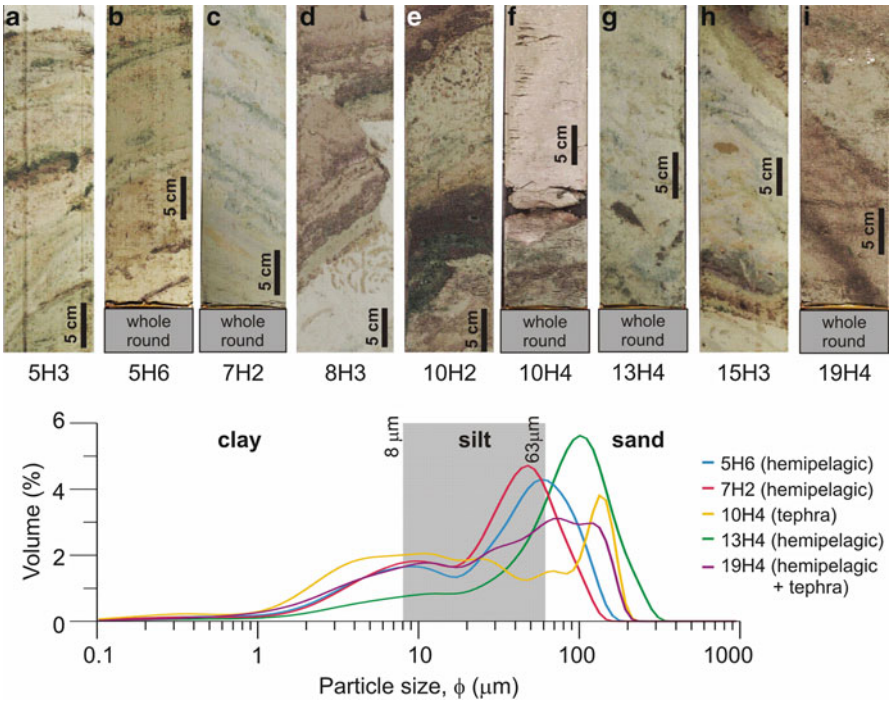

Fig. 7.4 *a* to *i*, examples of facies and structures present at Hole U1400C. *Bottom*: particle size distribution of whole-round samples

(Fig. 7.4). The 19H4 result is consistent with the Su/σ'_v profile, but the 10H4 result is anomalous with σ'_p and OCR exceedingly low, compared to adjacent Su values that indicate OCR ~ 1. The result might reflect unusual properties of tephra but should be considered suspect. U1400C show tilted beds and in some cases faulting or folding (Fig. 7.4), and such deformation could affect the stress state.

7.3.3 Hydraulic Conductivity

Measurements of hydraulic conductivity confirm that hemipelagic sediments and fine-grained tephras have low k. At effective stress conditions, the highest k measured corresponds to the deepest sample (19H4; $2.8 \cdot 10^{-9}$ m·s^{-1}), and the shallowest (5H6; $2.0 \cdot 10^{-9}$ m·s^{-1}), with similar grain size (Table 7.1). A slightly lower value ($1.2–2.1 \cdot 10^{-9}$ m·s^{-1}) is found for relatively coarser 13H4 (Table 7.1). Values of k an order of magnitude less ($3.4 \cdot 10^{-10}$ and $1.5 \cdot 10^{-10}$ m·s^{-1}) are found for the other two samples (7H2 and 10H4). Values of k at higher stresses are an order of magnitude less except for sample 7H2, which shows a smaller decrease, and sample 19H4, in which no change in k was noted.

7.4 Discussion and Conclusion

Our results suggest that in general, the upper 200 m of the drilled sediments west of Martinique have pore fluid pressures in excess of hydrostatic, except Site U1400 where overpressure appears only deeper than 180 mbsf. The inferred overpressure is explained by slow pore fluid escape during the burial of permeable sediment (turbidities and tephras) sandwiched within minimally permeable hemipelagic sediment. The Δu values obtained at Hole U1400C suggest that materials with low k (10^{-9}–10^{-10} m·s^{-1}) can maintain overpressure at depth, as shown by $\Delta u = 35\ \%\sigma'_v$ at 159 mbsf (19H4).

At Site U1400, overconsolidation likely reflects compression by sediment deformation rather than erosion. This is consistent with a compressive zone within deposit D2, evidenced by the transverse ridges observed on bathymetry (Fig. 7.1; Le Friant et al. 2003). At Site U1400, normal consolidation in the transition zone (85–120 mbsf) is implied by our data despite deformation revealed by sediment structures (Fig. 7.4).

No clear conclusions can be drawn about the link between the grain size and k, since calculated k is not proportional to sand content (Table 7.1), though we have measurements on a limited number of samples. This suggests that grain shape, sorting, and other micro-structural properties must control hydraulic conductivity, perhaps explaining why tephra of anomalous sample 10H4 indicates overpressure (a suspect result). At other sites (U1397, U1398, U1399) the presence of a relatively higher abundance of thicker turbidites (Fig. 7.2) and coarser tephra, compared to the sediment succession at Site U1400, results in a higher storage of pore water and thus higher overpressure, as deduced from S_u/σ'_v ratios (Fig. 7.2).

We found a general correlation between *Su* profiles and results of consolidation experiments, though *Su* measurements could be compromised in some holes and at some depths. Some *Su* values measured in split cores may be lower because of anisotropy and/or remoulding during coring. We cannot quantify the reliability of our *Su* measurements but three of the consolidation samples were of high quality (Table 7.1), and four of five appear relatively consistent with Su/σ'_v trends. Only one sample (10H4) is anomalous. Hence, we consider that our approach provides reliable first evidence of overpressures as a preconditioning factor for sediment deformation and failure. Overpressure can be enhanced by undrained loading (Voight et al. 2012) and/or seafloor acceleration (Moretti et al. 2012) triggered by debris avalanche emplacement, resulting in low shear strengths, which could account for the deformation of sediments at Site U1400.

Acknowledgments This research is based on shipboard data and core samples provided by IODP and is supported by the Institut de Physique du Globe de Paris. The authors thank University of Barcelona and M. Guart for use of laboratory facilities for grain size analyses. We thank J. Locat and N. Sultan for reviews.

References

Boudon G, Le Friant A, Komorowski J-C et al (2007) Volcano flank instability in the Lesser Antilles Arc: diversity of scale, processes, and temporal recurrence. J Geophys Res 112:B8

Bryant W, Wetzel A, Taylor E et al. (1986) Consolidation characteristics and permeability of Mississippi Fan sediments. In: Initial reports deep sea drilling project, vol 96. Washington, pp 797–809

Deplus C, Le Friant A, Boudon G et al (2001) Submarine evidence for large-scale debris avalanches in the Lesser Antilles Arc. Earth Planet Sci Lett 192:145–157

Expedition 340 Scientists (2012) Lesser Antilles Volcanism and landslides: implications for hazard assessment and long-term magmatic evolution of the arc. IODP Prelim Rep 340, pp 103. doi:10.2204/iodp.pr.340.2012

Feng T-W (2001) A linear log d-log w model for the determination of consistency limits of soils. Can Geotech J 38:1335–1342

Grozic JLH, Lunne T, Pande S (2003) An oedometer test study on the preconsolidation stress of glaciomarine clays. Can Geotech J 40:857–872

Harbitz CB, Glimsdal S, Bazin S et al (2012) Tsunami hazard in the Caribbean: regional exposure derived from credible worst case scenarios. Cont Shelf Res 38:1–23

Le Friant A, Boudon G, Deplus C et al (2003) Large-scale flank collapse events during the activity of Montagne Pelée, Martinique, Lesser Antilles. J Geophys Res 108:1–15

Le Friant A, Harford CL, Deplus C et al (2004) Geomorphological evolution of Montserrat (West Indies): importance of flank collapse and erosional processes. J Geol Soc 161:147–160

Le Friant A, Boudon G, Arnulf A et al (2009) Debris avalanche deposits offshore St. Vincent (West Indies): impact of flank-collapse events on the morphological evolution of the island. J Volcanol Geotherm Res 179:1–10

Le Friant A, Ishizuka O, Stroncik N (2011) Drilling volcanic landslides deposits and volcanoclastic sediments in the Lesser Antilles arc: implications for hazard assessment and long-term magmatic evolution of the arc. Integr Ocean Drill Progr Sci Prospect Exped 340:86

Lebas E, Le Friant A, Boudon G et al (2011) Multiple widespread landslides during the long-term evolution of a volcanic island: Insights from high-resolution seismic data, Montserrat Lesser Antilles. Geochem Geophys Geosyst 12:5

Lunne T, Berre T, Andersen KH et al (2006) Effects of sample disturbance and consolidation procedures on measured shear strength of soft marine Norwegian clays. Can Geotech J 750:726–750

Moretti L, Mangeney A, Capdeville Y et al (2012) Numerical modeling of the Mount Steller landslide flow history and of the generated long period seismic waves. Geophys Res Lett 39:L16402

Smith WHF, Sandwell DT (1997) Global sea floor topography from satellite altimetry and ship depth soundings. Science 277(5334):1956–1962

Terzaghi K, Peck RB, Mesri G (1996) Soil mechanics in engineering practice, 3rd edn. Wiley, New York

Voight B, Komorowski JC, Norton GE et al (2002) The 26 December (Boxing Day) 1997 sector collapse and debris avalanche at Soufrière Hills Volcano, Montserrat. In: Druitt TH, Kokellar BP (eds) The Eruption of Soufrière Hills Volcano, Montserrat, from 1995 to 1999. Geological Society, London, pp 363–407

Voight B, Le Friant A, Boudon G et al (2012) Undrained sediment loading key to long-runout submarine mass movements: evidence from the Caribbean Volcanic Arc. In: Kawamura K, Ikehara K, Yamada Y et al (eds) Submarine mass movements and their consequences. Springer, Dordrecht, pp 417–428

Watt SFL, Talling PJ, Vardy ME et al (2012a) Combinations of volcanic-flank and seafloor-sediment failure offshore Montserrat and their implications for tsunami generation. Earth Planet Sci Lett 319–320:228–240

Watt SFL, Talling PJ, Vardy ME et al (2012b) Widespread and progressive seafloor-sediment failure following volcanic debris avalanche emplacement: landslide dynamics and timing offshore Montserrat, Lesser Antilles. Mar Geol 323–325:69–94

Part II
Gas Hydrates and Role of Interstitial Fluids in Submarine Slope Failure

Chapter 8
Interrelationship Between Sediment Fabric, Pore Volume Variations as Indicator for Pore Pressure Changes, and Sediment Shear Strength

Lutz Torbahn and Katrin Huhn

Abstract The physical characterization of sediments forms the basis for slope stability analysis. The shear strength of water-saturated sediments is a function of sediment properties and pore pressure conditions. A reduction in strength, e.g., as a result of transient pore pressure changes, can cause the collapse of the sediment matrix and subsequently slope sediment fails. As failure processes in the sediment elude from direct observation, matrix deformation processes, sediment grain interactions, and the associated stresses can be examined by numerical simulations. The major aim of this study was to evaluate the effects of varied sediment fabric on pore volume changes and sediment strength in sheared samples. For all sediment fabrics, an inversely proportional relationship between strength and porosity was observed. A controlling effect of grain shape on the maximum friction coefficient value was demonstrated.

Keywords Sediment strength • Pore volume change • Sediment fabric • Failure mechanism • Discrete element method

8.1 Introduction

Numerous studies have shown that mineralogical composition and pore fluid pressure control the mechanical behaviour of water-saturated sediments (e.g., Lambe and Whitmann 1979; Marone 1998), which can be described by the Mohr-Coulomb failure criterion (Handin 1969; Byerlee 1978). If the pore pressure exceeds the characteristic material strength, the stress-imposed granular matrix will fail (Mitchell and Soga 2005; Goren et al. 2010). Therefore, transient pore pressure changes are

L. Torbahn (✉) • K. Huhn
MARUM – Center for Marine Environmental Sciences, University of Bremen, Leobener Str, D-28359 Bremen, Germany
e-mail: ltorbahn@marum.de

S. Krastel et al. (eds.), *Submarine Mass Movements and Their Consequences*, Advances in Natural and Technological Hazards Research 37, DOI 10.1007/978-3-319-00972-8_8,

widely accepted as a potential trigger mechanism for landslides (e.g., Hampton et al. 1996; Locat and Lee 2002). Various processes can cause such transient pore pressure variations, e.g., sea level changes and gas hydrate dissolution. The latter will be of particular importance in the near future, especially in higher latitudes, because gas hydrate dissociation will be driven by global warming (Mienert et al. 2010). Accordingly, an improved understanding of the interplay between sediment fabric, pore pressure (or indicative pore volume variations), and sediment shear strength is of increasing importance to define the potential trigger mechanisms of submarine landslides.

To examine these processes occurring prior to and during failure of submarine slopes, which elude from direct observation, we developed a 3D numerical direct shear test based on the Discrete Element Method (DEM). With this the relationship between sediment fabric, pore volume variations, and shear strength was examined. In our simulations, the sheared samples represented the basal shear plane of submarine landslides, whereas the fixed part of the shear box represented the undisturbed slope sediment. The mobilized sediment of the landslide was represented by the movable part of the shear box. The shear plane evolved inside the sheared sample as the localized failure. This experimental setting allowed for investigation of failure initiation and failure evolution. Sediment fabrics were created based on idealized fundamental grain shapes of spheres and aggregates of rod-like and plate-like shape as numerical replacements for natural silt and clay grains. The simulations were designed to address the following key questions:

1. How is sediment strength linked to pore volume changes during failure?
2. Does sediment fabric or sediment-grain complexity control sediment shear strength and pore volume evolution during shearing?
3. Are there any local effects of pore volume changes during the evolution of failure planes?

8.2 Method

In recent years, numerical simulations using the DEM came into focus for investigation of physical aspects of grain interactions and localized deformation inside granular brittle materials (Morgan 1999; Hazzard and Mair 2003; Abe and Mair 2009). The principle functionality of the DEM (e.g., Cundall and Strack 1978; Potyondy and Cundall 2004) provided the framework for the current study in which the three-dimensional DEM code PFC3D (ITASCA©) was used.

We developed a numerical direct shear device (Fig. 8.1) comparable in function to laboratory direct shear experiments. For each test, 120,000 spherical grains of uniform size (2 μm) filled a six-sided rectangular shear box (100 μm $\times$ 100 μm). The spherical grains approximated the shape of natural rounded silt with a grain size equivalent to the transition from clay to silt. Frictionless walls were used to enable (i) comparable boundary conditions in all experiments and (ii) to exclude

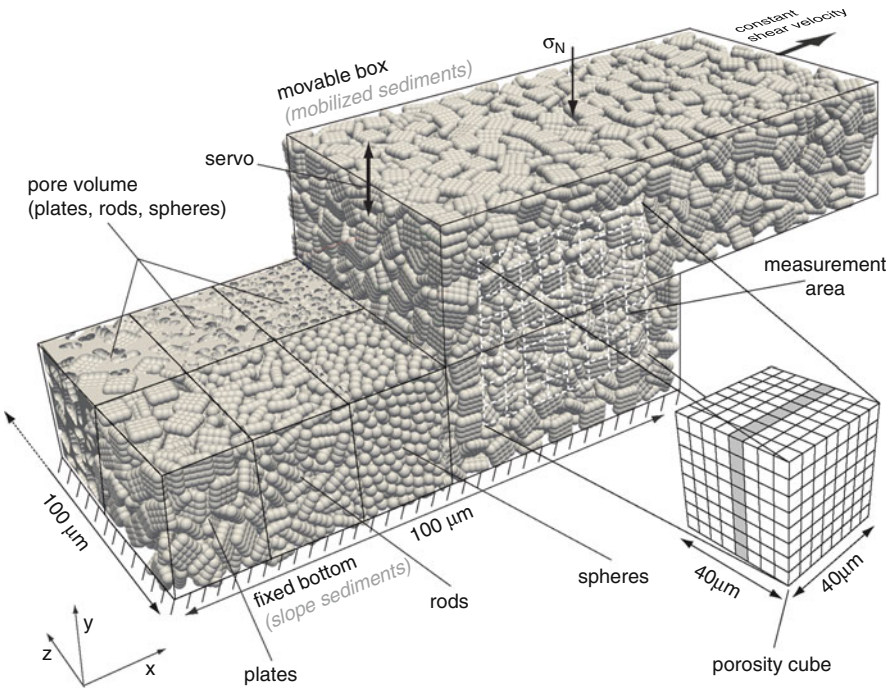

Fig. 8.1 Compilation of shear sample components including the realized fabrics of plate-like grains, rod-like grains, and spherical grains and visualization of pore volume for the three grain fabrics. The *dashed white mesh* shows the measurement area for material friction and porosity inside the sample. The *cube* and *sub-cubes* illustrate the measurement volume for porosity, whereas the *grey sub-cubes* indicate the layer of local pore volume investigation

influences caused by the roughness of the driving plate on the friction coefficient and shear strain distribution, which has been observed in lab and numerical shear tests (Anthony and Marone 2005; Abe and Mair 2009).

In order to create naturally packed samples, grains were created inside a higher box and then compressed by a downward moving top wall until the packing conformed to natural sediment conditions (Hazzard and Mair 2003; Abe and Mair 2005). A stable load on the top wall was maintained by a servo-mechanism throughout the entire shear process (Fig. 8.1). A constant shear velocity (1 µm/s) (with no acceleration) was enacted on the upper wall of the shear box inducing shear deformation in the positive x-direction.

Increased grain complexity and, thus, sediment fabric, was achieved by aggregating single spherical particles using unbreakable bonds (Fig. 8.1). The rod-like or plate-like shapes were stable throughout shear and were not susceptible to bending or abrasion. After aggregation, the aggregates were randomly oriented.

To simulate natural slope sediments, e.g., silt and clay, numerical grain properties were defined as follows: the coefficient of particle friction (μ_P) = 0.6 and as we used

a linear contact model, normal (k_N) and shear (k_S) grain stiffness were required: (k_N, k_S) = 10^9 N/m. This friction coefficient and according stiffness values have previously been successfully used to simulate marine sediments (e.g., Kock and Huhn 2007). Moreover, using the same particle properties for both numerical 'clay' and 'silt'- shaped particles ensures fair comparison and focuses the study to the influences of the grain shape. An artificially large particle density was used to force quasi-static deformation conditions by using a density scaling method. Thus, a sequence of equilibrium states was simulated to ensure that dynamical features, such as masses and grain inertia were negligible. This method ensures that dry and water-saturated sands exhibit the same behaviour when using the same static properties (Roux and Combe 2002).

Three measurement routines were used for the interpretation of model results: (1) The friction coefficient was calculated from the stress states at individual grain contacts using the Mohr-Coulomb failure criterion (e.g., Potyondy and Cundall 2004), e.g., for dry and cohesionless material, such as that used here. Inside the sheared sample the measured friction coefficient varied. Therefore, we calculated the average friction coefficient in certain areas during shear deformation. (2) The norm of the particle movement vector was used to determine zones of small and large grain slip along vertical slices through the central part of the sheared sample. Areas of relatively large grain motion highlighted areas of localized slip or failure planes in the sediment (Kock and Huhn 2007). (3) Porosity variations were calculated to quantify the influences of grain complexity on the pore volume evolution by:

$$\eta = V_{\text{pore volume}} / V_{\text{sample volume}}. \tag{8.1}$$

We used the Visualization Toolkit (VTK) (Schroeder et al. 2004) which allowed for calculation and visualization of the 3D pore space. VTK generates a volume model for the inner part of the sheared sample (40 μm × 30 μm or 40 μm × 40 μm) consisting of a Cartesian regular grid (Fig. 8.2I b, c). After the grain volumes were subtracted from the entire volume model (Fig. 8.2I d), a grid triangulation was necessary to calculate the pore volume (Alyassin et al. 1994).

The pore volume error, therefore, depends on the number of grid sections per grain diameter (Fig. 8.2). A benchmark (Fig. 8.2II) showed an acceptable pore volume error of 0.38 % for 30 grid sections per diameter (2 μm). For the entire volume model (Fig. 8.1), a total number of 600 × 600 × 600 grid sections were required to ensure volume accuracy.

8.3 Results

All numerical shear experiments revealed a direct influence of grain complexity and, hence, sediment fabric, on material behaviour (see results of measurement routines (1)–(3) below). In particular, the friction coefficient, as an indicator for

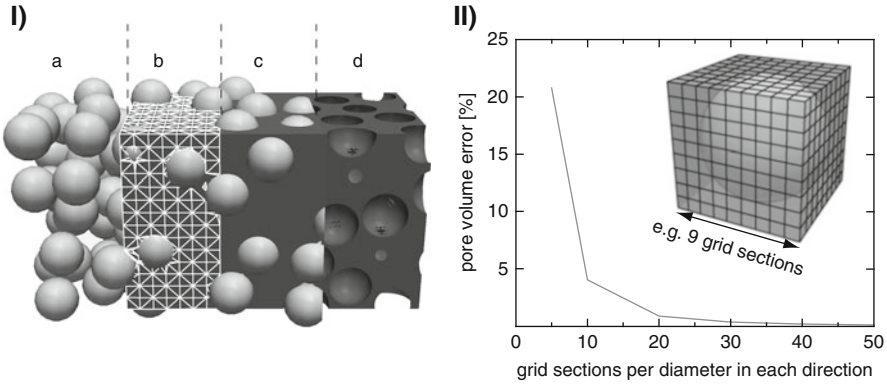

Fig. 8.2 (I) Schematic illustration of stepwise pore volume calculation: (**a**) a loosely packed sediment grain assembly, (**b**) a rough triangulated volume mesh, (**c**) a pore volume mesh with sediment grains, and (**d**) a pure mesh of pore volume. (II) Pore volume error estimation for different numbers of sections per grain diameter. For the applied 30 grid sections per basic grain diameter a pore volume error lower than 1 % occurred

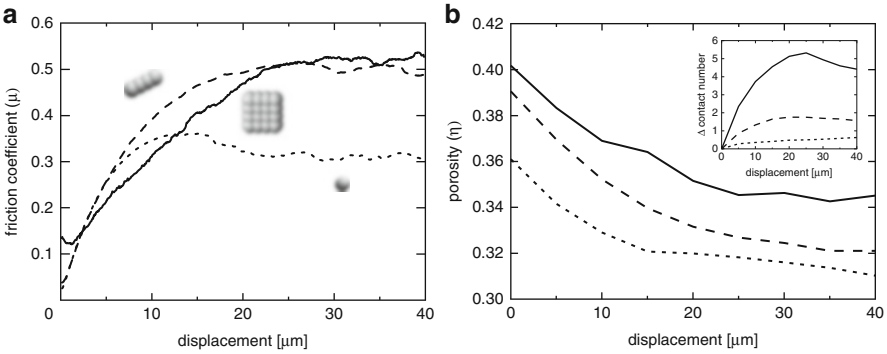

Fig. 8.3 Characteristic curves of (**a**) friction coefficient and (**b**) porosity vs. displacement for the three aggregates: sphere (*dotted line*), rod (*dashed line*), and plate (*solid line*)

the sediment strength (Fig. 8.3) and the porosity changes as an indicator for pore pressure variations (Fig. 8.4), showed direct relationships with grain complexity.

(1) For all experiments, we observed – independent of grain shape – an increase of the friction coefficient and a corresponding decrease in the porosity (Fig. 8.3). However, the curve shapes of the friction coefficient and porosity indicated specific distinctions in material behaviour that were influenced by the grain or, especially, aggregate shapes.

With increasing grain complexity, the friction coefficient at initial shear deformation increased (Fig. 8.3a). The curves for spheres and rods were nearly identical before the curve bifurcated at 6 μm displacement, whereas the curve for tabular aggregates differed at low strain.

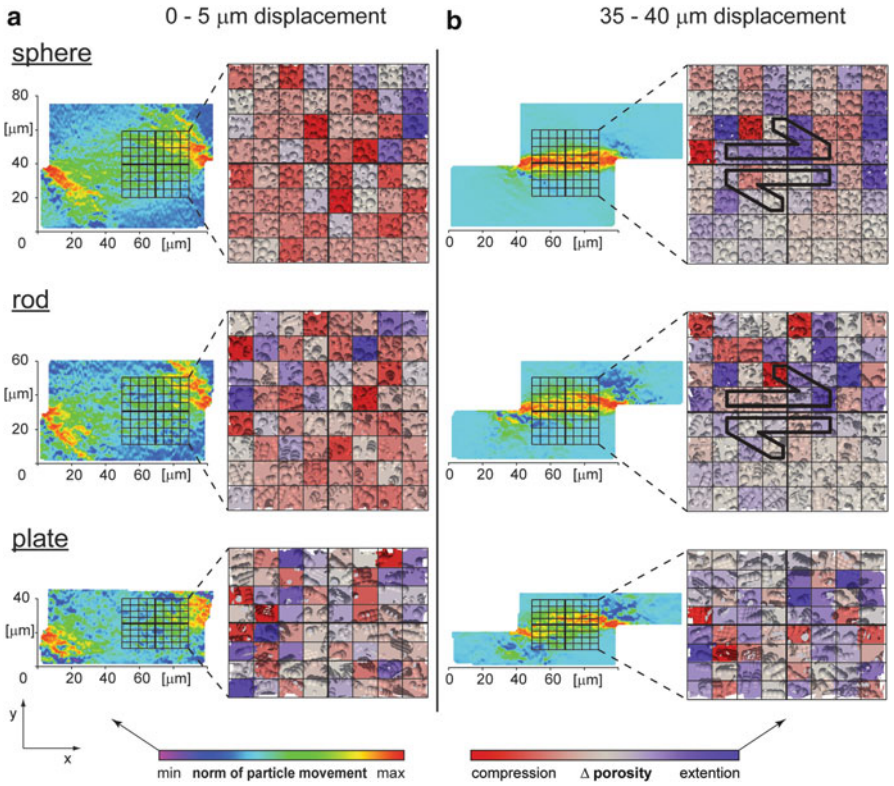

Fig. 8.4 Visualization of sediment slip behaviour derived from the particle movement as well as pore volume changes as an indicator for the pore pressure distribution within the initial and final 5 µm displacement. *Large arrows* in the pore volume plot represent the position and orientation of the developed failure plane

Subsequent deformation was affected by material hardening as evidenced by an increase in the friction coefficient towards the peak friction for all grain types. A peak friction coefficient of 0.37, in case of spheres, and 0.51 for rods, was observed after ~14 µm and ~26 µm displacement, respectively (Fig. 8.3a). Following peak friction, an overall material softening process was indicated by a decrease in the friction coefficient towards a steady or critical state. This phase of material softening and subsequent stable friction was only observed for spheres and rods. Furthermore, only the spherical particle experiments clearly attained a critical state. In contrast, even after 40 µm displacement, peak friction was not attained during shearing of the plate-like aggregates. Instead, the friction coefficient continuously increased. For the same strain, the experiment with plate-like aggregates only achieved a pre-peak state.

Peak friction appears to depend on grain complexity. In fact, increasing grain shape complexity led to an increased peak friction coefficient. However, the friction coefficient curves of rods and plates showed very similar variations.

(2) All pore volume curves exhibited different initial and final porosity values (Fig. 8.3b). It was demonstrated that porosity increases with increasing grain shape complexity, but decreases universally with increasing strain. The porosity gradient was also a function of grain complexity: the porosity magnitude decreased by 5.1 % for spheres, 7 % for rods, and 5.5 % for plates during the 40 μm displacement.

(3) At 0–5 μm displacement, the relative grain movements were identical for all sediment fabrics (Fig. 8.4a). No distinct failure planes were observed except in small areas at the side wall edges. The sediment matrix was dominated by compression for spheres and rods, whereas plates showed a more balanced distribution between compression and extension.

In contrast, both grain movements and porosity changes showed different patterns for the different grain shapes from 35 to 40 μm displacement (Fig. 8.4b). For spheres and rods, a horizontally oriented zone of larger grain slip was observed. The most significant pore volume change occurred above this shear plane in the upper part of the shear box, while the underlying part was unaffected. After failure, when the sediment matrix broke and a stable shear plane evolved, only the upper shear box part underwent progressive heterogeneous pore volume changes. This pattern clearly mirrored the location of the shear plane by separation of areas of low vs. high pore volume changes. In contrast, no distinct horizontal slip area of large grain motion was observed for plate-like grains (Fig. 8.4b). Instead, two parallel areas of minor slip evolved shortly before development of a stable shear plane. At that time, the porosity changes were still randomly balanced and distributed throughout the entire sample.

8.4 Discussion

8.4.1 Interplay: Sediment Strength and Pore Volume Changes

This study was designed to assess the relationship of sediment strength and pore volume changes during shearing. An increase in the friction coefficient and a corresponding decrease in porosity occurred with increasing shear strain in all experiments (Fig. 8.3). Hence, the densification of the sediment matrix caused an increase in the number of grain contacts. This was directly associated with an increase in sediment shear strength because a larger number of contacts must break to generate a failure plane. This finding correlates with laboratory shear experiments, e.g., Lohrmann et al. (2003), where the initial sediment compaction and the respective porosity evolution was attributed to control the shear strength of granular materials.

8.4.1.1 Effect of Grain Shape Complexity

Detailed analyses of the relationship of sediment strength and pore volume changes revealed a direct effect from fabric complexity. Generally, increasing grain

complexity caused an increase in sediment strength and porosity (Fig. 8.3) or an increase in particle contacts, particularly in case of plate-like grains (Fig. 8.3b). With strain, the contact numbers and the homogeneity of the stress network increased which also caused a restricted grain motion. Moreover, the increase in porosity with increasing grain complexity likely resulted from the generation of heterogeneous aggregate structures of complex microfabric, which create additional pore volumes. These results are consistent with those of other studies and suggest that the growth in sediment strength is also attributable to the resistance of grain rotation (Iwashita and Oda 1998; Yan 2009).

Our simulations also showed that particle complexity affects the amplitude of the coefficient of friction as well as the critical strain rate required to reach the peak friction value. However, Moore and Lockner (2007) found similar shear strength values for more complex sediment textures, e.g., dry montmorillonite, and mostly rounded grains, e.g., sand and silt. These differences can be explained by the fact that natural aggregates break down during heavy loading. As a predefined boundary condition, however, our aggregates were not able to disaggregate. Therefore, a low confining pressure regime was simulated resulting in a breakdown of only the fabric structure. The collapse of the different fabric structures was, nonetheless, sufficient ($\Delta\eta > 5$ %) to cause specific compaction rates.

In summary, a more complex grain shape or sediment fabric caused an increase in pore volume and an increase in sediment strength. This observation correlates to natural materials with respect to porosities. However, natural wet clays typically have much lower strength values compared to silt and sand. This aspect cannot be simulated with our modelling approach because fluids or fluid effects and cohesive forces have been excluded so that the focus is only on microfabric effects (Lupini et al. 1981; Saffer and Marone 2003).

Based on the general assumption that a reduction in pore volume resulted in a pore pressure increase (Goren et al. 2010), all fabrics displayed different increases in the potential pore pressures caused by pore volume reduction during densification (Fig. 8.3). The failure of a simple grain shape occurred at lower porosity changes indicating that less complex grains, e.g., non-cohesive sands or silts, more readily react to pore pressure changes compared to more complex sediment textures. Hence, our results confirm that non-cohesive slopes will fail in the case of lower transient pore pressure changes compared to cohesive slopes.

8.4.2 Local Pore Volume Changes

After the initial deformation, the pore volume change for the spherical fabric was dominated by compression (Fig. 8.4a). With increasing grain shape complexity, a more heterogeneous distribution of porosity changes was observed. This effect was a result of grain motion and rotation during shearing, which destroyed the initial

grain microfabric and re-oriented the elongated grains of higher shape complexity. In contrast, the lowest compaction rate and most homogeneous porosity change were observed for the spherical grain fabric, which allowed an ideal packing scenario.

At the final deformation stage from 35 to 40 μm displacement, particle re-arrangement was finished for spheres and rods (Fig. 8.4b). Constant porosities evolved in the lower part of the shear box, whereas the upper part was still dominated by compression and extension. In both experiments, stable friction after peak was achieved and a shear plane developed at the transition from homogenous to heterogeneous pore volume changes. In contrast, pore volume changes were still homogenously distributed through the sheared sample and no shear plane was observed for plate-like grains. This finding indicates that the pore volume below a landslide failure plane is not significantly changed after plane initiation, while pore volume changes above the shear plane continue.

8.5 Conclusions

The aim of this study was to assess the effect of grain shape and pore volume changes on sediment strength. The following general conclusions can be drawn:

- For increasing shear deformation, we observed an increase in the friction coefficient and a simultaneous decrease in porosity. Thereby, the reduction in porosity (matrix densification) caused an increase in the grain contact number which resulted in an increase in the coefficient of friction. In addition, increasing grain shape complexity caused a further increase in sediment strength and porosity as a consequence of a non-ideal packing and the associated grain rotation restriction. The breakdown of the microfabrics in the case of more complex textures resulted in a reduction of porosity and a significant increase in grain contacts, which again caused an increase in the friction coefficient.
- Non-cohesive slopes exhibit lower porosities and densifications prior to failure and are more prone to lower transient pore pressure changes compared to cohesive slopes, hence failing under lower triggers.
- This new approach indicates the evolution of domains of compressional and extensional behaviour during the evolution of the failure plane. The underlying undisturbed sediments below the failure plane show no pore volume changes, while the upper part exhibits significant porosity fluctuations. Hence, high resolution porosity analyses should allow for the identification of the basal failure planes of landslides.

Acknowledgments We wish to thank, S. Abe and I. Görz for very constructive reviews and M. Stipp. Further we thank L. Podszun, L. Wenk, B. Flaim, G. Bartzke, J. Kuhlmann and Y. Hellmann for assistance. This work was funded through the DFG-Research Center/Excellence Cluster MARUM "The Ocean in the Earth System".

References

Abe S, Mair K (2005) Grain fracture in 3D numerical simulations of granular shear. Geophys Res Lett 32:1–4

Abe S, Mair K (2009) Effects of gouge fragment shape on fault friction: new 3D modelling results. Geophys Res Lett 36:1–4

Alyassin AM, Lancaster JL, Downs Iii JH, Fox PT (1994) Evaluation of new algorithms for the interactive measurement of surface area and volume. Med Phys 21:741–752

Anthony JL, Marone C (2005) Influence of particle characteristics on granular friction. J Geophys Res 110:B08409. doi:10.1029/2004JB003399

Byerlee JD (1978) Friction of rocks. Pure Appl Geophys 116:615–625

Cundall PA, Strack ODL (1978) BALL – a program to model granular media using the distinct element method. Dames and Moore, London

Goren L, Aharonov E, Sparks D, Toussaint R (2010) Pore pressure evolution in deforming granular material: a general formulation and the infinitely stiff approximation. J Geophys Res 115:B09216

Hampton MA, Lee HJ, Locat J (1996) Submarine landslides. Rev Geophys 34:33–59

Handin J (1969) On the Coulomb-Mohr failure criterion. J Geophys Res 74:5343–5348

Hazzard JF, Mair K (2003) The importance of the third dimension in granular shear. Geophys Res Lett 30:1708–1711

Iwashita K, Oda M (1998) Rolling resistance at contacts in simulation of shear band development by DEM. J Eng Mech 124:285–292

Kock I, Huhn K (2007) Numerical investigation of localization and micromechanics in a stratified soil specimen. J Struct Geol 29:1679–1694

Lambe TW, Whitmann RV (1979) Soil mechanics. John Wiley & Sons, New York

Locat J, Lee HJ (2002) Submarine landslides: advances and challenges. Can Geotech J 39:193–212

Lohrmann J, Kukowski N, Adam J, Oncken O (2003) The impact of analogue material properties on the geometry, kinematics, and dynamics of convergent sand wedges. J Struct Geol 25: 1691–1711

Lupini JF, Skinner AE, Vaughan PR (1981) The drained residual strength of cohesive soils. Geotechnique 31:181–213

Marone C (1998) Laboratory-derived friction laws and their application to seismic faulting. Annu Rev Earth Planet Sci 26:643–696

Mienert J, Vanneste M, Haflidason H, Bünz S (2010) Norwegian margin outer shelf cracking: a consequence of climate-induced gas hydrate dissociation? Int J Earth Sci 99:207–225

Mitchell JK, Soga K (2005) Fundamentals of soil behaviour, 3rd edn. Willey, Hoboken

Moore DE, Lockner DA (2007) Friction of the smectite clay montmorillonite. In: Dixon T, Moore C (eds) The seismogenic zone of subduction thrust faults. Columbia University Press, New York, pp 317–345

Morgan JK (1999) Numerical simulations of granular shear zones using the distinct element method 2. Effects of particle size distribution and interparticle friction on mechanical behavior. J Geophys Res 104:2721–2732

Potyondy DO, Cundall PA (2004) A bonded-particle model for rock. Int J Rock Mech Min Sci 41:1329–1364

Roux J-N, Combe G (2002) Quasistatic rheology and the origins of strain. C R Phys 3:131–140

Saffer DM, Marone C (2003) Comparison of smectite- and illite-rich gouge frictional properties: application to the updip limit of the seismogenic zone along subduction megathrusts. Earth Planet Sci Lett 215:219–235

Schroeder W, Martin K, Lorensen B (2004) The visualization toolkit, 3rd edn. Kitware Inc., USA

Yan WM (2009) Fabric evolution in a numerical direct shear test. Comput Geotech 36:597–603

Chapter 9
Slope Instability of Glaciated Continental Margins: Constraints from Permeability-Compressibility Tests and Hydrogeological Modeling Off Storfjorden, NW Barents Sea

J. Llopart, R. Urgeles, A. Camerlenghi, R.G. Lucchi, B. De Mol, M. Rebesco, and M.T. Pedrosa

Abstract Climate variations control sediment supply to the continental slope as well as glacial advances and retreats, which (a) cause significant stress changes in the sedimentary column and redistribution of interstitial fluids, (b) induce a particular margin stratigraphic pattern and permeability architecture and (c) are at the origin of isostatic adjustments that may reactivate faults. We test this hypothesis using a combination of geophysical and geotechnical data from the Storfjorden Trough Mouth Fan, off southern Svalbard. The results of compressibility and permeability testing are used together with margin stratigraphic models obtained from seismic reflection data, as input for numerical finite elements models to understand focusing of interstitial fluids in glaciated continental margins and influence on timing and location of submarine slope failure. Available results indicate values of overpressure of 0.23–0.5 (slope-shelf) that persist to present-day. This overpressure started to develop in response to onset of Pleistocene glaciations and reduced by half the factor of safety of the continental slope.

Keywords Overpressure • Hydrogeology • Factor of safety • Storfjorden • Barents Sea • Hydrogeologic model

J. Llopart (✉) • B. De Mol • R. Urgeles
Dept. Geociències Marines, Institut de Ciències del Mar (CSIC), Barcelona, Spain
e-mail: jaume.llopart@gmail.com

A. Camerlenghi • R.G. Lucchi • M. Rebesco
Geophysics Research Section, Istituto Nazionale di Oceanografia e Geofisica Sperimentale-OGS, Trieste, Italy

M.T. Pedrosa
Instituto Andaluz de Ciencias de la Tierra-IACT, Granada, Spain

S. Krastel et al. (eds.), *Submarine Mass Movements and Their Consequences*, Advances in Natural and Technological Hazards Research 37, DOI 10.1007/978-3-319-00972-8_9,

9.1 Introduction

During the last decades large submarine landslides have been widely discovered in Polar Regions. The Norwegian margin has been subject of a comprehensive study motivated by the occurrence of gas and oil fields associated to nearby landslides. Large and medium-size landslides are well documented (i.e. the Trænadjupet Slide and the Andøya Slide), including the largest known submarine landslide, the Storegga Slide with a volume of 5600 km^3 (Haflidason et al. 2005; Laberg et al. 2000; Laberg et al. 2002). The thick deposits accumulated during glacial and interglacial cycles have been subject to ice sheet dynamics, loading and unloading by the grounded ice sheet, glacio-eustatic sea-level variations, glacio-isostatic rebound and associated seismicity (Bugge et al. 1987; Mulder and Moran 1995). Continental margin development must have played a significant role in controlling the migration of interstitial fluids, determining the occurrence of sediment instability when combined with depositional oversteeping (Dimakis et al. 2000). The aim of this study is therefore to: (1) characterize the compression and permeability characteristics of glacial-deglacial-interglacial marine sediments of a polar continental margin; (2) reconstruct the paleohydrogeological evolution; and (3) determine how continental margin architecture and physical properties couple to control the location of submarine slope instability.

The study area (Fig. 9.1) is located in the Storfjorden Trough Mouth Fan (TMF) south of the Svalbard archipelago. This TMF covers an area of about 40.000 km^2 and has a radius of about 190 km, developed concentrically off the Storfjorden trough.

9.2 Data and Methods

Consolidation and permeability tests were performed using a GDS Rowe & Barden-type Consolidation cell equipped with three 2 MPa advanced pressure/volume controllers. Atterberg limit were also determined. The liquid limit was determined using an 80 g, 60° apex fall cone device, while the plastic limit was estimated from the hand rolled thin thread of sediment method (Karlsson et al. 1977).

The stratigraphy and 2D architecture of the different units used to perform the hydrogeological modeling correspond to the seismic units defined in between seismic reflections R1-R7 described in Faleide et al. 1996. These seismic reflections were picked on seismic line ITEG08-09 acquired during the Italian cruise EGLACOM (Fig. 9.2). The R7 and the OB (top of Oceanic Basement) reflectors correspond to the projected position of these reflectors on line ITEG08-09 made from the two seismic lines north and south of Storfjorden included in Faleide et al. (1996) as the line ITEG08-09 did not have enough penetration to image these reflectors. The velocities for the time to depth conversion have been approximated from ODP Leg 162 holes 986C and 986D sonic data.

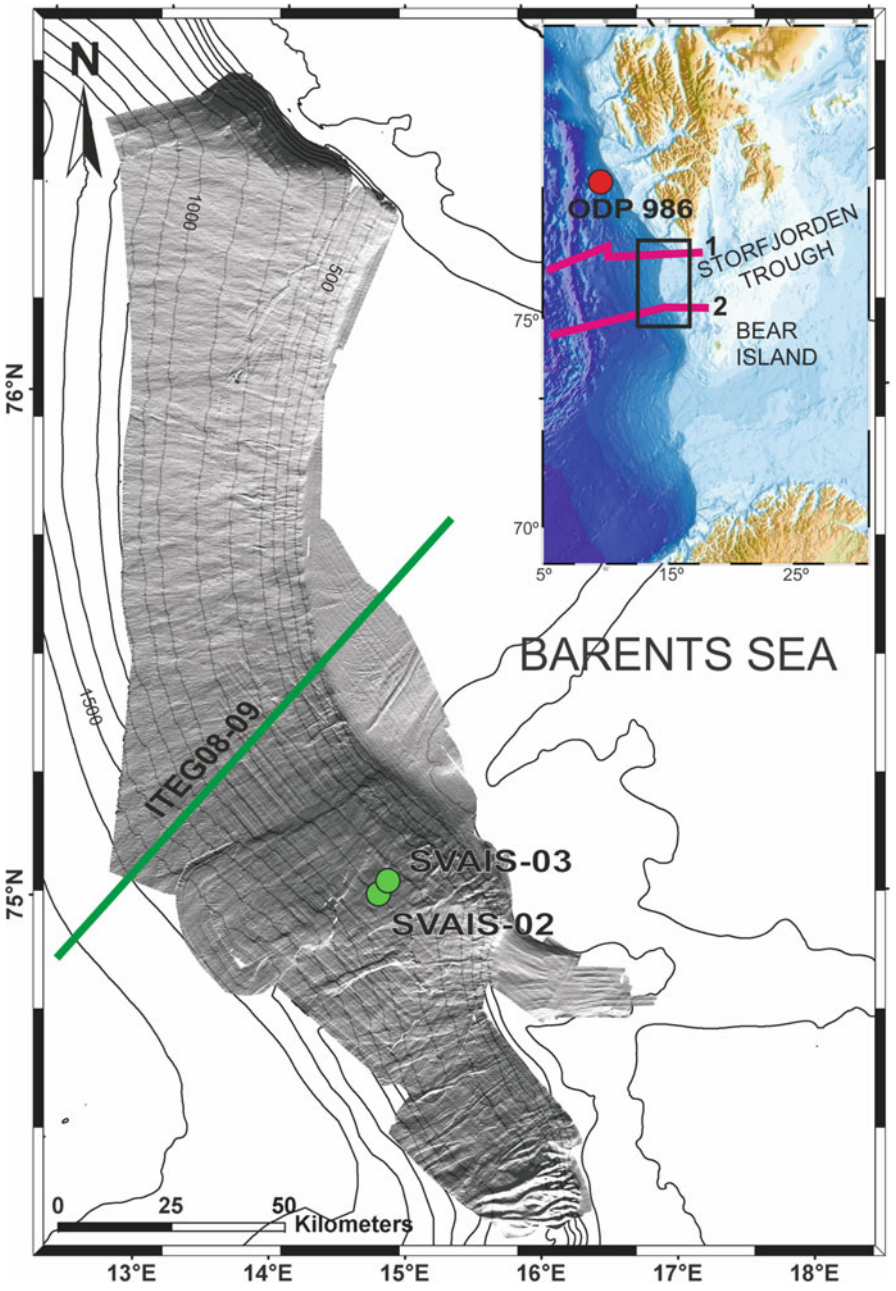

Fig. 9.1 Location of the study area. Bathymetric *shaded* relief showing submarine landslides beyond the shelf break. Seismic lines 1 and 2 (in *pink*) extracted from Faleide et al. 1996 [6] and ITEG08-09 (in *green*) from EGLACOM cruise report (REL OGS 2008/111). *Green dots* are gravity cores. *Red dot* is the Site ODP 986

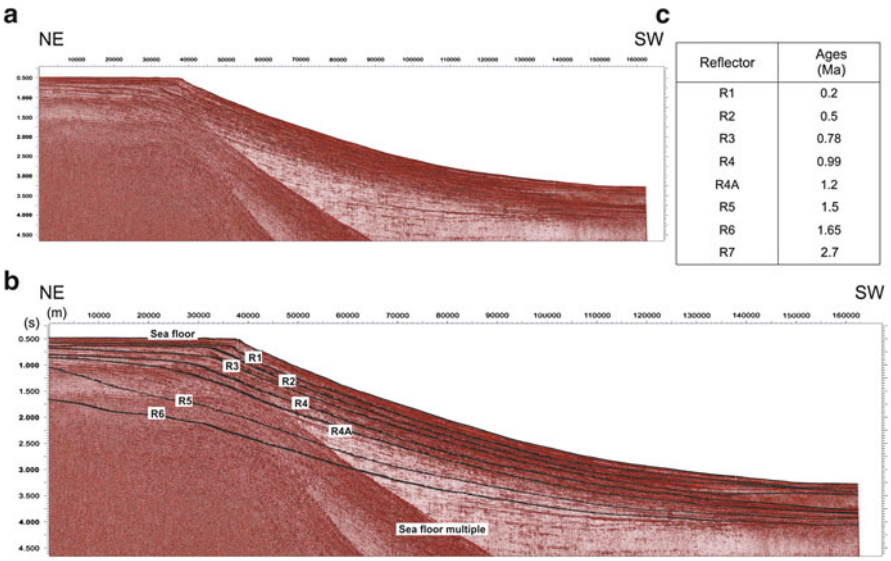

Fig. 9.2 (**a**) uninterpreted and (**b**) interpreted EGLACOM ITEG08-09 seismic line used for "BASIN" modelling. (**c**) ages for seismic reflectors [11]

Using the Finite Element Software "BASIN" (Bitzer 1996; 1999) continental margin hydrogeological modelling has been carried out to simulate the fluid migration and pore pressure development. In this study pore pressure is also described in terms of overpressure (λ), defined as (Flemings et al. 2008):

$$\lambda = (P - P_h)/(\sigma_v - P_h) \tag{9.1}$$

where P is pore pressure, P_h is the hydrostatic pressure and σ_v is lithostatic or total stress. The initial thickness (H_i) of different strata used as input for the model was calculated using van Hinte's decompaction equation (Van Hinte 1978):

$$H_i = H_f\,[(1 - \phi_f)/(1 - \phi_i)] \tag{9.2}$$

where ϕ_i is the initial porosity, ϕ_f is the present-day porosity and H_f is the present sediment thickness.

The total length of the modeled transect is around 162 km and the mesh nodes are equally spaced every 4 km. Ice-induced stresses or erosion by ice have not been considered. Sedimentary facies are often represented by a mixture of sediment types, whose composition will vary according to the relative abundance of each sediment type for a given area and unit. Physical properties are also averaged according to the sediment mixture. Time intervals were extracted from Knies et al. (2009) (Fig. 9.2c).

9.3 Results

Consolidation and permeability testing were performed on two sediment types: laminated sediments interpreted as plumites, and glacigenic debris flows (GDFs) (Table 9.1). Pre-consolidation pressures indicate normally consolidated sediments for plumites and GDFs (Table 9.1). Plumites also have higher initial hydraulic conductivity (4.8×10^{-8} m/s compared to 2.9×10^{-8} m/s) and compressibility (0.36 versus 0.19) than GDFs. The specific storage and permeabilities show also a more marked decrease with increasing stress for plumites than for GDFs (Table 9.1 and Fig. 9.3). Geotechnical tests (Fig. 9.3) show that climatically controlled sedimentation changes on polar continental margins produce sediments with contrasting physical properties. The steeper trend in the virgin consolidation and theoretical permeability

Table 9.1 Most important parameters derived from geotechnical tests in this study

	Sediment type	Wi (%)	e_0	k_0 (m^2)	S_0 (m^{-1})	σ_c
SVAIS-02-02	Plumites	44.16	1.804	$5.97E^{-15}$	0.06742	36
SVAIS-02-03	Plumites	42.02	1.894	$5.53E^{-16}$	0.04019	52
SVAIS-02-04	Plumites	39.89	1.729	$5.57E^{-15}$	0.03773	61
SVAIS-02-05	GDF	26.63	1.110	$2.49E^{-15}$	0.01334	67
SVAIS-02-06	GDF	23.14	0.899	$3.31E^{-15}$	0.03003	69
SVAIS-03-06	Plumites	47.86	1.854	$6.85E^{-15}$	0.0327	64

GDF Glacigenic Debris Flows, *Wi* initial water content, e_0 initial void ratio, k_0 initial permeability, S_0 initial specific storage, σ_c pre-consolidation pressure

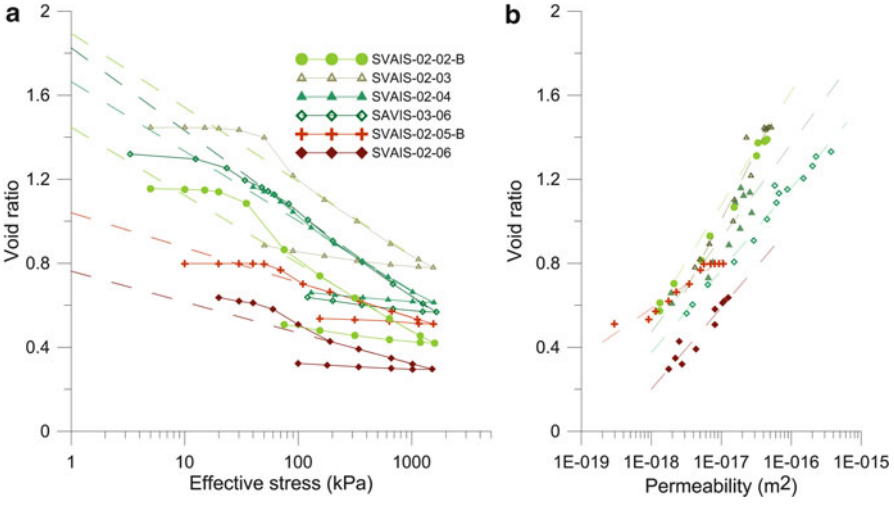

Fig. 9.3 Consolidation tests: (**a**) effective stress/void ratio relationship for the tested samples. (**b**) Flow-through permeability versus void ratio. Extrapolation to 1 kPa is used to determine initial parameters for the simulation. Greenish lines correspond to plumites and reddish to GDFs

Table 9.2 Parameters used for "BASIN" and fluid flow modeling

	Plumites	GDFs	Till	Hemipelagic sediments
Initial porosity	0.64[a]	0.5[a]	0.4[b]	0.778[c]
Grain density (kg/m^3)	2650	2650	2650	2650
Init. Specific storage (m^{-1})	0.025[a]	0.015[a]	0.0056[b]	0.044[c]
Init. hydraulic conductivity (m/s)	4.8E^{-8a}	2.9E^{-8a}	5.3E^{-11b}	3.0E^{-9d}

[a]This study, [b]Shaver (1998), [c]ODP sites 986C/D data, [d]Urgeles et al. (2010)

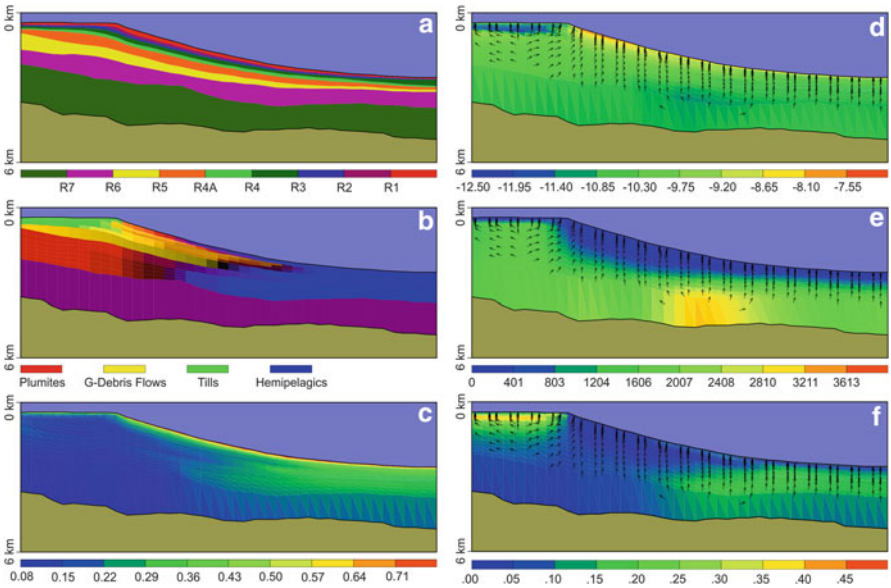

Fig. 9.4 Margin stratigraphic and hydrodynamic modeling with "BASIN" at final simulated present condition. (**a**) Margin stratigraphy according to seismic units described by Faleide et al. (1996). (**b**) Facies composition. (**c**) Fractional porosity. (**d**) Log hydraulic conductivity. (**e**) Excess pore pressure (kPa). (**f**) Overpressure (λ)

lines of plumites clearly highlights these differences (Fig. 9.3). Tests performed on split plumites cores SVAIS-02 and SVAIS-03 indicate higher water content and lower shear strength than the GDFs for a similar burial depth (Lucchi et al. 2012).

The parameters obtained from consolidation/permeability testing (see Table 9.2) have been used as input for the hydrogeological modeling. The last output stage in terms of physical properties and sedimentological/architectural characteristics from the model are presented in Fig. 9.4. At the end of the simulation (present day), the minimum porosities are around 10 % in the continental shelf and upper slope, mainly corresponding to the units consisting of tills and glacigenic debris flows. Hydraulic conductivities for these units have values between 10^{-12} and 10^{-10} m/s, but the values start decreasing at ~1.2 Ma. Overpressure reaches values of ~0.15 near the shelf break and upper slope where the sediment thickness is maximum.

A sensitivity analysis showed that hydraulic conductivity is the parameter that has larger influence on the resulting overpressure than other the parameters involved in the calculations as porosity or specific storage.

9.4 Discussion

"BASIN" modeling allows us to investigate how physical properties, sedimentology and stratigraphic architecture couple to control margin hydrogeology and fluid flow pathways. The simulation shows that low porosities (10–30 %) develop in most of the continental margin, specially the continental shelf and upper-middle slope, due to consolidation and the initial low porosity of till and glacigenic debris flow sediments.

Accumulation of GDFs on the upper-middle continental slope, which has low initial permeability and compressibility, determines the formation of fluid flow divergence beneath the continental shelf and lower slope. Most of the margin shows vertical fluid flow which is a normal situation for a fluid flow trend in a continental margin dominated by consolidation processes. The low porosity and permeability of the tills act as an impervious boundary which results in shallow moderate pore pressure and high overpressure. A more marked reduction in permeability of hemipelagic sediments due to their higher compressibility induces high pore pressures at depth but only moderate overpressure.

Onset of glaciation between 1.8 and 1.6 Ma (Butt et al. 2000; Laberg et al. 2010) provides abundant glacigenic sediments (tills and GDFs) to the continental shelf and upper slope, particularly since intensification of glaciation from 0.99 Ma (∼R4) (Knies et al. 2009). These sediments control to a large extent overpressure development. A maximum value of 0.5 is reached on the continental shelf, while the shelf edge and upper slope (where most of the landslides occur in that area) display a lower maximum value of 0.15.

High overpressure in glaciated continental margins may favor onset of slope failure (Kvalstad et al. 2005) and recent and buried landslides have also been identified off Storfjorden (Fig. 9.1) (Lucchi et al. 2012; Rebesco et al. 2012). A preliminary analysis of the factor of safety (FoS) using Eq. (9.3) (Flemings et al. 2008):

$$FoS = \frac{\tan \phi_f}{\sin \phi \cdot \cos \phi} \left(\cos^2 \phi - \lambda\right) \tag{9.3}$$

where ϕ_f is the friction angle (set constant at 28º) and ϕ the slope, shows that overpressure significantly reduced the FoS (FoS > 1 stable and FoS < 1 unstable), but not enough to induce slope failure. Along the reflector R2 (0.5 Ma) (where the largest slope failure is rooted), the steepening during margin development induced a slight decrease of the FoS in the upper slope since its deposition to present day, but an increase in some areas of the lower slope (Fig. 9.5). Close to the seafloor

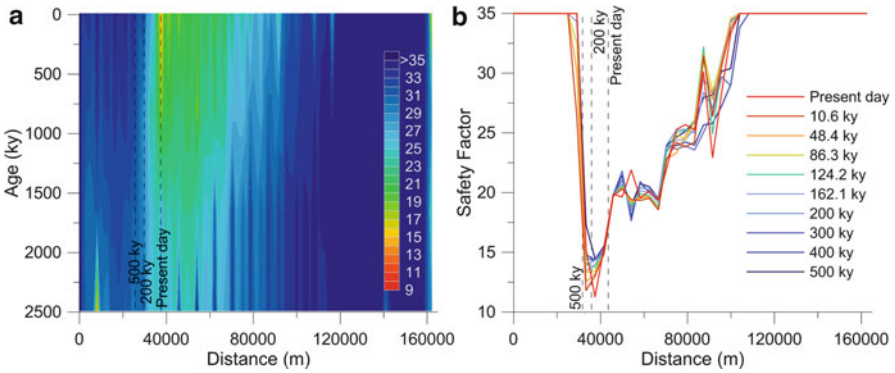

Fig. 9.5 (**a**) Evolution of the safety factor on the layer immediately below the seafloor. (**b**) Evolution of the safety factor on the R2 surface (∼0.5). *Dashed lines* represent the position of the shelf edge at different times during simulation

(layer immediately beneath) the FoS decreases with time in the slope area, but the lower values of FoS are still above 9. This fact shows that the slope has a higher control on the stability of the continental slope than overpressuring in the study area. At the maximum slope angle of 3º in the model, a minimum value of overpressure of 0.89 is needed for the slope to fail, highlighting that external mechanisms are needed to induce failure.

Weak layers are often involved in slope failure of Arctic and peri-Arctic regions (Vanneste et al. 2006). The high water content interglacial sediments that occur beneath rapidly deposited tills and GDFs can develop locally high overpressure zones which cannot be resolved in our model. Future work also needs to explore the effects of ice sheet erosion and isostatic compensation due to ice advance and retreat.

9.5 Conclusions

Consolidation tests of glacial and glacially influenced sediments of the upper slope of the Storfjorden TMF, western Barents Sea show that plumites (glacial melt-water plumites) have high void ratios, consolidation coefficients and permeabilities with respect to glacigenic debris flows at initial deposition conditions.

The compressibility and permeability values, together with stratigraphic input from seismic reflection profiles, were used in "BASIN" modeling. The modeling shows that onset of glacial sedimentation has a significant role in developing permeability barriers (tills) and/or allowing pore water drainage (GDFs). Occurrence of relatively uncompressible GDFs on the continental slope controls the margin fluid migration pathways.

Present day overpressure reaches a maximum value of 0.5 in the shelf area, 0.15 in the upper slope and 0.23 in the lower slope. These values of overpressure cannot trigger submarine landslides alone, but reduce the FoS of the margin by up to one half. Given the relatively reduced overpressure the FoS is mainly controlled by the evolution of the slope gradient during the margin development. An overpressure of more than 0.89 is needed to bring the FoS below 1. Also trigger mechanisms as glacio-eustatic rebound earthquakes can be considered.

Acknowledgements This study is funded by the "Ministerio Economia y Competitividad" through grants DEGLABAR, (CTM2010-17386), CORIBAR-ES (CTM2011-14807-E) and SVAIS (POL2006-07390). UNESCO and IUGS are also acknowledged for funding through project IGCP-585. The "Generalitat de Catalunya" is acknowledged for support through an excellence research group grant (2009-SGR-146). K. Andreassen and S. Clarke are thanked for their comments and positive criticism.

References

Bitzer K (1996) Modelling consolidation sedimentary and fluid basins flow. Comput Geosci 22:467–478

Bitzer K (1999) Two-dimensional simulation of clastic and carbonate sedimentation, consolidation, subsidence, fluid flow, heat flow and solute transport during the formation of sedimentary basins. Comput Geosci 25:431–447

Bugge T, Befring S, Belderson RH et al (1987) A giant three-stage submarine slide off Norway. Geo-Mar Lett 7:191–198

Butt FA, Elverhoi A, Solheim A et al (2000) Deciphering Late Cenozoic development of the western Svalbard Margin from ODP Site 986 results. Mar Geol 169:373–390. doi:10.1016/S0025-3227(00)00088-8

Dimakis P, Elverhoi A, Hoeg K et al (2000) Submarine slope stability on high-latitude glaciated Svalbard–Barents Sea margin. Mar Geol 162:303–316. doi:10.1016/S0025-3227(99)00076-6

Faleide JI, Solheim A, Fiedler A et al (1996) Late Cenozoic evolution of the western Barents Sea-Svalbard continental margin. Global Planet Change 12:53–74. doi:10.1016/0921-8181(95)00012-7

Flemings P, Long H, Dugan B et al (2008) Pore pressure penetrometers document high overpressure near the seafloor where multiple submarine landslides have occurred on the continental slope, offshore Louisiana, Gulf of Mexico. Earth Planet Sci Lett 269:309–325. doi:10.1016/j.epsl.2007.12.005

Haflidason H, Lien R, Sejrup HP et al (2005) The dating and morphometry of the Storegga Slide. Mar Petrol Geol 22:123–136. doi:10.1016/j.marpetgeo.2004.10.008

Karlsson R, Swedish Geotechnical Society, Laboratory Committee (1977) Consistency limits: a manual for the performance and interpretation of laboratory investigations. Statens rad for byggnads-forskning, Stockholm, pp 1–40

Knies J, Matthiessen J, Vogt C et al (2009) The Plio-Pleistocene glaciation of the Barents Sea–Svalbard region: a new model based on revised chronostratigraphy. Quat Sci Rev 28:812–829. doi:10.1016/j.quascirev.2008.12.002

Kvalstad TJ, Andresen L, Forsberg CF et al (2005) The Storegga slide: evaluation of triggering sources and slide mechanics. Mar Petrol Geol 22:245–256. doi:10.1016/j.marpetgeo.2004.10.019

Laberg J, Vorren T, Dowdeswell J et al (2000) The Andøya Slide and the Andøya Canyon, north-eastern Norwegian–Greenland Sea. Mar Geol 162:259–275. doi:10.1016/S0025-3227(99)00087-0

Laberg JS, Vorren TO, Mienert J et al (2002) Late Quaternary palaeoenvironment and chronology in the Trænadjupet Slide area offhore Norway. Mar Geol 188:35–60

Laberg JS, Andreassen K, Knies J et al (2010) Late Pliocene-Pleistocene development of the Barents Sea ice sheet. Geology 38:107–110. doi:10.1130/G30193.1

Lucchi RG, Pedrosa MT, Camerlenghi A et al (2012) Recent submarine landslides on the continental slope of Storfjorden and Kveitehola Trough – Mouth Fans (NW Barents Sea). In: Yamada Y et al (eds) Submarine mass movements and their consequences, vol 31, Advances in natural and technological hazards research., pp 735–745. doi:10.1007/978-94-007-2162-3

Mulder T, Moran K (1995) Relationship among submarine instabilities, sea level variations, and the presence of an ice sheet on the continental shelf: an example from the Verrill Canyon Area, Scotia Shelf. Paleoceanography 10:137–154

Rebesco M, Pedrosa MT, Camerlenghi A et al (2012) One million years of climatic generated landslide events on the northwestern Barents Sea continental margin. In: Yamada Y et al (eds) Submarine mass movements and their consequences, vol 31, Advances in natural and technological hazards research. Springer, Dordrecht, pp 747–756

Shaver RB (1998) The determination of glacial till specific storage in North Dakota. Ground Water 32:552–557

Urgeles R, Locat J, Sawyer DE et al (2010) History of pore pressure build up and slope instability in mud-dominated sediments of Ursa Basin, Gulf of Mexico continental slope. In: Mosher DC (ed) Submarine mass movements and their consequences, vol 28, Advances in natural and technological hazards research. Springer, Dordrecht, pp 179–190

Van Hinte JE (1978) Geohistory analysis; application of micropaleontology in exploration geology. AAPG Bull 62:201–222

Vanneste M, Mienert J, Bunz S (2006) The Hinlopen Slide: a giant, submarine slope failure on the northern Svalbard margin, Arctic Ocean. Earth Planet Sci Lett 245:373–388. doi:10.1016/j.epsl.2006.02.045

Chapter 10
Baiyun Slide and Its Relation to Fluid Migration in the Northern Slope of Southern China Sea

Wei Li, Shiguo Wu, Xiujuan Wang, Fang Zhao, Dawei Wang, Lijun Mi, and Qingping Li

Abstract A large-scale submarine landslide (Baiyun Slide) covering an area of 10,000 km^2 was identified from the multibeam bathymetric data, high-resolution 2D and 3D seismic data acquired in the Baiyun Sag, Pearl River Mouth Basin, northern South China Sea (SCS). Numerous polygonal faults are also found below the translational domain of the Baiyun Slide. Enhanced reflections, bright spots and pull-down reflection have been illustrated from the 2D and 3D seismic data, indicating the presence of gas. The headwall scarps of the slide are located stratigraphically above the sediments where the amplitude anomalies are identified. The focused fluid flow maybe leak from the gas reservoir and migrate upward into the base of the Baiyun Slide. Though the triggering mechanism of the Baiyun Slide is still poorly known, the fluid trapped below the slide will reduce the strength of the sediments and trigger the slope failure. We propose a conceptual model of the relationship between fluid migration and slope stability.

Keywords Baiyun Slide • Slope stability • Focused fluid flow • South China Sea

W. Li • S. Wu (✉) • X. Wang • F. Zhao • D. Wang
Key Laboratory of Marine Geology and Environment, Institute of Oceanology, Chinese Academy of Sciences, Qingdao 266071, China
e-mail: iocasliwei@gmail.com; swu@qdio.ac.cn

L. Mi
Department of Exploration, CNOOC, Beijing 100010, China

Q. Li
Key Laboratory of Deepwater Engineering, CNOOC Research Centre, Beijing 100029, China

S. Krastel et al. (eds.), *Submarine Mass Movements and Their Consequences*, Advances in Natural and Technological Hazards Research 37, DOI 10.1007/978-3-319-00972-8_10,

10.1 Introduction

Submarine landslides, are commonly observed on passive continental margins. They can transport significant volumes of sediments to offshore areas and control the seafloor morphology (Masson et al. 2006). With the development of hydrocarbon exploration into deepwater areas, submarine landslide is one of the most important geohazards, which poses a direct threat to submarine installations such as oil platforms and pipelines and may cause severe damage onshore due to the generation of destructive tsunami waves (Locat and Lee 2002; Krastel et al. 2006; Masson et al. 2006; Yamada et al. 2012).

The critical preconditioning factors and triggering mechanisms of a single submarine landslide is still poorly known. However, numerous studies demonstrate that the significance and recurrence of submarine landslide on continental margins depend on various factors, such as sea-level fluctuations, earthquakes, tectonic activity, high-sediment supply or fluid overpressure (Canals et al. 2004; Leynaud et al. 2004; Tripsanas et al. 2008; Mulder et al. 2009; Strozyk et al. 2009). Over the last decade focused fluid flow structures have gained increasing attention due to their role in the assessment of slope stability (Bünz et al. 2005; Micallef et al. 2011; Berndt et al. 2012). The focused fluid flow systems usually serve as pathways for upward migration of fluids from gas reservoirs (Cartwright et al. 2007; Huuse et al. 2010; Sun et al. 2012). Numerous structures of over-pressured focused fluid flow, mostly manifested in gas chimneys and polygonal faults, have been documented in the Pearl River Mouth Basin (Sun et al. 2012).

In this article, we use a combination of the multibeam bathymetric data and the high-resolution 2D/3D seismic reflection data acquired in the Pearl River Mouth Basin (Fig. 10.1) to: (1) identify the distribution and morphology characteristics of Baiyun Slide; and (2) discuss the possible relationship between fluid migration and Baiyun Slide. This study highlights the significance of fluid flow system on slope stability in the South China Sea (SCS), which has been poorly studied to date.

10.2 Geological Setting

The northern SCS is a typical passive margin which experiences complex rifting, thermal subsidence and sediment deposition during Cenozoic. It is comprised by five main Cenozoic rift basins, such as Yinggehai Basin (YGHB), Beibuwan Basin (BBWB), Qiongdongnan Basin (QDNB), Pearl River Mouth Basin (PRMB) and Taixinan Basin (TXNB), from west to east (Fig. 10.1a). The structural evolution of all the basins was divided into two stages: an Eocene-Oligocene rift stage and a Neogene-Quaternary postrift stage characterized by thermal subsidence (Gong 1997; Huang et al. 2003; Zhu et al. 2009).

The PRMB is a NE-elongated Cenozoic marginal rift basin developed on the pre-Tertiary basement. It lies in the central part of the northern SCS and covers an area

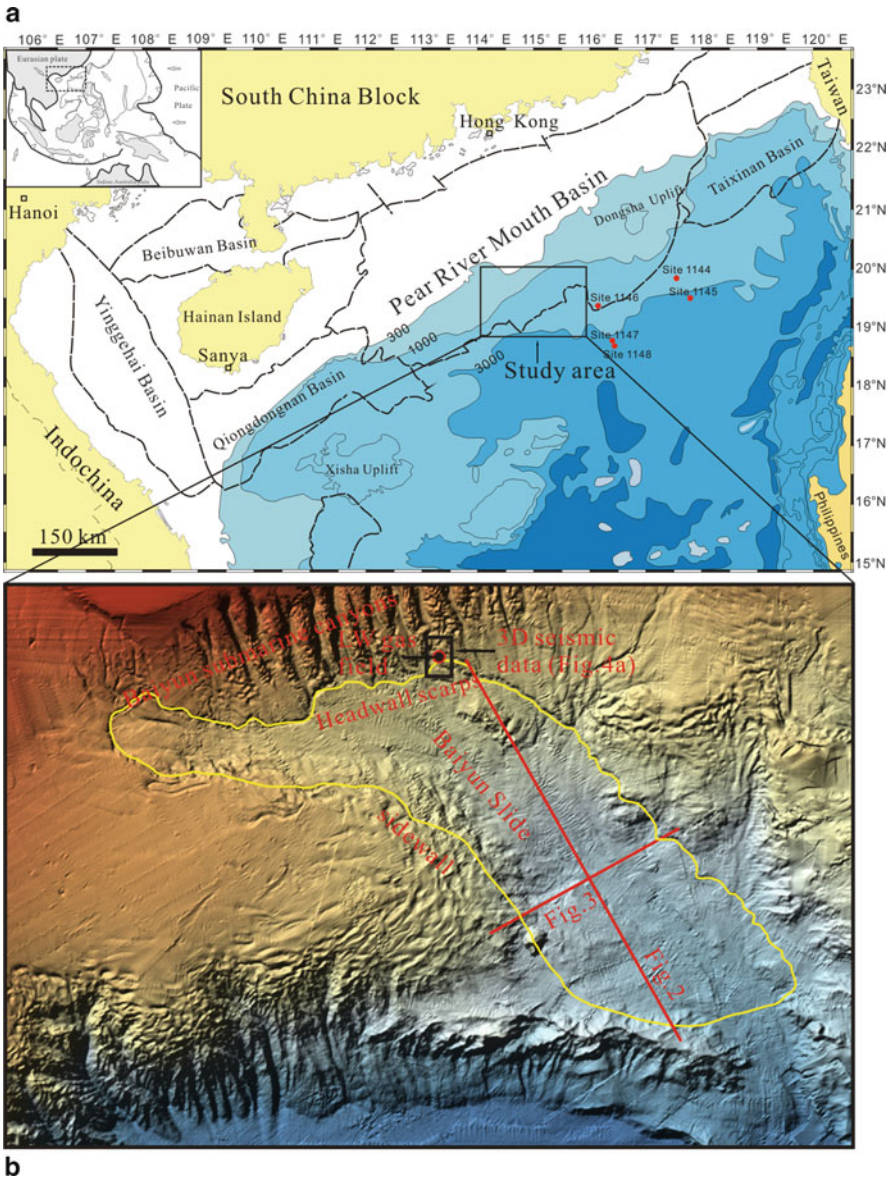

Fig. 10.1 Map of the Baiyun Slide Complex (**a**) at the continental margin of South China Sea. (**b**) The map also shows the LW gas field and Baiyun submarine canyons near the headwall of the Baiyun Slide

of $17.5 \times 104\ km^2$ (Fig. 10.1). The gas source of PRMB is relatively mature in terms of hydrocarbon exploration and production compared to other basins in the northern SCS. The study area located at the southeastern part of the PRMB. The water depth ranges from 500 to 3,000 m (Fig. 10.1). Several submarine canyons, called Baiyun

submarine canyons (Zhu et al. 2009), are developed in the north of the headwall of the slide, which provide important pathways for downslope sediment transportation. Li Wan (LW) gas field is in the north of the slide for a few kilometres, northward of the eastern headwall (Fig. 10.1). Gas and oil prospecting and production in this area necessitate a better understanding of submarine slope stability.

10.3 Data and Methods

The main database for this study includes a 3D seismic dataset covering an area of approximately 2,500 km^2, two 2D seismic lines and a multibeam bathymetry dataset covering an area of 30,000 km^2. The seismic acquisition system consists of a 3,000 m long 120-channel streamer, with hydrophone group interval of 25 m. The sampling interval was 4 ms. In 2008, about 20,000 km^2 of multibeam bathymetry was collected from the study area and adjacent area, in water depths of 300–3,000 m using differential GPS positioning and processed using the software CARIS HIPS of the Institute Oceanology, Chinese Academy of Science. We use part of this dataset in the present study. The data density is suitable for the production of raster grids, at ca. 100 m resolution (cell size), and the vertical resolution is ca. 1–3.3 m in the study area (3‰ of the water depth), which provides enough sufficient for our studies of seabed morphologies, such as headwall scarps and sidewall scarps of Baiyun Slide. Most imaging and analyzing steps included Digital Elevation Model (DEM) constructing, contour describing and Slope Analyzing, generation of ArcGIS v9.3.

10.4 Results

10.4.1 Morphology and Distribution of Baiyun Slide

Baiyun Slide is one of the largest submarine landslides located at N 19°–20° on the northern SCS (Fig. 10.1b). It has a run-out distance of ~150 km and an estimated affected area of ~10 000 km^2. We calculate that the average thickness of Baiyun Slide is 50 m, thus the total estimated volume of Baiyun Slide is 500 km^3. The continental slope angle is typically 1–3° and flattens at 2,500–3,000 m water depth to <1° (Fig. 10.2). The headwall domain of Baiyun Slide is located above the LW gas field (Fig. 10.1) characterized by high sedimentation rate of 11.3 cm/year (Zhang et al. 2002) with a water depth of ~1,000 m. We divide Baiyun Slide into three domains: the headwall domain, the translational domain and the toe domain (after Bull et al. 2009). Headwall scarps are clearly shown on the seismic section, which are considered as important kinematic indicators in the headwall domain of a slide (Bull et al. 2009). The direction of sediment transportation is usually perpendicular to the scarps. The Baiyun Slide develops

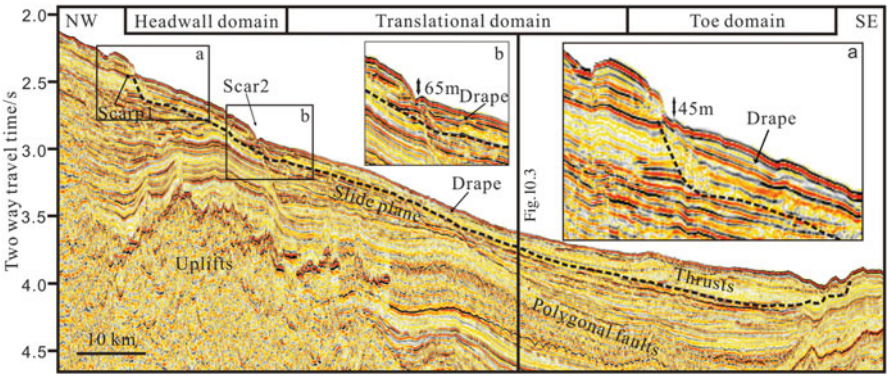

Fig. 10.2 Seismic profile crossing the entire Baiyun Slide Complex. It shows two main scars, the slide plane, and numerous polygonal faults below. Location of profile is shown of Fig. 10.1

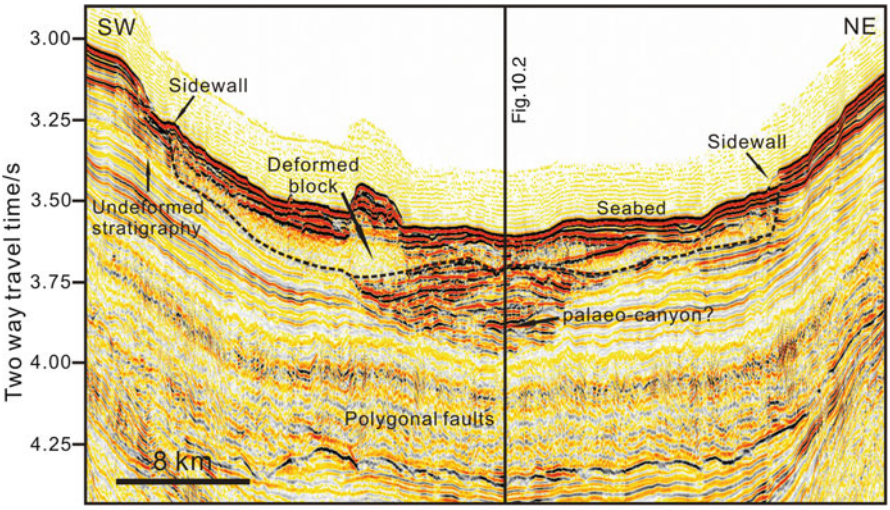

Fig. 10.3 The sidewalls and a huge remnant block are identified on the seismic profile. Numerous polygonal faults develop beneath the Baiyun Slide. Location of profile is shown of Fig. 10.1

in a retrogressive fashion, characterized by a stepped pattern of two major slide scars, 45 and 65 m in height, respectively (Fig. 10.2). The scarps dips steeply from 10° to 20° with sediments being transported directly down slope and away from the scarps. A large deformed block is showed in the translational domain of Baiyun Slide (Fig. 10.3). The movement of the failed material downslope across the slide plane can lead to intense deformation, and the formation of deformed block can provide kinematic information. The sidewalls form parallel to the gross flow direction, and offer a primary constraint on the gross general direction of sediment transport (Fig. 10.1b). Sidewalls are often associated with strike-slip

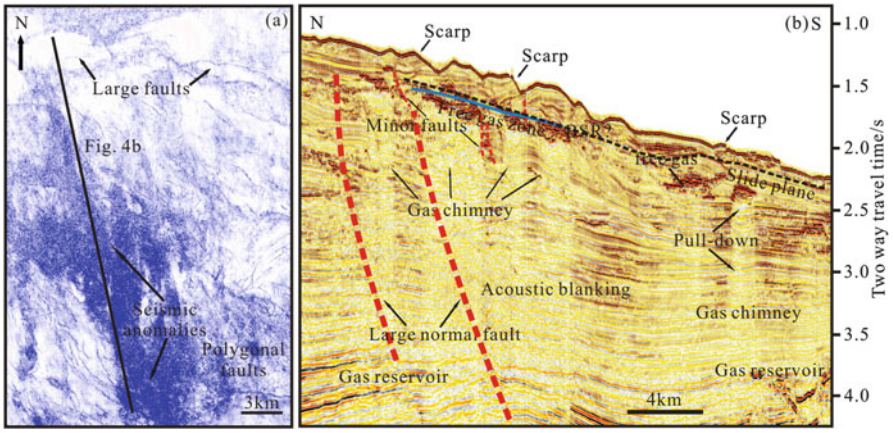

Fig. 10.4 (**a**) Coherence map at 3500 ms of the 3D seismic data in the study area (see Fig. 10.1 for location). Acoustic anomalies zones, polygonal faults and tectonic faults are clearly visible; (**b**) Seismic profile crossing the headwall domain of Baiyun Slide. It shows five gas chimneys and two major large normal faults connected with the deep gas reservoirs. A BSR (*blue solid line*) may exist above the free gas zone parallel to the slide plane (*black dashed line*)

movement. The seismic section across a sidewall shows that the seismic facies change from high amplitude, continuous reflections outside of the area affected by slope failure to disorder or chaotic reflections within the slide (Fig. 10.3). Based on the high sedimentation rate of 11.3 cm/year and the thickness of sedimentary drape overlying the slide, we estimate that the age of Baiyun Slide is 0.6 Ma.

10.4.2 Seismic Indications of Gas and Fluid Migration

10.4.2.1 Active Faults Related to Gas and Fluid Migration

The role of normal faults as fluid migration pathways has been intensively studied due to their significance in leakage, re-migration and re-accumulation of hydrocarbon and gas hydrates (Bünz et al. 2003; Gay et al. 2006; Cartwright et al. 2007; Sun et al. 2010a, b). In the study area, the normal faults can be divided into three classes, namely deep-seated large normal faults, shallow minor normal fault and polygonal faults (Sun et al. 2012).

The deep-seated large faults with steep fault-plane dips are widely observed in the headwall domain of Baiyun Slide (Fig. 10.4b). They are several kilometers long and often connect with gas reservoir. The seismic reflections are usually phased-reversed and have anomalously high amplitudes at different stratigraphic levels along a fault (Fig. 10.4); it is reasonable to assume that the large normal faults

are or have been acting as pathways for upward migration of gases and pore fluids. The shallow minor normal faults are often observed within the free gas zone and at the crests of gas chimneys (Fig. 10.4). The seismic data reveal that the enhanced reflections (free gas) are commonly distributed along with the minor normal faults, which also serve as pathways for fluid migration.

Polygonal faults are extensional non-tectonic faults with small throws and play a vital role in migration, accumulation and release of fluids (Gay et al. 2006; Cartwright et al. 2007; Sun et al. 2010a, b). Polygonal faults are widely developed beneath the Baiyun Slide, especially in the headwall domain and translational domain of Baiyun Slide (Figs. 10.3 and 10.4). The polygonal faults occur within the lower Miocene tier and are formed during earlier burial upon compaction-related dewatering and hence are associated with flow and release of fluids (Bünz et al. 2003; Sun et al. 2010a, b; Cartwright 2011). The chaotic seismic reflections within the palaeo-canyon provide strong evidence that the canyon fill may be courser grained material and gas may be present in the pore space (Fig. 10.3). The migrated fluids may accumulate at the base of the palaeo-canyon and caused the sediments overpressured. These observations indicate that the polygonal faults below Baiyun Slide would be a good pathway for migration of hydrocarbons or other fluids.

10.4.2.2 Gas Chimneys

Gas chimneys are vertical disturbances in the seismic profiles often related to the propagation of fluids (especially gas) through fissures and fractures in rocks. Such features are generally inferred to be associated with fluid expulsion and imply overpressures in the sediments. Gas chimneys occur widely spread at the northern flank of the giant Baiyun Slide on the northern SCS margin. Five gas chimneys can be identified below the headwall domain of Baiyun Slide based on the seismic profile in the study area (Fig. 10.4). They are more than 1200 m in diameter with a circular plan-view and connected with overpressured gas reservoirs.

Gas chimneys consist of columnar zones of vertically stacked, downward bending reflections (Fig. 10.4b) compared with surrounding stratal reflections, which is attributed to low velocity (pull-down) due to gas (Wang et al. 2010; Sun et al. 2012). The generated gas diffused between fractures, and between clusters of fracture networks, containing different levels of gas saturation (Arntsen et al. 2007). In fact only mere presence of gas in a network of fractures will lead to a decrease of the compressional- and shear-wave velocities. The gas chimneys are therefore well-exposed anomalies on coherency attribute slice (Fig. 10.4a).

Enhanced reflections are often located near the top of gas chimneys. They provide evidence for the occurrence of gas in the shallow sediments. The gas is most likely mainly sourced from deep-seated gas reservoirs and source rock through gas chimneys or large normal faults. These observations provide evidence that gas chimneys provide pathways for thermogenic fluids to migrate upward to the shallow sediments and to form the shallow gas accumulation. The root of gas chimneys is

crucial for understanding their origin depth, and hence the fluid source. The root zone is seismically defined as the stratigraphic depth where stratal reflections no longer have the characteristic of a down-bending reflection architecture (Fig. 10.4b).

10.5 Discussion

10.5.1 Relationship Between Fluid Migration and Slope Stability

The linkages of fluid flow and sliding is the occurrence of the gas chimneys and faults terminating at the basal shear surface of Baiyun Slide and shallow gas accumulations adjacent to this surface (Figs. 10.2, 10.3, and 10.4b). A BSR (bottom simulating reflector) observed on seismic profiles marks the base of free gas zone and is thus used as an indicator for the presence of gas hydrates (Fig. 10.4b). Acoustic blanking may indicate the presence of free gas or high pore-water contents below the BSR (Fig. 10.4b) (Bünz et al. 2005; Berndt et al. 2012). It also indicates widespread excess pore pressures in sediments.

Based on these observations, we develop a conceptual model of the spatial association between slide scars observed in the 3D data and underlying fluid migration features (Fig. 10.5). It is known that gas and oil can migrate into the overlying sediments through these focused fluid flow structures from the deep reservoirs (Bünz et al. 2003; Sun et al. 2012). Gas in the sediments will increase pore pressure in marine clays that are already weakened because of rapid accumulation of sediments. Fluid migration and the resulting decrease in effective stress may add to present-day landslide risk (Berndt et al. 2012). It is reasonable to assume that expulsion of fluids and subsequent accumulation of gas in the upper slope and outer

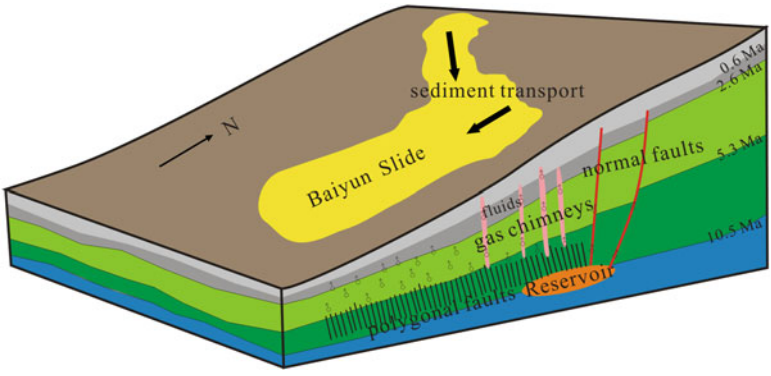

Fig. 10.5 Conceptual model illustrating the relationship between fluid migration and slope instability

shelf sediments have contributed to slope instability. Alternatively, it is possible that sliding happened first, causing a pressure drop, expansion of gas in underlying reservoirs and subsequent upward gas migration.

10.5.2 Possible Trigger Mechanisms

Baiyun Slide is one of the largest retrogressive submarine landslide in the northern SCS, however, its trigger mechanism is still poorly understood. Excess pore pressures within the sediments is considered to be the main possible triggering mechanism. Processes including rapid sediment deposition and fluid migration as well as gas hydrate decomposition increase the pore pressure and decrease the effective strength of sediments, hence increasing the potential for slope failure. During the Plio-Pleistocene period, the PMRB experienced rapid deposition of sediments, the highest accumulation rates are about 16 cm/year (Zhu et al. 2009), which may lead to excess pore pressures and decreasing slope stability. Identified leaking faults (e.g. polygonal faults etc.) and the occurrence of shallow gas by the identification of gas chimneys below Baiyun Slide are therefore direct evidences demonstrating the relationship between fluid migration and slope instability. Fluids including free gas that leak from the gas reservoir migrate upward through these fluid flow structures and accumulate in the shallow sediments, which may reduce the shear strength of the sediments and trigger slope failure.

10.6 Conclusions

The analysis of 2D/3D seismic data in combination with high-resolution multibeam bathymetric data in the southeastern Pearl River Mouth River Basin allows a detailed discussion of Baiyun Slide for the first time. The main conclusions are:

1. We identified the Baiyun Slide with a total volume about 500 km^3 over an area of 10,000 km^2 and with an estimated age of 0.6 Ma.
2. Numerous polygonal faults and gas chimneys are widely developed beneath the Baiyun Slide. We suggest a close relationship between fluid migration and slope instability.
3. The excess pore pressures within the sediments may be the main trigger mechanism of Baiyun Slide. It is important to assess the geohazard potential related to submarine mass wasting in northern SCS, especially as the study area is a current focus for hydrocarbon exploration and production.

Acknowledgments We acknowledge editor Christian Berndt, and the two reviewers Michael Strasser and Katrin Huhn for their constructive comments which greatly improved this manuscript. Our research is supported by National Natural Science Foundation of China (40930845 and 41276053) and the National Science and Technology Major Project (2011ZX05026-004-06).

References

Arntsen B, Wensaas L, Loseth H, Hermanrud C (2007) Seismic modeling of gas chimneys. Geophysics 72(5):SM251–SM259

Berndt C, Costa S, Canals M, Camerlenghi M, De Mol B, Saunders M (2012) Repeated slope failure linked to fluid migration: the Ana submarine landslide complex, Eivissa Channel, Western Mediterranean Sea. Earth Planet Sci Lett 319:65–74. doi:10.1016/j.epsl.2011.11.045

Bull S, Cartwright J, Huuse M (2009) A review of kinematic indicators from mass-transport complexes using 3D seismic data. Mar Petrol Geol 26(7):1132–1151

Bünz S, Mienert J, Berndt C (2003) Geological controls on the storage gas-hydrate system of the mid-Norwegian continental margin. Earth Planet Sci Lett 209:291–307

Bünz S, Mienert J, Bryn P, Berg K (2005) Fluid flow impact on slope failure from 3D seismic data: a case study in the Storegga Slide. Basin Res. doi:10.1111/j.13652117.2005.00256.x

Canals M et al (2004) Slope failure dynamics and impacts from seafloor and shallow sub-seafloor geophysical data: case studies from the COSTA project. Mar Geol 213:9–72. doi:10.1016/j.margeo.2004.10.001

Cartwright JA (2011) Diagenetically induced shear failure of fine-grained sediments and the development of polygonal fault systems. Mar Petrol Geol 28:1593–1610

Cartwright JA, Huuse M, Aplin A (2007) Seal bypass systems. AAPG Bull 91:1141–1166

Gay A, Lopez M, Cochonat P, Séranne M, Levache D, Sermondadaz G (2006) Isolated seafloor pockmarks linked to BSRs, fluid chimneys, polygonal faults and stacked Oligocene–Miocene turbiditic palaeochannels in the Lower Congo Basin. Mar Geol 226:25–40

Gong ZS (1997) The major offshore oil and gas fields in China. Petroleum Industry Press, Beijing, pp 221–223 (in Chinese)

Huang BJ, Xiao XM, Zhang MQ (2003) Geochemistry, grouping and origins of crude oils in the Western Pearl River Mouth Basin, offshore South China Sea. Org Geochem 34:993–1008

Huuse M, Jackson CAL, Van Rensbergen P, Davies RJ, Flemings PB, Dixon RJ (2010) Subsurface sediment remobilization and fluid flow in sedimentary basins: an overview. Basin Res 22: 342–360

Krastel S, Wynn RB et al (2006) Mapping of seabed morphology and shallow sediment structure of the Mauritania continental margin, Northwest Africa: some implications for geohazard potential. Nor J Geol 86:163–176

Leynaud D, Mienert J, Nadim F (2004) Slope stability assessment of the Helland Hansen area. Offshore the mid-Norwegian margin. Mar Geol 213(1–4):457–480. doi:10.1016/j.margeo.2004.10.019

Locat J, Lee HJ (2002) Submarine landslides: advances and challenges. Can Geotech J 39(1): 193–212. doi:10.1139/t01-089

Masson DG, Harbitz CB, Wynn RB, Pedersen G, Løvholt F (2006) Submarine landslides: processes, triggers and hazard prediction. Philos Trans R Soc Lond A 364:2009–2039

Micallef A, Berndt C, Debono G (2011) Fluid flow systems of the Malta Plateau, Central Mediterranean Sea. Mar Geol 1–4:74–85

Mulder T, Gonthier E, Lecroart P, Hanquiez V, Marches E, Voisset M (2009) Sediment failures and flows in the Gulf of Cadiz (eastern Atlantic). Mar Petrol Geol 26(5):660–672

Strozyk F, Huhn K, Strasser M, Krastel S, Kock I, Kopf A (2009) New evidence for massive gravitational mass-transport deposits in the southern Cretan Sea, eastern Mediterranean. Mar Geol 263:97–107

Sun QL, Wu SG, Lu FL, Yuan SQ (2010a) Polygonal faults and their implications for hydrocarbon reservoirs in the southern Qiongdongnan Basin, South China Sea. J Asian Earth Sci 39:470–479

Sun YB, Wu SG, Wang ZJ (2010b) The geometry and deformation characteristics of Baiyun submarine landslide. Mar Geol Quat Geol 28(6):69–77 (in Chinese)

Sun QL, Wu SG et al (2012) Shallow gas and focused fluid flow systems in the Pearl River Mouth Basin, northern South China Sea. Mar Geol. doi:10.1016/j.margeo.2012.05.003

Tripsanas E.K, Piper DJW, Campbell DC (2008) Evolution and depositional structure of earthquake-induced mass movements and gravity flows: Southwest Orphan Basin, Labrador Sea. Mar Petrol Geol 25(7):645–662, http://dx.doi.org/10.1016/j.marpetgeo.2007.08.002

Wang X, Wu SG, Yuan SQ, Ma YB, Wang DW (2010) Geophysical signatures associated with fluid flow and gas hydrate occurrence in a tectonically quiescent sequence, Qiongdongnan Basin, South China Sea. Geofluids. doi:10.1111/j.1468-8123.2010.00292.x

Yamada Y, Kawamura K, Ikehara K, Ogawa Y, Urgeles R, Mosher D, Chaytor J, Strasser M (2012) Submarine mass movements and their consequences. In: Yamada Y et al (eds) Submarine mass movements and their consequences, vol 31, Advances in natural and technological hazard research. Springer, Dordrecht, pp 1–12, doi:10.1007/978-94-007-2162-3_1

Zhang WY, Zhang FY, Chen RH, Zhang XY (2002) Constituents of matter and sedimentation fluxes and sedimentation rates of deep-water sedimentation during the Late Pleistocene in the South China Sea. Acta Sedimentol Sinica 20(4):668–674 (in Chinese with English abstract)

Zhu W, Huang B, Mi L, Wilkins RWT, Fu N, Xiao X (2009) Geochemistry, origin, and deep-water exploration potential of natural gases in the Pearl River Mouth and Qiongdongnan basins, South China Sea. AAPG Bull 93:741–761

Chapter 11
Post-failure Processes on the Continental Slope of the Central Nile Deep-Sea Fan: Interactions Between Fluid Seepage, Sediment Deformation and Sediment-Wave Construction

Sébastien Migeon, Silvia Ceramicola, Daniel Praeg, Emmanuelle Ducassou, Alexandre Dano, João Marcelo Ketzer, Flore Mary, and Jean Mascle

Abstract Voluminous mass-transport deposits (MTD) have been identified on seismic profiles across the central Nile Deep-Sea Fan (NDSF). The youngest MTDs are buried under 30–100 m of well-stratified slope deposits that, in water depths of 1,800–2,600 m, are characterized by undulating reflectors correlated with slope-parallel seabed ridges and troughs. Seabed imagery shows that, in the western part of the central NDSF, short, arcuate undulations are associated with fluid venting (carbonate pavements, gas flares), while to the east, long, linear undulations have erosional furrows on their downslope flanks and fluid seeps are less common. Sub-bottom profiles suggest that the western undulations correspond to rotated fault-blocks above the buried MTDs, while those in the east are sediment waves generated by gravity flows. We suggest that fluids coming from dewatering of MTDs and/or from deeper layers generate overpressures along the boundary between MTDs and overlying fine-grained sediment, resulting in a slow downslope movement of the

S. Migeon (✉) • A. Dano
Géoazur, UMR7329, UNS-UPMC-CNRS-OCA, Rue Albert Einstein, 06560 Valbonne, France
e-mail: migeon@geoazur.unice.fr

S. Ceramicola • D. Praeg
OGS (Istituto Nazionale di Oceanografia e di Geofisica Sperimentale), Borgo Grotta Gigante 42c, 34010 Trieste, Italy

E. Ducassou
Université Bordeaux 1, UMR5805 EPOC, Av. des facultés, 33405 Talence cedex, France

J.M. Ketzer
Center of Excellence in Research and Innovation in Petroleum, Mineral Resources and Carbon Storage (CEPAC), Pontifical University of Rio Grande do Sul (PUCRS), Av. Ipiranga 6681, Prédio 96J, CEP 90619-900, Porto Alegre-RS-, Brazil

F. Mary
UMR7329 Géoazur, UPMC-UNS-CNRS-OCA, rue A. Einstein, 06560 Valbonne, France

J. Mascle
Géoazur, UMR7329, UNS-UPMC-CNRS-OCA, Porte de la Darse, Villefranche-sur-Mer, France

S. Krastel et al. (eds.), *Submarine Mass Movements and Their Consequences*, Advances in Natural and Technological Hazards Research 37, DOI 10.1007/978-3-319-00972-8_11,

sediment cover and formation of tilted blocks separated by faults. Fluids can migrate to the seafloor, leading to the construction of carbonate pavements. Where the sediment cover stabilizes, sediment deposition by gravity flows may continue building sediment waves. These results suggest that complex processes may follow the emplacement of large MTDs, significantly impacting continental-slope evolution.

Keywords MTDs • Sediment waves • Deformation • Fluid seepages

11.1 Introduction

Gravity-driven sediment failure is an ubiquitous process on continental margins, resulting in a wide range of possible morpho-sedimentary expressions (McAdoo et al. 2000; Canals et al. 2004). Most studies of submarine landslides have concentrated on the triggering and dynamics of failures and their impacts as geohazards. In contrast, less attention has been given to processes following the emplacement of landslides on continental slopes. Although slope failures are known to decrease slope angles, which should inhibit further landslides, it has been shown that a return to stable conditions may involve several processes of erosion/deposition (Joanne et al. 2010). Moreover, observations of fluid seeps in the vicinity of slide scars raises the question of their role prior to and/or following failure (e.g. Lastras et al. 2004).

In this study, we examine sedimentary records of post-failure activity in the central Nile Deep-Sea Fan (NDSF), using a large dataset including multibeam seabed imagery, seismic-reflection profiles, and deep-towed side-scan sonar and 2–5 kHz data collected during the FANIL (2001) and APINIL campaigns (2011). Previous studies of the NDSF have shown its stratigraphic architecture to be characterised by large Mass-Transport Deposits (MTDs) (Garziglia et al. 2008; Loncke et al. 2009). In the central NDSF, stratified sediments form slope-parallel seabed undulations interpreted to record slope destabilisation in association with widespread fluid seepage, the latter recorded by high-backscatter carbonate pavements (Bayon et al. 2009). Here we present a first examination of lateral variability in the character of the undulations and fluid seeps, and consider it in relation to the interaction of processes of deformation and downslope deposition.

11.2 Methods

Multibeam bathymetric and backscatter data were acquired using hull-mounted Simrad EM300 and EM302 systems during the FANIL and APINIL campaigns, respectively. In the water depths of interest (1,800–2,600 m), the EM300 resulted in DTMs with a spatial resolution of 50 m (bathymetry) and 25 m (backscatter), while the EM302 yielded higher resolution DTMs of 25 m (bathymetry) and 10 m (backscatter). Subbottom profiles were acquired during both campaigns using a hull-

mounted chirp system. During the APINIL campaign, a deep-towed acoustic system (*Système Acoustique Remorqué*: SAR) deployed c. 70 m above the seabed provided both sidescan sonar imagery (resolution of 25 cm across swaths up to 1 km wide) and 2–5 kHz profiles (vertical resolution of 80 cm). Deeper penetration seismic-reflection profiles were acquired during FANIL using a 24-channel streamer and 2 mini-GI guns.

11.3 Results

Due to suspected interaction between buried bodies and seafloor features, we first describe the continental-slope architecture then the main seafloor morphologies.

11.3.1 Architecture and Age of MTDs and Slope Deposits

Seismic-reflection profiles show the upper 400 ms of the central NDSF to be characterised by up to 10 stacked lenticular bodies with a chaotic acoustic facies, interpreted as MTDs, and interbedded with high-amplitude reflection packages interpreted as turbidite channels (Fig. 11.2). The MTDs are 22–220 m (20–200 ms) thick, with sharp or erosive basal contacts and irregular tops. The youngest (MTD13) is about 150-km long and 35-km wide (Figs. 11.1 and 11.2; Rouillard 2010) and corresponds in cores to a debrite facies dated at c. 73 kyrs (Ducassou et al. 2013). MTD13 is buried by a stratified seismic facies 33–55 m (30–50 ms) thick (Fig. 11.2), corresponding in cores to alternating hemipelagite and turbidite deposits (Ducassou et al. 2009). To the east across the central NDSF, the stratified facies thickens up to 110 m above buried MTDs of unknown age but older than MTD13 (Fig. 11.2).

11.3.2 Seabed Sediment Undulations

Multibeam data show the seafloor of the central NSDF across water depths of 1,800–2,600 m to be dominated by sediment undulations, comprising elongate ridges alternating with trough-like depressions (Fig. 11.1). From east to west across a field of about 3,400 km^2, a clear change is observed in both the plan-form morphology and internal architecture of the undulations.

In the eastern part of the field, the mean slope angle is $\leq 0.8°$ and undulations are mainly slope-parallel (Fig. 11.1). Ridge crests are continuous for 2–9 km; most are linear and parallel with consistent wavelengths of 0.5–1 km, although some are arcuate and convex upslope or downslope in plain view. Ridges are 10–20 m high on the upper slope and decrease downslope to ≤ 5 m. In cross-section, the ridges

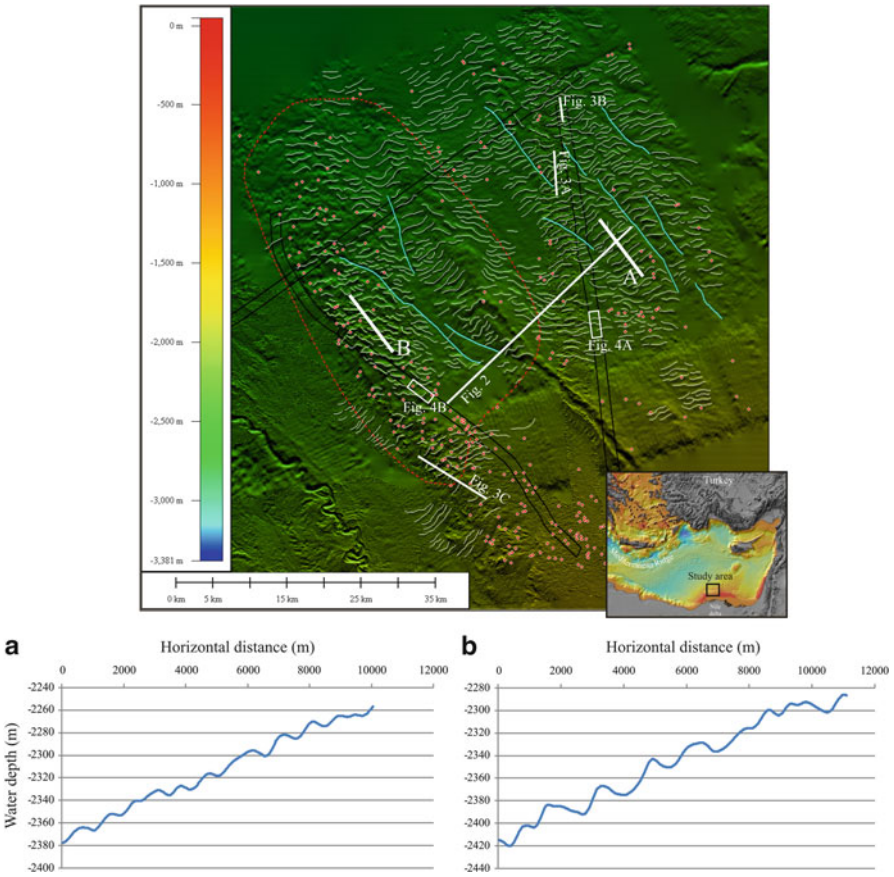

Fig. 11.1 Bathymetric map of the study area in the central NDSF. *Red dots* are multibeam high-backscatter patches. *White continuous lines* display crests of seabed undulations. *Blue lines* are small sediment pathways. The *red dashed line* displays the limit of MTD13. (**a**) and (**b**) are topographic profiles. The inset shows location of the study area on the Nile margin

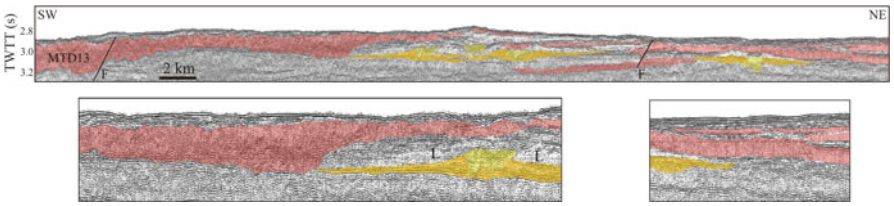

Fig. 11.2 Seismic profile illustrating occurrence of buried MTDs (*red bodies*) in the central NDSF. Some MTDs are affected by faults (*F*). *Yellow and orange bodies* are turbidite-channel infillings with adjacent levees (*L*). Profile location shown on Fig. 11.1

are mostly asymmetrical, with shorter upslope flanks (Figs. 11.1, and 11.3a, b), but symmetrical undulations also occur. In profile, the ridges consist of a well-layered echofacies, the first 30 ms of which thickens on upslope flanks, indicating higher sediment deposition, and thins on downslope flanks where truncations are common, indicating reduced deposition or erosion (Fig. 11.3a, b). Thus these structures have migrated upslope through time (Fig. 11.3a, b). They overlie a disorganized unit in which reflectors are tilted, disrupted and shifted vertically by faults (Fig. 11.3a). This unit overlies a MTD (Figs. 11.2, and 11.3a) which top itself exhibits relief (Fig. 11.3a). Sidescan sonar imagery across most of ridges (downslope flanks) reveal abundant furrows, 300–500-m long and 10–20-m wide, oriented parallel or oblique to slope (Fig. 11.4a), suggesting recent seafloor erosion by downslope flows.

In the western part of the field, overall slope angles are about 2.5° and in places up to 5.2°. The undulations are mainly arcuate and oriented oblique (10–40°) to slope, exhibiting a heterogeneous plan-form organisation that changes westwards (Fig. 11.1). In the eastern area of the western part, most arcuate crests are convex downslope; they are subparallel and up to 3 km long, with wavelengths of 1–1.5 km, and heights of 10–20 m with no downslope change. In the western area, most ridges are disrupted and <1 km long, with sharp changes of orientation (Fig. 11.1); they are 5–10 m high and ≤ 500 m in wavelength and distributed randomly along the slope (Fig. 11.1). In some places, they display a blocky pattern, more chaotic to the west. In profile, ridges are mainly asymmetrical with shorter and steeper downslope flanks (Figs. 11.1 and 11.3c), the reverse of the eastern part of the field, but also include symmetrical shapes with flat tops. Subbottom reflectors are continuous between adjacent ridges (Fig. 11.3c), parallel to seafloor and slightly wavy with wave amplitude constant with depth (Fig. 11.3c). Sediment thickness is nearly constant between reflectors across the ridges, providing no evidence for upslope or downslope migration (Fig. 11.3c). Small vertical offsets in reflectors across some troughs suggest faulting processes (Fig. 11.3c). Troughs are characterized by higher-amplitude reflections vertically aligned and resembling chimney-like structures (Fig. 11.3c; Loncke et al. 2004). Sidescan sonar imagery show the troughs to contain abundant intermediate-backscatter elongate patches trending parallel to the trough orientation, as well as smaller numbers of high-backscatter rounded patches (Fig. 11.4b), both inferred to be carbonate pavements related to gas venting (Dano et al. 2013). Gas flares identified in the water column above some of the high-backscatter patches indicate active fluid vents (Dano et al. 2013; Praeg et al. 2013). An absence of furrows suggests limited recent downslope particle transport/deposition.

11.3.3 Sediment Pathways

Several slope-perpendicular linear structures are located on the continental slope in water depths of 2,100–2,600 m (Fig. 11.1). They are 6–19-km long and V-shaped in cross section. They are interpreted as small-scale sediment-transport pathways.

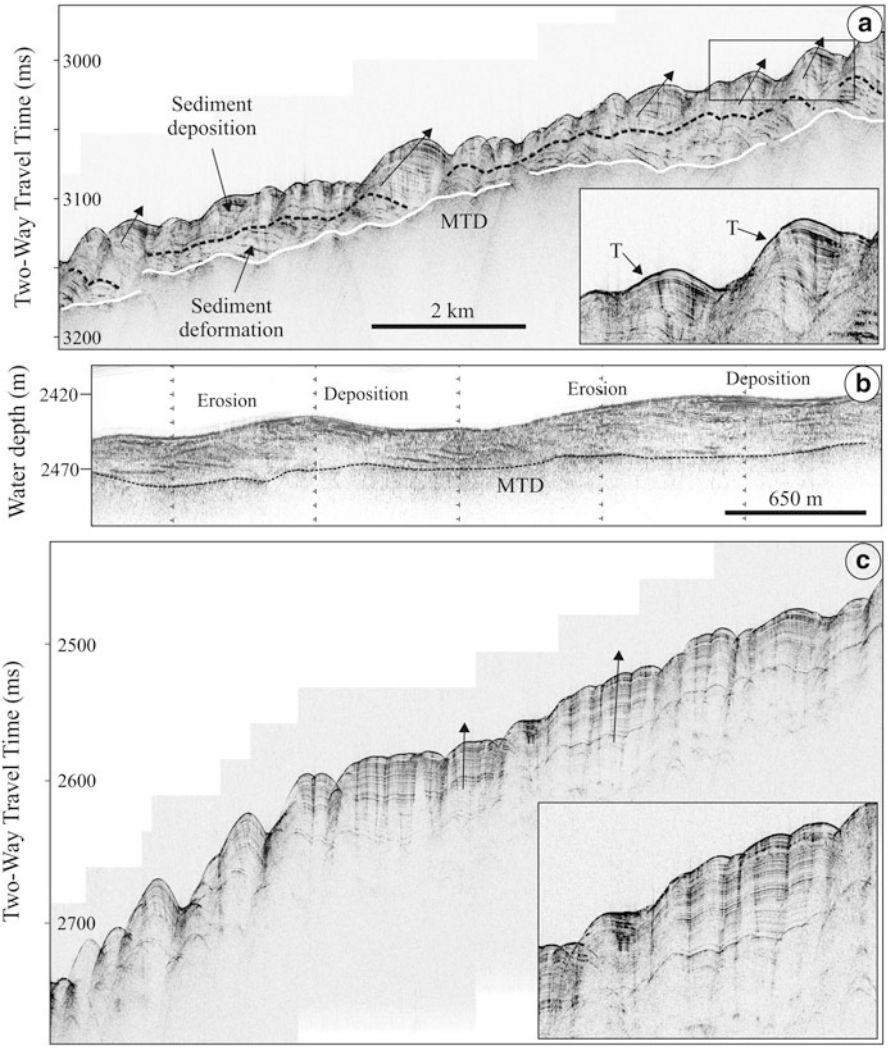

Fig. 11.3 (**a**) Hull-mounted subbottom profile illustrating sediment-waves; the *white line* is the *top* of a MTD and the *dashed line* is the *top* of a deformed interval (see text). (**b**) SAR subbottom profile illustrating sediment-waves; the *dotted line* is the *top* of a MTD. (**c**) Hull-mounted subbottom profile illustrating extensional deformations associated with fluid upward migration. Profiles location shown in Fig. 11.1

A well-developed channel-levee system (named DSF4 by Ducassou et al. 2009) is also located in the middle part of the study area, in water depths of 1,800–2,300 m (Fig. 11.1). It formed between 73 and 10 kyrs and is now being progressively buried by the undulations.

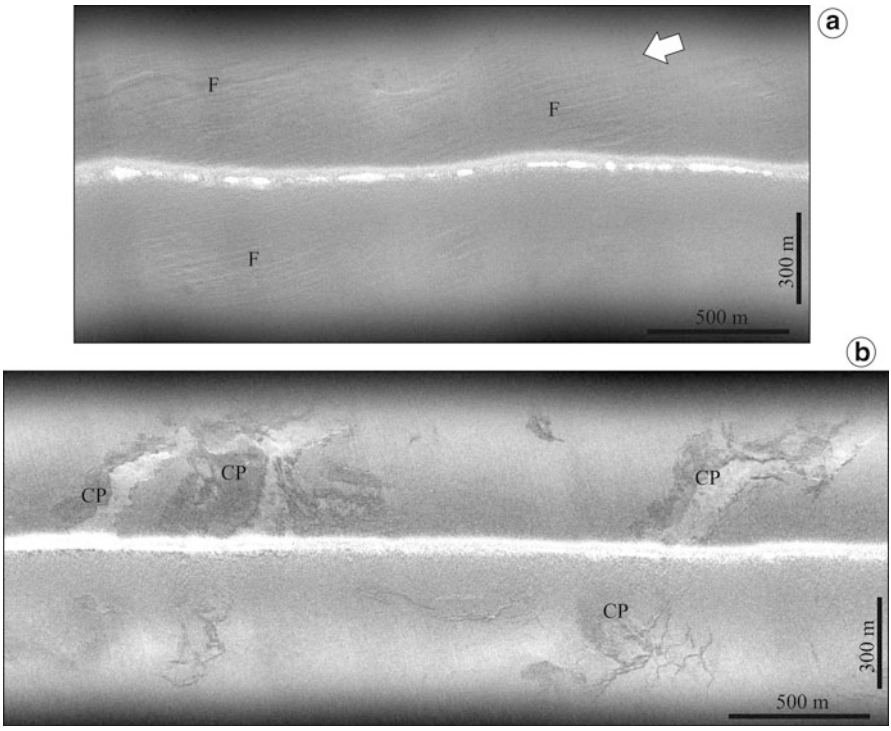

Fig. 11.4 SAR imagery illustrating (**a**) furrows (*F*) associated with sediment waves in the eastern study area, and (**b**) carbonate pavements (*CP*) flooring troughs of extensional deformations in the western study area. The *white arrow* indicates the main direction of turbulent flows that generated furrows. Images location shown in Fig. 11.1

11.4 Discussion

Undulating seabed sedimentary structures have been described on levees adjacent to turbidite channels, open continental slopes and submarine pro-deltas (Migeon et al. 2004; Hoffmann et al. 2011; Urgeles et al. 2011). They have been interpreted as either sediment waves deposited by turbulent flows, or deformation structures recording gravity-driven displacement of pre-existing sediment. The seabed undulations of the central NDSF have previously been interpreted as purely creeping/gliding features (Loncke et al. 2004; Bayon et al. 2009). We argue instead that the undulations provide evidence of both depositional and deformational processes. We first show the two main types of sediment undulations observed across the study area to correspond to end-member cases of these processes, then consider their overall relation to the underlying MTDs.

11.4.1 End-Members: Sediment Waves Versus Deformation Structures

In the eastern part of the study area, the plan-form morphology of the ridge crests and their downslope decrease in amplitude and wavelength are consistent with construction from turbulent gravity flows of decreasing velocity and particle load downslope (Normark et al. 2002). The presence of furrows on the downslope flanks of ridges confirms the role of these flows, at least during recent times, as does the occurrence of small-scale sediment pathways (Fig. 11.1). At the scale of individual ridges, the activity of successive turbulent flows caused preferential sediment deposition on their upslope flanks and by-passing or erosion of their downslope flanks (Fig. 11.3a), leading to upslope migration of the ridges. A similar pattern was observed in other slope settings, resulting in comparable slope-parallel sediment waves built by turbidity currents (Migeon et al. 2001; Normark et al. 2002).

In the western part of the study area, the chaotic convex-downslope morphology of the undulations, their 'reversed' asymmetry and absence of furrows suggest a limited impact of gravity flows in their formation. Their internal architecture provides no evidence of migration over time (Fig. 11.3c), consistent with either low-energy depositional draping of a pre-existing wavy topography, or with extensional deformation of the sediment cover. The presence of faults beneath the intervening troughs, many associated with gas seepage (Figs. 11.3c and 11.4b), favours the role of post-depositional rotational movements generated along shallow normal faults, as noted by previous authors (Loncke et al. 2004; Bayon et al. 2009).

The end-member cases of sediment-wave construction and extensional deformation are not exclusive. Thus in the eastern part of the study area, rotational structures are observed at depth (Fig. 11.3a), sandwiched between the undulating seabed sediments and the top of the MTD, suggesting that extensional deformation following MTD emplacement provided the pre-existing morphology that led to sediment-wave growth, as has been described in other areas (Hoffmann et al. 2011). In contrast, in the western part of the study area, sediment geometries continue to be dominated by extensional deformation involving rotating fault blocks, with widespread fluid venting along troughs aligned with fault planes.

11.4.2 Post-failure Slope Evolution

This work suggests that across the central NDSF, the formation of undulating sediment structures is initially linked to extensional deformation following the emplacement of large MTDs. Many extensional faults root within the MTDs and could result from differential compaction of these deposits, while others only affect

the overlying sediment cover and suggest slow gliding above MTDs. Because MTDs are younger and shallower to the west and the sediment cover thickens to the east (Fig. 11.2), extensional features should not be synchronous over the study area but must become younger to the west. Thus the west-east transition from irregular extensional features to well-developed sediment waves could reflect the increasing age of post-MTD processes affecting the slope.

After the emplacement of a large MTD, new sediment pathways develop on the slope and facilitate the deposition of a sediment drape. With time, the MTD experiences compaction, dewatering and eventual fluid release. Overpressures generated between the MTD and the overlying fine-grained sediment cover could then facilitate the slow gliding of the sediment cover along extensional faults rooting in the MTD. However, fluid seepage taking place across the central NDSF are also likely to be derived from deeper layers, including suspected gas hydrates (Praeg et al. 2008). This suggests another hypothesis that gas may accumulate at the base of an MTD, forming an overpressured horizon that contributes to the deformation of the overlying (and thickening) sediment mass and the development of fluid migration pathways allowing gas release.

In either case, rotational movements must be favoured by upward fluid flow along faults acting as conduits (Dano et al. 2013; Praeg et al. 2013). At seabed, gas-rich fluids lead to the construction of carbonate pavements. Carbonate precipitation may also take place within the conduits characterized by high-amplitude reflections (Fig. 11.3c). Such a process is thought to increase the cohesion of deposits and could contribute to the progressive stabilization of the sediment cover. Where sediment pathways exist, inactive rotational features will gradually be buried by gravity flows that may build sediment waves.

Additional high-resolution seismic profiles and 3D seismic data are now necessary to investigate the sediment cover above older MTDs to see whether this evolution is applicable or not to any time intervals.

11.5 Conclusion

An integrated analysis of multibeam and side-scan seabed imagery, and seismic profiles reveals lateral variations in the character of undulating features built on top of large MTDs across the central NDSF. They are interpreted to record the interaction of two end-member gravity-driven processes, extensional deformation associated with faulting and fluid migration, and sediment waves built by turbulent flows. Deformation features provide an initial morphology for sediment deposition and, where extension is reduced or ceases, may be progressively transformed into sediment waves. These results indicate that complex processes of continental-slope evolution may follow the emplacement of MTDs.

Acknowledgments The authors thank captains and crew of the RV Le Suroit and their colleagues present during the campaigns. The authors are thankful to Guillaume St Onge, Sam Johnson and David Völker for their reviews and constructive comments. This work was funded by the CNRS-INSU and the French program Action Marges.

References

Bayon G, Loncke L, Dupré S et al (2009) Multi-disciplinary investigation of fluid seepage on an unstable margin: the case of the Centre Nile deep sea fan. Mar Geol 26:92–104

Canals M, Lastras G, Urgeles R et al (2004) Slope failure dynamics and impacts from seafloor and shallow sub-seafloor geophysical data: case studies from the COSTA project. Mar Geol 213:9–72

Dano A, Praeg D, Migeon S et al (2013) Fluid seepage in relation to seafloor deformation on the central Nile Deep-Sea Fan, part 1: evidence from side-scan sonar data. In: Krastel S, Behrmann J-H, Völker D, Stipp M, Berndt C, Urgeles R, Chaytor J, Huhn K, Strasser M, Harbitz CB (eds) Submarine mass movements and their consequences. Advances in Natural and Technological Hazards Research 37, Springer, Heidelberg

Ducassou E, Migeon S, Mulder T et al (2009) Evolution of the Nile Deep-Sea Turbidite system during Late Quaternary: influence of climate change on fan sedimentation. Sedimentology 56:2061–2090

Ducassou E, Migeon S, Capotondi L, Mascle J (2013) Run-out distance and erosion of debris flows in the Nile deep-sea fan system: evidence from lithofacies and micropalaeontological analyses. Mar Petrol Geol 39:102–123

Garziglia S, Migeon S, Ducassou E et al (2008) Mass-transport deposits on the Rosetta province (NW Nile Dea-sea turbidite system, Egyptian margin): characteristics, distribution, and potential causal processes. Mar Geol 250:180–198

Hoffmann G, Silver E, Day S et al (2011) Deformation versus deposition of sediment waves in the Bismarck Sea, Papua New Guinea. Mass-transport deposits in deepwater settings. SEPM Spec Publ 96:455–474

Joanne C, Collot JY, Lamarche G, Migeon S (2010) Continental slope reconstruction after a giant mass failure, the example of the Matakaoa Margin, New Zealand. Mar Geol 268:67–84

Lastras G, Canals M, Urgeles R et al (2004) Shallow slides and pockmarks swarms in the Eivissa Channel, western Mediterranean Sea. Sedimentology 51:837–850

Loncke L, Mascle J, Scientific Party FANIL (2004) Mud volcanoes, gas chimney, pockmarks and mounds in the Nile deep-sea fan (Eastern Mediterranean): geophysical evidences. Mar Petrol Geol 21:669–689

Loncke L, Gaullier V, Droz L et al (2009) Multi-scale slope instabilities along the Nile deep-sea fan, Egyptian margin: a general overview. Mar Petrol Geol 26:633–646

McAdoo BG, Pratson LF, Orange DL (2000) Submarine landslide geomorphology, US continental slope. Mar Geol 169:103–136

Migeon S, Savoye B, Zanella E et al (2001) Detailed seismic-reflection and sedimentary study of turbidite sediment waves on the Var Sedimentary Ridge (SE France): significance for sediment transport and deposition and for the mechanisms of sediment-wave construction. Mar Petrol Geol 18:179–208

Migeon S, Savoye B, Babonneau N, Spy-Andersson FL (2004) Processes of sediment-wave construction along the present Zaire deep-sea meandering channel: role of meanders and flow-stripping. J Sediment Res 74:580–598

Normark WR, Piper DJW, Posamentier H, Pirmez C, Migeon S (2002) Variability in form and growth of sediment waves on turbidite channel levees. Mar Geol 192:23–58

Praeg D, Geletti R, Mascle J, Unnithan V, Harmegnies F (2008) Geophysical exploration for gas hydrates in the Mediterranean Sea and a bottom-simulating reflection on the Nile Fan. In: Riassunti Estesi, 27° Convegno Nazionale GNGTS, Trieste, Italy, pp 467–469

Praeg D, Ketzer JM, Augustin AH, et al (2013) Fluid seepage in relation to seafloor deformation on the central Nile Deep-Sea Fan, part 2: evidence from multibeam and sidescan imagery. In: Krastel S, Behrmann J-H, Völker D, Stipp M, Berndt C, Urgeles R, Chaytor J, Huhn K, Strasser M, Harbitz CB (eds) Submarine mass movements and their consequences. Advances in Natural and Technological Hazards Research 37, Springer, Heidelberg

Rouillard P (2010) Modèles architectural et lithologique des dépôts quaternaires du système de Rosetta (Delta Profond du Nil, Méditerranée orientale) : implication pour un analogue actuel de réservoirs pétroliers. PhD thesis, University of Nice-Sophia Antipolis, 421 pp

Urgeles R, Cattaneo A, Puig P et al (2011) A review of undulated sediment features on Mediterranean prodeltas: distinguishing sediment transport structures from sediment deformation. Mar Geophys Res 32:49–69

Chapter 12
Fluid Seepage in Relation to Seabed Deformation on the Central Nile Deep-Sea Fan, Part 1: Evidence from Sidescan Sonar Data

Alexandre Dano, Daniel Praeg, Sébastien Migeon, Jean-Marie Augustin, Silvia Ceramicola, João Marcelo Ketzer, Adolpho Herbert Augustin, Emmanuelle Ducassou, and Jean Mascle

Abstract The central Nile Deep-Sea Fan contains a broad area of seabed destabilisation in association with fluid seepage: slope-parallel sediment undulations are associated with multibeam high-backscatter patches (HBPs) related to authigenic carbonates. During the 2011 APINIL campaign, a deep-towed sidescan and profiling system (SAR) was used to acquire high-resolution data along three transects across water depths of 1,700–2,650 m. Three seabed domains are distinguished, all developed within stratified sediments overlying mass-transport deposits (MTDs). Upslope of the undulations (<1,950 m), sidescan HBPs record focused fluid seepage via seabed cracks. In the western area of undulations, sidescan HBPs are distinct from intermediate-backscatter patches (IBPs) that extend up to 850 m parallel to the undulations, mainly along their downslope flanks; some contain sub-circular HBPs up to 300 m wide, three associated with smaller (<10 m) hydroacoustic gas flares. Focused fluid seeps are inferred to have shifted over time

A. Dano (✉) • S. Migeon
Géoazur, UMR7329, UNS-UPMC-CNRS-OCA, Rue Albert Einstein, 06560 Valbonne, France
e-mail: dano@geoazur.unice.fr

D. Praeg • S. Ceramicola
OGS (Istituto Nazionale di Oceanografia e di Geofisica Sperimentale), Borgo Grotta Gigante 42c, 34010 Trieste, Italy

J.-M. Augustin
IFREMER, Technopôle Brest-Iroise, Plouzané, France

J.M. Ketzer • A.H. Augustin
Center of Excellence in Research and Innovation in Petroleum, Mineral Resources and Carbon Storage (CEPAC), Pontifical University of Rio Grande do Sul (PUCRS), Av. Ipiranga 6681, Prédio 96J, CEP 90619-900, Porto Alegre-RS-, Brazil

E. Ducassou
Université Bordeaux 1, UMR5805 EPOC, Avenue des facultés, 33405 Talence, France

J. Mascle
Géoazur, UMR7329, UNS-UPMC-CNRS-OCA, Porte de la Darse, Villefranche-sur-Mer, France

S. Krastel et al. (eds.), *Submarine Mass Movements and Their Consequences*, Advances in Natural and Technological Hazards Research 37, DOI 10.1007/978-3-319-00972-8_12,

to form elongate carbonate pavements, preferentially along the footwalls of faults beneath the undulations that provide pathways for fluid flow. In contrast, in the eastern area of undulations, sidescan imagery reveal only slope-transverse furrows formed by turbulent flows, interpreted to indicate that fossil carbonates sampled during submersible operations have been exhumed by erosion.

Keywords Fluid seepage • Sediment deformation • Backscatter • Gas flares

12.1 Introduction

Slope instabilities may be associated with features of seabed seepage (Lastras et al. 2004; Ramprasad et al. 2011), but it remains unclear whether fluid migration and release over time is a cause or consequence of sediment deformation. The Nile Deep-Sea Fan (NDSF) provides a useful study area, as investigations over the last decade have shown it to contain a rich variety of features of sediment destabilisation as well as of fluid migration and seepage (Loncke et al. 2004, 2009; Garziglia et al. 2008). The central NDSF contains a broad area of slope-parallel seabed undulations (Fig. 12.1), composed of stratified sediments overlying large mass transport deposits (MTDs), interpreted to record downslope deformation in association with fluid venting (Loncke et al. 2004; Bayon et al. 2009; Migeon et al. 2014). The undulations contain internal shear planes consistent with creeping and/or gliding of sediment blocks, while fluid seepage is recorded by patches of high acoustic backscatter up to 400 m across corresponding to pockmarks and/or low mounds (Loncke et al. 2004). Submersible observations show the high-backscatter patches to coincide with authigenic carbonate pavements, and suggest a model in which downslope sediment deformation above a decollement at the top of the MTDs has created pathways for fluid seepage through the troughs of the undulations, while apparently causing fossil carbonates to be exhumed along their crests (Bayon et al. 2009). In contrast, submersible observations upslope from the undulations suggest that carbonate pavements record ongoing seepage by diffuse fluid flow through undeformed sediments overlying MTDs (Bayon et al. 2009).

New information on the central NDSF was acquired during the 2011 APINIL campaign, using high-resolution swath/profiling systems. These data provide evidence of a lateral change in character of the seabed undulations, interpreted to record the interaction of gravity-driven deformation with downslope depositional processes over time: younger structures recording ongoing deformation and fluid venting in the west, give way eastwards to older deformation structures that are being transformed into sediment waves (Migeon et al. 2014). Here we focus on results from deep-towed sidescan swaths (Fig. 12.1), which provide the highest resolution seabed imagery yet available from the central NDSF. We examine the variation in seabed character across the area, with particular interest in the relation of seabed seepage to sediment deformation.

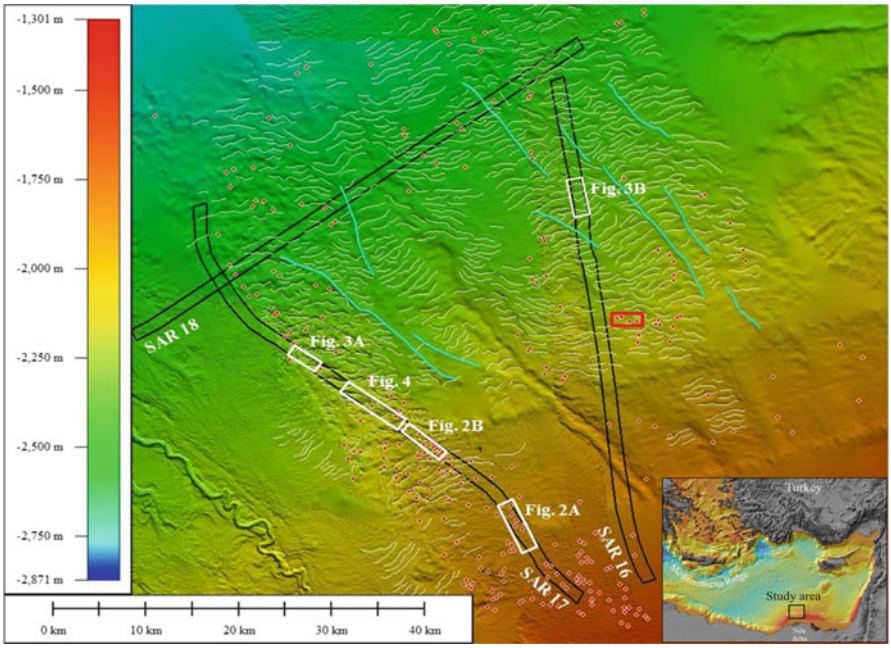

Fig. 12.1 Bathymetric map of the study area in the central NDSF. *Red dots* are multibeam high-backscatter patches. *White continuous lines* display crests of seabed undulations. *Blue lines* are small sediment pathways. The *red square* locates submersible investigations of carbonate pavements (Bayon et al. 2009)

12.2 Methods

Sidescan sonar imagery and 2–5 kHz sub-bottom profiles were acquired using the deep-towed SAR (*Système Acoustique Remorqué*) developed by Ifremer, towed 80–100 m above the seafloor at an average speed of 1 ms^{-1} and positioned using a short-baseline acoustic system. The sidescan sonar insonified an 1,100 m wide seabed swath with a spatial resolution of 0.25 m across-track and 1 m along-track, here gridded to 1.5 m pixels. High frequencies (170/190 kHz) and low incidence angles mean that penetration is minimal and backscatter intensity is mainly controlled by seabed morphology and sediment type. The different data types, including water column gas flares, were visualised using Sonarscope software (Ifremer).

12.3 Results

Subottom profiles across the central NDSF in water depths of 1,700–2,650 m (Fig. 12.1) show that the entire area is underlain by MTDs overlain by stratified sediments, both of which are thinner in depths <1,950 m (Figs. 12.2 and 12.3), here

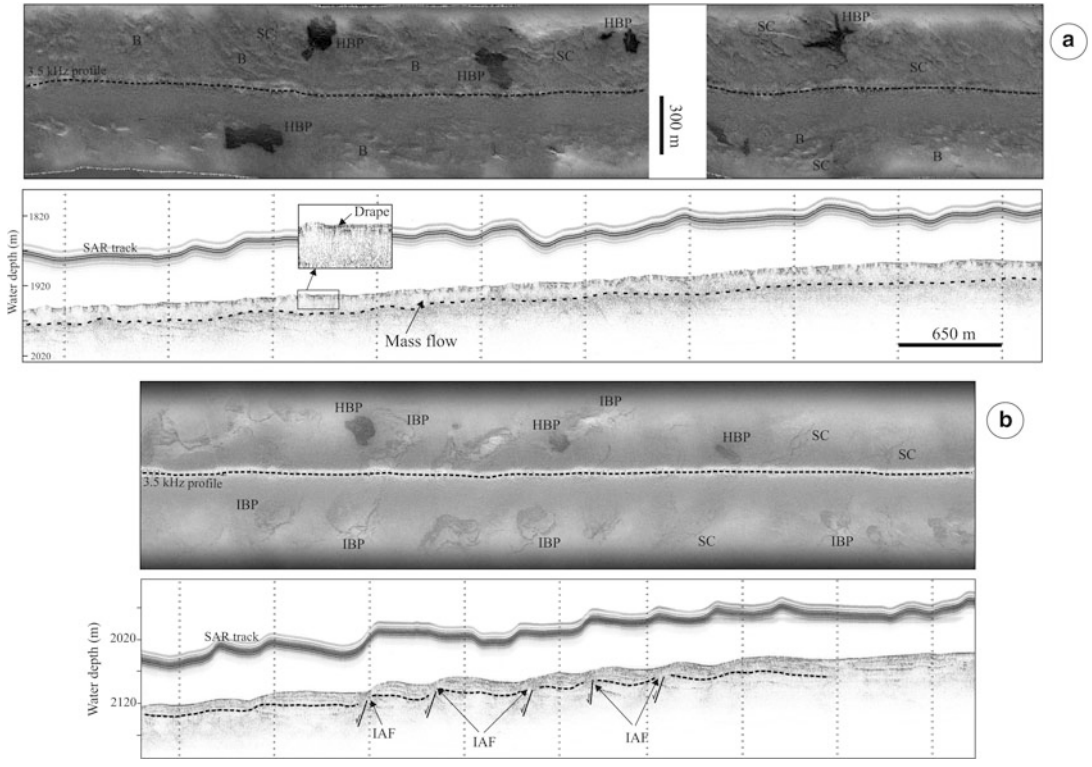

Fig. 12.2 SAR sidescan imagery (*upper*) and 3.5 kHz sub-bottom profiles (*lower*): (**a**) middle slope, across a mass-flow deposit with blocks (**b**), high-backscatter patches (*HBP*) and sediment cracks (*SC*); (**b**) lower slope, across sediment undulations associated with HBPs and intermediate-backscatter patches (*IBP*), as well as sediment cracks (*SC*); the IBPs (and cracks) are oriented parallel to the undulations and correlate at depth with incoherent acoustic facies (*IAF*) interpreted as gas-rich signatures along faults bounding the deformation structures (Locations in Fig. 12.1)

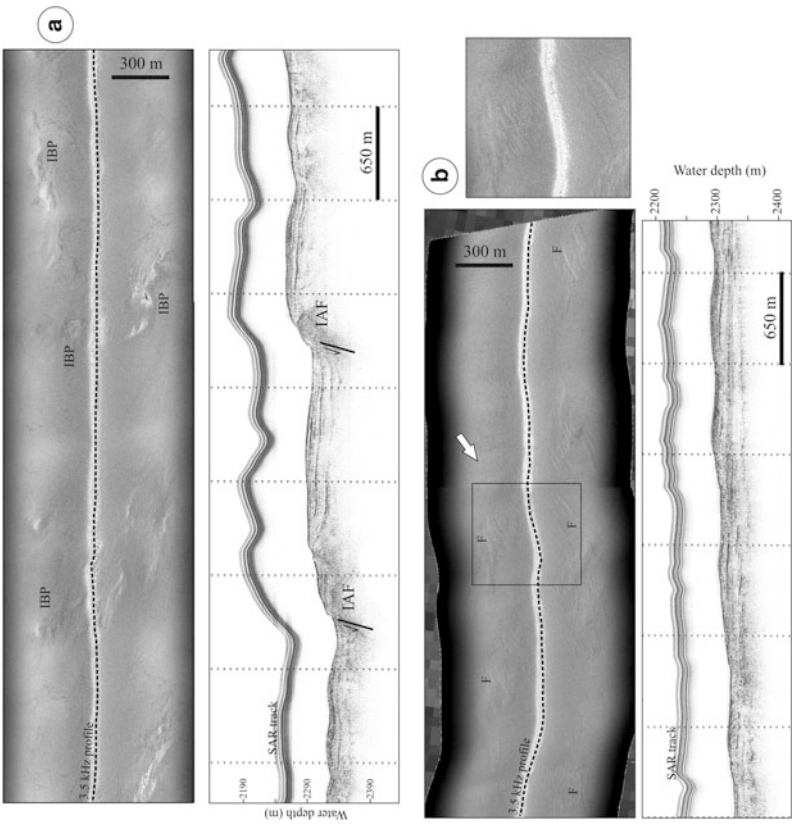

Fig. 12.3 SAR sidescan imagery (*upper*) and 3.5 kHz profiles (*lower*): (**a**) across sediment undulations associated with intermediate-backscatter patches (*IBP*) located along the footwalls of faults seen at depth and correlated with incoherent acoustic facies (*IAF*) indicative of gas; (**b**) across sediment undulations affected by downslope-oriented furrows (*F*) related to recent turbulent flows. The *white arrow* indicates the main direction of flows (Locations shown in Fig. 12.1)

called the middle slope (cf. Bayon et al. 2009). Across the lower slope in depths >1,950 m, the stratified sediments are deformed into seabed undulations that thicken and change in character eastwards: in the west short, arcuate features correspond to rotated fault blocks, while in the east longer, linear features are interpreted as older deformation structures that are being progressively transformed into sediment waves (Migeon et al. 2014).

Four types of seabed feature were identified: (1) erosional furrows, (2) sediment cracks, (3) carbonate pavements and (4) hydroacoustic gas flares rising from seabed into the water column.

12.3.1 Erosional Furrows

Seabed furrows consist of parallel lineaments 5–10 m wide and up to 800 m long, oriented transverse to slope (Fig. 12.3b). They are only observed along the eastern SAR transect (Fig. 12.1), from 2,150 to 2,500 m water depth, oriented N-NW. They are located on the downslope flanks of the larger seabed undulations and on both upstream and downstream flanks of the smaller ones. They are interpreted to record erosion of the seabed by turbulent flows moving downslope, as part of the ongoing sedimentary accretion of undulations in this part of the slope (see Migeon et al. 2014).

12.3.2 Sediment Cracks

Superficial sediment cracks are observed as radiating networks of lineaments of high backscatter (Figs. 12.2a, b and 12.3a), up to 4 m wide and 250 m long. Cracks were observed along the western SAR transect (Fig. 12.1) in two different settings, on the middle and lower slope. On the middle slope, in water depths of 1,690–1,970 m, they are associated with a blocky seabed morphology developed above an acoustically unstratified unit, together indicative of a mass transport deposit buried by thin stratified sediments (Fig. 12.2a). The radiating cracks could result from compaction following the emplacement of cohesive MTDs; some are associated with seabed carbonates (Fig. 12.2a, see below) and could have either guided upward fluid migration or been created by fluid flows. On the lower slope, they are seen on or near the crests of stratified sediment undulations that have undergone rotational tilting (Figs. 12.2b and 12.3a). The cracks lie parallel to the crest undulations and are inferred to be extensional structures related to fault block rotation.

12.3.3 Carbonate Pavements

Carbonate pavements are inferred from sidescan backscatter anomalies of varying intensity, here referred to as high and intermediate backscatter patches (HBPs and IBPs; Figs. 12.2 and 12.3a). On sidescan imagery, HBPs are up to 300 m in diameter, sub-circular to irregular in shape. They occur on the middle slope, on top of a blocky mass flow, in association with seabed cracks (Fig. 12.2a). They also occur on the lower slope, in the western area of seabed undulations, in association with more extensive IBPs (Figs. 12.2b and 12.3a), which exhibit lower but variable backscatter intensities and are elongate parallel to the seabed undulations, with widths up to 200 m and lengths up to 850 m. The IBPs and HBPs are preferentially located along the downslope flanks of the seabed undulations (Figs. 12.2b and 12.3a), although they can also extend across their troughs and crests. SAR 3.5 kHz profiles show many downslope flanks to be underlain by an incoherent acoustic facies consistent with the presence of gas (Figs. 12.2b and 12.3a). The HPBs and IBPs are interpreted as carbonate pavements formed in response to upward seepage of gas-rich fluids, as shown by submersible observations elsewhere in the central NDSF (Bayon et al. 2009). They overlap with backscatter anomalies observed on lower frequency multibeam data (Fig. 12.1) but are more extensive (see Praeg et al. 2014); however, there are none along the lower part (water depths >1,950 m) of the eastern SAR transect where no multibeam anomalies are observed (Fig. 12.1).

12.3.4 Hydroacoustic Flares

The SAR encountered gas flares in the water column at three sites, each near HBPs observed on sidescan imagery. The flares are observed on data uncorrected for slant-range, as vertical or slightly inclined features 3–10 m wide and up to 100 m high, i.e. the depth of the SAR above the seabed (Fig. 12.4). At each site a pair of flares was observed, c.60 m apart, recording separate bubble streams rising into the water column. It was not possible to position the flares relative to the sidescan swath, although they could be seen to lie to port or starboard of the SAR; in one case flares are seen to pass from one side to the other, indicating near-range features. Positioning of the flares using multibeam water column data (see Praeg et al. 2014) confirms that the flares lie at the edges of sidescan HBPs and indicates that features >250 m from the SAR are not observed.

12.4 Discussion

Analysis of sidescan sonar data across the central NDSF allows the identification of three open-slope domains characterized by differing associations of sediment deformation and fluid seepage: a middle slope (depths <1,950 m), and western and eastern areas of seabed undulations on the lower slope (depths >1,950 m).

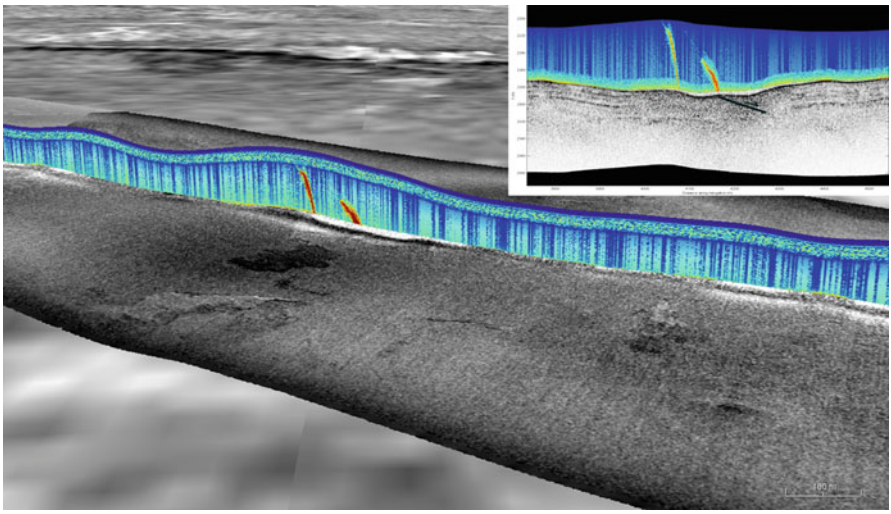

Fig. 12.4 Identification of gas flares in the side-scan sonar water column data, in colour and projected into vertical plane. The flares are 3–10 m wide and c. 60 m apart, inferred to lie within 250 m of the high-backscatter patch observed at seabed (the swath is 1,100 m wide on figure, 550 m on each side). *Inset*: correlation of these gas flares to gas signatures (*IAF*) on 2–5 kHz sub-bottom profile

12.4.1 Mid-slope Domain: Focused Fluid Flow Through MTDs

The southern domain corresponds to the middle slope, in water depths of 1,700–1,950 m, which is dominated by blocky MTDs 20–30 m thick on average, draped by layered deposits up to 2 m thick (Fig. 12.2a). From sedimentation rates estimated from cores in the area (Ducassou et al. 2009), the MTDs could be at least 10 kyrs old. Isolated HBPs observed above the MTDs in association with seabed cracks (Fig. 12.2a) indicate authigenic carbonate pavements formed from seepage of gas-rich fluids, unlikely to have come from dewatering of the relatively thin MTDs following their emplacement. Gas-rich fluids suggest focused fluid flow from depth, which exploited pathways offered by the cracks. This is in contrast to results from submersible observations on the slope to the east, in water depths of 1,650 m, where seabed carbonate pavements above MTDs were shown to record downward growth over the last 5 kyrs and suggested to record diffuse fluid flow (Bayon et al. 2009). The broad carbonate pavements (including IBPs up to 1.4 km across) are more likely to record growth over time by lateral displacement of sites of focused seepage, as suggested by Dupré et al. (2010).

12.4.2 Western Undulations: Fluid Flow Along Faults Rooted in MTDs

The western domain of seabed undulations contains abundant backscatter patches of high to intermediate intensity (Figs. 12.2 and 12.3a), indicative of carbonate formation in response to the migration and seepage of gas-rich fluids (cf. Bayon et al. 2009). The carbonate pavements are oriented sub-parallel to the seabed undulations, which record gravity-driven deformation of the upper sediment cover, in an area where the mean slope angle is 2.5° (Migeon et al. 2014). As gas charging is known to decrease sediment shear strength through time, which can contribute to creeping and/or landsliding processes (Locat and Lee 2002), fluid circulation is inferred to play a key role in the development of shallow instabilities on the central NDSF. In turn, our results provide evidence that sediment deformation has influenced fluid circulation.

Results from SAR sidescan imagery in the west of the study area indicate a distinction between sub-circular HBPs up to 300 m across, several of which are associated with smaller (<60 m) sites of gas venting, and broader areas of intermediate backscatter (IBPs) that extend up to 850 m along the seabed undulations. Backscatter patches of varying intensity have also been observed on 75 kHz sidescan sonar imagery from the central NDSF, upslope of the seabed undulations, which showed areas of variable (intermediate) backscatter up to 1,400 m across, within which occur smaller HBPs, some with gas flares at their edges (Dupré et al. 2010). The authors suggested that blocking of fluid flow by carbonate growth leads to lateral displacement of sites of seepage and the formation over time of broad carbonate sheets. Our results are consistent with this mechanism, which we apply to explain variable backscatter intensities in terms of successive stages of carbonate formation: IBPs correspond to fossil seepage sites, which may be covered by a thin veneer of sediment, while HBPs correspond to exposed areas of carbonates, within which backscatter may be enhanced both by micro-relief and by bioactivity related to active gas seepage (Dupré et al. 2010).

The SAR imagery shows that, in the western part of the study area, the growth over time of carbonate pavements is taking place along elongate zones, parallel to the seabed undulations. The formation of carbonate pavements appears to be favoured along the downslope facing flanks of the undulations, above faults assumed to bound rotated sediment blocks (Fig. 12.3a; Migeon et al. 2014). We infer that the faults act as fluid migration pathways, leading to preferential formation of carbonates along their footwalls.

12.4.3 Eastern Undulations: Exhumation of Fossil Carbonates

In the eastern domain of seabed undulations, neither IBPs nor HBPs were observed on sidescan imagery, consistent with the eastward decrease in density of HBPs

observed on multibeam data (Fig. 12.1; Migeon et al. 2014). A reduced fluid flux is supported by submersible observations in an area 2 km east of the SAR transect (Fig. 12.1, red square), which found dissolved methane anomalies in the troughs of some undulations but did not encounter gas bubbles (Bayon et al. 2009). The same study showed carbonate pavements on the crest of one undulation to be fossil features, dated at c. 8 kyrs, suggested to have been exhumed by deformation associated with formation of the seabed undulations. Our results suggest instead that these carbonates have been exposed by seabed erosion associated with the formation of elongated furrows, recording downslope particle transport by gravity flows (Fig. 12.3b). The predominance of sediment transport and deposition in the eastern domain, and the reduced importance of fluid circulation and gas venting, is consistent with an interpretation of the seabed undulations as older deformation structures that are being transformed into sediment waves (Migeon et al. 2014). Sedimentation could also contribute to the burial of seeps on the upslope flanks of undulations, a further explanation for their limited observation.

12.5 Conclusions

Changes in seabed character across the central NDSF observed on sidescan sonar imagery distinguish three main slope associations of sediment deformation and fluid seepage. A mid-slope (<1,950 m) area contains evidence of focused fluid flow from depth that has exploited seabed cracks developed above recent mass failure deposits. On the lower slope (>1,950 m), a broad area of seabed undulations changes in character from west to east. In the west, abundant evidence of seabed seepage correlates with shallow faults recording ongoing sediment deformation, which are inferred to have provided pathways for active seeps that have shifted over time to form broad carbonate pavements elongate along the seabed undulations. In the east, decreased evidence of seepage activity correlates with an increase in sediment furrows recording erosion by turbulent flows, which is inferred to have exhumed fossil carbonates sampled during submersible observations.

Acknowledgements The authors thank the captain and crew of the RV Le Suroît and their colleagues at sea and ashore who supported the APINIL campaign. This work was funded by CNRS-INSU and the French programme Action Marges. The manuscript was improved by helpful reviews from Renato Kowsmann (Petrobras, Rio di Janeiro) and Dave Long (BGS, Edinburgh).

References

Bayon G, Loncke L, Dupré S et al (2009) Multi-disciplinary investigation of fluid seepage on an unstable margin: the case of the Centre Nile deep sea fan. Mar Geol 26:92–104

Ducassou E, Migeon S, Mulder T et al (2009) Evolution of the Nile deep-sea turbidite system during the Late Quaternary: influence of climate change on fan sedimentation. Sedimentology 56:2061–2090

Dupré S, Woodside J, Klaucke I et al (2010) Widespread active seepage activity on the Nile deep Sea Fan (offshore Egypt) revealed by high-definition geophysical imagery. Mar Geol 275:1–19

Garziglia S, Migeon S, Ducassou E et al (2008) Mass-transport deposits on the Rosetta province (NW Nile deep-sea turbidite system, Egyptian margin): characteristics, distribution, and potential causal processes. Mar Geol 250:180–198

Lastras G, Canals M, Urgeles R et al (2004) Shallow slides and pockmarks swarms in the Eivissa Channel, Western Mediterranean Sea. Sedimentology 51:837–850

Locat J, Lee HJ (2002) Submarine landslides: advances and challenges. Can Geotech J 39:193–212

Loncke L, Mascle J, Fanil Scientific Parties (2004) Mud volcanoes, gas chimney, pockmarks and mounds in the Nile deep-sea fan (Eastern Mediterranean): geophysical evidences. Mar Petrol Geol 21:669–689

Loncke L, Gaullier V, Droz L et al (2009) Multi-scale slope instabilities along the Nile deep-sea fan, Egyptian margin: a general overview. Mar Petrol Geol 26:633–646

Migeon S, Ceramicola S, Praeg D et al (2014) Post-failure processes on the continental slope of the central Nile deep-sea fan: interactions between fluid seepage, sediment deformation and sediment-wave construction. In: Krastel S, Behrmann J-H, Völker D, Stipp M, Berndt C, Urgeles R, Chaytor J, Huhn K, Strasser M, Harbitz CB (eds) Submarine mass movements and their consequences, 6th international symposium. Springer, Switzerland/Heidelberg/New York/Dordrecht/London, pp 141–150

Praeg D, Ketzer JM, Augustin AH et al (2014) Fluid seepage in relation to seabed deformation on the central Nile deep-sea fan, part 2: evidence from multibeam and sidescan imagery. In: Krastel S, Behrmann J-H, Völker D, Stipp M, Berndt C, Urgeles R, Chaytor J, Huhn K, Strasser M, Harbitz CB (eds) Submarine mass movements and their consequences, 6th international symposium. Springer, Switzerland/Heidelberg/New York/Dordrecht/London, pp 117–127

Ramprasad T, Dewangan P, Ramana MV et al (2011) Evidence of slumping/sliding in Krishna-Godavari offshore basin due to gas/fluid movements. Mar Petrol Geol 28:1806–1816

Chapter 13
Fluid Seepage in Relation to Seabed Deformation on the Central Nile Deep-Sea Fan, Part 2: Evidence from Multibeam and Sidescan Imagery

Daniel Praeg, João Marcelo Ketzer, Adolpho Herbert Augustin, Sébastien Migeon, Silvia Ceramicola, Alexandre Dano, Emmanuelle Ducassou, Stéphanie Dupré, Jean Mascle, and Luiz Frederico Rodrigues

Abstract On the central Nile deep-sea fan, stratified sediments overlying mass-transport deposits (MTDs) are deformed into slope-parallel seabed undulations associated with fluid seepage. The western part of this system, in water depths of 1,950–2,250 m, is examined using multi-frequency data from hull-mounted and deep-towed swath/profiling systems. Sub-bottom profiles show sub-vertical fluid pipes that terminate both at and below seabed, and gas signatures along fault planes bounding the undulations. Fluid seepage is recorded by high- to intermediate-backscatter patches (HBPs, IBPs) that differ in appearance on multibeam imagery (30 kHz, $\leq$3 m penetration) and sidescan swaths (170/190 kHz, <0.1 m penetration). Comparison of the two suggests a distinction of (a) buried carbonates (0.1–3 m), (b) broad near-seabed (<0.1 m) carbonate pavements elongate along the undulations, (c) sub-circular areas of seabed seepage up to 300 m across. Four of the latter have narrower gas flares at their edges rising 400–800 m above seabed. These

D. Praeg (✉) • S. Ceramicola
OGS (Istituto Nazionale di Oceanografia e di Geofisica Sperimentale), Borgo Grotta Gigante 42c, 34010 Trieste, Italy
e-mail: dpraeg@ogs.trieste.it

J.M. Ketzer • A.H. Augustin • L.F. Rodrigues
Center of Excellence in Research and Innovation in Petroleum, Mineral Resources and Carbon Storage (CEPAC), Pontifical University of Rio Grande do Sul (PUCRS), Av. Ipiranga 6681, Prédio 96J, CEP 90619-900, Porto Alegre-RS-, Brazil

S. Migeon • A. Dano
Géoazur, UMR7329, UNS-UPMC-CNRS-OCA, Rue Albert Einstein, 06560 Valbonne, France

J. Mascle
Géoazur, UMR7329, UNS-UPMC-CNRS-OCA, Porte de la Darse, Villefranche-sur-Mer, France

E. Ducassou
Université Bordeaux 1, UMR5805 EPOC, Avenue des facultés, 33405 Talence, France

S. Dupré
IFREMER, Technopôle Brest-Iroise, 29280 Plouzané, France

S. Krastel et al. (eds.), *Submarine Mass Movements and Their Consequences*, Advances in Natural and Technological Hazards Research 37, DOI 10.1007/978-3-319-00972-8_13,

results are consistent with an evolving system of narrow fluid conduits that support the growth and burial of carbonate pavements, shifting over millennial timescales along linear zones parallel to fault planes rooted in MTDs. Sediment deformation above MTDs is inferred to provide pathways for fluid escape, but migration of gas-rich fluids from depth is likely to have facilitated slope destabilisation.

Keywords Slope undulations • Fluid seeps • Backscatter • Carbonates • Pipes • Faults

13.1 Introduction

Fluids play a key role in submarine slope stability (Sultan et al. 2004), but the relation of sediment failure to fluid migration and seepage remains poorly understood (Locat and Lee 2002). Seabed seepage may occur in association with different types of slope destabilisation (e.g. Lastras et al. 2004; Loncke et al. 2004; Paull et al. 2008), but it is unclear whether as consequence or cause. The central Nile Deep-Sea Fan (NDSF) provides an interesting example: slope-parallel seabed undulations, composed of stratified sediments up to 100 ms thick above mass-transport deposits (MTDs), are interpreted to record gravity-driven deformation in association with fluid seepage (Loncke et al. 2002, 2004; Bayon et al. 2009b; Migeon et al. 2014). Sub-bottom profiles indicate internal structures consistent with creeping and/or gliding, while fluid seepage is recorded by multibeam backscatter anomalies up to 400 m across corresponding to depressions or low mounds (Loncke et al. 2002, 2004). Submersible observations show backscatter anomalies to correspond to exposed carbonate pavements and suggest a model in which deformation of sediment above a decollement at the top of the MTDs has created pathways for fluid migration along the troughs of the undulations (Bayon et al. 2009b).

New high-resolution information was acquired across the central NDSF during the 2011 APINIL campaign (Fig. 13.1), using hull-mounted and deep-towed swath/profiling systems. The results provide evidence that whereas undulations in the east correspond to deformation structures that are being progressively transformed into sediment waves, in the west younger undulations record ongoing deformation and fluid venting, above an MTD dated to c.73 ka (Migeon et al. 2014; Dano et al. 2013). Here we focus on part of the western area (Fig. 13.1) where coincident data were acquired using multibeam, sidescan and sub-bottom systems, allowing a multi-frequency analysis of seabed features of fluid seepage in relation to sub-bottom evidence of fluid migration through the deformation structures.

13.2 Methods

Multibeam data were acquired using a hull-mounted Simrad EM302 (27–33 kHz), yielding DTMs with cell-sizes of 25 m (bathymetry) and 10 m (backscatter). Water column data were acquired along selected swaths and processed using Fledermaus

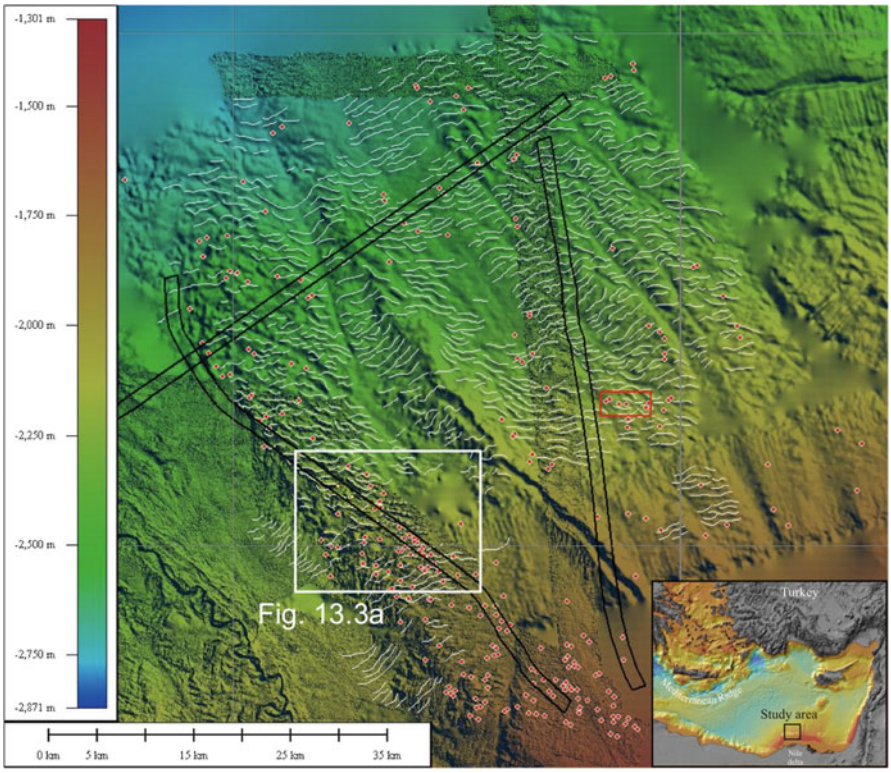

Fig. 13.1 Bathymetric map of central NDSF showing study area location. *Black parallel lines* denote SAR sidescan transects. *White continuous lines* are the crests of seabed undulations; *red dots* are multibeam high-backscatter patches. The *red square* locates an area of submersible investigations of carbonate pavements (Bayon et al. 2009b)

Midwater. Sub-bottom profiles were acquired with a hull-mounted Chirp system (1.8–5.3 kHz). Sidescan sonar imagery and 2–5 kHz profiles were acquired using the deep-towed SAR (*Système Acoustique Remorqué*) developed by Ifremer, towed 80–100 m above seabed. The sidescan sonar (170/190 kHz) insonified a swath up to 1,100 m wide with a theoretical resolution up to 25 cm across-track and 1 m along-track, here gridded to 1.5 m pixels. SAR water column data were visualised using Sonarscope software (see Dano et al. 2013). In comparing seabed imagery, penetration of marine muds by sonar systems decreases with frequency and offset (Mitchell 1993), such that a deep-towed 170/190 kHz sidescan will penetrate $\leq$10 cm, while a hull-mounted 30 kHz multibeam may penetrate up to 3 m (as demonstrated by Migeon et al. 2010).

13.3 Results

13.3.1 Faults and Fluid Indicators on Sub-bottom Profiles

Sub-bottom profiles across undulations in the study area show that stratified sediments up to 70 ms thick, and the top of the underlying MTD, are both offset by faults to form rotated sediment blocks (Fig. 13.2b); in places rollover anticlines suggest listric faults (Fig. 13.2c). Most faults lie beneath the downslope faces of undulations (Fig. 13.2; see also Fig. 2 in Dano et al. 2013), although a few dip upslope (Fig. 13.2b).

The profiles also reveal two kinds of near-seabed amplitude anomaly within the stratified sediments, incoherent acoustic facies (IAF) and pipes (Fig. 13.2). IAF are diffuse zones of amplitude enhancement, typical of free gas on high-frequency profiles; such an interpretation is supported by their coincidence with hydro-acoustic flares in the water column at two sites, both above faults (Fig. 13.2a, b). Pipes are common across the study area, as sub-vertical to inclined amplitude anomalies up to 15 m wide, most not coincident with faults (Fig. 13.2b, c); some terminate a few meters below seabed (Fig. 13.2c-inset), and not all of those that reach seabed coincide with backscatter anomalies (cf. Fig. 13.3). These observations are coherent with interpretations of pipes as products of past or ongoing fluid migration, fracturing and cementation (Andresen 2012).

13.3.2 Seabed Backscatter Anomalies at Differing Frequencies

Multibeam and sidescan sonar imagery across the same area of seabed undulations are shown in Fig. 13.3. The 10 m multibeam DTM shows many high-backscatter patches (HBPs), sub-circular to elongate, up to 400 m across, with no obvious pattern in their distribution or orientation. Smaller and/or intermediate-backscatter patches are also observed, but are difficult to distinguish from noise (Fig. 13.3). The larger HBPs are comparable to those previously observed on the central NDSF using a 50 m DTM based on 12–30 kHz multibeam imagery (Loncke et al. 2004; Bayon et al. 2009b). Comparison to the sidescan sonar swath shows the multibeam HBPs to correspond to three possible signatures: (1) areas of ‘normal’ backscatter (i.e. no anomalies); (2) patches of variable but intermediate backscatter (IBPs), elongate up to 850 m along the seabed undulations (see Dano et al. 2013), many of which overlap with the multibeam anomalies but are generally of greater extent; (3) sub-circular high-backscatter patches (HBPs) up to 300 m wide that coincide with, or lie within, the multibeam HBPs. Conversely, a comparison of the broad sidescan IBPs with multibeam backscatter suggests that many have some expression as intermediate multibeam amplitudes that are difficult to delineate.

These differences can be explained by differing penetration of the 30 kHz multibeam and 170/190 kHz sidescan sonar systems: multibeam backscatter integrates

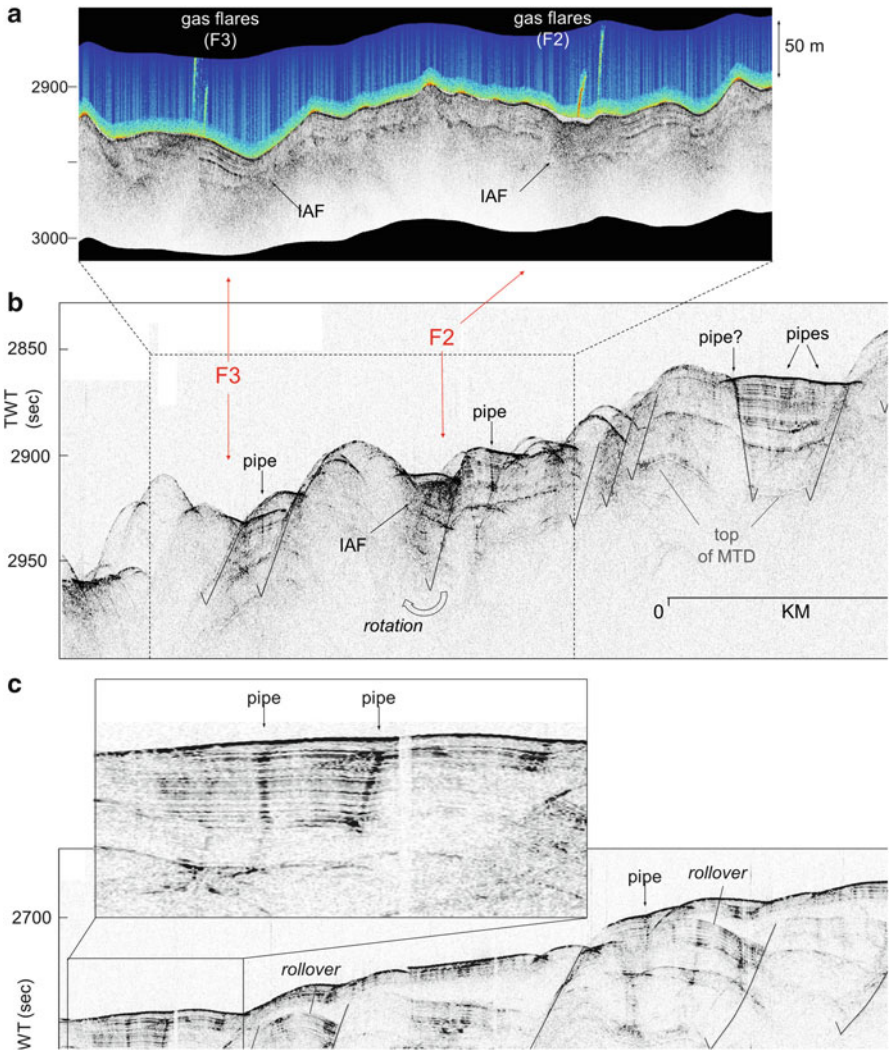

Fig. 13.2 Sub-bottom profiles across seabed undulations (locations in Fig. 13.3): (**a**) SAR 2–5 kHz profile showing incoherent acoustic facies (*IAF*), coincident with gas flares observed on 170/190 kHz sidescan data (in colour, water column swaths projected into vertical plane – see Dano et al. 2013); (**b**) hull-mounted Chirp 1.8–3.5 kHz profile subparallel with above (see Fig. 13.3a,d) showing fault-block rotations, sub-vertical fluid pipes and IAF; (**c**) hull-mounted Chirp profile across an area lacking seabed backscatter anomalies, showing sub-vertical fluid pipes, two of which do not reach seabed, and rollover anticlines consistent with listric faults

acoustic anomalies to depths of several meters, while the sidescan only sees features within 0.1 m of seabed (at higher resolution). Thus we infer that some multibeam HBPs are buried to depths of 0.1–3 m, whereas sidescan IBPs vs HPBs distinguish different kinds of feature at or near seabed. Assuming backscatter anomalies to

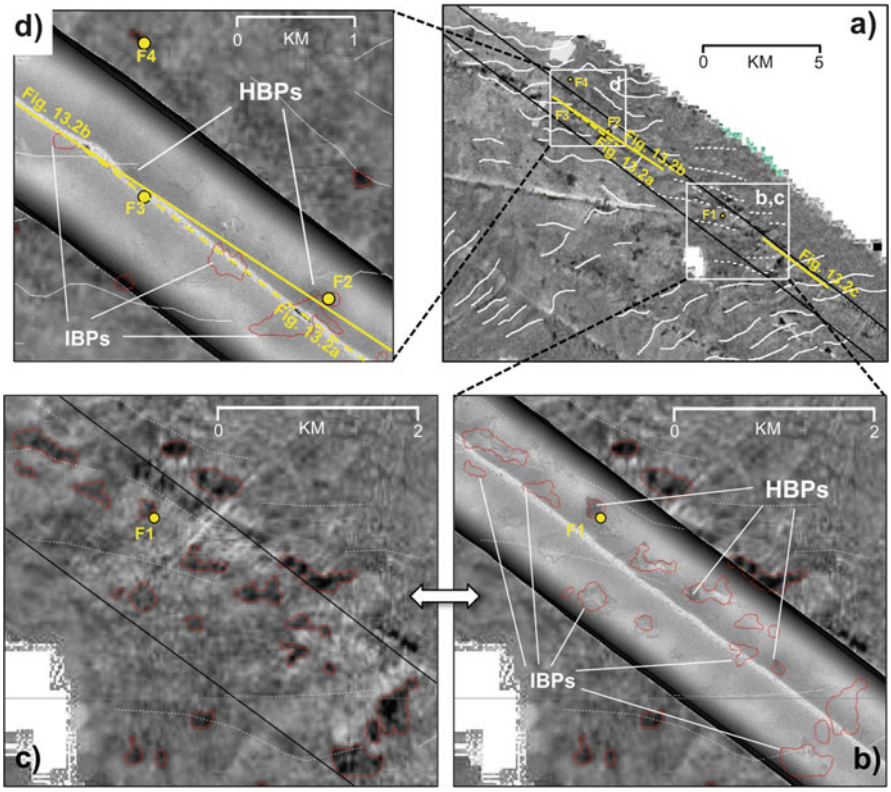

Fig. 13.3 Comparison of seabed imagery from multibeam and sidescan sonars (location in Fig. 13.1): (**a**) EM302 multibeam backscatter (10 m DTM) showing high-backscatter patches and the locations of four gas flares (F1-4); (**b**, **c**) comparison of multibeam backscatter anomalies (*left*) with high- and intermediate-backscatter patches (*HBPs*, *IPBs*) seen on SAR sidescan imagery (*right*); (**d**) comparison of multibeam and SAR backscatter anomalies as in (**b**)

be caused by authigenic carbonates, sidescan amplitudes may be enhanced by bioactivity and micro-relief in areas of gas venting, and/or reduced by a thin sediment veneer (cf. Dupré et al. 2010). In support of burial, patches of intermediate-(variable) and high-backscatter have been observed on 75 kHz sidescan imagery (penetration <1 m) on the central Nile fan upslope of the seabed undulations, and submersible transects only encountered exposed carbonates, and bioactivity, across the HBPs (Bayon et al. 2009b; Fig. 13.4). One question is why the elongate IPBs, if within 0.1 m of seabed, are of greater extent than multibeam HBPs (Fig. 13.3)? This could be explained if multibeam backscatter strength depends on the total thickness of reflective material within the upper <3 m sub-seabed; then parts of large sidescan IBPs could correspond to thin near-seabed sheets, within which occur smaller areas of thicker material (e.g. carbonates).

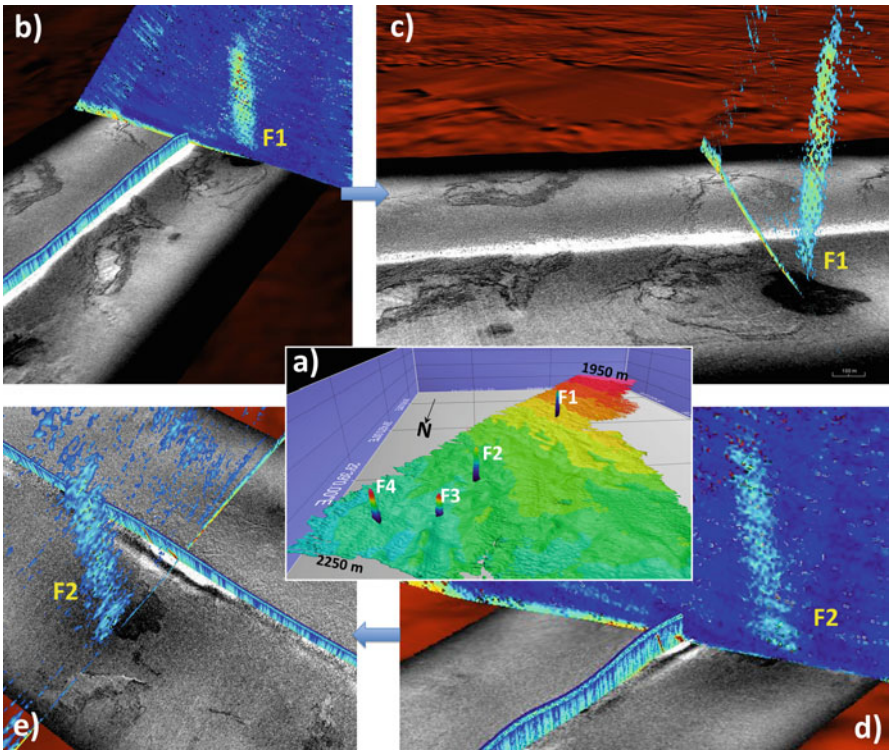

Fig. 13.4 Visualisation of water column gas flares on multibeam and sidescan imagery relative to seabed HBPs: (**a**) location of flares F1-4 from multibeam water column data, c.100 m wide and rising 400–800 m above seabed (locations also in Fig. 13.3a); (**b**, **c**) flare F1 at the edge of an HBP, >250 m from the centre of the c.1,100 m wide SAR swath; (**d, e**) flare F2 at the edge of an HBP, <250 m from the SAR water column profile which resolves two smaller flares ≤10 m wide and c.60 m apart

13.3.3 Water Column Gas Flares

Multibeam water column data allow the identification and positioning of four hydroacoustic flares, rising 400–800 m above seabed to water depths of 1,400–1,800 m (Figs. 13.3 and 13.4). The base of each flare is c.100 m wide and lies at the edge of a multibeam HBP (Fig. 13.3); three lie within the SAR swath and are seen to coincide with the edges of sidescan HBPs (Fig. 13.4). Two of the flares (<250 m from the swath centre) were visualised on higher resolution sidescan water column data (Fig. 13.2a), which shows each to correspond to a pair of narrower flares ≤10 m wide and c.60 m apart (Fig. 13.4d, e; see Dano et al. 2013). Thus gas is rising from multiple relatively small (≤10 m) sites at the edges of larger backscatter anomalies (corresponding to HPBs on both sidescan and multibeam imagery).

13.4 Discussion

13.4.1 Growth and Burial of Carbonate Pavements

Backscatter anomalies on the central NDSF have been correlated to seabed exposures of authigenic carbonates, formed in response to the upward flow of methane-rich fluids (Bayon et al. 2009a, b). Our comparison of multibeam and sidescan backscatter signatures suggests instead that multibeam HBPs indicate the presence of carbonates within the upper few meters of sediment, not necessarily exposed at seabed. Moreover, sidescan imagery indicate a near-seabed (<0.1 m) distinction between sub-circular high-backscatter patches (HBPs), several associated with gas flares at their edges, and larger intermediate-backscatter patches (IBPs) inferred to correspond to elongate carbonate pavements resulting from past seepage (see Dano et al. 2013). Interestingly, the sidescan IBPs overlap with but are of greater extent than multibeam HBPs, which can be explained if the IBPs include relatively thin near-seabed carbonate sheets. Water column data show gas is currently venting from only a few sites at the edges of HPBs, via flares ≤10 m wide on sidescan imagery, comparable to the widths of fluid pipes observed on sub-bottom profiles (Fig. 13.2).

These results are consistent with changes in fluid seepage over time to drive the growth of carbonate pavements and their progressive burial within near-seabed sediments. As suggested by Dupré et al. (2010), blockage of upward flow by carbonate growth provides a mechanism to laterally displace seepage sites and allow the formation over time of broad sheets. Dating of carbonate crusts elsewhere on the central NDSF indicates downward growth (Bayon et al. 2009a), and the diversion of flow beneath carbonate pavements is one means to allow the lateral growth of thin sheets. In addition, our observations of sub-vertical pipes, some of which do not reach seabed (Fig. 13.2b), show that individual fluid conduits may be abandoned. We infer an evolving system of sub-vertical conduits, feeding sites of seepage and the lateral growth of broad carbonate sheets, both of which can cease to be active and become progressively buried.

The timescales over which carbonates form and are buried may be estimated from sedimentation rates. Two cores from the central NDSF near the study area indicate rates of 2 cm/ka over the last 5 ka, 10–16 cm/ka from 5 to 15 ka and 2–11 cm/ka from 15 to 70 ka (Ducassou et al. 2009). Thus carbonates observed with sidescan imagery, assuming they are within 10 cm of seabed, must have formed during the last 5 ka, while features within the upper 2–3 m of sediment may date back at least to the last glacial maximum. This suggests changes in sites of seepage over millenial timescales, to allow the growth of elongate carbonate pavements. This estimate is consistent with a c.8 ka age obtained by U/Th dating of carbonate pavements on the central Nile fan to the east (Fig. 13.1; Bayon et al. 2009a), in an area where buried pavements are inferred to have been exposed by seabed erosion by turbulent flows (Migeon et al. 2014; Dano et al. 2013).

13.4.2 Fluid Migration Along Fault Planes

We infer that sites of fluid flow and seepage shift over relatively short (millenial) timescales to allow the growth of carbonate pavements along linear zones parallel to the seabed undulations. The formation of pavements appears to be favoured along the downslope-facing flanks of the undulations (see Dano et al. 2013), which correspond to fault planes bounding rotated sediment blocks (Fig. 13.2). This suggests the faults are acting as preferential pathways for fluid migration and influencing the localisation of fluid conduits. The distribution of pipes clearly shows that fluid conduits are not restricted to the faults (Fig. 13.2), nonetheless the observation of elongate carbonate pavements on sidescan imagery suggests that over time fluid seepage shifts along zones parallel to the fault planes.

This finding concurs with the model of Bayon et al. (2009b), who suggested that sediment deformation controls fluid escape on the central NDSF. However, their model envisages fluid flow along a planar boundary at the top of the MTDs, serving as a decollement for deformation driven by dewatering. In our study area, faults are observed to offset the top of the MTD (Fig. 13.2), and so must extend downward into it (see also Migeon et al. 2014; Dano et al. 2013). Given that fluid seepage on the NDSF is not confined to the area of seabed undulations (e.g. Loncke et al. 2004), it seems unlikely that gas-rich fluids are derived only from the MTDs and the <70 ms of sediment overlying them. We suggest that gas-rich fluids are derived from greater depths, and pass through the MTDs to reach seabed, exploiting pathways created by sediment deformation. If fluid migration pathways are indeed a consequence of deformation, the question remains whether fluids are contributing to the deformation? One hypothesis is that rising gas-rich fluids pass through the MTDs to generate overpressures below the base of the overlying fine-grained sediment cover, such that the upper part of the MTD acts as a decollement to superficial failure (see Migeon et al. 2014). Another possibility is that the MTDs instead act as barriers to fluid flow so that, following their emplacement, gas accumulation at their base leads to overpressures that drive or enhance post-failure deformation, ultimately impacting on the sediment cover to allow fluid escape.

13.5 Conclusions

A multi-frequency comparison of seabed backscatter signatures on the central Nile fan using multibeam and sidescan sonars indicates three types of anomaly linked to fluid seepage: buried carbonates (0.1-3 m), elongate near-seabed (<0.1 m) pavements produced by past fluid seepage and smaller areas of ongoing seabed seepage. Sites of seepage through vertical conduits are inferred to have shifted over timescales of millennia to build up broader carbonate sheets, preferentially along linear zones above fault planes bounding rotated sediment blocks that root

in underlying MTDs. Sediment deformation has thus provided pathways for fluid escape to seabed above the MTDs, but upward fluid migration beneath the MTDs is likely to have driven or enhanced sediment destabilisation.

Acknowledgments The authors thank the captain and crew of the r/v Le Suroît and their colleagues at sea and ashore who supported the APINIL campaign. This work was funded by CNRS-INSU and the French program Action Marges. We thank John Woodside (Amsterdam) and Fernando Freire (Petrobras, Rio de Janeiro) for useful reviews of the manuscript.

References

Andresen KJ (2012) Fluid flow features in hydrocarbon plumbing systems: what do they tell us about the basin evolution? Mar Geol 332–334:89–108

Bayon G, Henderson GM, Bohn M (2009a) U-Th stratigraphy of a cold seep carbonate crust. Chem Geol 260:47–56

Bayon G, Loncke L, Dupré S et al (2009b) Multi-disciplinary investigation of fluid seepage on an unstable margin: the case of the Centre Nile deep sea fan. Mar Geol 26:92–104

Dano A, Praeg D, Migeon S et al (2014) Fluid seepage in relation to seafloor deformation on the central Nile Deep-Sea Fan, part 1: evidence from side-scan sonar data. In: Krastel S Behrmann J-H, Völker D, Stipp M, Berndt C, Urgeles R, Chaytor J, Huhn K, Strasser M, Harbitz CB (eds) Submarine mass movements and their consequences, 6th international symposium. Springer, Switzerland/Heidelberg/New York/Dordrecht/London, pp 129–139

Ducassou E, Migeon S, Mulder T et al (2009) Evolution of the Nile deep-sea turbidite system during the Late Quaternary: influence of climate change on fan sedimentation. Sedimentology 56:2061–2090

Dupré S, Woodside J, Klaucke I et al (2010) Widespread active seepage activity on the Nile deep sea fan (offshore Egypt) revealed by high-definition geophysical imagery. Mar Geol 275:1–19

Lastras G, Canals M, Urgeles R et al (2004) Shallow slides and pockmarks swarms in the Eivissa Channel, Western Mediterranean Sea. Sedimentology 51:837–850

Locat J, Lee HJ (2002) Submarine landslides: advances and challenges. Can Geotech J 39:193–212

Loncke L, Gaullier V, Bellaiche G et al (2002) Recent depositional patterns of the Nile deep-sea fan from echo-character mapping. AAPG Bull 86:1165–1186

Loncke L, Mascle J, Parties FS (2004) Mud volcanoes, gas chimney, pockmarks and mounds in the Nile deep-sea fan (Eastern Mediterranean): geophysical evidences. Mar Petrol Geol 21: 669–689

Migeon S, Ducassou E, Le Gonidec Y et al (2010) Lobe construction and sand/mud segregation by turbidity currents and debris flows on the western Nile deep-sea fan (Eastern Mediterranean). Sediment Geol 133:265–293

Migeon S, Ceramicola S, Praeg D et al (2014) Post-failure processes on the continental slope of the central Nile deep-sea fan: interactions between fluid seepage, sediment deformation and sediment-wave construction. In: Krastel S, Behrmann J-H, Völker D, Stipp M, Berndt C, Urgeles R, Chaytor J, Huhn K, Strasser M, Harbitz CB (eds) Submarine mass movements and their consequences, 6th international symposium. Springer, Switzerland/Heidelberg/New York/Dordrecht/London, pp 117–127

Mitchell NC (1993) A model for attenuation of backscatter due to sediment accumulations and its application to determine sediment thicknesses with GLORIA sidescan sonar. J Geophys Res 98:22,477–22,493

Paull CK, Ussler W, Holbrook WS et al (2008) Origin of pockmarks and chimney structures on the flanks of the Storegga Slide, offshore Norway. Geo-Mar Lett 28:43–51

Sultan N, Cochonat P, Canals M et al (2004) Triggering mechanisms of slope instability processes and sediment failures on continental margins: a geotechnical approach. Mar Geol 213:291–321

Part III
Slope Stability and Risk Assessment

Chapter 14
Advances in Offshore Seismic Slope Stability: A Case History

Omar Zanoli, Claudio Piatti, Lorenzo Zuccarino, and Eric J. Parker

Abstract This paper presents a case history showing how the integration of detailed geophysical and geotechnical data and advanced numerical modeling can overcome the limitations of conventional analysis in predicting seismic stability of deepwater slopes. Submarine landslides represent one of the most critical geohazards for offshore pipelines and deepwater hydrocarbon developments. This is particularly true for seismically active regions where earthquakes are expected to be a triggering mechanism. A typical issue encountered in these cases is the coexistence of several detrimental aspects: poor geomechanical properties of shallow sediments; presence of steep slopes; and/or severe seismic input. The combination of these aspects often makes it difficult to match results of conventional pseudo-static slope stability analysis with field observations. These methods are generally conservative for deepwater conditions and are not able to reproduce observed past failures modes. This case history is of a complex slope system in the Mediterranean Sea. Morphologically the system presents a number of canyons and large-scale landslide features, overlain by a limited number of shallow planar slides. Geochronological testing constrained the large, deep slides to the distant past while confirming the shallow slides as recent phenomena. The use of high quality sampling and advanced laboratory tests provided the necessary input for dynamic nonlinear FEM analyses using OpenSees software. Numerical results based on a set of real time histories confirmed field observations and highlighted the possible formation of seismically triggered shallow slides. The paper describes how geophysical data, accurate soil sampling and advanced laboratory testing together with an advanced numerical model can develop reliable slope stability assessments for projects in difficult environmental conditions.

O. Zanoli (✉) • C. Piatti • L. Zuccarino • E.J. Parker
D'Appolonia S.p.A, Siting Division, Genoa, Italy
e-mail: omar.zanoli@dappolonia.it

S. Krastel et al. (eds.), *Submarine Mass Movements and Their Consequences*, Advances in Natural and Technological Hazards Research 37, DOI 10.1007/978-3-319-00972-8_14,

Keywords Submarine landslide • Advanced geotechnical testing • Seismic slope stability • Dynamic numerical modeling • Marine geophysics • Marine geohazards

14.1 Introduction

The combination of poor geomechanical properties, steep slopes and severe seismic input often leads to discrepancies between the results obtained from conventional pseudo-static slope stability methods and field observations (e.g. Biscontin and Pestana 2006). These methods are generally conservative for deepwater conditions and are not able to reproduce observed past failures modes. More advanced approaches (e.g. numerical modeling) are thus necessary to provide more realistic evaluations. This case study provides a description of an advanced slope stability assessment approach for seismic active environments.

14.2 Geomorphological and Geotechnical Data

14.2.1 Site Investigations

The study is based on data from a Detailed Marine Survey (DMS) including both geophysical and geotechnical/geological data.

Geophysical data comprise high-resolution, multi-beam bathymetry, sub-bottom profiling (SBP) and side scan sonar (SSS) data collected from an AUV (Autonomous Underwater Vehicle), 2D Ultra High Resolution (UHR) multi-channel seismic data, hull-mounted Pinger (HMP) profiles and Mini Sleeve Gun (MSG) profiles.

The geotechnical campaign included an extensive in-situ testing (Piezocone Penetration Test – PCPT) and sampling (Piston Gravity Core and Box Core) program, followed by standard and advanced laboratory testing. Detailed geological logging and dating (i.e., C^{14} radiocarbon and biostratigraphic analyses) were also carried out on undisturbed samples.

14.2.2 Geomorphological Setting

The area of interest comprises a major submarine canyon (Fig. 14.1) in water depths ranging from 250 to 1,250 m. The head of the canyon presents a steep-sided upper section with gradients up to 35º. This zone is followed by a perched mid-canyon section, with significantly lower gradients. Farther downslope, the canyon becomes steeper again and enters a lower canyon section. The complex can be described as a confined canyon system with intervening spurs. Slope failure deposits within the complex are characterized by a chaotic mixture of materials.

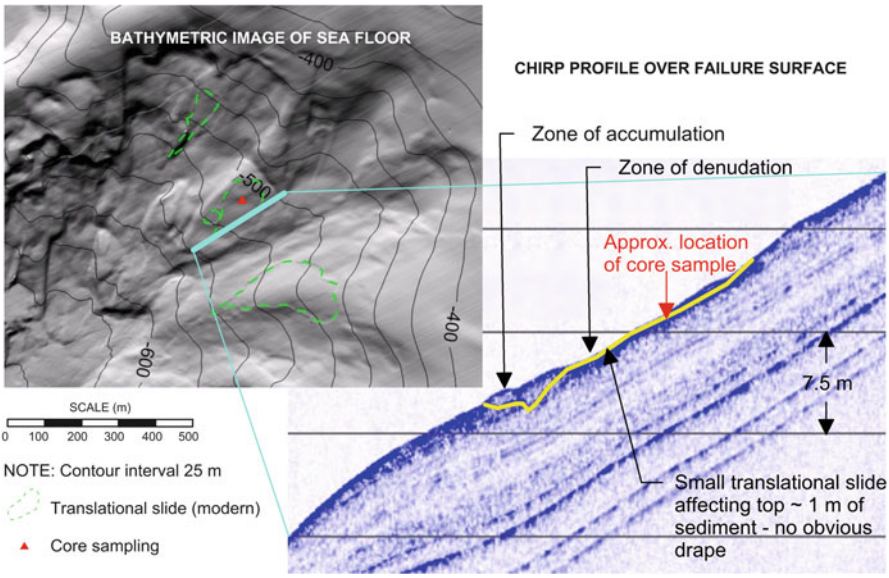

Fig. 14.1 Shaded relief map of the head of the canyon with indication of recent translational failures (*left*). CHIRP profile along section A-A′ with evidence of recent shallow translational slide (*right*)

These deposits originated primarily as translational failures at the canyon heads and flowed downslope, often as blocky runout, ending as debris flows interbedded with stratified clays.

In terms of lithology, the slope is covered by very soft to soft, well-layered hemipelagic clays of varying thicknesses. Sapropel horizons are frequently encountered within the shallow sediments. Soil sampling shows that underlying slope failure deposits consist of very soft to stiff clays and sandy clays. No evidence of gas hydrates was inferred from geophysical data in the area.

Three small translational failures manifested by seafloor scars are located near the head of the main canyon (Fig. 14.1). These translational slides are a few meters thick and appear to be the most recent failures in the upper slope. Dating of box core samples collected in the evacuation zone of one of these slides suggests they occurred in the last 800–1,000 years. Geochronologic testing indicates that the age of the main canyon failures is much greater, between about 17,000 and 18,500 years BP.

14.2.3 Geotechnical and Geophysical Data Integration

In principle, geotechnical data from an individual location can be extended to the nearby volume of soil only if the soil can be expected to be laterally continuous. Lateral variability can be assessed using geophysical data.

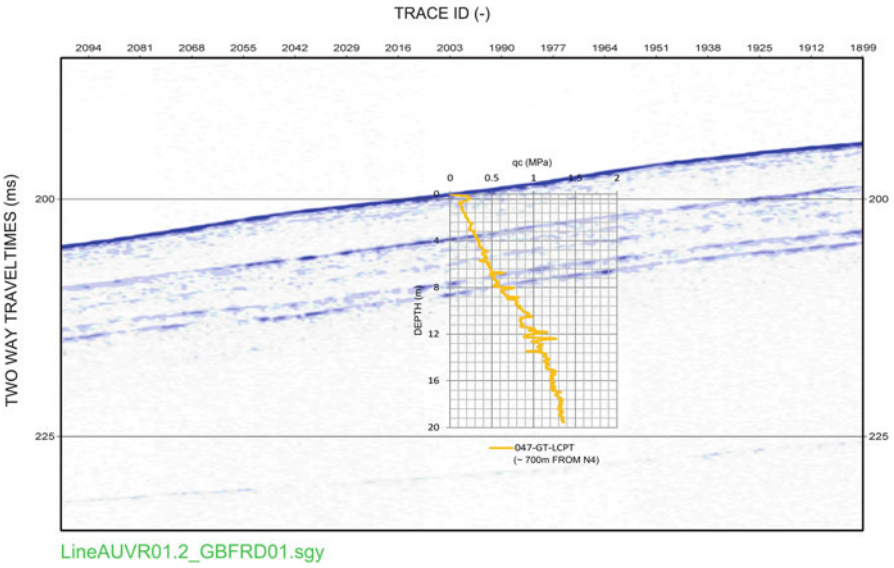

Fig. 14.2 Example of seismic and CPT data integration

The comparison between in-situ geotechnical and geophysical data was qualitatively evaluated through the superimposition of cone tip resistance plots on seismic sections. The correspondence between reflectors and peaks in cone tip resistance or sudden changes in cone tip resistance can be of value. An example is reported in Fig. 14.2. In this particular case no evident correlation between cone resistance and seismic reflectors is present, but the seismic section shows high lateral continuity of the sediments, confirming that the PCPT tests can be extended to the surrounding soil.

14.2.4 Soil Sampling

Obtaining high quality geotechnical samples is always challenging for deepwater projects. For this investigation a combination of box cores and long piston cores was chosen as the best solution for the expected soil conditions. Specifically, the Carma® Gravity Piston Corer technology (Magagnoli 2003) was used. This sampler retrieves large diameter (100 mm) cores, up to 30 m long, in fine sediments. An active piston allows for the reduction of compressive stress on the core top caused by the barrel's penetration, thus avoiding breakage of the core and liner implosion upon recovery.

An assessment of sample quality was performed using the Lunne et al. (1997) criteria, as shown in Fig. 14.3. This criteria is based on the evaluation of change in pore volume relative to the initial pore volume ($\Delta e/e_0$). The pore volume change

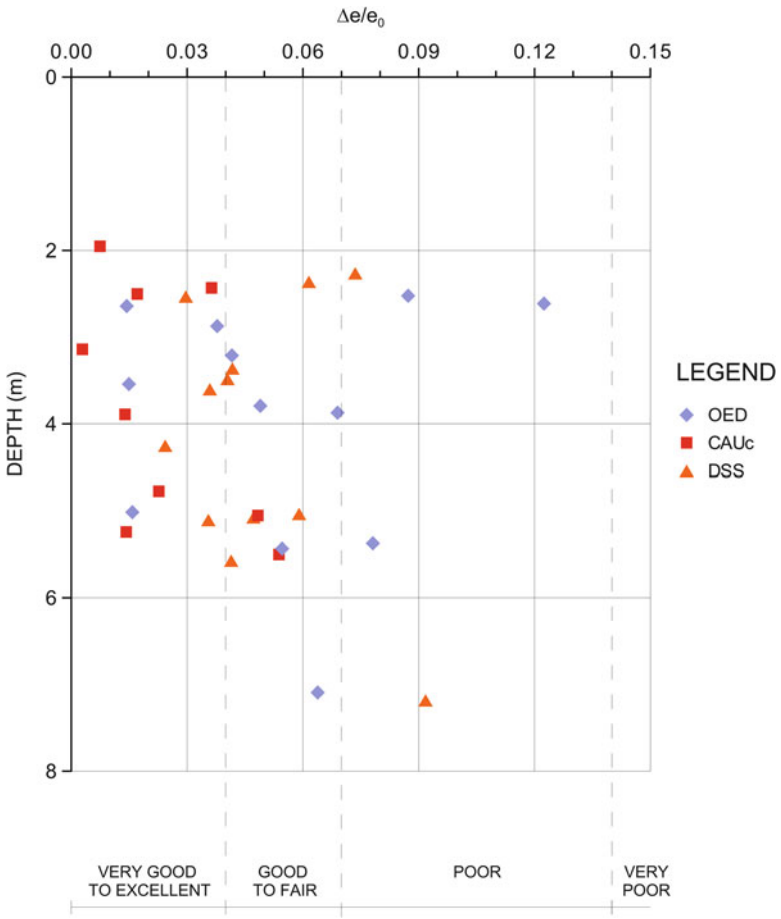

Fig. 14.3 Sample quality index following Lunne et al. (1997) for the recovered samples

(Δe) was evaluated after reconsolidation to in-situ stress in triaxial, direct simple shear (DSS) and oedometer tests. As shown in Fig. 14.3 most of the samples were good to very good quality, thus indicating that advanced laboratory test results would not to be unduly influenced by soil sampling.

14.2.5 Advanced Laboratory Testing

In addition to the standard geotechnical testing, a complete and detailed advanced laboratory test program was performed. The scope of testing was:

1. evaluate the influence of anisotropic consolidation stress on soil strength due to sloping ground condition;

2. study the effect of cyclic loading on soil strength;
3. verify post-earthquake soil strength;
4. quantify soil stiffness degradation and damping increase during cycling loading.

Classification/consolidation test results indicate that the sampled soil is a slightly overconsolidated low to medium plastic clay.

The advanced laboratory program comprised Anisotropic Consolidated Undrained triaxial tests in Compression (CAU_C) and Extension (CAU_E), Direct Simple Shear tests (DSS), Cyclic Direct Simple Shear (CSS), Bender Elements tests (BE) and Resonant Column tests (RC).

All samples were anisotropically consolidated to the estimated in-situ effective vertical and horizontal stresses. Specific triaxial tests were performed prior to the main program to evaluate the coefficient of lateral pressure at rest (K_0).

The effect of cyclic loading and average shear stress imposed by sloping conditions on undrained shear strength was measured through CSS tests performed under stress controlled conditions with cyclic frequency of 1 Hz. The cyclic strength of soils, as defined by Andersen (2009), is given by the sum of average and cyclic shear stresses at failure:

$$\tau_{cy,f} = \tau_a + \tau_{cy}$$

For the tested soils, $\tau_{cy,f}$ was found to be 45 % greater than the static strength for slope angles from 10° to 20°. This outcome is in line with literature results on clays and is the result of:

1. loading rate effects (faster loading in cyclic test leads to higher strength than in standard monotonic shear);
2. cyclic degradation effects (strength decreases as number of cycles increases);
3. anisotropic consolidation effects (τ_a).

Field experience shows that submerged slope failures are not usually triggered by inertial force during the seismic event. Rather, failure occurs some time after ground shaking stops due to soil structure weakening which is often related to pore pressure increase (Biscontin and Pestana 2006). In order to quantify this aspect, CSS tests were loaded for a specified number of cycles and then monotonically sheared to failure. The purpose of the initial cyclic phase was to induce a permanent strain (γ_p) in the specimen to simulate the effects of a seismic event. Once the cyclic phase was terminated, samples were monotonically loaded to failure. The test results show that the post cyclic undrained shear strength was about 85 % of the static undrained strength.

Soil response to seismic loading is also strongly influenced by the shear modulus decay (G/G_{max}) and damping ratio (D). The shear modulus at small strain (G_{max}) was measured with bender element tests (BE) and Resonant Columns tests (RC). The latter also gave G/G_{max} and damping ratio for a shear strains <0.1 %. Shear

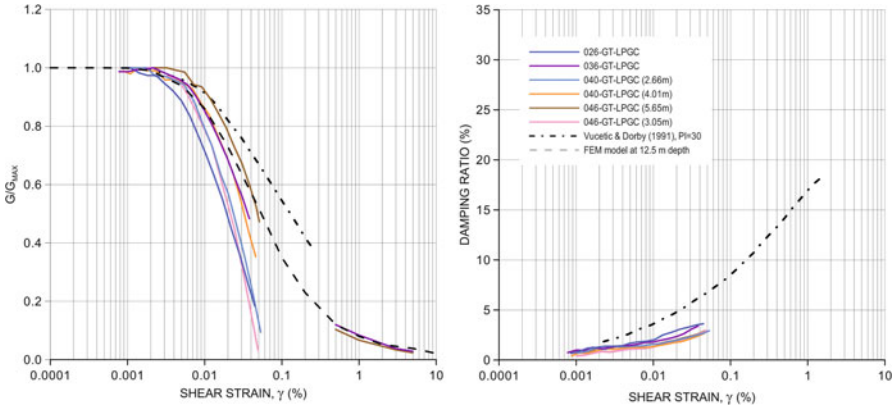

Fig. 14.4 Shear modulus and damping curves versus shear strain as result of some of the advanced laboratory tests (Resonant Column and strain-controlled CSS). Modulus reduction curve adopted in the model at 12.5 m depth is shown as an example

modulus at higher strain levels (>0.1 %) were derived from hysteresis loops in strain controlled CSS tests. Figure 14.4 shows laboratory results and reference curves from the literature. There was fairly good correspondence between measured values and results by Vucetic and Dobry (1991). Modulus degradation (G/G_{max}) was more severe for the tested samples than the published results; this is primarily attributed to the very low confining stress levels used in testing.

14.3 Stability Analyses

Stability analyses were conducted for static (pre- and post-earthquake) and seismic loading conditions, with both conventional and advanced approaches. Relevant results described in this section are primarily focused on comparison between the pseudo-static and advanced dynamic approaches.

The results presented refer to a specific section located in the northern flank of the canyon. This section was considered the most critical along the scarp, because it presents gradients exceeding 30° and poor geomechanical properties. The upper part of the section descends a steep slope, and seismic reflections from sub-bottom profiles appear to be generally parallel and unbroken. The stratigraphy consists of a thin superficial layer (0–0.5 m) of hemipelagic deposition that overlies a thick unit of very soft to firm slightly sandy clay. At the base of the slope, a slope failure unit designated as a Mass Transport Deposit (MTD) is observed. It is characterized by chaotic internal reflectors and highly undulating, rough seabed. The MTD comprises very soft to stiff clay and sandy clay.

14.3.1 Conventional Approach

Slope stability was initially evaluated using some of the more common limit equilibrium formulations, all of which are based on the method of slices. Soil was modelled in terms of unit weight and undrained shear strength. Total unit weights range from 16.0 kN/m^3 (0–2 m depth) to 18.0 kN/m^3 (2–13 m) and 19.0 kN/m^3 (below 13 m). Measured undrained shear strength at the mudline is 5 kPa. The strength increase with depth is of the order of 4.5 kPa/m in the first 3 m decreasing to 3.0 kPa/m below. Hydrostatic pore pressure was assumed in the analysis. Static analyses gave satisfactory safety factors (SF > 1.65). The least resistant slip surface was found at a depth of approximately 40 m.

Pseudostatic analyses were performed considering peak ground acceleration (PGA) values derived from a site-specific Probabilistic Seismic Hazard Assessment (PSHA) study considering return periods of 100, 1,000 and 10,000 years. A seismic coefficient of 0.5 was applied consistent with recommendations of EN 1998–5 (2004). The resulting factor of safety resulting from the pseudostatic analyses was marginal (SF $\approx$ 1) for 100 year return period and unsatisfactory (SF < 1) for both 1,000 and 10,000 year return periods. The critical slip surface was found to be approximately 60 m below the mudline.

This location for the critical surface contradicts field evidence. In fact, relatively superficial, probably seismically triggered, slides have been recognized rather than deep-seated failures. Furthermore, the age of the surficial slide is of the order of 1,000 years, significantly older that would be implied by the critical 100 year return period.

Post-earthquake stability assessment was performed using the aforementioned reduced undrained shear strength. Safety factors greater than 1.4 were assessed, indicating low susceptibility to post-earthquake failure.

14.3.2 Dynamic Approach

As an alternative to the pseudostatic approach, the slope response to earthquake loading was evaluated using a 2D dynamic finite element model. The model was implemented using the OpenSees finite element framework (PEER 2010). The soil domain was represented using a PressureIndependMultiYield material model. This is a general constitutive model in which the soil is represented as a nonlinear hysteretic material (Parra 1996; Yang 2000; Yang et al. 2003) with a Von Mises multi-surface (Iwan 1967; Mróz 1967) kinematic plasticity model. Plasticity is exhibited only in the deviatoric stress-strain response. The volumetric stress-strain response is linear-elastic and is independent of the deviatoric response. Plasticity is formulated based on the multi-surface (nested surfaces) concept, with an associative flow rule, according to Prevost (1977). The nonlinear shear stress strain backbone curve is represented by the Kondner hyperbolic model (Kondner 1963). The model

utilized a 9-node quadrilateral plane-strain element. This element is implemented for simulating dynamic response of solid-fluid fully coupled material, based on Biot's theory of porous medium.

The base of the model is a non-reflecting boundary modelled as a Lysmer-Kuhlemeyer (1969) dashpot. This approach simulates an infinite elastic half space, allowing some of the energy imparted by the event to radiate out of the model. To ensure that free-field conditions exist at the vertical boundaries of the model, a significantly more massive column of soil elements was simulated along the two vertical boundaries of the model. When the horizontal excitation is applied to the model, the reaction of these massive columns is equivalent to the free-field response.

The model size was chosen to be sufficiently large to incorporate the steepest portion of the slope and sufficiently deep to reach an average shear wave velocity greater than 300 m/s at the base of the model where input time histories were applied. The final model was 116 to 38 m high and 600 m long. The mesh consisted of 2,380 elements. The maximum size of any element was limited to one-fifth (Kramer 1996) of the shortest wavelength represented in the analysis. The mesh was dimensioned to pass a maximum frequency of 10 Hz.

A suite of seven real earthquake time histories was considered for the dynamic analyses. These accelerograms were recorded on stiff soil conditions, and chosen to match the characteristic magnitude/distance from the deaggregation results from the PSHA. The time histories were scaled to the PGA associated with the three return periods considered (100 year, 1,000 year and 10,000 year).

The dynamic FE model showed that the slope would be stable under the 100 year return period event, but that it would experience some distress for the 1,000 and 10,000 year return period ground motion. For the stronger ground motion a sliding surface develops at a depth of about 7 m (Fig. 14.5). The failed zone is of the order of 100 m long, and the length does not significantly increase for the larger earthquake. The soil in the failure zone develops significant shear strain, ~10 % for the 1,000 year event increasing to 20 % for the 10,000 year earthquake. The interpretation of the results is that at these strain levels failure is expected. The FE results reproduced both the physical size and estimated return periods of the slides observed in the field. Calculated displacements shall be read in terms of qualitative trends rather than quantitative values because strongly dependant on constitutive model assumptions.

14.4 Conclusions

The results obtained from a detailed survey comprising both geophysical and geotechnical data were used to develop an advanced geotechnical FE model using OpenSees. The required input data were gathered from an extensive advanced laboratory program which was used to define soil behavior under cyclic loading. Conventional pseudo-static analysis and advanced numerical modeling were performed for seismic slope stability assessment and then compared.

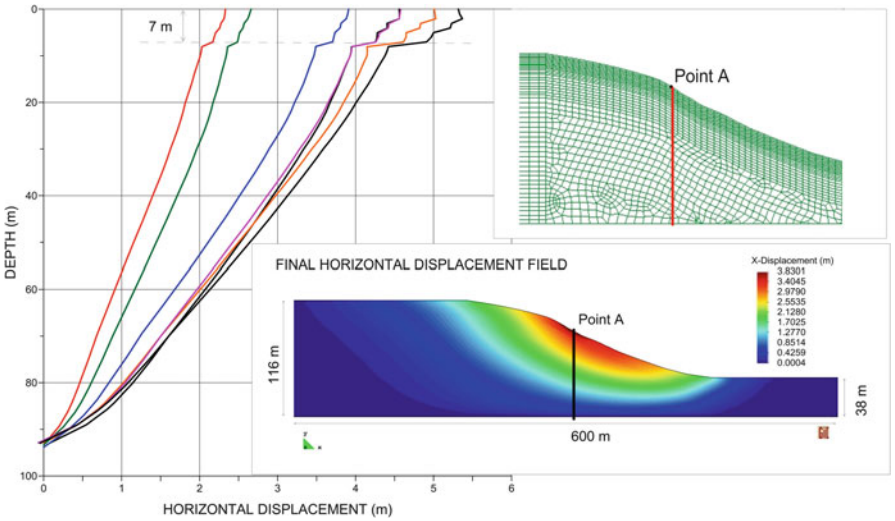

Fig. 14.5 Results of the dynamic FE model for 10,000 year return period. The graph on the *left* shows the horizontal final displacement profile below Point A (see location in *left top*) for the seven considered time histories. *Bottom right picture* shows the final horizontal displacement field (*blue* associated with lowest displacement, *dark red* with highest displacement)

The results of the 2D FE analysis are in good agreement with field observations. Based on the FEM, slopes are considered stable for short return period events (100 year), and in fact, extensive recent run-out sliding is not evident. Moderate to long return period events are expected to cause small (100's of meter size) and shallow slides, such as the three features in the upper canyon. The analysis did not predict massive deep sliding, and in fact no such slides are observed after the major sea level rise that started about 18,000 year BP and triggered worldwide submarine failures (e.g., Tappin 2010; Ducassou et al. 2009).

The FE results also highlight the degree of conservatism in the pseudo-static analysis. The simplified analysis suggested that the stability of the considered slope was marginal for 100 year, while deep failure was predicted for the 1,000 and 10,000 year earthquakes. FE analysis and field observations show the situation is much less severe.

Acknowledgements We would like to thank William J. Johnson and Federico Pisanò for their valuable review and improvement of the manuscript.

References

Andersen KH (2009) Bearing capacity under cyclic loading – offshore, along the coast, and on land. The 21st Bjerrum lecture presented in Oslo, 23 November 2007. Can Geotech J 46:513–535

Biscontin G, Pestana JM (2006) Factors affecting seismic response of submarine slopes. Nat Hazards Earth Syst Sci 6:97–107

Ducassou E, Migeon S, Mulder T, Murat A, Capotondi L, Bernasconi SM, Mascle J (2009) Evolution of the Nile deep-sea turbidite system during the late quaternary: influence of climate change on fan sedimentation. Sedimentology 56:2061–2090. doi:10.1111/j.1365-3091.2009.01070.x

EN 1998–5 (2004) Eurocode 8: design of structures for earthquake resistance – Part 5: foundations, retaining structures and geotechnical aspects. European Committee for Standardization (CEN), Brussels, Belgium

Iwan WD (1967) On a class of models for the yielding behaviour of continuous and composite systems. J Appl Mech ASME 34:612–617

Kondner RL (1963) Hyperbolic stress-strain response: cohesive soils. J Soil Mech Found Div 89(SM1):115–143

Kramer SL (ed) (1996) Geotechnical earthquake engineering. Prentice Hall, Upper Saddle River

Lunne T, Berre T, Andersen KH, Strandvik S, Sjursen M (1997) Sample disturbance effects in soft low plastic Norwegian clay. In: Proceedings of the conference on recent developments in soil and pavement mechanics, Rio de Janeiro, Brazil, 25–27 June 1997

Lysmer J, Kuhlemeyer RL (1969) Finite dynamic model for infinite media. J Eng Mech Div ASCE 95(EM4):859–877

Magagnoli A (2003) "CP-20" Carotiere a pistone per carote di sedimento lunghe fino a venti metri. Rapporto Tecnico n. 83. CNR – ISMAR, Bologna

Mróz Z (1967) On the description of anisotropic work hardening. J Mech Phys Solids 15:163–175

Pacific Earthquake Engineering Research Center (2010) Open system for earthquake engineering simulation (OpenSees). http://opensees.berkeley.edu. Accessed 20 Feb 2010

Parra E (1996) Numerical modelling of liquefaction and lateral ground deformation including cyclic mobility and dilation response in soil systems. PhD thesis, Department of Civil Engineering, Rensselaer Polytechnic Institute, Troy, NY

Prevost JH (1977) Mathematical modelling of monotonic and cyclic undrained clay behaviour. Int J Numer Anal Methods Geomech 1:195–216

Tappin DR (2010) Submarine mass failures as tsunami sources: their climate control. Philos Trans R Soc A 368:2417–2434. doi:10.1098/rsta.2010.0079

Vucetic M, Dobry R (1991) Effect of soil plasticity on cyclic response. J Geotech Eng 117(1):89–107

Yang Z (2000) Numerical modelling of earthquake site response including dilation and liquefaction. PhD thesis, Department of Civil Engineering and Engineering Mechanics, Columbia University, New York

Yang Z, Elgamal A, Parra E (2003) Computational model for cyclic mobility and associated shear deformation. J Geotech Geoenviron Eng 129(12):1119–1127

Chapter 15
Size-Frequency Relationship of Submarine Landslides at Convergent Plate Margins: Implications for Hazard and Risk Assessment

Jan H. Behrmann, David Völker, Jacob Geersen, Rieka Harders, and Wilhelm Weinrebe

Abstract We use complete inventories of submarine landslides from the Middle America (MA) and the Central Chile (CC) trench and forearc systems to analyze the size-frequency relationship of such structures on active continental slopes. The MA forearc is characterized by subduction erosion, and the CC forearc has had an accretionary tectonic history since the Late Neogene. Both are end-member types of convergent margins around the world. Both margin segments have been mapped by high-resolution swath bathymetry at strike lengths of about 1,300 km (MA) and 1,000 km (CC). The Middle America forearc has 143 discernible slides with sizes ranging from 0.38 to 1,426 km^2. Offshore Central Chile, the 62 mapped slides are 0.9–1,285 km^2 in size. Slide localization is markedly different at both margin types. While they also vary strongly along strike of the individual margin, depending on forearc slope gradient, kinematic coupling between plates, or topographic structure of the downgoing plate, the size-frequency relationships are remarkably similar. This allows quantification of the incidence of a submarine slide of given size per margin segment. The relationships hold for slide sizes from 10 to 1,000 km^2, with the cut-off defined by slide size (smaller slides) and sample size (larger slides). As slide traces of 100–300 km^2 size are obliterated by tectonic deformation after about 200,000 years, recurrence rates for slides of a given size can be estimated. This offers a chance to assess hazard and risk resulting from such events. It is suggested that it takes 20 to 200 plate boundary earthquakes to set off a medium-sized (>10 km^2) or larger slump or slide.

J.H. Behrmann (✉) • D. Völker • R. Harders • W. Weinrebe
GEOMAR, Helmholtz Centre for Ocean Research Kiel, Wischhofstr. 1-3, 24148 Kiel, Germany
e-mail: jbehrmann@geomar.de

J. Geersen
National Oceanography Centre Southampton, University of Southampton, Waterfront Campus, European Way, Southampton SO14 3ZH, UK

S. Krastel et al. (eds.), *Submarine Mass Movements and Their Consequences*, Advances in Natural and Technological Hazards Research 37, DOI 10.1007/978-3-319-00972-8_15,

Keywords Convergent plate boundary • Tectonics • Erosion • Accretion • Submarine landslide • Chile • Central America

15.1 Introduction

Submarine slides scar the continental slopes worldwide (e.g. Summerhayes et al. 1979). While such mass wasting structures of all sizes have been well documented for many passive continental margins (e.g. Lee 2008; Tripsanas et al. 2004), the exploration of active continental margins for such structures has proved difficult, mainly for two reasons. First, the forearc relief is to a large extent shaped by tectonic deformation, and by a variety of surface processes that work against accumulation of unstable sedimentary piles over long stretches of time. Deformation creates hummocky terrain, characterized by fold structures and thrust ridges. Also, vigorous oversteepening by subduction erosion, and rapid sediment loading on the continental shelf edges and upper slopes tend to define an environment of downslope transport in erosional gullies and/or submarine canyons. The second reason is that large, coherent bathymetric surveys of active continental margins have only recently become available. In this paper, we present and discuss the results of two large-scale surveys of submarine slumps and slides along the Middle America (MA) and Central Chile (CC) forearcs, derived from high-resolution bathymetric mapping (Harders et al. 2011; Völker et al. 2012). The strike lengths of the surveyed areas are 1,300 km (MA) and 1,000 km (CC), respectively. The forearc areas are completely covered. This allows quantitative assessment of numbers and sizes of structures, and can answer the question whether there is a size-frequency relationship for the slumps and slides, akin to that established for earthquakes (e.g. Rundle 1989). With the data available we also discuss the question how long it takes forearc deformation processes to obliterate the traces of a slide of given size. This way it becomes possible in principle to make estimates about recurrence times of slumping and sliding on a margin of a given strike length.

15.2 Tectonic Setting of the MA and CC Convergent Margins

The evolution of the MA forearc between the Panama-Costa Rica border and the Guatemala-Mexico border (between 8° N and 14° N) has been dominated by subduction erosion at least since the Neogene (e.g. von Huene et al. 2000). The Cocos Plate is subducted beneath the Caribbean Plate at a rate of 85 mm/a (DeMets 2001) in a direction slightly oblique to the NW-SE striking margin since the Late Oligocene/Early Miocene (Kimura et al. 1997). The most obvious feature (see e.g. Harders et al. 2011) is a well-defined and narrow deep-sea trench. The geomorphic expression of the downgoing Cocos Plate is strongly variable along strike, reflecting different processes of plate construction and alteration (e.g. Werner et al. 1999;

Barckhausen et al. 2001). Forearc morphology and the width of the shelf vary greatly along the margin, paralleling the changes in crustal structure and relief of the downgoing plate (e.g. Harders et al. 2012). There is rugged topography landward of the Cocos Ridge and the oceanic plate segment with numerous seamounts immediately to the NW. Offshore Nicoya Peninsula and Nicaragua the more subdued relief of the downgoing oceanic plate faces a continental margin with a less irregular morphology and a well developed canyon system on the middle and upper slopes. Offshore Central Chile the N-S striking forearc between 32° S and 42° S has recorded an important episode of frontal accretion at least since the Late Neogene, after a long history of subduction erosion (e.g. Kukowski and Oncken 2006). The present subduction rate of the Nazca Plate is around 66 mm/a, slightly dextrally oblique with an azimuth of about 80° (Angermann et al. 1999). The age of the subducting Nazca Plate increases northward from the Chile Triple Junction (e.g. Behrmann et al. 1994) to about 35 Ma around 32° S, where the Juan Fernandez Ridge, a shallow ENE-WSW trending rise with a series of seamount groups, enters the marine forearc (Tebbens and Cande 1997). Where it approaches the Chile Trench the elevated rise forms a barrier for trench parallel sediment transport from the south. In the area between 32° S and 42° S the Chile trench is filled with about 1.5–2 km of sediment (Völker et al. 2006), and submarine canyons operate as major sediment pathways. The tectonic processes that constrain the morphology and structure of the overriding South American Plate vary strongly from north to south, and also show distinct across-slope segmentation (Geersen et al. 2011a). From the trench to about 2,500 m water depth, the CC forearc is an active accretionary prism, dominated by a sequence of landward dipping thrust sheet packages (Bangs and Cande 1997; Geersen et al. 2011a). Further landward there is a Mesozoic paleo-accretionary prism with much smoother bathymetric expression, mainly due to a cover of 0.5–2 km of slope and shelf sediments, followed by continental metamorphic basement (e.g. Bangs and Cande 1997; Contreras-Reyes et al. 2010) closer to the coastline. Active faulting in the latter domains is restricted, including out-of-sequence thrusting, but also normal faulting in response to forearc uplift and collapse (Geersen et al. 2011a).

15.3 MA and CC Slumps and Slides: Observations and Data

Altogether 143 submarine mass wasting structures along the Central America forearc were detected and mapped by Harders et al. (2011). Sizes and coordinates of the structures are given in Table 15.1. The largest one is the Nicoya Slump offshore Nicoya Peninsula (Fig. 15.1a). It covers a total area of 1,425 km^2, and is one the most extensive areas of submarine mass wasting on any active margin on Earth. It affects the whole forearc down to the plate boundary (von Huene et al. 2004).

Other spectacular very large rotational slumps (see e.g. Mulder and Cochonat 1996 for issues of nomenclature) are the Jaco and Parrita structures (Fig. 15.1a, b), each about 120 km^2 in size. Both are retrogressive, cohesive failures of the whole

Table 15.1 Inventory of slumps and slides on the MA forearc. Evaluation of maps published by Harders et al. (2011) Given are centroid locations and sizes in km^2. Slide numbers refer to the original data inventory by Rieka Harders

Slide	N Lat (°)	W Long (°)	size	Slide	N Lat (°)	W Long (°)	size	Slide	N Lat (°)	W Long (°)	size
#	Centroid	Centroid	km^2	#	Centroid	Centroid	km^2	#	Centroid	Centroid	km^2
10	13.621	−92.722	2.091	319	12.059	−88.933	1.514	590	9.989	−86.139	4.367
5	13.576	−92.160	10.024	320	11.945	−88.738	32.992	610	9.814	−86.028	34.301
16	13.382	−92.410	6.579	330	11.932	−88.921	4.817	630	9.562	−85.950	43.504
17	13.156	−91.966	15.053	335	12.374	−88.943	3.617	680	9.534	−85.805	11.266
18	13.420	−92.464	6.069	336	12.440	−89.087	6.382	690	9.556	−85.804	4.908
20	13.604	−92.634	68.003	338	12.172	−88.638	3.035	670	9.571	−85.750	67.81
30	13.588	−92.532	4.354	339	12.262	−88.838	2.428	700	9.544	−85.702	12.571
33	12.740	−91.062	4.284	340	12.479	−89.238	0.776	710	9.578	−85.682	28.251
34	12.766	−91.124	3.405	341	12.414	−89.183	4.422	720	9.641	−85.645	43.635
35	13.290	−91.344	12.821	342	12.434	−89.202	6.246	760	9.527	−85.662	37.485
36	13.296	−91.301	6.071	343	12.348	−89.048	1.223	750	9.576	−85.613	8.971
37	13.270	−91.279	9.067	344	12.366	−89.104	1.361	740	9.615	−85.577	17.211
38	13.266	−91.258	10.228	347	12.372	−89.063	7.357	730	9.657	−85.543	21.165
40	13.513	−92.485	35.551	350	12.422	−89.134	4.618	780	9.569	−85.580	5.173
61	13.422	−92.383	3.187	351	12.405	−89.128	0.765	785	9.429	−85.524	283.461
63	13.187	−91.595	8.381	352	12.203	−88.732	0.272	770	9.557	−85.588	1.708
64	13.178	−91.478	13.574	353	11.887	−88.821	16.046	650	9.306	−85.807	59.073
65	13.043	−91.390	3.965	360	12.442	−89.060	1.738	820	9.384	−85.108	62.544
66	13.031	−91.400	3.674	370	12.341	−89.012	9.406	660	9.212	−85.581	1, 425.89
68	13.083	−91.439	8.665	378	12.001	−87.794	1.833	790	9.294	−85.503	5.541
69	13.008	−91.447	6.409	380	12.349	−88.900	1.437	800	9.242	−85.394	5.374
75	13.551	−92.331	12.881	390	11.637	−87.821	8.276	830	9.353	−84.886	21.087
80	13.516	−92.210	8.229	400	11.486	−87.807	8.513	840	9.051	−84.869	115.574
100	13.281	−91.899	38.715	401	11.477	−87.671	27.713	850	8.975	−84.932	11.753
114	12.636	−90.749	15.707	402	11.440	−87.632	29.071	860	8.895	−84.664	119.167

120	13.285	−91.778	93.348	403	11.371	−87.652	22.696	880	9.201	−84.732	0.891
130	13.048	−91.294	38.423	413	11.284	−87.681	10.412	890	9.194	−84.665	3.491
140	12.826	−91.020	53.258	415	11.248	−87.514	26.698	900	9.194	−84.626	4.794
150	12.830	−90.917	47.671	420	11.266	−87.449	5.581	870	9.201	−84.742	0.381
155	13.047	−90.618	25.559	430	11.218	−87.410	78.467	910	9.031	−84.551	10.792
160	12.795	−90.515	3.554	425	11.129	−87.513	6.209	970	8.709	−84.431	55.341
165	13.100	−90.672	61.718	440	11.218	−87.317	81.908	940	8.830	−84.236	33.557
170	12.726	−90.489	38.001	450	11.152	−87.300	6.589	961	8.801	−84.216	6.459
222	12.591	−90.623	15.04	460	11.091	−87.249	74.713	920	8.994	−84.549	0.923
230	12.700	−90.329	6.509	480	10.910	−87.197	53.197	941	8.831	−84.233	16.756
240	12.697	−90.431	8.539	510	10.858	−87.086	9.991	960	8.796	−84.227	12.116
250	12.661	−90.343	1.966	500	10.731	−86.882	4.809	961	8.801	−84.216	6.459
260	12.620	−90.339	2.311	520	10.484	−86.719	333.129	980	8.663	−84.306	1.545
285	12.387	−90.138	15.539	531	10.513	−86.529	2.667	990	8.493	−84.103	0.565
287	12.303	−89.941	13.623	534	10.449	−86.399	1.138	1000	8.403	−83.945	21.611
300	12.322	−89.778	2.215	532	10.417	−86.367	3.664	1035	8.401	−83.891	12.682
311	12.335	−89.765	1.172	530	10.140	−86.564	27.219	1010	8.375	−83.864	4.503
312	12.159	−89.204	1.751	540	10.109	−86.532	13.568	1020	8.385	−83.834	4.612
313	12.290	−89.515	1.925	550	10.181	−86.319	13.976	1030	8.320	−83.658	34.438
314	12.305	−89.524	2.063	570	10.154	−86.284	7.681	1050	8.359	−83.612	35.273
315	12.436	−89.437	2.071	560	10.148	−86.274	6.132	1060	8.349	−83.562	30.824
317	12.368	−89.300	1.678	565	10.121	−86.251	20.889	1070	8.294	−83.530	7.596
318	12.290	−89.141	0.668	580	10.138	−86.266	4.994				

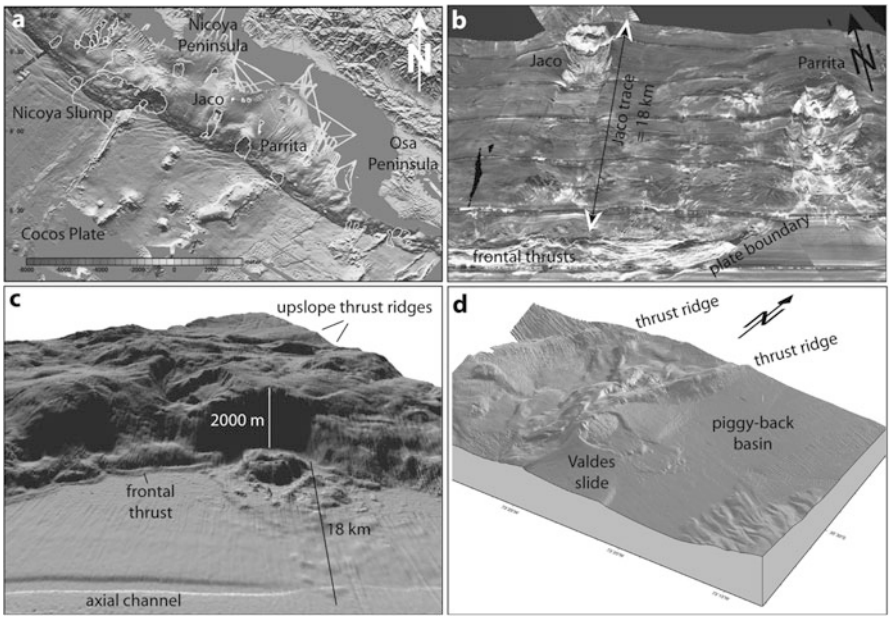

Fig. 15.1 Bathymetric maps showing examples of slumps and slides of the MA (**a**, **b**) and CC (**c**, **d**) forearcs. (**a**). The MA margin offshore the Nicoya and Osa peninsulas (**b**) oblique view from SSW showing the Jaco and Parrita structures. Bathymetric image with superimposed sidescan sonar image (after Harders et al. 2011) (**c**) Reloca slide (Völker et al. 2009). Oblique view from WNW. Note burial of the axial channel of the Chile trench by slide products. (**d**) Valdes Slide (Anasetti et al. 2010), located on the landward side of an active thrust ridge. Oblique view from SE

continental slope that developed behind subducting seamounts (Harders et al. 2011). Given the plate convergence rate (85 mm/a) and the downslope preserved length of the Jaco slump structure (about 18 km; Fig. 15.1b) it can be inferred that it takes about 200,000 years for such a slump to be obliterated by deformation and depositional processes in the forearc. While the very large slumps are rotational, a large number of the medium-sized to large (10–100 km^2) and small (<10 km^2) mass wasting structures have translational geometries. These are not related to mechanical obstacles ploughing into the overriding plate, but are caused by extensive failure of oversteepened forearc slope. The slope and strata-parallel attitude of translational slides suggests preconditioning by weak layers (Harders et al. 2010).

The regional overview picture for MA forearc slumps and slides is as follows (Fig. 15.2a). Offshore Guatemala, between 93° W and 90° W numbers of slides vary between 10 and 19 per degree western longitude, and sizes are small to intermediate, with averages around 20 km^2. Here, relatively smooth oceanic crust of the Cocos Plate is subducted (Fig. 15.2a), failures mostly occur where the slope is undercut and steepened by active normal faulting. The segment between 90° W and 88° W (the El Salvador Segment of Harders et al. 2011) has numerous (10–20 per degree longitude) small slides with average sizes of 3.48 km^2 and 7.25 km^2, respectively.

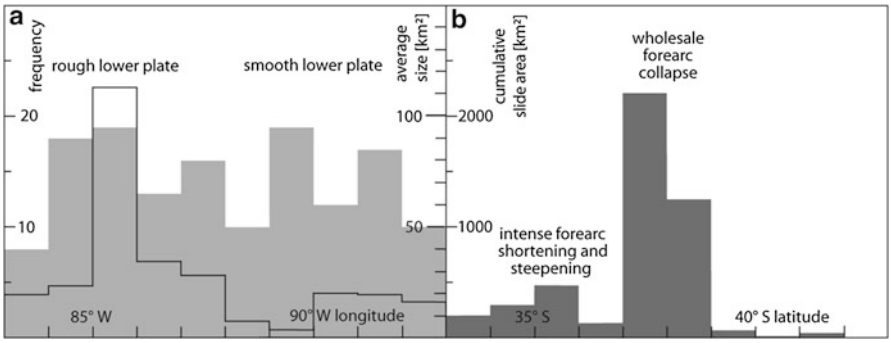

Fig. 15.2 (**a**) slide frequency (*grey histogram*) and average size along the MA forearc between 83° W (Costa Rica) and 93° W (Guatemala). (**b**) cumulative slide area plotted against southern latitude for the CC forearc

These mainly result from sidewall collapse of erosional gullies on the upper slope. East of 88° W slides are more numerous again and average size is medium-sized to large (18.93–34.18 km^2), mainly owing to the subduction of numerous seamounts and ridges. The single maximum in average size (112.92 km^2) is clearly due to the Nicoya Slump (see Fig. 15.2a).

On the CC forearc three groups of mass wasting structures were identified by Völker et al. (2012) in their survey of 62 slumps and slides between 32° and 42° S, mainly on grounds of their geographical and tectonic setting along the margin. The database can be found as an electronic supplement to Völker et al. (2012). The three groups differ in size to some extent, and have distinct failure geometries. The first group comprises relatively small translational slides related to canyon wall collapse. This phenomenon is widespread north of 37° S, where 40–60 % of the canyon walls have collapsed. Canyons south of 37° S show few canyon wall collapses and related translational slides (<10 % of affected canyon walls). This variability, as discussed by Völker et al. (2012), may be explained either by (1) absence or presence of weak sediment layers (e.g. volcanic ashes), (2) differences in the activity and geometry of the canyon systems due to tectonic deformation (bends undercutting canyon walls controlled by active thrust ridges), or (3) latitudinal shifts in sediment composition and deposition rate. The second group are collapses of steep parts of the lower continental slope. Six slides with sizes between 15 and 217 km^2 are preserved in water depths between 2,100 and 5,000 m, and two smaller slides lie on the flanks of sediment thrust ridges at the deformation front of the subduction zone (Völker et al. 2012). In this category, the Reloca Slide (Fig. 15.1c) is the most noticeable because of its size and volume (Völker et al. 2009), and because the displaced rocks are preserved as prominent features in the Chile Trench. The lower continental slope is steep (20–30°). The slide has an arcuate headscarp at about 2,900–3,000 m water depth, and a steep and straight slide ramp of 2,000 m elevation. Three major displaced blocks rise some 100 m above the trench floor, and are surrounded by about 25 smaller blocks (Fig. 15.1c). The debris field has a run-out distance of 18 km

and partly buries the axial channel of the Chile Trench, attesting to a Holocene age of the slide. The third group are supergiant failures of the whole continental slope (Geersen et al. 2011b). Offshore Arauco Peninsula. Three very large slope indentations with areas of 1,285, 924 and 1,145 km^2, shape the continental slope down from to shelf edge to the abyssal plain, and slide products change the seismic reflection pattern of the sedimentary trench fill (Geersen et al. 2011b). The failure structures are evident as elongate embayments with steep, up to 500 m high lateral and headwalls and chaotic seafloor morphology in the centers. The morphological differences between failed and unfailed slope suggests that 300–500 km^3 per slide have been involved in each failure. The regional overview of slump and slide areas (Fig. 15.2b) shows that the margin segment between 33° S and 37° is affected by intense mass wasting (125–477 km^2 per degree southern latitude). The very large figures between 37° S and 39° S relate to the three giant slides mentioned above. Further south, slumping and sliding is insignificant. In contrast to the MA forearc, where localization of mass wasting structures is mainly related to the structure of the downgoing plate (Harders et al. 2012) slide localization on the CC forearc is constrained by the action of intense frontal and mid-slope deformation between 33° S and 37° S in a region of high kinematic and frictional coupling between the converging plates (see Geersen et al. 2011a). Apart from Reloca Slide, a spectacular illustration of this fact is provided by the translational Valdes Slide (Fig. 15.1d; see also Anasetti et al. 2010), located on the eastern flank of an active thrust ridge, and moving material landward. Material underplating and resulting uplift caused wholesale slope collapse on the overriding plate between 37° S and 39° S, a situation unique to the CC forearc.

15.4 Size-Frequency Relationships

The database of Völker et al. (2012) for the CC forearc and that in Table 15.1 for the MA forearc can be used to investigate size-frequency relationships of the slumps and slides. The logarithmic plots in Fig. 15.3 show that both margins have very few supergiant structures (area >1,000 km^2), and the normalized incidence is less than one per 1,000 km of margin for the MA forearc, and two for the CC forearc. Numbers of very large (area >100 km^2) structures are almost similar, and constrain an incidence of about four per 1,000 km of margin. Small, and medium-sized to large (10–100 km^2) slides are almost twice as frequent on the MA forearc if compared with the CC forearc. Incidences are about 40 % higher (Fig. 15.3b), probably reflecting the more irregular topography of the downgoing plate. For the MA forearc this means that a slide at least of small (i.e. >3 km^2) size occurs every 12 km along the strike of the margin. For the Chile forearc this number is about 20 km. Only few very small slides have been identified in both studies (Harders et al. 2011; Völker et al. 2012). This may be because structures of less than 3 km^2 are in danger of being overlooked even in high-resolution bathymetric surveys, despite of a $<100 \times 100$ m footprint of modern multibeam echosounders. Likely causes are

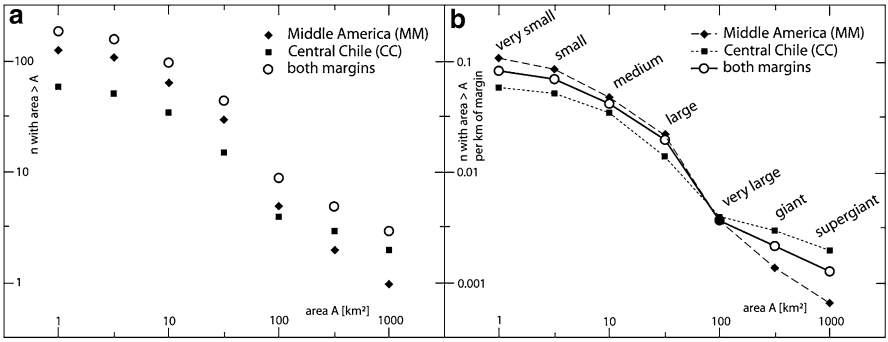

Fig. 15.3 Logarithmic plots showing frequency-size relationships. (**a**) area vs. number, (**b**) area vs. slide incidence per km of margin

low headwall and sidewall heights, relief deterioration by small-scale downslope mass transport, and the generally low modification small slides impose on overall forearc topography.

15.5 Discussion and Conclusion

Figure 15.3 shows a very rough power law relationship between sizes and frequencies of submarine mass wasting structures in the two data sets, at least for the size interval between 10 and 1,000 km^2. Fully quantitative evaluation akin to that relating to instrumental seismicity (e.g. Rundle 1989) should be treated with caution at this stage, because of the relatively small data set from a limited sample of margins. From the incidence data (Fig. 15.3b) it is apparent, however, that very large to supergiant slides (>100 km^2) occur every 250 km along strike of a convergent margin (incidence is 0.004 per 1,000 km). If we suppose that the traces of structures of very large or greater size can become obliterated after approximately 200,000 years, like in the example of Jaco Scar (Fig. 15.1b; slide # 840, 115 km^2 in Table 15.1), then one mass movement event of this size would have to occur along 1,000 km of margin within this time frame. A similar recurrence interval is also suggested by the age estimates for the CC margin giant and supergiant slides, which occurred roughly every 200,000 years over the last 0.6 Ma (Geersen et al. 2011b). This interpretation is contingent on the assumption that submarine mass wasting is a steady surface process at convergent margins. Coulomb wedge theory (e.g. Davis et al. 1983), which predicts that forearc wedges of critical slope angle are on the verge of failure throughout, including the possibility of slope destabilization, supports this assumption. Slides down to medium size (>10 km^2) have an average incidence roughly ten times higher (0.042; Fig. 15.3b). Thus, the recurrence interval of medium-sized or larger slides could be around 20,000 years. This means that major slumps and slides are rare events at convergent margins, although they can

be enormous in size and very hazardous. Any systematic causal relationship with plate boundary earthquakes, however, would be at best tentative. Given the length of interseismic cycles (100–1,000 years) for individual seismotectonic segments of active plate boundaries, only one out of 20–200 plate boundary earthquakes may set off a medium-sized or larger slide. This highlights the fact that the tsunami hazard and risk at convergent margins is mainly constrained by seismic events, and only to a second degree by earthquake-related slope instability.

Acknowledgements We are grateful for the reviews of this manuscript by Yuzuru Yamamoto and Achim Kopf, which helped to improve the original manuscript.

References

Anasetti A, Krastel S, Weinrebe W et al (2010) Detailed analysis of the Valdes Slide: a landward facing slope failure off Chile. Abstract EGU2010-13497, 2010 General Assembly of the EGU, Vienna, 2–7 May 2010

Angermann D, Klotz J, Reigber C (1999) Space-geodetic estimation of the Nazca-South America Euler vector. Earth Planet Sci Lett 171:329–334. doi:10.1016/S0012-821X(99)00173-9

Bangs NL, Cande SC (1997) Episodic development of a convergent margin inferred from structures and processes along the southern Chile margin. Tectonics 16:489–503. doi:10.1029/97TC00494

Barckhausen U, Ranero CR, von Huene R et al (2001) Revised tectonic boundaries in the Cocos Plate off Costa Rica: implications for the segmentation of the convergent margin and for plate tectonic models. J Geophys Res 106:19207–19220

Behrmann JH, Lewis SD, Cande S et al (1994) Tectonics and geology of spreading ridge subduction at the Chile Triple Junction; a synthesis of results from Leg 141 of the Ocean Drilling Program. Geol Rundsch 83:832–852

Contreras-Reyes E, Flueh ER, Grevemeyer I (2010) Tectonic control on sediment accretion and subduction off south central Chile: Implications for coseismic rupture processes of the 1960 and 2010 megathrust earthquakes. Tectonics 29:TC6018. doi:10.1029/2010TC002734

Davis D, Suppe J, Dahlen FA (1983) Mechanics of fold-and-thrust belts and accretionary wedges. J Geophys Res 88(B2):1153–1172

DeMets C (2001) A new estimate for present-day Cocos-Caribbean plate motion: implications for slip along the Central America volcanic arc. Geophys Res Lett 28:4043–4046

Geersen J, Behrmann JH, Völker D et al (2011a) Active tectonics of the South Chilean marine fore arc (35° S–40° S). Tectonics 30:TC3006

Geersen J, Voelker D, Behrmann JH et al (2011b) Pleistocene giant slope failures offshore Arauco Peninsula, Southern Chile. J Geol Soc 168:1237–1248

Harders R, Kutterolf S, Hensen C et al (2010) Tephra layers: a controlling factor on submarine translational sliding? Geochem Geophys Geosyst 12:Q05S23. doi:10.1029/2009GC002844

Harders R, Ranero CR, Weinrebe W et al (2011) Submarine slope failures along the convergent continental margin of the Middle America Trench. Geochem Geophys Geosyst 12:Q05S32. doi:10.1029/2010GC003401

Harders R, Ranero CR, Weinrebe W et al (2012) An overview of the role of long-term tectonics and incoming plate structure on segmentation of submarine mass wasting phenomena along the Middle America Trench. In: Yamada Y, Kawamura K, Ikehara K (eds) Submarine mass movements and their consequences. Springer, Dordrecht/Heidelberg/London/New York, pp 391–402. doi:10.1007/978-94-007-2162-1

Kimura G, Silver E, Blum P et al (1997) Proceedings of the ocean drilling program, Initial reports, 170. Ocean Drilling Program, College Station, 458 pp

Kukowski N, Oncken O (2006) Subduction erosion – the "normal" mode of fore-arc material transfer along the Chilean Margin? In: Oncken O, Chong G, Franz G et al (eds) The Andes – active subduction orogeny. Springer, Berlin, pp 217–236

Lee HJ (2008) Timing of occurrence of large submarine landslides on the Atlantic ocean margin. Mar Geol. doi:10.1016/j.margeo.2008.09.009

Mulder T, Cochonat P (1996) Classification of offshore mass movements. J Sediment Res 66:43–57

Rundle JB (1989) Derivation of the complete Gutenberg-Richter magnitude-frequency relation using the principle of scale invariance. J Geophys Res 94:12337–12342

Summerhayes C, Borold B, Embley R (1979) Surficial slides and slumps on the continental slope and rise of South West Africa: a reconnaissance study. Mar Geol 31:265–277

Tebbens SF, Cande SC (1997) Southeast Pacific tectonic evolution from early Oligocene to present. J Geophys Res 102:12061–12084. doi:10.1029/96jb02582

Tripsanas EK, Bryant WR, Doyle EH (2004) Slope-instability processes caused by salt movements in a complex deep-water environment, Bryant Canyon area, northwest Gulf of Mexico. AAPG Bull 88:801–823

Völker D, Wiedicke M, Ladage S et al (2006) Latitudinal variation in sedimentary processes in the Peru-Chile Trench off Central Chile. In: Oncken O, Chong G, Franz G et al (eds) The Andes – active subduction orogeny. Springer, Berlin, pp 193–216

Völker D, Weinrebe W, Behrmann JH et al (2009) Mass wasting at the base of the south central Chilean continental margin: the Reloca Slide. Adv Geosci 22:155–167

Völker D, Geersen J, Behrmann JH et al (2012) Submarine mass wasting off Southern Central Chile: distribution and possible mechanisms of slope failure at an active continental margin. In: Yamada Y, Kawamura K, Ikehara K, Ogawa Y, Urgeles R, Mosher D, Chaytor J, Strasser M (eds) Submarine mass movements and their consequences. Springer, Dordrecht/Heidelberg/London/New York, pp 379–389. doi:10.1007/978-94-007-2162-3_34

von Huene R, Ranero CR, Weinrebe W (2000) Quaternary convergent margin tectonics of Costa Rica, segmentation of the Cocos Plate, and Central American volcanism. Tectonics 19:314–334

von Huene R, Ranero CR, Watts P (2004) Tsunamigenic slope failure along the Middle America Trench in two tectonic settings. Mar Geol 203:303–317. doi:10.1016/S0025-3227(03)00312-8

Werner R, Hoernle K, van den Bogaard P et al (1999) Drowned 14 m.y. old Galapagos archipelago off the coast of Costa Rica: Implications for tectonic evolutionary models. Geology 27:499–502

Chapter 16
A Numerical Investigation of Sediment Destructuring as a Potential Globally Widespread Trigger for Large Submarine Landslides on Low Gradients

Morelia Urlaub, Peter Talling, and Antonis Zervos

Abstract Submarine landslides on open continental slopes can be far larger than any slope failure on land and occur in locations worldwide on gradients of <2°. Significantly elevated pore pressure is necessary to overcome the sediment's shearing resistance on such remarkably low gradients, but the processes causing such overpressure generation are contentious, especially in areas with slow sedimentation rates. Here we propose that the progressive loss of interparticle bonding and fabric could cause such high excess pore pressure. Slow sedimentation may favour the formation of a structural framework in the sediment that is load-bearing until yield stress is reached. The bonds then break down, causing an abrupt porosity decrease and consequently overpressure as pore fluid cannot escape sufficiently rapidly. To test this hypothesis, we implement such a loss of structure into a 2D fully coupled stress-fluid flow Finite Element model of a submerged low angle slope, and simulate consolidation due to slow sedimentation. The results suggest that destructuring could indeed be a critical process for submarine slope stability.

M. Urlaub (✉)
Dynamics of the Ocean Floor, GEOMAR Helmholtz Centre for Ocean Research Kiel, Wischhofstr. 1-3, 24148 Kiel, Germany
e-mail: murlaub@geomar.de

P. Talling
Marine Geosciences, National Oceanography Centre Southampton, University of Southampton Waterfront Campus, European Way, Southampton SO14 3ZH, United Kingdom

A. Zervos
Engineering and the Environment, University of Southampton, Southampton, UK

S. Krastel et al. (eds.), *Submarine Mass Movements and Their Consequences*, Advances in Natural and Technological Hazards Research 37, DOI 10.1007/978-3-319-00972-8_16,

16.1 Introduction

Submarine landslides are one of the main processes for moving sediment in the ocean, and in some cases there is strong evidence that they have generated far travelled tsunamis (Masson et al. 2006). Submarine landslides can contain >1,000 km^3 of sediment and be two orders of magnitude larger than the biggest terrestrial slides. The largest of these landslides occur on open continental slopes at passive margins, and as the tsunamigenic potential of a submarine landslide scales up with the volume of displaced material, these landslides are of specific socioeconomic interest. In order to enable a thorough evaluation of the geohazard of a particular region, as well as for potential mitigation efforts, there is a need to understand what causes these large landslides. However, the inability to observe submarine landslides directly makes them more difficult to analyse than many other geohazards. Our understanding of what causes these landslides is limited to hypotheses that are difficult to test rigorously and involve large uncertainties.

The largest open continental slope landslides tend to occur on extremely shallow slope angles of 2° or less. They also have similar headwall heights of about 100–250 m (Hühnerbach et al. 2004; Twichell et al. 2009), and occur as translational slab slides along bedding parallel glide planes (Masson et al. 2006). The morphological similarity among these large landslides, albeit being located in very different depositional environments, is striking and suggests a common trigger mechanism.

Mechanically, failure of such shallow slopes can only be explained by pore pressures that greatly exceed hydrostatic pressures, and thereby decrease the sediment's shearing resistance. However, the potential excess hydrostatic pressure sources that are discussed in the literature are often not capable of explaining the observed landslides. The dissociation of gas hydrates for example may act at the upper end of the gas hydrate stability zone (<600 m water depth). However, headwall depths of landslides at low gradient slopes cluster at 1,800–2,500 m water depth, and some headwalls occur down to 3,600 m water depth (Hühnerbach et al. 2004; Twichell et al. 2009). Gas hydrates are stable at these deeper water depths, suggesting that at least some large landslides are not triggered by hydrate dissociation. In the Gulf of Mexico high excess pore pressures (up to 70 % of the vertical effective stress in hydrostatic conditions) could be attributed to the rapid burial of low permeable sediment at deposition rates >30 m/ky (Dugan and Flemings 2000; Flemings et al. 2008). It is, however, difficult to generate such high overpressures, or to drive fluid laterally, in areas of slow sedimentation (<1 m/ky) such as north-west Africa, south-east Australia, or parts of the US east coast (Urlaub et al. 2012). Di Prisco et al. (1995) showed that even minor earthquakes can potentially cause failure of shallow (<20 m) submerged slopes, although some recent very large earthquakes have caused few submarine slope failures (Sumner et al. 2013). Nevertheless, deep-seated failures require significantly stronger ground acceleration due to higher effective

stresses at large sediment depths (Di Prisco et al. 1995). It is therefore more likely that the excess pore pressure provided by an earthquake acts as a final trigger on a slope that already is in an overpressured state. But what other general mechanism that is independent of burial rates, and that could be global rather than local, could cause excess pore pressure at depths corresponding to those of failure planes of large volume landslides?

16.1.1 Destructuring of Cemented Hemipelagic Clay as a Source of Overpressure

Sediment cores from passive continental slopes often contain hemipelagic clay intervals with 70–85 % calcium carbonate content. Visual observations, for example from the north-west African continental slope, show that the calcareous hemipelagic clay is often very stiff and has a comparatively high porosity at 5–6 m below seafloor (Masson, personal communication). This same stiff clay layer is remarkably uniform over hundreds of kilometres and a large range of water depths, and it is conceivable that those layers could form regionally extensive failure planes.

The stiffness of hemipelagic sediment is likely a result of early cementation that takes place during deposition and before the skeleton has the opportunity to readjust to the new, leaving a particularly open structure and high porosity. Post-depositional processes such as bioturbation, interaction of organic matter, electrostatic bonding or creep may also contribute to the formation and preservation of such an open structure (Locat et al. 2003). There is, however, a critical depth at which the vertical stress would be equal to the resistance of the bonding strength generated by cementation (Skempton and Northey 1952). If loaded further the bonds are liable to break leading to a progressive degradation of the open structure ('destructuring'). This comparatively rapid collapse of pore space, along with corresponding reduction in permeability causes overpressure as the excess pore fluid cannot dissipate.

The structural resistance provided by the cement is highly variable and depends strongly on the physical and chemical conditions applied during its formation, as well as the sediment's composition (Locat et al. 2003). In laboratory measurements the onset of structure degradation often occurs for overburden of ~100–500 kPa (e.g. Liu and Carter 1999; Tanaka and Locat 1999). This pressure range equals depths of ~20–100 m below seafloor (using a submerged unit of weight of 5 kN/m^3), which corresponds to the depths of failure planes for large volume landslides. Destructuring is stress-controlled, and thus independent of sedimentation rates. Considering that structure is a general property of marine clays, excess pore pressure generation as a result of destructuring could therefore be a rather general process, hence explaining the global distribution of major landslides.

16.1.2 Aims and Approach

In this paper we explore whether the progressive loss of structure during burial and shearing could cause sufficient excess pore pressure to cause failure of a low gradient continental slope. This contribution is novel because previous submarine slope stability analyses have not addressed destructuring effects.

We use a Finite Element model to simulate consolidation and burial of a cemented hemipelagic clay layer in a typical continental slope with a gradient of 2°. Consolidation occurs as a result of self weight and a continuous, spatially varying load. The cemented hemipelagic layer is initially stiff and load-bearing, but as it reaches critical pressures gradually looses its strength and stiffness.

16.2 Methodology

The Finite Element model uses fully coupled transient 2D plane strain pore fluid diffusion and stress analysis. The fluid is governed by Darcy's law while the mechanical part is based on the effective stress principle. The sediment is assumed homogeneous and fully saturated with a single incompressible pore fluid (sea water).

16.2.1 Material Model

The modelled material represents fine grained hemipelagic sediments. The elasto-plastic, isotropic hardening Modified Cam Clay model accounts for compaction, and is adjusted slightly to include destructuring effects. Permeability is nonlinear, anisotropic and changes as a function of porosity (Table 16.1). We choose the porosity-permeability relationship for hemipelagic clays of Binh et al. (2009), as it is one of the few to include samples from depth >10 m below seafloor. The physical-mechanical properties are average values for hemipelagic clays based on published data (Table 16.1), except for the slope of the consolidation curve (λ), which is explained in the following paragraph.

The consolidation path of structured sediment subjected to loading is shown in Fig. 16.1. In the following, the slope of the curve in the volume-pressure plot, λ, is referred to as compressibility. At low pressures, the structured (undisturbed) sediment is comparatively stiff (A to B in Fig. 16.1b), and structure allows the sediment to maintain high porosity. As pressure increases and exceeds the resistance provided by the structure, the sediment progressively looses its cement, and the structure-permitted porosity decreases rapidly (B-C). This destructuring phase is characterised by a steep slope of the consolidation curve. As loading and the loss of structure continues, the compression curve appears asymptotic to the equilibrium curve for structureless sediment (C-D). Kinematic hardening models have been developed that include the effect of destructuring, which require an extensive set

Table 16.1 Material model parameters representing hemipelagic clay. Refer to Fig. 16.1c for explanations of λ_c, λ_d and λ_{sl}.

Notation		Value	Remarks	References
κ	Swelling index	0.028		Powrie (2002)
ν	Poisson ratio	0.3		Powrie (2002)
λ_c	Slope of normal consolidation line (Fig. 16.1c)	0.10	Undisturbed: $p' < 100$ kPa	Hattab and Favre (2010)
λ_d		1.20	Destructuring: 100 kPa $< p' <$300 kPa	
λ_{sl}		0.48	Remoulded: $p' > 300$ kPa	
φ_{crit}'	Friction angle	30°	$M = \frac{\sin\phi_{crit}' \cdot 6 \cdot \sqrt{1-b+b^2}}{3+\sin\phi_{crit}' \cdot 2b - \sin\phi_{crit}'}, b = 0.5$	Powrie (2002)
M	Slope of critical state line	0.87		
k_y [ms]	Vert. permeability	$10^{-15}e^{18.93n}$	n = porosity	Binh et al. (2009)
k_x [ms]	Horiz. permeability	$10*k_y$		

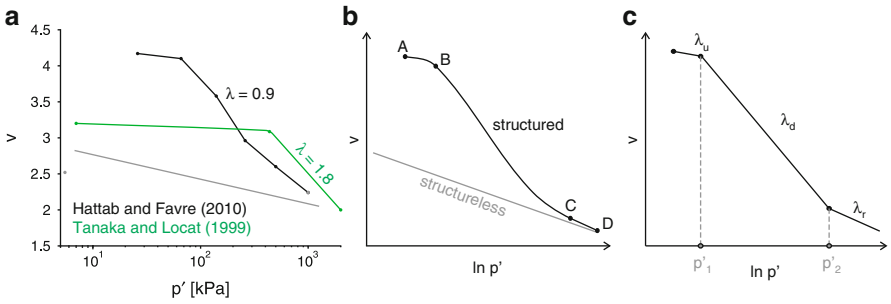

Fig. 16.1 Destructuring during compression in plots of specific volume, v, against mean effective pressure, p′: (**a**) Oedometric paths of two deep sea sediment samples with slope λ. The *grey line* represents the oedometric path of a structureless sample. The *black line* represents cemented hemipelagic (Hattab and Favre 2010) and the *green line* microfossil rich clay (Tanaka and Locat 1999). (**b**) Schematic representation of a typical consolidation path of structured sediment, and its structureless counterpart (*grey line*). (**c**) Definitions of material parameters for the implementation of destructuring in the material model

of parameters. We deliberately refrain from using such constitutive models as these specific parameters are hardly known for deep sea sediments. To account for destructuring effects instead, we introduce compressibility as a function of pressure in our elastoplastic material definitions. Three different λ values for different pressure ranges represent three stages of the material: cemented (λ_c, $p' < 100$ kPa), destructuring (λ_d, $100\ \text{kPa} < p' < 300$ kPa) and structureless (λ_{sl}, $p' > 100$ kPa, Fig. 16.1c).

We use the λ and critical pressure values reported by Hattab and Favre (2010). The authors conducted consolidation tests on cemented hemipelagic clay samples from the deep sea Gulf of Guinea, where sedimentation rates are about 0.3 m/ky For stresses below 90 kPa the sediment is stiff without a significant porosity decrease ($\lambda_c < 0.10$). Between 100 and 300 kPa cementation degrades progressively and the volume loss is significant ($\lambda_d = 0.90$). We choose a slightly higher λ_d. This is because it is likely that the true compressibility during destructuring is underestimated, as a considerable part of the structure has been lost due sampling and recovery (Locat and Lee 2002). For higher stresses λ_{sl} decreases to 0.48.

16.2.2 Model Description

Although slope failure is expected in the upper 250 m, large overall model depths are necessary to avoid boundary effects. Hence, the model is 5,500 m deep in z-direction at the shelf, and 2,000 m at the abyssal plain. The entire model is 120 km long in x-direction with a slope angle of 2°. The shelf and abyssal plain are each 10 km long. Water depth is 200 m at the shelf break and 3,700 m the abyssal plain.

The lateral boundaries of the model are fixed in the horizontal direction, but are free to move vertically. The base of the model is fixed in both vertical and horizontal directions. The upper boundary is free to move in either vertical or horizontal direction. The landward boundary of the model is impermeable, but pore fluid is allowed to flow through the abyssal plain boundary. No flow takes place through the basal boundary as sediments at this depth are highly lithified and virtually impermeable.

The water column is not modelled as such but represented by a pressure load corresponding to the hydrostatic pore pressure at the seafloor. The newly added sediment is simulated by an equivalent vertical vector load on the seafloor that increases linearly over time. The maximum loading rate along the shelf corresponds to 0.15 m/ky and decreases linearly downslope to 0.01 m/ky at the right side boundary.

Before loading by sediment deposition begins, all stresses are in equilibrium with the gravitational load ($g = 9.81\ m/s^2$), and pore pressures are hydrostatic throughout the model. As only slow deposition is considered in this study, the sediment in the model is initially normally consolidated. The initial porosity corresponds to a depth-porosity relationship for deep sea clays (Kominz et al. 2011). A detailed description of the model can be found in Urlaub (2012).

16.2.3 Assumptions and Limitations

Newly deposited sediment only provides a surface load in the models. Compaction and pore fluid generation and the build up or degradation of structure within the newly deposited sediment would occur in nature, but are not simulated here. Consequently, the model is not capable of simulating failure within this interval of newly deposited sediment. However, as the failure surface for the landslides considered here is typically at depths of 100–250 m below seafloor, this limitation is only critical if the thickness of deposited sediment exceeds 100 m. This is only the case when significantly longer time scales or higher deposition rates than the ones considered here (800 ky for 0.15 m/ky) are modelled.

The model is a first attempt of testing the effect of a cemented layer whose resistance has been exceeded on the stability of a submarine slope. The mechanical model is a highly simplified representation of a cemented sediment. Destructuring as implemented here neglects the effect of shearing and kinematic hardening, as well as the loss of strength. More complex material models are available that can be used to model structured clays. However, these constitutive models require a large number of parameters. Such parameter sets do not exist for marine sediments, mainly due to sample disturbance during recovery. The model thus predicts excess pore pressure generation, but may not truly represent failure mechanisms.

16.3 Results

The model is run for 800 ky. To evaluate excess pore pressure generation and slope stability during the analysis we show the temporal evolution of overpressure ratio u* (the ratio of excess pore pressure to vertical effective stress in hydrostatic conditions), porosity n, vertical effective stress σ'_v, and total shear strain γ, at six nodes of different depths at the upper slope (Fig. 16.2a–d). The upper two nodes are located at 0 and 19 m below the model surface and they are not affected by destructuring. Changes in porosity are comparatively small and u* is always <0.05. Effective stress increases continuously and shear strains do not exceed 3 %. The node at 28 m below the model surface begins at the upper boundary of the destructuring pressure range. Hence, it compacts rapidly but upwards drainage of pore fluid is possible as the overlying sediment is intact and maintains its high porosity and permeability. Consequently, u* is small and σ'_v increases as loading goes on. Shear strains increase at a constant rate to about 0.145. The three deeper nodes (36–63 m below model surface) are actively destructuring from the start of the model run, as indicated by a rapid porosity decrease. No drainage paths exist due to rapid collapse of pore spaces in the material above and below, so that u* rapidly increases to 0.6. If the model would run for longer, u* is expected to reach even higher values as it is continuously rising with time. The load is increasingly carried by the pore fluid and σ'_v remains constant. Shear strains reach up to 15 % with a decrease in the rate at which γ increases towards later stages of loading.

2D contour plots of the overpressure ratio and incremental shear strains, $\Delta\gamma$, for the entire model area show the final stage of the analysis after loading of the slope for 800 ky (Figs. 16.2e, 16.3). Maximum values of u* reach up to 0.6 within the destructuring layer at about 40–50 m below the model surface at the upper slope (Fig. 16.2e). In addition to such high excess pore pressures, a zone of particularly high incremental shear strains just above the u* maximum appears (Fig. 16.3). This indicates the development of a shear zone that can accommodate a failure plane.

16.4 Discussion

We implemented the gradual loss of structure of hemipelagic clay in a low angle continental slope model. When subjected to 800 ky of continuous and asymmetric sediment deposition at a maximum rate of 0.15 m/ky, high excess pore pressures reaching up to 60 % of the vertical effective stress in hydrostatic conditions develop, along with a zone of locally high shear strains. The excess pore pressures are still increasing when the run was terminated. These patterns indicate that failure may occur along a plane at 100–150 m below seafloor, which is in agreement with the depths of glide planes observed in field data. Similar continental slope models subjected to slow sedimentation without the effect of destructuring do not show any indications of instability (Urlaub et al. 2012). The presence of a pressure-dependent

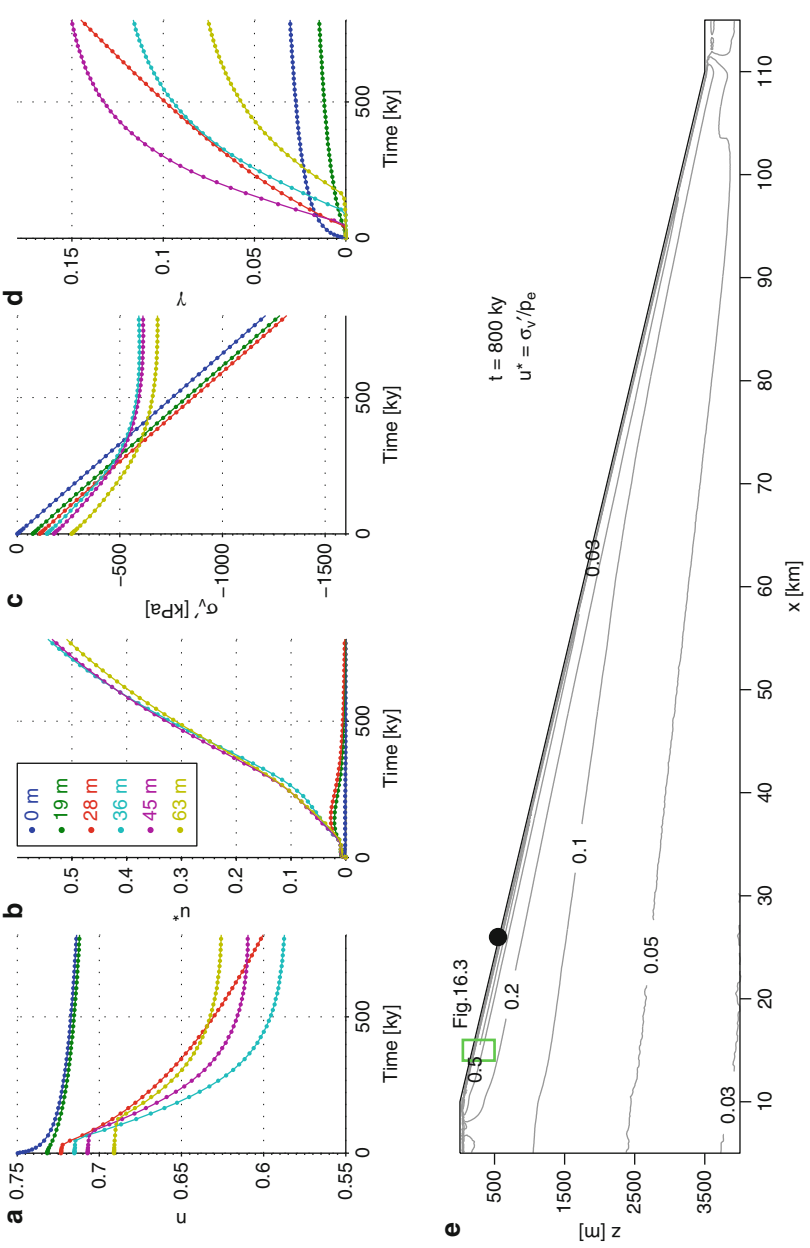

Fig. 16.2 Temporal evolution of (**a**) porosity n, (**b**) overpressure ratio u*, (**c**) vertical effective stress σ'_v and (**d**) shear strain γ at six nodes at different depths. The nodes locate 16 km from the shelf break as indicated by the *black dot* in the *lower panel*, and their initial depths before loading are given in *panel* (**b**). The *bottom panel* (**e**) shows overpressure ratio contours for the entire model domain after 800 ky of continuous loading. The *green square* indicates the close-up section shown in Fig. 16.3

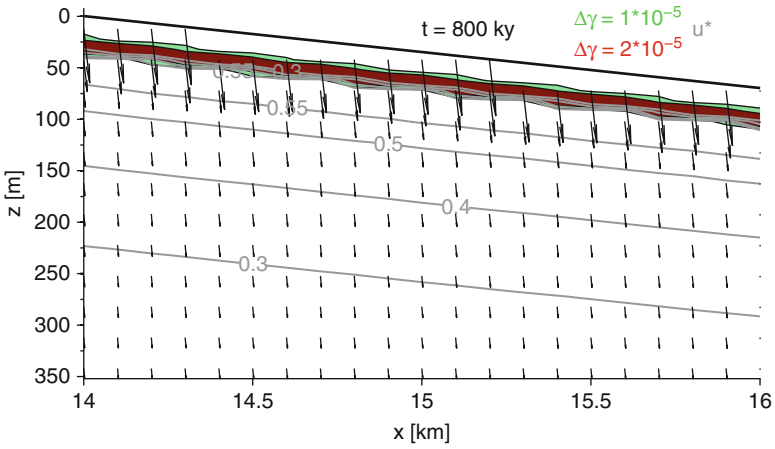

Fig. 16.3 Close-up of a surface-near section showing the overpressure ratio (*grey contour lines*) after 800 ky of constant sediment deposition. *Filled coloured contours* show the incremental shear strain of the last numerical increment. A surface-parallel zone of intense shearing lies just above the maximum overpressure ratio contour line. Taking into account the newly deposited sediment (which is not physically modelled or illustrated), the model surface at this time and distance from the shelf corresponds to a depth of about 115 m below seafloor

high compressibility (destructuring) zone seems the only mechanism that could cause failure of a low gradient slope when slow sedimentation acts as the only pressure source. It is therefore possible that destructuring may be important for the stability of continental slopes, and can help to explain failure of low angle slopes at continental margins with little sediment input. It is a process that could operate in many locations worldwide.

It is important to emphasise that the pressure range in which destructuring takes place and compressibility is high ($p'_1 > p' < p'_2$, Fig. 16.1c) directly controls the depth of the failure plane. The rate of porosity reduction during the destructuring phase (λ_d) controls the magnitude of excess pore pressure, and therefore the overall stability. Hence, whether failure occurs, and at which depth the failure plane is located, is prescribed by the mechanical behaviour of the sediment. Further investigations into the role of destructuring on slope stability require a thorough evaluation of these material properties.

Crushing of microfossils during compaction is a process with similar effects on excess pore pressure generation as destructuring of clay. Sediments rich in microfossils do not consolidate to as low porosities as other marine clays owing to microfossil shells acting as a structural component (Tanaka and Locat 1999). However, a "delayed compressibility" that can reach λ values of up to 2.0 is typical for such microfossil rich sediments (e.g. diatomaceous ooze shown in Fig. 16.1a). As a critical pressure is overcome during burial these shells collapse, porosity decreases rapidly and excess pore pressure builds up.

16.5 Conclusion

We investigate whether destructuring of cemented hemipelagic clay can cause sufficient overpressure to cause failure of a low gradient continental slope in an environment with low sedimentation rates. Under the conditions used here for the numerical modelling of the burial of such hemipelagic clay on a 2° slope indicates the development of a bedding parallel failure plane after ~800 ky. These initial results suggest that the loss of structure has the potential for causing wide spread weak layers that could cause large volume landslides at low gradient slopes globally.

Acknowledgements We would like to thank the reviewers Jean-Sebastien L'Heureux and Jacques Locat for their thoughtful reviews.

References

Binh NTT, Tokunaga T, Nakamura T, Kozumi K, Nakajuma M, Kubota M, Kameya H, Taniue M (2009) Physical properties of the shallow sediments in late Pleistocene formations, Ursa Basin, Gulf of Mexico, and their implications for generation and preservation of shallow overpressures. Mar Petrol Geol 26:474–486

Di Prisco C, Matiotti R, Nova R (1995) Theoretical investigation of the undrained stability of shallow submerged slopes. Géotechnique 45(3):479–496

Dugan B, Flemings PB (2000) Overpressure and fluid flow in the New Jersey continental slope: implications for slope failure and cold seeps. Science 289:288–291

Flemings PB, Long H, Dugan B, Germaine JT, John CM, Behrmann JH, Sawyer DE et al (2008) Erratum to "pore pressure penetrometers document high overpressure near the seafloor where multiple sub- marine landslides have occurred on the continental slope, offshore Louisiana, Gulf of Mexico". Earth Planet Sci Lett 274:269–283

Hattab M, Favre JL (2010) Analysis of the experimental compressibility of deep water marine sediments from the Gulf of Guinea. Mar Petrol Geol 27(2):486–499

Hühnerbach V, Masson DG et al (2004) Landslides in the North Atlantic and its adjacent seas: an analysis of their morphology, setting and behaviour. Mar Geol 213:343–362

Kominz MA, Patterson K, Odette D (2011) Lithology dependence of porosity in slope and deep marine sediments. J Sediment Res 81(10):730–742

Liu MD, Carter JP (1999) Virgin compression of structured soils. Géotechnique 49(1):43–57

Locat J, Lee HJ (2002) Submarine landslides: advances and challenges. Can Geotech J 39:193–212

Locat J, Tanaka H, Tan TS, Dasari GR, Lee HJ (2003) Natural soils: geotechnical behavior and geological knowledge. In: Tan TS et al (eds) Characterisation & engineering properties of natural soils, vol 1. A.A. Balkema Publishers, Lisse, p 3

Masson DG, Harbitz CB, Wynn RB, Pedersen G, Løvholt F (2006) Submarine landslides: processes, triggers and hazard prediction. Philos Trans R Soc 364:2009–2039

Powrie W (2002) Soil mechanics. Spon, London

Skempton AW, Northey RD (1952) The sensitivity of clays. Géotechnique 3:30–52

Sumner E., Siti MI, McNeill L, Talling PJ, Henstock TJ, Wynn RB, Djajadihardja Y, Permana, H (2013) Can turbidites be used to reconstruct a palaeoearthquake record for the central Sumatran margin? Geology. http://dx.doi.org/10.1130/G34298.1

Tanaka H, Locat J (1999) A microstructural investigation of Osaka Bay clay: the impact of microfossils on its mechanical behaviour. Can Geotech J 36(3):493–508

Twichell DC, Chaytor JD, ten Brink US, Buczkowski B (2009) Morphology of late quaternary submarine landslides along the U.S. Atlantic continental margin. Mar Geol 264:4–15

Urlaub M (2012) The role of sedimentation rate on the stability of low gradient submarine continental slopes. PhD thesis, University of Southampton, Southampton

Urlaub M, Zervos A, Talling PJ, Masson DG, Clayton CI (2012) How do 2° slopes fail in areas of slow sedimentation? A sensitivity study on the influence of accumulation rate and permeability on submarine slope stability. In: Yamada Y et al (eds) Submarine mass movements and their consequences. Springer, Dordrecht, pp 277–287

Chapter 17
How Stable Is the Nice Slope? – An Analysis Based on Strength and Cohesion from Ring Shear Experiments

Sylvia Stegmann and Achim Kopf

Abstract The upper shelf of the landslide-prone Ligurian Margin (Western Mediterranean Sea) off Nice well-known for the 1979 Airport Landslide is a natural laboratory to study preconditioning factors and trigger mechanisms for submarine landslides. For this study low-stress ring shear experiments have been carried out on a variety of sediments from >50 gravity cores to characterise the velocity-dependent frictional behaviour. Mean values of the peak coefficient of friction vary from 0.46 for clay-dominated samples (53 % clay, 46 % silt, 1 %) sand up to 0.76 for coarse-grained sediments (26 % clay, 57 % silt, 17 % sand). The majority of the sediments tested show velocity strengthening regardless of the grain size distribution. For clayey sediments the peak and residual cohesive strength increases with increasing normal stress, with values from 1.3 to 10.6 kPa and up to 25 % of all strength supported by cohesive forces in the shallowmost samples. A pseudo-static slope stability analysis reveals that the different lithologies (even clay-rich material with clay content ≥50 %) tested are stable up to slope angles <26° under quasi-drained conditions.

Keywords Ring shear • Submarine landslide • Slope stability analysis

17.1 Introduction and Geological Setting

The upper shelf off Nice (Southern France) along the Ligurian Margin is recognised for the 1979 Airport Landslide (e.g. Dan et al. 2007). Beside the reconstruction of the tsunamigenic 1979 landslide, an on-going project (Ifremer Brest [France],

S. Stegmann (✉) • A. Kopf
MARUM – Center for Marine Environmental Sciences, Marine Geotechnics, University of Bremen, Leobener Strasse, 28359 Bremen, Germany
e-mail: stegmann@uni-bremen.de

S. Krastel et al. (eds.), *Submarine Mass Movements and Their Consequences*, Advances in Natural and Technological Hazards Research 37, DOI 10.1007/978-3-319-00972-8_17,

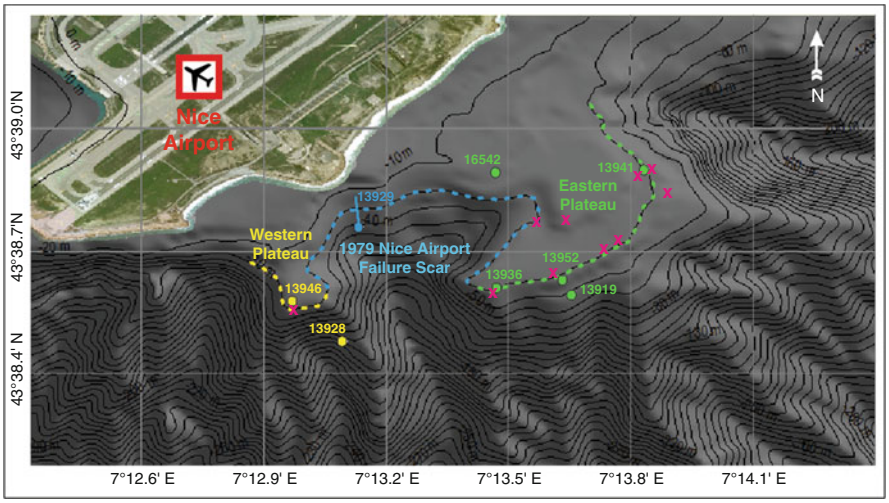

Fig. 17.1 Map of the continental slope off Nice including the 1979 landslide scar (*blue*) and the adjacent meta-stable plateaus east (*yellow*) and west (*green*) of it. *Coulor-coded circles* mark the positions of the cores used in this study. Static *in situ* CPTu locations are given by *pink crosses* (for details see Sultan and Shipboard Party 2008; Sultan et al. 2010)

Marum Bremen [Germany]) concentrates on the sediment-mechanical behaviour of the non-failed, but apparently meta-stable portion of the Nice Slope (Leynaud and Sultan 2010; Sultan et al. 2010; Stegmann et al. 2011).

In this study we focus on the frictional behaviour of sediments in and around the Nice Airport landslide scar (Fig. 17.1). Given the proximity to the dynamic sedimentary system of the Var river and coastal aquifer along the shelf off Nice, coarse-grained turbidites, thin silt layers, homogeneous sand packets are embedded in soft silty clay deposits (e.g. Sultan and Shipboard Party 2008; Kopf et al. 2008, 2009). Reddish, mottled or slumped clayey layers indicate incipient soft sediment deformation. Occurrence of fresh water, fluid-rich pockets and piping in cored sediments as well as pore pressure transients attest to active fluid flow processes (Kopf et al. 2008, 2009; Sultan et al. 2010; Stegmann et al. 2011). *In situ* CPTu data (see Fig. 17.1) reveal a significant decrease of sleeve friction initiating between 4 and 8 mbsf and indicate a disturbed/softened state of the sediments (Sultan et al. 2010). This is further supported by 3.5 kHz seismic data showing disturbance and gas blankening within the stratified soft deltaic sediments on both plateaus (Sultan and Shipboard Party 2008; Sultan et al. 2010). Based on these findings we want to investigate peak as well as residual shear behavior of key lithologies of the deltaic sequences (Fig. 17.1).

17.2 Methods

17.2.1 Coring and Sedimentological Analysis

Gravity cores were collected during the expeditions POS386 and POS429 in the 1979 Airport landslide scar as well as on the non-failed western and eastern plateaus and along its slopes (Fig. 17.1; Kopf et al. 2008, 2009).

After splitting and visual core description the sediments underwent a non-destructive determination of physical properties (e.g. bulk density) with a Geotek multi-sensor core logger (MSCL). Grain-size analyses on discrete samples were carried out using the laser diffraction method (Coulter LS-13320) quantifying 117 grain size classes from 0.04 to 2,000 μm as volume percent (vol%). Water content was determined by weighing the wet and dry samples.

17.2.2 Shear Experiments with the Ring Shear Apparatus

For this study ring shear experiments determine the drained shearing behaviour at large shear strains of remoulded specimens at moderate to low shear rates at a desired normal stress. In addition to the intrinsic shear characteristics of the different samples, e.g. coefficient of friction ($\mu = \tau/\sigma'_n$), the rate-dependent frictional stability was monitored, which is controlled by the velocity dependence of the steady-state friction parameter (a-b) (Scholz 1998). We used the Bromhead ring-shear device *TORSHEAR* manufactured by Wykeham Farrance (Bishop et al. 1971). The remoulded sediment sample is confined radially between concentric rings while a uniform normal stress is applied by a lever loading system (Fig. 17.2a, b). During shearing shear force, vertical displacement, and rotation are logged at a sampling rate of 10 s. Withering of the sediment is avoided as the shear box is inside a water container. Drainage of fluids is enabled by porous filter plates at the base and top of the specimen.

The Nice Slope sediments were tested under effective normal stress σ'_n of 27, 51, 100 and 198 kPa, with consolidation carried out slowly so that complete dissipation of any excess pore pressure is assumed. At each loading state the same shear rate sequence (0.06–0.6–6.0–0.03 mm/min) was applied until 200 mm horizontal displacement was reached. Peak shear strength (τ_{peak}) is obtained during the first shear phase at 0.06 mm/min at each stress increment, when the sample is assumed to be intact and no sliding surface is developed or is healed due to the consolidation under the increasing load (Hight et al. 1979). The constitutive stability parameter (a-b) was determined at the step from initial velocity of 0.06 to 0.6 mm/min on the residual path of the experiment. After completion of the shear sequence of four velocities at each σ'_n state, the sample was unloaded. Cohesive shear strength $\tau_{cohesion}$ was then measured in the absence of any external stress ($\sigma'_n \sim 0$ kPa) following Ikari and Kopf (2011).

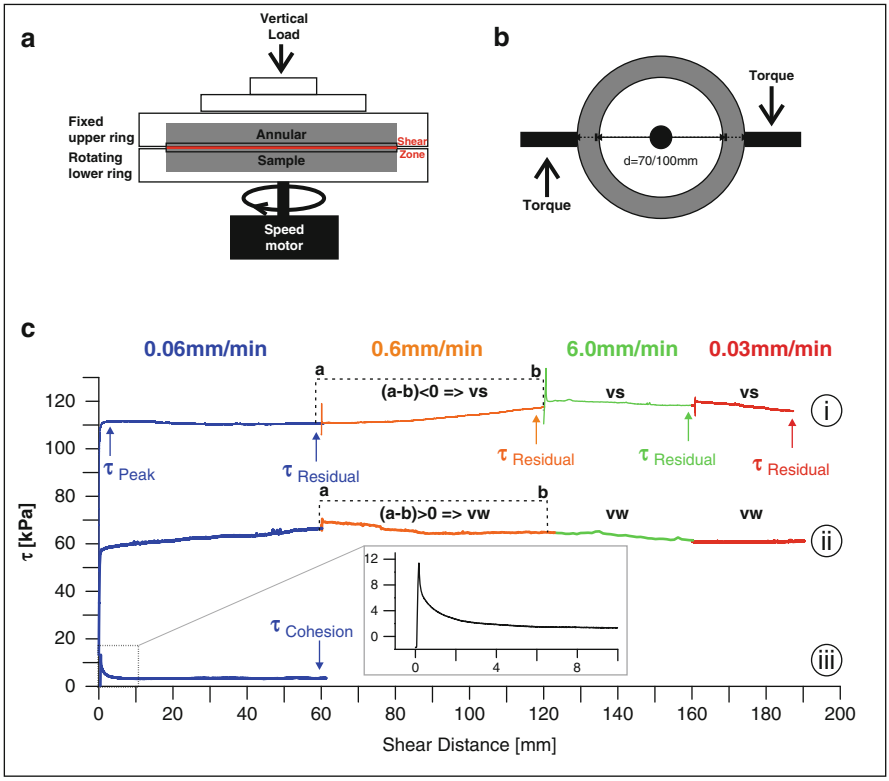

Fig. 17.2 (**a**) Schematic diagram of the ring shear device in cross section; (**b**) *top view* of the sample cell; (**c**) Examples for typical shear test protocols with shear strength τ plotted versus shear distance. Shearing related to different rates is marked with various *colours*. The rate sequence presented here was used for all tests. Experiment (i) was carried out on sample GeoB13952-422 cm bsf at 101 kPa; experiment (ii) was carried out on sample GeoB13929-54 cm bsf at 51 kPa. Graph (iii) represents a so-called cohesion test, which was limited to one shear sequence with v = 0.06 mm/min for sample GeoB13946-381 cm bsf at 51 kPa. See text

17.2.3 Stability Assessment of the Nice Slope Sediments

The stability of selected Nice Slope lithologies was assessed by the calculation of the Factor of Safety (FS). We use the infinite slope approximation for a static slope stability analysis under drained conditions (Løseth 1999), following:

$$FS = \frac{c + \gamma' z \left(cos^2\beta - \lambda^*\right) tan\varphi}{\gamma'\, z\, sin\beta\, cos\beta}$$

with c = cohesion, γ' = unit weight (submerged), z = depth, β = slope angle, φ = friction angle, and $\lambda^* = \Delta u/\sigma_n$ (being the pore pressure ratio). The numerator of this equation originates from the Mohr-Coulomb failure criterion $\tau = c' + \sigma'_n \tan\varphi$, where τ = shear strength, c' = intercept of cohesion, σ'_n = effective normal stress, and φ = internal friction angle (e.g. Hampton and Lee 1996). We use this relationship for intercomparison between the stability of the different lithologies and also to oppose ring shear data on cohesion (measured cohesive strength) with the graphical intercept at zero effective stress.

The Factor of Safety (FS) was obtained for each lithology for a mean effective stress of 51 kPa, corresponding to 6 m subbottom depth based on the calculation of overburden stress using the mean bulk density of 1.9 g/cm^3. This depth reflects a distinct decrease in CPTu data in many profiles through the sedimentary sequence (see Sultan et al. 2010, in particular Figs. 5 and 7). φ_{peak} and $\varphi_{residual}$ are obtained directly from the ring shear data. For the pore pressure ratio we generalise $\Delta u = 2$ kPa for the superficial portion of sediment of the plateau (see Fig. 11, Stegmann et al. 2011). The analysis encompasses a range of relevant slope angles along the Nice slope (plateau: <6°, slope: 7–19° and steep flanks along the slope: 25–29°).

17.3 Results

17.3.1 Sedimentological Analysis and Physical Properties

The samples selected for the shear experiments comprise representative lithologies of the Nice Slope surface sediments (Kopf et al. 2008, 2009). The deposits consist predominantly of silt (46–70 %). Depending on whether cohesive or granular material is predominantly coexisting clay (22–53 %) and sand contents (1–17 %) vary (Table 17.1). Bulk density ranges from 1.51 to 2.07 g/cm^3 (average 1.9 g/cm^3) and reflect both grain size distribution and consolidation state. Natural water content ranges from 31.5 to 44.8 %wt for the clay-rich sediments, but could be as low as 26.6 % for the coarse-grained or overconsolidated material of the 1979 landslide scar (see Table 17.1).

17.3.2 Frictional Behavior of the Nice Slope Sediments

In total, eleven ring shear experiments were carried out. A typical protocol of our multistage testing procedure for three different σ'_n stages is given in Fig. 17.2c. The silty specimens tested fail (peak strength) typically between 1 and 4 mm shear

Table 17.1 Summary of (i) selected index/sedimentary properties of Nice slope sediments used for ring shear experiments (e.g. grain size distribution, water content) and (ii) their frictional characteristics (coefficient of friction, cohesive strength, frictional stability expressed by velocity weakening [*vw*] and velocity strengthening [*vs*]). The samples were selected with respect to their geological setting (failed [1979 landslide scar] vs. stable [western/eastern flanks]) and their sedimentological properties (e.g. bulk density, grain size distribution); Note that *colour coding* corresponds to that of Fig. 17.1

				Grain size distribution [%]			μ_{Peak}				$\mu_{Residual}$				$\tau_{Cohesion}$ [kPa]				Frictional stability
							σ'_n [kPa]				σ'_n [kPa]				σ'_n [kPa]				Shear rate [mm/min]
Sample ID	Core (GeoB)	Water depth [m]	Water content [%]	Clay	Silt	Sand	27	51	100	198	27	51	100	198	27	51	100	198	0.06 → 0.6
9	13,946–420 cm	15	38.7	46	53	1	0.56	0.53	0.49	0.48	0.57	0.54	0.49	0.49	1.3	1.5	2.0	1.8	vs
10	13,946–381 cm	15	36.0	45	54	1	0.54	0.49	0.49	0.49	0.47	0.50	0.50	0.49	2.1	3.6	10.6	7.8	vs
11	13,928–104 cm	76	32.7	39	56	5	0.60	0.59	0.56	0.56	0.53	0.58	0.56	0.54	1.9	1.9	2.3	3.8	vs
1	13,929–56 cm	29	39.2	22	61	17	0.55	0.59	0.58	0.57	0.56	0.68	0.66	0.67	1.9	4.7	4.0	6.0	vs/vw
2	13,929–112 cm	29	26.7	50	49	1	0.58	0.60	0.55	0.55	0.59	0.59	0.59	0.57	2.0	1.9	1.9	2.2	vs/vw
3	13,929–160 cm	29	26.6	27	57	17	0.60	0.76	0.56	0.59	0.64	0.67	0.68	0.61	4.4	2.8	2.6	3.5	vs
4	13,936–225 cm	29	33.2	43	54	7	0.57	0.53	0.47	0.48	0.55	0.48	0.49	0.48	3.2	3.7	4.5	No data	vs
5	13,941–478 cm	14	31.5	33	56	12	0.57	0.57	0.56	0.55	0.50	0.55	0.55	0.57	1.8	1.5	1.5	2.4	vs
6	16,542–298 cm	13	44.8	53	46	1	0.50	0.49	0.46	0.54	0.49	0.50	0.51	0.55	1.4	1.7	2.0	3.5	vs
7	13,919–300 cm	35	38.0	42	55	3	0.56	0.59	0.56	0.52	0.54	0.55	0.59	0.56	1.9	2.3	2.1	5.4	vs
8	13,952–422 cm	21	32.7	37	53	10	0.59	0.56	0.56	0.56	0.59	0.56	0.56	0.55	No data				vs/vw

displacement. The friction value at high strains (post-yield) is lower than the peak value in some cases (Fig. 17.2c, i) but is higher in others (Fig. 17.2c, ii). The shear behaviour during the cohesion tests (Fig. 17.2c, iii) differs as the curve shows brittle failure with a more accentuated drop from peak to residual strength. As the residual value of the cohesion test should be consistent with the non-brittle strength of normally consolidated material (Lupini et al. 1981) we define the cohesive strength of the normally consolidated Nice Slope sediments with the value obtained after a shear distance of 60 mm, termed $\tau_{cohesion}$.

The coefficient of friction (μ) varies between 0.46 and 0.76 for μ_{peak} and between 0.49 and 0.68 for the residual state ($\mu_{residual}$). Both μ_{peak} and $\mu_{residual}$ reveal a clear stress-dependency as they generally decrease with increasing σ'_n. The opposing trend is observed in shear tests where the sand content (17 %, e.g. GeoB13929-56 cm) or clay content (>50 %, e.g. GeoB16542-298 cm) are high (Table 17.1).

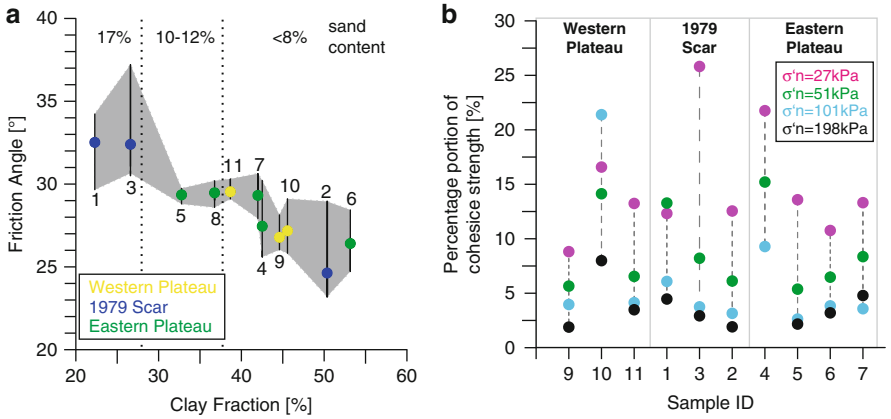

Fig. 17.3 (**a**) Correlation between peak friction angle φ and clay content. The *line* marks the corridor of the peak friction angle for the four different normal stress states. (**b**) Percental portion of cohesive strength relative to the residual strength measured at corresponding load increments

The influence of grain-size distribution on friction is reflected by the relationship between (peak) friction angle and clay fraction (Fig. 17.3a). Clay contents exceeding 30 % result in peak friction angles ranging from 23° to 30°, whereas higher friction angles (up to $\varphi = 37°$) are caused by a sand content up to 17 %. The corridor of σ'_n related peak friction angle of the different shear experiments scatters more widely when sand or clay is more abundant (see grey shading in Fig. 17.3a).

Cohesive strength was determined for the majority of the σ'_n stages of the individual shear tests (Table 17.1). Minimum and maximum values of $\tau_{cohesion}$ range from 1.3 kPa ($\sigma'_n = 27$ kPa) up to 10.6 kPa ($\sigma'_n = 198$ kPa), both measured in clay-rich samples with only 1 % sand of the Western Plateau (Table 17.1).

In general, $\tau_{cohesion}$ indicates a σ'_n-dependency as an increase of σ'_n generally causes the cohesive strength to increase as well (Fig. 17.3b), most likely a result from consolidation alone. Other than that, an unambiguous correlation between the grain size composition and the cohesive strength cannot be established (Table 17.1). The cohesive proportion of shear strength represents 2–27 % of the residual strength at the load increments tested (Fig. 17.3b).

17.3.3 Stability Assessment of the Nice Slope Sediments

The underlying criteria for using remoulded samples in a ring shear device have been the fact that (i) the Nice sediment is compositionally very heterogeneous and often disturbed, and that (ii) earlier *in situ* work suggested that a decrease in q_c (cone resistance) and, more prominently, f_s (sleeve friction) reflects remoulded strata (see Lunne et al. 1997; Sultan et al. 2010). If we compare cohesive background sediment

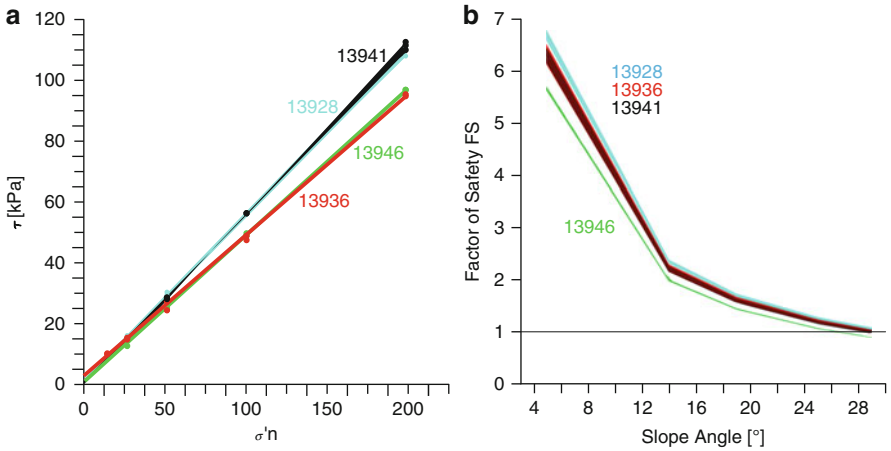

Fig. 17.4 (**a**) Stability of the different Nice slope lithologies in terms of the Mohr-Coulomb failure criterion. Shear strength data (the corridor of each curve represents the range between peak and residual value) are plotted versus effective normal stress; (**b**) the factor of safety (*FS*) was calculated using drained ring shear data for slope angles, which represent the plateau (1–6°), the slope (7–19°) and outcropping portions along the slope (25–29°)

of the stratified foresets of the deltaic sedimentation sequences (GeoB13936 and -46) and slope apron (GeoB13928) including cohesive, reddish layers, which have been observed in several cores (e.g. GeoB13946), the corresponding Mohr-Coulomb critical failure lines define two distinct corridors (Fig. 17.4a). The weakest lithologies originate from the clay-bearing sediments of the western (GeoB13946-381 cm [reddish layer]) and eastern (GeoB13936-225 cm) plateau (Fig. 17.4a). Cohesion c' (i.e. intercept of the failure line at zero effective normal stress) varies between 0.8 kPa (GeoB13946-381 cm) and 2.9 kPa (GeoB13936) for the peak strength. For comparison measured $\tau_{cohesion}$ ranges is ~1.3–1.5× higher for most samples. However, the weakest material (GeoB13946-381 cm) encountered in the shallow Nice Slope deposits shows extraordinarily high cohesive strength (a factor of 4.5 larger than that determined from the intercept of the failure criterion) and is also characterised by macroscopic deformation in the core. However, cohesive strength measured in normally consolidated ring shear samples may overestimate c since water contents may be lower than *in situ*.

When using c', the FS analysis indicates stability for the plateau as well as the adjacent slope with FS > 1 for angles up to 26°, with minor variations caused by the lithological variability off Nice (see graphs in Fig. 17.4b). With the higher values of $\tau_{cohesion}$ used, slope stability assessment would tend towards even higher slope angles until FS = 1 is reached.

17.4 Discussion

In general, our data agree well with the variations in clay content (Fig. 17.3a), although the difference between μ_{peak} and $\mu_{residual}$ is relatively small for the clay-rich samples. The Nice Slope specimens plot along a similar corridor as marine sediments from Nankai (Brown et al. 2003, their Fig. 4) and onshore soils of known mineral composition (Skempton 1985; Lupini et al. 1981), and corresponds quantitatively with the earlier findings (Fig. 17.3a).

Cohesive strength usually rises with increasing σ'_n and could not be related to grain-size distribution (Table 17.1, Ikari and Kopf 2011). We interpret this trend as a result of the bonding forces between clay particles, but also of interlocking of single grains with increasing compaction in the more granular specimens. At low σ'_n, the relative amount of strength attributed to cohesive forces can reach 12–14 % in normally consolidated sediment, and may be even higher in overconsolidated materials (e.g. from inside the 1979 scar). The cohesive forces are further governing slope stability of the area since they represent the tensile strength to be overcome by gas or other fluids that progressively weaken the seaward edge of the eastern plateau (see Sultan et al. 2010).

Both μ_{peak} and $\mu_{residual}$ reveal a clear stress-dependency as they generally decrease with increasing σ'_n. This has been observed in earlier studies (e.g. Ikari et al. 2009), and reflects *in situ* results from the Nice Slope (see Sultan et al. 2010; Leynaud and Sultan 2010). At the shelf-slope break, f_s values drop drastically in appx. 4–8 mbsf, which has been attributed to sediment remoulding and incipient shear zones (Sultan et al. 2010, their Fig. 5). Similar drops in strength are reflected by a decrease in both q_c between 12–18 mbsf (ibid., Fig. 6) and 21–23 mbsf (ibid., Fig. 4) and by decreasing q_c and f_s below 20 mbsf (ibid., their Figs. 5 and 7). The strong decrease in f_s is further evidencing high sensitivity of the clay (Lunne et al. 1997), which has been seen before in the area (Dan et al. 2007), but can barely be supported by our data because of the limited total length of the gravity cores.

The majority of our samples show velocity strengthening when increasing the initial velocity of 0.06 mm/min by an order of magnitude (Table 17.1). The associated stable sliding behaviour generally favours (aseismic) creep, as known from landslide-prone slopes, fault zones, and other geological settings (e.g. Marone et al. 1991).

Residual strength is usually not relevant for first-time slope failures, but the strength of clayey sediments may be similar to the residual state if the sediment structure has been disturbed and indicates progressive deformation (e.g. on slip surfaces in previous landslides, creeping slopes, in progressive shears, or after an embankment failure; see Skempton 1985). Those processes are all highly relevant for the Nice Airport area (e.g. Dan et al. 2007; Sultan et al. 2010). However, based on our data the slope stability analysis indicates little difference between peak and

residual state (Fig. 17.4b). For the low σ'_n, drained condition (51 kPa) cohesion plays a significant role in stabilising the slope. It is also worth noting that cohesive forces measured in our experiments range in the same order of magnitude as pore pressure fluctuations from seasonal charging of the aquifer system by precipitation and snow melt off Nice (Stegmann et al. 2011).

Our slope stability analysis attests that wide portions of the Nice Slope are characterised by FS > 1 and are stable under drained conditions as long as slope angles are <26° (see Fig. 17.4b). The clay-dominated reddish sediment (GeoB13946-381 cm) represents here the lithology most prone to instability. However, this picture may change in case external triggering events affect the Ligurian margin. These include earthquakes (Courboulex et al. 2007), groundwater charging (Stegmann et al. 2011), gas migration and creep (Sultan et al. 2010) or human impact (Dan et al. 2007). Those factors may evidently lower the effective stress drastically, so that less conservative stability analyses based on dynamic data (e.g. Leynaud and Sultan 2010) are appropriate to apply. Hence, we conclude that our analysis is best suited for the "background situation" whereas stability analysis work by Leynaud and Sultan (2010) is simulating the "event case".

Acknowledgments We are grateful to Mary Belke-Brea for help with grain size analysis and Gauvain Wiemer and Alois Steiner for assistance in the geotechnical laboratory. We thank both referees Marten Vanneste and Demian Saffer for constructive criticism. The study was funded by DFG via MARUM Cluster of Excellence.

References

Bishop AW, Green GE, Garga VK, Andresen A, Browns JD (1971) A new ring shear apparatus and its application to the measurements of residual strengths. Géotechnique 21:273–328

Brown KM, Kopf A, Underwood M, Steurer J, Weinberger JL (2003) Frictional and mineralogic properties of sediments entering the western Nankai subduction zone: Implications for state of stress on the subduction thrust. Earth Planet Sci Lett 214:589–613

Courboulex F et al (2007) Seismic hazard on the French Riviera: observations, interpretations and simulations. Geophys J Int 170:387–400

Hampton MA, Lee HJ, Locat J (1996) Submarine landslides. Rev Geophys 34(1):35–59

Dan G, Sultan N, Savoye B (2007) The 1979 Nice harbour Catastrophe revisited: trigger mechanism inferred from geotechnical measurements and numerical modelling. Mar Geol 245(1–4):40–64

Hight, DW, El Ghamraway MK, Gens A (1979) Some results from a laboratory study of a sandy clay and implications regarding its in situ behavior. In: Proceedings of the 2nd international conference on behaviour off off-shore structure. London, vol 1, pp 133–150

Ikari MJ, Kopf AJ (2011) Cohesive strength of clay-rich sediment. Geophys Res Lett 38:6309. doi:10.1029/2011GL047918

Ikari MJ, Saffer DM, Marone C (2009) Frictional and hydrologic properties of clay-rich fault gouge. J Geophys Res 114:B05409. doi:10.1029/2008JB006089

Kopf A et al (2008) REPORT AND PRELIMINARY RESULTS OF METEOR CRUISE M73/1: LIMA-LAMO. Berichte aus dem Fachbereich Geowissenschaften der Universität Bremen, Bremen (Germany), No. 264, p 169

Kopf A et al (2009) REPORT AND PRELIMINARY RESULTS OF POSEIDON CRUISE P386: NAIL (Nice Airport Landslide). Berichte aus dem Fachbereich Geowissenschaften der Universität Bremen, Bremen (Germany), No 271, p 161

Leynaud D, Sultan N (2010) 3-D slope stability analysis: a probability approach applied to the Nice slope (SE France). Mar Geol 269:89–106

Løseth TM (1999) Submarine massflow sedimentation: computer modelling and basin-fill stratigraphy. Springer, New York, p 156

Lupini JF, Skinner AE, Vaughan PR (1981) The drained residual strength of cohesive soils. Geotechnique 31(2):181–213

Lunne T, Robertson PK, Powell JJM (1997) Cone penetration testing in geotechnical practice. Blackie Academic/Chapman & Hall/E&FN Spon, London, 312 p, 3rd printing

Marone C, Scholz CH, Bilham R (1991) On the mechanics of earthquake afterslip. J Geophys Res 96:8441–8452

Scholz CH (1998) Earthquakes and friction laws. Nature 391: 37–42

Skempton AW (1985) Residual strength of clays in landslides, folded strata and the laboratory. Geotechnique 35(1):3–18

Stegmann S, Sultan N, Kopf A, Apprioual R, Pelleau P (2011) Hydrogeology and its effect on slope stability along the coastal aquifer of Nice, France. Mar Geol 280:168–181

Sultan N, Shipboard Party (2008) Prisme Cruise (R/V Atalante Toulon—Toulon; 2007): reports and preliminary results. IFREMER internal report, Ref: IFR CB/GM/LES/08

Sultan N, Savoye B, Jouet G, Leynaud D, Cochonat P, Henry P, Stegmann S, Kopf A (2010) Investigation of a possible submarine landslide at the Var delta front (Nice-slope – SE France). Can Geotech J 47:486–496. doi:10.1139/T09-105

Chapter 18
Regional Slope Stability Assessment Along the Caucasian Shelf of the Black Sea

Vsevolod Yu. Ionov, Ernest V. Kalinin, Igor K. Fomenko, and Sergey G. Mironyuk

Abstract Construction of submarine pipelines across the Caucasian shelf of the Black Sea draws a necessity of a detailed study of submarine landslides, which were discovered during a recent survey. The most probable triggers for landslide generation for the Caucasian shelf include earthquakes, wave loading and human activity. Slope stability assessment of the study area was carried out in order to reveal the most important triggering mechanisms. 1-D slope stability modelling was implemented for the purpose of landslide prediction. Gravity force, seismic loading and storm waves' loading were taken into consideration in the present slope stability assessment. The results indicate that for static conditions, landslides formation would most probably occur within the shelf break area where the surface inclination is ~30°. For the shelf area, landslide formation only occurs with additional triggers, such as seismic or wave loading.

Keywords Submarine landslides • Triggering mechanisms • The Black Sea • Slope stability • Shelf • Shelf break

V.Yu. Ionov (✉) • E.V. Kalinin
Geological Department, Lomonosov Moscow State University, GSP-1, Leninskie Gory, 119991 Moscow, Russia
e-mail: sevaionov@gmail.com

I.K. Fomenko
Gulf Interstate Engineering Company, Moscow, Russia

S.G. Mironyuk
Peter Gaz LLC, Moscow, Russia

S. Krastel et al. (eds.), *Submarine Mass Movements and Their Consequences*, Advances in Natural and Technological Hazards Research 37, DOI 10.1007/978-3-319-00972-8_18,

18.1 Introduction

For the past 20 years there has been an active development of oil and gas fields on the shelf of the Russian Federation along with major construction projects of extensive submarine pipelines such as “Blue Stream”, “Dzhubga-Lazarevskoe-Sochi” and “South Stream”. All the submarine pipelines mentioned above cross the Black Sea shelf area (Fig. 18.1) with two of them – Blue Stream and South Stream – crossing the continental slope, which is the most hazardous area with regard to the formation of submarine landslides.

Though the shelf and continental slope of the Black Sea are broadly utilized for the purpose of oil and gas development as well as transportation, scientific publications devoted to prediction and mathematical modeling of submarine landslides are missing.

The presented manuscript aims to predict submarine landslide formation on the Caucasian shelf area and continental slope of the Black Sea. In accordance with the proposed scope, the following objectives were analyzed:

1. investigation of geological engineering conditions within the study area;
2. setting up a model to assess slope stability in accordance with the geological engineering conditions within the study area;

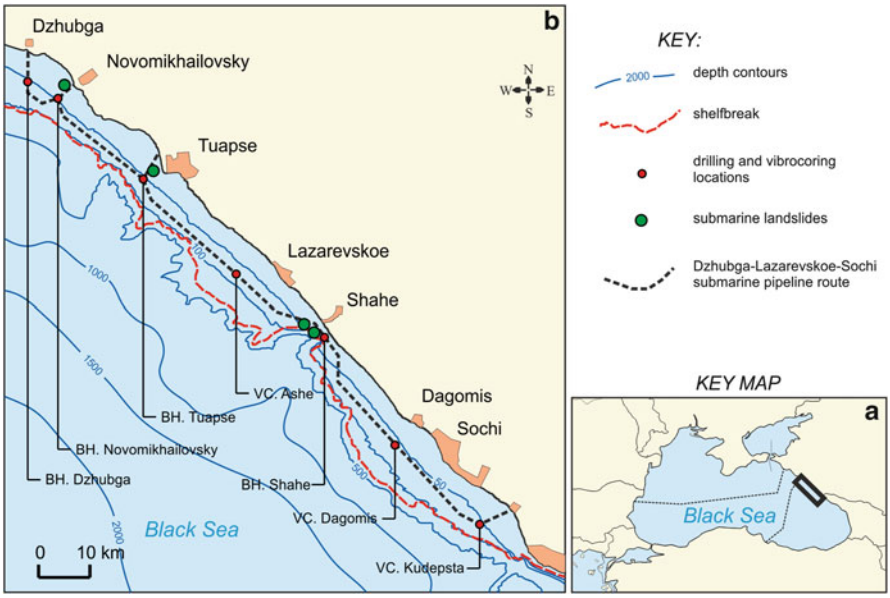

Fig. 18.1 (**a**) Map showing location of the study area (*black box*) and Blue Stream (Russia - Turkey) and South Stream (Russia - Bulgaria) submarine pipelines (*dashed lines* crossing the Black Sea). (**b**) Detailed map showing locations of analyzed cores (*BH* drilling, *VC* vibrocoring)

3. regional and local slope stability assessment within the study area on the Caucasian shelf.

The area shown on Fig. 18.1 was selected for the chosen approach.

18.2 Geological Engineering Conditions Along the Caucasian Shelf of the Black Sea

The shelf within the boundaries of the study area can be characterized as the abrasion-accumulative plain. Its width varies from 1.5 km (near Shahe village) up to 14 km (Sochi city, see Fig. 18.1 for locations). The shelf area can be divided into three zones: wave-cut bench, inner shelf and outer shelf.

The *wave-cut bench* forms a zone of abrasion type relief, which stretches as a narrow belt along the shoreline. Its width is about 500 m and it reaches a depth of about 8–15 m. The wave-cut bench zone is formed by rocks, which are associated with terrigenous-carbonate flysch deposits.

The *Inner shelf* forms a zone of accumulative relief. It is under the frequent influence of wave loading and is bounded by the 10 and 30 m depth contours.

The *Outer shelf* is also an accumulative type relief situated beyond the area of frequent wave loading influence. It is bounded by the shelf break. Here, the shelf area is rather flat with slope inclinations of less than 1° towards the shelf break. The shelf break itself is located in the depths ranging from 30 m (near the mouth of the Shahe River) up to 180 m (near Lazarevskoe village).

Geological engineering conditions of the study area were analysed on the basis of Peter Gaz LLC repository survey data, which include results of drilling, vibrocoring and geophysical surveying along the Dzhubga-Lazarevskoe-Sochi submarine pipeline route (geotechnical and geophysical cruises took place in 2008). The drilling and vibrocoring locations are 1–7 km off the shoreline and in the 15–70 m depth range. The geological section was examined and sampled to a depth of 20 m. The top 20 mbsf of the section are formed by the deposits of Paleocene-Eocene and Quaternary periods. Paleocene-Eocene deposits are presented by terrigenous and terrigenous-carbonate flysch. Quaternary sediments are unconformably overlying the flysch and are presented by a variety of sediment types (Table 18.1). Physical and mechanical properties of samples taken during the survey were determined in the onshore laboratory. All laboratory data was statistically reprocessed using a standard approach (GOST20522-96 1996). Physical and mechanical properties of Quaternary sediments are presented in the Table 18.1.

Sands with shells and shell debris are predominantly observed in the inner shelf zone. Mostly clayey sediments with high organic content and very soft to soft consistency may be observed in the outer shelf zone. Abundant shells and shell debris are found in these sediments. Quaternary sediments are deposited parallel to the seabed within the shelf and shelf break area. The geological setting in the shelf and shelf break area is not changing along the whole study area. Soft-sediment thickness in the shelf area is about 20 m according to geophysical data.

Table 18.1 Physical and mechanical properties of quaternary sediments on the Caucasian shelf of The Black Sea

					Triaxial shear tests			
					In terms of total stresses		In terms of effective stresses	
Soil type	Water content, %	Density, g/cm^3	Density of solid particles g/cm^3	Undrained Shear Strength, Cu, KPa	φ, deg	*c*, KPa	φ′, deg	*c*′, KPa
Very soft organic clay	45.6–105.5	1.44–1.79	2.63–2.76	2.4–13.0	8	10.5	13	10.5
	59.8 (0.13)	1.66 (0.04)	2.72 (0.01)	7.9 (0.26)				
Very soft organic silty clay	32.8–88.9	1.49–1.89	2.64–2.78	4.7–12.1	10	7.7	14	8.5
	49.2 (0.17)	1.75 (0.04)	2.71 (0.01)	7.7 (0.26)				
Firm clay and silty clay	32.4–56.2	1.67–1.91	2.64–2.74	6.5–21.0			15	9.8
	43.6 (0.159)	1.78 (0.04)	2.71 (0.01)	13.7 (0.42)				
Shells and shell debris	30.3–31.6	1.95–1.98	2.75–2.85				37	17
	30.6 (0.02)	1.97 (0.01)	2.79 (0.012)					
Gravelly sand with shells	25.5–28.7	1.97–1.99	2.71–2.78		33	15	34	15
	27.7 (0.03)	1.99 (0.01)	2.74 (0.01)					
Fine sand with shells	28.5–32.2	1.90–1.97	2.69–2.76		34	12	35	12
	30.0 (0.04)	1.94 (0.01)	2.72 (0.01)					
Fine sand	28.2–28.9	1.96–1.96	2.70–2.73				32	6
	28.8 (0.01)	1.96 (0)	2.73 (0.004)					
Silt	27.7–34.4	1.89–1.95	2.69–2.74		29	7	28	10
	31.1 (0.07)	1.92 (0.01)	2.71 (0.01)					
Very soft silty clay	33.7–37.8	1.87–1.89	2.69–2.76				25	12
	34.5 (0.01)	1.88 (0.004)	2.72 (0.01)					
Stiff clay and silty clay	35.5–38.0	1.80–1.88	2.71–2.73	25.0–39.0				
	36.8 (0.028)	1.85 (0.02)	2.72 (0.004)	32.0 (−)				

The numerator gives minimum and maximum values for individual soil types; the denominator shows mean values and the coefficient of variation (in *brackets*)

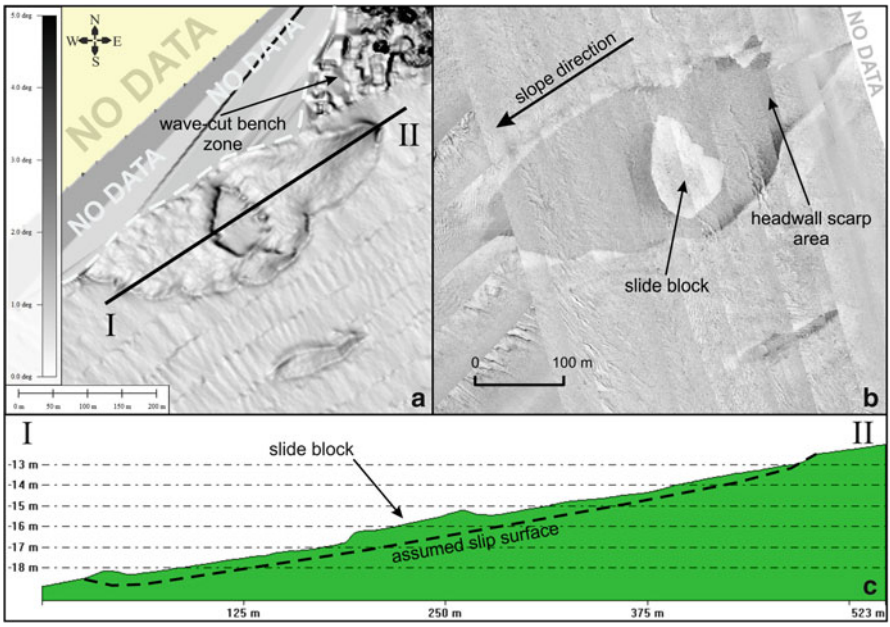

Fig. 18.2 (**a**) Part of the DTM (Global Mapper slope shader) showing the landslide area near Novomikhailovsky village. The *white dashed line* shows the edge of available bathymetric data. See Fig. 18.1 for location of slide. (**b**) Side-scan sonar image of the same area. (**c**) Profile across the landslide area (see (**a**) for profile location)

Very soft organic clay and *very soft organic silty clay* are the most widespread sediments in the study area. Thickness of these sediments at several sites reaches up to 12 m, and the layer's base lies at 16 m depth.

During the geological engineering survey on the Caucasian shelf of the Black sea between Dzhubga and Kudepsta villages, the authors discovered four submarine landslides in the inner shelf area (see Fig. 18.1 for location) by analyzing the digital terrain model (DTM). One of the discovered landslides is shown on Fig. 18.2. These landslides are about 1–2 m thick, up to 1,000 m long, and 500 m wide. According to the classification presented by Locat and Lee (2002) these landslides may be classified as translational slides. In general, average inclination of the surface within areas affected by landslides is not more than 1°. Length and width of the discovered landslides is 2–3 orders of magnitude larger than their thickness, which explains why these landslides form a thin deposit on top of the slightly inclined shelf surface.

Due to large spacing between sampling locations along the submarine pipeline route, none of the locations hit the landslide deposits. However, according to the sediments sampled closest to the landslide locations, we assume that landslide deposits are dominated by sandy soils.

For the territory of the Caucasian shelf and continental slope of the Black Sea, the most likely triggering mechanisms would include earthquakes, wave loading and human activity (e.g. bottom trawling, ship anchoring, dumping of soil, munitions clearance during submarine installations construction).

The presence of landslides in the study area indicates a necessity of slope stability assessment of Caucasian shelf of the Black Sea.

18.3 Methods

We follow a 1D approach based on limit equilibrium methods, which was utilized to perform the regional and local slope stability assessment.

Most limit equilibrium methods are based on the computation of a factor of safety along the slip surface (Duncan and Wright 2005). For static conditions, the following equation was used for the factor of safety (FS) computation (Hampton et al. 1996):

$$FS = \frac{c' \cdot \beta + W' \cdot \cos\alpha \cdot \tan\varphi'}{W' \cdot \sin\alpha} \tag{18.1}$$

where:

- FS – factor of safety,
- W' – submerged weight of a slice,
- β – length of the slice base,
- α – angle between the slice base (slip surface) and the horizontal,
- φ' - effective angle of internal friction,
- c' – effective cohesion.

In the present article, slope stability assessment was implemented with strength parameters in terms of effective and total stresses. Calculations with seismic and storm wave loading was performed only with strength parameters in terms of total stresses. For clayey soils, an additional analysis was carried out by means of undrained shear strength.

It is important to mention, that modeled profiles were used instead of real geological profiles during the 1D slope stability assessment. Modeled profiles are formed by one type of soil. Application of this approach is reasonable because width and length of discovered landslides is several orders of magnitude larger than their thickness; hence the modeled profiles may be seen as infinite objects. This approach anticipates a stability assessment along the whole slip surface, though it could be used for a single slice with a unit length base. Furthermore, it should be mentioned, that the slip surface is parallel to the seabed surface within the 1D slope stability approach.

Slope stability assessment was implemented for different inclinations of the seabed surface (1–40°) of the modeled profiles, thickness of the sliding mass

Table 18.2 Peak ground accelerations and seismic coefficients used during the slope stability assessment (degrees according to MSK-64 scale, VII – very strong earthquake, VIII – damaging, IX – destructive, and X – devastating earthquake)

	Degree (MSK-64)			
	VII	VIII	IX	X
Design ground acceleration, m/s^2	1	2	4	8
Seismic coefficient in horizontal direction	0.09	0.18	0.36	0.72
Seismic coefficient in vertical direction	0.0297	0.0594	0.1188	0.2376
	−0.0297	−0.0594	−0.1188	−0.2376

(1–20 mbsf), strength parameters (in total, effective stresses and with c_u) and for additional loading (seismic and storm wave). Thus, we suppose that the presented modeling approaches match with the geological engineering conditions of the study area and can be applied for preliminary landslide prediction purposes in the study area.

Slope stability analysis including seismic forces was implemented by means of seismic coefficients (pseudostatic approach) using the following equation (Ionov et al. 2012; Stability modelling with SLOPE/W, 2008):

$$FS = \frac{c \cdot \beta + (W' + k_v \cdot W) \cdot \cos\alpha \cdot \tan\varphi}{(W' + k_v \cdot W) \cdot \sin\alpha + k_h \cdot W \cdot \cos\alpha} \tag{18.2}$$

where:

- c – cohesion in terms of total stresses,
- φ – angle of internal friction in terms of total stresses,
- W – total weight of slice,
- k_h and k_v – seismic coefficients in horizontal and vertical direction accordingly.

Slope stability assessment was implemented for seismic loading with intensity VII to X (degrees according to Medvedev-Sponheur-Karnik scale or MSK-64). All seismic coefficients used in the calculations are presented in Table 18.2.

Storm wave loading was applied in the modeling process using the equations presented by Seed and Rahman (1978):

$$FS = \frac{c \cdot \beta + W' \cdot \cos\alpha \cdot \tan\varphi}{W' \cdot \sin\alpha + \dfrac{\gamma_\omega \cdot H \cdot z \cdot \pi}{L \cdot \cosh\left(\frac{2\pi d}{L}\right)}} \tag{18.3}$$

where:

- z – is the distance from the seabed to the slip surface,
- γ_w – the unit weight of water,
- H – wave height,
- L – wave length,
- d – water depth.

Table 18.3 Extreme wave parameters for the Caucasian shelf of the Black Sea between Dzhubga and Kudepsta villages

Return period	Water depth, m	Wave height, m Probability 0.1 %	Wave height, m Probability 50 %	Mean wave length, m
10 years	60	10.5	3.5	118
	20	6.1	2.2	70
100 years	60	13.6	4.6	152
	20	7.2	2.7	80

Extreme wave parameters for 10 and 100 years periods were used during the calculations (Table 18.3). Wave heights are presented for 0.1 and 50 % probabilities.

18.4 Regional Submarine Slope Stability Assessment Based on 1D Modelling

Slope stability assessment was carried out according to the model described above for each type of soil of the study area (Table 18.1).

Modeling results indicate that soils in the shelf area stay stable for static conditions (without additional triggers). Closer to the shelf break with increasing surface inclination, landslide formation, however, becomes possible even for static conditions. The most unstable soil is *very soft organic clay*. It should be mentioned that this type of soil is most widespread within the study area. According to the modeling within the shelf break area, formation of landslide with a thickness of up to 16 m is possible for static conditions.

Results for sandy soils essentially differ from those derived for very soft and soft clayey types of soils. Strength parameters for sandy soils are higher than for clayey soils. This difference is caused by the fact that sandy soils occur predominantly in the inner shelf zone and these soils are subjected to frequent storm wave loading. Calculations revealed that failure in sandy soils are almost independent from the strength parameters used in the model, either in terms of effective or total stresses. For static conditions, sandy soils in the shelf area and on relatively gentle sites of continental slope area stay stable. A failure in sandy soils on the continental slope will occur only at sites where the surface inclination exceeds 28°.

In general, the modeling results for static conditions show that gravitational forces are not sufficient for landslide formation in the shelf area.

Slope stability assessment with applied seismic loading shows that landslides are likely to occur in very soft and soft clayey soils both in the shelf area and in the continental slope area with seismic intensities of more than VII. In sandy soils within the shelf area, landslides may appear with seismic intensities of XI–X, and on the continental slope with seismic intensities of VII–VIII and more.

According to the modeling with applied storm wave loading, landslides may predominantly form in very soft and soft clayey soils. Formation of landslides triggered by storm waves in sandy soils may only be possible in the shelf break area, especially near the mouth of Shahe River.

18.5 Local Submarine Slope Stability Assessment Based on 1D Modelling

1D modelling results were also used for local slope stability assessment for several sites shown on the Fig. 18.1.

Local slope stability assessment was done using borehole and vibrocoring data; lithological information of these cores are shown on Fig. 18.3. Seabed surface inclination for all studied sites does not exceed 1°.

18.5.1 Dzhubga

For static conditions, this site is considered as stable. With respect to seismic loading landslides formation would occur only with seismic intensities greater than VII. It

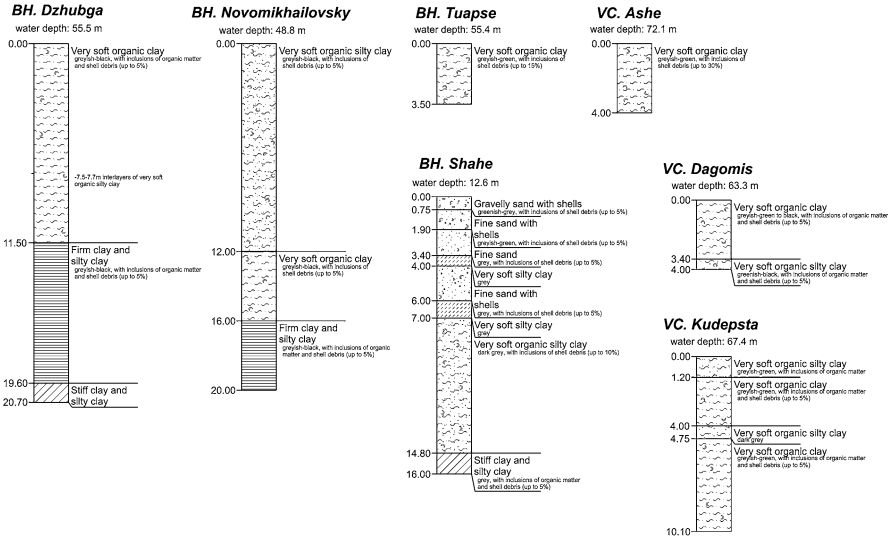

Fig. 18.3 Boreholes and vibrocores showing the most typical geological profiles of Caucasian shelf of the Black Sea used for local 1D slope stability assessment (see Fig. 18.1 for location of sites)

should be mentioned that the entire soil profile would then be affected by landslide processes. Modelling with storm wave loading indicates that failure may only occur at maximum wave heights of 13.6 m, and with undrained shear strength applied in the calculations. In this case, the sliding mass would be 10–20 m thick.

18.5.2 Novomikhailovsky

For static conditions the whole Quaternary soils stay stable. Landslides may occur only with seismic loading with intensity greater than VII. In this case, the whole thickness of soil mass becomes unstable. According to the modelling with applied storm wave loading (wave height of 13.6 m) the soil at depth up to 10 mbsf will stay in limit equilibrium, but from 10 to 20 m depth the soil mass would become unstable.

18.5.3 Tuapse

The available core for Tuapse is only 3.5 m long. For static conditions the soil mass stays stable. Modeling with applied seismic loading indicates that very soft organic clays become unstable with seismic intensity greater or equal to VII, if the slip surface is located at 5 mbsf and would stay stable if the slip surface is located at 2 mbsf. Therefore, if very soft organic clays occur at 5 m depth below the seabed, the soil mass would become unstable. If very soft organic clays are underlain by soil with higher strength parameters the whole soil mass would stay stable. Our storm wave loading model suggests that the soil mass would stay stable up to 3.5 mbsf. If the base of very soft organic clays lies at depths of 20 mbsf landslide formation would be possible with extreme wave heights such as $>$13 m.

18.5.4 Ashe

Due to identical geological setting of this location with the Tuapse location, all results are comparable to it.

18.5.5 Shahe

The borehole is located on the shelf and 470 m away from the shelf break at 12.6 m water depth. The width of the shelf area near the mouth of Shahe river is 1.5 km and the shelf break is located at water depths about 15–30 m. Inclination of the seabed

surface in the shelf break area does not exceed 15°. Assuming a low variability of geological engineering conditions across the shelf area, it is likely that geological profiles in the shelf break area close to the Shahe submarine canyon would be the same as the studied borehole location and, therefore it is reasonable to extrapolate the modeling results for Shahe borehole to the shelf break.

For static conditions, the examined shelf area stays in stable condition. In the shelf break area, landslide formation may be related to *very soft organic silty clays* (7.0–14.8 mbsf). Under earthquake loading in the shelf and shelf break area, landslide formation is possible with seismic intensities larger than VII. Modeling with applied storm wave loading indicates that landslide may occur in the shelf break area with *very soft organic silty clays* at wave heights of 2.2 or 7.2 m.

18.5.6 Dagomis

Modeling in static conditions shows that examined soil mass stays stable. Calculations with applied seismic loading revealed that a soil mass with a thickness >5 m becomes unstable under seismic loading with an intensity of VII. According to the modeling with applied storm wave loading, the examined soil mass stays stable. However, if the base of the very soft sediments layer is located at 20 mbsf, landslides may occur with waves of 13.6 m height.

18.5.7 Kudepsta

For static conditions the examined soil mass stays stable. Under seismic loading with intensity of VII the soil mass becomes unstable and in this case, the maximum thickness of the sliding mass would be 5 m and more. Storm wave modeling indicates that landslides with thickness of 10 m may occur on the Kudepsta location with wave heights exceeding 13.6 m.

18.6 Discussion and Conclusion

In the present article we investigated geological engineering conditions along the Caucasian shelf of the Black Sea. Four submarine landslides are present in the study area where slope inclination of the seabed surface is about 1°. The sliding masses presumably are represented by different types of sand. The landslides may be classified as translational slides. The most likely triggering mechanisms are earthquakes and storm waves. Slope stability assessment was carried out for the purposes of examining possible triggering mechanisms.

Regional slope stability assessment revealed that the shelf area is stable implying that submarine landslides only occur if additional triggers are present, whereas landslides may occur on the continental slope only under gravitational force loading.

Local slope stability assessment indicates that in static conditions all seven locations examined within the shelf area are stable. We would expect formation of massive landslides within the shelf area during an earthquake of seismic intensities of VII and higher. In addition, storm wave loading may also trigger landslides on all examined locations. It should be mentioned that landslides may only occur if we consider extreme wave heights such as >13 m in water depth of 60 m, which is very unlikely for the Black Sea according to statistical data (see Table 18.3).

Interestingly, a landslide with thicknesses of about 15 m is likely to occur even under static conditions and with storm wave heights of 2.2 and 7.2 m at the drilling location near Shahe village located very close to the shelf break.

It should be mentioned that triggering mechanisms for the four discovered landslides were not revealed.

Acknowledgements The authors would like to thank Dr. Katja Lindhorst, Dr. Vadim V. Pendin, Ivan Aschaulov, and Dr. Sebastian Krastel for critically reviewing and improving this manuscript. We also thank all Peter Gaz LLC employees who participated in "Dzgubga-Lazarevskoe-Sochi" submarine pipeline project especially Ksenia S. Popova, Sergey M. Kleschin, Denis A. Naumenko, Alexander P. Demonov, Irina A. Ostroverkhova, Olga A. Verbitskaya, Yuri A. Reva, Dmitry E. Besedin, Dmitry A. Savin.

References

Duncan J, Wright S (2005) Soil strength and slope stability. Wiley, Hoboken

GOST 20522–96. Soils. Statistical Treatment of the Test Results (1996) Minstoy Rossii. MNTKS, Moscow

Hampton M, Lee H, Locat J (1996) Submarine landslides. Rev Geophys 34(1):33–59

Ionov V, Kalinin E, Fomenko I et al (2012) Submarine landslides formation in the shelfbreak sediments of The Black Sea near Archipo-Osipovka. Injenernaya Geologiya 5:36–46

Locat J, Lee H (2002) Submarine landslides: advances and challenges. Can Geotech J 39:193–212

Seed H, Rahman M (1978) Wave-induced pore pressure in relation to ocean floor stability of cohesionless soils. Mar Geotechnol 3:123–150

Stability Modeling with SLOPE/W 2007 Version. An Engineering Methodology (2008) GEO-SLOPE International Ltd., Canada

Chapter 19
A Semi-empirical Method to Assess Flow-Slide Probability

Geeralt A. van den Ham, Maarten B. de Groot, and Dick R. Mastbergen

Abstract Flow-slides in submerged slopes in non-lithified sand and silt-sized sediments form a major threat for flood defences along (estuary) coastlines and riverbanks in the Netherlands. Flow slide is a complex failure mechanism including both soil mechanical and hydraulic features. Two important sub-mechanisms are static liquefaction and breaching. Both result in a flowing sand-water mixture, that eventually re-sediments under a gentle slope. Therefore, when analyzing historical flow slides it is often not clear to what extent static soil liquefaction and/or breaching played a role.

This paper presents a practical, semi-empirical method for assessing dike failure probability due to flow-sliding. It is based on statistical information about documented historical flow slides, in which the results of complex theoretical models, describing physics of static liquefaction or breach-flow, are incorporated.

Keywords Flow slides • Dike failure • Risk analysis

19.1 Introduction

Flow slides in submerged slopes in non-lithified sandy or silty sediments form a major threat for flood defences along (estuary) coastlines and riverbanks in the Netherlands. Such flow slides may result in severe damage to dikes and structures. Measures to prevent, mitigate, or repair the damage caused by flow slides are costly. Due to the complexity of flow slides, methods enabling an accurate quantitative risk assessment are under-developed, especially compared to methods currently available for other failure mechanisms (e.g. backward erosion below the dike or macro-instability of the dike).

G.A. van den Ham (✉) • M.B. de Groot • D.R. Mastbergen
Deltares, Delft, The Netherlands
e-mail: Geeralt.vandenHam@deltares.nl

S. Krastel et al. (eds.), *Submarine Mass Movements and Their Consequences*, Advances in Natural and Technological Hazards Research 37, DOI 10.1007/978-3-319-00972-8_19,

In the past, dike failure probability due to flow-sliding was predicted using either simple but conservative empirical rules based on documented historical flow slides, in which no distinction between sub-mechanisms such as static liquefaction or breach-flow was made, or rather complex theoretical models describing the physics of these sub-mechanisms. This paper presents how both approaches can be combined into a practical, semi-empirical method for assessing dike-failure probability due to flow-sliding, accounting for uncertainties of the main influence factors.

19.2 Failure Mechanisms

Flow slide includes both soil-mechanical and hydraulic features. Two important types are static soil liquefaction and breaching. Both result in a flowing sand-water mixture, exhibiting the same post-event failure scarp morphology, characterized by a very gentle slope. Therefore in the analysis of historical flow slides it is often not clear to what extent each of the two phenomena was responsible.

19.2.1 Static Liquefaction

Static soil liquefaction entails the sudden loss of strength of loosely packed saturated sand or silt, resulting in a sudden collapse of the sand body. Contrary to "ordinary" slope failure, in which the instable soil mass slides along a clear rupture surface while staying more or less intact, in a liquefaction flow slide the instable mass of sand (or silt) flows laminar like a viscous fluid.

Generally, for static liquefaction in an under-water slope the following conditions are required (1) the presence of a sufficiently large zone of loosely packed, non-lithified, and water-saturated sand or silt; (2) the stress state of the loosely packed sand elements should be close to the so-called metastability point (i.e. the intermediate maximum in the stress path). For this, both mean stress and shear stress should be sufficiently large, which is only the case in a sufficiently high and steep slope; and (3) the presence of a trigger, for example a (small) load change.

19.2.2 Breach Flow-Slide

Unlike liquefaction and "ordinary" shear slope failure, *breaching* only takes place at the sand surface: a local steep part of the slope, the so-called "breach", retrogresses upslope and generates a turbulent sand-water mixture flow over the sand surface downslope. The velocity and discharge of this mixture will grow by erosion of the sand surface and entrainment of ambient water if (a) the initial perturbation

generates a sufficiently high flow velocity carrying enough sand, and (b) if the local slope is steep enough. Since the retrogression velocity of the initial breach is relatively small a breaching flow slide generally takes much more time (several hours) than a liquefaction flow slide (several minutes).

Generally, for a breach-flow slide in an under-water slope the following conditions are required: (1) the presence of a sufficiently large zone of fine sand or silt; (2) a sufficiently high and steep slope; and (3) the presence of a trigger, for example scour or a local slope instability yielding a small but very steep slope section (breach).

19.3 Physical-Based Models

19.3.1 Static Liquefaction

Static liquefaction is widely discussed in literature (e.g. Jefferies and Been 2006). Examples of publications on the assessment of liquefaction-induced slope failure are Olson and Stark (2003) and Stoutjesdijk et al. (1998). Application of physical-based models usually requires an extensive local site-investigation and a large number of laboratory tests to assess necessary soil parameters. Insufficient accuracy in such assessments requires conservative estimations, resulting in unrealistically high failure probabilities.

19.3.2 Breach Flow-Slide

Validated equations governing the 1-dimensional stationary 2-layer flow and erosion processes, comparable with turbidity currents in combination with breaching can be found in Mastbergen and Van den Berg (2003). They are incorporated in the computer code HMBreach. The code allows assessing the sensitivity of an under-water slope with given geometry and sand properties to breaching, by calculating the minimum size of the initial breach for it to trigger a self-accelerating breach-flow. However, the tool has been validated only for restricted cases and the results are very sensitive to the applied friction and erosion model. Nor is exactly clear how the process develops when an upslope retrogressing breach reaches a contractive sand layer. Most likely, a local liquefaction flow slide, similar to the ones observed during large-scale flume tests (de Groot et al. 2012), will be initiated, which may trigger a breach flow slide upslope and/or downslope of a failed slope section.

A more advanced fully 3-dimensional flow model including turbulence generation, density flow, and sand transport processes is being developed in the software Delft3D-Flow (Lesser et al. 2004). Recently, computations simulating a breach-flow slide in the Eastern Scheldt have been performed successfully. However, the results still have to be validated with HMBreach and (scarce) field measurements.

19.3.3 Applicability of Physical-Based Models

Application of the theoretical models describing (parts of) flow-sliding is costly and does not always result in a reliable prediction of the flow-slide probability. The prediction accuracy of a flow slide depends on the (statistical and systematic) uncertainty of the input parameters and imperfection of the theoretical models themselves. High-level expertise is required to estimate the flow-slide probability using theoretical models, even when knowledge is available on local soil properties, slope geometry, and possible triggers. Although the theoretical liquefaction and breach-flow models are capable to quantify the relative influences of geometry and soil parameters, the reliability of the estimated probability remains limited.

19.4 Empirical Method

19.4.1 Basic Information and Mean Flow-Slide Frequency

A purely empirical method is based on documented historical flow slides in Zeeland, in the southwest of the Netherlands, as described by Wilderom (1979) and summarised by Silvis and De Groot (1995). Zeeland is a group of islands separated by tidal estuary channels which are part of the Rhine-Meuse-Scheldt delta. This dynamic area is characterised by alternating sedimentation and erosion along the channels. The consequent continuous gradual change in geometry of the submerged slopes results from time to time in a flow slide. These are probably initiated by a trigger (such as a rapid drop of water level), shortly after gradual erosion and sedimentation have caused a critical combination of slope angle and slope height.

According to Wilderom, the total number of flow slides along estuary banks in Zeeland between 1800 and 1978 was approximately 710. From the total length of (merely unprotected) estuary banks of approximately 190 km, the frequency of flow slides was found to be 0.02/km/year. This frequency can be used as a first rough estimate of the flow-slide probability in a similarly dynamic area with similar slopes and similar soil conditions.

19.4.2 General Applicability to Other Regions in the Netherlands

To what extent can the experience in Zeeland be applied in other parts of the Netherlands? The dynamic character of the shoals and channels in Zeeland may be similar to that of other tidal estuaries, but it is less in rivers and even less so in lakes. Application of the probability of occurrence found in Zeeland would result in overestimation of flow-slide probability. The similarity in slope geometry needs to

be compared from case to case, as will be discussed below. The general similarity in soil conditions follows from a comparison between the geology of other parts in the Netherlands with that of Zeeland, as presented in the following sections.

The geological past of Zeeland is characterised by rapidly shifting coastlines. Generally the upper 30 m of soil consists of Holocene deposits. Most of these consist of (medium) fine sand, which, in general, is loosely packed due to high deposition rates. The variation in tidal currents often resulted in thin clay layers in between the thicker sand layers.

The depositional environments in which sand accumulations formed in other parts of the Netherlands have been rivers, tidal waters, open coast shorelines, coastal sand flats, and periglacial sand deserts (see for example Schokker et al. 2007). Loose packing of sand is present in all these deposits. The combination with clay and peat layers (determines dissipation of excessive pore pressures) makes these deposits sensitive to liquefaction (Hicks and Onisiphorou 2005).

Thus, soil conditions relevant for the occurrence of flow slides in other parts of the Netherlands can be considered to be generally similar. Nevertheless, *local* soil conditions may significantly deviate from the mean conditions in Zeeland and need to be considered for each case separately.

19.4.3 Influence of Local Soil Characteristics and Slope Geometry

Application of the mean probability on a flow slide may be justified for a specific stretch of slope which has the characteristics of a "mean slope". For cases with lower or higher packing or other slope characteristics the probability will be different. Below we discuss how the expected probability can be adjusted to local characteristics.

A first source of information for such adjustment can be found in Wilderoms documentation of each flow slide. It includes parameters of the under-water slope geometry prior to the flow slide and general information about the local soil conditions and triggers for various bank stretches along the shores of Zeeland. Part of this information is illustrated in Figs. 19.1 and 19.2.

Figure 19.1 shows the influence of the type of deposits. Generally, the flow-slide frequency decreases with increasing age of the deposits. There is, however, a large variability among the different bank stretches. Some are much more sensitive than others; others even show an opposite tendency with respect to the influence of geology. The variability shows the large influence of other factors than the soil type in geological terms.

Large variability can also be observed if only slope angle is considered (Fig. 19.2).

Although these data contain a wealth of information, until now it has only been used to relate average site properties to an average flow-slide probability (i.e. a mean slope height (H_R) of 24 m, a mean slope angle of 1:5, an estimated mean relative

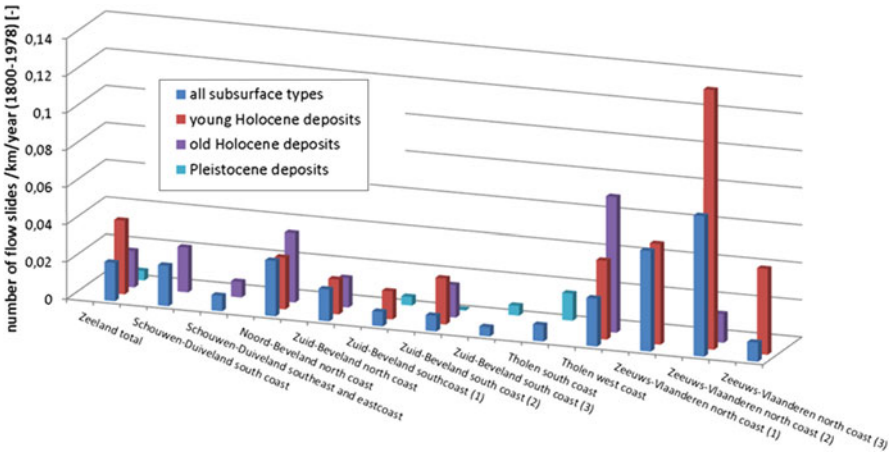

Fig. 19.1 Flow-slide frequency for all Zeeland banks documented by Wilderom (1979) and its 12 bank stretches as a function of geology

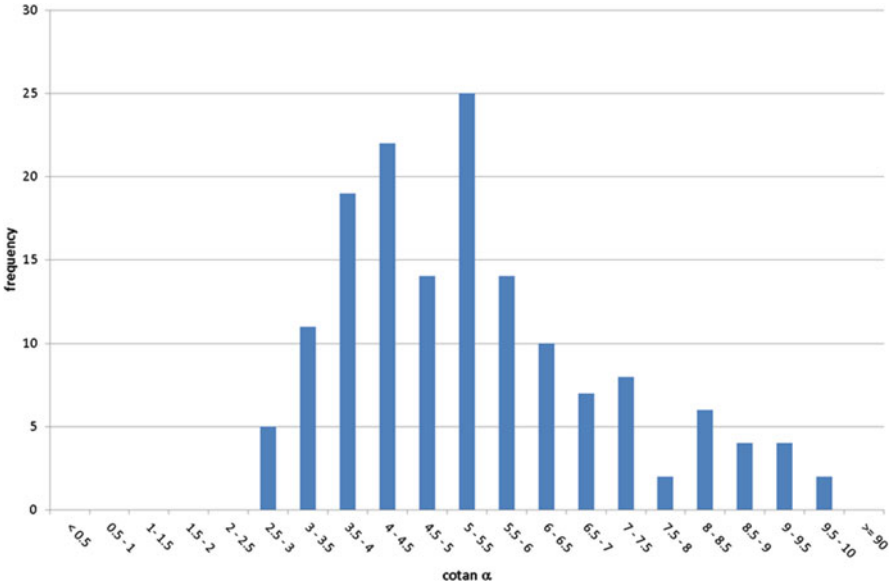

Fig. 19.2 Histogram with cotangent of average slope angle (α) of flow slides in Zeeland documented by Wilderom (1979)

density of 30 % (corresponding with $\psi = -0.05$, see Van Duinen et al. 2013) and an estimated mean median grain size of $2 \cdot 10^{-4}$ m). A multiple regression analysis would have been a good option, had the observations on the different site characteristics and flow-slide occurrences been paired. Unfortunately they were not.

19.5 Semi-empirical Method

Due to the limited possibilities for quantifying the influence of site characteristics on flow-slide probability using empiric data only, a semi-empirical method has been developed. The method takes the flow-slide probability for the mean slope as a starting point, and quantifies the influence of local deviations using the theoretical models described earlier.

Since other information is lacking, it may be assumed that half of all flow slides registered by Wilderom (1979) have been pure liquefaction flow slides while the other half concerned pure breach flow-slides (in reality many flow slides were presumably a combination of both mechanisms).

Therefore the flow-slide probability can be written as:

$$P\,(ZV) = 0.5 \cdot P\left(ZV_{liquefaction}\right) + 0.5 \cdot P\left(ZV_{breachflow}\right) \tag{19.1}$$

It is assumed that the occurrence of liquefaction is mainly influenced by (1) the stress state, which can be expressed by a so-called fictitious slope height (in which the influence of the above-water part of the slope is included (H_R)) and an average under-water slope angle (cotanα_R); and (2) the packing of the potentially liquefiable layer (expressed by relative density, I_D, or state parameter, ψ). The thickness of this layer is assumed to be 5 m, since this is the minimal thickness required for slope instability due to liquefaction.

Besides slope height and angle the occurrence of an unstable breach flow is assumed to be mainly influenced by medium grain size.

The probabilities on a liquefaction flow-slide and breach flow-slide can thus be expressed by:

$$P\left(ZV_{liquefaction}\right) = f1\,(H_R) \cdot f2\,(cotan\alpha_R) \cdot f3\,(density) \tag{19.2}$$

and

$$P\left(ZV_{breachflow}\right) = f4\,(H_{RB}) \cdot f2\,(cotan\alpha_R) \cdot f5\,(D_{50}) \cdot f6\,(claylayers) \tag{19.3}$$

which can, together with Eq. (19.1), be combined into:

$$P\,(ZV) = f2\,(cotan\alpha_R) \cdot \{0.5 \cdot f1\,(H_R) \cdot f3\,(density) + 0.5 \cdot f4\,(H_{RB}) \cdot f5\,(D_{50}) \cdot f6\,(claylayers)\} \cdot 0.02km^{-1} \cdot year^{-1} \tag{19.4}$$

Note that for breach flow the definition of slope height may be different than for liquefaction. For that reason different symbols are used (H_R vs. H_{RB}).

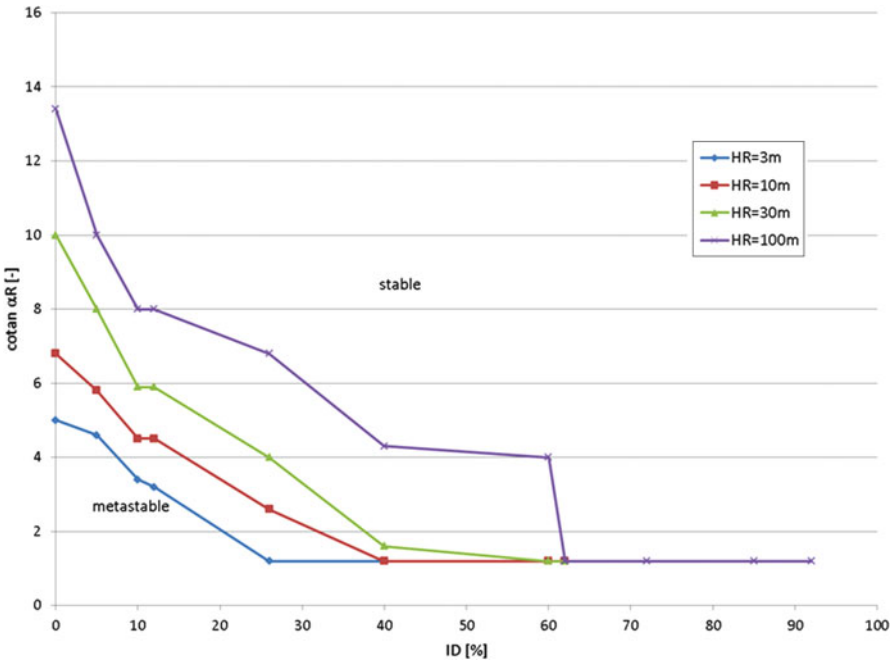

Fig. 19.3 Influence slope height (H_R), slope angle (cotα) and relative density (I_D) on the occurrence of metastability, as calculated with SLIQ2D (Modified from Stoutjesdijk et al. 1998)

19.5.1 Determination of P(ZV$_{liquefaction}$)

Figure 19.1 shows that the flow-slide frequency in "young Holocene deposits" is roughly twice as much as in "old Holocene deposits". Thus the frequency increases by a factor two if the relative density decreases by 10 %, or a corresponding increase of the state parameter by 0.05.

From sensitivity analyses with the liquefaction programme SLIQ2D (Stoutjesdijk et al. 1998) it appears that a decrease in relative density has roughly the same effect on the size of the metastable area as an increase of the slope height by a factor three (e.g. from 10 to 30 m) or an increase of slope angle by a factor 1.5 (e.g. from 1:6 to 1:4), see Fig. 19.3.

This leads to:

$$f1\,(H_R) = \left(\frac{H_R}{24}\right)^{2.1} \tag{19.5}$$

$$f2\,(cotan\alpha_R) = \left(\frac{5}{cotan\alpha_R}\right)^{5.7} \tag{19.6}$$

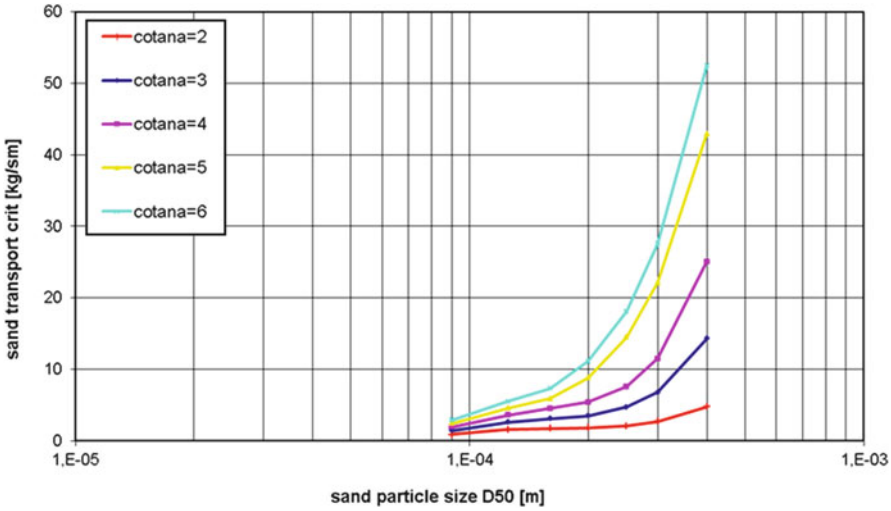

Fig. 19.4 Influence of grain size and slope angle on critical perturbation according to HMBreach

$$f3\,(density) = \left(\frac{1}{3}\right)^{\mathbf{10}\cdot(I_D-\mathbf{0.3})} \tag{19.7}$$

In the above equations the term describing the influence of relative density $\left(\frac{1}{3}\right)^{\mathbf{10}\cdot(I_D-\mathbf{0.3})}$ can be replaced by a term based on state parameter (ψ).

Reduction in slope angle from 1:5 to 1:11 yields a 100 times smaller probability. This agrees with the observations in Fig. 19.2.

Since it is unknown whether the flow slides registered by Wilderom are liquefaction or breaching flow-slides, the term $\left(\frac{5}{cotan\alpha_R}\right)^{5.7}$ applies for breach flow-slides as well.

19.5.2 Determination of P(ZV$_{breachflow}$)

Figure 19.4 presents the result of a series of HMBreach calculations for homogeneous sandy slopes. The critical value of the initial breach, i.e. the value that just causes a self-accelerating turbulent sand-water mixture flow and here expressed as sand transport sz, is presented on the vertical axis. The horizontal axis presents the mean grain size, whereas each curve is valid for a certain slope angle. The same value of the critical initial breach is assumed to correspond to the same probability on a breach flow. This makes clear that a decrease in grain size from $D_{50} = 2 \cdot 10^{-4}$ m to $1.25 \cdot 10^{-4}$ m yields the same value of the critical perturbation (i.e. sz = 5 kg/sm) if the slope angle is reduced from cotan$\alpha = 4$ to cotan$\alpha = 6$.

This means that f5 can be expressed as:

$f5\,(D_{50}) = \left(\frac{2\cdot10^{-4}}{\boldsymbol{D_{50}}}\right)^{\boldsymbol{E}}$ where $\frac{f5\left(1.25\cdot10^{-4}\right)}{f5\left(2\cdot10^{-4}\right)} = \frac{f2(6)}{f2(4)}$ or $\left(\frac{1.25\cdot10^{-4}}{2\cdot10^{-4}}\right)^{E} = \left(\frac{6}{4}\right)^{5.7}$, which yields E = 5.

In a similar way $f4\,(H_{RB}) = \left(\frac{\boldsymbol{H_{RB}}}{\boldsymbol{24}}\right)^{\boldsymbol{D}}$ with $D = 4$ is found.

Finally $f6$ is introduced because the presence of cohesive layers within the sand body increases the probability of a trigger. Undermining of these layers by the upslope moving breach may cause these layers to break down resulting in a sudden increase in the height of the vertical breach. This leads to a sudden increase in sand discharge and increase of erosion. Cohesive layers start to play a role if their (individual) thickness is larger than 0.5 m. If their thickness exceeds 5 m it can be assumed that the breach will stop.

In case a small number of relatively thin clay layers is present, as in the Holocene deposits in Zeeland, $f6\,(claylayers) = F = 1$ holds. Since the present version of HMBreach cannot account for cohesive layers, values for F for other situations have been estimated. F may vary between 1/3 (no clay layers) to 3 (many clay layers).

This results in:

$$\boldsymbol{P}\,(ZV) = \left(\frac{5}{cotan\alpha_R}\right)^{5.7}\left\{0.5\cdot\left(\frac{H_R}{24}\right)^{2.1}\cdot\left(\frac{1}{3}\right)^{10\cdot(I_D-0.3)} + 0.5\cdot\left(\frac{H_{RB}}{24}\right)^{4}\cdot\left(\frac{2\cdot10^{-4}}{D_{50}}\right)^{5}\cdot F_{cohesivelayers}\right\}\cdot 0.02\ \mathrm{km}^{-1}\cdot year^{-1} \tag{19.8}$$

19.6 Concluding Remarks

The presented semi-empirical method for calculating the probability of occurrence of flow slides has a solid base in the documentation of historical flow slides. The incorporation of the results of theoretical models describing the physics is promising, but needs further development. The theoretical models on breach flow-slide need further development and validation, including the interaction with static liquefaction. The respective factors in the semi-empirical equation need to be adapted accordingly. The role of the dynamic character of banks needs to be investigated such that the effects of gradual change of geometry and triggers can be incorporated. This will likely result in lower predicted probabilities for slopes in banks with a less dynamic character.

Acknowledgements The research is part of the programme "Strength and Loading on Flood Defence Structures" (SBW), funded by Rijkswaterstaat – Center for Water Management – on behalf of the Ministry of Infrastructure and the Environment, the Netherlands.
We kindly acknowledge Ir. Wim Kortlever of Rijkswaterstaat Dienst Infrastructuur and Dr. Janrik van den Berg of Utrecht University for reviewing the manuscript.

References

De Groot MB, Lindenberg J, Mastbergen DR, Van den Ham GA (2012) Large scale sand liquefaction flow-slide tests revisited. Eurofuge, Delft

Hicks MA, Onisiphorou C (2005) Stochastic evaluation of static liquefaction in a predominantly dilative sand fill. Géotechnique 55(2):123–133

Jefferies M, Been K (2006) Soil liquefaction – a critical state approach. Taylor & Francis, London/New York

Lesser GR, Roelvink JA, Van Kester JATM, Stelling GS (2004) Development and validation of a three-dimensional morphological model. Coast Eng 51(8–9):883–915

Mastbergen DR, Van den Berg JH (2003) Breaching in fine sands and the generation of sustained turbidity currents in submarine canyons. Sedimentology 50(4):625–637

Olson SM, Stark TD (2003) Yield strength ratio and liquefaction analysis of slopes and embankments. J Geotech Geoenviron Geol 129(8):727–737

Schokker J, Weerts HJT, Westerhoff WE, Berendsen HJA, Den Otter C (2007) Introduction of the Boxtel formation and implications for the quaternary lithostratigraphy of the Netherlands. J Geosci/Geologie en Mijnbouw 86(3):197–210

Silvis F, De Groot MB (1995) Flow slides in the Netherlands: experience and engineering practice. Can Geotech J 32:1086–1092

Stoutjesdijk TP, De Groot MB, Lindenberg J (1998) Flow-slide prediction method: influence on slope geometry. Can Geotech J 35(1):43–54

Van Duinen TA, Bezuijen A, Van den Ham GA, Hopman V (2013) Field measurements to investigate submerged slope failures. Submitted to 6th international symposium on submarine mass movements and their consequences, GEOMAR, Kiel, Germany, 23–25 September 2013

Wilderom NH (1979) Resultaten van het vooroeveronderzoek langs de Zeeuwse stromen. Rijkswaterstaat, Nota 75.2

Chapter 20
Submarine Slope Stability Assessment of the Central Mediterranean Continental Margin: The Gela Basin

Fei Ai, Jannis Kuhlmann, Katrin Huhn, Michael Strasser, and Achim Kopf

Abstract This study investigates slope stability for a relatively small scale (5.7 km^2, 0.6 km^3), 8 kyr old landslide named Northern Twin Slide (NTS) at the slope of the Gela Basin in the Sicily Channel (central Mediterranean). The NTS is characterized by two prominent failure scars, forming two morphological steps of 110 and 70 m height. Geotechnical data from a drill core upslope the failure scar (GeoB14403) recovered sediments down to ~52 m below seafloor (mbsf). The deposits show low over consolidation ratio (OCR = 0.24–0.4) and low internal friction angle (20–22°) around 28–45 mbsf, which suggests this mechanically weak interval may act as potential location of instability in a future failure event. Oedometer tests attest the sediments are highly under consolidated and the average overpressure ratio (λ^*) is ~0.7. Slope stability analyses carried out for different scenarios indicate that the slope is stable both under static undrained and drained conditions. A relatively small horizontal acceleration of 0.03–0.08 g induced by an earthquake may be sufficient to cause failure. We propose that moderate seismic triggers may have been responsible for the twin slide formation and could also cause mass wasting in the future.

Keywords Slope stability • Submarine landslide • Geotechnical characteristics • Central Mediterranean

F. Ai (✉) • J. Kuhlmann • K. Huhn • A. Kopf
MARUM-Center for Marine Environmental Sciences, and Faculty of Geosciences, University of Bremen, Leobener Straße, 28359 Bremen, Germany
e-mail: aifei@uni-bremen.de; jkuhlmann@marum.de; khuhn@uni-bremen.de; akopf@uni-bremen.de

M. Strasser
Geological Institute, ETH Zurich, Sonneggstrasse 5, 8092 Zurich, Switzerland
e-mail: strasser@erdw.ethz.ch

S. Krastel et al. (eds.), *Submarine Mass Movements and Their Consequences*, Advances in Natural and Technological Hazards Research 37, DOI 10.1007/978-3-319-00972-8_20,

20.1 Introduction

Submarine landslides are ubiquitous on continental margins. Overpressure near the seafloor plays a significant role in the occurrence of submarine landslides (Flemings et al. 2008). Seismic activity is considered as an important triggering mechanism of submarine landslides (Masson et al. 2006). It is therefore important to evaluate the effects of overpressure as a preconditioning factor and seismic shaking as triggering mechanism for submarine slope instability in earthquake-prone regions.

The study area is located between 200 and 800 m water depth along the eastern margin of the Gela Basin of the Sicily Channel, central Mediterranean. The continental slope has a general gradient (approx. 3°) and steep slide head scarps (up to 32° in places) (Fig. 20.1a). Two recent slides (termed Northern Twin Slide and Southern Twin Slide) show subrounded scars on the upper slope and are characterized by bathymetric bulges at the base of the slope (Minisini et al. 2007). These landslides are described as multiple failures likely controlled by specific stratigraphic surfaces acting as glide planes (Minisini and Trincardi 2009; Trincardi and Argnani 1990).

In order to provide a possibility to assess future slope instabilities due to overpressure and seismic shaking, undrained and drained infinite slope stability models are introduced to model slope stability under both static and pseudostatic conditions.

20.2 Geological Setting

The Gela Basin is the most recent (Plio-Quaternary) foredeep of the Maghrebian fold-and-thrust belt (Argnani et al. 1986). The extensional basin originated in the late Miocene to early Pliocene with the emplacement of the Gela nappe, which lasted until the early Pleistocene (Grasso 1993). Sequence stratigraphic interpretation on the shelf and upper slope area on the Gela Basin (Minisini and Trincardi 2009; Kuhlmann et al. 2013) identify, from top to bottom (Fig. 20.1b): (I) deposits resting on top of erosive unconformity ES1, (II) a progradational wedge pinching out towards NE and (III) deposits beneath sequence boundary SB1. In general, the studied northern slope of the Gela Basin shows high sedimentation rates of 85–250 mm/kyr area result of abundant supply of fine-grained material and tectonic subsidence (Emeis et al. 1996).

The NTS is characterized by two prominent failure scars forming two morphological steps of 110 and 70 m height (Fig. 20.1b). The slope angle of the slide headwall is around 16°, while the surfaces of the displaced masses dip at 1.5–4.5° (Minisini et al. 2007). The accumulation area of the NTS is characterized by a morphologic bulge at the seafloor which extends 7 km downslope and 1.5 km in width. The source area of the NTS is 5.7 km^2 and the average height of the failure section is approx. 100 m. The runout of the NTS is 11.7 km (Minisini et al. 2007).

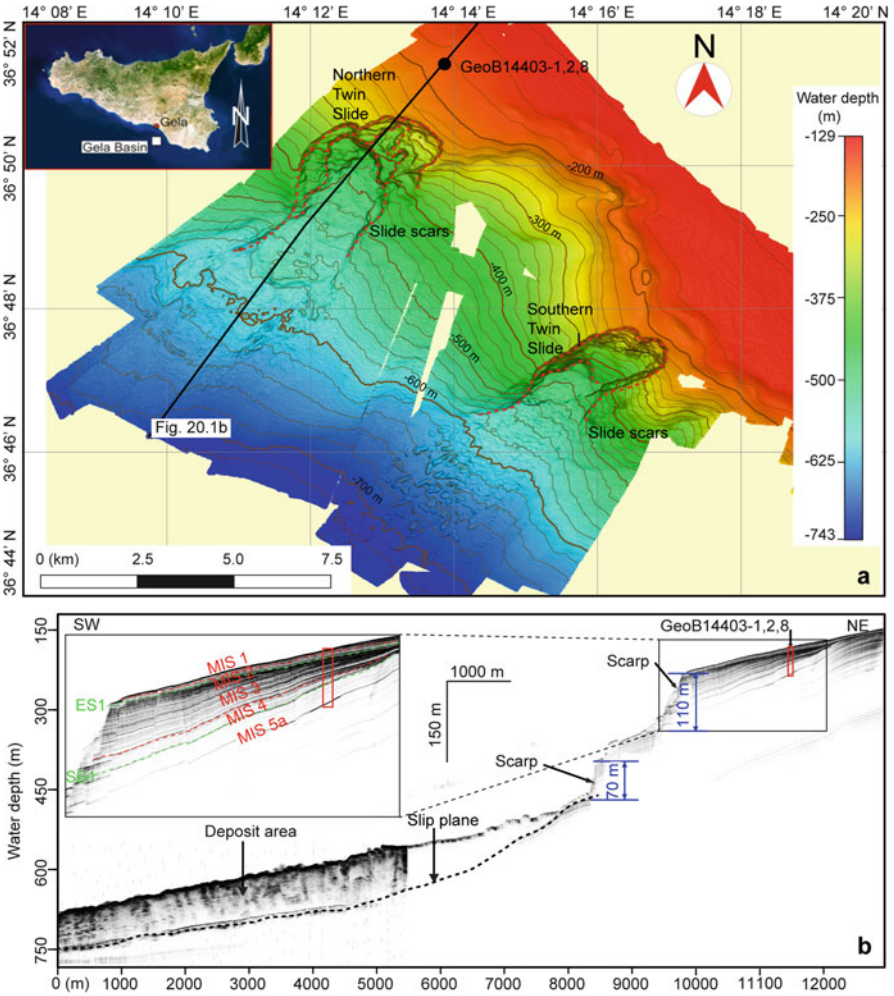

Fig. 20.1 (**a**) Overview map showing the morphology of the Twin Slides in the Gela Basin offshore Sicily (Italy). *Black dot* indicates the location of core GeoB14403. *Red dashed lines* indicate the scarps of the Twin Slides. *Black lines* indicate the locations of parasound profiles presented in (**b**). (**b**) Parasound sub-bottom profile crossing the NTS. *Red rectangle* shows the location of the core GeoB14403. *Green dashed lines* indicate the Erosion surface 1 (ES1) and the sequence boundary1 (SB1). *Red dashed lines* indicate the boundaries of different Marine Oxygen Isotope Stages (MIS) (Minisini et al. 2007; Kuhlmann et al. 2013). *Black dashed line* indicates the slip surface of the upper retrogressive landslide

20.3 Material and Methods

20.3.1 Shipboard and Laboratory Analysis

The principal data set for this study is based on a MeBo (MARUM seafloor drill rig) core and a co-located gravity short core, both acquired during Cruise MSM15/3 in 2010. A 51.9 m-long succession from the undisturbed slope apron upslope the NTS scar was recovered. Visual core description was carried out on board shortly after core recovery on the split core. Discrete samples were taken on board to measure water content and bulk density using oven drying method and pycnometer (Blum 1997). Undrained shear strength (S_u) was estimated using a Mennerich Geotechnik (Germany) vane shear apparatus (Blum 1997) and Wykeham Farrance cone penetrometer (Wood 1985).

Laboratory experiments consisted of grain size distribution analysis using a Beckman Coulter LS 13320 particle size analyzer and Atterberg limits using the Casagrande apparatus and rolling thread method (Casagrande 1932). Consolidation tests were performed using uniaxial incremental loading oedometer system (ASTM 2004a), with permeability being estimated from the consolidation test results (Lamb and Whitman 1969). The drained sediment strength parameters, cohesion (c') and internal friction angle (ϕ'), were determined using drained direct shear tests (ASTM 2004b).

20.3.2 Overpressure Estimation

Effective stress is an important parameter for slope stability analysis. Overpressure impacts the effective stress as seen in Terzaghi et al. (1996). Overpressure (Δu) is defined as fluid pressure (u) in excess of hydrostatic equilibrium (u_0) (Dugan and Sheahan 2012). The Terzaghi's effective stress relationship is:

$$\begin{aligned}\sigma'_v &= \sigma_v - u = \sigma_v - (u_0 + \Delta u) = (\rho_b - \rho_w)\, gz - \Delta u \\ &= (\gamma - \gamma_w)\, z - \Delta u = \gamma' z - \Delta u\end{aligned} \tag{20.1}$$

Where σ'_v is vertical effective stress, σ_v is total overburden stress, ρ_b is bulk density (assuming constant), ρ_w is density of water (assuming constant), γ is unit weight, γ_w is unit weight of water, γ' is buoyant weight, z is overburden depth, and g is the acceleration due to gravity.

Preconsolidation stress (σ'_{pc}) interpreted from consolidation test is an approach to evaluate overpressure (Casagrande 1936):

$$\Delta u = \sigma'_{vh} - \sigma'_{pc} \tag{20.2}$$

Where σ'_{vh} is vertical effective stress for hydrostatic conditions ($\sigma'_{vh} = \gamma' z$). The overpressure was used to perform back analysis of slope stability under drained conditions.

20.3.3 Slope Stability Analysis

The infinite slope stability analysis is used to calculate the factor of safety (*FS*). In the infinite slope approximation FS ≥ 1 represents stability and FS < 1 represents instability. For static conditions the *FS* calculation after Morgenstern (1967) and Løseth (1999) follows:

$$FS = \frac{S_u}{\gamma' z \sin\theta \cos\theta} \text{ (Undrained)} \tag{20.3}$$

$$FS = \frac{c' + \gamma' z \left(\cos^2\theta - \lambda^*\right) \tan\phi'}{\gamma' z \sin\theta \cos\theta} \text{ (Drained)} \tag{20.4}$$

Where θ is slope angle (also assumed angle for slip surface) and λ^* is overpressure ratio ($\lambda^* = \Delta u / \sigma'_{vh}$). The evaluation of slope stability under earthquake loading is commonly based on pseudostatic analysis (ten Brink et al. 2009; Morgenstern 1967). The overpressure that may be generated during an earthquake is not taken into account for the slope stability analysis. The seismic response included in the FS calculation is the integrated horizontal ground acceleration *kg* (where *k* is horizontal acceleration coefficient and *g* is the acceleration due to gravity), which is assumed to be applied over a time period long enough for the induced shear stress can to be considered constant.

$$FS = \frac{S_u}{\gamma' z \left[\sin\theta \cos\theta + k \left(\gamma / \gamma'\right) \cos^2\theta\right]} \text{ (Undrained)} \tag{20.5}$$

$$FS = \frac{c' + \gamma' z \left(\cos^2\theta - \lambda*\right) \tan\phi'}{\gamma' z \left[\sin\theta \cos\theta + k \left(\gamma / \gamma'\right) \cos^2\theta\right]} \text{ (Drained)} \tag{20.6}$$

The aim of the stability analysis is to estimate the static FS of the slope and the minimum seismic acceleration required to trigger a slope failure under undrained and drained conditions, respectively.

20.4 Results

20.4.1 Physical and Geotechnical Properties

The physical properties and geotechnical results are presented in Fig. 20.2. The dominant lithology is homogeneous silty clay to clayey silt with a narrow range

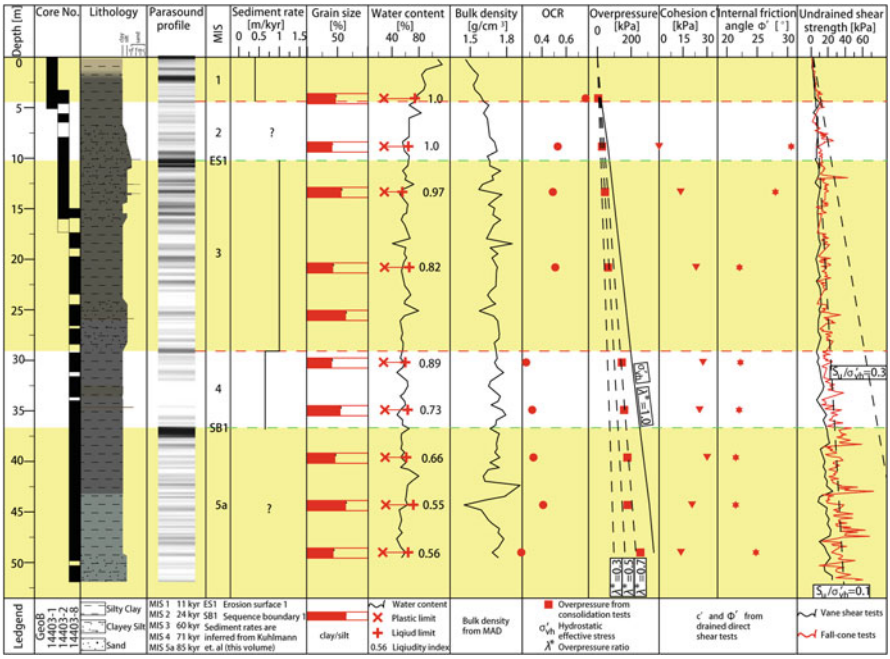

Fig. 20.2 Lithological, physical properties and geotechnical properties profile of core GeoB14403 for slope stability assessment

of particle sizes. The sediment's plastic limit is ~28 %, while the liquid limit ranges from 55 to 74 %. Natural water content is close to the liquid limit and gradually decreases with depth, while bulk density gradually increases with depth. Undrained shear strength values range from a few kPa near the seafloor to ~50 kPa at depth, where the pocket penetrometer generally shows slightly higher values than vane shear. The undrained shear strength-depth relation obtained from pocket penetrometer tests is: $S_u = 0.6z + 37$ (kPa, $R^2 = 0.64$). The sediment appears to be under consolidated as inferred from low ratios between the undrained shear strength and vertical effective stress at static condition ($S_u / \sigma'_{vh} \approx 0.1$) (Locat and Lee 2002).

Consolidation tests indicate sediments are slightly under consolidated ($OCR = \sigma'_{pc}/\sigma'_{vh} = 0.76$ at 4.08 mbsf)at shallow subsurface depth and become strongly under consolidated deeper downhole(OCR = 0.23 at 49 mbsf). Overpressures estimated from consolidation test results using Eq. 20.2 indicate that overpressure increases with depth and λ^* ranges from 0.24 to 0.77. Drained direct shear tests indicate that sediments from 28 to 45 mbsf have somewhat lower angle of internal friction (approx. 20°) compared to one sample from shallow depth (approx. 30°). Values of the effective cohesion intercept (c'), range from 0 to 30 kPa for granular to clay-rich sediments.

Table 20.1 Parameters used for slope stability calculations (Data derived from Fig. 20.2)

	Static or variable/value (in different scenarios)			
Input parameters	Undrained static	Drained static	Undrained seismic	Drained seismic
Undrained shear strength, S_u(kPa)	Static/0.6z + 3.7		Static/33.7	
Depth of the failure surface, z (m)	Variable/10–100		Static/50	
Slope angle, θ (°)		Variable/1–5.5		
Cohesion, c′ (kPa)	–	Static/23.5	–	Static/23.5
Internal friction angle, Φ′ (°)	–	Static/21	–	Static/21
Overpressure ratio, λ*	–	Variable/0.4–1.0	–	Static/0.7
Unit weight, γ (kN/m^2)	–	–	Static/16.4	
Horizontal acceleration coefficient, k	–	–	Variable/0–0.09	
Buoyant weight, γ′ (kN/m^2)		6.6		
Gravitational acceleration, g (m/s^2)		9.81		
FS/k	1.9/0	3.6/0	1/0.02	1/0.053

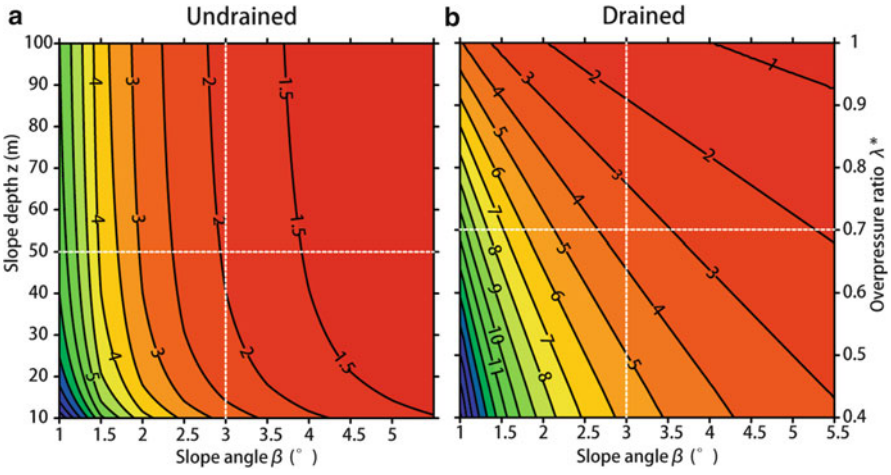

Fig. 20.3 Slope stability analysis under undrained (**a**) and drained (**b**) conditions for the NTS. *Contour plots* indicate FS values. *Dashed white lines* indicate current mean values of the parameters in the NTS

20.4.2 Slope Stability Analysis

Factor of safeties for four different cases were calculated using Eqs. 20.3, 20.4, 20.5, and 20.6 with two parameters changing within a certain range and other parameters keeping at constant value (Table 20.1 and Figs. 20.3 and 20.4). According to

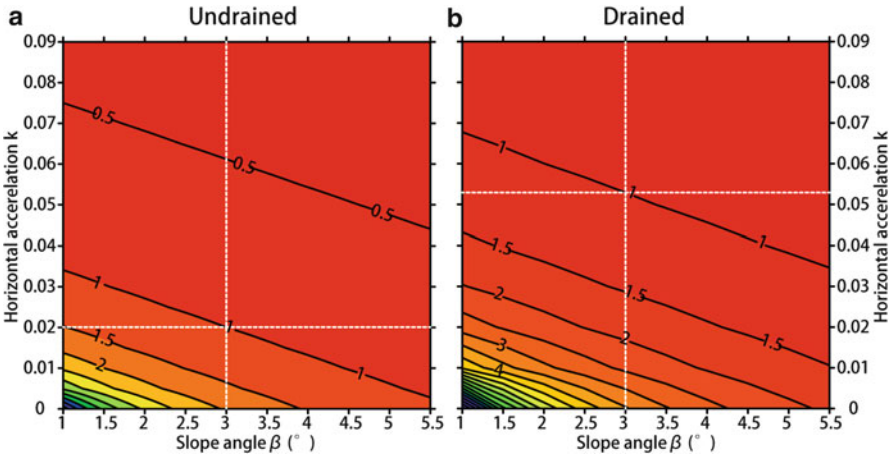

Fig. 20.4 Back-calculation of pseudostatic horizontal acceleration ratio showing FS as a function of slope angle and pseudostatic horizontal acceleration ratio under undrained (**a**) and drained (**b**) conditions for the NTS. *Contour plots* indicate FS values. *Dashed white lines* indicate the value of pseudostatic horizontal acceleration required to trigger slope failure (FS = 1) at current mean value of the slope angle

the parameters of current situation, the factor of safeties of static undrained and drained cases can be constrained (Fig. 20.3). Horizontal acceleration coefficients in earthquake undrained and drained cases were back-calculated using Eqs. 20.5 and 20.6 while FS = 1. The slope appears to be presently stable both under static undrained and drained conditions. The depth of the failure surface shows less influence on FS compared to slope angle in the undrained slope stability analysis. Overpressure ratios $\lambda^* \geq 0.93$ are required to fail a drained slope at an angle of 5.5°. Pseudo-static analysis indicates that slope is vulnerable in undrained earthquake case. Horizontal acceleration coefficient $k = 0.02$ is need to trigger slope failure in undrained earthquake case, while higher horizontal acceleration coefficient ($k = 0.053$) is required to trigger slope failure (FS = 1) at current mean values of the slope angle (3°) in drained earthquake case.

20.5 Discussion

20.5.1 Preconditioning Factors

Generally factors such as high sedimentation rate, slope steepening and the presence of intrinsically weak layer scan greatly reduce the factor of safety of slope under static loading conditions. High sedimentation (≥m/kyr) of low permeability sediments (permeability $\leq 10^{-16}$ m^2) can generate overpressure, a condition known

as under consolidated (Dugan and Sheahan 2012). Undrained shear tests and consolidation tests presented here suggest the sediments are strongly under consolidated (OCR = 0.27–0.77). The state of overpressure in the Gela basin most likely results from deposition of fine-grained sediments with high sedimentation rates. Based on seismostratigraphic interpretation and shallow cores a high sedimentation rate (0.3–0.6 m/kyr) was proposed since the Last Glacial Maximum at 18–24 kyr B.P. (Minisini and Trincardi 2009). Kuhlmann et al. (2013) estimate the sedimentation rate was ~0.5 m/kyr during MIS 1 and ~1 m/kyr during MIS 3 according to results from the MeBo core recovered in the undisturbed slope apron of the NTS. Based on our oedometer experiments, the coefficient of permeability of sediment is on the order of 10^{-10} m/s (permeability $\leq 10^{-16}$ m^2). Such a low permeability may inhibit fluid seepage and thereby induce the overpressure buildup (Dugan and Sheahan 2012).

The slope stability analysis suggests the slope angle has a larger influence on the FS than on depth of failure plane. Since FS decreases with increasing slope angle, one possible mechanism for failure could be rapid wedge-shaped sediment accumulation during sea level low stand (Minisini et al. 2007) or bottom currents leading to net erosion and undercutting the toe of slope (Bennett and Nelsen 1983). Both mechanisms have been hypothesized to occur in the study area (Minisini et al. 2007; Verdicchio and Trincardi 2008). Based on low internal friction angle derived from direct shear test, sediments from 28 to 45 mbsf appear to be weaker, potentially forming a preferential slip plane for future slope failure. Slope stability analysis further suggests the slope is stable in static conditions. To reach FS = 1 or lower, an overpressure ratio of 0.93 at slope angle of 5.5° would be required, which is not observed at present. Hence additional triggers are needed to generate slope failure.

20.5.2 Triggering Factors

Pseudostatic slope stability analysis suggests that pseudostatic horizontal acceleration in the order of 0.02–0.053 g is required to fail the slope (FS = 1) in undrained as well as drained conditions. Strasser et al. (2011), based on the principles by Seed and Idriss (1971) and Seed (1979), suggested that the pseudostatic horizontal acceleration only represent ~65 % of the effective earthquake peak ground acceleration (PGA = 0.03–0.08 g). In order to explore plausible scenarios for earthquake events, which might induce seismic shaking in this intensity range and thus could trigger slope failure of the NTS, PGA is estimated using empirical attenuation equations after Bindi et al. (2011) that depend on the combination of magnitude and source distance of earthquake (Fig. 20.5).

The Sicily channel show slow seismic activity (Fig. 20.5a). Over the last 40 year, only small earthquakes occurred, which are too low to trigger instabilities (Fig. 20.5b). The attenuation relationship combined with the critical threshold condition for instability, as revealed from our analysis, indicates that moderate earthquakes with magnitudes M = 4.0–4.8 near or at the location of the study area,

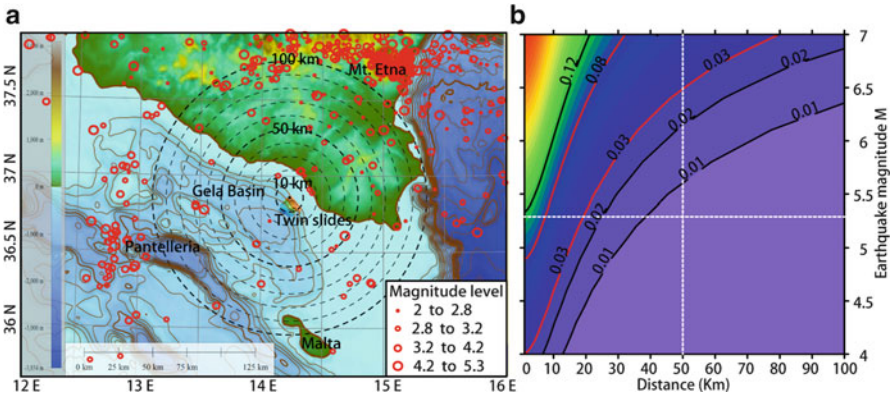

Fig. 20.5 (**a**) Earthquake record of the Sicily channel since 1970 (USGS database). *Dashed black circles* indicate the distance to the study area. *Red circles* indicate magnitude levels of earthquakes. (**b**) PGA estimation using empirical attenuation equations after Bindi et al. (2011) that depends on combination of magnitude and source distance of earthquake. *Contour plots* indicate the PGA. *Red lines* indicate the PGA values are required to trigger slope failure. *Dashed white lines* indicate the largest and closest earthquake in the study area during last 40 year

or strong (M = 7), far-field events in epicentral distance <20–80 km are required to trigger the slope failure. Past landslide occurrence in the study area indicates that over a longer time scale, larger magnitude earthquakes than those recorded during the instrumental period may have occurred. We propose that moderate seismic triggers may have been responsible for NTS formation and could also cause mass wasting in the future.

20.6 Conclusions

In summary, we have demonstrated geotechnical properties of sediments and slope stability analysis of the Gela Basin. Strongly under consolidation of the sediments in the study area are mainly attributed to rapid sedimentation in fine sediments. Despite of the high overpressure presented in the sediments, the stability analysis suggests the slope is stable under static conditions. Slope failure may be triggered by moderate earthquake (M4.0–M4.8) in the study area, or even strong events if farther away. Additional studies of in-situ pore pressure measurement and pore pressure change during the seismic loading are needed in order to further investigate the dynamic response and better assess the slope stability.

Acknowledgments We thank the captain and crew of the RV Meteor for their support during the cruise MSM 15/3. Matthias Lange is thanked for outstanding technical assistance with the geotechnical laboratory devices. This study has been funded through DFG-Research Center/Cluster of Excellence "The Ocean in the Earth System". We also like thank reviewers Brandon Dugan and Vasilios Lykousis for their constructive remarks.

References

Argnani A, Cornini S, Torelli L, Zitellini N (1986) Neogene-quaternary foredeep system in the strait of Sicily. Mem Soc Geol Italy 36:123–130

ASTM (2004a) Standard test methods for one-dimensional consolidation properties of soils using incremental loading (Standard D2435-04). ASTM International, West Conshohocken, p 10

ASTM (2004b) Standard test method for direct shear test of soils under consolidated drained conditions (Standard D3080-04). ASTM International, West Conshohocken, p 7

Bennett RH, Nelsen TA (1983) Seafloor characteristics and dynamics affecting geotechnical properties at shelf breaks. SEPM Spec Publ 33:333–355

Bindi D, Pacor F, Luzi L, Puglia R, Massa M, Ameri G, Paolucci R (2011) Ground motion prediction equations derived from the Italian strong motion database. Bull Earthq Eng 9(6):1899–1920. doi:10.1007/s10518-011-9313-z

Blum P (1997) Physical properties handbook: a guide to the shipboard measurement of physical properties of deep-sea cores. ODP Tech Notes 26:118

Casagrande A (1932) Research on the Atterberg limits of soil. Public Roads 13(8):121–136

Casagrande A (1936) The determination of the pre-consolidation load and its practical significance. In: Proceedings of the 1st international conference of soil mechanics and foundation engineering 3, pp 60–64

Dugan B, Sheahan TC (2012) Offshore sediment overpressures of passive margins: mechanisms, measurement, and models. Rev Geophys 50(3), RG3001. doi:10.1029/2011rg000379

Emeis K, Robertson A, Richter C (1996) Site 963. Proceedings ODP, Initial Report 160, pp 55–84

Flemings PB, Long H, Dugan B, Germaine J, John CM, Behrmann JH, Sawyer D, Scientists IE (2008) Pore pressure penetrometers document high overpressure near the seafloor where multiple submarine landslides have occurred on the continental slope, offshore Louisiana, Gulf of Mexico. Earth Planet Sci Lett 269(3–4):309–325. doi:10.1016/j.epsl.2007.12.005

Grasso M (1993) Pleistocene structures along the Ionian side of the Hyblean Plateau (SE Sicily): implications for the tectonic evolution of the Malta Escarpment. In: Max MD, Colantoni P (eds) Geological development of the Sicilian-Tunisian platform, vol 58, UNESCO report marine science. UNESCO, Paris, pp 49–54

Kuhlmann J, Asioli A, Strasser M, Trincardi F, Huhn F (2013) Integrated stratigraphic and morphological investigation of the Twin Slide complex offshore southern Sicily. In: Krastel S et al (eds) Submarine mass movements and their consequences. Springer, Heidelberg

Lamb TW, Whitman RV (1969) Soil mechanics. Massachusetts Institute of Technology, Cambridge, MA

Locat J, Lee HJ (2002) Submarine landslides: advances and challenges. Can Geotech J 39(1):193–212. doi:10.1139/t01-089

Løseth TM (1999) Submarine massflow sedimentation: computer modelling and basin-fill stratigraphy. Springer, New York

Masson DG, Harbitz CB, Wynn RB, Pedersen G, Løvholt F (2006) Submarine landslides: processes, triggers and hazard prediction. Philos Trans R Soc A Math Phys Eng Sci 364(1845):2009–2039. doi:10.1098/rsta.2006.1810

Minisini D, Trincardi F (2009) Frequent failure of the continental slope: the Gela Basin (Sicily Channel). J Geophys Res 114(F3), F03014. doi:10.1029/2008jf001037

Minisini D, Trincardi F, Asioli A, Canu M, Foglini F (2007) Morphologic variability of exposed mass-transport deposits on the eastern slope of Gela Basin (Sicily channel). Basin Res 19(2):217–240. doi:10.1111/j.1365-2117.2007.00324.x

Morgenstern NR (1967) Submarine slumping and the initiation of turbidity currents. In: Richards AF (eds) Marine Geotechnique. University of Illinois Press, Urbana, pp 189–210

Seed HB (1979) Considerations in earthquake-resistant design of earth and rock-fill dams. Géotechniques 29:215–263

Seed HB, Idriss IM (1971) Simplified procedure for evaluating soil liquefaction potential. J Soil Mech Found Div Proc Am Soc Civil Eng 97:1249–1273

Strasser M, Hilbe M, Anselmetti F (2011) Mapping basin-wide subaquatic slope failure susceptibility as a tool to assess regional seismic and tsunami hazards. Mar Geophys Res 32:331–347. doi:10.1007/s11001-010-9100-2

ten Brink US, Lee HJ, Geist EL, Twichell D (2009) Assessment of tsunami hazard to the U.S. East Coast using relationships between submarine landslides and earthquakes. Mar Geol 264(1–2):65–73. doi:http://dx.doi.org/10.1016/j.margeo.2008.05.011

Terzaghi K, Peck RB, Mesri G (1996) Soil mechanics in engineering practice. Wiley Inter Science, New York

Trincardi F, Argnani A (1990) Gela submarine slide: a major basin-wide event in the plio-quaternary foredeep of Sicily. Geo-Mar Lett 10(1):13–21. doi:10.1007/bf02431017

Verdicchio G, Trincardi F (2008) Mediterranean shelf-edge muddy contourites: examples from the Gela and South Adriatic basins. Geo-Mar Lett 28(3):137–151. doi:10.1007/s00367-007-0096-9

Wood DM (1985) Some fall-cone tests. Geotechnique 38:64–68

Part IV
Monitoring, Observation and Repeated Surveys of Active Slope Failure Processes

Chapter 21
The 1930 Landslide in Orkdalsfjorden: Morphology and Failure Mechanism

Jean-Sebastien L'Heureux, Oddvar Longva, Louise Hansen, and Maarten Vanneste

Abstract The 1930 landslide and associated 15-m high tsunami along the shore of Orkdalsfjorden, mid Norway, killed one person and caused major damage to port facilities. The combination of witness testimony with swath bathymetry data, high resolution seismic reflection data and gravity cores show that the failure propagated rapidly (up to 25 m/s) and progressively over a clay layer in a retrogressive manner. The volume of sediment evacuated downslope of the 8–12 m high and 3 km long headwall amounts $18.5 \cdot 10^6$ m^3 during this event. The transformation of the failed mass into a sediment gravity flow caused subsequent slope failures on the opposite side of the fjord and the breakage of submarine cables at distances of 3 and 18 km away from the initial landslide.

Keywords Historical landslide • Fjord • Morphology • Failure mechanism • Tsunami

21.1 Introduction

Landslides occur frequently along Norwegian fjords and are therefore a threat to coastal communities and near-shore facilities or infrastructure. In many cases, shoreline landslides develop following a common pattern, initiating offshore, retrogressing towards and in several cases across the shoreline and ultimately generating tsunamis (e.g. L'Heureux et al. 2011). The causes for these failures are not easy to pinpoint; however, this information is essential to correctly perform

J.-S. L'Heureux (✉) • M. Vanneste
Norwegian Geotechnical Institute (NGI), Oslo, Norway
e-mail: jean-sebastien.lheureux@ngi.no

O. Longva • L. Hansen
Geological Survey of Norway (NGU), Trondheim, Norway

S. Krastel et al. (eds.), *Submarine Mass Movements and Their Consequences*, Advances in Natural and Technological Hazards Research 37, DOI 10.1007/978-3-319-00972-8_21,

hazard assessment in such areas. To this aim, the analysis of past landslide events can give important knowledge on factors contributing to failure, landslide dynamics, the timing and the links between mass-wasting processes and their tsunamigenic potential. In this study, we investigate the 1930 landslide in Orkdalsfjorden, mid-Norway, using an integrated data set consisting of swath bathymetry data, high-resolution seismic reflection profiles and several gravity cores.

21.2 The 1930 Orkdalsfjorden Landslide

Orkdalsfjorden is an 11 km long tributary to the larger Trondheimsfjorden and is situated ~25 km southwest of Trondheim, mid Norway (Fig. 21.1b). The fjord basin is up to 400 m deep and has steep flanks. The water depth increases further northwards to more than 500 m in Trondheimsfjorden. A major river, Orkla, enters Orkdalsfjorden just north of the town of Orkanger.

The Orkdalsfjorden landslide occurred close to the mouth of the Orkla river in the early morning of May 2nd, 1930. The landslide was registered when about 1,250 m^3 of a minor recently-placed landfill disappeared into the fjord (location X; Fig. 21.1c). The failure occurred at 7:48 a.m. at an exceptionally low tide, and stretched ~500 m along the fjord (Bjerrum 1971). A few minutes later and approximately 2 km southwest, a 600- to 700-m-long stretch of land disappeared at Orkanger (location Y; Fig. 21.1). During this event, piers and harbour constructions were destroyed. A picture of the onshore encroachment is shown in Fig. 21.1d. Shortly afterwards, more shoreline failures took place on the opposite side of the fjord between 7:55 and 8:00 a.m. (location Z; Fig. 21.1c). This multiphase sequence of submarine landslides has, up to now, been considered to result from collapse and liquefaction of sandy material (Bjerrum 1971).

During the 1930 landslide event, an up to 15 m high wave caused severe damage to harbour installations and one man perished during this event. At 7:55 a.m., a telephone cable situated 3 km to the north of location X on Fig. 21.1b, and at a depth of 350 m, broke. This indicates that the landslide propagated with a velocity of approximately 7 m/s. Approximately 18 km further north along the fjord another cable was broken at 9:40 a.m. (Fig. 21.1b). This corresponds to a speed of 3.1 m/s since the occurrence of the initial landslide.

21.3 Data and Methods

Bathymetric data from Orkdalsfjorden were collected in 2003 and again in 2009 using a 250 kHz interferometric sidescan sonar system (GeoAcoustics) mounted onboard the R/V Seisma. The bathymetric grids have 1 m by 1 m cell size. During

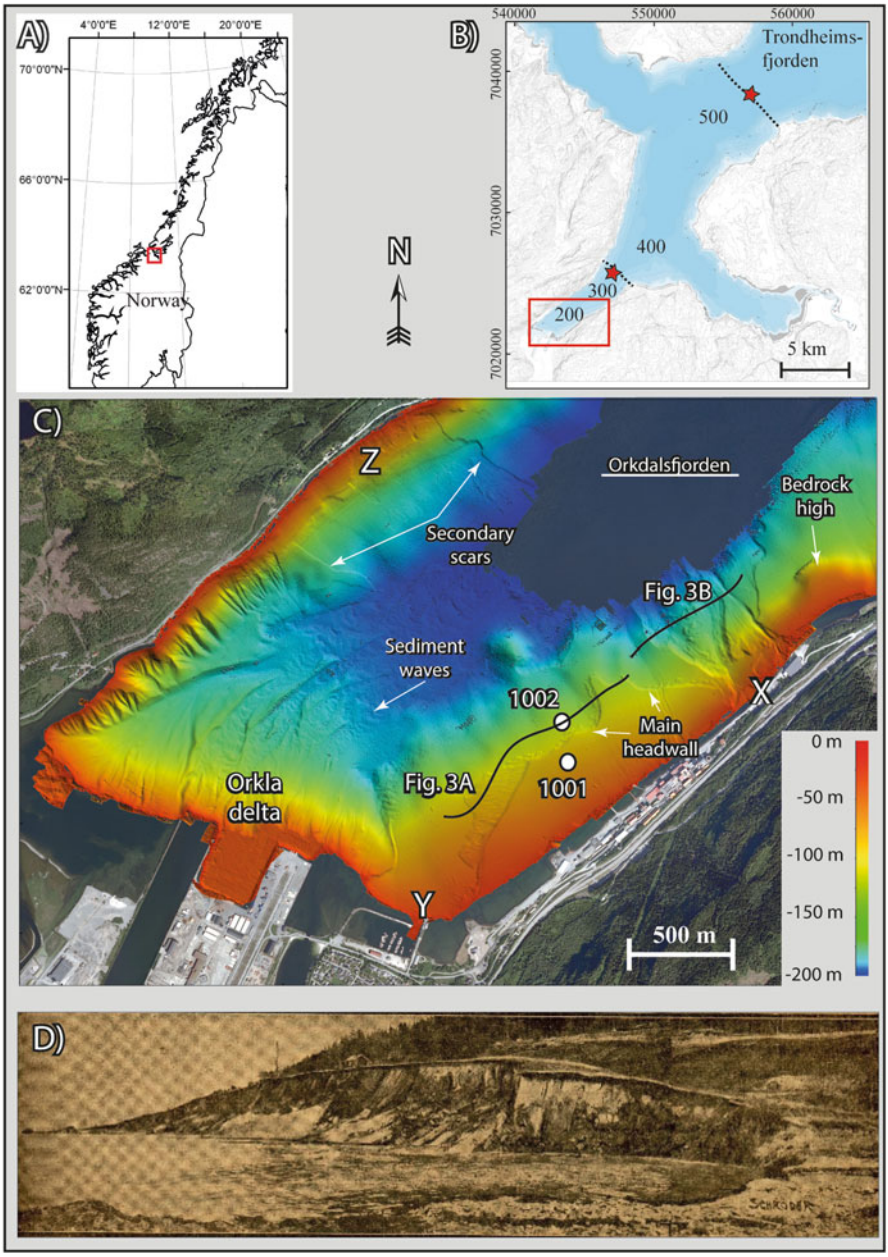

Fig. 21.1 Location of Orkdalsfjorden landslide, (**a**) the study area, (**b**) location of broken telephone cables, (**c**) swath bathymetry over the landslide area with tracks of seismic lines and core locations, (**d**) photography of the onshore escarpment at location Y (Courtesy of Adresseavisen)

the 2009 surveying, 14 lines of parametric sub-bottom profiler (TOPAS) were acquired over the landslide scar area. Also in 2009, a total of 9 gravity cores up to 1 m long were retrieved. X-ray imagery, detailed visual sedimentological description and measurements of magnetic susceptibility at every 1 cm with a Bartington MS2 probe were performed on the cores. Measurements of undrained shear strength were performed on clay samples using the Swedish fall-cone.

21.4 Results and Interpretation

The geomorphology in Orkdalsfjorden is characterized by steep slopes with gradients from about 6° close to the shoreline to over 25° near the foot of the slopes. To the southwest, the Orkla river delta is a pronounced morphological feature with distinct channels, gullies and sediment waves (Figs. 21.1c and 21.2). Sediment waves are found from the foot of the delta at approximately 100 m water depth to water depths beyond 300 m in the fjord basin. The slopes off the northwestern shoreline are at some locations deeply incised by gullies originating from small creeks onshore (Fig. 21.1b). At either side of the fjord, landslide scars of varying dimensions and mass-wasting deposits can be observed.

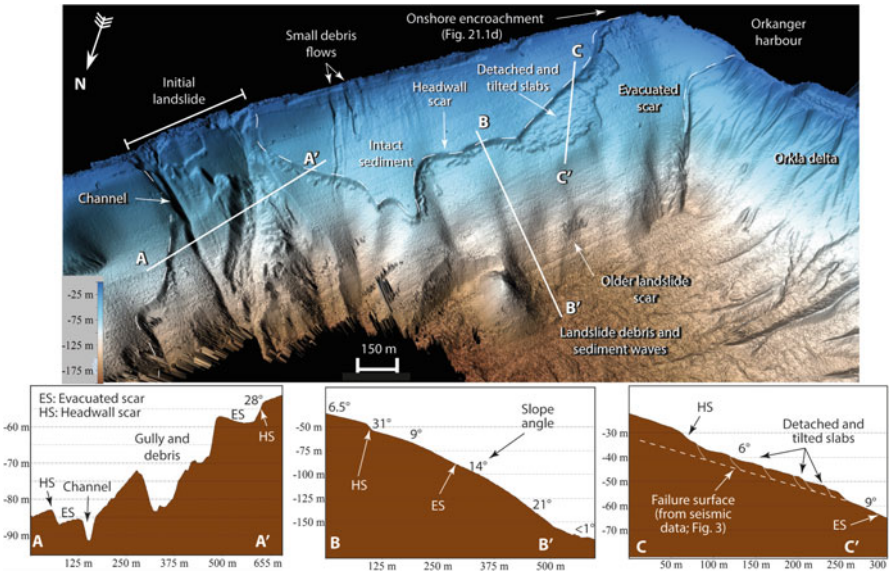

Fig. 21.2 Oblique view of the Orkdalsfjorden landslide with morphological interpretation and bathymetric profiles

21.4.1 Geomorphological and Stratigraphical Landslide Features

The bathymetry data clearly reveals that the entire southwestern flank of the fjord is affected by mass movement processes, including the presence of multiple escarpments, detached slabs, channels, and smaller debris flows (Figs. 21.1c and 21.2). A distinct escarpment or headwall connects the initial landslide area (X) with the landslide affecting the harbour at Orkanger (Y). The headwall varies between 8 and 12 m in height, and has a slope between 24° and 34°. Most of the area downslope of the 3 km long headwall has a smooth, relatively flat surface devoid of landslide debris.

Based on the bathymetric data, the volume of material evacuated during this slope failure (from X to Y) is estimated at $15–17 \cdot 10^6$ m^3. The slope within the evacuated slide scar area increases from about 6–7° at the foot near the headwall to over 20° close to the fjord bottom. Some landslide debris can be observed along the foot of the headwall, and also as a cluster shown along profile C–C′ in Fig. 21.2. There, the seafloor displays a staircase pattern, which is attributed to the detachment and tilting of blocks during the landslide. Combining the observations from the bathymetry data with the seismic profiles, one can notice that the tilted blocks rest on a high-amplitude reflector corresponding to the evacuated surface (Fig. 21.3). This reflection continues within unfailed sediments upslope of the headwall scar (Fig. 21.3).

The headwall scar close to the initial landslide area is incised by a channel and a more than 20 m deep "V-shaped" gully (Profile A–A′; Fig. 21.2). Within the gully, close to shore, planar surfaces at two different levels indicate that more than one layer were involved in the failure process. At 200 m off the shoreline, the hummocky gully floor indicates accumulation of debris and blocks from the initial landslide event and/or from the sidewalls of the gully. These mass wasting deposits are up to 20 m thick and acoustically transparent with chaotic reflections on the seismic data (Fig. 21.3). These landslide deposits are underlain by acoustically stratified sediments which likely represent marine to glacio-marine clays such as encountered in the surrounding fjord system (e.g. Bøe et al. 2003; Rise et al. 2006). On the seismic profile, one can observe a deep truncation within the clays deposits which has been filled in by landslide debris (Fig. 21.3). A laminated block, up to 20 m high, is also seen at the interface between the intact sediments and the landslide debris. The laminations in the block are oblique to those observed in the surrounding intact sediment. The block must therefore have been transported and/or rotated.

On the north-western side of the fjord and close to where the last shoreline failure was registered in 1930 (i.e. location Z; Fig. 21.1), the bathymetric data shows two distinct landslide scars. The 2 m high scars start at the shoreline and vanish in the landslide debris at the bottom of the fjord ~700 m away. Based on the bathymetric data, the sediment evacuated from this secondary landslide is estimated at $1.0–1.5 \cdot 10^6$ m^3 summing up a total landslide volume of approximately $16–18.5 \cdot 10^6$ m^3 for the 1930 event.

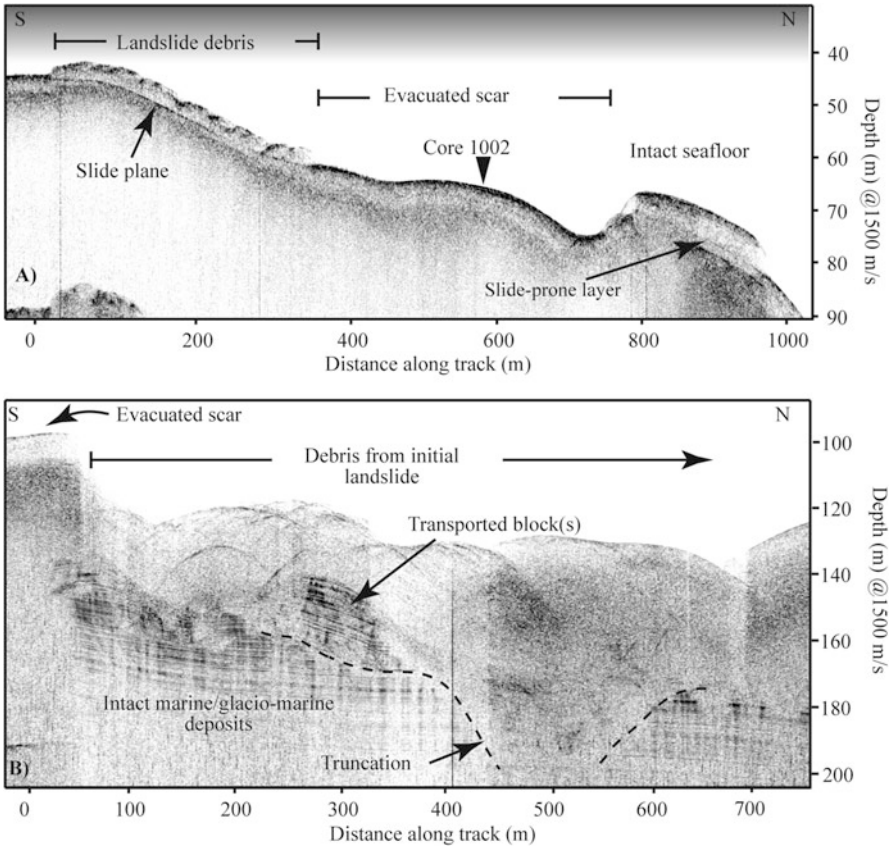

Fig. 21.3 (**a**) Seismic reflection profile showing detached and tilted slabs, and the evacuated landslide scar. Note the reflector corresponding to the sliding place below the debris and also within the intact sediment wedge. (**b**) Seismic reflection profile across the gully outside the initial landslide area (see Fig. 21.1c for location)

21.4.2 Core Data

Results from two representative gravity cores are presented in Fig. 21.4. Core 1001 was collected upslope of the headwall escarpment and consists of three different lithofacies. The bottommost interval (48–110 cm) consists of bioturbated silty sand to fine sand with little variation in magnetic susceptibility. A middle interval from 19 to 48 cm is made of sandy silt with little to absent bioturbation. The 19 cm thick topmost interval consists of dark, laminated, organic-rich silty clay including sulfurous layers. The lowest values of magnetic susceptibility in the core are found in this layer.

The top unit likely represents natural fjord-marine sedimentation affected by industrial waste from the nearby metal factory at Thamshavn, which has been

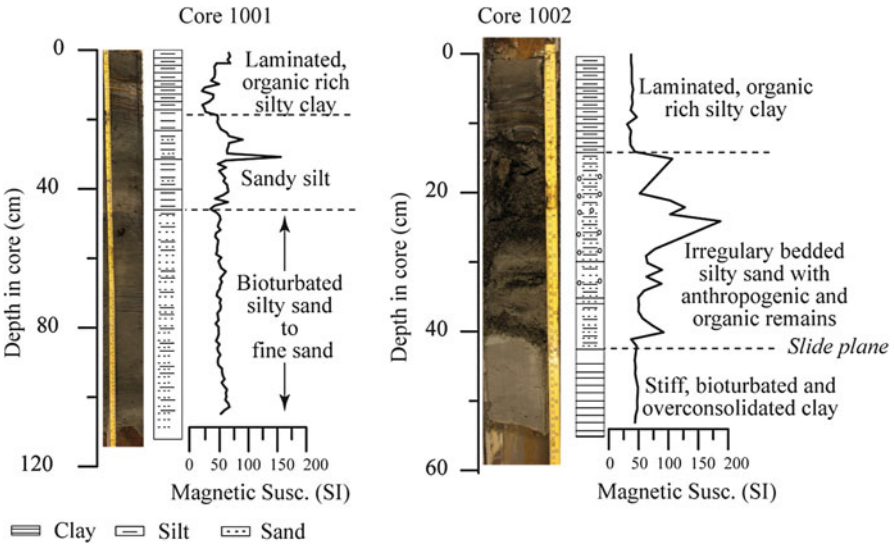

Fig. 21.4 Description of cores 1001 and 1002 collected outside and within the 1930 landslide scar respectively. Note the difference in depth scale between the two cores

operating since 1931. Core 1002 was collected within the evacuated landslide area (Fig. 21.1c). The topmost 13 cm consists of the same laminated and organic-rich silty clay as described in core 1001 and clearly represent the sedimentation since 1931 (Fig. 21.4). Below, the sediment consists of irregular beds of silt, sand and gravel with anthropogenic remains interpreted as landslide debris. A overconsolidated clay with an undrained shear strength of 12–13 kPa is found at the bottom. The overconsolidation of the clay is attributed to the removal of overburden (8–12 m) during the 1930 landslide and its depth corresponds to the level of the seismic reflection interpreted as a slide plane on Fig. 21.3a.

21.5 Discussion and Conclusions

Results from a gravity core and correlated seismic reflection data show that a clay layer forms the main slip surface of the 1930 Orkdalsfjorden landslide. The morphology and seismic profiles indicate that the initial failure took place on top of this clay layer and most likely at the boundary between this layer and the sandy fjord sediments. No core data describing the sediments immediately above or below this clay bed is available. However, data from similar fjord environment in the Trondheim harbour (L'Heureux et al. 2009, 2010) and Finneidfjord (L'Heureux et al. 2012; Vardy et al. 2012) have shown that clay-rich event beds deposited in the fjord as distal debris from terrestrial quick clay slides have functioned as slide planes

Table 21.1 Summary of estimated velocities for the different failure stage during the 1930 Orkdalsfjorden landslide

Event	Distance (km)	Time (h)	Velocity (km/h)	Velocity (m/s)	Stage
Landfill failure	0	7:48	–	–	Initial failure
Harbour failure	2–3	7:50	60–90	17–25	Failure propagation
First cable break	3	7:55	25	7	Post-failure
Second cable break	18	9:40	11	3	Post-failure

Note that the distance for each event is estimated from the area of the initial landslide

for submarine translational slides. Similarly, the valley of Orkla has thick deposits of glacio-marine sediments onshore and a history of quick-clay slides. We therefore interpret this clay bed to result from a quick-clay landslide in the catchment of the fjord. In such case, the slide plane lies at the boundary between the clay and the sandy fjord sediments above.

The causes for the 1930 landslide are attributed to a combination of human activity along the fjord shoreline (fill) combined with unfavourable groundwater conditions (low spring tide) and steep shoreline slopes.

The flow of debris following landward encroachment and failure of the fill in the early stage of the landslide caused intense seabed erosion and the formation of gullies in the deeper marine and glacio-marine sequences. The unloading caused prior and during the erosion may have led to intense strain accumulation in the clay layer in the western slopes, while the shoreline slopes to the east were supported by the outcropping bedrock (Fig. 21.1c). From this point, failure propagation took place relatively fast since the harbour in Orkanger was witnessed to fail only a couple of minutes after the initial landslide. A rough estimate yields a velocity of about 17–25 m/s for the failure propagation (Table 21.1). Based on the geomorphology and the seismic data, the failure propagated progressively over the clay layer in a retrogressive spreading manner upward and sideward. However, more geotechnical data are needed to assess whether or not the landslide mechanisms is associated to the brittleness and the sensitivity of the clay. The retrogressive process continued until the slope gradients reached a value of ~6°. At this stage, the potential energy in the slope was not sufficient for remoulding the sediments. The dip of the main headwall with slope angles up to 34° is representative of the internal friction angle for the sandy material found in nearby cores. These deposits may also have helped slowing down the retrogressive process. Following the main landslide event the sediments transformed into a debris flow and subsequently into a turbidity current, as suggested by the sediment waves in the deeper fjord basin (Fig. 21.1c, see also Bøe et al. 2003). The early acceleration phase of this landslide towards the deeper fjord basin likely caused the 15-m high tsunamis. Simultaneously, the bottom slope erosion caused by the sediment flow likely triggered the subsequent slope failures registered on the northern side of the fjord (Fig. 21.1c).

The 1930 Orkdalsfjorden event is one of the few known submarine/coastal landslide where timing of all stages of land sliding (i.e. failure initiation, propagation and

post-failure development) can be assessed (Table 21.1). It provides a good example showing that extensive areas of the seabed may fail in a relatively short period of time with important implication for tsunami generation. The potential hazard posed by mass movement processes must therefore be assessed regionally when planning construction activity in near-shore and coastal environments.

Acknowledgments We thank Oddbjørn Totland and John Anders Dahl for help during data acquisition onboard the RV SEISMA (NGU). Drs. Ariane Locat and G. Lastras are acknowledged for their constructive reviews.

References

Bjerrum L (1971) Subaqueous slope failures in Norwegian fjords. Norwegian Geotechnical Institute, Publication no. 88, pp 1–8

Bøe R, Rise L, Blikra LH et al (2003) Holocene mass movements process in Trondheimsfjorden, Central Norway. Nor J Geol 83:3–22

L'Heureux JS, Hansen L, Longva O (2009) Development of the submarine channel in front of the Nidelva River, Trondheimsfjorden, Norway. Mar Geol 260(1):30–44

L'Heureux JS, Hansen L, Longva O et al (2010) A multidisciplinary study of submarine landslides at the Nidelva fjord delta, Central Norway–implications for geohazards assessments. Nor J Geol 90:1–20

L'Heureux JS, Sylfest S, Longva O et al (2011) The 1888 shoreline landslide and tsunami in Trondheimsfjorden, central Norway. Mar Geophys Res 32(1–2):313–329

L'Heureux JS, Longva O, Steiner A et al (2012) Identification of weak layers and their role for the stability of slopes at Finneidfjord, northern Norway. In: Yamada Y et al (eds) Submarine mass movements and their consequences, vol 31, Advances in natural and technological hazards research. Springer, Dordrecht, pp 321–330

Rise L, Bøe R, Sveian H et al (2006) The deglaciation history of Trondheimsfjorden and Trondheimsleia, Central Norway. Nor J Geol 8:419–437

Vardy ME, L'Heureux JS, Vanneste M et al (2012) Multidisciplinary investigation of a shallow near–shore landslide, Finneidfjord, Norway. Near Surf Geophys 10:267–277

Chapter 22
Imaging Active Mass-Wasting and Sediment Flows on a Fjord Delta, Squamish, British Columbia

John E. Hughes Clarke, Carlos R. Vidiera Marques, and Danar Pratomo

Abstract An active fjord head delta in Squamish British Columbia, was selected as the location for a repetitive multibeam survey program to monitor temporal evolution of the prodelta morphology. Daily resurveys in 2011 established the style and extent of submarine mass movements, their typical periodicity and the conditions associated with the most active periods. This has now been followed by an hourly resurvey program in 2012 during those most active periods to actually witness the progression of activity immediately preceding, during and subsequent to a singular event.

The delta front in depths of 20–50 m is often the apparent start point for trains of sequential erosive and depositional events associated with upslope bedform migration along prodelta channels. Heavy targets on the channel floors were monitored in 2011 and indicated rare, abrupt down channel displacements of a few hundred metres, indicating that a small subset of events involved bulk translation of the seabed. In 2011, a bottom-mounted ADCP beyond one channel mouth recorded clear turbidity current events for a subset of the channel bedform migration periods.

In 2012, using multibeam water column imaging and a rapidly dipping towed optical backscatter probe, the evolution of a descending suspended sediment plume below the overlying river plume was monitored on an hourly basis. Towards low water, that descending plume was seen to occasionally feed a near seabed higher suspended sediment layer. On the development of this layer, the water column imaging revealed a thin basal flow that lasted about an hour and corresponded directly with the period of migration of the channel floor bedforms. Delta-lip failures are associated with the upslope end of about half of the bedform trains suggesting an alternate initiating mechanism.

J.E. Hughes Clarke (✉) • C.R. Vidiera Marques • D. Pratomo
Department of Geodesy and Geomatics Engineering, University of New Brunswick, P.O. Box 4400, Fredericton NB, Canada E3B 5A3
e-mail: jhc@omg.unb.ca

S. Krastel et al. (eds.), *Submarine Mass Movements and Their Consequences*, Advances in Natural and Technological Hazards Research 37, DOI 10.1007/978-3-319-00972-8_22,

Keywords Prodelta mass wasting • Surface differences • Cyclic steps • Bedform translation • Turbidity current • Water column imaging

22.1 Introduction

The majority of inferences about mechanisms for submarine mass wasting and sediment flows are based on interpretation of either outcrop geology, the resulting morphology of deposits on the seabed or comparisons to laboratory-scale experiments. To confidently describe a specific event, the seabed needs to have been surveyed prior to, and immediately after the event. For most descriptions of inferred mass wasting, only the result is imaged. To actually observe the process, instrumentation needs to be present (and survive) during an event.

Periodicity of deep-sea mass wasting or turbidity current events is usually too long to set up a specific monitoring program. Serendipitous interruptions of large scale infrastructure like deep-sea cables have provided the first (Heezen and Ewing 1952) and most detailed (Hsu et al. 2008) evidence for the passage of a specific event. In shallow water, where periodicity is expected to be higher, monitoring of natural flows is possible (Prior et al. 1987; Xu et al. 2004). With the advent of precise shallow water multibeam surveys, change analysis has also become feasible, most notably the work of Hill (2012).

The Squamish experiments, described herein, build on the repetitive survey approach of Hill (2012), but rather than address change on a seasonal scale (representing the cumulative sum of many events), examine it on a daily and hourly timescale. The specific objectives were to try to constrain:

- Initiating mechanisms – whether delta lip failure or hyperpycnal-like conditions could be associated with the onset of flow.
- The character of the near-seabed flow – whether they are fully turbulent or involve grain-to-grain interaction.
- The timing and mechanism of the bedform migration – how are they formed and what do they imply?

22.1.1 Geological Setting

The Squamish delta lies at the head of Howe Sound, British Columbia and is the major source of sediment into the sound. Hickin (1989) estimated that approximately one million cubic metres of sediment are delivered annually. The basin is approximately 16 km long, extending from the delta to a ponded basin in 285 m of water. The focus of this project is on the first 2 km extending down to a water depth of ∼200 m.

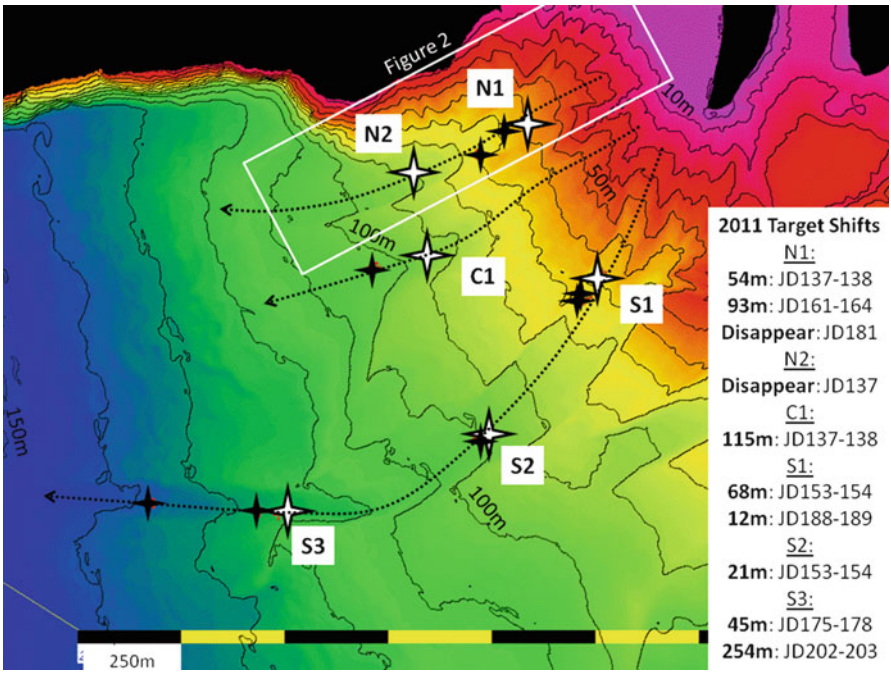

Fig. 22.1 Squamish prodelta bathymetry and block displacements. Starting location indicated by *larger white star*. Subsequent translated positions indicated by *black stars*. Ten metres contour intervals. For each shift, the horizontal translation and the pair of Julian days over which the shift took place are indicated. Where and when blocks disappeared, the date is indicated

The first complete survey of the prodelta occurred in 1973, 2 years after the river mouth had been radically altered through the construction of a training dyke (Hickin 1989). Change between the 1973 and 1990 single beam surveys and multibeam surveys from 2004 to 2006 were analyzed by Brucker et al. (2007). They noted that, on average, the proximal prodelta is accreting at a rate of about 1 m per year, with almost all the change attributable to the summer freshet period. That accretion, however, is punctuated by local incisions pertaining to three main channels on the prodelta (Fig. 22.1). Within those channels active transverse bedforms are well developed. What was not clear from the 2004–2009 surveys, spaced at 6–24 months apart, was whether the cumulative summer's change corresponded to a few major events or a large number of relatively minor events. Also no measurement had been made of any flow characteristics such as velocity, duration or suspended sediment concentration. The 2011 and 2012 programs, reported herein were specifically designed to address these deficiencies.

22.1.2 Methods

To investigate mass wasting activity on the Squamish prodelta a series of methods have been employed:

Bathymetry: For the 2011 and 2012 field seasons, an EM710 multibeam operating at 70–100 kHz utilizing 1° × 2° beams was employed. Together with RTG-GPS and aided inertial navigation, confident accuracy in the range 1 m or 2.5 % of depth horizontally and ~30 cm or 0.5 % of depth vertically (Hughes Clarke et al. 2012) is achievable.

Water Column Acoustic Scattering Imagery: the multibeam sonar provides a measure of the 3D acoustic scattering field within a cylinder of radius of the minimum slant range to the seafloor. The 70–100 kHz sonar is not attenuation limited in these depths and thus can usefully distinguish scattering from noise close to the seabed.

Current Measurements: In 2011 a bottom mounted ADCP was deployed for a 4 month period with the exception of a 20 day period when it was buried. The ADCP location was seaward of the mouth of the northern channel and thus could only detect events in that channel. The ADCP was not deployed in 2012 due to concerns about burial in the more proximal channel environment.

Temperature and Salinity Structure: In order to calculate the density deficit between the incoming cold fresh water and the generally warmer salty waters of the fjord, a towed dipping sensor with a CTD was deployed. The dip periodicity depends on the depth desired and the vessel speed. Dips within the river plume (about 10 m depth) could be obtained every 100 m. A maximum depth of 125 m was possible if the vessel slowed to less than 1 knot.

Suspended Sediment Concentrations: The same towed sensor was equipped with an optical backscatter probe. In 2011, a single probe was deployed which saturated at sediment concentrations of about 0.07 kg/m^3. The river plume rarely exceeded this value, but deep dips into bottom-following flows often caused saturation. In 2012 a second probe with a 100x lower sensitivity was added to examine the higher concentrations in the basal flows.

Correlation between output voltage and sediment load was attempted but complicated by some ambient light sensitivity. Nevertheless, agreement between estimated plume suspended loads and values previously reported by Syvitski and Murray (1981) and Hickin (1989) suggest that the values are within ~20 % of actual levels. Therefore suspended load is reported here in absolute kg/m^3 units.

Bulk Seafloor Displacements: While the ADCP indicated turbulent suspension flow beyond the channel sections, it was not clear whether the sediment displacements in the channels could be attributed to traction by the overriding turbulent flow or whether there was bulk displacement (sliding or grain flow) along the channel floor.

In order to monitor whether there was bulk displacement of the channel floors after the manner pioneered by Paull et al. (2010), concrete blocks (either 24 or 36 kg) were placed on the channel floors with three air filled spheres

suspended above. An automated algorithm was developed for the multibeam water column imagery (Marques 2012) to unambiguously identify and locate the spheres amongst the other mid-water scattering targets due to gas or zooplankton.

In 2011 six of these blocks with buoyed markers were laid in the thalwegs of the major channels (Fig. 22.1). The location of each of these blocks was monitored on a daily basis.

2011 Survey Design: A one to 3 day period for resurvey was conducted in 2011 over a period of 4 months (Hughes Clarke et al. 2012) during the summer high discharge period. From this, cumulative daily change could be assessed to infer correlations with tidal range and river discharge.

2012 Survey Design: Based on the inference from the 2011 daily surveys, the period of highest probability of mass wasting was selected for resurveys at periods of about 1 h in 2012. The survey plan involved running the channel corridors from about 4 h before low water, to about 2 h after low water. Immediately preceding the start of the channel surveying, the delta lip was imaged to see if there had been any change since the previous evening. And at the end of the day, the delta lip was resurveyed to compare with the morning and the following day. The overnight low-tide was weak due to the diurnal inequality and no overnight change in the either the delta lip or the channel floors was ever observed.

For the first 2 days all channels were sequentially surveyed with a repetition period of about 1.5 h. On the subsequent 4 days only a single channel was surveyed with a repetition period of about 0.5 h. Results for the first 3 days, during a river surge are presented.

22.2 Results

The 2011 campaign (Hughes Clarke et al. 2012) is herein briefly reviewed together with a new analysis of the 2011 block displacements. This provides a context for the 2012 operations which directly address the stated objectives.

22.2.1 2011 Daily Sequence of Events

On each survey weekday in 2011, the active delta lip was mapped from the edge (at ~1 m below chart datum) to 50 m depth. From that point, transects were run along the thalwegs of the three active channels down to 200 m. By running the channel axes, the centre beams of the multibeam with the highest accuracy were used to try and detect bathymetric change. This was also the geometry in which the best acoustic water column imaging could be obtained.

The terrain model for each day was subtracted from the previous day to assess resolvable change. On an active day, regions of erosion and deposition along one or more of the channels were observed (Fig. 22.2) almost always indicating upslope

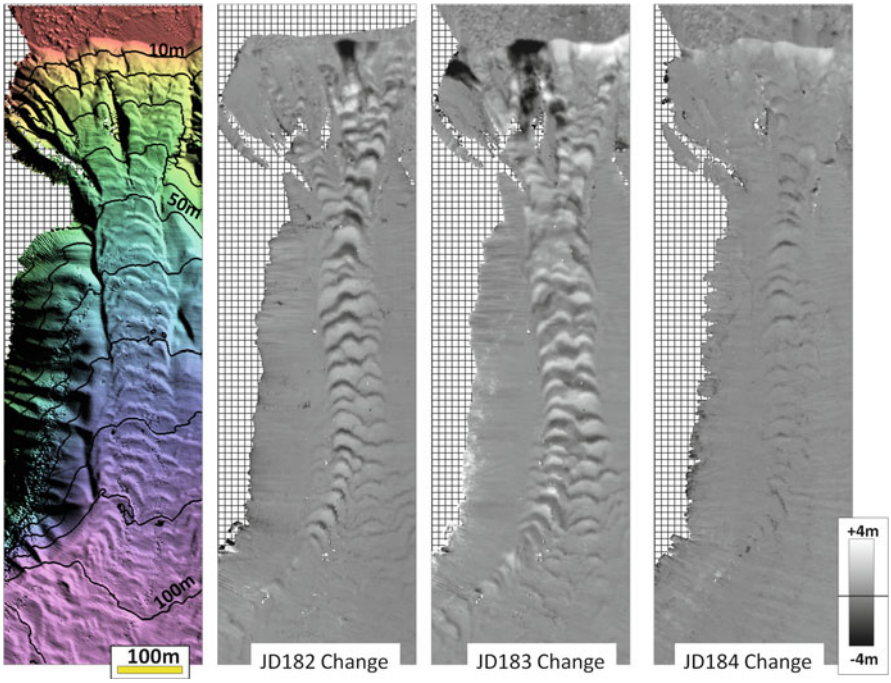

Fig. 22.2 2012 daily cumulative depth differences along a 1,000 m long section down the North Channel (*white box* in Fig. 22.1). *Left* shows the bathymetry with 10 m contours

migration of the transverse bedforms. The only time that the bedform migration direction was ambiguous was during larger events when displacements exceeded ½ a wavelength and thus crest to crest ambiguity exists. Some of these active bedform trains appear to initiate upslope in an erosive headscarp, but many appeared to extend gradually downslope without any discrete initiating source location.

Often more than one channel was active in the same day. Using 93 sequential surveys, a total of 103 channel-specific daily events were detected in 2011, of which 49 were in the northern channel (Fig. 1 in Hughes Clarke et al. 2012). For 20 of the northern channel events, a corresponding turbidity current surge was detected at the ADCP. A typical flow was 5–15 m thick, with a duration of about an hour and peak velocity of about 0.5 m/s (Hughes Clarke et al. 2012).

For each transect, a vertical section of the acoustic volume scattering along the channel axis from the surface to the seabed was obtained. For most days all this revealed was the zooplankton stratification in the fjord. As the summer progressed, it became apparent that the deep scattering layer would occasionally be perturbed by a bottom-following low scattering layer.

These bottom-following low-scattering layers were typically associated with low tide. During the low water period, the discharge of the river is constricted to a narrower cross section which results in a stronger off-delta flow.

For the majority of days, even if a seabed change clearly happened in the channel the blocks did not move. On just 8 of the 52 days on which change occurred, the blocks were translated by between 12 and 253 m (Fig. 22.1). It is notable that the spatial patterns of erosion and deposition do not look discernibly different on days when there was block displacement and days when there was not. Thus, while mass displacement must have occurred on those days, subsequent current activity appears to have moulded the sediments in a way that makes it indistinguishable from other mechanisms.

22.2.2 2012 Hourly Sequence of Events

The 2011 daily results suggested that events were preferentially correlated with lower-low water spring tide and thus in 2012 sequential 0.5–1.5 h period surveys were focused around that time to try to capture an event in progress.

Over 7 days, three days revealed active events. The cumulative bathymetric changes in the northern channel are presented in Fig. 22.2. The sampling interval for the first 2 days was 1.5 and 0.5 h for the third day. On the first day (JD182), the change extended over two epochs (inter-survey periods) implying all activity within a maximum of a 3 h period. On JD183 and JD184 all change was constrained to a single epoch implying less than 1.5 h and 0.5 of activity respectively.

The JD182 sequence of events in the northern channel is presented in Fig. 22.3 by showing the evolution of the bathymetric change within 5 discrete epochs. For that event, motion started in the shallowest end of the first line (Fig. 22.3 top). For the next two difference pairs (over a maximum of 3 h), changes were seen indicating upslope migration of the bedforms in both the one main and multiple feeder channels. Note that the active feeder channels change between epochs suggesting that there were multiple overprinting flows from separate sources.

For the same five survey lines, the acoustic water column volume scattering is presented (Fig. 22.4) with superimposed suspended sediment profiles. There was no activity at the start of the day. During the migration period a distinct basal flow was visible with an associated near-seabed suspended sediment peak and drop in salinity. For subsequent images, an upward expanding low acoustic backscatter anomaly was seen above the seabed in the wake of the flow. This anomaly has an increasingly thick but more dilute suspended sediment signature which slowly died away along with the salinity anomaly.

As well as a positive suspended sediment anomaly associated with each of the underflows, there was often also a notable drop in salinity (Figs. 22.4 right and 22.5). This is an indicator that the source of the fluid associated with these flows is derived from shallower depths. More significantly, it indicates a potential density deficit for that fluid compared to the ambient water into which it is intruding. Any drop in salinity should make the intruding water inherently lighter. That the flow remains on the seabed implies that there must be (or recently have been) sufficient suspended sediment to offset the negative density anomaly due to the salinity drop.

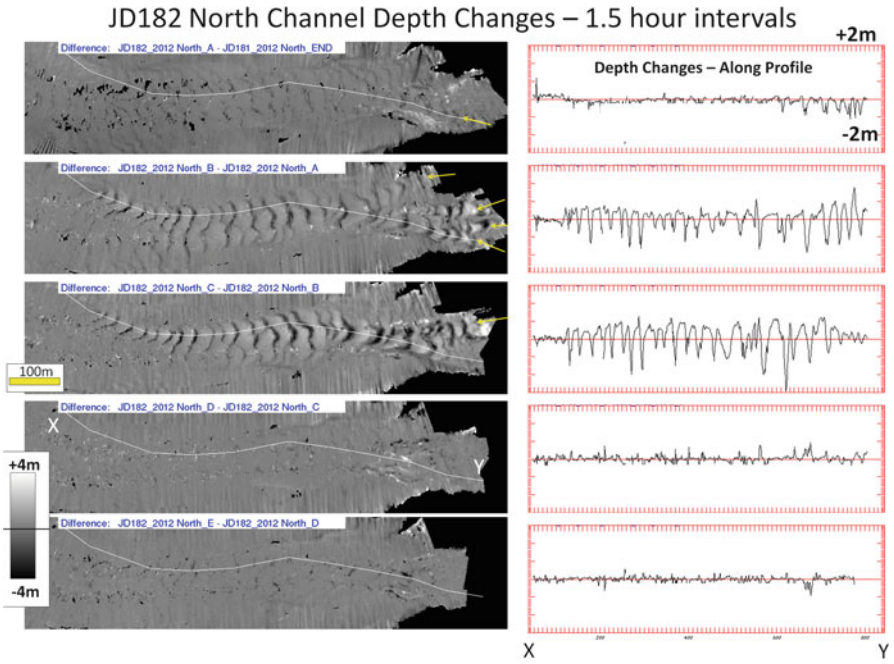

Fig. 22.3 *Left*: 5 inter-survey depth difference maps obtained on JD182 along the first 900 m of the northern channel (*uphill to right*). For each map, a representative transect is plotted on the *right* along the thalweg as indicated by a *white line*. *Arrows* indicate active feeder channels

Figure 22.5 illustrates the calculation of the density profile of the ambient water (using a profile taken before the flow arrived) and the instantaneous density profile through the active underflow. Note that these densities are based on temperature, salinity and pressure alone and thus only reflect the density of a clear watermass. By subtracting the two density profiles, a density anomaly can be calculated.

22.3 Discussion and Conclusion

Initiating Mechanisms: Two plausible initiation mechanisms are suggested from the observations:

1. Input of sediment from a delta-lip failure
   The delta lip can only be examined at high tide and thus only the cumulative daily change can be seen (Fig. 22.2), not by epoch. For JD182 and JD183, discrete amphitheatre-like delta lip scarps are present at the upstream end of some of the active bedform trains. Thus some of the trains could be fed from a discrete failure. The failure scarps could, alternately however, just be a result of oversteepening

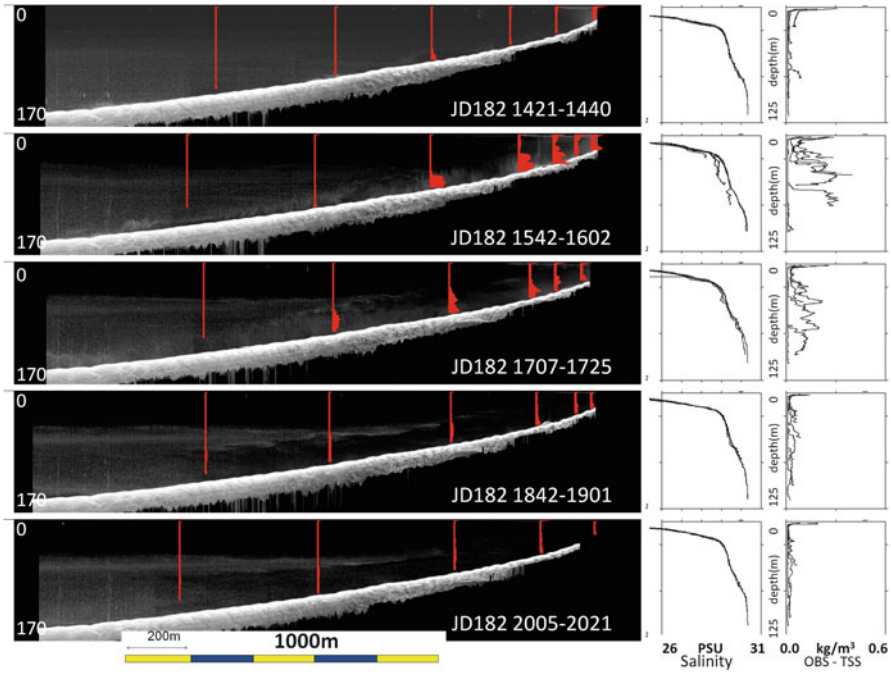

Fig. 22.4 Illustrating the EM710 90 kHz water column acoustic scattering images for an extended distance along the same five transects as Fig. 22.3. *Lighter tones* are higher acoustic backscatter. The *red* profiles are superimposed optical backscatter sections. On the *right*, the salinity and optical backscatter profiles of the upper 125 m are plotted in detail

due to bedform translation below. Significantly about half of the bedform trains are sourced from locations on the delta lip that accreted over the day without evidence of failure. This implies that another mechanism is required.

2. Fallout of sediment from river discharge.
   While enhanced suspended sediment is seen within the plume, at no point do the values provide nearly enough excess density to cause plunging of the river water (Mulder and Syvitski 1995). The suspended load however, is observed to be transferred from the fresh water layer to the brackish underlying layers (Figs. 22.4 and 22.5), reminiscent of the mechanism proposed by Parsons et al. (2001). This avoids the need to overcome the bulk of the freshwater excess buoyancy. The presence of a brackish anomaly in the under flows requires at least some entrainment of overlying water. To establish whether this is really the driving mechanism, however requires insights into the character of the near-seabed flow.

The character of the near-seabed flow: The density deficit near the seabed implied by the drop in salinity bears directly on the nature of the turbid underflow. For that flow to continue to hug the seabed, there must be a matching suspended load

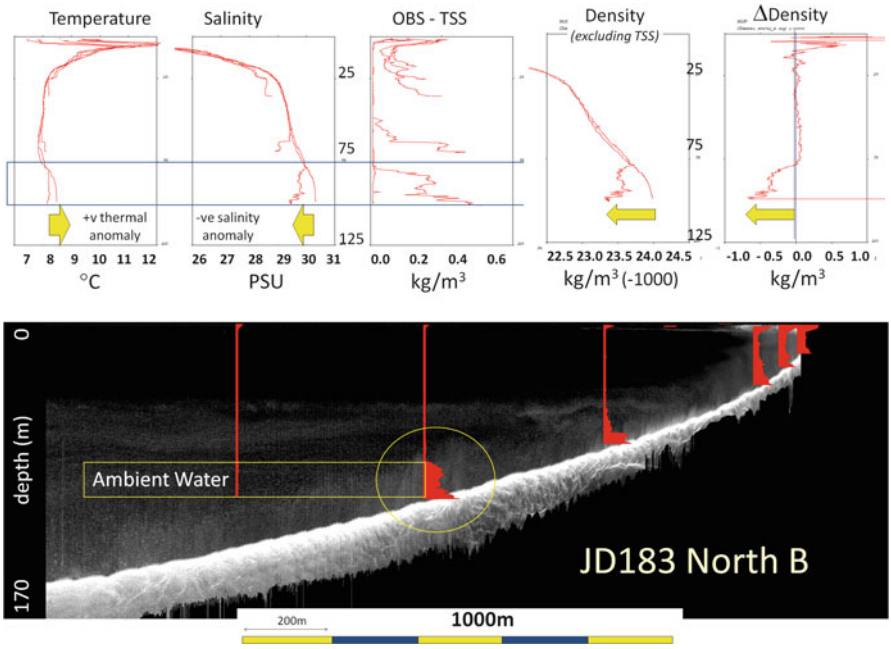

Fig. 22.5 *Lower*: showing optical backscatter profiles superimposed over the multibeam water column nadir section during the peak flow on JD183. *Upper*: plots showing temperature, salinity and suspended sediment profiles for the six dips and for the deepest two the density and density difference (assuming clear water)

that at least matches the surfeit of density. For the example shown in Fig. 22.5, it is clear that a suspended load of at least 0.7 kg/m^3 would be required. Yet the dipping optical backscatter probe never recorded a value higher than ~0.4 kg/m^3.

The fact that the measured suspended load at the seabed is not greater than the density deficit due to the brackish nature of the flow implies that there must be an as-yet unmeasured source of excess density. The probe was designed to freefall towards the seabed and automatically stops at least 2 m above the seabed thereby missing the base of the flow. It is speculated that there must be a very thin (<2 m) higher density and more brackish flow, whether a turbulent suspension or grain flow, that drives the observed bedform translations and sheds the positively buoyant turbid plume. The displacement of heavy concrete blocks during a small proportion of the flows in 2011, suggests occasional very strong basal flow, possibly grain-supported.

The measured tops of the underflows appear inherently positively buoyant. This is supported by the observation that in the wake, the flows appear to rise up, as shown by a diluting and thickening turbid layer. This would be expected as the suspended sediment concentration drops leaving a positively buoyant remnant plume. The rising turbid layer matches the anomalously low water column scattering. It is apparent that acoustic scattering at 90 kHz (~1.7 cm wavelength) is responding

to scatterers at the scale of the zooplankton rather than the much smaller suspended sediment. It is thus speculated that the reduction in scattering is due to the retreat of the deep scattering layer (zooplankton) away from the brackish intrusion.

Timing and Mechanism of Bedform Migration: For all the events detected in 2012, the onset of seabed change occurred within 1 h of low water. Either proposed initiating mechanism is most likely at that time due to the enhanced river suspended load and off-delta current speed. For the smaller event on JD184, only a single train of bedforms is seen and all activity is constrained within a 0.5 h period. For JD182 and JD183, as multiple trains of bedforms clearly emanate from differing feeder channels on the delta lip, it is apparent that there were multiple flows coalescing and the constraining time interval is correspondingly longer at up to 3 h or 1.5 h respectively. By spanning two observation epochs, the event on JD182 can be seen to have progressively shifted source feeder channels (Fig. 22.3 arrows). The feeder channel with the longest duration is notably associated with the major delta lip failure.

The bedform migration appears coincident with the first occurrence of near-seabed enhanced suspended load and does not continue during the rising wake. On all days, upstream migration was unambiguous for all bedforms indicating preferential erosion on the upstream faces and deposition on the downstream sides. Without knowledge of the nature of the near seabed flow, however, the manner in which this happens remains unknown.

In conclusion, the Squamish observations provide important new insights into the triggers and character of mass wasting and sediment flows on delta fronts. However, there still remains a need to image the near-bed (< 2 m) layers within these flow events, and to understand the character and triggers for up-slope migrating bedforms. Until this is done key questions will remain unanswered.

Acknowledgements This research has been funded by an NSERC Discovery Grant "Precise Seabed Change Monitoring" to the first author as well as research sponsorship of the Chair in Ocean Mapping at UNB from Rijkswaterstaat and Kongsberg Maritime. The professional operation of the CSL Heron was undertaken by Gordon Allison. The implementation of much of the survey component was undertaken by Steve Brucker, Ian Church, Doug Cartwright, James Muggah, Travis Hamilton and Pim Kuus. This paper significantly benefited from reviews by Peter Talling and Phil Hill.

References

Brucker S, Hughes Clarke JE, Beaudoin J, Lessels C, Czotter K, Loschiavo R, Iwanowska K, Hill P (2007) Monitoring flood-related change in bathymetry and sediment distribution over the Squamish Delta, Howe Sound, British Columbia. In: Proceedings of the United States hydrographic conference 2007, 16 pp. The 2007 conference paper is maintained by the Hydrographic Society of America on their website: http://www.thsoa.org/us07papers.htm

Heezen BC, Ewing M (1952) Turbidity currents and submarine slumps, and the 1929 Grand Banks earthquake. Am J Sci 250:849–873

Hickin EJ (1989) Contemporary Squamish River sediment flux to Howe Sound, British Columbia. Can J Earth Sci 26:1953–1963

Hill P (2012) Changes in submarine channel morphology and slope sedimentation patterns from repeat multibeam surveys in the Fraser River delta, western Canada. Int Assoc Sedimentol Spec Publ 44:47–70

Hsu S-K, Kuo J, Lo C-L, Tsai C-H, Doo W-B, Ku C-Y Sibuet J-C (2008) Turbidity currents, submarine landslides and the 2006 Pingtung earthquake off SW Taiwan. Terr Atmos Ocean Sci 19(6):767–772

Hughes Clarke JE, Brucker S, Muggah, J, Church I, Cartwright D, Kuus P, Hamilton T, Pratomo D, Eisan B (2012) The Squamish ProDelta: monitoring active landslides and turbidity currents: Canadian hydrographic conference 2012, proceedings, 15 pp. The 2012 conference paper is maintained by the Canadian Hydrographic Association on their website: http://hydrography.ca/2012-conference.html

Marques CRV (2012) Automatic mid-water target detection using multibeam water column. M.Sc. Eng. thesis, University of New Brunswick, 209 pp

Mulder T, Syvitski JPM (1995) Turbidity currents generated at river mouths during exceptional discharges to the world oceans. J Geol 103:285–299

Parsons JD, Bush JWM, Syvitski JPM (2001) Hyperpycnal plume formation from riverine outflows with small sediment concentrations. Sedimentology 48:465–478

Paull CK, Ussler W III, Caress DW, Lundsten E, Barry J, Covault JA, Maier KL, Xu J, Augenstein S (2010) Origins of large crescent-shaped bedforms within the axial channel of Monterey Canyon. Geosphere 6:755–774

Prior DB, Bornhold BD, Wiseman WJ Jr, Lowe DR (1987) Turbidity current activity in a British Columbia fjord. Science 237:1330–1333

Syvitski JPM, Murray JW (1981) Particle interaction in fjord suspended sediment. Mar Geol 39:215–242

Xu JP, Noble MA, Rosenfeld LK (2004) In-situ measurements of velocity structure within turbidity currents. Geophys Res Lett 31:L09311. doi:10.1029/2004GL019718

Chapter 23
Coastal and Submarine Landslides in the Tectonically-Active Tyrrhenian Calabrian Margin (Southern Italy): Examples and Geohazard Implications

Daniele Casalbore, Alessandro Bosman, Domenico Ridente, and Francesco Latino Chiocci

Abstract High-resolution multibeam bathymetry is used as basis for detecting instability processes on the Tyrrhenian margin offshore Calabria (Italy). Among the many evidence at different spatial scale, we focus on selected cases that may represent a potential geohazard because of their scale, shallow/proximal location and state of activity. These include failures along coastal cliffs and canyon headwalls indenting narrow shelves. Coastal rocky failures impacting shallow water offshore Scilla and Palmi retain significant tsunamigenic potential, as proved by the 1783 Scilla event. Slide scars at canyon headwalls offshore Bagnara Calabra and Gioia Tauro indicate retrogressive failure active at water depth <10 m, just few hundreds of meters from the coast and the settlements and infrastructures there present. Geohazard related to these features is therefore relevant as testified by the failure induced during construction of the Gioia Tauro harbour in 1977.

Keywords Rocky-failures • Canyons • Continental margins • Seafloor mapping • Tsunami

23.1 Introduction

In the last decades, the exploitation of offshore natural resources and of the coastal zone has become a relevant socio-economic issue. As a consequence, the intensified deployment of seafloor-lying structures has determined the rapid settlement of coastal sea stretches and an increasing human impact, raising the importance

D. Casalbore (✉) • A. Bosman • D. Ridente
CNR-IGAG, National Research Council, P.le Aldo Moro 5, Rome 00185, Italy
e-mail: daniele.casalbore@igag.cnr.it; daniele.casalbore@unibo.it

F.L. Chiocci
Dip. Scienze della Terra, Sapienza, Università di Roma, P.le Aldo Moro 5, Rome 00185, Italy

S. Krastel et al. (eds.), *Submarine Mass Movements and Their Consequences*, Advances in Natural and Technological Hazards Research 37, DOI 10.1007/978-3-319-00972-8_23,

of marine geohazard assessment and management. In this perspective, a special interest has to be dedicated to submarine instability in shallow-water and coastal environment, particularly in areas where a narrow shelf is present. The Tyrrhenian margin offshore Calabria is tectonically and seismically active and provides a favorable setting for depositional dynamics predisposing and/or triggering mass failure processes. In this view, one of the most catastrophic events occurred in 1783 and was a coastal landslide from Mt. Pacì, near Scilla, which entered the sea triggering a local tsunami that resulted in ~1,500 casualties (Mazzanti and Bozzano 2011 and reference therein). More recently, in 1977, failure at the headwall of Gioia Canyon generated a local tsunami that damaged the nearby Gioia Tauro harbour, with the loss of some vehicles (Colantoni et al. 1992). Because of the growing human impact in this sector, a more comprehensive understanding of the distribution and frequency of failure-prone features and related geohazard potential is needed. The recent acquisition of high-resolution bathymetry enabled the recognition of more than 400 submarine slide scars along this margin (from coast down to 2,000 m wd), covering a broad spectrum of dimensional scale and depth range (Casas et al. 2012). We focus on the characterization of coastal and very shallow-water slope failures, as they represent an ongoing geohazard in the study area.

23.2 Geological Setting

The Tyrrhenian Calabrian margin originated as a rifted margin during the spreading of the Southern Tyrrhenian Sea (Fig. 23.1), in turn controlled by the NW subduction of the Ionian plate beneath the Calabrian Arc (e.g. Malinverno and Ryan 1986). Regional uplift along the Calabrian Arc (~1 mm/a since Middle Pleistocene) is accommodated by NW-SE to E-W extension along fault systems (Antonioli et al. 2006; Ferranti et al. 2008 and reference therein). These fault systems define a seismic belt where several historical and pre-instrumental strong (ca. $M \geq 6$) earthquakes have been recorded, as for instance the February 5–March 28, 1783 sequence (e.g. CPTI Working Group 2004), also responsible for the Scilla tsunamigenic landslide (Bozzano et al. 2011).

Largely due to its tectonic evolution, the Calabrian margin is characterized by a very narrow to nearly absent continental shelf abruptly passing to steep slopes (Fabbri et al. 1980). In this view, two different geomorphic settings can be distinguished in the study area (Fig. 23.1):

(a) the southern setting between Scilla and Palmi, where the continental shelf is extremely narrow, connecting to a very steep slope (gradients up to 30°);
(b) the northern setting between Palmi and Gioia Tauro, where a wider shelf is locally interrupted by the head region of the two, down-slope coalescing (not shown in Fig. 23.1), Gioia and Mesima Canyons (hereafter Gioia-Mesima Canyon system; GMC). The GMC is fed by mountainous creeks with short, steep courses known as “fiumara”, characterized by torrential discharges and high sediment yields.

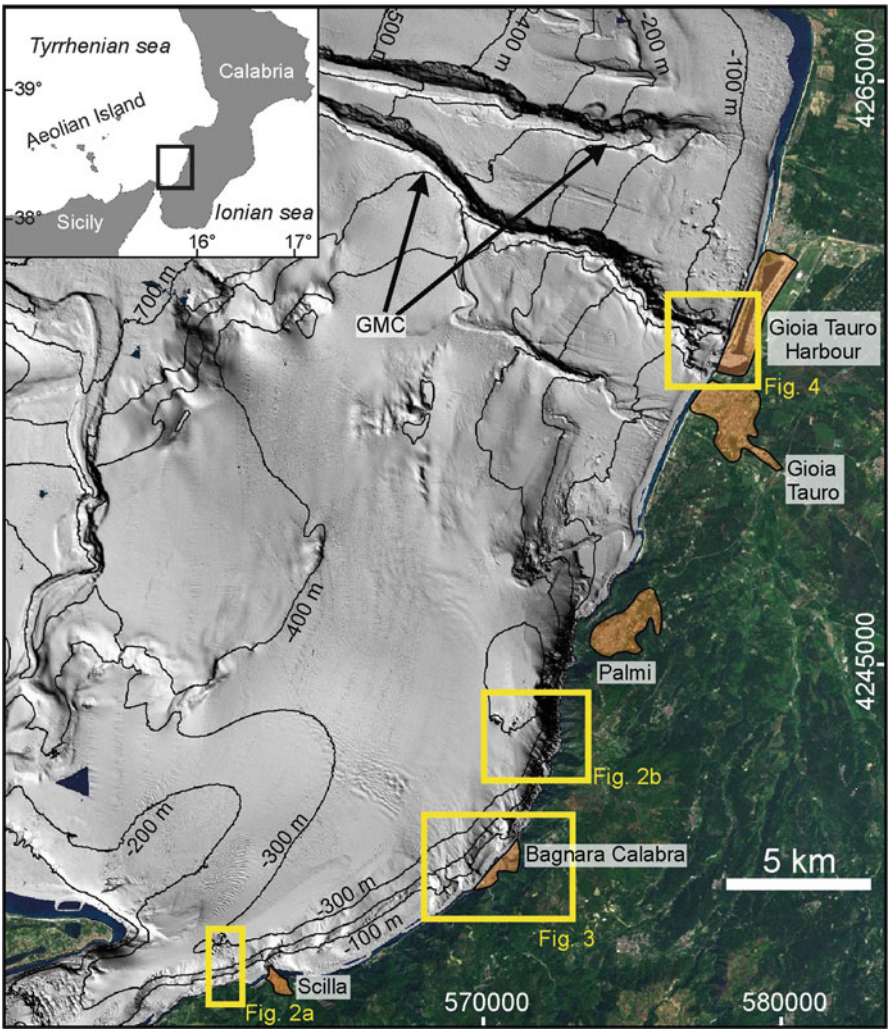

Fig. 23.1 Shaded relief of the study area and main morpho-bathymetric features; GMC: Mesima (to the north) and Gioia (to the south) Canyons. *Brown areas* indicate the extent of main coastal towns and infrastructures. Location of detailed maps are shown as *yellow boxes*

23.3 Data and Methods

This work relies on the interpretation of high-resolution morpho-bathymetric data collected during several cruises carried out over the last 10 years aboard R\Vs *Urania* and *Universitatis* (and small boats for shallow-water surveys). Data were acquired using multibeam systems operated at different frequencies (from 50 to 455 kHz) and DGPS- or RTK-positioning for assuring maximum resolution at all

the water depths. Volume of material mobilized from slope failures was estimated from landslide scars and deposits through the morphological reconstruction of a pre-failed surface according to the regional slope. Time lapse multibeam surveys were also used to generate residual maps for monitoring rapid morphological changes in unstable and/or highly dynamic environments, such as canyon headwalls.

23.4 Results

Morpho-bathymetric analysis indicates that sediment mass failures display different geomorphic features and variable spatial scale and depth range. Among the over 400 landslide scars mapped in this margin (Casas et al. 2012), we focus only on selected cases where (a) the slide scars and deposits are well-defined, (b) occur in coastal or very shallow-water, and (c) show evidence of recent activity and/or are related to known tsunamigenic failures.

Coastal landslides with hummocky deposit are described offshore Scilla (Fig. 23.2a) and Palmi (Fig. 23.2b). In the first case, two slide scars are presented, one affecting the coastal cliff (Mt. Pacì) and one carving the narrow shelf immediately in front of it, suggesting two genetically related events.

The landslide deposits lie between −270 and −305 m, where slope gradients abruptly decrease from 8–10° to <2°. The deposits cover an area of ~700.000 m^2 and show a rough morphology due to several hummocks ranging 20–180 m in length and 2–30 m in relief. Mobilized volume from the subaerial and submarine scars is estimated in the order of 5 (Bozzano et al. 2011) and 3×10^6 m^3, respectively. The total volume of the landslide deposits is estimated in the order of $6–8 \times 10^6$ m^3, 12–14 % of which consists of hummocks that increase in size toward the more distal part of the deposit.

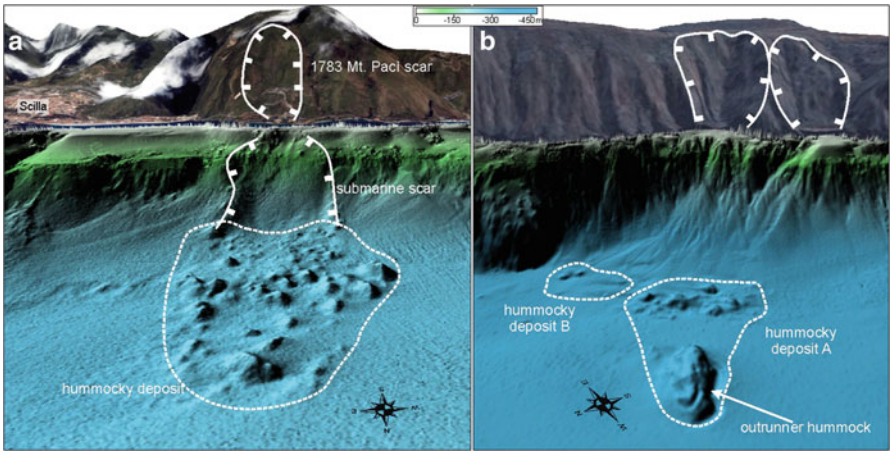

Fig. 23.2 3-D view of landslide deposits with hummocky morphology identified offshore Scilla (**a**) and Palmi (**b**) (see Fig. 23.1 for location)

Offshore Palmi a landslide deposit at water depth between −390 and −410 m, where slope gradients decrease from 6–8° to 2–3°, shows hummocky morphology as well (Fig. 23.2b). It likely relates to two distinct slide scars carving the coastal cliffs, by this displaying a patchy distribution, with a main depocentre (A in Fig. 23.2b) extending over ∼700.000 m^2 and a smaller one (∼100.000 m^2) east of the former (B in Fig. 23.2b). The main deposit forms a cluster of hummocks (ranging 40–120 m in length and 5–12 m in height) at the base of the slope (total volume of ∼800.000 m^3), 300 m from which lays a large out-runner hummock (470 m long, 230 m wide and 50 m high; 2×10^6 m^3 estimated volume). Deposit B consists of hummocks up to 70 m long and 10 m high, summing up to an estimated volume of 90.000 m^3. No submarine slide scar is observed in addition to the two sub-aerial scars and the littoral wedge (LW, hereafter) is well-preserved in this sector.

Submarine scars at canyon headwalls are observed offshore Bagnara Calabra and Gioia Tauro, displaying a retrogressive pattern and resulting in more than 50 detectable slide scars (Figs. 23.3 and 23.4).

Offshore Bagnara Calabra, three channels show headwalls extending from −15 to −200 m as the result of several coalescing landslide scars (up to 50–100 m wide, Fig. 23.3) that affect the littoral wedge, suggesting very recent erosion. Indeed, based on the comparison between geo-referenced aerial photo acquired in 2003 and multibeam bathymetry acquired in 2007, the erosional edge of the LW shows two loci of erosional retreat: one affects an area of 50.000 m^2 and is quantifiable as a coastward retreat of 40 m (Fig. 23.3b); the other affects an area of 5.000 m^2 and results in a retreat of 50 m along a newly formed landslide scar (Fig. 23.3c). A residual bathymetric map (derived from surveys on July 2007 and October 2008) of one of the channel headwall shows a neat semi-circular retrogressive slide scar at ∼15 m water depth (Fig. 23.3e). Thalwegs are marked by crescent-shaped, concave-down bedforms, with tens to hundreds of meters wavelength and amplitude of few meters.

The Gioia Canyon headwall (Fig. 23.4) shows two retrogressive branches that deeply indent the continental shelf at water depth of only 5–10 m, each branch consisting of several small (100–200 m wide) landslide scars; downslope, the thalweg shows a frame of crescent-shaped bedforms similar in size and shape to those recognized in the canyons offshore Bagnara.

23.5 Discussion and Conclusions

We define two types of mass failure yielding potential geohazard over a large number of geomorphic features indicative of mass movement along the Calabrian Tyrrhenian margin: (1) rocky coastal failures that evolve into submarine rock/debris avalanche (e.g. Locat et al. 2004; Shea and van Wyk de Vries 2008; Romagnoli et al. 2009); (2) submarine retrogressive scars confined at canyon headwalls.

Type 1 is documented by hummocky landslide deposits offshore Scilla and Palmi, where coastal failure has been interpreted as a fault zone deformation effect

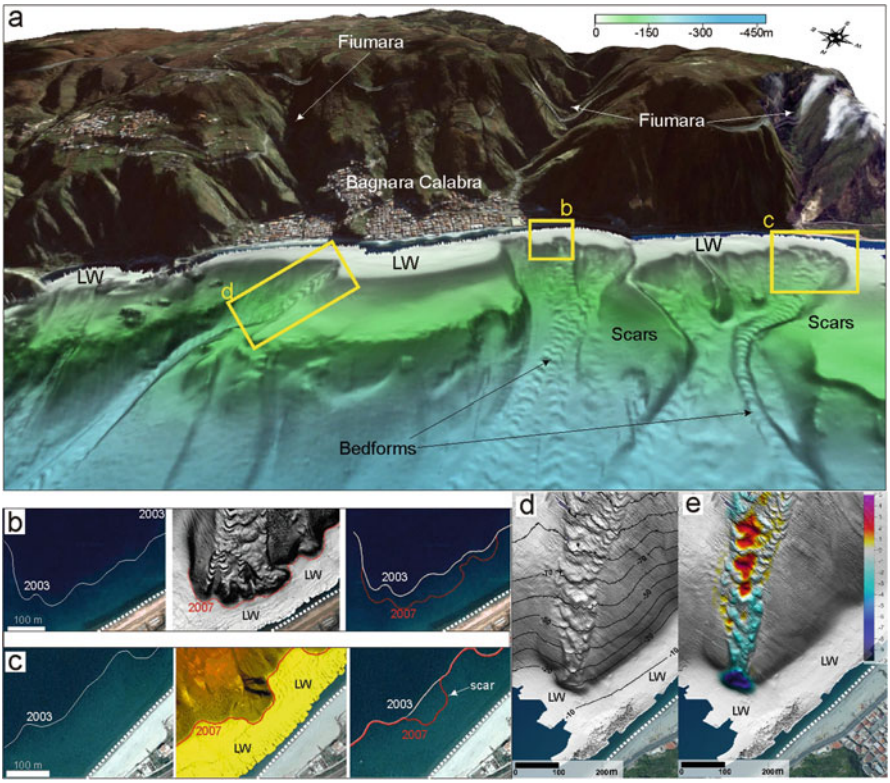

Fig. 23.3 (**a**) 3-D view of channels offshore Bagnara Calabra, deeply indenting the littoral wedge; note the entrenchment of fiumara and the vicinity of their mouths to the channel headwalls (see Fig. 23.1 for location of image). (**b**) and (**c**) the *left panels* show geo-referenced aerial photo (acquired in 2003, *dotted white lines* indicate the coastlines), where the different color of the sea allows to map the edge of the littoral wedge (*LW*), indicated by *solid white line*; the *middle panels* show the multibeam bathymetry (2007), where the edge of LW is indicated by *red lines*; the *right panel* show the comparison of LW edge mapped in 2003 and 2007, where a coastward retreat is observed. (**d**) and (**e**) Shaded relief related to the 2008 survey and residual map obtained as difference between 2007 and 2008 bathymetries of the channel headwall offshore Bagnara, providing evidence of a new slide scar

in relation with known active fault systems (e.g. Ferranti et al. 2008). In this view, the hummocky deposit offshore Scilla relates to the Mt. Pacì slide, triggered during the second main shock of the 1783 earthquake sequence (Bozzano et al. 2011). However, the recognition of a submarine scar coaxial with the subaerial one suggests a multiple event and poses a question on the timing/triggering relationships between the two failures (Fig. 23.2a). Unraveling such question would bring relevant insights in geohazard perspective, especially in the case of a shallow submarine landslide affecting retrogressively the instable coastal sectors, as proposed for other coastal landslide complexes (Cauchon-Voyer et al. 2008).

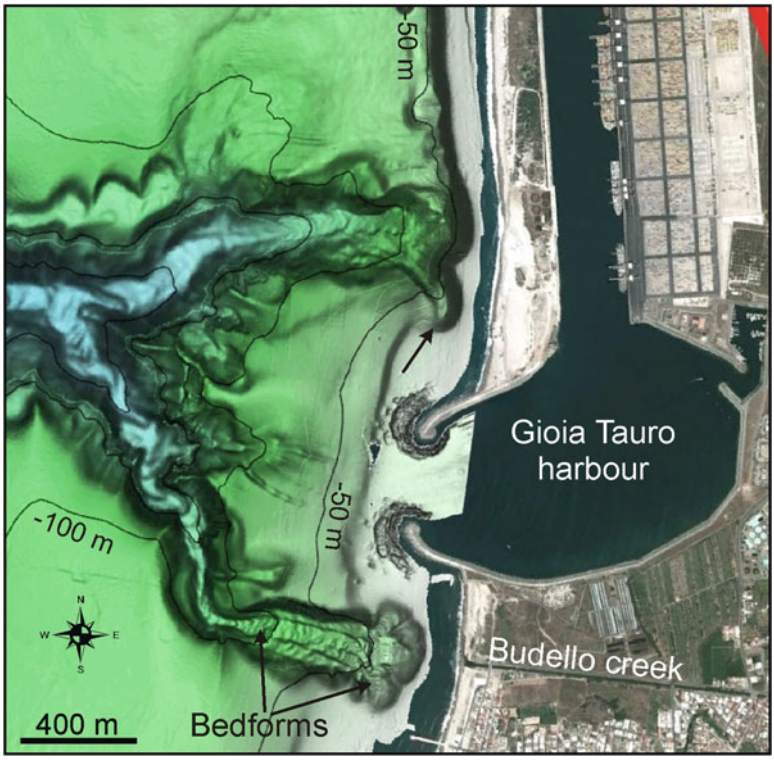

Fig. 23.4 Shaded relief of Gioia Tauro Canyon multiple headwall, deeply indenting the continental shelf and confining the Gioia Tauro harbour entrance

The landslide deposits offshore Palmi are interpreted as older failures with respect to the Scilla event, as the presence of a well-preserved littoral wedge and the lack of related submarine scars indicate that these events occurred before the development of the littoral wedge.

The shape and distribution of the hummocky landslide deposit offshore Palmi and Scilla also provide hints on post-failure processes. Failed deposits lie in correspondence of a marked decrease of slope gradients, in agreement with the fact that cohesionless inertial flows rapidly stop when gradients decrease (Jaeger et al. 1996). However, the average increase in hummock size with distance from the source area contrasts with common behavior of subaerial rock/debris avalanche (Yoshida et al. 2012). A possible explanation to this may reside in the low run out of these failure events, which would have hampered fragmentation of the hummocks by reducing time and distance available for blocks to partition according with the expected kinetic energy/size relationship.

Type 2 is documented by retrogressive scars within the headwalls of canyons offshore Bagnara Calabra and GMC; the lack of related slide deposits may indicate disintegrative failures (e.g. McAdoo et al. 2000). This type denotes the importance

of multiple predisposing factors, including high-rate, rapid sedimentation supplied both by coastal creeks (Fiumara in Fig. 23.3 and Budello in Fig. 23.4) directly discharging throughout the narrow shelf and onto steep slope settings and by sediment transported by long-shore currents that can be trapped within canyon heads (Fig. 23.3). High-energy sedimentary dynamics is further proved by the widespread crescent-shaped bedforms on the canyon thalwegs, similar to those observed in other active canyons (e.g. Monterey Canyon; Paull et al. 2010). Related to this depositional dynamics are also some possible triggering mechanisms, as for instance the load exerted by hyperpycnal flows generated during flash-flood events (Casalbore et al. 2011); more in general, an additional triggering mechanism is represented by cyclic load due to earthquakes and storm-waves.

From a geohazard perspective, the examples described indicate that coastal and shallow-marine failures cluster in a seismically active margin sector and may be independently solicited or even interact by triggering each other. Coastal rocky landslides have a high tsunamigenic potential, as demonstrated by the 1783 Scilla event that was able to generate up to 16 m-high waves in the near-field, rapidly decreasing far from the source; however, the recurrence time of these failures should be relatively low, as testified by the recognition of only two to three events along the entire margin. Conversely, shallow-marine failures at canyon heads mobilize lower volume, and consequently have a minor tsunamigenic potential, but their frequency is very high. Indeed, in spite of the lack of chronological constraints, the recognition of several slide scars at canyon headwalls that indent the present-day littoral wedge testifies frequent retrogressive failure, also in recent time. Given the proximity of the canyon headwalls at the coast ($\approx$100 m) and their retrogressive evolution, future slope failures could have head-scarps intersecting the shoreline, thus representing a major hazard for coastal settlements. Altogether these results allow to better define regional geohazard along the Calabrian (Tyrrhenian) margin, enlarging the previous knowledge based only on historical reports related to catastrophic events, such as the 1783 Mt. Pacì and the 1977 Gioia Tauro slope failures.

Acknowledgements Crew of R/V Urania and Maria Grazia are acknowledged along with the shipboard party; a special thank is due to Martina Pierdomenico for providing part of the material shown in Fig. 23.3. This research was funded by PRIN2006 and MaGIC Projects and carried out in the frame of RITMARE Project. We thank Francesca Budillon, Leonardo Macelloni and Sebastian Krastel for thoughtful and constructive reviews.

References

Antonioli F, Ferranti L, Lambeck K et al (2006) Late Pleistocene to Holocene record of changing uplift rates in southern Calabria and northeastern Sicily (southern Italy, Central Mediterranean Sea). Tectonophysics 422:23–40

Bozzano F, Lenti L, Martino S et al (2011) Earthquake triggering of landslides in highly jointed rock masses: reconstruction of the 1783 Scilla rock avalanche (Italy). Geomorphology 129:294–308

Casalbore D, Chiocci FL, Scarascia Mugnozza G et al (2011) Flash-flood hyperpycnal flows generating shallow-water landslides at Fiumara mouths in Western Messina Straits (Italy). Mar Geophys Res 32:257–271

Casas D, Chiocci FL, Casalbore D, Ercilla G (2012) Size Distribution of Submarine Landslides along the Gioia Basin. Tyrrhenian Sea (Italy). Rendiconti online della Società Geologica Italiana 21:948–950

Cauchon-Voyer G, Locat J, St-Onge G (2008) Late-Quaternary morpho-sedimentology and submarine mass movements of the Betsiamites area, Lower St. Lawrence Estuary, Quebec, Canada. Mar Geol 251:233–252

Colantoni P, Gennesseaux M, Vanney JR et al (1992) Processi dinamici del canyon sottomarino di Gioia Tauro (Mare Tirreno). Giornale di Geologia 3(54/2):199–213

CPTI Working Group (2004) Catalogo Parametrico dei Terremoti Italiani, version 2004 (CPTI04). INGV, Bologna. http://emidius.mi.ingv.it/CPTI

Fabbri A, Ghisetti F, Vezzani L (1980) The Peloritani-Calabria range and the Gioia basin in the Calabrian arc (Southern Italy): relationships between land and marine data. Geol Romana 19:131–150

Ferranti L, Monaco C, Morelli D et al (2008) Holocene activity of the Scilla Fault, Southern Calabria: insights from coastal morphological and structural investigations. Tectonophysics 453:74–93

Jaeger HM, Nagel SR, Behringer RO (1996) The physics of granular materials. Phys Today 49:32–36

Locat J, Lee HJ, Locat P, Imran J (2004) Numerical analysis of the mobility of the Palos Verdes debris avalanche, California, and its implication for the generation of tsunamis. Mar Geol 203:269–280

Malinverno A, Ryan WBF (1986) Extension in the Tyrrhenian sea and shortening in the Apennines as result of arc migration driven by sinking of the lithosphere. Tectonics 5:227–245

Mazzanti P, Bozzano F (2011) Revisiting the February 6th 1783 Scilla (Calabria, Italy) landslide and tsunami by numerical simulation. Mar Geophys Res 32:273–286

McAdoo BG, Pratson LF, Orange DL (2000) Submarine landslide geomorphology, US continental slope. Mar Geol 169:103–136

Paull CK, Ussler W, Caress DW et al (2010) Origins of large crescent-shaped bedforms within the axial channel of Monterey Canyon, offshore California. Geosphere 6:1–20

Romagnoli C, Casalbore D, Chiocci FL, Bosman A (2009) Offshore evidence of large-scale lateral collapses on the eastern flank of Stromboli, Italy, due to structurally-controlled, bilateral flank instability. Mar Geol 262:1–13

Shea T, Van Wyk de Vries B (2008) Structural analysis and analogue modeling of the kinematics and dynamics of rockslide avalanches. Geosphere 4:657–686

Yoshida H, Sugai T, Ohmori H (2012) Size–distance relationships for hummocks on volcanic rockslide – debris avalanche deposits in Japan. Geomorphology 136:76–87

Part V
Understanding Failure Processes from Submarine Landslide Geomorphology

Chapter 24
Recurrent Superficial Sediment Failure and Deep Gravitational Deformation in a Pleistocene Slope Marine Succession: The Poseidonia Slide (Salerno Bay, Tyrrhenian Sea)

Francesca Budillon, Massimo Cesarano, Alessandro Conforti, Gerardo Pappone, Gabriella Di Martino, and Nicola Pelosi

Abstract A large number of exposed scars, originated by multievent sediment failures, have been identified on the southern flank of a deep submarine valley in Salerno Bay (Southern Tyrrhenian Sea), between depths of 300 and 700 m. A 200 km^2 complex landslide lies across a 17 km-long SW-NE trending anticline, which is exposed 40 m above the seafloor of the continental slope and folds a Pleistocene marine successions. The exposed anticline, as well as others which are more subdued, have been formed by gravity-driven deformation of a deep and unconsolidated slope succession. The deep deformation seems to be coeval with recent stages of regional tectonic activity, given that a regional unconformity related to MIS 6 lowstand seals both the deep landslide features and the fault planes. A combined dataset of 2D high resolution seismics, swath-bathymetric digital elevation model of the seafloor and a gravity core was used to establish a possible relation between recurrent sediment failures at the seabed and the stack of positive reliefs in the compressional toe region of the buried landslide system and to learn more on the timing of the deformation phases.

Keywords Slope sediment failure • Compressional fold • Extensional fissure

F. Budillon (✉) • G. Di Martino • N. Pelosi
IAMC, National Research Council of Italy, Loc. Sa Mardini, Torregrande, 09170 Oristano, Italy
e-mail: francesca.budillon@iamc.cnr.it

M. Cesarano
DiBT, Università degli Studi del Molise, Contrada Fonte Lappone, 86090 Pesche (IS), Italy

A. Conforti
IAMC, National Research Council of Italy, Loc. Sa Mardini, Torregrande, 09170 Oristano, Italy

G. Pappone
DiSAm, Università Parthenope, Centro Direzionale di Napoli - Isola C4, 80143 Napoli, Italy

S. Krastel et al. (eds.), *Submarine Mass Movements and Their Consequences*, Advances in Natural and Technological Hazards Research 37, DOI 10.1007/978-3-319-00972-8_24,

24.1 Introduction

Toe regions of submarine landslide deposits may assume a wide variety of configurations including thrust ramps or displaced fronts as end members in unconfined systems, and folds, buttressed horse toe and/or compressional ridges in confined systems (Trincardi and Argnani 1990; Gamberi et al. 2011). It has long been recognized that unconfined landslides lean towards more accentuated depletion areas, more effective evacuation of scars and considerable run out distances if compared to the volume of involved material; in comparison confined systems show deep basal shear surfaces and accommodate limited differential depth, with relatively modest downslope transfer of displaced sediment (Frey-Martinez et al. 2006). Recently, a tri-dimensional slope stability assessment has demonstrated that compressive structures could favor slope failures, despite a low mean slope angle and low gravity loading of sediment weight, because of a reduction of the shear strength (Sultan et al. 2007).

Surficial and slides on steep continental slopes or on the flanks of compressional structures are often characterized by unconfined displaced masses. The run-out distances of these landslide can be long due to the initial inertia of the displaced masses and the low frictional resistance between them and the undeformed seabed Additionally, large landslide systems are often clues to deeper and older instability processes (Minisini and Trincardi 2009).

This paper reports the first results of an integrated morpho-stratigraphical reconstruction in an unstable slope area within Salerno Bay (Fig. 24.1) that has undergone repeated slope failures since the Middle Pleistocene, driven by different processes and at different spatial scales. Remarkably, the exposed compressional folds in the toe region of a buried large landslide system have themselves become source areas of sediment failures, developing small-scale unconfined slides.

24.1.1 Geological Setting

Half-graben basins (Gaeta, Naples and Salerno bays) separated by structural highs (Mt. Massico, Sorrento Peninsula and Cilento) along the Tyrrhenian side of the Southern Apennine range (Fig. 24.1) resulted from Quaternary extensional tectonics (Casciello et al. 2006 and references therein). The extensive vertical displacement was also accompanied by intense volcanic activity from Somma-Vesuvius, Campi Flegrei and Ischia Island, that produced tephra layers which represent good chronostratigraphic markers for the surrounding areas.

The overall thickness of the Pleistocene basin infill in Salerno Bay, which extends toward the mainland beneath the Sele Plain, ranges between 1,500 and 2,000 m, but can locally exceed a thickness of 3,000 m (AGIP 1977; Bartole et al. 1984; Casciello et al. 2004). These basin fills comprise marine clastic, epicontinental and volcanoclastic sediments which record the interactions between the glacio-eustatic sea level fluctuations and tectonic activity (Aucelli et al. 2012). The bedrock of the

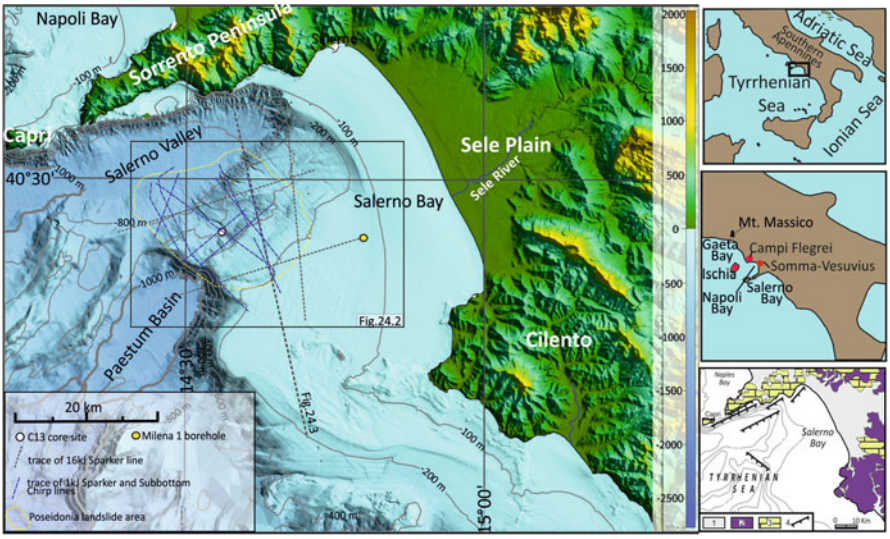

Fig. 24.1 (**a**) DEM of Salerno Bay and studied area; tracks of available seismic profiles across the Poseidonia landslide. (**b**) Schematic representation of the main structural lineaments of the continental margin and inland geology: *1* Quaternary deposits, *2* Meso-Cenozoic basinal units, *3* Meso-Cenozoic carbonate platform units, *4* extensional fault

Quaternary infill is stacked tectonic slices, whose higher terms consist of basinal units with their syn-tectonic siliciclastic deposits (Casciello et al. 2004). Extensive vertical displacements (up to 1,500 m) resulting from extensional tectonics and the accompanying seismic activity are seen as the main agents of gravity-driven mass wasting processes recorded in the stratigraphic succession of the peri-Tyrrhenian basins (Aiello et al. 2009; Milia et al. 2009).

24.2 Methods

This study uses bathymetric and stratigraphic data, collected by the *Istituto per l'Ambiente Marino Costiero* (IAMC) of the National Research Council of Italy (CNR) during the Arcose cruise aboard the R/V Urania in 2010. Chirp sonar profiles were acquired by using a 2–7 kHz sweep-modulated bandwidth. A Digital Elevation Model (DEM) with 10 m grid resolution was derived from bathymetry data collected with a Kongsberg EM710 multi-beam echo-sounder (100 kHz). A 7 m-long gravity core was retrieved from a large erosional scar (LES) of the Poseidonia landslide (Fig. 24.2).

A complete bathymetric basemap of Salerno Bay (Fig. 24.1) was created by compilation of data acquired as part of a national cartographic project conducted by IAMC CNR, between 2002 and 2009. Additional seismic profiles used (Fig. 24.3) were acquired in 1994 by IAMC and DiSAM of Parthenope University using a prototype 16 kJ Sparker source.

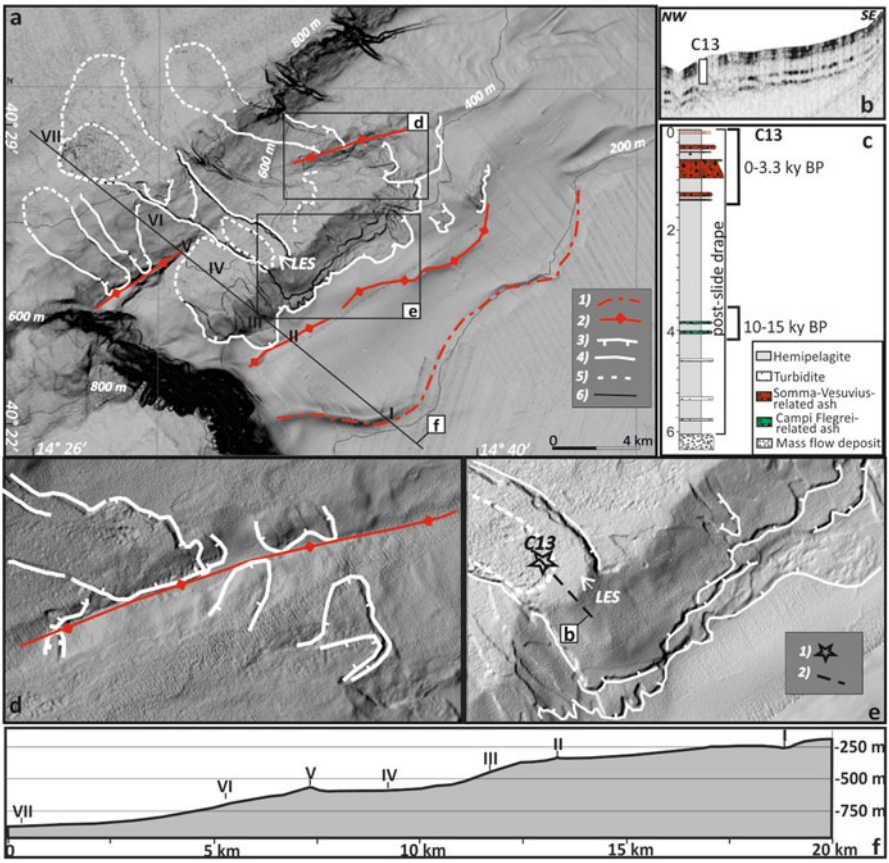

Fig. 24.2 (**a**) Morphological features of Poseidonia landslide system; *red* lineaments mark the morphologies related to the subdued landslide, *white* lineaments outline recent landslide features, 1 extensional fissure, 2 anticline axis, 3 headscar, 4 lateral scar, 5 landslide deposit, 6 track of profile in (**f**); (**b**) *Chirp line* with core location: the core enters a hemipelagic succession and below, a mass flow deposits; (**c**) core stratigraphy, showing the thickness of the post-slide drape above the mass flow deposit, failed from upslope scars; (**d**) detail of the failure scars from the anticline axis; (**e**) the complex erosional front on the upper slope made by several superimposing failure events, 1) core location, 2) track line of fig. (**b**); (**f**) topographic profile across the Poseidonia landslide system (see text for explanation)

24.3 Observations

24.3.1 Submarine Topography of the Poseidonia Landslide Area

The seafloor within the study area slopes, via a series of steps, to the northwest from 200 m to approximately 800 m into what is termed the Salerno Valley (SV) (Figs. 24.1 and 24.2). South of the SV and separated by a steep, fault-controlled

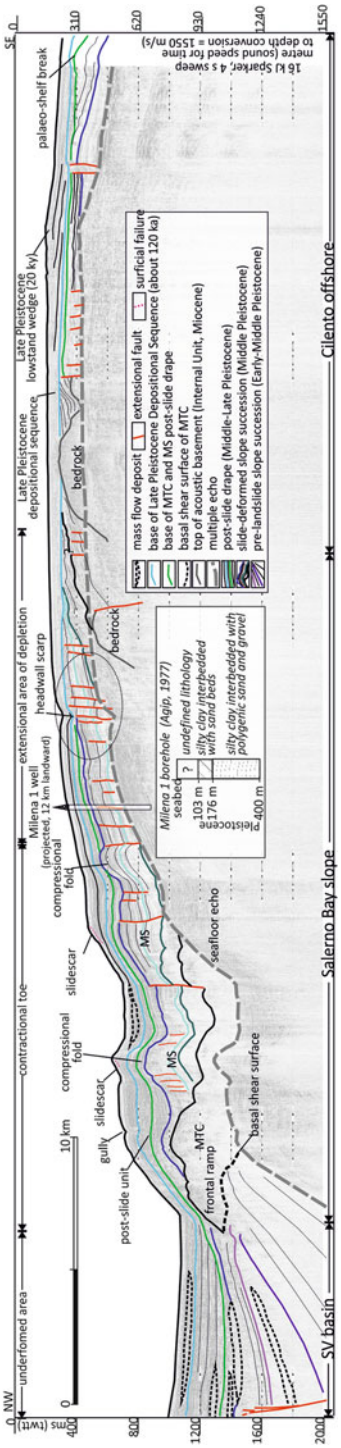

Fig. 24.3 16 kJ Sparker profile (location in Fig. 24.1) across the Poseidonia landslide depicts the features of the buried slides. A chaotic deposit (MTC) thrust over a slope marine succession, (Early?-) Middle Pleistocene in age. Thickness exceeds 200 m in the frontal ramp but seems to diminish in the rear. Above MTC a well-stratified slope succession has successively collapsed (MS), causing the stack of confined compressional folds against the relieved slice of MTC and the formation of an extensional fissure upslope. The landslides are sealed by an undeformed unit that includes the Late Pleistocene depositional sequence

scarp, is the Paestum Basin. The slope has several morphological features that reflect the tectonic and failure processes of the area and the stratigraphic context of the sub-seafloor (Fig. 24.2a, f). From −200 m down to the SV are:

- an arcuate depression 800 m wide and 18 km long (I), running in the 200–350 m depth range, and concave toward the SV; it is almost 20–30 m deep and becomes less evident toward the coast;
- a 4 km-long narrow anticline (II) at west end of the studied area, elevated 15 m above the surrounding seafloor; toward the north-east it turns into a 6° smooth step that deepens the seafloor by about 40 m;
- a gentle slope (III), 2 km wide with a dip of 3–6°, where a 14 km-long erosional front characterized by several headwall scars occurs; failure scarps exceed 20 m high and appear to have failed along stratigraphic surfaces since they show mostly flattened transfer areas;
- an almost flat area (IV), 2–3 km wide and 16 km long, where a 1.2 km-wide slidescar occurs (LES, Fig. 24.2a, e); this sector also accommodates part of the mass waste derived from upslope scars.
- a 18 km-long anticline (V), SW-NE oriented and slightly convex seaward; the structure is elevated 40 m above the surrounding seafloor but deepens in the middle segment where it is crossed by the LES; several other minor scars on the lateral sides, caused its progressive narrowing (Fig. 24.2d);
- a 3 km-wide transfer area (VI), 3–8° dip, where lateral scars of major surficial failures ensue;
- the SV seafloor (VII) that is base level for recent slope mass movements.

24.3.2 Seismic Stratigraphy

The availability of 2D seismic reflection data at different resolutions allows for the recognition of a multievent superficial landslide system with exposed morphologies (Figs. 24.2 and 24.4) and a buried large-scale landslide system (MTC and MS in Fig. 24.3), whose features still affect to some extent the present-day slope seafloor.

The exposed landslide system formed a 14 km-wide erosional front made of numerous intersecting, retrogressive and basinward-progressive scars between −300 and −700 m. Failures removed the uppermost part of the Pleistocene succession (Fig. 24.4) along stratigraphic planes, as the transfer surfaces are mostly planar and height of lateral walls in each individual scar is nearly constant. Major scars are as deep as 10–15 m but exceed 50 m in *LES* (Fig. 24.4b); the volume of removed material ranges between 0.025 and 0.54 km^3. Chirp profiles show that recent failures are localized preferentially on over steepened slopes that occur on top of buried anticlines and fault scarps. The occurrence of acoustically transparent and chaotic deposits beneath the scars indicates that the areas of mass transport deposition have become in turn areas of sediment dismantling. Small scars are also observed carving former scars (Fig. 24.2a), reflecting a seaward propagation of slope instability.

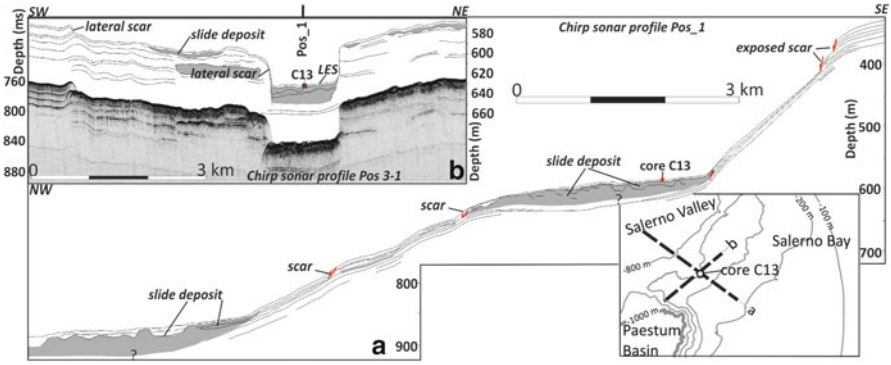

Fig. 24.4 Chirp profiles across the Poseidonia landslide depict the exposed features of the surficial landslide system and the relative deposits; (**a**) profile *Pos3_1* crosses a large exposed slidescar (*LES*) filled with mass flow deposits failed from upslope scars (refer also to Fig. 24.2); (**b**) line drawing of *Pos_1* shows that the landslide deposits settled within two main depocentres: the shallowest is confined on a slope terrace controlled by the emergency of a compressional fold of the buried landslide system, the deepest is at the base of the slope in the SV, beyond the fold

The sub-seafloor of the SV basin consists of 0.4 s-thick (about 320 m), of well-layered, mostly horizontal marine deposits (sheet turbidities and hemipelagites), interbedded with thin mass-transport lenses, overlaying a 0.8 s-thick (about 640 m) unit of inclined reflectors that truncate against a south-east-dipping growth normal fault (Fig. 24.3).

The Salerno Bay slope (Fig. 24.3) shows 0.06–0.12 s-thick (about 50–100 m) undeformed surface unit, consisting of subparallel laterally continuous reflectors that includes the Late Pleistocene depositional sequence (Budillon et al. 2011) formed during the last 4th order glacio-eustatic cycle (100–120 ky cal. BP). Below this unit, a 0.1 s-thick (about 50 m) wedge-shaped unit occurs (MS). Reflector geometries document post-depositional deformation since they are faulted and downthrown toward the basin in the upper slope, and folded and buttressed against the underlying chaotic body (MTC) at the base of slope (Fig. 24.3). Despite the deformation disturbance, reflectors are traceable for long distances along-slope and allow the slide deformation offset to be defined. Down-throw of about 0.23 s (twtt) in the depletion area results from movement on extensional faults that bound the detached tilted blocks, and a resultant shortening of about 10–15 % along the compressional segment occurs. This unit is interpreted as a confined rotational landslide, here referred as a mega-slump (MS), whose headwall scarp has left an extensional fissure in the upper slope, visible as an arcuate depression between −200 and −350 m bsl (Fig. 24.2a, f). The depth of the fissure gradually diminishes from west to east, for two possible reasons: (a) the whole downthrown is reduced at the lateral margin of the headwall scarp; (b) the post-slide sediment wedge has partially filled up the feature.

Below MS is a 0.3–0.4 s-thick (about 240−320 m) unit (MTC in Fig. 24.3) made of chaotic reflectors and topped by an irregular surface separated from the truncated reflectors of the SV by a sharp basal shear surface. The basal shear surface is visible partially since it is covered by multiple echoes in shallow water. However, a deep multichannel seismic record, shot for oil explorations in 1968, and mostly coincident with Fig. 24.3 profile, shows that this shear surface develops from 1.8 s (twtt), up to 1 s (twtt) for about 15 km landwards (Sacchi et al. 1994). According to this observation, the MTC basal shear surface extends nearly underneath the extensional fissure of Fig. 24.2a.

24.3.3 Core Stratigraphy

Gravity core C13 (Fig. 24.2) recovered about 6.7 m of sediment from the *LES* of the exposed landslide system. The core stratigraphy (Fig. 24.2c) consists of olive grey, slightly laminated, fine-grained sediment (hemipelagites), inter-layered with thin deposits of graded fine-sand (turbidites) and several ash layers that correlate to well-known tephras already recognized in Salerno Bay (Insinga et al. 2008; Sacchi et al. 2009; Lirer et al. 2013). The established tephro-stratigraphic framework for this area allows us to constrain the age of the upper 4 m of the *LES* post-slide to the younger than 15ky BP (D. Insinga, personal communication). Resulting depositional rates (of about 24 cm/ky) are in good agreement with those calculated using Palaeo-Secular Variation of Magnetic Field in a slope core, 13 km north-eastward which spans the last 26 ky BP (Iorio et al. 2009). Therefore, the same depositional rate is assigned to the whole drape layer down to a depth of 6 m, resulting in an minimum age of 24–24 ky BP, assuming no erosion at the base of the turbidites. However, the age of the post-slide drape in the *LES* (Figs. 24.2 and 24.4) is likely the age of the failures on the upper slope, whose deposits have partially filled the *LES*, rather than the failure responsible for creating the *LES*.

24.4 Discussion and Conclusion

Using the aforementioned observations a model of the Poseidonia landslide evolution and the relations among events is proposed (Fig. 24.5). Slope oversteepening due to the growth of a SE-dipping fault in the SV (Fig. 24.3) appears to be the preconditioning factor for the failure and emplacement of MTC and successively MS, as they are both sealed by the same marker bed (dark green line, Fig. 24.3). We believe that the activity along the SE-dipping fault was continuous during the Early-Middle Pleistocene, as the basin fill in the SV has regularly accreted against the fault plane and deep reflectors are progressively steeper with depth (Figs. 24.3 and 24.5a). Therefore, sediment failures should have occurred when the slope gradient

overcame the internal shear strength of sediment packages, possibly triggered by the coseismic activity, related to the fault displacement, as most often assumed (Canals et al. 2004).

24.4.1 Emplacement History

MTC emplaced first along a seafloor-emergent basal shear surface, overlying undeformed base-of-slope strata (Fig. 24.5b). Thickness of mass deposit was less than appears now; there are no elements to define the run-out, given that no correlation has been achieved among the undeformed slope reflectors and their counterpart involved in the failure. After the MTC emplacement, the deposition of a wedge-shaped unit ensued, tapering toward the SV. About 0.35 s (twtt) of sediments were accommodated in the depletion area of the MTC, and downlapping reflections developed on the irregular surface MTC (Fig. 24.5c). Further slope over-steepening caused the deformation of the wedge together with the MTC, possibly via reactivated of internal slip planes (Trincardi and Argnani 1990) (Fig. 24.5d). The stack of MTC relief in the toe region acted as a physical confinement for MS, which, as a result, was folded and buttressed against the MTC frontal ramp. On the whole, a 15 % contraction of the total length of the rotational slides is possible. The cumulative height of the headwall drop (about 0.23 s twtt, or 170 m) is probably underestimated, since the foot-wall has undergone extensive erosion and progressive leveling during ensuing lowstand phase of Late Pleistocene.

We believe that the formation of internal shear planes could explain both the remarkable over-thickness and the chaotic character of MTC with respect to MS.

The anticlines, rapidly stacked within MS and accompanied by internal disruption along their axis (Fig. 24.3), underwent frequent failures possibly due to the reduced competency of geotechnical properties resulting from excess pore pressure and reduced shear strength (Canals et al. 2004; Sultan et al. 2007). Indeed, the fold profile gets progressively sharper toward the top for the presence of several scars carving its sides and several thin lenses of mass flow deposits occur at the foot of lateral flanks.

Once active deformation of MTC and MS ceased, a drape of shelf margin sediments were deposited. The age of the drape roughly marks the end of the faults' activity and deep-rooted landslide emplacement, which we think occurred shortly before the last interglacial (Fig. 24.3).

The upper part of the drape is carved in turn by several small-scale translational slides, still evident on the seafloor (Figs. 24.2 and 24.4). On the whole, recent scars are confined within the boundaries defined by the older events (Fig. 24.2); however distinct run-outs from LES and other scars on the seaward side of the anticline extend much farther than MTC toe. Disintegrative behavior of the remobilized mass is assumed based on the evacuation efficiency of the scars and distally flattened deposits. Where small, more recently developed scars cut into the stratigraphically

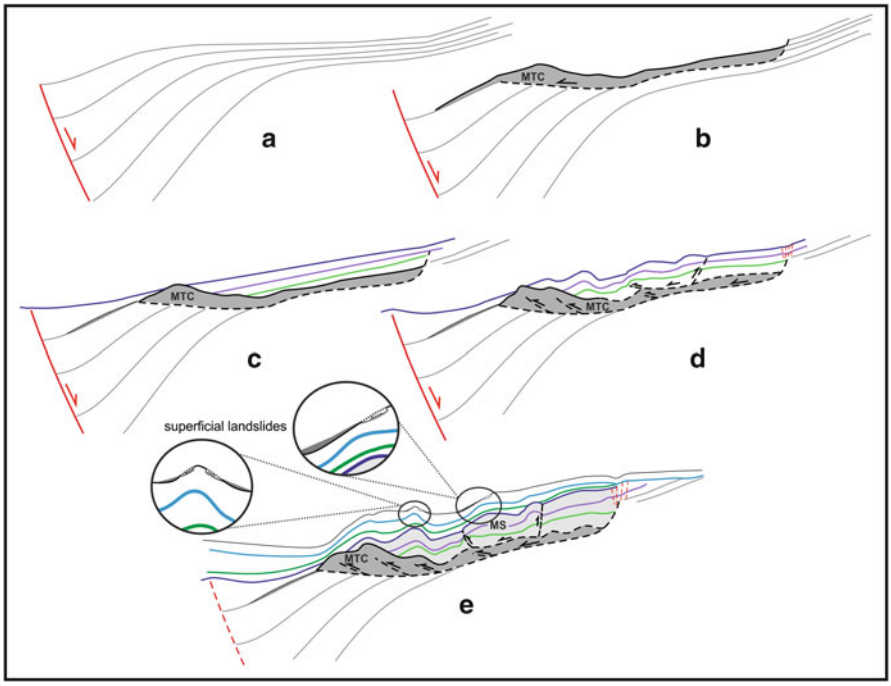

Fig. 24.5 Emplacement history of the Poseidonia landslide by a semi-quantitative evaluation according to thickness (in time), geometries and extension of seismic units (See text for discussion)

deeper and more cohesive sediments exposed by the pre-existing larger scars (i.e., basin ward-progressive scar evolution), the associated deposits show hummocky features and pressure ridges (Fig. 24.2a), indicative of minimal disintegration during transport (Minisini and Trincardi 2009).

It is believed that a different run-out and internal character among slides reflect the lithology of the material involved in the collapse (Gamberi et al. 2011). The stratigraphy of Milena 1 borehole highlights a lithologic change at 170 mbsf (Fig. 24.3) that could approximately correspond to the base of Late Pleistocene drape. Generally, the MTC and MS rotational slides could have involved a coarser lithology, while recent translational slides may have rooted in fine-grained successions punctuated by ash layers from Campania volcanic vents, mostly Late Pleistocene in age. Although the assessment of the timing of recent slides failure is a difficult task, we tentatively date the erosional front (Fig. 24.2) to the last glacial lowstand on the basis of the post-slide drape that holds several ash layers from last 15 ky of activity from the Somma-Vesuvius and Campi Flegrei vents (Fig. 24.2c).

Acknowledgment The authors are particularly grateful to Jan Sverre Laberg and Silvia Ceramicola for reviewing the manuscript. Donatella Insinga provided us with useful information on tephras. This study benefited with the contribution of RITMARE Flagship Project, funded by MIUR (NRP 2011–2013).

References

AGIP (1977) Temperature sotterranee. AGIP, Segrate Milano, 1390 pp

Aiello G, Marsella E, Di Fiore V, D'Isanto C (2009) Stratigraphic and structural styles of half-graben offshore basins in Southern Italy: multichannel seismic and Multibeam morpho-bathymetric evidences on the Salerno Valley (Southern Campania continental margin, Italy). Quaderni di Geofisica 77:1–33

Aucelli PPC, Amato V, Budillon F, Senatore MR, Amodio S, D'Amico C, Da Prato S, Ferraro L, Pappone G, Russo Ermolli E (2012) Evolution of the Sele River coastal plain (southern Italy) during the Late Quaternary by inland and offshore stratigraphical analyses. Rend Fis Acc Lincei 23:81–102

Bartole R, Salvelli D, Tramontana M, Forese C (1984) Structural and sedimentary features in the Tyrrhenian margin off Campania, southern Italy. Mar Geol 55:163–180

Budillon F, Conforti A, Tonielli R, De Falco G, Di Martino G, Innangi S, Marsella E (2011) The Bulgheria canyon-fan: a small-scale proximal system in the eastern Tyrrhenian Sea (Italy). Mar Geophys Res 32(1):83–97

Canals M, Lastras G, Urgeles R et al (2004) Slope failure dynamics and impacts from seafloor and shallow sub-seafloor geophysical data: case studies from the Costa project. Mar Geol 213:9–72

Casciello E, Cesarano M, Conforti A, D'Argenio B, Marsella E, Pappone G, Sacchi M (2004) Extensional detachment geometries on the Tyrrhenian margin of the Southern Apennines (the Salerno district). In: Pasquarè G, Venturini C (eds) Mapping geology in Italy. APAT, Servizio Geologico d'Italia, Firenze, pp 29–34

Casciello E, Cesarano M, Pappone G (2006) Extensional detachment faulting on the Tyrrhenian margin of the Southern Apennines contractional belt (Italy). J Geol Soc 163(4):617–629

Frey-Martinez J, Cartwright J, James D (2006) Frontally confined versus frontally emergent submarine landslides: A 3D seismic characterisation. Mar Petr Geol 23(5):585–604

Gamberi F, Rovere M, Marani M (2011) Mass-transport complex evolution in a tectonically active margin (Gioia Basin, Southeastern Tyrrhenian Sea). Mar Geol 279:98–110

Insinga DD, Molisso F, Lubritto C, Sacchi M, Passariello I, Morra V (2008) The proximal marine record of Somma-Vesuvius volcanic activity in the Naples and Salerno bays, Eastern Tyrrhenian Sea, during the last 3 kyr. J Volcanol Geotherm Res 177(1):170–186

Iorio M, Liddicoat J, Budillon F, Incoronato A, Tiano P, Coe R, Marsella E (2009) Palaeomagnetic secular variation time constraint of Late Neogene geological events in sediment from Eastern Tyrrhenian Sea margin. In: Kneller BC et al (eds) External controls on deep-water depositional systems, SEPM special publication 92. SEPM, Tulsa, pp 233–243

Lirer F, Sprovieri M, Ferraro L, Vallefuoco M, Capotondi L, Cascella A, Petrosino P, Insinga DD, Pelosi N, Tamburrino S, Lubritto C (2013) Integrated stratigraphy for the Late Quaternary in the eastern Tyrrhenian Sea. Quat Int 292:71–85

Milia A, Turco E, Pierantoni PP, Schettino A (2009) Four-dimensional tectono- stratigraphic evolution of the Southeastern peri-Tyrrhenian Basins (Margin of Calabria, Italy). Tectonophysics 476:41–56

Minisini D, Trincardi F (2009) Frequent failure of the continental slope: the Gela Basin (Sicily Channel). J Geophys Res 114:1–17

Sacchi M, Infuso S, Marsella E (1994) Late Pliocene–Early Pleistocene compressional tectonics in offshore Campania (eastern Tyrrhenian Sea). Boll di Geof Teoricaed Applicata 36(141–44):469–482

Sacchi M, Molisso F, Violante C, Esposito E, Insinga D, Lubritto C, Porfido S, Tòth T (2009) Insights into flood-dominated fan-deltas: very high-resolution seismic examples off the Amalfi cliffed coasts, eastern Tyrrhenian Sea. In: Violante C (ed) Geohazard in rocky coastal areas, Special publication 322. The Geological Society, London, pp 33–71

Sultan N, Voisset M, Marsset B, Marsset T, Cauquil E, Colliat J (2007) Potential role of compressional structures in generating submarine slope failures in the Niger Delta. Mar Geol 237(3–4):169–190

Trincardi F, Argnani A (1990) Gela submarine slide: a major basin wide event in the Plio-Quaternary foredeep of Sicily. Geo-Mar Lett 10:13–21

Chapter 25
Mass Wasting Features on the Submarine Flanks of Ventotene Volcanic Edifice (Tyrrhenian Sea, Italy)

Daniele Casalbore, Alessandro Bosman, Eleonora Martorelli, Andrea Sposato, and Francesco Latino Chiocci

Abstract High-resolution multibeam bathymetry acquired around Ventotene and S. Stefano islands (eastern Pontine Archipelago, Italy) enabled us to map main mass wasting features affecting their submarine portions. Large-scale instability morphological features are absent (apart from a 4×2.5 km caldera in the western sector), whereas 126 landslide scars of 100-m of length scale were identified between 130 and 1,150 m of water depth (wd). Two main groups of scars can be distinguished: the first one affects the edge of the insular shelf between 130 and 260 m wd. The second group affects the lower slope and surrounding basins, representing cases of retrogressive failure at the heads of channelized features. The different morphological relief of the scars coupled with the recognition of crescent-shaped bedforms made it possible to distinguish two mass-wasting/erosive stages and consequently to map the more active sectors of the edifice. The future evolution of the mass wasting processes will produce the enlargement of erosive sectors with possible formation of large channels, which will carve wide sectors of the edifice, as suggested by available geological constraints and by comparison with the nearby and older western sector of the Pontine archipelago, where a more mature organization of mass wasting processes is observed. The present study can provide useful insights for hazard assessment and future planning of risk mitigation in such islands that are densely populated and touristically exploited during the summer months.

Keywords Submarine landslide • Caldera • Multibeam • Morphometric analysis • Retrogressive failures

D. Casalbore (✉) • A. Bosman • E. Martorelli • A. Sposato
CNR-IGAG, P.le Aldo Moro 5, Rome 00185, Italy
e-mail: daniele.casalbore@igag.cnr.it; daniele.casalbore@unibo.it

F.L. Chiocci
Dip. Scienze della Terra, Sapienza, University of Rome, P.le Aldo Moro 5, Roma 00185, Italy

S. Krastel et al. (eds.), *Submarine Mass Movements and Their Consequences*, Advances in Natural and Technological Hazards Research 37, DOI 10.1007/978-3-319-00972-8_25,

25.1 Introduction

Over the last decades, advances in seafloor mapping have greatly contributed to improve our knowledge of marine volcanic edifices and to document the common occurrence of gravity-related processes on the flanks of insular volcanoes (e.g. Boudon et al. 2007). Such studies are usually related to the submarine portions of active insular volcanoes, such as Stromboli (Bosman et al. 2009), Vulcano (Romagnoli et al. 2013 and reference therein) and Ischia (Chiocci and De Alteriis 2006) for the Italian seas, confirming the occurrence of widespread mass wasting processes on their flanks. In this manuscript, we present the results of a recent investigation of the mass wasting processes on the submarine portions of the Ventotene edifice, an extinct Pleistocene volcano located in the central Tyrrhenian Sea (Fig. 25.1). A morphometric analysis of the landslide scars affecting the seafloor is presented in order to determine the key factors that control such slope instability. Moreover, a qualitative comparison of the spatial distribution of landslide scars at Ventotene with respect to that observed on the nearby Plio-Pleistocene western Pontine islands (Chiocci et al. 2003) was realized in order to provide insights on how the submarine morphology of the Ventotene edifice might develop in the future.

25.2 Geological Setting

The Pontine islands, located in the central Tyrrhenian Sea, lie on a basement that was thinned and stretched by Plio-Pleistocene extensional deformation, related to the opening of the Vavilov basin (Zitellini et al. 1984). This setting gave rise to a very steep, NW-SE trending continental slope and to intra-slope basins (e.g., the Ventotene and Palmarola basins), promoting intense volcanic activity during late Pliocene – late Pleistocene in the Pontine Archipelago (Cadoux et al. 2005). Seismic activity is generally low in the central Tyrrhenian Sea; in detail, the Pontine Archipelago is characterized by frequent, but weak earthquakes (Favali et al. 2004).

The western sector of the archipelago includes Ponza, Zannone and Palmarola islands (Fig. 25.1), which developed during two main volcanic cycles dated between 4.2–2.9 Ma and 1.6–0.9 Ma (Cadoux et al. 2005). The eastern sector includes Ventotene and S. Stefano islands, representing the tip of a large strato-volcano (i.e. Ventotene edifice) emplaced at the centre of the subsiding Ventotene basin and bounded southward by NW-SE regional features (Marani and Gamberi 2004). Ventotene and S. Stefano islands are composed of basaltic to trachytic effusive and pyroclastic products that erupted during the time span of 0.92–0.33 Ma (Metrich et al. 1988). The volcanic activity ended with a large explosive eruption, i.e. the Parata Grande lgnimbrite (0.15–0.3 Ma, Perrotta et al. 1996). According to stratigraphic, magnetic and low-resolution bathymetric data, Metrich et al. (1988) identified a possible caldera collapse, 2–3 km off the western coast of Ventotene Island, where the eruptive center of the edifice was presumably located.

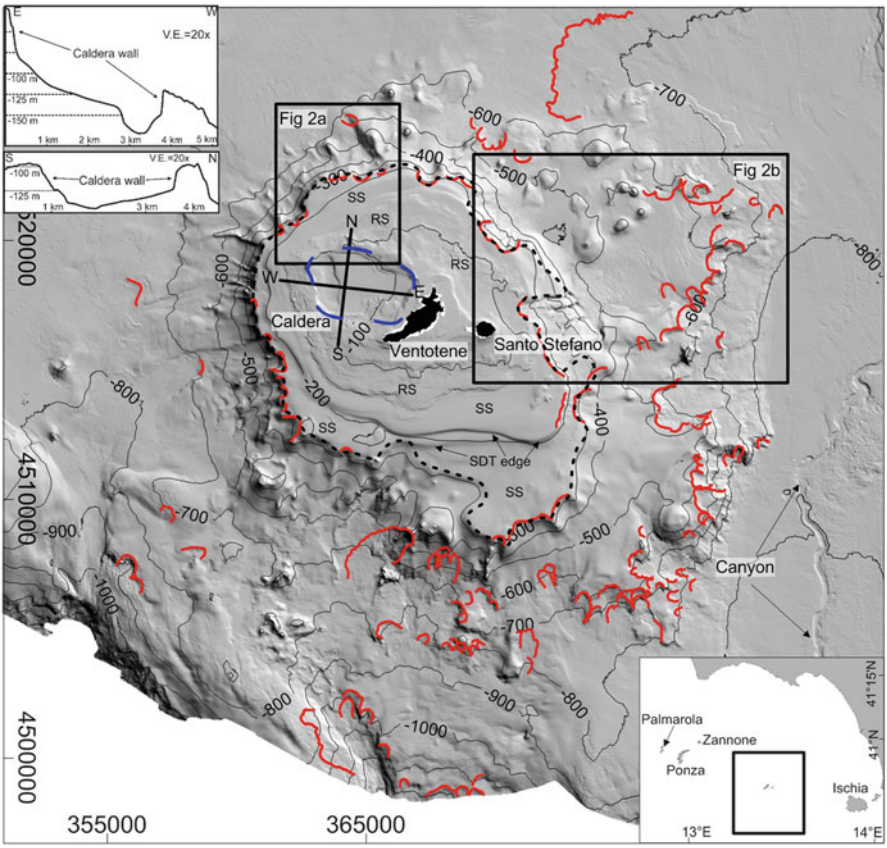

Fig. 25.1 Shaded relief of Ventotene edifice, isobaths each 100 m. The *dashed blue line* represents the caldera limit; in the *upper left*, two cross-sections show its shape. The *red* and *dotted black lines* represent the recognized landslide scars and the outer edge of the insular shelf, respectively; *SDT* submerged depositional terrace, *RS* rough seafloor, *SS* smooth seafloor, *V.E.* vertical exaggeration. *Bold black boxes* represent the following figures and inset on *lower right* represents the location of the study area within the central Tyrrhenian Sea

25.3 Data and Methods

Multibeam data were acquired from Ventotene edifice with systems operating at frequencies of 70 and 300 kHz (EM710 and EM3002D) aboard RV *Urania* and *Maria Grazia* (CNR, Italy) between 2009 and 2012. Data are DGPS-positioned and their processing was performed with Caris HIPS and SIPS software to generate digital terrain models with cell-size ranging from 1 m in shallow water (<100 m wd) to 10 m at greater depths. Slide scars were identified on bathymetric data through the recognition of abrupt scarps. We also used DEMs to calculate slope gradients,

a useful tool to classify the recognized scars as well as a critical factor for slope stability. The volumes of the slides were calculated by using headscarp height, scar gradient and area, and assuming a wedge geometry.

25.4 General Morphology

The Ventotene edifice has a diameter of about 23 km and rises from 600 m wd in the NW sector to 800 m wd in the E and SE sectors. The upper part of the edifice is characterized by a 6–8 km wide insular shelf, with the outer edge located at variable depths (between 130 and 260 m wd, dotted line in Fig. 25.1). The insular shelf is characterized by gradients <3–4°, and its largest portion is characterized by a rough seafloor (RS) in the first 100 m wd, whereas a smoother seafloor (SS) is recognized at greater depths (RS and SS in Figs. 25.1 and 25.2). The RS type mostly corresponds to rocky outcrops and the SS to a terraced morphology due to the presence of prograding sedimentary bodies located at different depths. These bodies are a common sedimentary feature found on steep and narrow Italian shelves in volcanic and non-volcanic setting, where they have been interpreted as submarine depositional terraces (SDT in Figs. 25.1 and 25.2, Chiocci and Orlando 1996; Chiocci et al. 2004). On the western part of the shelf, a 4×2.5 km depression, delimited by 30–40 m height scarp, is present (dashed blue lines in Fig. 25.1). The floor of the depression has a smooth morphology due to the presence of a sedimentary infill, so that the original height of the scarp was larger than the present day. Below the shelf edge, gradients increase to values >20° and the seafloor is characterized by an uneven morphology, due to the presence of volcanic outcrops alternating with erosive-depositional features (Fig. 25.1).

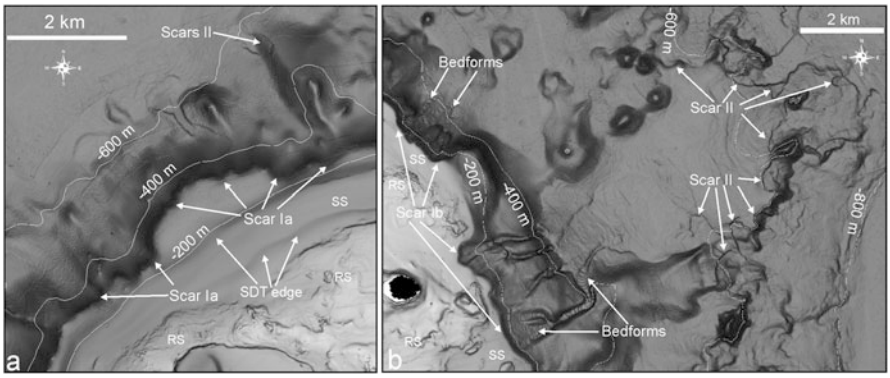

Fig. 25.2 Shaded relief of the north-western (**a**) and north-eastern (**b**) sectors of Ventotene edifice, where landslide scars type Ia, Ib and II are present, see text for details. Location of these figures can be found on Fig. 25.1 as well as the acronyms' definitions

Table 25.1 Landslide statistics for the total distribution of scars identified on Ventotene submarine flanks and subdivided according to their depth and location, i.e. shelves and submerged depositional terraces (SDT), volcanic flanks and basin

	Number of cases	n\a cases	Minimum	Maximum	Mean	Median	Standard deviation
Total distribution							
Water depth (mbsl)	126	0	130	1,157	548	576	233
Length (m)	126	0	66	2,900	322	246	323
Width (m)	126	0	136	4,400	492	390	472
Headscarp height (m)	101	25	5	83	19	15	14
Headscarp gradient (°)	101	25	5	43	18	18	7
Scar gradient (°)	113	13	2	29	11.8	10	6.9
Area (10^6 m^2)	126	0	0.006	9.8	0.248	0.086	0.9192
Volume (10^6 m^3)	101	25	0.036	68.6	3.2361	0.6525	10.2768
Shelves and SDT							
Water depth (mbsl)	29	0	130	260	217	240	44
Length (m)	29	0	100	990	309	194	248
Width (m)	29	0	200	1,860	512	400	340
Headscarp height (m)	10	19	13	83	33	22	26
Headscarp gradient (°)	10	19	18	27	21	21	2.7
Scar gradient (°)	29	0	7	29	18.7	19	6.5
Area (10^6 m^2)	29	0	0.02	1.6	0.2141	0.086	0.3332
Volume (10^6 m^3)	10	19	0.16	64	11.883	1.3125	22.0411
Volcanic flanks and basin							
Water depth (mbsl)	97	0	297	1,157	647.06	630	165.61
Length (m)	97	0	66	2,900	326.35	254	344.4
Width (m)	97	0	136	4,400	486.98	370	507.01
Headscarp height (m)	91	6	5	55	17.5	14	10.8
Headscarp gradient (°)	91	6	5	43	18	17	7.27
Scar gradient (°)	84	13	2	28	9.43	8	5.21
Area (10^6 m^2)	97	0	0.006	9.8	0.2582	0.086	1.033
Volume (10^6 m^3)	91	6	0.036	68.6	2.2859	0.637	7.71654

Water depth is referred to the minimum depth of the headscarp
n\a non-available cases are used to indicate the morphometric parameters that cannot be measured

25.4.1 Morphometric Analysis of Landslide Scars

A total of 126 landslide scars were recognized between 130 and 1,150 m wd, and their main morphometric parameters were measured (Table 25.1). The slide scars are few hundreds of meters long in the downslope direction and some hundreds of meters wide across. They witness the mobilization of estimated debris volumes ranging from few tens of thousands to some tens of millions of cubic meters; however, downslope related landslide deposits are commonly lacking.

Although slide scars were recognized at different depths all over the flanks, their distribution is not random. Two main groups can be recognized according to their distribution around specific sectors and depth intervals:

(a) the first group (29 scars) affects the edge of the insular shelf and the overlying terraced features between 130 and 260 m wd, and it shows the highest scar gradients (median value of 19°, Table 25.1). Two different scar morphologies are present in this group: the first type mainly affects the outer edge of the shelf (scar Ia in Fig. 25.2a) and it is characterized by the lack of a marked headwall. The second type (scar Ib in Fig. 25.2b) occurs at shallower depths, indenting the edge of the deeper SDTs and it shows a marked headwall, with median height of 22.5 m and gradient of 21.5° (Table 25.1). These scars often represent headwalls of channelized features, where crescent-shaped bedforms are present (Fig. 25.2b). The bedforms have wave-length of 70–110 m, amplitudes of 3–5 m and their crest-lines are concave downslope and perpendicular to the maximum gradient direction;
(b) the second group (97 scars) is observed on the volcanic flanks and the surrounding basins between 300 and 1,150 m wd (median value at 630 m wd, Table 25.1 and Fig. 25.2). The scars are longer and higher than in the previous group and most of them are characterized by a well-defined headscarp, with median height of 14 m and gradient of 8°. It is also noteworthy that a higher spatial density of slide scars is recognized in the south-eastern and southern flanks with respect to the western one (Fig. 25.1).

25.5 Discussions and Conclusions

25.5.1 Large-Scale Instability Processes

The high-resolution bathymetry of Ventotene edifice allowed us to recognize a large number of small and medium-scale landslides with landslide volumes ranging between tens of thousands up to some tens of millions m^3, whereas morphological features related to large-scale slope instabilities are absent. The latter features are quite common features on flanks of volcanic islands, where the seafloor morphology is dominated by debris avalanche and slump deposits related to large-scale sector collapses (e.g. Moore et al. 1994; Urgeles et al. 1997; Boudon et al. 2007; Casalbore et al. 2010 and reference therein). This is also the case at the nearby Ischia island that was affected by large-scale instability processes promoted by intermittent caldera resurgence, that caused a rapid uplift of the 780 m high Mt Epomeo in the past 33 ka (Chiocci and De Alteriis 2006).

The Ventotene edifice formed within the confined and subsiding Ventotene basin and is characterized by low relief (<1,000 m) and by the lack of a well-defined axial rift. Other volcanic islands morphologically similar to Ventotene (Pico and Faial at Azores and Vulcano at Eolie; Mitchell et al. 2012; Quartau et al. 2012; Romagnoli et al. 2013, respectively) do not show large-scale mass wasting features as well and we suggest that this type of islands has a low potential to generate large-scale instability processes. The presence of one (or more) axial zones is,

indeed, a common character of collapsed volcanic edifices, as demonstrated by field examples and laboratory studies (e.g. Tibaldi 2001 and reference therein). In contrast, the volcano-tectonic evolution of Ventotene was characterized by summit caldera collapse, as supported by the recognition of an old and partially filled depression in the western part of the edifice (Fig. 25.1). According to its shape and size, this depression can be interpreted as a caldera collapse, as was similarly suggested by Metrich et al. (1988). Its formation may be related to the last explosive eruption that ended the volcano-tectonic history of Ventotene at 0.15–0.3 Ma, as hypothesized by Perrotta et al. (1996).

25.5.2 Small-Scale Instability Processes

Another interesting characteristic of the mass wasting processes at Ventotene is the absence of small- and medium-scale landslide scars at depths shallower than 130 m wd. This is likely due to the extensive outcropping of volcanic bedrocks in the inner part of the shelf, as testified by the rough seafloor in the first 100 wd (RS in Figs. 25.1 and 25.2). In contrast, the shallowest scars affect the outer edge of the insular shelf and the deeper SDTs, where the smoother seafloor is related to the presence of a sedimentary cover (SS in Figs. 25.1 and 25.2). These failures may be promoted by over-steepening of non-cohesive sediments near the shelf edge (Table 25.1), similar to slope failures observed around the insular shelves of Stromboli (Casalbore et al. 2011), Faial (Quartau et al. 2012) and Vulcano (Romagnoli et al. 2013). At Ventotene, we tend to exclude a major role of cyclic load due to earthquakes or storm-waves as triggering processes, because of the low seismicity of the area and high depths (>130 m wd) The analysis of the morphological relief of the scars allows to distinguish between two mass-wasting/erosive stages: the deeper scars (Scar Ia in Fig. 25.2a) show a low relief and can be interpreted as older features, partially infilled by the prograding sequences of the SDTs. Contrastingly, the shallower scars (Scar Ib in Fig. 25.2b) have well-defined headscarps and indent the deeper SDTs, witnessing a younger erosive stage, as is also supported by the presence of crescent-shaped bedforms at their base. These bedforms are similar in size and morphology to those recognized at Monterey Canyon head (Paull et al. 2010), and at channelized features at Stromboli and Vulcano submarine edifices (Casalbore et al. 2010; Romagnoli et al. 2013), where they have been interpreted as a proxy of recent sedimentary activity/transport. This evidence has important implications for geohazard assessment at Ventotene, because it allows us to identify the NE sector as the more active of the edifice. This sector need be further investigated and carefully monitored, given that the occurrence of future slope failures at such shallow-water depths could generate local tsunamis.

The other main cluster of slide scars was identified on the lower flanks of Ventotene edifice and the surrounding basins (Table 25.1 and Fig. 25.1). Most of them are present in the southern and south-eastern flanks, where the base of the edifice lie at the greater depths (see Sect. 25.4 and Fig. 25.1), likely in response to

structural control related to regional NW-SE oriented tectonic features. Most of the scars are characterized by a high morphological relief, suggesting a relatively recent activity. Furthermore, they often coalesce to form the headwall of wide channelized features that develop downslope, suggesting a retrogressive mechanism for their origin, as proposed for similar features in other volcanic settings (Chiocci et al. 2003; Casalbore et al. 2010). The lack of landslide deposits at the base of the scars may reflect the disintegrative nature of the failures, where landslide masses either lose cohesion during failure or failed as a cohesive mass and disintegrated downslope, evolving in both cases into debris flows and/or turbidity currents.

25.5.3 Evolution of Mass Wasting Processes

According to the afore mentioned evidence, the evolution of mass wasting at Ventotene may be related to a twofold process. On the one hand, slope failures have affected the shelf edge, where easily removable volcaniclastic material is deposited. This process likely was most active during sea-level low stand and may have been triggered by storm loading. On the other hand, slope instability seems to be related to the progressive upslope migration of slope failures and related channelized features of the lower flanks due to retrogressive instability processes. This evolution should lead to a more mature organization of mass wasting features within some main channels, carving wider sectors of the flanks of the edifice. An extreme case of this evolution is represented by the nearby and older sector of the western Pontine Archipelago and the facing continental slope, affected by pervasive mass wasting processes (up to 98 % of the seafloor is affected by instability; Bosman et al. 2011). Indeed, the cannibalization (slope retreat) of this continental margin is a consequence of extremely high seafloor gradients (8–12°, locally up to 30°) as well as of the presence of regional NW-SE tectonic features active during the Plio-Pleistocene (Chiocci et al. 2003).

Acknowledgments The crews of R/V Urania and Maria Grazia are gratefully acknowledged as well as the people who participated in the surveys. This research is funded by the National "MaGIC" Project and carried out in the frame of "RITMARE" Project. We thank David Völker, Aaron Micallef and Rui Quartau for thoughtful and constructive reviews.

References

Bosman A, Chiocci FL, Romagnoli C (2009) Morpho-structural setting of Stromboli volcano revealed by high-resolution bathymetry and backscatter data of its submarine portions. Bull Volcanol 71(9):1007–1019

Bosman A, Calarco M, Casalbore D et al (2011) Volcanic islands: the tip of large submerged volcanoes that only marine geology may reveal (examples from W Pontine Archipelago, Ischia,

Stromboli and Pantelleria). In: Brugnoli E et al (eds) Marine research at CNR, Department of Earth and Environment (CNR), Rome, pp 433–444

Boudon G, Le Friant A, Komorowski JC et al (2007) Volcano flank instability in the Lesser Antilles Arc: diversity of scale, processes, and temporal recurrence. J Geophys Res 112. http://dx.doi.org/10.1029/2006JB004674

Cadoux A, Pinti DL, Aznar C et al (2005) New chronological and geochemical constraints on the genesis and geological evolution of Ponza and Palmarola volcanic islands (Tyrrhenian Sea, Italy). Lithos 81:121–151

Casalbore D, Romagnoli C, Chiocci F, Frezza V (2010) Morphosedimentary characteristics of the volcanic apron around Stromboli volcano. Mar Geol 269:132–148

Casalbore D, Romagnoli C, Bosman A, Chiocci FL (2011) Potential tsunamigenic landslides at Stromboli Volcano (Italy): insights from marine DEM analysis. Geomorphology 126:42–50

Chiocci FL, De Alteriis G (2006) The Ischia debris avalanche: first clear submarine evidence in the Mediterranean of a volcanic island prehistorical collapse. Terra Nova 18:202–209

Chiocci FL, Martorelli E, Bosman A (2003) Cannibalization of a continental margin by regional scale mass wasting: an example from the central Tyrrhenian Sea. In: Locat J, Mienert J (eds) Submarine mass movements and their consequences. Kluwer Academic, Dordrecht, pp 409–416

Chiocci FL, Orlando L (1996) Lowstand terraces on Tyrrhenian Sea steep continental slopes. Mar Geol 134:127–143

Chiocci F, D'Angelo S, Romagnoli C (eds) (2004) APAT, Atlante dei Terrazzi Deposizionali Sommersi lungo le coste italiane (Memorie Descrittive della carta Geologica d'Italia). Systemcart, Roma

Favali P, Berenzoli L, Maramai A (2004) Review of the Tyrrhenian Sea seismicity: how much is still to be known? Mem Descr Carta Geol d'It XLIV:57–70

Marani MP, Gamberi F (2004) Structural framework of the Tyrrhenian Sea unveiled by seafloor morphology. Mem Descr Carta Geol d'It XLIV:97–108

Metrich N, Santacroce R, Savelli C (1988) Ventotene, a potassic Quaternary volcano in central Tyrrhenian Sea. Rendiconti della Società Italiana di Mineralogia e Petrologia 43:1195–1213

Mitchell NC, Quartau R, Madeira J (2012) Assessing landslide movements in volcanic islands using near-shore marine geophysical data: south Pico Island, Azores. B Volcanol 74:483–496

Moore JG, Normark WR, Holcomb RT (1994) Giant Hawaiian landslides. Annu Rev Earth Planet Sci 22:119–144

Paull CK, Ussler W, Caress DW et al (2010) Origins of large crescent-shaped bedforms within the axial channel of Monterey Canyon, offshore California. Geosphere 6:1–20

Perrotta A, Scarpati C, Giacomelli L, Capozzi AR (1996) Proximal depositional facies from a caldera-forming eruption: the Parata Grande Tuff at Ventotene Island (Italy). J Volcanol Geotherm Res 71:207–228

Quartau R, Tempera F, Mitchell NC et al (2012) Morphology of the Faial Island shelf (Azores): the interplay between volcanic, erosional, depositional and mass wasting processes. Geochem Geophys Geosyst. doi:10.1029/2011GC003987

Romagnoli C, Casalbore D, Bosman A et al (2013) Submarine structure of Vulcano volcano (Aeolian islands) revealed by high-resolution bathymetry and seismo-acoustic data. Mar Geol. doi:10.1016/j.margeo.2012.12.002

Tibaldi A (2001) Multiple sector collapses at Stromboli volcano, Italy: how they work. Bull Volcanol 63:112–125

Urgeles R, Canals M, Baraza J, Alonso B, Masson D (1997) The most recent megalandslides of the Canary Islands: El Golfo debris avalanche and Canary debris flow, west El Hierro Island. J Geophys Res 102:20305–20323

Zitellini N, Marani M, Borsetti M (1984) Post-orogene tectonic evolution of Palmarola and Ventotene basins (Pontine Archipelago). Memorie della Società Geologica Italiana 27:121–131

Chapter 26
Submarine Mass-Movements Along the Slopes of the Active Ionian Continental Margins and Their Consequences for Marine Geohazards (Mediterranean Sea)

Silvia Ceramicola, Daniel Praeg, Marianne Coste, Edy Forlin, Andrea Cova, Ester Colizza, and Salvatore Critelli

Abstract The Ionian margins of Calabria and Apulia (IMCA) have been affected by mass movements of varying style, scale and age. Here we present examples of seabed and subsurface features identified along more than 400 km of the IMCA from multibeam seabed imagery and subbottom profiles acquired by OGS since 2005. Four different types of mass movement phenomena are recognized with expression at seabed and in the shallow subsurface: (1) mass transport complexes (MTCs) within intra-slope basins, (2) isolated slide scars (ISS) along open slopes, (3) slope-parallel sediment undulations (SPSU) recording block-rotations linked to fluid migration, and (4) headwall and sidewall scarps (HSC) in submarine canyons. Preliminary analyses of sedimentary processes suggest that both open-slope failures capable of triggering tsunamis and retrogression of canyon headwalls within 1–3 km of the Calabrian coast represent potential geohazards for coastal populations and offshore infrastructures.

Keywords Slope failures • Morpho-bathymetry • Seismics • Marine geohazards • Calabrian and Apulian margins

S. Ceramicola (✉) • D. Praeg • M. Coste • E. Forlin • A. Cova
OGS (Istituto Nazionale di Oceanografia e di Geofisica Sperimentale), Borgo Grotta Gigante 42c, 34010 Trieste, Italy
e-mail: sceramicola@ogs.trieste.it

E. Colizza
Dipartimento di Matematica e Geoscienze, Università di Trieste, Trieste 34126, Italy

S. Critelli
Dipartimento di Scienze della Terra, Università della Calabria, Arcavacate di Rende (CS) 87036, Italy

S. Krastel et al. (eds.), *Submarine Mass Movements and Their Consequences*, Advances in Natural and Technological Hazards Research 37, DOI 10.1007/978-3-319-00972-8_26,

26.1 Introduction

Gravity-driven submarine processes on continental margins are important geomorphic agents for transporting sediments downslope into deep-marine environments. Advances in shallow geophysical surveying methods have significantly improved our ability to map and describe the morpho-sedimentary features that record submarine mass movements over time (Chiocci and Ridente 2011). Any activity that affects the seabed represents a potential geohazard. An improved understanding of the spatial distribution and timing of geomorphic features related to mass movement is relevant both to understanding triggering factors (e.g. seismicity, faulting, fluid migration), and to assessing potential hazards for offshore infrastructures and adjacent coastal areas (e.g. tsunamis).

The Ionian margins of Calabria and Apulia (IMCA) provide an interesting laboratory to study active sedimentary processes related to submarine failures (Fig. 26.1). The two tectonically-active margins lie on opposite sides of the suture due to the subduction of the African and Adrian plates beneath southern Italy, and contain a variety of slope settings related to different tectonic activity (Rossi and Sartori 1981; Sartori 2003). The seabed dynamics of the IMCA and its linkages to deeper structures are currently being examined at OGS in the context of the Italian projects MAGIC and RITMARE, with the overall aim of defining and mapping geological features and processes that may constitute geological risks for surrounding coastal areas.

In this paper, we present examples of seabed and subsurface features identified from multibeam and subbottom data acquired over the last several years from the IMCA, supplemented by public seismic data held by OGS. The objective is to describe the variety of features related to mass movements, and to assess their potential hazard for coastal areas and offshore infrastructures.

26.2 Geological Setting

The IMCA includes two margins affected by subduction and accretionary tectonism. The Ionian Calabrian margin (ICM) records two main processes: compression and fore-arc extension during the SE advance of the Calabrian accretionary prism since the late Miocene (Sartori 2003), and rapid uplift (up to 1 mm/year) of onshore and shallow shelf areas since the mid-Pleistocene (Westaway 1993). This has resulted in steep slopes (3–8°) in the south, landward of the deep-water Crotone and Spartivento forearc basins, and irregular slopes (2–4°) in the north across the offshore extension of the southern Apennine thrust-fold belt, where intraslope basins of the western Gulf of Taranto correspond to piggy-back structural highs and lows (Fig. 26.1). The passive Ionian Apulian margin (IAM) is the result of westward subduction of the Adria plate under the southern Apennines, resulting in a steep (4–6°) slope characterised by several morphological steps resulting from the uneven structural setting of the underling Mesozoic carbonate platform. The seismicity of the IMCA

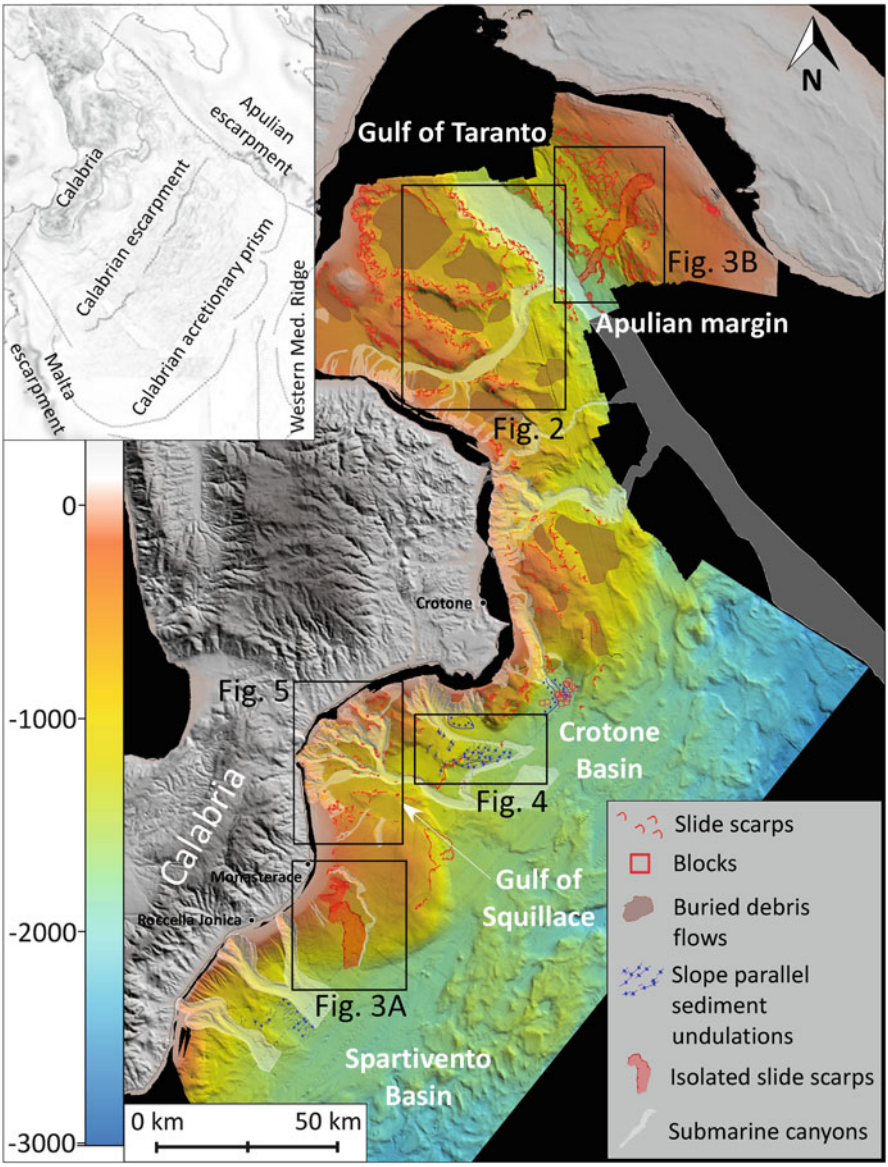

Fig. 26.1 Location of the IMCA study area and the main seabed morpho-sedimentary features related to downslope sediment movements. Offshore bathymetry based on DTMs of variable resolution (5–50 m grids, shaded relief illuminated from NE)

during the last century is mainly located along the onshore to nearshore parts of the Apennine-Calabrian accretionary system and decreases in foreland areas (DISS Working Group 2010). However, in 1743 an earthquake of estimated magnitude 7.0 affected a large area of the Ionian Sea from the Salento peninsula to the Greek island of Lefkas (Boschi et al. 2000).

26.3 Data and Methods

This study is primarily based on high-resolution geophysical data (multibeam and subbottom profiles) acquired by the RV OGS Explora during campaigns in 2009 and 2005. Swath bathymetric data were acquired over an area of about 30,000 km^2 using Reson 8150 (12 kHz) and 8111 (100 kHz) multibeam systems to obtain DTMs of variable cell size (5–50 m). Subbottom data consist of ca. 10,000 line-km of Chirp profiles (2–7 kHz). Our interpretive method consists of mapping seabed morpho-bathymetric elements in relation to acoustic facies identified on the sub-bottom profiles, in order to identify the principal tectonic and sedimentary features of the margin. Linkages to deeper structures are made using public multichannel seismic datasets (Videpi Project), held in a digital database at OGS.

26.4 Results

The seabed morphology and subsurface data together allow the recognition of four main types of mass movement phenomena along the slopes of the IMCA: mass transport complexes (MTCs) within intra-slope basins, isolated slide-scars (ISS) and slope-parallel sediment undulations (SPSU) on open slopes, and headwall and sidewall scarps in submarine canyons (HSC).

26.4.1 Mass Transport Complexes (MTCs) Within Intra-slope Basins

MTCs are recognised within piggy-back basins on the Calabrian slope of the Gulf of Taranto, in water depths of 600–900 m, as features including both seabed slide scarps and buried failure deposits together extending over areas of 30–200 km^2 (Fig. 26.1). Slide scarps are observed around the steep (up to 5–9°) flanks of the intra-slope basins as linear to crescentic features, some showing "*fresh*" sharp morphologies in contrast to others showing more rounded ruptures, that record multiple failure events. Blocks of various sizes are observed both along runoff and at the base of the slopes (Fig. 26.2). Sub-bottom profiles show the adjacent basins to contain unstratified (acoustically transparent) bodies up to tens of meters thick beneath thinner acoustically stratified units, interpreted as buried debris flows (Fig. 26.2). In places, stacked debris flows are observed, indicating that the MTCs record multiple episodes of failure along the intra-slope basin margins.

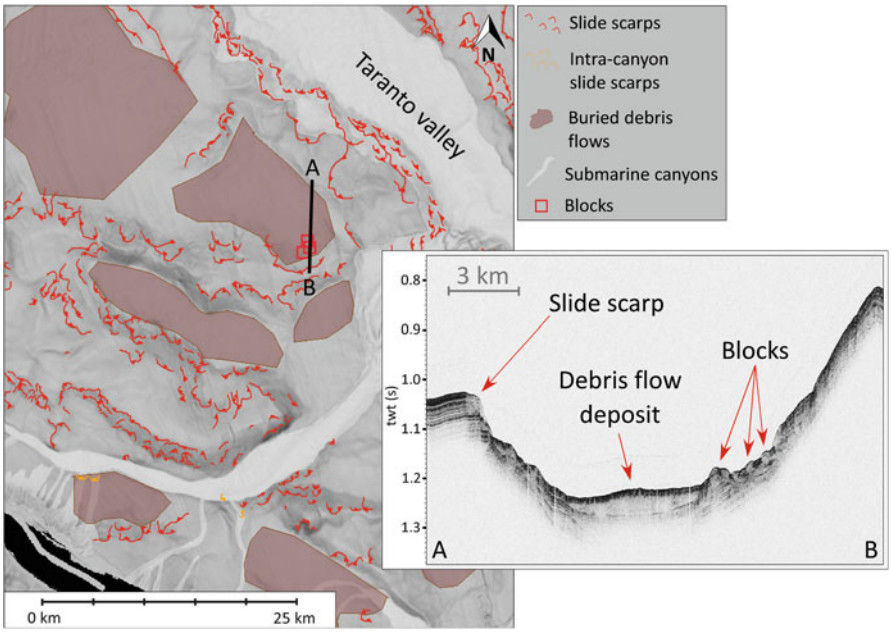

Fig. 26.2 Examples of mass transport complexes (MTCs) within intra-slope piggy-back basins of the Ionian Calabrian margin. Location is indicated in Fig. 26.1. Chirp sonar profile AB across a basin shows slide scarps and blocks above an unstratified debris flow deposit

26.4.2 Isolated Slide Scars on Open Slopes (ISS)

The steep (3–8°) open slopes offshore southern Calabria and western Apulia contain evidence of repeated failures, recorded by multiple slide scars at seabed and, in places, stacked slide deposits (Fig. 26.1). On both slopes larger isolated slide scars are observed: the Assi and Manduria failures (Fig. 26.3).

The Assi failure lies 8 km offshore Calabria on slopes of ca. 3° and in water depths of 400–1,400 m, where seabed scarps up to 50 m high define an elongate slide scar up to 6 km wide and at least 18 km long (Fig. 26.3A). Sub-bottom profiles show the slide deposits to include both acoustically stratified sediments and unstratified bodies and blocks (Fig. 26.3a). The profiles also show the slide to cut older debris flow deposits, linked to seabed scarps observed upslope (Fig. 26.3a). We infer the Assi to be the most recent isolated failure to affect this slope, and estimate that it mobilized in total ca. 2 km^3 of sediment, in one or more events.

The Manduria failure lies 30 km offshore Apulia on slopes of 4–5° and is an elongate depression up to 250 m deep and 34 km long, extending across water depths of 400–1,800 m to join the Taranto canyon (Fig. 26.3B). The feature resembles

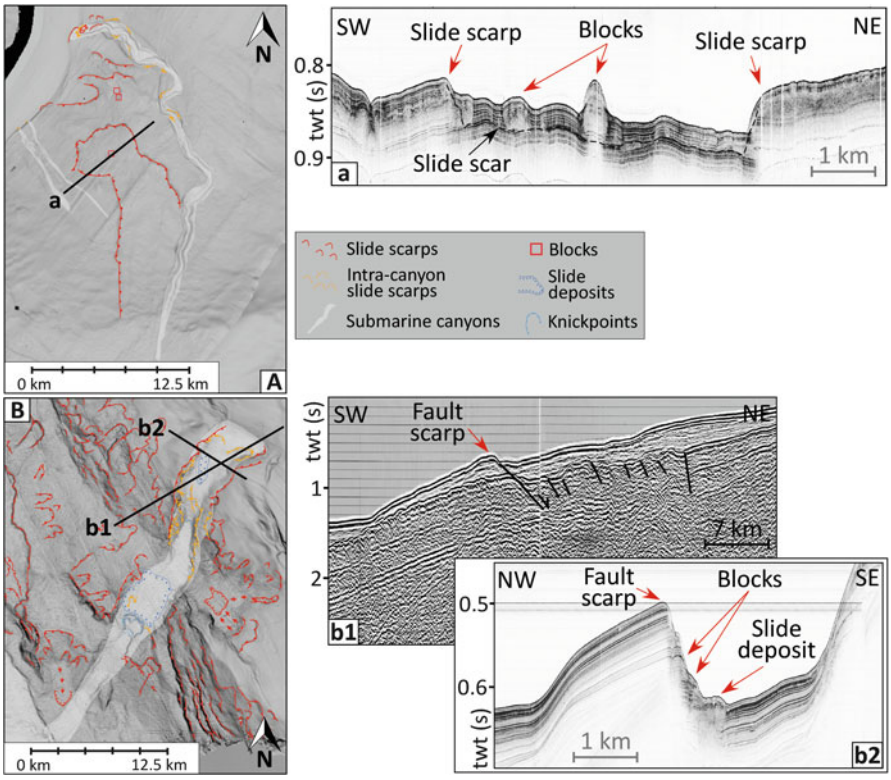

Fig. 26.3 Isolated slide scars on the Calabrian and Apulian open slopes (locations in Fig. 26.1). (**A**) Assi failure, the Chirp profile (*a*) shows the upper failure to include stratified and unstratified sediments, and to cut older debris flow deposits; (**B**) Manduria failure, the Chirp profile (*b2*) shows slide scarps and deposits, while the multichannel profile (*b2*) suggests a link to faults

a canyon, but is in part bounded by seabed slide scarps that are linked to seabed blocks and subsurface slide deposits on subbottom profiles (Fig. 26.3b). A concave axial profile includes two knick-points at 900 m and at 1,190 m depths, suggesting retrogressive failure activity. The total volume of the feature is estimated at 13 km^3. No deposits are observed at the base of the slide as they have probably been redistributed into the Ionian abyssal plain via the Taranto canyon. Seismic lines show that the Manduria failure coincides with faults in the Mesozoic carbonate platform (Fig. 26.3) suggesting a possible tectonic control on the localization of failures.

26.4.3 Slope-Parallel Sediment Undulations (SPSU)

In two areas south of Calabria, each on slopes of ca. 2°, multibeam data reveal distinctive slope-parallel sediment undulations, with lengths up to 12 km and

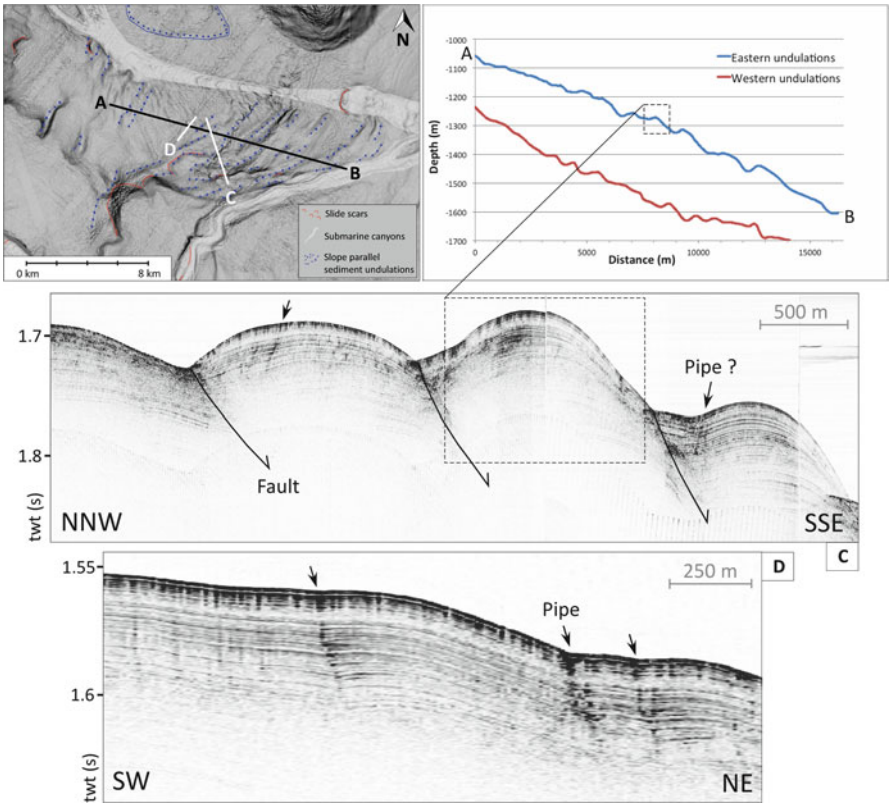

Fig. 26.4 Slope-parallel seabed undulations (SPSU) of the southern Calabrian margin (see Fig. 26.1). *Top right*: bathymetric profiles across the two areas of asymmetric SPSU, location of profile *A–B* shown at *left*. *C* and *D* are Chirp profiles showing interpreted faults and fluid escape pipes

spacing of 0.6–1.4 km (Fig. 26.1). The undulations are up to 100 m in relief and asymmetric in profile, with steeper upslope-facing flanks (Fig. 26.4 top-right). On subbottom profiles they consist of stratified sediments, mainly conformable with seabed to form anticline-like structures, but laterally discontinuous across seaward-dipping surfaces beneath their troughs interpreted as fault planes (Fig. 26.4c, d). The stratified sediments also contain inclined zones of high amplitudes near seabed, resembling fluid escape pipes (Andresen 2012). The SPSU are interpreted as fault-bounded sediment blocks recording downslope rotation in association with fluid migration, comparable to slope-parallel undulations observed elsewhere, notably on the Nile fan (Loncke et al. 2004; Migeon et al. 2013; Praeg et al. 2013).

The undulations provide evidence of a linkage between seabed sediment deformation and subsurface fluid flow. An interpretation of rotated sediment-blocks is consistent with evidence from deeper seismic profiles across the eastern area, showing the SPSU to form part of a folded/faulted Pleistocene interval developed

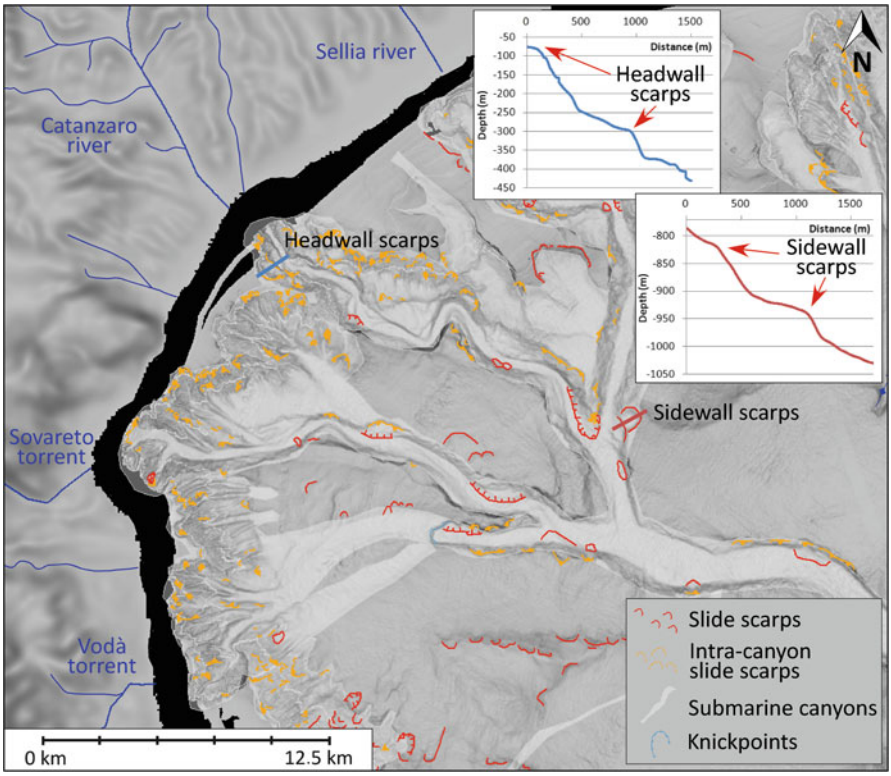

Fig. 26.5 Headwall and sidewall scarps in the Squillace canyon system (location in Fig. 26.1). The cauliform headwall lies 1–3 km from the coast, not all branches of the dendritic network connect with the hydrographic system onshore (in *blue*)

above diapiric structures affecting thick Pliocene sediments (Capozzi et al. 2012). The diapiric structures were originally suggested to be halokinetic (Rossi and Sartori 1981), but recently to be mud mobilized by upward fluid migration along normal faults (Capozzi et al. 2012). Our results indicate that the diapric structures are associated with fluids and show that their buried crests coincide with slope-parallel sediment blocks bounded by normal faults. We infer that overpressured fluids continue to facilitate progressive downslope rotation of sediment blocks along faults rooted in the diapiric structures. It is notable that the fluids have not resulted in mud volcanism, in contrast to adjacent areas (Praeg et al. 2009; Morelli et al. 2011).

26.4.4 Headwall and Sidewall Scarps in Submarine Canyons (HSC)

The Calabrian slopes are incised by numerous submarine canyons, of varying sizes and morphometries, not all connected to onshore drainage systems (Fig. 26.5). In the

Gulf of Taranto, the canyons extend 50–70 km offshore to join the Taranto canyon, which drains 250 km to the Ionian abyssal plain. South of Calabria canyons extend up to 70 km into the Crotone-Spartivento fore-arc basins (Morelli et al. 2011). Seismic profiles across the Squillace canyon in the Crotone basin show incision of relatively young (Pleistocene) sediments (Capozzi et al. 2012). All of the canyons are marked by semi-circular scarps, overlapping along their headwalls and isolated along sidewalls (Fig. 26.1), recording smaller-scale failures. The largest canyon system is located in the Gulf of Squillace (Fig. 26.1), where the headwall has a total perimeter of 62 km and an area of ca. 630 km^2. The canyon system is highly dendritic, the first-order branches of the cauliform headwall extending to within 1–3 km of the coastline. Headwall scarps are on average 30 m high and 60 m long, with a density of occurrence of ca. 50/km^2. Sidewall scarps are bigger in size (50–150 m high and 50–500 m long on average) with a lower density of occurrence (12/km^2).

Headwall and sidewall scarps show that failures of the canyon walls represents an important mechanism for their retrogressive growth. Considering only headwall scarps in the first-order canyon branches of the Squillace system, we estimate the volume of sediment removed by failure to be of the order of 6 km^3. Retrogressive scars are observed to be larger where canyons cut structural highs (e.g. Squillace), suggesting ongoing adjustment to tectonically-created topography.

26.5 Discussion – Mass Movements and Geohazards in the IMCA

The four types of mass movement described above constitute different degrees of marine geohazard for the Ionian coastal and deep-sea areas.

The slopes of the IMCA are marked by seabed slide scarps, which are particularly abundant along the Calabrian and Apulian margins of the Gulf of Taranto (Fig. 26.1). MTCs of the western Gulf of Taranto are located away from the coasts in water depths of $\geq$600 m and confined in intra-slope basins, and so do not represent a significant hazard for coastal areas. Nonetheless, they record a history of recurrent failure that is likely to be linked to seismogenic activity along the Apenninic belt, thus reflecting a wider potential for seismically-triggered failures. The Apulian slope is dissected by slide scars (Fig. 26.1), some of which appear to be linked to faults (Fig. 26.3B). This is interesting as this area has been considered seismically quiet, and raises the question of to what extent the observed failures may reflect distal versus proximal effects of seismicity. In our opinion, seismicity represents a significant potential trigger for geohazards along the IMCA in the Gulf of Taranto.

Isolated slide scars (ISS) on the Calabrian and Apulian open slopes also reflect a potential for larger submarine failures that may be capable of triggering tsunamis or anomalous waves. Tsunami modelling has been performed for the Assi slide, one scenario showing the area most affected to be the adjacent coast between Roccella Jonica and Monasterace (Fig. 26.1), where waves up to 1 m high could cause damage to coastal infrastructures (Zaniboni et al. 2012). Thus future open-slope failures similar to Assi could constitute geohazards for adjacent coastal areas,

as well as for deep-sea infrastructures (pipelines, cables etc.). A better understanding of failures on the IMCA is relevant to the monitoring of tsunamigenic failures in the Mediterranean Sea, where tsunami early-warning systems are less effective than in open oceans. This is an important issue as, in contrast to earthquakes, tsunamigenic failures can be monitored.

Slope-parallel seabed undulations (SPSU) represent a low potential hazard because they record slow gravity-driven deformation of slope sediments. However, the SPSU are associated with fluid pipes that we infer to reflect fluid overpressures associated with underlying mud diapirs. A sudden release of fluid overpressures could present a hazard for deep-sea infrastructures, as reflected in near-by mud volcanoes (Praeg et al. 2009).

Retrogressing canyon headwalls represent an important geohazard along the southern Calabrian margin, where they are located within 1–3 km of the coastline (see also Morelli et al. 2011). Headwall regression can lead to coastal erosion, with risks for coastal infrastructures (highways, harbours, railways). Retrogressive canyon erosion has caused of the repeated collapse of the pier of the harbour of Cirò Marina (Casalbore et al. 2012), which could have been avoided with more efficient geohazard assessment and coastal management. We recommend monitoring and higher sensibility of national and regional stakeholders to this important issue.

26.6 Conclusions

The Ionian margins of Calabria and Apulia, including the Gulf of Taranto, provide a natural laboratory to study submarine geohazards, due to ongoing convergent tectonism and a wide range of mass failure phenomena. Mapping of over 400 km of the IMCA show the seabed and shallow subsurface to contain four main types of sedimentary record of failure over time: (1) mass transport complexes within intra-slope basins, (2) isolated slide scars along open slopes, (3) slope-parallel sediment undulations recording gravity-driven block rotations linked to over pressured fluids, and (4) headwall and sidewall scarps in submarine canyons. Preliminary analyses of sedimentary processes occurring along the IMCA indicates that open-slope failures capable of triggering tsunamis represent potential geohazards both for coastal populations and for deep-sea infrastructures, whereas retrogression of canyon headwalls lying <1–3 km off the Calabrian coast represents an important geohazard that requires regular monitoring. Seismic hazard remains a major issue to be addressed in the IMCA.

Acknowledgments The seabed dynamics of the IMCA are being examined in the context of the Italian projects MAGIC (MArine Geohazards along the Italian Coasts), funded by the Civil Protection Department, and Ritmare (La ricerca italiana per il mare), funded by the Ministry of University and Research (MIUR). Data were acquired during four campaigns of the r/v OGS Explora: in 2005 for three projects, HERMES (EC Integrated Project), MESC (collaboration with

the University of Trieste) and WGDT (collaboration with the University of Calabria), all funded by OGS, and in 2009 for MAGIC. All campaigns were coordinated by Riccardo Ramella. All data were processed and interpreted at OGS; Andrea Caburlotto and Dario Civile of OGS are thanked for contributions to the mapping. This work as well as Marianne Coste's PhD programme are funded in the framework of MAGIC and Ritmare. Global Mapper software was customized for MAGIC interpretative purposes. The software package IHS Kingdom Suite is provided via an Academic Grant. The authors thank Sébastien Migeon and Dimitris Sakellariou for their constructive reviews.

References

Andresen KJ (2012) Fluid flow features in hydrocarbon plumbing systems: what do they tell us about the basin evolution? Mar Geol 332–334:89–108

Boschi E, Guidoboni E, Ferrari G, Mariotti D, Valensise G, Gasperini P (2000) Catalogue of strong Italian earthquakes from 461 B.C. to 1997. Ann Geophys 43(4):609–868

Capozzi R, Artoni A, Torelli L, Lorenzini S, Oppo D, Mussoni P, Polonia A (2012) Neogene to Quaternary tectonics and mud diapirism in the Gulf of Squillace (Crotone-Spartivento Basin, Calabrian Arc, Italy). Mar Pet Geol 35(1):219–234

Casalbore D, Bosman A, Chiocci FL (2012) Study of recent small-scale landslides in geologically active marine areas through repeated multibeam surveys: examples from the Southern Italy. In: Yamada Y et al (eds) Submarine mass movements and their consequences, Advances in natural and technological hazards research 31. Springer, Dordrecht, pp 573–582

Chiocci FL, Ridente D (2011) Regional-scale seafloor mapping and geohazard assessment. The experience from the Italian project MaGIC (Marine Geohazards along the Italian Coasts). Mar Geophys Res 32:13–23

DISS Working Group (2010) Database of Individual Seismogenic Sources (DISS), Version 3.1.1: a compilation of potential sources for earthquakes larger than M 5.5 in Italy and surrounding areas. http://diss.rm.ingv.it/diss/. Accessed 31 Jan 2013

Loncke L, Mascle J, Fanil Scientific Parties (2004) Mud volcanoes, gas chimney, pockmarks and mounds in the Nile deep-sea fan (Eastern Mediterranean): geophysical evidences. Mar Pet Geol 21:669–689

Migeon S, Ceramicola S, Praeg D et al (2014) Post-failure processes on the continental slope of the central Nile deep-sea fan: interactions between fluid seepage, sediment deformation and sediment-wave construction. In: Krastel S, Behrmann J-H, Völker D, Stipp M, Berndt C, Urgeles R, Chaytor J, Huhn K, Strasser M, Harbitz CB (eds) Submarine mass movements and their consequences, 6th international symposium. Springer, Switzerland/Heidelberg/New York/Dordrecht/London, pp 117–127

Morelli D, Cuppari A, Colizza E, Fanucci F (2011) Geomorphic setting and geohazard-related features along the Ionian Calabrian margin between Capo Spartivento and capo Rizzuto (Italy). Mar Geophys Res. doi:10.1007/s11001-011-9130-4

Praeg D, Ceramicola S, Barbieri R, Unnithan V, Wardell N (2009) Tectonically driven mud volcanism since the late Pliocene on the Calabrian accretionary prism, central Mediterranean Sea. Mar Pet Geol 26:1849–1865

Praeg D, Ketzer JM, Augustin AH et al (2014) Fluid seepage in relation to seabed deformation on the central Nile deep-sea fan, part 2: evidence from multibeam and sidescan imagery. In: Krastel S, Behrmann J-H, Völker D, Stipp M, Berndt C, Urgeles R, Chaytor J, Huhn K, Strasser M, Harbitz CB (eds) Submarine mass movements and their consequences, 6th international symposium. Springer, Switzerland/Heidelberg/New York/Dordrecht/London, pp 141–150

Rossi S, Sartori R (1981) A seismic reflection study of the external Calabrian Arc in the northern Ionian Sea (eastern Mediterranean). Mar Geophys Res 4:403–426

Sartori R (2003) The Tyrrhenian back-arc basin and subduction of the Ionian lithosphere. Episodes 26(3):217–221

Westaway R (1993) Quaternary uplift of Southern Italy. J Geophys Res 98:21741–21772

Zaniboni F, Tinti S, Pagnoni G, Ceramicola S, Planinsek P, Marson I (2012) Evaluation of tsunami hazard associated to the Assi submarine landslide along the Ionian Calabrian margin, Italy. EGU General Assembly, Vienna, Austria. GeophysResAbstr14:EGU2012-8569-1

Chapter 27
Evidence for Submarine Landslides Offshore Mt. Etna, Italy

Felix Gross, Sebastian Krastel, Francesco Latino Chiocci, Dominico Ridente, Jörg Bialas, Julia Schwab, Julio Beier, Deniz Cukur, and Daniel Winkelmann

Abstract Mt. Etna is the largest and one of the best-studied volcanoes in Europe. It represents a highly active basaltic volcano on top of the active Apennine thrust belt. The instability of its eastern flank has been described as an important preconditioning factor for the occurrence of submarine mass wasting events. In order to better understand the processes that may cause submarine slope failures, a new dataset including seismic, hydroacoustic and core data was collected during RV Meteor cruise M86/2 from December 2011 to January 2012. Seismic profiles and sediment cores reveal repeated mass transport deposits (MTD), indicating a long history of landslides in the working area. Some of the sampled MTDs and their surrounding strata contain volcaniclastic debris, indicating that slope failures may be controlled by volcanic and non-volcanic processes. Several tephra layers directly cover MTDs, which is regarded as an indicator for the possibility that several flank failures occur immediately before or very early during an eruption.

Keywords Volcano flank • Mt. Etna • Submarine sliding • Slope instability • Tephra

F. Gross (✉) • J. Bialas • J. Schwab • D. Cukur • D. Winkelmann
GEOMAR Helmholtz Centre for Ocean Research Kiel, Wischhofstr. 1-3, 24148 Kiel, Germany
e-mail: fgross@geomar.de

S. Krastel • J. Beier
Institute of Geosciences, Christian-Albrechts-Universität zu Kiel, Kiel, Germany

F.L. Chiocci
Dip. Scienze della Terra, University "La Sapienza", Rome, Italy

D. Ridente
IGAG-CNR, National Research Council, Rome, Italy

S. Krastel et al. (eds.), *Submarine Mass Movements and Their Consequences*, Advances in Natural and Technological Hazards Research 37, DOI 10.1007/978-3-319-00972-8_27,

27.1 Introduction

Mt. Etna (Sicily, Italy) is known as the largest active volcano in Europe (Fig. 27.1) (Gvirtzman and Nur 1999). It represents a highly active basaltic volcano overlying the active plate boundary between the African and Eurasian Plate (Chiocci et al. 2011; Doglioni et al. 2001), and builds up on continental crust (Gvirtzman and Nur 1999).

The eastern flank of Mount Etna is well known for its instability (Branca and Ferrara 2013) and its ongoing deformation (Argnani et al. 2012), which is controlled by spreading of an extensional fault system (Borgia et al. 1992). Chiocci et al. (2011) consider this ongoing deformation as an important factor controlling subaerial and submarine mass wasting events. Pareschi et al. (2006) postulate a long-lasting history of mass movements after the built-up of Mt. Etna, as long run-out debris slumps could be imaged offshore Mt. Etna. Chiocci et al. (2011) observed a large bulge offsetting the margin that is deeply affected by widespread semicircular steps, which have been interpreted as being associated with large-scale gravitational instabilities.

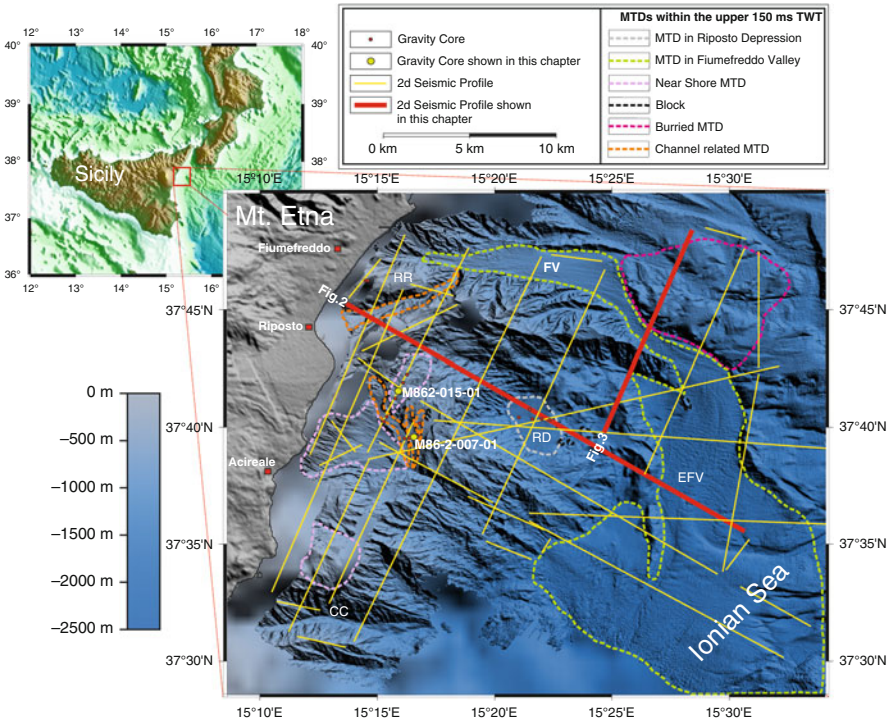

Fig. 27.1 Bathymetric map showing locations of seismic profiles collected during cruise M86/2 offshore Mt. Etna. *Dashed colored lines* display near-surface MTDs (Mass Transport Deposits). The *inset* map shows the general location of the working area. *RR* Riposto Ridge, *FV* Fiumefreddo Valley, *EFV* Extension of Fiumefreddo Valley, *RD* Riposto Depression, *CC* Catania Canyon

A variety of processes leading to a destabilization of the flank and possible catastrophic slope failures may act in addition to the ongoing deformation in the working area. These mechanisms include tectonic activity due to frequent earthquakes in the Calabrian Arc (e.g. Azzaro et al. 2000; Ferreli et al. 2002), high recurrence rate of volcanic eruptions and volcanic tremor (e.g. Simkin and Siebert 1994), and liquefaction of tephra layers, which was observed in comparable settings, e.g. by Harders et al. (2010). Furthermore, widespread incised gullies indicate ongoing highly variable hydrodynamic and gradational activity (Micallef and Mountjoy 2011), controlling the recent morphology in this area.

All these implications reveal that the area east of Mount Etna is a region, which is highly prone to submarine mass wasting. Several questions, however, remain open, including the spatial distribution of mass wasting and the role of abundant and widespread tephra layers. Based on new data collected during RV Meteor cruise M86/2 (December 2011/ January 2012), we focus on the relationship between widespread tephra layers and MTDs as well as on the identification of large- and small-scale features contributing to slope failures off Mt. Etna.

27.2 Data

All data presented in this manuscript are newly collected during RV Meteor cruise M86/2 (December 2011 to January 2012) and are presented here for the first time. High-resolution 2d reflection seismic data were acquired using a 1.7 l GI-Gun and a digital Geometrics GeoEel 104-channel streamer with a total length of 162.5 m and a hydrophone spacing of 1.56 m. Seismic data were processed with GEDCO Vista Seismic Processing V.11 including setting up the geometry, frequency filtering, normal move correction (NMO) with a constant velocity, stacking and time migration. Bin size was set to 2 m resulting in an average fold of 10. Bathymetric data were collected using the hull mounted Kongsberg EM120 and Kongsberg EM710 multi-beam echo-sounders. Parasound sediment echo-sounder data were acquired by an ATLAS DS-3/P70. In addition, a 10 m gravity corer was used for sediment sampling. All sediment cores were only examined visually as a detailed sedimentological analysis of the cores is not objective of this manuscript.

27.3 Results

27.3.1 Morphology of the Eastern Flank of Mt. Etna

Fiumefreddo Valley (FV) and its southern prolongation (EFV) (Fig. 27.1) mark the northern boundary of the eastern flank of Mt. Etna. This valley system hosts a wide spread hummocky topography, which is a strong implication for mass transport

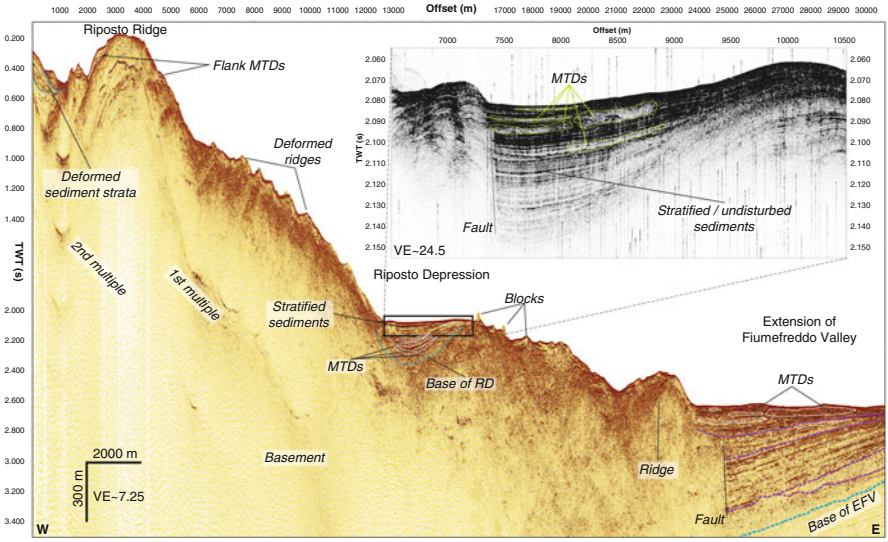

Fig. 27.2 2d reflection seismic profile M86-2-p407 and Parasound echo-sounding zoom-in of the Riposto Depression. The seismic section shows the distribution of proximal and distal sedimentary units and illustrates steep slope gradients. The Parasound echo sounding shows near-surface transparent units intercalated with well-stratified reflectors in the Riposto Depression. See Fig. 27.1 for location of profile

deposits (MTDs) at the seafloor. Riposto Ridge (RR) represents a major ridge in the North, which extends offshore in a curved shape towards the southern part of Fiumefreddo Valley; RR is strongly reworked by submarine canyon- and gully structures (Fig. 27.1).

Riposto Depression (RD, Figs. 27.1 and 27.2) is a flat depression, which covers an area of 7.25 km^2 and is surrounded by an amphitheater-like structure. This structure most likely represents the remnant of a major flank failure (Chiocci et al. 2011). Ridges surrounding the Riposto Depression show slope gradients of up to 20°. Large blocks and MTDs are visible especially on its eastern margin (Fig. 27.1), which can also be observed in seismic profiles (Fig. 27.2). The near-shore areas are characterized by funnel-shaped sedimentary systems, which host several incisions running down-slope to the East (Fig. 27.1). The southern boundary of the deforming part of Mt. Etna is marked by the Catania Canyon (Chiocci et al. 2011). In general, the entire flank offshore Mt. Etna is characterized by numerous small scale gully- and canyon like structures carving into the background morphology, which is commonly observable at steeply dipping continental margins (Micallef and Mountjoy 2011; Vachtman et al. 2013).

27.3.2 Seismic Evidence for MTDs

Most of the seismic units displaying high amplitude and discontinuous reflectors can be interpreted as MTDs. Profile M86-2-p407 (Fig. 27.2) represents a typical cross-section from the near shore areas to the southern extension of Fiumefreddo Valley. The profile shows four different settings:

- The Riposto Ridge is characterized by slope angles of up to 20° and prominent deformed ridges. The slope shows headwall-like structures, as indicated by widespread erosional truncations. Most of the depressions show an interlayering of chaotic seismic units interpreted as MTDs, and well-stratified sediments.
- The Riposto Depression is a small basin with a complex internal structure. The seismic record (Fig. 27.2) images well-stratified sediments in the uppermost 100 ms TWT underlain by three major high amplitude discontinuous units, which can be found below 2,150 ms TWT in the seismic record (Fig. 27.2). We interpret those units as MTDs. Parasound echo-sounder data allow a detailed view of the upper ~50 m of the sediments illustrating transparent units close to the sea floor as well as inter-bedded well stratified sediments (Fig. 27.2). The transparent/discontinuous units are interpreted as MTDs.
- The transition from Riposto Depression to the southern prolongation of Fiumefreddo Valley shows a rough topography. It reveals a field of blocks outcropping at the seafloor (Figs. 27.1 and 27.2). This hummocky topography may be formed as a result of one major or several smaller slope failures.
- The southern prolongation of Fiumefreddo Valley is imaged as a half-graben-like feature on the seismic profile (Fig. 27.2). The upper units are characterized by high amplitudes, discontinuous and more or less horizontal reflectors, while the lower units show a clear tilt. Further to the North, Fiumefreddo Valley is filled by high amplitude reflectors with varying continuity (Fig. 27.3).

A profile showing widespread MTDs around the Fiumefreddo Valley (Fig. 27.1) is shown in Fig. 27.3. Several chaotic units interpreted as MTDs are inter-bedded with well-stratified reflector packages representing the undisturbed background sediments. The area NE of Fiumefreddo Valley is of special interest. Billi et al. (2008) interpreted the morphology in this area as a large MTD originating from the head region of Fiumefreddo Valley based on an older data set. They considered a major sediment slide in this area as a potential trigger mechanism for the devastating tsunami, which followed the 1908 Messina earthquake. This hypothesis is strongly doubted by Argnani et al. (2009) based on modern bathymetric data. Argnani et al. (2009) show, that the morphology of the area is a product of long-lasting erosion without any trace of a 100 year-old large-scale landslide. The interpretation by Argnani et al. (2009) is well supported by the new seismic data. Thick stratified

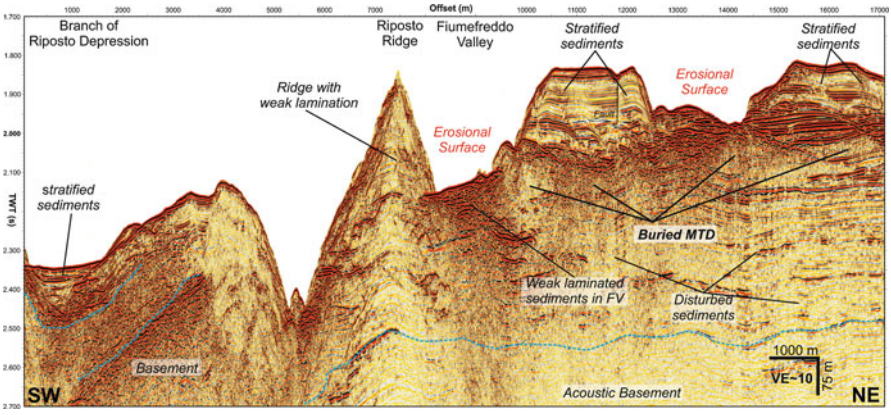

Fig. 27.3 2d reflection seismic profile M86-2-p404 traversing the northern edge of the survey area in a SW to NE direction. Especially the section from offset 8,000–14,500 reveals a stratified sedimentary unit, which is underlain by a large MTD. See Fig. 27.1 for location of profile

sedimentary units are found immediately below the sea floor (Fig. 27.3). These units are underlain by large MTDs, which were most likely deposited during the evolution of the Fiumefreddo Valley but not in present times. The buried MTDs indicate a long history of mass wasting at the eastern flank of Mt. Etna.

27.3.3 MTDs and Tephra Layers in the Sedimentary Record

Gravity cores were taken at several locations in order to sample near surface MTDs. Most of the cores show clear indications for MTDs, all of which host major tephra layers. To illustrate some typical features, sediment cores M86/2-007-01 and M86/2-015-01 were chosen. Gravity core M86/2-007-01 (Fig. 27.4a) with a total length of 433 cm was recovered southwest of the amphitheater structure at the eastern flank off Mt. Etna edifice (see Fig. 27.1 for location of core). It reveals a strong variation of deposits through the sediment column. Major tephra fallout deposits can be observed at 20–22, 58–61 and 325–331 cm (Fig. 27.4). In addition, two chaotic facies can be identified yielding intraclasts of up to 6 cm in diameter. Most remarkable feature in this gravity core is the section between 325 and 370 cm (Fig. 27.4b), as it bears a tephra layer with a thickness of ca. 6 cm, which is directly underlain by a ca. 40 cm thick chaotic unit.

Gravity core M86/2-015-01 (Fig. 27.4c) with a total length of 356 cm was recovered at the western edge of the amphitheater structure. Especially the lower section from 270 to 328 cm is of special interest, as it hosts a similar succession of MTD and tephra as described for the core M86/2-007-01 (Fig. 27.4d), as this MTD is directly overlain by a tephra layer. This chaotic layer features intraclasts of up to 9 cm in size with different compositions. Most prominent are tephra- as well

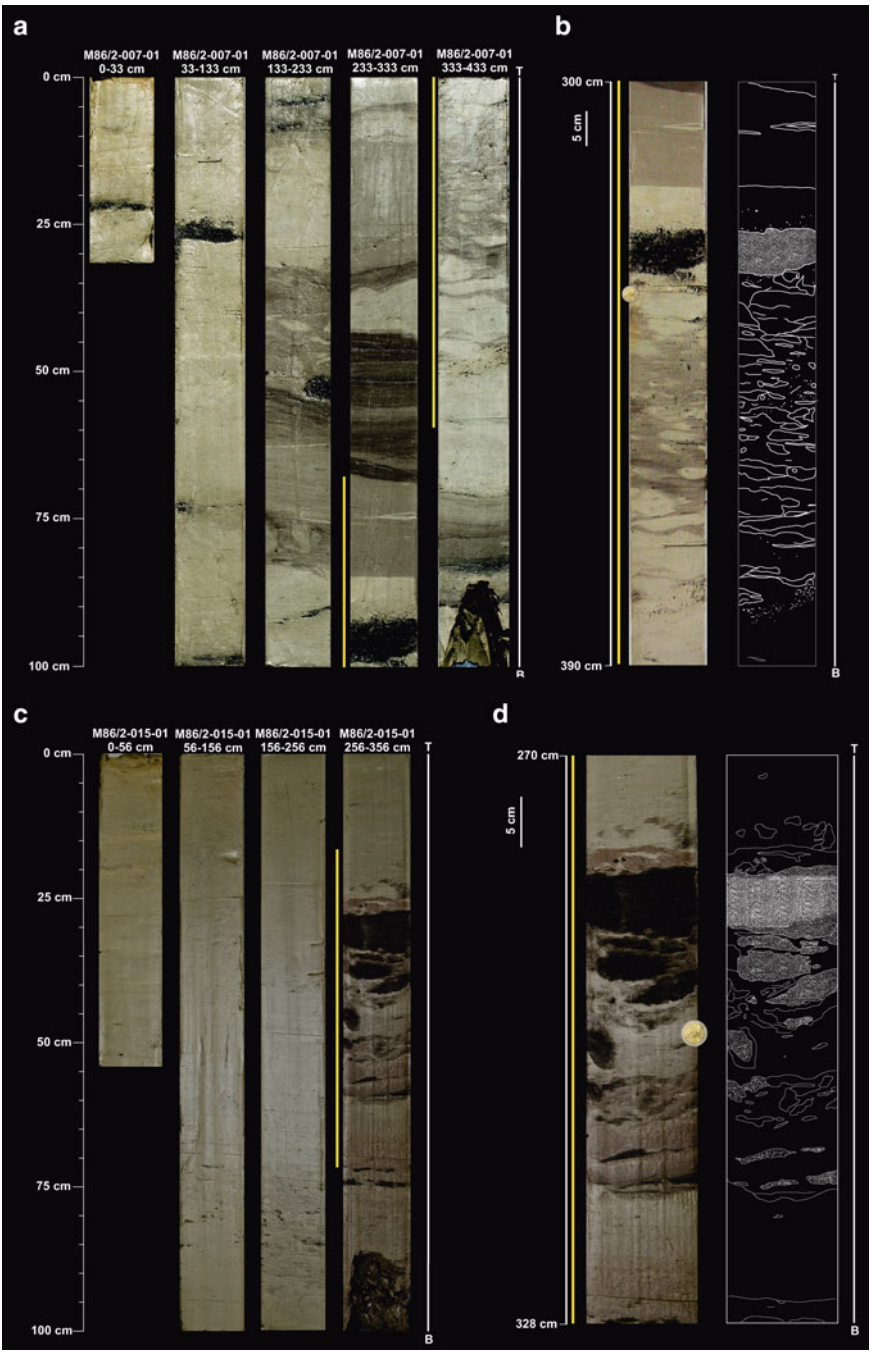

Fig. 27.4 (**a**) Gravity core M86/2-007-01 (**b**) Close up of Gravity Core M86/2-007-01 from 300 to 390 cm (**c**) Gravity core M86/2-015-01 (**d**) Close up of Gravity Core M86/2-015-01 from 270 to 328 cm

as clasts made out of fine to medium sands. As the composition of this chaotic unit hosts a mixture of sedimentary material available at the submarine slope of Mt. Etna, we consider this chaotic unit as a representative MTD for this region.

27.4 Discussion

27.4.1 MTD Distribution and History of Sliding

As previously described and discussed by Pareschi et al. (2006) and Chiocci et al. (2011), the entire survey area is strongly affected by submarine mass wasting. The new M86/2 high-resolution dataset reveals new insights into a long history of mass wasting and its strong connection to morphological features like the Riposto Depression. Especially seismic profile p404 (Fig. 27.3) provides indications for one or more ancient slope failure, as the prominent MTD is overlain by a well-stratified sedimentary unit with a thickness of ca. 200 ms TWT. Furthermore, Fiumefreddo Valley and its prolongation to the South (Figs. 27.1 and 27.2) seems to act as an important conduit. It collects debris and MTDs from the eastern flank of Mt. Etna and appears to restrict the sedimentary transport to the East and the Ionian Sea. The analysis of all available seismic data allows to document the regional and temporal distribution of large and small scale MTDs. Distal areas such as the southern prolongation of Fiumefreddo Valley show relatively small mass wasting deposits in the deeper sediment record, whereas high amplitude, discontinuous reflectors in the upper sediment column indicate larger scale MTDs in more recent times. For proximal areas, larger scale MTDs can be traced in sediment units deeper than 200 ms TWT. These MTDs can especially be traced within the Riposto Depression (Fig. 27.2), which shows a focus of large MTDs in the lower sedimentary units. The Riposto Depression represents a basin, which is strongly affected by mass wasting. It collects large amounts of transported sediments from the surrounding amphitheater structure with flank gradients of up to 20°.

Exposed and buried MTDs imply a long history of sliding and recent MTD generation in the working area strongly support the hypothesis of large-scale gravitational instabilities (Chiocci et al. 2011) and a long time activity of mass movements as run-out debris slumps (Pareschi et al. 2006).

27.4.2 Relationship between Tephra Layers and MTDs

The entire survey area is strongly affected by MTDs. Most general factors controlling slope failures include strong tectonic control and associated seismicity, over steepening of flanks due the deformation of the flank (Chiocci et al. 2011), volcanic eruptions, and possible liquefaction of tephra layers, which may act as a

slide plain and therefore entrain overlying sediments (Harders et al. 2010). Here we would like to focus on the role of tephra layers, as the identified succession of tephra layers directly on top of MTDs may be important for understanding possible slide triggering mechanisms in the working area. Harders et al. (2010) suggested for a comparable setting at the Middle America Trench that tephra layers act as detachment planes due to liquefaction during seismic activity. Nevertheless, no indication for such a process could be found in the working area offshore Mt. Etna. On the contrary the location of tephra layers immediately above the MTDs suggest a close link between emerging volcanic activity and slope failure. Volcanic tremor before an eruption may induce high seismicity and may trigger slope failures. Deformation of volcanic flanks during the rise of magma before an eruption and associated hydrothermal activity may further contribute to slope instability (van Wyk de Vries et al. 2000). Hence a slope failure would be followed by an eruption and the deposition of a tephra layer would occur immediately afterwards on top of the MTD. The consecutive succession of deposits was observed at several cores at different locations. No correlation between cores is possible but the different compositions of the tephra layers overlying MTDs suggest that different stratigraphic intervals were cored at different locations. We are aware that tephra does not behave like other particles in the water column (Carey 1997) as it may build vertical gravity currents, which lead to an inhomogeneous distribution of the widespread tephra layers. However, we are convinced that we sampled several slides with different ages, which show the typical succession of a MTD covered by a tephra. Hence, we consider the triggering of MTDs during emerging volcanic activity as being of general importance for the eastern submarine flank of Mt. Etna.

We also identified MTDs without a tephra layer on top indicating that other processes for slope stability are important as well. They may include oversteepening of the slope, toe erosion in areas with deep incisions, seismicity not related to volcanic activity, and high sediment accumulation rates. We also would like to point out that we have not cored any of the large MTDs identified in the seismic record as they cannot be reached without deep drilling. The clear indications even between small near-surface MTDs (identified in the cores) and volcanic activity let us assume that large failures are triggered by volcanic activity in a similar matter though a time lag between the MTD generation and the settling of tephra could lead to a similar observation in the sedimentary record.

27.5 Conclusion

Widespread MTDs could be mapped off the eastern flank of Mt. Etna edifice. MTDs at different stratigraphic levels indicate a long history of mass wasting. The distribution of MTDs is mainly controlled by pre-existing morphology. A typical succession of MTDs directly overlain by tephra layers indicate that volcano induced seismicity and flank deformation prior to an eruption act as important trigger mechanisms for slope failures on the eastern flank of Mt. Etna. This observation

was established at relatively small scale slides with thicknesses of up to 50 cm and in sediment depth less than 5 m. Seismic data show significantly larger buried MTDs, which were most likely triggered by similar volcanic processes in the past.

Acknowledgments Many thanks to the crew of RV Meteor for their help during the collection of data. The authors are thankful to Dina Vachtman and Klaus Reicherter for their reviews and constructive comments. This project was funded by the DFG and the Cluster of Excellence "The Future Ocean".

References

Argnani A, Chiocci FL, Tinti S, Bosman A, Lodi MV, Pagnoni G, Zaniboni F (2009) Comment on "On the cause of the 1908 Messina tsunami, southern Italy" by Andrea Billi et al. Geophys Res Lett 36:L13307

Argnani A, Mazzarini F, Bonazzi C, Bisson M, Isola I (2012) The deformation offshore of Mount Etna as imaged by multichannel seismic reflection profiles. J Volcanol Geotherm Res 251:50–64

Azzaro R, Bella D, Ferreli L, Michetti AM, Santagati F, Serva L, Vittori E (2000) First study of fault trench stratigraphy at Mt. Etna volcano, Southern Italy: understanding Holocene surface faulting along the Moscarello fault. J Geodyn 29:187–210

Billi A, Funiciello R, Minelli L, Faccenna C, Neri G, Orecchio B, Presti D (2008) On the cause of the 1908 Messina tsunami, Southern Italy. Geophys Res Lett 35:L06301

Borgia A, Ferrari L, Pasquare G (1992) Importance of gravitational spreading in the tectonic and volcanic evolution of Mount Etna. Nature 357:231–235

Branca S, Ferrara V (2013) The morphostructural setting of Mount Etna sedimentary basement (Italy): implications for the geometry and volume of the volcano and its flank instability. Tectonophysics 586:46–64

Carey S (1997) Influence of convective sedimentation on the formation of widespread tephra fall layers in the deep sea. Geology 25:839–842

Chiocci FL, Coltelli M, Bosman A, Cavallaro D (2011) Continental margin large-scale instability controlling the flank sliding of Etna volcano. Earth Planet Sci Lett 305(1–2):57–64

Doglioni C, Innocenti F, Mariotti G (2001) Why Mt Etna? Terra Nova 13:25–31

Ferreli L, Michetti AM, Serva L, Vittori E (2002) Stratigraphic evidence of coseismic faulting and aseismic fault creep from exploratory trenches at Mt. Etna volcano (Sicily, Italy). In: Ettensohn FR, Rast N, Brett CE (eds) Ancient seismites, Geological Society of America Special Paper 359, Geological Society of America, Boulder, pp 49–62

Gvirtzman Z, Nur A (1999) The formation of Mount Etna as the consequence of slab rollback. Nature 401:782–785

Harders R, Kutterolf S, Hensen C, Moerz T, Brückmann W (2010) Tephra layers: a controlling factor on submarine translational sliding? Geochem Geophys Geosyst 11(5):1–18

Micallef A, Mountjoy JJ (2011) A topographic signature of a hydrodynamic origin for submarine gullies. Geology 39:115–118

Pareschi MT, Boschi E, Mazzarini F, Favalli M (2006) Large submarine landslides offshore Mt. Etna. Geophys Res Lett 33:L13302

Simkin T, Siebert L (1994) Volcanoes of the world. Geoscience Press, Tucson, 349 pp

Vachtman D, Mitchell NC, Gawthorpe R (2013) Morphologic signatures in submarine canyons and gullies, central USA Atlantic continental margins. Mar Pet Geol 41:250–263

van Wyk de Vries B, Kerla N, Petley D (2000) Sector collapse forming at Casita volcano, Nicaragua. Geology 28:167–170

Chapter 28
The Malta-Sicily Escarpment: Mass Movement Dynamics in a Sediment-Undersupplied Margin

Aaron Micallef, Aggeliki Georgiopoulou, Timothy Le Bas, Joshu Mountjoy, Veerle Huvenne, and Claudio Lo Iacono

Abstract The Malta-Sicily Escarpment (MSE) is a steep carbonate escarpment that appears to have largely remained isolated from inputs of fluvial and littoral sediments since the Messinian Salinity Crisis. Mass movement activity has so far only been inferred from sediment cores at the base of the MSE. In this study we use geophysical and sedimentological data acquired from the upper MSE and outer Malta Plateau to: (i) map and characterise the dominant forms of mass movements, and (ii) determine the nature and origin of these mass movements, and their role in the evolution of the MSE. We document 67 mass movement scars across 370 km^2 of seafloor. Slope instability entailed translational slides, spreads and debris flows that mobilised Plio-Pleistocene outer shelf hemipelagic/pelagic sediments or carbonate sequences across the upper continental slope. Slope failure events are caused by loss of support associated with the formation of channels, gullies, canyon heads and fault-related escarpments. Mass movements play a key role in eroding the seafloor and transferring material to the lower MSE. In particular,

A. Micallef (✉)
Department of Physics, Faculty of Science, University of Malta, Msida, Malta

GRC Geociències Marines, Universitat de Barcelona, Barcelona, Spain
e-mail: aaron.micallef@um.edu.mt; micallefaaron@gmail.com

A. Georgiopoulou
Marine & Petroleum Geology Group, UCD School of Geological Sciences, University College Dublin, Dublin, Ireland

T. Le Bas • V. Huvenne
Marine Geosciences, National Oceanography Centre, Southampton, UK

J. Mountjoy
National Institute of Water and Atmospheric Research, Wellington, New Zealand

C. Lo Iacono
Marine Geosciences, National Oceanography Centre, Southampton, UK

Institut de Ciències del Mar (CSIC), Barcelona, Spain

S. Krastel et al. (eds.), *Submarine Mass Movements and Their Consequences*, Advances in Natural and Technological Hazards Research 37, DOI 10.1007/978-3-319-00972-8_28,

they control the extent of headward and lateral extension of submarine canyons, facilitate tributary development, remove material from the continental shelf and slope, and feed sediment and drive its transport across the submarine canyon system.

Keywords Submarine mass movement • Submarine canyon • Sediment-undersupplied margin • Malta-Sicily Escarpment • Mediterranean

28.1 Introduction

The Malta-Sicily Escarpment (MSE) is one of the principal physiographic elements of the central Mediterranean (Fig. 28.1). Consisting of a steep, NNW-SSE trending slope that extends southwards from the east coast of Sicily, the escarpment is 250 km long and has a vertical relief of almost 3 km. The MSE is the expression of a passive margin separating the continental crust of the Malta Plateau from the oceanic crust of the Ionian Basin (Argnani and Bonazzi 2005). Triassic-Neogene sedimentary and volcanic sequences outcrop along the escarpment (Casero et al. 1984; Scandone et al. 1981). Reconstructions of past sea level changes (Imbrie et al. 1989) and stratigraphic analyses (Max et al. 1993; Osler and Algan 1999) suggest

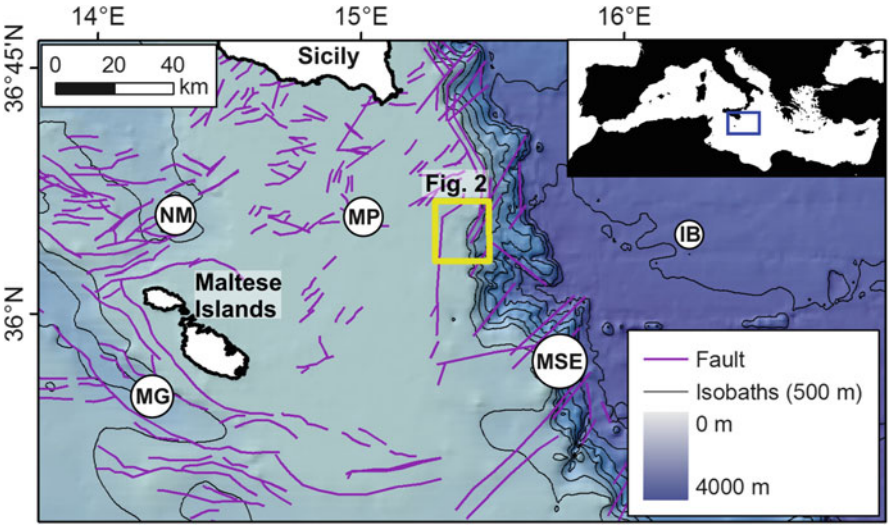

Fig. 28.1 Bathymetric map of the MSE, central Mediterranean Sea, showing the principal morphological features of the region. *IB* Ionian Basin, *MG* Malta Graben, *MP* Malta Plateau, *MSE* Malta-Sicily Escarpment, *NM* North Malta Basin (Source: IOC et al. 2003). Faults are mapped from published seismic reflection data; some of them have been reactivated in the early Pliocene (Casero et al. 1984; Gardiner et al. 1995)

that, following the Messinian Salinity Crisis (~5.9 Ma), the majority of the MSE has largely remained isolated from inputs of fluvial and littoral sediments, and that it has experienced low sedimentation rates; the escarpment may thus be classified as a sediment-undersupplied margin. The MSE is also located at the convergence between the eastward flowing Atlantic Ionian Stream and the westward passage of the denser Levantine Intermediate Water. Sediment drift accumulations, indicative of bottom current activity, have been reported at the foot of the MSE (Marani et al. 1993).

The role of slope instability in the overall evolution of the MSE is not well-understood. Mass movement activity has mainly been inferred from sediment cores. Volcaniclastic and terrigenous turbidites and debrites have been reported from the lower reaches of a submarine canyon system that incises the MSE (Casero et al. 1984; Scandone et al. 1981). Slumping across the MSE itself has only been reported from seismic reflection profiles (Jongsma et al. 1985). In this study we use geophysical and sedimentological data recently acquired from the outer Malta Plateau and upper MSE to: (i) map and characterise the dominant forms of mass movements, and (ii) determine the nature and origin of these mass movements, and their role in the evolution of the MSE.

28.2 Data and Methods

Our study is based on four types of data acquired from the MSE during the CUMECS research cruise (2012).

(i) Multibeam echosounder (MBES) data: An area of ~370 km^2 of seabed was surveyed using a Kongsberg-Simrad EM-710 system (70–100 kHz) (Fig. 28.1). Both bathymetry and backscatter grids with 10 m × 10 m bin size were derived (Fig. 28.2). These grids were visually interpreted and standard morphometric attributes (gradient, aspect, curvature) were extracted.

(ii) Sub-bottom profiles: 500 km of high resolution seismic reflection profiles were acquired simultaneously with the MBES data. The profiles were collected using a hull-mounted CHIRP-II profiler with operating frequencies of 2–7 kHz. For conversion of two-way travel time to depth we used a standard seismic p-wave velocity of 1,600 m s^{-1}.

(iii) Gravity cores: A total of 28 m of sediment cores were obtained from nine sites using a 6-m gravity corer (Fig. 28.2a). The cores were visually logged, photographed, and analysed in terms of sediment colour, magnetic susceptibility, p-wave velocity, and gamma density using a Geotek® Multi-Sensor Core Logger.

(iv) Dredge samples: Samples were acquired with a cylindrical metallic dredge from one selected site at a depth of 320 m (Fig. 28.2a).

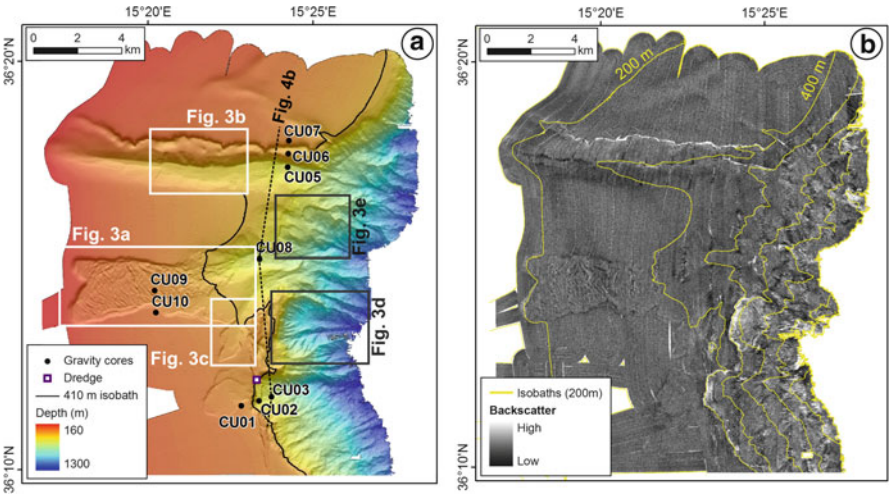

Fig. 28.2 (**a**) Bathymetric data draped on a shaded relief map and (**b**) backscatter map of the study area (isobaths at 200 m intervals). Location in Fig. 28.1

28.3 Results

28.3.1 Seafloor Morphology and Composition

The study area comprises two morphologically diverse provinces (outer Malta Plateau and MSE) that are divided by the 410 m isobath (Fig. 28.2a).

28.3.1.1 Outer Malta Plateau

The seafloor between 160 and 410 m depth is predominantly smooth, very gently sloping (0.8–1.8°) towards the east, and characterised by low backscatter response. Across the Outer Malta Plateau we identify three morphological elements of interest:

(i) Escarpments
Steep breaks of slope, up to 12.5 km long and 60 m high, occur in three orientations: W-E, N-S and SW-NE. They are straight to non-linear, and they generally correspond to high backscatter (Figs. 28.2 and 28.3b).

(ii) Scars
Located just upslope of the 410 m isobath are four scars that range from 1 to 18 km^2 in area. The scars have ellipsoidal to elongated plan-form shapes oriented east to north-eastwards; their lateral and upslope limits are characterised by escarpments with gradients of up to 15° and heights of up

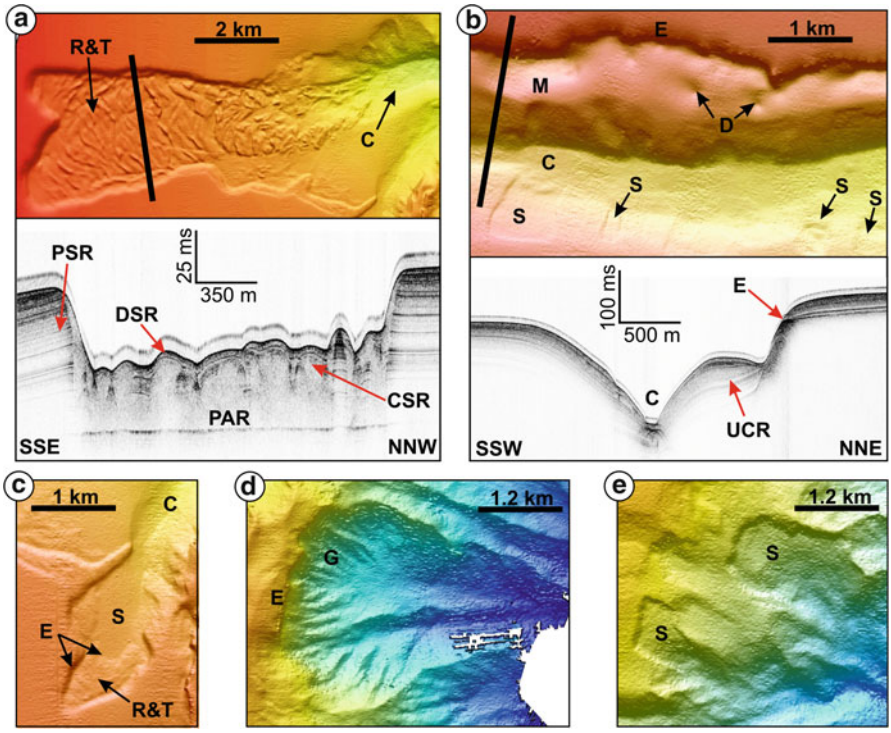

Fig. 28.3 Bathymetric map and sub-seafloor image of the: (**a**) Largest scar in the Outer Malta Plateau; (**b**) longest channel in the Outer Malta Plateau, the elongated morphology and escarpment across its northern wall. Bathymetric map of (**c**) small scar in Outer Malta Plateau; (**d**) amphitheatre-shaped depression in the upper MSE; (**e**) shallow scars in the upper MSE. Depth legend in Fig. 28.2. *C* channel, *CSR* chaotic seismic reflections, *D* circular depressions, *DSR* draping seismic reflections, *E* escarpment, *G* gullies, *M* mounded morphology, *PAR* planar high amplitude reflector, *PSR* parallel seismic reflections, *R&T* ridges & troughs, *S* scar, *UCR* upwardly-convex high amplitude reflectors

to 50 m. The largest scar comprises a series of sub-parallel linear ridges and troughs (Fig. 28.3a). The other three scars, on the other hand, are intersected by gently-sloping escarpments (Fig. 28.3c). The downslope section of these scars consists of smooth, near-planar seafloor whereas the upslope section comprises a ridge and trough pattern (Figs. 28.3a, c). The downslope limit of all the scars is contiguous with another scar, a channel or an escarpment.

(iii) Channels

The deepest part of the Outer Malta Plateau is incised by four channels. Two other channels connect scars with the upper MSE (Figs. 28.3a, c). The longest channel (12 km long) dominates the northern part of the study area (Fig. 28.3b). Its steeper northern wall is characterised by an elongated mounded morphology, up to 1 km wide, which extends along the foot of a

70 m high escarpment. Two 90 m wide circular depressions are also observed in that location. The walls of the long channel are affected by 16 small scars (0.03–0.4 km^2 in area), all of which slope towards and connect to the channel bed. The scars are shallow (maximum depth of 5 m), smooth, planar and have low aspect ratios.

28.3.1.2 Upper MSE

The seafloor deeper than 410 m is considerably different from that upslope. The slope is steeper (mean gradient of 11°) and is heavily incised by a dense network of gullies and distinct larger and wider channels that extend all the way from the shelf break to the limit of data coverage (Fig. 28.2). The gullies have steep sidewalls and sharp interfluves, whilst their beds generally coincide with high backscatter values. Some gullies are carved into large amphitheatre-shaped depressions (Fig. 28.3d), the upslope limits of which are high escarpments (up to 150 m in height) that have a very high backscatter response (Fig. 28.2b). The southernmost of these depressions intersects a N-S trending ridge; dredged material from this ridge consists of hard carbonate rocks. A large proportion of the gullied slope is affected by numerous, shallow scars (Fig. 28.3e). These are oriented downslope with a predominantly elongate plan shape, and they have upslope limits that are generally linear, steep and have a high backscatter character. The lower limit is difficult to identify from the bathymetric data. The scars are mostly located upslope or adjacent to gullies and channels.

28.3.2 Sub-seafloor Architecture

The seismic expression of the sub-seafloor in most of the shallow province comprises a sequence of continuous, parallel, high amplitude seismic reflections that is at least 50 m thick in places. At abrupt changes in slope, the sequence thins and seismic reflections converge. Sub-bottom profiles across scars in the shallow province show that this parallel seismic reflection pattern is truncated at escarpments (Fig. 28.3a). At the downslope limit of the scars, the seismic signature is predominantly chaotic. Where ridge and trough morphology occurs, the seismic pattern is predominantly represented by an irregular, chaotic, low reflectivity unit, which has variable thickness and is draped by an up to 5 m thick unit of coherent, moderate reflectors (Fig. 28.3a). The base of the irregular unit is a planar, high amplitude reflector.

The internal stratigraphy of the elongated mound on the long channel's northern wall is characterised by an asymmetric package of sub-parallel, upwardly-convex, high-amplitude reflectors (Fig. 28.3b). This sequence is also draped by a coherent, moderately reflective, 5 m thick unit.

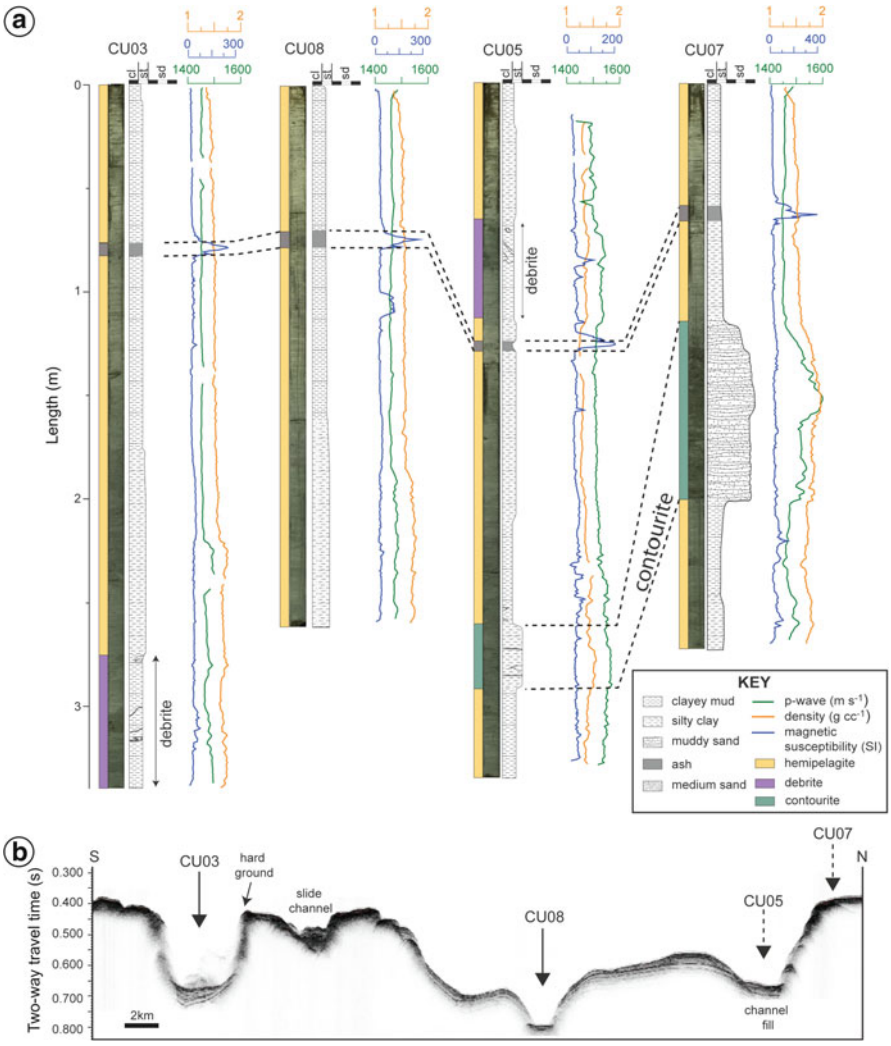

Fig. 28.4 (**a**) Data and interpretation of sediment cores from sites CU03, CU08, CU05 and CU07, and (**b**) their location on a sub-seafloor transect. The *coloured bar* to the *left* of the core photographs represents lithological interpretation. Location of cores and transect in Fig. 28.2a

28.3.3 Sub-surface Sedimentology

The sediment in all nine gravity cores is predominantly clay to silty clay of homogeneous lithology and physical properties, and punctuated by infrequent variations (Fig. 28.4). These include:

(i) Between 60 and 75 cm downcore in most cores, there is a layer of volcanic ash that generates a characteristic high peak in the magnetic susceptibility curve, which is used to correlate cores. This peak is found deeper downcore in core CU05, at about 120 cm.
(ii) The last 60 cm of core CU03 shows inclined laminae, sand clasts and erratic variability of the physical properties. Similar characteristics are found between 70 and 120 cm downcore in core CU05, 10 cm above the ash layer.
(iii) Between 260 and 290 cm downcore in CU05 there is a sequence of silty clay containing medium sand laminae alternating with clay laminae, characterised by relatively higher gamma ray density and p-wave velocity.
(iv) A 1 m thick sequence of unsorted, roughly-graded, medium to fine sand intermixed with clay occurs in core CU07. This sequence is characterised by relatively higher gamma ray density and p-wave velocity than the rest of the core, which correlates with the layer described above in core CU05.

28.4 Discussion and Conclusions

28.4.1 Nature of Mass Movements and Sediment Transport

We interpret the scars documented across the study area as evidence of widespread slope instability. The 67 mass movements identified can be divided into two classes – shelf mass movements that affect the outer Malta Plateau, and slope mass movements that occur across the MSE. Their areal extents range across three orders of magnitude and display up to three levels of retrogression.

On the outer Malta Plateau, mass movements have occurred on very gentle slopes of stratified fine sediments, which is likely of hemipelagic and pelagic origin and deposited during the Plio-Pleistocene (Micallef et al. 2011; Tonarelli et al. 1993). The style of deformation observed is indicative of both translational slides and debris flows. The ridge and trough morphology is the signature of spreading, which involves extension of a sediment unit and its break up into blocks that slide above a planar failure surface (Micallef et al. 2007). Spreading occurs in the largest scar as well as in the upslope sections of the smaller scars located at the shelf break. The chaotic seismic signature of the downslope limit of the scars is indicative of internal deformation, most likely caused by the occurrence of debris flows. The core retrieved from the long channel thalweg (CU05) has a sequence with the deformed sediments and erratic physical properties (Fig. 28.4), which we interpret as a debrite.

On the upper part of the MSE, slope instability has taken place in carbonate sequences with a steeply inclined exposure (Scandone et al. 1981). Due to the composition of the failed material, the chaotic seismic signature of the deposits, and their linear to arcuate steep headwalls, we infer that the style of failure was either a translational slide or debris avalanche (e.g. ten Brink et al. 2006). The amphitheatre-shaped depressions are likely canyon heads that result from coalescing, arcuate scars

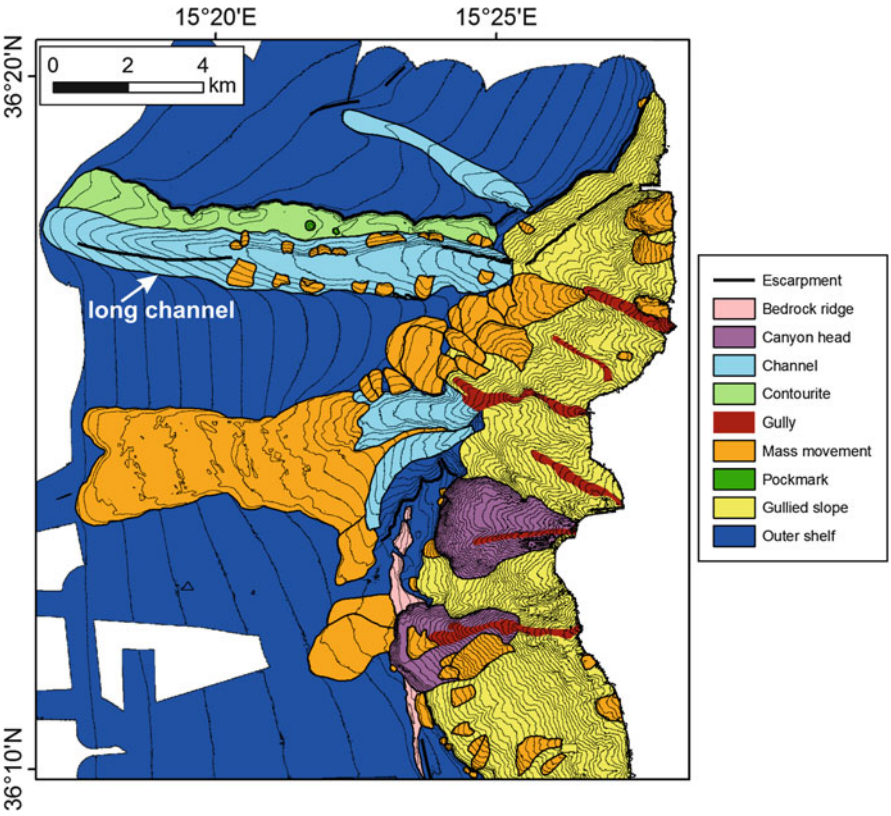

Fig. 28.5 Interpretation map of the study area (isobaths at 25 m intervals)

(Mulder et al. 2012). Mass movements associated with the upslope development of the southernmost of these canyon heads were powerful enough to erode a structurally-controlled bedrock ridge at its headwall (Fig. 28.5).

From the geophysical and sediment core data in Figs. 28.3b and 28.4, we interpret the elongated mounded morphology along the northern wall of the long channel as a contourite (Rebesco and Stow 2001; Stow et al. 2002).

28.4.2 Causes of Slope Instability

We propose four potential causes of slope instability across the outer Malta Plateau and upper MSE:

(i) **Loss of support**: The retrogressive nature of the mass movements – with their location upslope of other mass movements, escarpments, channel/gully

beds or canyon heads – indicates that loss of support plays an important role in triggering slope instability in the study area. Across the MSE, the incision of gullies and channels triggers slope failures across their walls due to oversteepening and loss of support (e.g. Micallef et al. 2012). These flank failures are responsible for widening and extending the gullies and channels upslope. The same dynamics characterise the long channel in the outer Malta Plateau. In this case, the formation of a contouritic drift on the northern wall indicates that bottom currents may play a role in channel incision. Otherwise, loss of support is the result of a mass movement taking place downslope or associated with the upslope development of a submarine canyon head.

(ii) **Sedimentation**: Hemipelagic and pelagic sedimentation, as well as contouritic deposition along the northern wall of the long channel, provide the material that fails across the outer Malta Plateau. Sedimentation rates across the Malta Plateau in the last 5 Ma are reported to be low, in the range of ~6 cm per 1,000 year on the Malta Plateau (Max et al. 1993; Osler and Algan 1999). Thus, we believe that sediment loading and associated excess pore pressure development are not a pre-conditioning factor for slope instability in the region.

(iii) **Faulting and seismicity**: Faults, linked to the different rates of underthrusting between the buoyant Malta Plateau and the Ionian crust (Adam et al. 2000; Grasso 1993), are common across the study area (as shown in Fig. 28.1 and inferred from the escarpments in Fig. 28.5) and likely to have exerted a predominant control on the physiography and, indirectly, on the location of mass movements (e.g. occurrence of steep slope gradients, seafloor deformation, escarpments, and channels). Seismic activity has mostly been restricted to the northern section of the MSE (Argnani and Bonazzi 2005). Ground shaking associated with distal earthquakes could thus have played a minor role in triggering slope instability across the study area.

(iv) **Fluid flow**: Deep fluid flow systems, sourced by Late Mesozoic sedimentary units, have been reported in parts of the outer Malta Plateau (Micallef et al. 2011). Fluid, likely transferred to the surface by faults in the Tertiary carbonate sequences, may thus play a role in reducing the stability of the outer Malta Plateau by elevating pore pressures in the sediments. The circular depressions identified on the northern wall of the long channel may be evidence of fluid escape at the seabed.

28.4.3 Role of Mass Movements in the Evolution of the MSE

The evolution of the MSE in the study area appears to have been determined by the interaction of: (i) fault activity associated with the tectonic regime of the central Mediterranean, (ii) sedimentary activity, driven by hemipelagic, pelagic and contouritic sedimentation, (iii) seafloor incision, related to bottom current activity and, possibly, to oceanographic and terrestrial processes that could have been active during sea level lowstands (e.g. Messinian Salinity Crisis). In this framework, the

role of mass movements across the MSE and outer Malta Plateau was to erode the seafloor and transfer material to the lower MSE. What is interesting about our study area is that it presents a very good example of how mass movements and canyon processes are interrelated. Submarine mass movements control the extent of lateral and headward extension of the canyons across the continental slope and shelf, as well as facilitate tributary development. They also remove material from the continental shelf and slope, feeding sediment and driving its transport down-canyon. Because of their size and position in the stratigraphic record, we believe that the mapped submarine mass movements do not constitute a significant geohazard to the central Mediterranean region.

Acknowledgments This research was supported by funding from the European Union 7th Framework Programme (FP7/2007–2013) under grant agreements n° 228344 (EUROFLEETS), n° 252702 (CAGE), n° 29874 (Geo-Habit) and ERC Starting Grant n° 258482 (CODEMAP). Additional funding was provided by the Crown Research Institute Core funding to NIWA and from the Griffith Geoscience Awards of the Department of Communications, Energy and Natural Resources under the National Geoscience Programme 2007–2013 of Ireland. We are indebted to the CUMECS shipboard party, the captain, crew and technicians of *RV Urania*, and to Suzanne Maclachlan and Jeremy Sothcott for their assistance with core analyses. Federica Foglini, Jan Sverre Laberg and Sebastian Krastel are thanked for their insightful reviews.

References

Adam J, Reuther CD, Grasso M et al (2000) Active fault kinematics and crustal stresses along the Ionian margin of southeastern Sicily. Tectonophysics 326:217–239

Argnani A, Bonazzi C (2005) Malta escarpment fault zone offshore eastern Sicily: Pliocene-Quaternary tectonic evolution based on new multichannel seismic data. Tectonics 24:TC4009

Casero P, Cita MB, Croce M et al (1984) Tentative di interpretazione evolutiva della scarpata di Malta basata su dati geologici e geofisici. Mem Soc Geol Ital 27:233–253

Gardiner W, Grasso M, Sedgeley D (1995) Plio-Pleistocene fault movement as evidence for mega-block kinematics within the Hyblean-Malta Plateau, Central Mediterranean. J Geodyn 19:35–51

Grasso M (1993) Pleistocene structures along the Ionian side of the Hyblean Plateau (SE Sicily): implications for the tectonic evolution of the Malta Escarpment. In: Max MD, Colantoni P (eds) Geological development of the Sicilian-Tunisian platform. UNESCO, Urbino, pp 49–54

Imbrie J, McIntyre A, Mix AC (1989) Oceanic response to orbital forcing in the late quaternary: observational and experimental strategies. In: Berger A et al (eds) Climate and geosciences: a challenge for science and society in the 21st century. Reidel Publishing Company, Dordrecht

IOC, IHO, BODC (2003) Centenary edition of the GEBCO digital atlas. Published on CD-ROM on behalf of the Intergovernmental Oceanographic Commission and the International Hydrographic Organisation as part of the General Bathymetric Chart of the Oceans, British Oceanographic Data Centre, Liverpool

Jongsma D, Van Hinte JE, Woodside JM (1985) Geologic structure and neotectonics of the North African continental margin south of Sicily. Mar Pet Geol 2:156–177

Marani M, Argnani A, Roveri M et al (1993) Sediment drifts and erosional surface in the central Mediterranean: seismic evidence of bottom-current activity. Sediment Geol 82:207–220

Max MD, Kristensen A, Michelozzi E (1993) Small scale Plio-Quaternary sequence stratigraphy and shallow geology of the west-central Malta Plateau. In: Max MD, Colantoni P (eds) Geological development of the Sicilian-Tunisian platform. UNESCO, Urbino, pp 117–122

Micallef A, Masson DG, Berndt C et al (2007) Morphology and mechanics of submarine spreading: a case study from the Storegga Slide. J Geophys Res 112:F03023

Micallef A, Berndt C, Debono G (2011) Fluid flow systems of the Malta Plateau, Central Mediterranean Sea. Mar Geol 284:74–85

Micallef A, Mountjoy JJ, Canals M et al (2012) Deep-seated bedrock landslides and submarine canyon evolution in an active tectonic margin: Cook Strait, New Zealand. In: Yamada Y et al (eds) Submarine mass movements and their consequences. Springer, London, pp 201–212

Mulder T, Ducassou E, Gillet E et al (2012) Canyon morphology on a modern carbonate slope of the Bahamas: evidence of regional tectonic tilting. Geology 40:771–774

Osler J, Algan O (1999) A high resolution seismic sequence analysis of the Malta Plateau. Saclantcen report

Rebesco M, Stow DAV (2001) Seismic expression of contourites and related deposits: a preface. Mar Geophys Res 22:303–308

Scandone P, Patacca E, Radoicic R et al (1981) Mesozoic and Cenozoic rocks from Malta Escarpment (Central Mediterranean). Am Assoc Pet Geol B 65:1299–1319

Stow DAV, Faugeres JC, Howe JA et al (2002) Bottom currents, contourites and deep-sea sediment drifts: current state-of-the-art. In: Stow DAV et al (eds) Deep-water contourite systems: modern drifts and ancient series, seismic and sedimentary characteristics. Geological Society, London, pp 7–20

ten Brink US, Geist EL, Lynett P et al (2006) Submarine slides north of Puerto Rico and their tsunami potential. In: Mercado A, Liu PLF (eds) Caribbean Tsunami hazard. World Scientific Publishers, Hackensack

Tonarelli B, Turgutcan F, Max MD, Akal T (1993) Shallow sediments at four localities on the Sicilian-Tunisian platform. In: Max MD, Colantoni P (eds) Geological development of the Sicilian-Tunisian platform. UNESCO, Urbino, pp 123–128

Chapter 29
Submarine Mass Movements Along a Sediment Starved Margin: The Menorca Channel (Balearic Islands – Western Mediterranean)

Claudio Lo Iacono, Roger Urgeles, S. Polizzi, J. Grinyó, M. Druet, M. Agate, J.M. Gili, and J. Acosta

Abstract Sediment starved passive margins, particularly those of insular slopes, display significant mass transport activity despite the absence of environmental stresses from high sedimentation rates. The "Menorca Channel" represents the up to 120 m deep shelf sector connecting the Menorca and Mallorca Islands (Balearic Islands – Western Mediterranean). South of the Menorca Channel submarine gravitational processes have been mapped and interpreted from swath-bathymetry, TOPAS parametric echosounder and deep-towed videos. The shelf-break is located at an average depth of 140 m, and sediment instability is a widespread phenomenon. The slope region south the Menorca Channel shows a number of submarine canyons disrupting the outer shelf. The north-easternmost canyon is the more active feature, with an incised axis and scars shaping the flanks up to their edges. Headwall scarps, between 140 and 700 m depth, are up to 20 m high. The shallower scarps producing slab-type failures have carved the outer edges of planar sedimentary bodies interpreted as formed in shallow environments during previous glacial stages. Results show that a variety of sediment instability processes extensively shape the southern upper slope of the Menorca Channel. Submarine canyons develop on the

C. Lo Iacono (✉)
Marine Geosciences, National Oceanography Centre, Southampton, UK

Institut de Ciències del Mar (CSIC), Barcelona, Spain
e-mail: cllo@noc.ac.uk; loiacono@cmima.csic.es

R. Urgeles
Dept. Geociències Marines, Institut de Cències del Mar (CSIC), Barcelona, Spain

J. Grinyó • J.M. Gili
Institut de Ciències del Mar (CSIC), Barcelona, Spain

S. Polizzi • M. Agate
Dipartimento delle Scienze della Terra e del Mare dell'Universitá di Palermo, Palermo, Italy

M. Druet • J. Acosta
Insituto Espaňol de Oceanografia, Madrid, Spain

S. Krastel et al. (eds.), *Submarine Mass Movements and Their Consequences*, Advances in Natural and Technological Hazards Research 37, DOI 10.1007/978-3-319-00972-8_29,

Emile Bodout Escarpment (EBE), a passive tectonic feature which bounds the slope region of the study area. A number of knickpoints within the canyons suggest backward erosion control on mass wasting and, at the same time, that slope failure is one of the main drivers for canyon upslope migration. Steep gradients of the upper slope, the presence of weak layers and the action of major storms during lowstand stages are additional factors likely to influence the distribution and frequency of mass wasting processes in this area.

29.1 Introduction

Submarine landslides are present across the full range of continental margins, tectonic settings (Hampton et al. 1996) and oceans (Weaver et al. 2000; Huhnerbach et al. 2004; Chaytor et al. 2009). Seafloor instability is triggered when the driving stresses acting on the slope exceed the resisting forces (Hampton et al. 1996). The factors that may induce submarine slope failure are divided between those that increase the driving stress (e.g. earthquakes) and those that reduce the shear resistance (e.g. high sedimentation rates, non-equilibrium consolidation and pore pressure build-up). Earthquakes typically occur on tectonically active margins, while high sedimentation rates are characteristic of continental margins fed by large river systems. Passive margins of insular slopes are devoid of large earthquakes and onshore watersheds are relatively small, implying that large river systems cannot be formed and therefore sediment delivery to the adjacent continental margins is rather limited. Despite the overall lack of these typical trigger mechanism and pre-conditioning factors for slope instability, submarine landslides are ubiquitous on some sediment-starved insular slopes such as those of the study area. In this study we present a morphological characterization of the mass wasting processes observed along the southern margin of the Balearic Promontory, between Menorca and Mallorca Islands (Balearic Islands – Western Mediterranean) (Fig. 29.1a). The main aims are to explore the factors that induce submarine slope failure in this environment and to better highlight the controls on the long-term evolution of sediment undersupplied insular slopes.

29.2 Geological Framework

The Balearic Promontory is a structural elevation including four major islands (from west to east: Ibiza, Formentera, Mallorca and Menorca) resulting from successive pre-Oligocene subduction of Africa beneath Eurasia, Oligocene rifting and oceanic accretion during the Miocene (Acosta et al. 2001). The Promontory separates the Balearic–Provençal Basin to the north from the Algero-Balearic Basin to the south (Acosta et al. 2002). The study area lies on the southern flank of the Menorca Channel between the islands of Mallorca and Menorca (Fig. 29.1a). A NE–SW steep scarp, the Emile Baudot Escarpment (EBE) bounds the southern margin of

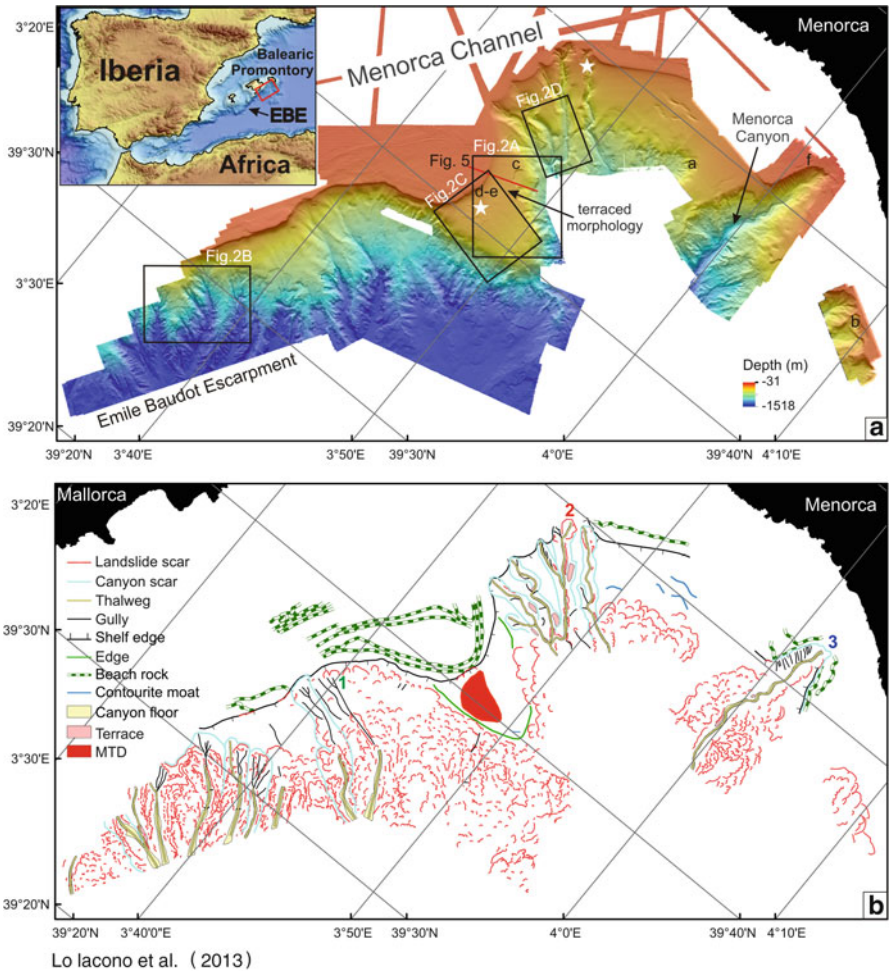

Fig. 29.1 (**a**) Bathymetry of the study area south of the Menorca Channel. *Black boxes* mark locations of detailed maps shown in Fig. 29.2. *Lower case letters* indicate the position of the images in Fig. 29.4. *Red line* shows location of parametric profile in Fig. 29.5. *White stars* show dredging locations. *Inset* shows location of the study area. (**b**) Interpretation of bathymetric data. *Colored numbers* indicate thalweg long profiles in Fig. 29.3

the Promontory, including the Menorca Channel (Fig. 29.1a). The EBE has been interpreted as evidence of the right-lateral strike–slip fault system that bounds the south Algero- Balearic basin (Mauffret et al. 2004). It is worthy to note the absence of earthquakes along the fault in the last 80 years (IGN, USGS), indicating the aseismic character of this feature. In the study area, the Menorca submarine canyon and other minor incisions converge towards a narrow channel (the South Mallorca Trough) that feed the Menorca Fan, a wide fan-shaped area along the base of the EBE (Camerlenghi et al. 2009). The Menorca channel has reduced or

null river sediment inputs. Sediments composing the seafloor mainly originate from local coastal erosion processes and by a variable carbonate production of bioherms (Barberà et al. 2012).

29.3 Methods

The data presented in this study was primarily collected for the INDEMARES-LIFE Project (www.indemares.es) of the Instituto Español de Oceanografia (IEO) and the Institut de Ciències del Mar (ICM-CSIC). Multi beam data were acquired during five cruises between 2010 and 2012 with a Simrad EM302 on the RV Miguel Oliver. Processing and visualization of bathymetric data were performed with CARIS HIPS system and ARC-GIS respectively. TOPAS PS18 high-resolution seismic records and rock dredges were collected in 2012 by IEO on the RV Miguel Oliver. Video surveys were conducted using the manned submersible JAGO (GEOMAR) in depths of 120–400 m. Video analysis was performed with the Final Cut software.

29.4 Results

The continental margin south off the Menorca and Mallorca Islands presents a width of ∼10–20 km and is mainly characterized by several lineations. These features display a curved morphology generally parallel to the bathymetric contours (Fig. 29.1). At least 8 bars, likely representing beachrock deposits, are recognized for a 90–110 m depth range (Fig. 29.1b). The shelf break, 120 m deep, is relatively sharp and indented by few canyons, particularly off Mallorca (Fig. 29.1). Off the shelf break, the upper slope is relatively smooth and has a terraced morphology (Figs. 29.1a and 29.2a). These terraces display also a smooth morphology that is only disturbed by Mass Transport Deposits (MTD) with hummocky morphology (Figs. 29.1b and 29.2c). The upper reaches of the slope display few canyons in the whole survey area. The only major canyon is the Menorca Canyon which evolves from the southern Menorca slope; it is well incised on the continental shelf and has well developed side valleys (Fig. 29.1). In between Menorca and Mallorca, off the Menorca Channel, the erosional features are rather shallow and do not incise significantly on the shelf (Fig. 29.1). These features resemble channels rather than canyons. Off south Mallorca, no major canyons develop, despite the middle slope showing pervasive gullying (Figs. 29.1 and 29.2). From north to south, the long profile of the canyons-channels-gullies shows increasing evidence of non-equilibrium conditions, with several knickpoints present within the gullies off Mallorca (Fig. 29.3), some of them related to failure scars (Figs. 29.1 and 29.3). Some knickpoints show elevations that exceed 200 m, with long-profile slopes that are remarkably different upslope and downslope from the knickpoint (Fig. 29.3).

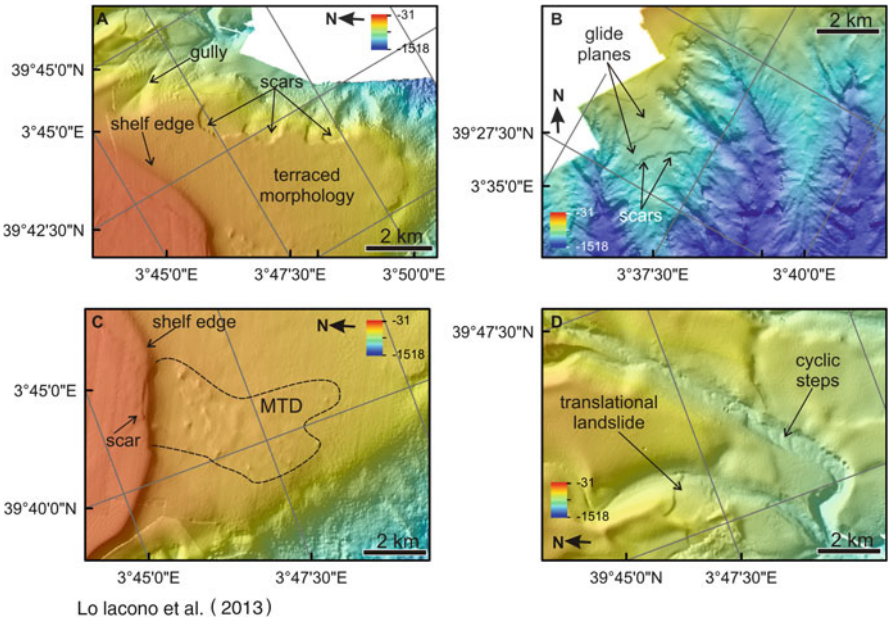

Fig. 29.2 Details of multi beam bathymetry showing (**a**) slab slides at the side flank of a submarine canyon (**b**) slab like stepped landslide scars at the head and interfluve of submarine canyons (**c**) hummocky MTD originating from littoral terrace/depositional body with beach rocks and (**d**) cyclic steps within submarine channel/canyon (see Fig. 29.1a for location)

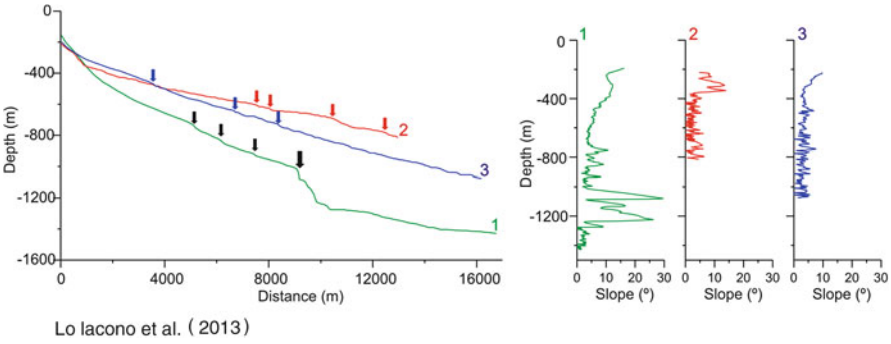

Fig. 29.3 Canyon long profiles (*left*) of selected canyons along the southern margin of the Menorca southern slope showing prominent and some more conspicuous knickpoints (*arrows*). Slope gradients with depth for the same canyons are shown to the *right*. For location of long-profiles see *colored numbers* in Fig. 29.1b

Analysis of video records (Fig. 29.4) shows that rocky outcrops generally coincide with the headscarps of landslides and show strata heads (Fig. 29.4a) and sub-vertical walls (Fig. 29.4b). Sediments along the shelf margin and the upper slope are mainly composed of bioclastic medium to coarse sands and gravels,

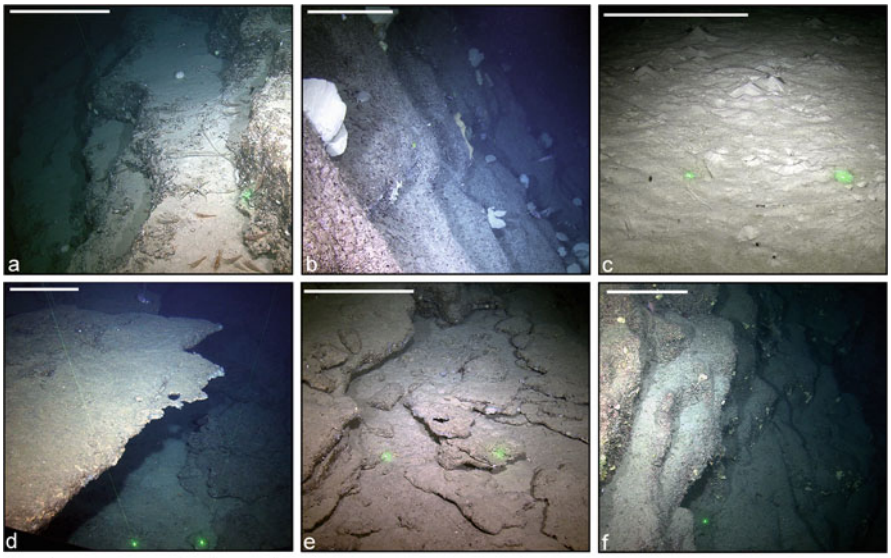

Fig. 29.4 Images extracted from the Jago video records on the Menorca upper slope, (**a**) strata head outcrops along a landslide scar, (**b**) tens of meters deep sub-vertical scar entirely encrusted by red algae, (**c**) bioclastic sands, (**d–f**) landslide composed of carbonate bioclastic deposits (beachrocks?), (**f**) vertical walls in the Menorca Canyon head. Location of the images is indicated with the letters on Fig. 29.1a. *White bar* corresponds to the length of 50 cm

coming from the degradation of the wide benthic assemblages present in the area (Fig. 29.4c). Most of the rocks observed along the shelf margin and in the head of the Menorca Canyon are likely composed of cemented bioclastic deposits (Fig. 29.4d, e). The substrate along the deep sub-vertical walls (Fig. 29.4f) is probably composed of the Tertiary carbonate rocks outcropping on-land in Menorca. Dredge rock samples collected on the 230 m deep landslide deposit (Fig. 29.2c) and in the Menorca Canyon head (−120 m) present the same lithological typology. Samples correspond to graded bioclastic and lithoclastic cemented coarse sands to gravels with a minor fine sediment component (Fig. 29.4d, e). Grains are sustained by secondary carbonate cements and several entire or partially fragmented shells are observed.

Parametric TOPAS sub-bottom profiles display typical downlap and toplap geometries for the sedimentary body that defines the shelf break (Fig. 29.5). Below the shelf break the seismic facies is initially well stratified and sub-parallel in areas where the seafloor shows relatively smooth relief. The stratified facies are often truncated at scarps 10–20 m high that root at distinct stratigraphic levels (Fig. 29.5). In deeper water with a more gullied relief some stratification is visible, although this is masked by the presence of hyperbolae induced by canyon roughness.

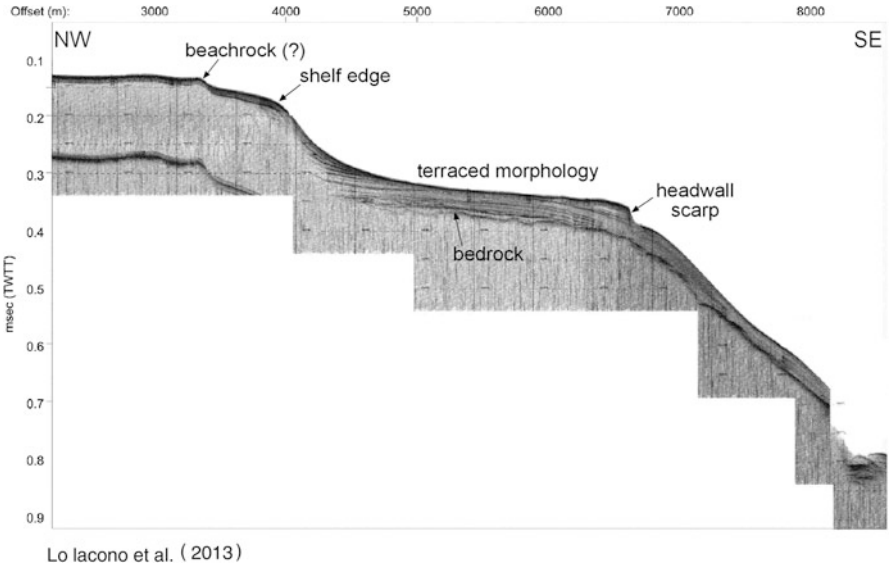

Fig. 29.5 TOPAS high-resolution parametric profile displaying slab slides on the upper slope of the southern Balearic Margin. See Fig. 29.1a for the location of the profile

The canyon's thalweg often displays opaque acoustic facies, but in some instances transparent deposits are observed within the canyons or at their foot.

29.5 Discussion

29.5.1 Factors Pre-conditioning Failure in Sediment Starved South Balearic Margin

The South Balearic margin is devoid of significant seismic activity and sedimentation rates are low (from 0.2 to 0.9 m kyr^{-1}) (Betzler et al. 2011), without major rivers delivering sediment in the adjacent coastal zone. Nevertheless, the large amount of scars and slab-like features surprisingly indicate a dominance of mass-wasting processes (Fig. 29.1b). Most of these landslides, however; appear to be associated to canyon heads and flanks. The bathymetric data, particularly the southern half, shows that there is a clear distinction in slope smoothness between the upper and lower continental slope and that most of the incisions do not indent the shelf edge (Fig. 29.1). Also the prominent knickpoints observed within some of the canyons and gullies (Fig. 29.3) highlight backward erosion processes along those canyons. The ultimate process responsible for such backward erosion is not clear from the data set presented in this study, but it is tentatively ascribed to nowadays inactive

tectonic features such as the Emile Baudot Escarpment (Acosta et al. 2001). Along the SW Mallorca slope, slope failure appears to be associated with drift deposits (Lüdmann et al. 2012). Contrary to that area, we hypothesize that mass-wasting in the SE Balearic margin is mainly driven by local slope steepening, canyon undercutting and axial incision, with slope gradients of around 5° along the open slope affected by mass wasting processes, 3° along the canyon axis and 30° across the headwall scarps. The gullies, channels and tributaries that drain into the Menorca Canyon (north of the spur with a mass transport deposit sitting on it, MTD in Fig. 29.2c) appear to have a profile that is more in equilibrium, which would explain significantly lower mass-wasting activity compared to those that drain the southern Mallorca slope. It is worth noting, that some of the canyons and gullies also display cyclic steps (Fig. 29.2d): these are believed to be formed by hydraulic jumps in which a flow makes a rapid change from thin, rapid supercritical flow to thick, tranquil sub-critical flow (Fildani et al. 2006). However, repeated lake surveys and analog experiments have shown that cyclic steps and knickpoint migration can also be controlled by submarine landslides (Tourmel et al. 2010).

Translational landslides are common features in the upper slope, with downslope dipping strata inducing the sliding of large slabs, conferring a local stratigraphic control in their generation (Figs. 29.1a and 29.2a, d) and implying that weak layers may be a factor in controlling sediment stability. Nonetheless available data do not allow to highlight the occurrence of weak layers as preferential sliding planes. Evidences of rocky landslides and small avalanches can be found in the cutting of strata heads along the southern Menorca slope and Mallorca shelf, creating sub-vertical to overhanging walls along the shelf edge and canyon heads and flanks (Figs. 29.2 and 29.4). Collected rocks are most probably part of Quaternary sedimentary bodies formed in shallow coastal environments during low sea level conditions. Mechanisms that would explain those landslides involve depositional steepening and loading of the upper slope by cemented planar deposits.

29.5.2 Relevance and Timing of Mass/Wasting Processes in Shaping the South Balearic Insular Margin

Data suggest that mass wasting is a pervasive and widespread sedimentary processes along the southern margin of the Menorca Channel (Fig. 29.1a, b). More than 700 km^2 of the 1,000 km^2 covering the entire study area are carved by landslide scarps, gullies and submarine canyons, corresponding to 82 % of the mapped slope region. This shows the relevance of sediment instability processes in slope shaping sediment-undersupplied insular margins. Absence of fluvial inputs and reduced clastic sedimentation can contribute to the formation of a thin Plio-Quaternary succession over a steep structurally controlled margin, favoring the dominance of erosive processes over depositional regimes (see also Micallef et al. 2013). Given their extension, retrograding mass transport processes have been likely carving the

slope region for a relatively long time. We infer that most landslides probably occurred during the glacial phases, when the outer shelf-upper slope system and the canyon heads suffered stronger hydrodynamic conditions related to storms and sediment transport processes (Hernandez-Molina et al. 2002; Lo Iacono et al. 2011). On top of that, occurrence of biogenic encrustations by benthic communities such as sponges, bryozoans and cold water corals on most of the landslide scars, in some case extensively covering large surfaces (Fig. 29.4b), demonstrate a reduced activity in the present-day, although univocal and reliable data on accretion rates of observed benthic organisms are still not available in scientific literature.

29.6 Conclusions

Multi beam bathymetry and high resolution seismic data reveal widespread presence of mass wasting features in the southern margin of the Menorca Channel, Balearic Islands (Western Mediterranean). Open slope translational landslides, gullies and submarine canyons and channels are the most prominent sediment instability features mapped in the area. Data suggest that dynamics of gravity processes in the area results from the interaction between backward erosion on structurally controlled slopes, stratigraphy and Quaternary sea level oscillations. Mass wasting features cover up to the 80 % of the mapped slope region and suggest a preponderant role in shaping sediment-undersupplied insular margins. Nonetheless, video runs from the study area did not show fresh scars and/or landslide deposits, advocating for a present-day inactivity of mass movement processes, as also confirmed by the extension of encrusting organisms over the observed features.

Acknowledgements This work was supported by the FP7 2011–2013 EU Marie Curie Action "Geo-Habit" – GA29874 and by the European project INDEMARES (Life-NAT/E/000732). UNESCO and IUGS are also acknowledged for funding through project IGCP-585. Reviewers Joshu Montjuoy (NIWA –Taihoro Nukurangi, New Zealand) and Claudia Romagnoli (Universitá di Bologna, Italy) are thanked for their comments and positive criticism.

References

Acosta J, Muñoz A, Herranz P et al (2001) Geodynamics of the Emile Baudot escarpment and the Balearic Promontory, western Mediterranean. Mar Pet Geol 18:349–369

Acosta J, Canals M, Lopez-Martinèz J et al (2002) The Balearic Promontory geomorphology (western Mediterranean): morphostructure and active processes. Geomorphology 49:177–204

Barberà C, Moranta J, Ordines F et al (2012) Biodiversity and habitat mapping of Menorca Channel (western Mediterranean): implications for conservation. Biodivers Conserv 21:701–728

Betzler C, Braga JC, Jaramillo-Vogel D et al (2011) Late Pleistocene and Holocene cool-water carbonates of the Western Mediterranean Sea. Sedimentology 58:643–669

Camerlenghi A, Accettella D, Costa S et al (2009) Morphogenesis of the SW Balearic continental slope and adjacent abyssal plain, Western Mediterranean Sea. Int J Earth Sci 98:735–750

Chaytor JD, ten Brink US, Solow AR et al (2009) Size distribution of submarine landslides along the U.S. Atlantic margin. Mar Geol 264:16–27

Fildani A, Normark WR, Kostic S et al (2006) Channel formation by flow stripping: large-scale scour features along the Monterey East Channel and their relation to sediment waves. Sedimentology 53:1265–1287

Hampton MA, Lee HJ, Locat J (1996) Submarine landslides. Rev Geophys 34:33–59

Hernandez-Molina FJ, Somoza L, Vàzquez JT et al (2002) Quaternary stratigraphic stacking patterns on the continental shelves of the southern Iberian Peninsula: their relationship with global climate and palaeoceanographic changes. Quat Int 921:5–23

Hühnerbach V, Masson DG, COSTA Project Partners (2004) Landslides in the north Atlantic and its adjacent seas: an analysis of their morphology, setting and behaviour. Mar Geol 213: 343–362

IGN Catalogue – Instituto Geografico Nacionál. Catàlogo y Boletines Sismicos. www.ign.es

Lo Iacono C, Sulli A, Agate M, Lo Presti V, Pepe F, Catalano R (2011) Submarine canyon morphologies in the Gulf of Palermo (Southern Tyrrhenian Sea) and possible implications for geo-hazard. Mar Geophys Res 32:127–138

Lüdmann T, Wiggershaus S, Betzler C et al (2012) Southwest Mallorca Island: a cool-water carbonate margin dominated by drift deposition associated with giant mass wasting. Mar Geol 307–310:73–87

Mauffret A, Frizon de Lamotte D et al (2004) E–W opening of the Algerian Basin (Western Mediterranean). Terra Nova 16:257–264

Micallef A, Georgiopoulou A, Huvenne V et al (2013) The Malta-Sicily Escarpment: mass movement dynamics in a sediment-undersupplied margin. In: Krastel S, Behrmann J-H, Völker D, Stipp M, Berndt C, Urgeles R, Chaytor J, Huhn K, Strasser M, Harbitz CB (eds) Submarine mass movements and their consequences, 6th international symposium. Springer, Heidelberg, pp 317–328

Tourmel D, Locat J, Parker G (2010) Upstream migration of knickpoints: geotechnical considerations. In: Yamada Y et al (eds) Submarine mass movements and their consequences. Springer, Dordrecht, pp 123–131

USGS National Earthquake Information Centre – NEIC. http://earrthquake.usgs.gov/regional/neic

Weaver PPE, Wynn RB, Kenyon NH et al (2000) Continental margin sedimentation, with special reference to the north-east Atlantic margin. Sedimentology 47:239–256

Chapter 30
The Detection of Volcanic Debris Avalanches (VDAs) Along the Hellenic Volcanic Arc, Through Marine Geophysical Techniques

P. Nomikou, D. Papanikolaou, A. Tibaldi, S. Carey, I. Livanos, K.L.C. Bell, F.A. Pasquarè, and G. Rousakis

Abstract Recent marine oceanographic surveys using geophysical techniques have revealed a number of volcanic debris avalanche deposits (VDAs) on the external flanks of Antimilos, Santorini and Nisyros volcanoes in the South Aegean Sea. Swath bathymetry and side-scan sonar surveys led to the recognition of characteristic hummocky topography on all of these deposits. On seismic profiles the VDAs are identified by chaotic facies, with incoherent areas bordered by continuous undisturbed seismic reflectors. High-resolution examination of the morphological characteristics of the VDAs was accomplished by using Remotely Operated Vehicles (ROVs), in order to distinguish them from other clastic deposits. In some cases the VDAs can be traced upslope to horseshoe-shaped collapse depressions and represent the expression of the complex evolution of these volcanic edifices. Recognition of VDAs at these volcanic centers has important implications for geohazard assessments as flank collapses have the potential for triggering of

P. Nomikou (✉) • D. Papanikolaou • I. Livanos
Department of Geology and Geoenvironment, University of Athens, Panepistimiopoli Zografou, 15784 Athens, Greece
e-mail: evinom@geol.uoa.gr

A. Tibaldi
Department of Earth and Environmental Sciences, University of Milan Bicocca, Milan, Italy

S. Carey
Graduate School of Oceanography, University of Rhode Island, Narragansett, RI, USA

K.L.C. Bell
Graduate School of Oceanography, University of Rhode Island, Narragansett, RI, USA

Ocean Exploration Trust, Mystic, CT, USA

F.A. Pasquarè
Department of Theoretical and Applied Sciences, Insubria University, Varese, Italy

G. Rousakis
Institute for Oceanography, Hellenic Centre for Marine Research, Anavyssos, Greece

S. Krastel et al. (eds.), *Submarine Mass Movements and Their Consequences*, Advances in Natural and Technological Hazards Research 37, DOI 10.1007/978-3-319-00972-8_30,

large-scale tsunamis. The relationship between the distribution/emplacement mechanisms of the VDA deposits and the source flank collapses remains an area of ongoing research.

Keywords Aegean volcanoes • Submarine landslide • Swath and seismic data • ROV exploration

30.1 Introduction

Repetitive eruptions at a single location frequently construct a volcanic edifice in the form of a subaerial stratovolcano or an ocean island volcano with highly unstable slopes (Manville et al. 2009). A variety of different mechanisms, such as magma intrusion, phreatic eruption, earthquakes, sea-level changes or erosion, can trigger huge sector collapses generating submarine volcanic landslides (McGuire 1996). Debris avalanches are blocky landslides originating directly from collapse of the subaerial and/or submarine island flanks that can travel for tens of kilometers across the sea floor (Siebert 1984). Globally, debris avalanches have been reported around volcanic islands in subduction zones (Tibaldi 2001; Romagnoli et al. 2009; Watt et al. 2012) or large oceanic shield volcanoes such as the Canary islands (Urgeles et al. 1997; Gee et al. 2001; Krastel et al. 2001; Masson et al. 2002) and Hawaiian islands (Clague and Moore 2002; Mitchell et al. 2002).

The largest landslides from volcanic islands may generate disastrous tsunamis at an ocean-basin scale (Waythomas et al. 2009). Understanding how volcanic island landslides can destabilize adjacent seafloor sediment is important for understanding landslide evolution and tsunami generating potential (Crutchley et al. 2013). Tsunamis may cause damage and destruction at coastal infrastructure and loss of lives. Thus identification of the products of such landslides, Volcanic Debris Avalanche deposits (VDAs), on the seafloor is critical to evaluating the potential tsunami hazard in coastal environments near island volcanoes.

Here we present the results of our study identifying VDAs along the Hellenic volcanic arc in the South Aegean Sea, where five separate deposits have been defined using marine geophysical techniques. This work is an extension of previous geophysical investigations on the submarine flanks of Antimilos (Alexandri et al. 2001), Santorini (Bell et al. 2013) and Nisyros (Tibaldi et al. 2008; Nomikou et al. 2009; Livanos et al. 2012) volcanoes.

30.1.1 Geological Setting

The Hellenic Volcanic arc was formed along the convergent plate boundary of the northward-subducting African Plate underneath the active margin of the European Plate (McKenzie 1972; Le Pichon and Angelier 1979). This structure is an important

supplier of volcaniclastic sediments to the Aegean Sea floor. The study of the Tertiary volcanic rocks on several islands of the Aegean, has shown a southward migration of the Volcanic Arc since Late Eocene which started from the North Aegean area and has progressed to its present day configuration along the southern margin of the Cycladic platform and the northern margin of the Cretan Basin (Papanikolaou 1993). The migration rate has been estimated to be 10 km/Myr, since the total displacement has been approximately 400 Myr over the past 40 Myr (Royden and Papanikolaou 2011). According to geochronological data the actual Hellenic Volcanic Arc has been active since the early Pliocene with significant activity during the Quaternary (Pe-Piper and Piper 2002).

Four groups of volcanic complexes occur in the volcanic arc, including both subaerial and submarine outcrops (Nomikou et al. 2013). The Methana group, including Paphsanias submarine volcano, is located at the western edge of the volcanic arc in western Saronikos Gulf. Both the Milos and Santorini groups together with Kolumbo volcanic chain northeast of Santorini, occur in the central arc. At the easternmost end of the arc, the Nisyros group includes several submarine volcanic features.

Nomikou et al. (2013) suggest that the volcanic centers are usually located within neotectonic grabens formed by normal faulting that are sometimes overprinted by subvertical dextral strike-slip structures, especially in the Santorini and Nisyrosvolcanic groups. This strike-slip component has been proposed to have a NE-SW direction in the Santorini – Kolumbo volcanic line. Thus, the overall tectonic regime in the central and eastern part of the arc is better described as transtensional with a prevailing NE-SW structural direction. In contrast, the prevailing tectonic trend in the Milos and Methana groups is in the NW-SE direction, following the general Miocene orientation of the Hellenic arc. This NW-SE tectonic trend was overprinted by younger E-W normal faults creating neotectonic horst and graben structures.

30.1.2 Methods

Bathymetric and seismic data were obtained during several cruises along the submarine volcanoes of the Hellenic Volcanic Arc with R/V Aegaeo and E/V Nautilus. Additional ROV dives have been performed in 2010 and 2011 during different oceanographic cruises.

The multibeam bathymetric surveys were carried out by the R/V Aegaeo of the Hellenic Centre for Marine Research, using a SEABEAM 2120 swath system. GPS navigation (Trimble 4000) provided the average position of the ship to within +/−10 m. High resolution seismic profiling of the Nisyros Volcanic Field, utilized a 10 in^3 air gun system coupled to a single channel streamer towed at 50 m and analog recorder. Around the Santorini Volcanic Field, a 40 in^3 air gun was used with the same streamer but with digital data acquisition. For the seismic survey SE of Nisyros, a 2 kJ sparker comprised by S.I.G.hydrophones, a receiver and a digital recording system, was used. For the ROV surveys, we used the E/V Nautilus's

Hercules and Argus ROVs. The Argus was outfitted with EdgeTech 4200 MP sidescan system with sonar frequency 300/600 kHz, for the acoustic survey of the hummocky area.

30.2 Results

30.2.1 Antimilos

The Milos-Antimilos volcanic group occurs at the southwestern margin of the Cycladic platform, near the Myrtoon Basin, an asymmetric tectonic graben of WNW–ESE direction with very steep morphological slopes (Fig. 30.1a) (Nomikou et al. 2013). Antimilos Island is a geometric volcanic dome formed exclusively of andesitic and dacitic lavas, tuffs and various types of flows ending at abrupt sea cliffs (Marinos 1961).

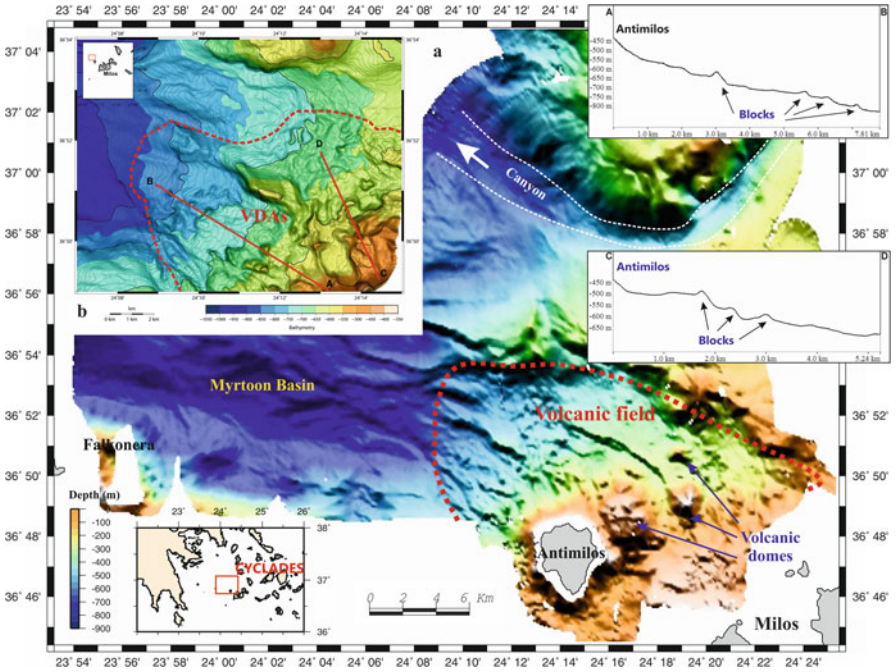

Fig. 30.1 (**a**) Shaded relief bathymetric map of Antimilos volcanic field based on multibeam bathymetric data (Nomikou et al. 2013). The *inset* map shows the location of Antimilos volcano in the Aegean Sea. (**b**) Detailed swath bathymetric map of the northern part of the Antimilos volcanic field. *Red lines* indicate two surface profiles across VDA deposits and shown as *insets* in the *upper right hand side* of the figure

The shaded relief bathymetric map reveals an area of rather irregular small-scale rough relief NW of Antimilos Island and a series assembly of three volcanic domes of decreasing size eastwards. Lobate volcanic deposits are emplaced at depths between 200 and 500 m with diameter of about 100–300 m and maximum height of the order of 50 m (Fig. 30.1b). Several channels (200 m wide and 4 km long) are cut into the seafloor from the shallow platform down to the slope, suggesting high transportation rates of volcaniclastic sediment from the island to the proximal part of the VDA deposits, where the hummocks appear subdued and partially buried (Fig. 30.1b).

The large volcanic field covers about 260 km^2 and appears to be very similar in character to the on-land outcropping volcanic features. The large scale of the hummocks, covering an area approximately 56 km^2, may reflect a larger-volume volcanic collapse of a pre-existing complex that may have been connected with the volcanic structure of Antimilos, further work is necessary to confirm this potential relationship.

30.2.2 Santorini

Santorini is an active caldera system in the central part of the Aegean Volcanic Arc (Druitt et al. 1999). Historic volcanic centres in the region include the submarine Kolumbo volcano, which lies 7 km north-east of Santorini (Sigurdsson et al. 2006; Nomikou et al. 2012), and the intra-caldera Kameni Islands which have been the site of the most recent eruptions in the region.

Numerous offshore geophysical surveys reveal the spectacular seafloor morphology around Santorini, such as prominent hummocky morphology on the eastern submarine flank of the island (Bell et al. 2013). The VDA deposit covers an area 6 km wide by 20 km long and up to 75 m thick in the central region (Fig. 30.2a). The northern extent of the VDA appears to be bounded by a large ridge from the eastern slope of Santorini, and similarly the southern extent coincides with a channel running down the Santorini's eastern slope. The extent of the layer to the south also appears to be bound by bathymetric features including the submarine slope of the nearby island of Anafi. Hummocks within the VDA are composed of individual blocks from a few meters to hundreds of meters in diameter that protrude up to tens of meters above the surrounding seafloor. The run-out distance of most blocks was less than 9 km, but some traveled up to 15 km into water depths of 600 m.

A seismic profile from the southern margin of the VDA (Fig. 30.2b) reveals two important features: (i) an upper layer characterized by chaotic undulating reflectors, and (ii) hyperbolic reflectors corresponding to large hummocks. The total volume of the deposit is estimated to be approximately 4.4×10^9 m^3 (Bell et al. 2013). This kind of landslide facies occurs near the island flanks and is associated with an irregular deposit surface. The hummocky seafloor is likely the result of a multi-stage landslide event that was caused by one of several earthquakes or volcanic eruptions

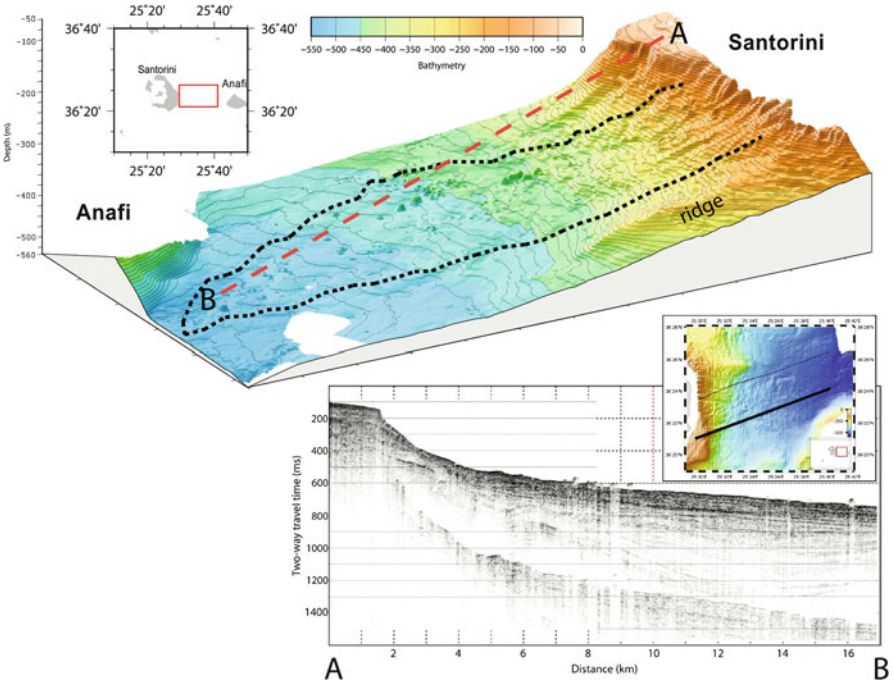

Fig. 30.2 (**a**) Three-dimensional swath bathymetric map of the eastern submarine flanks of Santorini, showing the extent of the hummocky seafloor. (**b**) The southernmost SW-NE longitudinal seismic profile showing a transect through the VDA deposit

that have occurred in and near Santorini after the Minoan eruption (1627–1600 BC) in the Late Bronze Age (Friedrich et al. 2006).

Side scan sonar data reveal a more complex morphology in the central part of the VDA. ROV observations reveal that some blocks have several areas of pumiceous scree and other areas of subvertical to vertical walls that are composed of pyroclastic flow deposits, sometimes covered by brown crust (Fig. 30.3a, d). Some others have communities of benthic megafauna, including corals (*Callogorgia* spp.) and sponges (Fig. 30.3b) and have flat tops (Fig. 30.3c).

30.2.3 Nisyros

The general trend of the recent volcanic centers between Kos and Tilos islands is ENE-WSW, demonstrating the intense geodynamic processes of the eastern edge of the active Hellenic volcanic arc (Nomikou and Papanikolaou 2011). The island of Nisyros is composed mostly of Quaternary volcanic rocks represented by alternating lava flows, pyroclastic layers and viscous lava domes, ranging in age from 160 to 25 ka (Papanikolaou et al. 1991).

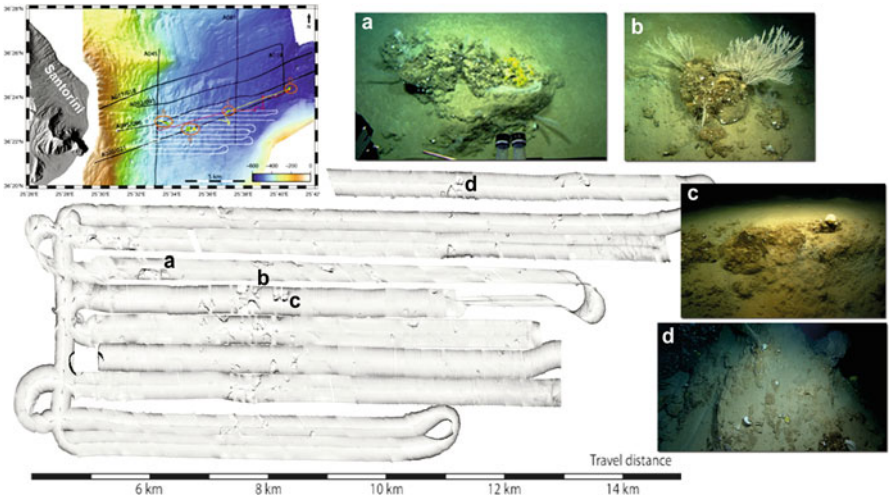

Fig. 30.3 Mosaic of 300 kHz sidescan sonar data; high backscatter is *black*, low backscatter (*shadow*) is *white*. Bathymetric map at the *upper left corner* shows the locations of the airgun profiles (*black lines*), ROV dive tracklines (*red lines*), sidescan survey tracklines (*white lines*) and collected samples (*red circles*). *Bottom* photographs recorded on high definition video of selected block are shown as *a*, *b*, *c*, *d* in the mosaic map

In the area south of Nisyros, VDAs composed of three fields of large blocks and longitudinal ridges (Fig. 30.4). VDA 1 extends 10 km offshore with a concentration of large blocks at its terminus while VDA 2 extends further, out to 16 km from the island and has a higher concentration of large blocks. VDAs 1 & 2 cover a total area of 58 km^2, extending down to 740 m depth. The largest elongated blocks are 520 m across in VDA 1 (with volume ~0.7 km^3), standing 60 m above the surrounding seafloor. A few smaller blocks (up to 400 m across) protrude 45 m above the seafloor at the central part of VDA 2 (with volume ~0.37 km^3). These deposits are bordered by NE-SW marginal fault zones of the South Nisyros Basin and may represent a multi-staged landslide event. In the seismic profiles A-B and C-D (Fig. 30.4), the upper seismic unit that defines the VDA deposits, is characterized by convex-upwards rounded reflectors, diffraction hyperbolae, and wavy or broken reflectors, often with high amplitudes.

The hummocky topography at the SE flanks of Nisyros (VDA 3) forms a lobate-shaped deposit with southeast flow direction and covers an area of approximately 4.8 km wide by 4.6 km long (about 22 km^2) (Fig. 30.4). Most of the hummocks are located at the center of the VDA (250–370 m depth) having either elongated or irregular shape. Using an average thickness of 30 m, Livanos et al. 2012 estimated the total VDA volume to be 6.6×10^8 m^3. ROV and side scan surveys over the blocks show that most are covered by biological encrustation (Fig. 30.5a, A) while others are rounded with black surface color (Fig. 30.5a, B). In some cases the northern slope of the hummock is smoother than the southern one, forming a ridge with NE-SW direction (Fig. 30.5a, C).

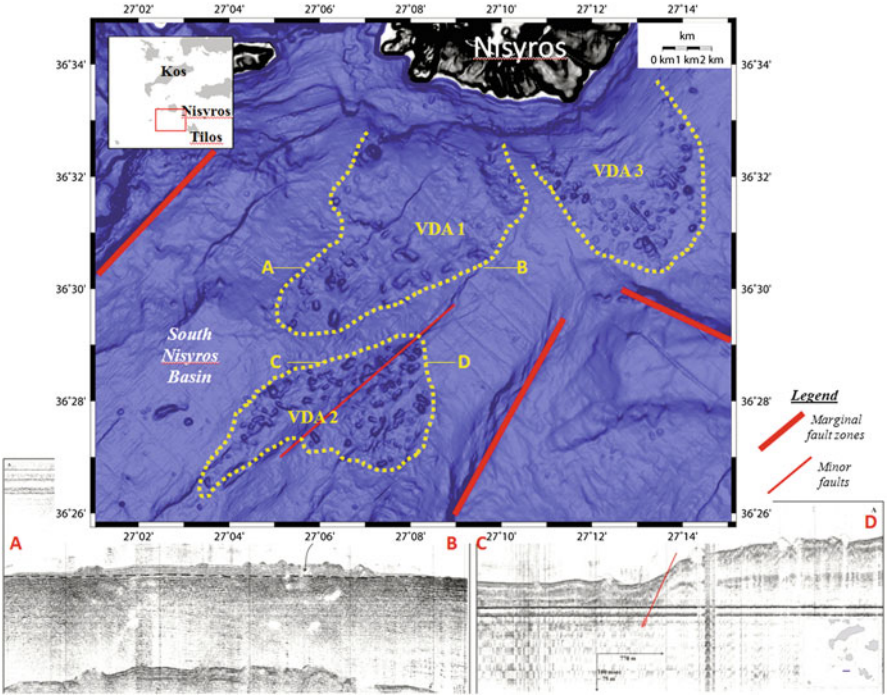

Fig. 30.4 Gradient-shaded swath bathymetry map showing multiple VDA deposits, south of Nisyros Volcano. *Red lines* indicate fault zones. The *inset* map shows the regional location of Nisyros, in the eastern edge of Hellenic volcanic arc. *Lower panel*: Seismic profiles across VDA deposits 1 (*A–B*) and 2 (*C–D*). *Red lines* indicate fault zones

Hyperbolic reflectors in the seismic profile (Fig. 30.5b) correspond to the location of large blocks within the VDA 3 and illustrate the relationship of the avalanche deposits to the recent stratigraphy of the sediments within Tilos Basin. The Tilos marginal fault zone borders the VDA to the south whereas the volcanic basement of Nisyros Volcano, which is the source of the VDA, is observed to the North. Due to the shape characteristics and the uniform appearance along the lobate-shaped deposit, we believe that the flank collapse was a singular failure, involving a rapid, virtually instantaneous movement of the entire slide mass into the sea. Unfortunately, there are no cores from the debris avalanche area that can be used to date the event.

30.3 Discussion and Conclusion

A combination of marine geophysical techniques has allowed us to identify and characterize five volcanic debris avalanche (VDA) deposits from three volcanic centers along the Hellenic Volcanic Arc in the southern Aegean Sea. All of the

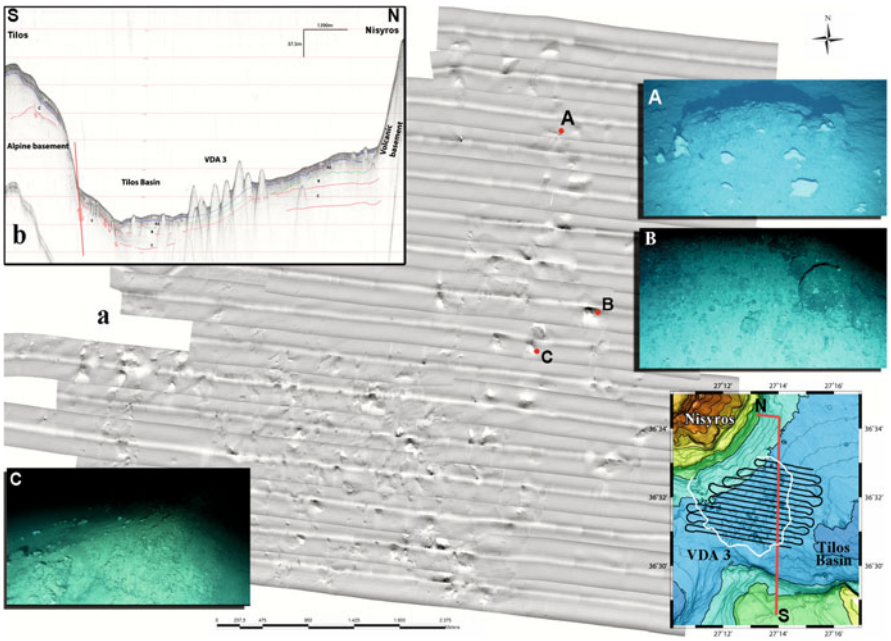

Fig. 30.5 (**a**) Mosaic of 300 kHz sidescan sonar data; The locations of side scan survey (*black line*) and the seismic profile (*red line*) are indicated in the inset bathymetric map in the lower *right side* of the figure. *A*, *B*, *C*: *Bottom* photographs recorded by high definition video of selected blocks. (**b**) Seismic profile across the eastern part of VDA deposit

landslide deposits appear to have been associated with volcanic edifice collapse, because they contain large structureless blocks dispersed from a source around the island flanks of Antimilos, Santorini and Nisyros (Lebas et al. 2011). While the ages of the VDAs cannot be precisely determined, those at Santorini appeared to be the youngest (post Late Bronze Age) and the rest of the deposits may have occurred in the last 100 ka based on the absence of significant sediment cover and their penetration into recent sediments.

Two substantially different morphologies are observed in the submarine VDA deposits. The first variety, "Type I" VDA deposit, includes large volume VDA, with elongate shape and less abundant and smaller blocks near the source zone, like the eastern flank of Santorini volcano. The second variety, "Type II" VDA deposit tend to be smaller in volume, exhibit lobate shapes, and are not as extensively dispersed from their source areas. This type contains many large scattered blocks over the entire surface of the deposit, like Antimilos VDAs and Nisyros VDAs.

Tsunamis around volcanic islands may be triggered less frequently by catastrophic flank collapse than by earthquakes, but nevertheless they have the potential to produce highly destructive events. Additional marine geophysical surveys around these volcanic islands, coupled with sediment coring and dating, are necessary to better resolve the mechanisms of VDA formation and timing of these important processes in the Hellenic Volcanic Arc of the Southern Aegean Sea.

Acknowledgments The officers and the crew of the R/V Aegaeo and E/V Nautilus are gratefully acknowledged for their important and effective contribution to the field work and sampling. Jason Chaytor and Vasilis Lykousis are acknowledged for their useful and constructive comments.

References

Alexandri M, Papanikolaou D, Nomikou P, Ballas D (2001) Geological structure of the Myrtoon basin (Aegean Sea) based on swath bathymetry. Rapport Commission International pour l'explorationscientifique de la MerMediterranee 36:3

Bell KLC, Carey S, Nomikou P, Sigurdsson H, Sakellariou D (2013) Submarine evidence of a debris avalanche deposit on the eastern slope of Santorini volcano, Greece. Tectonophysics 597/598:147–160

Clague DA, Moore JG (2002) The proximal part of the giant submarine Wailau landslide, Molokai, Hawaii. J Volcanol Geotherm Res 113:259–287

Crutchley GJ, Karstens J, Berndt C et al (2013) Insights into the emplacement dynamics of volcanic landslides from high-resolution 3D seismic data acquired offshore Montserrat, Lesser Antilles. Mar Geol 335:1–15

Druitt TH, Edwards L, Mellors RM, Pyle DM et al (1999) Santorini volcano. Geol Soc Lond Mem 19:1–178

Friedrich WL, Kromer B, Friedrich M, Heinemeier J, Pfeiffer T, Talamo S (2006) Santorini eruption radiocarbon dated to 1627–1600 B.C. Science 312:548

Gee MJR, Watts AB, Masson DG, Mitchell NC (2001) Landslides and the evolution of El Hiero in the Canary Islands. Mar Geol 177:271–293

Krastel S, Schmincke HU, Jacobs CL, Rihm R, Le Bas TM, Alibés B (2001) Submarine land-slides around the Canary Islands. J Geophys Res 106:3977–3997

Lebas E, Le Friant A, Boudon G et al (2011) Multiple widespread landslides during the long-term evolution of a volcanic island: insights from high-resolution seismic data, Montserrat, Lesser Antilles. Geochem Geophys Geosyst 12(5), May 2011. doi:10.1029/2010GC003451

Le Pichon X, Angelier J (1979) The Hellenic arc and trench system: a key to the neotectonic evolution of the eastern Mediterranean area. Tectonophysics 60:1–42

Livanos I, Nomikou P, Papanikolaou D, Rousakis G (2012) Volcanic Debris Avalanche at the SE submarine slopes of Nisyros Volcano, Greece. In: Abstracts of 2012 international earth science colloquium on the Aegean Region, Izmir, 1–5 October 2012

Manville V, Nemeth K, Kano K (2009) Source to sink: a review of three decades of progress in the understanding of volcanoclastic processes, deposits, and hazards. Sediment Geol 220:136–161

Marinos G (1961) The Antimilos volcano in Aegean Sea. Bull Geol Soc Greece IV(1):38–50

Masson DG, Watts AB, Gee MJR et al (2002) Slope failures on the flanks of the western Canary Islands. Earth Sci Rev 57:1–35

McGuire WJ (1996) Volcano instability: a review of contemporary issues. In: McGuire WJ, Jones AP, Neuberg J (eds) Volcano instability on the earth and other planets, vol 110, Geological Society of London special publication. Geological Society, London, pp 1–23

McKenzie DP (1972) Active tectonics of the Mediterranean region. Geophys JR Astron Soc 30:109–185

Mitchell NC, Masson DG, Watts AB, Gee MJR, Urgeles R (2002) The morphology of the submarine flanks of volcanic ocean islands: a comparative study of the Canary and Hawaiian hotspot islands. J Volcanol Geotherm Res 115:83–107

Nomikou P, Papanikolaou D (2011) Extension of active fault zones on Nisyros Volcano across the Yali–Nisyros channel based on onshore and offshore data Vol: SI Seafloor mapping. Mar Geophys Res. http://dx.doi.org/10.1007/s11001-011-9119-z

Nomikou P, Tibaldi A, Pasquare F, Papanikolaou D (2009) Submarine morphological analysis based on multibeam data of a huge collapse at the SE flank of Nisyros volcano. Rend Online Soc Geol Ital 7:177–179

Nomikou P, Carey S, Papanikolaou D, Bell CK, Sakellariou D, Alexandri M, Bejelou K (2012) Submarine Volcanoes of the Kolumbo volcanic zone NE of Santorini Caldera, Greece. Glob Planet Chang 90–91:135–151

Nomikou P, Papanikolaou D, Alexandri M, Sakellariou D, Rousakis G (2013) Submarine volcanoes along the Aegean volcanic arc. Tectonophysics 597/598:123–146

Papanikolaou D (1993) Geotectonic evolution of the Aegean. Bull Geol Soc Greece XXVII:33–48

Papanikolaou D, Lekkas E, Sakelariou D (1991) Geological structure and evolution of the Nisyros volcano. Bull Geol Soc Greece 25:405–419

Pe-Piper G, Piper D (2002) The igneous rocks of Greece. Beitragezurperionalengeologie der erde 30:573

Romagnoli C, Casalbore D, Chiocci FL, Bosman A (2009) Offshore evidence of large-scale lateral collapse on the eastern flank of Stromboli, Italy, due to structurally-controlled, bi-lateral flank instability. Mar Geol 262:1–13

Royden LH, Papanikolaou DJ (2011) Slab segmentation and late Cenozoic disruption of the Hellenic arc. Geochem Geophys Geosyst 12(3), 29 March 2011. doi:10.1029/2010GC003280

Siebert L (1984) Large volcanic debris avalanches: characteristics of source areas, deposits, and associated eruptions. J Volcanol Geotherm Res 22:163–197

Sigurdsson H, Carey S, Alexandri M et al (2006) Marine investigations of Greece's Santorini volcanic field. EOS 87(34):337–339

Tibaldi A (2001) Multiple sector collapses at Stromboli volcano, Italy: how they work. Bull Volcanol 63:112–125

Tibaldi A, Pasquarè FA, Papanikolaou D, Nomikou P (2008) Discovery of a huge sector collapse at the resurgent caldera of Nisyros, Greece, by onshore and offshore geological-structural data. J Volcanol Geotherm Res 177:485–499

Urgeles R, Canals M, Baraza J, Alonso B, Masson DG (1997) The most recent mega slides on the Canary Islands: the El Golfo Debris avalanche and the Canary Debris flow. J Geophys Res 102(20):305–323

Watt SFL, Tailing PJ, Vardy ME et al (2012) Widespread and progressive seafloor-sediment failure following volcanic debris avalanche emplacement: landslide dynamics and timing offshore Montserrat, Lesser Antilles. Mar Geol 323–325:69–94

Waythomas CF, Watts P, Shi F, Kirby JT (2009) Pacific Basin tsunami hazards associated with mass flows in the Aleutian arc of Alaska. Quat Sci Rev 28:1006–1019

Chapter 31
Submarine Mass Movements and Trigger Mechanisms in Byfjorden, Western Norway

Berit Oline Hjelstuen and Jo Brendryen

Abstract High-resolution TOPAS seismic profiles, bathymetric records and gravity cores from Byfjorden, surrounding the city of Bergen on the west coast of Norway, have been analysed in order to identify mass failures and their trigger mechanisms during the last 15,000 years. The seismic profiles show that Byfjorden comprises four 20–50 m deep sediment basins. These basins are characterised by glacimarine and hemipelagic acoustically laminated successions and acoustically transparent lens-shaped features, interpreted to be slide debrites. The gravity cores, taken from the sediment basin close to Bergen Harbour, penetrate the upper 2.4 m of the sediment infill in Byfjorden and reveal a 1.5 m thick turbidite above a larger-scale slide debrite. The turbidite is radiocarbon dated to c. 1,180 cal years BP, noting that such an age also has been assigned as a minimum age for a turbidite identified in the neighbouring Fensfjorden system. These turbidites are considerably younger than turbidites found in other western Norwegian fjord systems, which commonly cluster around 8,200, 2,800 and 2,100 cal years BP. We suggest an earthquake as trigger mechanism for the 1,180 cal years BP event, whereas the larger-sized slide debrites identified may be related to changes in depositional environments due to the last withdrawal of the Fennoscandian Ice Sheet in the Weichselian.

Keywords Fjords • Submarine slides • Turbidity currents • Trigger mechanisms

31.1 Introduction

The NW European coastline is intersected by numerous fjord systems. These onshore-offshore border zones are commonly heavily populated and fjord seabeds have lately become areas for seabed installations. Thus, it is of importance to

B.O. Hjelstuen (✉) • J. Brendryen
Department of Earth Science, University of Bergen, Allégt 41, N-5007 Bergen, Norway
e-mail: Berit.Hjelstuen@geo.uib.no

S. Krastel et al. (eds.), *Submarine Mass Movements and Their Consequences*, Advances in Natural and Technological Hazards Research 37, DOI 10.1007/978-3-319-00972-8_31,

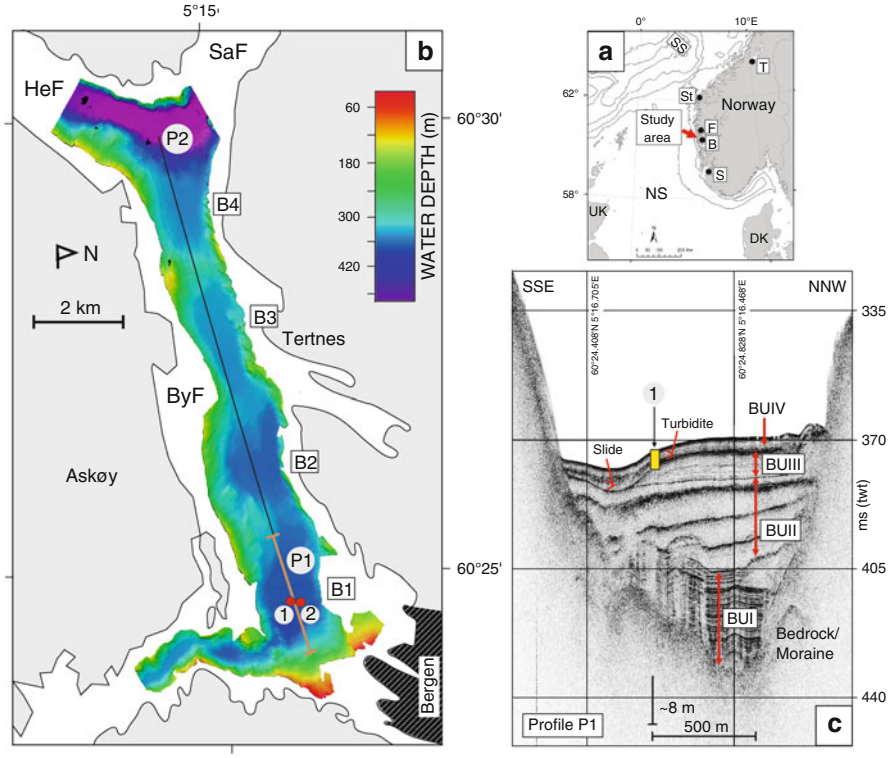

Fig. 31.1 (**a**) Location of study area. *S* Stavanger, *St* Stad, *B* Bergen, *F* Fensfjorden, *T* Trondheim, *SS* Storegga Slide, *NS* North Sea. (**b**) Bathymetry of Byfjorden. P1 (**c**) and P2 (Fig. 31.2a) indicate location of TOPAS profiles shown in this study. Numbers "1" and "2", in addition to *red dots*, show location of gravity cores HB11-170-05GC and HB11-170-01GC, respectively. *B1–B4* Identified sediment basins. *ByF* Byfjorden, *HeF* Herdlefjorden, *SaF* Salhusfjorden. (**c**) TOPAS seismic profile P1 (location in b and Fig. 31.2a), showing typical seismic facies in Byfjorden. Location of gravity core HB11-170-05GC is shown by a *yellow bar* and is marked "1". *BUI-BUIV* Identified seismostratigraphical units

have knowledge on mass failures within fjords, their frequencies and their trigger mechanisms as mass failures might represent a geohazard both to people and infrastructure.

During the last few years an increasing number of high resolution data sets from Norwegian fjord systems have been acquired, allowing for a detailed investigation of sedimentary processes within such depositional environments. Here, we analyze and discuss a data set from Byfjorden (Fig. 31.1), comprising EM300 bathymetric records, TOPAS high-resolution seismic profiles and gravity cores, in order to identify submarine mass movement episodes within this fjord system the last 15,000 years. We compare our findings with reported failure events from other western Norwegian fjord systems in order to address potential trigger mechanisms for the Byfjorden mass failures.

31.2 Geological Setting

The NNW oriented Byfjorden system is about 10 km long, has a width of 1.8–3.0 km and is located on the west coast of Norway, surrounding the city of Bergen (Figs. 31.1a, b). The northern boundary of the fjord system is defined as a triple-junction between Byfjorden, Herdlefjorden and Salhusfjorden. The fjord is, furthermore, situated within the Bergen Arches (Wennberg and Milnes 1994) and is surrounded by up to 400–600 m high mountains.

Byfjorden has, most likely, been emptied for most of its sediments during major glacial stages and refilled during deglaciation and interglacial periods (e.g. Aarseth 1997). We note that Byfjorden has a perpendicular orientation to the proposed regional ice-flow direction, suggesting that sediments in the deepest part of the fjord may have survived glacial erosion. However, we infer that most of the present day sediments within Byfjorden have been deposited during, and after, the last withdrawal of the Fennoscandian Ice Sheet (FIS) for about 15,000 years ago. We note that the FIS had a last readvance during the Younger Dryas time period, at c. 11,500 years BP (e.g. Mangerud et al. 2011). Dates on shells found in till units in Bergen (Bondevik and Mangerud 2002) suggest that the study area was ice free during the warm Allerød interstadial before the FIS readvanced during the Younger Dryas time period. Byfjorden was, most likely, covered with ice during the Younger Dryas. However, as the main ice movement followed Salhusfjorden and Herdlefjorden (Fig. 31.1b), glacial erosion might have been limited in Byfjorden.

CTD profiles taken in the southern part of Byfjorden in February and September 2009 (Hjelstuen et al. 2009b, c) showed that the surface water held a temperature of 2.5 °C during the winter months and 14.5 °C in the early autumn, whereas at 300 m water depth the water mass had a temperature around 8 °C both in the winter and in the early autumn. The salinity values showed only minor variation over the actual time period, measured to 27–28 in the surface layer and 34.8–34.9 at 330 m water depth.

31.3 Data and Methods

The data base used in this study comprises high resolution TOPAS seismic profiles, EM300 bathymetric records and gravity cores.

31.3.1 TOPAS Seismic Profiles and EM300 Bathymetric Data

The TOPAS seismic profiles were collected during an R/V G.O. Sars cruise in January 2010 to Byfjorden (Hjelstuen et al. 2010). During this field campaign a length profile and several cross profiles were collected, covering all identified fjord

basins in Byfjorden. The TOPAS profiles have been manually interpreted, and the sediment package has been divided into several sub-units based on differences in seismic facies character. A sediment velocity of 1,500 m/s has been utilised in order to estimate sediment thicknesses in metres.

Contemporaneous with the seismic profiling, EM300 bathymetric data were acquired from the fjord system (Fig. 31.1b). The bathymetric data has been gridded with a cell size of 10 m × 10 m, allowing for a detailed analyse of the fjord bottom.

31.3.2 Gravity Cores

Two gravity cores, HB11-170-05GC (60°24.649′N, 5°16.580′E, 346 m water depth) and HB11-170-01GC (60°24.636′N, 5°16.667′E, 346 m water depth) were taken from the deep fjord basin outside Bergen Harbour (Figs. 31.1b and 31.2). The cores were split longitudinally into a working half and an archive half, before they were visually described and X-radiographic imaged (top 195 cm of core HB11-170-05GC and top 130 cm of core HB11-170-01GC). Sediment colour was determined following the Munshell soil colour charts. Non-destructive logging of the cores were performed at 0.5 cm steps by a Geotek^{tm} Multi Sensor Core logging (MSCL) unit, where the bulk density was determined by Gamma-ray attenuation measurements and magnetic susceptibility was measured by a Barlington MS2E point sensor.

Core HB11-170-05GC was subsampled for radiocarbon dating at 36–37 cm core depth (Fig. 31.2b). Within this depth interval an almost perfectly preserved pine cone scale (*Pinus sylvestris*) was found and submitted to Beta Analytical Inc laboratory in Florida, USA, for AMS ^{14}C measurement. The result was calibrated using the Calib 6.0 software (Stuiver and Reimer 1993) and the Intcal09 calibration curve (Reimer et al. 2009) (Table 31.1).

31.4 Results

31.4.1 Fjord Bathymetry

Flat sea floor regions within fjord systems are commonly associated with sedimentary basins of variable thicknesses. Thus, the EM300 bathymetric records from Byfjorden indicate that this fjord system comprises four sediment basins (B1–B4 in Figs. 31.1b and 31.2a). These basins are all localised in water depths of 320–350 m, and are separated from each other by fjord transverse ridges. Across the ridges the water depth is as shallow as c. 270 m. The water depth in Byfjorden increases significantly at its northern part, reaching a maximum of 486 m where the fjord merges with Herdlefjorden and Salhusfjorden (Fig. 31.1b). The water depth shallow rapidly towards land, creating steep fjord flanks.

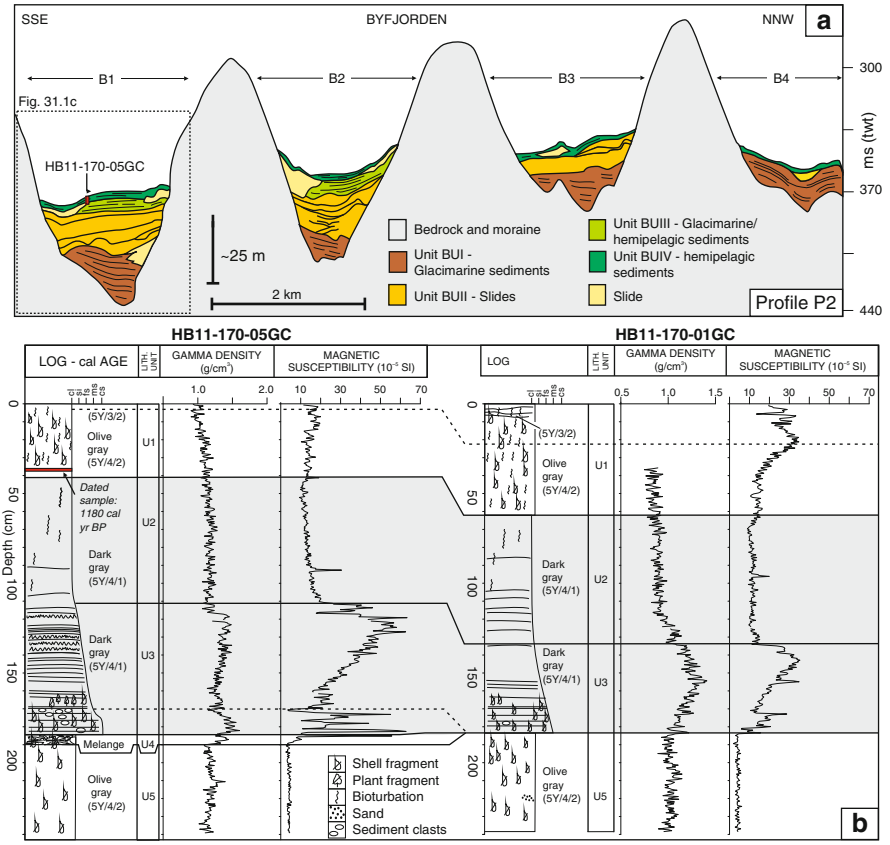

Fig. 31.2 (**a**) Interpreted TOPAS seismic profile P2 showing established seismostratigraphy (BUI-IV) for Byfjorden. *B1–B4* Identified sediment basins. Profile location in Fig. 31.1b. Location of gravity core HB11-170-05GC is shown. (**b**) Lithology, sediment colour, identified lithological units, gamma density and magnetic susceptibility for gravity cores HB11-170-05GC and HB11-170-01GC

Table 31.1 Radiocarbon date from core HB11-170-05GC

Lab no	Core depth (cm)	Dated material	^{14}C age, BP (conventional)	Calibrated age (median probability, BP)	Range of multiple calibrated 1σ age intervals (BP)	Calibrated age, 2σ interval (BP)
BETA-315215	36–37	Pinus sylvestris (cone scale)	1,240 ± 40	1,180	1,091–1,260	1,068–1,270

31.4.2 Seismic Stratigraphy and Seismic Facies

The TOPAS high resolution seismic records reveal that the sedimentary basins identified in the bathymetric data reach a maximum thickness of 70 ms(twt) [52 m] (Figs. 31.1c and 31.2a). The basin successions are characterised by stacks of low to high amplitude parallel to sub-parallel reflectors or lens-shaped features which are dominated by an acoustic transparent seismic facies. Based on this seismic facies character the sedimentary succession has been divided into several units. The lowermost unit identified, Byfjorden Unit I (BUI), is characterised by high amplitude parallel to sub-parallel reflectors (Fig. 31.1c). This unit reaches a maximum thickness of c. 20 ms(twt) [c. 15 m]. We note that smaller-scaled acoustically transparent lenses, locally, are observed in the upper part of the BUI (Fig. 31.1c). BUII comprises a stack of acoustic transparent lenses, separated from each other by high amplitude reflectors (Figs. 31.1c and 31.2a). We note that some of these lenses have eroded into the underlying unit. The lenses show variable thicknesses, reaching a maximum of c. 8 ms(twt) [c. 6 m]. BUIII is in the study area reaching a maximum thickness of c. 7 ms(twt) [c. 5 m], and is characterised by low amplitude parallel to sub-parallel reflectors. Locally, this unit appears to have been eroded and acoustic transparent lenses interfinger the unit at the basin edges (Figs. 31.1c and 31.2a). BUIII is only identified in the two southernmost sediment basins in Byfjorden. The youngest unit mapped in Byfjorden, BUIV, is dominated by parallel to sub-parallel low to medium amplitude reflectors, and is locally separated from the underlying unit by two high-amplitude reflectors. BUIV is identified in all four sediment basin in Byfjorden and does not exceed a thickness of 3 ms(twt) [2 m]. Similarly to the underlying unit, acoustic transparent lenses interfinger the BUIV sediments.

31.4.3 Core Stratigraphy and Chronology

Based on interpretation of visual structure, texture and colour, X-radiographic imagery and the MSCL data, the gravity cores have been correlated and divided into 5 informal lithological units (U1–U5 [oldest]) (Fig. 31.2b). The most prominent feature in both cores is an erosive base, olive gray to dark gray, generally laminated sandy fining upward unit, U3, that is capped by a dark gray homogeneous clay unit, U2, having occasional lamina and well-defined long bioturbation burrows. While U2 is similar in both thickness and appearance in both cores, U3 is coarser at the base in core HB11-170-05GC than in core HB11-170-01GC and contains rounded mud-clasts with different colours (olive gray and dark greenish gray) as well as plant fragments. We also note that U3 is about 14 cm thicker in core HB11-170-05GC.

Units U1 and U5 are characterized by olive gray, heavily bioturbated mud, with abundant shell fragments. Unit U4 is only found in core HB11-170-05GC, immediately below unit U3. U4 is characterized by an erosive lower boundary and

consists of a melange between two sediment types, olive gray mud (resembling the material in units U1 and U5) that is chaotically mixed with a denser dark-greenish to grey mud.

Dating of a cone scale, found immediately above the U1–U2 boundary (Fig. 31.2b), gave a calibrated age of 1,180 cal years BP (Table 31.1).

31.5 Discussion

The seismic facies character of the Byfjorden sedimentary succession is comparable to those observed within other western Norwegian fjords where similar seismic data have been analysed (e.g. Hjelstuen et al. 2009a). From these previous studies we conclude that BUI, BUIII and BUIV (Figs. 31.1c and 31.2a) are dominated by glacimarine and hemipelagic sediments, where BUI most likely were deposited during the Bølling-Allerød time period. We infer that the acoustically transparent lens-shape features are larger-scale slide debrites. Even also identified within units BUI and BUIV, these slide debrites are dominating the BUII unit. Furthermore, it seems that recurrent mass failure episodes have been most frequent in the two southernmost sediment basins in Byfjorden (B1 and B2 in Fig. 31.2a).

Similarly to previous findings within western Norwegian fjord systems (e.g. Bøe et al. 2004; Lysså et al. 2010) we infer that the mass failures which occurred during the BUII time period are related to rapid glaci-isostatic adjustments of the fjord area within a time period of about 1,000–1,200 years after the Younger Dryas time period. Glaci-isostatic adjustments can cause earthquakes and changes in depositional environments that may initiate submarine slides.

It has been inferred that a pulse of high seismicity, in the response to the removal of the last FIS, has occurred. The evidence for such a pulse is, however, still sparse and has only been documented by the large postglacial faults in northern Fennoscandia, along which Magnitude (M) >7 earthquakes could have been initiated (Bungum et al. 2005). Rapid glaci-isostatic rebound during and immediately after the last withdrawal of the FIS also caused a relative lowering in the sea level. As the sea level fell previously drowned fjord flanks may have been exposed to erosion e.g. by rivers, allowing for initiation of slides within rapidly deposited sediments (Lysså et al. 2008).

The gravity cores analysed in this study penetrate the seismostratigraphic units BUIII and BUIV in the southernmost identified fjord basin (Fig. 31.1c). Lithological unit U5 correlates to seismic unit BUIII, confirming that BUIII comprises hemipelagic sediments in its upper parts. Seismostratigraphic unit BUIV comprises lithological units U1–U4.

Due to the lower erosive boundary, the fining upward sequence and the capping clay unit, units U2 and U3 (Fig. 31.2b) are interpreted as a turbidite deposit. Unit U1 is, as unit U5, interpreted to consist of hemipelagic sediments, whereas U4 is interpreted to be a slide deposit due to its chaotic melange structure and a lower erosive boundary. We interpret the turbidite (U2 and U3) to have been emplaced by

a turbidity current triggered by the sliding event recorded in unit U4 (Fig. 31.2b). This interpretation is also supported by the TOPAS seismic profiles showing, at the core site, an acoustic transparent lens-shaped unit, inferred to be a slide debrite, which pinches out immediately below a complex of high amplitude reflectors which we interpreted to correlate with the turbidite deposit (Figs. 31.1c and 31.2a).

The dating immediately above the UI–U2 boundary (Fig. 31.2b) gave a calibrated age of c. 1,180 cal years BP (Table 31.1), indicating that the identified turbidite-slide debrite complex was deposited shortly before this. Such young ages on turbidite events in western Norwegian fjord systems have, so far, only been reported from the Fensfjorden system (Hjelstuen et al. 2013). Fensfjorden is located only about 30–35 km north of our study area (Fig. 31.1a), and the turbidite layer identified has been assigned the same minimum age as the turbidite in Byfjorden.

We note that previous studies in western Norwegian fjord systems have shown that turbidity currents, commonly, cluster around three time periods, 8,200, 2,800 and 2,100 cal years BP (Bøe et al. 2004). The 8,200 cal years BP event has been related to the tsunami following the Storegga Slide (Fig. 31.1a) on the Norwegian continental slope, whereas the 2,800 and 2,100 cal years BP events have been related to climatic variations and an earthquake, respectively.

The apparently contemporaneous age of the Byfjorden and Fensfjorden turbidity currents make us suggest that they were trigged by an earthquake. We note that Byfjorden and the neighbouring onshore and offshore areas between Stavanger and Stad (Fig. 31.1a) represent that region in Fennoscandia that have had the highest densities of $M > 3.0$ earthquakes the last three decades (Bungum et al. 2005); showing that earthquakes can be a likely trigger mechanism in this region. Bungum et al. (2005) also inferred that this region typically reveals one M5 earthquake every 10 years and one M7 earthquake every 1,100 year, indicating that large enough earthquakes could have occurred in the past in order to initiate the turbidity current observed in Byfjorden.

31.6 Conclusions

Investigation of a data set, comprising TOPAS seismic profiles, gravity cores and bathymetric data, show that Byfjorden the last 15,000 years has been heavily influenced by mass failures. Recurrent, larger-scale sliding events are suggested to have occurred as a response to isostatic rebound in the time period immediately after the last withdrawal of the FIS from the study area. The slide debrites deposited reach a maximum thickness of 6 m. An up to 1.5 m thick turbidite layer is observed in the studied gravity cores. The contemporaneous ages, c. 1,180 cal years BP, between this turbidity current and a turbidity current in the neighbouring Fensfjorden system may indicate that an earthquake was the trigger mechanism.

Acknowledgments We acknowledge the captains, ship crews and scientific crews onboard R/V G.O. Sars and R/V Hans Brattstrøm for all help during the acquisition of data utilised in this paper. Special thanks to Asgeir Steinsland, Institute for Marine Research, for processing of

EM300 data, and Stig Monsen, University of Bergen, for all technical assistance before, during and after the cruises. We are grateful to the reviewers, Dr Liv Plassen and Dr Michele Rebesco, for helpful comments.

References

Aarseth I (1997) Western Norwegian fjord sediments: age, volume, stratigraphy, and role as temporary depository during glacial cycles. Mar Geol 143:39–53. doi:10.1016/S0025-3227(97)00089-3

Bøe R, Longva O, Lepland A, Blikra H, Sønstegaard E, Hafliason H, Bryn P, Lien R (2004) Postglacial mass movements and their causes in fjords and lakes in western Norway. Nor J Geol 84:35–55

Bondevik S, Mangerud J (2002) A calander age estimate of a very late Younger Dryas ice sheet maximum in western Norway. Quat Sci Rev 21:1661–1676. doi:10.1016/S0277-3791(01)00123-8

Bungum H, Lindholm C, Faleide JI (2005) Postglacial seismicity offshore mid-Norway with emphasis on spatio-temporal-magnitudal variations. Mar Pet Geol 22:137–148. doi:10.1016/j.marpetgeo.2004.10.007

Hjelstuen BO, Haflidason H, Sejrup HP, Lysså A (2009a) Sedimentary processes and depositional environments in glaciated fjord systems – evidence from Nordfjord, Norway. Mar Geol 258:88–99. doi:10.1016/j.margeo.2008.11.010

Hjelstuen BO, Kleiven HF, Monsen S, Student Team (2009b) Marine geological cruise report from Byfjorden, Salhusfjorden and Herdlefjorden. Report No. 100-01/09, Department of Earth Science, University of Bergen, Bergen, Norway, 12 p

Hjelstuen BO, Kleiven HF, Monsen S, Student Team (2009c) Marine geological cruise report from Byfjorden and Herdlefjorden. Report No. 100-02/09, Department of Earth Science, University of Bergen, Bergen, Norway, 11 p

Hjelstuen BO, Alvheim S, Kjennbakken H, Monsen S, Steinsland A, Waldmann N, Bleikli VM, Bråten M, Elgåen HL, Ersland RA, Karlsen A, Hatleseth S-M, Kvilhaug S, Sand GK (2010) Marine geological cruise report from Fensfjorden, Bjørnafjorden and Byfjorden. Report No. 100-01/10, Department of Earth Science, University of Bergen, Bergen, Norway, 31 p

Hjelstuen BO, Kjennbakken H, Bleikli V, Ersland RA, Kvilhaug S, Euler C, Alvheim S (2013) Fjord stratigraphy and processes – evidence from the NE Atlantic Fensfjorden system. J Quat Sci 28:421–432. doi:10.1002/jqs.2636

Lysså A, Hansen L, Christensen O, L'Heureux J-S, Longva O, Olsen HA, Sveian H (2008) Landscape evolution and slide processes in a glacioisostatic rebound area; a combined marine and terrestrial approach. Mar Geol 248:53–73. doi:10.1016/j.margeo.2007.10.008

Lysså A, Hjelstuen BO, Larsen E (2010) Fjord fill in high-relief area: rapid deposition influenced by deglaciation dynamic, glacio-isostatic rebound and gravitational activity. Boreas 39:39–55. doi:10.1111/j.1502-3885.2009.00117

Mangerud J, Gyllencreutz R, Lohne Ø, Svendsen JI (2011) Glacial history of Norway. In: Ehlers J, Gibbard PL (eds) Quaternary glaciations – extent and chronology, Part IV – a closer look. Elsevier, Amsterdam, pp 279–298. doi:10.1016/B978-0-444-53447-7

Reimer PJ, Baillie MGL, Bard E, Bayliss A, Beck JW, Blackwell PG, Bronk Ramsey C, Buck CE, Burr GS, Edwards RL, Friedrich M, Grootes PM, Guilderson TP, Hajdas I, Heaton TJ, Hogg AG, Hughen KA, Kaiser KF, Kromer B, McCormac FG, Manning SW, Reimer RW, Richards DA, Southon JR, Talamo S, Turney CSM, van der Plicht J, Weyhenmeyer CE (2009) IntCal09 and Marine09 radiocarbon age calibration curves, 0–50,000 years cal BP. Radiocarbon 51(4):1111–1150

Wennberg O, Milnes A (1994) Interpretation of kinematic indicators along the northeastern margin of the Bergen Arc system: a preliminary field study. Nor J Geol 74:166–173

Stuiver M, Reimer PJ (1993) Extended ^{14}C database and revised CALIB radiocarbon calibration program. Radiocarbon 35: 215–230

Chapter 32
New Imaging of Submarine Landslides from the 1964 Earthquake Near Whittier, Alaska, and a Comparison to Failures in Other Alaskan Fjords

Peter J. Haeussler, Tom Parsons, David P. Finlayson, Pat Hart, Jason D. Chaytor, Holly Ryan, Homa Lee, Keith Labay, Andrew Peterson, and Lee Liberty

Abstract The 1964 Alaska M_w9.2 earthquake triggered numerous submarine slope failures in fjords of southern Alaska. These failures generated local tsunamis, such as at Whittier, where they inundated the town within 4 min of the beginning of shaking. Run-up was up to 32 m, with 13 casualties. We collected new multibeam bathymetry and high-resolution sparker seismic data in Passage Canal, and we examined bathymetry changes before and after the earthquake. The data reveal the debris flow deposit from the 1964 landslides, which covers the western 5 km of the fjord bottom. Individual blocks in the flow are up to 145-m wide and 25-m tall. Bathymetry changes show the mass transfer deposits originated from the fjord head and Whittier Creek deltas and had a volume of about 42 million m^3. The 1964 deposit has an average thickness of ~5.4 m. Beyond the debris flow, the failures likely deposited a ~4.6-m thick megaturbidite in a distal basin. We have studied the 1964 submarine landslides in three fjords. All involved failure of the fjord-head delta. All failures eroded basin-floor sediments and incorporated them as they travelled. All the failures deposited blocks, but their size and travel distances varied greatly. We find a correlation between maximum block size and maximum tsunami run-up regardless of the volume of the slides. Lastly, the fjord's margins were influenced by increased supply of glacial sediments during the little ice age, which along with a long interseismic interval (~900 years) may have caused the 1964 earthquake to produce particularly numerous and large submarine landslides.

P.J. Haeussler (✉) • K. Labay
U.S. Geological Survey, 4210 University Dr., Anchorage, AK, USA
e-mail: pheuslr@usgs.gov

T. Parsons • D.P. Finlayson • P. Hart • H. Ryan • H. Lee
U.S. Geological Survey, 345 Middlefield Rd., Menlo Park, CA, USA

J.D. Chaytor
U.S. Geological Survey, 384 Woods Hole Road, Woods Hole, MA, USA

A. Peterson • L. Liberty
Department of Geosciences, Boise State University, Boise, ID, USA

S. Krastel et al. (eds.), *Submarine Mass Movements and Their Consequences*, Advances in Natural and Technological Hazards Research 37, DOI 10.1007/978-3-319-00972-8_32,

Keywords Submarine landslide • 1964 Alaska earthquake • Fjord • Tsunami • Little ice age

32.1 Introduction

The 1964 Alaska M_w9.2 earthquake remains the second largest event ever recorded. In Alaska, 106 of 122 deaths from the earthquake were related to tsunamis, and 85 of these 106 deaths were associated with submarine landslide generated tsunamis (Fig. 32.1; NGDC tsunami database). Local submarine landslide-triggered tsunamis

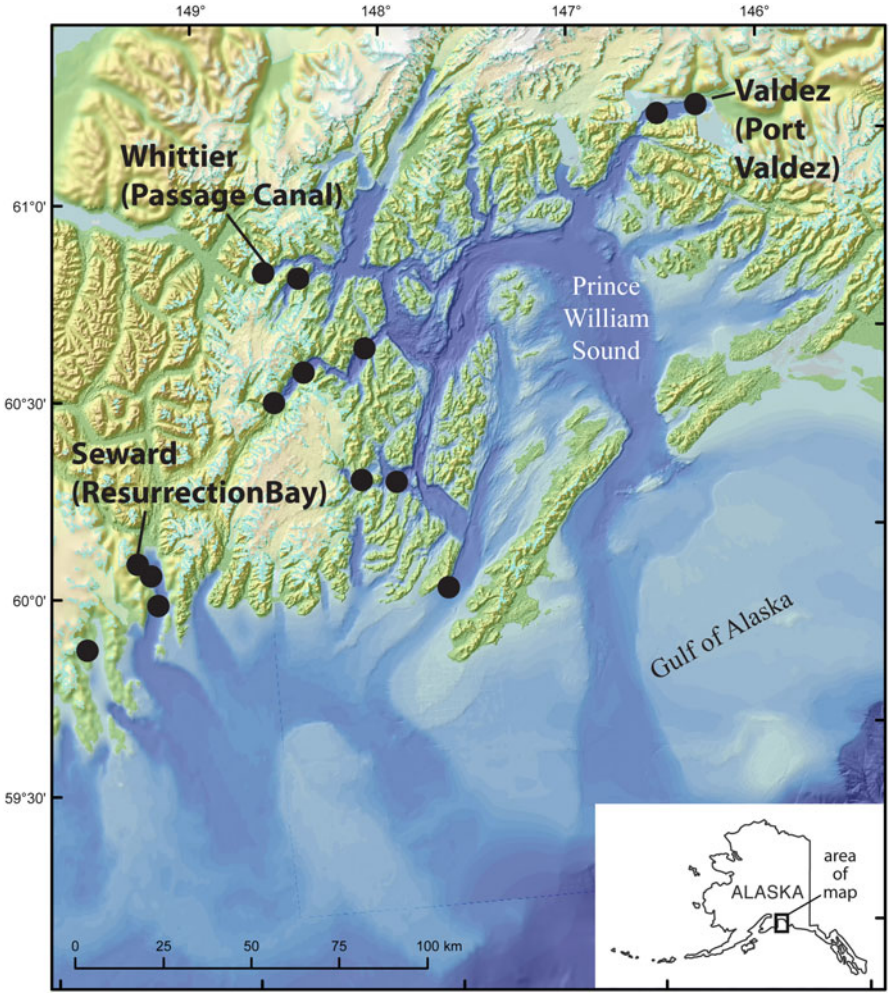

Fig. 32.1 Overview bathymetric and topographic map of the southern Alaska margin. *Black circles* show the locations we infer submarine landslides from data of Plafker et al. (1969) and our observations. Town names are listed with adjacent water body names in *parentheses*

were the biggest single cause of deaths in this earthquake. This is in contrast to other great megathrust earthquakes, where most casualties come from the tectonic tsunami.

Here we provide the first geologic examination of submarine landsliding in Passage Canal, since pioneering work completed soon after the 1964 earthquake (Fig. 32.1; Kachadoorian 1965; Wilson and Tørum 1972). Tsunami inundation maps were recently produced for this area, based on hypothetical source scenarios (Nicolsky et al. 2011a). Our new data could be used to benchmark tsunami models and validate scenarios. Whittier, Alaska, is a small (population 223) port town on the southern edge of Passage Canal, which is a fjord in western Prince William Sound (Fig. 32.1). The town is built on the Whittier Creek alluvial fan at the edge of the fjord. Whittier was, and remains, an unusual community in that the majority of the residents live(d) in a 14-story building, which lies about 450-m inland. Between this apartment building and the shoreline lies the industrial part of town with the port and harbor facilities, ferry dock, and railroad yard. The fjord ends about 2 km west of town, where two streams empty into Passage Canal and construct the fjord head delta.

There was about 4 min of strong, sustained, ground shaking in Whittier during the 1964 earthquake. Plafker (1969) determined that Whittier and all of Passage Canal subsided about 1.6 m during the event.

At least three waves inundated Whittier soon after the earthquake (Kachadoorian 1965). About a minute after shaking began, a large glassy wave formed in the middle of Passage Canal. This wave had a height of ~8 m above the sea level, but did not cause any damage. About a minute later, a muddy 12-m-high breaking wave inundated the port and railroad facilities. About 45 s later, a smaller third wave hit the town. The waves caused extensive destruction and 13 fatalities.

After the earthquake, Kachadoorian (1965) documented the tsunami run-up, changes in bathymetry along three profiles, and showed that failure of the fjord-head delta and the Whittier Creek fan generated the local tsunami.

32.2 Data and Methods

In the summer of 2011, we collected multibeam bathymetry and sparker seismic data in Passage Canal. We also examined bathymetry changes between a 1948 survey and our survey. Our goals were to better map the location and characteristics of the landslides, and to compare them to submarine landslides near Seward and Valdez (Fig. 32.1; Lee et al. 2006, 2007; Haeussler et al. 2007; Ryan et al. 2010).

We collected high-resolution bathymetric data for the westernmost 14 km of Passage Canal (Fig. 32.2). In total, we obtained 25 km^2 of multibeam data with a Reson 7111 system. Sound velocity casts were collected at six locations to improve depth calculations. In the survey area, we covered all areas deeper than about 20 m. Data processing removed noise and artifacts, and we produced a final DEM at a 5-m

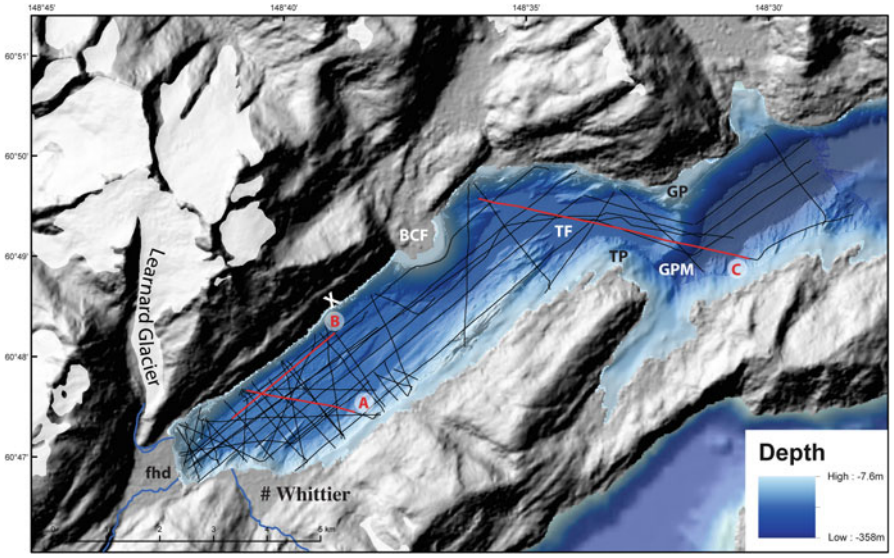

Fig. 32.2 Combined topography and bathymetry of the Passage Canal and Whittier area. *Black lines* are high-resolution seismic tracklines. Tracklines in *red*, labeled A, B, C, are shown in Fig. 32.3. Location X is where Nicolsky et al. (2011b) found evidence for cracking in bedrock indicating rockfall potential. *GP* Gradual Point, *GPM* Gradual Point moraine, *TP* Trinity Point, *TF* Trinity flats, *BCF* Billings Creek fan, *fhd* fjord-head delta

grid spacing. A 1995 NOAA conventional survey (H-10655) was combined with our final multibeam DEM to produce a combined DEM (Fig. 32.2).

For high-resolution seismic imaging, we used a single-channel streamer and a SIG 2Mille 50-tip mini-sparker as the source. The sparker was operated at a power of 500 J with a frequency range of 160 Hz to 1.5 kHz and a shot spacing of about 2.4 m. We collected about 168 km of data (Fig. 32.2) and found coherent reflections up to about 90 m below the sea bottom (Fig. 32.3). After data collection, a spectral shaping filter was applied to sharpen the seismic wavelet, then a coherency filter and automatic gain control were applied to produce the final image.

For examining bathymetric changes, we compared the depths from our survey to those of a 1948 NOAA survey (H-7161 with depths recorded in fathoms). We digitized more than 6,000 soundings from the smooth sheet, which averaged 93-m apart. As the entire area subsided about 1.6 m in 1964, the 1948 data were lowered this amount. The 2011 survey was then subtracted from the 1948 survey to show areas of depth changes.

The subsequent bathymetry difference map (Fig. 32.4) has some errors. As navigational accuracy was low in 1948, we discount most difference values on the fjord walls. The flat areas both east and west of the Gradual Point moraine are good locations to compare values as the effects of navigational errors are minimized. We refer to the basin west of the moraine as Trinity flats. It is possible a ~4-m-thick turbidite was deposited here in 1964, which we discuss later. Thus, we either

expect no depth change or a shallowing by about 4 m. Instead, we find depths are approximately 2.5–4.0 m deeper, and east of the moraine, depths are about 9 m deeper. A uniform water velocity of 800 fathoms/s (that is 1,463 m/s) was used for soundings in the 1948 survey, which would result in only a 1 m discrepancy from our values, so the source of the error remains unknown. The smaller error west of the moraine is consistent with the ~4 m thick turbidite hypothesis. Thus, the difference map is probably not accurate to <10 m in the deep fjord.

32.3 Results and Interpretations

The bathymetry data reveal the Holocene geologic processes at work (Fig. 32.2). Glacial scouring emphasizes the NW-SE strike of bedding. At the west end of the fjord, the lumpy character of the bottom shows blocks from the 1964 failures. This region extends about 5 km down the fjord center (Figs. 32.2 and 32.4). The Billings Creek fan is the next major feature, which shows small rills and gullies typical of fans. There are no indications of failures on the fan on the bathymetry or seismic data. We identify a submerged moraine south of Gradual Point with a shallowest depth of 141 m. West of the Gradual Point moraine is the Trinity flats basin. Nicolsky et al. (2011b) showed evidence of an incipient subaerial rock fall on the north shore of Passage Canal (point X on Fig. 32.2), and the authors model potential tsunami impact at Whittier. No evidence of rock fall is observed on the fjord bottom at this location.

High-resolution seismic reflection data show the base of the 1964 submarine landslide deposit (Fig. 32.3). We consider the seismic data in two parts divided by the Billings Creek fan. These areas have different characteristics at all stratigraphic levels, and the relationship between the two is obscured by channelization along the southern margin of the fan.

At the west end of the fjord, the uppermost seismic-stratigraphic unit consists of a hummocky, acoustically transparent facies with low-amplitude internal reflections (Fig. 32.3A, B). This unit correlates with the geomorphic expression of a blocky debris flow, and we conclude this is the mass transfer deposit (MTD) triggered by the 1964 earthquake. This deposit is typically 2- to 8-m thick, assuming a velocity of 1,500 m/s. Truncations of reflectors at the base of this unit indicate it was eroding as it flowed. Blocks within the deposit are up to 25-m tall and 145-m long. They have a velocity pull up beneath, indicating they consist of relatively high velocity material, possibly till. We infer a volume of about 20 million m^3 based on mapping the deposit with the seismic reflection data.

Below the 1964 deposit, we observe reflectors that we interpret as mostly background fjord sedimentation (Fig. 32.3). Blocks in the 1964 deposit make it difficult to better image the lower strata. Nonetheless, the reflectors usually parallel the bottom and pinch and swell slightly. There are acoustically transparent regions, but these do not have lateral continuity beyond a few hundred meters (Fig. 32.3A). These likely represent sediments deposited in small debris flows off the fjord-head

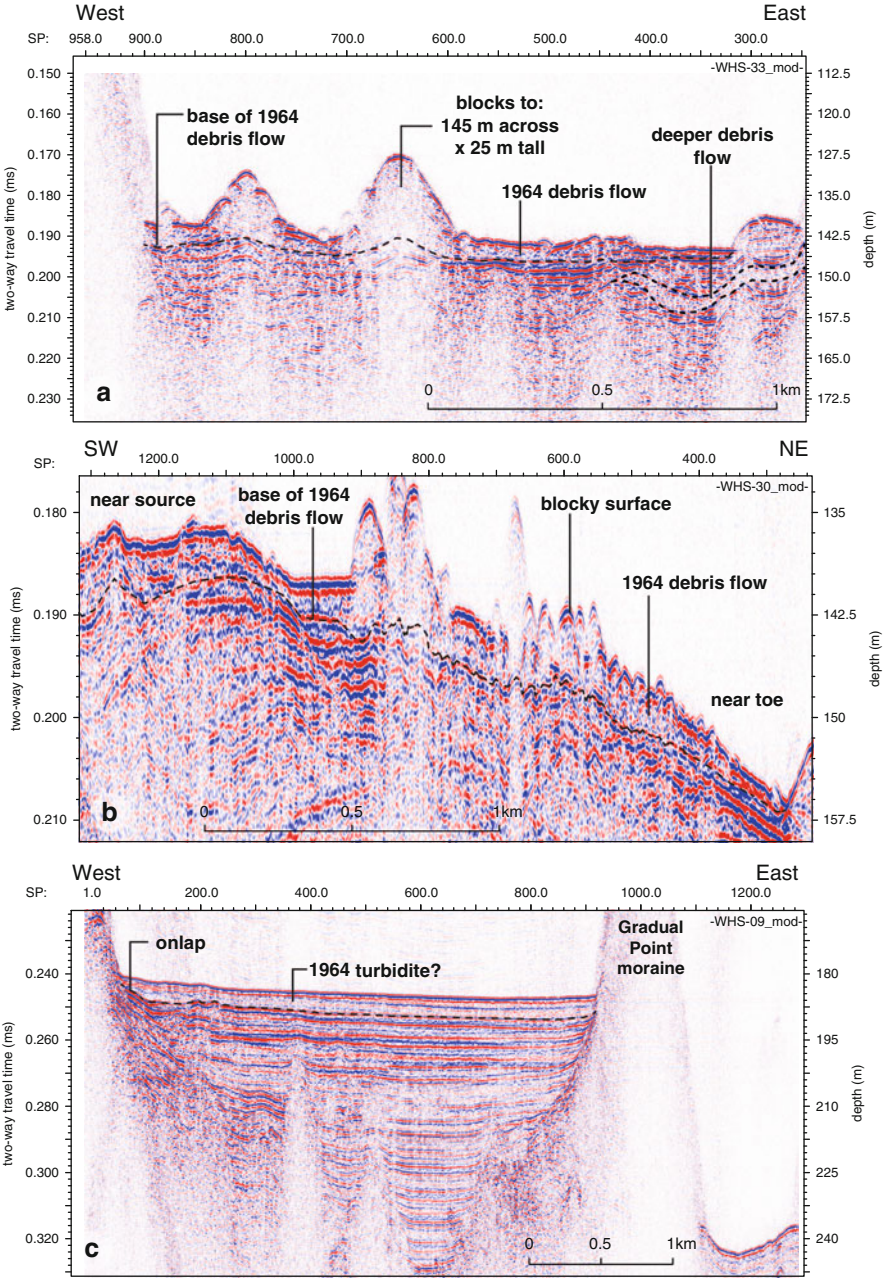
West
East
SP: 958.0 900.0 800.0 700.0 600.0 500.0 400.0 300.0
-WHS-33_mod-
base of 1964 debris flow
blocks to: 145 m across x 25 m tall
deeper debris flow
1964 debris flow
two-way travel time (ms)
depth (m)
0.150 0.160 0.170 0.180 0.190 0.200 0.210 0.220 0.230
112.5 120.0 127.5 135.0 142.5 150.0 157.5 165.0 172.5
a
0 0.5 1km
SW
NE
SP: 1200.0 1000.0 800.0 600.0 400.0
-WHS-30_mod-
near source
base of 1964 debris flow
blocky surface
1964 debris flow
near toe
two-way travel time (ms)
depth (m)
0.180 0.190 0.200 0.210
135 142.5 150 157.5
b
0 0.5 1km
West
East
SP: 1.0 200.0 400.0 600.0 800.0 1000.0 1200.0
-WHS-09_mod-
onlap
1964 turbidite?
Gradual Point moraine
two-way travel time (ms)
depth (m)
0.240 0.260 0.280 0.300 0.320
180 195 210 225 240
c
0 0.5 1km

delta or Whittier Creek. We have not been able to confidently trace seismic-stratigraphic packages from line to line. We see no evidence for large-scale MTDs beneath the 1964 deposit.

East of the Billings Creek fan, beneath the Trinity flats, the uppermost deposit is possibly a turbidite from the 1964 earthquake (Fig. 32.3C). The uppermost 0.005 s TWT (~4 m) is a coherent seismic stratigraphic unit with low amplitude and 1 or 2 weak internal reflectors. It locally shows onlap, and has a volume of about 14 million m^3. Given the large 1964 debris flow at the west end of the fjord, it is reasonable to expect that a turbidite developed and travelled farther eastward. The stratigraphic position, onlap, acoustic properties, and setting are consistent with a turbidite generated in 1964.

The bathymetry difference map shows redistribution of sediment during the 1964 earthquake (Fig. 32.4). The primary features of the map are an increase in depth up to 80 m at the west end of the fjord and off Whittier, and the deposition of the block field and debris flow in the area north of Whittier. This conclusion is the same as that of Kachadoorian (1965), who did 2D bathymetry differencing in this area and found broadly similar results. Based on differencing just the source regions, we calculate the volume of failed sediment was approximately 42 million m^3. This volume is greater than the calculated volume of the deposit from the seismic data (32 million m^3 ($32 = 20 + 14$ million m^3)), and moreover, we found evidence of erosion at the base of the debris flow, which indicates the deposit volume should be greater than the source region volume. This leads us to infer that there are errors in one of these two numbers, possibly related to incorrect mapping of flow margins or bathymetry on the older survey.

32.4 Discussion and Comparison

The new data provide a clear picture of the submarine landslide deposit generated in the 1964 earthquake. Simply, the fjord head delta and the Whittier Creek delta failed, and the landslide material slid eastward up to 5 km. A large turbidite was likely generated and deposited farther eastward across the Trinity flats. We can compare the characteristics of this slide and fjord to Port Valdez and Resurrection Bay where there were also submarine landslides in 1964.

Fig. 32.3 Seismic reflection profiles showing features of the 1964 mass transfer deposit. Location of profiles shown on Fig. 32.3. Horizontal scale is shot points, vertical scale is two-way travel time in seconds. 0.01 s TWT is approximately 8 m. (**A**) Line (WHS-33) across the largest blocks in the area north of Whittier. (**B**) Line (WHS-30) shows the main debris flow deposit from near the source region on the left to the distal end of the debris flow to the right. (**C**) Profile (WHS-09) across the Trinity flats and the Broad Point moraine that shows the nature of sedimentation beneath this basin. The uppermost ~4 m may be a turbidite generated in 1964. It onlaps older sediments at the west end of the profile. Older deposits may also contain turbidites

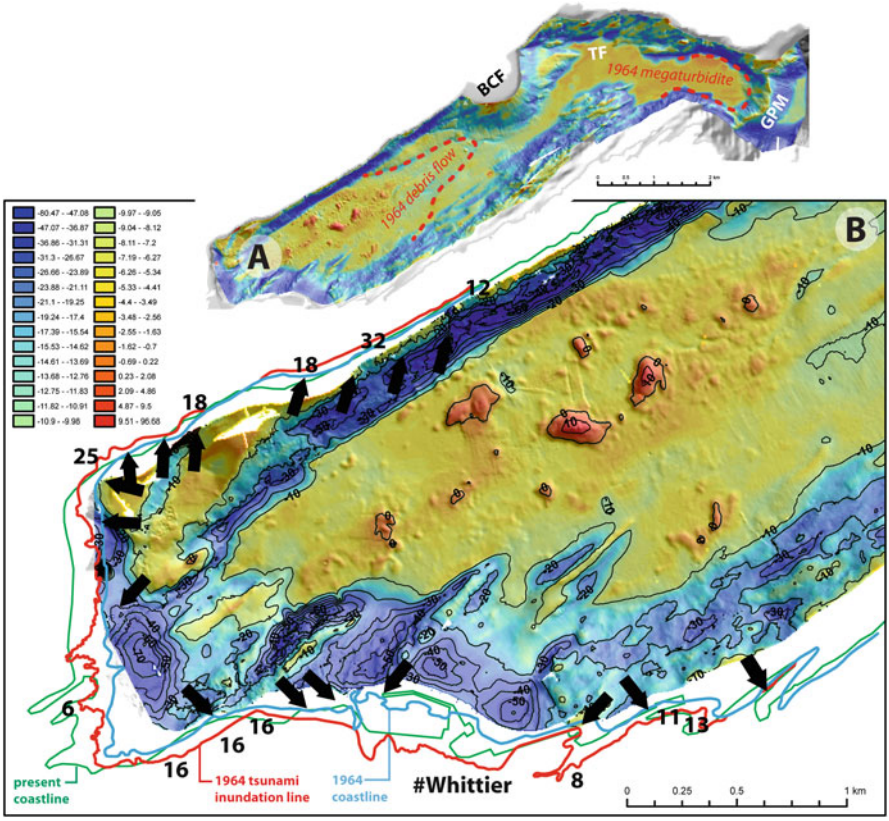

Fig. 32.4 Bathymetry difference, in meters, draped onto shaded relief image of Passage Canal. Note zero depth change color is *orange*. Older bathymetric survey is from 1948, our multibeam survey was in 2011. *Cool* colors indicate deeper values in 2012, *warm* colors indicate shallower depths in 2011. (**A**) Overview map of entire area of multibeam survey. *BCF* billings creek fan, *TF* trinity flats, *GPM* Gradual Point moraine. *Dashed red lines* show the limits of the 1964 debris flow, and the 1964 megaturbidite deposit. (**B**) Detail map of west end of Passage Canal near Whittier, which also shows the coastline and inundation line, tsunami runup directions (*arrows*) and heights, in meters (Data from Kachadoorian 1965)

At Port Valdez, the Shoup Bay moraine failed (Ryan et al. 2010). Blocks are up to 40-m tall and 400-m wide, extend 25 m below the sea floor, and the nearby tsunami run-up reached 67 m. In Passage Canal, the blocks are up to 25-m tall and 145-m wide, and extend ~5 m below the sea floor. Nearby tsunami run-up (Fig. 32.4) reached 32 m. The blocks may be composed of till, because a little ice age moraine is located on the modern shoreline adjacent to material that failed in 1964. The lack of seismic penetration and the velocity pull up beneath the blocks is consistent with blocks composed of till. In Resurrection Bay, the maximum block size off Seward was 12-m tall and 75-m across. Maximum tsunami runup was 12 m. The blocks were likely composed of sand and gravel. Although the nature of the failed material

varies, and likely influences block size and the ability of the blocks to remain intact, we find a correlation between the size of landslide blocks and maximum runup. Blocks may be more important than slide volume for generating tsunamis in some circumstances.

There are similarities and differences in the failures we have studied. All the landslides have evidence of erosion at their bases. Thus the landslide volume increased as the landslide progressed, leaving a larger deposit than the initial failure. Fan deltas almost always fail. In Resurrection Bay, every fan failed in the 1964 earthquake (Haeussler et al. 2007), and the Whittier Creek fan failed in Passage Canal. It is remarkable there is no evidence of failure of the Billings Creek fan. There is cryptic evidence of pre-1964 slides in Passage Canal, as described previously. Both Resurrection Bay and Port Valdez have clear evidence for pre-1964 slides, with Port Valdez showing five older failures (Ryan et al. 2010).

The little ice age (LIA) probably had a significant influence on the size of the submarine landslides in the 1964 earthquake. The little ice age consisted of multiple advances of glaciers, with three main pulses of expansion: 1180–1320 AD, 1540–1720 AD, closely followed by 1810–1880 AD (Barclay et al. 2009), all of which post-dated the last major megathrust earthquake around 900 years ago (Carver and Plafker 2008). These glacial advances transported additional sediment to the margins of these fjords, which then failed in 1964. Port Valdez has the clearest link to LIA advances, in that the Shoup Bay moraine was likely built during the LIA (Post and Viens 1994). At Resurrection Bay the relationship is less clear as there are no moraines near the waters edge. Nonetheless, it seems likely the fjord-head delta and the fan deltas built out during the LIA with increased sediment supply. The same arguments can be made for Passage Canal. Moreover, the Learnard Glacier (Fig. 32.2) extended to the shoreline at LIA time, and possibly generated diamicts that favored the generation of large cohesive blocks during failures.

Acknowledgements We thank Captain Greg Snedgen of the RV Alaskan Gyre for support during data collection. We thank Jasper Moernaut and Jean-Sébastien L'Heureux for reviews of the manuscript.

References

Barclay DJ, Wiles GC, Calkin PE (2009) Holocene glacier fluctuations in Alaska. Quat Sci Rev 28(21–22):2034–2048. doi:10.1016/j.quascirev.2009.01.016

Carver G, Plafker G (2008) Paleoseismicity and neotectonics of the Aleutian subduction zone – an overview. In: Freymueller JT, Haeussler PJ, Wesson RL, Ekström G (eds) Active tectonics and seismic potential of Alaska, Geophysical monograph series 179. American Geophysical Union, Washington, DC, pp 43–63

Haeussler PJ, Lee HJ, Ryan HF, Labay K, Kayen RE, Hampton MA, Suleimani E (2007) Submarine slope failures near Seward, Alaska, during the M9.2 1964 earthquake. In: Lycousis V, Sakellarion D, Locat J (eds) Submarine mass movements and their consequences. Springer, Dordrecht, pp 269–278

Kachadoorian R (1965) Effects of the earthquake of March 27, 1964, at Whittier, Alaska. US Geol Surv Prof Paper 542-B: B1–B21, 3 sheets, scale 1:4,800

Lee HJ, Ryan HF, Kayen RE, Haeussler PJ, Dartnell P, Hampton MA (2006) Varieties of submarine failure morphologies of seismically-induced landslides in Alaskan fjords. Nor J Geol 86:221–230

Lee HJ, Ryan HF, Haeussler PJ, Kayen RE, Hampton MA, Locat J, Suleimani E, Alexander CR (2007) Reassessment of seismically induced, tsunamigenic submarine slope failures in PortValdez, Alaska, USA. In: Lycousis V, Sakellarion D, Locat J (eds) Submarine mass movements and their consequences. Springer, Dordrecht, pp 357–365

National Geophysical Data Center (NGDC). Tsunami database. http://www.ngdc.noaa.gov/hazard/tsu.shtml. Accessed 27 Jan 2013

Nicolsky DJ, Suleimani EN, Combellick RA, Hansen RA (2011a) Tsunami inundation maps of Whittier and western Passage Canal, Alaska. Alaska Division of Geological and Geophysical Surveys Report Investigation 2011–7: 65

Nicolsky DJ, Wolken GJ, Combellick RA, Hansen RA (2011b) Potential rockfall-generated tsunami at Whittier, Alaska. Alaska Division of Geological and Geophysical Surveys Report Investigation 2011–7, Appendix B: 57–65

Plafker G (1969) Tectonics. US Geological Survey Professional Paper 543-I: G1–G74

Plafker G, Kachadoorian R, Eckel E, Mayo L (1969) Effects of the earthquake of March 27, 1964 on various communities. US Geological Survey Professional Paper 542-G: 1–50

Post A, Viens RJ (1994) Preliminary bathymetry of Shoup basin and late Holocene changes of Shoup Glacier, Alaska. US Geological Survey Water-Resources Investigations Report 94–4093: 1–11

Ryan HF, Lee HJ, Haeussler PJ, Alexander CR, Kayen RE (2010) Historic and paleo-submarine landslide deposits imaged beneath Port Valdez, Alaska: implications for tsunami generation in a glacial fiord. In: Mosher DC et al (eds) Submarine mass movements and their consequences. Springer, Dordrecht, pp 411–421

Wilson BW, Tørum A (1972) Effects of the tsunamis: an engineering study. In: The great Alaska earthquake of 1964, Engineering, National Academy of Sciences. National Academy of Sciences, Washington, DC, pp 361–526

Chapter 33
A Geomorphological Analysis of the Veatch Slide Complex Off Massachusetts, U.S.A.

Jacques Locat, Uri S. ten Brink, and Jason D. Chaytor

Abstract A geomorphological analysis of the Veatch slide complex is presented here indicting the presence of at least two major slides presenting different morphological characteristics and involving different type of sediments (in terms of strength and grain size). These slides took place after the erosion of the Veatch Canyon which had been the locus of many bank failures. It is shown that a more refined morphological analysis of similar landslide areas may lead to the definition of a greater number of slides and a greater role of channels both leading to a more complex interpretation on their mobility.

Keywords Submarine landslide • Mass-failure • Mass-transport • Slope failure • Passive continental margin • Yield strength • Mobility

33.1 Introduction

The U.S. Atlantic continental margin exhibits many deposits of submarine mass movements of various magnitudes (Booth et al. 1993; Twichell et al. 2009; Chaytor et al. 2009). Until about year 2000, most of the inventory had only been mapped by a large aperture side-scan sonar (GLORIA). With improving technology, multibeam bathymetry surveys have led to a re-examination of many previously identified landslides areas. As part of an effort carried out jointly between the USGS and

J. Locat (✉)
Laboratoire d'études sur les risques naturels, Laval University, Québec, Canada
e-mail: jacques.locat@ggl.ulaval.ca

U.S. ten Brink
United States Geological Survey, Quisset Campus, Wood's Hole, MA, USA

J.D. Chaytor
U.S. Geological Survey, 384 Woods Hole Road, Woods Hole, MA, USA

S. Krastel et al. (eds.), *Submarine Mass Movements and Their Consequences*, Advances in Natural and Technological Hazards Research 37, DOI 10.1007/978-3-319-00972-8_33,

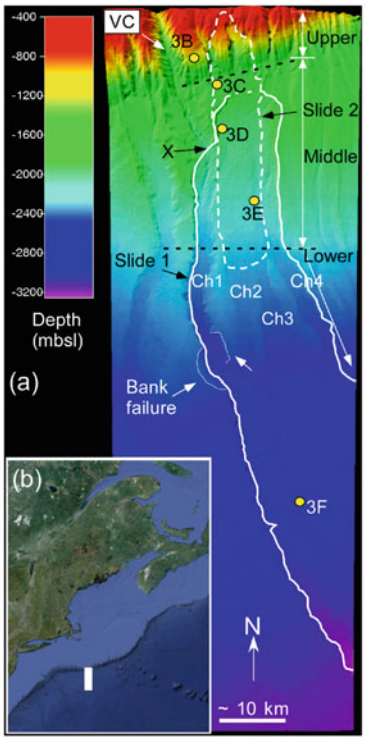

Features (c)	L (km)	W (km)	H (m)	V (km^3)	bus (°)	bfs (°)	bs (°)
Upper							
S1	2.6	2.8	100	0.73	2-4	5-6	10-14
S2	4.4	1.5	100	0.66	3-5	5-6	15-23
S3	3.8	3.2	100	1.22	4-6	6-7	25-34
S4	3.6	1.0	75	0.27	5-6	10-11	16-18
S5	4.0	2.0	50	0.40	4-6	8-12	14-15
S6	4.2	2.1	50	0.44	5-6	9-12	-
S7	1.9	2.1	50	0.20	4-6	8-11	-
S8	3.5	2.5	-	-	-	8-11	
Slide 2	8	8	100-150	6.4-9.6	2-6	5-12	10-34
Middle							
Slide 1	25	14	100	35.0	2-4	2-4	15-21
Lower							
Bank failure	5.1	3.7	160	3.01	1	-	10-23
	L (km)	W (km)	Hls (m)	Hrs (m)	bls (°)	brs (°)	bsu (°)
Ch1 V.C.	>75	~3	100-200	80-100	15-20	6-20	0.5-1.0
Ch2	22	2.5	5-15	20-25	1-2	2-5	0.8
Ch3	~25 or +	3-7	10	10-20	2-4	2-4	0.8
Ch4	~26 or +	1.5-3	30-40	60	8-10	5-10	0.8

Fig. 33.1 (**a**) View of the Veatch slide complex (*slide 1* and *2*) with its location shown in (**b**, image from Google Earth), (illuminated from the northeast); *3B*, *3C*, *3D*, and *3 F* are core locations; *Ch1* to *Ch4* are channels; (**c**) this table presents geometric characteristics of features discussed in the text. *L*, *W*, *H*, and *V* stands for length, width, height and volume. Meaning of subscripts for slope angles are: *us* upper surface, *fs* failure surface, *s* scarp, *rs* right scarp, *ls* left scarp, *su* surface of the channel, Visible failure surfaces are noted *S1* to *S8*

the U.S.-Nuclear Regulatory Commission to assess tsunami hazard from landslides along the U.S. Atlantic margin, a revised inventory of submarine mass movements along the eastern seaboard was obtained and published in a series of papers (e.g. Ten Brink et al. 2009; Locat et al. 2009; Twichell et al. 2009; Chaytor et al. 2009). Extending this series, this paper presents a detailed analysis of the morphology of the Veatch slide complex area, off Nantucket Island (Massachusetts, Fig. 33.1), in order to illustrate how better bathymetry displays more details of the seafloor and a more refined interpretation of the sliding processes. The Veatch canyon was named after A.C. Veatch, an American surveyor of the United States Coast and Geodetic Survey who pioneered marine surveys in this area (e.g. Veatch 1937).

Forde (1981) was the first to investigate the Veatch canyon and mostly focussed on sedimentary processes. The Veatch canyon slide as such was first identified as part of an inventory presented by Booth et al. (1993) based on GLORIA sidescan sonar imagery and concurrent seismic surveys. More recent multibeam surveys

have provided an opportunity to revisit the various landslides in the area (Twichell et al. 2009; Chaytor et al. 2009). An interpretation of the Veatch slide extent was presented by Blondel (2009) who suggests that the aerial coverage of the slide is about 11,000 km^2 (about 275 km × 40 km). Twichell et al. (2009) proposed a similar estimate using recent multibeam surveys.

This paper provides a more detailed analysis of the area referred to as the Veatch slide complex, which has been divided into three regions: upper, middle and lower (Fig. 33.1). It is shown hereafter that the Veatch slide can be seen as a complex slide with a morphology revealing various scars at different water depths. This analysis leads to some discussion of the uncertainty related to the definition of the size of a submarine mass movement when limited seismic data is available. Such a definition has an impact on the evaluation of slide initiation and mobility.

33.2 Methods

Bathymetric dataset used here has been acquired during 2004 by the U.S. Navy Ship Henson (Gardner et al. 2006) and by the NOAA ship Ronald H. Brown in 2009 (soundwaves.usgs.gov/2009/08/fieldwork.html). For the purpose of this study, the multibeam data was gridded with a cell size having a horizontal resolution of 25 m. Analog 3.5 kHz and airgun geophysical surveys were acquired as part of the GLORIA sidescan imagery (EEZ-SCAN 887 1991). A sound velocity of 1,500 m/s is used is the depth estimates. Core data is taken from the National Geophysical Data Center core repository (http://www.ngdc.noaa.gov). For more details on the methodology the reader is refer to Twichell et al. (2009).

33.3 The Veatch Slide Complex

In the Veatch slide complex region, the maximum extent of the Quaternary ice sheet more or less remained along the present coastline (Twichell et al. 2009). During that time of low sea levels, rivers carried sediments as far as the shelf edge to form a series of shelf-edge deltas. The delta foreset beds prograded as clinoforms (Sheridan et al. 2000) with angles of deposition of about 5°. According to Poag and Sevon (1989) the Quaternary sequence can reach a thickness varying from 400 to 800 m on the outer shelf and upper part of the slope.

Sediment texture in the vicinity of the Veatch slide complex decreases in size from the shelf to the abyssal plain (Bennet et al. 1980; Lambert et al. 1981): the shelf is mostly sandy, the upper slope consists of silty sand; the lower slope consists of sand silt and clay while silty clay dominates on the upper rise. Physical properties of surficial samples (less than 2 m deep, see Fig. 33.1a) obtained from the lower slope and upper rise regions indicate that sediments are mostly inorganic and of low activity, which is very similar to those reported for the Hudson Apron area to the south by Locat et al. (2003).

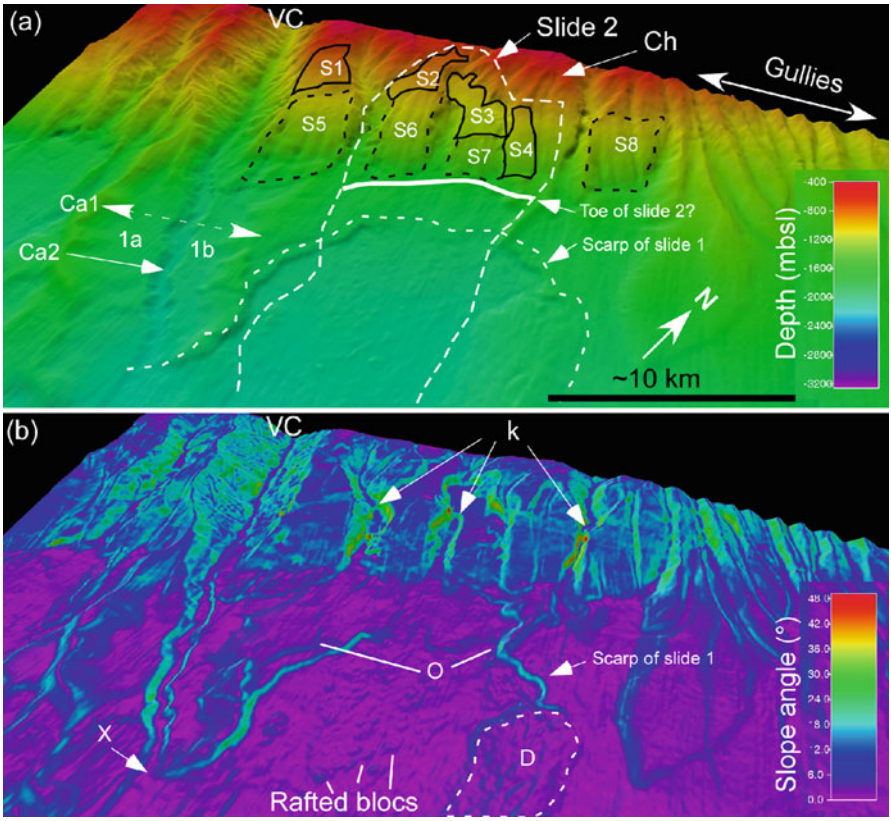

Fig. 33.2 (**a**) Upper part of the Veach slide complex showing the various failure surfaces (see Fig. 33.1c for specific geometric data); (**b**) slope map of the same area as in 'a' with the identification of few blocks generated by slide 2. ('a' and 'b' are illuminated from azimuth 315°, but illumination angle is 44° and 61° for 'a' and 'b' respectively; vertical exaggeration is 2.0)

A general view of the Veatch slide complex is shown in Fig. 33.1. The mass movements within the Veatch slide complex can be seen from the slope area down onto the upper rise, i.e. over a distance of more than 200 km. As it will be described below, the Veatch slide complex includes at least three distinct slide events: a first large slide originating from the upper rise area (slide 1), another slide originating from the continental slope (slide 2) and a small bank failure on the banks of the Veatch canyon (Fig. 33.1a).

From a geomorphological viewpoint the Veatch slide complex area has been divided into three regions: (1) Upper region (~400 to 1,750 mbsl) (2) Middle region (1,750 to 2,270 mbsl) and (3) Lower (>2,270 mbsl). The limit between the Upper and Middle regions is set at the location considered to be the toe of slide 2 near the base of the slope (see Figs. 33.1 and 33.2a).

33.3.1 Geomorphological Overview

The Upper region covers the slope and a limited part of the upper rise down to a depth of about 1,750 m. The lower boundary coincides with the location of the upper scarp of slide 1. A more detailed morphological view of the Upper region is provided in Fig. 33.2. A ∼17-km-wide slope region of detachment surfaces lies east of Veatch Canyon (VC), and likely corresponds to failure surfaces (1–8) with their associated head scarps, and changes eastward fairly abruptly to a gully system.

The Veatch Canyon is nearly a straight feature that has entrenched the slope with a relief of about 700 m and a thalweg dip of 2–4°. The slopes bordering the canyon are inclined at angles locally reaching nearly 30°. The average slopes of the canyon walls are greater in the upper part of the canyon (see Fig. 33.2b). The continental rise morphology in the vicinity of the canyon suggests that at least two periods of erosion took place: an older period represented by a higher floor level (Ca1) and a more recent erosion represented by Ca2 (slide ?). The Ca1 (see surface 1a and 1b in Fig. 33.2a) would have been about 150 m higher than the present canyon floor (Ca2). The height difference between the Ca1 level and the surrounding hills suggest an erosion of about 200 m of sediments. The slope of surface Ca1 toward the axis of the canyon is about 2° while the slopes of the canyon walls surrounding level Ca2 canyon are about 17°. The width of the present canyon valley (Ca2) is about 0.6 km. This may suggest that the Ca2 phase of canyon incision took place in sediments with a higher strength than for phase Ca1.

The main part of the Upper region is occupied by a series of surfaces (marked S1–S8 in Fig. 33.2a) that may correspond to various failures planes. Surfaces S1 to S4 are more distinct compared with surfaces S5 to S8. Surfaces S1 to S4 are smooth and dip more or less at the same angles (except for S4, see Fig. 33.3 for details). Except for S3, the head scarps can be quite steep with values between 10° and 25° (see table in Fig. 33.1). Surfaces S5 to S7 show rounded gullies and are generally steeper (between 8° and 12°) than the surfaces above. The surfaces have been eroded by gullies and may represent the original slope or at least an erosional surface formed by sediments having a greater strength.

The Middle region is seen both in Figs. 33.2 and 33.3 and is occupied by the upper scarp of slide 1 with its upper slope partly truncated ('O' in Fig. 33.2b) by the slide 2 event. This area is also limited to the west by the right bank of the Veatch Canyon and to the East by the lateral scarp of slide 1, and by the left bank of an abandoned canyon. It ends at the point where the debris field becomes channelized (Ch1 to Ch4 in Figs. 33.1b and 33.3c). The overall slope in that area is about 1°.

The Lower region is detailed in Fig. 33.3c and consists mostly of a channelized system developed between the banks of the Veatch Canyon to the West and an unnamed canyon to the East. The characteristics of the channels are summarized in Fig. 33.1c. This region also includes a bank failure (Fig. 33.3d) developed within the Veatch canyon.

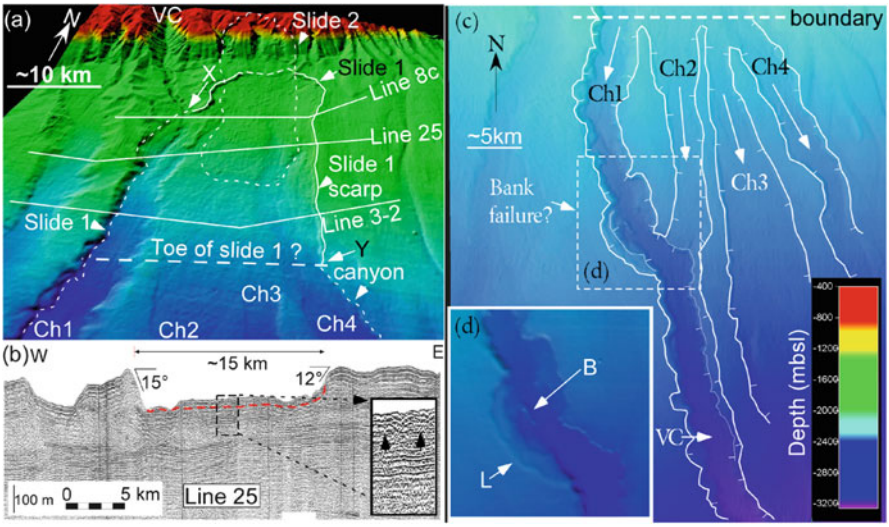

Fig. 33.3 (**a**) View of the Middle and Upper regions of the Veatch slide complex with the location of the available seismic lines; (**b**) air gun seismic line 25 showing the potential position of the failure plane or the flow surface (see insert) with a the debris about 50 m thick; (**c**) the lower region; (**d**) details of the bank failure with location shown by the dashed box. (Sun azimuth is same for 'a', 'c' and 'd' at 315°, but sun angle is 44°; the vertical exaggeration is 2.0)

Using these morphological observations we propose the following sequence of failures with time from oldest to youngest: bank failures, slide 1 and slide 2. The geometric characteristics of these slides are provided in Fig. 33.1c. Banks failures will not be detailed here. They are comparatively small and are found along the abandoned walls of the Veatch Canyon with the largest one indicated on Figs. 33.1 and 33.3. The following analysis will concentrate on slide 1 and 2.

33.3.2 Slide 1

Slide 1 extends from the Middle region to the Lower region (Figs. 33.1 and 33.3). It can be divided into two zones: (1) the area covering the evacuation of slide 1, and (2) the run out zone where the debris was deposited. The head scarp is well defined (Figs. 33.2b and 33.3a). The extent of the right lateral scarp of slide 1 stops at a point, noted 'X' in Fig. 33.1a, where the debris of the slides were more or less restrained by the walls of the Veatch Canyon. The left lateral scarp extends much farther to a point also where the walls of an older canyon start to confine the debris into a channel (point Y in Fig. 33.3a). The failure surface of slide 1 cannot be seen directly. A seismic line (air gun) shown in Fig. 33.3b presents an approximately 50 m layer of debris showing some deformations (see black arrows showing the base

in the insert in Fig. 33.3b) that are interpreted to be the debris from slide 2 which flowed over the slide 1 failure surface (red line in Fig. 33.3b) that may include some debris of slide 1.

The transition into the run out zone of the slide is shown as the dashed line in Figs. 33.1 and 33.3. The transition between the two parts is also used as a boundary between the Middle and Lower regions. More or less at that location there is an abrupt change in the morphology of slide 1 where at least four channels are present: Ch1: constrained to the west by the Veatch Canyon right wall over a distance of at least 74 km; Ch2: which is short (∼18 km) and comes back into the Veatch Canyon; Ch3: which widens downstream, and Ch4 which is constrained by the left wall of an abandoned canyon.

The morphological characteristic of slide 1 and the channels are summarized in the table in Fig. 33.1c. Using the above description, the volume of slide 1 is estimated to be at about 35 km^3. The head scarp has a slope ranging between 15° and 21° and the slope of the floor in the channel varies between 0.5° and 1°. According to Twichell et al. (2009) and Blondel (2009), the run out distance extends seaward for another 50 km for a total distance of about 160 km.

33.3.3 Slide 2

Slide 2, shown in Figs. 33.1, 33.2 and 33.3, originated in the continental slope. Although there are many failure surfaces seen in Fig. 33.2a, only surfaces 2, 3, 4, and 7 are considered to be part of slide 2. It is believed that these surfaces represent most of the failure plane which has been later partly eroded as seen by the presence of 3 knickpoints ('k' in Fig. 33.2b). The width and length of the overall failure surface is about 8 km by 8 km with an estimated thickness of the failed mass of about 100 m yielding an estimated volume of 6.4 km^3. Scarp slopes reach values as high as 30° with heights of about 100 m. The slope of the failure surface varies from about 5° in the upper part to close to 12° in the lower part of the slope.

The failed mass flows away onto the continental rise encroaching upon the head scarp of slide 1 ('O' in Fig. 33.2b) and spreading over the small depositional basin generated by slide 1. It appears to have stopped more or less before the head of channels seen in Figs. 33.1a and 33.3c. The apparently higher strength of the sediments involved in slide 2, compared to those of slide 1, may be deduced from the large amounts of rafted (?) blocks seen on the surface of the debris flow deposit of slide 2 (see 'rafted blocks' in Fig. 33.2b) which are not seen in the channels below. These blocks have a maximum length of 500 m, with a height of less than 20 m flanks slopes reaching up to 6°. In the lower part of the run out zone of slide 2, the debris is resting on a slope of about 1°. Using topographic cross sections, the overall mound created by the accumulation of the debris of slide 2 varies in height between 15 and 40 m. The surface of the deposition area of slide 2 is estimated at 133 km^2 which, for a displaced volume of 6.4 km^3 would yield an estimated average

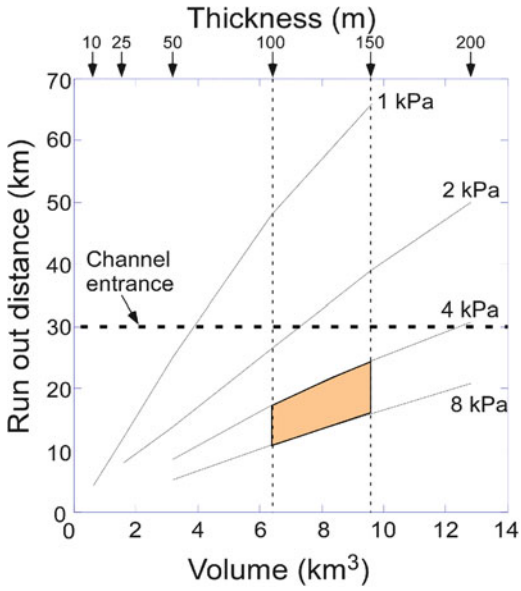

Fig. 33.4 Simulation of the run out distance of slide 2 as a function of slide volume and yield strength (1–8 kPa). The Herchel-Buckley model was used here with coefficient 'n' equal to 1, a reference strain rate of 1.0, and a unit weight of 16 kN/m^3

thickness of about 50 m which is similar to what has been estimated from the seismic line in Fig. 33.3b. This is assuming that all the debris covering the failure surface are from slide 2.

Based on these observations the parameters governing the mobility of this slide can be ascertained to some degree. First the strength of the material during the flow event can be estimated from the geometry of the deposit including both the slope and the thickness. Using the critical height and slope approach for an undrained infinite slope failure (Locat and Lee 2002) and using an average buoyant unit weight of 4–8 kN/m^3 (Locat et al. 2003), the yield strength for a debris thickness of 15 and 50 m would vary from 1 to 7 kPa respectively. The geotechnical profile available for the Hudson canyon (35 m deep, Locat et al. 2003) indicates a remoulded shear strength varying between 5 and 10 kPa. Using this information, the run out of slide 2 was estimated using BING (Imran et al. 2001) with an average buoyant unit weight of 6 kN/m^3, and a range of yield strength between 4 and 8 kPa. Results of the simulations are shown in Fig. 33.4. These results indicate that the estimated volume of the sliding mass may explain why the debris flow associated with slide 2 did not reach farther. Even assuming an initial thickness of 150 m, the flow would not enter the channels. An observed shorter run out distance compare to the computed one using BING could also be explained by a remoulding of the sliding mass that was not complete, as seen by the presence of rafted blocks.

33.4 Discussion and Concluding Remarks

Because of space limitations, we only briefly discuss two elements, The first one relates to the relative timing of these events and the second about the use of morphological information to deduce the volume and mobility of a slide.

The timing and triggering of these slides in this region have been discussed by many authors (e.g. Lee 2009; Twichell et al. 2009; Chaytor et al. 2009). They would, for most of them, be pre-conditioned by an increase in pore pressure due to the high sedimentation rate, gas hydrates dissociation and they would likely be triggered by erosion or earthquakes. When we compare slide 1 and slide 2, slide 1 appears to show a much greater disintegration of the failed mass although it was initiated on a much gentler slope than slide 2. This may indicate that it took place in younger sediments having a lower strength or involving less cohesive sediments which would disintegrate more easily. Considering the higher angles of the scarps of slide 2 relative to slide 1 this would indicate that slide 2 likely took place in normally consolidated sediments thus reducing the possibility that it could have been triggered by sedimentation rates at the time of low sea levels. Coring for dating the failure surfaces would greatly help answer this question.

Regarding the relationship between volume and mobility (e.g. Locat and Lee 2002; Issler et al. 2005), the most difficult element is to define which volume is involved in the slide and how much of the flow was channelized. For our region of interest most of the run out zone was defined by the GLORIA imagery. The use of higher resolution bathymetry, as shown here, leads to the identification of various slides in addition to channels used as conduits in the run out zone. These may have been involved in slide 1, resulting in potentially higher run out distances than expected for a given volume flowing on an open space. Slide 2 event, however, appears more or less confined to the space left by slide 1 and did not reach the lower region. The run out characteristics of slide 2 appear consistent with the estimated geotechnical and rheological parameters.

As a concluding remark, this geomorphological analysis of the Veatch slide complex has shown the presence of at least two major slides presenting different morphological characteristics and involving different type of sediments (in terms of strength and grain size). Finally, it is shown that a more refined morphological analysis of similar landslide areas may lead to the definition of a greater number of slides and a greater role of channels all leading to a more complex interpretation on their mobility. Recent acquisition of multibeam data may bring about a revised interpretation of the Veatch slide complex.

Acknowledgments This work funded by U.S.-Nuclear Regulatory Commission grant N6480 Physical study of tsunami sources and the U.S. Geological Survey. We also thank Home Lee and Nabil Sultan for their constructive review of the manuscript.

References

Bennett RH, Freeland GL, Douglas NL, Lambert DN, Sawyer WB, Keller GH (1980) Geotechnical properties of surficial sediments in a mega-corridor: U.S. Atlantic continental slope, rise and deep-sea basin. Mar Geol 38:123–140

Blondel P (2009) Chapter 7: Continental margins. In: The handbook of sidescan sonar. Springer/Praxis Books, Berlin/Chichester, pp 147–183

Booth JS, O'Leary DW, Popenoe P, Danforth WW (1993) U.S. Atlantic continental slope landslides: their distribution, general attributes, and implications. In: Submarine landslides: selected studies in the U.S. exclusive economic zone, U.S. Geological Survey Bulletin 2002. U.S. G.P.O., Washington, DC, pp 14–22

Chaytor JD, ten Brink AR, Solow JD, Andrews BD (2009) Size distribution of submarine landslides along the U.S. Atlantic margin. Mar Geol 264:16–27

EEZ-SCAN 87 (1991) Atlas of the U.S. exclusive economic zone, Atlantic continental margin, U.S.G.S. Miscellaneous investigations series I-2054. U.S. Geological Survey, Reston, 174 pp

Forde AB (1981) Evolution of Veatch, Washington, and Norflok submarine canyons: inference from strata and morphology. Mar Geol 39:197–214

Gardner JV, Mayer LA, Armstrong AA (2006) Mapping supports potential submission to U.N. law of the sea. EOS Trans Am Geophys Union 87:157–159

Imran J, Parker G, Locat J, Lee H (2001) A 1-D numerical model of muddy subaqueous and subaerial debris flows. J Hydraul Eng 127:959–968

Issler D, De Blasio FV, Elverhøi A, Bryn P, Lien R (2005) Scaling behaviour of clay-rich submarine debris flows. Mar Pet Geol 22:187–194

Lambert DN, Bennett RH, Sawyer WB, Keller GH (1981) Geotechnical properties of continental upper rise sediments – Veatch Canyon to Cape Hatteras. Mar Geotechnol 4:281–306

Lee HJ (2009) Timing of occurrence of large submarine landslides on the Atlantic Ocean margin. Mar Geol 264:53–64

Locat J, Lee HJ (2002) Submarine landslides: advances and challenges. Can Geotech J 39:193–212

Locat J, Desgagnés P, Leroueil S, Lee HJ (2003) Stability of the Hudson Apron slope off New Jersey. In: Locat J, Mienert J (eds) Submarine mass movements and their consequences, Kluwer series on natural and technological hazards 19. Kluwer, Dordrecht, pp 257–270

Locat J, Lee H, ten Brink U, Twichell D, Geist E, Sansoucy M (2009) Geomorphology, stability and mobility of the Currituck slide. Mar Geol 264:28–40

Poag CW, Sevon WD (1989) A record of Appalachian denudation in postrift Mesozoic and Cenozoic sedimentary deposits of the U.S. middle Atlantic continental margin. Geomorphology 2:119–157

Sheridan RE, Ashley GM, Miller KG, Walduer JS, Hall DW, Uptegrove J (2000) Offshore-onshore correlation of upper Pleistocene strata, New Jersey Coastal Plain to continental shelf and slope. Sediment Geol 134:197–207

ten Brink US, Lee HJ, Geist EL, Twichell DC (2009) Assessment of tsunami hazard to the U.S. East Coast using relationships between submarine landslides and earthquakes. Mar Geol 264:65–73

Twichell DC, Chaytor JD, ten Brink US, Buczkowski B (2009) Morphology of La Quaternary submarine landslides along the U.S. Atlantic continental margin. Mar Geol 264:4–15

Veatch AC (1937) Recent advances in marine surveying: work of the United States Coast and Geodetic Survey. Geogr Rev 27:625–629

Chapter 34
Characterization of Submarine Landslide Complexes Offshore Costa Rica: An Evolutionary Model Related to Seamount Subduction

Rieka Harders, César R. Ranero, and Wilhelm Weinrebe

Abstract Offshore Costa Rica large seamounts under-thrust the continental convergent margin causing slides of complex morphology. The large dimension of the structures has attracted previous investigations and their basic characteristics are known. However, no detailed mapping of their complex morphology has been reported. Here we present a detailed mapping of the failure-related structures and deposits. We use deep-towed sidescan sonar data, aided by multibeam bathymetry to analyze their geometry, geomorphologic character, backscatter intensity, and spatial distribution. Those observations are used to analyze the relationship between landslide characteristics and abundance, to the changes in the style of deformation caused by the subduction of seamounts to progressively greater depth under the margin.

Keywords Seamount subduction • Landslides • Deformation • Convergent margin • Model

34.1 Introduction

Underwater mass wasting processes occur at slopes of continental margins, flanks of volcanoes and large lakes. In this work we concentrate on submarine landsliding at the active subduction zone of the Middle America Trench (MAT) where the

R. Harders (✉) • W. Weinrebe
Geomar, Helmholtz-Zentrum für Ozeanforschung Kiel, Kiel, Germany
e-mail: riekaharders@gmx.de

C.R. Ranero
Barcelona Center for Subsurface Imaging (Barcelona-CSI), ICM, ICREA at CSIC, Barcelona, Spain

S. Krastel et al. (eds.), *Submarine Mass Movements and Their Consequences*, Advances in Natural and Technological Hazards Research 37, DOI 10.1007/978-3-319-00972-8_34,

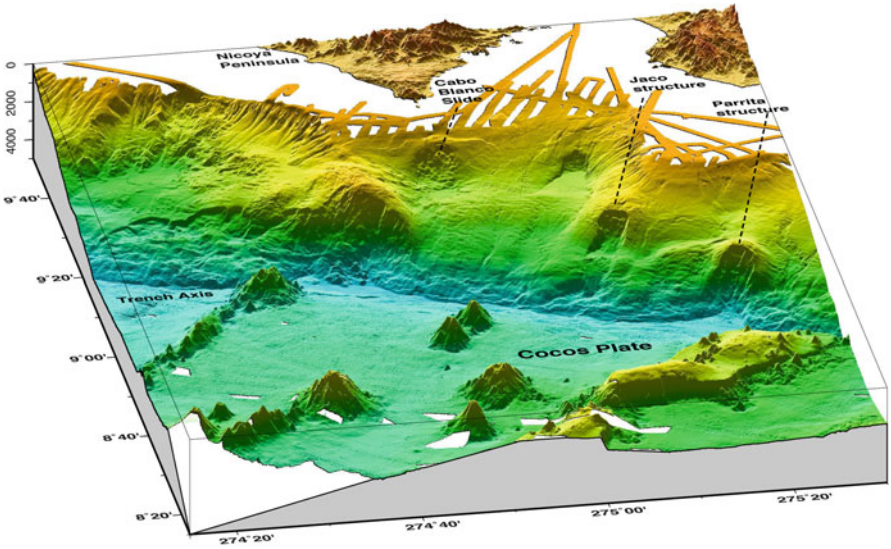

Fig. 34.1 Multibeam bathymetric map of the Middle America Trench offshore Costa Rica showing large-scale deformation and mass wasting structures in the margin related to seamount subduction

oceanic Cocos plate under-thrusts the Caribbean plate. Subduction zones can be differentiated between those with large accretionary prisms and those dominated by tectonic erosion, as the MAT, where tectonic processes gradually thin the overriding plate.

The convergent margin of the MAT has been extensively surveyed during the past two decades. Previous studies along >1,000 km of the MAT have shown that there exist more than 100 landslides with variable characteristics and origin. Work along the continental slope from Guatemala to Costa Rica identified submarine slides ranging in width and length from a few hundred meters to tens of km (Harders et al. 2011). The MAT slope displays evidence of mass-wasting structures with a distribution in segments, which appears similar to the segmentation of the morphology of the Cocos plate (Harders et al. 2011, 2012). Most large slides along the MAT occur where large seamounts subduct (Fig. 34.1). The seamounts are ~2–4 km high, ~20–30 km wide at their base, and cover ~40 % of the ocean plate offshore Costa Rica (Werner et al. 1999; von Huene et al. 2004).

Previous studies of slope failure at the MAT have been largely based on bathymetry data gridded at 100 m, with sufficient spatial resolution to detect large failure-related structures but not enough to map their internal structures and related deposits (Fig. 34.1). Sidescan sonar data have been locally used to complement those studies to classify large-scale failure structures (Hühnerbach et al. 2005; Ranero et al. 2008; Harders et al. 2011). However, the available sidescan sonar data permit detection of structures with a spatial resolution similar to a 25 m grid of high-quality multibeam bathymetry data (Kluesner et al. 2013). Thus, the

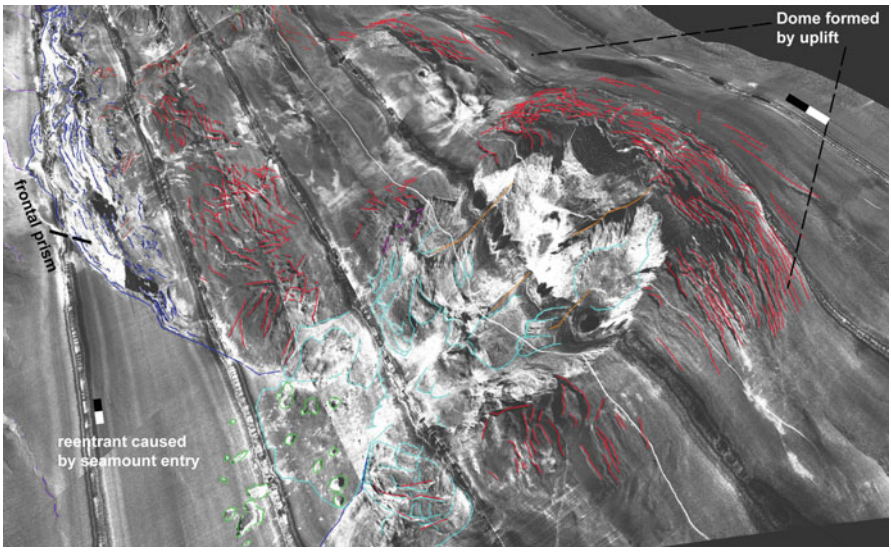

Fig. 34.2 Sidescan sonar imagery of Parrita structure. It shows a reentrant caused by seamount collision of Stage 1, a failed slope and associated structures, and the dome and deformation above an under-thrusting seamount of Stage 2. *Dark blue lines* are faults of the frontal prism. *Red lines* are fractures in slope sediment and possibly underlying margin wedge. *Pale blue* delineate debris flows. *Green polygons* delineate boulders from rock avalanches. *Orange lines* mark the crest of ridges. The *black-white bar* is 2 km long

sidescan sonar data allow for an improved analysis over previous work. Here we use sidescan sonar imagery draped on bathymetry for detailed mapping of Parrita and Jaco structures, and Cabo Blanco slide complex (Fig. 34.1). We differentiate deformational and mass-wasting related features based on morphology, geometry, and backscatter character (Figs. 34.2, 34.3, and 34.4). We use the three characteristic structures to propose a model of slope failure related to different stages of seamount under-thrusting that develop during the evolution in the subduction process.

34.2 Geological Framework

The bulk of the MAT overriding plate is made of competent crystalline rock, the so-called margin wedge, formed dominantly by igneous rock of the Caribbean flood basalt province and indurated sediment. The margin wedge is covered by ~0.5–2 km of slope sediment that is typically involved in landsliding. The front of the convergent margin is made of a 1–10 km wide sediment prism (Ranero and von Huene 2000; von Huene et al. 2000; Ranero et al. 2008). The frontal prism is formed by thrust sheets striking parallel to the trench, and is usually characterized by high backscatter caused by the rough relief produced by active faulting (Fig. 34.2).

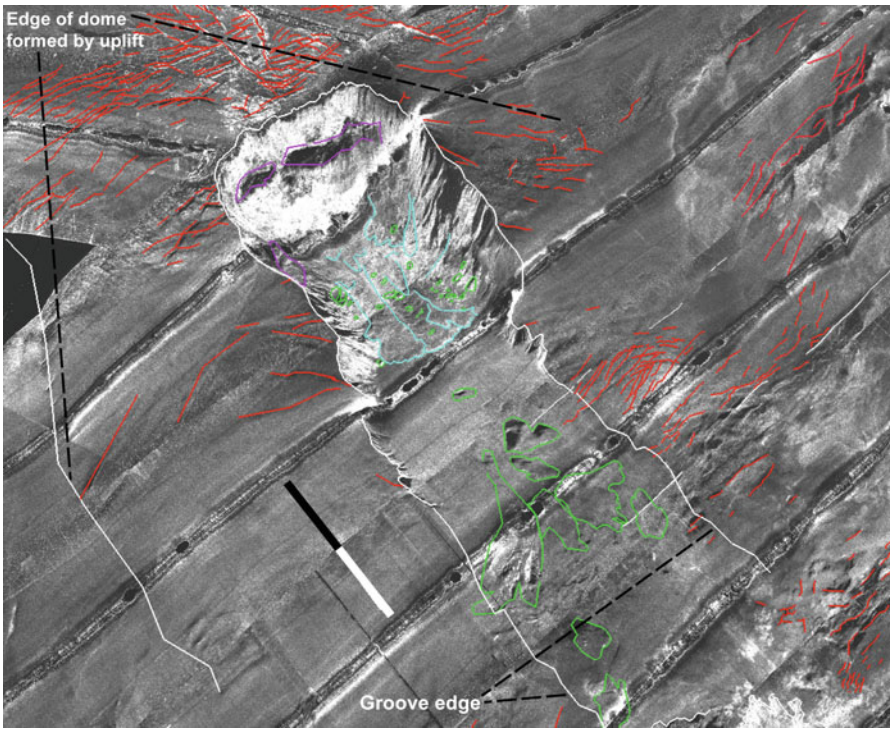

Fig. 34.3 Sidescan sonar imagery of Jaco structure. The dome, associated deformation, and the linear groove trailing the subducting seamount and mass-wasting structures define Stage 3. *Lilac polygons* delineate the *top* of blocks sliding on headwall and sidewall. *Red lines* mark fractures in slope sediment and possibly underlying margin wedge. *Pale blue* delineate debris flows. *Green polygons* delineate boulders from rock avalanches. The *black-white bar* is 4 km long

34.3 Mass Wasting Evolutionary Model

We discuss sequentially four evolutionary Stages of seamount subduction that produce distinct landsliding styles and abundance (Fig. 34.5). For each Stage we first describe the characteristic structures and then interpret the processes potentially controlling landsliding.

34.3.1 Stage 1: Seamount Collision with the Continental Margin Front

The initial collision of large seamounts is not currently occurring offshore Costa Rica, but the resulting structures can be studied from the morphology of deformational features at the base of the slope (Fig. 34.2).

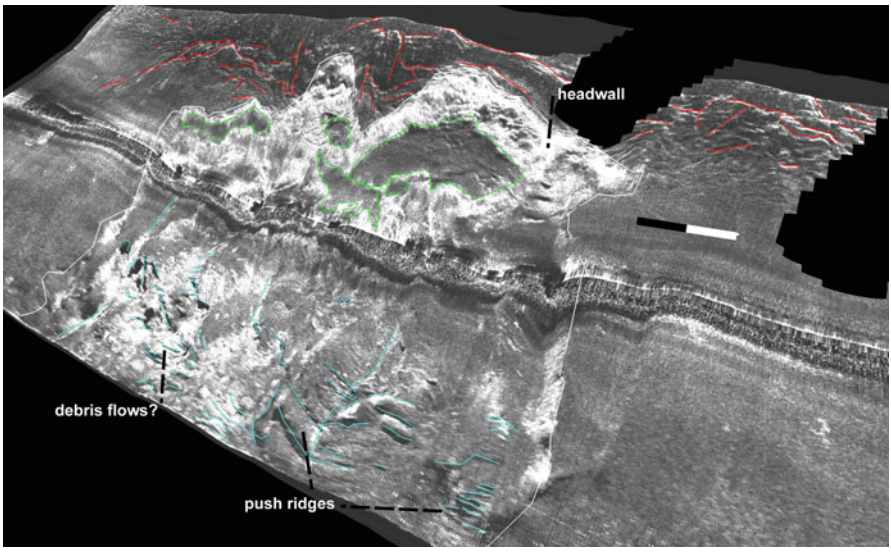

Fig. 34.4 Sidescan sonar imagery of Cabo Blanco translational slide complex. Sliding blocks and push ridges define Stage 4 processes. *Red lines* delineate main fractures of the swarm cutting slope sediment. *Pale blue lines* mark deformation structures in debris flows and push ridges. *Green polygons* delineate blocks. The *black-white bar* is 1 km long

The locus of recent collision are ~30–20 km wide by ~10 km deep landward indentations of the margin front clearly visible in multibeam bathymetry data (Fig. 34.1) that have been previously indentified (Ranero and von Huene 2000; von Huene et al. 2000, 2004). The smooth reentrant seafloor narrows inboard from ~20 km width where the entire frontal sediment prism has been removed, to ~5 km width. The transfer of upper plate material removed to form the indentations is unclear.

The fracture pattern of the lower slope changes from roughly trench parallel to strongly oblique near the reentrant (red fractures in Fig. 34.2) indicating that the seamount fractured and pushed sideways the margin basement and overlying sediment.

We interpret that during collision, before seamounts fully under-thrust the overriding plate, slope material is not uplifted above a seamount crest to fail in its wake, but is pushed in front and aside (Fig. 34.5a). Material pushed in front probably accumulates abutting the seamount flank and is under-thrust, which may involve at least part of the large mass of missing material in the reentrant (Fig. 34.2).

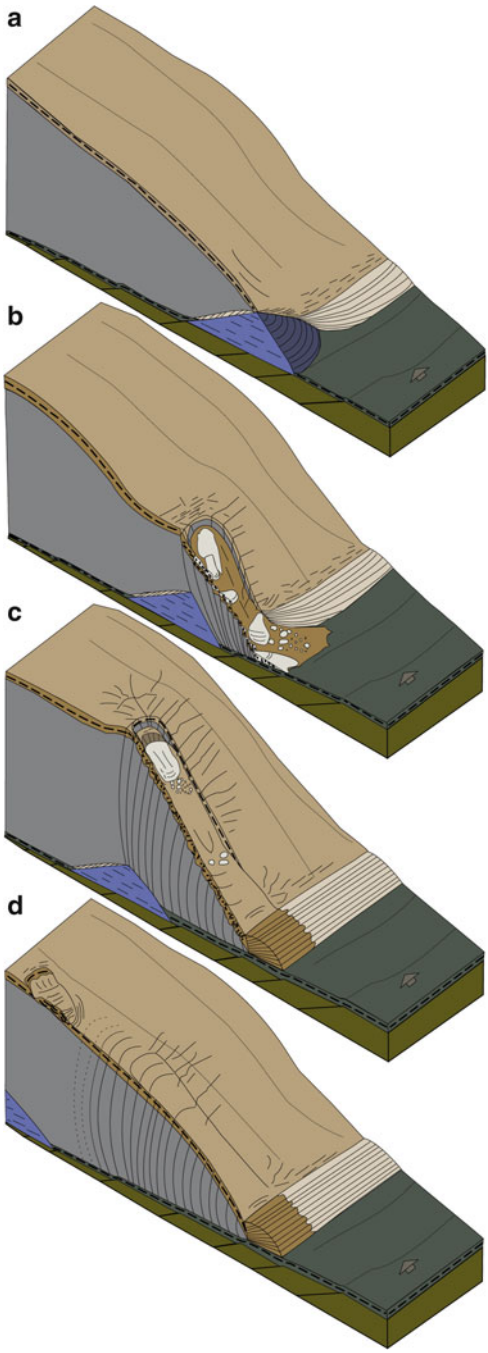

Fig. 34.5 Conceptual model of deformation and associated mass wasting processes related to seamount subduction. (**a**) Stage 1: Seamount collision with continental margin front. (**b**) Stage 2: Initial seamount thrusting under the *upper* plate and associated rock avalanches. (**c**) Stage 3: Seamount tunneling of overriding plate and associated rotational slumps. (**d**) Stage 4: *Upper* plate flexing and associated translational slides

34.3.2 Stage 2: Initial Seamount Thrusting Under the Continental Slope: Formation of Rock Avalanches

As a whole seamount under-thrusts the competent margin-wedge rock, upper-plate deformation and mass wasting processes change. The seamount uplifts the slope forming a fractured dome, and mass wasting occurs localized in the wake trailing the seamount (Fig. 34.1). Parrita shows an uplifted slope with a dome intensely cut, principally by trench-parallel fractures, ~1–5 km long, and a few hundreds of meters apart (Fig. 34.2). Radial fractures, described in analog models (Dominguez et al. 1998) are rare at Stage 2.

The terrain produced by failure forms trench-perpendicular depressions and intervening ridges that indicate the maximum width of failed rock masses (Fig. 34.2). The relief of the failed slope is characterized by sidewalls and headwalls up to 1 km high and 20–30° steep, that reach up to 35° in the uppermost sector.

We interpret that trench parallel fractures of the dome precondition the upper plate to fail in a complex mode. The steepest uppermost sector conforms a headwall that strikes parallel to fractures at the dome, which may indicate that it was formed by failure along a pre-existing fracture.

Types of mass-wasting deposits change from the foot to the top of the scar, possibly indicating an evolution in mass wasting processes. The smooth seafloor of the re-entrant from Stage 1 is covered close to the slope by a large (~4 × 6 km) debris flow containing coherent blocks generated during the first failures of Stage 2 (Fig. 34.2). Failed blocks littering the trench axis range from a few tens to several hundreds of meters. Blocks contained in the debris flow may be contemporary with that event. Others are away of the debris flow and possibly come from a different rock avalanche. Upslope along the scar, most of the seafloor is covered by overlapping debris flows, ranging from a few hundreds of meters to ~2 km in width and ~2–4 km long, that often appear to derive from the sidewalls and flanks of ridges (Fig. 34.2).

In the upper third of the scar, debris flows are rare. Here, sidescan sonar imagery is characterized by high backscatter, possibly indicating more recent mass wasting processes related to the disintegration of detached blocks that travel downhill, creating rock avalanches, that may turn into turbidities traversing down slope before reaching the trench axis. Turbidites fill the re-entrant produced in Stage 1 smoothing the seafloor between Parrita scarp and bending-related faults in the oceanic plate.

The deformation inferred from surface structures may involve fracturing of the entire overriding plate (Fig. 34.5b). Stage 2 occurs when a 2–4 km tall seamount is a ~1–4 km thick upper plate, as under Parrita (Ranero and von Huene 2000). We interpret that first the upper plate is uplifted and fractured possibly to a shallow depth where stresses are tensile. Fractures initially have small vertical offsets, but when the seamount subducts further, the fractures grow in its wake to 1 km offsets as the

entire upper plate collapses. Gravitational processes include sediment mass-wasting described above, and perhaps creep of fracture-bounded blocks involving the entire upper plate (Fig. 34.5b).

34.3.3 Stage 3: Seamount Tunneling of Overriding Plate: Formation of Rotational Slumps

As a large seamount travels deeper in the subduction zone, overriding plate deformation creates a trailing groove (Figs. 34.3 and 34.5c). The 3–4 km wide groove has sidewalls 25–30° steep that define fairly continuous faults. The sidewalls extend for >10 km from the edges of the headwall scarp, where they are ∼1 km high, to diminish in height and disappear where sediment fills the groove (Fig. 34.3).

The uplift above the seamount forms a dome, with fracture spacing larger than in Stage 2. Fractures are ∼1–5 km long, typically trench-parallel, but some are radial with morphology similar to analog models (Dominguez et al. 1998). The groove located trenchward of the dome, formed in the trailing wake of the subducting seamount, is narrower than fractures at the dome.

We interpret that groove formation involves upper-plate thinning and resulting subsidence through material removal by tectonic erosion by the subducting seamount (Ranero and von Huene 2000). The seamount dimensions and the elastic thickness of the upper plate probably control the constant width of the groove.

The length of the dome trench-parallel fractures does not control mass wasting during Stage 3. The dimensions of failing blocks appear preconditioned by the same characteristics that control the constant groove width. At Jaco, a $\sim 4 \times 1$ km block, abutting the headwall, has slid hundreds of meters (Fig. 34.3) indicating that, at least during a first phase, some blocks creep rather than catastrophically fail. The block seems cut by one oblique fracture into two sub-blocks that have slid slightly different amounts. The vertical dimension of the block is unclear and might be as thick as the entire headwall, so that the block is a coherent rotational slump that initially maintains its integrity. However, several debris flows located down-slope indicate that blocks may eventually disintegrate near the base of the headwall. In a similar process, a 1×0.5 km block has slid along the groove sidewall. The sidewalls foot is covered by comparatively smaller debris flows with tens-to-hundreds-of-meter-large blocks (Fig. 34.3).

We interpret that the surface deformation associated to Stage 3 occurring when a seamount is ∼4–8 km deep under the seafloor involves deep faulting across the entire upper plate (Fig. 34.5c). The 1-km-high headwall and sidewalls dimensions mean deep penetrating faults. In addition to the slumps abutting the headwall, the entire upper plate is collapsing at depth along the flanks of the seamount as several-km-thick rotational blocks.

34.3.4 Stage 4: Upper Plate Flexing: Formation of Translational Slides

Above a large seamount that has subducted to a depth of 8–12 km the overriding plate flexes but fractures little, the deep grooves of Stage 3 no longer form and mass wasting processes become more sporadic and produce comparatively smaller scale structures (Fig. 34.4). The relief of the continental slope above the seamount displays comparatively little uplift and minor fracturing. The Cabo Blanco landslide complex shows a slope cut by a swarm of small, hundreds-of-meter-long fractures with an anastomosing pattern that form irregular slide headwalls, a few hundreds of meters high (Fig. 34.4).

At Stage 4, mass wasting appears dominated by translational sliding affecting the upper few hundreds meters of slope sediment. Sliding produces groups of detached blocks that have moved down-slope a few-hundreds-of-meters distance (Fig. 34.4). The characteristic push ridges at the front of the slid mass also support relatively short displacements, compared to slide events occurring during the other Stages.

We interpret that the processes active at Stage 4 are fundamentally different from those of previous Stages. The competent ~8–12 km thick overriding plate above the seamount does not break as in previous Stages (Fig. 34.5d). In addition to the attenuation through increased thickness of the upper plate, the material progressively eroded by seamount tunneling flows around the seamount and reduces the relief of the ocean plate. As a consequence, associated seafloor relief comparatively diminishes and minor uplift, related tilting and minor fracturing trigger shallow translational sliding probably using pre-existing weak layers, like ash layers that have been shown to precondition the slope sediment structure in the region (Harders et al. 2010). Thus, deformation and stresses related to seamount subduction, which precondition sediment landsliding for Stages 1–3, are not the only preconditioning factor at Stage 4.

34.4 Conclusions

Upper plate deformation resulting from subduction of tens-of-km wide and 2–3-km tall seamounts varies as seamounts traverse under an overriding plate. During Stage 1, seamounts breach the margin front, creating re-entrants by removing material, possibly by pushing some aside and also transporting some material abutting their frontal flank into the subduction zone. During Stage 2, seamounts first under-thrust the overriding plate, causing intense trench-parallel fracturing that preconditions complex mass-wasting processes. During Stage 3, seamounts move deeper, under a 4–8 km thick plate. Here, uplift creates trench-parallel and radial fractures. Material removal by seamount tunneling forms linear grooves with steep ~1 km

high headwalls and sidewalls that promote rotational slumps. These slumps creep some distance along the scarps to disintegrate down-slope into debris flows. During Stage 4 a seamount is under an 8–12-km-thick plate that is competent and deforms by minor fracturing and tilting. Here dominates translational sliding of shallow sediment, possibly using pre-existing weak planes. In summary, Stages 1–3 failures are preconditioned by deformation by seamount subduction, whereas Stage 4 failure appears preconditioned by a combination of deformation and pre-existing factors.

Acknowledgements Side scan sonar data were collected with the R/V Sonne using the TOBI system from National Oceanographic Center Southampton. We acknowledge the constructive reviews of R. von Huene and C. Lo Iacono.

References

Dominguez S, Lallemand SE, Malavieille J et al (1998) Upper plate deformation associated with seamount subduction. Tectonophysics 293:207–224

Harders R, Kutterolf S, Hensen C et al (2010) Tephra layers: a controlling factor on submarine translational sliding? Geochem Geophys Geosyst 11:Q05S23. doi:10.1029/2009GC002844

Harders R, Ranero W, Weinrebe CR et al (2011) Submarine slope failures along the convergent continental margin of the Middle America Trench. Geochem Geophys Geosyst 12:Q05S32. doi:10.1029/2010GC003401

Harders R, Ranero CR Weinrebe W et al (2012) An overview of the role of long-term tectonics and incoming plate structure on segmentation of submarine mass wasting phenomena along the Middle America Trench. Chapter 35 In: Yamada Y et al (eds) Submarine mass movements and their consequences. Advances in natural and technological hazards research, vol 31, Springer Science + Business Media B.V., Dordrecht. doi: 10.1007/978-94-007-2162-3_35

Hühnerbach V, Masson DG, Bohrmann G et al (2005) Deformation and submarine landsliding caused by seamount subduction beneath the Costa Rica continental margin—new insights from high-resolution sidescan sonar data. In: Hodgons DM, Flint SS (eds) Submarine slope systems: processes and products, Geological society special publication 244. The Geological Society, London, pp 195–205

Kluesner JW, Silver EA, Bangs NL et al (2013) High density of structurally-controlled, shallow to deep water fluid seep indicators imaged offshore Costa Rica. Geochem Geophys Geosyst 11:1525–2027. doi:10.1002/ggge.20058

Ranero CR, von Huene R (2000) Subduction erosion along the Middle America convergent margin. Nature 404:748–752

Ranero CR, Grevemeyer I, Sahling H et al (2008) The hydrogeological system of erosional convergent margins and its influence on tectonics and interplate seismogenesis. Geochem Geophys Geosyst 9:Q03S04. doi:10.1029/2007GC001679

von Huene R, Ranero CR, Weinrebe W et al (2000) Quaternary convergent margin tectonics of Costa Rica, segmentation of the Cocos Plate, and Central American volcanism. Tectonics 19:314–334

von Huene R, Ranero CR, Watts P et al (2004) Tsunamigenic slope failure along the Middle America Trench in two tectonic settings. Mar Geol 203:303–317

Werner R, Hoernle K, van den Bogaard P et al (1999) Drowned 14-m.y.-old Galápagos archipelago off the coast of Costa Rica: implications for tectonic and evolutionary models. Geology 27:499–502. doi:10.1130/0091-7613

Chapter 35
Morphological Expression of Submarine Landslides in the Accretionary Prism of the Caribbean Continental Margin of Colombia

Javier Idárraga-García and Carlos A. Vargas

Abstract Morphological analyses of ~14,500 km^2 of high-resolution-bathymetric data in the Caribbean continental margin of Colombia has allowed us to identify submarine landslides in the Sinú Accretionary Prism (SAP) and Magdalena submarine fan (MSF) areas.

In the MSF area most of submarine failures are disintegrative, i.e. with no obvious deposit near or at the base of the scar, and are related to a system of canyons belonging to the Magdalena turbidite system and to an abrupt slope break at the border of the continental shelf. Landslides in the SAP area are mainly associated to the steeper flanks (12–18°) of anticline-related ridges. In many cases, the associated landslide deposits are buried by subsequent sediments related to broad fans formed in the mouth of channels and canyons. The cohesive landslides identified exhibit blocky deposits with rubble masses up to 50 m high and runout distances between 3.6 and 11 km.

Morphometric analyses of scarps allowed us to calculate landslides ages in function of the constant κ of diffusivity. Estimations using a κ value of 0.015 m^{2}y^{-1} suggest ages ranging between 13.8 and 9,761.9 ky for the MSF and ages between 12.2 and 1,031.8 ky for the SAP.

Keywords Submarine landslides • Canyons • Anticline-related ridges • Morphometric dating • Colombian Caribbean

J. Idárraga-García (✉)
Graduate Program of Geophysics, Universidad Nacional de Colombia, Bogotá, Colombia
e-mail: jidarragag@unal.edu.co

C.A. Vargas
Department of Geosciences, Universidad Nacional de Colombia, Bogotá, Colombia
e-mail: cavargasj@unal.edu.co

S. Krastel et al. (eds.), *Submarine Mass Movements and Their Consequences*, Advances in Natural and Technological Hazards Research 37, DOI 10.1007/978-3-319-00972-8_35,

35.1 Introduction

The mapping and characterization of submarine failures have attracted much attention in the past two decades, including with regard to their role as potential geohazards for marine and coastal infrastructure. The active Colombian Caribbean continental margin is characterized by a rough morphology and the presence of four active deltas fed by large Andean rivers. These features provide *a priori* high susceptibility to the occurrence of landslides with a wide range of sizes and types. Submarine landslides are triggered either by an increase in the driving stresses, a decrease in strength, or a combination of the two (Lee et al. 2007). The following possible triggers show the interplay of these factors: sediment accumulation, erosion, earthquakes, volcanism, waves, gas and gas hydrates, diapirism and human activity (Moore et al. 1989; Hampton et al. 1996; Mulder and Cochonat 1996; McAdoo et al. 2000).

The main objective of this paper is to present the morphological characteristics of the submarine landslides in the MSF and the SAP areas (Fig. 35.1) and discuss their possible origins and ages.

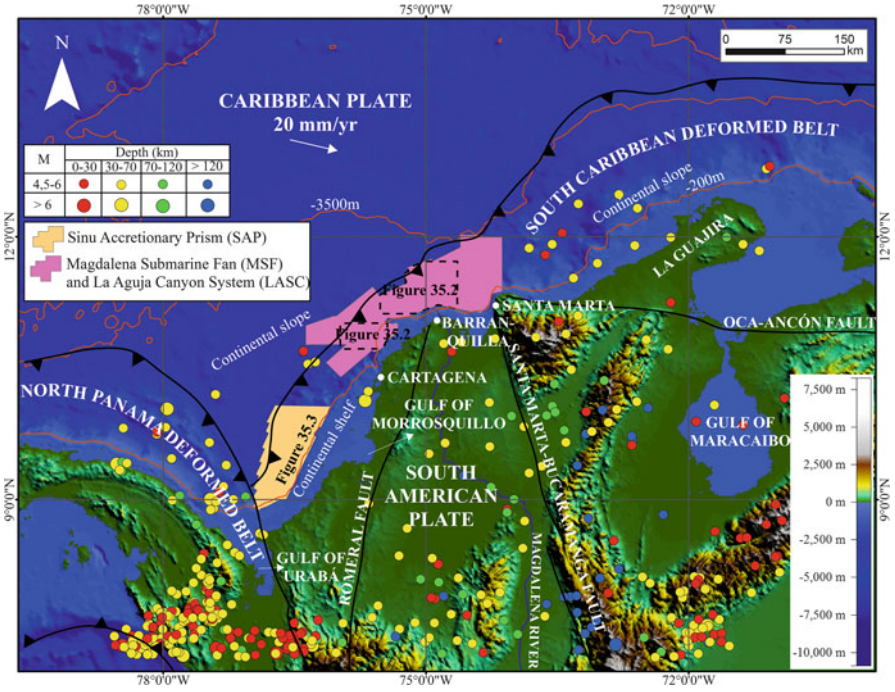

Fig. 35.1 Location of the studied areas (SAP and MSF) and the instrumental seismicity with magnitudes greater than 4.5. *Dashed line boxes* indicate Figs. 35.2 and 35.3. *Black bold lines* indicate major structures

35.2 Geologic Setting of the Study Area

35.2.1 Seismotectonic Setting

The Colombian Caribbean is located in a complex zone formed by the interaction between South American and Caribbean plates (Vargas and Mann 2013). The Caribbean oceanic plate is being subducted beneath the northwestern edge of the South American plate. The South Caribbean Deformed Belt represents the boundary between these two plates and corresponds to a NW-verging highly deformed sequence of sediments (Vinnels et al. 2010). The SAP is the offshore part of the belt and is made up of deformed sedimentary rocks that range in age from Middle Eocene to Late Oligocene (INGEOMINAS 2003).

Seismicity in the region is mainly located onshore. According to the Colombian National Seismological Network, there have been 8,821 earthquakes with Mw ranging from 2.5 to 7.3 and focal depths from 10 to 280 km in the period 1973–2013. Four of these events occurred close to the study zone with Mw >6 and focal depths <70 km (Fig. 35.1).

35.2.2 Morphology of the Colombian Caribbean Continental Margin

The Colombian Caribbean continental margin has a pronounced relief, in which two main elements are recognized (Fig. 35.1). The continental slope extends from 200 to 3,500 m depth and has a width less than 100 km (López 2005). The continental shelf has a maximum depth of 200 m and is 1,100 km-long from the Gulf of Urabá to the peninsula of La Guajira; its width varies from 5 km around the city of Santa Marta to over 50 km offshore the Gulf of Morrosquillo (López 2005).

In the study area, the margin can be divided into two contrasting sectors: the SAP, from the Gulf of Urabá to immediately north of the Gulf of Morrosquillo and the MSF, between the cities of Cartagena and Barranquilla (Fig. 35.1).

The SAP area exhibits typical flow geoforms as channels and canyons, and structural geoforms such as ridges and escarpments. Strong tectonic activity is manifested by the presence of NE-SW-oriented scarps and ridges related to axial zones of anticlines (Flinch 2003).

The MSF is a turbiditic system originated by the accumulation of the sediments delivered by the Magdalena River since Middle Pliocene (Ercilla et al. 2002). The continental shelf does not exceed 5 km in width so much of the sediment delivered by the river is directly deposited on the continental slope through a system of submarine canyons.

35.3 Data and Methods

Multibeam bathymetric data was acquired in 2002 aboard the R/V Baruna Jaya III using both ResonSeaBat 8160 (50 kHz) and Simrad EM12D (13 kHz) systems, and in 2006 aboard the M/V Ocean Endeavour using both Simrad EM1002 (93/98 kHz) and Simrad EM120 (11.25/12.75 kHz). Digital Terrain Models were subsequently created from the raw data with spatial resolutions between 50 and 25 m. These models were used to identify and describe submarine landslides. We used the nomenclature of McAdoo et al. (2000) to determine the type of mass movement.

We performed a quantitative scarp analysis in order to constrain a range of ages for the occurrence of the failures. In this sense, dating was carried out following the methodology of Hanks (2000) by applying a diffusion equation under transport-limited conditions. This equation relates the change in elevation to time using a proportionality constant κ of diffusivity $[L^2T^{-1}]$ and measurements associated to the fan-slope angle (θ_f), the scarp-slope angle (θ_s) and the effective vertical displacement of the scarp ($2a$).

35.4 Results

35.4.1 MSF Area

The area offshore of the current mouth of the Magdalena River is cut by a submarine canyon system through which sediments are conducted to abyssal depths. Based on bathymetric data, we differentiated three parallel canyons bounded by a series of structural highs; these canyons are incised by 260–400 m into the continental slope (Fig. 35.2). Most of the failures identified are disintegrative, i.e. the deposits originated from the landslide were probably transported downstream through the canyons or are buried by subsequent mass flow deposits (Fig. 35.2). Otherwise, we distinguished two cohesive landslides in this area: one associated with the eastern canyon and the other with the central one (Fig. 35.2).

The eastern canyon landslide has an area of 72.6 km^2; the headscarp is located at a depth of ~950 m and has an average height of 235 m and a slope of 13°. The scar is 341 m high and there is a deposit at its base which is evidenced by a rough surface composed of angular blocks with maximum height of 40 m (Fig. 35.2); the morphology of the scar is complex, with several arcuate indentations especially in the SW part, suggesting that the whole area of the scar does not correspond to a single event for the blocky deposit, but rather, to multiple events. The maximum runout distance is 11 km until the debris abuts a structural high (Fig. 35.2).

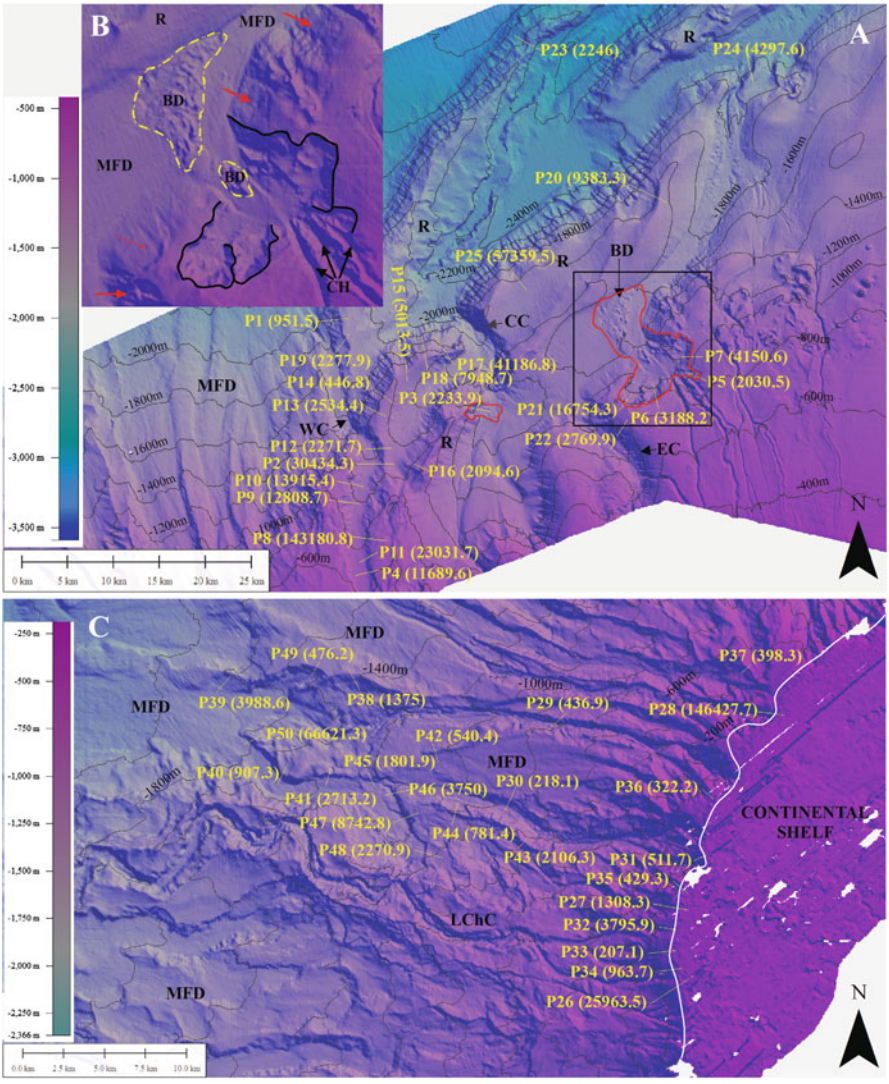

Fig. 35.2 (**A**) Bathymetry offshore of the Magdalena River current mouth. Two cohesive landslides are marked by the solid *red line*. *Black box* indicates zoom shown in (**B**). (**B**) Zoom view of the cohesive landslides present in the MSF. *Solid black lines* indicate the headscarps and the *dashed yellow lines* outline the blocky deposits. *Red arrows* point to some disintegrative landslides. (**C**) Bathymetry west of the current mouth of the Magdalena River. *κt* values are shown in parentheses next to the respective profile. *MFD* mass flow deposits, *R* ridge, *EC* eastern canyon, *CC* central canyon, *WC* western canyon, *BD* blocky deposit, *CH* channels, *LChC* leveed channel complex (For location see Fig. 35.1)

The slope failure associated with the central canyon has an area of 5.8 km^2; its headscarp is 1,200 m deep and reaches an average height of 74 m and a slope of 22°; the scar is 266 m high and exhibits a regular morphology; there is a deposit at the base of the scar which surface shows an intermediate roughness given by the presence of rubbles (Fig. 35.2); the runout distance reaches 3.6 km (Fig. 35.2).

The zone located westward of the current mouth of the Magdalena River is characterized by the presence of leveed channel complexes and large-scale mass flow deposits on the continental slope. All the landslides are associated with gullies, channels and canyons present on the border of the continental shelf that are the feeder of the mass flow deposits downslope (Fig. 35.2). The slope gradient at the shelf edge ranges between <1° and 5.6°.

Regarding the analysis of the 50 scarps (two cohesive and 48 disintegrative landslides), the measurement of θ_s, θ_f and $2a$ allowed estimating κt. Calculated values range between ~207.1 and ~14,6427.8 m^2 (Fig. 35.2), which is equivalent to an age range of 13.8–9,761.9 ky (see Sect. 35.5 below).

35.4.2 SAP Area

Most of the submarine landslides in the SAP are related to flanks of anticlines that control formation of ridges extending to a depth of 3,000 m (Fig. 35.3). These ridges exhibit an asymmetric cross section with the steeper seaward flanks sloping between 12° and 18°. There are failures on the walls of some submarine canyons located to the north of the area. These canyons have their headwaters in the middle of the continental slope and extend cutting a series of ridges until ending at 2,500 m water depth, where they form submarine fans in several ridge-bounded intraslope basins (Fig. 35.3). The distal sector of the canyons shows a large number of disintegrative landslides in their walls that give them an asymmetrical U-shaped cross section.

The landslides associated with the ridges are both cohesive and disintegrative. These two types of failures are more distributed towards the middle continental slope where the appearance of the margin is very rough (average slope angle of 15°). In contrast, the margin tends to be smoother on the upper slope, as there are almost no landslides (Fig. 35.3).

We focused on the detailed description of the three cohesive landslides best imaged in the bathymetry (Landslide 1, Landslide 2 and Landslide 3) (Fig. 35.4).

35.4.2.1 Landslide 1

This failure is associated with the outermost ridge of the SAP and has an area of 90.8 km^2. The headscarp has a NNW-SSE-oriented arcuate shape with a slope of ~20.6°; this feature has a height of ~316 m and is located in 2,100 m water depth (Fig. 35.4). The scar has a maximum height of 750 m and exhibits a very complex geometry which suggests the occurrence of multiple failure events. A blocky deposit

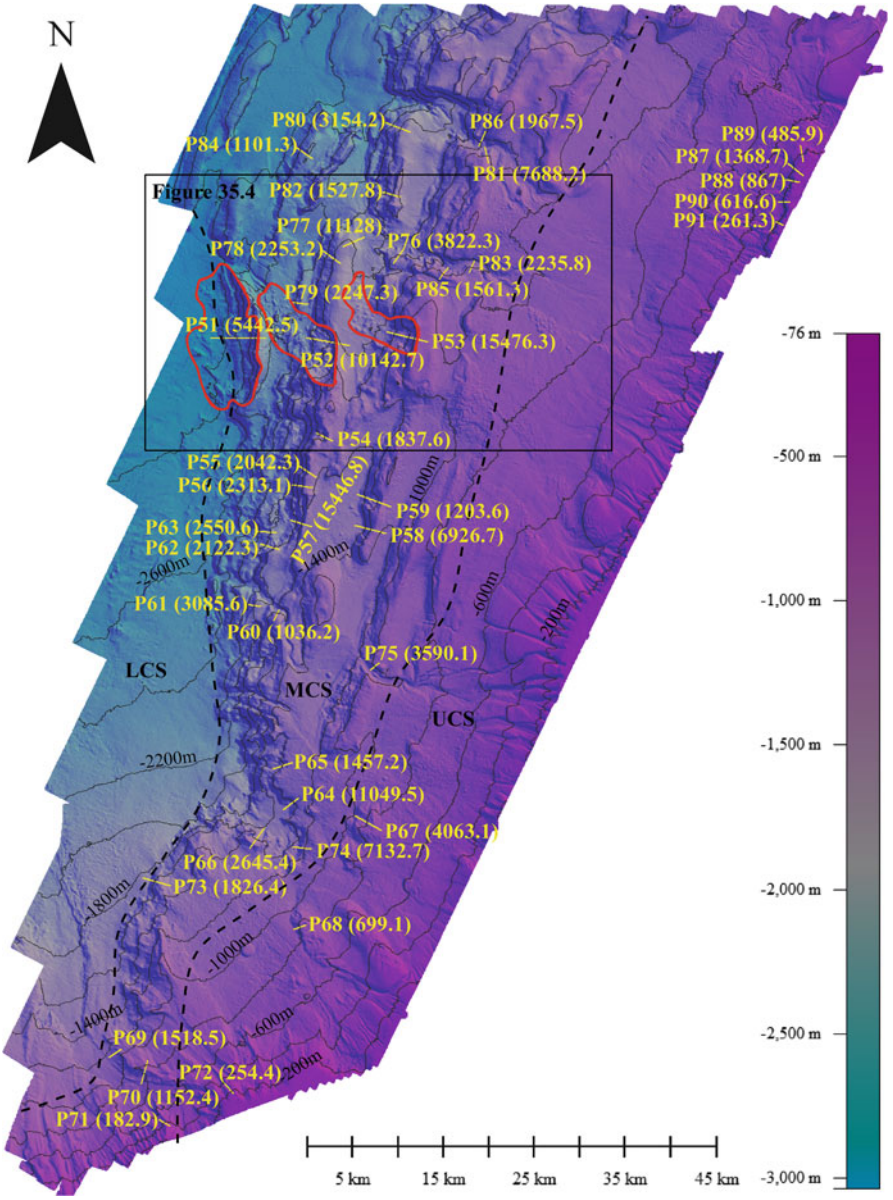

Fig. 35.3 Bathymetry of the SAP where a set of anticline-related ridges is present in the continental slope. *Red lines* indicate cohesive landslides highlighted in Fig. 35.4 (*black box*). κ*t* values are shown in parentheses next to the respective profile

is present at the base of the scar where the rubble masses are evidenced as irregular angular-shaped bathymetric highs reaching maximum heights of 50 m; this deposit extends to a depth of 2,915 m and has a maximum runout distance of 6.5 km (Fig. 35.4).

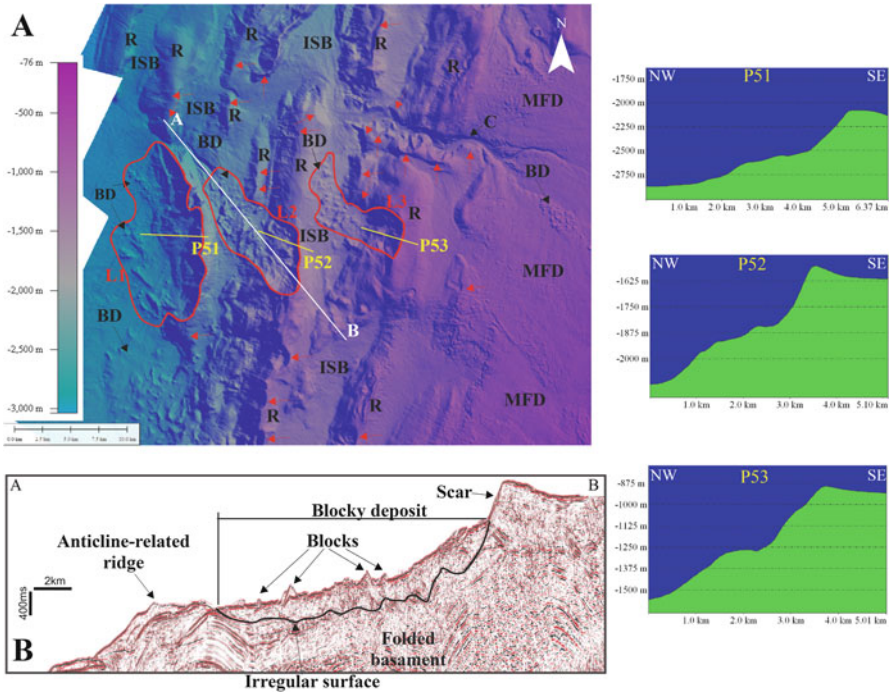

Fig. 35.4 (**A**) Detail of the landslides L1, L2 and L3 (*red lines*) in the SAP. L2 and L3 are frontally confined by ridges. The respective profiles are shown to the *right*. The *white line* AB indicates the location of seismic profile shown in (**B**). *Red arrows* point to some disintegrative landslides. (**B**) 2D seismic profile modified from Vinnels et al. (2010) where the main features of L2 are highlighted. *R* ridge, *ISB* intraslope basin, *MFD* mass flow deposit, *BD* blocky deposit, *C* canyon

35.4.2.2 Landslide 2

This landslide has an area of 48.1 km^2. Its headscarp exhibits a rectilinear trend oriented NS and has a height of ~248.2 m with a slope of 20.4°; it is located at 1,400 m water depth (Fig. 35.4). The scar is less complex than of the Landslide 1, indicating that it could be product of a single mass wasting event; its height is 496 m. The deposit caused by this event is frontally confined by the presence of a ridge at its downslope end and extends to a maximum depth of 2,730 m with a maximum runout distance of 11 km. Its appearance is rougher than Landslide 1 due to the presence of many angular-shaped rubble deposits rising up to 40 m (Fig. 35.4).

35.4.2.3 Landslide 3

This landslide has an area of 30.8 km^2. The headscarp has a slightly arcuate appearance oriented NNE to NNW with a slope of 17.1°; it is located at 875 m

water depth and has an average height of 132.6 m (Fig. 35.4). The scar has a height of 566 m and its appearance is similar to the Landslide 2, suggesting that it may also be the result of a single event of mass wasting. The associated deposit has a runout distance of 8 km and is frontally confined by the presence of a ridge. The presence of some angular up to 30 m high blocks results in an intermediate surface roughness (Fig. 35.4).

The κt values obtained from the morphometric analysis of 41 scarps (three cohesive and 38 disintegrative failures) range between ~182.9 and ~15,476.3 m^2 (Fig. 35.3). According to our approach (see Sect. 35.5 below) these values are equivalent to an age range of 12.2–1,031.8 ky.

35.5 Discussion and Conclusion

35.5.1 Origin of the Landslides

The origin of the landslides described in the MSF is related to the sedimentary dynamics that characterize the evolution of the Magdalena River delta. This hypothesis is supported by the fact that the MSF is an active turbidite system since the Middle Pliocene (Ercilla et al. 2002). Modern offshore instability of this system is well documented by the numerous submarine cable breaks that have occurred since the 1950s (Heezen 1956). The system is fed by the Magdalena River which is considered the most important river of Colombia with a sediment load of 144×10^6 t yr^{-1} (Restrepo and Kjerfve 2004) and whose evolution has been marked by several migrations of its mouth over time (Ercilla et al. 2002). The vast majority of sediments brought by the river are deposited on the continental slope through a canyon system, this being a preconditioning factor for generating mass movements. This adds to the fact that the MFS is located in a tectonically active area where there have been several earthquakes with magnitudes greater than 5 (Fig. 35.1).

The failures present in the SAP are associated with anticlines-related ridges. Here the preconditioning factor for the generation of landslides is the steep slopes (between 12° and 18°) on the seaward-flanks of the ridges, in contrast to the more gentle slopes on the opposite flanks (4–10°). The orientations of the scars slopes have a preferential NW direction product of the landslide occurrence on the westward-oriented steeper flanks of the ridges.

35.5.2 Approach to the Age of Landslides

We presented κt values obtained from the morphometric analyses of 91 profiles throughout the study zone. Nowadays there is no consensus on the constant κ values for underwater environments, which can range up to several orders of magnitude.

Mitchell (1996) reported a value of ~0.007 m^2y^{-1} for the Galapagos spreading center. McAdoo and Simpson (2005) suggest values ranging between 10^{-3} and 10^{-4} m^2ky^{-1} for slides on continental slopes. On the other hand, Vargas et al. (2012) attempted to date the Mira submarine canyon (Colombia) and obtained that the most probable κ values range between 0.001 and 1.33 m^2y^{-1} for an event occurred in 3,200 y BP. However, Ratzov et al. (2012) using other methods suggested that the Mira canyon age may range between 53 and 67 ky. According to this, the κ values in the canyon area oscillate between 0.015 and 0.057 m^2y^{-1}, which are consistent with the range suggested by Vargas et al. (2012). We tested these new limits of κ value to calculate ages. Estimations using a κ value of 0.015 m^2y^{-1} suggest landslides ages ranging between 13.8 and 9,761.9 ky for the MSF and ages between 12.2 and 1,031.8 ky for the SAP. The large contrast of the results suggests a complex slope dynamics in the two study areas. However, this work is one of the first attempts to date the submarine landslides in the Colombian Caribbean.

Acknowledgments This work was conducted under the Seismotectonic Research of the Graduate Program of Geophysics of the Universidad Nacional de Colombia. The authors are grateful to the Assigned Editor Dr. David Völker and the reviewers Dr. Gueorgui Ratzov and Dr. Geoffroy Lamarche. We also thank ANH-INVEMAR for giving us the permission to use the bathymetric database. We are grateful to the COLCIENCIAS Doctoral Fellowship Program as well.

References

Ercilla G, Alonso B, Estrada F et al (2002) The Magdalena turbidite system (Caribbean Sea): present-day morphology and architecture model. Mar Geol 185:303–318

Flinch JF (2003) Structural evolution of the Sinú-Lower Magdalena area (Northern Colombia). In: Bartolini C, Buffler RT, Blickwede J (eds) The Circum-Gulf of Mexico and the Caribbean: hydrocarbon habitats, basin formation, and plate tectonics, vol 79, AAPG Memoir. American Association of Petroleum Geologists, Tulsa, pp 776–796

Hampton MA, Lee HJ, Locat J (1996) Submarine landslides. Rev Geophys 34:33–59

Hanks TC (2000) The age of scarplike landforms from diffusion-equation analysis. In: Nollet JS, Sowers JM, Lettis WR (eds) Quaternary geochronology: methods and applications. American Geophysical Union, Washington, DC, pp 313–338

Heezen BC (1956) Corrientes de turbidez del Río Magdalena. Boletín de la Sociedad Geográfica de Colombia 51–52:135–143

INGEOMINAS (2003) Geología de los Cinturones Sinú-San Jacinto. Planchas 50 Puerto Escondido, 51 Lorica, 59 Mulatos, 60 Canalete, 61, Montería, 69 Necoclí, 70 San Pedro de Urabá, 71 Planeta Rica, 79 Turbo, 80 Tierralta. Escala 1:100.000, 225 p

Lee HJ, Locat J, Desgagnés P et al (2007) Submarine mass movements on continental margins. In: Nittrouer CA, Austin JA, Field ME et al (eds) Continental margin sedimentation: from sediment transport to sequence stratigraphy. IAS, Oxford, pp 213–274

López E (2005) Evolución tectónica de la región Caribe de Colombia. Informe Interno Ingeominas no 78. Bogotá, 56 pp

McAdoo BG, Simpson G (2005) Morphometric dating of submarine landslide scarps. Geophysical research abstracts, vol 7, 00629, SRef-ID: 1607-7962/gra/EGU05-A-00629

McAdoo BG, Pratson LF, Orange DL (2000) Submarine landslide geomorphology, US continental slope. Mar Geol 169:103–136

Mitchell NC (1996) Creep in pelagic sediments and potential for morphologic dating of marine fault scarps. Geophys Res Lett 23(5):483–486

Moore JG, Clague DA, Holcomb RT et al (1989) Prodigious submarine slides on the Hawaiian Ridge. J Geophys Res 94(B12):17465–17484

Mulder T, Cochonat P (1996) Classification of offshore mass movements. J Sediment Res 66:43–57

Ratzov G, Sosson M, Collot JY et al (2012) Late Quaternary geomorphologic evolution of submarine canyons as a marker of active deformation on convergent margins: the example of the South Colombian margin. Mar Geol 315–318:77–97

Restrepo JD, Kjerfve B (2004) The Pacific and Caribbean rivers of Columbia: water discharge, sediment transport, and dissolved loads. In: de Lacerda LD, Santelli RE, Duursma EK et al (eds) Environmental geochemistry in tropical and subtropical environments. Springer, Berlin/New York, pp 169–187

Vargas CA, Mann P (2013) Tearing and breaking off of subducted slabs as the result of collision of the Panama arc-indenter with northwestern South America. Bull Seismol Soc Am 103(3):2025–2046

Vargas CA, Mann P, Gomez C (2012) Morphologic expression of accretionary processes and recent submarine landslides along the southwestern Pacific margin of Colombia. In: Yamada Y et al (eds) Submarine mass movements and their consequences, vol 31, Advances in natural and technological hazards research. Springer, Dordrecht, pp 365–377

Vinnels J, Butler R, McCaffrey W et al (2010) Depositional processes across the Sinú Accretionary Prism, offshore Colombia. Mar Petrol Geol 27(4):794–809

Chapter 36
Contrasting Development of the Latest Quaternary Slope Failures and Mass-Transport Deposits in the Ulleung Basin, East Sea (Japan Sea)

Sang Hoon Lee, Jang-Jun Bahk, Han Joon Kim, Gil-Young Kim, Seong-Pil Kim, Sueng-Won Jeong, and Sung-Sik Park

Abstract In order to understand how the variations in shelf morphology and sediment supply to the shelf within a basin can change the occurrence styles of slope failures and mass-transport deposits (MTDs), this chapter details dimensions and morphology of the latest Quaternary slope failures and MTDs on the western and southern margins of the Ulleung Basin. On the western margin, the slides and slumps have relatively small dimensions with a few small, scoop-shaped scars and gullies deeper than 700 m water depth. The downslope mass-flow deposits occur as small, solitary lobes restricted at the base-of-slope. On the western margin, the small sediment input to the shelf and the prominent Hupo Bank and Hupo Trough blocking sediment delivery to the slope probably caused relatively low accumulation of muddy sediments in the slope, most likely resulting in the small dimensions of slope failures, and the restricted occurrence of small MTDs at the base-of-slope. In contrast, the southern margin is characterized by large dimensions of gullied scars with huge slides and slumps deeper than 250 m water depth. These catastrophic failures evolved into extensive mass flows, which travelled downslope for several tens of kilometers. On the southern margin, the flat, broad shelf and the high sediment supply to the shelf during the last glacial period probably caused relatively high accumulation of mixed muddy and sandy sediments in the upper slope. These conditions could have promoted large-scale slope failures along the entire upper slope, forming the extensive occurrence of MTDs in the middle to lower slopes.

S.H. Lee (✉) • H.J. Kim
Department of Marine Environment Research, Korea Institute of Ocean Science and Technology, Ansan 426-744, South Korea
e-mail: sanglee@kordi.re.kr; sanglee@kiost.ac

J.-J. Bahk • G.-Y. Kim • S.-P. Kim • S.-W. Jeong
Korea Institute of Geoscience and Mineral Resources, Daejeon 305-330, South Korea

S.-S. Park
Kyungpook National University, Daegu 702-701, South Korea

S. Krastel et al. (eds.), *Submarine Mass Movements and Their Consequences*, Advances in Natural and Technological Hazards Research 37, DOI 10.1007/978-3-319-00972-8_36,

This study provides an example that the variations in shelf morphology and sediment supply to the shelf within a basin can affect the styles of slope failures and MTDs by controlling sediment input and sediment types to the slope.

Keywords Submarine slope failure • Submarine mass-transport deposits • Mass-flow deposits • Ulleung Basin • East Sea (Japan Sea)

36.1 Introduction

Submarine slope failures are common in various sedimentary environments worldwide, particularly along open continental slopes, submarine canyons, flanks of volcanic ridges and islands, prodelta slopes, and fjord slopes (Piper et al. 1985; Hampton et al. 1996; Locat and Lee 2002). These slope failures are generally controlled by various factors, such as sedimentation rate, sediment types, sea-level changes, earthquakes, gas-hydrate dissociation, etc., giving rise to a variety of the slope-failure styles (Mulder and Cochonat 1996; Locat and Lee 2002; Canals et al. 2004). The styles of submarine slope failures affect sedimentary features (dimension, run-out distance, geometry, etc.) of the downslope associated mass-transport deposits (Mulder and Cochonat 1996; Piper et al. 1999; Lastras et al. 2004; Lee et al. 2004; Tripsanas et al. 2008).

In the Ulleung Basin, East Sea (Japan Sea), a variety of slope failures and mass-transport deposits (MTDs) formed during the last glacial period occur along the entire basin margins (Fig. 36.1; Chough et al. 1997; Lee et al. 1999, 2004). Even though the MTDs and slope failures show a contour-parallel distribution along the basin margins in general (Fig. 36.1), the styles of slope failures and MTDs are contrasting between the western and the southern margins, reflecting different types of shelf morphology and sediment supply to the shelf along the margins. In this chapter, we detail the dimensions, occurrence and morphology of slope failures and MTDs and the linked shelf morphology on the western and southern margins. Based on these characteristics, this chapter illustrates how the variations in shelf morphology and sediment supply to the shelf within a basin can affect the occurrence styles of slope failures and MTDs by controlling sediment input and sediment types to the slope.

36.2 Geological Setting

The Ulleung Basin is a semi-enclosed back-arc basin formed behind the Japanese Arc (Fig. 36.1; Yoon and Chough 1995). The basin is bordered by the continental margin of the Korean Peninsula, the Korea Plateau, the Oki Bank and the Japanese Arc. The continental shelf of the Korean Peninsula is narrow (<25 km wide) and is flanked by a steep (4–10°) slope (Fig. 36.1). The shelf includes the N–S-trending

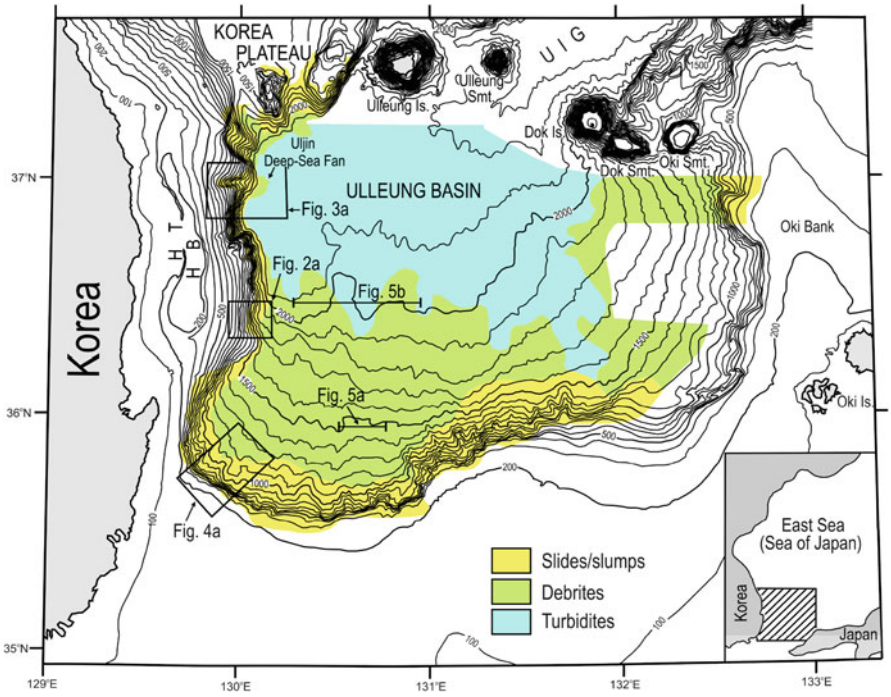

Fig. 36.1 Physiography of the Ulleung Basin and adjacent areas in the East Sea. Nearly contour-parallel distribution of slides/slumps, debrites and turbidities identified from chirp (2–7 kHz) profiles (Lee et al. 1999, 2004). Water depth in meters. *HB* Hupo Bank, *HT* Hupo Trough, *Smt.* seamount, *UIG* Ulleung Interplain Gap

topographic low (Hupo Trough; >150 m deep) and high (Hupo Bank). The Hupo Bank is about 84 km long, and rises more than 100 m above the surrounding seafloor (Fig. 36.1). Along the east coast of the Korean Peninsula, there are a few small streams without major rivers, resulting in small amount of sediment input into the continental shelf of the Korea Peninsula (Chough et al. 2000). In the south and east, the Ulleung Basin is bordered by broad (30–150 km wide) shelf and rather gentle (less than 2°) slope (Fig. 36.1). The northeastern part of the basin is punctuated by volcanic islands (Ulleung and Dok islands) and seamounts. The basin floor gradually deepens toward the northeast, and is connected to the Japan Basin through the Ulleung Interplain Gap.

On the entire margins and plain of the basin, the uppermost sedimentary sequence (less than ca. 30 m thick) of the Ulleung Basin consists mostly of various MTDs formed during the last glacial period (Chough et al. 1997; Lee et al. 2004). The MTDs in the basin show a contour-parallel distribution: slides and slumps on the upper to middle slope, debris-flow deposits on the lower slope (or base-of-slope), and turbidities on the basin plain (Fig. 36.1; Chough et al. 1997). The zonal distribution of MTDs suggests that mass transports were mostly derived from

regional slope failures with large-scale transformation from slide/slump through debris flows to turbidity currents (Chough et al. 1997). The sediment failures were plausibly triggered by earthquakes, in combination with the last sea-level lowering and the associated gas-hydrate dissociation (Lee et al. 2004, 2010).

36.3 Materials and Methods

In order to describe sedimentary features of the slope failures and associated MTDs, we used bathymetric/back-scattering data, high-resolution subbottom profiles, and single-channel air-gun seismic profiles. The bathymetric and back-scattering data were acquired using a 13 kHz deep-water multi-beam echo sounder (EM12S). The high-resolution subbottom profiles were obtained using a chirp (2–7 kHz) sub-bottom profiling system (Datasonics CAP-6000W and Benthos Chirp II). Seismic profiles were acquired using a single channel streamer (MESH200P Hydrophone Array) and air-gun sources (299 cubic inches).

36.4 Sedimentary Features of Latest Quaternary Slope Failures and Mass-Transport Deposits

36.4.1 Western Basin Margin

On the western basin margin, slope sediments failed deeper than 700 m water depth where the slope gradient begins to increases. A few distinct scoop-shaped (or horseshoe-shaped) slope-failure scars are present at water depths of 700–1,200 m (Figs. 36.2a and 36.3a). These scars rarely coalesce with neighboring ones. The horseshoe-shaped scars are less than 15–20 km^2 in area, and less than 50 m in scarp height (Fig. 36.2b). Some scars are associated downslope with gullies which extend to the base-of-slope (Figs. 36.2a and 36.3a). Besides the scoop-shaped scars, the slope failures also occur as very small-scale, subdued gullies deeper than 1,200 m water depth (Fig. 36.3a). On the upper to lower slopes of the western margin, core sediments (3–11 m long) from the undisturbed areas are dominated by hemipelagic mud consisting of more than 60–70 % of clay fractions with less than 1 % of sand fractions (Chough and Lee 1987; Lee et al. 2004).

At the base-of-slope, the downslope mass-flow deposits generally occur as small-scale, solitary lobes (Figs. 36.2a and 36.3). Near 37°00′N, a distinct fan-shaped lobe (Uljin deep-sea fan) occurs at the downslope of gully mouth (Fig. 36.3). This fan consists of acoustically transparent masses with slightly convex-up, smooth surfaces (Fig. 36.3b). It is about 5 km long in longitudinal direction. Its thickness is up to ca. 10 m off the gully mouth, and thins laterally (Fig. 36.3b). Except Uljin deep-sea

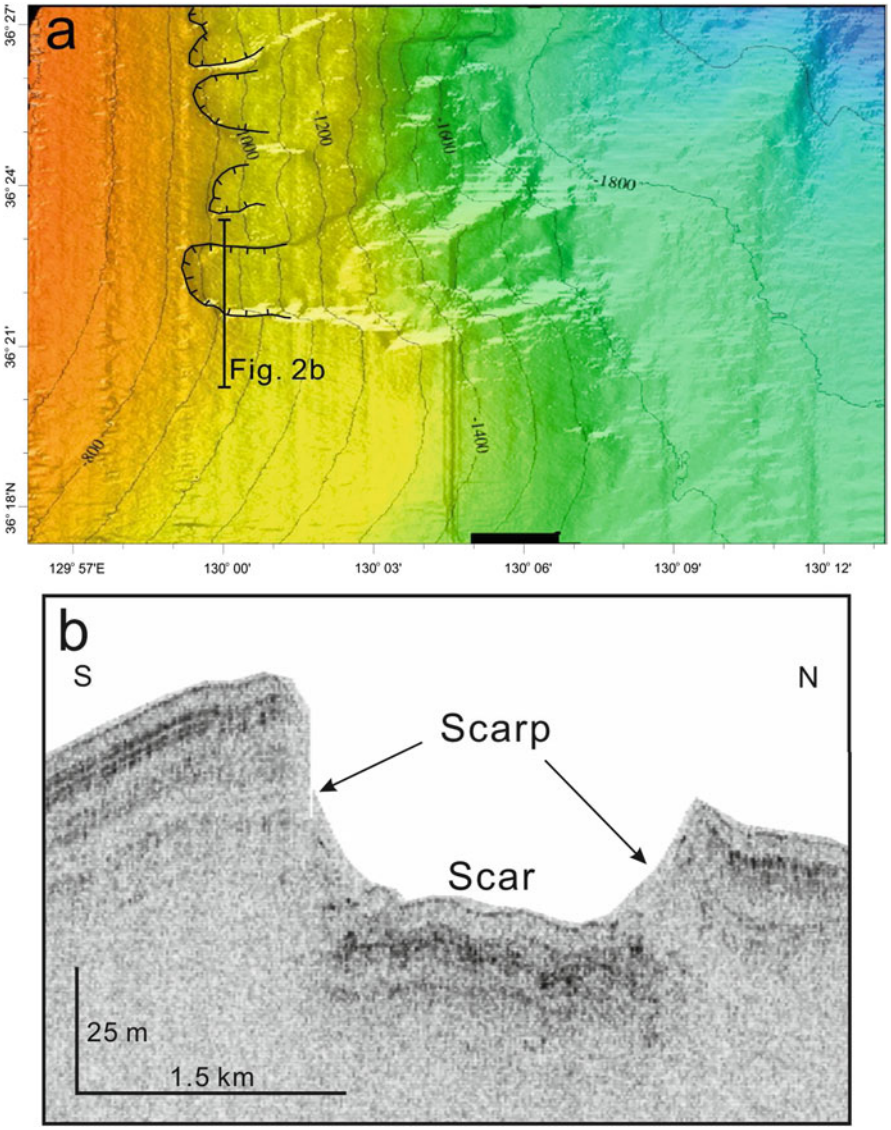

Fig. 36.2 (**a**) *Scoop-shaped* slope-failure scars on the western slope of the Ulleung Basin. Water depth in meters. For location of Fig. 36.2a, see Fig. 36.1. (**b**) A chirp (2–7 kHz) subbottom profile showing sedimentary features of the *scoop-shaped* scars in cross section

fan, most mass-flow deposits at the base-of-slope are very small (<2 km long in longitudinal direction) and subdued (Fig. 36.3a). These subdued mass-flow lobes cannot be easily recognized in chirp (2–7 kHz) subbottom profiles, indicating that the deposits are most likely thin in thickness.

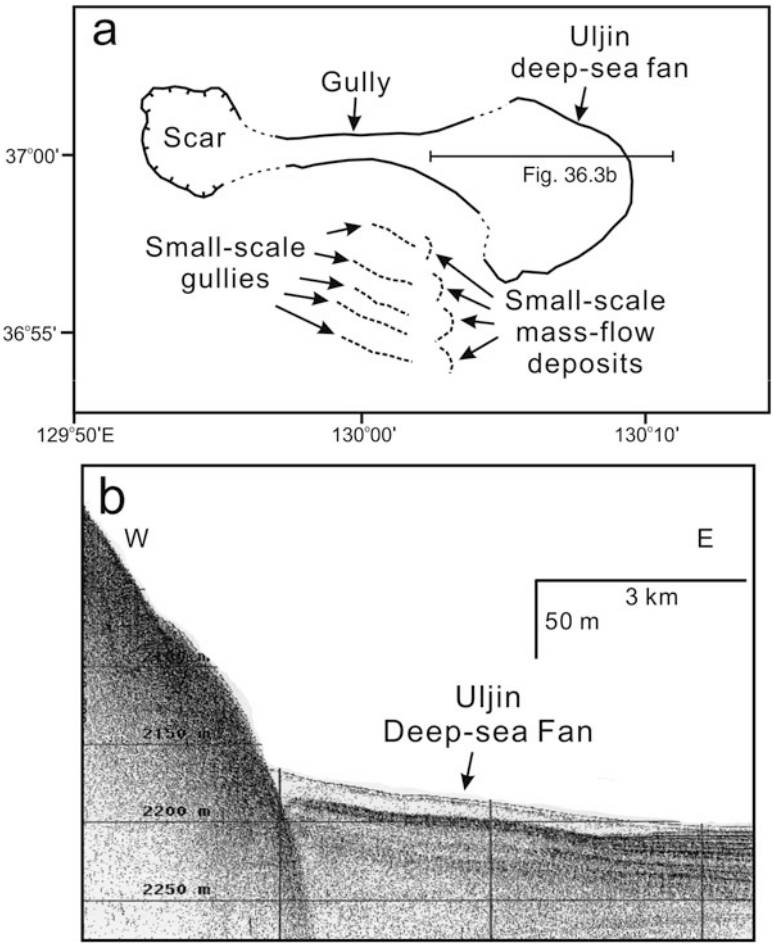

Fig. 36.3 (**a**) Line drawings of *scoop-shaped* scars, gullies, and downslope associated mass-transport deposits (MTDs) from sonar images on the western slope of the Ulleung Basin. For location of Fig. 36.3a, see Fig. 36.1. (**b**) A chirp (2–7 kHz) subbottom profile showing a distinct fan-shaped mass-flow deposits (Uljin deep-sea fan) at the base-of-slope

36.4.2 Southern Basin Margin

Along the entire southern margin, slope failures occur extensively at water depths of ca. 250–1,000 m, and there are no prominent submarine canyons and channels on the upper to lower slope (Fig. 36.1). The uppermost slope in water depths of 250–500 m is dominated by gullied slope-failure scars (Fig. 36.4), showing steep (4.0–10.3°) slope gradient. These gullied slope-failure scars are more than ca. 70–80 m deep and several kilometers wide, and coalesce downslope with adjacent ones,

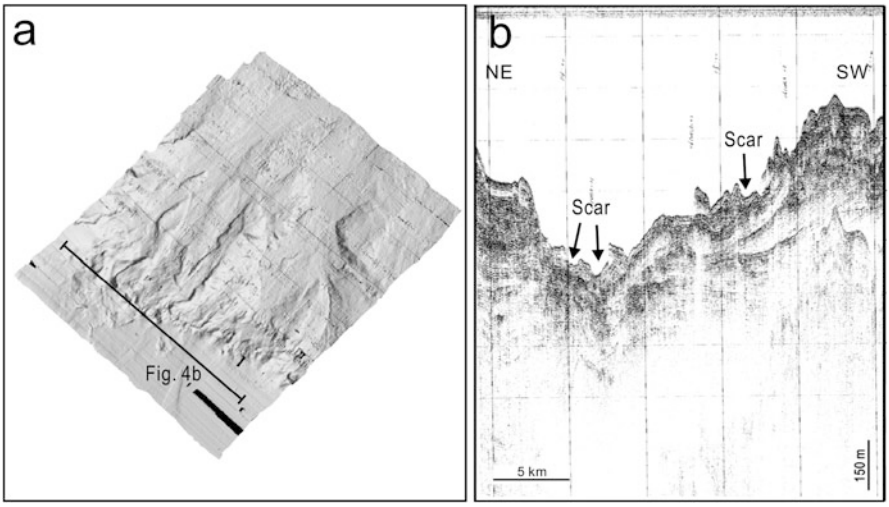

Fig. 36.4 *Shaded relief* image (**a**) and a single-channel air-gun seismic profile (**b**) showing gullied slope-failure scars on the *upper* slope of the southern Ulleung Basin. For location of images and seismic profile, see Fig. 36.1

forming larger-scale gullied morphology. Within the gullied slope-failure scars, highly rugged or irregularly blocky failed masses occasionally present along the axis of scars (Fig. 36.4). On the upper slope of the southern margin, core sediments (4–10 m long) from the undisturbed areas, deeper than 350–400 m water depth, consist mostly of hemipelagic muds (>70 % clay contents) with interbedded fine-sand layers (Lee et al. 2004). In contrast, sediment cores (several meters long) retrieved from the uppermost slope, shallower than 350–400 m water depth, consist mostly of fine to medium sands with abundant shell fragments (Chough and Lee 1987; Lee et al. 1993).

Along the entire southern margin, large-scale, composite failed masses showing irregularly rugged, blocky, or lumpy morphology are dominantly present at downslope of the gullied scars (Chough et al. 1997). These slide and slump masses change downslope to mass-flow deposits showing hyperbolic surface echoes with convex-up upper surface geometry in transverse section (Fig. 36.5a). These deposits cover extensively on the middle slope (Chough et al. 1997; Lee et al. 1999). The lower slope area is mostly dominated by mass-flow lobes consisting of lens- or wedge-shaped, acoustically transparent masses (Fig. 36.5b; Lee et al. 1999). Each mass-flow lobe is elongated downslope (i.e., N–S direction), and commonly fills topographic depressions, forming shingled internal architecture (Fig. 36.5b). These lobes are 10–40 km thick and >20 km long, and range from several meters to ca. 30 km in width. The mass-flow lobes were transported downslope for more than at least several tens of kilometers from the slope failing areas (i.e., upper to middle slope).

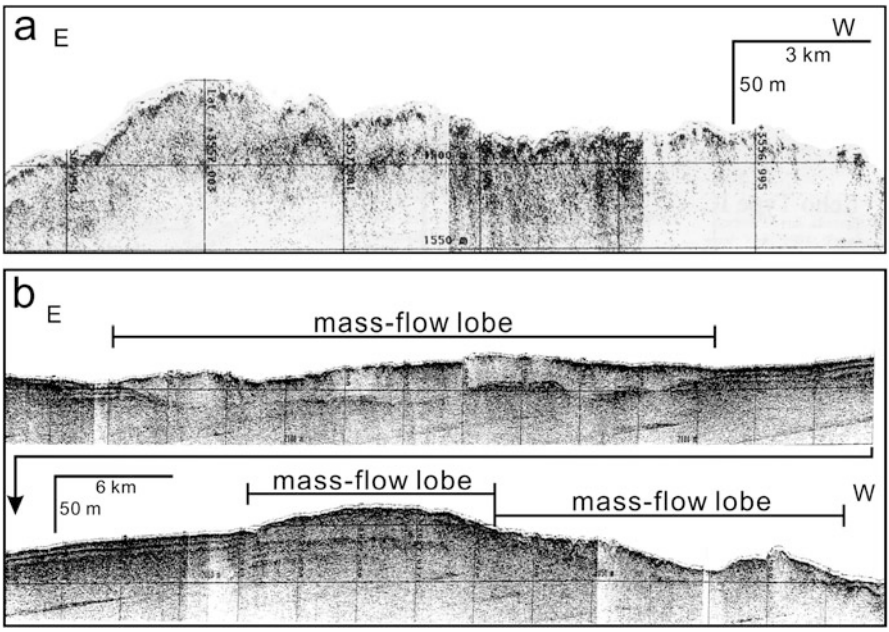

Fig. 36.5 Chirp (2–7 kHz) subbottom profiles showing hyperbolic surfaced mass-flow deposits on the southern middle slope (**a**) and sedimentary features of mass-flow lobes on the southern lower slope (**b**). For location of profiles, see Fig. 36.1

36.5 Discussion and Conclusions

The Ulleung Basin shows contrasting styles of the MTDs between the western and southern margins. The contrasting styles of MTDs can be ascribed to difference in dimensions of slope failures between the two basin margins. On the western basin margin, a few small-scale, scoop-shaped slope-failure scars with small gullies suggest that small amount of slope sediments failed. The small volume of failed sediment masses in the western basin margin would have formed small-sized slides and slumps on the middle slope and small, subdued solitary mass-flow deposits restricted at the base-of-slope. In contrast, the southern basin margin exhibits extensive occurrence of large-scale, gullied slope-failure scars along the entire upper slope, implying that huge amount of slope sediments failed. The large volume of failed sediment masses would have caused the extensive occurrence of large-scale, composite slides and slumps on the entire upper to middle slopes. Furthermore, the large momentum induced by the huge volume of failed sediments along the southern margin could have formed the extensive mass-flow deposits in the middle to lower slope areas, which travelled for more than several tens of kilometers from the failing areas (Lee et al. 1999, 2010).

The difference in dimensions of slope failures between the western and southern basin margins could be closely linked to the variation in shelf morphology and supply of riverine sediments to the shelf which can control sediment input and sediment types to slope. The western basin margin is characterized by a narrow (<25 km wide) shelf including the N–S-trending, prominent Hupo Trough and Hupo Bank (Fig. 36.1). Along the shelf of the western margin, there are only a few small streams without major rivers, implying a relatively small amount of sediment input into the western shelf during the last glacial period (Chough et al. 2000). The prominent Hupo Trough and Hupo Bank in the narrow western shelf (Fig. 36.1) could most likely block the sediment delivery from the shelf to the slope. These features suggest that relatively low accumulation of hemipelagic muds with rare sands prevailed in the western slope. These conditions probably caused the small-dimension of a few scoop-shaped slope-failure scars and gullies in the western slope. In contrast, the southern basin margin has a broad (30–150 km wide) shelf consisting of sandy sediments with paleo-channels, probably fed from the Nakdong River, during the last glacial period (Chough et al. 1997; Bahk et al. 2004). The high input of the riverine sediments to the southern shelf could form the prograding sedimentary sequences to the shelf break (Chough et al. 1997, 2000). These features indicate that relatively large amount of muddy and sandy sediments transported from the southern shelf most likely accumulated in the upper slope. The relatively high accumulation of sediments could probably promote large-scale, gullied slope failures along the entire southern slope.

Acknowledgments This study is supported by the KIODP project and the KIOST project (PE98742). We are grateful to the Korea Hydrographic and Oceanographic Administration for providing chirp subbottom profiles. We thank Prof. Strasser, Dr. Lafuerza, and Prof. Yoon for their constructive comments.

References

Bahk JJ, Han SJ, Khim BK (2004) Variations of terrigenous sediment supply to the southern slope of the Ulleung Basin, East/Japan Sea since the Last Glacial Maximum. Geosci J 8:381–390

Canals M, Lastras G, Urgeles R, Casamor JL, Mienert J, Cattaneo A, De Batist M, Haflidason H, Imbo Y, Laberg JS, Locat J, Long D, Longva O, Masson DG, Sultan N, Trincardi F, Bryn P (2004) Slope failure dynamics and impacts from seafloor and shallow sub-seafloor geophysical data: case studies from the COSTA project. Mar Geol 213:9–72

Chough SK, Lee HJ (1987) Stability of sediments on the Ulleung Basin slope. Mar Geotechnol 7:123–132

Chough SK, Lee SH, Kim JW, Park SC, Yoo DG, Han HS, Yoon HS, Oh SB, Kim YB, Back GG (1997) Chirp (2–7 kHz) echo characters in the Ulleung Basin. Geosci J 1:143–153

Chough SK, Lee HJ, Yoon SH (2000) Marine geology of Korean seas. Elsevier, Amsterdam

Hampton MA, Lee HJ, Locat J (1996) Submarine landslides. Rev Geophys 34:33–59

Lastras G, Canals M, Urgeles R, De Batist M, Calafat AM, Casamor JL (2004) Characterisation of the recent BIG'95 debris flow deposits on the Ebro margin, Western Mediterranean Sea, after variety of seismic reflection data. Mar Geol 213:235–255

Lee HJ, Chun SS, Yoon SH, Kim SR (1993) Slope stability and geotechnical properties of sediment of the southern margin of Ulleung Basin, East Sea (Sea of Japan). Mar Geol 110:31–45

Lee SH, Chough SK, Back GG, Kim YB, Sung BS (1999) Gradual downslope change in high-resolution acoustic characters and geometry of large-scale submarine debris lobes in Ulleung Basin, East Sea (Sea of Japan), Korea. Geo-Mar Lett 19:254–261

Lee SH, Bahk JJ, Chough SK (2004) Late Quaternary sedimentation in the eastern continental margin of the Korean Peninsula. In: Clift P, Kuhnt W, Wang P, Hayes D (eds) Continent ─ ocean interactions within east Asian marginal seas, vol 149, Geophysical monograph. American Geophysical Union, Washington, DC, pp 205–233

Lee SH, Bahk JJ, Kim HJ, Lee KE, Jou HT, Suk BC (2010) Changes in the frequency, scale, and failing areas of latest Quaternary (<29.4 cal. ka B.P.) slope failures along the SW Ulleung Basin, East Sea (Japan Sea), inferred from depositional characters of densely dated turbiditic successions. Geo-Mar Lett 30:133–142

Locat J, Lee HJ (2002) Submarine landslides: advances and challenges. Can Geotech J 39:193–212

Mulder T, Cochonat P (1996) Classification of offshore mass movements. J Sediment Res 66:43–57

Piper DJW, Farre JA, Shor A (1985) Late Quaternary slumps and debris flows on the Scotian slope. Bull Geol Soc Am 96:1508–1517

Piper DJW, Cochonat P, Morrison ML (1999) The sequence of events around the epicentre of the 1929 Grand Banks earthquake: initiation of debris flows and turbidity current inferred from sidescan sonar. Sedimentology 46:79–97

Tripsanas E, Piper DJW, Jenner KA, Bryant WR (2008) Submarine mass-transport facies: new perspectives on flow processes from cores on the eastern North American margin. Sedimentology 55:97–136

Yoon SH, Chough SK (1995) Regional strike slip in the eastern continental margin of Korea and its tectonic implications for the evolution of Ulleung Basin, East Sea (Sea of Japan). Bull Geol Soc Am 107:83–97

Chapter 37
Seismic Characteristics and Distribution of Large Scale Mass Transport Deposits in the Qiongdongnan Basin, South China Sea

Dawei Wang, Shiguo Wu, Fuliang Lü, and George Spence

Abstract Large-scale mass-transport deposits (MTDs), here called the Huaguang MTDs, occur in the South China Sea region within the Qiongdongnan Basin, north of Guangle Uplift and west of Xisha Uplift. As a large-scale buried MTD system, the Guaguang MTDs cover an area of more than 18,000 km^2 and can be divided into four distinct sub-MTDs. Sediment sources for MTD1, MTD2 and MTD3 are from southern Guangle Uplift and eastern Xisha Uplift, and their transport directions are generally from south to north. However, the flow direction for MTD4, located in the northwest portion of the study area, is from west to east with a source in the Yinggehai Basin region. MTD1 and MTD4 merge to form two connected depocenters. Along their length, the MTDs are seen as continuous packages that extend to the northwest, with a maximum distance of ~180 km from Guangle Uplift. The maximum thickness of the deposits reaches ~950 ms two-way travel time. The Huaguang MTDs show prominent features characteristic of large landslides. The overall seismic facies includes highly disrupted reflectors, truncated reflectors, and steep side walls. The lateral margins are easily recognized on seismic profiles perpendicular to the flow direction as abrupt boundaries between the inner highly chaotic or weakly reflective seismic facies and the outer continuous undisturbed facies. The MTDs are widely distributed in the Late Miocene upper Huangliu

D. Wang (✉) • S. Wu
Key Laboratory of Marine Geology and Environment, Institute of Oceanology, Chinese Academy of Sciences, Qingdao 266071, China

Marine Oil & Gas Research Center, Institute of Oceanology, Chinese Academy of Sciences, Qingdao 266071, China
e-mail: wangdawei@qdio.ac.cn

F. Lü
PetroChina Hangzhou Institute of Geology, China National Petroleum Corporation, Hangzhou 310023, China

G. Spence
School of Earth and Ocean Sciences, University of Victoria, Victoria, CanadaV8W 3V6

S. Krastel et al. (eds.), *Submarine Mass Movements and Their Consequences*, Advances in Natural and Technological Hazards Research 37, DOI 10.1007/978-3-319-00972-8_37,

Formation (8.3–5.5 Ma). The analysis of the Huaguang MTDs provides constraints for Late Miocene tectonic activity on the passive continental margin of the South China Sea.

Keywords Mass transport deposits • Seismic characteristics • Qiongdongnan Basin • South China Sea

37.1 Introduction

In this chapter, we use new 2D/3D seismic data to study mass transport deposits (MTDs) in the Qiongdongnan Basin (QDNB) and its surrounding slopes. The study area, on the northwestern slope of the South China Sea (SCS, Fig. 37.1), includes the

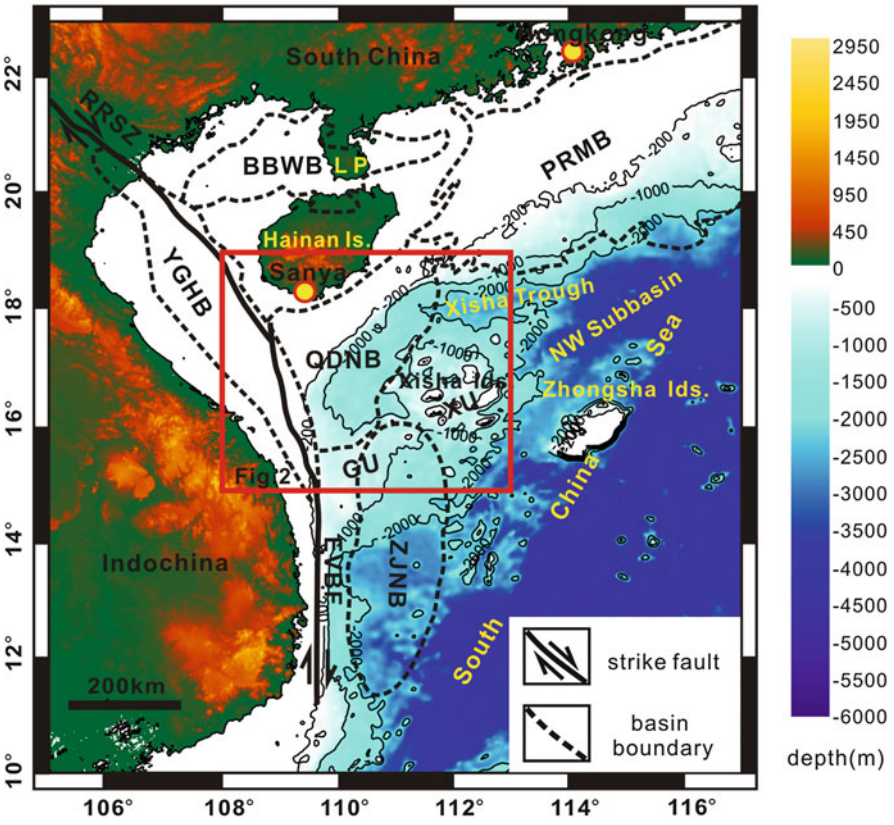

Fig. 37.1 Location of major Cenozoic basins in the western and northern part of the SCS. *BBWB* Beibuwan Basin, *YGHB* Yinggehai Basin, *QDNB* Qiongdongnan Basin, *PRMB* Pearl River Mouth Basin, *ZJNB* Zhongjiannan Basin, *LP* Leizhou Peninsula, *XU* Xisha Uplift, *GU* Guangle Uplift, *RRSZ* Red River Shear Zone

southern part of QDNB and the western part of the Xisha Uplift. The MTDs affect the upper Huangliu Formation of Late Miocene age. The top interface (5.5 Ma) of the upper Huangliu Formation is the marker of a reversal from left- to right-lateral motion of the Red River Shear Zone (RRSZ). We aim to understand the large-scale nature of the Late Neogene MTDs, including their seismic characteristics, architecture, distribution, transport direction and formation mechanism.

37.1.1 Geological Setting

The QDNB on the northwest slope of the SCS is bounded by the Yinggehai Basin (YGHB) to the west (Fig. 37.1). The basins along the northern SCS margin were formed by lithospheric stretching during the Paleocene and Oligocene, followed by thermal subsidence (Li et al. 1998). In the QDNB the rift phase was associated with the initial opening of the SCS in the Eocene and Oligocene (Ru and Pigott 1986), and post-rift subsidence followed after Early Miocene (∼21 Ma). The terrigeneous sediments were transported from two main sources during the Cenozoic: the South China Block and Indochina Peninsula (Yao et al. 2008). Sediment sources for the basins on the SCS western shelf and slope are rivers that are draining into the SCS along the Vietnam coast. These small narrow mountainous rivers are prominent in the central part of the coast.

The Xisha Uplift, lying south of the Xisha Trough and west of the NW Subbasin of the SCS (Fig. 37.1), is considered as a separate mini-block associated with Cenozoic rifting. Based on wide-angle seismic profiles and heat flow measurements along the northern margin of the South China Sea, Qiu et al. (2001) and Shi et al. (2002) suggested that the Xisha Uplift originated from the South China Block. Thus, the formation and evolution of the Xisha Uplift and the NW Subbasin were likely closely related (Taylor and Hayes 1983).

37.1.2 Data and Methods

The data used in this chapter include high resolution 2D seismic data acquired by the China National Petroleum Corporation in 2005 and drilling data from well YC35-1-2 (Fig. 37.2). The seismic data, with dominant frequencies of 40–60 Hz, cover an area of 26,000 km^2. The seismic stratigraphy was mapped and geological ages of the MTDs were determined using the well stratigraphy and previous research results.

MTDs are characterized by low amplitude, chaotic and translucent seismic reflections, surrounded by undisturbed sedimentary strata. Headwalls, lateral walls, top surfaces and basal surfaces can be identified in seismic profiles. The headwalls and lateral walls are continuous normal faults or escarpments (Gee et al. 2006; Bull et al. 2009; Moscardelli and Wood 2008; Perov and Bhattacharya 2011), and they form continuous boundaries between undisturbed and disturbed sedimentary strata.

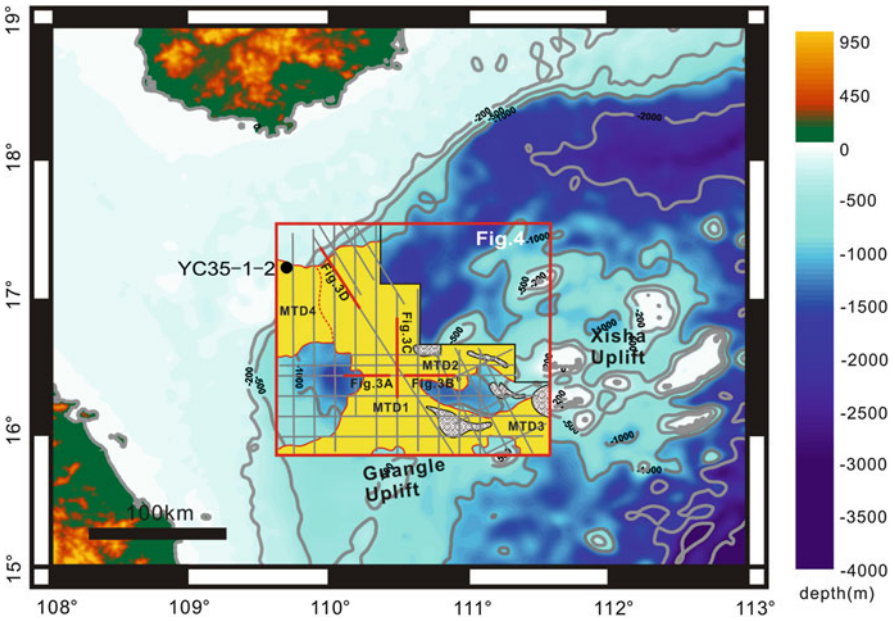

Fig. 37.2 Location of high resolution 2D seismic data and well YC35-1-2 used for this study. The *thick red lines* show the 2D seismic profiles discussed in this chapter. The polygon outlined by *thick red lines* marks the location of the research area. The *thick black dashed lines* mark the boundaries of the basins in the northwestern region of the SCS

The bottom surface of the MTDs is a shear erosional surface, while the top surface is the continuous surface between the lower chaotic strata and upper continuous strata. By recognizing diagnostic slide characteristics and calculating thicknesses of an MTD, we can determine the transport direction of the MTD, the sedimentary depocenter and the source region. The high resolution 2D seismic data enable us to map the distribution of MTDs, and to evaluate possible trigger mechanisms.

37.2 Results

37.2.1 The Margin of MTDs

Although the lateral and headwall boundaries of the MTDs are characterized by escarpments, the Huaguang MTDs show differences compared to typical submarine landslides in that there is a gradual transition between the MTDs and the undisturbed facies that surround them. Moreover, the Huaguang MTDs form a complex of many sub-MTDs, with characteristic transitions between the different sub-MTDs.

On seismic profiles, the character of the MTD boundaries varies from west to east, which corresponds to a direction normal to the main MTD transport direction.

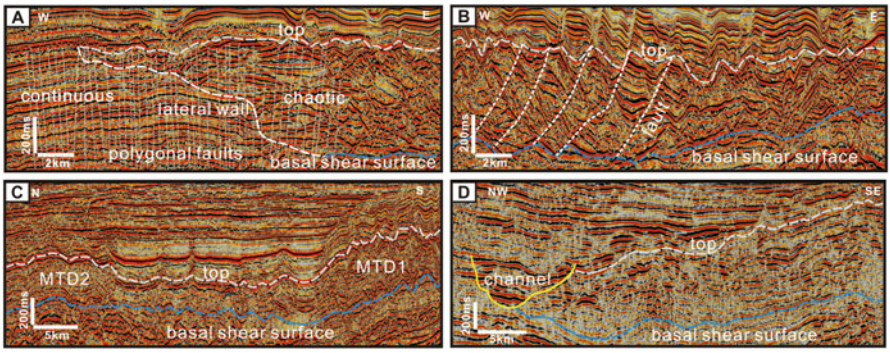

Fig. 37.3 Seismic characteristics of Huaguang MTDs. (**a**) The western lateral wall, (**b**) the eastern part of MTD1, (**c**) the transition region between MTD1 and MTD2, (**d**) the toe of the MTDs

At the western boundary of MTD1 (Fig. 37.3a), the deeper portion is a steep fault, while the shallow portion dips at a more gentle angle. Near the eastern boundary of MTD1 (Fig. 37.3b), a series of parallel normal faults can be interpreted. Seismic profiles across the headwall region of MTD1 are not shown in this chapter, since the headwall is not imaged as a typical normal fault. We consider that the buried MTDs were severely deformed by deformation after the mass wasting event, and therefore the typical characteristics of the headwall are difficult to identify.

On a north-to-south seismic profile crossing the transition between MTD1 and MTD2 (Fig. 37.3c), the MTD strata are thinner and deeper within the transition region than in the main body of the MTDs. On a profile that crosses the toe of the MTDs (Fig. 37.3d), it is clear that folds and faults have formed in the strata immediately overlying the MTDs, although details of these structures, such as the expected thrust faults or pressure ridges, cannot be resolved due to limitations in the 2D seismic data. However, a prominent channel is easily identified at the toe of the MTDs (Fig. 37.3d). This channel, the Central Canyon, has been mapped previously (Su et al. 2009; Yuan 2009) and has been shown to extend for a length of about 425 km, with a width of 3–12 km and an approximate area of 5,000 km^2. It shows that an MTD can be eroded by an overlying channel system after the MTD is formed.

On other seismic profiles, not shown, two additional sub-MTDs have been identified. MTD3 was deposited in a local bathymetric low in the south-eastern portion of the study area. MTD4 is located in the north-western area. Its sidewalls are easily identified on north-south seismic profiles, similar to how the sidewalls of MTD1 and MTD2 are identified on profiles in the cross-transport-direction. However, the boundary between MTD4 and MTD1 is difficult to recognize due to the sparse 2D seismic grid and low resolution. Nevertheless, as discussed in Sect. 37.2.3, we infer two separate depocenters and sources for these MTDs. The inferred boundary between the MTDs, indicated by a dashed line in the thickness isomap of Fig. 37.4, corresponds to the minimum deposit thickness between the two depocenters.

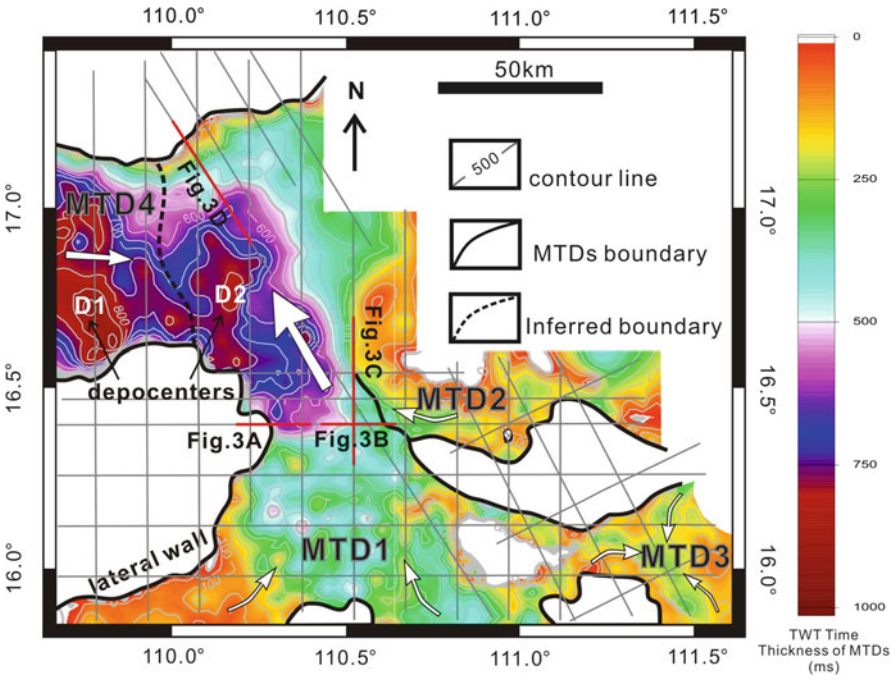

Fig. 37.4 The TWT time thickness isomap of MTDs. Two connected depocenters, D1 and D2, are identified in the northwestern part of the study area. They show that there are two separate sources and transport directions, from west to east and from south to northwest. The depocenters, which are located in the downstream region of the MTDs, usually occur in the translational and toe domains

37.2.2 Seismic Characteristics of MTDs

Bull et al. (2009) subdivided the typical MTD into a headwall domain, a translational domain, and a toe domain. Each domain exhibits distinct kinematic indicators, which are identified by key geometrical criteria. In the tensional headwall domain, rock fails by normal faulting, with the initial movement perpendicular to the steep headwall scarp. Downdip, there may be extensional ridges or blocks, separated by normal or listric faults. In the mainly strike-slip translational domain, debris flow speed gradually slows down with the gradually decreasing slope gradient. In the compressive toe domain, the translated material may be confined downslope against undisturbed strata, or it may continue freely across the seafloor and gradually lose kinetic energy due to frictional forces. Pressure ridges or thrust and fold systems form with an orientation parallel or sub-parallel to the flow direction or direction of maximum compression.

The Huaguang MTDs have some specific seismic characteristics similar to typical MTDs. It is a complex MTD system comprising four sub-MTDs. We will focus on the seismic characteristics of MTD1 and MTD2, which form the main

body of the Huaguang MTDs and are covered by a dense grid of 2D seismic lines. The strata in the transition region between MTD1 and MTD2 are deformed in a series of small anticlines (Fig. 37.3c). On the whole, discontinuous events are mixed with chaotic half-translucent facies. The discontinuous layers show a macroscopic sub-parallel convex-upward shape. These characteristics may be the result of compression produced by loading by the MTDs on either side of the transition region.

The western and eastern parts of MTD1 exhibit different seismic characteristics. In general, the internal strata of MTD1 show non-continuous seismic reflective events (Fig. 37.3a, b). In contrast, the strata above the top surface are more continuous parallel or sub-parallel layers. Within the western part of MTD1, some polygonal faults extend upward from the underlying strata (Fig. 37.3a). The polygonal faults are continuous, not cut or disrupted by the MTDs. Thus, the faulting must have occurred after the MTDs were formed. The internal strata in the eastern part of MTD1 are deformed in a series of fault blocks between normal faults that indicate an extensional strain environment (Fig. 37.3b). Within the fault blocks, the strata are sub-parallel and show macroscopic fold morphology. The upper parts of the strata are less disrupted than the more chaotic lower parts. This part of MTD1 belongs to the translational domain of the Huaguang MTDs. However, normal faults were found, not usual in the translational domain. The existence of the normal faults may indicate that the stress field of this area changes from an early compressional environment into a late extensional environment. The orientation of the normal faults indicates that the mass transport direction is from southeast to northwest in this local area. As well, the overlying strata have almost the same attitude as the top surface. However, underlying strata have a completely different attitude from the top surface and the internal strata of MTD1.

The strata at the toe, which were deposited after long-distance transport, show a chaotic, half-translucent, and locally continuous seismic reflectivity (Fig. 37.3d). That is, most strata have been completely deformed, but a small number of short continuous seismic events forming boudin-like structures may represent a portion of the strata that still retain their original form.

37.2.3 Distribution and Transport Direction of MTDs

Although the sparseness of the 2D seismic grid makes it difficult to determine the internal structure of the MTDs or their precise boundaries, we still can recognize the MTDs as chaotic zones that show discontinuous seismic reflections bounded above, below and laterally by regions of continuous reflections in the strata of upper Huangliu Formation (Fig. 37.4). As a large-scale buried MTD system, the Huaguang MTDs cover an area of more than 18,000 km^2. In the down-slope direction, the MTDs are seen as continuous packages that extend northwards to a maximum distance of ca.180 km from Guangle Uplift. In general, the thickness distribution of the MTDs shows that most deposits represent the translational and toe domains.

The thickness of MTD1 and MTD4 in the western portion of the study area is greater than that of MTD2 and MTD3 in the eastern portion (Fig. 37.4). We interpret two connected depocenters, D1 and D2, located in the northwestern part of study area. Here, the maximum MTD thickness reaches ca. 950 ms two-way travel time. As discussed below, D2 has a source located in the Guangle Uplift or Xisha Uplift. D1 has a separate source located in the western region outside the study area.

We reconstruct the transport direction from the topographic trends, seismic characteristics and deposit thicknesses (Fig. 37.4). The Huaguang MTDs include four sub-MTDs. The transport direction is different for each sub-MTD. For MTD1, located in the central part of the study area, the flow direction is from south to north-west in general. The initial transport direction for MTD2 is from north-east to south-west. The direction changes to north-west after MTD2 converges with the main body of MTD1. For MTD3, located in the southern portion of the study area, sediment is transported from local surrounding highs to a central low. The source regions for MTD1, MTD2 and MTD3 are the Guangle Uplift and the Xisha Uplift (Fig. 37.2). However, as the maximum deposit thickness is located in the north-westernmost portion of the study area and it is unlikely that the flow direction for MTD1 would turn by 90° towards higher topography, we infer that these thick deposits are a separate sub-MTD, identified here as MTD4. That is, there must be an additional source region to the west outside the study area, which we assume is the shallower shelf region occupied by the Yinggehai Basin. The transport direction for this source is from west to east. Hence the Huaguang MTD system originates from three source areas, including the Guangle Uplift, the Xisha Uplift and the Yinggehai Basin.

37.3 Discussion

In response to the collision of India and Eurasia, the Indochina Block and the region south of it were moved to the southeast through a series of major left-lateral fault zones. Three successive deformation phases for the offshore RRSZ include left-lateral movement from ~30 to 16 Ma, a transitional phase between 16 and 5.5 Ma when slip velocity decreased and eventually ceased, and a reversal to right-lateral movement with low rates after 5.5 Ma (Clift 2006; Zhu et al. 2009; Tapponnier et al. 2001). The top surface of the Huaguang MTDs corresponds to a stratigraphic horizon with an age of 5.5 Ma, based on correlations with well YC35-1-2. We thus infer that the MTDs formed at 5.5 Ma. This time is consistent with the time of RRSZ reversal from left- to right-lateral motion (Clift 2006).

Rapid sediment accumulation is a key factor for the formation of MTDs. In central Vietnam, a significant change in regional cooling rate during the Upper Miocene is linked to enhanced erosion and deposition of prograding sediments in adjacent offshore basins (Carter et al. 2000). Denudation rates also shifted at this

time from ~34 m/Myr to 390–500 m/Myr. Fyhn et al. (2009) suggested that these changes were the result of seaward tilting of the region onshore and offshore of central Vietnam during the Late Neogene. We suggest that the tilting affected most of east Indochina, including north Vietnam where mountain rivers can transport clastics into the Qiongdongnan Basin. From late Neogene to recent, detrital material of terrigenous origin has also gradually overlain the carbonate platform deposits of the Guangle Uplift (Fyhn et al. 2009), although the Xisha Uplift has remained a carbonate platform since the early Neogene.

Neogene volcanism is relatively widespread in extensive areas of the western SCS and southeastern Indochina. The magmatism was vigorous during the Pliocene-Recent in the Leizhou Peninsula and during the Quaternary in northern Hainan Island (Wang et al. 2001; Ho et al. 2000), but quiet or very weak before the Pliocene (5.5 Ma). Our seismic data image many basement highs in the study area. We interpret these as Late Miocene volcanoes, nearly coeval with the formation of the Huaguang MTDs.

We believe that the rapid sedimentation rate has a direct relationship with the increase in erosion rates caused by tectonic events during 10.5–5.5 Ma. The rapid offshore sediment accumulation associated with the upper Huangliu formation (8.3–5.5 Ma) led to the regional development of steep slopes, high pore pressures and weak cementation. These properties provide the basic conditions for the formation of mass transport deposits. The Late Miocene tectonic activities, including volcanism and fault activation or reactivation, supply the necessary trigger mechanisms for the initiation of the MTDs.

37.4 Conclusions

The Huaguang MTDs form a large-scale buried MTD system which covers an area of about 18,000 km^2 in the southern portion of QDNB. Most of the MTDs show a seismic facies characterized by a chaotic zone with discontinuous seismic reflections bounded by continuous strata. The MTDs come from the Guangle Uplift, the Xisha Uplift and the Yinggehai Basin region on the shelf. After Early Miocene, the offshore basins of Vietnam received abundant sediments. Fault activation or reactivation and volcanism were the immediate trigger mechanisms for the MTDs.

Acknowledgements We acknowledge editor David Völker, and the two reviewers Brandon Dugan and Thomas Lüdmann for their constructive comments which greatly improve this manuscript. We thank China National Petroleum Company and China National Offshore Oil Cooperation for their permissions to release the seismic and well data. This work was supported by the National Natural Science Foundation of China (40906028), the Open Fund of the Key Laboratory of Marine Geology and Environment, China Academy of Science (MGE2010KG07).

References

Bull S, Cartwright J, Huuse M (2009) A review of kinematic indicators from mass-transport complexes using 3D seismic data. Mar Petrol Geol 26:1132–1151

Carter A, Roques D, Bristow CS (2000) Denudation history of onshore Central Vietnam: constraints on the Cenozoic evolution of the western margin of the South China Sea. Tectonophysics 322:265–277

Clift PD (2006) Controls on the erosion of Cenozoic Asia and the flux of clastic sediment to the ocean. Earth Planet Sci Lett 241:571–580

Fyhn MBW, Boldreel LO, Nielsen LH (2009) Geological development of the Central and South Vietnamese margin: implications for the establishment of the South China Sea, Indochinese escape tectonics and Cenozoic volcanism. Tectonophysics 478:184–214

Gee M, Gawthorpe R, Friedmann S (2006) Triggering and evolution of a giant landslide, offshore Angola revealed by 3D seismic stratigraphy and geomorphology. J Sediment Res 76:9–19

Ho KS, Chen JC, Juang WS (2000) Geochronology and geochemistry of late Cenozoic basalts from the Leiqiong area, Southern China. J Asian Earth Sci 18:307–324

Li ST, Lin CS, Zhang QM (1998) Dynamic process of episodic rifting in continental marginal basin and tectonic events since 10Ma in South China Sea. Chin Sci Bull 43(8):797–810

Moscardelli L, Wood LJ (2008) New classification system for mass transport complexes in offshore Trinidad. Basin Res 20:73–98

Perov G, Bhattacharya JP (2011) Pleistocene shelf-margin delta: intradeltaic deformation and sediment bypass, Northern Gulf of Mexico. AAPG Bull 95:1617–1641. doi:10.1306/01271109141

Qiu X, Ye S, Wu S, Shi X, Zhou D, Xia K, Flueh ER (2001) Crustal structure across the Xisha Trough, northwestern South China Sea. Tectonophysics 341:179–193. doi:10.1016/S0040-1951(01)00222-0

Ru K, Pigott JD (1986) Episodic rifting and subsidence in the South China Sea. AAPG Bull 70(9):1136–1155

Shi X, Zhou D, Qiu X, Zhang Y (2002) Thermal and rheological structures of the Xisha Trough, South China Sea. Tectonophysics 351:285–300. doi:10.1016/S0040-1951(02)00162-2

Su M, Li JL, Jiang T, Tian S, Zhang C, Xie XL (2009) Morphological features and formation mechanism of Central Canyon in Qiongdongnan Basin, Northern South China Sea. Mar Geol Quat Geol 29(4):85–93

Tapponnier P, Xu Z, Roger F, Meyer B, Arnaud N, Wittlinger G, Yang J (2001) Oblique stepwise rise and growth of the Tibet Plateau. Science 294:1671–1677

Taylor B, Hayes DE (1983) Origin and history of the South China Sea Basin. In: Hayes DE (ed) The tectonic and geologic evolution of Southeast Asian seas and islands: Part 2. American Geophysical Union, Washington, pp 23–56

Wang JH, Yin A, Harrison TM, Grove M, Zhang YQ, Xie GH (2001) A tectonic model for Cenozoic igneous activities in the eastern Indo-Asian collision zone. Earth Planet Sci Lett 188:123–133

Yao GS, Yuan SQ, Wu SG, Zhong C (2008) The double provenance supply depositional model and its exploration prospect in the deepwater of Qiongdongnan Basin. Petrol Explor Dev 35(6):685–691. doi:10.1016/S1876-3804(09)60101-4

Yuan SQ, Wu SG, Lüdmann T, Yao GS, Lv FL, Gao F, Wang H, Li L (2009) Fine-grained Pleistocene deepwater turbidite channel system on the slope of Qiongdongnan Basin, northern South China Sea. Mar Pet Geol 26:1441–1451. doi:10.1016/j.marpetgeo.2009.03.007

Zhu MZ, Graham S, McHargue T (2009) The Red River Fault zone in the Yinggehai Basin, South China Sea. Tectonophysics 476(3–4):397–417. doi:10.1016/j.tecto.2009.06.015

Chapter 38
Modification of the Shape of Pacific Islands by Submarine Landslides: Banaba, Nauru, and Niue

Jens C. Krüger and Susanne M.L. Pohler

Abstract The three uplifted atoll islands Banaba, Nauru and Niue are shaped by submarine mass wasting. For each island, the most distinct submarine landslide is described using multibeam bathymetry. All three islands are fractured through tectonic uplift. Subaerial exposure caused further structural weakness through karstification and dolomitisation, which increased porosity and permeability of the limestone cap. Initial fractures became enlarged into chasms, caves and caverns which ultimately resulted in flank failure. The ages of these submarine landslides are poorly constrained, but were probably youngest for Home Bay, Banaba, (>10,000 BP); between 1.6 Ma and 10,000 BP for Anabar Bay, Nauru; and 700,000 BP or less for Tepa Point, Niue.

Keywords Central Pacific Ocean • Banaba • Nauru • Niue • Raised atolls • Slope failure • Submarine landslides

38.1 Introduction

Fairbridge (1950) first commented on the stellate shape of atolls and suggested mass wasting as the dominant process for this. Detailed bathymetry of Banaba, Nauru, and Niue showed large submarine slope failures along the flanks of the three raised carbonate islands. The three islands are located in the SW and central Pacific Ocean (Fig. 38.1) and are subject to tectonic forces associated with plate convergence (Kroenke et al. 2004).

J.C. Krüger (✉)
Applied Geoscience and Technology Division, Secretariat of the Pacific Community, Private Mail Bag, Suva, Fiji
e-mail: jensk@spc.int

S.M.L. Pohler
School of Marine Studies, University of the South Pacific, Private Mail Bag, Suva, Fiji

S. Krastel et al. (eds.), *Submarine Mass Movements and Their Consequences*, Advances in Natural and Technological Hazards Research 37, DOI 10.1007/978-3-319-00972-8_38,

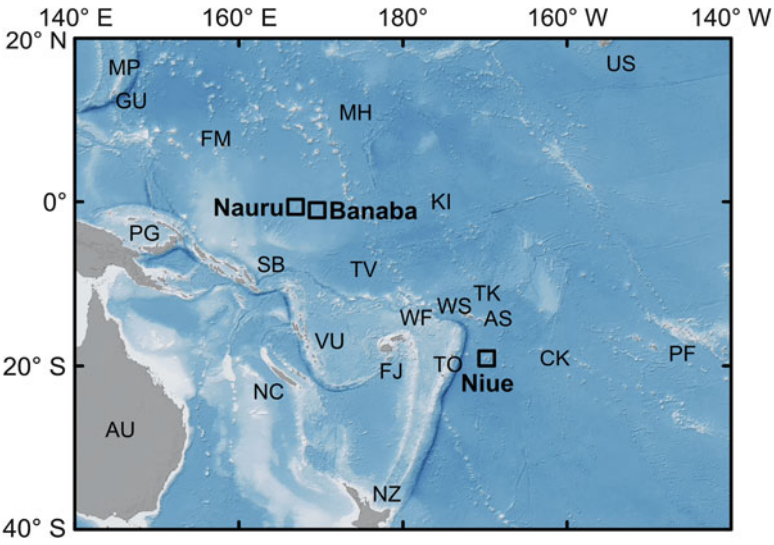

Fig. 38.1 Location diagram of the southwest Pacific Ocean with country and territory codes (except Nauru and Niue), showing raised limestone islands referred to in this study (*black boxes*). Shallow to deep bathymetry is shown using *white* to *dark blue* colours

38.2 Methodology

Bathymetry was obtained using a mid-ocean depth multibeam echosounder (Reson SeaBat 8160) operated from a 25 m survey vessel. A gyro compass provided heading information, and a motion sensor was used to correct for the heave, roll and pitch of the vessel. Positioning was provided by a stand-alone dual-frequency Global Positioning System. Sound velocity profiles were derived from conductivity, temperature and depth data collected to a maximum depth of 400 m on a daily basis. These data were supplemented with external sources of sound velocity data from ARGO floats (www.argo.ucsd.edu) and the Generalized Digital Environmental Model (128.160.23.42/gdemv/gdemv.html) for depths beyond 400 m.

Surveys were conducted at an average speed of six knots by circumnavigating the islands four or more times at increasing distances from the shoreline to the depth limit of the echosounder. The water depths in mapped areas ranged from 50 to 2,000 m. For acquisition and post-processing Hypack software was used (www.hypack.com). Digital elevation models (DEMs) were calculated and visualised using Surfer software (www.goldensoftware.com). DEMs were supplemented with publically available bathymetry from previous surveys, as well as satellite derived bathymetry. Further details of the surveys techniques, equipment, and data sources can be found in Kruger (2008), Kruger and Sharma (2008), and Sharma and Kruger (2008), for Niue, Nauru and Banaba, respectively.

38.3 Results

Between 2004 and 2008 high-resolution bathymetric surveys of three raised central and SW Pacific atoll islands (Banaba, Nauru and Niue) were completed.

38.3.1 Banaba Island

Banaba is located approximately 450 km southwest of Tarawa, Kiribati, at 0°51′S and 169°32′W (Fig. 38.1). Land area is about 2.5 km long (N-S) by 3.0 km wide (E-W), with a maximum elevation of 81 m, and an area of approximately 6 km^2. The coastline is formed by nine and a half kilometers of predominantly steep limestone cliffs which represent the former reef rim of the raised atoll. The island is surrounded by a fringing rock platform and reef complex up to 200 m wide.

38.3.1.1 Geological Setting

The uplift of Banaba maybe due to collision-related structural deformation of the Pacific plate at the Ontong Java Plateau, presumed to have intensified about 2.6 million years ago, and probably continuing today (Kroenke et al. 2004). The dolomite surface in the center of the island is dissected into pinnacles forming a *karrenfeld,* formed by radial and concentric cracking of the uplifted island (Hutchinson 1950).

38.3.1.2 Slope Geomorphology

The water depths within the survey area attain 2,100 m. Below the reef crest, 50 m-wide submarine terraces are found at 10 and 20 m (Fig. 38.2). Between water depths of 30–200 m, the seabed exhibits slopes of 40–60°. A distinct terrace scarp follows the 400 m isobath. There are several large submarine reef front landslides on the SW and NW flanks of the island, with headscarp slopes of 30–60°, originating at the 300 m isobath. Below a depth of 500 m, the north and east flanks of Banaba exhibit a variable relief on a slope of 30–60°, comprising numerous channels separated by minor mounds and lobes approximately 200 m in height.

Banaba's most distinct feature is Home Bay to the south of the island. The bay is the surface expression of the crown and headscarp of a large submarine landslide that breaches the terrace scarp and the reef front slope (Fig. 38.2). The seaward convex headscarp is two kilometers wide and up to 500 m high. The Home Bay slide is trending NE-SW and is about 1.5 km wide with flanks rising over 300 m above the canyon floor.

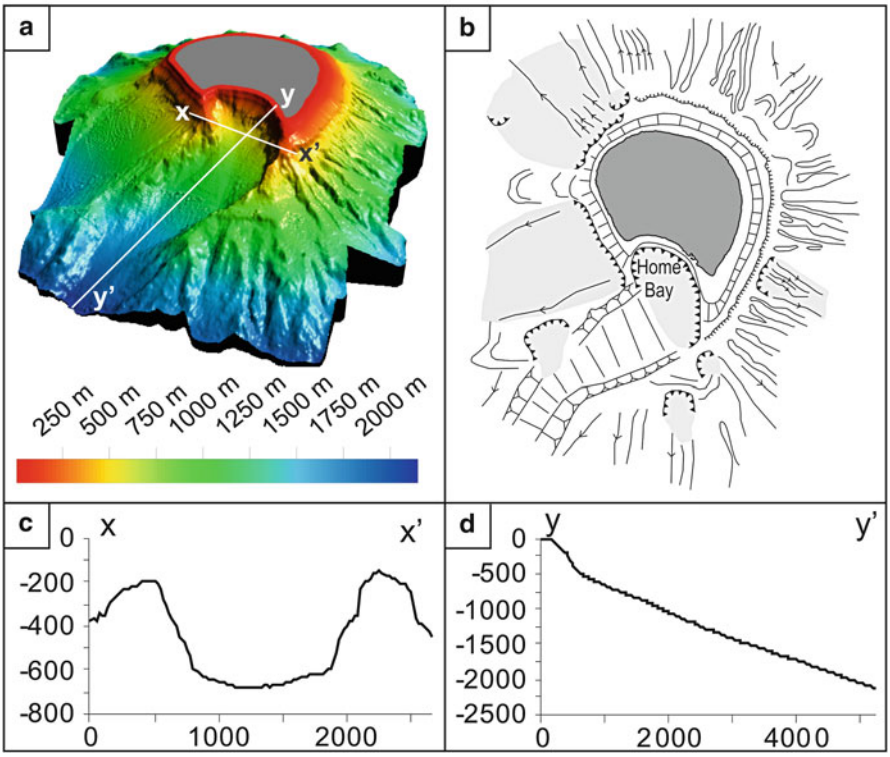

Fig. 38.2 (**a**) Three-dimensional perspective bathymetry of Banaba, Kiribati, looking north. The dominant feature is a large submarine scarp forming Home Bay, and breaching the Holocene reef platform. (**b**) Interpretation of principal geomorphology showing numerous mass wasting features (See Fig. 38.3b for legend). Profile across (**c**), and along canyon (**d**), with location shown in (**a**). Home Bay canyon is about 1.5 km wide and over 300 m deep, trending NE-SW

38.3.2 Nauru

Nauru Island, located at 0°31′S and 166°56′E (Fig. 38.1) is a raised atoll comprising a single island with a maximum elevation of 71 m, standing some 4–5 km above the surrounding ocean floor of the southern Nauru Basin. Total land area is about 21 km^2.

38.3.2.1 Geological Setting

The Nauru volcanic base was presumably constructed by hotspot volcanism during the mid-Eocene to Oligocene time, or 29–47 million years ago (Jacobsen et al. 1997). It is estimated that the seamount is capped by about 500 m of limestone, with uplift and subaerial exposure of the carbonate platform during the Pleistocene,

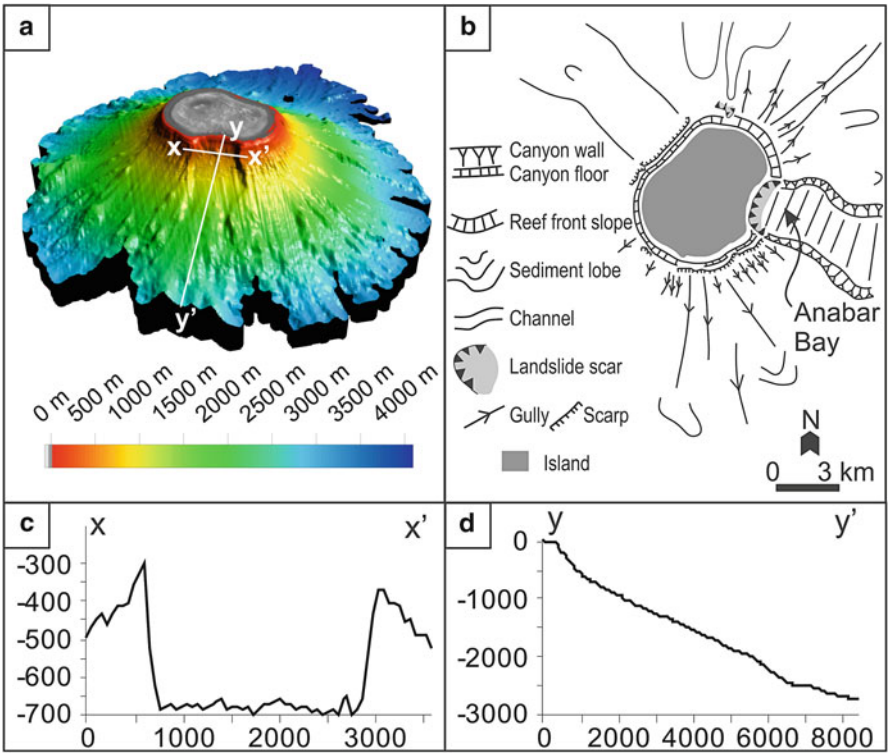

Fig. 38.3 (**a**) Three-dimensional perspective bathymetry of Nauru, looking west. The dominant feature is a large submarine scarp forming Anabar Bay. (**b**) Interpretation of principal geomorphology showing numerous mass wasting features. Profile across (**c**), and along canyon (**d**), with location shown in (**a**). Anabar Bay canyon is about 2.5 km wide and over 350 m deep, trending NW-SE

1.6 Ma ago (Jacobsen et al. 1997). Analogous to Banaba, the uplift of Nauru is presumed to be related to collision-related structural deformation of the Pacific plate at the Ontong Java Plateau (Kroenke et al. 2004).

38.3.2.2 Slope Geomorphology

The surveyed water depth around Nauru ranges from 3 to 1,735 m (Fig. 38.3). Within the 500 m isobath, or to a distance of approximately 800 m offshore, the submarine slope descends at about 45°. Beyond this, the seabed deepens an average gradient of 31° near the seaward limits of the survey area. A near continuous submarine scarp encircles the island in close proximity (350 m) to the coastline. The top of the scarp is at a water depth of approximately 120 m and descents to about 180 m. Further downslope, a second set of scarps, also sub-parallel to the

coastline, occur in water depths of approximately 300 m. These are concentrated to the south and northeast of the island with a scarp height of approximately 80 m, and are associated with numerous channels orientated radially downslope (Fig. 38.3).

The most distinctive seabed feature is the Anabar Bay submarine landslide located on the eastern flank of the Nauru edifice. The upslope arcuate scarp of this mass failure occurs in a water depth of 250 m and extends over a distance of approximately 4 km, with a maximum headscarp height of 400 m (Fig. 38.3). The side walls of the Anabar Bay submarine landslide are near vertical, exhibiting maximum slope angles at 80°.

38.3.3 Niue

Niue is located approximately 430 km east of Vava'u, Tonga at 19°03′S and 169°52′W (Fig. 38.1). Land area is about 21.5 km long (N-S) by 14.5 km wide (E-W), with a maximum elevation of 68 m, and an area of approximately 263 km^2. The coastline is formed by 78 km of predominantly steep limestone cliffs which represent the reef rim of a former atoll. The island is enclosed by a fringing rock platform and reef complex up to 150 m wide.

38.3.3.1 Geological Setting

The island of Niue is a carbonate platform capping a submarine volcanic cone that rises more than 4,000 m from the surrounding seafloor. Niue's westward movement toward the Tongan subduction zone has carried it onto a lithospheric bulge, subaerially exposing the previously subsiding atoll. The carbonate sedimentary rocks occur to a depth of 300–400 m (Hill 1996). The uppermost 300 m of the carbonate facies have been reported to be middle to late Miocene (Wheeler and Aharon 1997).

38.3.3.2 Seabed Morphology

The nearshore bathymetry at Alofi shows two terraces below the fringing reef platform (Fig. 38.4). The first is a 150 m-wide terrace at an average water depth of 13 m. The lower terrace is 80 m wide with an average depth of 34 m. Below these terraces, the seabed slopes at angles of 30–40° to depths of approximately 250 m. Depths to 800 m are characterised by gentler slopes of 0–20°. Depths of 800–1,400 m are characterized by maximum slopes of 30–60°, exceeding 60° to the north and northeast of the island. Depths exceeding 1,400 m are characterized by seabed that shows numerous escarpments, sidewalls and minor canyons. The morphological interpretation of publicly available data (Kruger 2008) in the vicinity of Niue shows a fault-bound graben structure to the NW, which has developed due to Niue's position on the peripheral bulge of the Tonga Trench. The southernmost fault

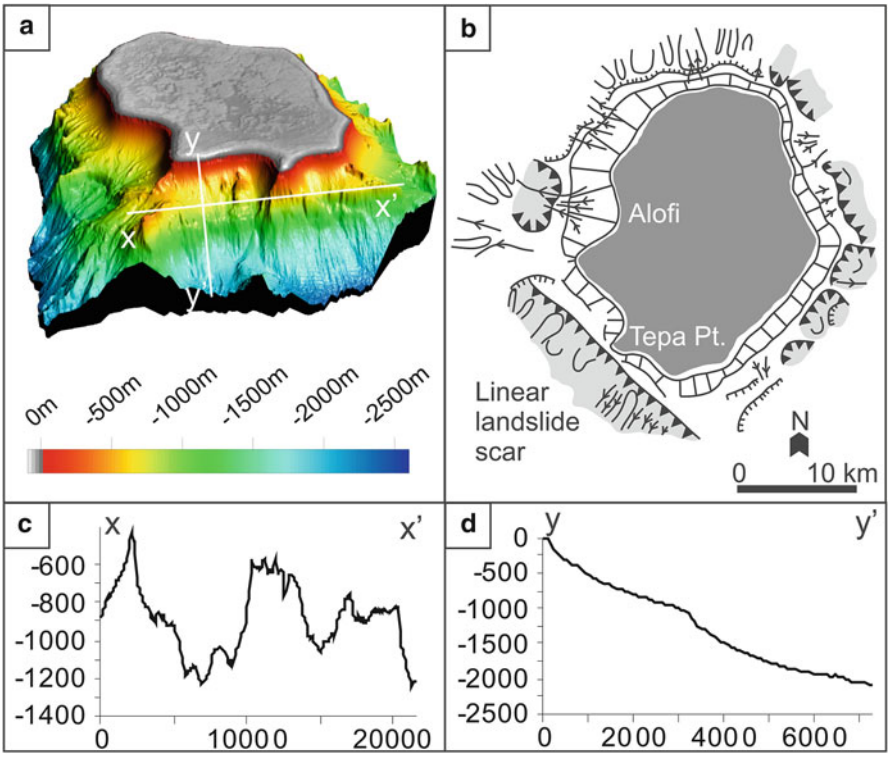

Fig. 38.4 (**a**) Three-dimensional perspective bathymetry of Niue NE. The dominant feature is a large linear submarine scarp off Tepa Point. (**b**) Interpretation of principal geomorphology showing numerous mass wasting features (See Fig. 38.3b for legend). Profile across (**c**), and along scarp (**d**), with location shown in (**a**). The scarp is approximately 18 km long originating at the 1,000 m isobaths, and trending NW-SE

mapped by Kruger (2008, Figure 5) continues along the 1,000 m isobath at Tepa Point, forming an approximately 18 km-long linear scarp along Niue's SW flank. The linearity of this scarp is in definite contrast to other collapse features observed on the bathymetric data, which are convex seaward and separated by terminal points that radially protrude from the coastline (Fig. 38.4).

38.4 Discussion

38.4.1 Causes of Submarine Landslides on Banaba, Nauru and Niue

The three surveyed islands have in common that they were subjected to structural stresses associated with uplift which resulted in radial and concentric cracking and

jointing (Banaba: Hutchinson 1950; Nauru: Jacobsen et al. 1997), and block-faulting (Niue: Schofield 1959). Keating and McGuire (2004) listed numerous factors for ocean island instability and suggested lithospheric flexure as one major cause for instability of Niue. Features associated with fracturing of Niue are water-filled chasms oriented sub-parallel to the coastline, and Schofield (1959) interpreted them as solution channels, which enlarged faults associated with slumping. He noted that "steep-dipping reverse-like faults do occur on the surface of landslides".

The morphology to the SW of Niue is interpreted as a mass flow deposit generated by downslope movement of debris from a fault-induced submarine landslide (Kruger 2008). The submarine landslide was presumably triggered by the growth of a normal fault, induced by the bending of the lithospheric plate, cutting across the southwest flank of the Niue edifice. Similar trench-parallel faulting was observed on the outer slopes of the Tonga Trench by Wright et al. (2000), where fault scarp heights of nearly 1 km have been reported (Mofjeld et al. 2004).

On Nauru the submarine landslide has significantly altered the subaerial shape of the island. The upslope region of the submarine mass failure is the arcuate eastern coastline of Nauru, forming Anabar Bay. Jacobson et al. (1997) speculated that the failure of the island flank was caused by the highly fractured nature of the island.

Keating and MacGuire (2004) listed karst mega-porosity resulting in low mechanical strength as main factor for instability of Johnston Atoll and Mururoa Atoll. On Niue deep cave systems (i.e. mega-porosity) were documented by Schofield (1959) and Banaba and Nauru have karstic surfaces which were exposed by mining activity on both islands. Karstification was caused initially by subaerial exposure of the atolls during eustatic sea level low-stands in glacial periods and now tectonic uplift has retained the atolls above sea level. Freshwater intrusion and mixing zone processes are associated with wide-spread dolomitization which occurred on all three islands and which exacerbated porosity through the recrystallisation process (Choquette and Pray 1970). It seems plausible that karst mega-porosity in addition to fracturing is responsible for the flank failures on all three islands.

38.4.2 Age of the Landslides

The modern reef terrace at Home Bay, Banaba, is much reduced in width, suggesting that the landslide involved the outer edge of the fringing reef complex. This indicates a Holocene age for the event, possibly even younger than the sea level maximum about 3,000 years BP.

The Nauru topography indicates that the Pleistocene atoll reef rim was removed by the Anabar Bay landslide, suggesting a maximum age of 1.6 Ma (post subaerial exposure). A Holocene minimum age is suggested as the modern reef platform is well developed.

The fault-induced landslide of Niue is associated with the ascend of the atoll onto the peripheral bulge in front of the Tonga Trench. Fieldes et al. (1960) calculated that uplift of the atoll commenced as early as 700, 000 years ago (Middle Pleistocene) and puts a maximum age on the landslide formation.

38.5 Conclusions

The multibeam bathymetry data of all three islands show that large submarine landslides have significantly altered the raised atoll perimeters, thus modifying the circular shape that would be expected from a carbonate cap that developed over a strato- or shield volcano. Large scale mass-wasting is known from many (if not most) atolls, seamounts and guyots world-wide and the reasons are many fold. In the case of the three raised atolls it appears that cracking and faulting of the islands associated with uplift and possibly in conjunction with karstification and dolomitisation has caused the massive flank failures. The ages of these submarine landslides are poorly constrained, but were probably youngest for Home Bay, Banaba, (>10,000 BP); between 1.6 Ma and 10,000 BP for Anabar Bay, Nauru; and 700,000 BP or less for Tepa Point, Niue. On all three islands uplift, fracturing and karstification are continuing and the hazards of landside-induced tsunamis and associated risks remain, as on other oceanic island e.g. Mangaia island, Cook Islands (Goff 2011).

Acknowledgements The authors would like to thank the European Community who funded this study through the 8th and 9th European Development Fund. Useful comments on the manuscript were received from John Collen and Brian McAdoo. Thanks also go to Tariq Rahiman for help in the production of the vector map for Banaba.

References

Choquette PW, Pray LC (1970) Geologic nomenclature and classification of porosity in sedimentary carbonates. AAPG Bull 54:207–250

Fairbridge RW (1950) Landslide patterns on oceanic volcanoes and atolls. Geogr J 115(1/3):84–88

Fieldes MG, Bearling G, Claridge GGC, Wells N, Taylor NH (1960) Mineralogy and radioactivity of Niue Island soils. N Z J Sci 3:658–675

Goff J (2011) Evidence of a previously unrecorded local tsunami, 13 April 2010, Cook Islands: implications for Pacific Island countries. Nat Hazard Earth Syst Sci 11:1371–1379

Hill PJ (1996) Niue and adjacent seamounts. In: Meylan MA, Glasby GP (eds) Manihiki Plateau and Capricorn seamounts, Niue, and Tofua trough: results of Tui Cruises, vol 10, SOPAC technical bulletin. South Pacific Applied Geoscience Commission, Suva, pp 31–44

Hutchinson GE (1950) Phosphatic Guano on the atolls of the Pacific Ocean, the biogeochemistry of vertebrate excretion. Bull Am Mus Nat Hist 96:160–259

Jacobsen G, Hill PJ, Ghassemi F (1997) Geology and hydrogeology of Nauru Island. In: Vacher HL, Quinn T (eds) Geology and hydrogeology of carbonate islands, vol 54, Developments in sedimentology., pp 707–742

Keating BH, McGuire WJ (2004) Instability and structural failure at volcanic ocean islands and the climate change dimension. Adv Geophys 47:175–271

Kroenke LW, Wessel P, Sterling A (2004) Motion of the Ontong Java Plateau in the hot-spot frame of reference: 122 Ma-present. In: Fitton JG, Mahoney JJ, Wallace PJ, Saunders AD (eds) Origin and evolution of the Ontong Java Plateau, vol 229, Geological society, special publication. Geological Society, London, pp 9–20

Kruger JC (2008) Niue technical report: high-resolution bathymetry survey of Niue. SOPAC project report ER49, South Pacific Applied Geoscience Commission, Suva, 44 pp

Kruger JC, Sharma A (2008) Nauru technical report: high-resolution bathymetry survey. SOPAC project report ER116, South Pacific Applied Geoscience Commission, Suva, 28 pp

Mofjeld HO, Symons CM, Lonsdale P, Gonz Lez FI, Titov VV (2004) Tsunami scattering and earthquake faults in the deep Pacific Ocean. Oceanogr Spec Issue 17(1):38–46

Schofield JC (1959) The geology and hydrology of Niue Island, South Pacific. New Zealand Geological Survey, Bulletin, vol 62. New Zealand Department of Scientific and Industrial Research, Wellington, 28 pp

Sharma A, Kruger JC (2008) Kiribati technical report: high-resolution bathymetry survey in Kiribati. SOPAC project report ER114, South Pacific Applied Geoscience Commission, Suva, 55 pp

Wheeler CW, Aharon P (1997) Geology and hydrogeology of Niue. In: Vacher HL, Quinn T (eds) Geology and hydrogeology of carbonate islands, vol 54, Developments in sedimentology. Elsevier, Amsterdam, pp 537–564

Wright DJ, Bloomer SH, MacLeod CJ, Taylor B, Goodlife AM (2000) Bathymetry of the Tonga Trench and forearc: a map series. Mar Geophys Res 21:489–511

Part VI
Interaction Between Ocean Circulation and MTDs

Chapter 39
Submarine Landslides and Contourite Drifts Along the Pianosa Ridge (Corsica Trough, Mediterranean Sea)

A. Cattaneo, G. Jouet, S. Charrier, E. Théreau, and V. Riboulot

Abstract The Corsica Trough between the island of Corsica and the mainland of Italy is dominated on its western side by turbidite channel-lobe systems fed by high-gradient rivers during glacial epochs, while the eastern side is markedly different. It is flanked by the Pianosa Ridge, a prominent tectonic structure confining the distal reaches of turbidite lobes and it is characterized by the development of contourite drifts with evident seafloor expression. The southern part of the Pianosa Ridge hosts a submarine landslide called 'Pianosa Slump' (PS, 6 km long, 14 km wide). Multichannel Sparker and Chirp profiles reveal the internal geometry of the PS, formed by two sediment bodies of up to 0.85 and 0.34 km^3. A buried submarine landslide below the PS shows that mass wasting is a recurrent process in this area. Preliminary results suggest that submarine landslides have volumes and ages comparable with those of turbidite lobes from the Golo turbidite system and contribute actively to their confinement and to basin filling. Relatively steep gradients, rapid contourite drift accumulation during times of sea level lowstands, and fluid escape from distal turbidite sandy lobes are the main factors conducive to seafloor instability.

Keywords Submarine landslides • Contourite drifts • Multibeam bathymetry • Seismic profiles • Pianosa Ridge • Tyrrhenian Sea

A. Cattaneo (✉)
Géosciences Marines, IFREMER, Centre de Brest, BP70, 29280 Plouzané, France

Istituto di Scienze Marine (ISMAR-CNR), Bologna, Via Gobetti 101, Bologna 40129, Italy
e-mail: antonio.cattaneo@ifremer.fr

G. Jouet • S. Charrier • E. Théreau • V. Riboulot
Géosciences Marines, IFREMER, Centre de Brest, BP70, 29280 Plouzané, France

S. Krastel et al. (eds.), *Submarine Mass Movements and Their Consequences*, Advances in Natural and Technological Hazards Research 37, DOI 10.1007/978-3-319-00972-8_39,

39.1 Introduction

The Corsica Trough is a narrow (40 km) and shallow, north–south trending basin separating the Corsica shelf (to the west) from the Pianosa Ridge (to the east) and connecting the Tyrrhenian and Ligurian basins in the Western Mediterranean Sea (Viaris de Lesegno L 1978; Bacini Sedimentari 1979; Fig. 39.1). The Golo Basin within the Corsica Trough is characterized by a slope asymmetry with a gentle slope

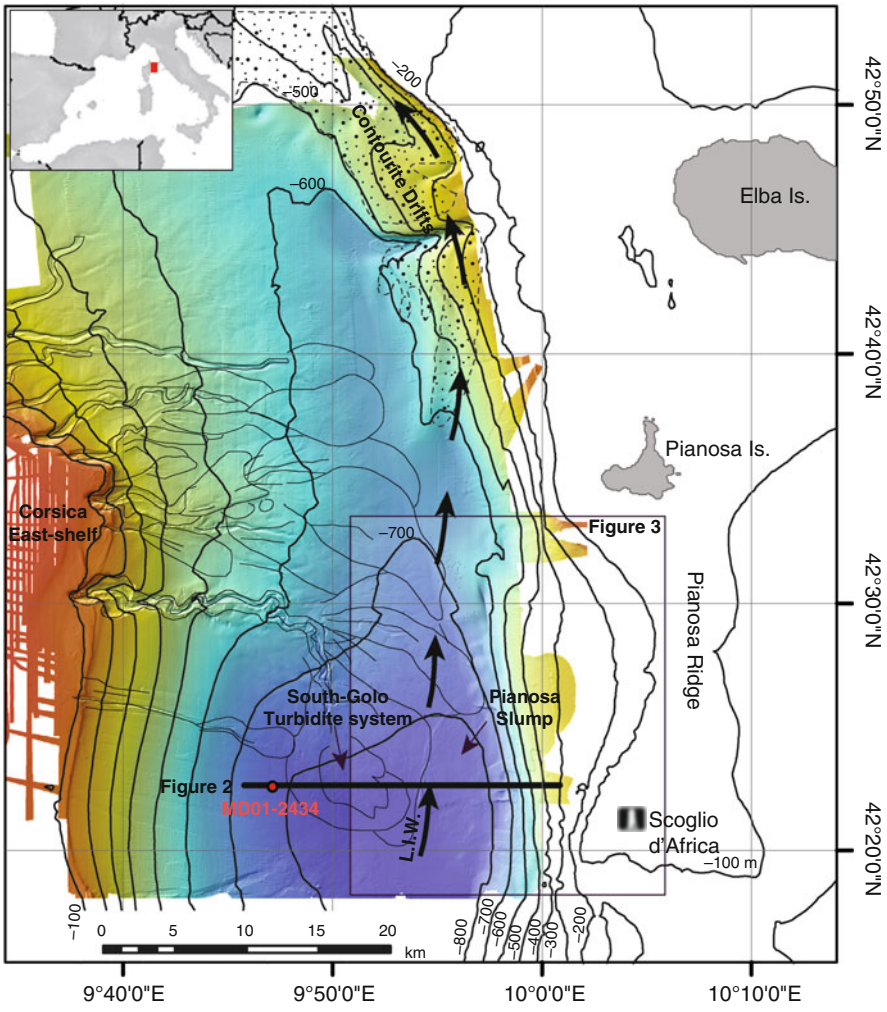

Fig. 39.1 Bathymetric map of the Corsica Trough (grid spacing 25 m) with location of a regional seismic profile (Fig. 39.2). The steep morphology of the Pianosa Ridge contrasts with the western side dominated by turbidite systems (outlined in *grey* from Deptuck et al. 2008). The study area is defined in Fig. 39.3. *LIW* Levantine Intermediate Waters

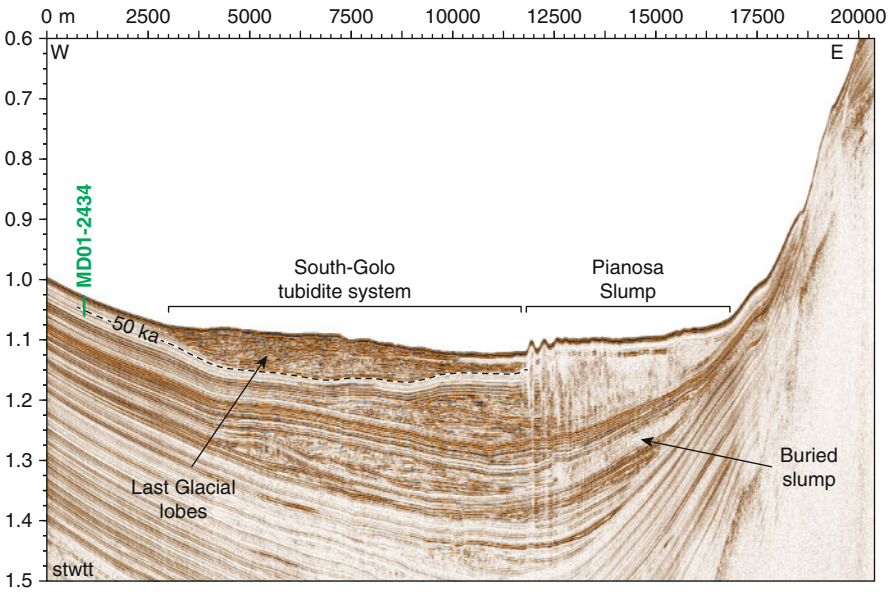

Fig. 39.2 Regional multichannel Sparker profile showing the overall filling of the Corsica Trough with well developed turbidite lobes (west side and basin floor), and slumps at the foot of the steep Pianosa Ridge (east side)

on the western side (east of the shelf break of Corsica with an average gradient of 2–3°) and a steep slope on the eastern side (Pianosa Ridge, with an average gradient from 3.5° to 7.5°; Stanley et al. 1980; Gervais et al. 2004; Fig. 39.2). The limited extension of the Golo sedimentary system from the Corsica catchment to the turbidite systems favoured recent exploration of the East-Corsica margin from source-to-sink (Bellaiche et al. 1994; Gervais et al. 2006; Deptuck et al. 2008; Sømme et al. 2011; Calvès et al. 2012). Several studies draw attention to the presence of contourite drifts along the Pianosa Ridge (Marani et al. 1993; Verdicchio and Trincardi 2008) and their dynamics (Roveri 2002; Toucanne et al. 2012). However, the detailed analysis of mass transport deposits, their role in filling and confining the basin and their relationships with turbidite lobes and contourite drifts have been neglected. The aim of this paper is to investigate the occurrence and distribution of submarine landslides along the Pianosa Ridge and to delineate a preliminary explanation of their genetic relationship with the encasing sediment.

39.2 Geological Setting

The Corsica Trough between East Corsica and West Tuscany is about 200 km long, 40 km wide (10–30 km at the 200 m isobath) with a maximum depth of 900 m (Fig. 39.1). In the Corsica Trough, the Pliocene-Quaternary sedimentation pattern

is dominated by deposits resulting from gravity-driven flows and bottom currents. Along the western side, high sediment input from the Golo River contributed during lowstands to the development of lobe complexes in the basin (Stanley et al. 1980; Gervais 2002; Deptuck et al. 2008; Figs. 39.1 and 39.2). Along the starved eastern side, the sedimentary record is dominated by the presence of submarine landslides (Gervais et al. 2006) and of elongated, mounded contourite drifts (Marani et al. 1993). According to the authors, contourite drifts have grown since middle Pliocene (Roveri 2002) or middle Late Pleistocene, with the opening and deepening of the Tyrrhenian Sea (Verdicchio and Trincardi 2008), favoured by topographic constriction (section narrowing and shoaling) and the Coriolis effect (Roveri 2002). The hydrographic dynamics of the Corsica Trough are dominated by a northward component of superficial Modified Atlantic Waters (0–200 m w.d.) and Levantine Intermediate Waters (LIW, up to 600–1,000 m w.d.; Artale and Gasparini 1990; Toucanne et al. 2012). Contourite drifts are located along the Pianosa Ridge and could record LIW intensification and enhanced ventilation throughout the last glacial interval, while weak intermediate ventilation characterised Holocene and Interglacial periods (Toucanne et al. 2012).

39.3 Methods

This study results from an integration of morpho-bathymetric data with seismic reflection profiles. EM1000 and EM300 multibeam echosounder data acquired during CORFAN 2 cruise (2001) were compiled in a DTM with a grid cell size of 25 m processed with the "Caraibes" software (©IFREMER). Chirp and multichannel Sparker data (72 traces) were simultaneously collected with the multibeam data. The frequency content ranges from 2 to 5 kHz and 130 to 750 Hz, respectively for the Chirp and Sparker seismic data. For the Sparker data, the seismic migration velocities vary spatially based on normal move-out velocity analysis every 250 common depth points. Within the study interval (0–500 ms TWT below seafloor) the interval velocity ranges between 1,500 and 1,750 m s^{-1}. Chirp data were processed in envelope attribute.

39.4 Submarine Landslides

The study area is comprised between 42°18′ and 42°35′ latitude N along the Pianosa Ridge (Fig. 39.3), and shows two morphologically distinct sectors. The sector south of 42°26′ latitude N and West of Scoglio d'Africa has a narrow continental slope (7 km) with a mean slope angle of 7°. A remarkable submarine landslide named 'Pianosa Slump' (PS) was identified by Gervais et al. (2004) at the toe of the Pianosa Ridge (Figs. 39.3 and 39.4). This submarine landslide appears to be composed of two adjacent landslides with a marked expression at the seafloor. The North Pianosa

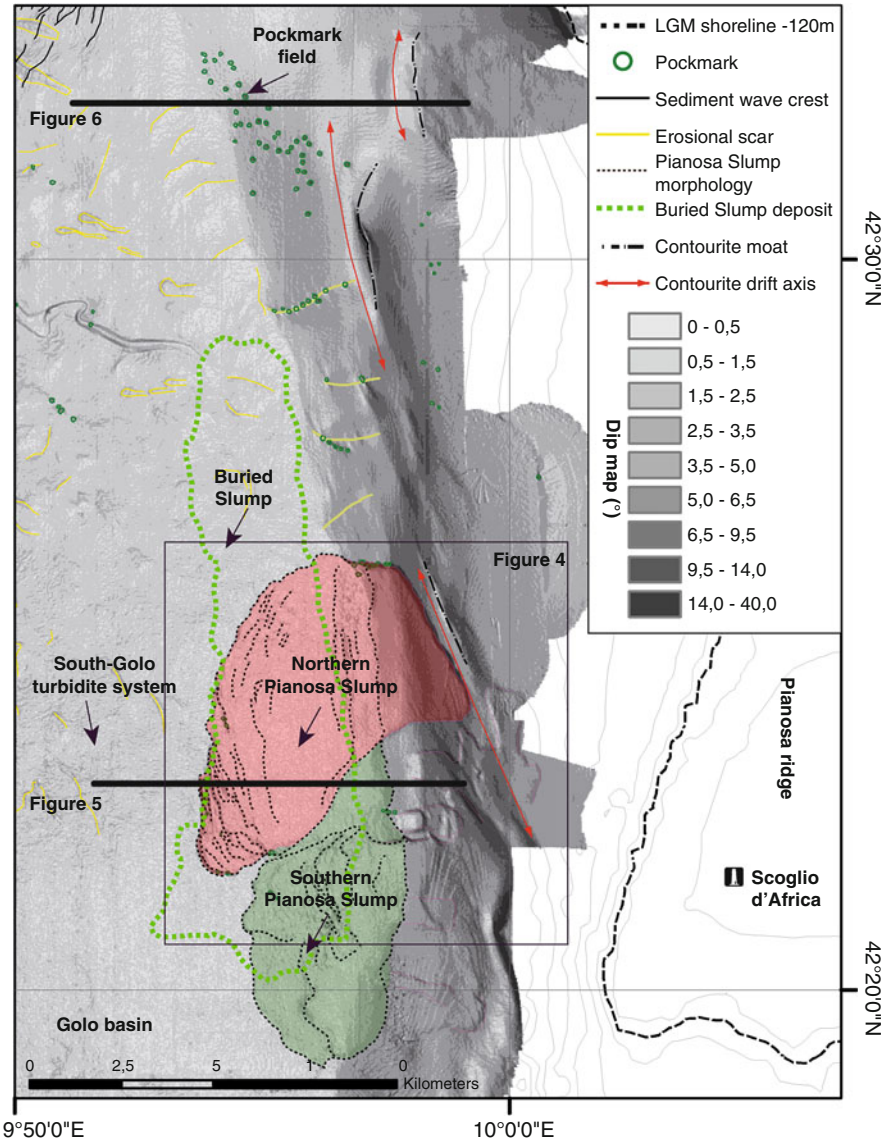

Fig. 39.3 Slope-angle map with observations based also on the interpretation of seismic profiles. Contourite drifts have a more pronounced relief towards the North

Slump (NPS, red pattern in Fig. 39.3) has a marked 30-m high headwall oriented NW-SE (Fig. 39.4). The evacuation zone of NPS extends from the head scar at 505–790 m w.d., over a distance of 2.5–8 km.

Pockmarks are present close to the landslide head scarp (Fig. 39.3). The NPS deposit has a positive relief, reaches down to 860 m w.d., and shows 10-m high

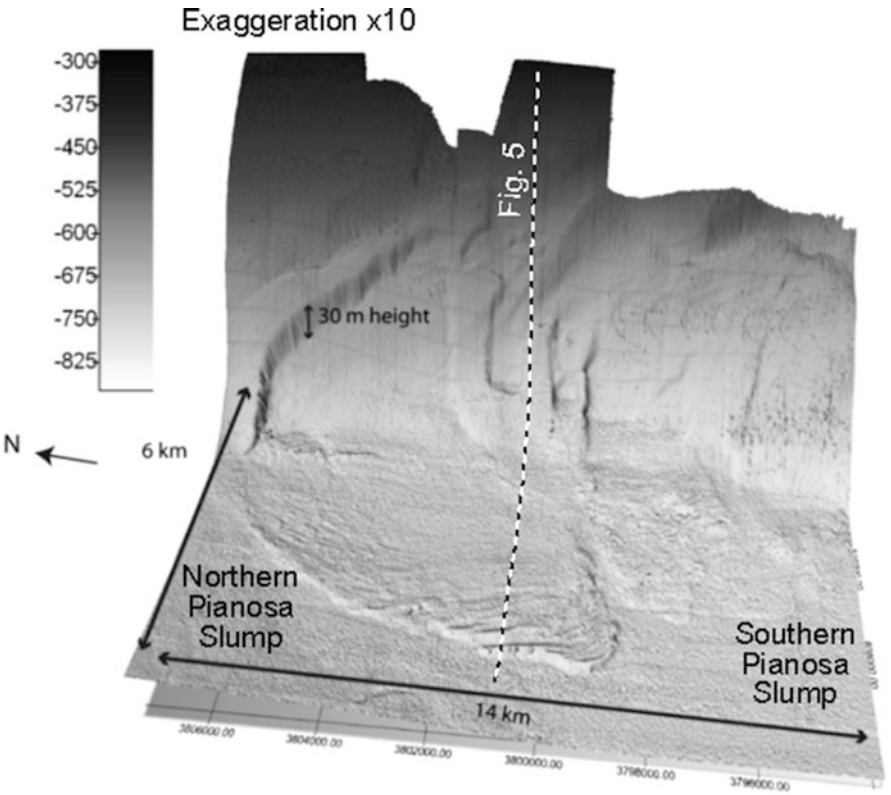

Fig. 39.4 Seafloor morphology of the Pianosa Slump in 3D. The NPS has well defined headwall scarp, deposit and pressure ridges. The SPS has a more complex (multi-source) headwall scarp area and a less developed deposit

arcuate pressure ridges with crests oriented NW-SE, suggesting a flow direction towards the SW (Fig. 39.4). NPS has a total area of 40 km^2. Seismic facies in the deposit are transparent to chaotic in the distal reach under the pressure ridges, as if this lower reach were characterised by a lesser degree of sediment disruption than the upper part of the deposit (Figs. 39.2 and 39.5). The deposit is covered by a 22-m thick layered seismic facies interpreted as a regional hemipelagite unit draping the whole basin. By seismic correlation with sediment core MD01-2434, the estimated age of the hemipelagite bottom is between 15.8 and 17.1 ka BP (Calvès et al. 2012). The seismic reflector J (Gervais et al. 2006; dashed line in Figs. 39.2 and 39.5) dated at 50 cal. kyr BP in core MD01-2434 (Calvès et al. 2012) is affected by the PS.

The basal slip plane of NPS is not easily identified, but it is estimated (assuming a velocity of 1,550 m s^{-1} for the sediment) with at a maximum depth of 66–42 m corresponding to a thickness of 36–23 m of the slump deposit. This gives a total volume of sediment affected comprised between 0.85 and 0.55 km^3.

The South Pianosa Slump (SPS, green pattern in Fig. 39.3) shows a series of small headwall scarps. The SPS deposit shows irregular relief without pressure

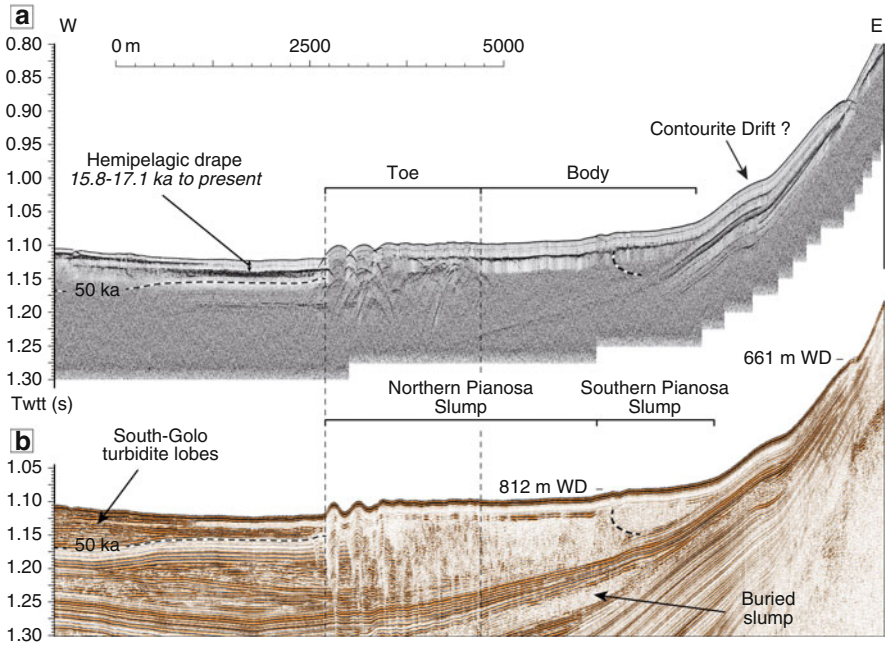

Fig. 39.5 Chirp (**a**) and Sparker (**b**) profiles parallel to Fig. 39.2 (location in Figs. 39.3, 39.4) crossing the body and toe of NPS. Note a buried, older slump deposit. The profiles cut out of the headwall scarp of the NPS on the side of Pianosa Ridge, where a subdued contourite drift appears

ridges but with some blocky areas (Fig. 39.4). Seismic reflection profiles show a partially transparent seismic facies overlaying a chaotic facies with disturbed reflections. The SPS deposit is covered by the same layered seismic facies of NPS, interpreted as hemipelagic deposits. The SPS affects a total area of 45 km^2 (20 km^2 of deposit). The SPS deposit has a mean thickness of 16 m (assuming a velocity of 1,550 m s^{-1} for the sediment) and a maximum of 39 m. The total volume of sediment affected is estimated at 0.34 km^3.

A buried submarine landslide deposit is recognized from Sparker seismic sections as a seismically chaotic and transparent facies along the Pianosa Ridge (Figs. 39.2 and 39.5). The extent of this submarine landslide deposit is tentatively outlined in Fig. 39.3. Pockmarks are observed close to some of the submarine landslide scars, but there are also pockmark fields in the northern sector that are possibly linked to fluid escape from the distal reaches of turbidite lobes.

39.5 Contourite Drifts

In the sector north of 42°26′ latitude N (Fig. 39.3), the slope becomes gentler (2–4°). The base of slope is as shallow as 600–750 m and it is associated with elongated mound morphologies and deep moats roughly parallel to the Pianosa Ridge

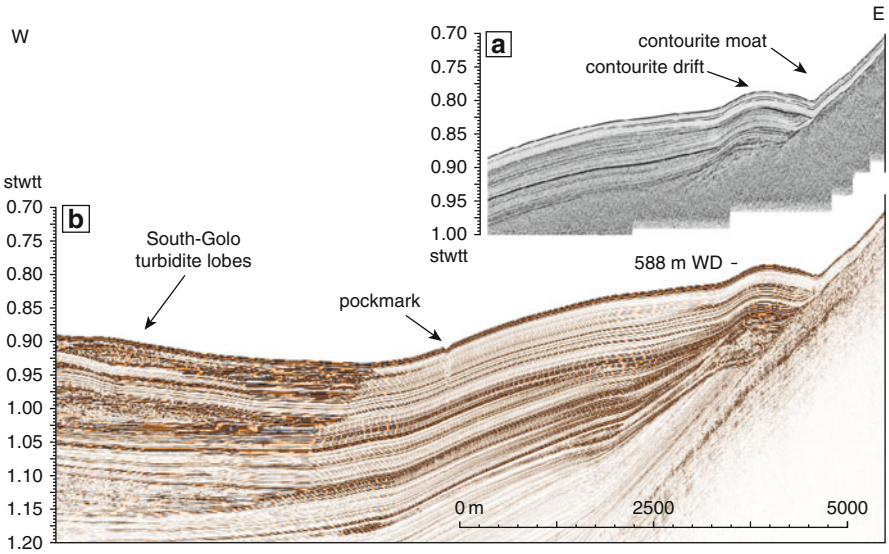

Fig. 39.6 Chirp (**a**) and Sparker (**b**) profiles showing a contourite drift with high amplitude reflections (reactivation and erosional surfaces) correlated to the base of Golo turbidite lobes

(Fig. 39.3). The main sedimentary structures observed are multi-crest contourite drifts. A major elongated contourite drift oriented N-S extends over more than 10 km and ends on a pockmark field (Figs. 39.3 and 39.6). Small contourite drifts can be also observed along the slope above the Pianosa Slump (Fig. 39.5). In general, a trend of enhanced contourite drift morphologies with more developed contourite drift crests and moats is visible from south to north. This trend continues out of the study area as north as the Capraia Sill, at 42°56′ latitude N (Roveri 2002).

The internal structure of contourite drifts is characterized by sets of stacked units composed of parallel seismic reflections bounded by high amplitude reflections (Fig. 39.6). Seimic units aggrade on a basal truncation marked by the toplap terminations within the underlying unit. The asymmetric mound with steep basinward and gentle landward sides, combined with the narrow moat parallel to the drift on its landward side, is a result of the general upslope migration of separate drifts (*sensu* Faugères et al. 1999). The seismic correlation of the high amplitude reflections suggests that the high amplitude reflections reach the base of turbidite lobes in the basin floor.

39.6 Discussion and Conclusion

In the Corsica Trough, submarine landslides are aligned along the western side of the Pianosa Ridge, but only in the southern sector (south of 42°26′ lat North). The Pianosa Slump, with evident seafloor expression, is composed by two landslide

bodies for a maximum of 1.19 km^3 in volume. Several buried landslides of apparently similar or even larger size prove that mass wasting has been relevant and recurrent in the filling of the Golo Basin.

Submarine landslides represent a significant volume of sediment infilling the Golo Basin and contribute to the confinement of turbidite lobes of the Golo turbidite system, at least in the uppermost stratigraphic units, with volumes comparable to those of turbidite sand lobes (see Calvès et al. 2012).

North of the Pianosa Slump, the morphology of the eastern Corsica Trough is dominated by the presence of elongated separate contourite drifts developed at the foot of the Pianosa Ridge along the pathway of LIW (Artale and Gasparini 1990).

The internal geometry of contourite drifts, with seismic units bracketed by high amplitude reflections, supports the interpretation of an uneven growth of the drifts. Variations in the climate-driven intensity and sea-level driven pathway of bottom currents may result in the possible demise or even cannibalization of older contourite drifts (Marani et al. 1993; Roveri 2002). Waxing and waning cycles of bottom-current strength in the Corsica Trough, reconstructed by means of mean sortable silt variations in sediment cores, appear cyclical and guided by climate change (Toucanne et al. 2012).

A possible relationship in terms of 'efficiency' of sediment transport and accumulation was proposed by Roveri (2002) linking low sea level stands to maximum growth of turbidite lobes and enhanced efficiency (and growth) of contourite drifts on the eastern side of the Corsica Trough. Here we propose an attempt to correlate times of enhanced sediment transport efficiency to the highest probability to develop seafloor instability in the same area. This is based on preliminary correlations of regional reflectors of the Pleistocene sediment filling (Gervais et al. 2004, 2006) with the revised chronology of the reflectors and age of lobes (Calvès et al. 2012; Toucanne et al. 2012). Mass wasting along the southern part of the Pianosa Ridge would thus be linked to the same external forcing (sea level fluctuations) alternating times of enhanced production of turbidite lobes (on the western side and central basin) and contourite drifts (eastern side). This preliminary result contributes to understand the timing of submarine landslides as a consequence of both local and global factors (see for example, for the effect of sea level, Trincardi et al. 2003; Lee 2009; Lafuerza et al. 2012).

Predisposing factors for the occurrence and recurrence of landslides in the southern sector of the Pianosa Ridge include: the presence of a steep seafloor; the presence of potentially unstable contourite drift deposits; and the expulsion of fluids. None of these predisposing factors appears at this stage sufficient to explain satisfactorily the location of submarine landslides. On-going work aims to understand the triggering factors of the landslides and to strengthen their chronology relative to contourite drifts and turbidite lobes. Further data to disentangle the mutual influence of bottom current, seafloor instability, fluid escape will be available after two research cruises planned for the end of 2013.

Acknowledgments We thank the Captain and crew of the Corfan2 (2001) campaign onboard R/V Le Suroît. We are grateful to reviewers D. Mosher and M. Roveri and guest editor D. Voelker for skilled insights that improved the manuscript. This is CNR-ISMAR contribution N. 1790.

References

Artale M, Gasparini GP (1990) Simultaneous temperature and velocity measurements of the internal wave field in the Corsican Channel (Eastern Ligurian Sea). J Geophys Res 95(C2):1635–1645

Bacini Sedimentari (1979) Primi dati geologici sul Bacino della Corsica (Mar Tirreno). Atti Convegno Scientifico Nazionale, P.F. Oceanografia e Fondi Marini: 713–727

Bellaiche G, Droz L, Gaullier V, Pautot G (1994) Small submarine fans on the eastern margin of Corsica: sedimentary significance and tectonic implications. Mar Geol 117:177–185

Calvès G, Toucanne S, Jouet G, Charrier S, Thereau E, Etoubleau J, Marsset T, Droz L, Bez M, Abreu V, Jorry S, Mulder T, Lericolais G (2012) Inferring denudation variations from the sediment record; an example of the last glacial cycle record of the Golo Basin and watershed, East Corsica, western Mediterranean sea. Basin Res 24:1–22

Deptuck ME, Piper DJW, Savoye B, Gervais A (2008) Dimensions and architecture of late Pleistocene submarine lobes off the northern margin of East Corsica. Sedimentology 55:869–898

Faugères J-C, Stow DAV, Imbert P, Viana A (1999) Seismic features diagnostic of contourite drifts. Mar Geol 162:1–38

Gervais A (2002) Analyse multi-échelles de la morphologie, de la géométrie et de l'architecture d'un système turbiditique sableux profound (système du Golo, marge est Corse, mer Méditerranée). Unpublished PhD thesis, University Bordeaux 1, no. 2 621, 285 pp. http://www.asf.epoc.u-bordeaux1.fr/theses/Manuscrits/GERVAIS_2002.pdf

Gervais A, Savoye B, Mulder T, Piper DJW, Cremer M, Pichevin L (2004) Present morphology and depositional architecture of a sandy submarine system: the Golo turbidite system (Eastern margin of Corsica). In: Lomas S, Joseph P (eds) Confined turbidite systems, Geological Society of London special Publication, vol 222, pp 59–89

Gervais A, Savoye B, Mulder T, Gonthier E (2006) Sandy modern turbidite lobes: a new insight from high resolution seismic data. Mar Petrol Geol 23:485–502

Lafuerza S, Sultan N, Canals M, Lastras G, Cattaneo A, Frigola J, Costa S, Berndt C (2012) Failure mechanisms of Ana Slide from geotechnical evidence, Eivissa Channel, Western Mediterranean Sea. Mar Geol 307–310:1–21

Lee HJ (2009) Timing of occurrence of large submarine landslides on the Atlantic Ocean margin. Mar Geol 264:53–64

Marani M, Argnani A, Roveri M, Trincardi F (1993) Sediment drifts and erosional surfaces in the central Mediterranean: seismic evidence of bottom-current activity. Sediment Geol 82:207–220

Roveri M (2002) Sediment drift of the Corsica Channel, northern Tyrrhenian Sea. In: Stow DAV, Pudsey CJ, Howe JA, Faugères J-C, Viana A (eds) Deep-water contourite systems: modern drifts and ancient series, seismic and sedimentary characteristics, Geological Society of London Memoirs, 22, pp 191–208

Sømme TO, Piper DJW, Deptuck ME, Helland-Hansen W (2011) Linking onshore-offshore sediment dispersal in the Golo source-to-sink system (Corsica, France) during the late Quaternary. J Sediment Res 81:118–137

Stanley DJ, Réhault JP, Stuckenrath R (1980) Turbid-layer bypassing model: the Corsican Trough, northwestern Mediterranean. Mar Geol 37:19–40

Toucanne S, Jouet G, Ducassou E, Bassetti M-A, Dennielou B, Minto'o CMA, Lahmi M, Touyet N, Charlier K, Lericolais G, Mulder T (2012) A 130,000-year record of Levantine Intermediate Water flow variability in the Corsica Trough, western Mediterranean Sea. Quat Sci Rev 33:55–73

Trincardi F, Cattaneo A, Correggiari A, Mongardi S, Breda A, Asioli A (2003) Submarine slides during relative sea-level rise: two examples from the eastern Tyrrhenian margin. In: Locat J, Mienert J (eds) Submarine mass movements and their consequences. Kluwer, Amsterdam, pp 469–478

Verdicchio G, Trincardi F (2008) Shallow water contourites. In: Rebesco M, Camerlenghi A (eds) 238 Contourites, Developments in sedimentology, Elsevier, Amsterdam, 60, pp 409–433

Viaris de Lesegno L (1978) Etude structurale de la Mer Tyrrhenienne Septentrionale. Thèse de iiième cycle, Université Paris 6, 170 pp

Chapter 40
Mass Transport Complexes from Contourite and Shelf-Edge Deposits Along the South-Western Adriatic Margin (Italy)

Giacomo Dalla Valle, Elisabetta Campiani, Federica Foglini, Fabiano Gamberi, and Fabio Trincardi

Abstract Seismic data and multi-beam bathymetry reveal the occurrence of several exposed or shallowly buried Mass Transport Complexes (MTCs) in the South-Western Adriatic margin (SWAM), which represents the outer sector of the Albanides-Dinarides foreland basin. MTCs are spatially diffused along the SWAM and characterized by high variability in size, morphology and internal geometry. MTCs are derived from the mobilisation of both contourite drift deposits and shelf-margin progradational deposits. The most prominent MTC of the SWAM is the Gondola Slide (GS), a large, deep-seated (~250 m) MTC located near the Gondola-Dauno fault zone (GDFZ), involving around 30 km^3 of shelf and slope sediments. In the northern sector of the margin, the Vieste Slide (VS) affects a low gradient upper slope sector, which is extensively dominated by contourite drifts and sediment waves. Seismic correlation shows that the first and main failure events of GS and VS were contemporaneous and impacted the entire margin (more than 2,000 km^2), and probably were trigger by large earthquake, while later events in both GS and VS appear more localised and asynchronous indicating, probably, slope readjustments governed by local stratigraphic factors.

Keywords Submarine landslide • Sediment drift • Cascading current • Multibeam bathymetry • Cross-cutting relationships

G. Dalla Valle (✉) • E. Campiani • F. Foglini • F. Gamberi
Istituto di Scienze Marine (ISMAR-CNR), Bologna, Via Gobetti 101, Bologna 40129, Italy
e-mail: giacomo.dalla.valle@bo.ismar.cnr.it

F. Trincardi
Istituto di Scienze Marine (ISMAR-CNR), Arsenale, Tesa 104, Castello 2737/F
30122 Venezia, Italy

S. Krastel et al. (eds.), *Submarine Mass Movements and Their Consequences*, Advances in Natural and Technological Hazards Research 37, DOI 10.1007/978-3-319-00972-8_40,

40.1 Introduction

Advancements in multibeam instruments allow detection of an increasing numbers of submarine mass transport complexes (MTCs) along passive and active continental margins (Canals et al. 2004; Masson et al. 2006). These new imaging capabilities show that the entire South-western Adriatic Margin (SWAM) has been impacted by repeated submarine slope failures of variable extent emanating from the shelf edge and upper slope areas generating MTCs with run outs up to tens of km. We study two adjacent MTCs on the open slope of the SWAM: the Gondola Slide MTC and the Vieste Slide MTC. We examine the differences in the materials affected by failure and the resulting morphology, internal geometry and stacking architecture. We discuss the factors that control these differences including the possible trigger mechanisms, the stratigraphy of the involved sedimentary succession and the oceanographic regime that impact the SWAM.

40.1.1 Geological Setting

The SWAM represents the outer foredeep of the west-verging Albanide-Hellenide thrust belt (Fig. 40.1b). Northward of Bari Canyon and seaward of a relatively steep upper slope (4° between 200 and 350 m of water depth) the SWAM continental slope is quite gentle (less than 2°) and is carved by multiple slide scarps affecting consolidated Pleistocene regressive deposits and late Quaternary contouritic drift deposits (Minisini et al. 2006; Verdicchio and Trincardi 2008; Fig. 40.1c). The SWAM is pervasively dominated by erosional and depositional features created by bottom-currents interacting with a complex morphology reflecting longer-term tectonic deformation and MTCs (Ridente and Trincardi 2006; Verdicchio and Trincardi 2006). A large variety of erosional and depositional features including sediment drifts and sediment waves have been interpreted to be a result of constructive interaction between two distinct southerly bottom water masses: the contour-parallel Levantine Intermediate Water and the North Adriatic Dense Water cascading seasonally across the slope (Verdicchio and Trincardi 2006).

The Gondola-Dauno Fault Zone (GDFZ) represents the main regional deformation zone (Ridente et al. 2008). It affects and shapes the central sector of the SWAM, with a marked seafloor expression in the slope and in the basin plain (Duano Seamount), developing also a marked middle-slope antiform that runs with a SW-NE trend (Fig. 40.1c). Two antiforms, linked to deeply buried structures of tectonic origin, cross the SWAM in a NS direction, one located in the middle slope sector, whereas the other one is located more distally in the basin plain (Fig. 40.1c).

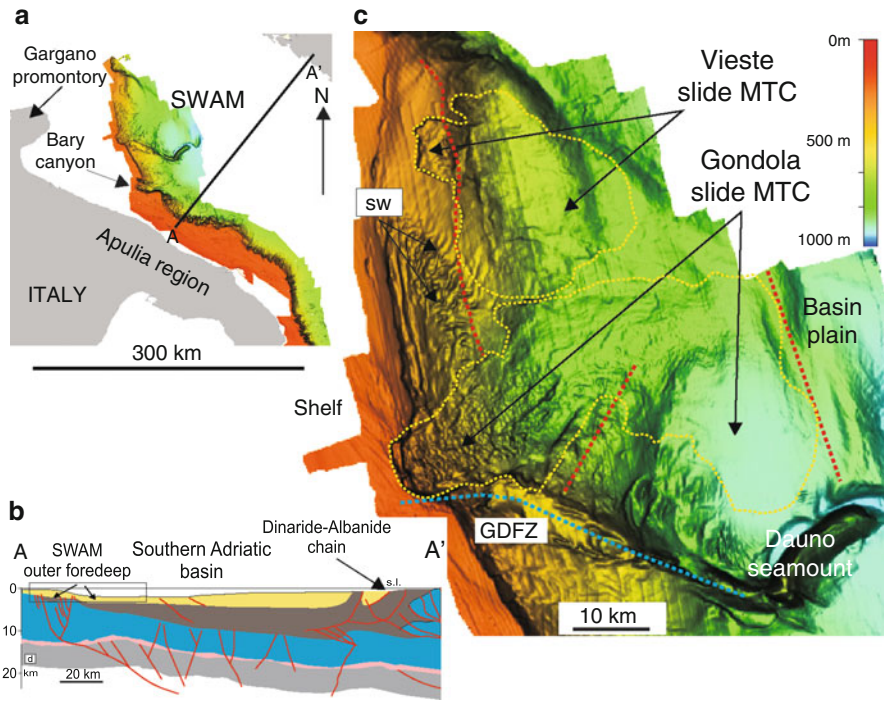

Fig. 40.1 (**a**) Location of study area with multibeam bathymetry of the South-Western Adriatic margin (SWAM) acquired by ISMAR-Bologna. (**b**) Schematic geological transect of the South Adriatic Basin (Modified from Fantoni and Franciosi 2010). See Fig. 40.1a for location of the profile (**c**) Shaded relief bathymetry of the SWAM sector impacted by the Gondola and Vieste slide MTC. *Red dotted lines* delineate axes of main antiforms affecting location of slide headwalls and sidewalls and confining the areal distribution of MTCs. *GDFZ* Gondola-Dauno fault zone, *SW* sediment waves

The studied MTCs are localized northward from the GFDZ: the largest one, the Gondola Slide MTC lies close to the GDFZ, and reach the outer continental shelf, whereas the Vieste Slide MTC, involves mainly slope contouritic deposits.

40.1.2 Material and Methods

Multibeam data used in the study were collected by ISMAR-Bologna using a Reson 8160 and EM300. Digital Elevation Models (DEMs) were created at grid resolution of 20 and 50 m. High-resolution seismic profiles were collected using

a 16 transducers hull-mounted Chirp-sonar profiler with a vertical resolution less than 0.5 m. Basic stratigraphic information used to infer the age of the main failure events is from published papers by Minisini et al. (2006), Verdicchio et al. (2007), Piva et al. (2008).

40.2 Results

Repeated mass-failure events along the SWAM have generated MTCs covering an area of 3.350 km^2. The two major MTCs are the Gondola Slide (GS-MTC) and the Vieste Slide (VS-MTC) (Fig. 40.1).

40.2.1 Gondola Slide (GS-MTC)

The Gondola Slide (GS-MTC) is the largest MTC of the Adriatic Sea and is located nearby the Gondola-Dauno fault zone (GDFZ) (Fig. 40.2a). The GS-MTC failed a 250-m-thick slope section composed of progradational Mid-Pleistocene deposits (Ridente and Trincardi 2006). The GS-MTC extends from the shelf-break, located in 180 m of water depth, to the abyssal plain (1,050 m of depth) with a run out of about 50 km, involving around 30 km^3 of material (Figs. 40.1 and 40.2a). The geomorphological analysis of multibeam data reveals that the GS-MTC is the result of at least three distinct failures resulting in discernible mass-transport deposits (MTDs): GS1-MTD, which represents the first and main mass failure; GS2-MTD, a second and more localized deposit; and GS3-MTD the least extensive and youngest deposit (Fig. 40.2a).

The headwall of the GS-MTC is 10 km wide and has an amphitheatre-like morphology with a relief of up to 250 m (Fig. 40.2b). The northern sidewall is a subdued, 6 km long scarp carved into the upper slope deposits. The southern sidewall is more pronounced and coincides with the E-W trending structural lineament of GDFZ (Fig. 40.2b). The southern sidewall is around 10 km long and forms a large, curvilinear scarp up to 150 m high and partially constitutes the GS2-MTD headwall (Fig. 40.2b). The proximal sector of GS1-MTD is characterized by the elongated ridges, upslope, and large blocks (Figs. 40.2a and 40.3a, b). The ridges are linear to slightly sinuous, have lengths between 600 m and 3 km, are up to 40 m high (Figs. 40.2b and 40.3a, b), and mainly consist of shelf-margin strata (as documented by ROV images Freiwald et al. 2009). On chirp-sonar profiles the ridges and the blocks correspond to a very irregular area with reduced acoustic penetration and diffraction hyperbolae (Fig. 40.3a, b). In some cases they appear to have maintained their original stratigraphy (Fig. 40.3a).

Beyond 500 m water depth, the ridges are replaced by rounded blocks with diameter less than 500 m (Fig. 40.2c). Ponded acoustically transparent deposits are interspersed within the ridge and blocky areas (Fig. 40.3a). We interpreted these

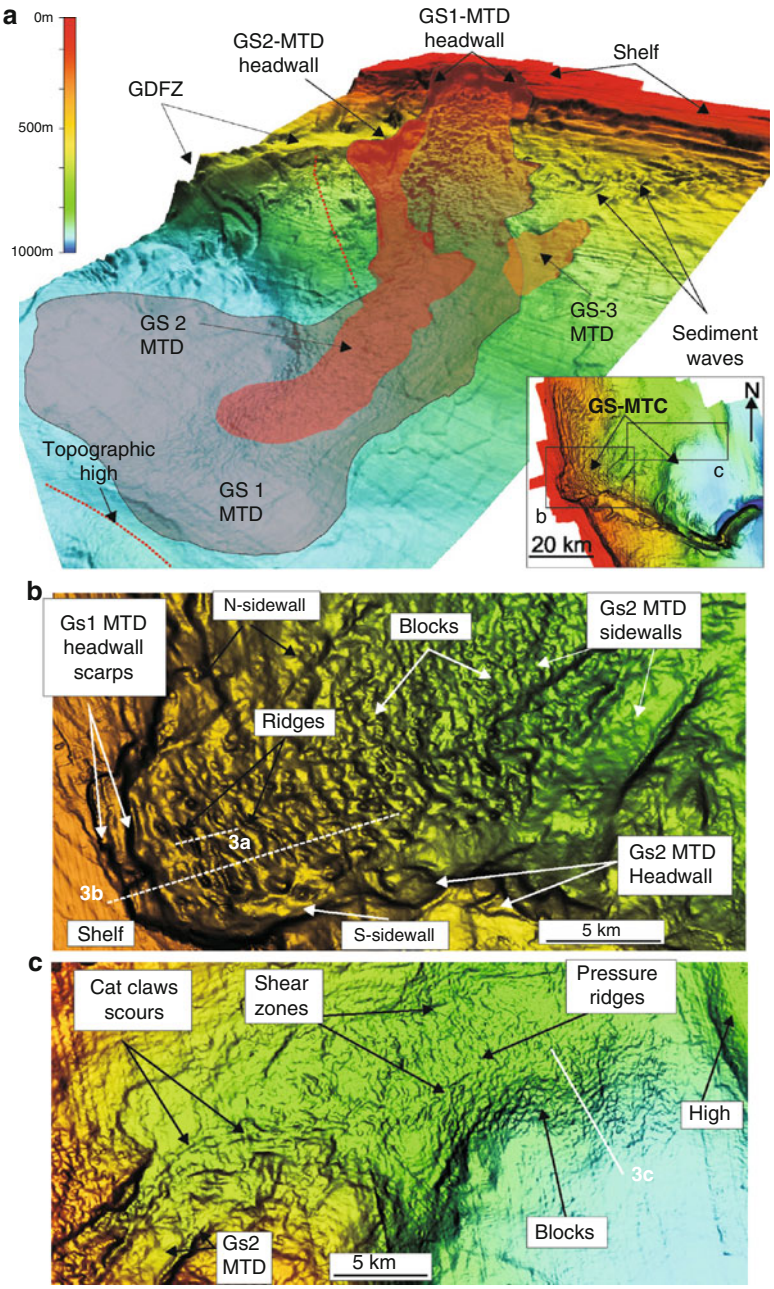

Fig. 40.2 (**a**) Multibeam bathymetry maps showing location of Gondola MTCs with the areal extension of its building MTDs (GS1, GS2, GS3). (**b**) Detail of exposed sector, with the upper slope character by elongated km-scale ridges, followed downlsope by a blocky area (**c**) The distal sector is buried but the morphology of the MTC is still discernible with the occurrence of pressure ridges, longitudinal shear zones and blocks. *GDFZ* Gondola-Dauno Fault zone

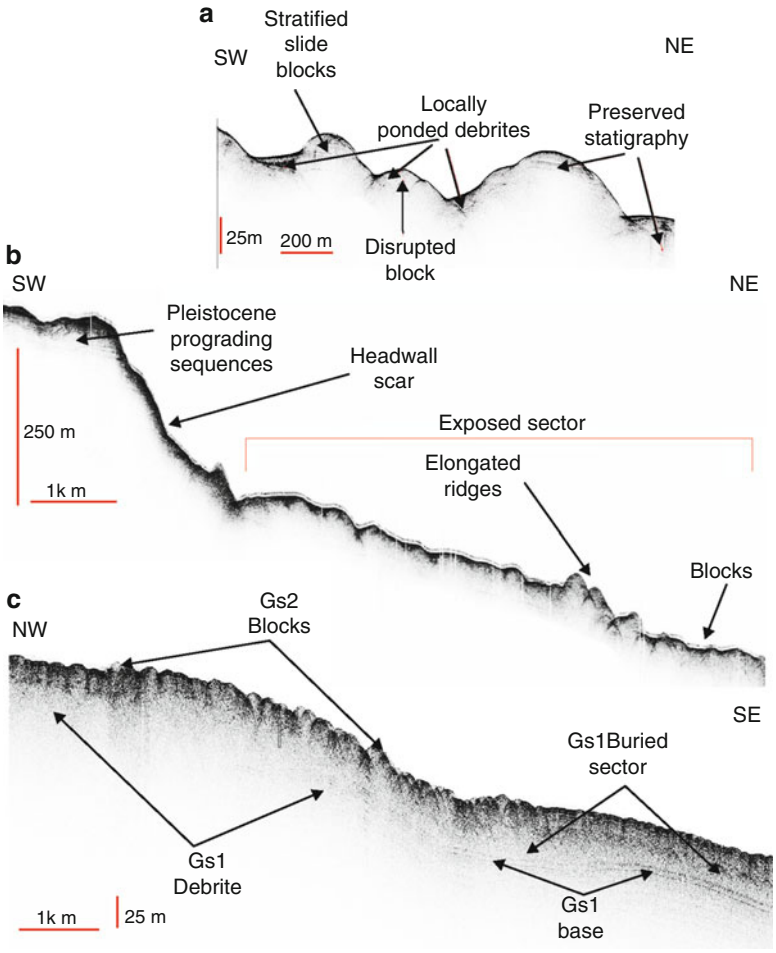

Fig. 40.3 Chirp sonar profiles illustrating the stratigraphic framework of Gondola MTCs. (**a**) Elongated ridges showing preserved stratigraphy. (**b**) On the upper slope ridges and blocks are exposed because of the continuous sweeping of the sea floor by powerful bottom currents capable to exceed 50 cm s^{-1} (Trincardi et al. 2007). (**c**) Buried, distal sector of GS1-MTD with superimposed GS2-MTD which appears to lack draping sediment cover (see Fig. 40.2 for the location of the profiles)

deposits as debrites resulting from blocks and strata disintegration during the failure (Fig. 40.3a). In the basin plain, between 700 and 1,000 m of water depth, GS1-MTD is characterized by weakly reflective to chaotic facies (debrites; Fig. 40.2c) covered by a 25 m thick hemipelagic drape (Fig. 40.3c).

The GS2-MTD resulted from a successive collapse that has involved the part of the southern sidewall of GS1-MTD (Fig. 40.2a, b). The GS2-MTD headwall is 5 km wide and 150 m high (Fig. 40.2b). The GS2-MTD has two marked sidewalls

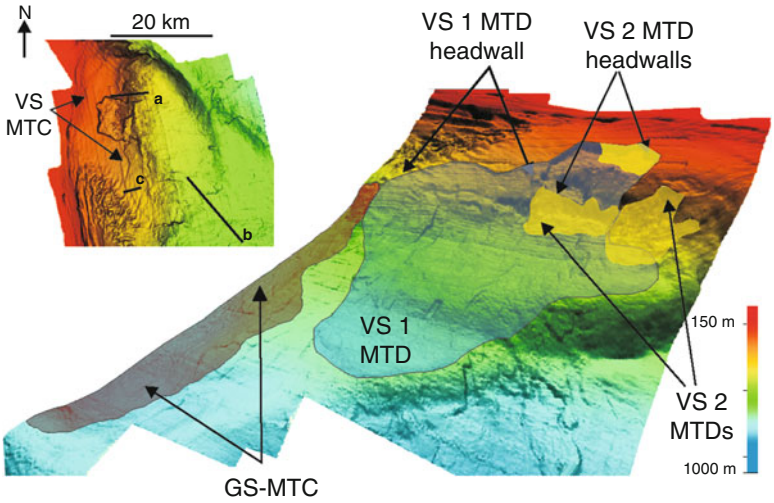

Fig. 40.4 Multibeam bathymetry of Vieste MTCs showing the areal extent of its composing MTDs (VS1, VS2-MTD) and their spatial relationship with the GS-MTC

running along a SW-NE trend (Fig. 40.2b). Its upper transitional zone is filled by post-slide contour-current deposits, whereas its distal sector is characterized by a series of curvilinear scours interpreted as cat-claw scours (sensu Moscardelli et al. 2006) (Fig. 40.2c). The accumulation zone of GS2-MTD is emplaced above the GS1-MTD, and is characterized by pressure ridge aligned in EW direction, laterally bounded by longitudinal shear zones (Fig. 40.2c). Blocks up to 3 m high are present at the distal toe of the accumulation zone (Figs. 40.2c and 40.3c).

The GS3-MTD is the youngest MTD of the GS-MTC representing a minor failure episode affecting well developed, along slope sediment waves deposited in on the slope sector northward from the GS-MTC (Fig. 40.2). The GS3-MTD is confined in the mid-slope sector and characterized by an arcuate headwall with a maximum relief of 75 m.

40.2.2 Vieste Slide (VS-MTC)

North of the GS-MTC, a network of headwall scars which affects the upper and middle continental slope of the SWAM with a linear extent of 42 km (Fig. 40.4).

This network of headwall scars run parallel to the axis of a buried tectonic antiform trending in a N-S direction at around 750 m of depth (Fig. 40.1). At the base of the slope, an old deeply buried MTC (Old-Vieste MTC) was deposited across the basin over an area of 290 km^2.

The VS MTC consists of two vertically stacked MTDs (VS1 and VS2) (Fig. 40.4). The evacuation area of VS1-MTD correspond to an arcuate headwall,

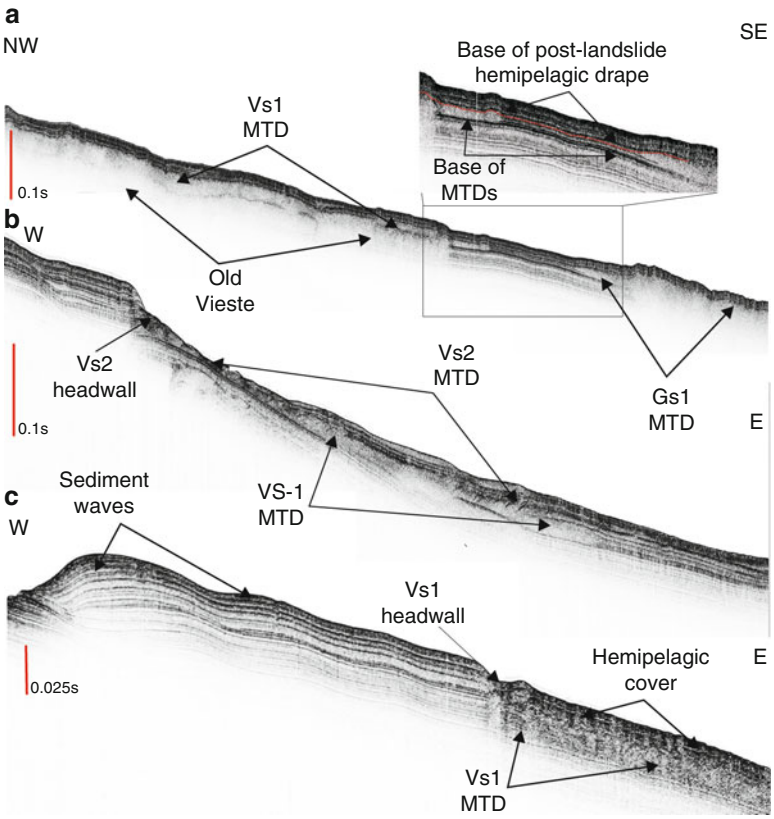

Fig. 40.5 (**a**) Chirp profile illustrating internal geometries and spatial relationship of GS1-MTD with VS1-MTD. (**b**) Chirp profile showing the vertical staking pattern of the VS1 and VS2 MTDs (see Fig. 40.4 for the location of the profiles). (**c**) Chirp profile showing the upperslope sediment drift affected by VS1 MTD

30 km long, set at depth of 530 m, which gives rise to a marked U-shaped headwall with relief less than 50 m further north (Fig. 40.4). The evacuation area is set just downslope of a field of sediment waves with up to 40 m of relief (Fig. 40.5c). The VS-1 MTD has an E-W extent of 24 km reaching the basin plain at 1,040 m of depth, while in an N-S direction it has a length of 25 km (Fig. 40.4). VS-1 MTD is made up of 30–40 m of weakly reflective, chaotic seismic facies that remains attached to the headwall scarp and is draped by a 10–20 m thick sedimentary succession (Fig. 40.5c). The VS-2 MTD consists of several, smaller scale deposits downslope of a U-shaped scar with an upper scarp at a depth of 360 m, and a lower scarp at 410 m (Fig. 40.4). Both of the two headwall scarps have a relief of 40 m (Fig. 40.4). In the accumulation zone the VS-2 MTDs consists of an around 3.5 km long acoustically transparent deposit exposed at the seafloor and deposited on top of the VS-1 MTD (Fig. 40.5b).

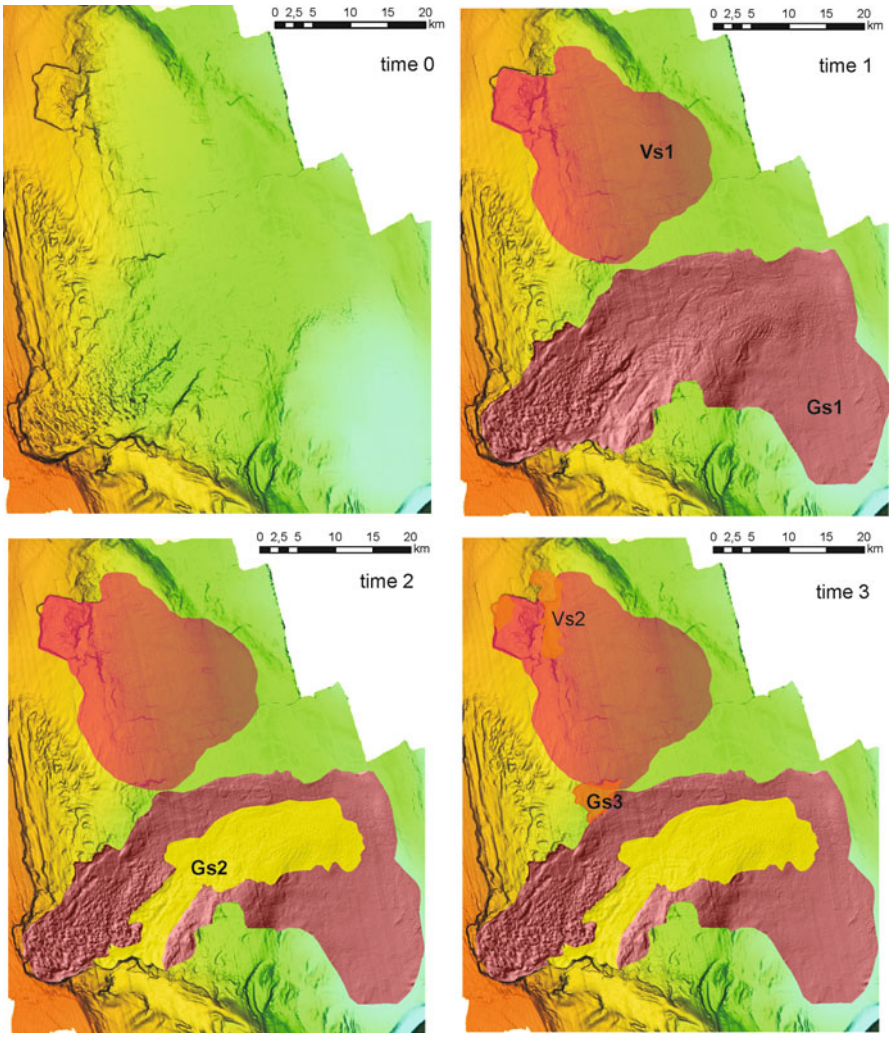

Fig. 40.6 Schematic sketch of the timing of emplacement of the MTDs that compose GS and VS MTCs

40.3 Discussion and Conclusions

Based on the analysis of multibeam bathymetric data, the re-examination of the multiple coalescing submarine MTCs on the SWAM allows reconstruction of the phase relationships among successive submarine failures.

Relative timing of the failures is based on "cross-cutting" relationships of the elementary MTD composing the MTCs of the SWAM. Seismic correlation based on newly acquired Chirp sonar profiles shows that the first mass failure event of both

GS1 MTD and VS1 MTD was contemporaneous and impacted the SWAM over more than 2,000 km^2 (Figs. 40.5a and 40.6). Following age data from Minisini et al. (2006) we can establish that GS1-MTD and VS-1 MTD occurred simultaneously within the MIS 2-glacial unit (in the order of 20–24 ky cal. BP). Considering the broad extent of the failure event responsible for the GS1 and VS1 MTD, and their impact in their stratigraphically dissimilar contexts (shelf *vs.* upperslope) across a wide region, we suggest that the most likely trigger be an earthquake. SWAM is a seismically active area and during the last 500 ky has experienced active tectonic deformation mainly along the GDFZ (Ridente and Trincardi 2006). The source sedimentary environment and the depth of rooting of the slide plane represent the main factors controlling the different morphologies and failure style of the SWAM MTCs.

The deep-seated GS1-MTD involved more than 200 m of Middle to Upper Pleistocene, lithified outer-shelf deposits (Ridente et al. 2008). A deep weak layer led to the formation of a MTC with great run out, characterized by sectors with different morphologies and different architectural elements. The GS-1 MTD shows a proximal sector with elongated ridges and blocks which have a rigid behaviour that in some cases preserve the original stratigraphy, and a distal sector characterized by debrites resulting from strata disruption.

On the contrary the VS-MTDs are shallow seated (<50 m), involving upper-slope, fine grained sediment drift which are Late Quaternary in age (Verdicchio and Trincardi 2006) and generate homogeneous chaotic, weakly reflective "thin-skinned" mudflows, where the original stratigraphy is completely disrupted (Fig. 40.5b). Later failures in both GS and VS MTCs appear more localised (Fig. 40.6) and asynchronous, possibly resulting from slope readjustments governed by local factors.

Acknowledgments The authors are thankful to Jason D. Chaytor and Gian Andrea Pini for their helpful reviews and constructive comments.

References

Canals M, Lastras G, Urgeles R, Casamor JL, Mienert J, Cattaneo A, De Batist M, Heflidason H, Imbo Y, La Berg JS, Locat J, Long D, Longva O, Masson DG, Sultan N, Trincardi F, Bryn P (2004) Slope failure dynamics and impacts from seafloor and shallow sub-seafloor geophysical data: case studies from the COSTA project. Mar Geol 213:9–72

Fantoni R, Franciosi R (2010) Tectono-sedimentary setting of the Po Plain and Adriatic Foreland. Rend Lincei 21:197–209. doi:10.1007/s12210-010-0102-4

Freiwald P, Beuck L, Rüggeberg A, Taviani M, Hebbeln D et al (2009) The white coral community in the Central Mediterranean Sea revealed by ROV surveys. Oceanography 22:58–74

Masson DG, Harbitz CB, Wynn RB, Pedersen G, Lovholt F (2006) Submarine landslides: processes, triggers and hazard prediction. Philos Trans R Soc A 364:2009–2039

Minisini D, Trincardi F, Asioli A (2006) Evidence of slope instability in the South-Western Adriatic margin. Nat Hazard Earth Syst Sci 6:1–20

Moscardelli L, Wood LJ, Mann P (2006) Mass-transport complexes and associated processes in the offshore area of Trinidad and Venezuela. AAPG Bull 90:1059–1088

Piva A, Asioli A, Trincardi F, Schneider R, Vigliotti L (2008) Late-Holocene climate variability in the Adriatic Sea (Central Mediterranean). Holocene 18:153–167

Ridente D, Trincardi F (2006) Active foreland deformation evidenced by shallow folds and faults affecting late-Quaternary shelf-slope deposits (Adriatic Sea, Italy). Basin Res 18:171–188

Ridente D, Di Bucci D, Fracassi U, Trincardi F, Valensise G (2008) Middle Pleistocene to Holocene activity of the Gondola Fault Zone (Southern Adriatic Foreland): deformation of a shear zone and seismotectonic implications. Tectonophysics 453:110–121

Trincardi F, Verdicchio G, Miserocchi S (2007) Sea-floor evidence for the interaction between cascading and along-slope bottom-water masses. J Geophys Res (Earth Surf) 112:F03011. doi:10.1029/2006JF000620

Verdicchio G, Trincardi F (2006) Short-distance variability in slope bed-forms along the Southwestern Adriatic Margin (Central Mediterranean). Mar Geol 234:271–292

Verdicchio G, Trincardi F (2008) Mediterranean shelf-edge muddy contourites: examples from the Gela and South Adriatic basins. Geo-Mar Lett 28:137–151

Verdicchio G, Trincardi F, Asioli A (2007) Mediterranean bottom current deposits: an example from the Southwestern Adriatic Margin. Geol Soc Lond Spec Publ 276:199–224

Chapter 41
Mass Wasting Along Atlantic Continental Margins: A Comparison Between NW-Africa and the de la Plata River Region (Northern Argentina and Uruguay)

S. Krastel, J. Lehr, D. Winkelmann, T. Schwenk, B. Preu, M. Strasser, R.B. Wynn, A. Georgiopoulou, and T.J.J. Hanebuth

Abstract The passive continental margins of the Atlantic Ocean are characterized by thick sedimentary successions, which might become unstable resulting in landslides of various sizes. The type of mass-wasting differs between individual margin sections but the reasons for these differences are not well understood. The NW-African continental margin is characterized by several large-scale but infrequent landslides, while the continental margin in the de la Plata River region (northern Argentina and Uruguay) shows widespread small-scale mass transport deposits. These different styles of mass wasting can be explained by different oceanographic and sedimentary settings. The margin off Northwest Africa is characterized by high primary productivity caused by oceanic upwelling as well as locally focused aeolian input resulting in relatively high sedimentation rates. This setting leads to sediment instabilities arising primarily from underconsolidation of deposited sediments and widespread weak layers. In contrast, the modern ocean margin off Uruguay and

S. Krastel (✉) • J. Lehr
Institute for Geosciences, Christian-Albrechts-Universität zu Kiel, Kiel, Germany
e-mail: skrastel@geophysik.uni-kiel.de

D. Winkelmann
GEOMAR Helmholtz Centre for Ocean Research Kiel, Kiel, Germany

T. Schwenk • B. Preu • T.J.J. Hanebuth
MARUM – Center for Marine Environmental Sciences, and Faculty of Geosciences, University of Bremen, Bremen, Germany

M. Strasser
Geological Institute, ETH Zurich, Zurich, Switzerland

R.B. Wynn
National Oceanography Centre, Southampton, UK

A. Georgiopoulou
University College Dublin, Dublin, Ireland

S. Krastel et al. (eds.), *Submarine Mass Movements and Their Consequences*, Advances in Natural and Technological Hazards Research 37, DOI 10.1007/978-3-319-00972-8_41,

northern Argentina is characterized by strong contour currents and a high amount of fluvial sediment resulting in widespread contouritic deposits. These contourites are potentially unstable leading to smaller but more frequent landslides.

Keywords Submarine landslides • Passive margins • Atlantic Ocean • Acoustic imaging

41.1 Introduction

Submarine landslides and sediment gravity flows are the dominant process for sediment transport from the continental shelf to the deep ocean. Sand-rich gravity flow deposits form many of the World's largest oil and gas reservoirs, while mud-rich deposits may sequester globally significant volumes of organic carbon (Galy et al. 2007). Landslides and sediment gravity flows are also a significant geohazard to seafloor infrastructure, e.g. pipelines and telecommunications cables (Camerlenghi et al. 2007). In some cases, submarine landslides have generated tsunamis that have caused widespread damage to coastal communities (Tappin et al. 2001; Bondevik et al. 2005).

The largest submarine landslides tend to occur on open areas of the continental slope, in tectonically quiet regions where large volumes of fine-grained sediment can accumulate over long periods of time (Masson et al. 2010). Significant changes concerning size and morphology, however, do exist for different sections of passive margins. E.g., a compilation of landslides in the North Atlantic shows a systematic difference between the eastern and western margin (Hühnerbach et al. 2004). The eastern North Atlantic is characterized by a few large slope failures, whereas the western North Atlantic shows abundant smaller failures. Hühnerbach et al. (2004) suggest that the larger numbers of small slope failures for the western North Atlantic can be explained by their association with submarine canyons (Booth et al. 1993; McAdoo et al. 2000) while similar canyoned slopes are relatively rare in the eastern North Atlantic. A first analysis of seismic and sediment core data from the continental margin in the de la Plata region (western South Atlantic) also show a pattern of abundant small landslides but only a few canyons and gullies (Krastel et al. 2011). Hence other processes control the size and pattern of landslides in this area.

The main objective of this manuscript is to compare the type and pattern of mass wasting off NW-Africa and in the de la Plata region. We briefly summarize the current knowledge of mass wasting off NW-Africa based on published literature, present new data for the de la Plata region, and analyze possible reasons for the different style of mass wasting. Finally we estimate the geohazard potential related to mass wasting in both settings.

41.2 Submarine Landslides Off NW-Africa

In this chapter we briefly summarize the sedimentary setting of the NW-African continental margin (south of 26°N) with a focus on submarine mass wasting based on published literature. The passive margin off NW-Africa is characterized by relatively high accumulation rates (locally exceeding 10 cm/ka, Martinez et al. 1999) as a result of high primary productivity caused by oceanic upwelling. Significant amounts of dust are imported from the Sahara desert (Sarnthein and Koopmann 1980) while fluvial input is very low. Mass wasting off NW-Africa has intensely been studied in the past (e.g., Weaver et al. 2000; Wynn et al. 2000; Krastel et al. 2006, 2012; Georgiopoulou et al. 2010). The NW-African continental margin is characterized by very large but infrequent mass wasting events (Weaver et al. 2000). The most recent compilation of Krastel et al. (2012) shows four mega-slides each affecting over 20,000 km^2 of seafloor in the area between 12° and 26°N, namely the Sahara Slide, the Cap Blanc Slide, the Mauritania Slide and the Dakar Slide from north to south (Fig. 41.1). All slides are complex in morphology and show clear indications for multiple failures and upslope retrogression. The failures occurred during periods of low or rising sea level (Georgiopoulou et al. 2010; Krastel et al. 2012). Seismic data show numerous buried landslides indicating a long history of mass wasting for these areas (Krastel et al. 2012). The areas between the slides are characterized by a large number of canyons and gullies. No landslides occur in these areas except for very small local failures of canyon walls.

41.3 Submarine Landslides in the de la Plata Region

The passive continental margin off Uruguay and Northern Argentina is characterized by a complex oceanographic regime (Preu et al. 2012) and significant fluvial input from large river systems such as the Rio de la Plata (Gilberto et al. 2004, Fig. 41.1). This setting leads to a complex interplay between gravitational downslope and contour-current driven alongslope sediment transport (Klaus and Ledbetter 1988). The most prominent sedimentary features are widespread contouritic deposits extending from the southern Argentine margin (Hernández-Molina et al. 2009) to the northern Argentine and Uruguayan slope (Preu et al. 2012). Preu et al. (2012) suggest that the modern slope morphology was generated under the influence of the full force of the Northern Source Deep Water after closure of the Central American Seaway leading to formation of mounded plastered drift sequences on the so called Ewing Terrace (Fig. 41.1).

Acoustic data collected off Uruguay and Northern Argentina allow a detailed investigation of mass wasting features in this area (Figs. 41.2 and 41.3). First analyses of this dataset document the continental slope offshore Uruguay

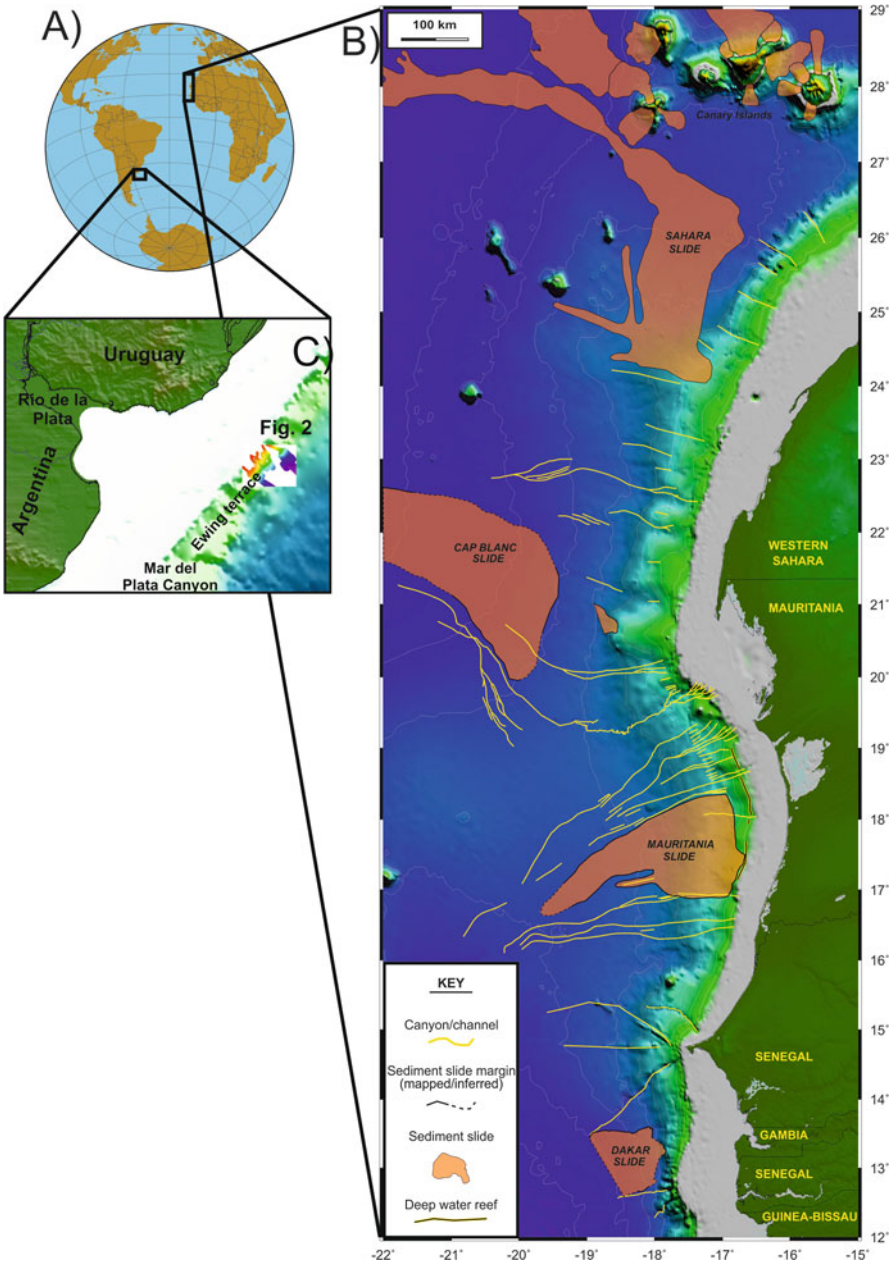

Fig. 41.1 (**a**) Location of study areas in the Atlantic Ocean. (**b**) Distribution of submarine landslides off NW-Africa (Modified after Krastel et al. 2012). (**c**) Close-up of the de la Plata region

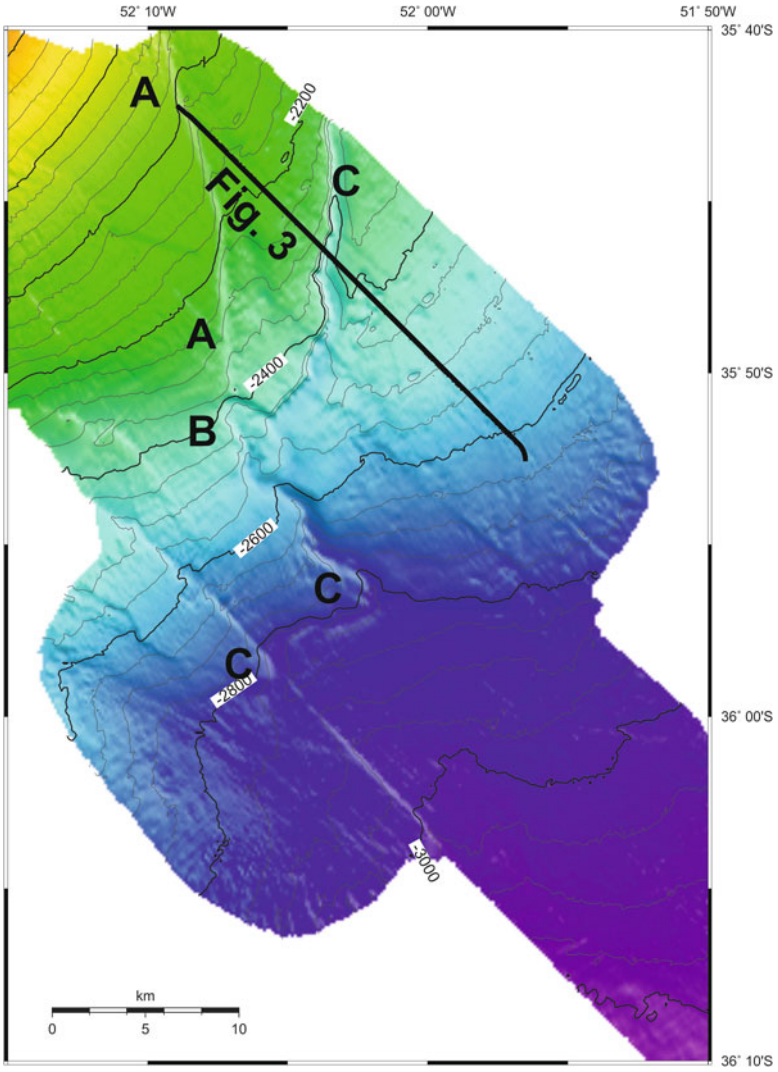

Fig. 41.2 Bathymetric map of a landslide area off Uruguay (see Fig. 41.1c for location of map)

to be the locus of submarine mass wasting in the survey area (Krastel et al. 2011). The combined analysis of hydro-acoustic (sediment echo sounder, multibeam bathymetry) (Fig. 41.2) and high resolution seismic data (Fig. 41.3) allows a detailed reconstruction of mass wasting in this area.

The bathymetric data (Fig. 41.2) image a complex pattern of morphological steps. Morphological step A (Fig. 41.2) is a linear structure of at least 20 km

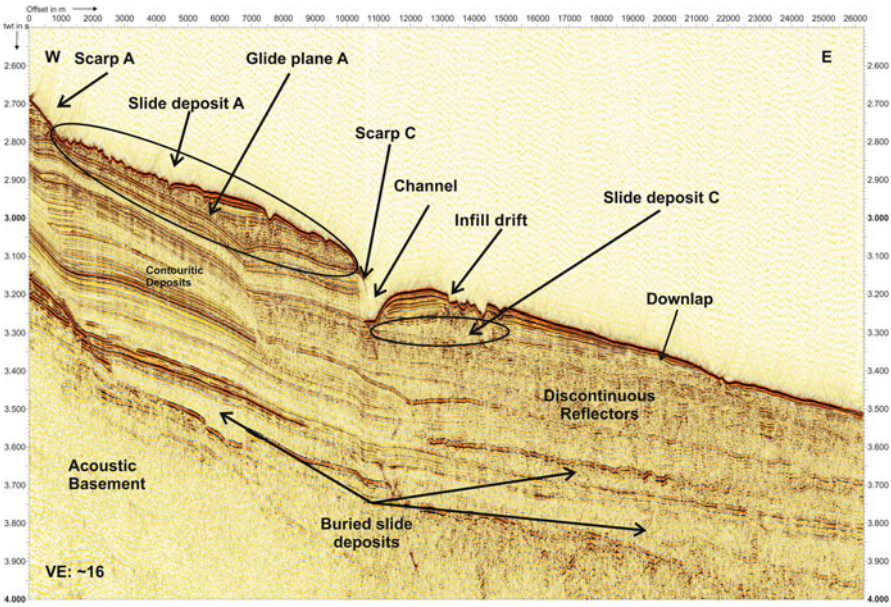

Fig. 41.3 Seismic profile crossing the scarps shown in Fig. 41.2

length (the northern edge is not covered by the data) and a height of 60–90 m. It runs subparallel to the contour lines. Morphological step A terminates against the 2 km-wide amphitheater-shaped incision B. This feature represents a classical landslide headwall, and young slide deposits are found beneath the headwall (Henkel et al. 2011). Incision B also cuts morphological structure C (Fig. 41.2), a more than 40 km-long and partly meandering feature. This feature is not a simple morphological step but a ~1 km-wide channel-like feature with an up to 150 m-high and steep (up to 30°) landward western wall and a shallower and more gentle sloping seaward eastern wall (Figs. 41.2 and 41.3).

A seismic cross section (Fig. 41.3) clearly images the temporal evolution of the morphological features. Young landslide deposits without a detectable drape are found beneath morphological step A. The landslide deposits show a chaotic to transparent seismic facies and a hummocky surface. Landslide deposits are also found beneath the morphological step C, but these deposits are clearly covered by a lense-shaped sedimentary body characterized by wavy reflectors of high amplitude. Such deposits are typical for an infill drift. Hence we suggest the following temporal evolution for this area (Fig. 41.4). Morphological step C was formed by one or a series of slope failures. The N-S orientated section of step C may connect two individual headwalls at slightly different water depths. Northward-flowing bottom currents were focused along this step as Coriolis-forces deflect the currents to the

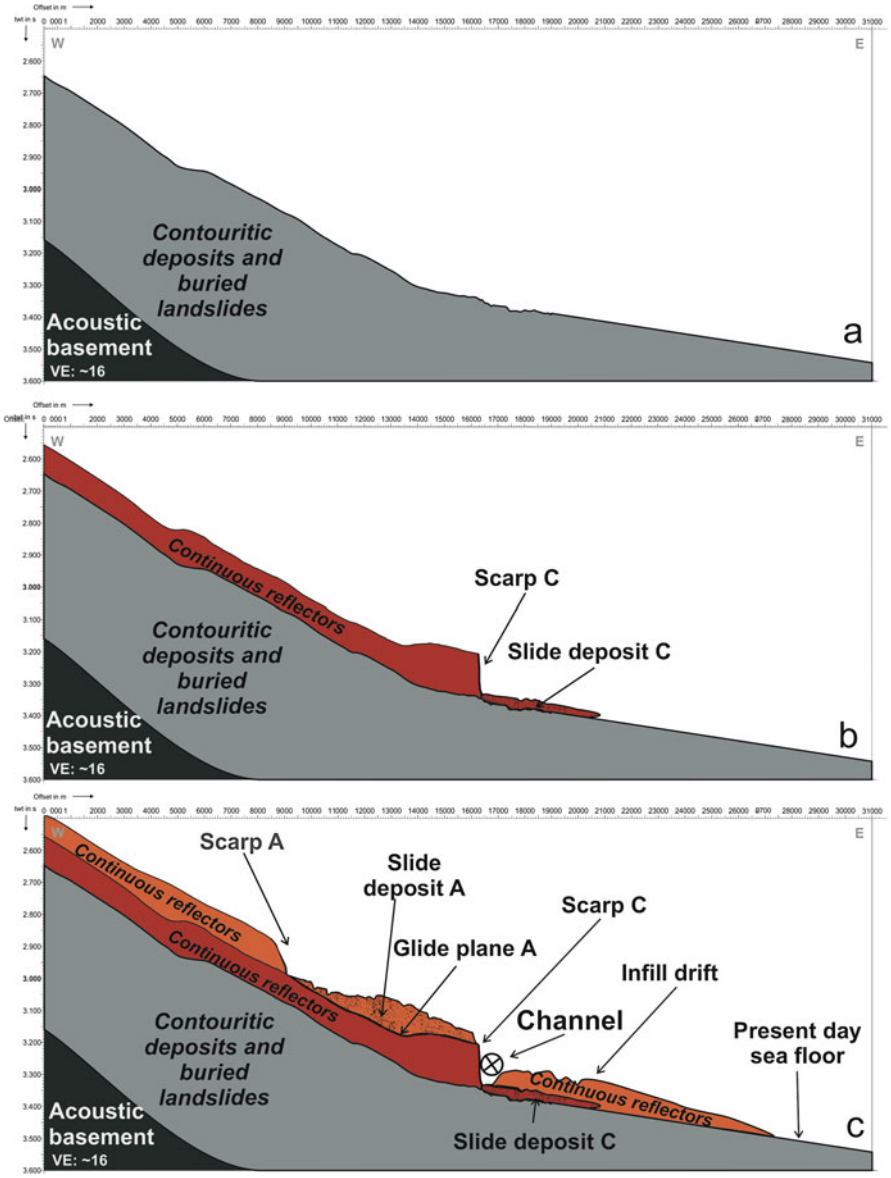

Fig. 41.4 Conceptual model showing the interaction of downslope and alongslope sediment transport reconstructed from seismic data: (**a**) pre-slide morphology. (**b**) Sediment accumulation and failure generating scarp C. (**c**) Focusing of contour currents leads to the formation of an infill drift and channel downslope of scarp C. Scarp A is formed by a second failure affecting more recent sediments

left against the morphological step. This process leads to the preservation of the morphological step and the deposition of an infill drift on the right-hand side of the current. The morphological step A was formed by a more recent failure as landslide deposits beneath this step are not covered by a major drape. No deposits of these failures are found in the channel beneath step C as these deposits were removed by the northward flowing bottom currents.

Incision B is the youngest morphological feature as it cuts all other features. A multidisciplinary study of a core taken in close proximity to incision B suggests an age of less than 30 years before present for the most recent landslide deposits (Henkel et al. 2011).

Seismic data (Fig. 41.3) also show deeply buried old landslides and widespread contouritic deposits. The margin in the de la Plata region is characterized by a long history of small-scale slope failures including failures in the recent past in a contouritic environment.

41.4 Discussion

41.4.1 Type of Landsliding: A Comparison Between NW-Africa and the de la Plata Region

The NW-African continental margin is characterized by very large but infrequent landslides (Fig. 41.1), while the de la Plata region shows smaller but more abundant landslides (Figs. 41.2, 41.3, and 41.4). These different styles of mass wasting may be explained by the different sedimentary and oceanographic setting of both regions.

Krastel et al. (2012) suggest that open slope areas off NW-Africa without major incisions allow rapid and undisturbed sediment accumulation beneath zones of high primary productivity, which in turn leads to sediment instabilities arising primarily from underconsolidation of deposited sediments and widespread lithological weak layers. The combination of infrequent triggers and high accumulation rates leads to the large size of individual landslides. The areas between the major landslides off NW-Africa are characterized by abundant canyons and gullies. These canyons act as effective pathways for regular downslope sediment transport by turbidity currents, preventing extensive slope failure.

A totally different setting is found in the de la Plata region. Canyons and gullies are rare, except for the major Mar del Plata Canyon (Fig. 41.1). The margin is characterized by significant fluvial input from large river systems and a complex oceanographic regime leading to widespread contouritic deposits. Contourites are well known to be potentially unstable especially as good grain-size sorting makes them weaker than poorly sorted sediments and excess pore pressure may develop within contourite units that are sandwiched between impermeable horizons

(Laberg and Camerlenghi 2008). Even small triggers would initiate mass failures in such environments. Despite the fact that the margin in the de la Plata region belongs to the passive Atlantic margin, it shows higher seismicity than the NW-African continental margin. E.g., a magnitude 5.2 m_b earthquake with an epicentre about 70 km southwest of the area shown on Fig. 41.2 occurred on June 26, 1988 (Benavídez Sosa 1998). Henkel et al. (2011) consider this earthquake as the most likely trigger for very young mass transport deposits in our study area. Once a landslide generated a headwall, the interaction between gravitational downslope and contouritic alongslope sediment transport is most evident. Currents are focussed at scarps generated by landslides, which leads to a preservation of them. Toe erosion may lead to further small failures of old landslide scarps.

41.4.2 Geohazard Potential

The geohazard potential for both margin settings is considered to be low but for different reasons. The landslides off NW-Africa are definitely large enough for triggering major tsunamis but these events are infrequent. Statistical analyses show that landslides in the northern Atlantic preferably occur at times of sea level rise and possibly lowstands (Lee 2009) suggesting relatively stable slopes during the present sea level highstand. However, Lee (2009) also pointed out that landslides during the present sea level highstands cannot be excluded; he listed three major dated landslides during the past 5,000 years including the Grand Banks landslide in 1929. Georgiopoulou et al. (2010) and Krastel et al. (2012) found some evidence for young landsliding in the source region of the Sahara Slide (see Fig. 41.1 for location) but exact age and size of this landslide is still under debate. Despite these findings, the likelihood for a major mass wasting event off NW-Africa in the near future is low and hence the geohazard potential is low.

Landslide frequency in the de la Plata region is much higher, though exact recurrence rates are unknown due to missing age control of individual slides. The only available data of one of the near-surface landslides is less than 30 years before present (Henkel et al. 2011). This date in combination with several additional near surface mass transport deposits proves that landslides in the de la Plata region occurred frequently in the recent past and will most likely be frequent in the near future. The volumes of these landslides, however, are small (usually <2 km^3) and they occur at relatively large water depths of more than 2,000 m. The deposits suggest quick disintegration of the landslide material. The tsunami potential of submarine landslides with these characteristics is estimated to be very low, despite the fact that the initial acceleration is known as an additional important parameter (Harbitz et al. 2006). Hence landslides in the de la Plata region may happen in the near future but they do not present a major hazard for coastal communities.

41.5 Conclusions

The NW-African continental margin is characterized by very large but infrequent slope failures, while the continental slope in the de la Plata region (Northern Argentina and Uruguay) shows abundant small landslides, which also occurred in the recent past. Long undisturbed sediment accumulation in combination with very rare triggers lead to very large landslides off NW-Africa, while smaller but more frequent failures of instable contouritic deposits result in the observed mass wasting patterns in the de la Plata region. Hence the sedimentary and oceanographic setting is one of the key factors controlling slope stability along passive continental margins. Despite the different settings, the geohazard potential is small for both settings, as the NW-African continental margin is currently stable, while the landslides in the de la Plata region are too small and too deep for triggering tsunamis which may endanger coastal communities.

Acknowledgments We thank all scientists and crew who supported data collection during numerous cruises. The authors are thankful to Domenico Ridente and Asrar Talukder for their reviews and constructive comments. Financial support was provided by the Deutsche Forschungsgemeinschaft.

References

Benavídez Sosa A (1998) Sismicidad y sismotectónica en Uruguay. Física de la Tierra 10:167–186

Bondevik S, Lovholt F, Harbitz CB et al (2005) The Storegga Slide tsunami – comparing field observations with numerical simulations. Mar Petrol Geol 22:195–208

Booth JS, O'Leary DW, Popenoe P et al (1993) U.S. Atlantic continental slope landslides: their distribution, general attributes, and implications. In: Schwab WC, Lee HJ, Twichell DC (eds) Submarine landslides: selected studies in the U.S. Exclusive Economic Zone, U.S. Geological Survey bulletin 2002. U.S. Geological Survey, Denver, pp 14–22

Camerlenghi A, Urgeles R, Ercilla G et al (2007) Scientific ocean drilling behind the assessment of geo-hazards from submarine slides. Sci Drill 4:45–47

Galy V, France-Lanord C, Beyssac O et al (2007) Efficient organic carbon burial in the Bengal fan sustained by the Himalayan erosional system. Nature 450:407–411

Georgiopoulou A, Masson DG, Wynn RB et al (2010) The Sahara Slide: initiation and processes from headwall to deposit of a giant submarine slide. Geochem Geophys Geosyst 11(7). doi:10.1029/2010GC003066

Gilberto DA, Bermec CS, Acha EM et al (2004) Large-scale spatial patterns of benthic assemblages in the SW Atlantic: the Rio de la Plata estuary and adjacent shelf waters. Estuar Coast Shelf Sci 61:1–13

Harbitz CB, Løvholt F, Pedersen G et al (2006) Mechanisms of tsunami generation by submarine landslides: a short review. Nor J Geol 86:255–264

Henkel S, Strasser M, Schwenk T et al (2011) An interdisciplinary investigation of a recent submarine mass transport deposit at the continental margin off Uruguay. Geochem Geophys Geosyst 12(Q08009). doi:10.1029/2011GC003669

Hernández-Molina FJ, Paterlini M, Violante R et al (2009) Contourite depositional system on the Argentine Slope: an exceptional record of the influence of Antarctic water masses. Geology 37:507–510

Hühnerbach V, Masson DG, Project Partners (2004) An analysis of submarine landslide dynamics and processes in the North Atlantic. Mar Geol 213:343–362

Klaus A, Ledbetter MT (1988) Deep-sea sedimentary processes in the Argentine Basin revealed by high-resolution seismic records (3.5 kHz echograms). Deep-Sea Res 35:899–917

Krastel S, Wynn RB, Hanebuth TJJ et al (2006) Mapping of seabed morphology and shallow sediment structure of the Mauritania continental margin, Northwest Africa: some implications for geohazard potential. Nor J Geol 86:163–176

Krastel S, Wefer G, Hanebuth TJJ et al (2011) Sediment dynamics and geohazards off Uruguay and the de la Plata River region (Northern-Argentina). Geo-Mar Lett 31:271–283

Krastel S, Wynn RB, Georgiopoulou A et al (2012) Large scale mass wasting at the NW-African Continental Margin: some general implications for mass wasting at passive continental margins. In: Yamada Y et al (eds) Submarine mass movements and their consequences, Advances in natural and technological hazards research 31. Springer, Dordrecht, pp 189–199

Laberg JS, Camerlenghi A (2008) The significance of contourites for submarine slope stability. In: Rebesco M, Camerlenghi A (eds) Contourites, vol 60, Developments in sedimentology. Elsevier, Amsterdam, pp 537–556

Lee HJ (2009) Timing of occurrence of large submarine landslides on the Atlantic Ocean margin. Mar Geol 264:53–64

Martinez P, Bertrand P, Shimmield GB et al (1999) Upwelling intensity and ocean productivity changes off Cape Blanc (Northwest Africa) during the last 70,000 years: geochemical and micropalaeontological evidence. Mar Geol 158:57–74

Masson DG, Wynn RB, Talling PJ (2010) Large landslides on passive continental margins: processes, hypotheses and outstanding questions. In: Mosher DC et al (eds) Submarine mass movements and their consequences, Advances in natural and technological hazards research 28. Springer, Dordrecht, pp 153–165

McAdoo BG, Pratson LF, Orange DL (2000) Submarine landslide geomorphology, US continental slope. Mar Geol 169:103–136

Preu BM, Schwenk T, Hernández-Molina J et al (2012) Sedimentary growth pattern on the northern Argentine slope: the impact of North Atlantic Deep Water on southern hemisphere slope architecture. Mar Geol 329–331:113–125

Sarnthein M, Koopmann B (1980) Late Quaternary deep-sea record on northwest African dust supply and wind circulation. Palaeoecol Afr 12:239–253

Tappin DR, Watts P, McMurtry GM et al (2001) The Sissano, Papua New Guinea tsunami of July 1998 – offshore evidence on the source mechanism. Mar Geol 175:1–23

Weaver PPE, Wynn RB, Kenyon NH et al (2000) Continental margin sedimentation with special reference to the Northeast Atlantic margin. Sedimentology 47:239–256

Wynn RB, Masson DG, Stow DAV et al (2000) The Northwest African slope apron: a modern analogue for deep-water systems with complex seafloor topography. Mar Petrol Geol 17:253–265

Chapter 42
Comparison of Mass Wasting Processes on the Slopes of the Rockall Trough, Northeast Atlantic

Aggeliki Georgiopoulou, Sara Benetti, Patrick M. Shannon, Fabio Sacchetti, Peter D.W. Haughton, Laia Comas-Bru, and Sebastian Krastel

Abstract The deep-water, sediment-starved Rockall Trough separates the western Irish shelf from the Rockall Bank. Both margins have narrow, steep slopes that connect the continental shelf with the deeper basin but differ in their underlying geological controls and sediment transport processes. We compare and contrast the opposing margins of the Rockall Trough and review the size, depth distribution and degree of mass wasting processes and associated geohazard risk on each margin.

Rapid contourite buildup, shallow underlying abrupt basement topography and slope oversteepening due to erosion at the base of the western margin have led to large slope failures such as the Rockall Bank Slide Complex.

In contrast, the eastern margin of the Rockall Trough marked the westernmost extent of the British Irish Ice Sheet, reflected on the shelf by the presence of end moraines. Sediment was delivered by meltwater discharged from the ice sheet which locally reached the shelf edge. In conjunction with the effect of erosion from bottom currents and localised slope failures, the waning of the ice sheet led to the formation of numerous canyons incising this slope.

Slope failures on the eastern margin were relatively small and sediment was progressively evacuated towards the deeper basin through canyons. In contrast, mass wasting on the western margin involved larger sediment volumes. Processes resulting in mass wasting on the western margin are likely to be still active.

A. Georgiopoulou (✉)
Marine & Petroleum Geology Group, UCD School of Geological Sciences, University College Dublin, Dublin, Ireland
e-mail: aggie.georg@ucd.ie

S. Benetti • F. Sacchetti
School of Environmental Sciences, University of Ulster, Coleraine, Northern Ireland, UK

P.M. Shannon • P.D.W. Haughton • L. Comas-Bru
UCD School of Geological Sciences, University College Dublin, Dublin, Ireland

S. Krastel
Institute of Geosciences, Christian-Albrechts-Universität zu Kiel, Kiel, Germany

S. Krastel et al. (eds.), *Submarine Mass Movements and Their Consequences*, Advances in Natural and Technological Hazards Research 37, DOI 10.1007/978-3-319-00972-8_42,

In contrast, the eastern margin that was glacially nourished is likely to be less active with only minor mass wasting resulting from contour current scour and local canyon margin collapse.

Keywords Submarine landslide • Slope failure • Scarp • Glacial environment • Statistical comparison

42.1 Introduction

The Rockall Trough is an elongate, steep-sided, NNE-SSW trending intracontinental basin west of Ireland and the UK (Fig. 42.1). It is 200–250 km wide, with water depths increasing from almost 3,000 m in the northern part to more than 4,000 m in the south where it opens to the Porcupine Abyssal Plain (Fig. 42.1).

It is bounded to the west by the Rockall Bank, a structural high with slopes of 5°–10° (Fig. 42.1). Its topography shows an almost flat plateau (0°–2°) at 300–400 m water depth (Fig. 42.1). The Rockall Bank Slide Complex (RBSC) excavates part of the Rockall Bank and deposits sediment onto the floor of the trough (Flood et al. 1979; Unnithan et al. 2001; Elliott et al. 2010; Georgiopoulou et al. 2013). Bottom current activity and contourite deposition have been invoked as partially responsible for the slope collapses (Elliott et al. 2010). Buried basement scarps of the Rockall Bank and contouritic deposition across them seems to play an important role on slope instability as well (Georgiopoulou et al. 2013).

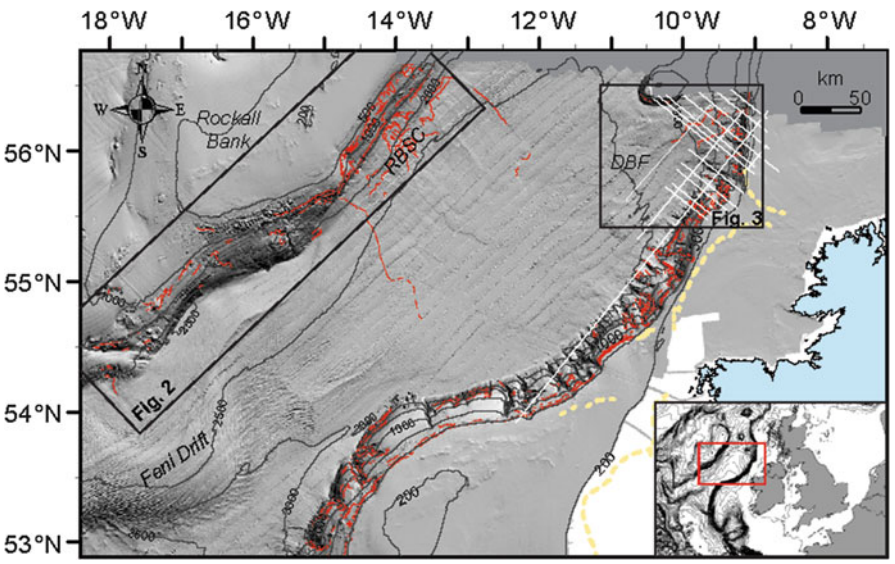

Fig. 42.1 Shaded relief bathymetric map of the study area. Marked with *red lines* are the mapped scarps. The *yellow dashed line* represents the maximum extent of the BIIS (After Benetti et al. 2010). The *white lines* show 2D seismic profiles of the DGER survey. Bathymetric contours are shown at 500 m intervals

The eastern margin crosses the boundary between the glaciated and glacially-influenced margins of the Northeast Atlantic (Weaver et al. 2000). It is characterised by the Donegal–Barra Fan (DBF) and a dense network of canyons dissecting the slope (Fig. 42.1). The DBF is a 450 m thick trough mouth fan that represents the southernmost glacial prograding wedge of Northern Europe and is built by sediments delivered from an expanded British Irish Ice Sheet (BIIS) during the Plio-Pleistocene (Armishaw et al. 1998; Dahlgren et al. 2005; Sejrup et al. 2005). Slope gradients are gentler (∼3°) than the opposite side of the trough as well as adjacent areas (3°–7°). The canyons were primarily active during sea level lowstands and glacial maxima, when sediment delivery to the slope was increased (Cronin et al. 2005; Elliott et al. 2006; Sacchetti et al. 2012). There is a remarkable correlation of the size and position of the canyons with the changing glacial features on the continental shelf (Sacchetti et al. 2012). Well-developed canyon systems formed where there was localised delivery of high volumes of meltwater and sediment from the ice front onto the slope (Sacchetti et al. 2012).

This study compares sediment mass movements from the margins of the Rockall Trough. It includes most of the previously published datasets and literature, together with some new data, to create a unique database of a statistically significant number of slope failure parameters (Fig. 42.1). The aim of the analysis is to describe and determine the parameters, such as number and density of scarps, scarp length, slope angle and water depth, that may have controlled the amount of sediment delivered to the basin floor through mass wasting. We also compare and contrast the causes and triggers of slope failure on the Rockall Trough margins and examine the potential present day geohazard.

42.2 Data and Methods

The study is based on high-resolution multibeam swath bathymetry and backscatter data acquired as part of the Irish National Seabed Survey between 1999 and 2002. The data were acquired in several phases with a Simrad EM120 multibeam echo sounder (MBES) and a Simrad EM1002 MBES. The processing and feature mapping methodologies are described in (Sacchetti et al. 2011).

The length, water depth and the slope gradient at the central point of scarps manually digitised were extracted and statistically analysed. Errors associated with manual digitisation may be present but every care was taken for correct mapping in order to digitise the slope just behind the break of slope.

A 2D seismic dataset of 1996 vintage was also integrated in the study. It extends across part of the depositional area of the Donegal-Barra Fan (Fig. 42.1). Dominant frequencies in the top second of the data, which is the interval of interest in this study, are in the range of 40–45 Hz which, with sediment velocities of 1,800–2,000 m s^{-1}, generate vertical resolutions of 10–12 m.

42.3 Results and Interpretations

42.3.1 Morphological Characteristics of the Rockall Trough Margins

42.3.1.1 Western Margin

Sedimentation on the western slope of the Rockall Trough is dominated by contouritic style deposition (Stoker et al. 2005) generating a slightly mounded topography built over buried deep fault scarps of the Mesozoic basement (Georgiopoulou et al. 2013). The slope is dissected by numerous scarps, the vast majority of which are found in the northern part of this slope (Figs. 42.1 and 42.2). Those scarps are responsible for the RBSC and have been described in detail by Elliott et al. (2010) and Georgiopoulou et al. (2013). They are linear to curvilinear, 15–60 m high, but some as high as 150 m, on average 20°–30° steep and occur on average on slope gradients of ~2°. Linear to curvilinear scarps are also found on the basin floor associated with the evacuation zone of the RBSC (Georgiopoulou et al. 2013). The distribution of the scarps and their different shapes have been attributed by Georgiopoulou et al. (2013) to different episodes of slope collapse.

The scarps on the southern part of this slope have not been described in detail before. In contrast to the northern slope here there are fewer scarps that appear to be distributed in eight clusters (A–H; Fig. 42.2). Most are linear and occur at different water depths (Fig. 42.2). The highest scarps are in cluster F (up to 170 m high) with gradients up to 30° on slopes that in places reach 10°–13°. Scarps in cluster A are similar to the RBSC scarps both in dimensions and water depth and also appear to relate to basement structures (Georgiopoulou et al. 2013, their Fig. 11b). Scarps in

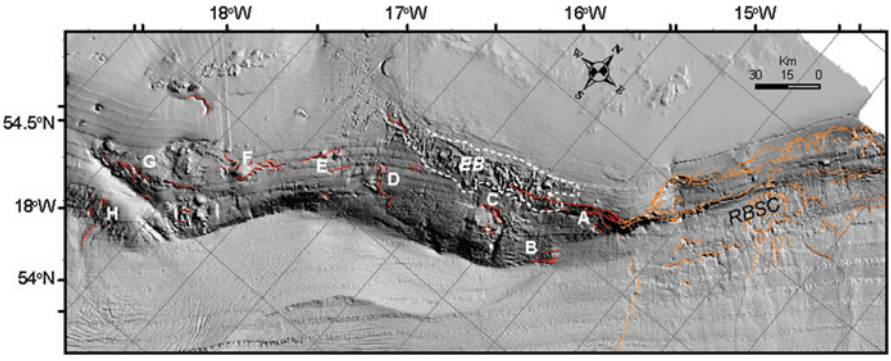

Fig. 42.2 Shaded relief of the western slope margin. *Red* and *orange lines* indicate the locations of mapped scarps. *Orange lines* represent scarps associated with the RBSC. The *white dashed line* outlines exposed bedrock (*EB*). Letters *A–H* refer to clusters of scarps (refer to text for more detail). For location see Fig. 42.1

clusters C, D and G seem to relate to channel-like features (Fig. 42.2); the ones in areas C and D incise the slope less than 10 km downslope of exposed basement bedrock, while those in cluster G mark the upslope margins of a channel that flows obliquely to the strike of the slope direction (Fig. 42.2). Finally clusters B and H involve scarps near the base of slope (Fig. 42.2). In B scarps are linear and aligned quasi-parallel to one another and the highest of them is 135 m high, while in H they are scoop-shaped and the highest of them is 60 m high.

42.3.1.2 Eastern Margin

The eastern slope is dissected by numerous canyons of various dimensions with associated channel wall and channel head collapses (Cronin et al. 2005; Elliott et al. 2006; Sacchetti et al. 2012). The formation of these canyons has been attributed to strong bottom current processes on the floor of the trough which destabilised the lower slope locally and created the initial erosional features in the form of scarps and slides (Elliott et al. 2006). These scars were subsequently developed and enlarged by headwall collapses propagating them upslope in a retrogressive manner (Elliott et al. 2006). These were subsequently cannibalised by flows deriving from the melting ice grounded at the shelf edge. Depending on the distance from the edge of the ice sheet and the duration of occupancy of the ice sheet at that location some canyons grew larger than others (Sacchetti et al. 2012).

Only three "open-slope" slide complexes, i.e. not related to canyon formation, are found on this margin (Sacchetti et al. 2012). Two are located on the upper slope in water depths of 500–1,000 m (S2 and S3 in Fig. 42.3) and are 10°–30° steep, 2–6 km long and 100–200 m high (Fig. 42.3). Both exhibit step-like morphology downslope. S2 is made up of four terraces distributed side-by-side, whereas S3 comprises two terraces, one narrower upslope that opens up to a double the width second terrace downslope. The two slides occupy inter-channel parts of the slope that have convex up morphology (Sacchetti et al. 2012).

The third slide is located within the area occupied by the DBF in the northeast and therefore lies on the trough floor (Fig. 42.3). Sacchetti et al. (2012) interpreted the westernmost scarp as the edge of a slide slab (their Fig. 42.3b). However, seismic profiles indicate that both the eastern and the western scarps represent sidewalls of a scar created by a slide that moved in a NE-SW direction following the general slope direction of the trough floor. This is in contrast to the interpretation of Sacchetti et al. (2012) who suggested two separate margins with a slide slab that had moved in a SE-NW direction following the margin slope direction. The previously interpreted slide slab in fact appears to be remnant seafloor with an undeformed internal character of layered reflectors that are sharply truncated (Fig. 42.3b, c). There is also evidence of stacked slide deposits (Fig. 42.3b, c). Syndepositional thrusts observed within buried slide deposits (Fig. 42.3d) also suggest a direction of flow (Bull et al. 2009) from the NE to the SW rather than SE to NW. Slides offshore Trinidad and Israel show similar syndepositional thrusts in the body of slide deposits instead of the

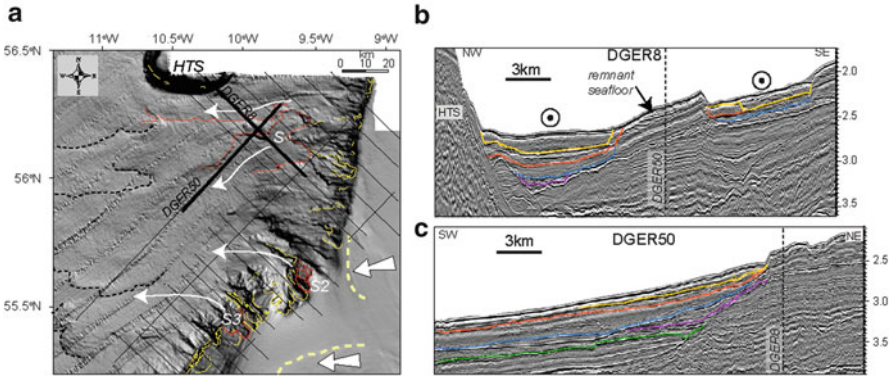

Fig. 42.3 (**a**) Shaded relief map of the NE margin showing the depositional lobes of the DBF (*dashed black lines*), with scarps in *yellow* (slides associated with canyons) and in *red* ("open" slope slides). *Yellow dashed lines* indicate the maximum extent of the BIIS on the shelf (After (Benetti et al. 2010). *White arrows* suggest sediment flow pathways. *Thin black solid lines* represent seismic data and with *thicker black figures* (**b**), (**c**) and (**d**). (**b**) and (**c**) Seismic profiles across scarps truncating seafloor reflectors. Note the stacked buried slides (bases marked with different colour for each event). (**d**) Seismic profile slowing syndepositional thrusts indicative of direction of movement to the SE. Slides were forced through the Hebrides Terrace Seamount (*HTS*) to the west and the rising Irish slope to the east constricting flows laterally. The vertical scale is two-way time in seconds. For location see Fig. 42.1

terminal toe, and they were attributed to lateral confinement during flow (Frey Martinez et al. 2005; Moscardelli et al. 2006), which may also be the case at the DBF that was forced through the Hebrides Terrace Seamount and the Irish slope.

42.3.2 Statistical Analysis and Distribution of Parameter Values

780 slope scarps were identified and analysed. 530 are located on the eastern Rockall slope in an area of about 23,000 km^2, and 250 are on the western slope in an area 20,000 km^2 in extent. The density of scarps on the eastern margin is 23 per 1,000 km^2, almost double that on the western margin (12.5 per 1,000 km^2).

The most abundant scarps are 2–6 km long (Fig. 42.4). However, the western slope has a higher frequency of scarps longer than 10 km (Fig. 42.4). A marked difference between the two margins is seen in the mean values of slope gradient at scarp locations. A mean of 8.7° occurs on the eastern slope, in contrast to 6° on the western slope. Kurtosis is a measure of how outlier-prone a distribution is, the higher the kurtosis the more outlier prone, which means that there is a wider distribution of values of slope gradient at the source area on the east (11.21) than on the west (5.98) (Fig. 42.4).

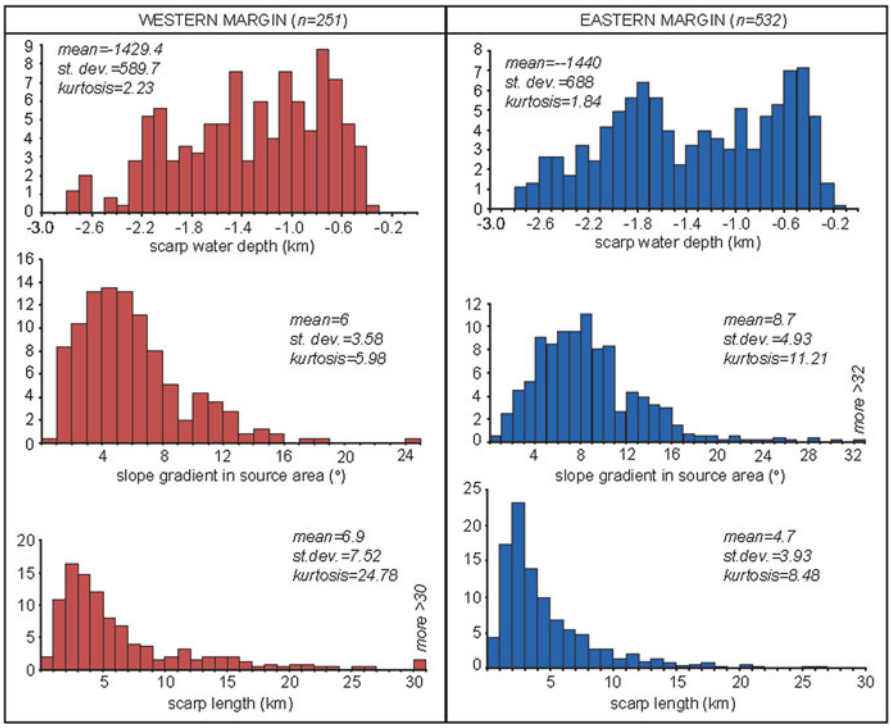

Fig. 42.4 Histograms of slope failure parameters for events on the Western and Eastern margins. The vertical axis in the graphs shows the percentage out of total number of events (*n*)

Scarps appear to initiate at different water depths on the two margins. On the west they are almost evenly distributed across water depths, with a slight preference for 600, 1,100, 1,500 and 1,900 m. In contrast there are two clear centres around 500 and 1,800 m on the eastern slope.

Spearman Rank coefficient (rho, ρ), which is used here as in (Hühnerbach et al. 2004) indicate that the parameters examined in this study correlate poorly apart from the water depth of scarps and slope gradient on the eastern margin, that show a weak negative correlation (Fig. 42.5).

42.4 Discussion and Conclusions

The western margin of the Rockall Trough can be regarded as reflecting "open slope" conditions as opposed to the eastern margin that may be regarded as reflecting "confined conditions" due to the dense distribution of canyons. Therefore their differences in mass wasting processes manifest the differences that arise from the conditions on such slope environments.

a

RHO	WEST		EAST	
	depth	gradient	depth	gradient
length	-0.12	0.05	0.19	-0.12
depth	------	0.05	-------	**-0.30**

b

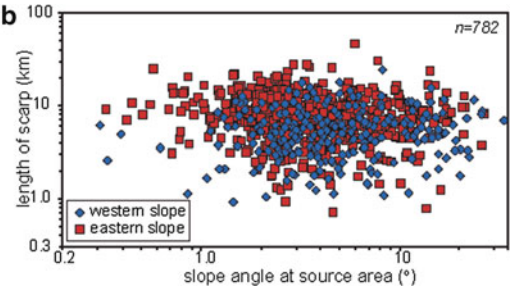

Fig. 42.5 (**a**) Table of correlation coefficients (Spearman Rank coefficient, rho) for the examined parameters and (**b**) scatter plots of scarp parameters expressed in log-log

The variation in mean slope gradient where slope instability has occurred may reflect different controlling mechanisms. Georgiopoulou et al. (2013) demonstrated that slide scarp location on the western margin was controlled by underlying structures as well as bottom current activity (Elliott et al. 2010), whereas on the eastern margin the main control was sediment supply and, by extension, canyon incision (Sacchetti et al. 2012). Most scarps on the eastern margin are located within canyons which have steeper slope gradients than the adjacent slope. This may also be the reason for the weak negative correlation seen between the water depth and slope gradient on this margin, with canyons having steeper margins at shallow than in deep water.

The canyon control may also explain the water depth distribution on the eastern slope as the two preferred water depths that are seen on the histogram (Fig. 42.4) seem to correspond to canyons that reached different stages of development (Elliott et al. 2006; Sacchetti et al. 2012). The peak at 500 m thus corresponds to the mature canyons that have reached the shelf edge whereas the deeper peak of 1,400 m corresponds to the mid-shelf canyons. The three "open slope" slide scarps found on the eastern margin cannot be distinguished within the population of scarps for this margin as they are limited in number and occur in various depths. In addition, scarps are also found aligned with an alongslope moat (Sacchetti et al. 2012), suggestive of the genesis mechanism for this moat. By contrast, on the west, scarps are more distributed across different water depths perhaps indicative of the basement control described by Georgiopoulou et al. (2013). The high percentage of events in deeper water depths there, potentially marks the effect of bottom currents near the break of slope, undercutting and removing support (Elliott et al. 2010).

The larger percentage of small slides on the eastern compared to the western margin may be explained by the fact that many of them are associated with submarine canyons and their interslope areas which have confined dimensions and therefore limit the extent to which scarps can extend. A similar distribution is also observed on the western Atlantic margin where it is also dominated by canyon-related mass movements (McAdoo et al. 2000). The mass wasting characteristics

on the eastern and western North Atlantic show many similarities with the present study, with the one margin being characterised by large infrequent slides and the other abundant smaller failures (Hühnerbach et al. 2004).

Considering that mass movement on the eastern slope was controlled by a sediment supply that no longer exists (the BIIS), slope failures will be scarce and only due to local slope instabilities within the canyons or where erosion due to bottom currents removes support. In contrast on the west where bottom currents are still active, there is sediment build up on top of the basement scarps, and hence a risk of further slope instability. How frequent the events are though remains to be determined. This change of focus of slope instability from the one margin to the other has also been observed in shallow sediment cores from the deep Rockall Trough (Georgiopoulou et al. 2012).

In conclusion, the scarp dimensions and distribution on the margins of the Rockall Trough differ in response to the underlying controls of sediment mass movement in each of these locations. They are controlled by canyon processes on the eastern margin and by contourite build up on top of buried Rockall Bank basement structures on the western margin.

Acknowledgements The UCD authors acknowledge funding from a Griffith Geoscience Research Award of the Irish Department of Communications, Energy and Natural Resources under the National Geoscience Programme 2007–2013 Ireland. We also thank the Petroleum Affairs Division of the Irish Department of Communications, Energy and Natural Resources for providing the seismic data used in the project and the Marine Institute (Ireland) and the Geological Survey of Ireland for access to the INSS dataset. We also acknowledge IHS for the license to use the KINGDOM software. The editor, Prof Michael Strasser, and the reviewers, Drs Jan Sverre Laberg and Lorena Moscardelli, are gratefully thanked for their comments and valuable input.

References

Armishaw JE, Holmes RW, Stow DAV (1998) Morphology and sedimentation on the Hebrides Slope and Barra Fan, NW UK continental margin. Geol Soc Spec Publ 129(1):81–104

Benetti S, Dunlop P, Ó Cofaigh C (2010) Glacial and glacially-related features on the continental margin of northwest Ireland mapped from marine geophysical data. J Maps 6(1):14–29

Bull S, Cartwright J, Huuse M (2009) A review of kinematic indicators from mass-transport complexes using 3D seismic data. Mar Petrol Geol 26(7):1132–1151

Cronin BT, Akhmetzhanov AM, Mazzini A, Akhmanov G, Ivanov M, Kenyon NH, Shipboard Scientists TTR (2005) Morphology, evolution and fill: implications for sand and mud distribution in filling deep-water canyons and slope channel complexes. Sediment Geol 179(1–2):71–97

Dahlgren KIT, Vorren TO, Stoker MS, Nielsen T, Nygard A, Petter Sejrup H (2005) Late Cenozoic prograding wedges on the NW European continental margin: their formation and relationship to tectonics and climate. Mar Petrol Geol 22(9–10):1089–1110

Elliott GM, Shannon PM, Haughton PDW, Praeg D, O'Reilly B (2006) Mid- to Late Cenozoic canyon development on the eastern margin of the Rockall Trough, offshore Ireland. Mar Geol 229(3–4):113–132

Elliott GM, Shannon PM, Haughton PDW, Øvrebø LK (2010) The Rockall Bank Mass Flow: collapse of a moated contourite drift onlapping the eastern flank of Rockall Bank, west of Ireland. Mar Petrol Geol 27(1):92–107

Flood RD, Hollister CD, Lonsdale P (1979) Disruption of the Feni sediment drift by debris flows from Rockall Bank. Mar Geol 32(3–4):311–334

Frey Martinez J, Cartwright J, Hall B (2005) 3D seismic interpretation of slump complexes: examples from the continental margin of Israel. Basin Res 17(1):83–108

Georgiopoulou A, Benetti S, Shannon PM, Haughton PDW, McCarron S (2012) Gravity flow deposits in the deep Rockall Trough, Northeast Atlantic. In: Yamada Y et al (eds) Submarine mass movements and their consequences, Advances in natural and technological hazards research. Springer, Dordrecht/Heidelberg/London/New York, pp 695–707

Georgiopoulou A, Shannon PM, Sacchetti F, Haughton PDW, Benetti S (2013) Basement-controlled multiple slope collapses, Rockall Bank Slide Complex. NE Atlantic Mar Geol. doi:10.1016/j.margeo.2012.12.003

Hühnerbach V, Masson DG, Participants of the COSTA-Project (2004) Landslides in the North Atlantic and its adjacent seas: an analysis of their morphology, setting and behaviour. Mar Geol 213:343–362

McAdoo BG, Pratson LF, Orange D (2000) Submarine landslide geomorphology, US continental margin. Mar Geol 169:103–136

Moscardelli L, Wood L, Mann P (2006) Mass-transport complexes and associated processes in the offshore area of Trinidad and Venezuela. AAPG Bull 90(7):1059–1088

Sacchetti F, Benetti S, Georgiopoulou A, Dunlop P, Quinn R (2011) Geomorphology of the Irish Rockall Trough, North Atlantic Ocean, mapped from multibeam bathymetric and backscatter data. J Maps 2011:60–81

Sacchetti F, Benetti S, Georgiopoulou A, Shannon PM, O'Reilly BM, Dunlop P, Quinn R, Ó Cofaigh C (2012) Deep-water geomorphology of the glaciated Irish margin from high-resolution marine geophysical data. Mar Geol 291–294(1):113–131

Sejrup HP, Hjelstuen BO, Dahlgren KIT, Haflidason H, Kuijpers A, Nygard A, Praeg D, Stoker MS, Vorren TO (2005) Pleistocene glacial history of the NW European continental margin. Mar Petrol Geol 22(9–10):1111–1129

Stoker MS, Praeg D, Hjelstuen BO, Laberg JS, Nielsen T, Shannon PM (2005) Neogene stratigraphy and the sedimentary and oceanographic development of the NW European Atlantic margin. Mar Petrol Geol 22(9–10):977–1005

Unnithan V, Shannon PM, McGrane K, Readman PW, Jacob AWB, Keary R, Kenyon NH (2001) Slope instability and sediment redistribution in the Rockall Trough: constraints from GLORIA. In: Shannon PM et al (eds) The petroleum exploration of Ireland's offshore basins, vol 188, Geol Society special publication., pp 439–454

Weaver PPE, Wynn RB, Kenyon NH, Evans J (2000) Continental margin sedimentation, with special reference to the north-east Atlantic margin. Sedimentology 47(suppl 1):239–256

Part VII
Landslide Generated Tsunamis

Chapter 43
The State-of-the-Art Numerical Tools for Modeling Landslide Tsunamis: A Short Review

Mohammad Heidarzadeh, Sebastian Krastel, and Ahmet C. Yalciner

Abstract We present a short review of the state-of-the-art numerical tools that have been used for modeling landslide-generated waves. A comparative study is conducted on the physical properties of earthquake- and landslide-generated waves suggesting that both dispersion and nonlinearity effects may be neglected for the former waves whereas they may be considered for the latter ones. We introduce landslide tsunami models and group them into three classes: (1) models treating the moving mass as a fluid, (2) models estimating the initial water surface, and (3) models fed by the transient seafloor deformation. Selection of a particular model from the list of models introduced here depends on: (1) the dimensions of the source, (2) the available computing capacities, (3) availability of fine bathymetric grid, and (4) the purposes of the modeling.

Keywords Submarine landslide • Landslide-generated waves • Tsunami • Numerical modeling

43.1 Introduction

Fifteen years after the 1998 Papua New Guinea (PNG) tsunami, a landslide tsunami triggered by a moderate earthquake (M_w 7) claiming 2,200 lives (Synolakis et al. 2002), the potential hazard posed by submarine mass failures remains

M. Heidarzadeh (✉)
Cluster of Excellence "The Future Ocean", Institute of Geosciences, Christian-Albrechts University zu Kiel, Kiel, Germany
e-mail: mheidarzadeh@geomar.de

S. Krastel
Institute of Geosciences, Christian-Albrechts-Universität University zu Kiel, Kiel, Germany

A.C. Yalciner
Department of Civil Engineering, Middle East Technical University, Ankara, Turkey

S. Krastel et al. (eds.), *Submarine Mass Movements and Their Consequences*, Advances in Natural and Technological Hazards Research 37, DOI 10.1007/978-3-319-00972-8_43,

poorly understood at least in comparison to tectonic-generated tsunamis. Although scientists were surprised by the significant death toll following a moderate offshore earthquake on that tragic day, now they are well aware that landslide-generated waves pose a major risk to coastal communities since they may be triggered by moderate or small earthquakes and sometimes even aseismically.

The 1998 PNG event was a milestone in tsunami research, as it brought the attention of scientific community to the potential large tsunami hazards associated with submarine mass movements (Synolakis et al. 2002) though the phenomenon has been known long before the PNG event (e.g., Gutenberg 1939). In the aftermath of this catastrophe, the tsunami hazard of several locations in USA, Japan and other parts of the World were revisited by taking into account possible submarine mass failures. However, these efforts require new tools and techniques as the tsunami-genesis and hydrodynamics of landslide tsunamis differs from those of tectonic tsunamis, in several ways.

To address the increasing need for conducting tsunami hazard assessments from submarine landslides, here we review available numerical tools which have proven their capabilities in accurate modeling of landslide-generated waves.

43.2 Physical Differences of Landslide and Tectonic Tsunamis

Table 43.1 compares the physical properties of landslides tsunamis with those of tectonic ones. The main differences are:

43.2.1 Difference in Source Dimensions

The seafloor deformation due to submarine tectonic displacements is normally of the order of hundreds of kilometers, whereas the dimensions of landslide sources are of the order of kilometers or less (Table 43.1). Therefore, tectonic tsunamis travel long distances with relatively little dispersion. Landslide-generated waves do not usually travel long distances due to their radial distribution of energy and their shorter wavelengths implying wave dispersion.

43.2.2 Difference in Initial Seafloor Deformation

Table 43.1 shows that the initial uplift or subsidence caused by submarine earthquakes is normally of the order of meters, but seafloor deformation due to landslides may be up to hundreds of meters. As a result of this relatively large seafloor

Table 43.1 Comparing the physical properties of some landslide tsunamis with those of tectonic ones

Type	Event name	Type of tsunami source	L[15] (km)	W[16] (km)	SD[17] (m)	R[18] (m)	T[19] (min)	FFE[20]	SS[21] (m/s)	μ[22]	ε[23]
Tectonic tsunamis	Dec. 26, 2004 (Indonesia)[1]	Earthquake (*Mw* 9.1)	900	200	14	>40	40–120[11]	Yes	4,000	0.002	8×10^{-6}
	Mar. 11, 2011 (Japan)[2]	Earthquake (*Mw* 9.0)	400	200	12	~40	40–100[12]	Yes	4,000	0.005	2×10^{-5}
	Feb. 27, 2010 (Chile)[3, 4]	Earthquake (*Mw* 8.8)	550	120	5	29	15–100[13]	Yes	4,000	0.004	5×10^{-6}
	July 12, 1993 (H-N-O)[5]	Earthquake (*Mw* 7.8)	150	35	4.2	31.7	20–90[14]	–	4,000	0.007	2×10^{-5}
Landslide tsunamis	July 17, 1998[6] (PNG)	Landslide after an earthquake (*Mw* 7.0)	4.5	5	760	15	2–5	No	10–15	0.22	2×10^{-3}
	Nov. 3, 1994 (Skagway)[7]	Construction works	0.33	0.16	15	9–11	1–3	No	35	0.1	8×10^{-3}
	Nov. 18, 1929 (Grand Banks)[8]	Landslide after an earthquake (*Mw* 7.2)	200	100	15	13	10–30	Yes	20	0.008	3×10^{-4}
	Dec. 30, 2002 (Stromboli)[9]	Landslide	2.2	0.7	30	11	0.5–1	No	30–60	0.5	4×10^{-3}
Mixed source	April 1, 1946 (Unimak)[10]	Both landslide and earthquake (*Mw* 8.2)	–	–	–	42	–	Yes	–	–	–

[1]Fujii and Satake (2007), [2]Fujii et al. (2011), [3]Rabinovich et al. (2012), [4]Fritz et al. (2011), [5]Satake and Tanioka (1995), [6]Synolakis et al. (2002), [7]Rabinovich et al. (1999), [8]Fine et al. (2005), [9]Tinti et al. (2006), [10]Okal et al. (2003), [11]Rabinovich and Thomson (2007), [12]Heidarzadeh and Satake (2013), [13]Rabinovich et al. (2012), [14]Myres and Baptsta (2001), [15]Length, [16]Width, [17]Seafloor deformation, [18]Maximum runup, [19]Period, [20]Far-Field effects, [21]Source speed, [22]Dispersion parameter, [23]Steepness parameter

deformation, landslides are capable of producing large runups in the near-field although their dimensions are usually small.

43.2.3 Difference in Modeling Techniques

Shallow water theory has been usually applied in the past decades for modeling of tsunamis which is based on the fact that tsunami wavelength (λ) is much larger than the water depth (d), or $\mu = d/\lambda \ll 1$ (Table 43.1) where μ is dispersion parameter. In fact, the effect of wave dispersion can be neglected for these long waves ($\lambda/d > 20$) because the phase velocity of waves ($c = \sqrt{gd}$) is a function of only water depth. However, landslide-generated waves are mostly classified as intermediate waves ($2 < \lambda/d < 20$) or deep-water waves ($\lambda/d < 2$). Due to the relatively small wavelengths of landslide-generated waves, dispersion plays a role in their propagation because the phase velocity of waves (e.g., for deep-water waves: $c = \sqrt{\frac{g\lambda}{2\pi}}$) is a function of wavelength for this type of waves indicating that longer waves propagate faster than the shorter ones. Therefore, long-wave equations may be applied cautiously for modeling of landslide tsunamis or an alternative set of equations needs to be employed.

43.2.4 Difference in Generation Mechanism

As the speed of seismic waves responsible for seafloor deformation (~4 km/s) is much larger than the propagation speed of long water waves (~0.1–0.2 km/s), it is often assumed that seafloor deformation due to a submarine earthquake occurs instantaneously. For landslides tsunamis, this is not a valid assumption because of the relatively lower speed of landslide movement on the seafloor (~0.01–0.1 km/s, Table 43.1). This means that the relatively slow motion of landslides during the generation process of a tsunami needs to be taken into consideration.

43.2.5 Linearity and Nonlinearity of the Waves

In deep water, landslide tsunamis are most often linear and thus the steepness coefficient $\varepsilon = a/\lambda$ is small (Table 43.1), where a is the wave amplitude. In shallow water, the waves become shorter and higher (steeper) until possible breaking. Here nonlinear models should be applied.

43.2.6 Differences in Warning Systems and Tsunami Countermeasures

The physical differences discussed between landslide and tectonic tsunamis necessitate different warning systems and tsunami countermeasures. While ground shaking and seismic records on seismometers provide useful warnings in many cases before the arrival of tectonic tsunamis, landslide tsunamis usually attack the coastal areas without warnings. As landslide tsunamis are normally characterized by extreme wave heights and are fairly unpredictable with regard to volume, location and release mechanism, construction of seawalls and other tsunami countermeasures may be less effective. Due to the unpredictability of landslide tsunamis, pre-computed landslide tsunami scenarios are not easily obtained for warning purposes whereas such pre-computed scenarios form the basis for tectonic tsunami warnings.

43.3 Modelling of Landslide Tsunamis

Landslide-generated waves are usually dispersive, nonlinear, and their source speed is relatively slow. In fact, different methods for modeling landslide tsunamis are based on the way that we incorporate the aforesaid criteria into the modeling method. Among the main characteristics of the landslide-generated waves, possibly the slow movement of the source at the tsunami generation phase is the most important. Different numerical models used for landslide tsunami modeling can be identified by the way that they treat the tsunami generation phase. This is the basis for our classification of landslide tsunami models in the next section.

43.4 Available Numerical Models for Modelling Landslide Tsunamis

In general, based on the way that a particular model treats the tsunami generation phase, we classify the landslide numerical models into three groups: (1) models that treat the submarine mass motion like the flow of a fluid with a particular density, (2) models that estimate the initial water surface using semi-empirical equations, and (3) models that are fed by the transient seafloor deformation at different times. Another classification was presented by Satake (2012). Table 43.2 presents a list of some numerical models that have been used for modeling of landslide-generated waves. Among the models presented in Table 43.2, some of them were originally developed for modeling of tectonic tsunamis which have been modified during the past decade to incorporate landslide sources (e.g., TUNAMI, and MOST). We briefly discuss below the classes of models.

Table 43.2 Numerical models used for modeling of landslide-generated waves

Type	Name	Developer	L/NL[1]	D/ND[2]	C/UC[13]	Case studies
Treating submarine mass as a fluid	–	Heinrich (1992)	NL	ND	C	Caribbean Sea[4]
	–	Jiang and LeBlond (1992)	NL	ND	C	–
	TWO_LAYER	Imamura and Imteaz (1995)	NL	ND	C	Marmara Sea[3]
	–	Tinti et al. (1999)	NL	ND	C	Stromboli, Italy
	–	Thomson et al. (2001)	NL	ND	C	1994 Skagway
	–	Assier-Rzadkieaicz et al. (2000)	NL	ND	C	1979 Nice event
	–	Kawamata et al. (2005)	NL	ND	C	1741 Oshima-Oshima
Estimating the initial water surface	–	Harbitz (1992)	L	ND	UC	Grand Banks (1929)
	MOST	Titov and Synolakis (1998)	NL	ND	UC	1998 PNG[6] South California[7]
	TUNAMI	Goto et al. (1997)	NL	ND	UC	Off. Indonesia[8]
	GEOWAVE	Watts et al. (2003)	NL	D	UC	1998 PNG 1994 Skagway
	NAMI DANCE	Insel (2010)	NL	D	UC	Marmara Sea[9]
	COULWAVE	Lynett and Liu (2002)	NL	D	UC	North Carolina[15]
	–	Weiss et al. (2006)	NL	D	UC	Valdes slide, Chile[14]
Transient Seafloor models	COMCOT	Liu et al. (1998)	NL	WD[10]	C	Mediterranean Sea[11]
	–	Satake (2001)	NL	ND	C	1741 Oshima-Oshima[12] Hawaii Island[12]
	–	Lynett and Liu (2002)	NL	WD[10]	C	1998 PNG[5]

[1]Linear model/non-linear, [2]Dispersive/non-dispersive, [3]Yalciner et al. (2002), [4]Heinrich et al. (1999), [5]Lynett et al. (2003), [6]Synolakis et al. (2002), [7]Borrero et al. (2004), [8]Brune et al. (2010), [9]Insel (2010), [10]Weak dispersion effect is included in which numerical dispersion is applied to mimic physical dispersion, [11]Iglesias et al. (2012), [12]Satake (2001, 2012), [13]Coupled/un-coupled, [14]Weiss et al. (2013), [15]Geist et al. (2009)

43.4.1 Models Treating the Submarine Mass Like a Fluid Flow

In this class of models, the movement of the submarine mass is treated like the flow of a fluid with the density of ρ_2. Therefore, two fluid layers with densities of ρ_1 and ρ_2 are modeled (Fig. 43.1). Long wave approximations are usually applied for

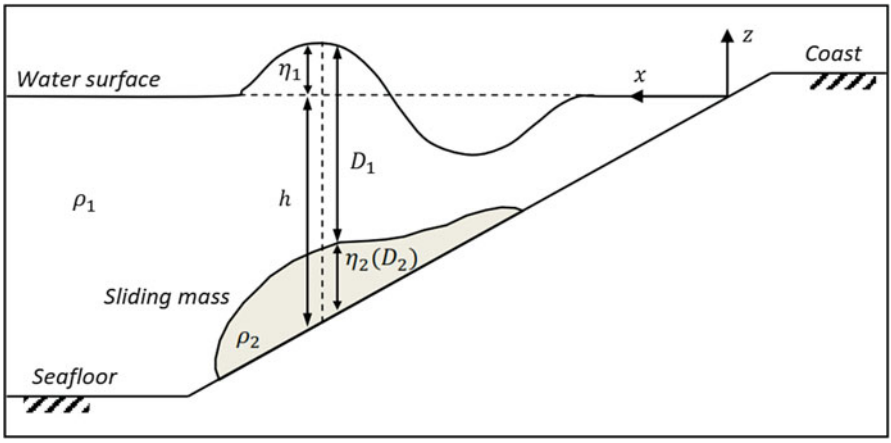

Fig. 43.1 Sketch showing the principles of the landslide models that treat the moving mass like the flow of a fluid with density $\boldsymbol{\rho_2}$. In this sketch, ρ_1 and $\boldsymbol{\eta_1}$ represent the density and wave height of the ocean water and η_2 is the thickness of the sliding mass

both the sliding mass and the resulting water waves. In this class of models, in some cases, only one flow with variable density in time and space is considered, e.g., the model by Heinrich (1992). For the simplest case in which the bottom friction and interfacial resistance are neglected, the 2D vertical (2DV) nonlinear long-wave equations (Imamura and Imteaz 1995) describing the system (Fig. 43.1) are:

For the water layer:

$$\frac{\partial(\eta_1 - \eta_2)}{\partial t} + \frac{\partial M_1}{\partial x} = 0 \tag{43.1}$$

$$\frac{\partial M_1}{\partial t} + \frac{\partial}{\partial x}\left(\frac{{M_1}^2}{D_1}\right) + gD_1\frac{d\eta_1}{dx} = 0 \tag{43.2}$$

And for the sliding mass:

$$\frac{\partial \eta_2}{\partial t} + \frac{\partial M_2}{\partial x} = 0 \tag{43.3}$$

$$\frac{\partial M_2}{\partial t} + \frac{\partial}{\partial x}\left(\frac{{M_2}^2}{D_2}\right) + gD_2\left(\alpha\frac{\partial D_1}{\partial x} + \frac{\partial \eta_2}{\partial x} - \frac{\partial h}{\partial x}\right) = 0 \tag{43.4}$$

in which g is the gravitational acceleration, M_1 and M_2 are flow discharges, α is density ratio $\left(\frac{\rho_1}{\rho_2}\right)$, and other parameters are shown in Fig. 43.1.

The TWO_LAYER model was successfully applied to the landslide sources in the Marmara Sea (Yalçıner et al. 2002). Other models of this class have been used for the modeling of the 1994 Skagway (Thomson et al. 2001) and the 1741 Oshima-Oshima (Kawamata et al. 2005) tsunamis (Table 43.2).

43.4.2 Models That Estimate the Initial Water Surface

Due to the complex nature of the generation phase of landslide tsunamis, some of the available numerical models simplify the generation phase by applying empirical equations. In fact, these models neglect the dynamic nature of the generation of waves by landslides. In this context, one set of empirical equations for modeling the generation phase of landslide tsunamis were proposed by Watts (1998) and described by Synolakis (2003). These authors estimated the 3D distribution of the initial sea level disturbance using 2DV numerical and experimental results. These empirical equations are based on a 2DV characteristic wave amplitude (η_{2d}). According to Watts et al. (2005):

$$\eta_{2d} = 0.0286\ T\ (1 - 0.75\ Sin\theta)\left(\frac{b \sin\theta}{d}\right)^{1.25} \tag{43.5}$$

in which, T and b are the thickness and length of the sliding mass, respectively, d is the submergence depth, and θ is the angle of the slope. Using Gaussian curve fits, Eq. (43.5) yields the 3D initial wave height of tsunami as follows (Synolakis 2003):

$$\eta_{3D}(x, y) = \frac{w}{\lambda + w} \sec h^2\left(\frac{3y}{w+\lambda}\right)\left[-1.2\ Z_{min} \exp\left(-\left\{1.2\ Z_{min}\frac{x - X_{min}}{\lambda\ Z_{max}}\right\}^2\right) + Z_{max} \exp\left(-\left\{\frac{x - X_{min} - \Delta x}{\lambda}\right\}^2\right)\right] \tag{43.6}$$

Here, Z_{min} is the maximum depression of the water surface calculated using $Z_{min} = 2.1\eta_{2d}$, Z_{max} is the maximum elevation obtained from $Z_{max} = 0.64\ \eta_{2d}\left(0.8 + \frac{0.2d}{b \sin\theta}\right)$, w is the width of the slide, λ is the characteristic wavelength given by $\lambda = \frac{u_t}{a_0}\sqrt{gd}$, g is gravitational acceleration, u_t is the terminal velocity of slide, and a_0 is the initial acceleration of slide. Δx is the distance between the crest of elevation wave and the trough of the depression wave, and given by $\Delta x = 0.5\ \lambda$, and X_{min} is the distance between the trough of the depression wave and the shoreline.

Figure 43.2 shows how a 3D initial wave of a landslide tsunami (η_{3D}) is calculated from its characteristic wave height (η_{2D}). To produce Fig. 43.2 (right panel), the characteristics of the 1998 PNG event were used for which the maximum elevation and depression in the initial profile of the water surface are 14 and 16 m, respectively. This class of landslide models is mostly composed of tectonic-tsunami models which have been modified to assign initial conditions using empirical equations.

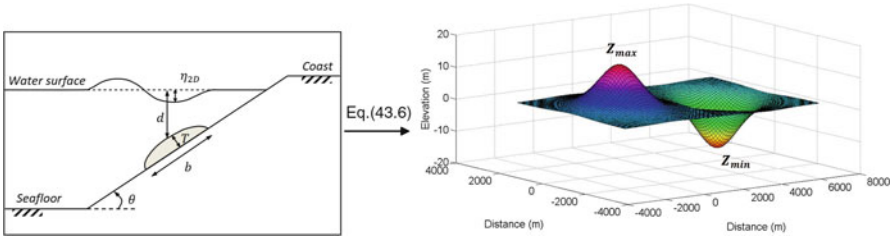

Fig. 43.2 Sketch showing the principles of the landslide model that estimate the initial wave height generated by landslide sources. Left panel shows the parameters used for calculation of the characteristic wave height (η_{2D}). Right panel shows the corresponding 3D initial wave height of tsunami (η_{3D}) calculated using Eq. (43.6)

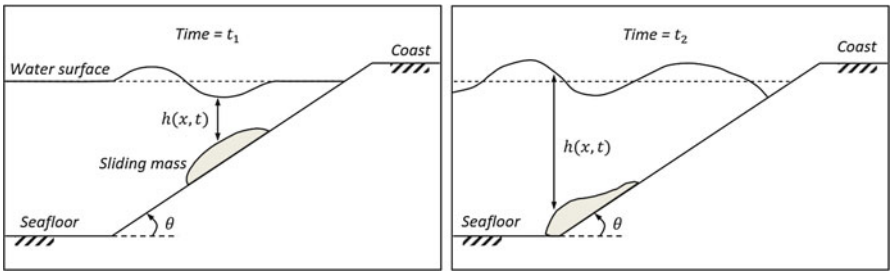

Fig. 43.3 Sketch showing the principles of the landslide models that are inputted by the transient seafloor deformation at different times. This figure shows the seafloor states at two different times during the evolution of a submarine landslide

43.4.3 Models Fed by the Transient Seafloor Deformation

These models are based on the assimilation of the numerical scheme of the shape of the seafloor deformation at different times. As an example, Fig. 43.3 shows the seafloor states at two different times of t_1 and t_2 which can be used as inputs for the numerical simulations. In this case, the landslide source will be treated by implementing the forcing term of $\frac{\partial h}{\partial t}$ in the continuity equation. By neglecting bottom friction and the Coriolis force, the nonlinear long-wave equations in a 2DV Cartesian domain take the following form (Wang 2009):

$$\frac{\partial \eta}{\partial t} + \frac{\partial M}{\partial x} = -\frac{\partial h}{\partial t} \tag{43.7}$$

$$\frac{\partial M}{\partial t} + \frac{\partial}{\partial x}\left(\frac{M^2}{h}\right) + gh\frac{\partial \eta}{\partial x} = 0 \tag{43.8}$$

in which the parameters are either as shown in Fig. 43.3 or were introduced above. The forcing term of $\frac{\partial h}{\partial t}$ at the right side of the Eq. (43.7) represents the forcing from

the landslide source which can be calculated by differentiating the seafloor states that are inputted to the program at different times.

According to Table 43.2, the COMCOT model (Liu et al. 1998) has been recently used for landslide tsunami modeling in the Mediterranean Sea (Iglesias et al. 2012). Another such model was proposed by Liu et al. (2005).

43.5 Discussions and Conclusions

A range of landslide tsunami models have been discussed (Table 43.2). These models are either linear or nonlinear, dispersive or non-dispersive, and coupled or uncoupled. The most accurate models for landslide tsunami modeling are likely those which are nonlinear, dispersive and coupled. However, application of such sophisticated and computationally-costly models is reasonable only if enough information about seafloor bathymetry and sliding mass is available, and only if it is needed for a proper description of the physical processes involved. Among the models studied here, GEOWAVE (Watts et al. 2003) is fully nonlinear and dispersive. NAMI DANCE is also nonlinear and dispersion effect is included in one of its versions. Two other models, e.g., COMCOT and the model by Lynett and Liu (2002), are weakly dispersive by applying numerical dispersion. Most of the models in Table 43.2 are nonlinear and non-dispersive. Our short review suggests that the numerical tools used for landslide-generated waves are not, in general, as standardized as those used for tectonic tsunamis indicating that the recommendations by Synolakis et al. (2008) need to be applied for their standardization.

All of the models presented in Table 43.2 have proven their capabilities in varying degrees in modeling of landslide tsunamis, by reproducing observations from past events. Therefore, we cannot propose a particular model from our Table 43.2 for landslide tsunami hazard assessment as superior or more capable. Application of a particular model from Table 43.2 depends on several factors:

1. The dimensions of the source whether the dispersion can be neglected for the landslide source or not.
2. The available computing capacities: for example, dispersive models like the model by Liu et al. (2005) usually need relatively long CPU times.
3. Availability of fine bathymetric grid: most of the landslide tsunami models need relatively small grid size compared to tectonic models.
4. The purpose of the modeling and the level of desired accuracy. In most cases, the final tsunami runup height and arrival time to coastlines are the purposes of modeling. In many cases dispersion is important for the propagation phase. The wave length is important for amplification and run-up.

Acknowledgments This study was funded by the Alexander von Humboldt Foundation in Germany. The first author is grateful to Prof. Kenji Satake (University of Tokyo, Japan) for his

supports and fruitful discussions. This manuscript benefited from detailed and constructive reviews by Dr. Carl B. Harbitz (Norwegian Geotechnical Institute, Norway), Prof. Costas E. Synolakis (University of Southern California, USA) and Dr. Anawat Suppasri (Tohoku University, Japan) for which we are sincerely grateful.

References

Assier-Rzadkieaicz S, Heinrich P, Sabatier PC, Savoye B, Bourillet JF (2000) Numerical modeling of a landslide-generated tsunami: the 1979 nice event. Pure Appl Geophys 157(10):1707–1727

Borrero JC, Legg MR, Synolakis CE (2004) Tsunami sources in the southern California bight. Geophys Res Lett 31(13):L13211

Brune S, Babeyko AY, Gaedicke C, Ladage S (2010) Hazard assessment of underwater landslide-generated tsunamis: a case study in the Padang region, Indonesia. Nat Hazards 53(2):205–218

Fine IV, Rabinovich AB, Bornhold BD, Thomson RE (2005) The Grand Banks landslide-generated tsunami of November 18, 1929: preliminary analysis and numerical modeling. Mar Geol 215:45–57

Fritz HM et al (2011) Field survey of the 27 February 2010 Chile tsunami. Pure Appl Geophys 168:1989–2010

Fujii Y, Satake K (2007) Tsunami source of the 2004 Sumatra–Andaman earthquake inferred from tide Gauge and satellite data. Bull Seismol Soc Am 97(1A):S192–S207

Fujii Y, Satake K, Sakai S, Shinohara M, Kanazawa T (2011) Tsunami source of the 2011 off the Pacific coast of Tohoku earthquake. Earth Planets Space 63:815–820

Geist EL, Lynett PJ, Chaytor JD (2009) Hydrodynamic modeling of tsunamis from the Currituck landslide. Mar Geol 264(1):41–52

Goto C, Ogawa Y, Shuto N, Imamura F (1997) Numerical method of tsunami simulation with the leap-frog scheme (IUGG/IOC time project), IOC Manual, UNESCO, No. 35

Gutenberg B (1939) Tsunamis and earthquakes. Bull Seismol Soc Am 29(4):517–526

Harbitz CB (1992) Model simulations of Tsunamis generated by the Storegge Slides. Mar Geol 105:1–21

Heidarzadeh M, Satake K (2013) Waveform and spectral analyses of the 2011 Japan Tsunami records on Tide Gauge and DART stations across the Pacific Ocean. Pure Appl Geophys 170(6–8):1275–1293. doi:10.1007/s00024-012-0558-5

Heinrich P (1992) Nonlinear water waves generated by submarine and aerial landslides. J Waterw Port, Coast, Ocean Eng ASCE 118(3):249–266

Heinrich P, Guibourg S, Mangeney A, Roche R (1999) Numerical modeling of a landslide-generated tsunami following a potential explosion of the Montserrat volcano. Phys Chem Earth A 24(2):163–168

Iglesias O, Lastras G, Canals M, Olabarrieta M, González M, Aniel-Quiroga Í, Otero L, Duran R, Amblas D, Casamor JL, Tahchi E, Tinti S, De Mol B (2012) The BIG'95 submarine landslide–generated tsunami: a numerical simulation. J Geol 120(1):31–48

Imamura F, Imteaz MA (1995) Long waves in two layer, governing equations and numerical model. Sci Tsunami Hazards 13:3–24

Insel I (2010) Landslide characteristics and tsunami generation, MSc thesis in METU Department of Civil Engineering, Coastal and Ocean Engineering Division

Jiang L, LeBlond PH (1992) The coupling of a submarine slide and the surface waves which it generates. J Geophys Res 97(C8):12731–12744

Kawamata K, Takaoka K, Ban K, Imamura F, Yamaki S, Kobayashi E (2005) Model of tsunami generation by collapse of volcanic eruption: The 1741 Oshima-Oshima tsunami. In: Satake K (ed) Tsunamis. Springer, Dordrecht, pp 79–96

Liu PL-F, Woo S-B, Cho Y-S (1998) Computer programs for tsunami propagation and inundation. Technical report, Cornell University

Liu PL-F, Wu T-R, Raichlen F, Synolakis C, Borrero JC (2005) Runup and rundown generated by three-dimensional sliding masses. J Fluid Mech 536:107–144

Lynett P, Liu PL-F (2002) A numerical study of submarine–landslide–generated waves and run–up. Proc R Soc Lond A 458:2885–2910

Lynett PJ, Borrero JC, Liu PL-F, Synolakis CE (2003) Field survey and numerical simulations: a review of the 1998 Papua New Guinea tsunami. Pure Appl Geophys 160:2119–2146

Myres EP, Baptsta AM (2001) Analysis of factors influencing simulations of the 1993 Hokkaido Nansei-Oki and 1964 Alaska tsunamis. Nat Hazards 23:1–28

Okal EA, Plafker G, Synolakis CE, Borrero JC (2003) Near-field survey of the 1946 Aleutian tsunami on Unimak and Sanak Islands. Bull Seismol Soc Am 93(3):1226–1234

Rabinovich AB, Thomson RE (2007) The 26 December 2004 Sumatra tsunami: analysis of Tide Gauge data from the World Ocean Part 1. Indian Ocean and South Africa. Pure Appl Geophys 164:261–308

Rabinovich AB, Thomson RE, Kulikov EA, Bornhold BD, Fine IV (1999) The landslide-generated tsunami of November 3, 1994 in Skagway Harbor, Alaska: a case study. Geophys Res Lett 26(19):3009–3012

Rabinovich AB, Thomson RE, Fine IV (2012) The 2010 Chilean tsunami off the west coast of Canada and the northwest coast of the United States. Pure Appl Geophys. doi:10.1007/s00024-012-0541-1

Satake K (2001) Tsunami modeling from submarine landslides. In: Proceedings of the international Tsunami symposium, Seattle, Washington (USA), 7–10 August 2001, vol 6, paper 6-4

Satake K (2012) Tsunamis generated by submarine landslides. Submarine mass movements and their consequences, Springer, pp 475–484

Satake K, Tanioka Y (1995) Tsunami generation of the 1993 Hokkaido Nansei-Oki earthquake. Pure Appl Geophys 144(3/4):803–821

Synolakis CE (2003) Tsunami and seiche. In: Chen WF, Scawthorn C (eds) Earthquake engineering handbook. CRC Press, Boca Raton, pp 1–90, Chapter 9

Synolakis CE, Bardet J-P, Borrero JC, Davies HL, Okal EA, Silver EA, Sweet S, Tappin DR (2002) The slump origin of the 1998 Papua New Guinea tsunami. Proc R Soc Lond A 458:763–789

Synolakis C, Bernard E, Titov V, Kanoglu U, Gonzalez F (2008) Validation and verification of tsunami numerical models. Pure Appl Geophys 165(11–12):2197–2228

Thomson RE, Rabinovich AB, Kulikov EA, Fine IV, Bornhold BB (2001) On numerical simulation of the landslide-generated tsunami of November 3, 1994 in Skagway Harbor, Alaska. In: Hebenstrait GT (ed) Tsunami research at the end of a critical decade, vol 18, Advances in natural and technological hazards research. Kluwer Academic Publishers, Dordrecht, pp 243–282, 304 p

Tinti S, Bertolucci E, Romagnoli R (1999) Modeling a possible Holocenic landslide-induced tsunami at Stromboli volcano. Phys Chem Earth 24(5):423–429

Tinti S, Maramai A, Armigliato A, Graziani L, Manucci A, Pagnoni G, Zaniboni F (2006) Observations of physical effects from tsunamis of December 30, 2002 at Stromboli volcano, southern Italy. Bull Volcano 68(5):450–461

Titov VV, Synolakis CE (1998) Numerical modeling of tidal wave runup. J Waterw Port Coast Ocean Eng 124(4):157–171

Wang X (2009) User manual for COMCOT version 1.7 (first draft), Cornel University, pp 65

Watts P (1998) Wavemaker curves for tsunamis generated by underwater landslides. J Waterw Port Coast Ocean Eng 124(3):127–137

Watts P, Grilli ST, Kirby JT, Fryer GJ, Tappin DR (2003) Landslide tsunami case studies using a Boussinesq model and a fully nonlinear tsunami generation model. Nat Hazards Earth Syst Sci 3(5):391–402

Watts P, Grilli ST, Tappin D, Fryer GJ (2005) Tsunami generation by submarine mass failure. II: predictive equations and case studies. J Waterw Port Coast Ocean Eng 131(6):298–310

Weiss R, Wunnemann K, Bahlburg H (2006) Numerical modelling of generation, propagation and run-up of tsunamis caused by oceanic impacts: model strategy and technical solutions. Geophys J Int 167:77–88

Weiss R, Krastel S, Anasetti A, Wuennemann K (2013) Constraining the characteristics of tsunami waves from deformable submarine landslides. Geophys J Int. doi:10.1093/gji/ggt094. http://gji.oxfordjournals.org/content/early/2013/04/05/gji.ggt094

Yalçıner AC, Alpar B, Altınok Y, Özbay İ, Imamura F (2002) Tsunamis in the Sea of Marmara: historical documents for the past, models for the future. Mar Geol 190(1):445–463

Chapter 44
Modeling Submarine Landslide-Generated Waves in Lake Ohrid, Macedonia/Albania

Katja Lindhorst, Sebastian Krastel, Cord Papenberg, and Mohammed Heidarzadeh

Abstract We study potential tsunami hazards associated with submarine landslides in Lake Ohrid, Macedonia/Albania. The transboundary Lake Ohrid located on the Balkan Peninsula shared by Macedonia and Albania is considered to be the oldest-continuously existing lake in Europe (2–5 Ma), though the age and the origin are not completely unraveled to date. Previous studies by means of hydroacoustic methods have shown that the western margin of Lake Ohrid has a long history of mass wasting. Based on seismic data, slide deposits are found in different stratigraphic levels as well as on the lake floor where they have affected a large area. This study is focused on the well-studied Udenisht Slide Complex covering an area of 27 km^2 within the southwestern part of Lake Ohrid. The Udenisht slide is by far the largest mass movement with an average thickness of 30–40 m and an estimated volume of about 0.11 km^3. It is therefore well within the limits of submarine landslides that are known to be capable of triggering tsunamis. Using numerical modeling, the propagation of a landslide-generated tsunami with an initial wave height of more than 5 m has been calculated. Run-up heights estimated for coastal communities around the lake are moderate in the north (2–3 m) can reach up to 10 m directly at the site where the slide initiated. This study is a first generation of landslide tsunami hazard assessment for Lake Ohrid and further detailed modeling is recommended for the region.

Keywords Lake Ohrid • Submarine landslide • Tsunami • Numerical modeling

K. Lindhorst (✉) • S. Krastel (✉)
Institute of Geosciences, Christian-Albrechts Universität zu Kiel, Kiel, Germany
e-mail: klindhorst@geophysik.uni-kiel.de; skrastel@geophysik.uni-kiel.de

C. Papenberg
Helmholtz Centre for Ocean Research Kiel, Kiel, Germany

M. Heidarzadeh
Cluster of Excellence – The Future Ocean, Institute of Geosciences, Christian-Albrechts University zu Kiel, Kiel, Germany

S. Krastel et al. (eds.), *Submarine Mass Movements and Their Consequences*, Advances in Natural and Technological Hazards Research 37, DOI 10.1007/978-3-319-00972-8_44,

44.1 Introduction and Study Area

Lake Ohrid situated on the Balkan Peninsula (Fig. 44.1) in a tectonically-formed basin is most likely the oldest lake in Europe (2–5 Ma, Albrecht and Wilke 2008). Surrounded by high mountains, the surface of Lake Ohrid is located at an altitude of 693 m above sea level. It extends 30 km north-south and 15 km east-west covering an area of about 360 km^2.

The total water volume of Lake Ohrid is 55 km^3; maximum water depth reaches 293 m (Popovska and Bonacci 2007). Previous geophysical investigations showed the importance of Lake Ohrid as a valuable archive to study the sedimentary evolution of a graben system over several million years (Lindhorst 2012).

Lake Ohrid has been formed as a pull-apart basin in Late Miocene with subsequent E-W extension within the South Balkan Extensional Regime (Burchfiel et al. 2008; Lindhorst 2012). The sedimentary infill within the central part of the basin indicates that Lake Ohrid existed continuously since its initial formation (Lindhorst et al. 2010). A first chronological model suggests that the oldest sediments within the deepest part of the basin are at least 2 Ma old (Lindhorst 2012). Acoustic data show widespread mass wasting deposits.

In this study we investigate the tsunamigenic potential of landslides within Lake Ohrid using numerical modeling. First, we briefly summarize mass wasting features within the basin. Afterwards we present results of our modeling approach with

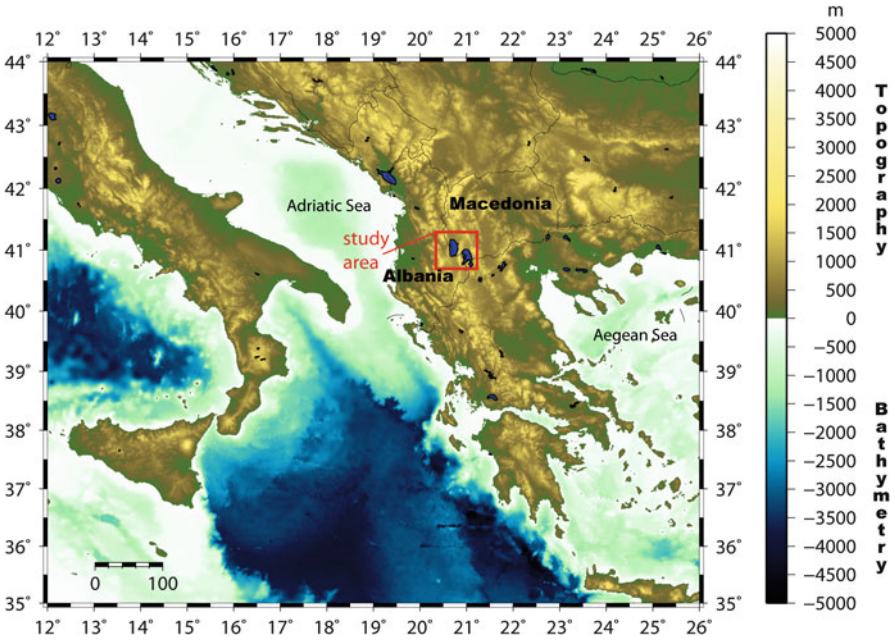

Fig. 44.1 General location map of Lake Ohrid on the Balkan Peninsula

a focus on wave amplitudes at several stations along the shore of Lake Ohrid. Our results increase the general understanding of landslide-generated hazard within active basins and can be seen as a case study for other deep lakes with steep flanks especially in regions with high seismic activities such as the alpine lakes.

44.1.1 Mass Wasting in Lake Ohrid

Slide deposits are widespread within the basin and can be found at different stratigraphic levels indicating that Lake Ohrid has a long history of mass wasting. Possible trigger mechanisms for submarine sliding events within Lake Ohrid were discussed in Lindhorst et al. (2012). The fact that Lake Ohrid is located within a seismically active region and the location of the Udenisht slide is along the active margin point to an earthquake as the most likely trigger for the Udenisht slide event. For example, Wagner et al. (2012) showed that an earthquake in the sixth century most likely triggered a slide in the northwestern part of Lake Ohrid.

Seismic cross sections of the southwestern part of Lake Ohrid show several chaotic units interpreted as mass wasting deposits within the youngest sedimentary succession (Lindhorst et al. 2012). In total, six slide deposits stacked on top of each other have been mapped. Up to 75 m-thick sediments overlay the oldest slide deposits (Lindhorst et al. 2012). The Udenisht slide complex is the most prominent subaquatic failure event in Lake Ohrid. Sediment echosounder profiles across the sliding area only show a thin sedimentary cover. Taking the sedimentation rate into account it was suggested that the event is younger than 1,500 years (Lindhorst et al. 2012). The sliding area can be identified by means of morphological data as shown in Fig. 44.2. The Udenisht slide covers almost 10 % of the entire lake surface. The Udenisht slide has a long run-out distance. Slide deposits are up to 50 m thick (Fig. 44.2). The volume of the slide is estimated to be $\sim$0.11 km^3 (Lindhorst et al. 2012). Interpretation of the slide morphology suggest that the slide can be classified as a retrogressive submarine mass movement with at least two sub-events and sudden failures of major blocks in the upper part of the slide area (Lindhorst et al. 2012). Although a distinct head wall of the slide has not been detected, we found evidence that the major event was initiated in shallow water depth. In 2009 a bathymetric survey was carried out by means of an ELAC Seabeam 1180 multibeam device resulting in a high resolution topography map (Fig. 44.2). The Udenisht slide area is characterized by an upper slope area bounded by distinct sidewalls and a run-out area where slide deposits up to a thickness of 60 m can be found (Lindhorst et al. 2010, 2012). Furthermore, the present topography excludes that the Udenisht slide was triggered onshore. Seismicity along an active fault trending in NW-SE direction and crossing the upper part of the sliding area, has been interpreted as a trigger for a sub-event in a water depth of about 120 m (Lindhorst 2012).

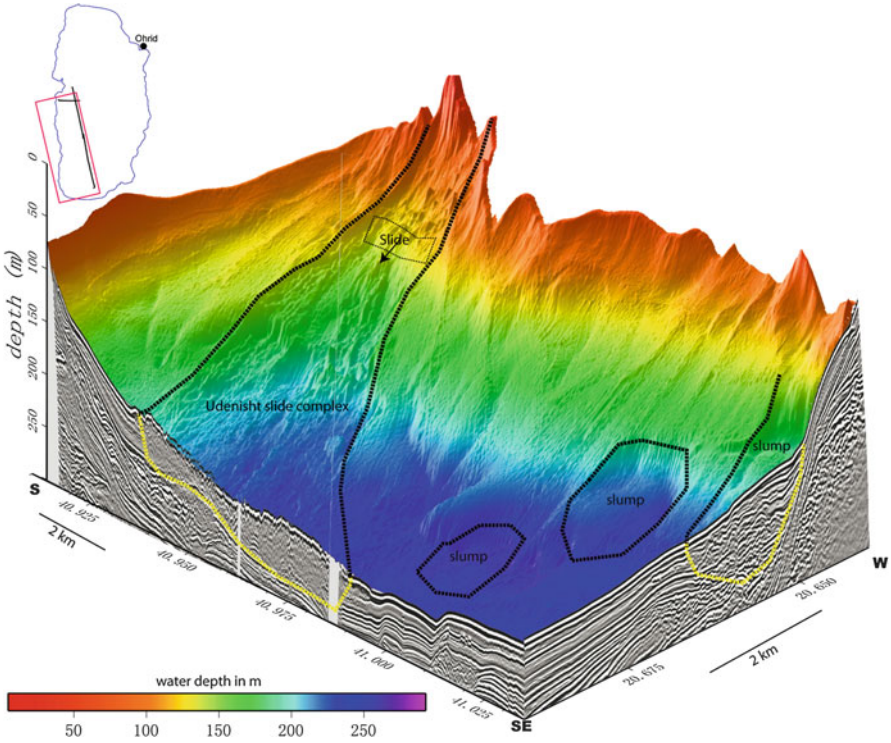

Fig. 44.2 Bathymetric map of the southwestern part of Lake Ohrid showing the morphology of the Udenisht slide complex. Two seismic cross sections showing the slide deposits of the Udenisht slide (*yellow dashed line* in S-N direction) and the slump (E-W profile) further to the north that we used for evaluating input parameters of the modeled tsunami. Two additional slumps along the western margin are marked

44.1.2 Numerical Approach

We use the numerical model TUNAMI-N2 (Imamura et al. 2006; Yalçiner et al. 2004) to simulate the propagation of long waves generated by possible submarine landslides within Lake Ohrid. Developed at the Tohoku University in Japan by Fumihiku Imamura and Nobou Shuto, TUNAMI is one the famous international numerical codes validated with both laboratory and field tsunami data (Yeh et al. 1996).

Tsunami modeling is usually composed of three steps of (1) generation, (2) propagation and (3) inundation. Here, we prevent the waves from inundation on dryland by imposing a vertical wall near the shoreline. To estimate the run-up heights at the main coastal communities around Lake Ohrid, we calculate tsunami wave height at offshore water depth and then apply an empirical equation to estimate the run-up heights. In our numerical simulations, wave evolution beyond water depth of 20 m is prohibited, and then empirical equations are used to

estimate run-up heights. Therefore, near-shore wave phenomena such as wave breaking are not considered here. This may imply an over-estimation of the run-up heights.

44.1.3 Initial Tsunami Wave

The initial tsunami wave amplitude will be build up during the acceleration time of the underwater slump. Combined information from high resolution bathymetric and seismic data within the area of the Udenisht slide provide input parameters to constrain the exact location, water depth, slide direction, and the geometry of the slide. However, the initial failure mechanism is difficult to reconstruct because we do not find a distinct headwall today. In order to overcome this problem, we assume that the Udenisht slide initially started as a slump similar to those observed further to the North (Fig. 44.2). Based on this assumption we apply the semi-empirical formulas proposed by Watts et al. (2003) and Grilli and Watts (2005) for our numerical modeling of landslide tsunamis.

The modeled submarine slide is located on the upper slope in a water depth of 120 m of the Udenisht slide complex and moves about 200 m downslope (Fig. 44.2). We further assume that a slide block rotates around a very small angle so that the movement can be described as a translation parallel to the slope. We do not account for deformation of the sliding block during the short acceleration time (t_0) until the maximum depression at the water surface is reach and the initial tsunami wave has been build-up. We assume a specific density of 1,900 g/cm^3 and slide geometry with width of 2,500 m, a length of 500 m, and a thickness of about 50 m resulting in a volume of 0.0625 km^3 for the simulated sliding block. This volume is half the volume of the Udenisht slide deposits (Lindhorst et al. 2012), which we consider as realistic initial slide volume because seismic data show significant entrainment of underlying sediments during slide propagation. The time t_0 until the maximum surface depression was generated is 14.7 s. The resulting wave has a wavelength $\lambda_0 = 510$ m and the characteristic wave height is 5.20 m. We calculated an initial acceleration of $a_0 = 0.8$ m/s^2, a maximum velocity of $u_{max} = 11.4$ m/s, a characteristic distance of motion of $S_0 = 170$ m, and a small angular displacement of $\Delta\Phi = 0.54$ rad.

44.2 Results

44.2.1 Wave Propagation and Estimated Run-Up Heights

The propagation of the modeled tsunami wave is shown in Fig. 44.3. Our modeled mass wasting event induces a tsunami wave reaching Progradec, Sveti Naum, Gradiste, Ohrid, and Struga after 0.5, 4, 4.5, 8, 10 min, respectively (Fig. 44.4).

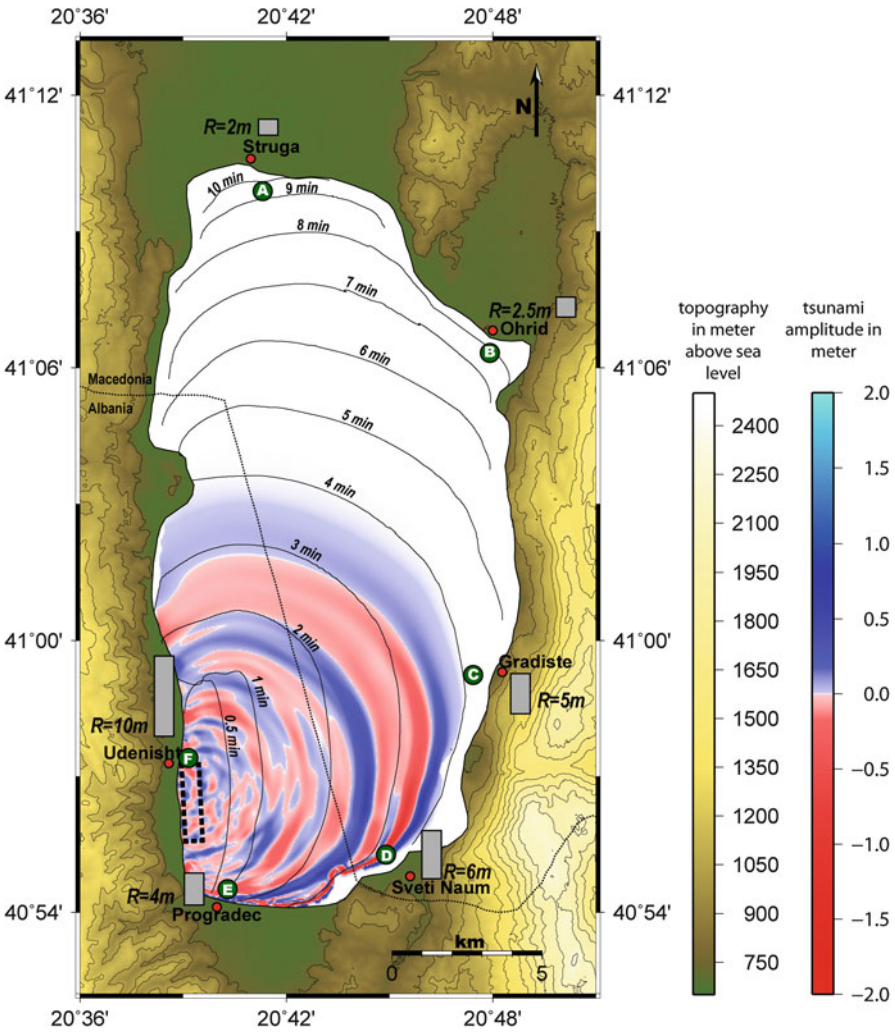

Fig. 44.3 Tsunami wave distribution (*red* and *blue colored*) in Lake Ohrid after 4 mins. Isolines show wave propagation after initiation at the slide location (*dashed square*) over a time period of 10 mins. After that time the tsunami has reached all the coastlines. *Grey bars* indicate run-up height normalized to the maximum run-up at Udenisht. *Green dots* are the virtual tidal gauge stations (Fig. 44.4)

Waves hit the coast at Udenisht immediately after failure occurs (Fig. 44.4). The maximum wave heights at the virtual gauge stations off Udenisht, Progradec, Sveti Naum, Gradiste, Ohrid, and Struga are 75, 60, 120, 60, 23, and 13 cm, respectively. The time histories of tsunami waves at selected locations are shown in Fig. 44.4. As shown, the artificial gauges are located at different water depths of 22, 18, 20, 18, and 20 m.

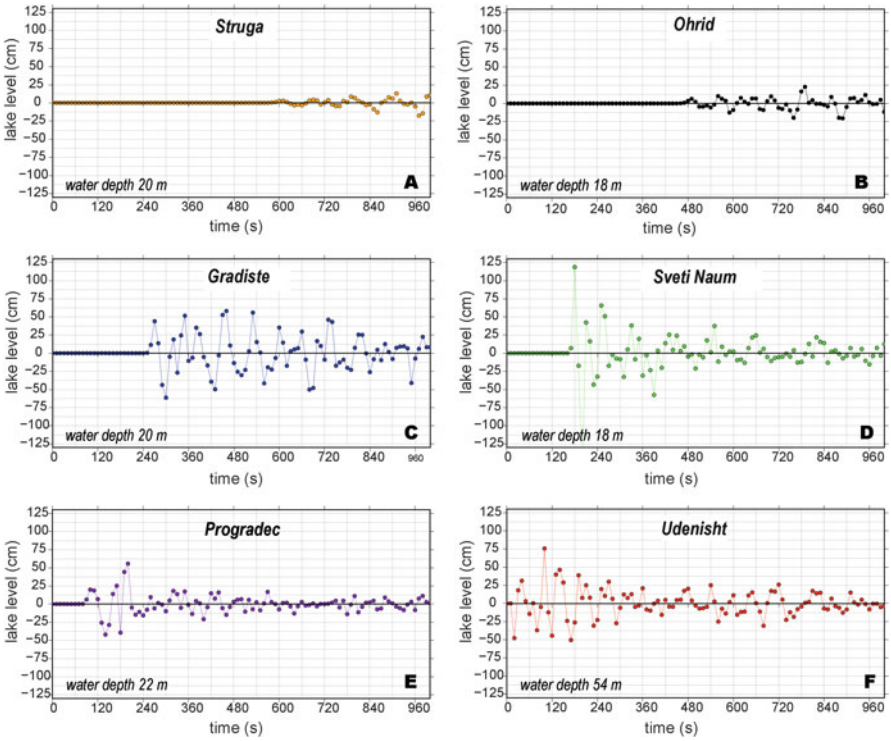

Fig. 44.4 Time histories of tsunami waves at some artificial gauges. Gauge locations are shown in Fig. 44.3

In general the maximum wave heights at Struga and Ohrid are relatively small (<25 cm). The highest waves are measured at Sveti Naum at a water depth of 18 m (Fig. 44.4). Table 44.1 presents our estimation of run-up values using two empirical equations. Whereas the first equation only considers the wave amplitude at a certain water depth and must be considered as a very simple approach to get a first impression of run-up heights at the coast. The second formula is an empirical approach including more parameters such as the slope angle and gives a more realistic estimation of run-up heights. In our cases we assume that the slope angles offshore Udenisht and Gradiste are greatest (∼4°) because they are located along the steep sides of Lake Ohrid. The slope angles in the north are small (∼2°) and for the southern region we assume medium slope values (∼3°). According to Table 44.1, in Udenisht, which is closest to the slide, the estimated run-up heights are greatest (2 and 10 m, Fig. 44.3). Run-up heights in Ohrid (0.5 and 2.5 m) and Struga (0.35 and 2 m) are moderate (Fig. 44.3). In the south the estimated run-up is about 5 m for the second formula (Fig. 44.4).

Table 44.1 Estimation of run-up values using empirical equation

Location	Offshore surface elevation (m)	Water depth (m)	Slope angle (°)	R1 (m)[a]	R2 (m)[b]
Udenisht	0.76	54	4	1.8	10
Progradec	0.6	22	3	0.8	4
Sveti Naum	1.2	18	3	2	6
Gradiste	0.6	20	4	1.2	5
Ohrid	0.23	18	2	0.5	2.5
Struga	0.13	20	2	0.35	2

[a]The empirical equation by Ward and Asphaug (2003) was used: $\mathrm{R1} = \sqrt[5]{\mathrm{A(d)}^4} \times \sqrt[5]{\mathrm{d}}$, where A(d) is the tsunami amplitude at water depth d

[b]The equation proposed by Ward and Day (2007): $R2 = 3.26 \times H_0 \times (\tan\beta)^{0.42} \times \left(\frac{A_0}{H_0}\right)^{0.41}$, in which H_0 is the offshore water depth in meters, A_0 is the wave amplitude at the water depth of H_0 in meters, β is the slope of the beach, and R is runup height in meters

44.3 Discussion and Conclusion

In order to discuss results of our modeled tsunami wave distribution across Lake Ohrid we compare our estimated run-up value to an empirical formula of Lynett and Liu (2005). In their approach they calculated run-up heights by taking the geometry, submergence depth and slope angle of the failure area into account to estimate a run-up at the coast closest to the submarine landslide event. The equation by Lynett and Liu (2005) gives a run-up value of about 6 m which is close to the values presented here.

According to a morphological analysis, the tsunamigenic potential for the Udenisht slide has been characterized as low (Lindhorst et al. 2012). A long run-out distance of slide material and the fact that the Udenisht slide has been characterized as a retrogressive event with at least two sub-events further reduce the absolute volume of individual failure events. However, this study illustrates that, in general, sub-lacustrine mass failure events as observed within the modern lake floor morphology inhibit a tsunamigenic potential. Results from our numerical modeling presented here show that an underwater slump with a shape similar to that in the northwestern part located at the site of the Udenisht slide is capable to trigger a tsunami wave. Our preliminary modeling shows that this wave would propagate across the entire lake in about 10 min but would have small to moderate estimated run-ups at the cities of Ohrid and Struga (see Table 44.1). At the village of Udenisht and in the southern area of Lake Ohrid we find that the estimated run-ups are large enough to cause significant damages along the coast and are hence a potential hazard for the coastal communities. The time between landslide and tsunami arrival at Udenisht, Progradec, Sveti Naum, and Gradiste is less than 5 min.

For our numerical solution we assume a simplistic scenario with the following assumptions: (1), a simple geometry of the sliding block (2) non retrogressive behavior of the slide, (3) the present of an intact block comparable to a slump, (4) a short horizontal displacement of ∼200 m, and (5) a submergence depth of about 120 m. A slump-type failure was considered in our modeling because, according to Watts et al. (2005), it has a higher potential to trigger a tsunami than submarine slides. The effect of retrogressive behavior of a landslide would reduce the maximum surface elevation and lead to smaller amplitudes (Bondevik et al. 2005; Harbitz et al. 2006). On the other hand, intense slide deformation in shallow water may increase coastal run-up by more than a factor of 2 and 3 (Grilli and Watts 2005). Hence tsunamis of significant height would be triggered, if further failures occur at the uppermost part of the Udenisht slide area.

In order to evaluate the influence of slide volume and initial submergence depth to the initial wave height we ran the tsunami model with higher and lower slide volumes as well as with higher submergence depth as input parameters than presented here which would then effect the coastal amplification. We found that the initial wave height increases dramatically if the tsunami initiates in shallower water depth. We considered these heights as unrealistic for Lake Ohrid because such an event during the last 2,000 years would have been mentioned in primary sources. Because our model does not allow wave breaking effect we could only simulate a tsunami in water depth greater than 50 m. The highest variability in input parameters is slide volume. Although we have a good estimation of the volume that got deposited after the failure along the western margin but it is uncertain whether these deposits are evidences for one single event. In addition our morphological data indicates that the Udenisht slide is a complex system of more than one event that is different in size and submergence depth. In general, an increase in volume would also increase the initial wave height and subsequently higher damages around the coast of Lake Ohrid.

In conclusion, this study gives a first impression of the tsunamigenic potential of sub-lacustrine mass movement events which are common within Lake Ohrid and have been found in different stratigraphic levels. Our study suggests that a potential tsunami hazard within Lake Ohrid cannot be neglected although our preliminary modeling showed that the run-up values would be small. This approach, however, points to the urgent need for more sophisticated modeling approaches for landslide generated tsunamis in Lake Ohrid and comparable lakes.

Acknowledgments We thank the reviewers Hendrik Vogel and Ahmet C. Yalciner as well as the editor Carl B. Harbitz for their comments and suggestions that improved the manuscript. The TUNAMI-N2 code used is this paper is originally authored by Professors Fumihiku Imamura and Nobou Shuto at the Tohoku University in Japan. TUNAMI-N2 is copyrighted to Professors Ahmet C. Yalciner, Fumihiku Imamura and Costas E. Synolakis. We acknowledge them for developing and making available the code to scientists around the world. We also would like to thank Sascha Brune for his constructive cooperation regarding landslide tsunami modeling. We also thank C. Berndt for valuable comments.

References

Albrecht C, Wilke T (2008) Ancient Lake Ohrid: biodiversity and evolution. Hydrobiologia 615:103–140. doi:10.1007/s10750-008-9558-y

Bondevik S, Løvholt F, Harbitz C, Mangerud J, Dawson A, Svendsen J (2005) The Storegga Slide tsunami—comparing field observations with numerical simulations. Mar Petrol Geol 22:195–208

Burchfiel B, Nakov R, Dumurdzanov N, Papanikolaou D, Tzankov T, Serafimovski T, King R, Kotzev V, Todosov A, Nurce B (2008) Evolution and dynamics of the Cenozoic tectonics of the South Balkan extensional system. Geosphere 4:918

Grilli ST, Watts P (2005) Tsunami generation by submarine mass failure. I: modeling, experimental validation, and sensitivity analyses. J Waterw Port Coast Ocean Eng 131(6):283–297

Harbitz C, Løvholt F, Pedersen G, Masson D (2006) Mechanisms of tsunami generation by submarine landslides: a short review. Nor J Geol 86:255–264

Imamura F, Yalciner AC, Ozyurt G (2006) Tsunami modelling manual. UNESCO IOC international training course on Tsunami Numerical Modelling

Lindhorst K (2012) Neotectonic and sedimentary evolution of Lake Ohrid (Albania/Macedonia): acquisition and interpretation of new hydro-acoustic and seismic data. Unpublished PhD thesis, Christian-Albrechts-Universität zu Kiel, Kiel

Lindhorst K, Vogel H, Krastel S, Wagner B, Hilgers A, Zander A, Schwenk T, Wessels M, Daut G (2010) Stratigraphic analysis of lake level fluctuations in Lake Ohrid: an integration of high resolution hydro-acoustic data and sediment cores. Biogeosciences 7:3531–3548. doi:10.5194/bgd-7-3651-2010

Lindhorst K, Gruen M, Krastel S, Schwenk T (2012) Hydroacoustic analysis of mass wasting deposits in Lake Ohrid (FYR Macedonia/Albania). In: Submarine mass movements and their consequences. Springer, Dordrecht, pp 245–253

Lynett P, Liu PL-F (2005) A numerical study of the run-up generated by three-dimensional landslides. J Geophys Res 110(C3):C03006

Popovska C, Bonacci O (2007) Basic data on the hydrology of Lakes Ohrid and Prespa. Hydrol Process 21(5):658–664

Wagner B, Francke A, Sulpizio R, Zanchetta G, Lindhorst K, Krastel S, Vogel H, Daut G, Grazhdani A, Lushaj B (2012) Seismic and sedimentological evidence of an early 6th century AD earthquake at Lake Ohrid (Macedonia/Albania). Climate Past 8:2069–2078

Ward SN, Asphaug E (2003) Asteroid impact tsunami of 2880 March 16. Geophys J Int 153(3):F6–F10

Ward SN, Day S (2007) Tsunami balls: a granular approach to tsunami runup and inundation. Commun Comput Phys 3(1):222–249

Watts P, Grilli S, Kirby J, Fryer G, Tappin D (2003) Landslide tsunami case studies using a Boussinesq model and a fully nonlinear tsunami generation model. Nat Hazards Earth Syst Sci 3(5):391–402

Watts P, Grilli S et al (2005) Tsunami generation by submarine mass failure. II: predictive equations and case studies. J Waterw Port Coast Ocean Eng 131:298

Yalçiner A, Pelinovsky E, Talipova T, Kurkin A, Kozelkov A, Zaitsev A (2004) Tsunamis in the Black Sea: comparison of the historical, instrumental, and numerical data. J Geophys Res 109(C12):C12023

Yeh HH-J, Liu PL, Synolakis C (1996) Long-wave runup models: Friday Harbor, USA, 12–17 September 1995. World Scientific, Singapore

Chapter 45
Modeling Potential Tsunami Generation by the BIG'95 Landslide

Finn Løvholt, Carl B. Harbitz, Maarten Vanneste, Fabio V. De Blasio, Roger Urgeles, Olaia Iglesias, Miquel Canals, Galderic Lastras, Geir Pedersen, and Sylfest Glimsdal

Abstract The BIG'95 landslide was emplaced 11,500 years ago and is one of the largest known submarine landslides in the Mediterranean Sea. The simulated landslide dynamics matches the observed run-out and deposited thickness. Water elevation simulated by using a dispersive tsunami model exceed 10 m close to the landslide area and at the nearest shorelines. Modeling further indicates that the tsunami probably had widespread consequences in the Mediterranean. Compared to previous studies, this new simulation provides larger waves. There is, however, still a need to better constrain the landslide dynamics in order to illuminate the uncertainties related to the tsunamigenic power of this, and other, submarine landslides.

F. Løvholt (✉)
Offshore Energy, Norwegian Geotechnical Institute (NGI), Oslo, Norway

Department of Mathematics, University of Oslo, Oslo, Norway
e-mail: finn.lovholt@ngi.no

C.B. Harbitz • S. Glimsdal
Natural Hazards, Norwegian Geotechnical Institute (NGI), Oslo, Norway

Department of Mathematics, University of Oslo, Oslo, Norway

M. Vanneste
Offshore Energy, Norwegian Geotechnical Institute (NGI), Oslo, Norway

F.V. De Blasio
Department of Earth Sciences, Università di Roma "Sapienza", Rome, Italy

Università di Milano "Bicocca", Milan, Italy

R. Urgeles
Dept. Geociències Marines, Institut de Cències del Mar (CSIC), Barcelona, Spain

O. Iglesias • M. Canals • G. Lastras
GRC Geociències Marines, Universitat de Barcelona, Catalonia, Spain

G. Pedersen
Department of Mathematics, University of Oslo, Oslo, Norway

S. Krastel et al. (eds.), *Submarine Mass Movements and Their Consequences*, Advances in Natural and Technological Hazards Research 37, DOI 10.1007/978-3-319-00972-8_45,

Keywords Submarine landslide • Slope failure • Tsunami • Frequency dispersion • BIG'95

45.1 Introduction

The BIG'95 landslide is one of the largest known submarine landslides in the Mediterranean Sea, with a volume of 26 km^3 (Canals et al. 2000) and an age of 11,500 years (Lastras et al. 2002). The landslide occurred at the Ebro margin at a water depth of about 1–1.5 km, and is thought to result from high pore-water pressures and differential compaction processes (Lastras et al. 2004; Urgeles et al. 2006). It evolved into a debris flow with intact rafted blocks, resulting in a run-out of 110 km for the debris flow and 15–20 km for the blocks (Fig. 45.1). The debris flow climbed some 20 m on the flanks of the Balearic Islands. At 11,500 year BP the contemporary sea level was some 80–120 m below today's level, and for this reason it is unlikely that onshore evidence of a possible tsunami can be found. Despite the lack of paleotsunami records, the large volume involved suggests that the landslide could have generated a significant tsunami. For a thorough assessment of the tsunamigenic potential, the dynamics of the landslide is crucial. Whereas a fast flowing landslide may be an efficient tsunami source, a large but slowly moving one may not generate a large tsunami (e.g. Løvholt et al. 2005).

Lastras et al. (2005) used a Bingham type rheology including both debris and transportation of rafted blocks to model the evolution of the BIG'95 landslide. Roughly mimicking both the total and the intact block run-out distances, maximum landslide velocities approaching 50 m/s were obtained. Using a shallow water model and basing their landslide model on Lastras et al. (2005), Iglesias et al. (2012) also simulated the possible tsunami, obtaining maximum water elevations up to 9.5 m at 9 m water depth offshore Mallorca. Tsunamis induced by landslides are, however, most often dispersive (e.g. Lynett et al. 2003; Harbitz et al. 2006; Glimsdal et al. in press), implying wavelength dependent wave speed. Hence, a more sophisticated model, for instance of Boussinesq type that incorporates dispersion, would give more reliable tsunami characteristics. Here, a reconstruction of the landslide as well as new landslide simulations building on the study of Lastras et al. (2005) is presented in Sect. 45.2. Compared to the study of Lastras et al. (2005) a series of transect simulations are employed for a representation of the tsunamigenic landslide in two horizontal dimension (Sect. 45.3). The tsunami modeling is presented in Sect. 45.3.

45.2 Simulated Landslide Evolution

The circumference of the BIG'95 landslide thickness is shown in Fig. 45.1. Further processing of the data is performed to shed light on the net erosion and deposition in the area, and thus constrain landslide dynamics and define the sliding planes.

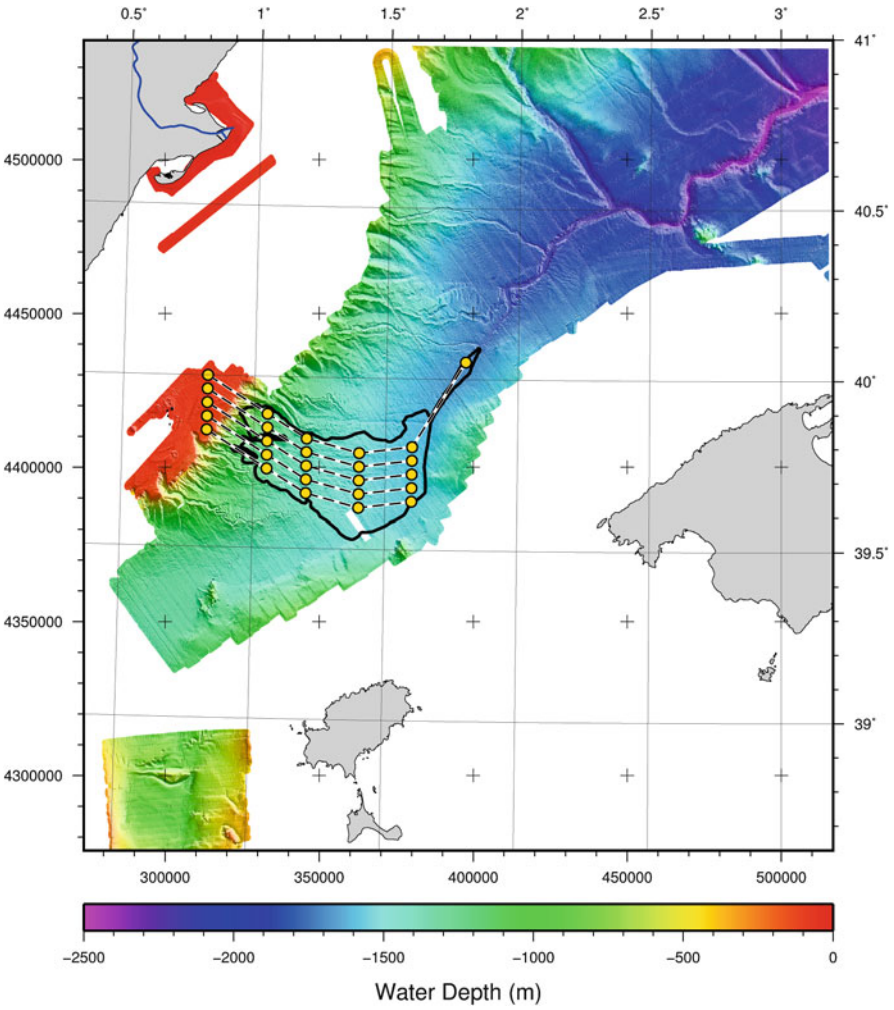

Fig. 45.1 Location of landslide deposits based on shallow sub-bottom profiling. The *dashed lines* show transects used for modeling the landslide dynamics

Post-failure evolution of the BIG'95 landslide is simulated along five "parallel" 2D transects (Fig. 45.1) using the Bing model (Imran et al. 2001). This simulation is based on the previous work by Lastras et al. (2005). However, the objective here is to provide a model of the landslide evolution in two horizontal dimensions for tsunami generation. Observed sediment distribution along the five selected transects is used to constrain the landslide run-out distance, debris thickness, pre-slide topography, etc. The landslide thickness along the transects is depicted in Fig. 45.2.

The BING model considers the landslide as a dense debris flow described by a Bingham rheology with a plug flow overlying a shear layer where no deformation

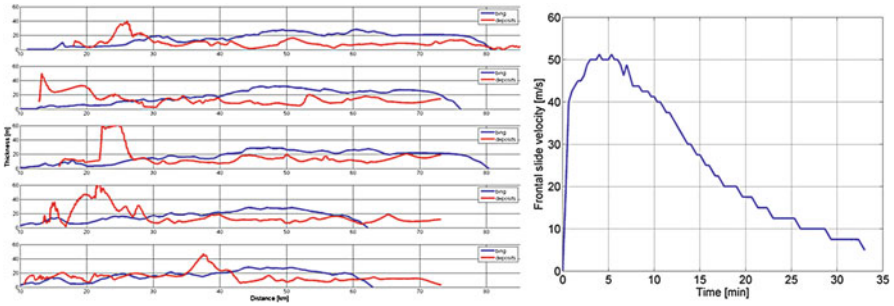

Fig. 45.2 *Left panel*: Comparison of the BIG'95 landslide thickness reconstructed from combining present day and pre-slide bathymetry (*red*), and thicknesses (*blue*) from landslide simulations after 33 min. The results are shown in descending order from north to south (the northernmost transect in Fig. 45.1 is the uppermost). *Right panel*: Frontal speed of the modeled BIG'95 landslide along the mid transect in Fig. 45.1

takes place until a certain yield strength is exceeded, after which the debris flows as a Newtonian fluid. The yield strength and the viscosity are tuned to 1 kPa and 1 kPa · s, respectively, to reproduce the observed landslide thickness (Fig. 45.1). A viscous drag with a skin friction of 0.002 (Norem et al. 1990) and a pressure drag coefficient of 0.8 are employed. Simplifying assumptions include constant parameter values no effects of possible hydroplaning. Hence, remolding effects implying reduction of the yield strength with time is not taken into account. Moreover, the Bing model does not take into account possible formation of low density turbidity currents (see e.g. Assier Rzadkiewicz et al. 1997).

Lastras et al. (2005) obtained best fit for slightly smaller yield strengths (0.5–0.8 kPa), while a yield strength of 0.8 kPa was utilized for the purpose of tsunami generation by Iglesias et al. (2012). Previous studies have employed different values for the Bingham rheologies: Marr et al. (2002) used viscosities of 30 and 300 Pa · s, as well as yield strengths ranging from 2 to 15 kPa to model the run-out of clay rich debris flows on the Bear Island fan, Norwegian Sea. Based on measurements from different sites, Locat and Lee (2002) exemplify yield strengths ranging from 0.01 to 1 kPa. Our employed yield strengths are in the upper range of those observed by Locat and Lee (2002). A high viscosity is used compared to Marr et al. (2002). Yet, as demonstrated below, the simulated landslide speed and acceleration are still relatively large.

At the start of the simulation, the landslide material is positioned upslope at locations corresponding roughly to the pre-landslide bathymetry. At the beginning, the frontal acceleration is too large. This is due to a large initial landslide thickness pushing the frontal part to a large acceleration. In addition, the constant value of the yield strength needed to mobilize the material is initially too low. Hence, the tsunami generation during the acceleration phase may be overestimated. The resulting run-out and landslide thicknesses after 33 min are compared with the slide thicknesses interpreted from the deposits as shown in Fig. 45.2. At this time, the landslide is

decelerating and is close to rest. The thicknesses are slightly overestimated, which may indicate that the employed yield strength needed to mobilize the landslide is somewhat too low. An example of the frontal slide speed is shown in Fig. 45.2, with a maximum of about 50 m/s. The slide speed corresponds well with the findings of Lastras et al. (2005). The maximum Froude number (defined as the ratio of the slide speed to the wave celerity) is approximately 0.5. Hence, the landslide speed is subcritical, which implies that the tsunami will run away from the landslide, limiting the build-up of the wave.

For each transect, the landslide consists of a combination of debris (Bingham fluid) and rafted blocks. The anomalous large thicknesses from the observed deposits are interpreted as intact blocks. It is noted that the blocks are present in the simulations (for details of the block motions see Lastras et al. 2005), but not displayed in Fig. 45.2. In Lastras et al. (2005), the block fraction reaches a maximum velocity of 20 m/s. The rafted blocks in the simulations move slower and are less effective in tsunami generation. Due to their limited wavelength, the tsunami amplitude induced by the rafted blocks would also attenuate faster with distance. Therefore, only the debris flow is retained to represent the tsunami source. For each output time step (1.5 s), the thickness of the Bingham fluid is interpolated between the transects, providing a time dependent landslide source in two horizontal dimensions as input to the tsunami model. In addition, time averaging is performed to provide a smoother velocity profile, providing landslide induced source terms every 20 s as input to the tsunami model. This is also the reason for the stepwise velocity profile depicted in Fig. 45.2. This procedure gives a volume of approximately 19 km^3 for the loose material phase, whereas the remaining 7 km^3 constituting the rest of the observed volume of 26 km^3 is interpreted as the rafted blocks.

45.3 Tsunami Propagation

Numerical simulations are performed using both a linear hydrostatic model (LSW) and a dispersive wave model GloBouss (Løvholt et al. 2008) with present day public domain ETOPO 1 bathymetry. The simulated time-dependent landslide thickness is interpreted as a time dependent distribution of source terms that are invoked in the continuity equation as the rate of change of the depth, whereas secondary source terms in the momentum equation are omitted. For further details on the landslide source terms in the tsunami model, see Løvholt et al. (2010).

First, the simulations are run on a grid resolution of 0.25′ (refined from ETOPO 1 using bi-linear interpolation) covering the Balearic Sea and the Balearic Islands for 1 h and 40 min of wave propagation. To ensure convergence, grid refinement tests were conducted for grid resolutions of 1′, 0.5′, and 0.25′ respectively, indicating an accuracy of about 1 % for the leading wave at 0.25′ resolution. Snapshots of the simulated surface elevations and maximum water levels for the whole duration are shown in Figs. 45.3 and 45.4, respectively. The wave displays an eastward sickle shaped positive wave, and a westward depression wave caused by the net mass

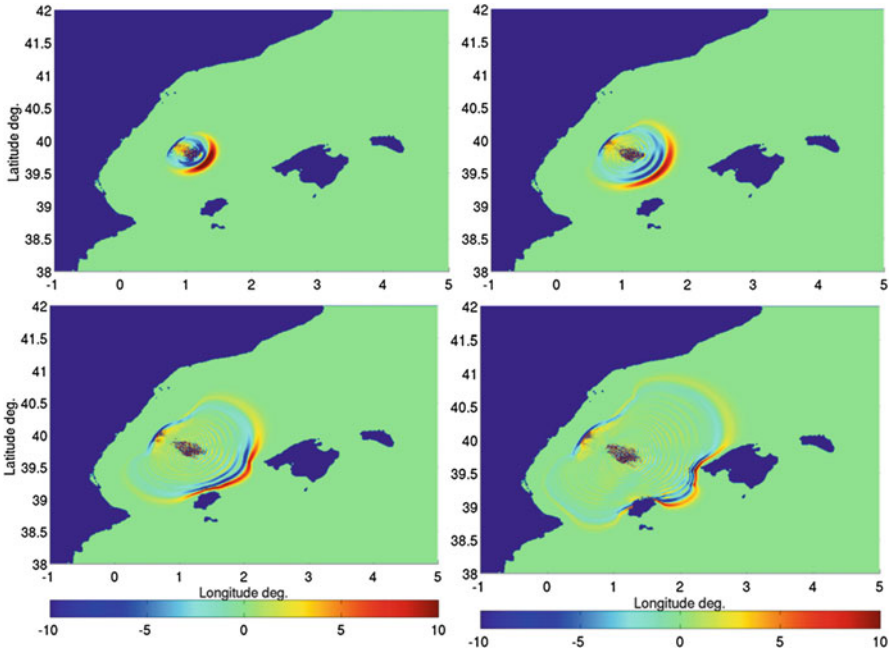

Fig. 45.3 Snapshots of the simulated sea surface elevation from the BIG'95 landslide tsunami near the source area and the Balearic Islands. *Upper left*: t = 5 min; *upper right*: t = 10 min; *lower left*: t = 15 min; *lower right*: t = 20 min

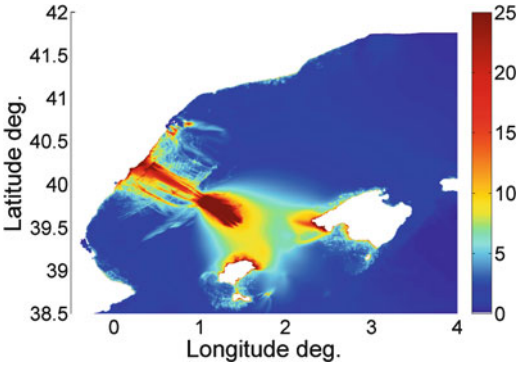

Fig. 45.4 Simulated maximum surface elevation over the whole simulation

withdrawal near the headwall. An elevation of more than 10 m is produced in the near field, indicating severe impact on the Balearic Islands and parts of eastern Spain. However, the tsunami has a pronounced directivity towards southeast and northwest, giving a narrower distribution of maximum surface elevation near the shoreline than typical for earthquake generated tsunamis (see Okal and Synolakis 2004, for a discussion). Far field simulations indicate water elevations exceeding 3 m offshore Catalonia and Africa (results not shown).

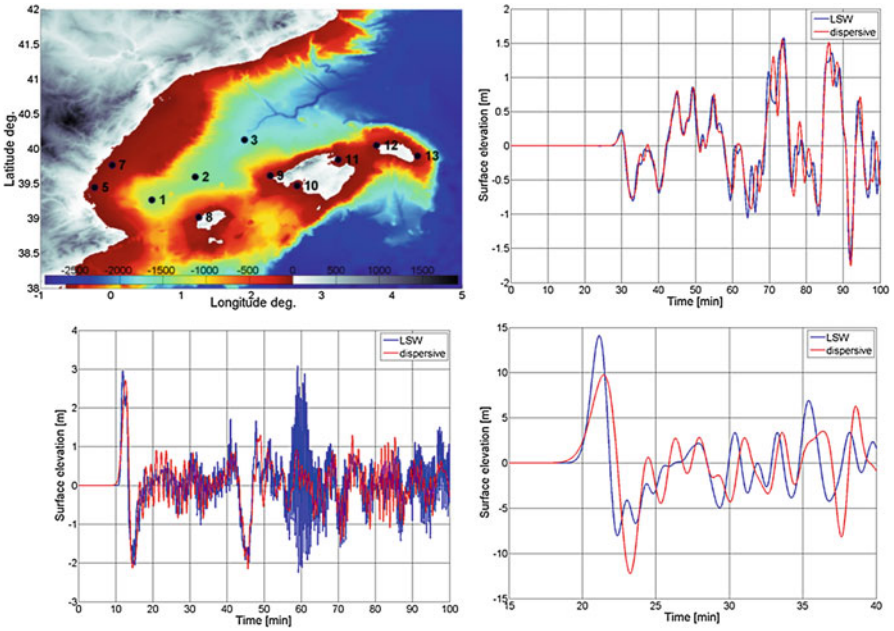

Fig. 45.5 *Upper left*: Location of synthetic gauges off the Ebro Margin and the Balearic Islands. *Upper right*: Surface elevation at gauge number 7. *Lower left*: Surface elevation at gauge number 3. *Lower right*: Surface elevation at gauge number 9

Figure 45.3 displays shorter trailing waves as compared to the leading one, most pronounced in the direction of landslide motion. This effect is interpreted as frequency dispersion. We clearly see some effects of dispersion for two of the gauges by comparing the LSW and dispersive models. The effect is most notable for gauge 9, located in the direction of the landslide motion, where LSW model gives a relative error of almost 50 % in the maximum surface elevation. This effect is typical for the points east of the source area shown in Fig. 45.5. We also note that for location 7 close to mainland Spain, the effects of dispersion are barely noticeable as a consequence of longer waves spreading azimuthally. Moreover, it is noted that the relative influence of dispersion increases with time. For a discussion of frequency dispersion of tsunamis, see Glimsdal et al. (in press).

Short crested spurious waves with a length within the grid size are also evident in the wave generation area in Fig. 45.5. These are artifacts due to sharp fronts in the progressing landslide, which are conveyed to the water surface. Although not attempted here, the short crested waves may be removed by applying dispersive filters that take into account the hydrodynamic response due to the seabed displacement (Kajiura 1963; Løvholt et al. 2012; Glimsdal et al. 2013). These waves move slowly and do not propagate far beyond the source generation area.

45.4 Discussion and Conclusion

Our simulations suggest that the 11,500 BP BIG'95 landslide along the Ebro margin may have been capable of generating a significant tsunami. A similar conclusion was found by Iglesias et al. (2012). However, an inspection of their map displaying the maximum water level indicates smaller waves. The discrepancy is due to differences in representation of the landslide dynamics and source terms in the numerical tsunami models. However, is noted that the shallow water assumption by Iglesias et al. (2012) is conservative with respect to the wave evolution. By performing this comparison, a challenge in hindcasting events of this kind is revealed: in both cases, the landslide run-out used for computing the tsunami is retrofitted roughly by the landslide simulation. Nonetheless, there is an inherent ambiguity as several parameter combinations including viscosity and yield strength that enter the landslide computation may produce more or less the same run-out distance. Hence, the simulated landslide dynamics may differ, affecting the tsunamigenic power. Parameter sensitivity analysis should be performed to demonstrate the possible parameter span in the landslide dynamics and its effect on tsunamigenesis. Unfortunately, such studies are rare for landslide induced tsunamis, and more research is needed within this field. We do not have paleotsunami evidence from the BIG'95 landslide. Maybe it remains concealed, unidentified, or maybe the landslide was actually not tsunamigenic because the mass release and flow evolved slower than modeled.

Acknowledgements The study was financially supported by the EU FP6 project TRANSFER (Tsunami Risk and Strategies for the European Region, contract no. 037058), and the Research Council of Norway (RCN) under project no. 205184. The Norwegian Geotechnical Institute (NGI), and the International Centre for Geohazards (ICG) are also thanked for supporting the work on this manuscript. Reviewers Dr. Peter Talling and Dr. Filippo Zaniboni are thanked for their valuable comments and positive criticism on the manuscript. This is contribution no. 418 of the International Centre for Geohazards (ICG).

References

Assier Rzadkiewicz S, Mariotti C, Heinrich P (1997) Numerical simulation of submarine landslides and their hydraulic effect. J Waterw Port Coast Ocean Eng ASCE 123(4):149–157

Canals M, Casamor JL, Urgeles R et al. (2000) The Ebro continental margin, Western Mediterranean Sea: interplay between canyon-channel systems and mass wasting processes. In: Nelson CH, Weimer P (eds) Deep-water reservoirs of the world: SEPM, Gulf Coast Section, 20th annual conference, Houston, TX, USA, pp 152–174

Glimsdal S, Pedersen G, Harbitz CB et al. (2013) Dispersive tsunamis; does it really matter? Nat Hazards Earth Syst Sci 13:1507–1526. www.nat-hazards-earth-syst-sci.net/13/1507/2013/. doi:10.5194/nhess-13-1507-2013

Harbitz CB, Løvholt F, Pedersen G et al (2006) Mechanisms of tsunami generation by submarine landslides: a short review. Nor J Geol 86:255–264

Iglesias O, Lastras G, Canals M et al (2012) The BIG'95 submarine landslide-generated tsunami: a numerical simulation. J Geol 120:31–48

Imran J, Harff P, Parker G (2001) A numerical model of submarine debris flow with graphical user interface. Comput Geosci 27:717–729

Kajiura K (1963) The leading wave of a tsunami. Bull Earthq Res Inst 41:535–571

Lastras G, Canals M, Hughes Clarke JE, Moreno A, De Batist M, Masson DG, Cochonat P (2002) Seafloor imagery from the BIG'95 debris flow, western Mediterranean. Geology 30:871–874

Lastras G, Canals M, Urgeles R et al (2004) Characterisation of a recent debris flow deposit after a variety of seismic reflection data, Ebro margin, western Mediterranean. Mar Geol 213:235–255

Lastras G, de Blasio FV, Canals M, Elverhøi A (2005) Conceptual and numerical modeling of the BIG'95 debris flow, Western Mediterranean Sea. J Sediment Res 75:784–797

Locat J, Lee H (2002) Submarine landslides: advances and challenges. Can Geotech J 39:193–212

Løvholt F, Harbitz CB, Haugen KB (2005) A parametric study of tsunamis generated by submarine slides in the Ormen Lange/Storegga area off western Norway. Mar Petrol Geol 22(1–2): 219–233

Løvholt F, Pedersen G, Gisler G (2008) Oceanic propagation of a potential tsunami from the La Palma Island. J Geophys Res 113:C09026. doi:10.1029/2007JC004603

Løvholt F, Pedersen G, Glimsdal S (2010) Coupling of dispersive tsunami propagation and shallow water coastal response. Open Oceanogr J Caribb Waves Spec Issue 4:71–82. doi:10.2174/1874252101004020071

Løvholt F, Pedersen GK, Bazin S, Kühn D, Bredesen RE, Harbitz CB (2012) Stochastic analysis of tsunami runup due to heterogeneous coseismic slip and dispersion. J Geophys Res 117:C03047. doi:10.1029/2011JC007616

Lynett PJ, Borrero JC, Liu PL-F, Synolakis CE (2003) Field survey and numerical simulations: a review of the 1998 Papua New Guinea tsunami. Pure Appl Geophys 160:2119–2146

Marr JG, Elverhøi A, Harbitz CB, Imran J, Harrf P (2002) Numerical simulation of mud-rich subaqueous debris flows on the glacially active margins of the Svalbard-Barents Sea. Mar Geol 188:351–364

Norem H, Locat J, Schieldrop BA (1990) An approach to the physics and the modeling of submarine flowslides. Mar Geotechnol 9(2):93–111

Okal EA, Synolakis CE (2004) Source discriminants for near-field tsunamis. Geophys J Int 158:899–912

Urgeles R, Leynaud D, Lastras G et al (2006) Back-analysis and failure mechanisms of a large submarine slide on the Ebro continental slope, NW Mediterranean. Mar Geol 226:185–206

Chapter 46
Modeling of Potential Landslide Tsunami Hazards Off Western Thailand (Andaman Sea)

Julia Schwab, Sebastian Krastel, Mohammad Heidarzadeh, and Sascha Brune

Abstract We model several scenarios of potential submarine landslide tsunamis in the Andaman Sea off the Thai west coast. Our results suggest that landslides may be capable of producing significant tsunamis. Two categories of submarine landslide scenarios were evaluated. Geometry parameters of the first category are taken from identified mass transport deposits (MTDs); the second category considers a potentially unstable block identified in seismic data. Our preliminary modeling approach shows that run-up values may reach significant tsunami heights for some scenarios. We point out that our results have to be regarded as only preliminary due to several limitations in our modeling approach. Our results, however, show the need for more sophisticated modeling of landslide tsunamis, especially regarding the failure process and inundation on dry land

46.1 Introduction

Due to its vicinity to the highly seismic Sunda Trench, the Thai west coast is vulnerable to tectonic tsunamis (e.g. Jankaew et al. 2008). Earthquakes, however, are not the only source of tsunami waves. Seismically triggered submarine slope failures

J. Schwab (✉)
Helmholtz Centre for Ocean Research, GEOMAR, Kiel, Germany
e-mail: jschwab@geomar.de

S. Krastel
Institute of Geosciences, Christian-Albrechts-Universität zu Kiel, Kiel, Germany

M. Heidarzadeh
Cluster of Excellence "The Future Ocean", Institute of Geosciences, Christian-Albrechts Universität zu Kiel, Kiel, Germany

S. Brune
GFZ German Research Centre for Geosciences, Potsdam, Germany

S. Krastel et al. (eds.), *Submarine Mass Movements and Their Consequences*, Advances in Natural and Technological Hazards Research 37, DOI 10.1007/978-3-319-00972-8_46,

are also known for producing large wave heights in the near field (Synolakis et al. 2002). However, tsunami warning is problematic, as landslides may initiate within minutes or hours of an earthquake (e.g. Fritz et al. 2012), and a seismic signal may not even be detectable prior to a landslide.

Schwab et al. (2012) identified several MTDs and indicators for potential future failures at the western edge of Mergui Ridge, which forms a part of the outer Thai shelf. By minimum volume estimations and submergence depth of identified deposits, they concluded that only a few slope failures may have been tsunamigenic, resulting in a low estimate for landslide tsunami hazards. In order to obtain a more detailed picture of the tsunamigenic potential that may arise from these slope failures, this study aims to quantitatively understand the landslide tsunami hazards off western Thailand by numerical modeling.

46.2 Geological Background

Schwab et al. (2012) examined 2D reflection seismic profiles across the Mergui Ridge-East Andaman Basin transition (Fig. 46.1a), and high resolution bathymetric data from the top of Mergui Ridge. They identified several stacked MTDs west of Mergui Ridge (Fig. 46.2a) indicating recurrent slope failures. Based on the thickness of undisturbed sediment packages between individual MTDs, long time intervals (hundreds of kyrs) were estimated between succeeding events. Possible causes for slope failures include ongoing tectonic activity, occurrence of potentially unstable drift deposits and the presence of fluids and resulting overpressure. Additionally, indicators for potential future failures were identified (Fig. 46.2b) at the faulted western edge of Mergui Ridge (Schwab et al. 2012).

46.3 Modeling and Data Set

Based on geometrical parameters derived from seismic and bathymetric dataset (Figs 46.1b and 46.2), different hypothetical scenarios of landslide tsunami generation were modeled. The dimensions of the modeled slides are comparable to those described by Brune et al. (2010b) from neighboring areas. We follow the modeling approach of these authors, which takes into account that small landslides do not fulfill the applicability conditions for more realistic source models (see Brune et al. 2010b for a discussion of the approach). Therefore initial wave heights are calculated by a set of semi-empirical formulas (Watts et al. 2005; Grilli and Watts 2005). These formulas describe the sea surface response to a simplified coherent rotational slump failure. Compared to other more realistic landslide formulas (e.g. Mohammed and Fritz 2012) they do not account for the deformation of the slide during the failure process. For calculating tsunami propagation, the TUNAMI-N2

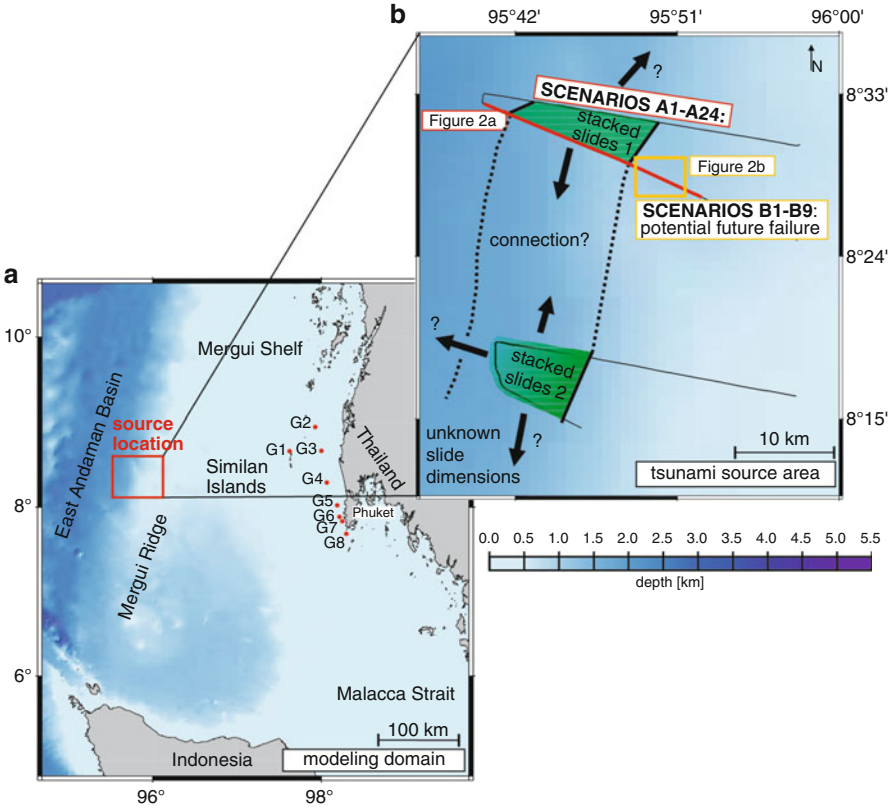

Fig. 46.1 (**a**) Bathymetric map of modeling domain and main structural features. G1–G8 indicate "artificial gauge stations" near the coast (20–50 m water depth) where maximum wave heights of tsunami are derived from. (**b**) Source location for chosen scenarios. *Green* areas indicate the locations where stacked slides have been identified in the basin on seismic profiles (*thin black lines*). *Black arrows* indicate the uncertainty in slide width

numerical code (e.g. Goto et al. 1997) was applied, and an extension of this code (Brune et al. 2010a) was used to test stability conditions of input parameters and to calculate initial wave heights as described above. The simulations were performed for a total time of 25,200 s for all scenarios with a time step of 0.5 s using the GEBCO bathymetric grid (IOC et al. 2003) resolved to 32 arc sec.

Calculated maximum wave heights are regarded at eight artificial gauge stations G1–G8 (Fig. 46.1a, Table 46.1) placed offshore at water depths of about 20 m (G1) and about 50 m (G2–G8). Empirical formulas were applied to obtain a first estimate of potential run-up heights R1 (Ward and Asphaug 2003) and R2 (Ward and Day 2008) from the maximum offshore wave heights at G1–G8. R1 depends only on water depth and tsunami wave height at an offshore location, whereas for R2 also the slope angle between offshore location and shore line is included.

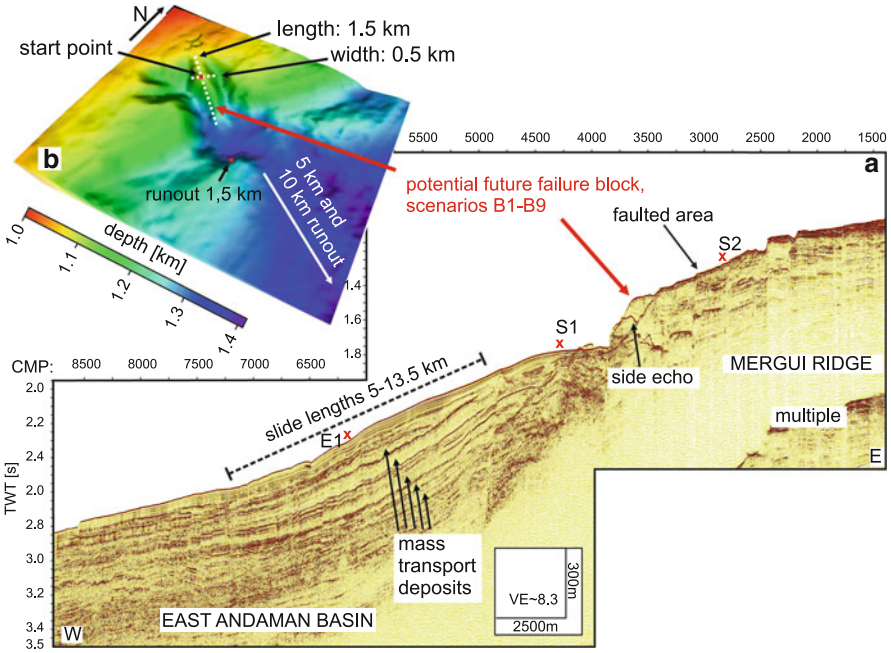

Fig. 46.2 (**a**) 2D reflection seismic profiles across the two source areas, "stacked slides location" and "potentially unstable block". *S1*: start point for slides of scenarios A1–A12, *S2*: start point for slides of scenarios A13–A24. *E1*: Endpoint for slides of scenarios A13–A24. (**b**) Bathymetry of the "potentially unstable block" (scenarios B1–B9). *CMP* Common Midpoint (See Fig. 46.1b for locations)

Table 46.1 Artificial gauge stations

Gauge	G1	G2	G3	G4	G5	G6	G7	G8
Lat [°]	8.6636	8.8639	8.6405	8.2704	8.011	7.8888	7.8404	7.7609
Long [°]	97.6254	98.2577	98.2286	98.27	98.2853	98.2524	98.284	98.3228
Water depth [m]	24	49	50	49	51	48	46	48
Coastal location	Similan Islands	Bang Muang	Khue-kakk	Khok Kloe	Chueng Tao	Patong	Karon	Rawai

46.3.1 Modeled Scenarios

We chose two source locations based on information derived from seismic and bathymetric data (Fig. 46.1). Scenarios A1–A24 correspond to a location of previously-identified, stacked MTDs. Scenarios B1–B9 consider a potentially unstable block (Fig. 46.2, Schwab et al. 2012).

46.3.1.1 Scenarios A1–A24, "Stacked Slides Location"

The "stacked slides location" is situated west of the Mergui Ridge (Fig. 46.1b). Four parallel seismic reflection profiles show a similar pattern of five stacked MTDs (Fig. 46.2a). Geometrical properties of the modeled slides were varied according to the dimensions of identified slides lengths between 5 and 13.5 km. Widths of 5, 7 and 30 km were chosen, the latter width value assuming that the two areas of stacked MTDs are connected, while the smaller values imply separate failure events. The slide thickness applied for these scenarios was 150 m, which is the maximum thickness measured for all detected MTDs. We use slope angles of 3° and 6°, corresponding to the range of slope angles in the source area. The origin of the MTDs is unknown, therefore we assume two different locations for slide initiation at the edge of the ridge in about 880 m water depth (run-out distance 15.5 km) and at the upper boundary of the basin in about 1,270 m water depth (run-out distance 7.5 km, Fig. 46.2a).

46.3.1.2 Scenarios B1–B9: "Potentially Unstable Block"

In scenarios B1–B9, we model the failure of a potentially unstable sedimentary block located at the edge of Mergui Ridge in about 1,100 m water depth (Fig. 46.2a) (Schwab et al. 2012). Its dimensions (Table 46.3) are derived from bathymetric data (Fig. 46.2b). Different run-out distances (1.5, 5 and 10 km) and slope angles (3°, 6° and 14.5) were used (Table 46.3).

46.4 Results

Initial positive wave heights (η_{plus}) for scenarios A1–A24 range between 1.5 and 118.1 m (Tables 46.2 and 46.3). η_{plus} values larger than 40 m are reached for scenarios with long run-out distances and short slide lengths of 5 km (A13, A15, A17, A19, A21, A23). Arrival times of the first tsunami waves at the coast (23–35 min) are similar for all scenarios. A_{20max}, the maximum offshore wave height at G1, ranges between 1.3 and 22.8 m for the A-scenarios. Run-up estimations from A_{20max} range between 2.3 and 23.1 m (R1) and 8.0 and 25.8 m (R2), respectively.

For scenarios B1–B9, η_{plus} ranges between 1.7 and 28.2 m. Arrival times are in the same range as for the A-scenarios (32–35 min). Compared to A1–A24, the A_{20max} values of B1–B9 are smaller (0.02 and 0.32 m). Run-up estimations are in the range of 0.04–0.61 m (R1) and 1.0–4.0 m (R1) respectively.

The maximum wave height distributions strongly depend on slide input parameters (Tables 46.2 and 46.3, Figs. 46.3 and 46.4). Despite its larger length, scenario A2 produces smaller wave heights compared to scenario A1 (Fig. 46.3a, b). Scenario

Table 46.2 Key modeling parameters for scenario A1–A24

Scenario	A1	A2	A3	A4	A5	A6	A7	A8	A9	A10	A11	A12
Runout [km]	7.5	7.5	7.5	7.5	7.5	7.5	7.5	7.5	7.5	7.5	7.5	7.5
SLA [°]	3	3	3	3	3	3	6	6	6	6	6	6
DIM [km × km]	5 × 5	5 × 13.5	7 × 5	7 × 13.5	30 × 5	30 × 13.5	5 × 5	5 × 13.5	7 × 5	7 × 13.5	30 × 5	30 × 13.5
Th [m]	150	150	150	150	150	150	150	150	150	150	150	150
Vol [km^3]	2.9	8.0	4.1	11.1	17.7	47.7	2.9	8.0	4.1	11.1	17.7	47.7
η_{plus} [m]	10.8	1.5	13.2	2.0	23.7	5.0	12.6	1.8	15.5	2.3	27.6	5.8
Ta [min]	35	34	34	35	34	34	34	34	35	35	34	34
A_{20max} [m]	2.3	1.3	3.0	1.8	7.7	5.6	2.6	1.5	3.5	2.1	8.7	6.6
R1 [m]	3.6	2.3	4.6	3.0	9.6	7.5	4.1	2.6	5.1	3.4	10.6	8.5
R2 [m]	10.0	8.0	11.3	9.1	16.5	14.5	10.6	8.5	11.9	9.7	17.4	15.5
Scenario	A13	A14	A15	A16	A17	A18	A19	A20	A21	A22	A23	A24
Runout [km]	15.5	15.5	15.5	15.5	15.5	15.5	15.5	15.5	15.5	15.5	15.5	15.5
SLA [°]	3	3	3	3	3	3	6	6	6	6	6	6
DIM [km × km]	5 × 5	5 × 13.5	7 × 5	7 × 13.5	30 × 5	30 × 13.5	5 × 5	5 × 13.5	7 × 5	7 × 13.5	30 × 5	30 × 13.5
Th [m]	150	150	150	150	150	150	150	150	150	150	150	150
Vol [km^3]	2.9	8.0	4.1	11.1	17.7	47.7	2.9	8.0	4.1	11.1	17.7	47.7
η_{plus} [m]	49.8	6.8	60.4	8.9	101.4	21.0	58.0	8.0	70.3	10.4	118.1	24.4
Ta[min]	32	33	23	23	33	32	32	33	35	35	32	33
A_{20max} [m]	7.3	5.2	9.2	7.1	15.9	20.3	8.2	6.1	10.2	8.3	16.5	22.8
R1 [m]	9.3	7.1	11.2	9.1	17.2	21.0	10.2	8.0	12.1	10.3	17.8	23.1
R2 [m]	16.2	14.1	17.8	16.0	22.2	24.6	17.0	15.0	18.6	17.1	22.6	25.8

SLA local slope angle, *Runout* run-out distance, *DIM* slide dimensions in width × length, *Th* thickness of slide, *Vol.* Volume of the slide, calculated as given in Grilli and Watts (2005), η_{plus} initial wave height, *Ta* arrival time, A_{20max} maximum wave height (surface elevation) at G1, *R1* run-up calculated for A_{20max} after Ward and Asphaug (2003), *R2* run-up calculated after Ward and Day (2008)

Table 46.3 Key modeling parameters for scenarios B1–B9

Scenario	B1	B2	B3	B4	B5	B6	B7	B8	B9
Runout[km]	1.5	5	10	1.5	5	10	1.5	5	10
SLA [°]	3	3	3	6	6	6	14.5	14.5	14.5
DIM [km × km]	0.5 × 1.5	0.5 × 1.5	0.5 × 1.5	0.5 × 1.5	0.5 × 1.5	0.5 × 1.5	0.5 × 1.5	0.5 × 1.5	0.5 × 1.5
Th [m]	150	150	150	150	150	150	150	150	150
Vol [km^3]	0.07	0.07	0.07	0.07	0.07	0.07	0.07	0.07	0.07
η_{plus}[m]	1.7	9.0	24.2	2.0	10.5	28.2	2.4	12.8	34.2
Ta[min]	35	35	33	35	35	35	32	34	35
A_{20max}[m]	0.01	0.06	0.17	0.01	0.070	0.20	0.01	0.09	0.24
R1[m]	0.04	0.20	0.47	0.04	0.23	0.53	0.05	0.27	0.61
R2[m]	1.0	2.3	3.5	1.0	2.4	3.7	1.1	2.7	4.0

SLA local slope angle, *Runout* run-out distance, *DIM* slide dimensions in width × length, *Th* thickness of slide, *Vol.* Volume of the slide, calculated after Grilli and Watts (2005), η_{plus} initial wave height, *Ta* arrival time, A_{20max} maximum wave height (surface elevation) at G1, *R1* run-up calculated for A_{20max} after Ward and Asphaug (2003), *R2*: run-up calculated after Ward and Day (2008)

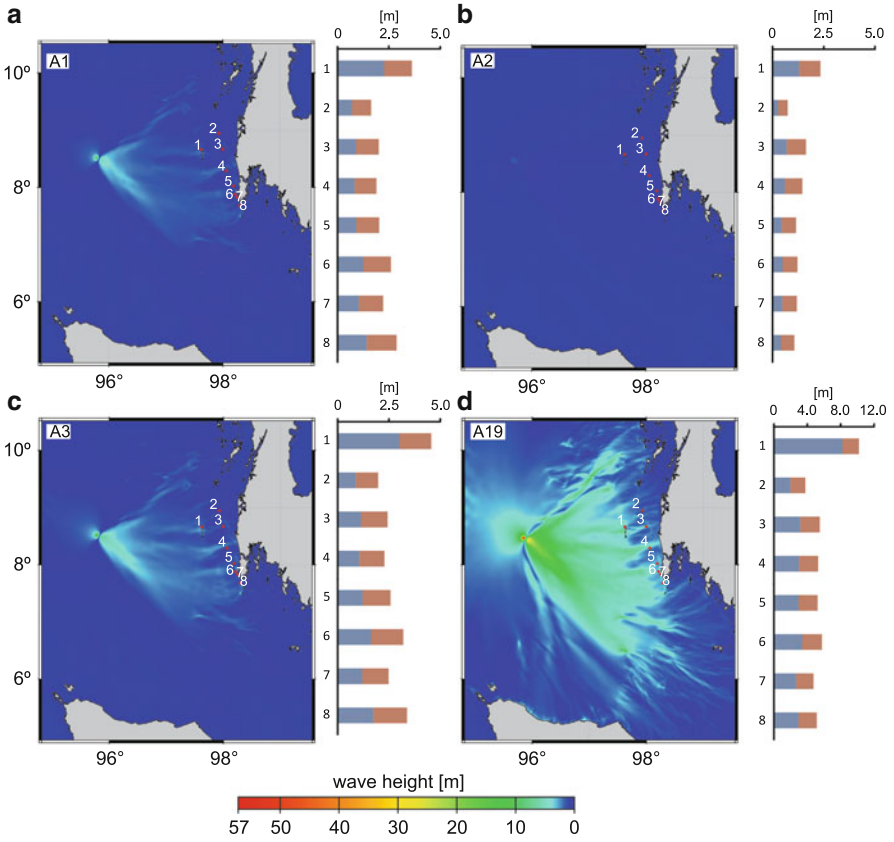

Fig. 46.3 Examples for wave height distributions from hypothetical failures at the "stacked slides location", as well as maximum wave heights (*blue bars*) and R1 run-up estimations (*red bars*) for artificial gauge stations G1–G8. Note the different scales for the wave height/run-up charts

A3 has a larger width compared to A1 and produces larger wave heights. Scenario A19 has the same slide dimensions as A1 but a larger run-out distance and larger slope angle (Fig. 46.3d, Table 46.2). This scenario also results in larger wave heights compared to A1.

Generally, largest maximum wave heights arise near the source area and in a triangular zone towards the coast. Regarding maximum wave heights at individual gauge locations, G1 records the largest run-up estimations (Fig. 46.3).

Figure 46.4 demonstrates the difference in wave heights for different run-out distances and slope angles of the B-scenarios (Table 46.3). Compared to the A-scenarios, the tsunami wave heights are smaller and not focused towards the coast, indicating reduced tsunami potential of the B-scenarios.

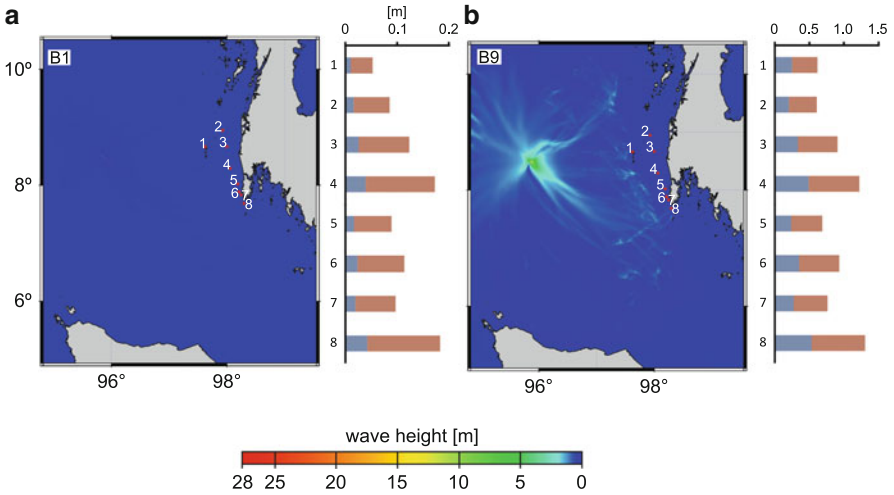

Fig. 46.4 Examples for wave height distributions from hypothetical failures at "potentially unstable block" location, as well as maximum wave heights (*blue bars*) and R1 run-up estimations (*red bars*) for artificial gauge stations G1–G8. Note the different scales for the wave height/run-up charts

46.5 Discussion and Conclusions

Our results give first insights into the tsunamigenic potential of slope failures off western Thailand. These results are only a preliminary assessment of landslide tsunami potential due to the limitations of the chosen approach:

1. The failure process that produced the MTDs in the working area is unknown. Therefore initial wave heights were calculated from failures, modeled as simplified coherent rotational slumps. More realistic failure scenarios such as translational and/or disintegrating slides or in the form of multiple events would produce smaller wave heights (Masson et al. 2006), but were not modelled in our preliminarily approach. Hence our modeled initial wave height is most likely overestimated.
2. In our numerical simulations, wave evolution beyond water depth of 20 m is prohibited, therefore run-up values were estimated by empirical equations using offshore wave heights at only a few isolated points (G1–G8), and inundation modeling was not performed at all. Empirical equations have limitations, the results vary for different equations (Tables 46.2 and 46.3), and near-shore wave phenomena reducing run-ups such as wave breaking are not considered by these empirical formulas.
3. Tsunami propagation was calculated from a coarse bathymetric grid and by shallow-water equations, which do not take into account effects such as dispersion. This may lead to inaccuracy of wave calculations.

4. The dimensions of the landslides in the A-scenarios are inferred from MTDs, as the pre-failure dimensions of the slides are not known. Thereby a thickness of 150 m was chosen for all scenarios, as thickness is the least determined value based on our seismic field data. This means that, as thickness is an important factor for wave generation, the calculation of initial wave height may contain inaccuracies.
5. The seismic images of the MTDs show clear signs of disintegration. This means that deformation occurred during the failure. According to Mohammed and Fritz (2012) deformation during the failure process leads to energy conversion and hence wave reduction. This again suggests that wave heights calculated in this study may be overestimated.

Landslide tsunamis are often described as a local phenomenon with large run-up heights limited to the near-field (Synolakis et al. 2002). Our results for the A-scenarios show such patterns (Fig. 46.3d), with a triangular zone of large maximum wave heights, presumably indicating a delimited area where tsunami hazard may occur at the coast. Some of the scenarios studied here show potential tsunami hazards comparable to the Papua New Guinea landslide tsunami of July 1998, where large run-up heights of more than 10 m were observed on a very limited coastline of about 20 km (Synolakis et al. 2002). A location especially exposed to a tsunami would then be around the gauge station G1, where the largest run-up heights were estimated.

Contrasting to the modeling results of A1–A24, the B-scenarios produce lower run-up height estimations, which are reasonable due to their smaller landslide volume and more realistic slide dimensions, and which are comparable to values described by Jintasaeranee et al. (2012).

Our results suggest that a landslide tsunami hazard for the coastal areas may exist, and wave heights and run-up estimations may increase with slope angle, run-out distance and slide volume. The width/length ratio of the slides is also affecting our preliminary results, as in most cases an increase in length leads to unexpected decrease in wave heights. This finding has to be examined in greater detail in the future.

Unlike tectonic tsunamis, landslide tsunami sources cannot not be located based on global networks and they may be located close to the shoreline (e.g. Fritz et al. 2012). Therefore landslide tsunamis are almost unpredictable making tsunami warning impossible. Short arrival times of around 30 min or less are typical for near-field tsunamis. The calculated arrival times of our model scenarios fall in this range, indicating that warning time for coastal areas would be short, adding to the unpredictability of landslide tsunamis.

Because of the previously mentioned limitations of our model approach, our results only represent worst case scenarios. This is especially true for the A-scenarios with largest volumes. Furthermore, recurrence rates for major tsunamigenic earthquakes in the area are estimated by 400 years (Monecke et al. 2008), whereas landslide recurrence is estimated to be in the range of 100 kyrs (Schwab et al. 2012). Hence, landslide tsunamis do not represent a major additional risk for the Thai coast.

However, they cannot be neglected and we recommend further geological surveys in the region to better locate sizes and distribution of submarine landslides, and sophisticated numerical modeling in order to reliably assess their hazard potential.

Acknowledgments The TUNAMI-N2 code is originally authored by Fumihiku Imamura and Nobou Shuto and copyrighted to Ahmet C. Yalciner, Fumihiku Imamura and Costas E. Synolakis. We acknowledge them for developing and making available the code. We thank the reviewers Hermann Fritz and Marc de Batist for their careful reviews and constructive comments that helped to improve the manuscript.

References

Brune S, Babeyko AY, Ladage S, Sobolev SV (2010a) Landslide tsunami hazard in the Indonesian Sunda Arc. Nat Hazards Earth Sys 10:589–604. doi:10.5194/nhess-10-589-2010

Brune S, Ladage S, Babeyko AY et al (2010b) Submarine landslides at the eastern Sunda margin: observations and tsunami impact assessment. Nat Hazards 54:547–562. doi:10.1007/s11069-009-9487-8

Fritz HM, Hillaire JV, Molière E, Wei E, Mohammed F (2012) Twin tsunamis triggered by the 12 January 2010 Haiti earthquake. Pure Appl Geophys. doi:10.1007/s00024-012-0479-3

Goto C, Ogawa Y, Shuto N, Imamura F (1997) IUGG/IOC TIME Project: numerical method of tsunami simulation with the leap-frog scheme. In Intergovernmental Oceanographic Commission of UNESCO, manuals and guides no. 35, UNESCO

Grilli ST, Watts P (2005) Tsunami generation by submarine mass failure. Part I: modeling, experimental validation, and sensitivity analysis. Waterw Port C-ASCE 131(6):283–297

IOC, IHO, BODC (2003) Centenary edition of the GEBCO digital atlas, published on CD-ROM on behalf of the Intergovernmental Oceanographic Commission and the International Hydrographic Organization as part of the general bathymetric chart of the oceans. British oceanographic data centre, Liverpool

Jankaew K, Atwater BF, Sawai Y et al (2008) Medieval forewarning of the 2004 Indian Ocean tsunami in Thailand. Nature 455:1228–1231. doi:10.1038/nature07373

Jintasaeranee P, Weinrebe W, Klaucke I et al (2012) Morphology of the Andaman outer shelf and upper slope of the Thai exclusive economic zone. J Asian Earth Sci 46:78–85

Masson DG, Harbitz CB, Wynn RB et al (2006) Submarine landslides: processes, triggers and hazard prediction. Philos Trans R Soc A 364:2009–2039

Mohammed F, Fritz HM (2012) Physical modeling of tsunamis generated by three-dimensional deformable granular landslides. J Geophys Res 117(C11):C11015

Monecke K, Finger W, Klarer D et al (2008) A 1,000-year sediment record of tsunami recurrence in northern Sumatra. Nature 455:1232–1234. doi:10.1038/nature07374

Schwab JM, Krastel S, Grün M et al (2012) Submarine mass wasting and associated tsunami risk offshore western Thailand, Andaman Sea, Indian Ocean. Nat Hazards Earth Sys 12:609–2630. doi:10.5194/nhess-12-2609-2012

Synolakis CE, Bardet J-P, Borrero JC et al (2002) The slump origin of the 1998 Papua New Guinea tsunami. Proc R Soc Lond A 458:763–789

Ward SN, Asphaug E (2003) Asteroid impact tsunami of 2880 March 16. Geophys J Int 153:F6–F10. doi:10.1046/j.1365-246X.2003.01944.x

Ward SN, Day S (2008) Tsunami balls: a granular approach to tsunami runup and inundation. Commun Comput Phys 3(1):222–249

Watts P, Grilli ST, Tappin D, Fryer GJ (2005) Tsunami generation by submarine mass failure. Part II: predictive equations and case studies. Waterw Port C-ASCE 131(6):298–310

Chapter 47
Morphology of Australia's Eastern Continental Slope and Related Tsunami Hazard

Samantha Clarke, Thomas Hubble, David Airey, Phyllis Yu, Ron Boyd, John Keene, Neville Exon, James Gardner, Steven Ward, and Shipboard Party SS12/2008

Abstract Morphologic characterisation of five distinct, eastern Australian upper continental slope submarine landslides enabled modelling of their tsunami hazard. Flow depth, run-up and inundation distance has been calculated for each of the five landslides. Future submarine landslides with similar characteristics to these could generate tsunami with maximum flow depths ranging 5–10 m at the coastline, maximum run-up of 5 m and maximum inundation distances of 1 km.

Keywords Submarine landslides • Wave height • Southeastern Australia • Upper slope • Flow depth • Run-up • Inundation distance

S. Clarke (✉) • T. Hubble • D. Airey • P. Yu • J. Keene
Geocoastal Research Group, University of Sydney, Sydney, NSW, Australia
e-mail: samantha.clarke@sydney.edu.au

R. Boyd
School of Environmental and Life Sciences, University of Newcastle, Newcastle, NSW, Australia

ConocoPhillips, Houston, TX, USA

N. Exon
Earth and Marine Sciences, Australian National University, Canberra, ACT, Australia

J. Gardner
CCOM, University of New Hampshire, Durham, NH, USA

S. Ward
Earth and Marine Science, University of California at Santa Crux, Cal. United States

Title of Team: Shipboard Party SS12/2008

S. Krastel et al. (eds.), *Submarine Mass Movements and Their Consequences*, Advances in Natural and Technological Hazards Research 37, DOI 10.1007/978-3-319-00972-8_47,

47.1 Introduction and Aims

Submarine landslides can damage seabed infrastructure, cause subsidence of coastal land, and generate tsunamis (Masson et al. 2006). Examples of large submarine landslide generated tsunamis include the 1929 Grand Banks' event (Fine et al. 2005), the 1946 Scotch Cap Alaska event (Fryer et al. 2004), and the 1998 Aitape Papua New Guinea event (Tappin et al. 2001). Submarine landslide generated tsunami are not as well understood as those associated with large earthquakes and consequently present a significant but poorly-quantified hazard (Sue et al. 2011).

The eastern Australia (EA) coast is potentially vulnerable to tsunamis due to the population concentration (∼85 %) and critical infrastructure within 50 km of the coast (Short and Woodroffe 2009). However, there has been little reason to suspect a local source for the generation of tsunami on the EA coastline. The identification of relatively recent, abundant submarine landslide scars has changed this perception (Boyd et al. 2010; Clarke et al. 2012; Keene et al. 2008) and established that submarine landsliding should be considered a common and ongoing characteristic of this passive continental margin (Clarke et al. 2012; Hubble et al. 2012).

This study uses data collected during the *RV Southern Surveyor* (*SS12/2008*) survey of the EA continental margin (Boyd et al. 2010) to (a) characterise slope morphology of the margin between Noosa Heads and Yamba, (b) determine the geometry of selected landslide features, and (c) quantify the size of tsunami potentially generated by these lands.

The study area (Fig. 47.1) is located along the EA continental slope between Noosa Heads to Yamba. We focus on five distinct landslide scars from the upper continental slope identified by Boyd et al. (2010) and one adjacent potential submarine landslide site. They are the: (1) Bribie Bowl Slide; (2) Coolangatta2 Slide; (3) Coolangatta1 Slide; (4) Cudgen Slide; (5) Byron Slide; and (6) Potential

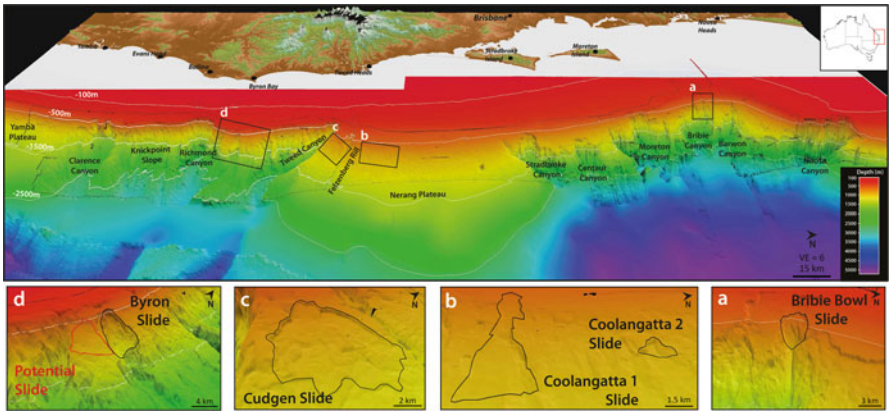

Fig. 47.1 Digital elevation model (*DEM*) of the slope geometry of the EA continental margin. Insets show details of actual (*black lines*) and potential landslides (*red outline*)

Table 47.1 Summary of the submarine landslide parameters

Landslide name / Parameter (m)	Canyon region Average slope angle >3°			Plateau region Average slope angle <3°		
	Bribie Bowl Slide	Bryon Slide	Potential Slide (adjacent to Bryon Slide)	Cudgen Slide	Coolangatta1 Slide	Coolangatta2 Slide
Thickness (t)	125	220	200	50	20	45
Length (L)	3,000	3,700	3,800	7,500	8,300	1,400
Width (W)	2,465	3,558	3,268	5,338	2,286	1,558
Water depth (h_0)	600	1,000	800	600	600	900

See Fig. 47.1 for landslide locations

Slide mass (c.f. Table 47.1). The five scars are representative of the failures that occur in the two contrasting slope morphologies in the study area: (1) the relatively steep (3–7°) and canyon incised slope (Bribie Bowl Slide, Bryon Slide and Potential Slide) and (2) the relatively gentle sloping (1–3°) Nerang plateau (Coolangatta1&2 Slides and Cudgen Slides). At least one gravity core was recovered from each of these landslides.

47.2 Data and Methods

47.2.1 Bathymetry and Landslide Geometry

Approximately 13,000 km^2 of bathymetric data was acquired using a 30-kHz Kongsberg EM300 multibeam echosounder. The multibeam data was processed to produce a 50 m gridded digital elevation model (DEM) (Boyd et al. 2010).

The DEM was used to examine the six individual sites using *Fledermaus V7.3.3b* software (http://www.qps.nl/). Landslide thickness (t), length (L), width (W), and water depth at landslide centre of mass (h_0), as well as distance from the adjacent coastline to head of the landslide source (r) were determined for each feature (Table 47.1). Landslide thickness is the maximum thickness within the landslide scar assuming the surface is continuous without the apparent landslide feature (McAdoo et al. 2000). Landslide length is the distance from landslide head to landslide toe. Landslide width is the average of measurements taken every 500 m down the landslide scar, perpendicular to the landslide axis. Water depth is taken from the landslide centre of mass.

47.2.2 Tsunami Calculations

The size of tsunami generated by potential of slope failures identified here has been assessed using empirical equations developed by Ward et al. (Chesley and

Ward 2006; Ward 2001; Ward 2011). Equations 47.1 and 47.2 use a landslide's geometric characteristics and an estimate of landslide mass velocity to generate maximum flow depth at the coastline *($F_d(0)$)* (i.e. tsunami height). Function 3 allows run-up *($R(X_{max})$)* and inundation distance (X_{max}) to be estimated where left and right sides are equal only at a particular X_{max} values, determined from site-specific coastline profiles perpendicular to the coastline and adjacent to each landslide site.

Flow depth at coastline:

$$F_d\,(\mathbf{0}) = [A_0 P\,(r)]^{4/5} h_0^{1/5} \tag{47.1}$$

Propagation and beaching factor:

$$A_0 P\,(r) = 0.7345t \left[\frac{W}{Lref}\right]\left[\frac{Lref}{h_0}\right]^{0.36} e^{-3.74\left[\frac{v_s - v_t}{v_t}\right]^2}\left[\frac{Lref}{r}\right]^{0.69} \tag{47.2}$$

Run-up and Inundation depth:

$$[R(X_{max}) - T(X_0)] + \frac{16.7n^2}{F_d\,(\mathbf{0})}(X_{max} - X_0) = F_d\,(\mathbf{0}) \tag{47.3}$$

Where A_0 is the initially generated surface elevation, *P(r)* is propagation factor *P* at distance *r* from the source of the wave v_s is landslide speed, v_t is tsunami speed at the landslide $= \sqrt{(gh_0)}$, L_{ref} is a reference length, taken here as 1 m, *X* is distance inland from the coastline ($X_0 = 0$ at coastline), *T(X)* is topographic elevation at location *X*. Land surface roughness is represented by Manning's coefficient *n* which is taken as 0.015 for very smooth topography, 0.03 urbanized/built land, and 0.07 densely forested landscape (Gerardi et al. 2008).

47.3 Results

47.3.1 Morphometric Characteristics of Individual Landslides

The five landslides (Fig. 47.2) are U-shaped in cross-section (3–6 km wide and 20–220 m deep) backed by an amphitheatre shaped crestal zone. In each case, landslide morphology is similar to the classical circular failure profile described by Varnes (1978), but elongated in the downslope, longitudinal profile.

The Bribie Bowl, Byron and Potential Slides are located within the steeper canyon regions (average slope 3–7°) and are thicker (>100 m) compared with landslides developed on the adjacent Nerang plateau. Both canyon landslides present an average slope of approximately 12° along the majority of the failure plane, increasing to 33° at the head scarp. In plan view the crown scarps present

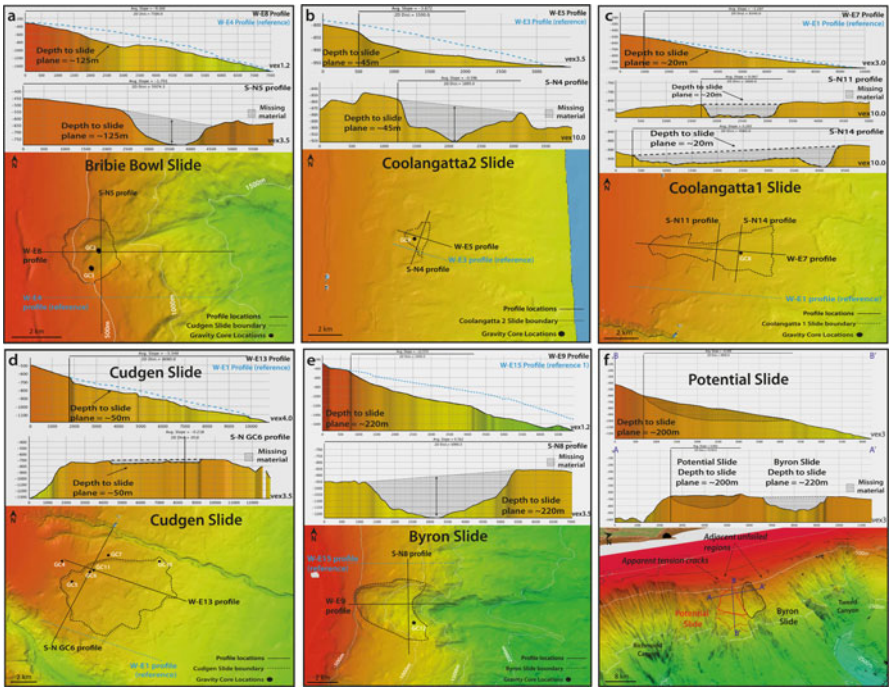

Fig. 47.2 Detailed DEM for each landslide showing slope geometry and cross-section profiles across slide (*black line* S-N) and down slide (*black line* W-E). Landslide outlines (*black* a-e and *red* f) and cross-sections for the Potential Slide (*dark blue*) are shown, along with tension cracks at the landslide head and slope break at the toe (*dashed red*). Reference profiles marked in *light blue*

distinctive semicircular shape, but the detached landslide slabs are essentially planar blocks, as the exposed failure surface is planar with a declination roughly parallel to the adjacent unfailed slope.

The Coolangatta1&2 and Cudgen Slides are located on the shallower Nerang plateau region (average slope 2–3°). These landslides are thinner (<50 m) and representative of the numerous upper slope failures that occur on this very gently dipping plateau (Boyd et al. 2010). All three landslides present a "hummocky" texture within the failure region, a gently concave landslide shape, and average slopes of approximately 3.5° within the failure plane, up to 7.5° at the head scarp.

The potential landslide mass identified adjacent to the Byron Slide protrudes anomalously out from the shelf in the heavily incised southern canyon section (Fig. 47.1). The extensive mass wasting surrounding this block and apparent tension crack features at the head of the identified mass (Fig. 47.2f) suggests it's possible future failure. The tension crack represents the landslide head, while a break in slope that presents as extant circular failures cresting at the 1,500 m contour defines the expected toe.

Table 47.2 Summary of the maximum flow depths

	Maximum flow depth at coastline $F_d(0)$ (m)					
	Average slope angle >3°			Average slope angle <3°		
Maximum landslide velocity (v_s) (ms^{-1})	Bribie Bowl Slide	Byron Slide	Potential Slide	Cudgen Slide	Coolangatta1 Slide	Coolangatta2 Slide
10	2.7	6.2	6.2	3.0	0.6	0.7
20	5.0	10.3	10.9	5.6	1.2	1.2
30	8.5	16.3	17.8	9.5	2.0	1.8
40	13.0	24.0	26.7	14.5	3.0	2.8

Failures are assumed to occur as one complete landslide block, rather than as a number of multiple landslides from the same site. This may generate an overestimated volume of the landslide block.

47.3.2 Calculated Characteristics of Landslide-Generated Tsunami

Table 47.2 summarises maximum flow depth at the coastline for the five landslides and the potential landslide using a range of maximum landslide velocities (v_s). The dimensions of the landslide mass, initial acceleration and maximum velocity of the sliding mass are important when assessing expected tsunami size (Ward 2001). The range of velocities tested has been constrained by minimum and maximum velocity values reported in the literature (Masson et al. 2006). The velocity at which submarine landslides travel after failure is not well defined due to a lack of direct measurements. The 1929 Grand Banks Slide was measured travelling at 25 ms^{-1} (Fine et al. 2005), while the 2006 SW Taiwan event measured turbidity current velocities between 17 and 20 ms^{-1} (Hsu 2008). Velocities are based on cable breakages during failure and are measured from the gentle upper slope, approximately 2° and <0.5° respectively. At the higher end, speeds of up to 80 ms^{-1} have been inferred for some large landslides based on landslide debris travel distances (Masson et al. 2006). We have tested a range of possible landslide velocities; however we consider 20 ms^{-1} a reasonable and conservative (i.e. minimum) value (Driscoll et al. 2000).

The calculations demonstrate that submarine failures along the EA continental margin have the potential to generate tsunami with flow depths at the coast ranging from 1.2 to 10.9 m for landslide velocities of 20 ms^{-1}. In particular, the Bribie Bowl, Byron, Cudgen and the Potential Slides all generate flow depths greater than 5 m at the coastline for landslide velocities of 20 ms^{-1} (Table 47.2).

Flow depth at the coastline directly relates to landslide thickness at a particular location. The thinner landslides considered, Coolangatta1&2 Slides (thickness 20 m and 45 m respectfully), produce smaller tsunami with inundation depths of 1 m. The

Table 47.3 Summary of the maximum inundation distance (X_{max}) and run-up ($R(X_{max})$)

Maximum landslide velocity (v_s) (ms^{-1})	Inundation distance (X_{max}) (m) & Run-up ($R(X_{max})$) (m)	Average slope angle >3°			Average slope angle <3°		
		Bribie Bowl Slide	Byron Slide	Potential Slide	Cudgen Slide	Coolangatta1 Slide	Coolangatta2 Slide
10	X_{max}	26	500	500	24	27	31
	$R(X_{max})$	2.4	2.08	2.08	2.75	0.15	0.15
20	X_{max}	398	898	901	50	54	53
	$R(X_{max})$	1.5	4.1	4.8	5.2	0.4	0.4
30	X_{max}	880	1,720	1,978	100	130	120
	$R(X_{max})$	1.95	5.95	6.3	8.8	0.42	0.37
40	X_{max}	1,715	3,252	3,805	732	220	220
	$R(X_{max})$	1.9	6.9	7.36	10	0.73	0.39

Cudgen Slide (50 m thick) and Bribie Bowl Slide (125 m thick) generated 5–6 m inundations, while the Byron Slide (220 m thick) and Potential Slide (estimated 200 m thick) generated inundation depths of 10 m.

Maximum flow depth at the coastline is larger for the thicker canyon landslides (e.g. Byron Slide and Potential Slide ~10 m; Bribie Bowl Slide ~5 m) which occur on steeper slopes in comparison to shallow plateau landslides which generally produce waves less than 1 m in height, except where landslide surface area was particularly large (e.g. Cudgen Slide: surface area ~50 km^2, flow depth ~5 m).

Table 47.3 summarizes maximum expected inundation distance and run-up for the identified landslides over a range of landslide velocities (v_s). Local topography greatly affect the ability of a wave to inundate past the immediate coastline (Gerardi et al. 2008) and these values are estimates which are less reliable than coastal inundation depth.

The results show that submarine landslides along the EA continental margin have the potential to generate inundation and run-up distances up to 1 km and 5 m respectively for landslide velocities of 20 ms^{-1}. Using 20 ms^{-1} landslide velocity as a benchmark, the two shallow Coolangatta1&2 Slides generate maximum inundation distances around 50 m and run-up about <0.5 m. The Cudgen Slide generates inundation distances around 50 m, however with much greater run-up at around 5 m. The Bribie Bowl Slide produced inundation distances around 400 m and run-up about 1.5 m, while the Byron and Potential Slides from the canyon regions generates maximum inundation distances around 1 km and run-up about 4 m.

47.4 Discussion

This study demonstrates that blocks shed from submarine scars have the potential to generate significant tsunami on the EA coast with flow depths of at least 10 m in height, run-up of ~5 m and maximum inundation distances of 1 km. These estimates

are based on relatively conservative estimates of landslide velocity given (a) the relatively steeply inclined slopes down which sliding material has moved and (b) the lack of evidence for a depositional site where the landslide mass ceased moving in mapped areas downslope of the landslide, indicating that the landslide material has travelled at least 15–20 km from its site of origin.

Evidence for historical tsunamis that have inundated the EA coastline is limited. A recently published tsunami catalogue (Dominey-Howes 2007) identifies historical events on the EA coast, of which 16 (∼30 %) have no identified cause (run-ups between <0.1 to 6 m asl). Nevertheless, our results show that upper slope landslides similar to those investigated in this study are a plausible source for the tsunami documented in catalogue (Dominey-Howes 2007). A growing body of evidence (Hubble 2013) is strengthening the contention that shedding landslides of the size investigated in this study should be considered to be a common, ongoing characteristic such that future failures are very likely to occur. Constraining estimates of landslide velocity is critical as coastal flow depth, inundation distance and run-up all increase with landslide velocity. We have used conservative estimates of landslide velocity and it is quite possible that these landslides can generate significantly more destructive events than we have suggested.

Evaluating possible triggering conditions for submarine sliding is also critical, as these conditions are not well understood (Masson et al. 2006). However, the majority of documented twentieth century submarine landslide tsunami events are related to moderate earthquakes (generally >M7). Such events are rare on the stable Australian continent and suggested recurrence intervals for such events are at multi-millennial timescales (Clark 2010).

47.5 Conclusions

The morphometric characterization of five distinct, geologically young, submarine landslides on the eastern Australian upper continental slope has enabled an estimation of tsunami size their related landslide masses probably generated and an insight into tsunami hazard that might be expected on the eastern Australian coast. Flow depth (1.2–10.9 m), run-up (0.4–4.8 m) and inundation distance (50–901 m) were calculated for five landslide sites assuming landslide velocities of 20 ms^{-1}. The reoccurrence of submarine landslides with similar characteristics to those shed from the margin in the geologically recent past would therefore be expected to generate tsunami with maximum flow depths between 5 and 10 m at the coastline, run-up of up to 5 m and inundation distances of up to 1 km. In particular, a potential landslide mass adjacent to the Byron Slide has been identified. If it was to fail it could generate maximum flow depths of ca. 10 m at the coastline, with inundation distances of ca. 1 km, for a conservative landslide velocity of 20 ms^{-1}. If these assumptions are correct, a tsunami this size would cause significant damage and possibly loss of life.

Acknowledgments We would like to acknowledge the P&O crew and scientific crews of the RV Southern Surveyor voyage (12/2008). Funding for this voyage was provided by ARC Australia and ConocoPhillips Pty Ltd. This paper benefitted from reviews by Dr Geoffroy Lamarche and Dr Julie Dickinson.

References

Boyd R, Keene J, Hubble T, Gardner J, Glenn K, Ruming K, Exon N (2010) Southeast Australia: a Cenozoic continental margin dominated by mass transport. In: Mosher DC et al (eds) Submarine mass movements and their consequences, vol 28, Advances in natural and technological hazards research. Springer, Dordrecht, pp 491–502

Chesley SR, Ward SN (2006) A quantitative assessment of the human and economic hazard from impact-generated tsunami. Nat Hazards 38(3):355–374

Clark DJ (2010) Large earthquake recurrence in New South Wales: implications for earthquake hazard. Earthquake hazard project. Geoscience Australia, Canberra

Clarke S, Hubble T, Airey D, Yu P, Boyd R, Keene J, Exon N, Gardner J (2012) Submarine landslides on the upper southeast Australian passive continental margin – preliminary findings. In: Yamada Y, Kawamura K, Ikehara K et al (eds) Submarine mass movements and their consequences, vol 31, Advances in natural and technological hazards research. Springer, Dordrecht, pp 55–66

Dominey-Howes D (2007) Geological and historical records of tsunami in Australia. Mar Geol 239:99–123

Driscoll NW, Weissel JK, Goff JA (2000) Potential for large-scale submarine slope failure and tsunami generation along the U.S. mid-Atlantic coast. Geology 28(5):407–410

Fine IV, Rabinovich AB, Bornhold BD, Thomson RE, Kulikov EA (2005) The Grand Banks landslide-generated tsunami of November 18, 1929: preliminary analysis and numerical modeling. Mar Geol 215:45–57

Fryer GJ, Watts P, Pratson LF (2004) Source of the great tsunami of 1 April 1946: a landslide in the upper Aleutian forearc. Mar Geol 203(3–4):201–218

Gerardi F, Barbano MS, De Martini PM, Pantosti D (2008) Discrimination of tsunami sources (earthquake versus landslide) on the basis of historical data in eastern Sicily and southern Calabria. Bull Seismol Soc Am 98(6):2795–2805

Hsu S-K (2008) Turbidity currents, submarine landslides and the 2006 Pingtung earthquake off SW Taiwan. TAO: Terr Atmos Ocean Sci 19(6):767

Hubble T (2013) Voyage summary SS2013-V01: marine geology and geohazard survey of the SE Australian Margin off Northern NSW and Southern Queensland. CSIRO, Hobart

Hubble T, Yu P, Airey D, Clarke S, Boyd R, Keene J, Exon N, Gardner J (2012) Physical properties and age of continental slope sediments dredged from the eastern Australian continental margin – implications for timing of slope failure. In: Yamada Y et al (eds) Submarine mass movements and their consequences, vol 31, Advances in natural and technological hazards research. Springer, Dordrecht, pp 43–54

Keene J, Baker C, Tran M, Potter A (2008) Geomorphology and sedimentology of the East Marine Region of Australia. Record 2008/10. Geoscience Australia, Canberra, 262 pp

Masson DG, Harbitz CB, Wynn RB, Pedersen G, Lovholt F (2006) Submarine landslides: processes, triggers and hazard prediction. Philos Trans R Soc A 364:2009–2039

McAdoo BG, Pratson LF, Orange DL (2000) Submarine landslide geomorphology, US continental slope. Mar Geol 169(1–2):103–136

Short AD, Woodroffe CD (2009) The coast of Australia. Cambridge University Press, New York

Sue LP, Nokes RI, Davidson MJ (2011) Tsunami generation by submarine landslides: comparison of physical and numerical models. Environ Fluid Mech 11(2):133–165

Tappin DR, Watts P, McMurtry GM, Lafoy Y, Matsumoto T (2001) The Sissano, Papua New Guinea tsunami of July 1998 – offshore evidence on the source mechanism. Mar Geol 175(1–4):1–23

Varnes DJ (1978) Slope movements and types and processes. Landslides: analysis and control, special report, vol 176. Transportation Research Board, National Academy of Sciences, Washington

Ward SN (2001) Landslide tsunami. J Geophys Res 106:11201–11215

Ward SN (2011) Tsunami. In: Gupta HK (ed) Encyclopedia of earth sciences series. Springer, Dordrecht, pp 1473–1493

Chapter 48
The Tsunami Generation Potential of Shovel and Bulli Slides in the Continental Margin SE Australia

Asrarur Rahman Talukder and David Völker

Abstract High-resolution bathymetric maps from offshore SE Australia have shown that the continental margin is characterised by numerous landslides of all sizes and shapes. We have studied two of the larger slides, Shovel Slide and Bulli Slide, located in the upper to mid continental margin offshore New South Wales (NSW), in detail. Morphometric analyses suggest that the slides had the potential to create tsunamis. We have calculated the initial wavelength and maximum amplitudes of those hypothetical tsunamis using the equations of Watts et al. (Nat Hazards Earth Syst Sci 3:391–402, 2003). The calculated initial wave heights above the mass centroid are in the same range of magnitude on the order of 10–25 m for both slides. The initial wavelengths vary between 75 and 104 km. If, on the other hand, the slides represent multiple (e.g. retrogressive) events, the tsunamigenic potentials were lower. Sizes, shapes, frequencies and the tsunami potentials of the submarine landslides from offshore NSW suggest that submarine landslides may well provide sources for local tsunamis. Precise dating of the landslide events and modelling of the calculated tsunami run up along the coast are yet to be performed.

Keywords Submarine landslides • Tsunami • SE Australian margins

A.R. Talukder (✉)
CSIRO, 26 Dick Perry Avenue, Kensington, WA 6151, Australia
e-mail: asrar.talukder@csiro.au

D. Völker
Geomar, Wischhofstr. 1-3, D24148 Kiel, Germany
e-mail: dvoelker@geomar.de

S. Krastel et al. (eds.), *Submarine Mass Movements and Their Consequences*, Advances in Natural and Technological Hazards Research 37, DOI 10.1007/978-3-319-00972-8_48,

48.1 Introduction

In 2006 Geoscience Australia (GA) carried out a mapping survey of the continental slope onboard the RV Southern Surveyor in the southern half of the SE Australian margins (Glenn et al. 2008). Subsequently in 2008, Boyd and the scientific party carried out a follow up mapping survey onboard the RV Southern Surveyor covering the northern half (Boyd et al. 2009). During these two surveys, high resolution bathymetry data for upper half of the continental slope were obtained together with some 2D seismic profiles and sediment samples. While submarine landslides in the margin were first reported by Jenkins and Keene (1992), a recompilation of the up to date bathymetry data revealed that the continental slopes off SE Australia are characterised by numerous slides ranging in size from 0.5–20 km^3 and associated with a variety of submarine canyons and debris flows (Boyd et al. 2010).

In this work we analyse the tsunami potential of two selected slides, the Shovel and Bulli Slides, both located offshore New South Wales (NSW) (Fig. 48.1). We have calculated the initial wavelengths and maximum amplitudes of the hypothetical tsunamis, which could be created by these slides using the equations of Watts et al. (2003). We used open source bathymetry and 2D seismic data from GA.

48.2 Neogene-Recent Deformation, Seismicity and Tsunami Record of the SE Australian Margins

The SE Australian margin (from 37°30′ S to 24°15′ S) offshore NSW and Queensland, is a narrow, sediment deficient rifted passive margin (Boyd et al. 2004; Colwell et al. 1993). The general geomorphic shape and orientation of the continental slope features have been inherited from the initial rifting of the continental crust related to the Tasman Sea opening during the Cretaceous (Colwell et al. 1993; Gaina et al. 1998). Recent sedimentation has dominantly occurred on the upper and middle slope since rifting (Glenn et al. 2008), while the lower slope has been subject to sediment removal due to vigorous bottom-water flow (Clarke et al. 2012). The morphology of the mid and lower slopes, particularly below 1,000 m water depth, is modified by canyons and mass wasting processes (Boyd et al. 2010).

This continental margin around Australia is passive, but the margin has been actively deformed from the Neogene in response to stress transmission from the plate boundaries (Hillis et al. 2008). Amongst the passive continental margins, Australia presents one of the highest rates of seismic activity in the World (Johnson 1994). The important characteristic of Neogene deformation in Australia, and associate seismic activities, is that they seem to be concentrated in four distinct regions, of which the SE Australian margin is the most active (Hillis et al. 2008).

The catalogue of Australian tsunamis, recently updated by Dominey-Howes (2007) recorded 44 individual tsunami events on the NSW coast; seven palaeo-tsunamis and 37 historic tsunamis that have occurred since AD1885. In the

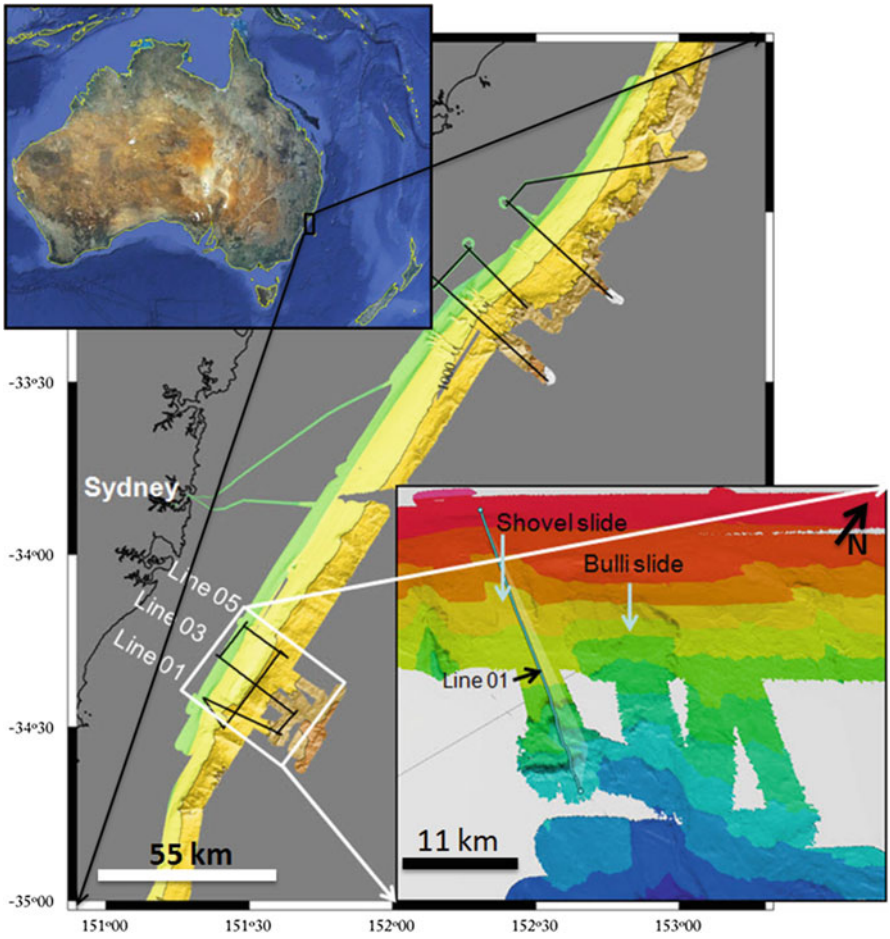

Fig. 48.1 Bathymetric maps offshore NSW with inset of the Shovel and Bulli Slides. *Black lines* refer the location of the 2D seismic lines (Data courtesy: GA)

catalogue, all the paleo-tsunamis on the NSW coasts are recorded from the work by Bryant, Young and others during 1990s and 2000s. According to these authors, the paleo-tsunamis were mega-tsunamis impacting repeatedly all along the coast of SE Australia (Dominey-Howes 2007 and references therein). The first paleo-tsunami event is apparently dated at around 105 ka (Young and Bryant 1992) with the rest being Holocene in age (Bryant and Nott 2001; Young et al. 1997). However, since 2000, the geological and chronological evidence of these paleo-tsunamis has become the subject of intense criticisms because many of the interpreted tsunamigenic deposits can be explained by non-tsunamigenic origins, or do not match with other regional palaeo-tsunami datasets (Courtney et al. 2012 and references therein, Dominey-Howes et al. 2006; Goff and Dominey-Howes 2009, 2010). In a recent

review paper, Courtney et al. (2012) re-examined all the published geological and chronological evidences and interpretations for the paleo-tsunamis and suggested only three localised tsunami events with much smaller run-up during Holocene. Goff and Dominey-Howes (2010) suggest the possibility of a mega-tsunami event at around 2.5 Ma ago depositing boulders on cliff-tops up to 33 m above sea level (Bryant and Nott 2001).

48.3 Shovel and Bulli Slides Offshore NSW

We have chosen these two slides because of their proximity to purported tsunami deposits in southern NSW and available 2D seismic coverage (Fig. 48.1). The initial interpretation of the bathymetry data is published in a GA post-cruise report (Glenn et al. 2008). Their brief description is also published in Boyd et al. (2010). Here we will only describe some of the geometry that is relevant for our calculations.

During the survey SS2006/10, six multichannel seismic lines were completed in the area of Shovel and Bulli Slides (Fig. 48.1). Glenn et al. (2008) described in detail the seismo-stratigraphy of these lines. Here we present our reinterpretation for the relative timing and possible recurrence of the mass wasting events in question. In order to describe the events, we will use the horizon marking the base of Cenozoic sequences which is labelled here as H1 (Fig. 48.2). This is a thin carbonate layer

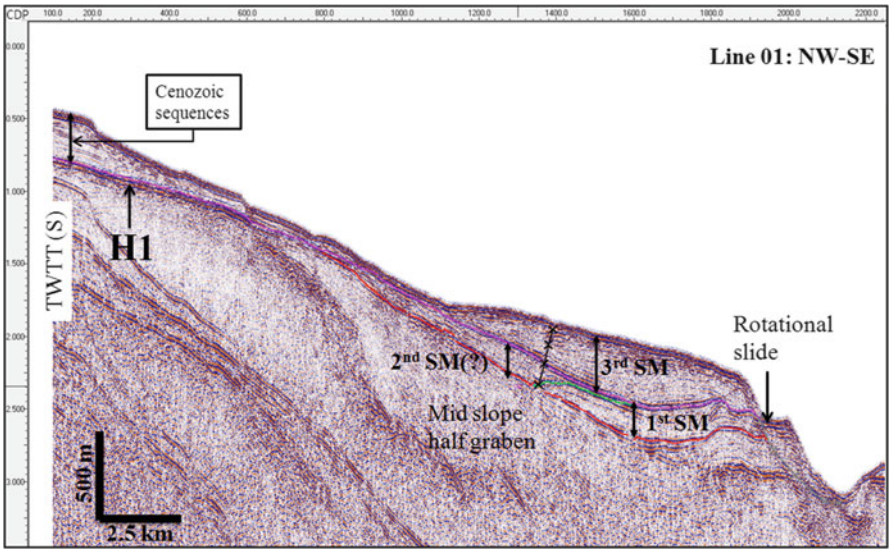

Fig. 48.2 2D seismic line 01 passing through the long axis of the Shovel Slide. Numbers 1st SM, 2nd SM and 3rd SM refer the interpreted failed mass (sedimentary wedges) indicating three mass wasting events, from 1st, the oldest to 3rd the youngest. *H1*: horizon marking the base of Cenozoic sequences. See the location of the line in Fig. 48.1 (Data courtesy: GA)

of Paleocene-Eocene age, seismically imaged as a thin packet of high amplitude and high continuity reflectors overlying an acoustic basement as well as Cretaceous syn-rift and post-rift sediments (Glenn et al. 2008).

Seismic line 01 passes through the long axis of the Shovel Slide (Fig. 48.2). The first head scarp is about 37 m high and lies at CDP 205 (at depth of 0.517 s TWTT). Between CDP 440 and CDP 580, the seismic line passes through the edge of the sidewall, creating a second 60 m high scarp at CDP 585 (at depth of 1.025 s TWTT). Between CDP 775 and CDP1100, almost the entire sedimentary packet above horizon H1 is missing. Down slope from CDP1100 however, a sedimentary wedge rests on top of H1. In seismic section, the wedge is thinner upslope and gradually thickens downslope (Fig. 48.2). This sedimentary body terminates down slope at CDP 1900 forming a high angle scarp (Fig. 48.2). Internally, the wedge is characterised by a chaotic reflection in its lower section but has a more coherent reflector in the upper part. This sedimentary body bears the characteristics of submarine slide deposits as established by Jenkins and Keene (1992). The geometry and the internal coherence of the wedge suggest that it could be the result of a single event in the Shovel Slide group with the slide plane going through H1 (Fig. 48.2: 3rd SM). By analogy, two other sedimentary wedges can be identified beneath H1 (Fig. 48.2: 1st and 2nd SM). The upper sedimentary wedge slumps further downslope at its toe at CDP 1900, while the lower one is folded (Fig. 48.2). Altogether these three sedimentary wedges are inferred to represent three separate Shovel Slide events.

Seismic line 03 lies along the long axis of the Bulli Slide (Fig. 48.1). The slide is located immediately down slope from the large Bulli Basement blocks but no depositional sediment from this event can be traced on the seismic lines. The upper part of another possible coherent slumped mass is also imaged along line 05 (Fig. 48.3).

48.4 Estimate of Tsunami Potential

The Watts et al. (2003) model was used for the purpose of estimating the height of the initial tsunami wave. This assumes an underwater slide as a rigid body of simplified geometry moving along a straight incline with the centre of mass motion parallel to the incline and subject to external forces from added mass, gravity, and dissipation. Assumptions include a specific density $\gamma = 1.85$, a negligible Coulomb friction coefficient ($Cn = 0$), an added mass coefficient ($Cm = 1$) and a drag coefficient ($Cd = 1$). The model produces a set of simple equations for the description of the underwater slide motion, the initial tsunami amplitude and wavelength above the middle of the initial slide position, using the geometrical parameters d (water depth of mass centroid prior to sliding), b (length of slide body), T (thickness of slide body) and θ (inclination of ramp) as input parameters. The relationships are largely empirical. We present values for the tsunami wavelength $\lambda 0$ and 2-D tsunami amplitude $\eta 2d$ using equations 3a and 3b of Watts et al. (2003)

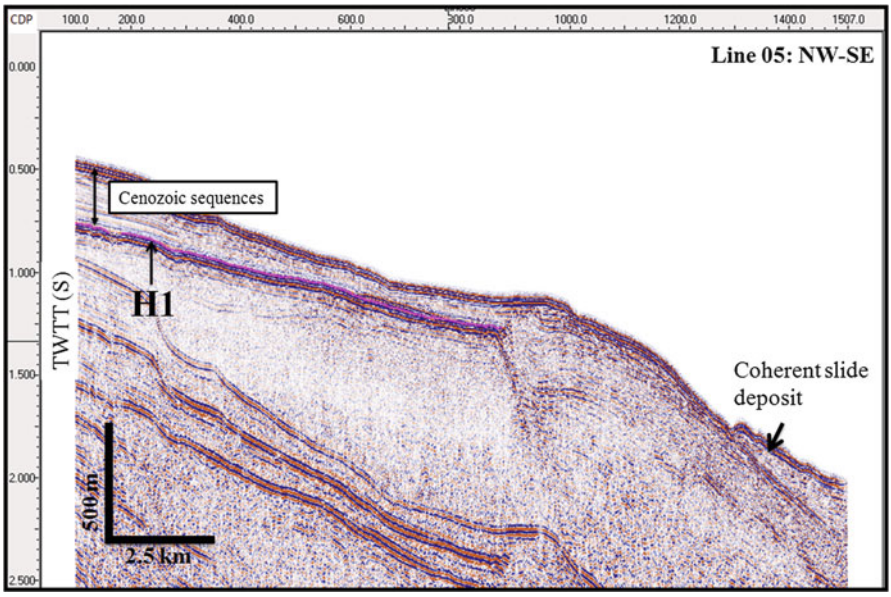

Fig. 48.3 2D seismic line 05 showing part of another coherent failed sediment mass. *H1*: horizon marking the base of Cenozoic sequences. See the location of the line in Fig. 48.1 (Data courtesy: GA)

The results of the tsunami wave calculation for maximum, minimum and mean value input parameters are shown in Tables 48.1 and 48.2. We consider the calculated values as upper limits, as (1) the condition of a Coulomb friction coefficient close to 0 is met only when the slide is completely decoupled and as (2) the model is calibrated to a rock density of 1.85 g/cm^3, whereas saturated bulk densities of slope sediments measured by Clarke et al. (2012) and Hubble et al. (2012) rather point towards 1.5 g/cm^3. The effect of Coulomb friction can be simulated if instead of the true ramp inclination a lower value (or effective inclination) θ' is assumed.

All calculations assume that the slides have developed as singular events and not as successive multiple failures. This assumption cannot be unequivocally confirmed from the morphology of the evacuation area alone.

48.4.1 Shovel Slide

Shovel Slide is present in the swath bathymetry data as a depression in the continental slope between 400 and 1,400 m water depth with 15–25° steep lateral walls (Figs. 48.1 and 48.2). The headwall has an elevation of ~50 m and sidewall

Table 48.1 Input and calculated parameters for an estimate of a hypothetical tsunami generated by the latest Shovel Slide event

Shovel Slide					
	Unit	Description	Max	Min	Mean
Input parameters					
b	m	Length of slide body	14,000	13,000	13,500
d	m	Water depth of mass centroid prior to failure	1,050	1,050	1,050
F	degree	Inclination of ramp	4	2	3
F′	degree	Effective inclination to simulate Coulomb friction	4	2	3
T	m	Thickness of slide body	90	60	75
Calculated parameters					
λ0	km	Wavelength of tsunami wave	56.2	76.5	63.7
η2d	m	Amplitude above mass centre	16.7	4.4	9.4

Table 48.2 Input and calculated parameter for an estimate of a hypothetical tsunami generated by the latest Bulli Slide event

Bulli Slide					
	Unit	Description	Max	Min	Mean
Input parameters					
b	m	Length of slide body	17,000	15,000	16,000
d	m	Water depth of mass centroid prior to failure	1,700	1,700	1,700
F	degree	Inclination of ramp	4	2	3
F′	degree	Effective inclination to simulate Coulomb friction	4	2	3
T	m	Thickness of slide body	200	200	200
Calculated parameters					
λ_0	km	Wavelength of tsunami wave	78.8	104.6	88.2
η2d	m	Amplitude above mass centre	25.9	9.6	17

height is up to 180 m at a water depth of around 1,000–1,300 m. A reconstruction of the missing rock body by restoration of the hypothetical initial slope surface produces a roughly wedge shaped body with a maximum thickness of 200 m and a mean thickness of 75 m (7.6 km^3 volume/96 km^2 area; method described in Völker 2010). The shape is unlike the shape that Watts et al. (2003) use for an idealised slide (mound with elliptical cross-section), but we can take the down-slope length of slide b as the distance from the headwall to the downdip position, where the thickness of the hypothetically missing rock body is <10 m, which gives a down slope length of 14 km. The slope gradient both within the slide depression as well as to the sides of it ranges between 2° and 6°, with a mean of 3°. The position of the mass centroid of the slide should be slightly upslope of the place where the maximum thickness of the missing rock volume is assumed, between the actual water depth of the depression and the reconstructed water depth at that location, which would be a water depth of 1,000–1,100 m.

48.4.2 Bulli Slide

Bulli Slide is only partly covered by the bathymetric dataset, which is missing the lower portion (Fig. 48.1). The slide is discernible as a bowl-shaped depression at the continental slope. The headscarp lies downslope of a mid-slope bathymetric high at a water depth of 1,000–1,100 m and the central depression has a maximum depth of 450 m in relation to the unfailed slope to the sides of the slide. A full reconstruction of the geometry of the missing volume of rock is impossible with the present dataset, but for the visible upper part, we assume a mean thickness of 200 m and a downslope length of 17 km. A maximum thickness of 450 m is reached at a water depth of 1,900 m, which results in a depth of the mass centroid prior to sliding of 1,700 m.

The calculated initial wave heights above the mass centroid are in the same range of magnitude (10–25 m) for both slides. Due to the larger thickness of Bulli Slide, its impact for tsunami generation must have been greater, an effect that is partly counteracted by the larger water depth of the Bulli Slide Site.

48.5 Discussion and Conclusion

The seismic images, where available, suggest that many of the failed masses were coherent sedimentary bodies, which is an important criterion to be tsunamigenic (Masson et al. 2006). The repeated failure of the Shovel Slide could also have generated repeated localised tsunamis along the coast. However, we don't have any precise dating of the latest events of Bulli or Shovel Slides. In the bathymetry data, the scarps of the Shovel Slide appear fresh. On the seismic line, no sedimentary cover on the slide plane is observed. Because of the lower frequency of the seismic source used, up to several meters of sediments would not be seen on the seismic profiles (Glenn et al. 2008). Coring attempts suggest that the latest events of these two slides could be at least 40 ka old (personal communication with Tom Hubble, 2012). In that case, a relation between Bulli and Shovel Slides and Holocene tsunamis can be ruled out.

The SE Australian margins are the most active earthquake zone in Australia (Hillis et al. 2008). Clarke et al. (2012) and Hubble et al. (2012) show that the upper continental slope deposits are inherently stable, but present a paradoxical high number of slide scars. They suggest that submarine landslides, which are very common in the margins, require some external triggers and earthquakes could be one of them. An earthquake/landslide coupled process could be more effective in creating tsunamis with run-ups greater than 4–5 m (Gusiakov 2003).

In conclusion, our work points towards the likelihood that submarine landslides off the NSW coast may well provide sources for local tsunamis although their run up and wave heights are yet to be determined. Precise dating of slide events and tsunami run up modelling along the coast are required to evaluate further the tsunami risk of the margin.

Acknowledgment We would like to thank GA for the bathymetric and seismic data used in this work. We explicitly thank the reviewers James Goff and Tom Hubble for their efforts to improve the manuscript. We also thank Dr. Cedric Griffiths for his careful and detailed linguistic revision of the manuscript and Carl Bonnevie Harbitz for the final review.

References

Boyd R, Ruming K, Roberts JJ (2004) Geomorphology and surficial sediments of the southeast Australian continental margin. Aust J Earth Sci 51:743–764

Boyd R, Keene J, Ruming K, Exon N, Shipboard Party SS12/2008 (2009) Voyage summary: marine geology and geohazard survey of the SE Australian margin off Northern NSW and Southern Queensland. CSIRO, Kensington, 23 pp

Boyd R, Keene J, Hubble T, Gardner J, Glenn K, Rumming K, Exon N, The crews of Southern Surveyor 10/2006 and 12/2008 (2010) Southeast Australia: a Cenozoic continental margin dominated by mass transport. In: Mosher DC, Shipp RC, Moscardelli L et al (eds) Submarine mass movements and their consequences, vol 28, Advances in natural and technological hazards research. Springer, Dordrecht, pp 491–502

Bryant EA, Nott J (2001) Geological indicators of large tsunami in Australia. Nat Hazards 24: 231–249

Clarke S, Hubble T, Airey D, Yu P, Boyd R, Keene JB, Exon N, Gardner J, Shipboard Party SS12/2008 (2012) Submarine landslides on the upper southeast Australian passive continental margin – preliminary findings. In: Yamada Y et al (eds) Submarine mass movements and their consequences, vol 31, Advances in natural and technological hazards research. Springer, Dordrecht, pp 55–65

Colwell JB, Coffin MF, Spencer RA (1993) Structure of the southern New South Wales continental margin, Southeastern Australia. BMR J Aust Geol Geophys 13(4):333–343

Courtney C, Dominey-Howes D, Goff J, Chague-Goff C, Switzer AD, McFadgen B (2012) A synthesis and review of the geological evidence for palaeotsunamis along the coast of southeast Australia: the evidence, issues and potential ways forward. Quat Sci Rev 54:99–125

Dominey-Howes D (2007) Geological and historical records of tsunami in Australia. Mar Geol 239:99–123

Dominey-Howes D, Humphreys GS, Hesse PP (2006) Tsunami and palaeotsunami depositional signatures and their potential value in understanding the late-Holocene tsunami record. The Holocene 16(8):1095–1107

Gaina C, Mueller DR, Royer JY, Stock J, Hardebeck J, Symonds P (1998) The tectonic history of the Tasman Sea: a puzzle with 13 pieces. J Geophys Res 103(B6):12413–12433

Glenn K, Post A, Keene J, Boyd R, Fountain L, Potter A, Osuchowski M, Dando N (2008) NSW continental slope survey – post cruise report. Geoscience Australia Record 2008/14, 160 pp

Goff J, Dominey-Howes D (2009) Australasian palaeotsunamis — do Australia and New Zealand have a shared trans-Tasman prehistory? Earth-Sci Rev 97:159–166

Goff J, Dominey-Howes D (2010) Does the Eltanin asteroid tsunami provide an alternative explanation for the Australian megatsunami hypothesis? Nat Hazards Earth Syst Sci 10: 713–715

Gusiakov VK (2003) Identification of slide generated tsunamis in the historical catalogues. In: Yalciner AC, Pelinovsky E, Okal E, Synolakis CE (eds) Submarine landslides and tsunamis, NATO science series: IV earth and environmental science. Kluwer Academic Publishers, Dordrecht/Boston/London, pp 17–32

Hillis RR, Sandiford M, Reynolds SD, Quigley MC (2008) Present-day stresses, seismicity and Neogene-to-Recent tectonics of Australia's 'passive' margins: intraplate deformation controlled by plate boundary forces. In: Johnson H, Dore´ AG, Gatlife RW et al (eds) The nature and origin of compressive margins, Geological Society Special Publication. Geological Society Publishing House, London, pp 71–89

Hubble T, Yu P, Airey D, Clarke S, Boyd R, Keene JB, Exon N, Gardner J, Shipboard Party SS12/2008 (2012) Physical properties and age of continental slope sediments dredged from the eastern Australian continental margin – implications for timing of slope failure. In: Yamada Y et al (eds) Submarine mass movements and their consequences, vol 31, Advances in natural and technological hazards research. Springer, Dordrecht, pp 43–54

Jenkins CJ, Keene JB (1992) Submarine slope failures of the Southeast Australian continental slope: a thinly sedimented margin. Deep-Sea Res Part A Oceanogr Res Pap 39(2):121–136

Johnson AC (1994) Seismic tectonic interpretations and conclusions from the stable continental region seismicity database. Report TR-102261-1, 4-1-4-102. The Earthquakes of Stable Continental Regions, Electric Power Research Institute

Masson DG, Harbitz CB, Wynn RB, Pedersen G, Løvholt F (2006) Submarine landslides: processes, triggers and hazard prediction. Philos Trans R Soc A 364:2009–2039

Völker DJ (2010) A simple and efficient GIS tool for volume calculations of submarine landslides. Geo-Mar Lett 30:541–547

Watts P, Grilli ST, Kirby JT, Fryer GJ, Tappin DR (2003) Landslide tsunami case studies using a Boussinesq model and a fully nonlinear tsunami generation model. Nat Hazards Earth Syst Sci 3:391–402

Young RW, Bryant EA (1992) Catastroohic wave erosion on the southeastern coast of Australia: impact of the Lanai tsunami ca. 105 ka? Geology 20:199–202

Young RW, Bryant EA, Price DM, Dilek SY, Wheeler DJ (1997) Chronology of Holocene tsunamis on the Southeastern coast of Australia. Trans Jpn Geomorphol Union 18(1):1–19

Part VIII
Long-Term Record of Submarine Landslides and MTD Paleoseismology

Chapter 49
Along-Strike Migration of Intermittent Submarine Slope Failures at Subduction Margins: Geological Evidence from the Chikura Group, Central Japan

Yuzuru Yamamoto and Shunsuke Kawakami

Abstract Ancient submarine slope failures are exposed in the Plio–Pleistocene trench–slope basin sediments of the Chikura Group. Based on the lateral tracing of a key tephra bed ("HF") and the sedimentology and geological structure at seven exposures of the failure deposit over a total distance of 5 km, we identified at least five discrete failure events and evidence of lateral variation in the age of the failures, younging to the west. The slope failure deposits therefore represent the lateral migration of intermittent submarine slope failures. The initial slope failure was triggered by earthquake-induced liquefaction at about 2 Ma, and subsequently failures propagated northwards perpendicular to the ancient trench axis. The geological evidence for the systematic lateral migration of intermittent submarine slope failures accords with the migration style identified by physical models of failure propagation.

49.1 Introduction

Submarine slope failures are a significant cause of submarine erosion at subduction margins (e.g., Underwood and Moore 1995; Lucente and Pini 2007; Yamamoto et al. 2007, 2009). Such slope failures originate from gravitational instability associated mainly with uplift of the hanging wall of subduction-related thrusts. Submarine slope failures have the potential to destroy infrastructure, including telecommunication cables (e.g., Heezen and Ewing 1952) and oil–gas platforms (e.g.,

Y. Yamamoto (✉)
IFREE, JAMSTEC, Yokohama 236-0001, Japan
e-mail: yuzuru-y@jamstec.go.jp; yuzupon.y@gmail.com

S. Kawakami
Asahi Geo Survey Co., Ltd, Shibuya-ku, Tokyo 151-0051, Japan

S. Krastel et al. (eds.), *Submarine Mass Movements and Their Consequences*, Advances in Natural and Technological Hazards Research 37, DOI 10.1007/978-3-319-00972-8_49,

Bea et al. 1983), and they may generate large tsunamis (e.g., Bondevik et al. 2005; Talling et al. 2007); consequently, such failure events pose a risk to human life.

Recent studies have examined various possible mechanisms for submarine slope failures, including the influence of fluid pressure (e.g., Flemings et al. 2008; Sawyer et al. 2009; Dugan and Germaine 2008), gas expansion (Morita et al. 2012), and earthquake-induced liquefaction (e.g., Yamamoto et al. 2007). Some previous investigations have analyzed the style and pattern of submarine slope failure formation (e.g., Yamada et al. 2010, 2012). Information about the generation of submarine slope failures should assist in the prediction of the occurrence of such events and in the prevention of disasters. However, the lack of research in this area may reflect the difficulty of making high-resolution, time-lapse observations of submarine slope failures on the deep ocean floor.

To address this shortcoming, in the present study we focus on ancient examples of submarine slope failures exposed in a Pliocene–Pleistocene trench–slope basin, Chikura Group, central Japan. Yamamoto et al. (2007) identified a paleo-slope failure deposit in these rocks in a newly excavated road section. The failure was caused by earthquake-induced liquefaction at around 2 Ma and the deposits related to it can be traced from east to west over a distance of 5 km (Fig. 49.1). Therefore, the deposits present a good opportunity to examine the along-strike variation of a submarine slope failure. The present study investigates the lateral variation in the geology and structure of the failure deposits by examining a west-to-east series of seven outcrops exposed along the strike of the paleo-slope. By analysing the geological sections, and tracing the key marker tephra bed "HF" (Kawakami and Shishikura 2006), spatial and temporal variations in the submarine slope failures are identified.

49.2 Geologic Setting

The unique tectonic setting of central Japan comprises two plate subduction systems: the Philippine Sea Plate is being subducted beneath the North America/Eurasia Plate, and the Pacific Plate is being subducted beneath both of these aforementioned plates (Fig. 49.1a). The Izu–Bonin island arc, on the Philippine Sea Plate, began colliding with the Honshu arc in the middle Miocene, resulting in the northward bending and rapid uplift of the geological architecture on Honshu (e.g., Koyama and Kitazato 1989; Yamamoto and Kawakami 2005). Young, non-metamorphosed sedimentary sequences of these subduction systems (e.g., accretionary prism, forearc basin, and trench–slope basin) have been rapidly uplifted and exposed on the Miura and Boso peninsulas of central Japan (Fig. 49.1b).

Two accretionary complexes (the upper Miocene to lower Pliocene Miura–Boso accretionary prism and the lower to middle Miocene Hota accretionary complex) are exposed in the southern parts of the Miura and Boso peninsulas. The Miura–Boso prism developed in the southernmost part of the peninsulas and comprises alternating beds of hemipelagic siltstone and volcaniclastic sandstone/conglomerate

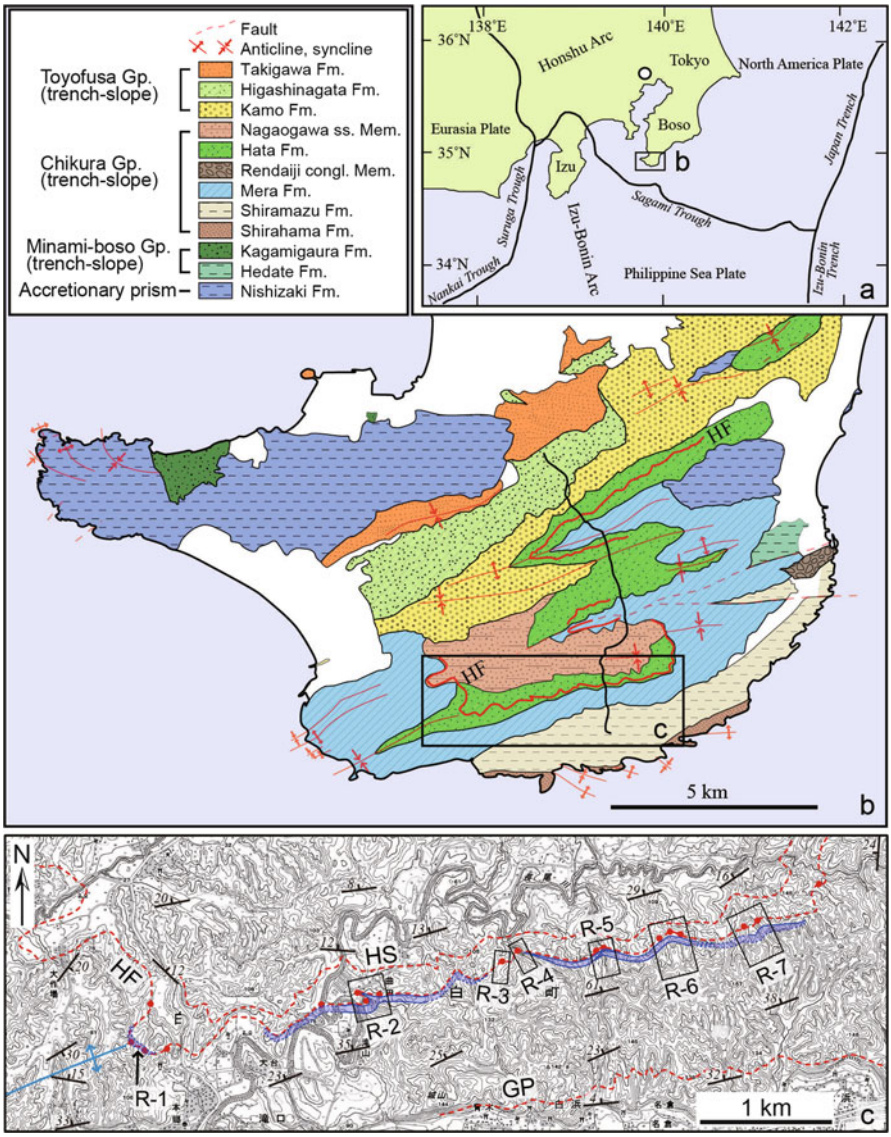

Fig. 49.1 Index (**a**) and geological (**b**) maps of the southern Boso Peninsula, Central Japan. (**c**) Topographic map showing the lateral distribution of slope failure deposits in *blue*. *HS*, *HF*, and *GP* are key beds described in Kawakami and Shishikura (2006). R-1 to R-7 are the exposures where the failure deposit was examined

derived from the Izu–Bonin island arc, representing an off-scraped accretionary prism that was buried to a depth of <1 km (Yamamoto et al. 2005; Yamamoto 2006). The accretionary prism is overlain by younger post-Pliocene trench–slope basin deposits of the Chikura and Toyofusa groups.

The Chikura Group is characterized by syn-sedimentary folding (Saito 1992), indicative of deposition in the tectonically controlled trench–slope basin. Detailed stratigraphy and chronology, including the tracing of key marker beds such as tephra layers, indicate that the sedimentary environment of the Chikura Group was reduced in dimension by shortening and uplifting of the underlying accretionary prism, and that the depo-center migrated to the north over time (Kawakami and Shishikura 2006).

49.3 Fossil Submarine Slope Deposits

The submarine slope failure deposits exposed in the Chikura Group are composed of large blocks (up to 15 m across) of siltstone and alternating beds of sand stone and siltstone, all within a sandy matrix (Figs. 49.2 and 49.3a). The thickness of the failure deposits ranges from 12 to 20 m. The large blocks have key beds that can be correlated with the coherent layers underlying the failure deposit (Awa Research Group 2008). The scoriaceous sandstone layer, which contains sedimentary structures associated with turbidity currents, caps the slope failure deposits and fills the irregular depressions between blocks (Fig. 49.3d). This observation indicates that the slope failures occurred on the seafloor.

The sandy matrix of the slope failure deposit is composed mainly of medium-size volcaniclastic sand containing coarser scoriaceous and pumiceous grains, and

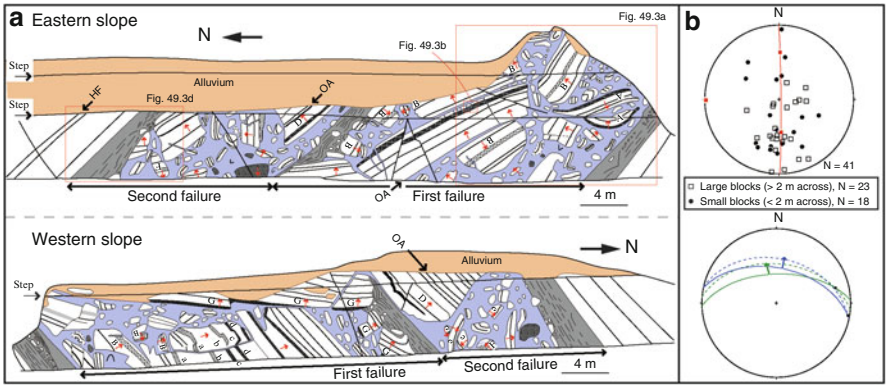

Fig. 49.2 (**a**) Sketch of the outcrop exposed at R-5 (after Yamamoto et al. 2007). *Blue-colored* parts denote matrices of the slope failure deposit composed of liquefied sand. *Red arrows* indicate the direction of younging, and *letters* represent individual layers that can be traced among different blocks. *HF* and *OA* are key beds. (**b**) Stereoplot diagrams (lower hemisphere projection) showing the poles of the bedding planes corresponding to the shortest axis of each block, presenting a girdle distribution trending N–S (*upper*) and a north-oriented paleo-turbidite current deduced from cross-lamination (*lower*) in the coherent part of the geological section at R-5, indicating that the paleo-slope had a north-facing aspect

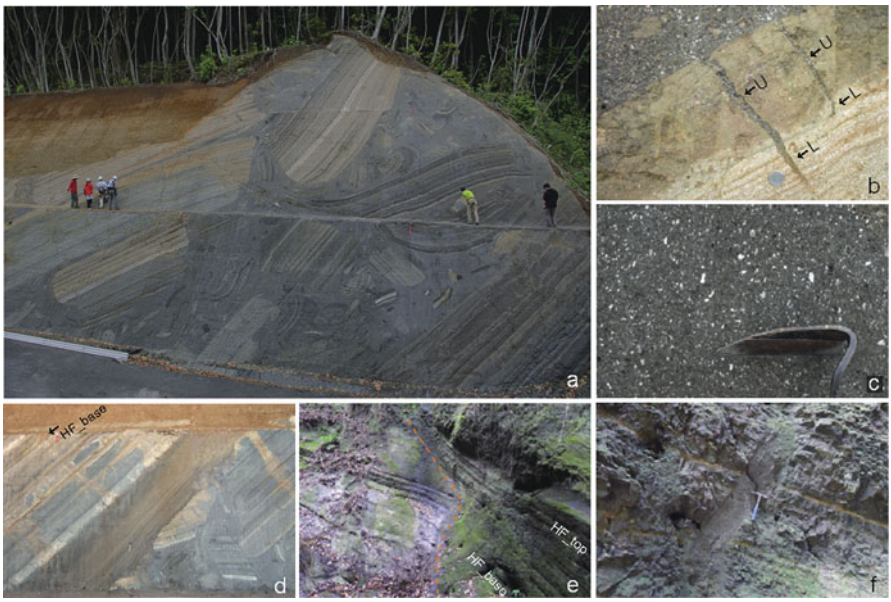

Fig. 49.3 Photographs of fossil submarine slope failures. The location of the photograph **a-d** is marked by the *red rectangle* in (Fig. 49.2). (**a**) Photograph of the slope failure deposit at R-5. (**b**) Minor neptunian-style intrusions by the matrix material. (**c**) close-up photograph of matrix. (**d**) Photograph of the upper boundary of the submarine slope failure deposit at R-5, showing the scoriaceous sandstone layer that overlies the failure deposit. *Black arrow* indicates position of the base of the key bed HF. (**e**) Onlap-style sedimentary interface between key bed HF and older units at R-4. A few tens of meters of geological section, including bed OA, is missing and no slope failure deposit is identified below bed HF. (**f**) Sand injection indicative of minor liquefaction at R-3.

presents no preferred orientation or foliation. The matrix commonly intrudes into the large blocks: some of these intrusions terminate in the blocks, while others penetrate completely through. Some examples of these clastic intrusions are composed of different components in the lower and upper parts: well-sorted medium grain sized sands are found in the lower parts of the intrusion, while poorly sorted matrices containing coarser grains are found in the upper parts (Fig. 49.3b). This indicates that two stages of matrix intrusion occurred, with the first intrusion subsequently driven in by the second. The sand layer which consists of the similar materials overlies the intruded silt layer. The first intrusion therefore apparently came from the sand layer originally deposited just above. On the other hand, the latter corresponds to the main phase of intrusion because it continues to the main body of sandy matrix.

Many blocks are rotated and some of them are overturned (Fig. 49.2). Smaller blocks (<1 m across) tend to be deformed in a ductile manner, whereas the larger blocks exhibit brittle deformation. The broadest surface on each block parallels to the bedding plane indicating the shape of blocks controlled by bedding planes. The attitudes of the shortest axes of these blocks inferred from bedding planes show a N–S-trending girdle distribution (Fig. 49.2b). The cross-laminations in the turbidite

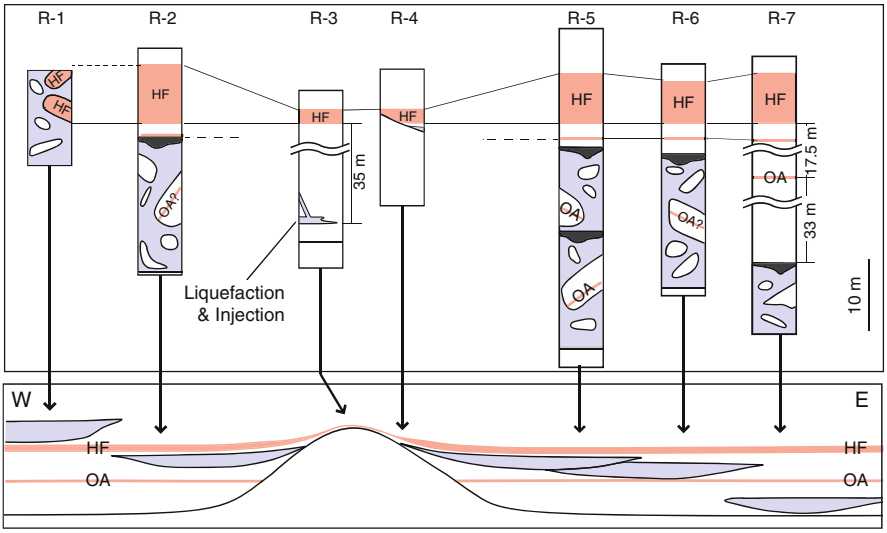

Fig. 49.4 Schematic E–W cross-section showing the spatial distribution of slope failure deposits (*blue-colored*). *White-* and *dark-grey colored* materials in the failure deposits denote blocks and failure-induced sandstone layers on the deposit, respectively. The failure deposits become younger to the west. *HF* and *OA* are key beds

sequence overlying the slope failure body indicate that the turbidity current moved in a northwards direction, indicative of a paleoslope inclined to the north. Based on the correspondence between the paleoslope indicators and attitude of blocks, we infer that the slope failure masses moved northwards and that blocks rotated on the paleo-slope during the movements.

To examine the lateral variation of the slope failure deposits, seven exposures of the key bed HF were chosen (Fig. 49.1c). Exposure R-5 corresponds to the outcrop reported by Yamamoto et al. (2007). At site R-5, the slope failure deposit is developed approximately 3.2 m below the key bed (HF) and contains another key bed, "OA", in the blocks (Figs. 49.2 and 49.4). The occurrence of two sets of slope failure deposits and overlying sandstone layer filling the irregular surfaces of the failure deposits indicate that two discrete slope failures are represented at R-5. The total thickness of the slope failures at site R-5 is about 30 m.

At site R-6, about 500 m east of R-5, a failure deposit is developed 4 m below HF. Although the interval represented is almost the same as that of R-5, only a single slope failure is identified. At site R-7, the easternmost exposure, the slope failure deposit is developed about 50 m below bed HF. Another key bed, "OA," is not included in the failure deposit but is exposed in the overlying part of the section.

At outcrops R-3 and R-4, although some sand injections (representing minor liquefaction) are identified, no slope failure deposit is identified below bed HF. At R-4 in particular, a few tens of meters of geological section including bed OA is missing, and the older stratigraphy is overlain by bed HF in an onlap style.

Although the outcrop at R-1, the westernmost exposure, has now been destroyed by topographic alterations, Kawakami and Shishikura (2006) reported a slope failure deposit containing bed HF.

49.4 Discussion

A fossil slope failure deposit is contained in the Plio–Pleistocene trench–slope basin, Chikura Group, occurred on the north-facing submarine slope and was probably generated by earthquake-induced liquefaction.

The inferred evolution of the slope failure is as follows. First, the sediments in the Chikura Group were deposited in the trench–slope basin (Fig. 49.5a). Although the basin has both north- and south-facing slopes (e.g., Kawakami and Shishikura 2006), the processes of slope failure occurred on the north-facing paleoslope. The probable initiating earthquake occurred soon after sedimentation (at around 2 Ma), and sand liquefaction formed small-scale sandstone dykes (Figs. 49.3b and 49.5b). Many of the liquefied sand layers connected with each other, leading to the formation of large blocks (Fig. 49.5c). Some previously formed small-scale sand dykes became further intruded, driven by the major liquefaction, to make intrusions composed of different materials in the lower and upper parts (Fig. 49.3b). The liquefied sand layers lost shear strength, leading to the formation of a submarine slope failure (Fig. 49.5d). The surface of the failure deposit had an irregular geometry and was filled in by the failure-induced turbidity current (Fig. 49.5e). At site R-5, a second failure occurred and covered the first one (Fig. 49.5f).

Basedon the lateral tracing of key tephra bed HF and the geological expression of slope failure deposits over a distance of 5 km, at least five different submarine slope failures can be identified. Since the slope failures are overlain by a failure-induced turbidite deposit, the ages of the failures are very close to the age of the sediments immediately overlying the failure deposits (Yamamoto et al. 2007). Therefore, the failures that developed in the western part of the study area are younger than those in the eastern part. No failure deposit was identified in exposures R-3 and R-4, with the geological section at R-4 revealing an unconformity just below key bed HF. Given that the unconformity corresponds to the interval represented by the failure exposed at R-5, this gap presumably corresponds to the slide scar where the liquefaction occurred and from which the failed mass evacuated.

Yamada et al. (2010) identified systematic patterns of the lateral migration of intermittent slope failures based on the results of sandbox experiments that simulated thrust-related uplifting and slope failures along the plate subduction zone. A major difference in conditions between that study and the slope failures examined in the present paper is that the modeled failures were generated only by altering slope inclinations; no triggers were applied such as earthquakes or liquefaction. However, given the geometry of the paleo-slope in the Chikura Group, and its tectonic history including the successive inclination and uplifting of the paleo-

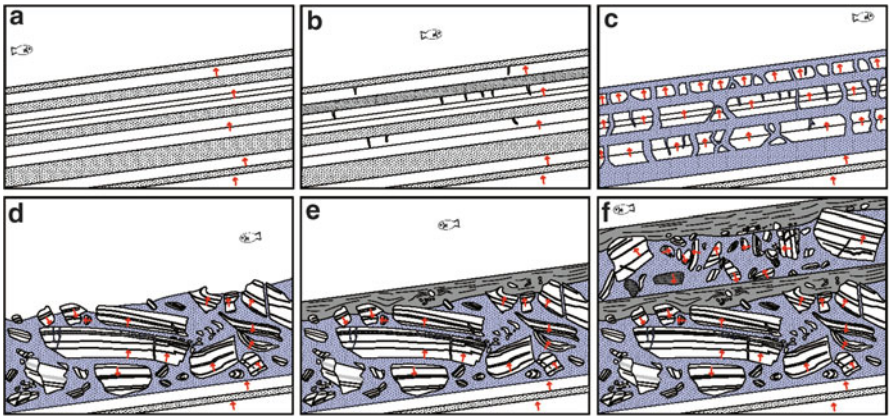

Fig. 49.5 Schematic figure illustrating the progressive formation of submarine slope failure in the Pliocene Chikura Group (using the example at site R-5). *Blue-colored* parts represent the matrices of the slope failure described in Fig. 49.2.a. (**a**) Initial state. (**b**) Earthquake-induced liquefaction occurs and associated small-scaled sandstone neptunian dykes are formed. (**c**) Soon after (**b**), liquefied sand layers interconnect, leading to the formation of large blocks. (**d**) The submarine slope failure occurred due to the loss of shear strength. The surface of the slump deposit has an irregular geometry. (**e**) The irregular surface was overlain by the failure-induced turbidite. (**f**) The second failure deposit covered the first one

slope, the geological conditions correspond quite closely to those represented in the physical models of Yamada et al. (2010).

In the experiments of Yamada et al. (2010), a slope failure produces a scar in the submarine topography, including a relatively steeply dipping scarp, triggering events in adjacent areas and leading to a lateral migration of discrete slope failures (Yamada et al. 2010). A large slide event should produce a large-scale unstable configuration of submarine topography, thereby initiating an extensive lateral migration of slides.

In conclusion, a detailed study of slope failure deposits in the Chikura Group, central Japan, reveals a systematic migrating pattern of submarine paleo-slope failures, consistent with the results of analog modeling reported by Yamada et al. (2010). The recognition of this failure pattern adds to our understanding of the mechanisms of submarine slope failures and will assist in the prediction of hazardous failures, particularly regarding the occurrence of series of intermittent failures on submarine slopes.

Acknowledgments This study was supported by a JSPS Research Grant (No. 21740363) awarded to the first author. We are grateful to Case J. Moore and Yasuhiro Yamada for their detailed reviews, which improved the manuscript. We sincerely thank Ryo Murakami and his family for their kind hospitality during fieldwork.

References

Awa Research Group (2008) Plio-Pleistocene sediments and fold formation in the southernmost of the Boso Peninsula. Field trip guide 62nd Annual meeting of Association for geologic collaboration in Japan, 11 pp

Bea RG, Sircar P, Niedoroda AW (1983) Wave-induced slides in South Pass Block 70, Mississippi Delta. J Geotech Eng 109:619–644

Bondevik S, Løvholt F, Harbitz CB et al (2005) The Storegga slide tsunami—comparing field observations with numerical simulations. Mar Petrol Geol 22:195–208

Dugan B, Germaine JT (2008) Near-seafloor overpressure in the deepwater Mississippi Canyon, northern Gulf of Mexico. Geophys Res Lett 35, L02304. doi:10.1029/2007GL032275

Flemings PB, Long H, Dugan B et al (2008) Pore pressure penetrometers document high overpressure near the seafloor where multiple submarine landslides have occurred on the continental slope, offshore Louisiana, Gulf of Mexico. Earth Planet Sci Lett 269:309–324. doi:310.1016/ j.epsl.2008.1006.1027

Heezen BC, Ewing M (1952) Turbidity currents and submarine slumps and the 1929 Grand Banks earthquake. Am J Sci 250:849–873

Kawakami S, Shishikura M (2006) Geology of the Tateyama District. Geological Survey of Japan. Quadrangle series, 1:50,000. AIST, Tokyo, p 82 (in Japanese with English abstract)

Koyama M, Kitazato H (1989) Paleomagnetic evidence for Pleistocene clockwise rotation in the Oiso Hills: a possible record of interaction between the Philippine Sea Plate and Northeast Japan. In: Hillhouse JW (ed) Deep structure and past kinematics of accreted terranes, vol 50, Geophysical monograph., pp 249–265

Lucente CC, Pini GA (2007) Basin-wide mass-wasting complexes as markers of the Oligo–Miocene foredeep-accretionary wedge evolution in the Northern Apennines, Italy. Basin Res 20:49–71

Morita S, Nakajima T, Hanamura Y (2012) Possible ground instability factor implied by slumping and dewatering structures in high-methane-flux continental slope. In: Yamada Y et al (eds) Submarine mass movements and their consequences, vol 31, Advances in natural and technological hazard researches. Springer, Dordrecht, pp 311–320

Saito S (1992) Stratigraphy of Cenozoic strata in the southern terminus area of Boso Peninsula, Central Japan. Contributions from the Institute of Geology and Paleontology Tohoku University, Sendai, Japan. 93, pp 1–37

Sawyer DE, Flemings PB, Dugan B, Germaine JT (2009) Retrogressive failures recorded in mass transport deposits in the Ursa Basin, Northern Gulf of Mexico. J Geophys Res 114, B10102. doi:10.1029/2008JB006159

Talling PJ, Wynn RB, Masson DG et al (2007) Onset of submarine debris flow deposition far from original giant landslide. Nature 450:541–544

Underwood MB, Moore GF (1995) Trenches and trench-slope basins. In: Busby CJ et al (eds) Tectonics of sedimentary basins. Blackwell Science, Cambridge, MA, pp 179–219

Yamada Y, Yamashita Y, Yamamoto Y (2010) Submarine landslides at subduction margins: Insights from physical models. Tectonophysics 484:156–167

Yamamoto Y (2006) Systematic variation of shear-induced physical properties and fabrics in the Miura–Boso accretionary prism: the earliest processes during off scraping. Earth Planet Sci Lett 244:270–284. doi:10.1016/ j.epsl.2006.01.049

Yamamoto Y, Kawakami S (2005) Rapid tectonics of the late Miocene Boso accretionary prism related to the Izu-Bonin arc collision. Isl Arc 14:178–198

Yamamoto Y, Mukoyoshi H, Ogawa Y (2005) Structural characteristics of shallowly buried accretionary prism: rapidly uplifted Neogene accreted sediments on the Miura–Boso Peninsula, Central Japan. Tectonics 24, TC5008. doi:10.1029/2005TC001823

Yamamoto Y, Ogawa Y, Uchino T, Muraoka S, Chiba T (2007) Large-scale chaotically mixed sedimentary body within the Late Pliocene to Pleistocene Chikura Group, Central Japan. Isl Arc 16:505–507

Yamamoto Y, Nidaira M, Ohta Y, Ogawa Y (2009) Formation of chaotic rock-units during primary accretion processes: examples from the Miura–Boso accretionary complex, Central Japan. Isl Arc 18:496–512

Yamamoto Y, Yamada Y, Yamashita Y et al (2012) Systematic development of submarine slope failures at subduction margins: fossil record of accretion-related slope failure in the Miocene Hota accretionary complex, Central Japan. In: Yamada Y et al (eds) Submarine mass movements and their consequences, vol 31, Advances in natural and technological hazards research series. Springer, Dordrecht, pp 355–364

Chapter 50
Quaternary Mass-Transport Deposits on the North-Eastern Alboran Seamounts (SW Mediterranean Sea)

B. Alonso, G. Ercilla, M. Garcia, J.T. Vázquez, C. Juan, D. Casas, F. Estrada, E. D´Acremont, Ch. Gorini, B. El Moumni, and M. Farran

Abstract The Quaternary stratigraphic architecture of seamounts and surrounding deposits in the eastern Alboran Sea reveals at least 53 stacked MTDs in the Pollux Bank, Sabinar Bank (Sabinar Platform and Western Sabinar), Maimonides Ridge, and Adra Ridge. These MTDs are grouped into two types based on their size: small-scale MTDs (length <5 km and thickness <18 ms) and large-scale MTDs (length >5 km and thickness >18 ms). The study of these deposits has allowed us to define a close relationship between size (thickness-length) and source area gradients. The frequency of MTD events has varied between 40 and 373 kyr throughout the Quaternary (1.8 Ma to present). Correlation between individual MTDs is difficult but could be done for at least one local MTD event between Sabinar Platform and Western Sabinar (Sabinar Bank); in addition, one regional MTD event has been recognized around all of the studied seamounts. These failure events could have been triggered by tectonically controlled seismicity at both regional and local scale.

B. Alonso (✉) • G. Ercilla • C. Juan • F. Estrada • M. Farran
Instituto de Ciencias del Mar, CSIC, Barcelona, Spain
e-mail: belen@icm.csic.es

M. Garcia
Instituto Andaluz de Ciencias de la Tierra, CSIC-Universidad de Granada, Granada, Spain

J.T. Vázquez
Instituto Español de Oceanografía, Centro de Málaga, Málaga, Spain

D. Casas
Instituto Geológico Minero de España, Madrid, Spain

E. D´Acremont • Ch. Gorini
UPMC Univ. Paris 06, ISTEP, Paris, France

CNRS, UMR 7193, F-75005 Paris, France

B. El Moumni
Doyen de la FP, Université Abdelmalek ESSAADI, Tangier, Morocco

S. Krastel et al. (eds.), *Submarine Mass Movements and Their Consequences*, Advances in Natural and Technological Hazards Research 37, DOI 10.1007/978-3-319-00972-8_50,

Keywords Mass-transport deposits • Seismic profiles • Seamounts • Alboran Sea

50.1 Introduction

Over the past decade, MTDs have been described in the Alboran Sea (Fig. 50.1) based on new geophysical data (TOPAS and Parasound seismic profiles) and multibeam bathymetric techniques (Muñoz et al. 2007; Martínez-García et al. 2011; Vázquez et al. 2010; Casas et al. 2011; Alonso et al. 2012a). The eastern Alboran Sea is special from the morphotectonic point of view as mass-transport features locally affect the seafloor of a seamount domain (Vázquez et al. 2010; Alonso et al. 2012a). The temporal and spatial relationships of MTDs in the seamount domain are still unknown. The purpose of this paper is to characterise the MTDs of four seamounts (Pollux Bank, Sabinar Bank_two sectors: W Sabinar and Sabinar Platform_, Maimonides Ridge and Adra Ridge) and the surrounding deposits of the eastern Alboran Basin (SW Mediterranean Sea, Fig. 50.1), and to understand their spatial and temporal distributions in terms of size (thickness-length) and event frequency, throughout the Quaternary stratigraphic divisions.

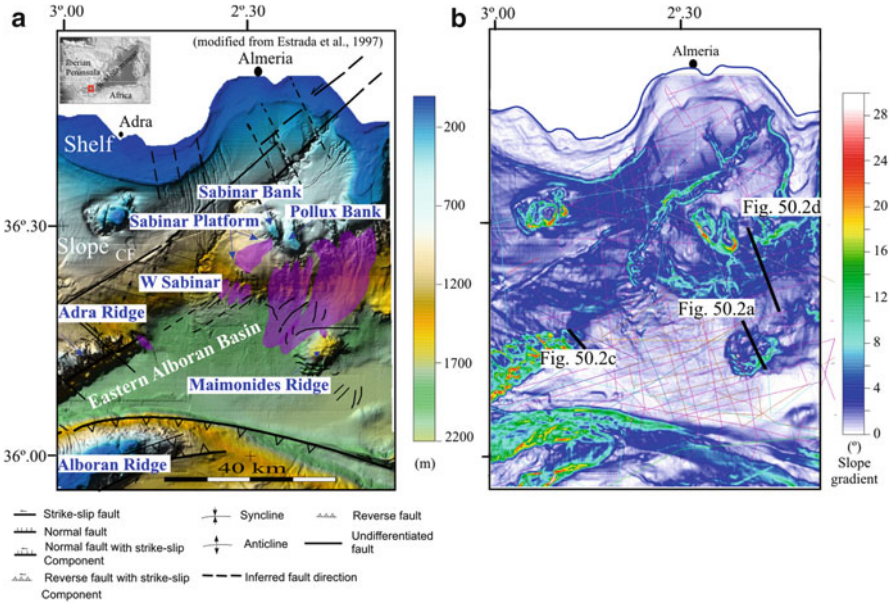

Fig. 50.1 General bathymetric map (**a**) and gradient map (**b**) of the north-eastern Alboran Sea. The main tectonic structures and the area affected by MTDs on seamounts (*shaded purple*) are shown on the bathymetric map. *CF* Carboneras Fault. *Black lines* show the location of Fig. 50.2a, c, d

50.1.1 Geological Setting

Numerous seamounts in the margins and basins of the Alboran Sea represent first order morphotectonic features (Auzende et al. 1975). The NE-SW trending structural and volcanic Alboran Ridge is the most striking feature reaching nearly 200 km in length (Fig. 50.1a; Woodside and Maldonado 1992). Other volcanic seamounts also characterise the physiography in the eastern Alboran Sea; they are, from east to west, Pollux Bank (270 m water depth), Sabinar Bank (Sabinar Platform at 780 m water depth and W Sabinar at 1,117 m water depth), Maimonides Ridge (1,438 m water depth) and Adra Ridge (716 m water depth) (Fig. 50.1a).

The Alboran Sea is a tectonically active region which has been affected by oblique compression that generated strike-slip and compressional tectonics during the Pliocene and Quaternary (Martínez-García et al. 2013). At present, it is subject to the continuous oblique NW-SE convergence of the African and Eurasian plates (Nocquet 2012). The main tectonic structures affecting the Pliocene and Quaternary sediments have two predominant directions NE-SW and NW-SE (Fig. 50.1a) (Woodside and Maldonado 1992; Estrada et al. 1997; Martínez-García et al. 2011). There are also minor faults and folds oriented ENE-WSW and NNW-SSE (Fig. 50.1a), which have controlled the uplift of the seamounts. The seismicity of the northeastern region is characterised by continuous, shallow earthquakes of low to moderate magnitude ($M_w < 5.5$) (Stich et al. 2003). The highest magnitude earthquake recorded instrumentally took place in the Carboneras Fault Zone and Adra area (M_w 6.1 in 1910). The regional stratigraphy, established recently by Juan et al. (2012), divides the Quaternary deposits into two seismic units, which are, from base to top: C (Lower Quaternary), and D (Upper Quaternary). These are respectively bounded at the bottom by two seismic boundaries: the base of the Quaternary Discontinuity-BQD- (2.6 Ma) and the Middle Pleistocene Revolution-MPR- (0.920 kyr).

50.1.2 Data and Methods

The data set is the result of a combination of several cruises, including, the GC-90 cruise (R/V Garcia del Cid), MARSIBAL-2006 cruise (BIO Hespérides), SAGAS-2011 (R/V Sarmiento de Gamboa) and MONTERA-2012 cruise (R/V Sarmiento de Gamboa) (Fig. 50.1b). This study uses integrated information from different types of seismic data, high and ultra-high resolution seismic profiles (airgun system, TOPAS and Parasound parametric sounders) and swath bathymetry data. The swath bathymetry was acquired from the Spanish Secretary General for Fisheries, Ministry of Agriculture, Food and Environment.

The establishment of the chronostratigraphic framework is based on previous high-resolution seismic stratigraphic studies in the Alboran Sea (Estrada et al. 1997; Alonso and Ercilla 2003; Juan et al. 2012; Ercilla et al. 2012; Alonso et al. 2012b). The method for estimating the potential age of each MTD is based on the

sedimentation rate per stratigraphic division and the depth of the MTD within its stratigraphic division. Each seismic subunit was decompacted using the method of Estrada et al. (1997) who applied Van Hinte's (1978) compaction law. The theoretical value of initial sediment porosity is given by Sclater and Christie (1980) and the present sediment porosity is given by the measurements conducted on similar deposits in the Alboran Sea (Comas et al. 1996). For the thickness of each seismic subunit (metres) and the depth of the MTDs, the seismic wave velocity defined for ODP-Site 976, located in the western Alboran Basin, is used (Comas et al. 1996).

50.2 Results

50.2.1 Characterisation of MTDs

The MTDs analyzed in this paper are aged from 1.8 Ma (upper section of seismic unit C) to the present day (seismic unit D), based on the stratigraphic context (Fig. 50.2). In this work, seismic units C and D have each been divided into two

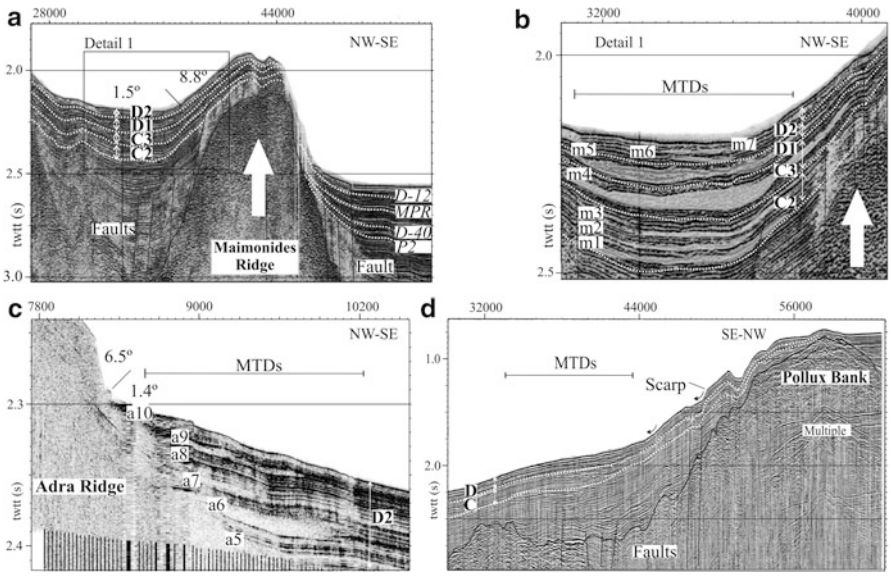

Fig. 50.2 Quaternary MTDs on the eastern Alboran Seamounts: (**a**) obliquely-oriented air-gun seismic profile showing the Quaternary stratigraphy of the Maimonides Ridge; (**b**) detail of the seven stacked MTDs (m1–m7) in the northern sector of Maimonides Ridge; (**c**) obliquely-oriented TOPAS seismic profile showing six MTDs (a5–a10) within seismic subunit D2 in the eastern sector of Adra Ridge; and (**d**) obliquely-oriented air-gun seismic profile showing the Quaternary stratigraphy of the Pollux Bank and the area affected by MTDs. Legend: C2, C3, D1, D2 Quaternary seismic subunits; P2, D-40, MPR, D-12 seismic reflectors; *letter/number* refer to MTD; *twtt* two-way travel time; and *s* seconds (See Fig. 50.1 for locations of profiles)

subunits which are, from base to top, C2, C3, D1 and D2 (Alonso et al. 2012b). These four subunits are bounded by regional discontinuities related to the following isotopic stages: P2 dated at MIS 60 (1.8 kyr), D-40 dated at MIS 40 (1.32 kyr), MPR dated at MIS 22 (0.920 kyr), and D-12 dated at MIS-12 (0.450 kyr) (Alonso et al. 2012b) (Fig. 50.2).

At least 53 stacked MTDs have been recognized for the first time within the Quaternary deposits of Pollux Bank, Sabinar Platform, Western Sabinar, Maimonides Ridge, Adra Ridge and surroundings (Fig. 50.3). These MTDs are acoustically defined by semitransparent, transparent, and chaotic facies with lenticular shape (Fig. 50.2b, c). Their upper and lower boundaries consist of high-amplitude seismic reflections. These deposits interrupt the lateral continuity of the surrounding stratified deposits and appear as stacked lobate bodies within the Quaternary unit (Fig. 50.2). Based on their dimensions, small-scale MTDs (length <5 km and thickness <18 ms) and large-scale MTDs (length >5 km and thickness >18 ms) have been identified (Fig. 50.3). The MTDs have been identified between 770 m and 1,920 m water depth. They occur at the foot of the studied seamounts and also on the platform adjacent to Sabinar Bank (770–920 m water depth) (Fig. 50.1a). The seamount walls display high but variable slope gradients (up to 20°) (Fig. 50.1b). The eastern sector of Pollux Bank shows a relatively moderate slope gradient (2.3°–5°) (Fig. 50.3).

50.2.2 Quantitative Analysis of MTDs

Each MTD was numbered starting with 1 for the oldest with a letter added in front of the number to represent the region (Figs. 50.2 and 50.3). The number was assigned according to the MTD's position within the stratigraphic subunit and the letter refers to the name of each seamount. MTDs located on seamounts exhibit significant spatial and temporal differences, in terms of thickness-length, within the Quaternary deposits (Fig. 50.3). They are generally thin (5–18 ms, two way travel time) and short (<7 km long) on most of the seamounts. One exception was found in the eastern sector of Pollux Bank where MTDs are relatively thicker (18–50 ms, two way travel time) and longer (7–18 km) (Fig. 50.3). Thicknesses show a cyclic pattern with alternating thinner and thicker MTDs (Fig. 50.3).

The potential age of each MTD, its recurrence and frequency are also defined (Fig. 50.3). The ages of most MTDs are different, with the exception of p3, s4, sp4, m4 and a3 which are estimated to have been deposited at 1.193, 1.195, 1.187, 1.195, and 1.190 kyr respectively (Fig. 50.3). The range of estimated recurrence within each seismic subunit allows two return frequencies to be established based on the frequency values obtained in other areas (Piper et al. 2003; Strozyk et al. 2010; Ratzov et al. 2010): (i) *low* (recurrence interval of >210 kyr) and, (ii) *medium* (recurrence interval of 40–210 kyr) (Fig. 50.3). A medium frequency of MTDs predominates throughout the Quaternary (1.8 Ma to present).

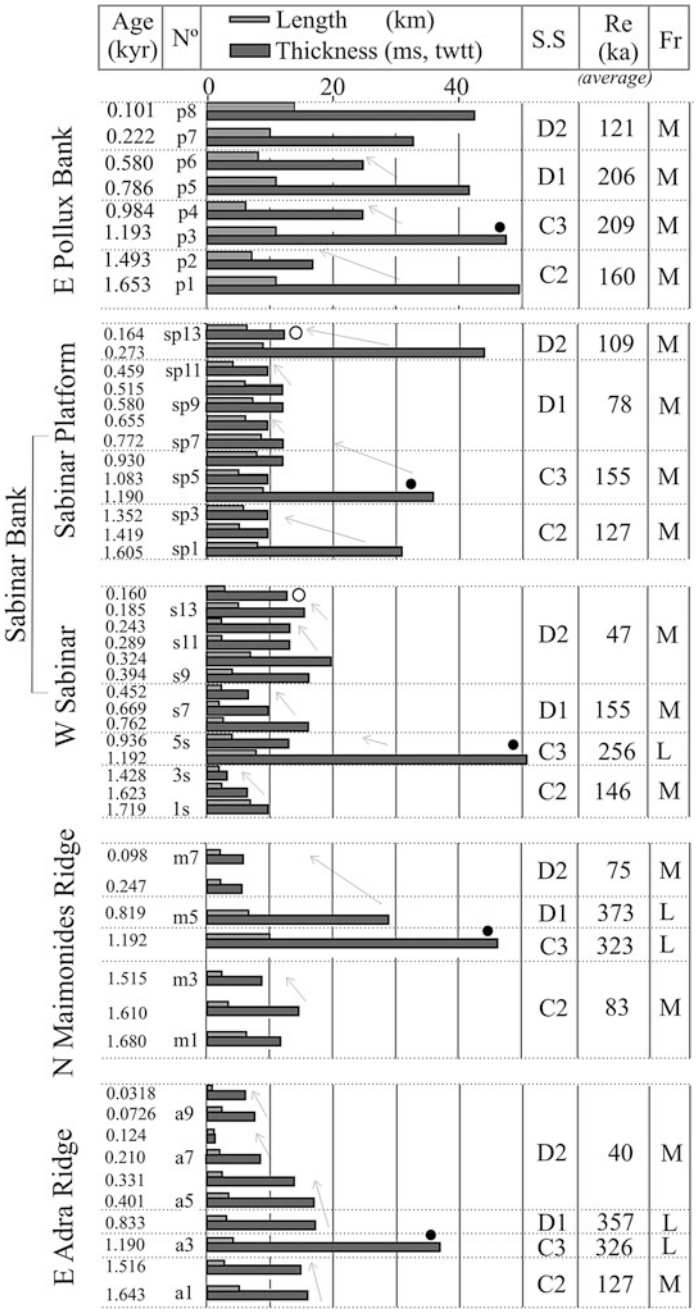

Fig. 50.3 Temporal and spatial distribution of the MTDs on the eastern Alboran seamounts showing the potential age estimate age (kyr), the size (thickness-length), the recurrence values (*Re*) and the frequency (*Fr*) of MTD events within the Quaternary seismic subunits (S.S) (C2, C3, D1, and D2). Legend: *ms* milliseconds; *black dots* refer to the possible regionally synchronic tectonic pulse and *white dots* refer to possible locally synchronic tectonic pulse

50.3 Discussion and Conclusions

Between 52 and 90 % of the Quaternary sedimentary record in the five sectors of studied seamounts of the north-eastern Alboran Sea and surroundings is made up of stacked MTDs (Fig. 50.2). This means that recurrent MTDs are common on the seamounts and surrounding areas. The following paragraphs focus on understanding the geological significance of the spatial and temporal distributions of the MTDs through the relationship of their thickness-lengths with seafloor gradients, and the footprints of potential causal processes.

Bathymetry and high resolution seismic records reveal that the thinner (<18 ms, twtt) and shorter (<5 km) MTDs are sourced from the Sabinar, Maimonides, and Adra (Figs. 50.1 and 50.3). Their walls are characterised by slope gradients of >5°–20° (Fig. 50.1b), outcropping basement and thin Quaternary sedimentary cover (<100 ms thick, twtt) (Woodside and Maldonado 1992). Contrastingly, the thicker (18–50 ms, twtt) and longer (5–18 km) MTDs (Fig. 50.3) come from the eastern Pollux Bank walls, characterised by relatively low slope gradients (2.5°–5°) (Fig. 50.1b) and thicker sedimentary cover (100–230 ms thick, twtt) (Fig. 50.2c). The temporal and spatial distributions of the 53 MTDs studied suggest an inverse correlation between MTD size (thickness-length) and the slope angle of the source area. Similar observations made elsewhere (McAdoo et al. 2000) suggested that high-slope angles prevent the development of thick slope sediment and large-scale failures.

MTD triggering usually includes several factors such as high amplitude sea-level changes, sediment overburden, storms, presence of bubble gas within the sediment and dissociation of gas hydrate, overstepping and tectonic-related earthquakes (Locat and Lee 2002). The seamounts of this study are isolated from continental sediment sources, meaning sea level changes could not directly influence sedimentary instability. Likewise, the high resolution seismic profiles do not show acoustic anomalies related to the presence of free gas within the sediments or gas hydrate in either the seamounts or in the surrounding areas. The scar zones of the mapped MTDs are located at sufficiently deep water depths (Pollux at 963 m, Sabinar Platform at 570 m, W Sabinar at 1,117 m, Maimonides at 1,477 m, and Adra at 1,584 m) not to be affected by the action of storm-wave loadings, even during the large amplitude and high frequency sea-level changes that characterise the Late Quaternary.

The steep slopes of the seamount walls, with gradients of between 2.5° and 20°, may also contribute to sedimentary instability as a preconditioning and/or triggering factor. The seamounts are morphologically tectonic in origin and/or their bounding faults are considered to be tectonically active in the upper Quaternary such as the Carboneras Fault which is seismically active (Gràcia et al. 2006; Estrada et al. 1997; Martínez-García et al. 2011). As consequence, the seismic activity is considered a likely triggering mechanism. In fact, locating the MTDs on the structural map reveals that they are sited along major and minor scale faults although no relationship of MTD size to major and minor scale faults has been observed

(Fig. 50.1a). Similar observations have been made along the recent structures on the Alboran Ridge and Yusuf Fault (Martínez-García et al. 2011). Likewise the interplay between seismicity and steep slopes can be considered a potential triggering mechanism as it could play a more significant control on critical slope condition over a longer time scale explaining the high variability of MTD recurrence (40–373 kyr) (Fig. 50.3).

The chronostratigraphic correlation of MTDs between seamounts is used to test their potential synchronicity and to discriminate between local and regional triggering. The ages obtained for the MTDs indicate that only one regional MTD event seems to have occurred, at about 1.191 kyr, the age obtained for MTDs p3, s4, sp4, r4 and a3 close to the lower boundary of seismic subunit C3 in the five study sites (Fig. 50.2). If tectonic-related seismicity is accepted as an important factor for MTD triggering mechanisms in the Alboran seamounts, it may be tentatively inferred that the mentioned MTDs could be related to a contemporaneous tectonic pulse at regional scale. The interpretation of a synchronous event at regional scale is also supported by the thickness of these MTDs (48–51 ms, twtt), which suggests a seismic event of significant magnitude. In addition, two more recent MTDs, at 0.160 kyr in the W Sabinar (s14 MTD) and 0.164 kyr on Sabinar Platform (sp13 MTD), are time correlated across the Sabinar Bank (Fig. 50.3). This correlation indicates at least one local tectonic pulse at the Sabinar Bank of minor magnitude if one considers the fact that the MTDs are thinner (<13 ms, Fig. 50.3). This hypothesis is further supported by the presence of similar sediments from the same source area (Sabinar Bank), but with different slope gradients, up to 20° in the Sabinar Platform and 4°–8° in the W Sabinar (Fig. 50.1b).

The non-coincident ages of the other MTDs and their irregular frequency (a recurrence interval of about 40–373 kyr) could be related to irregular activity of the tectonic structures affecting the geotectonic history of each seamount, different tectonic controls on critical slope condition, or the different geotechnical properties of the sediments affected. The generally cyclic thickness pattern, increase-decrease-increase, observed in the all seamounts studied seems to point to a greater tectonic influence. The decreases could be related to a lack of sediment for potential remobilisation after several strong seismic events that would have depleted the source area. Once the source area is re-charged in terms of sediment, MTDs with a larger thickness may develop. Geotechnical studies are necessary to establish the mechanical behaviour of the slope sediments during instability scenarios in order to investigate slope instability and factors controlling the frequency of MTDs.

Acknowledgements This work was funded by the MONTERA (CTM2009-14157-C02-02) and CONTOURIBER (CTM2008-06399-C04-04/MAR) projects of the Spanish R&D Plan (MINECO). The Continental Margins Group would also like to acknowledge the R&D system of Catalonia "*Generalitat de Catalunya*" for the financial support received as part of the 2009 SGR107 programme. We thank IHS for supporting us with the Kingdom Suite Program. We also extend our thanks to the Ministry of the Environment and Rural and Marine Affairs ("*Secretaria General del Mar*") for the bathymetric data. We also wish to thank Sebastian Migeon and Aggeliki Georgiopoulou for reviewing this paper.

References

Alonso B, Ercilla G (2003) Small turbidite systems in a complex tectonic setting (SW Mediterranean Sea): morphology and growth patterns. Mar Petrol Geol 19:1225–1240

Alonso B, Ercilla G, Juan C, Casas D et al. (2012a) Morpho-seismic characterization of Quaternary mass-movement deposits in the eastern sector of the Alboran Sea (SW Mediterranean). Geo-Temas 13:561–564

Alonso B, Ercilla G, Juan C, Casas D et al. (2012b) El abanico distal de Almeria: Arquitectura estratigráfica y evolución durante el Pleistoceno Superior (SO Mediterráneo). Geo-Temas 13:491–494

Auzende J, Bonin J, Olivet JL (1975) La marge nord-africaine considérée comme marge active. Bull Soc Géol de Fr 37:486–495

Casas D, Ercilla G, Yenes M, Estrada F et al (2011) The Baraza slide. Model and dynamics. Mar Geophys Res 32(1):245–256

Comas MC, Zahn R, Klaus A (1996) Proceedings of the ocean drilling program, initial reports, College Station, Texas, vol 161, pp 179–296

Ercilla G, Juan C, Estrada F, Casas D et al. (2012) Contourite sedimentation in the Alboran Sea: Morphosedimentary characterization. Geo-Temas 13:1809–1812

Estrada F, Ercilla G, Alonso B (1997) The tectosedimentary evolution of the northeastern Alboran Sea during the Plio-Quaternary. In: Cloetingh S et al. (eds) Structural controls on sedimentary casin formation. Tectonophysics 282 (1–4), pp 423–442

Gràcia E, Pallàs R, Soto JI, Comas MC et al (2006) Active faulting offshore SE Spain (Alboran Sea): implication for earthquake hazard assessment in the Southern Iberian Margin. Earth Planet Sci Lett 241:734–749

Juan C, Ercilla G, Estrada F, Casas D et al. (2012) Contourite sedimentation in the Alboran Sea: Plio-Quaternary evolution. Geo-Temas 13:1817–1820

Locat J, Lee HJ (2002) Submarine landslides: advances and challenges. Can Geotech J 39:193–212

McAdoo BG, Pratson LF, Orange DL (2000) Submarine landslide geomorphology, US continental slope. Mar Geol 169:103–136

Martínez-García P, Soto JI, Comas M (2011) Recent structures in the Alboran Ridge and Yusuf zones based on swath bathymetry and sub-bottom profiling: evidence of active tectonics. Geo-Mar Lett 31:19–36

Martínez-Garcia P, Comas M, Soto JI, Lonergan L, Watts AB (2013) Strike-slip tectonics and basin inversion in the western Mediterranean: the Post-Messinian evolution of the Alboran Sea. Basin Res 25:1–27

Muñoz A, Ballesteros M, Montoya I, Rivera J (2007) Alboran Basin, southern Spain-Part I: geomorphology. Mar Petrol Geol 25:59–73

Nocquet JM (2012) Present-day kinematics of the Mediterranean: a comprehensive overview of GPS results. Tectonophysics 579:220–242

Piper DJW, Mosher DC, Gauley BJ, Kenner K et al (2003) The chronology and recurrence of submarine mass movements on the continental slope off southern Canada. In: Locat J, Mienert J (eds) Submarine mass movements and their consequences, Advances in natural and technological hazard research 19. Kluwer Academic Publisher, Dordrecht, pp 299–306

Ratzov G, Collot JY, Sosson M, Migeon S (2010) Mass-transport deposits in the northern Ecuador subduction trench: result of frontal erosion over multiple seismic cycles. Earth Plan Sci Lett 296:80–102

Sclater JG, Christie PAF (1980) Continental stretching: an example of the post-mid-Cretaceous subsidence of the central North Sea basin. J Geophys Res 85:3711–3739

Stich D, Ammon CJ, Morales J (2003) Moment tensor solutions for small and moderate earthquakes in the Ibero-Magreb region. J Geophys Res 108:2148–2168

Strozyk F, Strasser M, Föster A, Kopf A et al (2010) Slope failure in active margin environment: constraints from submarine landslide in the Hellenic arc. J Geophys Res 115(B08103):1–13

Van Hinte JE (1978) Geohistory analysis. Application of micropaleontology in exploration geology. AAPG 62:201–222

Vázquez A, Bárcenas P, Palomino D, Alonso B et al. (2010) Sedimentary instabilities along the southwestern slope of the Alboran Ridge (SW Mediterranean). In: Abstracts of the 9th CIESM, Venice, Italy, 10–14 May 1978

Woodside JM, Maldonado A (1992) Styles of compressional neotectonics in the eastern Alboran Sea. Geo-Mar Lett 12(2/3):111–116

Chapter 51
Searching for the Record of Historical Earthquakes, Floods and Anthropogenic Activities in the Var Sedimentary Ridge (NW Mediterranean)

V. Hassoun, J. Martín, S. Migeon, C. Larroque, A. Cattaneo, M. Eriksson, J.A. Sanchez-Cabeza, B. Mercier de Lepinay, L. Liong Wee Kwong, I. Levy, L.-E. Heimbürger, and J.-C. Miquel

Abstract Submarine landslides on continental slopes are triggered by diverse mechanisms such as sea-level variations, climate-driven sediment supply fluctuations, slope steepening related to long term tectonics, earthquakes and human activities. In the present work, we try to discriminate the origin of major gravity events recorded in three sediment cores collected on the Var Sedimentary Ridge (NW Mediterranean) by means of X-ray imaging, grain-size distributions and ^{210}Pb-based chronologies supported by ^{137}Cs and AMS ^{14}C dating. An alternation of hemipelagic mud and sandy turbidite layers is apparent in all cores. In two of them, the topmost turbidite can be correlated to the well-known 1979 Nice-Airport

V. Hassoun (✉) • C. Larroque • B. Mercier de Lepinay
UMR7329 Géoazur, UNS-UPMC-CNRS-OCA, 06560 Valbonne, France
e-mail: hassoun@geoazur.unice.fr

J. Martín
ICM-CSIC, 08003 Barcelona, Spain

S. Migeon
Géoazur, UMR7329, UNS-UPMC-CNRS-OCA, Rue Albert Einstein, 06560 Valbonne, France

A. Cattaneo
Géosciences Marines, IFREMER, Centre de Brest, BP70, 29280 Plouzané, France

Istituto di Scienze Marine (ISMAR-CNR), Bologna, Via Gobetti 101, Bologna 40129, Italy

M. Eriksson • L. Liong Wee Kwong • I. Levy • J.-C. Miquel
IAEA–EL, 98000 Monaco, Monaco

J.A. Sanchez-Cabeza
Institut de Ciència i Tecnologia Ambientals, Universitat Autònoma de Barcelona, 08193 Bellaterra, Spain

Instituto de Ciencias del Mar y Limnología, Universidad Nacional Autónoma de México, 04510 Mexico D.F., Mexico

L.-E. Heimbürger
GET-OMP, 31400 Toulouse, France

S. Krastel et al. (eds.), *Submarine Mass Movements and Their Consequences*, Advances in Natural and Technological Hazards Research 37, DOI 10.1007/978-3-319-00972-8_51,

landslide. A sub-surficial sandy layer is identified in all three cores with an approximate age of 120 years, suggesting for the first time a relationship with the largest earthquake in the region (1887; $M_w = 6.9$). Below the depth of that major event, sand beds are tentatively related to older local earthquakes and centennial floods.

Keywords Ligurian margin • Turbidites • Hyperpycnites • Earthquakes • Floods • 1979 Nice event

51.1 Introduction

The triggering of submarine landslides on continental slopes is controlled by various factors acting differently in time and space (e.g. Lee et al. 2007). Earthquakes are classically evoked on both passive and active margins but it is difficult to correlate a specific failure-related scar to such a short-term event. Anyway, mass-transport deposits and turbidites found on the lower continental slope or in deep basins may preserve the record of past earthquakes and thus constitute a proxy for paleoseismic activity (Goldfinger et al. 2003; Gràcia et al. 2010; Ratzov et al. 2010). Although sedimentological criterions for the identification of landslide- and flood-triggered turbidites have been validated in some cases, earthquake-triggered turbidites are often identified by precise dating and correlation with earthquakes and tsunami deposits (Nakajima and Kanai 2000).

Along the Ligurian margin (NW Mediterranean; Fig. 51.1), sediment supply delivered by small mountain-supplied rivers is high and the hemipelagic background is disrupted by slumping, hyperpycnal flows and turbidity-currents (Migeon et al. 2006). In addition to a moderate seismic activity, large historical earthquakes with intensities $I_0 \leq$ IX MSK also affected the Ligurian margin, notably in years1564, 1644, 1818 and 1887 (Larroque et al. 2001). In a context of steep continental slope, these earthquakes should have triggered slope failures. The 1887 Ligurian earthquake is the most catastrophic historical event that affected the area ($M_w \approx 6.9$; Larroque et al. 2012). The epicenter is estimated to be located offshore the Italian city of Imperia (Fig. 51.1). This earthquake generated a tsunami along the Ligurian coast and triggered at least one slope failure close to the epicentral area (Hassoun et al. 2009).

In 1979, a sediment failure (8×10^6 m^3) occurred at shallow-water depth during infilling operations seaward of the Nice International Airport (Dan et al. 2007). This anthropogenic event generated a turbidity current (Mulder et al. 1997; Fig. 51.1) and a tsunami that affected the coastline between the cities of Nice and Antibes (Ioualalen et al. 2010). In addition, flood-generated turbidity currents are also common offshore the Var River and are responsible for deposition of inversely-graded hyperpycnites throughout the continental slope (Mulder et al. 2001).

To test the traceability of major historical events in the sedimentary record, sandy turbidites were studied from cores collected close to the crest of the eastern Var Sedimentary Ridge (VSR; Fig. 51.1). In this area, Holocene sedimentation rates are high (30 cm ky^{-1}; Migeon et al. 2001), offering a high-resolution record of the sedimentary processes occurred during the last centuries.

51.2 Methods

Three short cores were collected in the eastern VSR during the Malisar, Dycomed4 and ENVAR cruises in 2007, using respectively a Küllenberg, a B&C multicorer and a Reineck box sampler. Coring sites DYC and DYF were located along the crest of the VSR, on a topographic low and on a high, respectively. Site KNI27 was located 8 km southward from the VSR crest (Fig. 51.1). Analyses included visual core description, numerical X-ray (SCOPIX; Migeon et al. 1999) and grain-size distribution (Coulter® laser granulometer). In cores DYC and DYF, ^{210}Pb and ^{137}Cs concentrations were determined by gamma-spectroscopy and ^{226}Ra (assumed equal to supported ^{210}Pb) by Liquid Scintillation Counting (Martín et al. 2009; Sanchez-Cabeza et al. 2010). AMS ^{14}C analyses were conducted in foraminifera (planktonic shells and bulk) samples and wood fragments. Radiocarbon ages calibration was performed using the MARINE09 database of the software CALIB 6.0 (Stuiver et al. 2005). Raw bathymetric data were collected during the Malisar cruise using a Simrad EM300 and provided a 25-m resolution DTM.

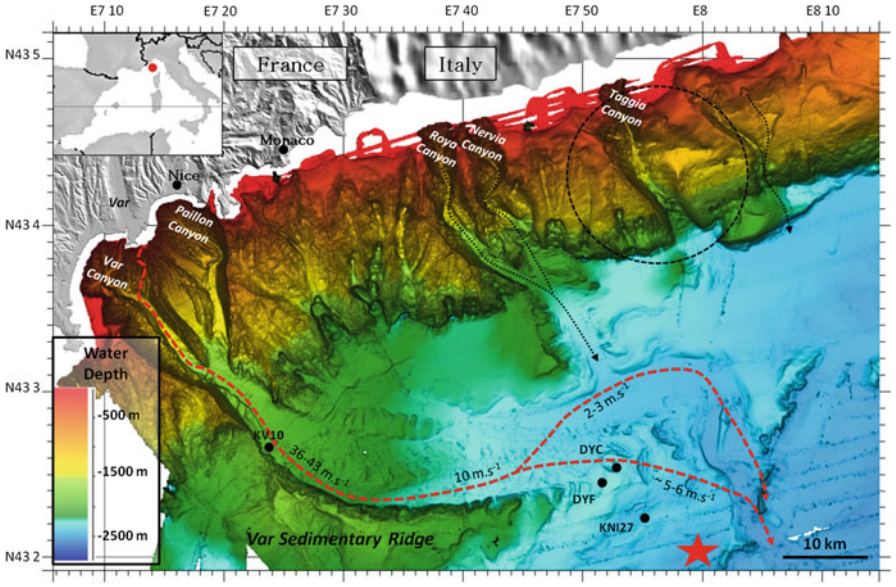

Fig. 51.1 Shaded bathymetric map of the Ligurian Margin (Géoazur-Ifremer) illustrating the location of cores DYF, DYC, KNI27 and KV10. The *red star* corresponds to the location of the cable broken by the 1979 flow (*red dashed arrows* from Mulder et al. 1997). The *dashed black circle* locates the 1887 epicentral area (Larroque et al. 2012) and the *black arrows* the potential pathways of landslides and turbulent flows triggered by the earthquake

51.3 Results

51.3.1 Age Models

In cores DYC (Fig. 51.2) and DYF (Fig. 51.3), measurements of ^{210}Pb excess activity allowed deducing a CRS (Constant Rate of Supply) age model, which was confirmed by ^{137}Cs. Sandy beds, identified below as turbidites (instantaneous deposition) were not taken into account in the calculation of the sedimentation rate and age estimation. ^{14}C dates are given in Table 51.1.

Within the three cores, several sandy layers (T1–T10) were identified. We will mostly focus on the most recent layers T1 and T2. In core DYC, sedimentation rate was estimated at 0.30–0.35 mm year^{-1} and the ^{14}C dating at the base of the core gave an age of AD 1398–1475. T1 and T2 would have been deposited in AD 1980 ± 4 and 1888 ± 9, respectively. In core DYF, the rate of hemipelagic sedimentation is about 0.27–0.33 mm year^{-1}. The ^{210}Pb age model supported by

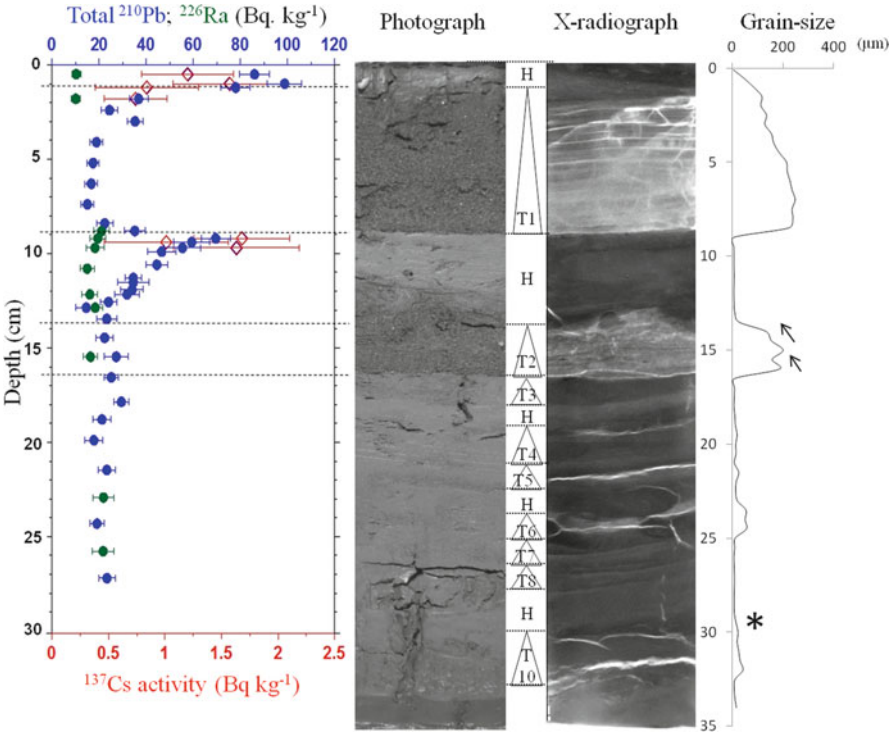

Fig. 51.2 From *left* to *right*: concentration of ^{210}Pb, ^{137}Cs and ^{226}Ra, core photograph, X-ray image, mean grain-size of core DYC. The *white arrows* indicate the two sub-intervals in turbidite T2. T1–T10 are turbidite layers described in the text. *H* corresponds to the hemipelagic intervals. The *black star* locates the sample for ^{14}C dating

Table 51.1 Location of the studied cores, AMS radiocarbon data and sample age calibrations based on the MARINE09 curve (Stuiver et al. 2005) including in CALIB 6.0 calibration software

Core	Coord.	Water depth (m)	Core depth (cm)	Material	Radiocarbon age (year BP $\pm$ 1σ)	ΔR^a	1σ Cal BP age ranges	Cal BP age median probability
DYC	N43°25.03 E07°51.98	2,345	36.5	Bulk planktic	880 $\pm$ 30	−27 $\pm$ 40	475–552	518
DYF	N43°24.66 E07°51.63	2,330	17.5	Bulk planktic	780 $\pm$ 30	−27 $\pm$ 40	404–497	443
			22.5	Bulk planktic	1,030 $\pm$ 30	−27 $\pm$ 40	591–664	624
			29.5	Bulk planktic	1,290 $\pm$ 30	−27 $\pm$ 40	799–913	856
KNI27	N43°21.41 E07°55.94	2,440	23.5	Wood	660 $\pm$ 30	−27 $\pm$ 40	282–391	341

[a]Local reservoir correction for Antibes, France (Siani et al. 2000; Reimer and McCormac 2006)

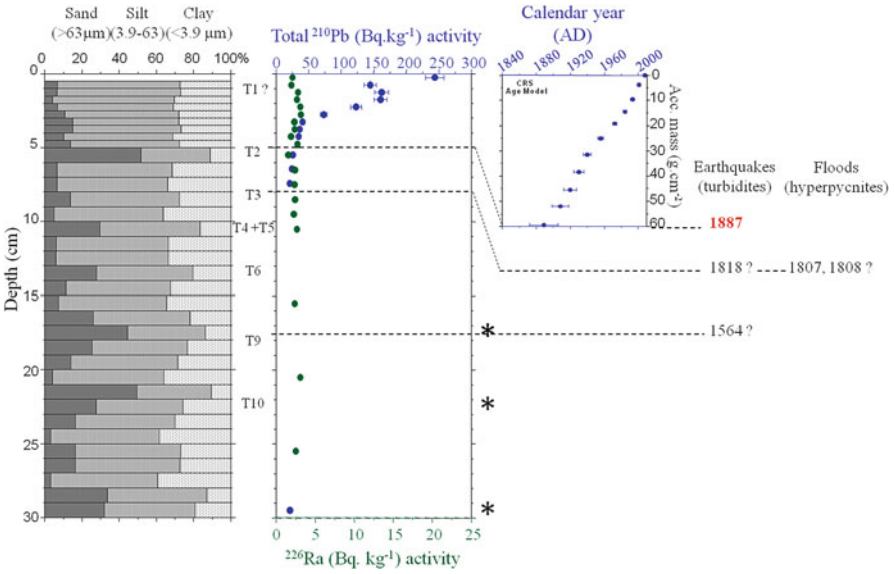

Fig. 51.3 Core DYF. From *left* to *right*: grain-size distribution; vertical profiles of ^{210}Pb and ^{226}Ra activity; CRS age model; assumption on the origin of the sandy intervals. T1–T10 are turbidite layers described in the text. The *black stars* indicate the depth of ^{14}C dating

the ^{14}C dating gave an age of AD 1887 ± 10 for T2 (4–6 cm deep). The activity of the excess ^{210}Pb does not follow a normal decaying curve but presents an anomalous peak at 1.2 cm depth corresponding to the 1968–1987 time interval. In core KNI27, only one ^{14}C dating was available and gave an age of 1559–1668 AD at depth 23.5 cm. Although the top of this core looks disturbed and is probably missing, a hemipelagic-sedimentation rate was estimated around 0.22–0.28 mm year^{-1}. Ages for T1 and T2 seem coherent with those found in DYC.

51.3.2 Cores and Facies Description

Sedimentological analysis of the cores revealed an alternation of hemipelagic intervals and coarse-grained beds corresponding to turbidites (Figs. 51.2, 51.3 and 51.4). Based on sedimentological analysis and age models, we proposed to correlate the turbidites from the three cores. This method is robust for the two uppermost turbidites T1 and T2 but only allows emitting hypotheses for older turbidites (T3–T10) which are not detailed in this study.

In the core DYC, the uppermost 17 cm consist of turbidites T1 and T2 (Fig. 51.2), topped by thin (1- and 3-cm thick, respectively) hemipelagic intervals. From 17 cm to the base of the core, sediments consist of hemipelagic layers alternating with seven silty to silty-clay turbidites (T3 to T10). Turbidite T1 exhibits a sharp to

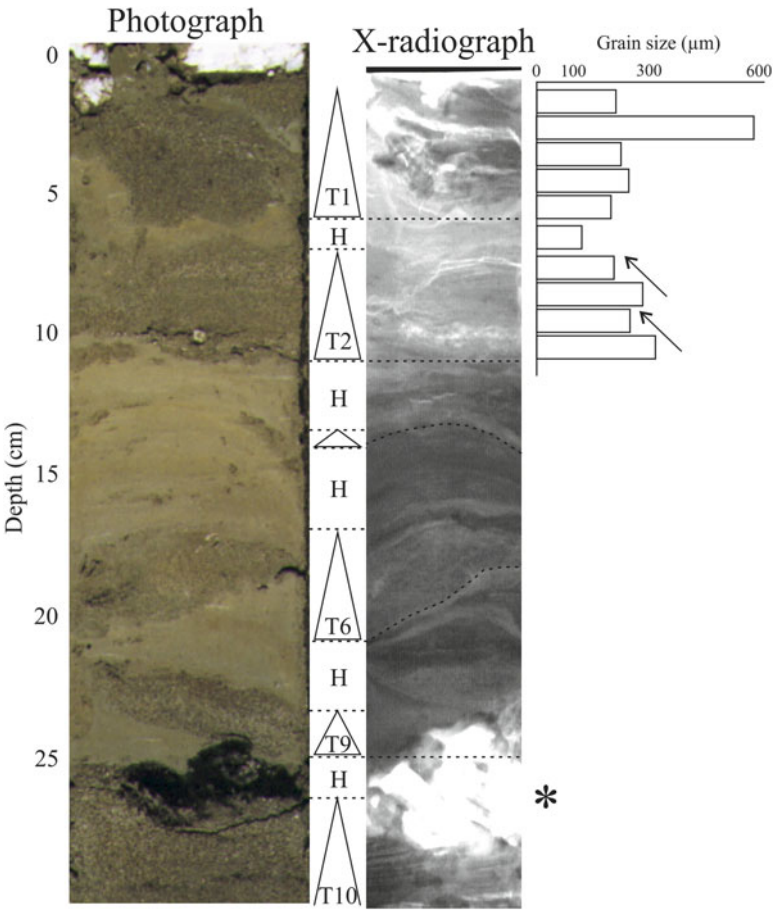

Fig. 51.4 Core KNI27. From *left* to *right*: core photograph, X-ray image and mean grain-size of turbidite T2. The *black arrows* indicate the two sub-intervals in turbidite T2. T1–T10 are turbidite intervals described in the text. *H* corresponds to the hemipelagic intervals. The *black star* indicates the location of the wood sample used for ^{14}C dating

erosive basal contact. It is normally graded and consists of a lower 5-cm thick structureless interval changing upward into a laminated interval. These intervals may correspond to the terms Ta and Tb of the Bouma Sequence (Bouma 1962). The 1-cm thick silty clays overlying T1 could correspond to the term Te of Bouma. The absence of the terms Tc and Td and the sharp contact between Tb and Te suggest a deposit resulting from a turbidity surge (Mulder and Alexander 2001).

Turbidite T2 also exhibits a sharp to erosive basal contact and two superimposed normally-graded intervals. The basal interval is structureless, while the upper interval exhibits laminae overlaid by a homogenous layer. This internal organization of T2 can be interpreted as the fast succession of two successive pulses of turbulent flows.

Core KNI27 presents the same organization with six turbidites alternating with clayey-silt deposits. T1 and T2 are structureless and exhibit an erosive basal contact. T2 consists of two superimposed normally-graded sub-intervals (Fig. 51.4).

The core DYF was cut in layers of 0.5–1-cm thick for geochemical analyses. The succession of lithofacies was inferred from grain-size analyses only, which suggest an alternation of fine-grained (hemipelagic) and coarser (turbidite) layers (Fig. 51.3). However, the sampling interval being high with respect to some bed thickness observed in the two previous cores, a single sandy layer could correspond to several successive events.

51.4 Discussion

Based on the sedimentological facies and age models described above, the topmost turbidites were correlated with well-known recent events. Turbidite T1 found in cores DYC and KNI27 is coherent with the 1979 Nice-Airport landslide (Figs. 51.2 and 51.4). Two submarine cables were broken by the turbidite surge of 1979 (Gennesseaux et al. 1980) just few kilometres south of the position of these cores; it is then not surprising to find a deposit related to this flow. In contrast, in core DYF a synchronous turbidite is lacking. In the uppermost 2 cm, the presence of the anomalous peak of ^{210}Pb activity (Fig. 51.3) suggests either punctual seafloor erosion or reworking by benthic fauna. Based on the age model, this peak may correspond to the 1979 flow, which could explain local seafloor erosion. Thus, the differences between cores DYC and KNI27 with core DYF could be explained by their specific location. All three cores recorded the very first phase of seafloor erosion probably related to the head of the 1979 flow, then turbidite deposition did not occur at DYF site as it is located on a topographic high (Fig. 51.1).

Turbidite T2 was identified in all three cores (Figs. 51.2, 51.3 and 51.4). The age models suggest a relationship with the 1887 Ligurian earthquake. This would be the first time that a sedimentary record related to this major earthquake is identified in the VSR. In cores DYC and KNI27, the presence in T2 of two sub-intervals interpreted as recording two successive turbulent flows is coherent with an earthquake event which may trigger multiple synchronous failures on the continental slope, resulting in stacked coarse-grained turbidites (e.g. Goldfinger et al. 2003). Only one failure-scar was correlated with the 1887 earthquake on its epicentral area (Hassoun et al. 2009): these results suggest that at least an additional failure event, large enough to generate a turbidity current, was also triggered.

In core (KV10; Fig. 51.1) collected on a terrace 30 m above the lower Var Canyon floor, Mulder et al. (2001) identified the 1979 turbidite and numerous hyperpycnites, but no sedimentary record corresponding to the 1887 earthquake. So the earthquake did not trigger a failure on the continental slope offshore the Var River but closer to the epicenter, possibly offshore the Roya and Taggia rivers. Additional cores collected at the mouth of the Roya and Taggia canyons are necessary to confirm this hypothesis.

Downcore, the correlation of turbidites with known events is more speculative. Based on the approximate ages of the coarse beds located below T2, we proposed that turbidites T3 and T9 (Figs. 51.2, 51.3 and 51.4) may have recorded the 1818 and 1564 historical earthquakes (I_0 MSK = VIII for the two earthquakes), respectively. Although epicentral area of the 1564 earthquake is thought to be located on land along the Vésubie Valley (40 km north of Nice), it could have triggered, offshore the Var River, slope failures large enough to produce gravity flows that followed the Var Canyon and Valley to the eastern VSR. The 1818 earthquake epicentral area was on the Ligurian coast, close to the 1887 epicenter (Larroque et al. 2001). Nevertheless the macroseismic intensity of the 1818 earthquake is at least 2 points lower on the MSK scale (Larroque et al. 2001). Therefore, potential failures triggered by the 1818 earthquake should be smaller but located close to the 1887 landslides, and their gravity flows might have followed similar pathways to the eastern VSR.

Some coarse layers do not coincide with historical earthquakes and could then record strong decennial and centennial floods (DDTM des Alpes-Maritimes 2011) and related hyperpycnal flows. In some cases, historical earthquakes and flood events being nearly synchronous, the precision of the age models does not allow discriminating between earthquake- and flood-triggered turbidites (Fig. 51.3).

51.5 Conclusions

Three short cores collected in the eastern VSR provide the sedimentary record of the main gravity-flow events occurred during the last centuries. Based on radionuclide chronologies, the origin of turbidite deposits has been associated with three different triggering mechanisms.

The sediment record of the 1979 Nice-Airport landslide was identified in the uppermost part of the cores, either by a 5–10 cm thick turbidite or by an erosive surface. Then, a turbidite less than 5-cm thick was correlated for the first time with the 1887 Ligurian earthquake, the strongest one known in the region. The sedimentological characteristics of this turbidite suggest that at least two synchronous failures large enough to generate turbidity currents were triggered on the continental slope. It is proposed that older turbidite layers in the three cores either recorded hyperpycnal currents derived from major floods or mass-movements triggered by local historical earthquakes.

Acknowledgements The authors thank the officers and crew of R/V Tethys-II and R/V Le Suroît and colleagues for their help at sea. We are grateful to C. Migon and D. Cossa for providing core DYC and to S. Schmidt who conducted part of the radionuclide measurements at University of Bordeaux1. The International Atomic Energy Agency is grateful to the Government of the Principality of Monaco for the support provided to its Environment Laboratories. We gratefully acknowledge the support of the Laboratoire de Mesure du Carbone 14 (UMS 2572, ARTEMIS, Saclay) and the US National Science Foundation for the ^{14}C dating of sediment samples at NOSAMS (Woods Hole Oceanographic Institution). This work was funded by the CNRS-INSU and by the French program Action Marges. The manuscript benefited from constructive reviews by Eulàlia Gràcia and Dimitris Sakellariou.

References

Bouma AH (1962) Sedimentology of some flysch deposits: a graphic approach to facies interpretation. Elsevier, Amsterdam

Dan G, Sultan N, Savoye B (2007) The 1979 Nice harbour catastrophe revisited: Trigger mechanism inferred from geotechnical measurements and numerical modelling. Mar Geol 245:40–64

DDTM des Alpes-Maritimes (2011), Rapport de Présentation: Historique-Partie 1 et 2- avril 2011. In: Plan de Prévention des Risques Naturels Prévisibles de la Basse Vallée du Var (PPRI), http://www.alpes-maritimes.equipement.gouv.fr/plan-de-prevention-des-risques-a385.html

Gennesseaux M, Mauffret A, Pautot G (1980) Les glissements sous-marins de la pente continentale niçoise et la rupture de câbles en mer Ligure (Méditerranée occidentale). C R Acad Sci Paris 290:959–962

Goldfinger C, Nelson CH, Johnson JE, The Shipboard Scientific Party (2003) Deep-water turbidites as Holocene earthquake proxies: the Cascadia subduction zone and Northern San Andreas Fault systems. Ann Geophys 46(5):1169–1194

Gràcia E, Vizcaino A, Escutia C et al (2010) Holocene earthquake record offshore Portugal (SW Iberia): testing turbidite paleoseismology in a slow-convergence margin. Quat Sci Rev 29(9):1156–1172

Hassoun V, Migeon S, Cattaneo A et al. (2009) Imbricated scars on the Ligurian continental slope: evidence for multiple failure events in the 1887 eathquake epicentral area. In: Seafloor mapping for geohazard assessment. Rendiconti online della Società Geologica Italiana, Ischia

Ioualalen M, Migeon S, Sardou O (2010) Landslide tsunami vulnerability in the Ligurian Sea: case study of the October 16th 1979 Nice airport submarine landslide and of identified geological mass failures. Geophys J Int 181(2):724–740

Larroque C, Béthoux N, Calais C et al (2001) Active and recent deformation at the Southern Alps-Ligurian basin junction. Neth J GeoSci 80:255–272

Larroque C, Scotti O, Ioualalen M (2012) Reappraisal of the 1887 Ligurian earthquake (western Mediterranean) from macroseismicity, active tectonics and tsunami modelling. Geophys J Int 190(1):87–104

Lee HJ, Locat J, Desgagnés P et al (2007) Submarine mass movements on continental margins. In: Nittrouer AC, Austin JA, Field ME, Kravitz JH, Syvitski PM, Wiberg PL (eds) Continental margin sedimentation: from sediment transport to sequence stratigraphy. Blackwell Publishing Ltd, Oxford, pp 213–273

Martín J, Sanchez-Cabeza J, Eriksson M et al (2009) Recent accumulation of trace metals in sediments at the DYFAMED site (Northwestern Mediterranean Sea). Mar Pollut Bull 59: 146–153

Migeon S, Weber O, Faugères JC, Saint-Paul J (1999) SCOPIX: a new X-ray imaging system for core analysis. Geo-Mar Lett 18:251–255

Migeon S, Savoye B, Zanella E et al (2001) Detailed seismic-reflection and sedimentary study of turbidite sediment waves on the Var Sedimentary Ridge (SE France): significance for sediment transport and deposition and for the mechanisms of sediment-wave construction. Mar Petrol Geol 18:179–208

Migeon S, Mulder T, Savoye B, Sage F (2006) The Var turbidite system (Ligurian Sea, northwestern Mediterranean)-morphology, sediment supply, construction of turbidite levee and sediment waves: implication for hydrocarbon reservoirs. Geo-Mar Lett 26:361–371

Mulder T, Alexander J (2001) The physical character of subaqueous sedimentary density flows and their deposits. Sedimentology 48(2):269–299

Mulder T, Savoye B, Syvitski JPM (1997) Numerical modelling of a mid-sized gravity flow: the 1979 Nice turbidity current (dynamics, processes, sediment budget and seafloor impact). Sedimentology 44:305–326

Mulder T, Migeon S, Savoye B, Faugeres JC (2001) Inversely graded turbidite sequences in the deep Mediterranean: a record of deposits from flood-generated turbidity currents? Geo-Mar Lett 21:86–93

Nakajima T, Kanai Y (2000) Sedimentary features of seismoturbidites triggered by the 1983 and older historical earthquakes in the eastern margin of the Japan Sea. Sediment Geol 135:1–19

Ratzov G, Collot JY, Sosson M, Migeon S (2010) Mass-transport deposits in the northern Ecuador subduction trench: Result of frontal erosion over multiple seismic cycles. Earth Planet Sci Lett 296(1–2):89–102

Reimer P, McCormac F (2006) Marine radiocarbon reservoir corrections for the Mediterranean and Aegean Seas. Radiocarbon 44(1):159–166

Sanchez-Cabeza JA, Liong Wee Kwong L, Betti M (2010) Method to Determine ^{226}Ra in Small Sediment Samples by Ultralow Background Liquid Scintillation. Anal chem 82:6847–6853

Siani G, Paterne M, Arnold M et al (2000) Radiocarbon reservoir ages in the Mediterranean Sea and Black Sea. Radiocarbon 42(2):271–280

Stuiver M, Reimer P, Reimer R (2005) CALIB radiocarbon calibration, execute version 6.0.2. In: http://calib.qub.ac.uk/calib/

Chapter 52
Integrated Stratigraphic and Morphological Investigation of the Twin Slide Complex Offshore Southern Sicily

J. Kuhlmann, A. Asioli, M. Strasser, F. Trincardi, and K. Huhn

Abstract The Holocene Twin Slides form the most recent of recurrent mass wasting events along the NE portion of Gela Basin within the Sicily Channel, central Mediterranean Sea. Here, we present new evidence on the morphological evolution and stratigraphic context of this coeval slide complex based on deep-drilled sediment sequences providing a >100 ka paleo-oceanographic record. Both Northern (NTS) and Southern Twin Slide (STS) involve two failure stages, a debris avalanche and a translational slide, but are strongly affected by distinct preconditioning factors linked to the older and buried *Father Slide*. Core-acoustic correlations suggest that sliding occurred along sub-horizontal weak layers reflecting abrupt physical changes in lithology or mechanical properties. Our results show further that headwall failure predominantly took place along sub-vertical normal faults, partly through reactivation of buried *Father Slide* headscarps.

Keywords Twin Slide complex • Gela Basin • Stratigraphy • Morphology • Isotope records

J. Kuhlmann (✉) • K. Huhn
MARUM – Center for Marine Environmental Sciences, University of Bremen, Bremen, Germany
e-mail: jkuhlmann@marum.de

A. Asioli
Istituto di Geoscienze e Georisorse, CNR-UOS di Padova, Padova, Italy

M. Strasser
Geological Institute, ETH Zurich, Zurich, Switzerland

F. Trincardi
Istituto di Scienze Marine (ISMAR-CNR), Venezia, Italy

S. Krastel et al. (eds.), *Submarine Mass Movements and Their Consequences*, Advances in Natural and Technological Hazards Research 37, DOI 10.1007/978-3-319-00972-8_52,

52.1 Introduction

Submarine landslides occur at all margins worldwide (Masson et al. 2006). To enhance knowledge on slope failure processes and trigger mechanisms, small-scaled slide complexes are uniquely positioned, as full data coverage often allows for a detailed definition of the internal structure (Canals et al. 2004; Lee 2005). One prominent example is the Twin Slide complex at the NE portion of Gela Basin within Sicily Channel, Central Mediterranean Sea. These coeval multistage failures occur only 6 km apart from each other and feature similar runout lengths and fall heights – yet their failure areas and mass-transport deposits (MTDs) show markedly different morphologies (Minisini et al. 2007; Minisini and Trincardi 2009).

To unravel the architecture of the Twin Slide complex and elaborate on available stratigraphic models, this study presents two deep-drilled sediment sequences recovered with gravity cores and Bremen seafloor drill rig MeBo (Freudenthal and Wefer 2007). We introduce a detailed age model relying on foraminifera-based eco-biostratigraphy as well as $\delta^{13}C$ and $\delta^{18}O$ records, and propose revised stratigraphic models based on the correlation of core data to acoustic sub-bottom profiles.

52.1.1 Geological Setting

The Twin Slide complex is located along the NE part of Gela Basin within the Strait of Sicily, Central Mediterranean Sea (Fig. 52.1). The basin represents a Pliocene-Quaternary foredeep of the Maghrebian fold-and-thrust belt and is filled with 2.5 km of shallowing-upward marine sediments (Colantoni 1975; Argnani 1990). In the north, Gela Basin is overthrusted by the Gela nappe, the southwest migrating outermost thrust wedge of the Maghrebian chain (Butler et al. 1992). Its tip parallels the present-day shelf break and plunges in direction of the basin, thus favouring a steeply sloped morphology (Trincardi and Argnani 1990).

52.1.2 Material and Methods

The data set for this study was acquired aboard RV Maria S. Merian during cruise MSM15/3 in 2010. Main devices used include a parametric sediment echosounder with dm-scale vertical resolution operating at 4 kHz (Atlas Parasound), two bathymetric multibeam echosounder operating at 12 kHz (Kongsberg Simrad EM120) and 95 kHz (EM1002), and coring devices (gravity corer up to 6 mbsf, MeBo up to 51.9 mbsf).

A GEOTEK Ltd. multi-sensor core logger (MSCL) was used for non-destructive measurements of core-physical properties including bulk density, compressional wave velocity, and magnetic susceptibility.

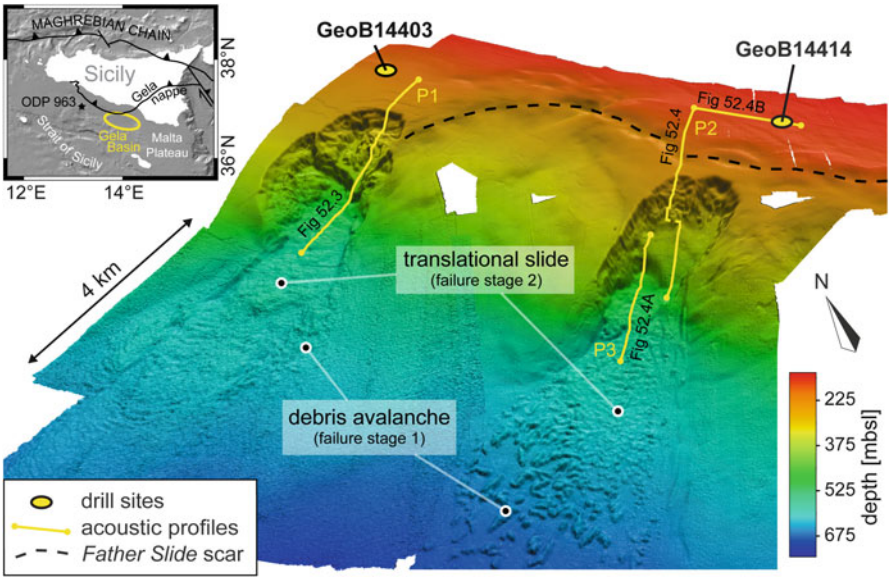

Fig. 52.1 3D multibeam shaded relief of the Twin Slides in the Gela Basin (lighting from NE, sun angle 35°, vertical exaggeration 5, grid spacing 10 m); *yellow circles* indicate core locations, *yellow lines* sub-bottom echosounder profiles P1 and P2/P3 shown in Figs. 52.3 and 52.4, respectively; *dashed black line* marks the outline of the *Father Slide* headscar (Minisini et al. 2007); variability in data resolution derives from the two distinct multibeam systems used. *Inset*: location of the Gela Basin in the Strait of Sicily, central Mediterranean (From GEBCO database)

Geochemical logging for light elements (Al to Fe) was performed on an Avaatech II core scanner using a generator setting of 10 kV, 0.2 mA and a sampling time of 20 s. Ca/Fe ratios served as an indicator for major lithological changes within the cored sequences.

For micropaleontology, sediment subsamples (20–50 g each) were taken with a vertical resolution of at least 20 cm. The sediment was freeze-dried, soaked in distilled water and washed through a 63 μm mesh sieve. A foraminifera-based eco-biostratigraphy relying on the identification of (temporary) disappearance and (re)occurrence of planktic species was developed to identify paleo-environmental changes already defined in Central Mediterranean (Minisini et al. 2007; Incarbona et al. 2010). Similarly, an isotope stratigraphy was established based on $\delta^{13}C$ and $\delta^{18}O$ records of benthic *Bulimina marginata* and planktonic *Globigerinoides ex gr. ruber*. Measurements were performed at MARUM using a Finnigan MAT 252 mass spectrometer coupled with a carbonate preparation device type "Bremen" (standard deviation <0.05‰ for $\delta^{13}C$ and <0.07‰ for $\delta^{18}O$).

52.2 Morphology and Stratigraphy

High resolution bathymetric data shows the Twin Slide complex as a prominent feature on the NE continental slope of the Gela Basin (Fig. 52.1). The upper slope exhibits the crescent-shaped, irregular morphological expression of an extensive buried slide termed *Father Slide* (Minisini et al. 2007). Southern Twin Slide (STS) affected the downslope area of this structure, while Northern Twin Slide (NTS) emanated from undisturbed sediment units along the edge of the *Father Slide* scar. Both failure areas expose two distinct MTDs of varying extend indicating individual failure stages: a debris avalanche deposit with blocks appearing elongated dominantly in the direction of motion (stage 1), and an overriding translational slide deposit likely affecting less consolidated units of the upper slope (stage 2).

Pre-failure depositional variation induced by the *Father Slide* manifests in the morphological appearance of upper failure areas as presented in Fig. 52.2. NTS shows a terrace-like structure (I on Fig. 52.2) with several individual slide scarps dipping by as much as 32°, reflecting multiple failure phases that affected planar, well-layered source units (see Sect. 52.2.1). Pronounced morphological steps of 1–2.5 m upslope of the headwall indicate incipient scarping through retrogressive failure (II on Fig. 52.2). In contrast, the upper failure area of STS exhibits a constant slope gradient of 8°–10° (III on Fig. 52.2) reflecting the underlying post *Father Slide* morphology (see Sect. 52.2.2) and is confined by steep lateral headwalls dipping 15°–20°. Upslope, contour-parallel crests with asymmetric slopes indicate erosional moat and related drift deposits (IV on Fig. 52.2), likely adding to the slopes instability through rapid sedimentation and successive generation of excess pore pressure (Verdicchio and Trincardi 2008).

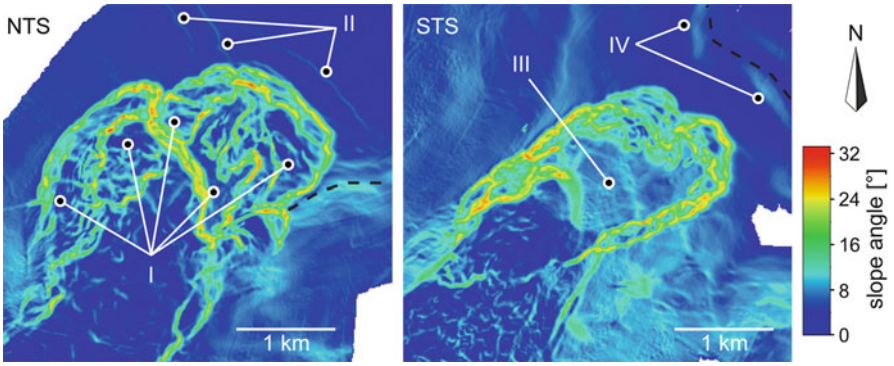

Fig. 52.2 Gradient maps of the upper failure zones of NTS and STS (grid spacing 10 m); *I*: individual slide terraces reflecting source sediments of NTS; *II*: scarps indicating retrogressive failure; *III*: constant slope gradient reflecting post *Father Slide* morphology; *IV*: moat structures indicating sediment drift

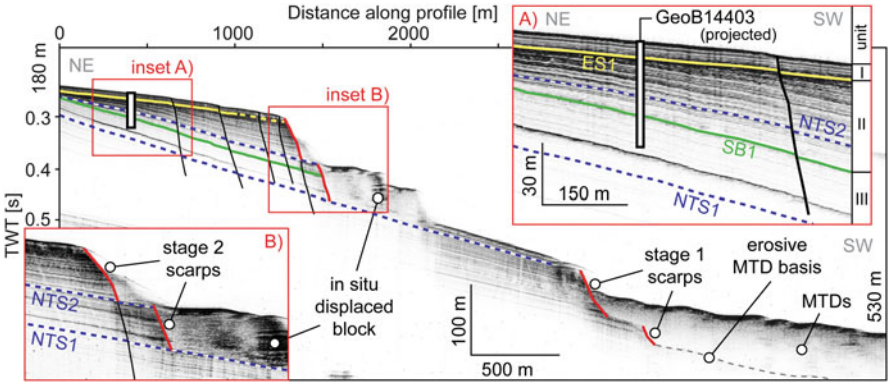

Fig. 52.3 Parasound profile P1 illustrating the stratigraphic framework of NTS. *Solid/dashed yellow line*: erosive unconformity/conformity ES1; *solid green line*: sequence boundary SB1; *dashed blue lines*: glide planes of stage 2 failure; *solid black lines*: faults indicating locations of potential retrogressive failure; *solid red lines*: slide scarps. *Inset A*: magnification of drill site area indicating sequence stratigraphic units. *Inset B*: magnification of stage 2 slide scarps showing glide planes beneath acoustically transparent units

52.2.1 Site GeoB14403 (NTS)

Parasound profile P1 (Fig. 52.3) across the upper failure zone of NTS reveals the stratigraphic context of site GeoB14403. The drilled sequence penetrates three sequence stratigraphic units (after Minisini et al. 2007, Fig. 52.3): (I) deposits resting on top of erosive unconformity ES1, (II) a progradational wedge pinching out towards NE and (III) deposits beneath sequence boundary SB1. Truncated acoustic reflections within units II and III mark two individual slide scarps, presumably deriving from failure stage 2 (solid red lines on Fig. 52.3). Upslope, prominent faults with clear reflection offsets show normal sense of shear and thus a downslope mass movement component, indicating locations of incipient scarping and retrogressive failure (solid black lines on Fig. 52.3). Two horizons acting as glide planes can be identified beneath the base of acoustically transparent units within this upper failure zone (dashed blue lines), one of which being intersected by the drilled cores. Downslope, older and potentially more consolidated sedimentary units were dissected and transported basinward in the debris avalanche of failure stage 1. Associated scars are filled with a thick, acoustically transparent layer. As suggested by the bathymetric data (Fig. 52.1) and estimations on the amount of involved material (Fig. 52.3), this layer represents the slide deposit of failure stage 2, possibly covering stage 1 avalanche deposits.

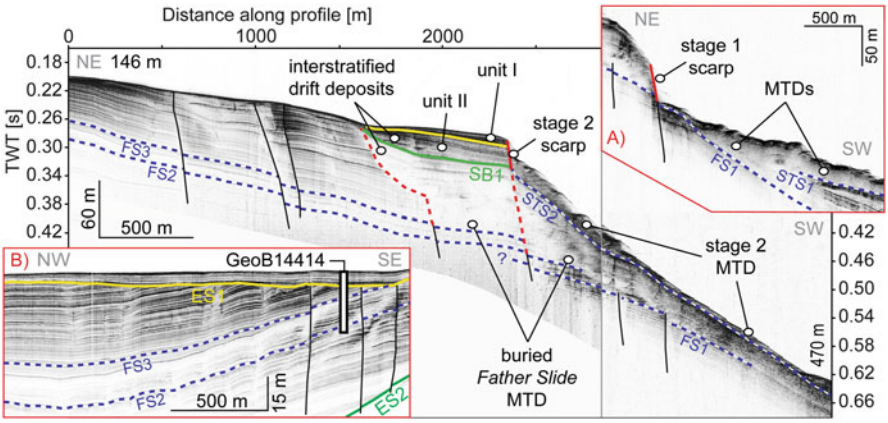

Fig. 52.4 Parasound profile P2 illustrating the stratigraphic framework of STS. Annotations analogue to Fig. 52.3. *Dashed blue lines*: glide planes of stage 2 failure (*STS*) and buried *Father Slide* (*FS*); *solid black lines*: faults; *dashed red lines*: *Father Slide* scarps. *Inset A*: lower slope showing headscarp of failure stage 1 and resulting MTDs (profile P3 in Fig. 52.1). *Inset B*: magnification of drill site area (For location see Fig. 52.1)

52.2.2 Site GeoB14414 (STS)

Parasound profiles P2 and P3 correlate drilled sediment units with the downslope failure area of STS and reveal a complex pre-failure setting dominated by buried *Father Slide* (Fig. 52.4). MTDs of this event can be traced as acoustically transparent facies into two prominent scarps (dashed red lines), which sharply truncate reflector packages of upslope sediment units. Post-failure deposits infilling the *Father Slide* scar appear to have failed by reactivation of the downslope scarp, which correlates with the position of sub-vertical normal faults, as indicated by offsets of neighbouring reflections. Similarly, the more recent and seafloor-exposed slide deposit of failure stage 2 dissected sedimentary sequences of units I, II and III along with interstratified, highly sensitive drift deposits (Verdicchio and Trincardi 2008). Downslope, a marked morphological step of 50 m indicates headwall failure of post *Father Slide* units associated with stage 1 debris avalanche (Fig. 52.4).

The location of the drill site upslope of *Father Slide* scar does not allow for an investigation of sediment units affected by STS. However, the bases of MTDs originating from the *Father Slide* event rest on top of three strong, bedding parallel acoustic reflectors (FS1–FS3). The upper two of these sub-horizontal layers can be traced back into the sediment sequence recovered at station GeoB14414 (Fig. 52.4). Besides the shallow ES1, a second discontinuity truncates underlying seismic reflectors in greater depth (ES2, solid green line), interpreted as a shelf-wide erosional unconformity of the penultimate sea level lowstand during Marine Isotope Stage 6 (MIS6; Sprovieri et al. 2006, and references therein).

52.3 Core Data and Age Model

At average recovery rates of 91 % (site GeoB14403) and 88 % (site GeoB14414) gravity and MeBo cores provide a sediment sequence reaching down to 51.9 mbsf and 27.0 mbsf, respectively. The dominant lithology is a silty nannofossil clay with quartzose silt, volcanic glass, and minor amounts of foraminifers and authigenic pyrite. A thin ash layer of dm-scale exhibiting normal grading and a relatively sharp base is intercalated at a depth of 25.7 mbsf (GeoB14403). A more detailed analysis of geotechnical properties of the sequence recovered at site GeoB14403 is presented by Ai et al. (2013).

52.3.1 Site GeoB14403 (NTS)

The composite plot depicted in Fig. 52.5 integrates physical/chemical log data with stable isotope measurements and related Marine Isotope Stages (MIS) and Dansgaard-Oeschger Interstadials (DOIS; Sprovieri et al. 2006, and references therein). A vertical acoustic profile of the drill site is added for reference, converted into depth scheme using core velocity logs. Magnetic susceptibility values are cut at 40 SI $\times 10^{-5}$ to reveal their general pattern. The combined data suggests a division of the drilled sediment sequence into the following intervals:

1. 0–4.5 mbsf. Holocene interval without systematic changes in lithology. Heavier values in the δ^{13}C *B. marginata* record indicate sapropel 1 equivalent (S1 eq), accompanied by high Ca/Fe ratios. Foraminifera assemblages suggest the presence of Pre-Boreal at the base of this interval as do correlations to the δ^{18}O records of core A236P09 from Gela Basin (Asioli and Trincardi, unpublished data).
2. 4.5–10.4 mbsf. Interval with scarce and cold planktic assemblage along with middle shelf benthic assemblage dominated by *Cassidulina laevigata carinata*, similar to an interval in core P08 (Minisini et al. 2007) referred to as MIS2. The erosive base correlates to the strong acoustic reflection of ES1.
3. 10.4–29.1 mbsf. Interval with scarce and cold planktic and middle shelf benthic assemblages interpreted as MIS3. In accordance with borehole PRAD1-2 (Piva et al. 2008) the bioevent Last Common Occurrence of *Globorotalia inflata* (LCO *G.i.*) is positioned in DOIS12. Accordingly, DOIS17 at the base of this interval marks MIS4/3 boundary, which correlates with the upper glide plane NTS2.
4. 29.1–36.8 mbsf. δ^{18}O records of *G. ruber* (up to 2.72‰) are comparable with MIS4 values of core KC01B (Lourens 2004) from the Ionian Basin. Sequence boundary SB1, accompanied by an offset in Ca/Fe ratio, marks the end of DOIS19 and defines MIS5/4 boundary according to Sprovieri et al. (2006).
5. 36.8–51.9 mbsf. Two relatively warm subintervals (42.0–46.5 and 49.6 downcore) alternate with colder ones marked by scarce planktic and middle shelf benthic assemblages. The presence of *G. ruber*, *Neogloboquadrina dutertrei* and

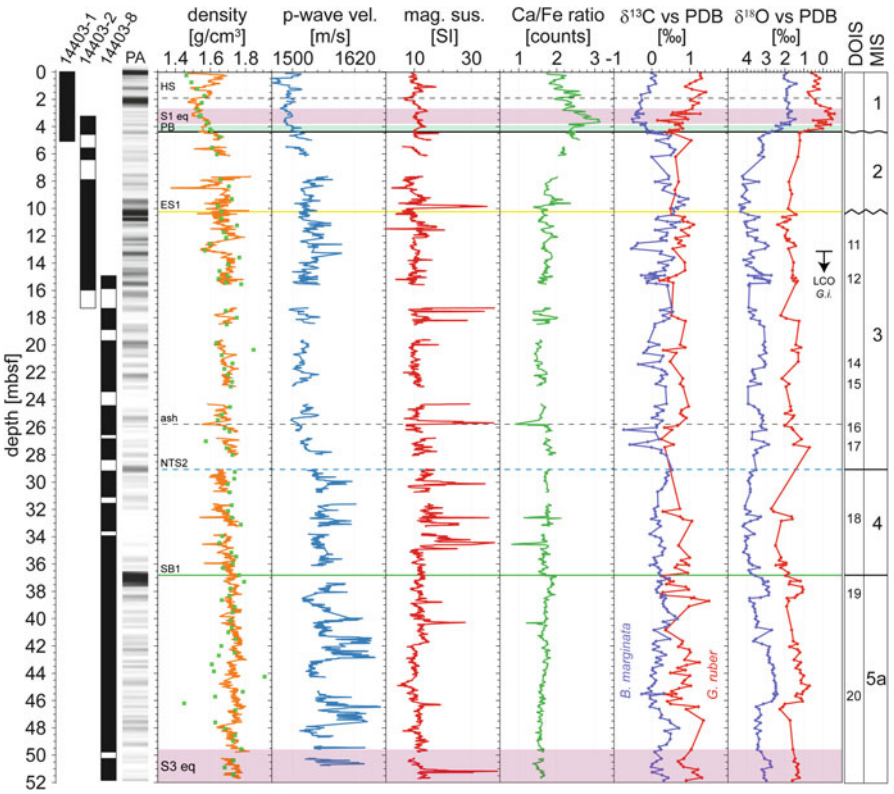

Fig. 52.5 Composite plot integrating acoustic, physical and chemical logs with stable isotope measurements of site GeoB14403. Chronological interpretations according to Marine Isotope Stages (*MIS*) and Dansgaard-Oeschger Interstadials (*DOIS*). *Green squares*: MAD density parameters determined according to IODP shipboard practices (Blum 1997); *light red area*: sapropel equivalents; *PB* Pre-Boreal, *HS* high-stand system tract, *LCO G.i.* bioevent Last Common Occurrence of *G. inflata, PA* vertical acoustic profile at drill site, *PDB* Pee Dee Belemnite standard

vegetal remains along with a benthic assemblage dominated by intermediate and deep infaunal taxa may indicate a sapropel equivalent deposition (S3 eq) at the lower warm interval.

52.3.2 Site GeoB14414 (STS)

Analogue to station GeoB14403, the combined data of the composite plot presented in Fig. 52.6 suggests a division of the sediment sequence into three intervals as follows:

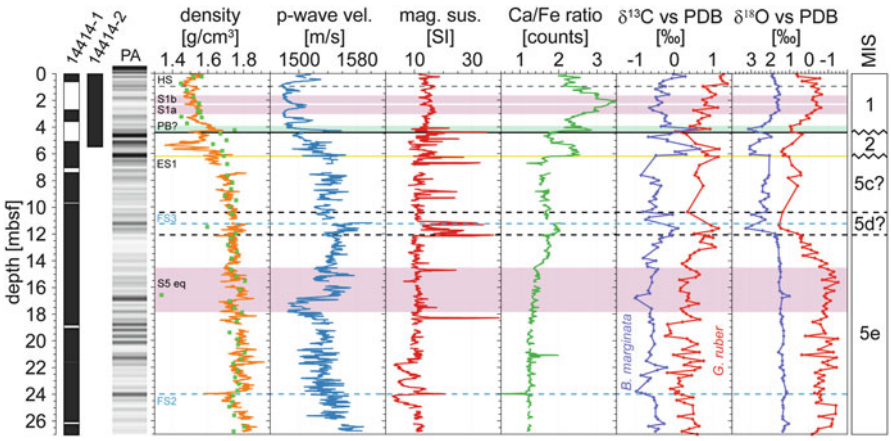

Fig. 52.6 Composite plot integrating acoustic, physical and chemical logs with stable isotope measurements of site GeoB14414. Annotations analogue to Fig. 52.5

1. 0–4.3 mbsf. Holocene interval coherent to that of site GeoB14403, but with a sharp erosive base that correlates to a pronounced acoustic reflection and is represented in all core logs (e.g., sudden decrease of Ca/Fe values from 2.8 to 2.0).
2. 4.3–6.2 mbsf. Short interval with augmented content of organic matter reflected by greater variability in magnetic susceptibility. Down-core, the interval is limited by an erosive base correlating to the strong acoustic reflection of ES1. At the interval top, lighter values in the $\delta^{18}O$ record of *B. marginata* suggest the presence of Bolling-Allerod. Though this interpretation cannot be validated by foraminifera assemblages (planktic taxa too scarce) the interval is ascribed to MIS2.
3. 6.2–27.0 mbsf. An extended interval that has been ascribed to MIS5 and may be further divided into three subintervals (from bottom to top):

   (III) 12.0–27.0 mbsf. A Sapropel equivalent deposit records very warm conditions (light red area). $\delta^{18}O$ records of *G. ruber* (up to −1.5‰) are compatible to MIS5a, c and e records from the Ionian Basin (core KC01B, Lourens 2004; ODP site 963, Sprovieri et al. 2006). However, the presence of *Globigerinoides sacculifer* and the absence of *Globorotalia inflata* suggest a quite expanded MIS5e interval (Incarbona et al. 2010).

   (II) 10.5–12.0 mbsf. Short interval with elevated values of p-wave velocity, magnetic susceptibility and Ca/Fe ratio. Both $\delta^{18}O$ records show values heavier than the underlying interval, which are too light to infer the presence of MIS4 (in comparison with core KC01B, Lourens 2004). Hence, this interval has been tentatively ascribed to MIS5d.

   (I) 6.2–10.5 mbsf. This interval shows values lighter than those of the underlying interval for both $\delta^{18}O$ records, indicating the relatively warmer phase related to MIS5c.

52.4 Discussion and Conclusions

Based on deep drilled cores and acoustic datasets, this study introduces an integrated chronological framework to the architecture of the Twin Slide complex, both revising and extending stratigraphic records presented earlier (Minisini et al. 2007; Minisini and Trincardi 2009). A conceptual model of the Twin Slides combining acoustic evidence (Sect. 52.2) with the developed age model (Sect. 52.3) is shown in Fig. 52.7. Both events appear to involve two failure stages, but are strongly controlled by their distinctive pre-failure architecture. NTS affected undisturbed units at the edge of buried *Father Slide* and cut down MIS5 deposits during failure stage 1, resulting in a debris avalanche preserved along the sides of the slide (Fig. 52.1). Most of this blocky outrun, however, is covered by a translational slide deposit of failure stage 2 deriving from retrogressive failure of younger units (predominantly MIS4/3) in the upslope region.

In contrast, STS rests on the infillings of buried *Father Slide*, which affected early MIS5(e-c) sedimentary units overlying the erosional unconformity of the penultimate sea level lowstand during MIS6. The stage 1 failure (debris avalanche) reworked *Father Slide* MTD as well as stratified post-failure deposits, while the stage 2 failure dissected progradational units of MIS4/3 – interstratified by drift deposits – along the reactivated shear zone of *Father Slide*. Unlike NTS, the resulting slide deposit only partly covers stage 1 debris avalanche (Fig. 52.1).

Summarizing these findings, failure stages of both Twin Slides appear to involve sedimentary units of similar stratigraphic age. This contrasts previous assumptions by Minisini et al. (2007), who related observed dissimilarities in geomorphology to distinct stratigraphic units affected by failure. Instead, these dissimilarities may simply reflect differences in the amount of material involved in the two failure stages. Similarly, core-acoustic correlations suggest that headwall failure of the Twin Slides predominantly occurs along sub-vertical normal faults (Figs. 52.3

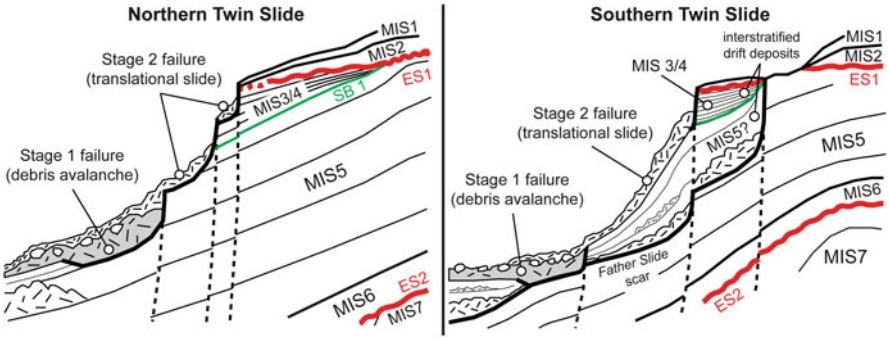

Fig. 52.7 Schematic sketch of NTS (*left*) and STS (*right*) illustrating implications of the presented stratigraphic record. *MIS* Marine Isotope Stage, *ES* unconformities associated with 100 ka glacial cycles, *SB* sequence boundary

and 52.4) and translational sliding along sub-horizontal weak layers reflecting abrupt physical changes in lithology or mechanical properties (Figs. 52.5 and 52.6). The shallowest part of NTS failed along the MIS4/3 boundary and correlates to a section identified by Ai et al. (2013) as a preferential slip plane due to its reduced internal friction angle. They further propose a moderate earthquake (M = 4.0–4.8) to be sufficient to trigger failure of this layer. Acoustic data suggests that similar mechanisms may have been responsible for the stage 2 failure of STS (Fig. 52.7). Stage 1 failure of STS, instead, partly reactivated the shear plane previously followed by *Father Slide* (Figs. 52.4 and 52.7). To further assess the role of these layers in sediment failure, however, additional data on their geotechnical properties is required.

Acknowledgments We gratefully acknowledge the constructive reviews by Yasuhiro Yamada and Frank Strozyk. $\delta^{13}C/\delta^{18}O$ analyses, MSCL and XRF core scanning were carried out at the lab facilities of MARUM. This study is funded through DFG-Research Center/Cluster of Excellence "The Ocean in the Earth System".

References

Ai F, Kuhlmann J, Huhn K et al (2013) Submarine slope stability assessment of the central Mediterranean continental margin: the Gela Basin. In: Krastel S, Behrmann J-H, Völker D, Stipp M, Berndt C, Urgeles R, Chaytor J, Huhn K, Strasser M, Harbitz CB (eds) Submarine mass movements and their consequences. Springer, Heidelberg

Argnani A (1990) The strait of Sicily rift zone: foreland deformation related to the evolution of a back-arc basin. J Geodyn 12:311–331

Blum P (1997) Physical properties handbook: a guide to the ship board measurement of physical properties of deep-sea cores. ODP Tech Note 26, College Station, TX

Butler RWH, Grasso M, LaManna F (1992) Origin and deformation of the Neogene-Recent Maghrebian foredeep at the Gela Nappe, SE Sicily. J Geol Soc Lond 149:547–556

Canals M, Lastras G, Urgeles R et al (2004) Slope failure dynamics and impacts from seafloor and shallow sub-seafloor geophysical data: case studies from the COSTA project. Mar Geol 213(1–4):9–72

Colantoni P (1975) Note di geologia marina sul Canale di Sicilia. Giorn Geol 40(1):181–207

Freudenthal T, Wefer G (2007) Scientific drilling with the sea floor drill rig MeBo. Sci Drill 5: 63–66

Incarbona A, Di Stefano E, Sprovieri R et al (2010) Millenial-scale paleoenvironmental changes in the central Mediterranean during the last interglacial: comparison with European and North Atlantic records. Geobios 43(1):111–122

Lee HJ (2005) Undersea landslides: extent and significance in the Pacific Ocean, an update. Nat Hazard Earth Syst Sci 5:877–892

Lourens LJ (2004) Revised tuning of Ocean Drilling Program Site 964 and KC01B (Mediterranean) and implications for the $\delta^{18}O$, tephra, calcareous nannofossil, and geomagnetic reversal chronologies of the past 1.1 Myr. Paleoceanography 19:20. doi:10.1029/2003PA000997

Masson DG, Harbitz CB, Wynn RB et al (2006) Submarine landslides: processes, triggers and hazard prediction. Philos Trans R Soc A 364:2009–2039

Minisini D, Trincardi F (2009) Frequent failure of the continental slope: the Gela Basin (Sicily Channel). J Geophys Res 114:F03014. doi:10.1029/2008JF001037

Minisini D, Trincardi F, Asioli A et al (2007) Morphologic variability of exposed mass-transport deposits on the eastern slope of Gela Basin (Sicily channel). Basin Res 19:217–240

Piva A, Asioli A, Schneider RR et al. (2008) Climatic cycles as expressed in sediments of the PROMESS1 borehole PRAD1-2, central Adriatic, for the last 370 ka: 1. Integrated stratigraphy. Geochem Geophys Geosyst 9(1):21. doi:10.1029/2007GC001713

Sprovieri R, Di Stefano E, Incarbona A et al (2006) Suborbital climate variability during Marine Isotopic Stage 5 in the Central Mediterranean basin: evidence from calcareous plankton record. Quat Sci Rev 25(17–18):2332–2342

Trincardi F, Argnani A (1990) Gela submarine slide: a major basin-wide event in the plio-quaternary foredeep of Sicily. Geo-Mar Lett 10:13–21

Verdicchio G, Trincardi F (2008) Mediterranean shelf-edge muddy contourites: examples from the Gela and South Adriatic basins. Geo-Mar Lett 28:137–151

Chapter 53
Mass Transport Deposits Periodicity Related to Glacial Cycles and Marine-Lacustrine Transitions on a Ponded Basin of the Sea of Marmara (Turkey) Over the Last 500 ka

C. Grall, P. Henry, G.K. Westbrook, M.N. Çağatay, Y. Thomas, B. Marsset, D. Borschneck, H. Saritas, G. Cifçi, and L. Géli

Abstract The Sea of Marmara (SoM) is affected by large earthquakes occurring on the North Anatolian Fault. Numerous submarine mass movements have occurred and the most recent turbidites in the basins of the SoM have been related to historical earthquakes. Within the SoM, the occurrence of submarine mass movements and their size appears modulated by eustatic changes that can be accompanied by transitions between a salty marine environment and a brackish lake environment. Detailed analysis, using a 3D high-resolution seismic dataset, of stratigraphy over the last 500 ka, within a ponded basin of the Western High, shows that intervals of draped sedimentary reflectors alternate with onlap sequences that followed episodes of rapid sea-level rise, with a periodicity of approximately 100,000 years (corresponding to glacial cycles). Mass Transport Deposits (MTDs) occur within the onlapping sequences. Detail analysis of the youngest large slide, which probably followed the lacustrine transition to during Marine Isotopic Stage 4 is presented; and the possible triggering processes are discussed. The potential triggers of MTDs

C. Grall (✉)
CEREGE, CNRS, Aix Marseille University, Marseille, France

IFREMER – French Research Institute for Exploration of the Sea, Marine Geosciences, Plouzané, France
e-mail: grall@cerege.fr

P. Henry • D. Borschneck
CEREGE, CNRS, Aix Marseille University, Marseille, France

G.K. Westbrook • Y. Thomas • B. Marsset • L. Géli
IFREMER – French Research Institute for Exploration of the Sea, Marine Geosciences, Plouzané, France

M.N. Çağatay
EMCOL and Department of Geological Engineering, Istanbul Technical University, Istanbul, Turkey

H. Saritas • G. Cifçi
Institute of Marine Sciences and Technology, Dokuz Eylul University, Izmir, Turkey

S. Krastel et al. (eds.), *Submarine Mass Movements and Their Consequences*, Advances in Natural and Technological Hazards Research 37, DOI 10.1007/978-3-319-00972-8_53,

during this transition, in the context of the SoM are: (i) gas hydrate dissociation by pressure drop; (ii) changes in sediments supply and transport dynamics; (iii) variations in pressure and/or ionic strength in pores. The latter case appears the most suitable hypothesis, as salt diffuses out of the pores of the marine clay-rich sediment dominated by smectite at the beginning of low stand/lacustrine stages. The pore water freshening induces clay swelling, which can potentially drive sediment slope failure.

Keywords High Resolution 3D seismic data • Mass Transport Deposits • Lacustrine/marine transitions • Sea of Marmara

53.1 Introduction

A great variety of factors can cause and/or promote submarine mass movements, including earthquakes (Masson et al. 2006), environmental changes such as sea-level changes and associated variations in sediment supply (Rothwell et al. 1998), and gas hydrate dissociation (e.g. Maslin et al. 2004). The Sea of Marmara (SoM) is an active seismotectonic setting, located along the western part of the North Anatolian major continental transform fault (Wong et al. 1995; Le Pichon et al. 2001). Submarine gas hydrates occur in the sediment at fluid emission sites (Bourry et al. 2009). It is likely that hydrates were more widely distributed in the past and were dissociated massively during the deglaciation (Menot and Bard 2010). The SoM has also been subjected to a history of connections and disconnections with Black and Aegean Seas via the Bosphorous and the Çannakale Straits respectively (Fig. 53.1a, e.g. Çağatay et al. 2009). These oscillations are related to global eustatic changes, and induce transitions between lacustrine and marine conditions. In such an environment, submarine mass-movements are very common, and 75 % of the sedimentation in basins is composed of gravity-induced deposits (e.g. Beck et al. 2007) and many of which were triggered by earthquakes (McHugh et al. 2006). Mass-wasting occurrence and size increased during the end of the glaciation period which may be attributed to thermal destabilization of gas hydrate or variations in sediment supply (Zitter et al. 2012).

During the last glacial period, the SoM was a mildly brackish lake (e.g. Londeix et al. 2009), as the global sea-level dropped below the level of the Çannakale sill (e.g. Çağatay et al. 2009) at the beginning of Marine Isotopic Stage 4 at ~70 ka (thereafter MIS-4). Sedimentation rates were at least two times higher during these glacial times than during modern marine environment (Çağatay et al. 2000; Vidal et al. 2010). Pore fluid composition profiles indicate diffusion of salts, between the lacustrine sediments and the seawater above, affecting a layer of 12–40 m thickness below the seafloor, that does not strongly depending on the sedimentation rates in the area considered (Zitter et al. 2008; Çağatay et al. 2004).

Little is known about older paleo-environmental changes induced by sea-level variations. Considering global sea-level variations (e.g. Lisiecki and Raymo 2005), marine to lacustrine transitions may not have occurred during all the glacial

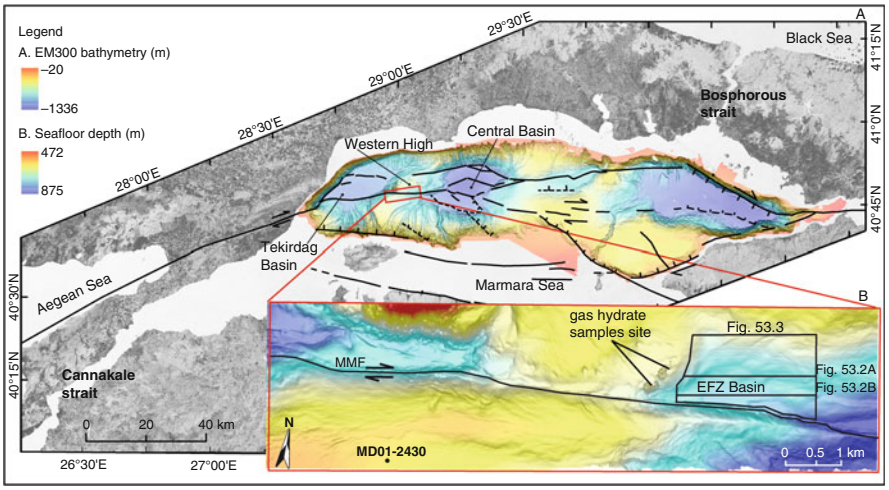

Fig. 53.1 (**a**) Tectonic map of the Sea of Marmara region with the Main Marmara Fault (*MMF*, Le Pichon et al. 2001) and secondary fault system (Grall et al. 2012). The *red box* locates the 3D seismic survey data. (**b**) Seafloor mapping from the 3D-seismic data, and the location of the Eastern Fault-Zone basin (annotated EFZ-basin). Locations of the seismic lines present on Fig. 53.2, MD01-2430 core, and sites where gas hydrates have been sampled are shown. The *black box* indicates the area shown in Fig. 53.3a

100,000-year cycles, as the timing of connection and disconnection depends not only on global sea-level but also on the depth of the Çannakale sill, which probably varied with time (e.g. Çağatay et al. 2009; Badertscher et al. 2011).

In this paper, the relationship between mass wasting and sea-level changes over the last 400–500 ka is evaluated using high resolution seismic records. The Mass-Transport Deposits (MTDs) related to sea-level oscillations and marine/lacustrine transitions are here characterized, and the possible MTDs trigger processes discussed.

53.2 Main Observations and Interpretations

53.2.1 Overview of Stratigraphic Sequences and Mass-Transport Deposits Position

The 3D seismic survey covers an area of 33 km^2 on the western part of the Western High, along the main strike-slip fault branch of the Main Marmara Fault (MMF, Le Pichon et al. 2001, Fig. 53.1b). We focus here on the Eastern Fault-Zone Basin, an asymmetric basin bounded on its southern side by the MMF (Fig. 53.1b). The seismic imaging (migration, bin size 6 m, Thomas et al. 2012) has a maximum

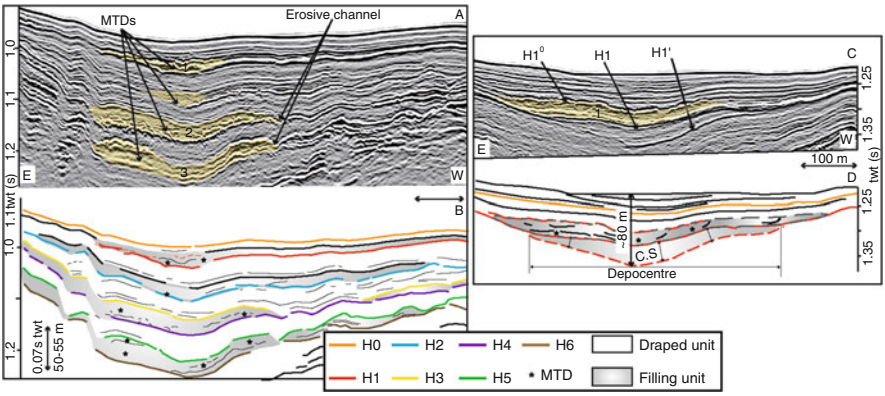

Fig. 53.2 (**a**) Seismic section across the northern edge of the Eastern Fault-Zone Basin. MTDs are highlighted in *yellow*, and numbers 1, 2, 3 refer to the three most remarkable MTDs discussed in the text. (**b**) Line drawing of the seismic section above. Horizon numbers mentioned increase from *top* to *bottom*. Stratigraphic sequences contain one basin filling unit (in *grey*) in which MTDs occurred (indicate by *black stars*), and one draped section (in *white*). The four main stratigraphic sequences in this characteristic seismic section have a thickness of around 65–75 ms twt, which represent around 50–63 m (P-wave velocity ranges between 1,515 (above H1) and 1,660 m/s (between H6 and H4), within the sediments, Thomas et al 2012). (**c**) Seismic section across the Eastern Fault-Zone Basin, showing details of the first stratigraphic sequence below the seafloor. (**d**) Line drawing of the seismic section above. The filling unit contains a condensed section (H1′–H1) on which MTDs occurred (between H1 and $H1^0$). The condensed section extension corresponds to the basin depocentre (represented in Fig. 53.3a) when the slides occurred. See Fig. 53.1c for the location of the seismic lines

sub-seabed seismic penetration of about 600 m in this basin. H0, the shallowest seismic horizon (Fig. 53.2) encountered over most of the 3D HR survey, is at around 15 m depth on core MD01-2430 location, at the same depth as an ash layer (Çağatay, pers. comm). Mean sedimentation rates over this time-scale have been derived from the H0 mapping. The sedimentation rates range between 0.3 and 1.1 mm/a, in the Eastern Fault-Zone Basin. Considering the seismic penetration and the sedimentation rates, the dataset gives access to the history of sedimentation over a time scale of about 500,000 years.

Sedimentary sections consist of the repetition of four sequences, each sequence has between 0 and around 80 m of thickness and contains two seismic units (Fig. 53.2a, b): (1) Draped units with moderate lateral variations of thickness, either acoustically transparent or bearing laterally continuous internal sub-parallel reflectors (2) Basin filling units displaying strong lateral variations of thicknesses and laterally correlative with either condensed sections (Fig. 53.2b) or hiatuses on the slopes and topographic highs. Sedimentary bodies that contain irregular lenses and chaotic reflections are observed at the base and/or within the filling sequences (Fig. 53.2a, b), and are interpreted MTDs (e.g. Alves 2010).

Three remarkable MTDs thus occur within the basin filling units (Fig. 53.2a). Prominent reflective horizons (H1, H4 and H6; Fig. 53.2b) which present significant disruption, mark the base of the MTDs. The top horizons of the MTDs ($H1^0$, H3 and H5, Fig. 53.2b), pinch out against a continuous basal horizons and display small-scale topography. Horizon H5 displays erosive channel geometry that may have developed concurrently with the deposition of the basin filling unit (Fig. 53.2a, b). Erosion affects the underlying MTDs and therefore must at least in part post-date the MTDs events. Horizon H3 is relatively smooth but small erosive channels affect H4 where H3 is absent, suggesting the MTD strata between H3 and H4 is correlative with an erosion surface (Fig. 53.2a, b).

The high-resolution age model from ^{14}C calibrated ages obtained from core MD01-2430 (Fig. 53.1b) indicates a sharp reduction of sedimentation rate from 0.6 to 0.2 mm/a following the reconnection at 14.7 ka (Vidal et al. 2010). In the Holocene, sedimentation rates subsequently increased back to 0.4 mm/a, although still not reaching the glacial sedimentation rate again (Vidal et al. 2010). We surmise this has been the case during previous glacial cycles, at least in cases when the SoM had been disconnected during a global sea-level low-stand, and possibly during all episodes of rapid seal-level rise. In this case, the repetition of filling unit/draped section corresponds to the sea level low and high stands oscillation at 100 ka time-scale. In particular, the onlap sequence on H1′ (Fig. 53.2c, d), first low-stand/filling units below the seafloor, probably results from a decrease of sedimentation rate during the marine high stand at MIS-5 (∼130 ka). The MTDs lying on H1 thus occurred during the sea level fall at MIS-4 (∼70 ka).

Variations of clay composition could explain differences of slope instabilities frequency between marine and lacustrine rich-clay sediments. Powder of clay fraction of 38 samples (of both marine and lacustrine muds) has been characterized by X-ray diffraction. The relative amount of smectite, illite, kaolinite and chlorite were determined by comparing the major XRD reflection peaks surfaces obtained on untreated, ethylene-glycolated, hydrazine monohydrate and heated smear slides. Lacustrine and marine clay compositions do not display significant differences. The clays fraction is dominated by swelling clay as the clay fraction is composed of, on average, 75 % smectite, 13 % illite, and around 5–7 % kaolinite and chlorite.

53.2.2 Characterization of MTDs on H1

The MTDs above H1 form a thick unstratified lens with a rough upper surface. Within this lens, we observed locally some highly reflective patches interpreted as stratigraphic reflectors within coherent blocks floating in a matrix of flowed mud that has lost coherence, at least at the scale of the HR data (Fig. 53.3d). The top of the MTDs is a highly reflective and rough reflector of reverse polarity to that of the seafloor, suggesting that the deposit has probably a higher content of fluid than the upper sediments. The top of the MTD is undulated, and we observed small-scale

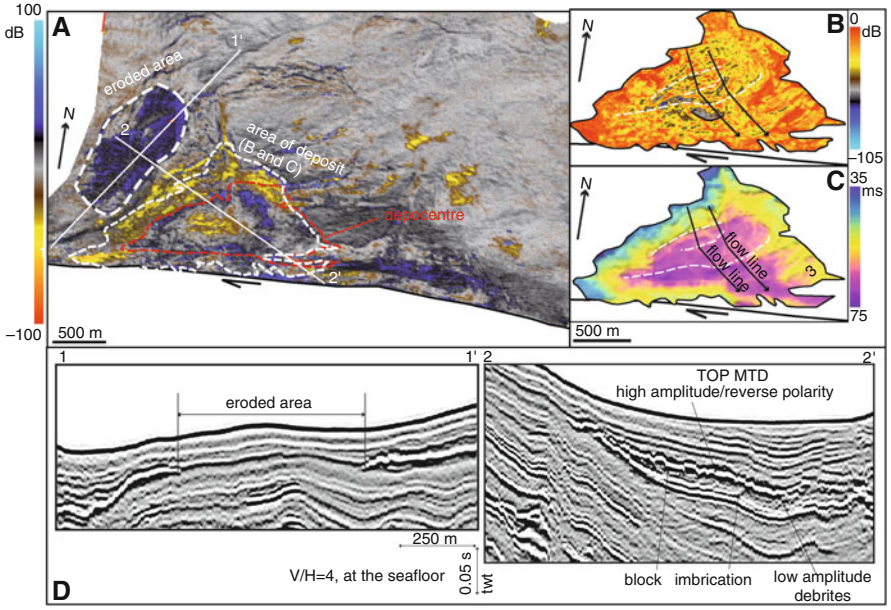

Fig. 53.3 Mapping and characteristics of the first remarkable MTDs below the seafloor, which probably occurred after the sea-level fall at MIS-4 (~70 ka). (**a**) Amplitude map of the basal surface of the MTDs (horizon H1). This map is located in Fig. 53.1b. Eroded area and area of deposits (which is detailed in Fig. 53.2b, c) correspond to the main scars of the slides and the zone of slide depositions. The depocentre is derived from the mapping of the condensed section below the MTDs (Fig. 53.2c, d). (**b**) Amplitude map of the top horizon of the MTDs. Amplitude anomalies alignment is indicated by *white dash lines*. (**c**) Topography of the top horizon of the MTDs. The *white dash lines* and the *black arrows* indicate the orientation of small undulations and the flow lines respectively. (**d**) Seismic sections along the scars of the slides (1–1′) and across the MTDs (2–2′)

ridges of higher reflectivity (in absolute value) with a NE-SW strike (Fig. 53.3b, c). The geometry of the structures suggests the mud flow occurred perpendicular to the western ridges (Fig. 53.3a) along a NW-SE sliding direction. The MTD covers an area of about 0.47 km^2 and has a total volume of 5.5 hm^3. Along the NW edge of the basin, the MTD thickness is around 7–8 m. It increases toward the southeast, reaching a maximum thickness of 23 m in the central part of the basin (Fig. 53.3c). H1 displays variable reflectivity below the MTDs. On the whole western edge of the MTDs but also its northeastern edge, H1 has negative polarity and high reflectivity (Fig. 53.3a). Below the central part of the MTDs, H1 appears composite with several sub-reflectors resulting in a concentric reflectivity pattern (Fig. 53.3a). On the slope west of the MTD, H1 is absent, or displays low reflectivity, over a 0.28 km^2 area (labeled eroded area in Fig. 53.3a). This area corresponds to a place where H1 but also others horizons above have been eroded and thus appears as the probable main source of the material forming the slide masses. The thickness of sediment removed during the event is estimated to 11 ± 5 m comparing the thickness of sediment on

either side of the slide with the thickness of sediment in the scar (Fig. 53.3d, section 1–1′). It also seems that most of the sediment deposited between H1 and H0 has been removed. The volume of sediment removed is thus $3 \pm 1.4 \times 10^6$ m^3, which represents only about 1/2 to 1/3 of the MTD volume. This paradox may be resolved if sediments deposited above H1 in the basin have been displaced and in part incorporated into the MTD. The eastern edge of the MTD is not sharp (Fig. 53.3d, section 2–2′) but appears as a gradational transition between disturbed sediments and an undisturbed layer of about 7–8 m thickness. Also, the base of the MTD is not erosive in the deepest parts of the basin but appears to follow closely H1, which may represent the basal sliding surface or layer immediately beneath it. In fact the volume and geometry of the MTD may be accounted for, if a 7.4 m average thickness layer of sediment covering both the area of sediment removal and the area now covered by the MTD was redistributed by the sliding event to the deeper part of the basin. This can suggest liquefaction occurred as the slide progressed, a common feature in slides and slumps, which can evolve into debris flow deposits (Mulder and Cochonat 1996).

53.3 Discussions About Possible Triggering Processes and Conclusions

During the last glacial cycle, the draped sequence in the basin corresponds to low-stand lacustrine deposits with a relatively high sedimentation rate. Parts of the underlying deposits, presumably marine sediments from the last interglacial (MIS-5), have been redistributed by gravitationally driven mass transport, resulting in lateral variations in sediment thickness. Sediment remobilization likely occurred after sea-level dropped at MIS-4. This pattern of alternating draping sedimentation and sediment redistribution is found to repeat cyclically in the stratigraphic record. This suggests that comparable sequences of events occurred during earlier glacial cycles. This is also supported by the thickness of these sequences, which would correspond to about 100,000 years of sedimentation extrapolating the mean sedimentation rates measured over the last ∼29 ka.

Sediment fluxes into the deep basins of the Sea of Marmara from continental shelves and slopes are higher during low stand than during high stand, and slope instabilities clustered at the end of the glaciation (Zitter et al. 2012). However, the Western High is relatively isolated from this influence, as canyons originating from the shelf edges bypass the Western High and supply sediments to the deep Central and Tekirdag basins (Fig. 53.1a). Nevertheless, we still observe cyclic local redistribution of sediments between slopes and ponded basins but probably with a different timing as the MTD in this study is inferred to correlate with the beginning of a low stand.

At the beginning of MIS-4 (∼70 ka), sea-level fell from −25 to −85 m below the modern sea level resulting in the disconnection of the Sea of Marmara (Çağatay et al. 2009). This also induced a pressure drop of 0.6 MPa and thus possible dissociation

of gas hydrate (Liu and Flemings 2009). Nonetheless, a temperature decrease of 1 °C at the seafloor of the Western High associated to this pressure drop should be sufficient to keep hydrates in their stability field (e.g., Henry et al. 1999). It is thus unlikely that widespread gas hydrate dissociation occurred at this time. On the other hand, pore fluid freshening by salt diffusion must have occurred. Since the post-glacial reconnection, water column salinization (that has been progressive over 2,000 years, Vidal et al. 2010) lead to the diffusion of salts downward into the pore fluids of the lacustrine sediments (Zitter et al. 2008) and the reverse process had occurred during the last glaciation after the disconnection. The diffusion length being proportional to the square root of time, the salt diffusion gradient below the seafloor affects a sediment layer of thickness 10–100 m for times ranging from 1,000 to 100,000 years. A layer of 11 ± 5 m of marine sediments has been remobilized, which appears consistent with the thickness of leached sediments after only a few thousand years. As the clay-fraction is dominated by smectite, clay swelling induced by osmotic stress during the desalinization of the pore water is expected (Charpentier and Bourrié 1997), reducing the cohesion of sediment and promoting submarine slope failures (Masson et al. 2006). Consequently, systematic destabilization of marine sediments on slopes at the beginning of lacustrine periods should occur.

We remarked that the cyclic occurrence of MTDs observed in a ponded basin of the Western High in the SoM could correlate with glacial-interglacial sequences. Despite that slope instabilities are presumably triggered by earthquakes, their size and/or frequency appears to be modulated by glacio-eustatic oscillations and the lacustrine/marine transitions associated to them. The swelling of clays in marine sediments under low salinity brackish water can promote slope instability after marine to lacustrine transitions, and may be one factor contributing to long-term cyclicity of slope instability occurrence in the Sea of Marmara.

Acknowledgements The Marmara-DM cruise was supported by ESONET NoE, Network of Excellence, coordinated by IFREMER and co funded by EU as part of FP6 (2009). This work is also co-funded by CNRS. We would like to thank Cedric Amiel, for his participation to the XRD laboratory manipulation. We thank Cecilia McHugh and Lies Loncke for their constructive comments that improved this manuscript.

References

Alves TM (2010) 3D Seismic examples of differential compaction in mass-transport deposits and their effect on post-failure strata. Mar Geol 271:212–224

Badertscher S, Fleitmann D, Cheng H et al (2011) Pleistocene water intrusions from the Mediterranean and Caspian seas into the Black Sea. Nat Geosci 4:236–239

Beck C, Mercier de Lepinay B, Schneider JL et al (2007) Late Quaternary co-seismic sedimentation in the Sea of Marmara's deep basins. Sediment Geol 199:65–89

Bourry C, Chazallon B, Charlou JL et al (2009) Free gas and gas hydrates from the Sea of Marmara, Turkey: chemical and structural characterization. Chem Geol 264:197–206

Çağatay MN, Gorur N, Algan O et al (2000) Late Glacial-Holocene palaeoceanography of the Sea of Marmara: timing of connections with the Mediterranean and the Black Sea. Mar Geol 167:191–206

Çağatay MN, Ozcan M, Gungor E et al (2004) Pore-water and sediment geochemistry in the Marmara Sea (Turkey): early diagenesis and diffusive fluxes. Geochem Explor Environ Anal 4:213–225

Çağatay MN, Eris K, Ryan WBF et al (2009) Late Pleistocene-Holocene evolution of the northern shelf of the Sea of Marmara. Mar Geol 265:87–100

Charpentier S, Bourrié G (1997) Deformation of saturated clays under mechanical and osmotic stress and its relation with the arrangement of the clays. Eur J Soil Sci 48:49–57

Grall C, Henry P, Tezcan D et al (2012) Heat flow in the Sea of Marmara Central Basin: possible implications for the tectonic evolution of the North Anatolian fault. Geology 40:3–6

Henry P, Thomas M, Ben Clennell M (1999) Formation of natural gas hydrates in marine sediments 2. Thermodynamic calculations of stability conditions in porous sediments. J Geophys Res 104:23005–23022

Le Pichon X, Sengor AMC, Demribag E et al (2001) The active Main Marmara Fault. Earth Planet Sci Lett 192:595–616

Lisiecki LE, Raymo ME (2005) A Pliocene-Pleistocene stack of 57 globally distributed benthic d18O records. Paleoceanography 20:PA1003

Liu X, Flemings P (2009) Dynamic response of oceanic hydrates to sea level drop. Geophys Res Lett 36:L17308

Londeix L, Herreyre Y, Turon JL et al (2009) Last Glacial to Holocene hydrology of the Marmara Sea inferred from a dinoflagellate cyst record. Rev Palaeobot Palynol 158:52–71

Maslin M, Owen M, Day S et al (2004) Linking continental-slope failures and climate change: testing the clathrate gun hypothesis. Geology 32:53–56

Masson DG, Harbitz CB, Wynn RB et al (2006) Submarine landslides: processes, triggers and hazard prediction. Philos Trans R Soc A Math Phys Eng Sci 364:2009–2039

McHugh CMG, Seeber L, Cormier MH et al (2006) Submarine earthquake geology along the North Anatolia Fault in the Marmara Sea, turkey: a model for transform basin sedimentation. Earth Planet Sci Lett 248:661–684

Menot G, Bard E (2010) Geochemical evidence for a large methane release during the last deglaciation from Marmara Sea sediments. Geochim Cosmochim Acta 74:1537–1550

Mulder T, Cochonat P (1996) Classification of offshore mass movements. J Sediment Res 66:43–57

Rothwell RG, Thomson J, Kahler G (1998) Low-sea-level emplacement of a very large late Pleistocene "megaturbidite" in the Western Mediterranean Sea. Nature 392:377–380

Thomas Y, Marsset B, Westbrook GK et al (2012) Contribution of high-resolution 3D seismic near-seafloor imaging to reservoir-scale studies: application to the active North Anatolian Fault, Sea of Marmara, Near Surf. Geophysics 10:291–301

Vidal L, Menot G, Joly C et al (2010) Hydrology in the Sea of Marmara during the last 23 ka: implications for timing of Black Sea connections and sapropel deposition. Paleoceanography 25:PA1205

Wong HK, Ludmann T, Ulug A et al (1995) The Sea of Marmara – a plate boundary sea in an escape tectonic regime. Tectonophysics 244:231–250

Zitter TAC, Henry P, Aloisi G et al (2008) Cold seeps along the main Marmara Fault in the Sea of Marmara (Turkey). Deep-Sea Res Part I-Oceanogr Res Pap 55:552–570

Zitter TAC, Grall C, Henry P et al (2012) Distribution, morphology and triggers of submarine mass wasting in the Sea of Marmara. Mar Geol 329:58–74

Chapter 54
Instability of Oceanic Volcanic Edifices: Examples of Sector Collapse, Debris Avalanches, and Debris Flows from Gran Canaria (Canary Islands)

Hans-Ulrich Schmincke and Mari Sumita

Abstract We review different types of mass transfer (landslides, debris avalanches, debris flows, turbidites) generated throughout the evolution of a long-lived volcanic island (Gran Canaria) from its emergence at ca. 16 Ma to the present. The choice of Gran Canaria is based on its unique characteristics in that the various types of downslope mass transfer are not only documented by acoustic methods and bathymetry, but also by lithology (ODP Leg 157 drilling and land deposits). The intermittent mass transfer caused by edifice instability and direct volcanic processes (pyroclastic flows) represents by far the greatest contribution of mass to the depot centers peripheral to the island, as contrasted with steady erosion. We speculate on the impact of long-term trade wind directions as major factors in deeply eroding and thus weakening the northern slopes and therefore preferentially localizing sector collapses on the windward sides of the islands.

Keywords Gran Canaria • Debris avalanche • Debris flow • Syn-ignimbrite turbidite

54.1 Introduction

The idea of major landslides having generated the magnificent Orotava valley in northern Tenerife (Figs. 54.1 and 54.2) was suggested early on by Alexander von Humboldt (1814). Undisputable collapse-generated debris avalanche deposits in the Canaries were first recognized on Gran Canaria (review in Mehl and Schmincke 1999) and subsequently on the sea floor off El Hierro by Holcomb and Searle (1991). The seismic and bathymetric evidence for offshore debris avalanches common

H.-U. Schmincke (✉) • M. Sumita
GEOMAR Helmholtz Centre for Ocean Research, Kiel, Germany
e-mail: h-u.schmincke@t-online.de

S. Krastel et al. (eds.), *Submarine Mass Movements and Their Consequences*, Advances in Natural and Technological Hazards Research 37, DOI 10.1007/978-3-319-00972-8_54,

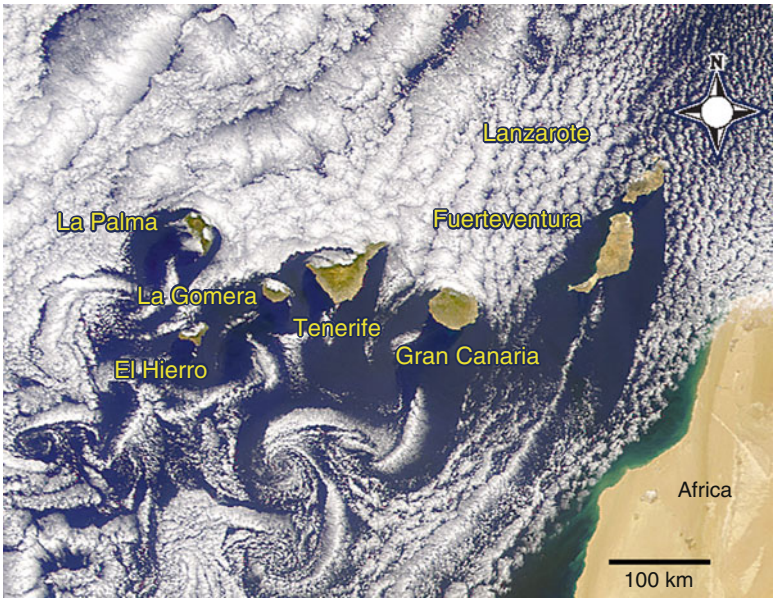

Fig. 54.1 Clouds pile up on the steep northern flanks of the Canary Islands due to the prevailing north-northeast trade wind directions constant since at least the middle Miocene. The higher erosional rates on the northern flanks resulted in steeper slope gradients and higher susceptibility for flank collapse (Image SeaWIFS project, NASA/Goddard Space Center, and ORBIMAGE)

around all of the seven major Canary Islands has been reviewed by Krastel et al. (2001). Older deposits around the eastern Canaries are largely or completely hidden in the volcanic aprons owing to high sedimentation rates. Masson et al. (2002) focus their review on Tenerife and the western islands La Palma and El Hierro where most of the 14 dominantly debris avalanche deposits – all younger than 1 Ma – are morphologically recognizable on the sea floor, most also being associated with landslide scars onshore. Volumes range from 50–500 km^3 and run out distances are up to 130 km from source.

Gran Canaria and its volcanic apron are arguably the oceanic island system with the highest number and greatest variety of volcanic mass flow deposits known as based on (a) its longevity, (b) development of a 20 km caldera, the source for >20 felsic ignimbrites emplaced over ca 5 Ma, whose submarine *syn-ignimbrite turbidites* have traveled tens to hundreds of km on the sea floor, (c) concentric as contrasted with focused transport of mass flows during at least three major periods and (d) a large post-erosional stratocone. Gran Canaria is typical of other volcanic centers throughout the Canary islands in that all have grown over millions of years, the eastern ones over 20 millions of years, while the youngest in the west are younger than 3 Ma (Schmincke and Sumita 2010).

54.2 Stages of Mass Transfer from Gran Canaria into the Sea

The uniqueness of the system is due to: (1) Numerous headwall scars not only along the coast but also in the interior of the island; (2) mass flow deposits exposed on land; (3) ODP Leg 157 drilling at 4 sites around the island, penetrating many stages of mass flow emplacement throughout ca. 15 Ma; (4) Seismic reflection and bathymetric analysis of the volcanic apron; (5) Dredged samples. Nine case histories are here briefly summarized (Fig. 54.2). These are only a minimum since several events such a major landslide scar above Valsequillo and Pleistocene basaltic debris flow deposits drilled at Site 954 are omitted.

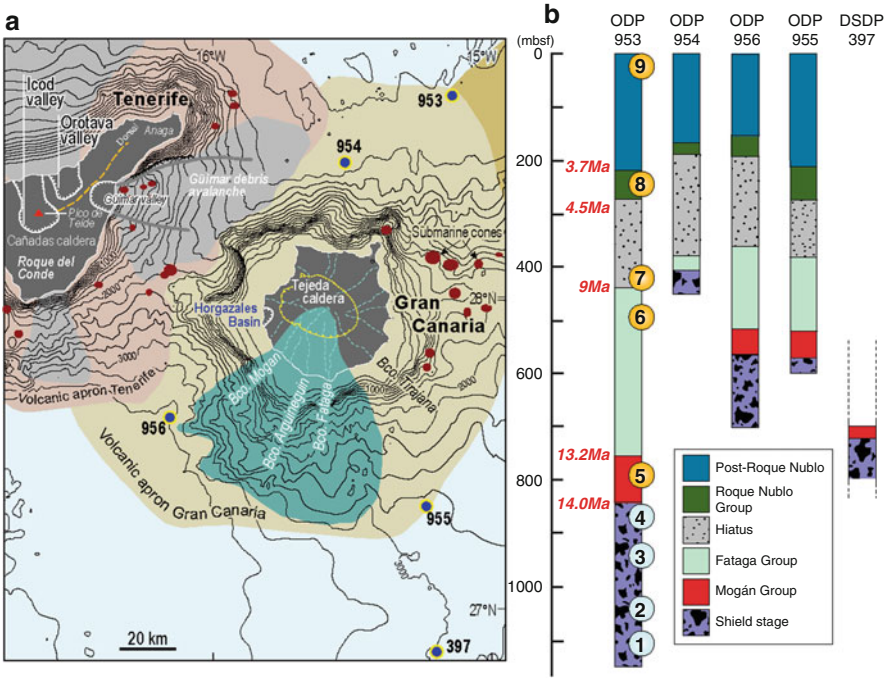

Fig. 54.2 (**a**) Gran Canaria and submarine contours. The volcanic apron (beige) is largely covered by the eastern apron of Tenerife (*light brown*). Volcanic cones are shown in *red*. The outline of the Miocene Tejeda caldera is shown inside Gran Canaria. The prominent southern onland and submarine fan of Roque Nublo debris avalanches is shown in *green*, other RN debris avalanches that entered the sea are not shown (Modified from Funck and Schmincke 1998; Krastel et al. 2001). (**b**) Stratigraphic correlation between four holes drilled in the volcanic apron of Gran Canaria and distal hole DSDP Site 397, based on the overall stratigraphy determined on land, drilled deposits being correlated precisely with the time-equivalent deposits onshore (Schmincke and Sumita 1998). *Numbers* indicate specific mass flow stages (See text)

54.2.1 Stages 1 and 2. Pre-shield Non-explosive and Moderately Explosive Submarine Activity

In a magnificent cross-section of an uplifted seamount in Barranco de las Angustias (La Palma) densely packed pillow lavas are overlain by a ca. 350 m of up to 5 m thick flow deposits consisting of variably rounded blocks of pillow basalt in the cm-dcm range (Staudigel and Schmincke 1984; see also figs. 4.20–4.23 in Schmincke and Sumita 2010). We interpret these as analogous to basaltic debris flows formed by partial collapse of up to four cones between 363 and 90 m bsl during the 2011–2012 shallow submarine eruptions off El Hierro (Rivera et al. 2013). Massive hyaloclastite debris flow deposits make up the upper part of the La Palma seamount section.

The basal 190 m of Site 953 (ODP Leg 157) consist of about sixteen 1–50 m thick well-sorted massive lapillistone to coarse hyaloclastite debris flows consisting dominantly of variably vesicular shards becoming finer grained and bedded upwards and more vesicular in the uppermost flows suggesting decreasing water depth (*stage 2*). Abundant largely non-vesicular basalt clasts up to 25 cm in diameter are concentrated near the base of each flow (*stage 1*). We interpret this association as representing a mixture of hyaloclastite mass flows recording episodic down slope transport from near the top of a shallowing seamount to a depth of ca. 3,000 m, en route picking up basalt blocks from fragmented lava flows recording an earlier stage of seamount growth (Schmincke and Segschneider 1998).

54.2.2 Stage 3. Shield Stage Noneruptive Flank Collapse

A major unconformity in the emergent amalgamated shield stage of Gran Canaria between lower shield-stage basalts (Güigüi Formation) and younger more evolved basalts (Hogarzales Formation) (Figs. 54.2 and 54.3) is interpreted as caused by sector collapse of the Güigüi Formation. A >70 m thick, strongly graded debris flow deposit drilled at Site 956 (ODP Leg 157) some 40 km southwest of Gran Canaria was interpreted as representing this collapsed flank (Fig. 54.4; Schmincke and Segschneider 1998). The poorly sorted deposit is made up dominantly of angular lapilli-sized blocks of tachylitic and poorly vesiculated basalt, shallow water biogenic debris being concentrated near the top. The angularity of the blocks indicates an origin by sudden collapse of subaerial shield basalts. An overlying sand deposit is tentatively interpreted as a tsunamis deposit generated by the emplacement of the huge debris flow. The scalloped steep subaerial-submarine morphology along western and northern Gran Canaria indicates several similar large slumps but the displaced masses are hidden in the volcanic aprons (Funck and Schmincke 1998). The fact that Miocene basalt lavas only crop out very sparsely in northeast Gran Canaria could be due to both high erosional rates and flank collapse.

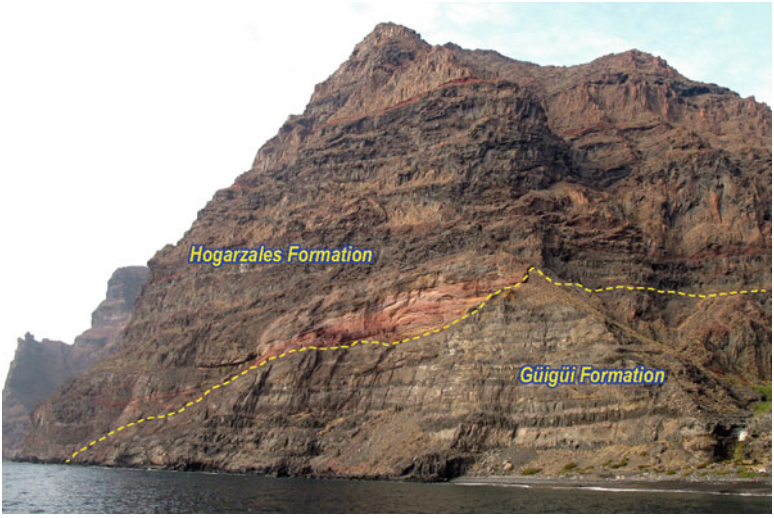

Fig. 54.3 Unconformity between *lower* (Güigüi Fm), strongly diked basalt shield lavas overlain with pronounced unconformity by *upper* (Hogarzales Fm) shield lavas. We interpret the unconformity by collapse of the older shield volcano edifice

54.2.3 Stage 4. Shield Stage Eruption-Associated Delta Collapse

The major debrite of *stage 3* is overlain by two moderately graded debris flow deposits 25 and 15 m thick. Their lithology differs significantly in that they contain fresh sideromelane "droplets" and vesicular shards, evidence that the debris flows were formed during eruptive events but accumulated adjacent to the coast as reflected by the presence of shallow water biogenic debris. Most likely, these flows – as well as similar delta deposits overlying *stage 1* and *2* deposits in Site 953 – were derived from delta deposits that form during advance of lava flows into the sea as described from Kilauea volcano (Moore et al. 1973). The more evolved basaltic composition suggests that these events are associated with the younger Hogarzales basalts that fill the huge morphological scar described.

54.2.4 Stage 5. Early Caldera Stage Syn-Ignimbrite Turbidites

Large-volume rhyolitic ignimbrites were erupted from a 20 km diameter caldera developed on the basaltic shield volcano complex between 14 and 13.3 Ma. Syn-ignimbrite turbidites spread concentrically away from the island up to hundreds of km (Sumita and Schmincke 1998). Some syn-ignimbrite turbidites drilled up to 60 km away from the island (Site 953) were correlated precisely with their onland

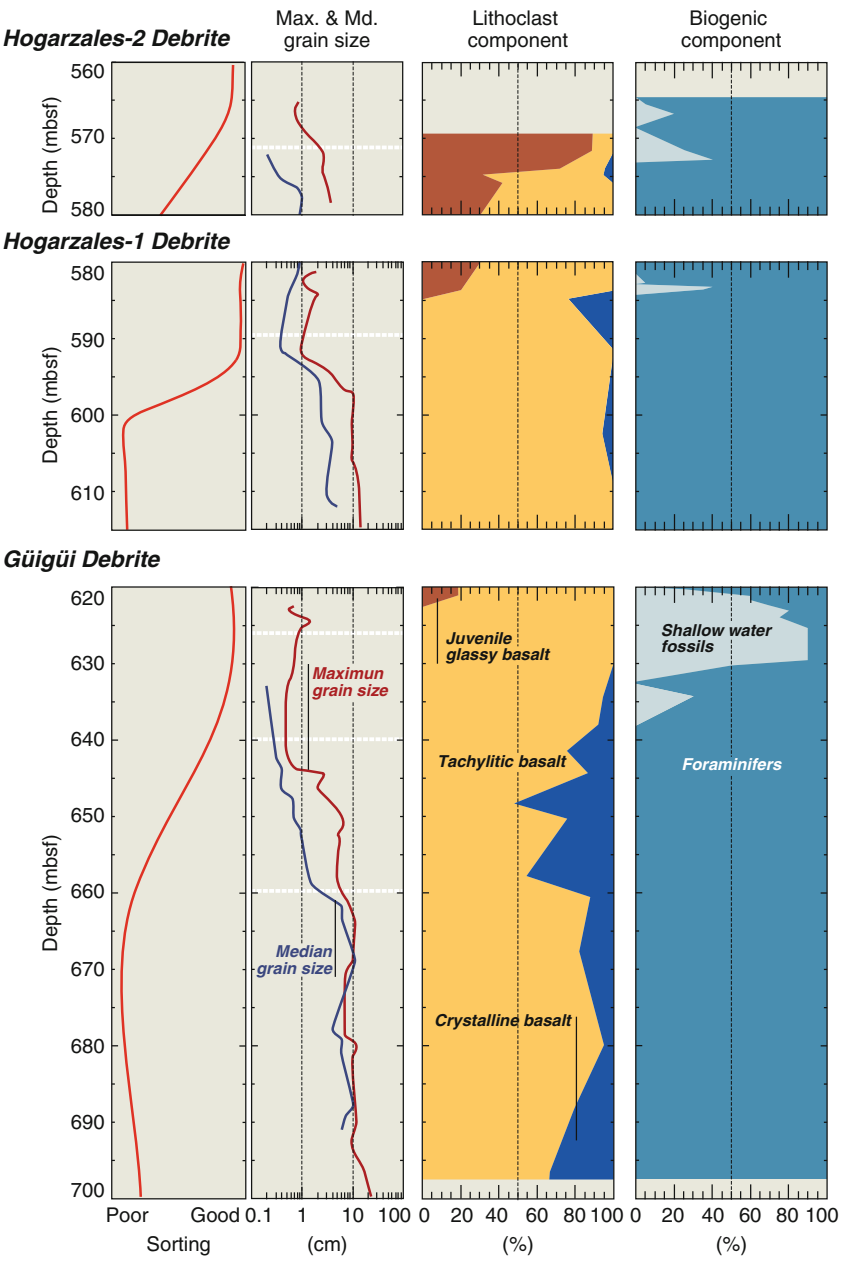

Fig. 54.4 Lithology of Güigüi and Hogarzales debris flow deposits drilled at Site 956. Simplified modal percentages of three clast types in the Güigüi Debrite, contrasting especially with Hogarzales Debrite-2 in which juvenile components dominate (all at Site 956). Maximum clast sizes and median of smaller clasts (not Md of total deposit) estimated in the core and thin section show pronounced decrease in all three flow deposits upwards while sorting increases with shallow water fossils becoming abundant near the top, evidence for shallow water derivation. (Modified from E. Hanenkamp, unpubl. Diplomarbeit, 2002, Univ. Hamburg)

Fig. 54.5 Distal facies of Miocene Fataga debris avalanche deposit ca. 1 km from south coast near Arguineguín. Angular blocks are dominantly *green* Fataga phonolite lava, ignimbrite and obsidian fragments while *white* soft pumiceous material is strongly deformed plastically. Person at base for scale

counterparts allowing for the calculation of total mass output, the estimated volume of basal ignimbrite P1 e.g. amounting to >100 km^3 (DRE) (Freundt and Schmincke 1998).

54.2.5 Stage 6. Late Caldera Stage Phonolitic Debris Avalanches and Debris Flows

Inland volcano collapse stages (Fataga Group) are documented in subaerial debris-avalanche deposits made of fragmented lava, non-welded ignimbrites and obsidian breccias (Fig. 54.5). Many are exposed close to shore e.g. near Arguineguín, mixed with, or grading into, debris flow deposits emplaced between ca. 11.5 and ca. 10 Ma. Poorly recovered breccias (Sites 953 and 956 (Leg 157)) do not allow reliable volume estimates of individual flows.

54.2.6 Stage 7. Post-caldera Collapse

At the western head of Tirajana basin in eastern Gran Canaria, Pliocene Roque Nublo deposits abut against Fataga Group phonolite lavas along a nearly vertical

Fig. 54.6 Distal and marginal facies of Pliocene Roque Nublo debris avalanche deposit ca. 2 km from south coast near Pasito Blanco filling a shallow channel in widespread conglomerate sheet. Partly rounded clasts including *green* Fataga lava and ignimbrite fragments picked up en route are suspended in fine-grained *brown* matrix

contact, probably a major post-Fataga sector collapse scar. Local debris avalanche deposits (DAD) of Fataga composition in northeastern Gran Canaria are interpreted as reflecting northward collapse of the thick pile of Fataga volcanics. The resulting debris avalanches must have entered the sea to the east and northeast. The deposits resemble the Holocene Fataga debris-avalanche deposits (Fig. 54.7).

54.2.7 Stage 8. Post-erosional Stratocone Collapse Deposits (Roque Nublo)

The morphologically and structurally most impressive subaerial debris avalanche deposits of any oceanic island were generated on Gran Canaria around 3.5 Ma during multistage collapse of the Roque Nublo (RN) stratocone. They traveled overland for some 20 km radially and overtopped canyons up to 500 m deep as between Barrancos de Fataga in the east, Mogán in the west and in the north and northeast of the island (Fig. 54.6). The debris avalanche deposits in the sea form a major seismic reflector (R3) at least as far as 50 km away from the island at a depth of ca. 200 m below the sea floor where they form a huge morphological debris fan (Funck and Schmincke 1998; Mehl and Schmincke 1999) (Fig. 54.2). Recovery of

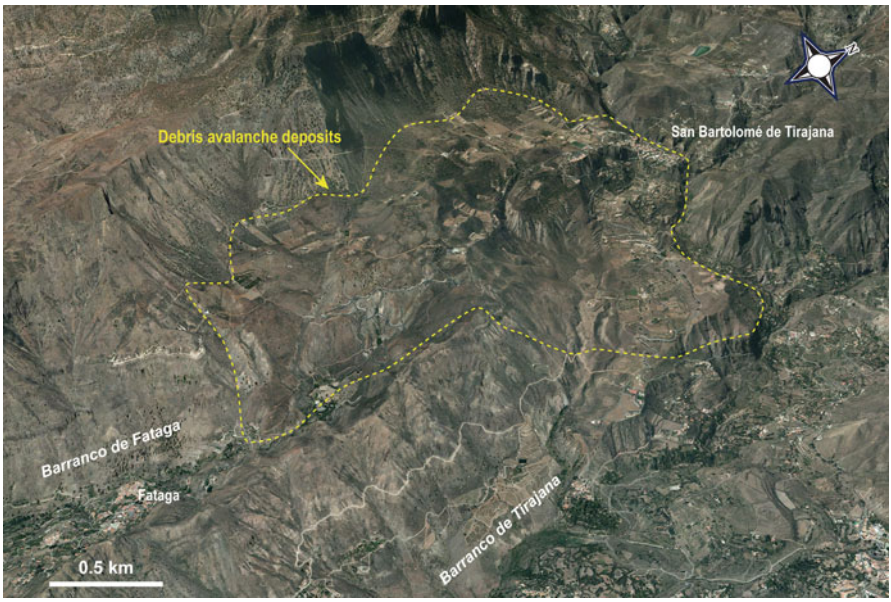

Fig. 54.7 Quaternary to Holocene (?) amalgamated debris avalanche deposits consisting entirely of Miocene Fataga Group phonolitic lava, ignimbrite, and volcaniclastic sediments. The town of San Bartolome de Tirajana and the plateau above are built on these debris flow deposits totaling >50 m in thickness (Aerial image adapted from Google Earth (2013))

the deposits in all ODP drill sites was poor but RN debris avalanche deposits were dredged in the channel between Gran Canaria and Fuerteventura (Schmincke and Graf 2000) documenting that RN debris avalanches were emplaced concentrically around the island. Altogether a minimum volume of >ca. 50 km^3 is estimated that, however, maybe much larger owing to intense erosion on land and poor control on the submarine deposits.

54.2.8 Stage 9. Late Quaternary to Holocene Mass Wasting

In Barrancos de Tirajana and Fataga, one or more Quaternary to Holocene (?) collapse events are interpreted to have plugged an older drainage system connecting the large Tirajana basin and Fataga canyon. As a result, the Fataga canyon was captured, drainage being diverted to the southern Tirajana basin. The >50 m thick huge debris slide(s) underlying the town of San Bartolomé de Tirajana are characterized by a distinctive hummocky surface topography and extend to the base of the switchback road leading from the Tirajana basin into Barrano de Fataga (Fig. 54.7). Fataga canyon, cutoff from its headwater water supply, is gradually being drowned along its course by numerous rock falls and debris avalanches some more than 150 m thick descending from the steep slopes.

54.3 Discussion

Many causes of sector collapse have been proposed ever since the north flank of Mt St Helens failed on May 18, 1980 (e.g. Siebert 1984). Two endmember processes can be defined with respect to the Gran Canaria mass flows: eruption-induced and instability-induced and a combination of both. The unusually thick lithics-dominated drilled debris flow deposit (*stage 3*) represents a relatively clear instability-induced endmember. Factors in the Canaries that contribute to such sector collapses are steep flank slopes (10°–15° vs. 3°–6° for subaerial Hawaiian volcanoes) (review in Masson et al. 2002) and growth of the volcanic edifices on top of thick submarine sediments, which, on the southern flanks, include methane-rich low-strength sediments. Sector collapse (*stage 3*) occurred at a time of decreasing magma supply and establishment of a high-level magma reservoir that quickly developed into a huge reservoir underlying the 20 km caldera exerting increased lateral stress to the shield volcano flank. Juvenile vesiculating lava lumps of the high temperature Mogán Group peralkaline ignimbrites (*stage 5*) were quenched when entering the sea, forming thick unstable piles of highly fragmented strongly welded ignimbrite, periodically collapsing to form voluminuous syn-ignimbrite turbidites drilled at all Leg 157 sites – an endmember for volcanic triggering. The debris avalanches generated during *stage 6* must have been associated with the growth of obsidian domes as reflected in their lithology. Generation of the large volume Roque Nublo debris avalanches (*stage 8*) was greatly facilitated by the abundance of epiclastic sediments interbedded with lava flows, contributing to high pore pressure that reduced the strength of the stratocone, especially in the central crater area where the debris avalanches were spawned. The wet Pliocene climate provided ample water and probably a high water table (Schmincke and Sumita 2010).

The present dominant NE trade wind direction in the Canary islands (Fig. 54.1) was roughly constant for at least 15 Ma (Schmincke and Sumita 1998). The northeastern flanks of the islands were thus much more strongly eroded than the southwestern flanks. Asymmetric mass wasting was invoked by Schmincke (1968) and contrasted with the then prevailing idea of major faults separating a "Canarian land mass" into separate islands. The asymmetric deep erosion may have caused major sector collapses to occur preferentially on the north flanks of several of the Canary Islands (Schmincke and Sumita 2010). Interestingly, the main dike directions on the island changed from roughly radial (Miocene shield) to approximately N-S during growth of the Pliocene Roque Nublo stratocone, excepting the dominantly concentric Miocene felsic cone sheet swarm reflecting the central caldera structure. In post-Roqublo times (younger than ca. 3 Ma), mafic dike directions changed abruptly to strongly NW-SE orientation that remained dominant until the Holocene. We speculate that the extremely voluminuous Roque Nublo mass wasting removing much of the northeastern flanks of the island aided by intense erosion during the Pliocene may have altered the stress field of the island to such a degree that ascending magmas used the gravitationally-reoriented stress field to intrude along directions that were fundamentally controlled by the orientation of

the weak flank of the island – and thus ultimately by climate. The causal and temporal relationship between internal and external causes of mass wasting is being explored in the Canaries along several lines of evidence. For example, sector collapse triggered by dike intrusion has been invoked for neighboring Tenerife (Walter et al. 2005). Longpré et al. (2011) redated the famous El Golfo flank collapse on El Hierro as having occurred during low sea level between ca. 87 and 39 ka, contrasting with earlier views postulating the El Golfo slide to have been facilitated by high sea level.

In summary, the cause of most sector collapses and resulting mass flows is a combination of external and internal forcing and complex feedback mechanisms. Massive and instantaneous downslope mass transfer to the deeper ocean depot centers greatly outweighed that by steady erosion throughout the history of Gran Canaria.

Acknowledgements Constructive comments by Steve Carey, Michelle Coombs and Jason Chaytor helped to improve the manuscript. Our work in the Canary Islands has been supported by the Deutsche Forschungsgemeinschaft.

References

Freundt A, Schmincke H-U (1998) Emplacement of ash layers related to high-grade ignimbrite P1 in the sea around Gran Canaria. In: Weaver PPE, Schmincke H-U, Firth JV, Duffield WA (eds) Proc ODP. Scientific results 157, College Station, TX (Ocean Drilling Program), pp 201–218

Funck T, Schmincke H-U (1998) Growth and destruction of Gran Canaria deduced from seismic reflection and bathymetric data. J Geophys Res 103:15393–15407

Holcomb RT, Searle RC (1991) Large landslides from oceanic volcanoes. Mar Geotechnol 10:9–32

Krastel S, Schmincke H-U, Jacobs CL, Rihm R, Le Bas TP, Alibés B (2001) Submarine landslides around the Canary Islands. J Geophys Res 106:3977–3998

Longpré M-A, Chadwick JP, Wijbrans J, Iping R (2011) Age of the El Golfo debris avalanche, El Hierro (Canary Islands): new constrains from laser and furnace $^{40}Ar/^{39}Ar$ dating. J Volcanol Geotherm Res 203:76–80

Masson DG, Watts AB, Gee MJR, Urgeles R, Mitchell NC, Le Bas TP, Canals M (2002) Slope failures on the flanks of the western Canary Islands. Earth Sci Rev 57:1–35

Mehl KW, Schmincke H-U (1999) Structure and emplacement of the Pliocene Roque Nublo debris avalanche deposit, Gran Canaria, Spain. J Volcanol Geotherm Res 94:105–133

Moore JG, Phillips RL, Grigg RW, Peterson DW, Swanson DA (1973) Flow of lava into the sea, 1969–1971, Kilauea Volcano, Hawaii. Geol Soc Am Bull 84:537–546

Rivera J, Lastras G, Canals M, Acosta J, Arrese B, Hermida N, Micallef A, Tello O, Amblas D (2013) Construction of an oceanic island: insights from the El Hierro (Canary islands) 2011–2012 submarine volcanic eruption. Geology 41:355–358. doi:10.1130/G33863.1

Schmincke H-U (1968) Faulting versus erosion and the reconstruction of the Mid-Miocene shield volcano of Gran Canaria. Geol Mitt 8:23–50

Schmincke H-U, Graf G (eds) (2000) DECOS/OMEX II, Cruise no. 43, 25 November 1998–14 January 1999. METEOR reports, Universität Hamburg, 00-2

Schmincke H-U, Segschneider B (1998) Shallow submarine to emergent basaltic shield volcanism of Gran Canaria: evidence from drilling into the volcanic apron. In: Weaver PPE, Schmincke H-U, Firth JV, Duffield WA (eds) Proc ODP. Scientific results 157, College Station, TX (Ocean Drilling Program), pp 141–181

Schmincke H-U, Sumita M (1998) Volcanic evolution of Gran Canaria reconstructed from apron sediments: synthesis of VICAP project drilling (ODP Leg 157). In: Weaver PPE, Schmincke H-U, Firth JV, Duffield WA (eds) Proc ODP. Scientific results 157, College Station, TX (Ocean Drilling Program), pp 443–469

Schmincke H-U, Sumita M (2010) Geological evolution of the Canary Islands. Görres-Verlag Koblenz, Germany

Siebert L (1984) Large volcanic debris avalanches: characteristics of source areas, deposits, and associated eruptions. J Volcanol Geotherm Res 22:163–197

Staudigel H, Schmincke H-U (1984) The Pliocene seamount series of La Palma/Canary Islands. J Geophys Res 89:11.195–11.215

Sumita M, Schmincke H-U (1998) Tephra event stratigraphy and emplacement of volcaniclastic sediments, Mogán and Fataga stratigraphic intervals, ODP Leg 157. Part I Mineral and chemical stratigraphy of volcaniclastic units and correlation to the subaerial record. In: Weaver PPE, Schmincke H-U, Firth JV, Duffield WA (eds) Proc ODP. Scientific results 157, College Station, TX (Ocean Drilling Program), pp 219–266

von Humboldt A (1814) Voyage aux régions équinoxiales du nouveau continent fait en 1799, 1800, 1801, 1802, 1803 et 1804. Paris

Walter TR, Troll V, Cailleau B, Belousov A, Schmincke HU, Pvd Bogaard, Amelung F (2005) Rift zone reorganization through flank instability on ocean island volcanoes: Tenerife, Canary Islands. Bull Volcanol 67:281–291

Chapter 55
Slope Failures and Timing of Turbidity Flows North of Puerto Rico

Jason D. Chaytor and Uri S. ten Brink

Abstract The submerged carbonate platform north of Puerto Rico terminates in a high (3,000–4,000 m) and in places steep (>45°) slope characterized by numerous landslide scarps including two 30–50 km-wide amphitheater-shaped features. The origin of the steep platform edge and the amphitheaters has been attributed to: (1) catastrophic failure, or (2) localized failures and progressive erosion. Determining which of the two mechanisms has shaped the platform edge is critically important in understanding landslide-generated tsunami hazards in the region. Multibeam bathymetry, seismic reflection profiles, and a suite sediment cores from the Puerto Rico Trench and the slope between the trench and the platform edge were used to test these two hypotheses. Deposits within trench axis and at the base of the slope are predominantly composed of sandy carbonate turbidites and pelagic sediment with inter-fingering of chaotic debris units. Regionally-correlated turbidites within the upper 10 m of the trench sediments were dated between ~25 and 22 kyrs and ~18–19 kyrs for the penultimate and most recent events, respectively. Deposits on the slope are laterally discontinuous and vary from thin layers of fragmented carbonate platform material to thick pelagic layers. Large debris blocks or lobes are absent within the near-surface deposits at the trench axis and the base of slope basins. Progressive small-scale scalloping and self-erosion of the carbonate platform and underlying stratigraphy appears to be the most likely mechanism for recent development of the amphitheaters. These smaller scale failures may lead to the generation of tsunamis with local, rather than regional, impact.

Keywords Radiocarbon • Multibeam bathymetry • Mass transport deposits • Seismic reflection

J.D. Chaytor (✉)
U.S. Geological Survey, 384 Woods Hole Road, Woods Hole, MA, USA
e-mail: jchaytor@usgs.gov

U.S. ten Brink
U.S. Geological Survey, Woods Hole Coastal and Marine Science Center,
Woods Hole, MA 02543, USA

S. Krastel et al. (eds.), *Submarine Mass Movements and Their Consequences*, Advances in Natural and Technological Hazards Research 37, DOI 10.1007/978-3-319-00972-8_55,

55.1 Introduction

The style, size, and hazard potential of slope failures along margins of the Puerto Rico Trench (PRT; Fig. 55.1) have been investigated and debated since the first geophysical surveys of the region more than 60 years ago. Thick deposits, primarily composed of turbidite layers in the PRT basins, thought to be the result of turbid flows originating from the Puerto Rico-Virgin Islands (PR-VI) carbonate platform, have received considerable attention through geophysical and sedimentological investigation (e.g., Ewing and Ewing 1962; Conolly and Ewing 1967; Doull 1983). Large-scale indentations (Fig. 55.1), crescentic fracturing, and block detachment along the northern edge of the carbonate platform have all been interpreted to be related to catastrophic failure (Schwab et al. 1991; Hearne 2004) or as a result of localized failures and progressive erosion (Scanlon and Masson 1996; ten Brink et al. 2006).

Determining the ages and mechanisms of major failure events is critically important in the evaluation of regional and Atlantic Ocean-wide geohazards. Catastrophic slope failure would have evacuated more than 1,500 km^3 of material (Schwab et al. 1991), capable of generating a locally destructive, and regionally damaging, tsunami. A smaller slope failure along part of the trench marginal slope (ten Brink et al. 2006), although potentially destructive in the near-field (e.g., the 1918 Mona Canyon tsunami, López-Venegas et al. 2008), would be far less damaging regionally.

Here we report on the analysis of new gravity cores and existing piston cores coupled to a new suite of geophysical data providing insight into mass transport processes (MTPs) in the PRT region. Radiocarbon ages for cores tied to previously identified and correlated turbidites elucidate the recent history of MTPs and landslide-tsunami hazards in the region.

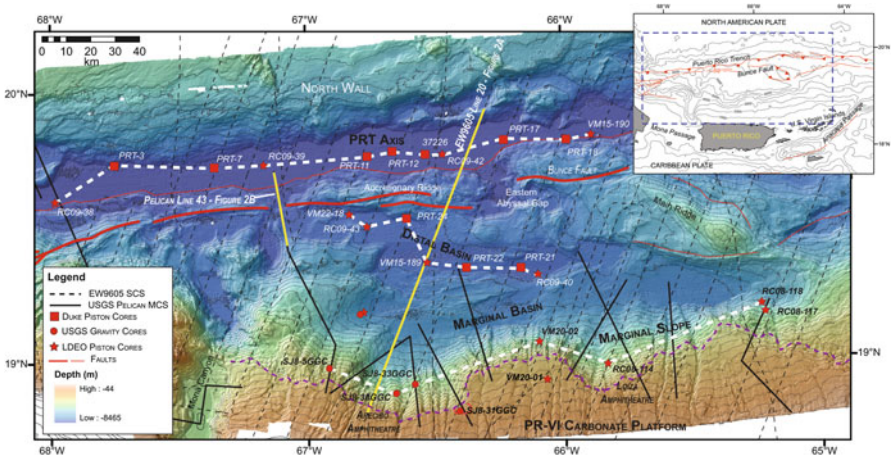

Fig. 55.1 Bathymetry of Puerto Rico Trench and adjacent regions, with primary physiographic features labeled. Core locations, multichannel and single channel seismic line tracks, major faults and the location of core correlation plots (Figs. 55.3, 55.4, and 55.5) are shown

55.1.1 Physiography and Geology

The physiographic subdivisions of the PRT based on the new bathymetry compilation are shown in Fig. 55.1. The Tertiary-age PR-VI carbonate platform, the primary source of material being transported into the PRT, extends from the coastal hills of northern Puerto Rico offshore to a depth of between ~2,500 m (within amphitheaters) and ~4,000 m, with a post-3.3 Ma northward dip of 4°. Deposits of skeletal calcareous sand and river-derived terrestrial material are found on the shelf and upper slope (Schneidermann et al. 1976). Small translational landslides, fractures and dissolution features, and predominantly N-S oriented canyon systems with relief between 100 and 400 m and U- and V-shaped floors (Scanlon and Masson 1996) ornament the carbonate platform. Although the canyon walls are steep (often >20°), covered by varying thicknesses of sediment, and cut by vertical fissures, Gardner et al. (1980) found them to be devoid of evidence of active depositional processes (e.g., turbidity currents, wall failure) and to now be acting as catchments for river-supplied terrestrial material. Based on GLORIA side-scan imagery, Scanlon and Masson (1996) noted that several of these canyons appeared to continue below the marginal escarpment down into the marginal slope, but their full downslope extent and relationship to deposition in the trench could not be determined. ten Brink et al. (2006) mapped 160 landslide evacuation zones along the marginal escarpment and slope, although none exceeded 20 km^3.

55.1.2 Data

Multibeam data, gridded at a resolution of 150 m, covering the bulk of the PRT, were collected by the U.S. Geological Survey (USGS) between 2002 and 2006 using the SeaBeam 2112 system on the National Oceanic and Atmospheric Administration (NOAA) ship *Ronald H. Brown* (Fig. 55.1). Additional bathymetry coverage of the upper carbonate platform (<1,700 m depth) was derived from the NOAA Puerto Rico DEM Discovery Portal (http://www.ngdc.noaa.gov/mgg/dem/demportal.html). Previously collected single-channel (SCS) and new multi-channel (MCS) seismic reflection data were analyzed to identify evidence of slope failure and mass transport processes. Approximately 670 km of MCS reflection profiles crossing the carbonate platform and trench were collected by the USGS in 2006 using a 35 in^3 generated injection gun, and a 24-channel streamer (see Chaytor and ten Brink 2010). SCS profiles used were collected in 1996 aboard the R/V Ewing (cruise EW9605; see van Gestel et al. 1998 for details).

Sedimentology data were derived from eight new gravity cores (SJ8 cores) collected by the USGS in 2008, from cores archived at the Lamont Doherty Earth Observatory (LDEO) core repository (core identifiers RC08/09-xx and VMxx-xx), and from unpublished sources (PRT and 372xx cores, Doull 1983). The USGS cores were collected at sites immediately below the carbonate platform marginal

Table 55.1 AMS ^{14}C radiocarbon ages and 2-σ calibrated age ranges of mixed planktonic foraminifera samples. Radiocarbon ages were converted to calibrated ages using Calib 6.0 (Stuiver and Reimer 1993), utilizing the Marine09 calibration curves (Reimer et al. 2009) and include open ocean 400 year marine reservoir correction

Core	Water depth (m)	Depth in core (cm)	Lab code	Radiocarbon age	2-σ Calibrated age range (BP)
RC08-118	6,190	17–21	OS-76016	6,960 ± 55	7,458 ± 105
RC09-38	8,292	400–403	OS-77358	19,300 ± 85	22,731 ± 504
RC09-39	8,316	694–697	OS-77360	19,350 ± 80	22,713 ± 531
RC09-40	7,817	368–370	OS-77359	16,650 ± 75	19,257 ± 323
		370–372	OS-77361	15,400 ± 60	18,268 ± 272
RC09-42	8,292	230–233	OS-77362	21,700 ± 90	25,449 ± 398
RC09-43	7,815	265–268	OS-76017	16,050 ± 65	18,787 ± 161
		334–338	OS-77363	14,250 ± 55[a]	16,943 ± 182
VM20-02	2,989	16–20	OS-76018	13,050 ± 80	14,848 ± 605
VM22-18	7,948	26–29	OS-76019	11,250 ± 50	12,742 ± 142
SJ8-33GGC	4,912	49–50.5	OS-86482	29,000 ± 120	32,948 ± 503
		90–92	OS-86483	29,300 ± 140	33,706 ± 737
SJ8-38GGC	4564	144–146	OS-86484	44,400 ± 550	47,262 ± 1,442

[a]Age from very small sample, not used in analysis

escarpment. These new cores were visually logged and underwent grain-size, wet bulk density, magnetic susceptibility, and X-ray fluorescence analyses.

Mixed planktonic foraminiferal assemblages (primarily *Globigerinoides ruber* [white], *Globigerinoides sacculifer*, and *Globigerinella aequilateralis*) extracted from the newly collected gravity cores and LDEO piston cores were radiocarbon dated at the National Ocean Sciences Accelerator Mass Spectrometry facility (Table 55.1). Although much of the PRT and adjacent area lies below the regional carbonate compensation depth, carbonate preservation in the samples was high, possibly due to rapid burial by turbidity currents and debris flows. Given the age (greater than 50 years) and sampling history of the LDEO cores, the sampled intervals often consisted of several centimeters of sediment below event layers and therefore their ages likely have lower precision.

55.2 Results

55.2.1 Slope Failure Features and Mass Transport Deposit Distribution

Mass Transport Deposits (MTD) associated with failures of the slope north of Puerto Rico appear to be confined to surficial slope deposits, base of slope debris wedges and turbidites, and thin debris flow layers in the marginal and distal

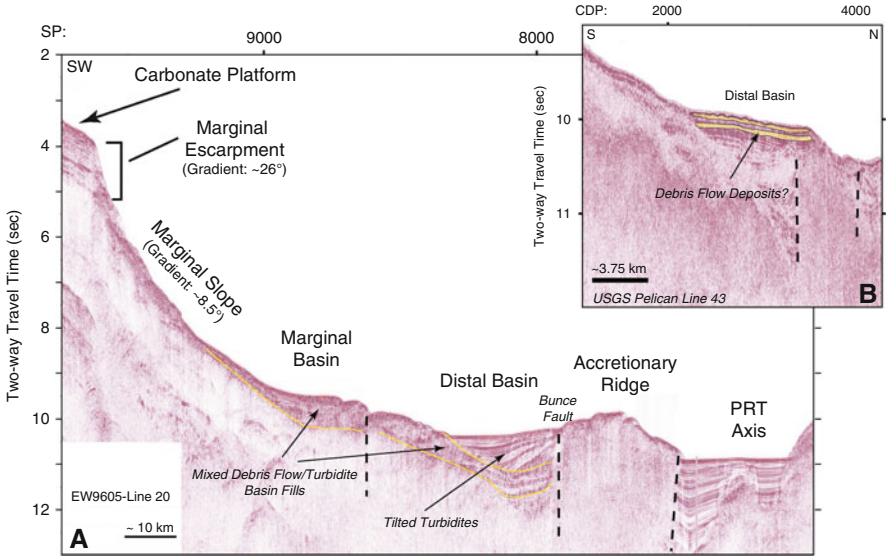

Fig. 55.2 (**a**) Stacked single-channel seismic line EW9605-Line 20 showing the general physiographic components of the trench and its margins (outlined by *yellow line*). Turbidite and debris flow deposition are seen on the marginal slope and in the marginal basin, while generally only turbidites are seen in the distal basin and PRT axis. *Dashed lines* mark the location of faults. (**b**) USGS MCS Line 43 showing the presence of a near-surface debris flow deposit at the western end of the distal basin (location in *yellow* on Fig. 55.1)

basins and the trench axis (Fig. 55.2a). While debris flow deposits appear to be generally confined to the marginal slope and basin, at least one debris flow, from an unknown source, is present in the near surface at the western end of the distal basin (Fig. 55.2b). Most notably, there is no evidence of blocky debris flows or rock falls that would be characteristic of catastrophic failure of amphitheater-scale sections of the competent carbonate platform material and older underlying units. Large-scale blocky submarine slope failures of coherent lithologies have been found to leave a prominent surficial and subsurface record for 10's of thousands to millions of years (e.g., Clague and Moore 2002; Le Friant et al. 2004). Using the new MCS data we have not been able to confirm the presence of detached and down-thrown blocks of carbonate platform material along the marginal slope as reported by Hearne (2004).

As noted by Scanlon and Masson (1996) and revealed in great detail by the new bathymetry data, many of the canyon systems developed in the carbonate platform continue across the marginal escarpment and down the marginal slope (Fig. 55.1). Below the marginal escarpment, the widths of the canyons increase substantially and develop flat to U-shaped floors. The canyon systems do not extend beyond the base of the slope and there is no surficial expression of depositional fans within the marginal or distal basins. The morphology of these canyon systems suggests that they are currently zones of accumulation and have been for some time.

55.2.2 *Correlation and Timing of Turbidite and Debris Flow Deposition*

Correlations of individual turbidite and pelagic units within the PRT basins based on detailed sedimentological analysis have been carried out by Conolly and Ewing (1967) and Doull (1983) and those correlations will generally be applied here. Sediments recovered in the LDEO, Duke and USGS cores along the marginal slope and within the trench basins are classified as (1) pelagic sediments including foraminifera oozes, (2) turbidites and debris flows consisting of calcareous sands often containing carbonate rock fragments, terrigenous material, foraminifera tests and pteropod shells, and often, shallow water organisms, or (3) sediment characterized by silty-clay size fraction composed of a mix of pelagic sediments and silt-sized carbonate and terrigenous rock fragments, usually present above turbidite sands. Sediments on the deeper parts of the carbonate platform are predominantly pelagic in origin, interrupted by only very thin sands containing shallow water material, the youngest of which in core VM20-01 was deposited after approximately 13,000 year BP. Core SJ8-31GGC from within a landslide scar at the edge of the marginal escarpment (Fig. 55.1) contains at least 12 cm of Holocene pelagic sediments (based on the presence of *Globorotalia menardii*).

55.2.2.1 Marginal Slope and Basin

A plot of cores from the marginal slope (Fig. 55.3) reveals strong along-slope variations in near surface sediments. Thick gravel layers in core VM20-01 and clay-breccia interval in core RC08-118 stand as evidence of deposition of small scale MTDs on the slope. Sand layers are almost always ungraded and some contain gravel-size clasts of carbonate rock at their base. All but one of the cores is capped by a layer of pelagic sediment, which in core RC08-118 has a basal age of $7{,}458 \pm 105$ year BP. Core RC08-114 is composed entirely of pelagic sediment layers, suggesting that if the record is complete, there has either been no significant downslope sediment transport or the marginal slope acts more as a "by-pass" slope (Schlager and Camber 1986). Dates of pelagic and silty-clay layers directly above thin sand layers in cores SJ8-33GGC and -38GGC collected on ridges between canyons within the Arecibo Amphitheatre, returned late-Pleistocene ages of $32{,}948 \pm 503$ and $47{,}262 \pm 1{,}442$ years BP, respectively.

55.2.2.2 Distal Basin

Doull (1983) identified four correlatable turbidites in the sediments of the distal basin (EP-1-EP-4), the thickest of which was EP-3 (Fig. 55.4). That said, many of the turbidite sands in the distal basin cores have particularly thick silty-clay tails and multiple sand pulses which complicate correlation along the full length of the

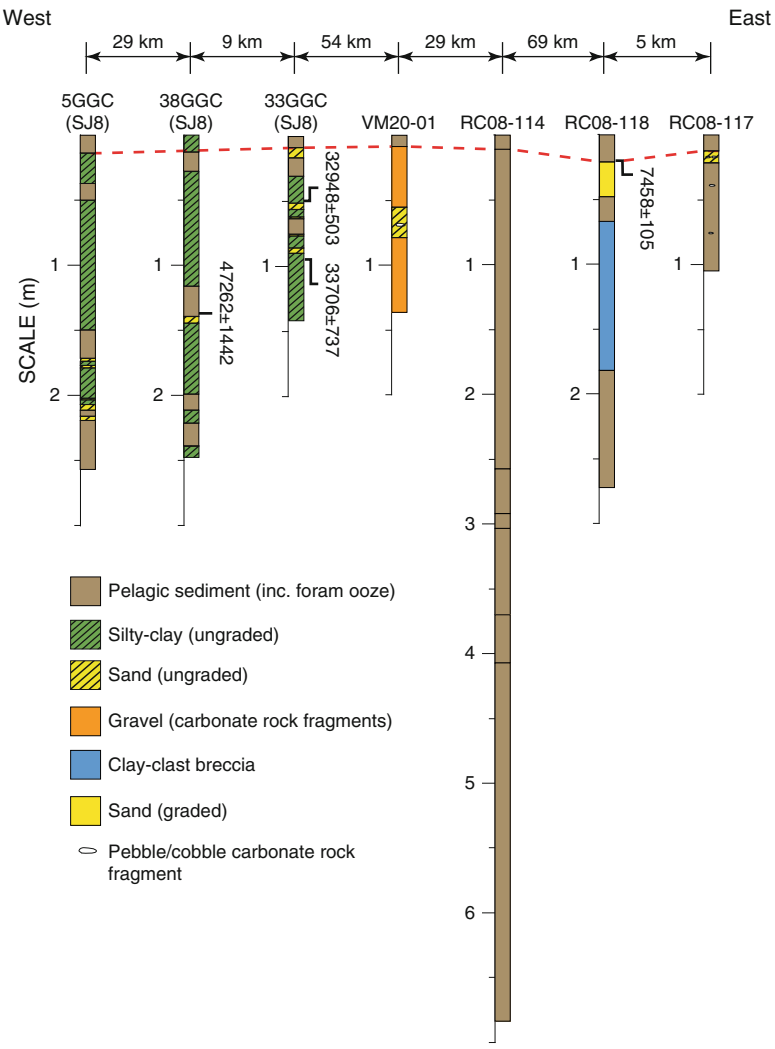

Fig. 55.3 Marginal slope core correlation plot revealing a dynamic and complex depositional environment which varies over relatively short distances. The *red-dashed line* marks the base of the capping pelagic layer. Calibrated AMS ^{14}C radiocarbon ages determined from mixed planktonic foraminifera samples are shown for selected cores (in years BP with 2-σ errors). Location of cores and correlation line shown on Fig. 55.1

basin. A prominent turbidite between the EP-3 and EP-4 turbidites in core RC09-40 interpreted by Doull (1983) to be a surge or pulse of the EP-3 event has an age of between 18,000 and 19,500 year BP (bioturbation may have caused mixing in the sediment prior to turbidity current arrival). A similar age of 18,787 years BP was determined for pelagic sediment at the base of the penultimate turbidite in

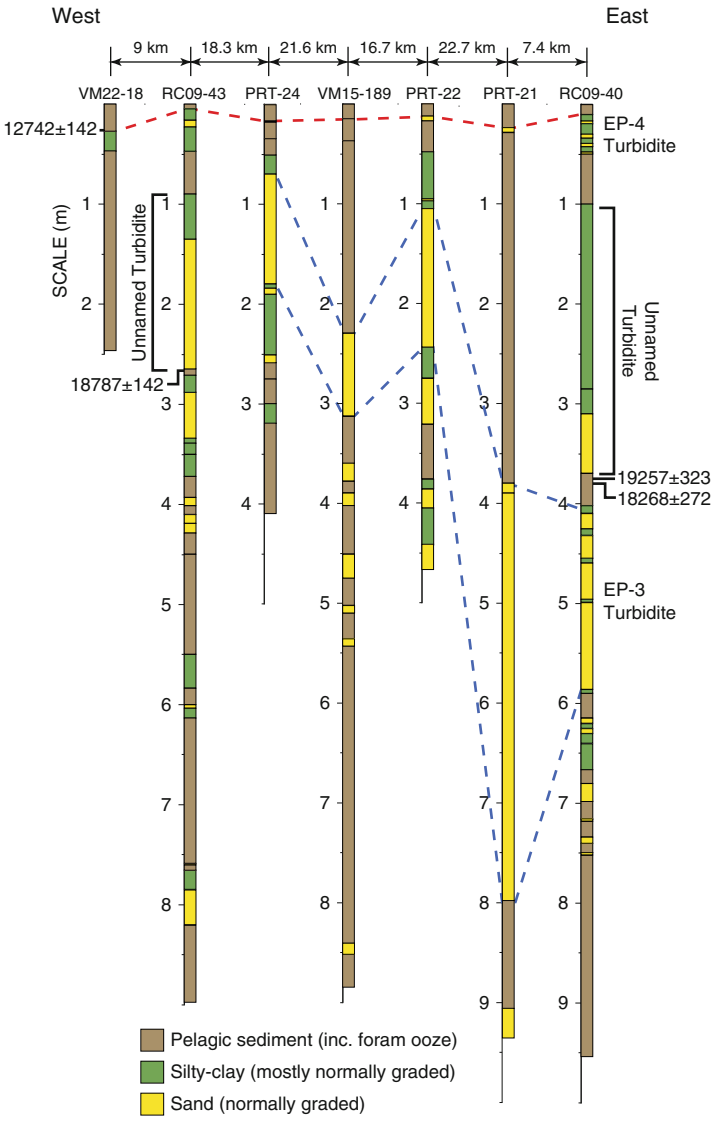

Fig. 55.4 Distal basin core correlation plot. Thick turbidites [Doull (1983) only assumes that the graded sands comprise the turbidite, but they often have a significant graded silty-clay tail] are present throughout the distal basin, the most prominent of which is the EP-3 turbidite. The youngest significant turbidite in RC09-40 (between the EP-4 and EP-3 turbidite of Doull (1983)) and RC09-43 has a basal age of between 18 and 19 ka. *Red dashed line* marks base of capping pelagic layer, *blue lines* mark upper and lower bounds of correlated turbidites. Correlation location shown on Fig. 55.1

RC09-38, which was not included in the Doull (1983) correlation. As with cores of the marginal slope, all cores analyzed in the distal basin are capped with a pelagic layer of variable, but not more than ~25 cm thickness. The age at the base of the capping pelagic layer in core VM22-8 at the western end of the distal basin (Fig. 55.4) is 12,742 ± 142 year BP (accumulation rate of ~2 cm/1,000 year).

55.2.2.3 PRT Axis

Sediments in the upper 9–10 m of the PRT axis are comprised primarily of pelagic sediments interrupted at various depths by sandy turbidites (Fig. 55.5). Doull (1983) identified three potentially correlative turbidites, although only turbidite MP-2 could be correlated well across the length of the PRT axis and based on turbidite thickness variations, entry point locations, and sand composition, attributed the Puerto Rico slope as the primary source of the material. The estimated volume of the combined MP-2 and EP-3 turbidites is approximately 1.9 km^3 (Doull 1983). As with sediments elsewhere throughout the trench, all cores have pelagic sediments of varying thickness at their top. Radiocarbon ages of pelagic sediment immediately below the MP-2 turbidites in cores RC09-38, RC09-39, and RC09-42 were found to be 22,731, 22,713, and 25,449 year BP, respectively. The 3,000 year older age in core RC09-42 may reflect additional erosion of pelagic material by the turbidity current, especially if this core was more proximal to the turbidity current entry point (eastern abyssal gap, Fig. 55.1) into the PRT axis.

55.3 Discussion and Conclusions

Geologic and geophysical data from the PRT show that mass transport processes, while prevalent across the entire region, may be spatially and temporally restricted. While attempts have been made to assign specific source areas along the edge of the carbonate platform to imaged deposits (Hearne 2004), such determinations are difficult and prone to error given the complex mixing of slope failure and channel flushing material from multiple sources and the ongoing tectonic deformation within the PRT.

Our analysis of available bathymetry, seismic reflection, and core data indicates that there has not been any large-scale collapse of the carbonate platform and/or marginal slope during the Late Pleistocene-Holocene. A lack of wide-spread deposition of blocky carbonate platform fragments in debris flow material strongly supports a process of progressive erosion and dissolution (scalloping, Mullins and Hine (1989); self-erosion, Schlager and Camber (1986)) and infrequent slope channel flushing as the primary sources of mass transport material entering the PRT basins. In fact the turbidites/debris flows penetrated by the cores are likely the result

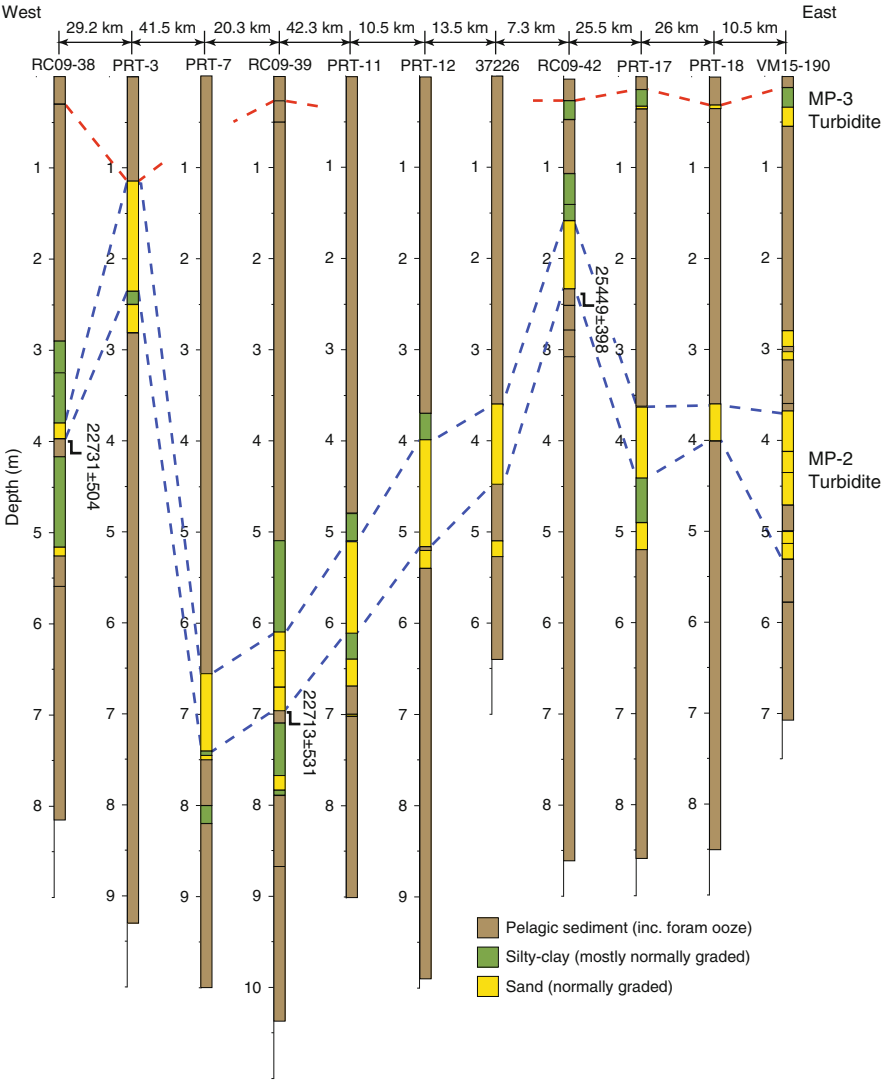

Fig. 55.5 PRT axis core correlation plot. Thick turbidites are less common than in the distal basin. The capping pelagic layer (base marked by *dashed red line*) is discontinuous across the PRT axis. Age of the MP-2 turbidite (*blue dashed lines*) is between 22.7 and 25.5 ka

of minor destabilization/channel flushing events given that Doull (1983) calculated the combined volume of the MP-2 and EP-3 turbidites to be only 1.9 km^3, ten times smaller than the maximum evacuation scar mapped by ten Brink et al. (2006) along the marginal slope. Interestingly, although the trench is a seismically active plate boundary, we find that there has not been significant turbidity current or debris flow activity within the trench for the last 18,000 years.

From a landslide-tsunami hazards perspective, long-term progressive margin erosion resulting in many small-scale failures suggests that there is currently a low probability of occurrence of a regionally destructive landslide-generated tsunami from the slope north of Puerto Rico. Non-catastrophic failure during the late Pleistocene-Holocene period may also indicate that the PRT has not experienced a high magnitude (>M8) earthquake capable of destabilizing large sections of the carbonate platform or marginal slope. That said, a landslide and local tsunami hazard does exist due to continued earthquake-triggered scalloping and/or self-erosion of the carbonate platform north of Puerto Rico as shown by the 1918 M7.2 Mona Passage earthquake/landslide and the resulting tsunami (López-Venegas et al. 2008).

Acknowledgments We would like to thank the captain and crew of the R/V Seward Johnson, Jim Broda, Heather Benway, Kate McMullen, and Rusty Lotti Bond and the staff of the LDEO core repository. EW9605 seismic data was acquired from the UTIG Academic Seismic Portal. Kathryn Scanlon, Lorena Moscadelli and Calvin Campbell provided valuable reviews. Any use of trade, product, or firm names is for descriptive purposes only and does not imply endorsement by the U.S. Government.

References

Chaytor JD, ten Brink US (2010) Extension in Mona Passage, Northeast Caribbean. Tectonophysics 493:74–92

Clague DA, Moore JG (2002) The proximal part of the giant submarine Wailau landslide, Molokai, Hawaii. J Volcanol Geotherm Res 113:259–287

Conolly J, Ewing M (1967) Sedimentation in the Puerto Rico Trench. J Sediment Res 37:44

Doull ME (1983) Turbidite sedimentation in the Puerto Rico Trench abyssal plain. Masters thesis, Duke University, 248 pp

Ewing J, Ewing M (1962) Reflection profiling in and around the Puerto Rico Trench. J Geophys Res 67:4729–4739

Gardner WD, Glover L, Hollister CD (1980) Canyons off northwest Puerto Rico: studies of their origin and maintenance with the nuclear research submarine NR-1. Mar Geol 37:41–70

Hearne ME (2004) Investigation of submarine landslide deposits the northern margin of Puerto Rico. MS thesis, University of North Carolina Wilmington, 84 pp

Le Friant A, Harford CL, Deplus C et al (2004) Geomorphological evolution of Montserrat (West Indies): importance of flank collapse and erosional processes. J Geol Soc Lond 161:147–160

López-Venegas A, ten Brink US, Geist EL (2008) Submarine landslide as the source for the October 11, 1918 Mona Passage tsunami: observations and modeling. Mar Geol 254:35–46

Mullins HT, Hine AC (1989) Scalloped bank margins: beginning of the end for carbonate platforms? Geology 17:30–33

Reimer P, Baillie M, Bard E et al (2009) INTCAL09 and MARINE09 radiocarbon age calibration curves, 0–50,000 years cal BP. Radiocarbon 51:1111–1150

Scanlon KM, Masson DG (1996) Sedimentary processes in a tectonically active region: Puerto Rico North Insular Slope. In: Gardner JV, Field ME, Twichell DC (eds) Geology of the US seafloor: the view from GLORIA. Cambridge University Press, Cambridge, pp 123–134

Schlager W, Camber O (1986) Submarine slope angles, drowning unconformities, and self-erosion of limestone escarpments. Geology 14:762–765

Schneidermann N, Pilkey OH, Saunders C (1976) Sedimentation on the Puerto Rico insular shelf. J Sediment Res 46:167–173

Schwab W, Danforth W, Scanlon K et al (1991) A giant submarine slope failure on the northern insular slope of Puerto Rico. Mar Geol 96:237–246

Stuiver M, Reimer PJ (1993) Extended 14C database and revised CALIB radiocarbon calibration program. Radiocarbon 35:215–230

ten Brink US, Geist EL, Andrews BD (2006) Size distribution of submarine landslides and its implication to tsunami hazard in Puerto Rico. Geophys Res Lett 33:L11307. doi:10.1029/2006GL26125

van Gestel JP, Mann P, Dolan JF et al (1998) Structure and tectonics of the upper Cenozoic Puerto Rico-Virgin Islands carbonate platform as determined from seismic reflection studies. J Geophys Res 103:30505–30530

Chapter 56
Age Estimation of Submarine Landslides in the La Aguja Submarine Canyon, Northwestern Colombia

Carlos A. Vargas and Javier Idarraga-García

Abstract La Aguja Submarine Canyon (LASC) is a remarkable bathymetric feature that cuts the continental margin of the Colombian Caribbean Coast offshore of the Santa Marta massif. This section of the margin is strongly influenced by two active strike-slip fault systems: the NNW-trending Santa Marta – Bucaramanga Fault (SMBF) and the EW-trending Oca- Fault (OF). Based on 6,500 km^2 of high resolution multibeam bathymetry and one 2D seismic reflection profile ($\sim$60 km), we identified submarine landslides associated with the LASC. Along the canyon we observe channel morphologies high sinuosity, variable widths (between 2 and 8 km), and both U- and V-shaped asymmetric cross sections. The occurrence of mud volcanoes in the surrounding area, some of which stand above the flanks of the canyon, is also common. The available data allowed us to identify 31 submarine landslides on the LASC flanks, between water depths of 1,200 and 3,285 m, with slopes ranging between 6.1° and 36.8°. Using numerical solutions of the diffusion equation of these scarps we estimate ages of between $<$1.0 to $\sim$631.6 ka. According to observations, the triggering mechanisms of landslides could be closely related to earthquakes originated in the convergence zone of SMBF and OF, and/or to the flanks instabilities driven by mud diapirism.

Keywords Submarine landslide • Scarp-fault dating • Diapirism • Continental margin

C.A. Vargas (✉)
Department of Geosciences, Universidad Nacional de Colombia at Bogotá, Bogotá, Colombia
e-mail: cavargasj@unal.edu.co

J. Idarraga-García
Colombian Institute for Marine and Coastal Research-INVEMAR, Santa Marta, Colombia
e-mail: javier.idarraga@invemar.org.co

S. Krastel et al. (eds.), *Submarine Mass Movements and Their Consequences*, Advances in Natural and Technological Hazards Research 37, DOI 10.1007/978-3-319-00972-8_56,

56.1 Introduction

Active continental margins are zones of high susceptibility to the occurrence of tsunamis in response to seismogenic events. These zones are also favorable for the development of submarine landslides due to tectonic and/or depositional over steepening of the continental slope. Many of these regions also support a wide array of infrastructure (ports, undersea cables, oil fields, etc.) with associated highly populated cities. The SW Caribbean region is a good example of one of these regions and is an area where rivers with high sediment flux as a result of erosion of the Andean Orogen, promote slope instability on the continental slope with or without participation of earthquakes.

While several studies have documented evidence of slope instabilities which move large amounts of sediments toward the Colombian and Venezuelan basins (e.g. Shepard 1973; Vernette et al. 1992), the geomorphologic characterization of the phenomenon has only been possible in the past decade due to the availability of high-resolution bathymetric data. One of the most prominent features detected in the bathymetry along the continental slope offshore the Colombian Caribbean Coast is the La Aguja submarine canyon. From early bathymetric surveys, it was thought that the LASC was seaward projection of a structure that crosses the NW segment of the Santa Marta Massif (Krause 1971).

In this work we present images on the geometry of the canyon, and describe some of its major geomorphologic features, such as associated submarine landslides. Using these geomorphic features and diffusion equations we estimate the age range over which the canyon was built. Also, we discuss the restrictions of the dating method used and the interpretations that may support its origin.

56.1.1 Geological Setting

The direction of relative motion of the Caribbean Plate with respect to South America Plate is generally agreed upon as being eastward, leading to a geodynamic configuration that results from a complex and evolving transpressive history throughout the Cenozoic (Mann and Burke 1984). The current active convergence of these plates is responsible for the current configuration of the South Caribbean Deformed Belt (SCDB), where ~2 cm/year Caribbean–South American convergence is accommodated along the Colombian Caribbean Coast in the form of low-angle thrust faults and fault-ramp folds (Audemard and Audemard 2002; Vargas and Mann 2013).

At least four geomorphological features dominating the study area: (a) the Magdalena Fan, a turbiditic system created by the accumulation of the sediments transported by the Magdalena river; (b) the Santa Marta massif (SMM), a pyramidal structure composed of Mesozoic and Cenozoic rocks which rises to 5,600 m and likely isostatically control a large segment NW of Colombia and Venezuela; (c) the

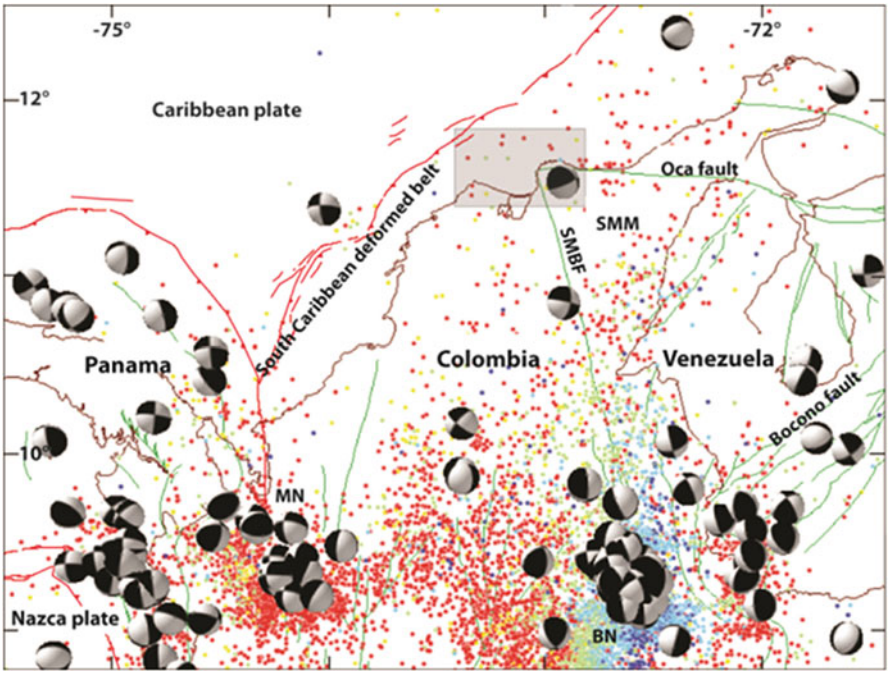

Fig. 56.1 Seismotectonic features of NW Colombia and location of the study area (*gray box*). Points correspond to hypocenters calculated by the National Seismological Network of Colombia (1993–2013). *Dots* represents events discriminated by depth, ranging from shallow (0–32 km in *red*) to intermediate depths (~170 km in *dark blue*). *Green lines* correspond to segments of regional faults. Surface expression of the boundary between the Caribbean and Nazca plates were drawn with *red lines*. Projected focal mechanisms were estimated by NEIC (1976–2013). The coast line has been drawn in *brown*. *BN* Bucaramanga earthquake nest, *MN* Murindo earthquake nest

Santa Marta – Bucaramanga fault (SMBF), which skirts the edge SW of the SMM; and (d) the Oca fault (OF), which runs along the northern edge of the SMM and possibly intersects the SMBF near the LASC (Fig. 56.1). Although seismotectonic activity associated with these geomorphic features is currently limited as shown by the sparse instrumental record of seismicity along their traces (Fig. 56.1), historical data suggests that they have been active in the recent past. In general, the seismic record is consistent with a convergence zone of low-angle accretion, that involves Mesozoic and Cenozoic lithologies, and where regional transpressional fault systems as SMBF and OF, partially dissipates movements along wide areas onshore and offshore.

Acoustic data and seismic surveys near the coast have indicated that some fluvial channels are connected to the LASC (Shepard 1973). Restrepo-Correa and Ojeda (2010) described the canyon as a feature that extends 115 km down the shelf and continental slope, from −10 to −3,200 m water depth. Restrepo-Correa and Ojeda (2010) also describe the presence of mud volcanoes which protrude from the

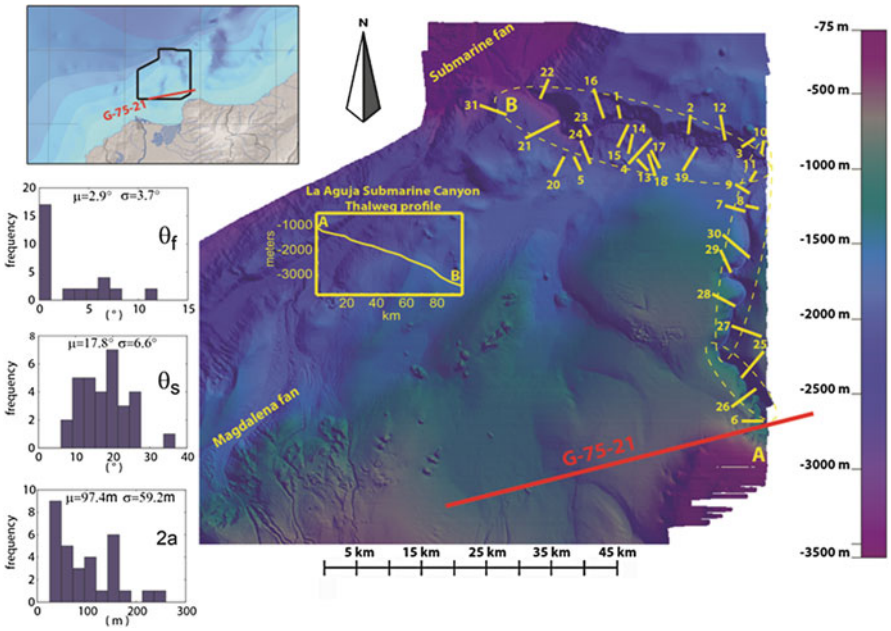

Fig. 56.2 *Inset on top left*: Location of bathymetric program in NW Colombia (*black polygon*) and screening of seismic line (*red line*) that crosses the headscarp of the LASC. *Center Image* presents the DTM showing the LASC and location of the seismic line. *Dashed yellow ellipses* indicate the three zones associated with changes in direction and suggested by Restrepo-Correa and Ojeda (2010) as: Inner, Middle and Outer reaches. A profile of the canyon thalweg, along points *A* and *B* have been drawn in *yellow lines*. *Smaller yellow lines* (1–31) have correspondence with scarp profiles where measurements were done. Histograms of the *left side* of the figure represent the statistical distributions of the measurements associated to the fan-slope angle (θ_f), scarp-slope angle (θ_s) and the effective vertical displacement of the scarp (*2a*)

seafloor adjacent to the canyon. These mud volcanoes make up to NW-SE trending belt over a 20-km wide zone. A steep scarp separates the continental slope from the abyssal plain of the Colombian Basin. The outflow end of the canyon coincides with a relatively flat area, which corresponds to a basin floor fan. Restrepo-Correa and Ojeda (2010) divided the canyon in three areas associated to breaks in direction: Inner, Middle and Outer reaches (Fig. 56.2).

56.1.2 Data and Methods

Bathymetric information used in the current study were acquired in 2002 aboard the R/V Baruna Jaya III using Reson SeaBat 8160 and Simrad EM12D multibeam

systems, and in 2006 aboard the M/V Ocean Endeavour using Simrad EM1002 and Simrad EM120 (11.25/12.75 kHz) multibeam systems by the National Hydrocarbon Agency of Colombia (ANH) and supplied to the Institute of Marine and Coastal Research of Colombia (INVEMAR). For the resulting Digital Terrain Models (DTM) these bathymetry data were gridded at spatial resolutions of 25 and 50 m. Although we utilized same data that used by Restrepo-Correa and Ojeda (2010) for describing geomorphology features of the canyon, our analyses were focused in proposing an age range of landslides which forming the LASC.

The LASC is the main feature detected by the bathymetric survey and is bounded by recent submarine mass failures. We performed quantitative geomorphologic scarp analyses to constrain the ages of its evolution. This study followed the methods of Hanks (2000) by applying the diffusion equation under transport-limited conditions. Equation (56.1) is a linear, second-order differential equation that relates the change in elevation H to time t using the proportionality constant κ and landscape curvature x (distance along the profile):

$$\frac{\partial H}{\partial t} = \kappa \frac{\partial^2 H}{\partial x^2} \tag{56.1}$$

where diffusivity $[L^2T^{-1}]$ varies with climate, scarp material, and scarp height. The slope aspect is considered constant over the timescales investigated. Scarp height reduction is expressed by Hanks (2000) as:

$$\left.\frac{\partial u}{\partial x}_{x=0}\right| - b = \frac{a}{\sqrt{\pi \kappa t}} \equiv tan\theta_s - tan\theta_f \tag{56.2}$$

In this reduction, $\theta_s = tan^{-1}\left(\left.\frac{\partial u}{\partial x}\right|_{x=0}\right)$ represents the maximum slope-scarp angle, $\theta_f = tan^{-1}b$ is the fan slope angle, and a is the effective half-vertical displacement.

Thirty-one bathymetric profiles of submarine landslides (see location and statistical distribution of associated parameters on Fig. 56.2) were compared with theoretical profiles estimated by numerical solutions of Eq. (56.1). A least-square fit was performed by iterative adjustment of measurements of the effective displacement ($2a$) and the angles θ_s and θ_f. Constant κ and variable t were merged for estimating values that best fitted the data. The resulting profiles are not exclusively dependent on κ or t, but rather their product. For example, the same profile will result for $\kappa = 1$ m^2/year and $t = 10$ year or $\kappa = 10$ m^2/year and $t = 1$ year. This methodology has been used in submarine scenarios (see e.g. Mitchell 1996; McAdoo and Simpson 2005; Vargas et al. 2012). Nevertheless, the applicability of method in underwater environments has not been widely used due to the limited knowledge of climate and erosion conditions on the evolution of submerged scarps.

One time-migrated seismic line of the "Bahia" Block (G-75-21; Fig. 56.3), acquired for oil exploration, was used for supporting interpretations regarding the substrate geometry of the canyon.

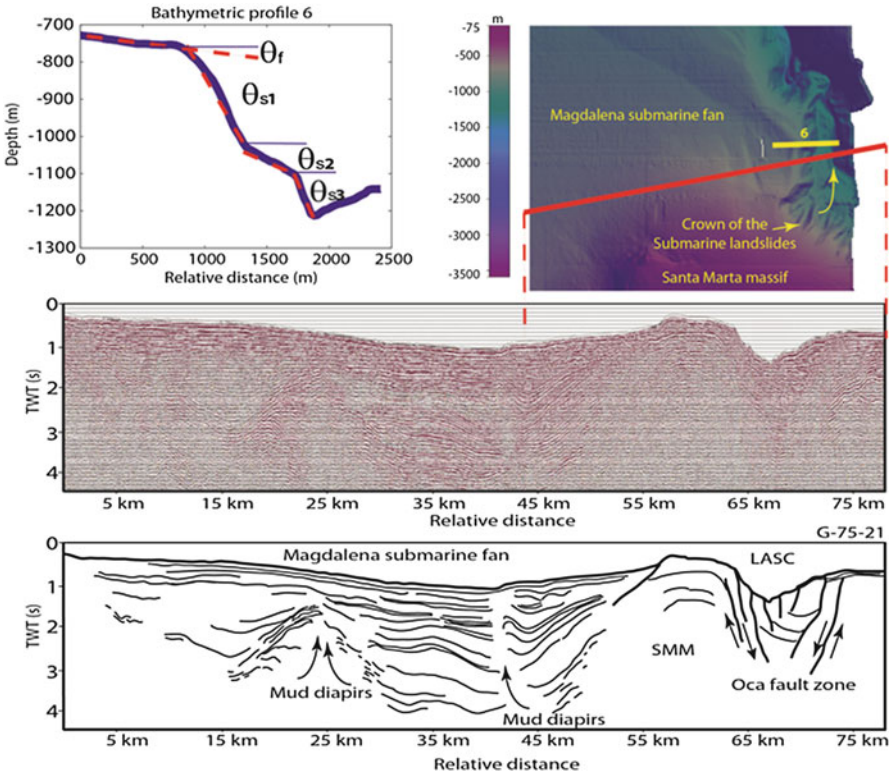

Fig. 56.3 *Inset top left*: Bathymetric profile #6 in the headscarp of the LASC suggesting at least three landslide events (θ_{s1}, θ_{s2} and θ_{s3}). *Inset top right*: Location of the profile (*yellow line*) and seismic line G-75-21 on the DTM. *Middle panel* correspond to the time-migrated seismic line without interpretation. *Lower panel* shows interpretation of the seismic record, where is possible to identify structural perturbations related to the OF, and intense diapirism in the western area. Large sedimentary sequence of the Magdalena fan is being intruded by diapirs

56.2 Results

The development of the canyon is complex and varies downslope which may be the result of changes in sedimentary processes, diapirism, and tectonic activity. Figure 56.3 illustrates bathymetric profile 6, located in the vicinity of the headscarp, which shows at least three scarp-slope changes with respect to the surrounding fan. These breaks in slope suggest three episodes of recent landsliding and highlight the present day geometry of the Inner Reach of the LASC. Seismic profiles suggests that the erosion-resistance contrast between the SMM and the zone of weakness related to the OF, could be responsible for enabling an area where the canyon was developed. Chowa et al. (2001) proposed a model that links the Kaoping submarine canyon in Taiwan with the development of diapiric activity surrounding

it, suggesting that the erosion process that favoured the canyon generated a reduction of confining pressures in sediments deposited and consequently promoted high diapirism activity in the area. This model may partially explain the diapiric activity that borders the LASC.

Bathymetric and seismic records did not reveal the trace of the SMBF within the study area suggesting that it has been recently inactive and easily disguised by recent sediments from the Magdalena Fan. However, following the model of Chowa et al. (2001), the trace of the fault may be associated with mud diapirism detected in the west of the canyon.

From the analysis of the 31 scarps, the measurements of θ_s, θ_f and $2a$, allowed estimation of κt values that indicate a broad range of relative diffusion ages of between ~407 and ~103.461 m^2 (Table 56.1). While measurements of slope remain low gradients ($\theta_f = 2.9° \pm 3.7°$; $\theta_s = 17.8° \pm 6.6°$) and are consistent with other observations in the region (e.g. Vargas et al. 2012); values of the vertical effective displacement are promoting high values of κt. Figure 56.4a illustrates the behaviour of these angles with respect to κt. Regardless of age, a relationship seems to exist between θ_s and θ_f when θ_f is greater than 2°.

56.3 Discussion and Conclusion

The Rio Magdalena has built throughout its recent history the largest delta influenced by waves in South America (Restrepo and Lopez 2008). Its sediment flux to the Caribbean Sea over the 27 years between 1972 and 1998 year-period yielded an annual sediment load of 144×10^6 t $year^{-1}$ (Syvitski et al. 2005), placing it as the main contributor of material in SW Caribbean. Its discharge is projected to several tens of kilometers offshore, contributing to a rapid accumulation of sediments on the continental slope, camouflaging the active tectonics and facilitating conditions for diapirism.

Although there is no global consensus on the mechanisms that explain the development of submarine landslides on continental shelves (active or passive) with slopes greater than 2°, the presence of these slopes in the study area (Fig. 56.4a) are indicative of instability and sensitivity to submarine landslides (e.g. Urlaub et al. 2012). The larger scarp-slope angles are located on the headscarp mainly, suggesting greater potential for the development of new submarine slides (Fig. 56.4b).

Although the κt map (Fig. 56.4b) does not show a clear pattern of κt values along the canyon, the highest values located in the middle portions of the directional segments identified in the canyon (Inner, Middle and Outer reaches), indicating greater stability in those areas.

The κ constant values for marine zones might vary by several orders of magnitude. Mitchell (1996) suggested values around 0.007 m^2 $year^{-1}$ for the Galapagos spreading centre. McAdoo and Simpson (2005) estimated values oscillating between 10^{-3} and 10^{-4} m^2 ka^{-1} for sedimentary landslides on continental slopes

Table 56.1 Results of the geomorphologic scarp-dating analyses in 31 bathymetric profiles located along of the LASC (Fig. 56.2)

Profile	Latitude (°)	Longitude (°)	Depth (m)	Fan slope (°) θ_f	Slope-scarp (°) θ_s	Effective vertical displacement (m) $2a$	Relative age (m^2) κt
1	11.984	−74.335	−2,440.6	0.0	10.2	73.5	13,204.6
2	11.877	−74.238	−2,115.1	0.0	16.3	158.3	23,290.8
3	11.852	−74.149	−2,021.3	0.0	18.7	149.3	15,537.4
4	11.830	−74.301	−1,724.2	0.0	10.4	43.5	4,453.6
5	11.821	−74.394	−2,070.1	3.0	23.7	57.0	1,732.8
6	11.464	−74.139	−1,136.5	11.9	36.8	43.4	519.1
7	11.760	−74.169	−1,714.2	6.4	21.3	40.7	1,695.1
8	11.761	−74.151	−1,814.0	0.0	19.6	25.5	407.2
9	11.788	−74.157	−1,753.6	0.0	27.5	153.1	6,878.4
10	11.844	−74.133	−1,744.4	0.0	17.0	36.9	1,157.8
11	11.804	−74.146	−1,925.4	0.0	24.2	71.6	2,025.5
12	11.871	−74.184	−1,708.6	0.0	10.7	44.6	4,429.3
13	11.814	−74.296	−1,756.2	5.6	19.1	46.3	2,760.4
14	11.840	−74.312	−1,924.4	0.0	13.8	259.7	88,403.9
15	11.862	−74.331	−2,391.7	0.0	15.7	151.7	23,103.5
16	11.909	−74.355	−2,404.6	0.0	14.8	102.7	12,057.7
17	11.826	−74.282	−1,913.8	8.2	26.5	38.8	956.4
18	11.817	−74.289	−1,819.4	6.8	18.4	96.8	16,494.4
19	11.829	−74.237	−1,877.7	4.7	15.1	62.2	8,724.3
20	11.821	−74.422	−1,865.9	0.0	25.0	113.8	4,754.8
21	11.865	−74.453	−2,292.0	3.9	14.6	134.0	38,758.5
22	11.918	−74.442	−3,002.3	0.0	21.5	171.9	15,127.4
23	11.875	−74.384	−2,418.6	11.2	20.9	163.0	62,753.1
24	11.830	−74.376	−2,138.1	0.0	20.5	83.5	3,952.3
25	11.545	−74.147	−871.2	0.0	7.9	158.4	103,237.5
26	11.492	−74.166	−952.7	8.2	13.2	96.0	90,261.1
27	11.584	−74.150	−931.1	2.8	6.1	55.7	71,465.0
28	11.629	−74.182	−1,297.6	5.8	10.8	44.9	19,710.4
29	11.681	−74.184	−1,352.3	6.4	16.6	213.0	103,461.2
30	11.697	−74.163	−1,551.1	6.2	11.2	57.6	32,007.4
31	11.898	−74.507	−2,612.9	0.0	24.8	73.5	2,011.8

of several regions in the world (North Sea; Gulf of Cadiz; western Mediterranean near to Ibiza Island; and Offshore Oregon). Nevertheless, Vargas et al. (2012) in their attempt to date the Mira submarine canyon (Colombia) found that the main uncertainty is the definition of a plausible diffusion constant κ and that a linear solution to the scarp-fault diffusion hypothesis may be far from an accurate solution. Testing of different scenarios by using a finite element diffusion model in order to identify the triggering event that initiated the Mira Canyon suggested a κ constant value ranging between 0.001 and 1.33 m^2 $year^{-1}$ for an associated event occurred in 3,200 year BP. Ratzov et al. (2012) using other methods suggested that the Mira Canyon age may range between 53 and 67 ka. Accepting this new age interval, the κ

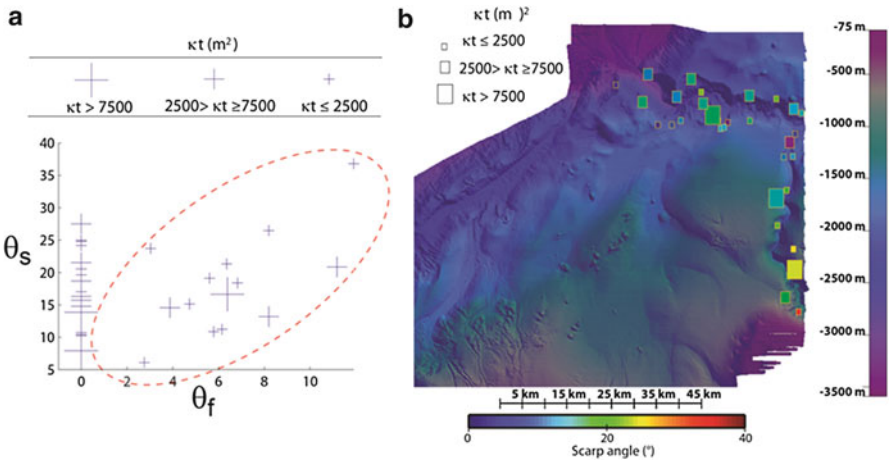

Fig. 56.4 (**a**) Slope of the fan (θ_f) *vs* slope of the escarpment for various ranges of κt. The *red dashed ellipse* indicates an apparent direct relationship between θ_s and θ_f for θ_f values greater than 2°, in similar form suggested by other authors (e.g. Urlaub et al. 2012). (**b**) Projection of the κt values and angles of the scarps in the DTM. Apparently the largest angles of the scarps are located near to the headscarp

values around the Mira canyon are oscillating between 0.015 and 0.057 m^2 $year^{-1}$, which are consistent with the previous range suggested by Vargas et al. (2012).

We tested the limits of the κ value inferred from data reported by Ratzov et al. (2012) for calculating ages. Estimations of the age of the landslide located in the headscarp (profile #6) suggest an origin time ranging between ~13.4 and ~16.9 ka. However, using $\kappa = 0.015$ m^2 $year^{-1}$, almost twice the value reported by Mitchell (1996), we got large contrasts of age along the canyon (between <1.0 and ~631.6 ka) that suggest a complex history of this structure. In any case, the estimations of this work constitute one of the first attempts to constrain the time of development of submarine landslides in SW Caribbean.

Acknowledgments The authors would like to express their appreciation to the ANH and the INVEMAR for permitting use of the data. We also thank to the Assigned Editor Dr. J. Chaytor and the reviewers Dr. L. Moscardelli and V. Huerfano. This study was partially supported by COLCIENCIAS and UPC-MICCIN-FEDER. Seismic sections were done with IHS software.

References

Audemard FE, Audemard FA (2002) Structure of the Merida Andes, Venezuela: relations with the South America–Caribbean geodynamic interaction. Tectonophysics 345:299–327

Chowa J, Leea JS, Liub CS, Leec BD, Watkins JS (2001) A submarine canyon as the cause of a mud volcano — Liuchieuyu Island in Taiwan. Mar Geol 176:55–63

Hanks TC (2000) The age of scarplike landforms from diffusion-equation analysis. In: Nollet JS, Sowers JM, Lettis WR (eds) Quaternary geochronology: methods and applications. AGU series. American Geophysical Union, Washington, DC

Krause DC (1971) Bathymetry, geomagnetism, and tectonics of the Caribbean Sea north of Colombia. In: Donnely TW (ed) Caribbean geophysical, tectonic, and petrologic studies: Geological Society of America Memoir. Geological Society of America, Boulder, pp 35–54

Mann P, Burke K (1984) Cenozoic rift formation in the northern Caribbean. Geology 12:732–736

McAdoo B, Simpson G (2005) Morphometric dating of submarine landslide scarps. Geophys Res Abstr 7:EGU05-A-00629

Mitchell NC (1996) Creep in pelagic sediments and potential for morphologic dating of marine fault scarps. Geophys Res Lett 23(5):483–486

Ratzov G, Sosson M, Collot JY, Migeon S (2012) Late quaternary geomorphologic evolution of submarine canyons as a marker of active deformation on convergent margins: the example of the South Colombian margin. Mar Geol 315–318:77–97

Restrepo JD, Lopez S (2008) Morphodynamics of the Pacific and Caribbean deltas of Colombia, South America. J S Am Earth Sci 25:1–21

Restrepo-Correa IC, Ojeda GY (2010) Geologic controls on the morphology of La Aguja submarine canyon. J S Am Earth Sci 29:861–870

Shepard F (1973) Sea floor off Magdalena Delta and Santa Marta Area, Colombia. Geol Soc Am Bull 84:1955–1972

Syvitski JPM, Kettner AJ, Correggiari A, Nelson BW (2005) Distributary channels and their impact on sediment dispersal. Mar Geol 222–223:75–94

Urlaub M, Zerbos A, Talling PJ, Masson DG, Clayton CI (2012) How do $\sim 2^{\circ}$ slopes fail in areas of slow sedimentation? A sensitivity study on the influence of accumulation rate and permeability on submarine slope stability. In: Submarine mass movements and their consequences. Advances in natural and technological hazards research 31. Springer, Dordrecht

Vargas CA, Mann P (2013) Tearing and breakoff of subducted slabs as the result of collision of the Panama arc-indenter with northwestern South America. Bull Seismol Soc Am. doi:10.1785/0120120328

Vargas CA, Mann P, Gomez C (2012) Morphologic expression of accretionary processes and recent submarine landslides along the southwestern Pacific margin of Colombia. In: Submarine mass movements and their consequences. Advances in natural and technological hazards research 31. Springer, Dordrecht

Vernette G, Mauffret A, Bobier C, Briceno L, Gayet J (1992) Mud diapirism, fan sedimentation and strike-slip faulting, Caribbean Columbia margin. Tectonophysics 202(2–4):335–349

Chapter 57
Deep-Sea Turbidite Evidence on the Recurrence of Large Earthquakes Off Shakotan Peninsula, Northeastern Japan Sea

Ken Ikehara, Takuya Itaki, Taqumi TuZino, and Koichi Hoyanagi

Abstract Twelve deep-sea turbidites were identified in the Holocene sequence of a core collected from the western foot of the Kaiyo Seamount, located near the fault area of the 1940 Shakotan-oki earthquake, northern Okushiri Ridge, eastern margin of the northern Japan Sea. On the basis of the geological, tectonic, and topographical settings of the site, the turbidites are interpreted as of earthquake origin (seismoturbidite). Age determinations on radiolarian remains in the sediments suggested that the uppermost sediments, younger than 3 ky BP, were lost during the coring. Four clear faunal boundaries, at 4, 6, 8.5, and 10.5 ka, were recognized. The turbidite recurrence interval in the deep-sea basin indicated an average recurrence interval for large earthquakes of 500–1,000 years around the Kaiyo Seamount during the early- to middle Holocene.

Keywords Turbidite • Japan Sea • Recurrence interval • Shakotan-oki earthquake • Radiolaria

57.1 Introduction

The eastern margin of the Japan Sea is thought to be the boundary between the Eurasian and North American plates (e.g. Nakamura 1983). The initiation of subduction along the boundary has been inferred to be 1.8 Ma (Tamaki et al. 1992), and no clear subduction structure has been observed (Tamaki and Honza 1985).

K. Ikehara (✉) • T. Itaki • T. TuZino
Institute of Geology and Geoinformation, Geological Survey of Japan, AIST, Tsukuba 305-8567, Japan
e-mail: k-ikehara@aist.go.jp

K. Hoyanagi
Institute of Geological Sciences, Faculty of Science, Shinshu University, Matsumoto 390-8621, Japan

S. Krastel et al. (eds.), *Submarine Mass Movements and Their Consequences*, Advances in Natural and Technological Hazards Research 37, DOI 10.1007/978-3-319-00972-8_57,

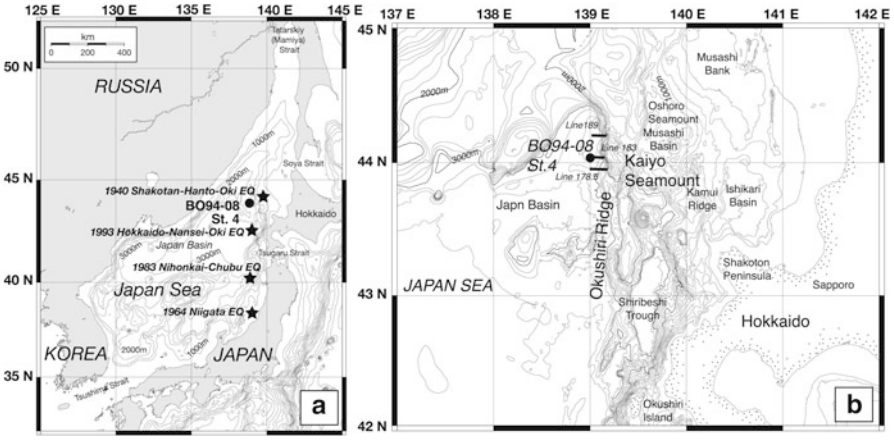

Fig. 57.1 Index (**a**) and bathymetric map (**b**) of the studied area showing the core site and the sub-bottom profile transects in Fig. 57.4. Epicenters of historic earthquakes are shown in **a**

Therefore, the eastern margin is thought to be a young, immature plate boundary. During the twentieth century, four large thrust-type earthquakes with magnitudes larger than 7.5 occurred along the margin: the 1940 Shakotan-oki, the 1964 Niigata, the 1983 Nihonkai-chubu, and the 1993 Hokkaido-nansei-oki earthquakes (Fig. 57.1). All of them generated tsunamis, and caused serious damages. To predict forth-coming large earthquakes along the margin and to reduce the damage they cause, it is very important to understand the recurrence interval and nature of each earthquake. Unfortunately, the epicenters of the four large earthquakes were located beneath the sea bottom. Furthermore, historical documents recording past large earthquakes are very limited for the northern part of the margin because of the low population in Hokkaido, the nearest land to the 1940 Shakotan-oki and 1993 Hokkaido-nansei-oki earthquakes. Therefore, it is very difficult to estimate the time interval between large earthquakes. Natural records such as of liquefaction, sudden changes in the sedimentary environment, event deposits by tsunamis, and slope failures are important for determining the occurrence of past large earthquakes. Heezen and Ewing (1952) in a classical paper showed that submarine slope failures and turbidity currents were initiated by the 1929 Grand Banks earthquake off Newfoundland, NW Atlantic. Furthermore, Adams (1990) estimated paleoseismicity by studying deep-sea turbidites, which were products of submarine slope failures, in the Cascadia subduction zone. Therefore, the seismo-turbidite has been used as a deep-sea paleoseimological tool (e.g. Goldfinger et al. 2007; Gutierrez-Pastor et al. 2013). The deep-sea basins of the northern Japan Sea are areas of modern mud deposition, where no strong currents move the sand on their floor. The deep-sea basins near Okushiri Ridge are far from land and coastal shelves, so large storm waves are unlikely to generate slope failures. Therefore, these deep-sea basins are suitable sites for a paleoseismicity analysis based on deep-sea turbidite.

Here, we report the occurrence of turbidites in a core collected from the western foot of the Kaiyo Seamount, which is just west of the fault area of the 1940 Shakotan-oki earthquake. Then the recurrence interval of large earthquakes is discussed on the basis of the radiolarian-based Holocene chronology in the core.

57.1.1 Geological and Seismological Settings

The Okushiri Ridge is a north-south trending topographic high about 400 km long. The ridge consists of asymmetric anticlines and thrusts (Tamaki and Honza 1985) reflecting E-W compression during the Quaternary. In the study area, two seamounts, the Kaiyo and Oshoro seamounts, compose the ridge. The Kaiyo Seamount rises 2,500 m above the flat seafloor of the Japan Basin, and its summit is at a water depth of 938 m. The Oshoro Seamount (summit water depth: 219 m) lies NNE of the Kaiyo Seamount. The ridge displays a clear asymmetric profile in E-W section. The western flank is a steep escarpment with slope >30°. In contrast, the eastern flank is more gently dipping with 5°. The Okushiri Ridge is composed of basaltic rocks overlain by oceanic sediments (Miyashita et al. 1989; Tokuyama et al. 1989, 1992). Many active faults (thrusts) are reported at the western foot of the Kaiyo Seamount and along the eastern and western feet of the Oshoro Seamount (Tokuyama et al. 1992; Okamura et al. 1998, 2002).

Large earthquakes have occurred along the Okushiri Ridge. The Shakotan-oki earthquake with surface wave magnitude Ms = 7.5 (Abe 1981) occurred at midnight, August 2, 1940. The tsunami generated by this earthquake caused the deaths of ten peoples. Satake (1986) re-examined the earthquake and estimated its fault area as 100 km × 35 km near the Oshoro Seamount. Therefore, large earthquakes can be generated in the study area. The recurrence interval of large earthquakes in this area is unknown, however, although a tsunami generating earthquake also occurred in 1792 (the Shiribeshi-oki earthquake, M = 7 1/4).

57.1.2 Materials and Methods

A sediment core, BO89-08 TB-4, was collected from the eastern margin of the Japan Basin, western foot of Kaiyo Seamount, northern Okushiri Ridge (latitude 44°04.1′ N, longitude 139°00.4′ E, water depth 3,500 m; Fig. 57.1). The core was described by Ishii et al. (1999). We re-examined the core and soft-X-ray radiographs and identified 13 thin sand or silt layers in the last deglacial-Holocene hemipelagic clay sequence of the core (Fig. 57.2). The thickest sand layer is 9.5 cm thick. All of the sand or silt beds had sharp and erosional basal contact, and some layers show a clear upward-fining graded structure and parallel and ripple lamination (Fig. 57.3). Thin layers less than 1 cm thick have no structure, but we interpreted all of the sand or silt layers as turbidites, because of their sharp and erosional basal contacts. To

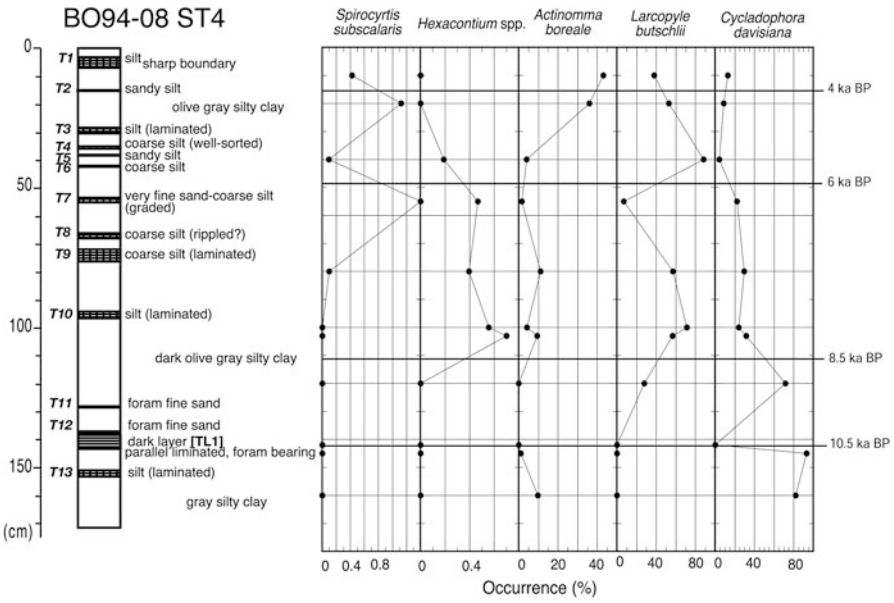

Fig. 57.2 Columnar section of the obtained core and occurrence of selected radiolarian species and radiolarian horizons

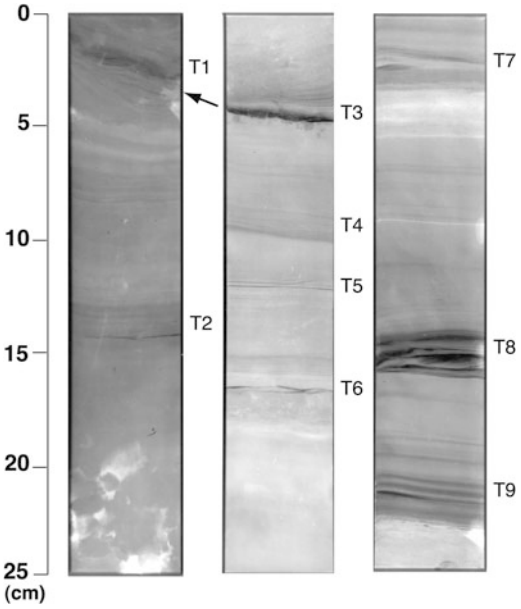

Fig. 57.3 Soft-X-ray radiographs of the uppermost 75 cm of the obtained core. *Arrow* indicates the horizon of sharp discontinuous boundary

determine the depositional age, we examined radiolarian faunal assemblages in the hemipelagic mud at intervals of a few to 20 cm, because of the shallow (around 2,000 m) calcium carbonate compensation depth in the modern Japan Sea. Itaki and Ikehara (2003), however, used radiolarian faunal assemblages to determine the late Quaternary sequence in the northern Japan Sea.

Ten sub-bottom profiles along the transects crossing the Kaiyo Seamount were obtained during the GH99 cruise by the Geological Survey of Japan. The acoustic facies of the records were analyzed, and the sedimentological processes of each facies were inferred from their acoustic characters.

57.2 Results and Discussions

57.2.1 Origin of Turbidites

Twelve turbidite layers were found above the 10.5 ky BP horizon. Several possible trigger mechanisms for turbidite deposition, such as the direct discharge of sediment suspended in water from rivers, storm waves, a sudden large sediment supply, tsunamis, and earthquakes, have been proposed. Because the studied site is far from land and coastal shelves, and because the Ishikari and Musashi Basins and the Kamui and Okushiri Ridges intervene between coastal shelves and the site (Fig. 57.1), we considered the influence of rivers and storms to be negligible. The top of the Kaiyo Seamount is at a water depth of 938 m, which is too deep for storm waves at the sea surface to trigger turbidite deposition. On the other hand, large earthquakes such as the 1940 Shakotan-oki and the 1993 Hokkaido-nansei-oki earthquakes occurred along the Okushiri Ridge. The studied core was collected at the western foot of the steep slope of the Kaiyo Seamount, which is west of the fault area of the 1940 Shakotan-oki earthquake. Occurrence of a major active fault at the foot slope by seismic reflection surveys (Tokuyama et al. 1992; Okamura et al. 1998, 2002) suggests the potential for earthquake generation in this area.

Three types of acoustic and topographic features were recognized on the foot slope: step type, talus type, and flat type. The step type occurred mainly in the southern part of the seamount (Fig. 57.4). Some of the observed mounds might have been formed by sediment sliding down the slope. Coarse-grained gravity flow deposits were found in short cores collected by the submersible Shinkai 6500 from the base of the slope of the southern Kaiyo Seamount (Okamura et al. 2002). The talus type typically dips gently basinward and is found in the central part of the seamount (Fig. 57.4). No internal reflector was observed. The talus-type sea bottom is smooth or has a small hyperbolic pattern. The smooth sea floor of the talus footslope has a reflector that was a little stronger than that of the basin floor, which is characterized by flat topography and finely stratified acoustic facies. The morphology of the sedimentary body of the talus footslope and its acoustic character indicates that the talus footslope is composed by the coarse materials derived

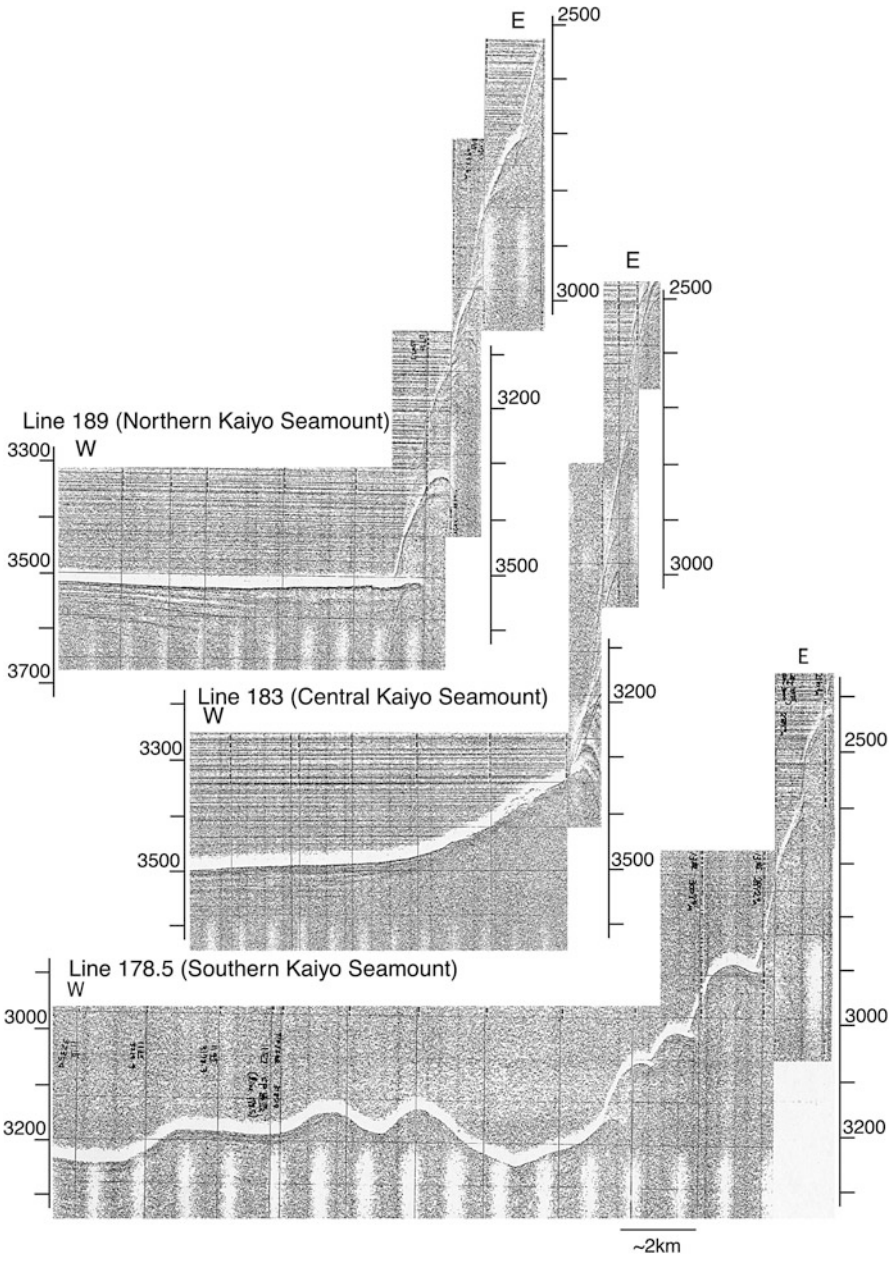

Fig. 57.4 Sub-bottom profile records from the western slope of the Kaiyo Seamont. Locations of the survey lines are shown in Fig. 57.1

from the slope. A flat but stronger reflection, sometimes with a small hyperbolic pattern, was found in the northern part (Fig. 57.4). The strong seafloor reflection and lower acoustic penetration suggest the presence of coarse-grained materials. These facts indicate that gravity flow deposits from the western slope of the Kaiyo Seamount are widely distributed on the foot slope. Therefore, the most probable trigger mechanism for the turbidite deposition is submarine slope failure along the western slope of the Kaiyo Seamount generated by shaking during large earthquake near the site.

57.2.2 Recurrence Intervals of Turbidites

Late Quaternary sediments of the Japan Sea are characterized by alternating of dark- and light-colored sediment layers (Tada et al. 1992). The youngest dark layer (TL1), which contains many foraminifer tests and high amount of organic carbon, was dated to 10.5 ky BP (Oba et al. 1995; Itaki and Ikehara 2003). In core BO89-08 TB-4, a clear dark-colored sediment layer with many foraminifer tests was observed at the depth of 138.5–143.5 cm from the core top. Radiolarian assemblages at and below the dark layer indicated that this dark layer corresponds to TL1. The rapid decrease in *Cycladophora davisiana* such as occurs at TL1 and the rapid increase of *Larcopyle butschlii* above TL1 (Itaki and Ikehara 2003) were clearly recognized. Furthermore, three additional chronological horizons (8.5, 6, and 4 ky BP; Itaki and Ikehara 2003) above 10.5 ky BP were identified in the core: a rapid increase in *Hexacontium* spp. and *Actinomma boreale* at 8.5 ky BP, a rapid decrease in *Hexacontium* spp. at 6 ky BP, and a decrease in *Spirocyrtis subscalaris* at 4 ky BP.

On the basis of the radiolarian chronology in the northern Japan Sea (Itaki and Ikehara 2003), two turbidite layers occur between the chronological horizons of 10.5 and 8.5 ky BP, four between 8.5 and 6 ky BP, four between 6 and 4 ky BP, and one between the 4 ky BP horizon and the uppermost sharp boundary below the uppermost turbidite. Therefore, the recurrence interval for turbidite deposition was estimated as 500–1,000 years. As mentioned above, the most probable trigger for the turbidite deposition was a large earthquake near the sampling site. Thus, we estimated the average recurrence interval of large earthquakes in the study area as 500–1,000 years.

Shimokawa and Ikehara (2002) suggested on the basis of deep-sea turbidite records from the Shiribeshi Trough that the recurrence interval of large earthquakes in the fault area of the 1993 Hokkaido-nansei-oki earthquake was 1,000–1,500. Nakajima and Kanai (1995) reported a recurrence interval in the 1983 Nihonkai-chubu earthquake fault area of 200–300 years. The present result is between those two estimates. Awata (2002) compiled the recurrence intervals of active faults on land in central to northern Japan, and found the shortest intervals (1,000–1,500 years) along the Shinano-gawa belt. The present result suggests a higher level of seismic activity along the Okushiri Ridge than along active land faults.

There are two possible source areas for the large earthquakes that triggered the turbidites west of the Kaiyo Seamount. One is a rupture of the active thrust at the western foot of the seamount (Tokuyama et al. 1992; Okamura et al. 1998), which would presumably cause a large collapse of the slope. Another possible origin is a rupture near the Oshoro Seamount. The source area of the 1940 Shakotan-oki earthquake, which is the largest earthquake known to have occurred near the Kaiyo Seamount, has been inferred to have been near the Oshoro Seamount (Satake 1986). Therefore, there is a possibility that the turbidites were triggered by different earthquakes near the Kaiyo Seamount, which may account for the relatively short recurrence interval of large earthquakes in this area. Even if each rupture occurred independently, the estimated recurrence interval is almost the same as that in the Shinano-gawa belt. Therefore, the study area has a high potential to generate large earthquakes.

57.3 Conclusion

Deep-sea turbidites in a core collected from the western foot of the Kaiyo Seamount, which is west of the fault area of the 1940 Shakotan-oki earthquake, were examined. The geological, tectonic, and topographic settings of the site suggest that the turbidites are of earthquake origin. On the basis of the radiolarian chronology for the Holocene sequence in the northern Japan Sea, the recurrence interval of large earthquakes is estimated as 500–1,000 years. This is shorter than that reported for active land faults in central to northern Japan, and indicates more tectonic activity along the Okushiri Ridge. However, there are two possible source areas for the large earthquakes that triggered the turbidite deposition: an active thrust at the western foot of the Kaiyo Seamount and active faults near the Oshoro Seamount, which is the fault area of the 1940 Shakotan-oki earthquake.

Acknowledgements We thank to the captain, officers, crew, and on-board scientists of the BO94-08 cruise, especially the late Prof. Jiro Ishii of Hokkaido Tokai University, for helping with the sampling, and those of the GH99 cruise, especially Dr. Kohsaku Arai of the Geological Survey of Japan for obtaining the sub-bottom profiling records. Thanks also to Dr. Yukinobu Okamura for his critical reading of an early version of the manuscript. We thank Prof. Michael Strasser and Dr. Toshiya Kanamatsu for their constructive comments, which improved the manuscript.

References

Abe K (1981) Magnitudes of large shallow earthquakes from 1904 to 1980. Phys Earth Planet Inter 27:72–92

Adams J (1990) Paleoseismicity of the Cascadia subduction zone: evidence from turbidites off the Oregon-Washington margin. Tectonics 9:569–583

Awata Y (2002) Highly stressed zones in late Quaternary. In: Otake M, Taira A, Ota Y (eds) Active faults and seismo-tectonics of the eastern margin of the Japan Sea. University of Tokyo Press, Tokyo, pp 122–132 (in Japanese)

Goldfinger C, Morey AE, Hans Nelson C, Gutierrez-Pastor J, Johnson JE, Karabanov E, Chaytor J, Eriksson A, Party SS (2007) Rupture lengths and temporal history of significant earthquakes on the offshore and north coast segments of the Northern San Andreas Fault based on turbidite stratigraphy. Earth Planet Sci Lett 254:9–27

Gutierrez-Pastor J, Hans Nelson C, Goldfinger C, Escutia C (2013) Sedimentology of seismo-turbidites off the Cascadia and northern California active tectonic continental margins, northwest Pacific Ocean. Mar Geol 336:99–119

Heezen BC, Ewing M (1952) Turbidity currents and submarine slumps, and the 1929 Grand Banks Earthquake. Am J Sci 250:849–873

Ishii J, Hoyanagi K, Sekijima Y, Maeda T, Ikehara K (1999) Piston core sample collected from the northern Japan Basin deep-sea floor. Earth Sci (Chikyu-kagaku) 53:135–146 (in Japanese with English abstract)

Itaki T, Ikehara K (2003) Radiolarian biozonation for the upper Quaternary in the Japan Sea. J Geol Soc Jpn 109:96–105

Miyashita S, Tanaka T, Monma H, Tokuyama H, Soh W, Kuramoto S, Ishii J (1989) Observation using the submersible "Shinkai 2000" at the northern part of the Okushiri Ridge – a section of the oceanic crust of the Japan Sea. JAMSTECR Deepsea Res 5:85–100 (in Japanese with English abstract)

Nakajima T, Kanai Y (1995) Recurrence intervals of earthquakes inferred from turbidites near the epicenter area of the 1983 Japan Sea Earthquake. Zisin 48:223–228 (in Japanese with English abstract)

Nakamura K (1983) Possible nascent trench along the eastern Japan Sea as the convergent boundary between Eurasian and North American plates. Bull Earthq Res Inst Univ Tokyo 58:711–722 (in Japanese with English abstract)

Oba T, Murayama M, Matsumoto E, Nakamura T (1995) AMS 14C ages of Japan Sea cores from the Oki Ridge. Quat Res (Daiyonki-kenkyu) 34:289–296 (in Japanese with English abstract)

Okamura Y, Kuramoto S, Sato M (1998) Active structures and their relation to earthquakes along the eastern margin of the Japan Sea. Bull Geol Surv Jpn 49:1–18 (in Japanese with English abstract)

Okamura Y, Satake K, Takeuchi A, Gamo T, Kato C, Sasayama Y, Nanayama F, Ikehara K, Kodera T (2002) Tectonic, geochemical and biological studies in the eastern margin of the Japan Sea – preliminary results of Yokosuka/Shinkai 6500 YK01-06 Cruise. JAMSTEC Deep-sea Res 20:77–114

Satake K (1986) Re-examination of the 1940 Shakotan-oki earthquake and the fault parameters of the earthquakes along the eastern margin of the Japan Sea. Phys Earth Planet In 43:137–147

Shimokawa K, Ikehara K (2002) Paleo-earthquake records in sediments. In: Otake M, Taira A, Ota Y (eds) Active faults and seismo-tectonics of the eastern margin of the Japan Sea. University of Tokyo Press, Tokyo, pp 95–108 (in Japanese)

Tada R, Koizumi I, Cramp A, Rahman A (1992) Correlation of dark and light layers and the origin of their cyclicity in the Quaternary sediments from the Japan sea. In: Pisciotto Ka, Ingle JC Jr, Von Bareymann MT, Barron J et al (eds) Proceedings of ODP, scientific results, 127/128, Part 1, College Station, TX (Ocean Drilling Program), pp 577–601

Tamaki K, Honza E (1985) Incipient subduction and obduction along the eastern margin of the Japan Sea. Tectonophysics 119:381–406

Tamaki K, Suyehiro K, Allan J, Ingle JC Jr, Pisciotto KA (1992) Tectonic synthesis and implications of Japan Sea ODP drilling. In: Tamaki K, Suyehiro K, Allan J, McWilliams M et al (eds) Proceedings of ODP, scientific results, 127/128, Part 2, College Station, TX (Ocean Drilling Program), pp 1333–1348

Tokuyama H, Kuramoto S, Soh W, Miyashita S, Takeuchi A, Monma H, Tanaka T (1989) Deep-sea submersible survey of the exposed profile of the Japan Basin Crust – observation on the fault scarps bounded by the western margin of the Okushiri Ridge, off west Hokkaido. JAMSTECR Deepsea Res 5:101–110 (in Japanese with English abstract)

Tokuyama H, Kuramoto S, Soh W, Miyashita S, Byrne T, Tanaka T (1992) Initiation of ophiolite emplacement: a modern example from Okushiri Ridge, Northeast Japan Arc. Mar Geol 103:323–334

Chapter 58
Characteristics of Magnetic Fabrics in Mass Transport Deposits in the Nankai Trough Trench Slope, Japan

Yujin Kitamura, Michael Strasser, Beth Novak, Toshiya Kanamatsu, Kiichiro Kawamura, and Xixi Zhao

Abstract Submarine landslides are a potential risk to coastal areas all over the world. Studies of mass transport deposit (MTD) contribute to our understanding of the nature and process of submarine landslides. Scientific drilling provides material containing geological records of past landslide events. However, MTDs may not always be uniquely discernible by visual inspection. We applied magnetic fabric analysis to the drilled cores to examine the potential of magnetic fabrics for use in identifying MTDs. Among the sites drilled in the framework of the Nankai Trough Seismogenic Zone Experiment (NanTroSEIZE), in Japan, of the Integrated Ocean Drilling Program (IODP), multiple occurrences of MTDs were observed in the recovered cores. We focused on the slope sediments in the footwall of the megasplay fault at Sites C0008 and C0018. The shape parameter (T) and the orientation of

Y. Kitamura (✉)
Department of Earth and Planetary Science, University of Tokyo, 7-3-1 Hongo, Bunkyo-ku, Tokyo 113-0033, Japan

Institute for Research on Earth Evolution, Japan Agency for Marine-Earth Science and Technology, Yokosuka, Japan
e-mail: ykitamura@eps.s.u-tokyo.ac.jp

M. Strasser
Geological Institute, ETH Zurich, Zurich, Switzerland

B. Novak
Department of Geology, Western Washington University, Bellingham, WA, USA

T. Kanamatsu
Institute for Research on Earth Evolution, Japan Agency for Marine-Earth Science and Technology, Yokosuka, Japan

K. Kawamura
Department of Geosphere Sciences, Yamaguchi University, Yamaguchi, Japan

X. Zhao
Department of Earth and Planetary Sciences, University of California Santa Cruz, Santa Cruz, USA

S. Krastel et al. (eds.), *Submarine Mass Movements and Their Consequences*, Advances in Natural and Technological Hazards Research 37, DOI 10.1007/978-3-319-00972-8_58,

the axes of magnetic ellipsoids are distinctively scattered in MTDs at Site C0018. Downward increments in the lineation parameter (*L)* near the bottom of the MTDs may result from shear localization near the basal sliding plane. This, in combination with visual observation, suggests cohesive mass flow. By contrast, the results from sediments previously described as mass transport complexes at Site C0008 showed the opposite trend, suggesting a different process during transportation; i.e. the mass transport body evolved to become a complete debris flow. Our results show that magnetic fabric analysis is potent for describing MTDs and their internal structures. This finding may extend the methodology for describing MTDs and add to the discussion of the dynamic formation process.

Keywords Submarine landslide • D/V Chikyu • NanTroSEIZE • Accretionary prism • Megasplay fault • IODP Expeditions 316 and 333

58.1 Introduction

The trench slope along subduction zones is a common location of submarine landslides. Submarine slope failures can be promoted by the intrinsic environment of subduction zones and their depositional conditions such as shaking due to earthquakes or tectonic steepening. The anisotropy of magnetic susceptibility (AMS) is a rapid and nondestructive mean of investigating rock fabrics. The AMS method has been used as a reliable strain indicator in geological settings where conventional strain markers are scarce and it is currently best to investigate subtle tectonic related fabrics in clay sedimentary rocks at the early stages of deformation. This method has successfully provided strain information for various types of accretionary prism material: e.g., present marine sediments (e.g. Owens 1993), ancient accretionary prisms (e.g. Kanamatsu et al. 1996; Yamamoto 2006) and even highly deformed plate boundary rocks (e.g. Kitamura et al. 2005; Kitamura and Kimura 2012).

Here we present magnetic fabric data for the trench slope sediments from Sites C0008 and C0018, from which mass transport deposits (MTDs) were recovered during IODP Expeditions 316 and 333, respectively. Our aim is to examine the potential of magnetic fabrics in identifying MTDs.

58.2 Geological Overview of IODP Sites C0008 and C0018

The Nankai Trough of southwest Japan is among the most extensively studied subduction zones in the world, and has a well documented 1,300-year history of great earthquakes and associated tsunamis (Ando 1975). Here, the Philippine Sea plate is being subducted beneath the Eurasian continental plate at a convergence rate of 4 cm/year (Seno et al. 1993). The expeditions were conducted as a part of the Nankai Trough Seismogenic Zone Experiment (NanTroSEIZE), a multi-expedition

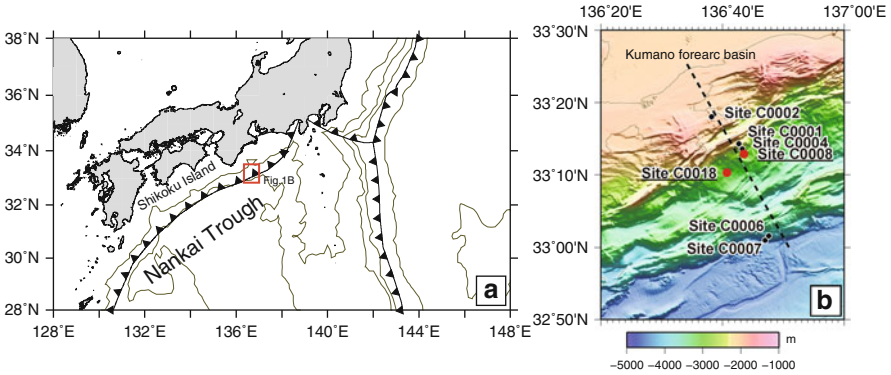

Fig. 58.1 Location map of Sites C0008 and C0018 in the Nankai Trough, off Japan

project for characterizing and monitoring the subducting plate boundary process in the Nankai Trough. Multiple drillings have recovered mass transport deposits in various places along a transect across the trough (e.g., Expedition 316 Scientists 2009; Kitamura and Yamamoto 2012; Strasser et al. 2012).

58.2.1 Site C0008

Site C0008 is located at a water depth of ~2,775 m, ~26 km landward of the trench axis and a few hundred meters seaward of the megasplay fault (Fig. 58.1) (Kinoshita et al. 2009). It recovered the slope sediments (Unit I) and underlying accretionary prism (Unit II) in the footwall of the megasplay fault. Two lithologic units were identified at Site C0008 (Expedition 316 Scientists 2009). The uppermost slope sediment (lithologic Unit I) consists of a 272 m (in Hole C0008A) thick succession of hemipelagic silty clay with thin sand beds and volcanic ash layers. In the shallow sediments in Subunit IA from 6.93 to 15.50 meter below the seafloor (mbsf) at Hole C0008A, a slump deposit was observed (Strasser et al. 2011). At the base of Unit I, a 40 m section of clayey gravel containing rounded clasts of clay and pumice constitutes Subunit IB. This subunit was interpreted as a series of mass-wasting deposits (described as a mass-transport complex (MTC) by Expedition 316 Scientists 2009) accumulated in the lower slope basin, possibly during an early stage of the Late Pliocene to the Early Pleistocene basin formation. Structural observations of the two holes drilled at Site C0008 indicate that the main structural features consist of subhorizontal bedding and normal faults (Expedition 316 Scientists 2009). Normal faults do not show any preferred orientation, suggesting that they reflect vertical compaction. In Hole C0008A, the porosity of discrete samples decreases with depth from ~65 % at the surface to 50 % at 270 mbsf (Expedition 316 Scientists 2009).

58.2.2 Site C0018

Site C0018 is located ~7.5 km southwest of Site C0008 and ~3 km seaward from the megasplay fault tip in a slope basin at 3,112 m water depth (Fig. 58.1). The site was selected to recover MTDs downslope from the megasplay fault zone (Expedition 333 Scientists 2012 and Strasser et al. 2012).

Sediments cored at Site C0018 were subdivided into two lithologic subunits, Units IA and IB (Expedition 333 Scientists 2012). Subunit IA is mainly composed of bioturbated hemipelagic mud intercalated with layers of varying coarse and fine volcanic ash and MTDs. Subunit IB consists of sandy turbidites interbedded with silty clay. The depositional ages of the sediments at Site C0018 are <1.67 Ma at the bottom of the borehole and about ~1 Ma at the boundary of Subunits IA and IB.

Six intervals of MTDs occur within Subunit IA. They range in thickness from 0.5 to 61 m and have a cumulative thickness of 98 m. For the recognition of MTDs in a single drill site, onboard imaging by X-ray computed tomography (CT) scans of recovered cores provided efficient and clear criteria in addition to the conventional visual core description (Expedition 333 Scientists 2012). Physical properties data show that MTD intervals display an increased compaction gradient compared with the average porosity-depth trend, and slight reversals (porosity increasing with depth) are observed near the base of MTDs 2, 3, 5 and 6 (Expedition 333 Scientists 2012; Strasser et al. 2012).

58.3 Method

In this study, AMS measurements were made on a total of 813 samples (7 or 10 cm^3 volume) from Sites C0008 ($n = 330$) and C0018 ($n = 483$). Clayey or silty samples were collected from every core section, avoiding specific features such as veins, nodules and shear bands, and were measured with a KLY-4S Kappabridge magnetic susceptibility meter at the Japan Agency for Marine-Earth Science and Technology. As much as possible, we selected fine-grained clayey samples. Onboard data suggest that the magnetic minerals may be a mixture of titano-magnetite and clay minerals as reported in this area (e.g. Kitamura et al. 2010).

Magnetic susceptibility is a proportion of the intensity of the induced magnetic field to that of the applied magnetic field. AMS represents the geometrical alignment and intensity of mineral fabrics as a magnetic ellipsoid, which is commonly linked with the strain ellipsoid. The ellipsoids expressed with the principal susceptibility axes (K1 > K2 > K3) and the minimum axis K3, in particular, are widely regarded as the orientation of maximum shortening.

We present the following parameters derived from the principal susceptibility axes for discussion: The lineation parameter L (= K1/K2) and the flattening parameter F (= K2/K3) commonly used for structural geology, the anisotropy

degree (P') and the shape parameter (T), an amended expression of the *L-F* diagram (Flinn diagram) in the polar coordinate system proposed by Jelinek (1981), *Km*, the bulk magnetic susceptibility.

Km reflects the amount of magnetically susceptible components in the specimen and thus displays the lithologic difference. *L-F* and P'-T are each a pair of factors expressing the shape of magnetic ellipsoids but are different in their main focus. L and F indicate the intensity of the shape components, lineation and flattening, respectively. Given both L and F, we know the shape of the ellipsoid. T itself provides the shape information (oblate if $0 < T < 1$ and prolate if $-1 < T < 0$), where the intensity of distortion compared to the true sphere is presented by P'. Therefore, P′-T are useful for discussing the shape in general while L-F are strong when focusing on the lineation or flattening components.

For normally deposited and compacted marine sediments, it is expected that P' shows a gradual increase with depth in association with the reduction of porosity and T displays random plots in the shallow part shifting to the oblate field (Kitamura et al. 2010). This compaction trend is seen as a stable L and increasing F with depth. A vertical K3 axis is expected for gravitational compaction (e.g. Kanamatsu et al. 2012).

58.4 Results

At Site C0008, AMS shape parameter T generally shows positive values, indicating that the sediments are under compactive conditions (Fig. 58.2). Porosity clearly decreases with depth for about 50 m from the top of the core, whereas it shows no significant change below 50 mbsf. A stable P' down to about 150 and 100 mbsf at Holes C0008A and C0008C, respectively, presumably supports impeded compaction in the shallow sediments. An increase in *Km* at the same depths is associated with an abundance of ash layers (Expedition 316 Scientists 2009). Steeply inclined K3 axes indicate vertical loading in general. The abrupt change in the inclination of the K3 axes in the cores in the top 25 m that are associated with similar shifts in other parameters such as porosity, T and the inclination of K1 suggests an early stage of compaction. However, gentle K3 values of less than 60° occasionally appear throughout Subunit IA below the sediments with early compaction. These samples do not show any particular tendency in other parameters. We speculate that these apparently rotated samples contain dispersed ash that is not visible, as the lower portion of Subunit IA that is abundant in ash shows similar outliers in the K1 and K3 inclinations. Sediments from Subunit IB of the MTD show signs of compaction: porosity reduction with depth; high F; high P′ and positive T; vertical K3. The higher value of *Km* in Subunit IB may enhance such distinct shape information. Regardless of the atypical samples of gentle K3 axes, the sediments at Site C0008 represent down-hole compaction with an interval of impeded compaction in the lower portion of Subunit IA.

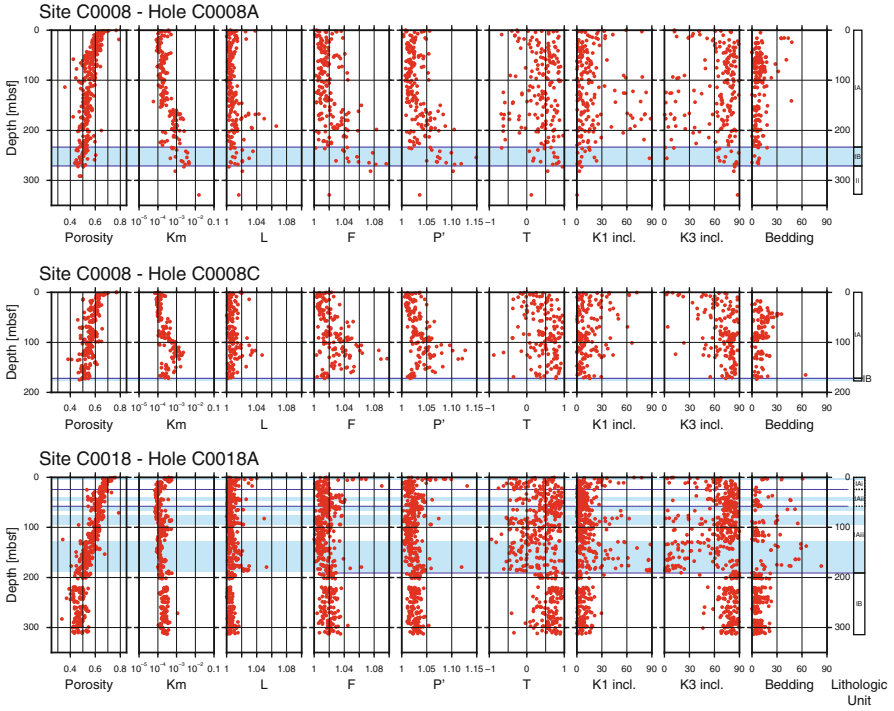

Fig. 58.2 Down-hole profile of porosity, AMS parameters and bedding dip at IODP Sites C0008 and C0018. Intervals of the mass transport deposits are highlighted (Expedition 316 Scientists 2009; Expedition 333 Scientists 2012)

At Site C0018, the T value shows a scattered distribution and low P' in the upper 50 mbsf, indicating unconsolidated deposits. Converging T to the positive value in the deeper succession, except within the MTDs, agrees with the trend of compaction against depth inferred from the porosity data. The parameters of T and the axes of magnetic ellipsoids (the inclination of K1 and K3) as well as the bedding dip show remarkable scatter in the MTD intervals. *Km* at Site C0018 reflects a slight difference in lithology between Subunits IA and IB. The sediments at Site C0018 are characterized by sediment compaction with positive T and vertical K3, although the down-hole progress of compaction is not clear, as well as MTDs with scattered T and K1/K3.

58.5 Discussion and Summary

The results from Site C0018 present AMS analyses as powerful tools for recognizing MTDs, in addition to visual descriptions and X-CT image analyses. In the MTD intervals at Site C0018, the scattered shape parameter T suggests the remobilization

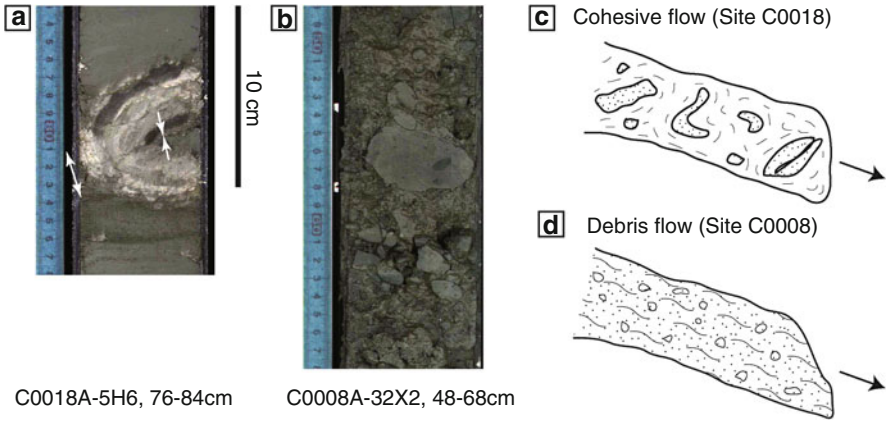

Fig. 58.3 Typical examples of MTDs from Sites (**a**) C0018 and (**b**) C0008. Arrows indicate the orientation of plausible maximum strain around the fold hinge. Schematic illustration of (**c**) cohesive flow in Site C0018 and (**d**) debris flow in Site C0008

and redeposition (or rearrangement) of the magnetic carrier particles. The low anisotropy degree P′ and variable T correspond to spherical magnetic ellipsoids, which show up accordingly in the disordered orientation of the ellipsoid axes. This change is more clearly recognizable in the P' and T diagrams (for example, in MTD 6 and Subunit IB) than in the L and F diagrams (Fig. 58.2). The remaining bedding planes indicate that the overall sedimentary structure is not completely destroyed within the MTDs. Thus the possible mechanism for magnetic fabric disorder in the MTD may be heterogeneous development of stretching and shortening fabrics in the sediments by slumping within the transporting mass, i.e. shortening in the inner hinges of local folds and stretching in the outer hinges (Fig. 58.3). Two intervals of coherent sediments between MTD 1 and 2 and MTD 5 and 6 also show scattered values of T. In the upper interval this is because of unconsolidated sediment, but no clear cause for the lower interval was identified. Table 58.1 shows the average of T in MTDs and coherent intercalated intervals presenting distinct T variations in MTDs. Here we learn that the MTDs can be identified by systematic change in the scattering of T and the orientation of the magnetic ellipsoid axes. Thus, AMS analysis can enforce the traditional method of MTD recognition by visual core description.

Some parameters bear information on the internal structure and processes of MTD formation. The lineation parameter slightly increases with depth near the base of MTDs 2, 3, 5 and 6 (Fig. 58.2). This increase is associated with a porosity kick back at the base of the MTDs; i.e., the sediments in the lowermost MTD appear to be overconsolidated. We speculate that the loading and shearing near the basal boundary of the transporting mass promoted mechanical dewatering and lineation fabrics. These observations may reflect localized shear flow near the basal sliding plane of transporting debris.

Table 58.1 Average T parameters in the MTDs and coherent intervals in between

	Depth interval (mbsf)	Average *T*		
		MTD	Coherent	
Site C0018				
	0.00–1.43		0.54	
MTD1	1.43–4.28	−0.02		
	4.28–39.45		0.29	
MTD2	39.45–46.73	0.18		
	46.73–58.01		0.68	
MTD3	58.01–65.75	0.46		
	56.75–66.44		0.30	
MTD4	66.44–66.93	0.19		
	66.93–75.91		0.63	
MTD5	75.91–94.37	0.12		
	94.37–127.55		0.32	
MTD6	127.55–188.57	0.11		
	188.57–313.66		0.59	
Average C0018		0.15	0.48	
Site C0008A				
Unit IA	0.00–234.55		0.34	
Unit IB (MTC)	234.55–272.46	0.46		
Unit II	272.46–329.36		(0.54)	*n=3*
Site C0008C				
Unit IA	0.00–170.90		0.42	
Unit IB (MTC)	170.90–176.20	(0.57)		*n=2*

The AMS results from MTD in Subunit IB at Site C0008 contradict the results from MTDs at Site C0018. A high P′ and positive *T* as well as high *F* indicate well-compacted sediment (Fig. 58.2). The average *T* value in MTD is higher than that in coherent interval by contrast (Table 58.1) and vertical K3 axes and horizontal bedding do not demonstrate disturbance, suggesting the promotion of compaction. The MTD was reported as unconsolidated "gravels" in Subunit IB (Expedition 316 Scientists 2009). Preliminary results from coring at Site C0022 located between Sites C0004 and C0008 confirmed similar occurrences of mudclast gravels (Moore et al. 2013). The visual inspection of the cores suggests submarine landslide deposits, although this was accompanied by no particular AMS anomaly. Similarly, the slump deposits in the shallow Subunit IA at Site C0008 (see Sect. 58.2.1) do not show scattering in the AMS parameters. The AMS data from chaotic sediments in Subunits IA and IB imply a different type of MTD, which can be ascribed to a different dynamic process during transportation. The mass transport process to create this AMS pattern would be a debris flow that enforced particles to redeposit, resulting in an isotropic magnetic fabric near the surface and oblate fabrics at greater depths, and such fabrics are commonly observed in sediments under diagenetic compaction. This means that the debris flow here is associated with the re-sedimentation process. This interpretation is consistent with what was previously inferred from sedimentological data (Strasser et al. 2011). Interestingly,

evidence for overconsolidation was found in the porosity data in the shallow slump and in the AMS data in the deeper MTD. This apparent overconsolidation is possibly due to uplift associated with the removal of mass at this site suggested by the scars (Expedition 316 Scientists 2009).

In summary, the MTDs that occurred at Site C0018 are formed by ductile flow during transportation, causing a scattered shape parameter and magnetic ellipsoid orientation, while in contrast, the MTDs at Site C0008 are formed by debris flows under conditions where both erosion and deposition take place (Fig. 58.3). These features correspond to the proposed classifications of submarine landslides, i.e. the MTDs in Site C0018 correspond to the "debris avalanche" (Masson et al. 2006) or "discrete cohesive slide" or "blocky flow" (Ogata et al. 2012), whereas the MTDs in Site C0008 match the definition of "debris flow" in both studies cited. Our results showed that the AMS analysis is (1) apt to detect a specific kind of MTD formed with cohesive flow, and (2) in combination with visual description and X-CT analysis, the AMS method can be used to discriminate another kind of MTD that had evolved to a debris flow in which all the transporting particles broke up and lost cohesion, leading to complete re-sedimentation.

Acknowledgements This research used samples and data provided by the Integrated Ocean Drilling Program. This work was partially supported by KAKENHI 19GS0211 and 21107001. We thank K. Tsuchida (Marine Works Japan Co. Ltd.) for providing technical support with regard to the AMS measurements. The IODP Expeditions 316 and 333 could not have been completed without the devoted contributions of those involved. Careful review and critical comments by David Völker and Yoshitaka Hashimoto improved this manuscript.

References

Ando M (1975) Source mechanisms and tectonic significance of historical earthquakes along Nankai Trough, Japan. Tectonophysics 27:119–140

Expedition 316 Scientists (2009) Expedition 316 site C0008. In: Kinoshita M, Tobin H, Ashi J, Kimura G, Lallemant S, Screaton EJ, Curewitz D, Masago H, Moe KT (eds) Expedition 314/315/316 scientists, Proceedings of the integrated ocean drilling program, vol 314/315/316. Integrated Ocean Drilling Program Management International, Inc., Washington, DC. doi:10.2204/iodp.proc.314315316.136.2009

Expedition 333 Scientists (2012) Site C0018. In: Henry P, Kanamatsu T, Moe K (eds) Expedition 333 scientists, Proceedings of the integrated ocean drilling program, vol 333. Integrated Ocean Drilling Program Management International, Inc., Tokyo. doi:10.2204/iodp.proc.333.103.2012

Jelinek V (1981) Characterization of the magnetic fabric of rocks. Tectonophysics 79:63–67

Kanamatsu T, Herroro-Bervera E, Taira A, Saito S, Ashi J, Furumoto AS (1996) Magnetic fabric development in the tertiary accretionary complex in the Boso and Miura Peninsulas of central Japan. Geophys Res Lett 23:471–474

Kanamatsu T, Pares J, Kitamura Y (2012) Pliocene shortening direction in Nankai Trough off Kumano southwest Japan, Sites IODP C0001 and C0002, Expedition 315; anisotropy of magnetic susceptibility analysis for paleostress. Geochem Geophys Geosyst 13:Q0AD22

Kinoshita M, Tobin H, Ashi J, Kimura G, Lallemant S, Screaton EJ, Curewitz D, Masago H, Moe KT, Expedition 314/315/316 Scientists (2009) NanTroSEIZE stage 1: investigations of seismogenesis, Nankai Trough, Japan. In: Proceedings of the integrated ocean drilling

program, vol 314/315/316. Integrated Ocean Drilling Program Management International, Inc., Washington, DC. doi:10.2204/iodp.proc.314315316.2009

Kitamura Y, Kimura G (2012) Dynamic role of tectonic mélange during interseismic process of plate boundary mega earthquakes. Tectonophysics 568–569:39–52

Kitamura Y, Yamamoto Y (2012) Records of submarine landslides in subduction input recovered by IODP Expedition 322, Nankai Trough, Japan. In: Yamada Y et al (eds) Submarine mass movements and their consequences. Springer, Dordrecht, pp 659–670

Kitamura Y, Sato K, Ikesawa E, Ikehara-Ohmori K, Kimura G, Kondo H, Ujiie K, Onishi CT, Kawabata K, Hashimoto Y, Mukoyoshi H, Masago H (2005) Melange and its seismogenic roof decollement: a plate boundary fault rock in the subduction zone – an example from the Shimanto Belt, Japan. Tectonics 24:TC5012. doi:5010.1029/2004TC001635

Kitamura Y, Kanamatsu T, Zhao X (2010) Structural evolution in accretionary prism toe revealed by magnetic fabric analysis from IODP NanTroSEIZE Expedition 316. Earth Planet Sci Lett 292:221–230. doi:210.1016/j.epsl.2010.1001.1040

Masson DG, Harbitz CB, Wynn RB, Pedersen G, Løvholt F (2006) Submarine landslides: processes, triggers and hazard prediction. Philos Trans R Soc A 364:2009–2039

Moore G, Kanagawa K, Strasser M, Dugan B, Maeda L, Toczko S, The Expedition 338 Scientists (2013) NanTroSEIZE Stage 3: NanTroSEIZE plate boundary deep riser 2. IODP preliminary report, 338. doi:10.2204/iodp.pr.338.2013

Ogata K, Mutti E, Pini GA, Tinterri R (2012) Mass transport-related stratal disruption within sedimentary mélanges: examples from the northern Apennines (Italy) and south-central Pyrenees (Spain). Tectonophysics 568–569:185–199

Owens WH (1993) Magnetic fabric studies of samples from Hole 808C, Nankai Trough. In: Hill IA, Taira A, Firth JV, et al (eds) Proceedings of the ODP scientific results, College Station, TX (Ocean Drilling Program), pp 301–310

Seno T, Stein S, Gripp A (1993) A model for the motion of the Philippine Sea plate consistent with NUVEL-1 and geological data. J Geophys Res 98(B10):17941–17948

Strasser M, Moore G, Kimura G, Kopf A, Underwood M, Guo J, Screaton E (2011) Slumping and mass-transport deposition in the Nankai forearc: evidence from IODP drilling and 3-D reflection seismic data. Geochem Geophys Geosyst 12:Q0AD13. doi:10.1029/2010GC003431

Strasser M, Henry P, Kanamatsu T, Moe KT, Moore GF, IODP_Expedition_333_Scientists (2012) Scientific drilling of mass transport deposits in the Nankai accretionary wedge: first results from IODP Expedition 333. In: Yamada Y et al (eds) Submarine mass movements and their consequences. Springer, Dordrecht, pp 671–681

Yamamoto Y (2006) Systematic variation of shear-induced physical properties and fabrics in the Miura-Boso accretionary prism: the earliest processes during off-scraping. Earth Planet Sci Lett 244:270–284

Part IX
Outcrops of Ancient Submarine Landslides

Chapter 59
New Concepts on Mass Wasting Phenomena at Passive and Active Margins of the Alpine Tethys: Famous Classical Outcrops in the Berchtesgaden – Salzburg Alps Revisited. Part A: Jurassic Slide/Debrite Complexes Triggered by Syn-Sedimentary Block Faulting

Rüdiger Henrich, Karl-Heinz Baumann, and Torsten Bickert

Abstract Jurassic strata exposed in outcrops along road cuts and trails as well as saw cut wall sections of "technical marmor" quarries at Adnet close to Salzburg and Waidring were studied for their depositional features, their geometries of sediment bodies, syn-depositional deformation and re-deposition structures as well as tectonic features. A spectacular mass wasting complex at Rote Wand/ Mount Steinplatte near Waidring (Austria, Tirol) was studied. Development of this complex indicates that in a first phase downward gliding almost intact slide blocks plugged into the underlying bedded nodular strata. In turn, this slide was immediately overrun by semi-consolidated slumped deposits, which partly disintegrated into pebbly mudstones. On top of the mass sealing by three debris flows is observed. We assume that the emplacement of the slide/slump complex occurred as one single event triggered by syn-sedimentary block faulting at the passive Early Jurassic Alpine margin. Eventually deposition of the first debrite covering the slide/slump complex was also related to this phase. In addition, a broad spectrum of mass wasting deposits is described from Liassic strata on the paleoslope of the drowned Rhaetian reef complex at Adnet and the surrounding basins.

Keywords Passive and active Alpine margins • Slides • Slumps • Debrites • Synsedimentary tectonics

R. Henrich (✉) • K.-H. Baumann • T. Bickert
MARUM and Faculty of Geosciences, University of Bremen, Bremen, Germany
e-mail: henrich@uni-bremen.de

S. Krastel et al. (eds.), *Submarine Mass Movements and Their Consequences*, Advances in Natural and Technological Hazards Research 37, DOI 10.1007/978-3-319-00972-8_59,

59.1 Introduction

59.1.1 Study Areas and Previous Studies

The Berchtesgaden–Salzburg Alps bear spectacular outcrops of Triassic to Cretaceous strata of the Alpine Tethys that are embedded in a fascinating alpine scenario. In addition, here in the Tyrolean nappe, wide areas are less affected by later tectonic overprinting providing the unique chance to study original paleogeogaphic settings as well as the geometries and evolutionary patterns of facies distribution.

At the end of the Triassic drowning of the huge Triassic reef – platform complexes of the East Alpine Shelf was induced by transgression associated with sea level rise concurrent with rifting and subsequent onset sea floor spreading in the Penninic ocean (Fig. 59.1). This induced an overall change of depositional regimes towards progressively deepening pelagic environments. These hemipelagic to pelagic Jurassic strata contain increasing amounts of various types of mass wasting deposits. Bernoulli and Jenkyns (1970) analysed the well exposed basinal pelagic Jurassic succession in the Glasenbach gorge south of Salzburg where a

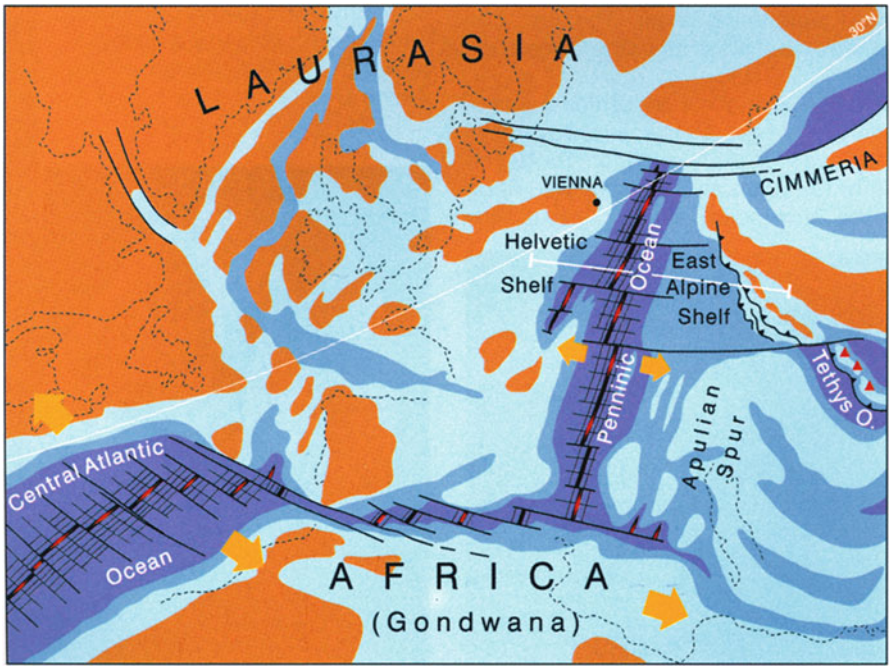

Fig. 59.1 Early Jurassic plate tectonic model of the Alpine Tethys (Modified from Rocky Austria 2000)

broad spectrum of mass wasting deposits including red nodular pebbly mudstones, slide/debrite complexes, and turbidite beds are exposed. Böhm (1992) and Böhm et al. (1995, 1999) studied the microfacies and analysed sedimentary regimes of Lower to Middle Jurassic strata including breccia occurrences deposited over submerged Rhätian reef mounds and on submarine swells in the Osterhorn mountains south of Salzburg.

59.1.2 Aims of This Study

Primary targets of this study are (1) to analyse the occurrences of different types of mass wasting deposits intercalated into Jurassic strata of the Berchtesgaden – Salzburg Alps, (2) to characterise and map their depositional features in detail, and (3) to develop new models displaying the changes in sediment dynamics and evolutionary trends during their formation. To achieve this, we will critically review the main findings of previous studies and evaluate their depositional models and evolutionary concepts. In, addition we characterise shifts in depositional settings of the background sediments and highlight which were the implications for their sustainability to mass wasting processes. Finally we discuss potential triggers and compare the evolutionary stages of the studied mass wasting complexes.

59.2 Methods

Jurassic strata in outcrops along road cuts, mountain trails and in gorges as well as the saw-cut wall sections of the famous technical "marmor" quarries around the small village Adnet were studied for their depositional features, their facies distribution patterns, geometries of sediment bodies, syndepositional deformation and re-deposition structures as well as tectonic features. Detailed mapping and geometrical analysis of a spectacular outcrop (Mount Steinplatte – Rote Wand) provide new insight into the succession and dynamic of mass wasting events occurring on passive (Early Jurassic) Alpine margins. During several field trips and teaching courses of the University of Bremen the structural and sedimentary inventory of these two classical outcrops have been mapped and measured up in detail by student groups. Line drawings of the major geometrical relationships between different sedimentary units were compiled and their internal sedimentary structures were documented. Based on this data new insights considering the succession and interaction of various types of mass wasting and the evolution of events on the studied slopes were gained.

59.3 Results and Interpretation

59.3.1 Mass Wasting Phenomena on the Paleoslope of the Drowned Rhaetian Reef Complex at Adnet and Within the Surrounding Basins

59.3.1.1 Stratigraphy and Palaeographic Setting

The Osterhorn Mountains southeast of Salzburg are part of the Tirolic nappe. The area is characterised by remarkably slight tectonic deformation. The paleogeographic configuration during Liassic time shows a pronounced differentiation. A southern plateau transits northward into two basins (Glasenbach basin and Trattberg basin), which are separated by deep swells (Fig. 59.2). Excellent outcrops of Triassic and Jurassic strata exist here, in particular, in the famous quarries around the little village of Adnet.

In the foundation of the Liassic strata Rhaetian alternating marl-limestone beds were deposited in a shelf basin setting (Fig. 59.2 – Kössen Formation), which interfinger locally with massive limestone of reef mounds (e.g. Adnet Reef, Guggen Reef – Fig. 59.3). The end-Rhaetian paleorelief at the Adnet reef mound has been reconstructed by Böhm et al. (1999) by measuring inclination of slope beds and

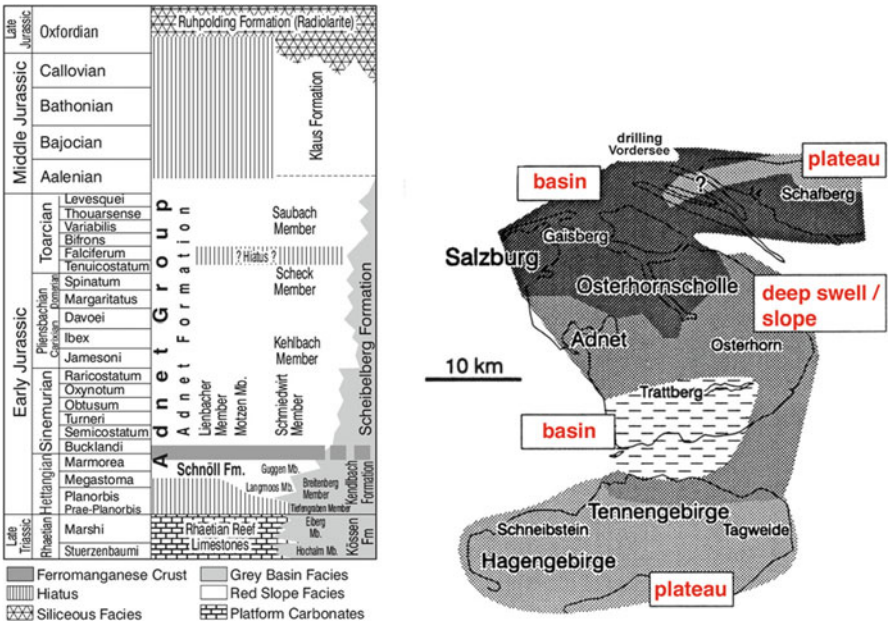

Fig. 59.2 Liassic paleogeography and stratigraphy around Adnet (Modified from Böhm et al. 1995, 1999)

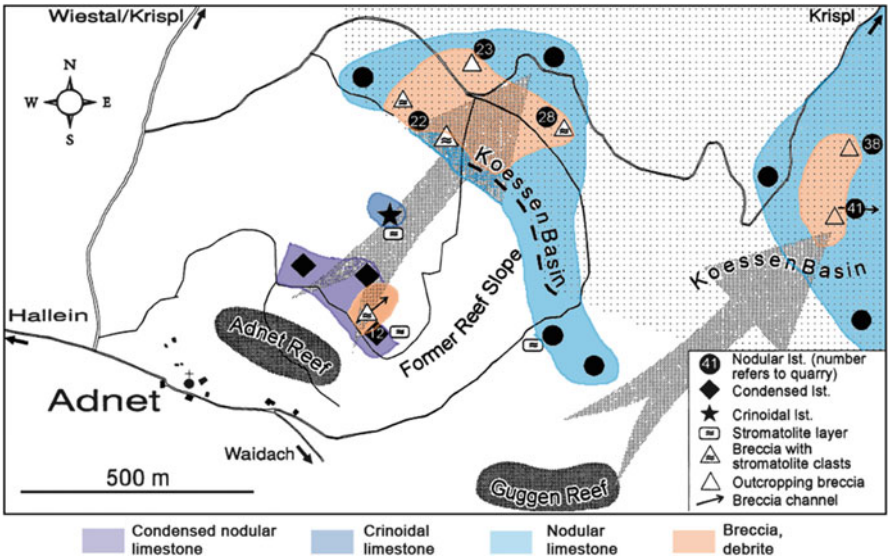

Fig. 59.3 Distribution pattern of Liasssic background facies and mass wasting deposits on the paleoslopes of drowned Rhätian reefs and within the surrounding basins around Adnet (Modified from Böhm et al.1995). *Large arrows* indicating presumed transport directions. *Numbers* refer to the position of quarries (12 = Lienbach quarry, 22 = Scheck quarry, 23 = Wimbach respectively Plattenbruch quarry, 28 = Schnöll quarry)

geopetal sediment infillings in cavities. The mound displays a horizontal sea floor forming a flat top plateau and a north to northeast dipping slope inclined by about 10°–15°. Total elevation of the mound was 50–80 m above the gently inclined sea floor. During end-Triassic reef drowning the deeply submerged, inherited relief gave rise to pronounced Liassic facies differentiation.

Grey spiculitic cherty limestone and marl beds were deposited in the former shelf basin areas (Scheibelberg, Formation Fig. 59.2), whereas red nodular limestones, and red condensed limestones rich in ammonites and often intercalated with Fe-Mn crusts as well as crinoidal limestones covered the slope and top areas of the former reef mound (Adnet Formation, Fig. 59.2). Various sub-members of the Adnet Formation are distinguished displaying distinct shifts in facies.

59.3.1.2 Facies Patterns of the Liassic Background Sediments

Different subfacies types of Liassic sediments cover the Rhaetian reef at Adnet depending on their paleoslope position on the drowned reef mound. Details are already presented and discussed (Böhm 1992; Böhm et al. 1995, 1999) and are beyond the scope of this study. Following we will present a general overview of facies occurrences, and discuss aspects relevant for their potential for sediment mobilisation and mass wasting. Over the top and the uppermost slope decimetre-sized bedded,

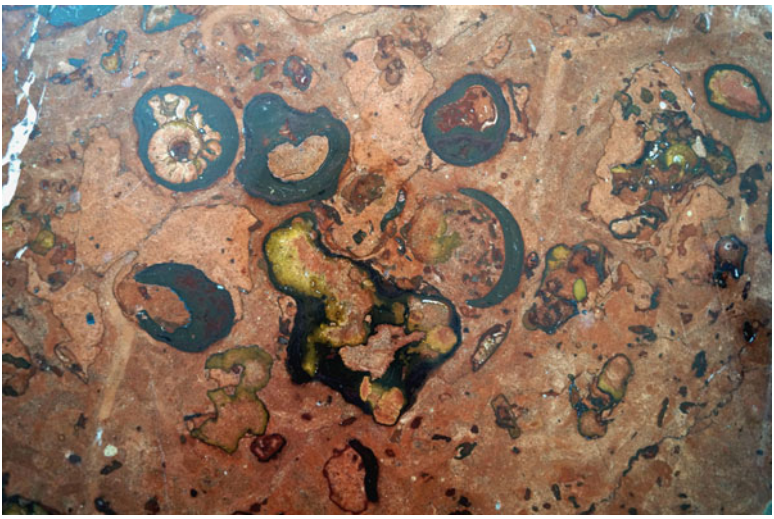

Fig. 59.4 A firm ground consisting of strongly bioturbated sandy mud with a broad spectrum of well-developed distinct burrow tubes is covered by a hard ground bearing abundant ammonites that are covered and embedded into a ferromanganese crust (polished section of a block from Schnöll quarry = No.28 in Fig. 59.3)

marl-poor blotchy red micritic limestones with layers bearing abundant centimetre- to millimetre-sized intraclasts with ferromanganese coatings directly cover the Rhaetian stata (Adnet Formation: Lienbach Member, Fig. 59.2). In the basal parts condensed sections with Fe-Mn crusts occur. Some horizons are particularly rich in ammonites (Fig. 59.4), which are often covered by, or respectively are embedded into Fe-Mn custs. The textural and sedimentary inventory of these layers clearly depicts temporal changes in sea floor properties documenting a clear trend towards increased sediment consolidation and sea floor cementation. Starting firm with grounds represented by semi-consolidated fine to medium grained strongly bioturbated sandy mud bearing a broad spectrum of well-developed distinct burrow tubes sea floor properties changed towards hard grounds in the condensed layers that are characterised by thick ferromanganese crusts (Fig. 59.4). The succession of environments documents a significant increase in bottom currents promoting erosion and resuspension and sea floor cementation. In middle to lower slope positions the typical Adnet Limestone "sensu strictu" represented by reddish medium to thin nodular-bedded intraclastic wacke/packstones with ostracods, foraminifers, sponge spicules and crinoidal debris (Adnet Formation: Schmiedwirt Member Fig. 59.2) was deposited.

Higher up in the section, in younger parts of the Adnet Formation, this subfacies type is much more widespread covering almost all parts of the original paleoslope and its transition into the adjacent basins. This occurrence pattern documents a general deepening of the entire area in the Upper Liassic period. A peculiar feature of the nodular Adnet Limestone is its layer-wise differential stage of consolidation

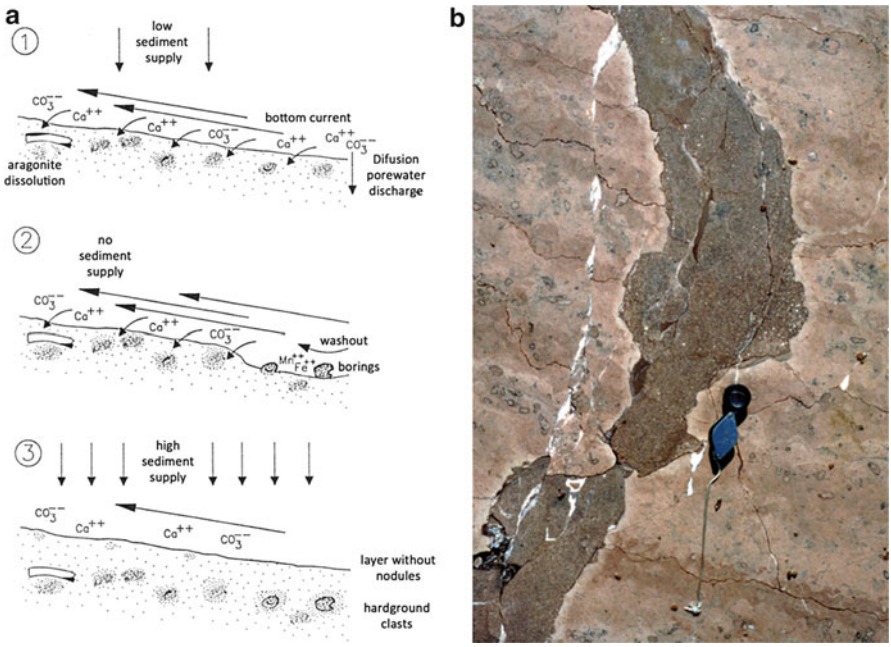

Fig. 59.5 (**a**) Schematic diagram illustrating the formation of red nodular Adnet limestone "sensu strictu"- see text for explanation (from Böhm). (**b**) Synsedimentary tectonic fissure (Neptunian dyke) dissecting bedded nodular Adnet limestone. Note ferromanganese coatings of micro-nodules, good fitting of both sides of the fissure and infilling of younger crinoidal rich muddy sediment (Photo from Lienbach quarry = No.12 in Fig. 59.3)

and cementation. Supply of the Ca^{2+} and $CO_3{}^2$ ions to maintain the growth of the cement concretions may be from seawater or by dissolution of carbonate minerals, in particular aragonite, within the sediment induced by microbial activity. Fine-grained muddy arenite layers enriched with micro-nodules, i.e. early diagenetic cement concretions, alternate with soft muddy sediment layers (Fig. 59.5a). Modern analog pelagic carbonate muds with cement concretions were formed on the slope of the Bahama Bank (Mullins et al. 1980). The alternate nodule rich and nodule poor layers document rhythmic variations in bottom current speed displaying coincident shifts of phases characterised by sediment deposition and phases characterised by erosion inducing excavation and ferromanganese encrustation of early-cemented micro nodules (Fig. 59.5a).

59.3.1.3 Mass Wasting Deposits and Indications for Synsedimentary Tectonics in the Liassic Strata Deposited Over the Submerged Adnet Reef and Within the Surrounding Basins

Debrites and breccias are intercalated at various stratigraphic levels into the Liassic red nodular limestone of the Adnet Formation as well as into the grey spiculitic

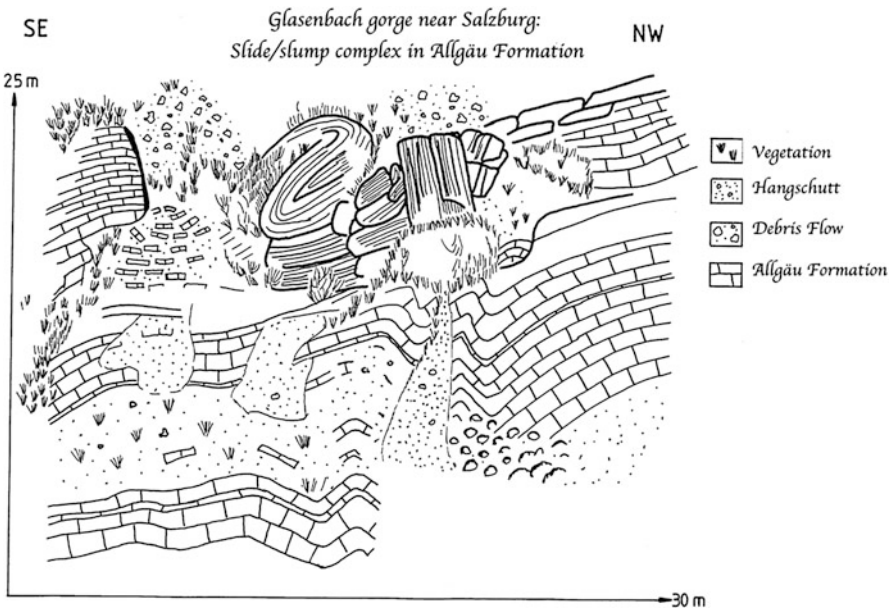

Fig. 59.6 Slide/slump/debrite complex intercalated into the Upper Scheiblberg (Allgäu) Formation (Glasenbach gorge south of Salzburg)

limestones of the Scheiblberg Formation; thicknesses varying from a few centimetres to a maximum of 40 m at Kehlbach (quarry No. 41 in Fig. 59.3). Typically the debrites consist of a mixture of variable sized clasts of the Liassic background sediments predominately red reworked deposits of the Adnet Formation embedded in a red muddy matrix. Occasionally grey clasts of the Scheiblberg Formation may be admixed. Depending on matrix content and stage of consolidation/cementation three basic types of breccias can be distinguished. Breccias with high proportions of slightly rounded clasts and intermediate matrix contents have been classified as nodular breccias. Debrites with high mud contents and a predominance of millimetre- to centimetre-sized, rounded to sub-rounded clasts are termed pebbly mudstones (Bernoulli and Jenkyns 1970).

Later on only locally slide – olistholithic debrite complexes occurred, which may be included into the upper part of the Scheiblberg Formation (Fig. 59.6). The textural and structural features of such complex mass wasting packages indicate release of a thicker pile of sediments with different stages of consolidation and cementation in various parts. The lower slide portion obviously was almost completely lithified, whereas the upper slumped part was semi-consolidated. Finally the package was sealed by a debrite.

For the Scheck breccia excellent outcrops in different quarries around Adnet exist. In proximal parts, like in the Scheck quarry which is situated on the upper slope of the former Adnet reef mound, the Scheck breccia consists of a chaotic

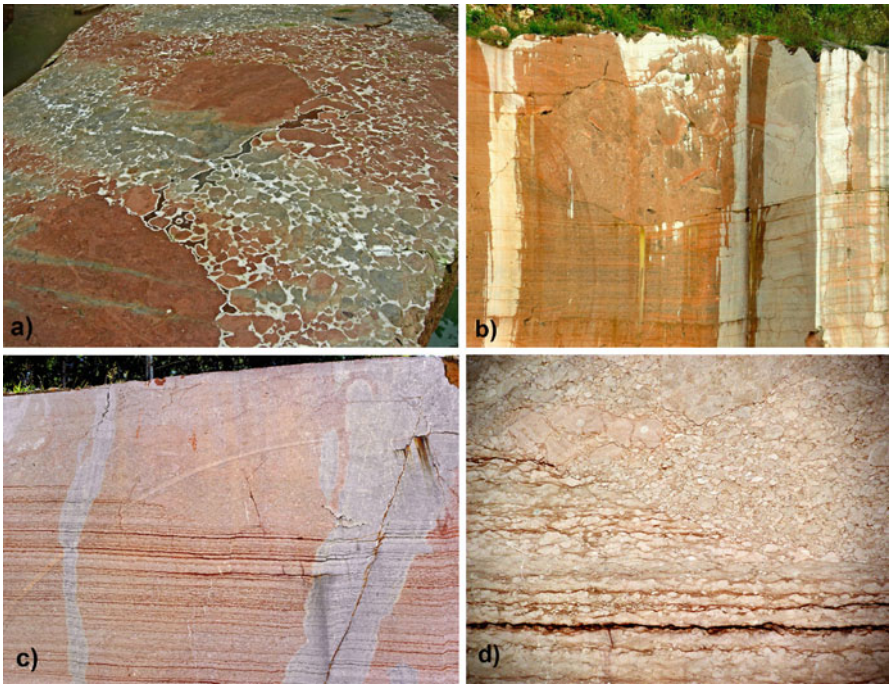

Fig. 59.7 (**a**) Cemented type of the Scheck breccia with huge blocks of nodular limestone (Scheck quarry = No.22 in Fig. 59.3), (**b**) Scheck breccia bearing huge blocks of nodular limestone and a chaotic clast fabric displaying a very nice channel structure that erosively undercuts deeply into nodular limestone beds of the Adnet formation (Lienbach quarry = No. 12 in Fig. 59.3), (**c**) Scheck breccia on the middle to lower slope erosively overlie nodular limestones of the Adnet formation (Plattenbruch quarry = No.23 in Fig. 59.3), (**d**) detail showing the erosive contact to the underlying nodular Adnet limestone

fabric of angular as well as rounded to sub-rounded clasts with extremely low mud contents (Fig. 59.7a). Metre-sized blocks of nodular limestone are included into the chaotic clast fabric. Pore spaces between the clasts are filled with two generations of white submarine cements. Also in an upper slope position, in the upper middle wall of Lienbach quarry, a more matrix rich variety of the Scheck breccia with huge blocks of nodular limestone and a chaotic clast fabric display a very nice channel structure erosively undercutting deeply into the underlying nodular limestone beds of the Adnet formation (Fig. 59.7b). The main occurrences of the Scheck breccia on the middle to lower slope erosively overlie nodular limestones of the Adnet formation (Plattenbruch quarry – Fig. 59.7c, d). Mud content is low and clasts are densely packed. Composition of the breccia clearly evidences, that the clasts were mainly derived by disintegration of the underlying eroded nodular limestone beds. Metre sized olistholithic blocks of nodular limestone may be included into the breccia. During downslope movement chaotic fabrics as well as packages showing alignment of clast along the flow pathway were developed (Fig. 59.7d).

59.3.2 The Liassic Slide/Slump/ Debrite Complex at the Foot of the Paleoslope of the Drowned Rhaetian Carbonate Ramp at Mount Steinplatte Near Waidring (Tirol)

At the mount Steinplatte near Lofer excellent outcrops, studied by numerous investigators during the past three decades (see latest review in Stanton and Flügel 1989) display sedimentary regimes on the paleo-slope of a Rhaetian reef complex to the adjacent Kössen shelf basin. Surprisingly less studied in this area is a spectacular masswasting complex exposed at Rote Wand at the northern slope of Plattenkogel. This unit developed after drowning of the Rhaetian platform during transgression in Early Jurassic time and displays a huge slide/slump/debrite complex. Ebli (1997) recognized that this 18–25 m thick mass wasting unit consisted of debrites and slide/slump blocks of Toarcian red nodular limestones. As a result of detailed measurements and mapping of this fantastic outcrop we clearly are able to distinguish at least three different structural units. The first unit starts with a huge slide block at the base transiting above into a slump/pebbly mudstone complex (Fig. 59.8b). Well-developed almost intact thick bedding is recognized in the basal slide block (Fig. 59.9a). The slide block erosively plugs into the underlying well-bedded nodular limestones of the Adnet Formation (Fig. 59.9b). In the overriding slump complex well-developed isoclinal slump folds (Fig. 59.9c) and nice examples for disintegration of slumps into pebbly mudstone flows are seen (Fig. 59.9d). This slide/slump complex above is sealed by three debrites at the top, each of them cutting with irregular erosion surfaces into the underlying flows (Figs. 59.8a and 59.9e). No background sediments are found between the debrites indicating that these flows were released within a short time.

The succession of structural units in the studied slide/slump/debrite complex at Mount Steinplatte provides clear evidence for destabilisation of a thick sediment package comprising lithified deposits at the base, overlain by semi-consolidated sediments in the middle portion, and soft to initially consolidated/cemented deposits at the top. During downslope displacement and movement of the entire pile, the basal lithified sediments disintegrated into almost intact slide blocks that plugged into the underlying bedded nodular strata.

In turn the slide was immediately overrun by semi-consolidated slumped deposits, which were derived from the middle portion of the dislocated sediment package. Slumps partly disintegrated into pebbly mudstones during the downslope movement of the mass.

59.3.2.1 Interpretation and Discussion

We assume that the emplacement of the slide/slump complex occurred as one single event. Eventually deposition of the first debrite can also be related to this phase. The following two debrites were released within a short time interval afterwards as evidenced by lack of background sediments between the debrite units. The observed

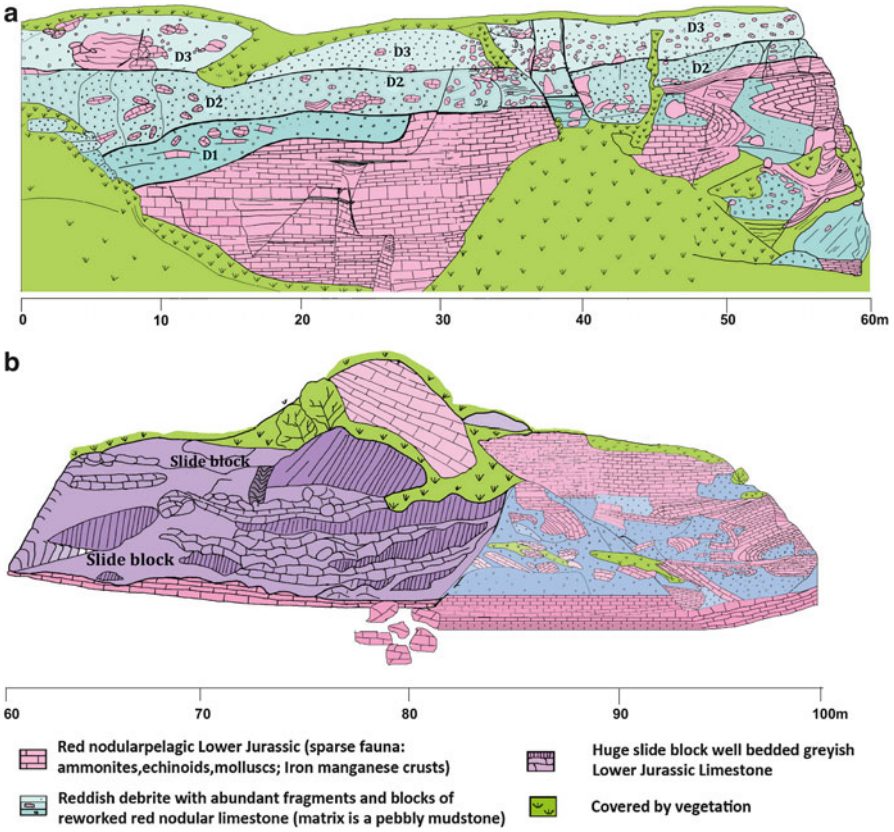

Fig. 59.8 Line drawing of detailed mapping of structural details of the Rote Wand Slide/Slump/Debrite complex plugging erosive into the underlying flat-bedded Adnet Formation (See text for further explanation)

features clearly call for an external trigger to release downslope movements of such a huge voluminous mass. In our view block faulting and tilting associated with rifting at the passive Early Jurassic Alpine margin, which was located between the opening Penninic Ocean to the northwest and the closing Meliata Ocean to the southeast, would be the best trigger. This assumption is in line with previous studies from various parts of the Northern Calcareous Alps (Eberli 1988; Lackschewitz et al. 1991; Böhm et al 1995; Ebli 1997). However, mega-slides and breccias also occur in Middle to Upper Jurassic post rift sediments (Rofan breccias – Wächter 1987, Schwarzenbergklamm breccia/Unken Syncline – Ortner et al. 2008, Strubberg Formation/Berchtesgaden – Gawlick et al. 1999; Missoni and Gawlick 2011). During this period tectonic settings changed in the Northern Calcareous Alps. The southern parts were affected by compression tectonics induced by progressive closure of the Meliata Ocean, whereas extensional tectonics including strike-slip faulting may have prevailed in the northern part. However, when and where these

Fig. 59.9 Structural features of the Steinplatte slide/slump/ debrite complex – (**a**) Well-developed almost intact thick bedding is recognized in the basal slide block, (**b**) Basal slide block erosive plugs into the underlying well-bedded nodular limestones, (**c**) Well developed isoclinal slump folds, (**d**) Nice examples for disintegration of slumps into pebbly mudstone flows, (**e**) Debrites D_1 and D_2 with irregular erosion surfaces at the base, (**f**) Detail showing debrite D_1 channel deeply eroding the underlying bedded nodular limestones of the Adnet Formation

shifts in plate tectonic regimes exactly occurred still is controversially debated. Hence also controversial models for the formation and trigger of these Upper to Late Jurassic breccias and slides are presented, including: (1) Activity at strike-slip faults and formation of pull-apart extensional basins (Frank and Schlager 2006;

Ortner et al. 2008), and (2) Nappe stacking and related compression with gravitative emplacement of Hallstatt melange in response to closure of the Meliata Ocean (Gawlick et al. 1999; Missoni and Gawlick 2011).

59.4 Conclusions

- Liassic strata of the Alpine Tethys include a broad spectrum of mass wasting deposits. Their spatial and temporal associations as well as their structural and textural features clearly proof that the state of consolidation and cementation of the dislocated sediments is essential for release, flow patterns and spreading mode of the different mass wasting deposits. Listed up according to increased cementation and consolidation the spectrum includes (1) matrix rich, far travelled **reddish pebbly mudstones** transiting upslope into (2) **red nodular debrites**, which may include increasing amounts of variable-sized blocks of initially consolidated red nodular limestones that were incorporated into the debris flows as rip-up clasts, and in further upslope position (3) **reddish, matrix-poor, semi-consolidated intraformational clast breccias with pore spaces between clasts being later filled by different generations of submarine cements, i.e. the so-called Adnet Scheck**. In outcrops the development and the lateral transition of types (2) and (3) into syn-sedimentary slumps and slides can often be observed.
- A spectacular Upper Liassic slide/slump/debrite complex at Rote Wand/Mount Steinplatte provides clear evidence for destabilisation of a thick sediment package. Development of this complex indicates that in a first phase downward gliding almost intact slide blocks plugged into the underlying bedded nodular strata. In turn the slide was immediately overrun by semi-consolidated slumped deposits, which partly disintegrated into pebbly mudstones. On top sealing by three debris flows is observed. Emplacement of the slide/slump complex occurred as one single event triggered by block faulting at the passive Early Jurassic Alpine margin. Eventually deposition of the first debrite was also related to this phase. The following two debrites were released within a short time interval afterwards as evidenced by lack of background sediments between the debrite units.

Acknowledgements Constructive comments by the editor Sebastian Krastel and reviewers Florian Böhm and Hugo Ortner are gratefully acknowledged. Many thanks go to Claudia Henrich for compiling the final versions of the line drawings.

References

Bernoulli D, Jenkyns HC (1970) A Jurassic basin: the Glasenbach Gorge, Salzburg, Austria. Verh Geol B-A 1970:504–531

Böhm F (1992) Mikrofazies und Ablagerungsmilieu des Lias und Dogger der Nordöstlichen Kalkalpen. Erlanger Geol Abh 121:52–217

Böhm F, Dommergues J-L, Meister C (1995) Breccias of the Adnet Formation: indicators of a Mid-Liassic tectonic event in the Northern Calcareous Alps (Salzburg/Austria). Geol Rdsch 84:272–286

Böhm F, Ebli O, Krystyn L, Lobitzer H, Rakus M, Siblik M (1999) Fauna, stratigraphy and deposition environment of the Hettangian-Sinemurian (Early Jurassic) of Adnet (Salzburg, Austria). Abh Geol B A 56:143–271

Eberli GP (1988) The evolution of the southern continental margin of the Jurassic Tethys Ocean as recorded in the Allgäu Formation of the Austroalpine Nappes of Graubünden (Switzerland). Eclogae Geol Helv 81:175–214

Ebli O (1997) Sedimentation und Biofazies an passiven Kontinentalrändern. Lias und Dogger des Mittelabschnitts der Nördlichen Kalkalpen und des frühen Atlantik (DSDP Site 547B, offshore Marokko). Münchner Geowiss Abh A 32:1–255

Frank W, Schlager W (2006) Jurassic strike-slip versus subduction in the Eastern Alps. Int J Earth Sci 95:431–450

Gawlick H-J, Frisch W, Vescei A, Steiger T, Böhm F (1999) The change from rifting to thrusting in the Northern Calcareous Alps as recorded in Jurassic sediments. Geol Rdsch 87:644–657

Krenmayr HG et al (2000) Rocky Austria – a brief earth history of Austria. Geological Survey of Austria, Vienna, pp 1–60

Lackschewitz KS, Grützmacher U, Henrich R (1991) Paleoceanography and rotational block faulting in Jurassic carbonate series of the Chiemgau Alps (Bavaria). Facies 24:1–24

Missoni S, Gawlick H-J (2011) Jurassic mountain building and Mesozoic-Cenozoic geodynamic evolution of the Northern Calcareous Alps as proven in the Berchtesgaden Alps (Germany). Facies 57:137–186

Mullins HT, Neumann AC, Willer JR, Boardman MR (1980) Nodular carbonate sediment of Bahamian slopes: possible precursors to nodular limestones. J Sediment Petrol 50:117–131

Ortner H, Ustaszewski M, Rittner M (2008) Late Jurassic tectonics and sedimentation: breccias in the Unken syncline, central Northern Calcareous Alps. Swiss J Geosci 101(Suppl 1):55–71

Stanton RJ, Flügel E (1989) Problems with reef models: the Late Triassic Steinplatte "Reef" (Northern Alps, Salzburg/Tyrol, Austria). Facies 20:1–138

Wächter J (1987) Jurassische Massflow – und Internbrekzien und ihr sedimentary-tektonisches Umfeld im mittleren Abschnitt der Nördlichen Kalkalpen. Bochumer geologische und geotechnische Arbeiten 27, 239 pp

Chapter 60
New Concepts on Mass Wasting Phenomena at Passive and Active Margins of the Alpine Tethys: Famous Classical Outcrops in the Berchtesgaden – Salzburg Alps Revisited. Part B: Stacking Patterns of Slide/Debrite Complexes in an Active Lower Cretaceous Foreland Wedge-Top Basin

Rüdiger Henrich, Karl-Heinz Baumann, and Torsten Bickert

Abstract Along the Rossfeld mountain road near Berchtesgaden a classical outcrop of Lower Cretaceous mass wasting is located. The debrites contain completely lithified boulders and blocks of highly variable dimensions of the stratigraphic pile of rock units included in the two overthrusted nappes as well as multiple reworked slide blocks and clasts of semiconsolidated siliciclastic turbidite beds. Alternations of these siliclastic turbidite beds and autochthonous marls form the background sediment, in which the debrites are intercalated. Our new results show that most of turbidite/marl successions are not autochthonous, but forms slide units, which were sheared and overthrusted at their base during gliding from the flanks into the central parts of the trench.

Keywords Passive and active Alpine margins • Slides • Slumps • Debrites • Synsedimentary tectonics

60.1 Introduction

60.1.1 Study Area and Previous Studies

The Berchtesgaden–Salzburg Alps bear spectacular outcrops of Triassic to Cretaceous strata of the Alpine Tethys that are embedded in a fascinating alpine scenario. In addition, here in the Tirolic nappe, wide areas are less affected by later

R. Henrich (✉) • K.-H. Baumann • T. Bickert
MARUM and Faculty of Geosciences, University of Bremen, Bremen, Germany
e-mail: henrich@uni-bremen.de

S. Krastel et al. (eds.), *Submarine Mass Movements and Their Consequences*, Advances in Natural and Technological Hazards Research 37, DOI 10.1007/978-3-319-00972-8_60,

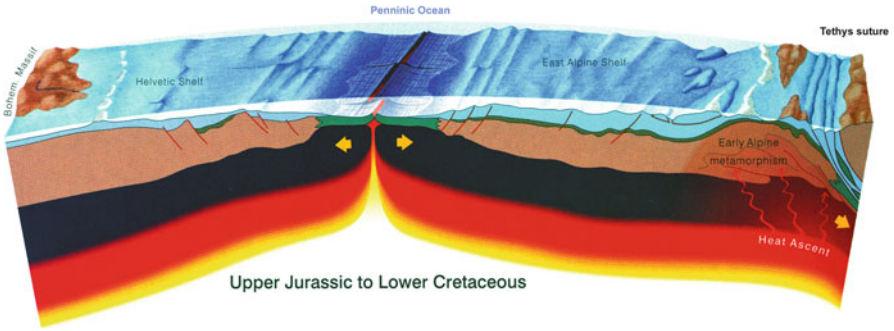

Fig. 60.1 Plate tectonic configuration of the Alpine Tethys during uppermost Jurassic and Lower Cretaceous time (Modified from Rocky Austria 2000)

tectonic overprinting providing the unique chance to study original paleogeographic settings as well as the geometries and evolutionary patterns of facies distribution. During uppermost Jurassic to lower Cretaceous time tectonic regimes in the Alpine Tethys changed towards compressional settings. At the southern margin of the Tethys compression and nappe tectonics occurred at so-called the Tethys suture (Fig. 60.1).

Along the Roßfeld mountain road near Berchtesgaden a classical mass-wasting outcrop is located. Previous investigators (Faupl and Tollmann 1979; Decker et al. 1987) have already highlighted the basic phenomenology, which is a complex interaction of debrites and syndepositional turbidite beds in a trench induced by the Lower Cretaceous Alpine tectonics. The lithostratigraphy of the Roßfeld Formation (see Fig. 60.2) comprises a basal marl unit, in which thin sandstone beds (sandy turbidites) are intercalated. Higher up in the section a few metre thick unit of thin bedded sandstones and an approximately 60 m thick package of thick-bedded sandstones (siliciclastic turbidites) occur. The top unit is formed by an around 30 m thick alternations of mass flow deposits (debrites) and siliciclastic turbidites.

The heavy mineral spectra of the siliciclastic turbidites are characterized by the occurrence of chromium spinell, green amphiboles and interestingly reddishbrown amphiboles, which may indicate alkaline rocks in the source area (Faupl and Tollmann 1979). Subsequent analysis by Faupl and Pober 1991 and Faupl and Wagreich 2000 confirmed the evidence that siliclastic, volcanic, and ophiolithic components were derived from eroding rocks of the ob-ducted Alpine Tethys suture (compare Fig. 60.1 for position of the Tethys suture). These authors introduced a conceptional model assuming interactions of debris flows derived from the submarine nappe pile with syndepositional turbidite beds in a trench-like structure in the middle region of the Northern Calcareous Alps induced by the Lower Cretaceous Alpine tectonics at the Tethys suture. A more modern frame of the thrust sheets of the NCA was presented by Ortner (2003) and Ortner and Gaupp (2007) interpreting the deposits of the Roßfeld Formation as wedge–top basins in the foreland of the Tethys suture. Preliminary component analysis of the debrites in the Roßfeld Formation presented in recent study by Missoni and Gawlick (2011) provides evidence that all material

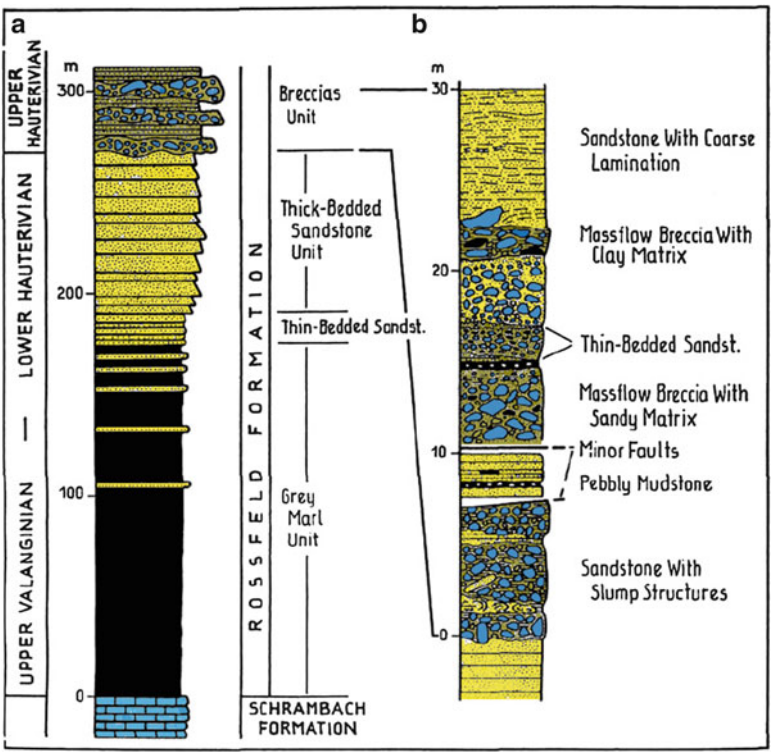

Fig. 60.2 Lithostratigraphy of the Roßfeld Formation at the type locality near Brechtesgaden (Modified from Decker et al. 1987)

was derived from erosion of a nearby upper Jurassic shallow water carbonate platform and basin strata in the foundation (Tauglboden-, Plassen- and Oberalm Formation), whereas older Triassic to Middle Jurassic lithologies were not found. Hence, Missoni and Gawlick (2011) propose an alternative model interpreting the sequence as "Roßfeld molasse" deposited in an under-filled foreland basin. So far the previous studies have not put sufficient emphasis on analysis of the entity of all structural details and the geometrical relationship of sediment bodies displayed in the outcrops. This aspect is in the central focus of the present study. It increases our knowledge considering the sediment dynamics and temporal evolution of these interesting mass wasting deposits.

60.1.2 Aims of This Study

Primary targets of this study are (1) to analyse the occurrences of different types of mass wasting deposits intercalated into Cretaceous strata exposed at the Roßfeld

road near Berchtesgaden, (2) to characterise and map their depositional features in detail, and (3) to critically evaluate the existing contrasting models and to develop new models on base of the observed changes in sediment dynamics and the temporal evolution of mass wasting phenomenon in the Roßfeld Formation.

60.2 Methods

Cretaceous strata exposed along the Roßfeld mountain road were studied for depositional features, facies distribution patterns, geometries of sediment-bodies, syndepositional deformation and re-deposition structures as well as tectonic features. During several field trips and teaching courses of the University of Bremen the structural and sedimentary inventory of this classical outcrop has been mapped and measured up in detail by student groups. Line drawings of the major geometrical relationships between different sedimentary units were compiled and their internal sedimentary structures were documented.

60.3 Results

Based on our detailed mapping and compilation of line drawings we were able to develop new ideas about the succession and evolution of mass wasting events contained in this impressive outcrop. The debrites contain completely lithified boulders and blocks of highly variable dimensions (cm^3-sized to several m^3-sized) of the stratigraphic pile of rock units included in the two overthrusted nappes (i.e. predominantly Triassic and Jurassic limestones, marls and dolomites) as well as multiple reworked slide blocks and clasts of semi-consolidated syndepositional siliciclastic turbidite beds. The debrites alternate with sediment packages consisting of thin to well-bedded siliclastic and partly silicified turbidite beds and marls. The earlier models assume autochthonous deposition of the siliclastic turbidite beds and marls. However, our new results clearly proof that most of the turbidite/marl successions exposed along the Roßfeld road are not autochthonous, but form slide units, which were sheared and overthrusted at their base during downward gravitational sliding from the flanks into more central parts of a trench (Fig. 60.3).

At the base of each slide unit a chaotic debrite occurs, which comprises variable sized clasts of limestone's and dolomites as well as clasts of semi-consolidated syndepositional siliciclastic turbidite beds in a marly matrix. Altogether six of these debrite/slide units are observed. In general slide units are strongly sheared at their base (Figs. 60.3 and 60.4), whereas the upper part of the slide appears to be unaffected and almost intact. The sheared slices at the base have often been syndepositionally folded (Fig. 60.5) or overthrusted during emplacement and

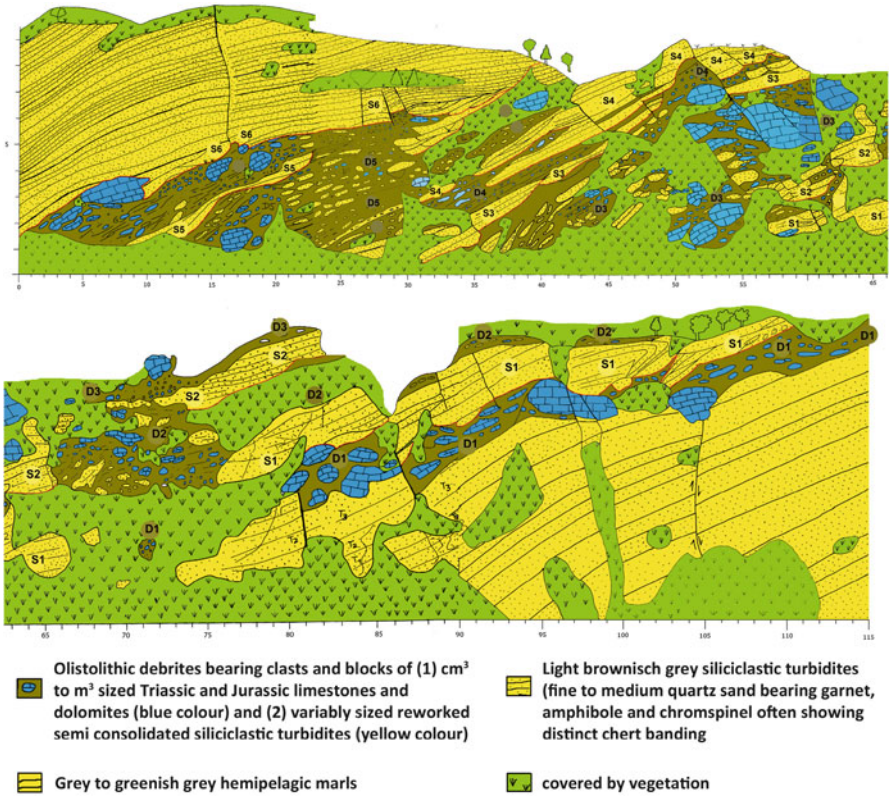

Fig. 60.3 Line drawing of detailed mapping of structural details of the Roßfeld road slide/debrite complex intercalated into the Lower Cretaceous Roßfeld Formation (See text for further explanation)

stacked on top of each other (Figs. 60.3 and 60.4). Due subsequent tectonics the slide/debrite complex was affected slightly by younger faults dissecting the slide debrite packages (Fig. 60.3).

60.3.1 Interpretation

Taken all observations into consideration we propose the following depositional model for the studied complex. Debris flows induced by syndepositional tectonic pulses at the northward propagading lower Cretaceous nappe pile moved downslope into the foreland trench. In turn collapse of the side-wall of the trench occurred. This triggered sliding of stacks of previously deposited semi-consolidated siliciclastic turbidite beds. The slides overrun, respectively travelled downslope on top of the debris flows. Basal parts of the slides were affected by slumping and

Fig. 60.4 Stack of sheared slices of packages of siliciclastic turbidite beds at the base of Slide 5 displaying syndepositional folding and stretching

Fig. 60.5 Syndepositional folding of siliciclastic turbidite beds at the base of Slide 1

shearing during downslope movement. Since six of these combined debrite/slide packages are stacked on top of each other without intercalation of any recognizable autochthonous sediments (i.e. grey pelagic marls respectively autochthonous deposited turbidites) in between. Hence, we assume that the entire mass wasting complex was deposited within short time, possibly triggered by a succession of retrogressive collapse events released from progressively higher parts of the trench flanks.

60.4 Critical Evaluation of Depositional Models, Triggers and Tectonic Settings Proposed for the Mass Wasting Complexes in the Roßfeld Formation

The original cartoon illustrating the depositional model for the Roßfeld Formation (Fig. 60.6) clearly depicts the transition from pelagic sedimentation (Schrambach Formation) to deposition of siliclastic turbidites, which intercalate with thick debrites of variable composition in the uppermost section (Roßfeld Formation, – Faupl and Tollmann 1979). Beside debris flows no other mass wasting deposits were recognized.

A critical evaluation of this model and the different new depositional models as well as their assumed plate tectonic settings implies first to summarize the main aspects and observations derived from outcrop analysis: (1) The Roßfeld Formation is characterized by increasing amount of terrigenous siliciclastic material displaying a clear coarsening upward trend of grain size spectra. In addition, with respect to provenance the siliciclastic turbidites in the Roßfeld Formation are derived from a source located at southeastern margin including different lithologies of the northwestward propagating initial Alpine pile and material from the overthrusted and abducted suture of the Vardar-/Meliata ocean. (2) The debrites intercalated into the Roßfeld Formation consist of a mixture of limestone/marl clasts and rip-up clasts of the siliciclastic turbidite beds. (3) A stack of slides consisting of siliclastic turbidite/ marl alternations bearing characteristic shear structures and slumps of semiconsolidated turbidite beds at the base is typical for the Upper Roßfeld Formation.

All these aspects would be fit with the model proposed by Ortner and Gaupp (2007) claiming wedge–top basins in the foreland of the Tethys suture. The "Roßfeld molasse" model proposed by Missoni an Gawlick (2011) explains the Roßfeld Formation by erosion of an uplifted local Plassen Carbonate Platform separating the Roßfeld basin to the north from a southern molasse basin situated close to the Vardar suture. This model is supported by preliminary component analysis of clasts of the debrites, but lacks to explain the observed large-scale tectonic structures, and how and were the siliciclastic turbidites bypassed the Plassen Carbonate platform swell. Further detailed studies of the mega-clasts incorporated into the debrites will shed

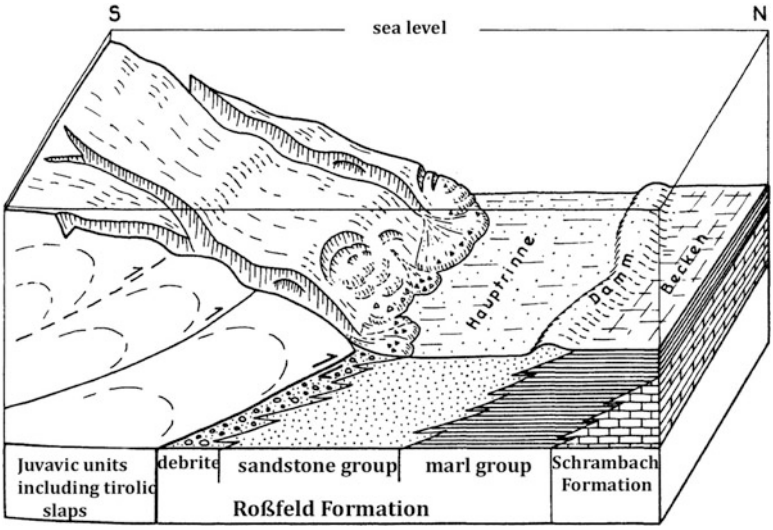

Fig. 60.6 Depositional model of the Roßfeld Formation (Modified from Faupl and Tollmann 1979)

new light on this problem. The crucial question is, was it really only local material or is also material from the Juvavic units included. Our new depositional model would perfectly fit into the tectonic frame of a wedge–top basin in the foreland of the northward prograding nappe pile at Tethys suture as suggested by Ortner and Gaupp (2007). However, at the present state of knowledge we cannot exclude the contrasting interpretation by Missoni and Gawlick (2011).

60.5 Conclusions

Based on detailed mapping of the road outcrops at the type locality of Lower Cretaceous Roßfeld Formation we provide a new conceptual model for the development of this classical mass-wasting complex. Olistholithic debris flows induced by syndepositional tectonic pulses in the accretion prism of the lower Cretaceous nappe pile moving down slope on the flanks of the trench initiated the collapse of the side walls of the trench and triggered sliding of stacks of previously deposited semiconsolidated siliciclastic turbidite beds. Since six of these combined debrite/slide events are stacked on top of each other without intercalation of any recognizable autochthonous sediments in between, this indicates that the entire mass wasting complex was deposited within short time, possibly triggered by a succession of retrogressive collapse events released from progressively higher parts of the trench flanks.

Acknowledgements Constructive comments by the editor Sebastian Krastel and reviewers Florian Böhm and Hugo Ortner are gratefully acknowledged. Many thanks go to Claudia Henrich for compiling the final versions of the line drawings.

References

Decker K, Faupl P, Müller A (1987) Synorogenic sedimentation on the Northern Calcareous Alps during the Early Cretaceous. In: Flügel HW, Faupl P (eds) Geodynamics of the Eastern Alps. Deuticke Verlag, Wien, pp 126–141

Faupl P, Pober E (1991) Zur Bedeutung detritischer Chromspinelle in den Ostalpen: Ophiolitischer Detritus aus der Vadarsutur. In: Lobitzer H, Csaszar G (eds) Jubiläumsschrift 20 Jahre Geologische Zusammenarbeit Österreich – Ungarn. Teil 1 Guidebook. Geologische Bundesanstalt, Wien, pp 133–143

Faupl P, Tollmann A (1979) Die Roßfeldschichten: Ein Beispiel für Sedimentation im Bereich einer tektonisch aktiven Tiefseerinne aus der kalkalpinen Unterkreide. Geologische Rundschau 68:93–120

Faupl P, Wagreich M (2000) Late Jurassic to Eocene paleogeography and geodynamic evolution of the Eastern Alps. Miteilungen Österreichische Geol Gesellschaft 92:79–94

Krenmayr HG et al (2000) Rocky Austria – a brief earth history of Austria. Geological Survey of Austria, Vienna, pp 1–60

Missoni S, Gawlick H-J (2011) Jurassic mountain building and Mesozoic-Cenozoic geodynamic evolution of the Northern Calcareous Alps as proven in the Berchtesgaden Alps (Germany). Facies 57:137–186

Ortner H (2003) Cretaceous thrusting in the western part of the Northern Calcareous Alps (Austria) – evidence from synorogenic sedimentation and structural data. Mitteilungen der Österreichischen Geologischen Gesellschaft 94:63–77

Ortner H, Gaupp R (2007) Synorogenic sediments of the western Northern Calcareous Alps. Geol Alp 4:133–148

ERRATUM

Submarine Mass Movements and Their Consequences

Sebastian Krastel, Jan-Hinrich, Behrmann David Völker, Michael Stipp, Christian Berndt, Roger Urgeles, Jason Chaytor, Katrin Huhn, Michael Strasser, Carl Bonnevie Harbitz

S. Krastel et al. (eds.), *Submarine Mass Movements and Their Consequences*, Advances in Natural and Technological Hazards Research 37, DOI 10.1007/978-3-319-00972-8,

DOI 10.1007/978-3-319-00972-8_61

Chapter 24
Recurrent Superficial Sediment Failure and Deep Gravitational Deformation in a Pleistocene Slope Marine Succession: The Poseidonia Slide (Salerno Bay, Tyrrhenian Sea)

Francesca Budillon, Massimo Cesarano, Alessandro Conforti, Gerardo Pappone, Gabriella Di Martino, and Nicola Pelosi

On page 273, Chapter 24, the correct address of *F. Budillon, G. Di Martino, N. Pelosi* should read: "IAMC, National Research Council of Italy, **Calata Porta di Massa, 80, 80133 Napoli, Italy**".

On page 280, Chapter 24 in the section 24.3.3 the value mentioned should be: "22–24 ky BP" instead of "24–24 ky BP".

The publisher apologizes for the inconvenience caused.

The online version of the original book can be found at
http://dx.doi.org/10.1007/978-3-319-00972-8

ERRATUM

Chapter 46
Modeling of Potential Landslide Tsunami Hazards Off Western Thailand (Andaman Sea)

Julia Schwab, Sebastian Krastel, Mohammad Heidarzadeh, and Sascha Brune

Abstract We model several scenarios of potential submarine landslide tsunamis in the Andaman Sea off the Thai west coast. Our results suggest that landslides may be capable of producing significant tsunamis. Two categories of submarine landslide scenarios were evaluated. Geometry parameters of the first category are taken from identified mass transport deposits (MTDs); the second category considers a potentially unstable block identified in seismic data. Our preliminary modeling approach shows, that run-up values may reach significant tsunami heights for some scenarios. We point out that our results have to be regarded as only preliminary due to several limitations in our modeling approach. Our results, however, show the need for more sophisticated modeling of landslide tsunamis, especially regarding the failure process and inundation on dry land.

Unfortunately this chapter was published without authors' corrections. The revised version is published as Erratum.

J. Schwab (✉)
Helmholtz Centre for Ocean Research, GEOMAR, Kiel, Germany
e-mail: jschwab@geomar.de

S. Krastel
Institute of Geosciences, Christian-Albrechts-Universität zu Kiel, Kiel, Germany

M. Heidarzadeh
Cluster of Excellence "The Future Ocean", Institute of Geosciences, Christian-Albrechts Universität zu Kiel, Kiel, Germany

S. Brune
GFZ German Research Centre for Geosciences, Potsdam, Germany

46.1 Introduction

Due to its vicinity to the highly seismic Sunda Trench, the Thai west coast is vulnerable to tectonic tsunamis (e.g. Jankaew et al. 2008). Earthquakes, however, are not the only source of tsunami waves. Seismically triggered submarine slope failures are also known for producing large wave heights in the near field (Synolakis et al. 2002). However, tsunami warning is problematic, as landslides may initiate within minutes or hours of an earthquake (e.g. Fritz et al. 2012), and a seismic signal may not even be detectable prior to a landslide.

Schwab et al. (2012) identified several MTDs and indicators for potential future failures at the western edge of Mergui Ridge, which forms a part of the outer Thai shelf. By minimum volume estimations and submergence depth of identified deposits, they concluded that only a few slope failures may have been tsunamigenic, resulting in a low estimate for landslide tsunami hazards. In order to obtain a more detailed picture of the tsunamigenic potential that may arise from these slope failures, this study aims to quantitatively understand the landslide tsunami hazards off western Thailand by numerical modeling.

46.2 Geological Background

Schwab et al. (2012) examined 2D reflection seismic profiles across the Mergui Ridge-East Andaman Basin transition (Fig. 46.1a), and high resolution bathymetric data from the top of Mergui Ridge. They identified several stacked MTDs west of Mergui Ridge (Figs. 46.1b and 46.2a) indicating recurrent slope failures. Based on the thickness of undisturbed sediment packages between individual MTDs, long time intervals (hundreds of kyrs) were estimated between succeeding events. Possible causes for slope failures include ongoing tectonic activity, occurrence of potentially unstable drift deposits and the presence of fluids and resulting overpressure. Additionally, indicators for potential future failures were identified (Fig. 46.2b) at the faulted western edge of Mergui Ridge (Schwab et al. 2012).

46.3 Modeling and Dataset

Based on geometrical parameters derived from seismic and bathymetric dataset (Figs. 46.1b and 46.2), different hypothetical scenarios of landslide tsunami generation were modeled. The dimensions of the modeled slides are comparable to those described by Brune et al. (2010a, b) from neighboring areas. We follow the modeling approach of these authors, which takes into account that small landslides do not fulfill the applicability conditions for more realistic source models (see Brune et al. 2010b for a discussion of the approach). Therefore initial wave heights are calculated by a set of semi-empirical formulas (Watts et al. 2005; Grilli and Watts 2005). These formulas describe the sea surface response to a simplified coherent rotational slump failure. Compared to other more realistic landslide formulas

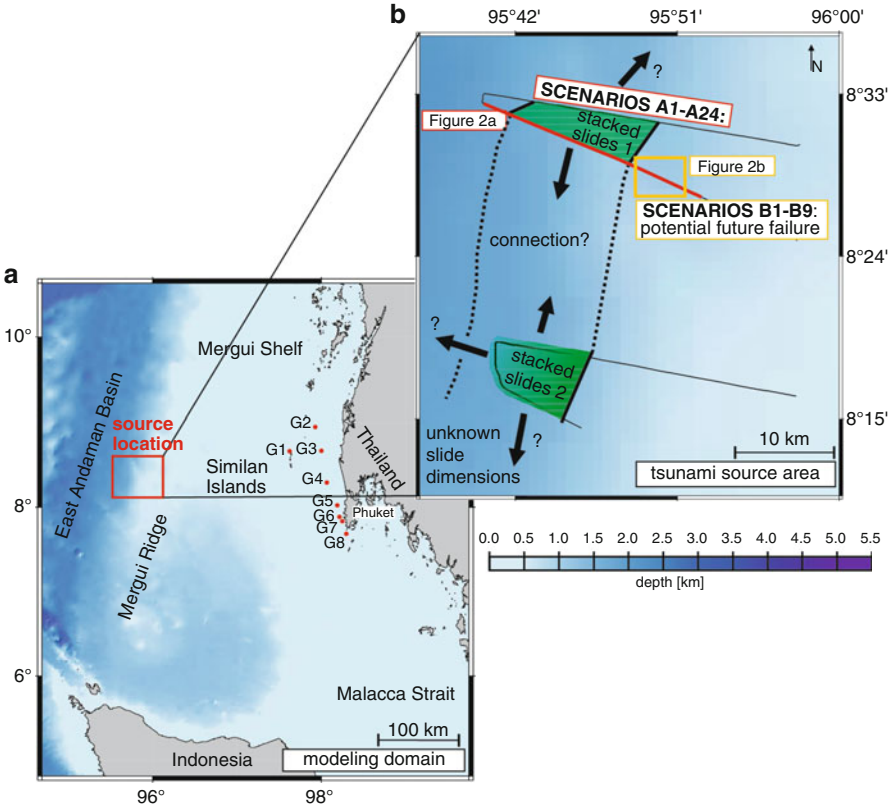

Fig. 46.1 (**a**) Bathymetric map of modeling domain and main structural features. G1–G8 indicate "artificial gauge stations" near the coast (20–50 m water depth) where maximum wave heights of tsunami are derived from. (**b**) Source location for chosen scenarios. *Green* areas indicate the locations where stacked slides have been identified in the basin on seismic profiles (*thin black lines*). *Black arrows* indicate the uncertainty in slide width

(e.g. Mohammed and Fritz 2012) they do not account for the deformation of the slide during the failure process. For calculating tsunami propagation, the TUNAMI-N2 numerical code (e.g. Goto et al. 1997) was applied, and an extension of this code (Brune et al. 2010b) was used to test stability conditions of input parameters and to calculate initial wave heights as described above. The simulations were performed for a total time of 25,200 s for all scenarios with a time step of 0.5 s using the GEBCO bathymetric grid (IOC et al. 2003) resolved to 32 arc sec.

Calculated maximum wave heights are regarded at eight artificial gauge stations G1–G8 (Fig. 46.1a, Table 46.1) placed offshore at water depths of about 20 m (G1) and about 50 m (G2–G8). Empirical formulas were applied to obtain a first estimate of potential run-up heights R1 (Ward and Asphaug 2003) and R2 (Ward and Day 2008) from the maximum offshore wave heights at G1–G8. R1 depends only on water depth and tsunami wave height at an offshore location, whereas for R2 also the slope angle between offshore location and shore line is included.

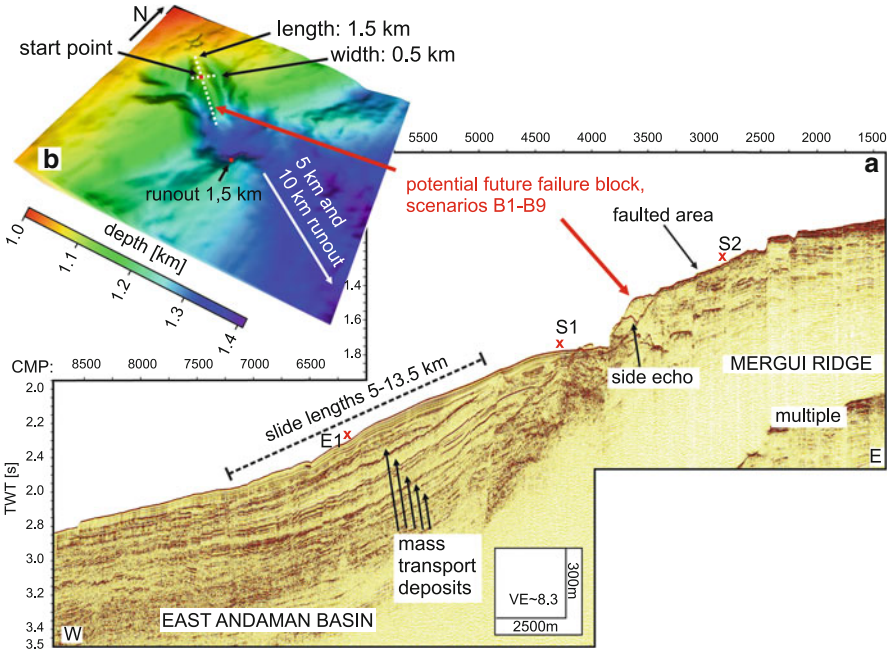

Fig. 46.2 (**a**) 2D reflection seismic profiles across the two source areas, "stacked slides location" and "potentially unstable block". *S1*: start point for slides of scenarios A1–A12, *S2*: start point for slides of scenarios A13–A24. *E1*: Endpoint for slides of scenarios A13–A24. (**b**) Bathymetry of the "potentially unstable block" (scenarios B1–B9). *CMP* Common Midpoint (See Fig. 46.1b for locations)

Table 46.1 Artificial gauge stations

Gauge	G1	G2	G3	G4	G5	G6	G7	G8
Lat [°]	8.6636	8.8639	8.6405	8.2704	8.011	7.8888	7.8404	7.7609
Long [°]	97.6254	98.2577	98.2286	98.27	98.2853	98.2524	98.284	98.3228
Water depth [m]	24	49	50	49	51	48	46	48
Coastal location	Similan Islands	Bang Muang	Khue-kakk	Khok Kloe	Chueng Tao	Patong	Karon	Rawai

46.3.1 Modeled Scenarios

We chose two source locations based on information derived from seismic and bathymetric data (Fig. 46.1). Scenarios A1–A24 correspond to a location of previously-identified, stacked MTDs. Scenarios B1–B9 consider a potentially unstable block (Fig. 46.2, Schwab et al. 2012).

46.3.1.1 Scenarios A1–A24, "Stacked Slides Location"

The "stacked slides location" is situated west of the Mergui Ridge (Fig. 46.1b). Four parallel seismic reflection profiles show a similar pattern of five stacked MTDs (Fig. 46.2a). Geometrical properties of the modeled slides were varied according to the dimensions of identified slides with lengths between 5 and 13.5 km. Widths of 5, 7 and 30 km were chosen, the latter width value assuming that the two areas of stacked MTDs are connected, while the smaller values imply separate failure events. The slide thickness applied for these scenarios was 150 m, which is the maximum thickness measured for all detected MTDs. We use slope angles of 3° and 6°, corresponding to the range of slope angles in the source area. The origin of the MTDs is unknown, therefore we assume two different locations for slide initiation at the edge of the ridge in about 880 m water depth (run-out distance 15.5 km) and at the upper boundary of the basin in about 1,270 m water depth (run-out distance 7.5 km, Fig. 46.2a).

46.3.1.2 Scenarios B1–B9: "Potentially Unstable Block"

In scenarios B1–B9, we model the failure of a potentially unstable sedimentary block located at the edge of Mergui Ridge in about 1,100 m water depth (Fig. 46.2a) (Schwab et al. 2012). Its dimensions (Table 46.3) are derived from bathymetric data (Fig. 46.2b). Different run-out distances (1.5, 5 and 10 km) and slope angles (3°, 6° and 14.5) were used (Table 46.3).

46.4 Results

Initial positive wave heights (η_{plus}) for scenarios A1–A24 range between 1.5 and 118.1 m (Table 46.2). η_{plus} values larger than 40 m are reached for scenarios with long run-out distances and short slide lengths of 5 km (A13, A15, A17, A19, A21, A23). Arrival times of the first tsunami waves at the coast (32–37 min) are similar for all scenarios. A_{20max}, the maximum offshore wave height at G1, ranges between 1.3 and 22.8 m for the A-scenarios. Run-up estimations from A_{20max} range between 2.3 and 23.1 m (R1) and 8.0 and 25.8 m (R2), respectively.

For scenarios B1–B9, η_{plus} ranges between 1.7 and 28.2 m (Table 46.3). Arrival times are in the same range as for the A-scenarios (37–40 min). Compared to A1–A24, the A_{20max} values of B1–B9 are smaller (0.01–0.24 m). Run-up estimations are in the range of 0.04–0.61 m (R1) and 1.0–4.0 m (R1) respectively.

The maximum wave height distributions strongly depend on slide input parameters (Tables 46.2 and 46.3, Figs. 46.3 and 46.4). Despite its larger length, scenario A2 produces smaller wave heights compared to scenario A1 (Fig. 46.3a, b). Scenario

Table 46.2 Key modeling parameters for scenario A1–A24

Scenario	A1	A2	A3	A4	A5	A6	A7	A8	A9	A10	A11	A12
Runout [km]	7.5	7.5	7.5	7.5	7.5	7.5	7.5	7.5	7.5	7.5	7.5	7.5
SLA [°]	3	3	3	3	3	3	6	6	6	6	6	6
DIM [km × km]	5 × 5	5 × 13.5	7 × 5	7 × 13.5	30 × 5	30 × 13.5	5 × 5	5 × 13.5	7 × 5	7 × 13.5	30 × 5	30 × 13.5
Th [m]	150	150	150	150	150	150	150	150	150	150	150	150
Vol [km^3]	2.9	8.0	4.1	11.1	17.7	47.7	2.9	8.0	4.1	11.1	17.7	47.7
η_{plus} [m]	10.8	1.5	13.2	2.0	23.7	5.0	12.6	1.8	15.5	2.3	27.6	5.8
Ta [min]	36	37	36	36	33	32	36	36	36	36	33	32
A_{20max} [m]	2.3	1.3	3.0	1.8	7.7	5.6	2.6	1.5	3.5	2.1	8.7	6.6
R1 [m]	3.6	2.3	4.6	3.0	9.6	7.5	4.1	2.6	5.1	3.4	10.6	8.5
R2 [m]	10.0	8.0	11.3	9.1	16.5	14.5	10.6	8.5	11.9	9.7	17.4	15.5
Scenario	A13	A14	A15	A16	A17	A18	A19	A20	A21	A22	A23	A24
Runout [km]	15.5	15.5	15.5	15.5	15.5	15.5	15.5	15.5	15.5	15.5	15.5	15.5
SLA [°]	3	3	3	3	3	3	6	6	6	6	6	6
DIM [km × km]	5 × 5	5 × 13.5	7 × 5	7 × 13.5	30 × 5	30 × 13.5	5 × 5	5 × 13.5	7 × 5	7 × 13.5	30 × 5	30 × 13.5
Th [m]	150	150	150	150	150	150	150	150	150	150	150	150
Vol [km^3]	2.9	8.0	4.1	11.1	17.7	47.7	2.9	8.0	4.1	11.1	17.7	47.7
η_{plus} [m]	49.8	6.8	60.4	8.9	101.4	21.0	58.0	8.0	70.3	10.4	118.1	24.4
Ta[min]	36	37	36	36	33	32	36	37	36	36	32	31
A_{20max} [m]	7.3	5.2	9.2	7.1	15.9	20.3	8.2	6.1	10.2	8.3	16.5	22.8
R1 [m]	9.3	7.1	11.2	9.1	17.2	21.0	10.2	8.0	12.1	10.3	17.8	23.1
R2 [m]	16.2	14.1	17.8	16.0	22.2	24.6	17.0	15.0	18.6	17.1	22.6	25.8

SLA local slope angle, *Runout* run-out distance, *DIM* slide dimensions in width × length, *Th* thickness of slide, *Vol.* Volume of the slide, calculated as given in Grilli and Watts (2005), η_{plus} initial wave height, *Ta* arrival time, A_{20max} maximum wave height (surface elevation) at G1, *R1* run-up calculated for A_{20max} after Ward and Asphaug (2003), *R2* run-up calculated after Ward and Day (2008)

Table 46.3 Key modeling parameters for scenarios B1–B9

Scenario	B1	B2	B3	B4	B5	B6	B7	B8	B9
Runout[km]	1.5	5	10	1.5	5	10	1.5	5	10
SLA [°]	3	3	3	6	6	6	14.5	14.5	14.5
DIM [km × km]	0.5 × 1.5	0.5 × 1.5	0.5 × 1.5	0.5 × 1.5	0.5 × 1.5	0.5 × 1.5	0.5 × 1.5	0.5 × 1.5	0.5 × 1.5
Th [m]	125	125	125	125	125	125	125	125	125
Vol [km^3]	0.07	0.07	0.07	0.07	0.07	0.07	0.07	0.07	0.07
η_{plus}[m]	1.7	9.0	24.2	2.0	10.5	28.2	2.4	12.8	34.2
Ta[min]	40	37	37	40	37	37	37	39	40
A_{20max}[m]	0.01	0.06	0.17	0.01	0.070	0.20	0.01	0.09	0.24
R1[m]	0.04	0.20	0.47	0.04	0.23	0.53	0.05	0.27	0.61
R2[m]	1.0	2.3	3.5	1.0	2.4	3.7	1.1	2.7	4.0

SLA local slope angle, *Runout* run-out distance, *DIM* slide dimensions in width × length, *Th* thickness of slide, *Vol.* Volume of the slide, calculated after Grilli and Watts (2005), η_{plus} initial wave height, *Ta* arrival time, A_{20max} maximum wave height (surface elevation) at G1, *R1* run-up calculated for A_{20max} after Ward and Asphaug (2003), *R2*: run-up calculated after Ward and Day (2008)

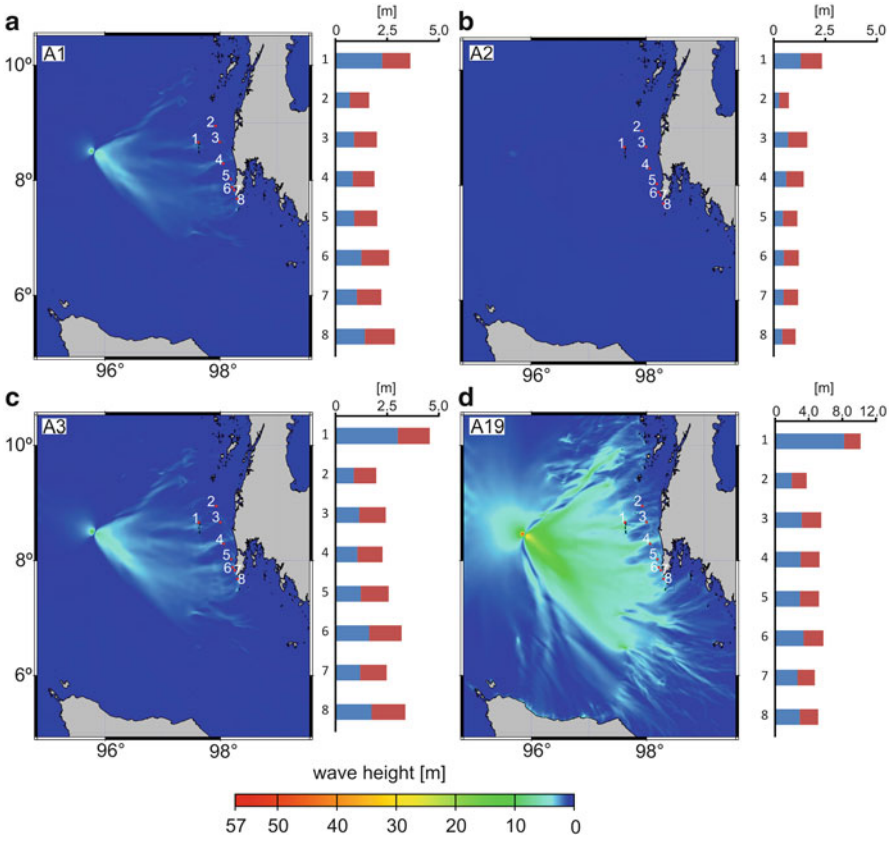

Fig. 46.3 Examples for wave height distributions from hypothetical failures at the "stacked slides location", as well as maximum wave heights (*blue bars*) and R1 run-up estimations (*red bars*) for artificial gauge stations G1–G8. Note the different scales for the wave height/run-up charts

A3 has a larger width compared to A1 and produces larger wave heights. Scenario A19 has the same slide dimensions as A1 but a larger run-out distance and larger slope angle (Fig. 46.3d, Table 46.2). This scenario also results in larger wave heights compared to A1.

Generally, largest maximum wave heights arise near the source area and in a triangular zone towards the coast. Regarding maximum wave heights at individual gauge locations, G1 records the largest run-up estimations (Fig. 46.3).

Figure 46.4 demonstrates the difference in wave heights for different run-out distances and slope angles of the B-scenarios (Table 46.3). Compared to the A-scenarios, the tsunami wave heights are smaller and not focused towards the coast, indicating reduced tsunami potential of the B-scenarios.

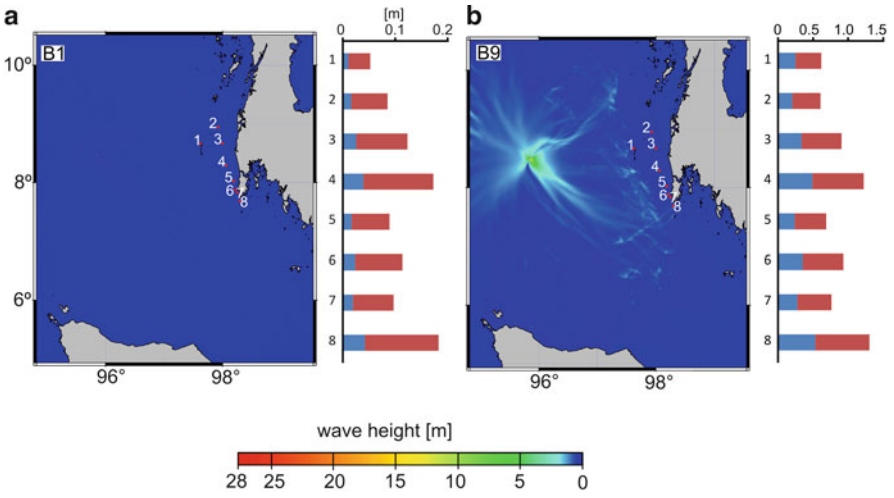

Fig. 46.4 Examples for wave height distributions from hypothetical failures at "potentially unstable block" location, as well as maximum wave heights (*blue bars*) and R1 run-up estimations (*red bars*) for artificial gauge stations G1–G8. Note the different scales for the wave height/run-up charts

46.5 Discussion and Conclusions

Our results give first insights into the tsunamigenic potential of slope failures off western Thailand. These results are only a preliminary assessment of landslide tsunami potential due to the limitations of the chosen approach:

1. The failure process that produced the MTDs in the working area is unknown. Therefore initial wave heights were calculated from failures, modeled as simplified coherent rotational slumps. More realistic failure scenarios such as translational and/or disintegrating slides or in the form of multiple events would produce smaller wave heights (Masson et al. 2006), but were not modeled in our preliminarily approach. Hence our modeled initial wave height is most likely overestimated.
2. In our numerical simulations, wave evolution beyond water depth of 20 m is prohibited, therefore run-up values were estimated by empirical equations using offshore wave heights at only a few isolated points (G1–G8), and inundation modeling was not performed at all. Empirical equations have limitations, the results vary for different equations (Tables 46.2 and 46.3), and near-shore wave phenomena reducing run-ups such as wave breaking are not considered by these empirical formulas.
3. Tsunami propagation was calculated from a coarse bathymetric grid and by shallow-water equations, which do not take into account effects such as dispersion. This may lead to inaccuracy of wave calculations.

4. The dimensions of the landslides in the A-scenarios are inferred from MTDs, as the pre-failure dimensions of the slides are not known. Thereby a thickness of 150 m was chosen for all scenarios, as thickness is the least determined value based on our seismic field data. This means that, as thickness is an important factor for wave generation, the calculation of initial wave height may contain inaccuracies.
5. The seismic images of the MTDs show clear signs of disintegration. This means that deformation occurred during the failure. According to Mohammed and Fritz (2012) deformation during the failure process leads to energy conversion and hence wave reduction. This again suggests that wave heights calculated in this study may be overestimated.

Landslide tsunamis are often described as a local phenomenon with large run-up heights limited to the near-field (Synolakis et al. 2002). Our results for the A-scenarios show such patterns (Fig. 46.3d), with a triangular zone of large maximum wave heights, presumably indicating a delimited area where tsunami hazard may occur at the coast. Some of the scenarios studied here show potential tsunami hazards comparable to the Papua New Guinea landslide tsunami of July 1998, where large run-up heights of more than 10 m were observed on a very limited coastline of about 20 km (Synolakis et al. 2002). A location especially exposed to a tsunami would then be around the gauge station G1, where the largest run-up heights were estimated.

Contrasting to the modeling results of A1–A24, the B-scenarios produce lower run-up height estimations, which are reasonable due to their smaller landslide volume and more realistic slide dimensions, and which are comparable to values described by Jintasaeranee et al. (2012).

Our results suggest that a landslide tsunami hazard for the coastal areas may exist, and wave heights and run-up estimations may increase with slope angle, run-out distance and slide volume. The width/length ratio of the slides is also affecting our preliminary results, as in most cases an increase in length leads to unexpected decrease in wave heights. This finding has to be examined in greater detail in the future.

Unlike tectonic tsunamis, landslide tsunami sources cannot not be located based on global networks and they may be located close to the shoreline (e.g. Fritz et al. 2012). Therefore landslide tsunamis are almost unpredictable making tsunami warning impossible. Short arrival times of around 30 min or less are typical for near-field tsunamis. The calculated arrival times of our model scenarios are close to this range, indicating that warning time for coastal areas would be short, adding to the unpredictability of landslide tsunamis.

Because of the previously mentioned limitations of our model approach, our results only represent worst case scenarios. This is especially true for the A-scenarios with largest volumes. Furthermore, recurrence rates for major tsunamigenic earthquakes in the area are estimated by 400 years (Monecke et al. 2008), whereas landslide recurrence is estimated to be in the range of 100 kyrs (Schwab et al. 2012). Hence, landslide tsunamis do not represent a major additional risk for the Thai coast.

However, they cannot be neglected and we recommend further geological surveys in the region to better locate sizes and distribution of submarine landslides, and sophisticated numerical modeling in order to reliably assess their hazard potential.

Acknowledgments The TUNAMI-N2 code is originally authored by Fumihiku Imamura and Nobou Shuto and copyrighted to Ahmet C. Yalciner, Fumihiku Imamura and Costas E. Synolakis. We acknowledge them for developing and making available the code. We thank the reviewers Hermann Fritz and Marc de Batist for their careful reviews and constructive comments that helped to improve the manuscript.

References

Brune S, Babeyko AY, Ladage S, Sobolev SV (2010a) Landslide tsunami hazard in the Indonesian Sunda Arc. Nat Hazards Earth Sys 10:589–604. doi:10.5194/nhess-10-589-2010

Brune S, Ladage S, Babeyko AY et al (2010b) Submarine landslides at the eastern Sunda margin: observations and tsunami impact assessment. Nat Hazards 54:547–562. doi:10.1007/s11069-009-9487-8

Fritz HM, Hillaire JV, Molière E, Wei E, Mohammed F (2012) Twin tsunamis triggered by the 12 January 2010 Haiti earthquake. Pure Appl Geophys. doi:10.1007/s00024-012-0479-3

Goto C, Ogawa Y, Shuto N, Imamura F (1997) IUGG/IOC TIME Project: Numerical method of tsunami simulation with the leap-frog scheme. In Intergovernmental Oceanographic Commission, manuals and guides no. 35, UNESCO

Grilli ST, Watts P (2005) Tsunami generation by submarine mass failure. Part I: modeling, experimental validation, and sensitivity analysis. Waterw Port C-ASCE 131(6):283–297

IOC, IHO, BODC (2003) Centenary edition of the GEBCO digital atlas, published on CD-ROM on behalf of the Intergovernmental Oceanographic Commission and the International Hydrographic Organization as part of the general bathymetric chart of the oceans. British oceanographic data centre, Liverpool

Jankaew K, Atwater BF, Sawai Y et al (2008) Medieval forewarning of the 2004 Indian Ocean tsunami in Thailand. Nature 455:1228–1231. doi:10.1038/nature07373

Jintasaeranee P, Weinrebe W, Klaucke I et al (2012) Morphology of the Andaman outer shelf and upper slope of the Thai exclusive economic zone. J Asian Earth Sci 46:78–85

Masson DG, Harbitz CB, Wynn RB et al (2006) Submarine landslides: processes, triggers and hazard prediction. Philos Trans R Soc A 364:2009–2039

Mohammed F, Fritz HM (2012) Physical modeling of tsunamis generated by three-dimensional deformable granular landslides. J Geophys Res 117(C11):C11015

Monecke K, Finger W, Klarer D et al (2008) A 1,000-year sediment record of tsunami recurrence in northern Sumatra. Nature 455:1232–1234. doi:10.1038/nature07374

Schwab JM, Krastel S, Grün M et al (2012) Submarine mass wasting and associated tsunami risk offshore western Thailand, Andaman Sea, Indian Ocean. Nat Hazards Earth Sys 12:609–2630. doi:10.5194/nhess-12-2609-2012

Synolakis CE, Bardet J-P, Borrero JC et al (2002) The slump origin of the 1998 Papua New Guinea tsunami. Proc R Soc Lond A 458:763–789

Ward SN, Asphaug E (2003) Asteroid impact tsunami of 2880 March 16. Geophys J Int 153:F6–F10. doi:10.1046/j.1365-246X.2003.01944.x

Ward SN, Day S (2008) Tsunami balls: a granular approach to tsunami runup and inundation. Commun Comput Phys 3(1):222–249

Watts P, Grilli ST, Tappin D, Fryer GJ (2005) Tsunami generation by submarine mass failure. Part II: predictive equations and case studies. Waterw Port C-ASCE 131(6):298–310